

SECOND SYMPOSIUM ON PROTECTION AGAINST RADIATIONS IN SPACE

FACILITY FORM 602

N65-34575

N65-34634

(ACCESSION NUMBER)

(THRU)

519

(PAGES)

1

(CODE)

(NASA CR OR TMX OR AD NUMBER)

(CATEGORY)

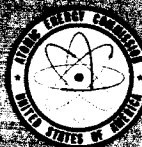
OCTOBER 1965

GPO PRICE \$ 3.25

CFSTI PRICE(S) \$ _____

Hard copy (HC) _____

Microfiche (MF) 2.50



SECOND SYMPOSIUM ON PROTECTION AGAINST RADIATIONS IN SPACE

GATLINBURG, TENNESSEE OCTOBER 12 - 14, 1964

SPONSORED BY:

National Aeronautics and Space Administration

U. S. Air Force

U. S. Atomic Energy Commission

EDITED BY:

ARTHUR REETZ, JR.

NASA Headquarters



Scientific and Technical Information Division

NATIONAL AERONAUTICS AND SPACE ADMINISTRATION

Washington, D.C.

1965

The Symposium Committee

FRED C. MAIENSCHN, *Chairman*
Oak Ridge National Laboratory

NATHANIEL F. BARR
U.S. Atomic Energy Commission

MYRON B. GILBERT
Air Force Cambridge Research Laboratories

GEORGE F. PEZDIRTZ
Langley Research Center, NASA

GEORGE F. PIEPER
Goddard Space Flight Center, NASA

ARTHUR REETZ, JR.
NASA Headquarters

IRVING J. RUSSELL
Air Force Weapons Laboratory

Foreword

All space vehicles will be exposed to natural charged particle radiation fields. The effects and possible problems imposed by such radiations are of great concern to those actively engaged in the exploration of space. Materials and components, which may be damaged by the radiation, frequently can be replaced by more radiation resistant items; however, replacement systems are not always possible or practical and, hence, protective measures in the form of shielding must be employed. (One of the more radiation-sensitive systems to be flown in space is man himself.) Many groups are engaged in research on the attenuation and penetration of high-energy space radiation and on the development of methods for the design of shielding which affords protection against the radiation. The purpose of the Second Symposium on Protection Against Radiations in Space, like that of the First, was to bring these groups together to exchange information and share ideas.

The First Symposium on the Protection Against Radiation Hazards in Space was held in Gatlinburg, Tenn., on November 5-7, 1962, and was sponsored by the NASA Manned Spacecraft Center, the Oak Ridge National Laboratory, and the American Nuclear Society. The proceedings of that symposium were published by the U.S. Atomic Energy Commission in a two-volume report numbered TID-7652.

Early in 1964, it became apparent that sufficient new information worthy of presentation in another symposium had been gathered. Because of its interest and role in space and related research, the U.S. Air Force joined NASA and AEC in the sponsorship of the Second Symposium at Gatlinburg in October 1964. The host, as before, was the Oak Ridge National Laboratory.

These proceedings are the written record of the Second Symposium. Invited papers covering the space radiation environment, radiobiological effects, and radiation effects on materials and components comprised the first three sessions. By defining the radiation problems in space and providing for the proper assessment of the radiation effects and shielding requirements, these papers helped to establish the necessary background for the shielding papers which followed in the fourth session.

Arthur Reetz, Jr.
Technical Editor

Contents

	PAGE
1—MAN-MADE RADIATION IN SPACE.....	1
WERNHER VON BRAUN	

Session I

RADIATION ENVIRONMENT IN SPACE

Chairman: George F. Pieper

2—THE GEOMAGNETICALLY TRAPPED RADIATION.....	7
J. W. FREEMAN, JR.	
3—REVIEW OF GALACTIC AND SOLAR COSMIC RAYS.....	19
F. B. McDONALD	
4—THE MAGNETOSPHERE AND ITS BOUNDARY LAYER.....	31
NORMAN F. NESS	
5—SOLAR PERTURBATIONS OF THE SPACE ENVIRONMENT.....	41
HENRY J. SMITH	
6—THE UPDATING AND DISSEMINATION OF THE KNOWLEDGE OF TRAPPED RADIATION—MODEL ENVIRONMENTS.....	47
JAMES I. VETTE	

Session II

BIOLOGICAL EFFECTS OF SPACE RADIATION

Chairman: Cornelius A. Tobias

7—METHODS IN THE EVALUATION OF RADIATION HAZARDS IN MANNED SPACE FLIGHT.....	59
DOUGLAS GRAHN AND WRIGHT H. LANGHAM	
8—LETHAL, MUTAGENIC, AND CYTOGENETIC EFFECTS OF FAST CHARGED PARTICLES ON VARIOUS BIOLOGICAL MATERIALS..	65
G. E. STAPLETON	
9—BIOLOGICAL EFFECTS OF PROTONS AND NEUTRONS IN LARGE ANIMALS.....	73
S. TOM TAKETA	

	PAGE
10—THE RADIOBIOLOGICAL CONSEQUENCES OF DOSE DISTRIBUTIONS PRODUCED BY SOLAR-FLARE-TYPE SPECTRA.....	85
ROBERT K. JONES, DUANE E. ADAMS, AND IRVING J. RUSSELL	
11—EFFECT OF HIGH-ENERGY PROTONS AND ALPHA PARTICLES ON SMALL MAMMALS.....	97
CHARLES A. SONDHAUS	
12—BIOLOGICAL EFFECTS OF HEAVY IONS.....	105
PAUL TODD	

Session III

THE EFFECTS OF SPACE RADIATION ON MATERIALS

Chairman: George F. Pezdirtz

13—A SUMMARY OF RADIATION EFFECTS THRESHOLDS.....	117
DONALD J. HAMMAN	
14—RADIATION EFFECTS ON SEMICONDUCTING MATERIALS.....	121
H. Y. FAN	
15—RADIATION EFFECTS IN OPTICAL MATERIALS.....	123
W. E. SPICER	
16—RADIATION-INDUCED ELECTRICAL PROPERTY CHANGES IN POLYMERIC SOLIDS.....	131
S. E. HARRISON AND E. A. SZYMKOWIAK	

Session IVA

SHIELDING AGAINST SPACE RADIATION

Chairman: Edward D. Harney

17—STATUS REPORT ON THE SPACE RADIATION EFFECTS ON THE APOLLO MISSION	
A. Apollo Dose Limits.....	139
JOHN BILLINGHAM	
B. Apollo Shielding Analysis.....	143
DONALD E. ROBBINS	
C. Apollo Radiation Environment Analysis.....	147
JERRY L. MODISETTE	
D. Operational Procedures for Apollo Dose Reduction.....	151
PETER W. HIGGINS	

	PAGE
18—PARTICLES EMITTED IN THE FORWARD DIRECTION FROM HIGH-ENERGY NUCLEON-NUCLEUS KNOCK-ON REACTIONS....	157
H. W. BERTINI	
19—CALCULATED TISSUE CURRENT-TO-DOSE CONVERSION FACTORS FOR NUCLEONS OF ENERGY BELOW 400 MeV.....	161
W. E. KINNEY AND C. D. ZERBY	
20—THE SECONDARY-PARTICLE CONTRIBUTION TO THE DOSE FROM MONOENERGETIC PROTON BEAMS AND THE VALIDITY OF CURRENT-TO-DOSE CONVERSION FACTORS.....	173
D. C. IRVING, R. G. ALSMILLER, JR., W. E. KINNEY, AND H. S. MORAN	
21—THE VALIDITY OF THE STRAIGHTAHEAD APPROXIMATION IN SPACE VEHICLE SHIELDING STUDIES.....	177
R. G. ALSMILLER, JR., D. C. IRVING, W. E. KINNEY, AND H. S. MORAN	
22—COSMIC-RAY SHOWER PRODUCTION IN MANNED SPACE VEHI- CLES—COPPER.....	183
K. A. MORE AND O. L. TIFFANY	
23—THE APPLICATION OF THE LIOUVILLE THEOREM TO MAG- NETIC SHIELDING PROBLEMS.....	189
A. D. PRESCOTT, E. W. URBAN, AND R. D. SHELTON	
24—MAGNETIC RADIATION SHIELDING USING SUPERCONDUCTING COILS.....	199
R. E. BERNERT AND Z. J. J. STEKLY	
25—PLASMA RADIATION SHIELDING.....	211
RICHARD H. LEVY AND G. SARGENT JANES	

Session IVB

SHIELDING AGAINST SPACE RADIATION

Chairman: Phillip Mittelman

26—FRACTIONAL CELL LETHALITY APPROACH TO SPACE RADIATION HAZARDS.....	219
S. B. CURTIS, D. L. DYE, AND W. R. SHELDON	

	PAGE
27—SYNTHESIS OF SPHERICAL MINIMUM-WEIGHT PROTON SHIELDS.....	225
J. CELNIK, A. D. KRUMBEIN, AND F. R. NAKACHE	
28—QUALITY FACTORS FOR DEGRADED PROTON SPECTRA.....	229
RICHARD MADEY AND THOMAS E. STEPHENSON	
29—RADIATION SPECTROMETRY IN SPACE: REQUIREMENTS FOR ACCURATE DOSE DETERMINATIONS.....	235
BENTON C. CLARK	
30—AN APPLICATION OF THE GENERALIZED CONCEPT OF DOSIMETRY TO SPACE RADIATIONS.....	245
H. A. WRIGHT, G. S. HURST, AND E. B. WAGNER	
31—PROTON FLUX, DOSAGE, AND DAMAGE ESTIMATES IN THE VAN ALLEN BELT.....	251
S. RUSSAK AND K. RICHARDSON	
32—A GAMMA-RAY PROBE SYSTEM FOR DETERMINING THE SHIELDING EFFECTIVENESS OF THE APOLLO VEHICLE.....	257
A. D. KRUMBEIN, R. C. ROSS, AND C. BEAULIEU	

Session IVC

SHIELDING AGAINST SPACE RADIATION

Chairman: R. G. Alsmiller, Jr.

33—THE EFFECT OF CHARGED-PARTICLE ENVIRONMENTS ON MANNED MILITARY SPACE SYSTEMS.....	265
F. L. KELLER AND R. G. PRUETT	
34—THE IONIZING RADIATIONS IN SUPERSONIC TRANSPORT FLIGHTS.....	287
TRUTZ FOELSCHÉ	
35—PRIMARY- AND SECONDARY-PROTON DOSE RATES IN SPHERES AND SLABS OF TISSUE.....	301
ROGER WALLACE, PALMER G. STEWARD, AND CHARLES SONDHAUS	
36—DIFFERENTIAL CROSS SECTIONS BY FLIGHT-TIME SPECTROSCOPY FOR PROTON PRODUCTION IN REACTIONS OF 160-MeV PROTONS ON NUCLEI.....	331
R. W. PEELLE, T. A. LOVE, N. W. HILL, AND R. T. SANTORO	

	PAGE
37—COMPARISON OF MEASURED NEUTRON AND PROTON SPECTRA WITH CALCULATED SPECTRA IN THE ENERGY REGION BETWEEN 50 AND 160 MeV.....	337
W. A. GIBSON, W. R. BURRUS, W. E. KINNEY, AND J. W. WACHTER	
38—SPECTRA OF GAMMA RAYS PRODUCED BY INTERACTION OF ~160-MeV PROTONS WITH Be, C, O, Al, Co, AND Bi.....	341
W. ZOBEL, F. C. MAIENSCHN, AND R. J. SCROGGS	
39—CALCULATION OF PROTON-INDUCED GAMMA-RAY SPECTRUM AND COMPARISON WITH EXPERIMENT.....	351
C. W. HILL AND K. M. SIMPSON, JR.	
40—SOME EXPERIMENTAL DATA ON THE NUCLEAR CASCADE IN THICK ABSORBERS.....	357
B. S. P. SHEN	

Session IVD

SHIELDING AGAINST SPACE RADIATION

Chairman: Norman M. Schaeffer

41—APOLLO SPACECRAFT NUCLEAR RADIATION PROTECTION STATUS REPORT.....	365
FREDERICK RAYMES	
42—OPTIMUM SOLAR CELL SHIELDING FOR THE ADVANCED ORBITING SOLAR OBSERVATORY.....	377
HOWARD WEINER	
43—A SPACE RADIATION PROTECTION SYSTEM FOR NEAR-EARTH MANNED ORBITAL SPACE STATIONS.....	397
FRANK L. BOUQUET, JR.	
44—THE IMPORTANCE OF SPACE RADIATION SHIELDING WEIGHT..	407
E. R. BEEVER AND D. H. RUSLING	
45—SHIELDING REQUIREMENTS FOR MANNED ORBITING SPACE STATIONS.....	415
T. M. JORDAN, E. F. KOPROWSKI, AND R. W. LANGLEY	
46—SOLAR FLARE HAZARD TO EARTH-ORBITING VEHICLES.....	429
E. KUHN, F. E. SCHWAMB, AND W. T. PAYNE	

Session IVE

SHIELDING AGAINST SPACE RADIATION

Chairman: Trutz Foelsche

	PAGE
47—RESULTS OF SOME RECENT TRANSPORT CALCULATIONS FOR ELECTRONS AND BREMSSTRAHLUNG.....	437
M. J. BERGER AND S. M. SELTZER	
48—BREMSSTRAHLUNG PRODUCTION IN THICK ALUMINUM AND IRON TARGETS BY 0.5- TO 3.0-MeV ELECTRONS.....	449
L. L. BAGGERLY, W. E. DANCE, B. J. FARMER, AND J. H. JOHNSON	
49—SPACE ELECTRON RADIATION SHIELDING—BREMSSTRAHLUNG AND ELECTRON TRANSMISSION.....	455
G. D. MAGNUSON AND A. W. McREYNOLDS	
50—ERRORS FROM GEOMETRIC APPROXIMATIONS INTRODUCED IN THREE COMPUTATIONAL MODELS FOR SPACE VEHICLE ELEC- TRON DOSE PREDICTION.....	465
R. P. MOSHOFSKY	
51—AN EVALUATION OF RADIATION SHIELDING BY VEHICLE ORIENTATION.....	473
B. W. MAR	
52—THE IMPORTANCE OF RADIATION ANISOTROPY IN DOSE CALCU- LATIONS.....	477
R. E. FORTNEY AND G. D. DUCKWORTH	

Session IVF

SHIELDING AGAINST SPACE RADIATION

Chairman: Charles W. Hill

53—ANALYTICAL FORMULATION OF PROTON DOSE RATES BEHIND SPHERICAL MULTILAYER SHIELDS.....	485
F. R. NAKACHE	
54—THE CALCULATION OF PROTON PENETRATION AND DOSE RATES.	493
MARTIN O. BURRELL	
55—LOCAL DOSE FROM PROTON AND ALPHA PARTICLE ENDERS BEHIND COMPLEX SHIELD SYSTEMS.....	507
HERMANN J. SCHAEFER	

	PAGE
56—RBE OF PROTONS AND ALPHA PARTICLES.....	513
J. W. HAFNER	
57—AN EXAMINATION OF THE RELATIVE MERITS OF STOCHASTIC AND NONSTATISTICAL METHODS OF COMPUTING PRIMARY IONIZATION DOSES.....	527
B. LILEY AND G. C. SCHAEDEL	
58—A SPACE RADIATION SHIELDING CODE FOR REALISTIC VEHICLE GEOMETRIES.....	535
K. M. SIMPSON, C. W. HILL, AND C. C. DOUGLASS	
SYMPOSIUM SUMMARY	
59—SUMMARY OF THE SECOND SYMPOSIUM ON PROTECTION AGAINST RADIATION HAZARDS IN SPACE.....	543
J. WARREN KELLER	
APPENDIX—LIST OF PARTICIPANTS.....	547

1.—Man-Made Radiations in Space

WERNHER VON BRAUN

George C. Marshall Space Flight Center, NASA

It is encouraging to see a joint assault on radiation in space by the three organizations most vitally concerned with its problems.

Problems involving the radiation environment in space, its biological effects, its effects on materials, and problems of shielding require careful study. In addition to the problems of natural radiations in space, which are under consideration at this conference, there are also the problems connected with the radiation which man himself and his equipment will take into space.

The task of the Marshall Space Flight Center is to provide NASA with heavy launch vehicles—such as the Saturn rockets for Project Apollo. Less publicized is our responsibility to perform advanced system studies for space transportation concepts of the future. To propel these vehicles, we are thinking in terms of nuclear propulsion. Not too far in the future huge nuclear propelled spacecraft will take crews of men on long voyages into space. And the problems of man-made radiation connected with these spaceships will prove far more challenging in the long run than those of the natural radiations in space.

With regard to natural radiations, I do not like the often-used phrase “hostile environment of space.” Space is *not* hostile. Hostility is willful. It is directed by someone with the intellect to act. Neither is it hospitable. It is neutral. Space is simply there, following the scientific principles of nature, neither assisting nor resisting the attempts of man to fathom its mysteries.

Of course there are hazards in space for man—if he ignores its immutable laws. Just as there is danger for man on earth if he walks off a cliff, stays out in the tropic sun too long,

or defies the arctic cold without adequate protection.

But man has learned to live in earth’s environment without undue danger. And he will learn to live in the environment of space, as he comes to know its characteristics and how to adjust to them.

Man interacts with his environment. Right now, the environment of space has a certain amount of mystery, or even magic, connected with it. We need to dispel this mystery, take the “hex” out of space. Fear and superstition feed on the unknown. The only way we can remove them from the picture is to learn more about the spatial environment. And the ultimate solution is for men to go there, to live and work in space for extended periods of time.

We have attempted to simulate the environment of space here on Earth to the best of our ability—which is quite limited. These experiments are increasing our knowledge of both materials and living organisms, and they should be continued. We are extending our knowledge of space by highly instrumented probes and Earth satellites. But it is impossible to program fully for the unknown and unexpected.

The best way to study space is to put men there. Of course, man isn’t equipped with senses to monitor intensity and frequencies of space radiation. But man can observe and think. He can control experiments. Man’s capacity and speed are limited as compared with a machine when he acts as transmitter, receiver, or control mechanism. But he adds judgment and reasoning power to the spacecraft. He can make sense of fragmentary information. He can solve problems by logical induction.

You can program a machine to react to the known or the expected. But only man can react intelligently to the unexpected. When man is there as the observer and controller of experiments, he has the ability to parley an unexpected development into something fruitful. A computer cannot react intelligently to the unforeseen.

Project Mercury showed us that when we place a man in the loop, the chances of mission success are greatly enhanced. Several of the Mercury missions might have ended in failure when programmed equipment malfunctioned if a man had not been aboard to operate manual controls. Man can be designed into the machinery of a spacecraft, with due regard for his strengths and weaknesses, as a priceless asset. The safety and well-being of these future astronauts depend in part on the scientists attending this conference.

I firmly believe that man will eventually explore the solar system. And he must do it on his own terms, without being dictated to by conditions of gravity, thermal considerations, or radiation environment. We must give him the tools he needs to live with the natural radiations of space and the radiation he creates there in the performance of activities. We must master these problems to the extent that man can live in space almost without conscious thought of the dangers of the environment, so that he can explore and perform experiments without interruption.

NASA's Manned Space Flight Program is currently concerned with projects Gemini and Apollo, both of which are carefully planned steps to increase our ability to sail on the new ocean of space. Apollo is by far the most ambitious space flight project yet attempted. It is an engineering demonstration of the feasibility of manned space travel in the broadest sense. It is a demonstration of the highest quality, undoubtedly the greatest engineering challenge we have ever faced. In Apollo we are building an operational space-faring capability that can take us a quarter of a million miles from earth to land on another heavenly body, and return safely to earth. This will be an epic achievement. But Apollo is just a scouting expedition, a demonstration that the

pilots and their machine can make the journey, like Lindbergh crossing the Atlantic.

After Apollo will come man's true assault on space. Pilots and passengers, scientists trained as observers and experimenters, will follow in wave after wave to explore space in a big way. We are not alone in thinking that this will happen. If we are to capture the reality of space, come to know it intimately, and exploit it to our advantage, we must send more men into space, like the waves of an advancing army. We must set up bases, establish logistics lines, maintain communications, and furnish replacements and reinforcements for a continual, frontal assault.

Our current space launch vehicles are not capable of sustaining such an advance. The Saturn V rocket will launch the 45-ton Apollo spacecraft from the earth with such velocity that it will coast upward to the moon, with no further propulsion needed except that for course correction and braking into lunar orbit. More advanced transportation systems must be developed to take larger payloads into earth orbit, and the moon and beyond.

I said earlier that you cannot simulate the total environment of space, qualitatively, for testing on earth. If we are to develop materials that will stand up under the rigors of space, we must test them in the true environment of space, where they are subjected at the same time to all the variables under which they will operate. For this we need orbital research laboratories. If we are to capture the realities of the lunar environment, we must establish bases on the moon, such as those established in Operation Deepfreeze for study of the antarctic. This requires a team of men and machines, and an efficient transportation system for getting them there and back.

Today we are planning such transportation systems of the future around nuclear propulsion. Our first major step will be application of nuclear fission in so-called nuclear blowdown or nuclear heat transfer rocket engines. And we are looking at nuclear-powered ion propulsion. Here the nuclear energy is first converted into electricity, and ions are expelled from the electric field. This method cannot provide large thrusts, but has phenomenal propellant efficiency, and operates for many

hundreds of hours. This appears very attractive for interplanetary explorations.

We are making cost effectiveness studies to determine whether a nuclear lunar ferry is feasible for exploration of the moon. In this transportation system we would place a nuclear powered space vehicle into orbit around the earth. This vehicle would be fueled with liquid hydrogen brought up from the earth's surface with chemical-powered rockets. The fully fueled nuclear vehicle would be capable of launching itself from its low earth orbit into an orbit of the moon. From there, another all-chemical lunar landing vehicle comparable to the Apollo Lunar Excursion Module would take over as a shuttle bus between the orbiting nuclear vehicle and the moon's surface. The module could land people, supplies, and equipment on the lunar surface, and pick up a group of people who had spent their tour of duty of perhaps 3 months on the moon.

The nuclear ferry vehicle, which all the while has remained in orbit around the moon, would then hurl itself back into the original earth departure orbit. It would use some of the remaining liquid hydrogen fuel to boost itself out of circumlunar orbit, and the remainder to return itself to the orbit of the earth. There would be no reentry of the ferry into the atmosphere. At the end of its orbit-to-orbit round-trip mission, its liquid hydrogen tank would be empty, but the reactor in its nuclear rocket engine would still be unexhausted. It seems to be entirely feasible to build a lunar ferry that can fly such a round-trip mission 50 times.

Each time the ferry returned to Earth orbit it would be unloaded, serviced, and refueled with liquid hydrogen. And here is where the problem of man-made radiation occurs. Think of the service crew that must go up and inspect the lunar ferry and prepare it for another run. They must inspect and check it, replacing anything that is broken, checking the environmental control system and gas pressurization systems. And, most important of all, they must refuel the nuclear propulsion system with liquid hydrogen. What will they do about that hot reactor? Approach it through a safety cone provided by a shadow shield? How will they handle a defective reactor engine? With remote handling equipment? Throw the

whole nuclear-powered shuttleship away? Or part of it? Remove the hot engine and leave it in a parking orbit, replacing it with another engine brought out of orbiting cold storage, where it has had an opportunity to cool down somewhat?

Providing maximum protection to the service crew and the occupants of the lunar ferry presents a real challenge to the nuclear design engineer and the nuclear shielding expert. Shielding by mass is always a possible solution, of course. But here you would be trading in weight. It may be possible to construct spacecraft configurations in a manner to take advantage of propellants, structure, and intervening equipment to assist in common protection from both natural and artificial radiation. What other solutions could be found? Would the creation of electromagnetic fields to deflect certain types of charged particle radiation be possible?

I have used a nuclear lunar ferry as an illustration of a possible transportation system that would present man-made radiation problems. There are other areas to be examined. We need a variety of more efficient space propulsion systems for expanding our capability to explore space in the post-Apollo period. And all of our currently foreseeable advanced space propulsion systems are based on nuclear energy sources.

The problems of protection from artificial radiation are drastically different from those of natural radiation, but it would be to our advantage to tackle them together for possible common solutions.

We need to improve our radiation shielding technology for possible future space projects that use nuclear power sources for operating on-board equipment, as well as for propulsion. Radiation problems will arise from all types of nuclear systems, whether they are solid core reactors, or nuclear/electric propulsion systems, or nuclear power sources. Even gaseous core reactors, whose feasibility NASA is studying, will have their radiation and shielding problems.

We have made some studies of nuclear/electric propulsion for Mars vehicles, placing the reactor far away on a pole, and providing protection to the crew through shadow shielding. We are also studying the use of nuclear rocket

engines in a cluster, the way we now cluster chemical engines. But the complex radiation and radiation heating environment in such nuclear engine clusters is little understood.

If those scientists concerned with natural radiation in space would extend the scope of their thinking to consider man-induced radiation as well, a tremendous impact could be made on the future of nuclear space propulsion.

For man to play an effective role in using nuclear space systems, we must develop a body of design criteria and concepts that will enable the designer to tie the man and machine together into an efficient team. Considerable work has been done on the problems of man's participation in Earth launch of vehicles with nuclear upper stages. We are just beginning, however, to examine in detail the human engineering design criteria and handling concepts for advanced nuclear vehicles. We need to investigate thoroughly the operational safety hazards associated with such systems as the

nuclear lunar ferry, nuclear planetary orbital launch vehicles, interorbital transport vehicles, and Earth orbital launch facilities employing nuclear power supplies.

The problems of natural radiation in space plus those of man-made radiation are indeed difficult. However, let us take comfort from recent history which indicates that solutions will be found. Remember that only 20 years ago professors of aerodynamics prophesied that we would never fly through the sound barrier. Little more than 10 years ago thermodynamicists predicted that we would never break the heat barrier in reentry flights. Only 8 years ago economists prophesied that our first satellite programs would never be able to pass the barrier of the Bureau of the Budget.

None of these barriers has withstood the advance of science and technology, and these experiences may give us confidence that we shall also succeed in breaking through the radiation barriers.

SESSION 1

RADIATION ENVIRONMENT IN SPACE

Chairman: GEORGE F. PIEPER
Goddard Space Flight Center, NASA

N 03 - 34576
N 65 - 34576

2—The Geomagnetically Trapped Radiation

J. W. FREEMAN, JR.

Rice University

It is well known that the supersonic flow of the solar wind past the earth results in the confinement or abrupt termination of the earth's magnetic field in all directions save perhaps the anti-solar direction. The region within this surface of abrupt termination of the geomagnetic field, that is, the region in which the magnetic field is ordered and roughly dipolar, has come to be called the magnetosphere. The surface of termination of the geomagnetic field is known as the magnetopause.

Figure 1 shows a pictorial diagram of a cross section of the magnetosphere taken through the

noon-midnight meridian. Those lines of force which lie within the shaded areas are closed, well confined, relatively stable, and capable of trapping charged particles. Lines of magnetic force which leave the earth in the polar regions may be extruded to great distances on the night side of the earth. The ultimate fate of these lines of force is not known at this time. It seems certain that the tail of the magnetosphere must extend at least to the orbit of the moon and probably much farther. By contrast, the magnetopause is found at some 10 earth radii in the direction of the sun and, as indicated in the figure, durable trapping fills the entire magnetosphere on the sunlit side of the earth.

Before launching into the description of the trapped radiation, a word or two about the appropriate coordinate system is necessary. In 1961 McIlwain introduced the B, L coordinate system for the description of Van Allen radiation (ref. 1). It can be shown that the first adiabatic invariant of the motion of a trapped particle in the geomagnetic field is the magnetic moment of the particle, treated as a current loop spiraling about a field line. This leads to the fact that a trapped particle will always mirror at the same value of magnetic field strength, B . The second adiabatic invariant, I_0 , defines the magnetic shell on which the particle stays as it drifts about the earth in *longitude*. McIlwain found a means of labeling these shells with the value L . The L value is nearly constant along a line of force and, for a perfect dipole, has the magnitude of the equatorial distance of the line of force in units of earth radii. In figure 2, the light lines which merge with the heavy lines represent magnetic field lines and, hence, contours of constant L .

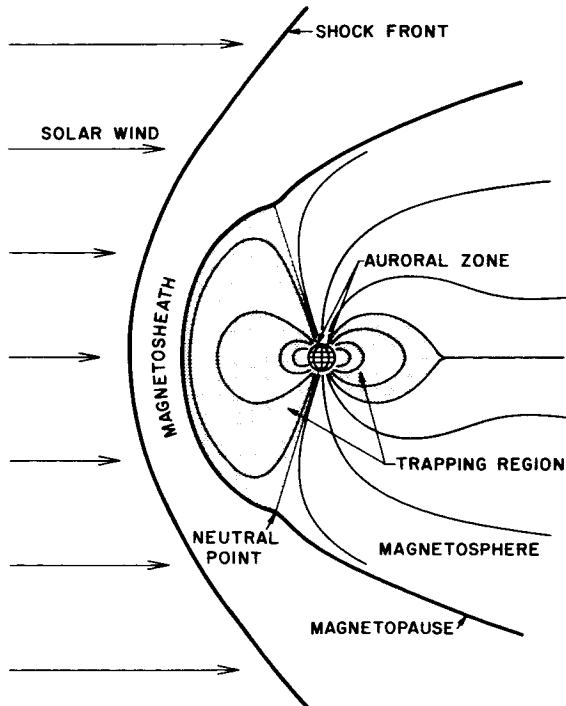


FIGURE 1.—Cross section of magnetosphere taken through noon-midnight meridian.

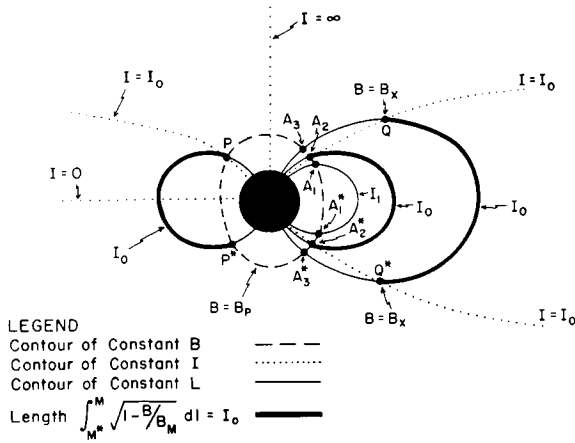


FIGURE 2.—Van Allen radiation, as shown by B, L coordinate system.

The Van Allen radiation consists predominantly of electrons and protons. A very small flux, less than 1%, of deuterons or tritons has been observed in emulsion experiments (refs. 2 and 3).

PROTONS

Let us consider first the distribution of trapped penetrating protons. As shown by figure 3, on the right-hand side, the radial dis-

tribution of protons of energy in excess of 40 MeV peaks on lines of magnetic force that cross the geomagnetic equator at 1.5 earth radii geocentric distance, or $L=1.5 R_E$. As first estimated by Van Allen in 1959, the peak intensities for protons capable of penetrating 3.5 gm/cm² of lead are of the order of 5×10^4 protons/cm²-sec. This band of energetic protons constitutes the most penetrating natural component of the region known classically as the inner radiation zone.

Recently McIlwain has discovered a secondary maximum in the penetrating proton component (ref. 4). In figure 4, this second peak is seen to lie at about $L \approx 2.2$ earth radii. This figure also shows the radial profile of intensities of somewhat lower energy protons. Note the complex changes in energy spectrum as a function of radial distance.

The detailed integral energy spectra for various L values are shown in figure 5. These data are all the work of McIlwain, based on Relay I data. Note that the spectra tend to soften with increasing L .

Prior to a year ago it was thought that these proton intensities were time stationary on a scale of at least months. However, on September 23, 1963, there occurred an intense magnetic storm which resulted in the

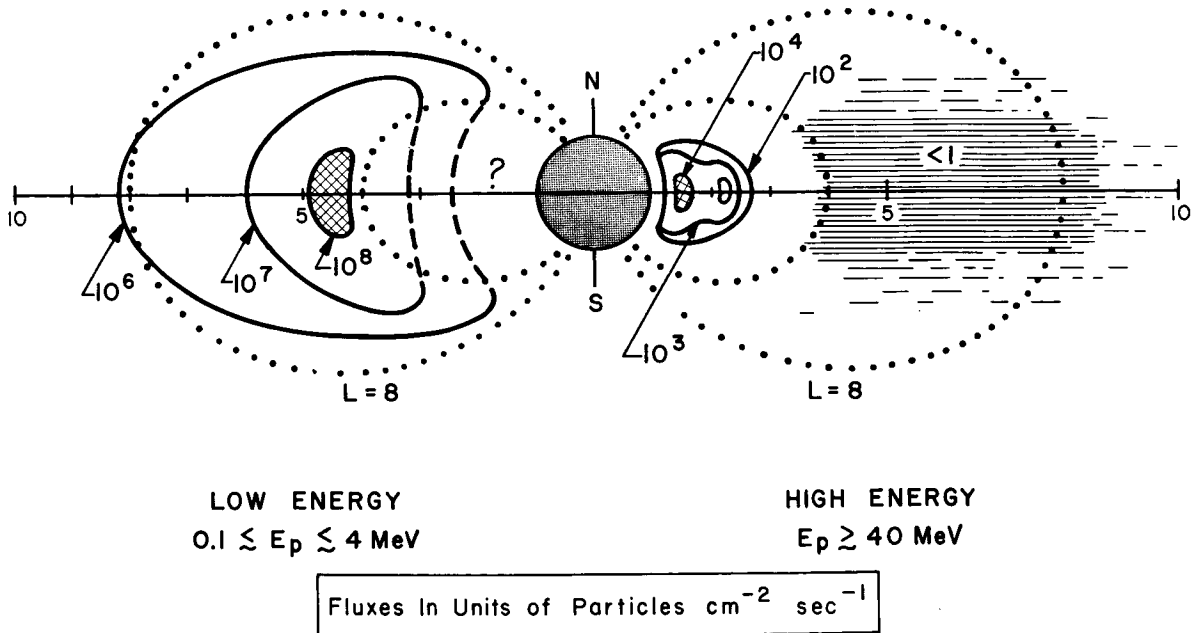


FIGURE 3.—Spatial distribution of trapped protons.

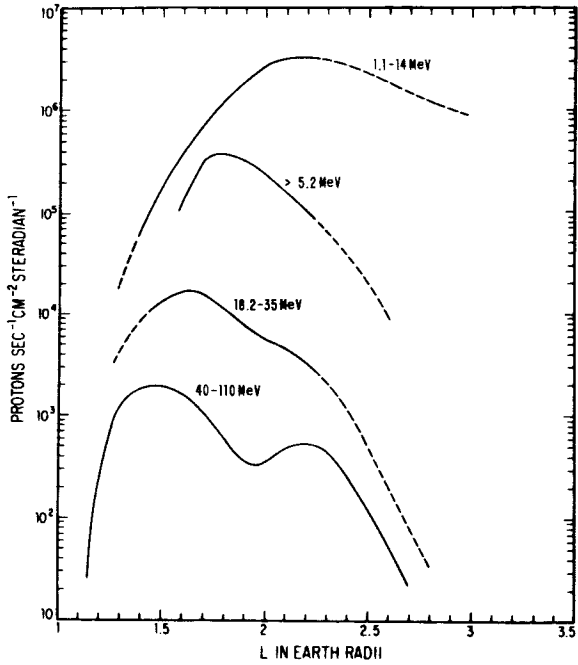


FIGURE 4.—Trapped protons: unidirectional intensity at magnetic equator.

redistribution and/or reductions of the trapped protons McIlwain had been studying with Relay I (ref. 5), figure 6 illustrates this change. Note the discontinuity in flux intensity on about 23 September. The majority of the change took place within a 6.5 hour period. It can be seen from the slide that the flux decreases were greater for greater L values. An additional interesting fact not evident from this figure is that the protons whose mirror points were farthest from the equator, that is, those with small equatorial pitch angles, suffered the greatest reduction. McIlwain states that indeed it is quite possible that the equatorial intensities on high lines of force may have even increased.

In figure 7, McIlwain has plotted the daily dose of energetic particles received by Relay I (ref. 6). The upper curve is for $E > 0.5$ MeV electrons, the middle curve for $E > 8.5$ MeV electrons, and the lower curve for 40 to 110 MeV protons. Note that the ordinate must be divided by 1000 to get the integrated

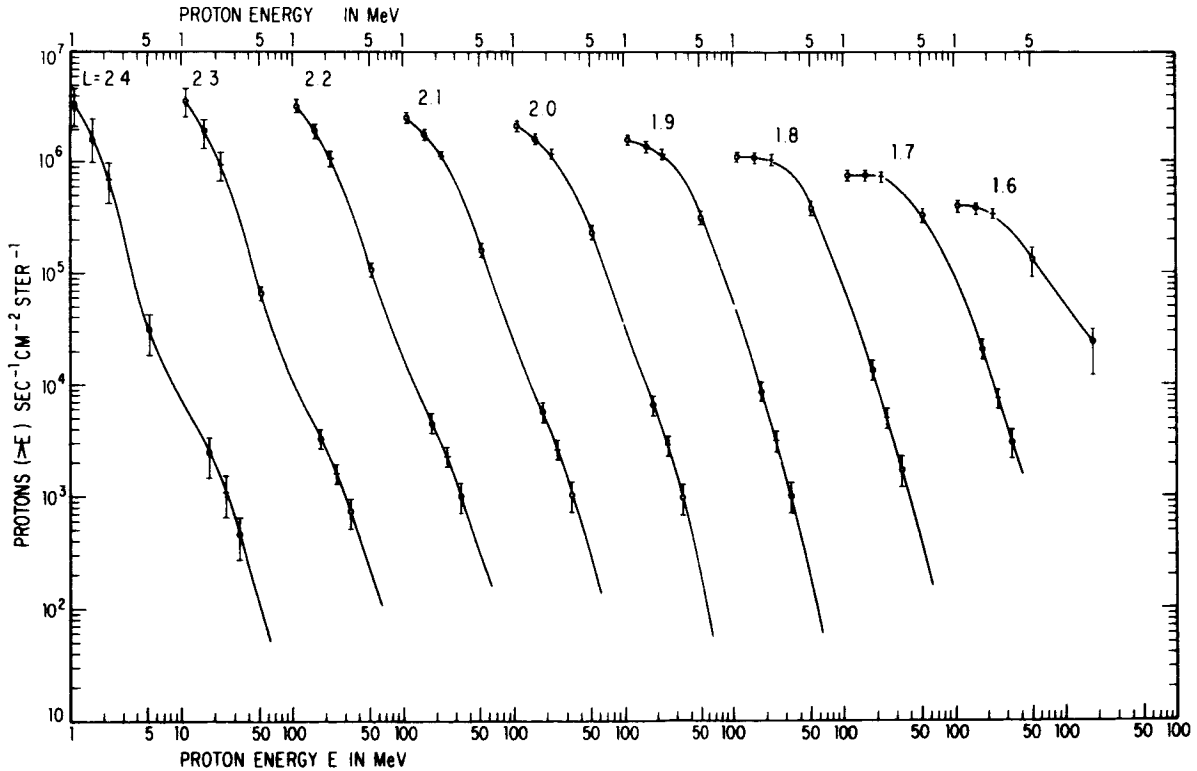


FIGURE 5.—Integral energy spectra for unidirectional protons at magnetic equator observed by Relay 1.

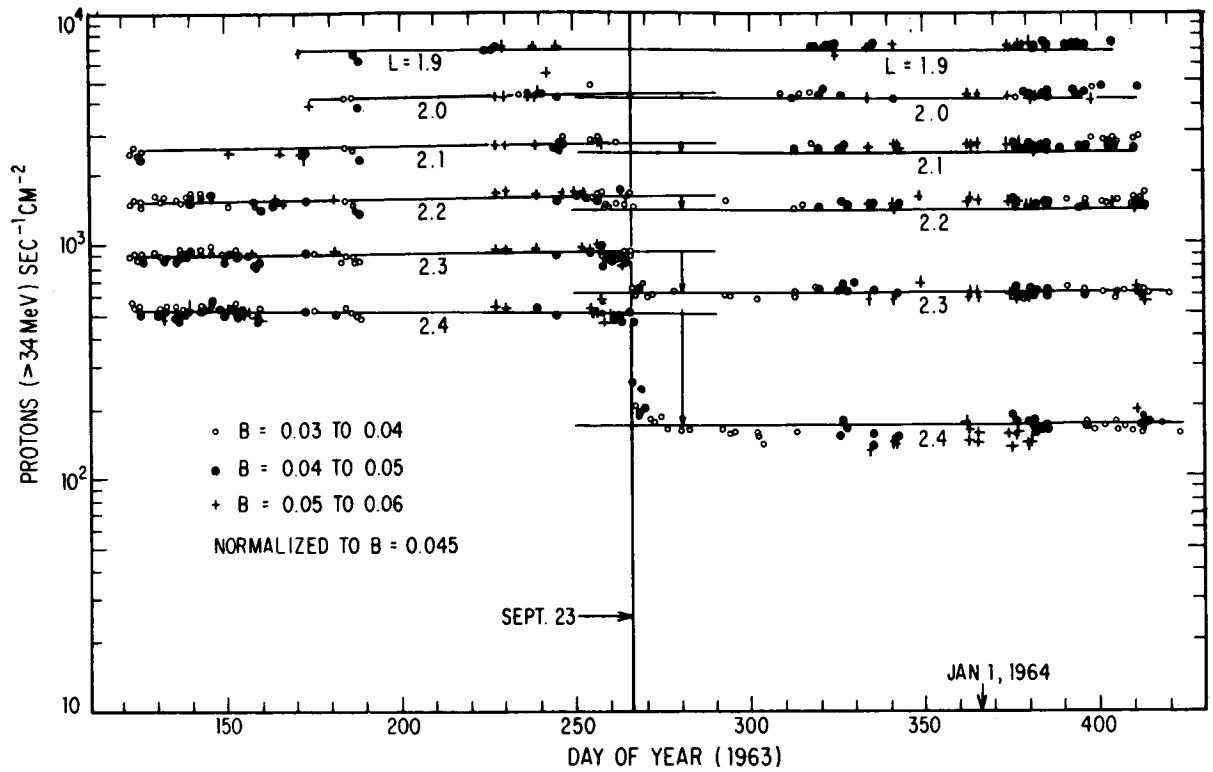


FIGURE 6.—Change in proton intensities following magnetic storm of 23 September 1963.

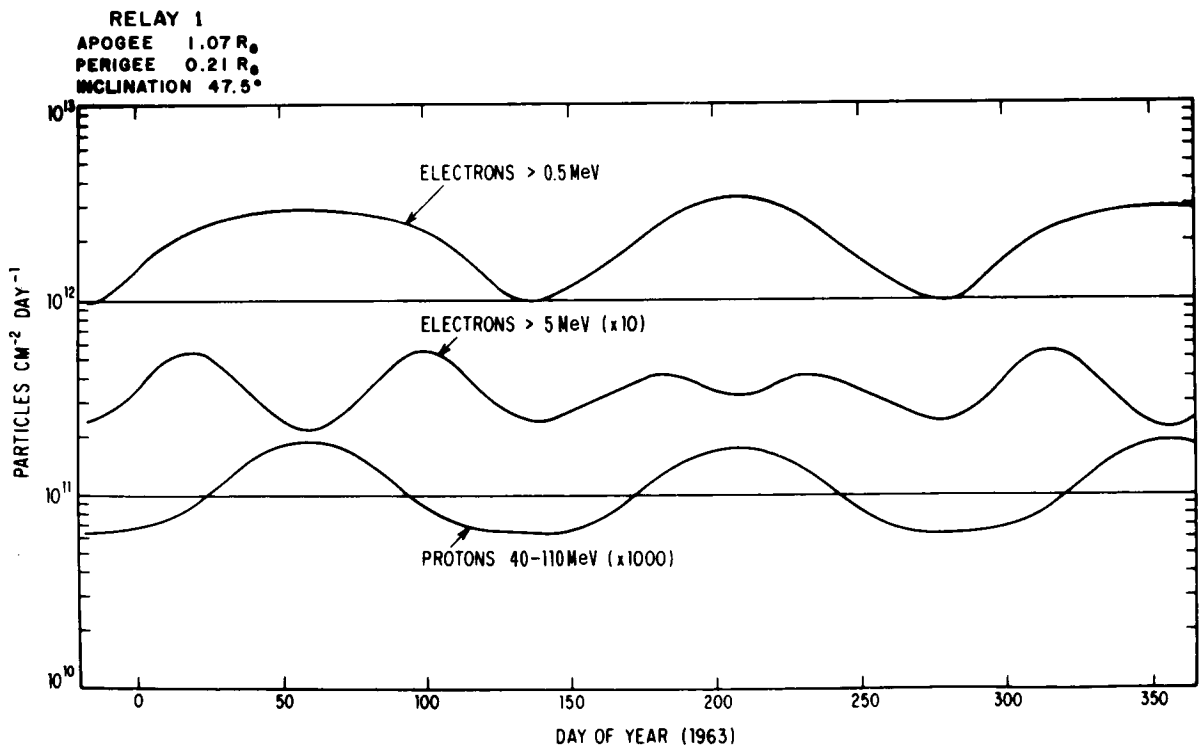


FIGURE 7.—Daily dose of energetic particles received by Relay 1.

flux of energetic protons. Thus the peak flux of protons greater than 40 MeV is about 2×10^8 protons/cm²-day and the minimum flux is about 7×10^7 protons/cm²-day. The periodic variation in the daily integrated intensity results, of course, from the latitudinal oscillations of perigee.

The *low energy* proton distribution is illustrated on the left-hand side of figure 3. Davis and Williamson (ref. 7), using a scintillation counter sensitive to protons in the energy range 120 keV to 4.5 MeV, have demonstrated the existence of an important proton component of the outer zone. As illustrated here, they find fluxes of the order of 10^8 protons/cm²-sec on magnetic field lines that cross the equator between 3 and 5 earth radii. The integral intensity of these low-to-moderate energy protons falls in direct proportion to the *geomagnetic field energy density* out to the boundary of durable trapping. As a general rule (for electrons as well as protons), beyond the outer zone peak at approximately $3.5R_E$ the particle energy spectra tend to soften with increasing radial distance. For example, fitting the energy spectrum to an exponential law, Davis and Williamson (ref. 7) find that the *e*-folding energy is 400 keV at $L \sim 2.8 R_E$, 120 keV at $L \sim 5.0$, and 64 keV at $L \sim 6.1$.

ELECTRONS

Let us turn now to the Van Allen electrons. Relatively high intensities of naturally occurring low-to-moderate energy electrons are found throughout the *entire region of durable trapping within the magnetosphere*. Unfortunately, the electron spectra of the inner zone had not been adequately studied prior to the Starfish nuclear detonation. However, it was known that a flux of some 10^8 electrons/cm²-sec of energy greater than 40 keV is found in the inner radiation zone. O'Brien (ref. 8) estimates that the integral intensity above 600 keV is only some two orders of magnitude below the $E > 40$ keV figure. Thus, the natural inner zone electrons outnumber their energetic proton companions by several orders of magnitude. With regard to spectrum, with Injun I data, Pizella et al. (ref. 9) obtained a fit to an exponential spectrum with an *e*-folding energy

of 160 keV. This was in reasonable agreement with the measurements of Holly, Allen, and Johnson, but in disagreement with the then popular neutron albedo theory of the source of the inner zone electrons.

The Starfish nuclear detonation of July 1962 liberated some 10^{27} energetic electrons within the magnetosphere. McIlwain (ref. 10) estimates from Explorer 15 measurements that by November 5, 1962, the total number of electrons with energies greater than 0.5 and 5 MeV on all magnetic shells labeled by $L \leq 1.62 R_E$ were 8.8×10^{24} and 9.8×10^{22} , respectively. This indicates that some 1.2% of the electrons available from the explosion were still trapped 120 days after the event.

Figures 8 and 9 illustrate the distribution of these electrons in space. Figure 8 is for electrons of energy greater than 5 MeV. It shows the contours of constant omni-directional intensity. (Actually plotted are logarithms of the omni-directional intensity.) The fluxes shown vary over some two-and-a-half orders of magnitude. The secondary maximum seen at $L \sim 1.75$ is presumably due to electrons injected by the Soviet nuclear detonations in late October and early November. Figure 9 shows a similar set of contours for $E > 0.5$ MeV electrons. Again the Starfish peak at $L \sim 1.3$ and the Soviet peak at $L \sim 1.75$ are evident.

Figure 10 shows the radial profiles of the electron intensities for several values of magnetic latitude. Also shown are the proton intensities. This slide represents the intensities found on 1 January 1963, or about $1\frac{1}{2}$ months after the data shown in the last two figures. It can be seen that the electrons from the Soviet bursts have almost disappeared or been masked by the Starfish or natural electrons. This is particularly evident in the >0.5 MeV energy electrons. The rise in intensities beyond $L \sim 3.5$ represents the heart of the outer radiation zone.

A matter of extreme interest is the decay time of the Starfish electrons themselves. Figure 11, also due to McIlwain, shows the measured decay times for $E > 0.5$ MeV electrons as a function of radial distance (ref. 10). These are the times required for the electron intensities to decrease by *e*. It is seen that in the region of the Starfish intensity peak, decay times of the order of 200 to 300 days are evident.

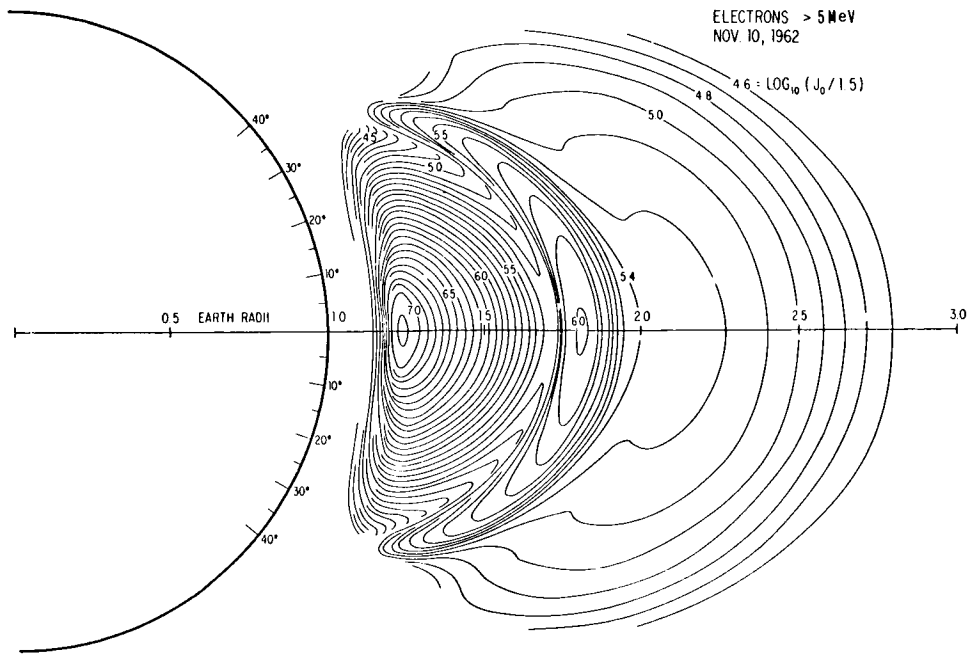


FIGURE 8.—Spatial distribution of trapped electrons (>5 MeV) 10 November 1962, following Starfish nuclear detonation of July 1962.

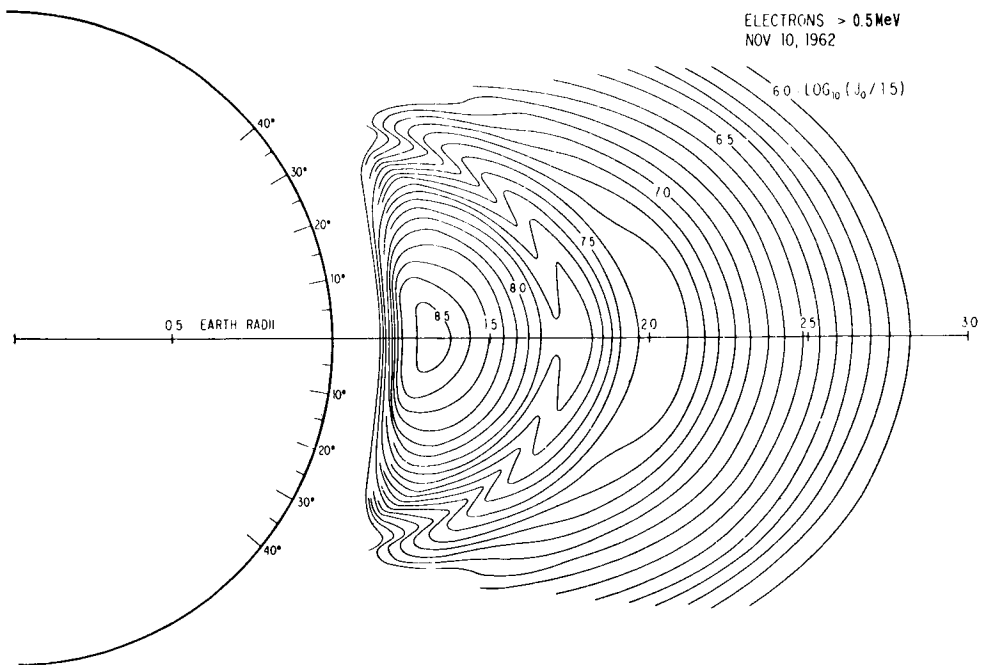


FIGURE 9.—Spatial distribution of trapped electrons (>0.5 MeV) 10 November 1962, following Starfish nuclear detonation of July 1962.

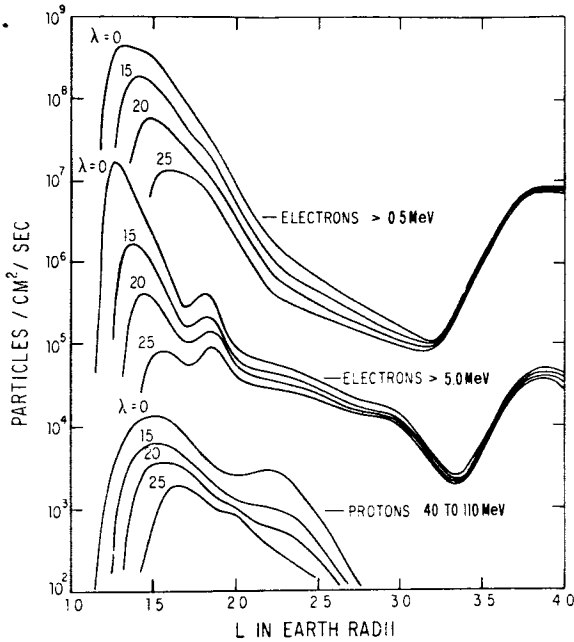


FIGURE 10.—Radial profiles of trapped electron and proton intensities for certain values of magnetic latitude found 1 January 1963.

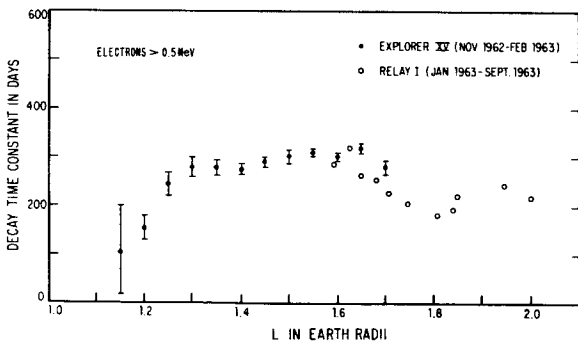


FIGURE 11.—Decay time of Starfish electrons.

It is believed that beyond $L \sim 1.7$ the trapped electrons are strongly perturbed by magnetic disturbances.

Recently Walt and MacDonald (ref. 11) have calculated the predicted effects of the ambient atmosphere on trapped electrons. Figure 12 shows the comparison between the Walt and MacDonald theoretical electron decay times and the experimental Starfish electron decay times. It is concluded that during periods of minimum solar activity, atmospheric collisions are the most important loss mechanism for electrons in the region $L \gtrsim 1.25$.

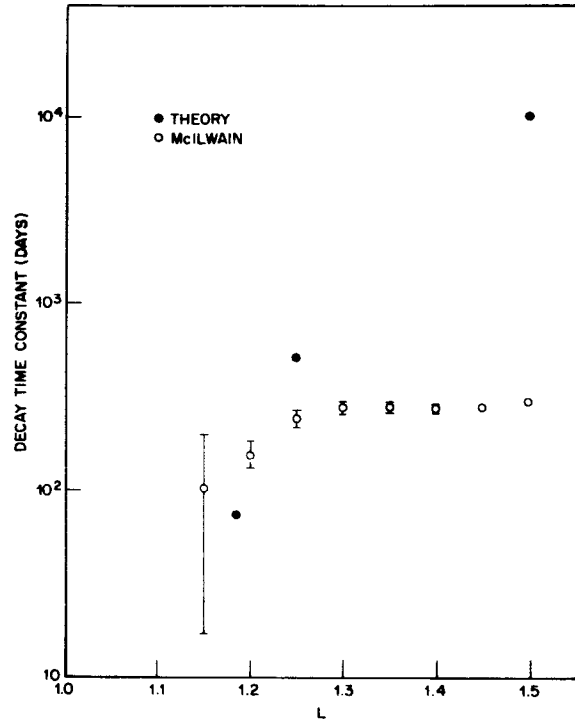


FIGURE 12.—Comparison of experimental and theoretical values of the decay rates of artificially injected electrons as a function of L . The time constants given here are appropriate to the time period $110 < t < 200$ days after the detonation and are the times required for the omnidirectional flux in the equatorial plane to decrease by a factor of 2.718. The open circles are experimental points of McIlwain; solid circles are theoretical values.

The Walt and MacDonald theory has also been used to predict the time variation of the count-rate of a small heavily shielded geiger tube of the type flown by Van Allen et al. on the satellites Injun I and III (refs. 11 and 12). The results of the comparison between theory and observation are shown in figure 13. The lines represent the theoretical prediction and the symbols the actual data. The various curves represent different values of B , all for L values from 1.175 to 1.195.

Figure 14 gives one some feel for the long time variation of the counting rates of the same detector (ref. 12). Also shown for comparison are the background rates derived from pre-Starfish Injun I data. Current estimates of the time required for evidence of the Starfish

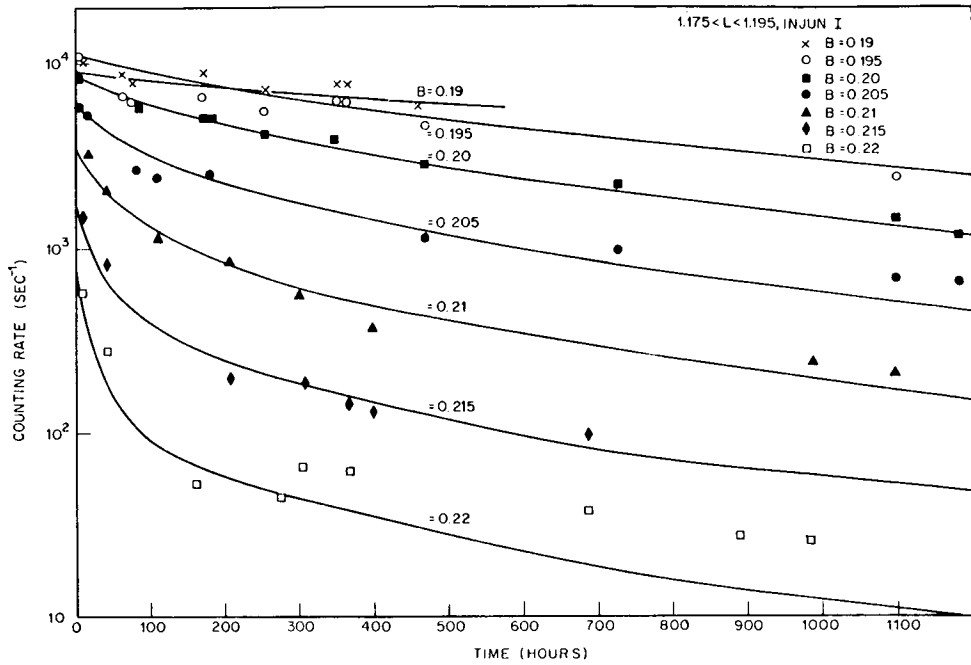


FIGURE 13.—Time variation of count-rate of a small, heavily shielded geiger tube. The lines represent the theoretical prediction and the symbols the actual data. The curves represent different values of B , all for L values from 1.175 to 1.195.

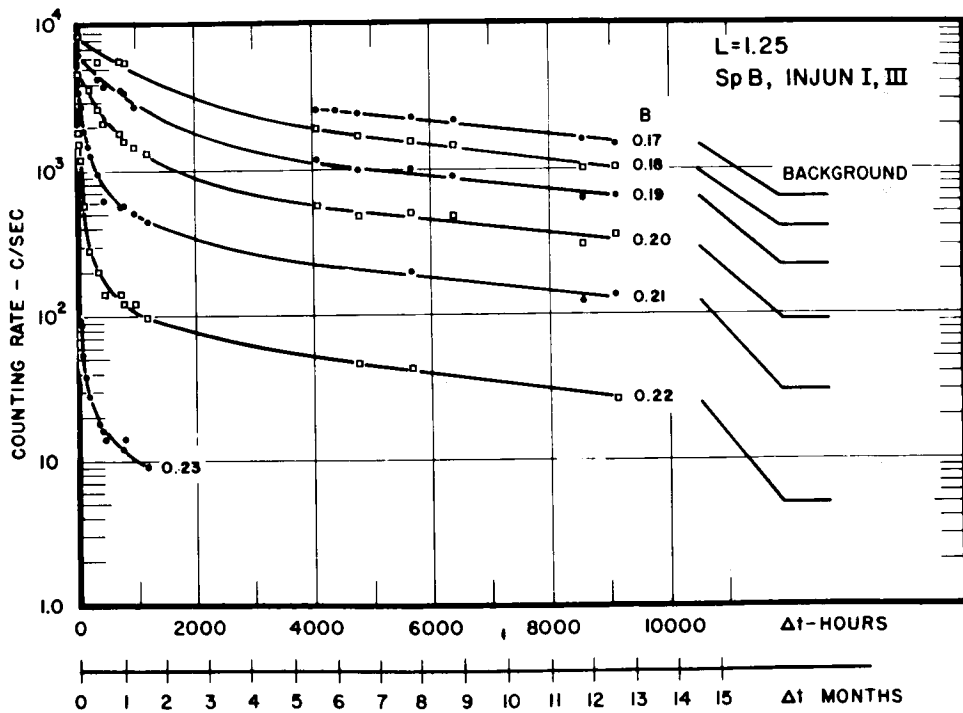


FIGURE 14.—Long-time variation of the counting rates of detector shown in figure 13.

electrons to disappear range from 10 to 20 years, although the enhanced atmospheric heating during the coming solar maximum may require that these estimates be modified somewhat.

Only *naturally* occurring electrons are found in the outer radiation zone, that is, beyond $L \approx 3$. Frank, Van Allen, Whelpley, and Craven (ref. 13), using Explorer 14 data, have found these sample values of the outer zone electron intensities at $L \approx 6$:

$$\begin{aligned} J_o(E_e \geq 40 \text{ keV}) &= 1.5 \times 10^8 / \text{cm}^2\text{-sec} \\ J_o(E_e \geq 230 \text{ keV}) &\leq 1.5 \times 10^6 / \text{cm}^2\text{-sec} \\ J_o(E_e \geq 1.6 \text{ MeV}) &= 2 \times 10^5 / \text{cm}^2\text{-sec} \end{aligned}$$

Figure 15 shows the radial profiles of the outer zone electron intensities. The *solid* circles represent the penetrating electron component. The sharp peak at 25 000 km represents the heart of the classical outer Van Allen belt. The *open* circles are the count-rates of an $E > 40$ keV electron detector. It has been found that as the measurements have been pushed to lower energies, the radiation is found to more nearly fill the entire magnetosphere, at least on the sunlit side of the earth. Here it can be seen that the $E > 40$ keV electron flux is uniform to within an order of magnitude out to the magnetopause, which here occurs at about 70 000 km. There is in reality a great deal of

fine structure in the soft electron flux which is not shown in this graph. This fine structure is absent in the energetic electron fluxes. Both the hard and soft electron components in the outer zone exhibit dramatic temporal variations during magnetic storms. With the onset of a magnetic storm sudden commencement, the outer zone soft electron flux increases suddenly, often by several orders of magnitude. At the same time there is a diminution of the hard electron flux, which subsequently undergoes a slow recovery, often to intensities above the prestorm level. The recovery time constants for both the hard and soft components are typically of the order of several days (ref. 14).

The most recent information on the soft electron fluxes in and near the magnetosphere comes from Explorer 18 or IMP-1. In figure 16, Kinsey Anderson (ref. 15) has depicted the distribution of $E > 40$ keV electron fluxes in the magnetosphere with an equatorial cut. The sun is on the left, the dashed line represents the bow wave shock front, and the solid line just inside it is the magnetopause. In addition to the trapped radiation near the earth, one notes that significant fluxes of energetic electrons are found on the night side of the earth at distances as great as 30 earth radii. The fluxes may continue at least as far as the orbit of the moon. The cut-off in this diagram represents satellite apogee and not the limit of the phenomenon.

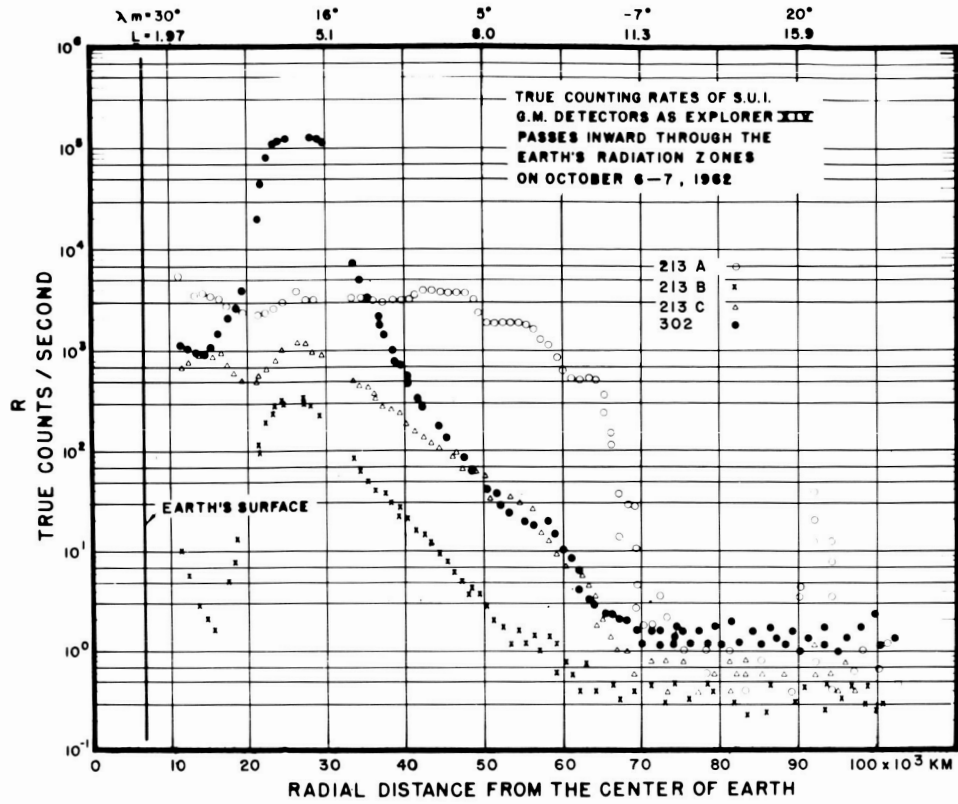


FIGURE 15.—Radial profiles of the outer zone electron intensities. The solid circles represent the penetrating electron component. The sharp peak at 25 000 km represents the heart of the classical outer Van Allen belt. The open circles are the count-rates of an $E > 40$ keV electron detector.

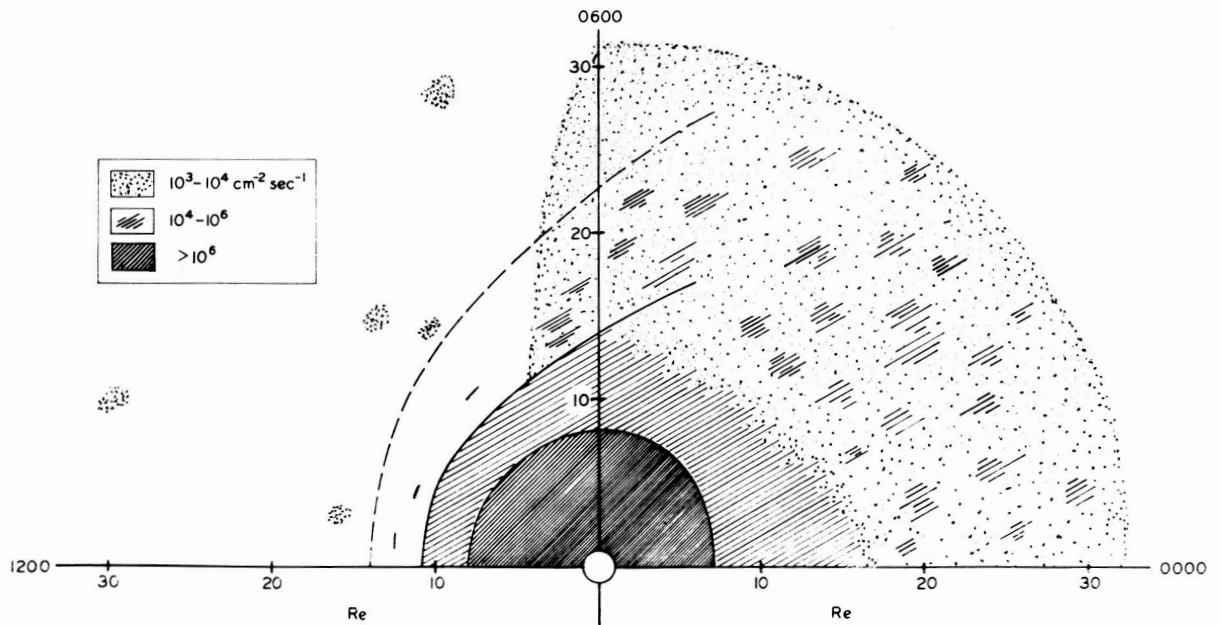


FIGURE 16.—Distribution of $E > 40$ electron fluxes in the magnetosphere. As represented, the sun is on the left, the dashed line is the bow wave shock front, and the solid line just inside that is the magnetopause.

REFERENCES

1. McILWAIN, C. E.: Coordinates for Mapping the Distribution of Magnetically Trapped Particles. *J. Geophys. Res.*, vol. 66, 1961, pp. 3681-3692.
2. FREDEN, S. C.; and WHITE, R. S.: Particle Fluxes in the Inner Radiation Belt. *J. Geophys. Res.*, vol. 65, 1960, pp. 1372-1383.
3. HECKMAN, H. H.; and ARMSTRONG, ALICE H.: Energy Spectrum of Geomagnetically Trapped Protons. *J. Geophys. Res.*, vol. 67, 1962, pp. 1255-1262.
4. FILLIUS, R. W.; and McILWAIN, C. E.: The Anomalous Energy Spectrum of Protons in the Earth's Radiation Belt. Univ. of Calif. (San Diego) Research Rept., 1964.
5. McILWAIN, C. E.: Redistribution of Trapped Protons During a Magnetic Storm. Univ. of Calif. (San Diego) Research Rept., Apr. 1964.
6. McILWAIN, C. E.; FILLIUS, R. W.; VALERIO, J.; and DAVÉ, A.: Relay 1 Trapped Radiation Measurements. Univ. of Calif. (San Diego) Research Rept., Mar. 1964.
7. DAVIS, L. R.; and WILLIAMSON, J. M.: Low-Energy Trapped Protons. NASA-GSFC Research Rept. X-611-62-89.
8. O'BRIEN, B. J.: Review of Studies of Trapped Radiation With Satellite-Borne Apparatus. *Space Science Reviews*, no. 1, 1963, pp. 415-484.
9. PIZELLA, G.; LAUGHLIN, C. D.; and O'BRIEN, B. J.: Note on the Electron Energy Spectrum in the Inner Van Allen Belt. *J. Geophys. Res.*, vol. 67, 1962, pp. 3281-3287.
10. McILWAIN, C. E.: Trapped Electron Intensities in November, 1962. Univ. of Calif. (San Diego) Research Rept., 1963.
11. WALT, M.; and MacDONALD, W. M.: The Influence of the Earth's Atmosphere on Geomagnetically Trapped Particles. *Reviews of Geophysics*, no. 2, 1964.
12. VAN ALLEN, J. A.: On the Lifetimes of Geomagnetically Trapped Electrons of Several MeV Energy. S.U.I. Research Rept., 64-34, 1964.
13. FRANK, L. A.; VAN ALLEN, J. A.; WHELPLEY, W. A.; and CRAVEN, J. D.: Absolute Intensities of Geomagnetically Trapped Particles With Explorer 14. *J. Geophys. Res.*, vol. 68, 1963, pp. 1573-1580.
14. FREEMAN, J. W., JR.: The Morphology of the Electron Distribution in the Outer Radiation Zone and Near the Magnetospheric Boundary as Observed by Explorer 12. *J. Geophys. Res.*, vol. 69, 1964, pp. 1691-1723.
15. ANDERSON, K. A.; HARRIS, H. K.; and PAOLI, R. J.: Energetic Electron Fluxes in and Beyond the Earth's Outer Magnetosphere. Rept. Series 5, Issue 50, Physics Department and Space Science Laboratory, Univ. of Calif. (Berkeley).

3—Review of Galactic and Solar Cosmic Rays

F. B. McDONALD

Goddard Space Flight Center, NASA

The energetic particle population in interplanetary space extends from "solar wind" protons in the keV range to ultrarelativistic particles associated with the galactic cosmic rays. The population in this region of space is highly variable. Not only are the galactic cosmic rays strongly modulated by the solar wind, but there are frequent great injections of solar cosmic rays that give rise to particle fluxes an order of magnitude greater than galactic cosmic rays. Interspersed with these events are small recurrent streams associated with particularly active solar regions and producing streams of protons in the 1 to 10 MeV range. This paper attempts to summarize some salient features of both the galactic and solar cosmic rays.

GALACTIC COSMIC RAYS

The galactic cosmic rays were first discovered some 50 years ago, but even now their study is one of the important problems in physics and astrophysics. Following World War I, until the late 1940's, cosmic ray studies were nearly synonymous with high energy physics. The nuclear interactions of the high energy primaries with the nuclei of the upper atmosphere, and the resulting electron and nuclear cascades down through the atmosphere, furnished the particle beam for discovering the positively charged electron (positron), the μ and π meson, and the early heavy mesons or "strange particles." Since the cosmic rays interact with air nuclei, it is clearly necessary to get beyond the earth's atmosphere to obtain quantitative studies of most of the properties of the primary beam. With the development of large Skyhook balloons and, more importantly, the advent of earth satellites and probes, it has been possible to obtain far more definitive information on

the nature of the primary radiation. Strongly coupled with this is the discovery of great discrete radio sources emitting polarized radio signals which can apparently be explained only in terms of synchrotron radiation from highly relativistic electrons. This important link to astrophysics is further emphasized when we realize that the energy density of the primary radiation is about 1 electron volt per cubic centimeter. This is comparable to the energy density of starlight, to the energy contained in the galactic magnetic fields, and to the energy due to turbulence through the galaxy. Because of the very great energy of the particles, we assume they cannot be contained in our solar system and are therefore generated in the galaxy, possibly by a variety of sources. When we observe them near the earth's orbit, they have already undergone three basic processes: (1) initial acceleration followed by diffusion through the galaxy; (2) possible post-acceleration; and, finally, (3) modulation by the solar wind. However, it is more convenient to order the experimental information in the following way: (1) chemical composition or charge distribution; (2) energy distribution; (3) spatial distribution.

Charge Distribution

The multiply charged particles observed in the primary cosmic ray beam furnish us a direct sample of galactic material. Figure 1 demonstrates one method of doing high energy chemistry (ref. 1). Illustrated here are tracks of heavy nuclei, ranging from hydrogen through iron, in a nuclear emulsion. As one progresses towards the heavier nuclei, the strong coulomb interaction between the stripped nucleus and the electrons of the elements in the emulsion produces delta rays or "knock-on" electrons,

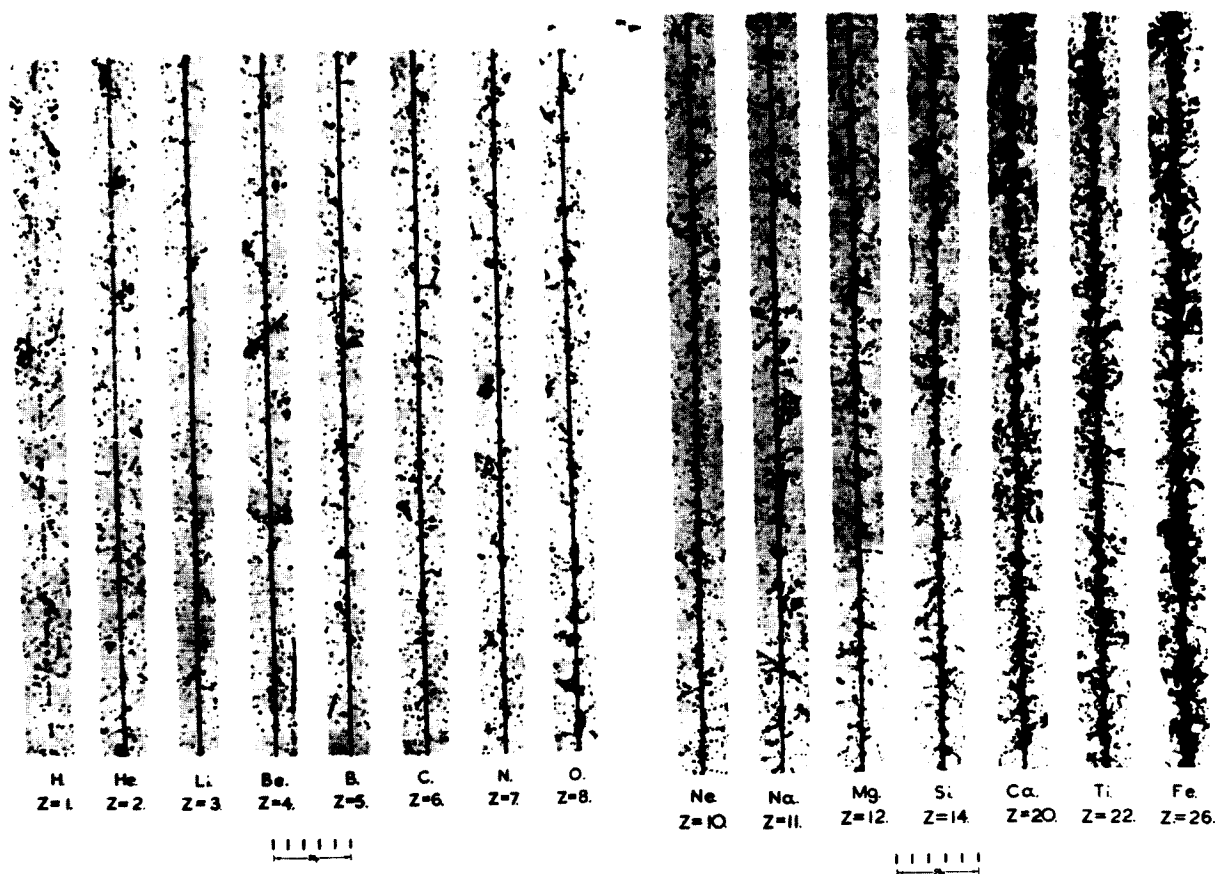


FIGURE 1.—Reproduction of tracks of primary cosmic rays of hydrogen to iron in nuclear emulsions.

which provide one means of charge identification. The measurements to date on the chemical abundances are summarized (refs. 2 and 3) in tables 1 and figure 2. The striking feature here is the overabundance of elements in the range greater than carbon and the presence of lithium, beryllium, and boron. This suggests two things: first, that the initial injection and acceleration of cosmic rays occur in a region rich in heavy nuclei; second, that the light nuclei Li, Be, and B are formed by fragmentation of these heavy nuclei in nuclear collisions with interstellar hydrogen. We know reasonably well (ref. 3) the fragmentation parameters for the production of Li, Be, and B in the breakup of heavy nuclei, and this makes it possible to estimate the average amount of material traversed by the cosmic rays. The best current estimate (ref. 4) is 2.5 gms/cm². Figure 2

shows further details of the chemical composition; it reveals that the nuclei of even Z tend to predominate over those of odd Z . There also appears to be a dearth of elements in the region just before calcium. Recent studies have indicated that electrons in the energy interval greater than 100 MeV constitute approximately 1% of the primary beam (refs. 5 and 6).

Energy Distribution

The next distinguishing feature of the galactic radiation is the energy spectrum. Observations now extend from 10^7 to 10^{19} electron volts. Particles with total energies of approximately 10^{20} electron volts have been observed (ref. 7). Figure 3 shows the integral flux values over the complete range. In the region up to approximately 20 GeV, data have been obtained (refs. 8 and 9) by direct observations with satellites,

TABLE I

*Chemical Composition
Galactic Cosmic Rays*

Group	Z	Intensity/meter ² -ster-sec > 1.5 GeV/Nuc	Intensity / Intensity Z ≥ 10	Average in universe *
Hydrogen.....	1	1300	680	3360
Helium.....	2	88	46	258
Li, Be, B.....	3 - 5	1.9	1.0	10 ⁻⁵
C, N, O, F.....	6 - 9	5.7	3.0	2.64
Z ≥ Neon.....	≥ 10	1.9	1.0	1.
Z ≥ Calcium.....	≥ 20	.53	.28	.06

* After Suess and Urey.

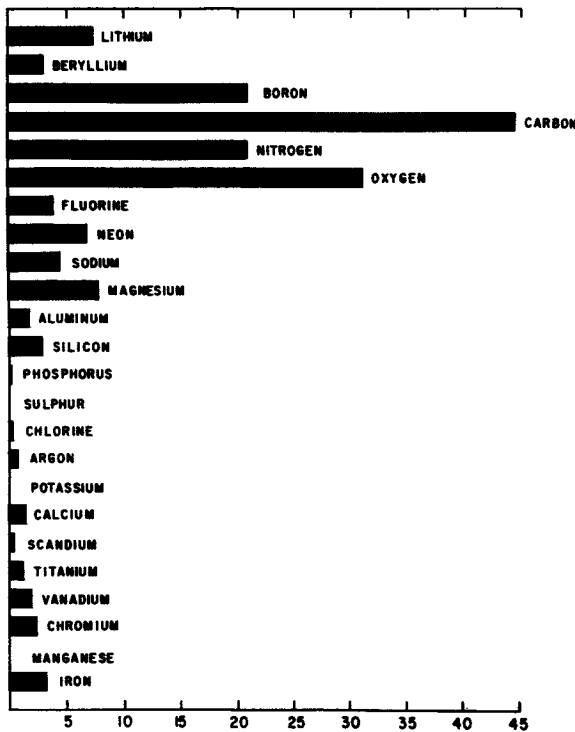


FIGURE 2.—Relative intensity of charge particles Z > 2.

space probes, or balloons. The intermediate region around 10¹² eV data have been obtained by the study of high energy interactions underground (refs. 10 and 11); and the highest energy (> ~10¹⁵ eV) data are based on studies of extensive air showers (refs. 12 to 14). The best estimate now is that if we represent the integral spectra in the form

773-446 O-65-3

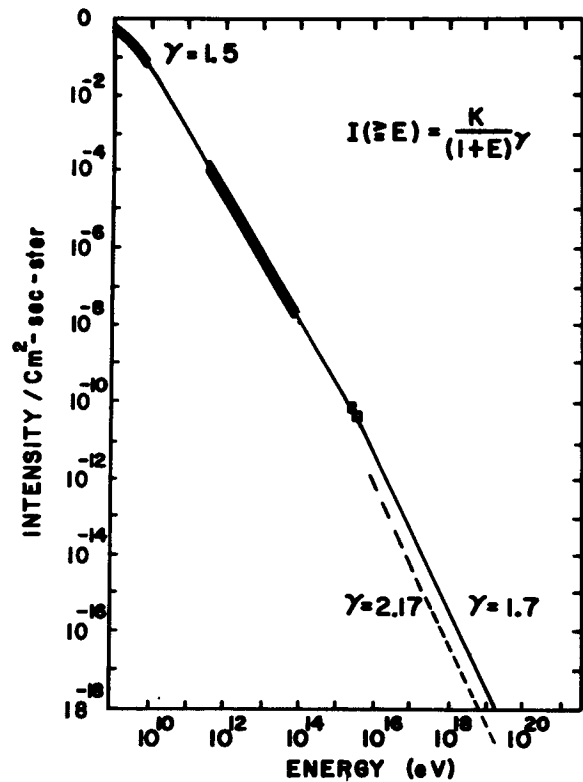


FIGURE 3.—Integral energy spectrum of primary nucleons.

$$J(\geq E) = \frac{K}{(1+E)^\gamma} \text{ particles/cm}^2\text{-sec-ster with kinetic energy } > E(\text{GeV})$$

γ changes from 1.5 at the lowest energy interval to a value in the range 1.7 to 2.17 at the highest. Recent data tend to suggest that at even higher energies γ possibly assumes a smaller value.

The best experimental evidence at present indicates that, in the range 10^9 to 10^{15} eV, the charge composition is not a function of energy. As one goes to much lower energies, it is expected that the energy loss in the traversal of the 2.5 gms/cm² of hydrogen will play an important role and one should then see different energy spectra in this region for different components. Figure 4 shows the low energy differential spectra for protons extending down to approximately 10 MeV. These measurements (refs. 15 to 19) were taken in mid 1963 and 1964 and presumably represent conditions just prior to solar minimum. It is observed that the low energy portion of the spectrum is steeply falling as a function of energy. In the region 10 to 100 MeV, these measurements were made aboard the IMP-1 spacecraft.

Spatial Distribution

It appears that the primary cosmic radiation is essentially isotropic over the celestial sphere. The amplitude of anisotropy (refs. 20 and 21) is probably not greater than 1% in the region up to approximately 10^{15} eV. At medium energies (greater than ~ 500 MeV), there may be small anisotropies associated with the solar modulation. Studies in the low energy range (10 MeV to approximately 300 MeV, for example) have not been made.

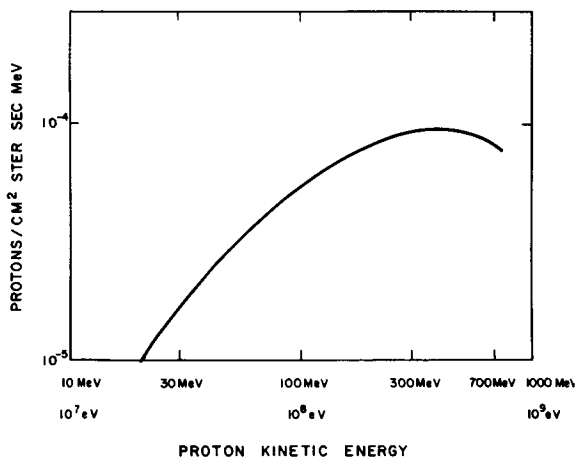


FIGURE 4.—Low energy differential energy spectra of primary cosmic ray protons in time interval close to solar maximum.

SOLAR COSMIC RAYS

During the period 1956 to 1963, there were at least 64 occasions when the sun accelerated nuclei to energies greater than a few MeV, and these particles were subsequently detected in the vicinity of the earth. These solar cosmic ray events are of fundamental scientific importance. Not only should they provide information on solar processes, but their propagation characteristics should give new clues to the magnetic field configurations in the vicinity of the sun and in interplanetary space. These solar particle outbursts also pose important considerations for manned space travel in such programs as the forthcoming Apollo flights. Some of the pertinent features of these events—size and frequency of occurrence, energy and charge spectra, and propagation characteristics—will be summarized here.

Frequency and Size Distribution

The solar production of cosmic rays was first observed by Forbush (ref. 22) in 1942 by means of sea level ionization chambers. Neutron monitors, introduced in 1949, offered greater sensitivity but still responded primarily to particles with kinetic energies >1 GeV at the top of the atmosphere. The identification of polar-cap absorption events with solar particle emission by Bailey (ref. 23) provided a means of extending the observations to much lower particle energies. This method was extended by Reid and Collins (ref. 24). It is based on the attenuation of galactic radio noise due to the enhanced ionization produced by these events in the vicinity of the polar *D* layer. Finally, the direct particle observations by balloon, rocket, and satellite-borne instrumentation have greatly extended our knowledge of these events. By using all these methods (ref. 25), some 64 events have been detected over the interval around solar maximum. There were probably additional small events which were not detected.

Because of the uncertainty in the detection of small events, it seems worthwhile to introduce a threshold and to consider only those events which are greater than this threshold. The arbitrarily chosen threshold is limited to those

with a minimum integrated intensity of 10^6 particles/cm² at energies >30 MeV observed at the earth. (This is comparable to the integrated intensity of the galactic cosmic radiation for one week.) This, then, reduces the total number of events to 30 over the six-year period (ref. 24).

The 12 and 15 November 1960 events certainly are two of the largest events ever recorded. Since these two events were studied in detail by a number of rocket, balloon, and satellite observations combined with numerous riometer and neutron monitor measurements, they are by far the best documented of the great events. The time history of these two events (ref. 26) is shown in figures 5 and 6. It is to be understood that the second event follows immediately after the first. In the 12 November event, there are two maxima displayed in the >500 MeV region. The second maximum is associated with the passage of a plasma cloud that also generated a large magnetic storm and produced a Forbush decrease (which can be

described as a depression or sweeping out of the galactic cosmic rays).

The event on 15 November 1960 was marked by strong anisotropy during the first hour (ref. 17). The high intensity phase has a very rapid rise followed by a regular decay (fig. 6). The integral flux greater than 20 MeV reached a maximum 20 hours after the flare. Again, in figure 6, the integral time history at three energy levels is shown.

Charge Composition

The charge composition of the cosmic radiation was first studied extensively by Fichtel et al. (refs. 28 and 29). They observed a proton/medium nuclei (medium nuclei=carbon, nitrogen and oxygen) ratio of ~ 2000 in the energy range 42.5 MeV to 95 MeV; a proton/helium ratio of 33 in the same energy interval; and a helium/medium ratio of 60. While these small abundances imply that heavy nuclei are not of importance from the manned space travel viewpoint, nevertheless the fact that the sun accelerates these nuclei to moderate energies is of enormous astrophysical significance. The charge spectrum of Biswas, Fichtel, and Guss is given in table II. All values have been normalized to a base of oxygen=10. Also shown for comparison is the relative abundance in the solar atmosphere and in the galactic cosmic rays. It is seen that the solar cosmic rays agree well with the relative abundance in the solar atmosphere and differ significantly in several areas from that observed in the galactic cosmic rays.

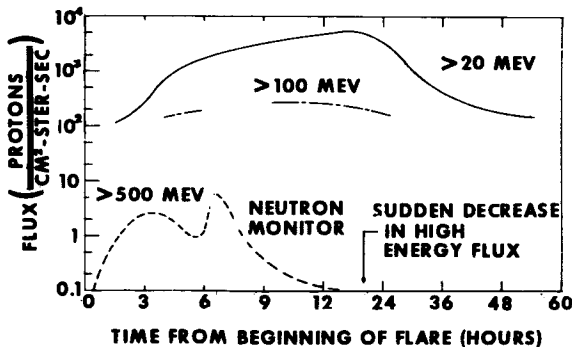


FIGURE 5.—Time history of three integral energy regions from 12 November 1960 event.

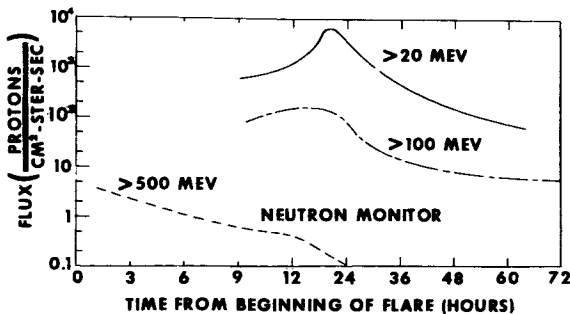


FIGURE 6.—Time history of three integral energy regions from 15 November 1960 event.

ENERGY SPECTRUM OF THE SOLAR COSMIC RAYS

It is important to determine the spectral characteristics of the solar cosmic rays. To date, the methods it has been possible to devise cover only a small dynamic range in energy for fixed n . The general practice has been to represent the differential spectrum of the solar particles in the form $dJ/dE = K/E^n$ where E is the kinetic energy and n varies over the range 1 to 6. In order to apply this formula over an extended dynamic range, it is necessary to vary n as a function of energy, that is, to have n decrease as the energy decreases. The measurements of alphas and heavy nuclei strongly suggest that both charge components display the

TABLE II

Relative Abundances of Nuclei Normalized to a Base of 1.0 for Oxygen

Element	Solar cosmic rays	Sun	Universal abundances	Galactic cosmic rays
${}^2\text{He}$	017 ± 14	?	150	48
${}^3\text{Li}$	-----	$\ll 0.001$	$\ll 0.001$	0.3
${}^4\text{B-}{}^9\text{B}$	< 0.02	$\ll 0.001$	$\ll 0.001$	0.8
${}^6\text{C}$	0.59 ± 0.07	0.6	0.3	1.8
${}^7\text{N}$	0.19 ± 0.04	0.1	0.2	≤ 0.8
${}^8\text{O}$	1.0	1.0	1.0	1.0
${}^9\text{F}$	< 0.03	$\ll 0.001$	$\ll 0.001$	≤ 0.1
${}^{10}\text{Ne}$	0.13 ± 0.02	?	0.40	0.30
${}^{11}\text{Na}$	-----	0.002	0.001	0.19
${}^{12}\text{Mg}$	0.043 ± 0.011	0.027	0.042	0.32
${}^{13}\text{Al}$	-----	0.002	0.002	0.06
${}^{14}\text{Si}$	0.033 ± 0.011	0.035	0.046	0.12
${}^{15}\text{P-}{}^{21}\text{Sc}$	0.057 ± 0.017	0.032	0.027	0.13
${}^{22}\text{Ti-}{}^{28}\text{Ni}$	≤ 0.02	0.006	0.030	0.28

same rigidity spectrum (ref. 28). It is most convenient to think of rigidity simply as momentum per unit charge. Freier and Weber (ref. 30) have proposed a representation in the form of exponential rigidity as given by the formula

$$\frac{dJ}{dP} = \frac{dJ_o(t)}{dP} \exp \left[-\frac{P}{P_o(t)} \right],$$

where P_o is a characteristic rigidity which is a function of time, dJ_o/dP also is a function of time, and P is the particle rigidity. This has produced a remarkable simplification of the spectra of the solar cosmic rays as shown in figure 7. It is still debatable how low in energy a rigidity representation can be extended. In most events it is not applicable in the region below 50–30 MeV; below 30 MeV, it predicts an intensity which is too low compared to the observations. It does, however, appear to be well followed in the higher energy regions. It has been observed that both P_o and J_o are functions of time. These are shown for the November 1960 events in figure 8. The conventional representation for these events has been discussed in a previous section of this paper. While P_o appears simply to decrease as a function of time, J_o displays a complex behavior which is probably strongly dependent on the interplanetary electromagnetic condi-

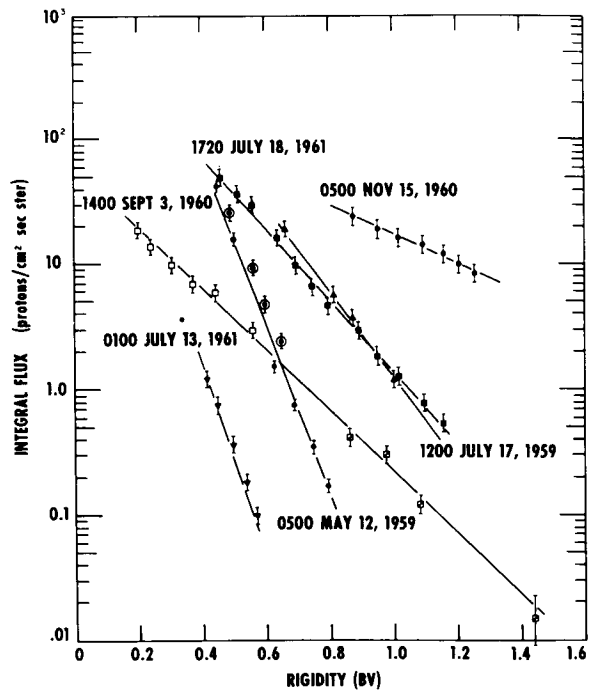


FIGURE 7.—Integral proton spectra are shown as exponentials in rigidity at selected times for six different solar flares. Data points taken from counter ascents are shown as solid symbols; those taken with emulsion are shown as open symbols.

tions near the earth's orbit. For example, at the time of the November 15 cosmic ray flare, a solar plasma front was enroute to the earth from

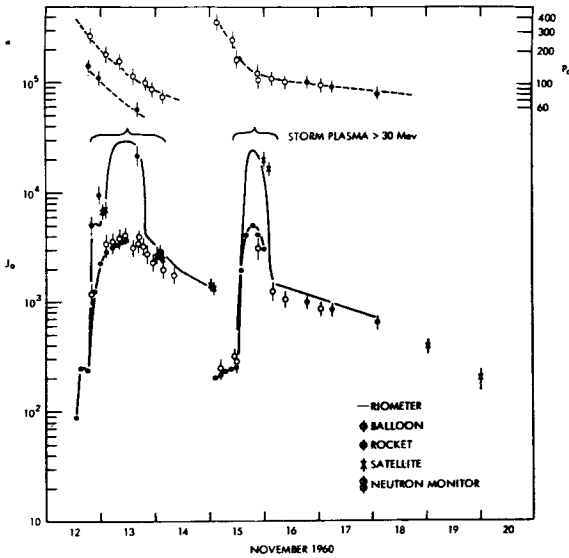


FIGURE 8.—Time history of the intensity and spectrum of solar particles during the events of November 1960. The values of J_0 are determined by various techniques and include riometer, balloon, rocket, satellite, and neutron monitors.

a previous flare in the same solar region. Following the sudden commencement on November 15, the total intensity of solar particles increased by an order of magnitude, and the spectrum steepened appropriately. This is reflected in the strong increase in J_0 at that time. A similar behavior is noted for the plasma cloud associated with the 12 November event. It is important to note that this technique is not applicable for the onset or beginning of the solar flare and applies only when a reasonable equilibrium has been established following flare maximum.

PROPAGATION CHARACTERISTICS

The data obtained from the satellites and space probes have made it possible to observe in detail the onset and decay phase for a number of solar proton events. One example of a great variety of data that has been collected by a number of observers is the 85 MeV data from Explorers XII and XIV which is shown in figure 9. The detailed energy spectrum for the 28 September 1961 event is shown as a function of time (refs. 31 and 32) (fig. 10). This particular event can be characterized as medium sized but contains several striking features.

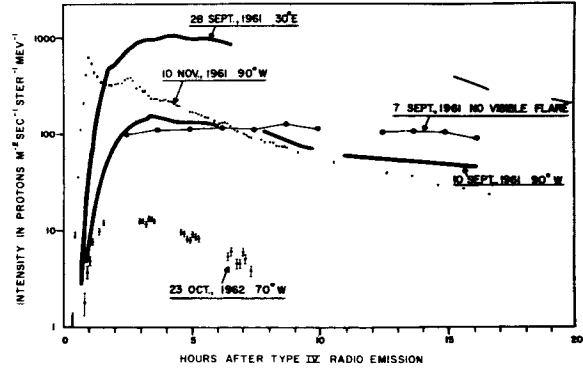


FIGURE 9.—The intensity of 85-MeV protons versus time after the type IV emissions during the five primary solar proton events. The shapes of only two events, those of 28 September 1961 and 23 October 1962, are seen to be quantitatively similar, as monitored in this manner.

For example, in figure 11 the behavior of the intensities of the various differential components for this event has been plotted not as a function of time but simply as a function of distance travelled. Distance travelled is simply the product of particle velocity and the time from the flare. The intensity curves of the various components have then been vertically scaled to give the best fit to a common curve. It is then noted that all components lie very closely on a common curve. This has been interpreted by the authors as a measure of the probability that a particle should travel a given distance before reaching the earth from the sun.

The fact that they fall on a common curve shows that particles of all energies travel a given path length with equal probabilities. The distance travelled by most particles is an order of magnitude larger than one astronomical unit. This indicates that propagation involves an important degree of scattering. Furthermore, in the energy region studied, that is, below 1 GeV, the degree of scattering is not a function of energy. This suggests that the mode of propagation is a diffusion-like process. A number of other observers (refs. 32 and 34) have been able to fit solar proton data to a simple diffusion process as represented by (ref. 33)

$$\mu(M, t) = \frac{N}{2\pi^{1/2}\tau^{3/2}} \exp\left(-\frac{MR}{4\tau}\right),$$

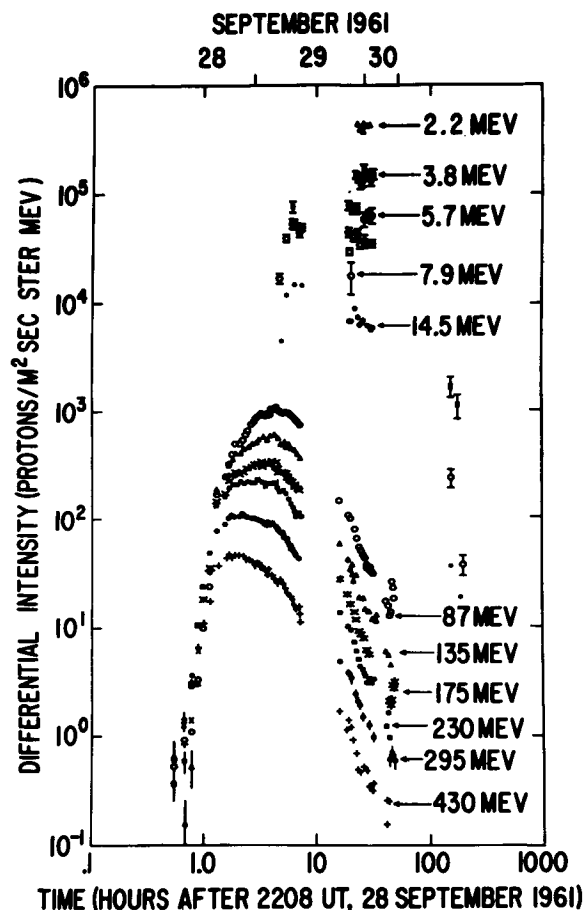


FIGURE 10.—The differential intensities of solar protons during the 28 September 1961 event plotted against time after the X-ray burst at the sun. The data were interrupted when the satellite passed through the magnetosphere and when the delayed increase occurred on 30 September 1961.

where

$$\begin{aligned}
 N &= \text{particle/unit energy/solid angle at} \\
 &\quad \text{source measured at } \tau=0, \\
 R &= \text{distance from source, and } \tau=Qt \\
 &\quad \text{where } Q=w\lambda/3, w=\text{particle velocity,} \\
 &\quad \lambda=\text{diffusion mean free path.}
 \end{aligned}$$

It has also generally been necessary to add a boundary to explain the observed change from a power law to exponential data. The present simple representation of velocity dependence makes it possible to extrapolate back to zero distance (ref. 31), and this extrapolation makes

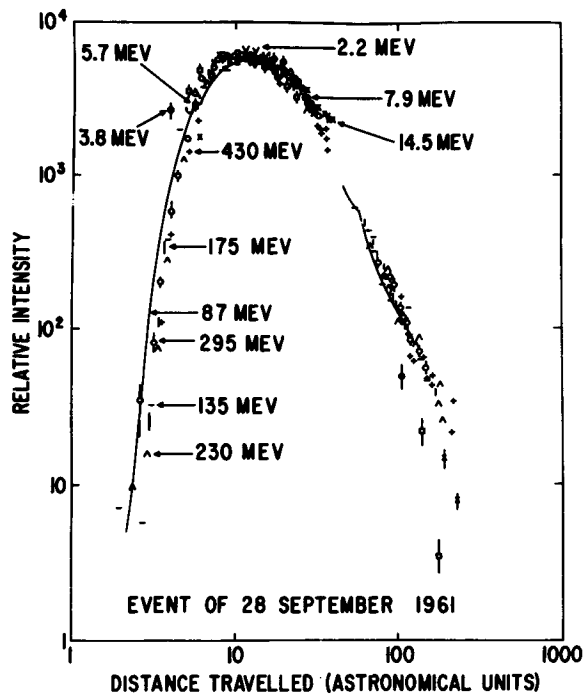


FIGURE 11.—The intensity versus time plots for the 28 September 1961 event (figure 10) converted to relative intensity versus distance plots. The distance is computed for each energy component by taking the product of the corresponding particle velocity and time from the event; the intensities are scaled to give the best fit to a common propagation curve. This fit occurs over a dynamic range in energy of a factor of a few hundred, a velocity range of a factor of 14, and a time duration of several days.

it possible to determine the source spectrum. These are shown for a number of events in figure 12. The source spectra appear to be well represented by power laws in kinetic energy. This is not in disagreement with the representation of the spectra in the form of exponential rigidity. In the latter case, one is dealing with particles after they have propagated through interplanetary space, while the source spectra represent the particles at the sun immediately following acceleration. In the event of 28 September 1961, a great increase was observed at the time of the large magnetic storm some 50 hours after the primary event. It was almost an order of magnitude increase in the low energy particles as seen in figure 13. This was followed by a small recurring event (fig. 14) some 27 days later

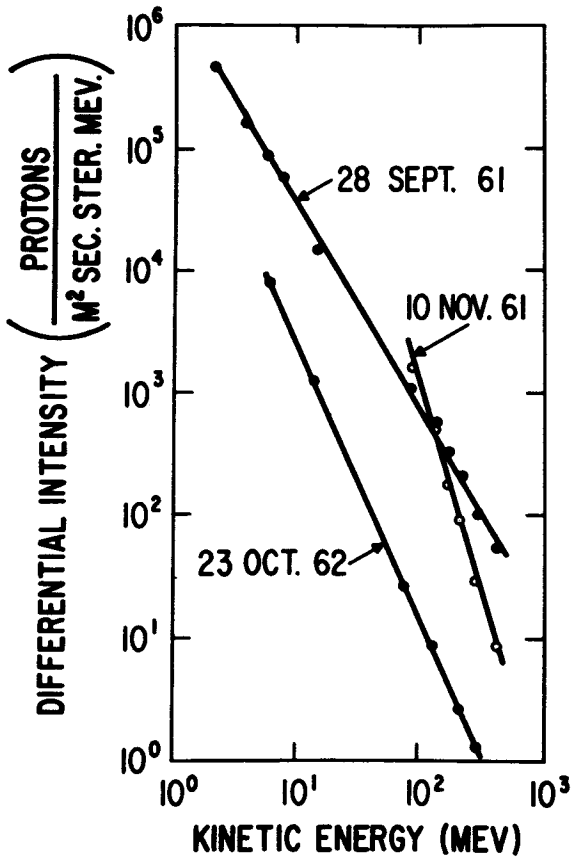


FIGURE 12.—The source spectra of three solar proton events. The intensities plotted are arbitrarily chosen to show the maximum intensities reached at the earth; as explained in the text, the relative scaling of the two sections of the spectrum of 10 November is not necessarily meaningful. In the case of the solar proton events which totally conform to a velocity-dependent behavior, such as those of 28 September 1961 and 23 October 1962, the source spectrum is the unique differential energy spectrum of the protons at the time of their escape from the sun; in each event the source spectrum is proportional to that shown here with a constant which depends in an unknown way on the geometry of propagation.

when the same solar region again passed central meridian.

It now appears that these recurring events are a common feature of active regions. However, they contain predominantly low energy particles, that is, less than ~ 50 MeV with steeply falling energy spectra, and do not change the picture in terms of the radiation hazards to man in space.

Consistent with these observations are the studies by Guss (ref. 35) of the distribution in

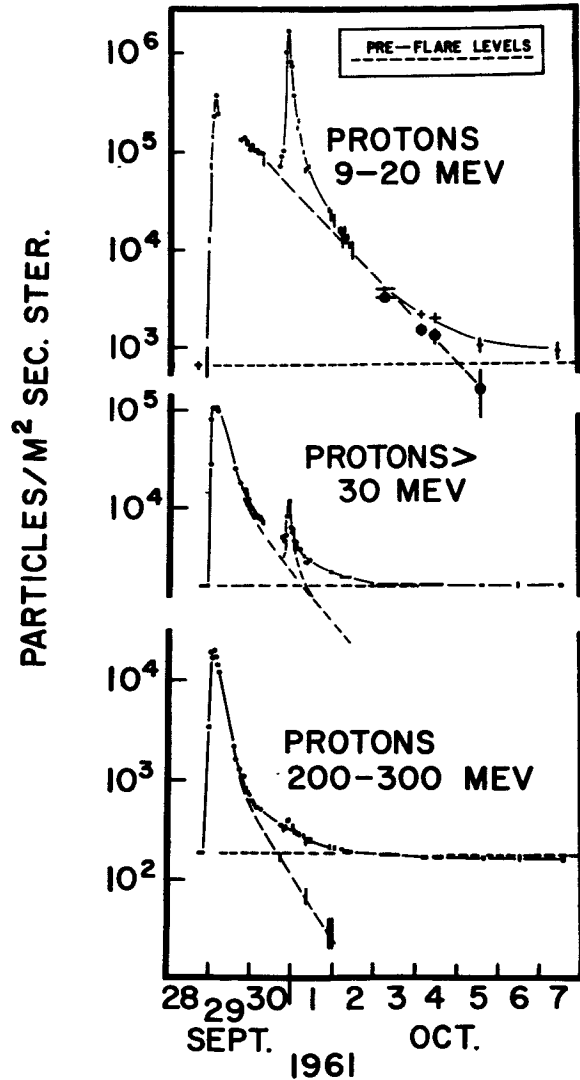


FIGURE 13.—Representative proton intensities between 28 September and 7 October, showing the delayed intensity increase of predominately lower-energy protons on 30 September 1961. The energy spectra of these particles are relatively constant with time, unlike those of the velocity-ordered primary solar proton event, and their arrival times are essentially constant with energy, occurring at the time of arrival of the enhanced solar plasma, two days after the flare.

heliographic longitude of flares which produce energetic solar particles. Guss has found that flares from a single 10° interval in heliographic longitude caused most of the large solar particle events over the last solar cycle. He has interpreted this to indicate the existence of a center for the formation of active regions which persisted for more than 73 rotations. Figure 15

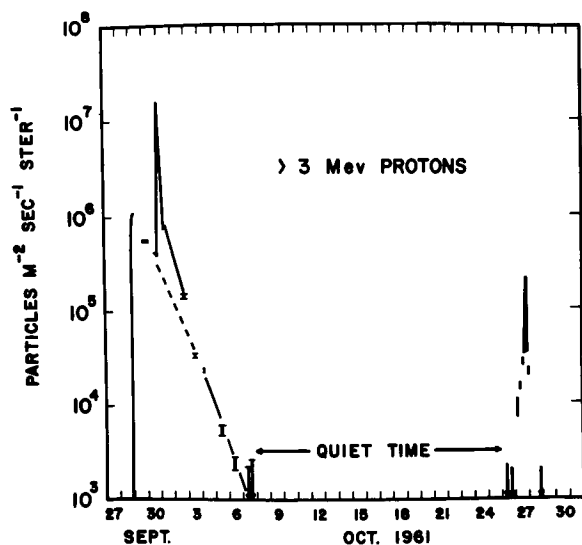


FIGURE 14.—The intensity of protons of energy above 3 MeV between 30 September and 28 October 1961. The delayed increase on 30 September is superposed on the primary solar-proton intensity decay, and the recurrent event on 27 October follows the completely event-free intervening period.

shows the heliographic longitudes for flares which produced solar particle events between 1955 and 1962 during the last solar cycle. The series of flares between 80° and 90° produced the largest particle events of that cycle—the event of 23 February 1956 and the multiple events of July 1959, November 1960, and July 1961. The remainder of the events during the last solar cycle also fall into longitude bands, but not so sharply defined. Guss found that the events between 240° and 280° , with one exception, occurred between 20 January 1957 and 23 March 1958, indicating the existence of an active site which lasted for more than a year. The events between 210° and 220° are those of March through September 1960. The interval between 160° and 190° contained events which occurred between 9 August 1957 and 10 May 1959. The interval between 110° and 140°

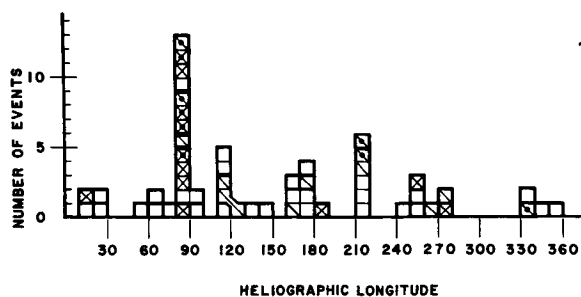


FIGURE 15.—Number of solar particle events versus heliographic longitude with the central meridian during the 23 February 1956 event set to 0° , and assuming a rotation period of 27.04 days. The particle intensity with kinetic energy >30 MeV detected at the earth⁸ integrated over the particle event is X, $I \geq 10^8$ particles/cm²; \square , $I \geq 5 \times 10^6$ particles/cm²; open squares, $I < 5 \times 10^6$ particles/cm². A dot in a square signifies that there was a neutron-monitor rate increase, indicating the presence of a significant number of particles with kinetic energy greater than about 5000 MeV. Light lines are used to separate individual events and heavy lines to separate individual active regions.

includes events from 6 June 1958 to 22 August 1958 and the two small events of 10 September and 28 September 1961. Finally, he observed a dearth of activity in the longitude interval between 280° and 80° . Thus, a single well-defined longitude region was responsible for most of the intense particle events of the last solar cycle. The fact that this region can be compressed into a 10° band of longitude with a suitable choice of the period of solar radiation would indicate that this site rotated at constant rate as observed through the variable rotation of the photosphere.

Several excellent summaries on solar protons have appeared. These include a review of solar cosmic ray events by W. R. Webber in the AAS-NASA Symposium on the Physics of Solar Flares (ref. 36) and D. K. Bailey (ref. 37) in the Tenth Report of the Inter Union Commission on Solar and Terrestrial Relationships.

REFERENCES

1. DAINTON, A. D.; FOWLER, P. H.; and KENT, D. W.: *Phil. Mag.*, vol. 43, 1952, p. 729.
2. McDONALD, F. B.: *Nuovo Cimento Suppl.*, vol. 8, 1958, p. 500.
3. WADDINGTON, C. J.: *J. Phys. Soc. Japan*, vol. 17, Suppl. A-III, 63, 1962.
4. BADHWAR, G. D.; DANIEL, R. R.; and VIJAYALAKSHMI, B.: *Prog. Theoret. Phys.*, vol. 28, 1962, p. 607.
5. EARL, J. A.: *Phys. Rev. Letters*, vol. 6, 1961, p. 125.
6. MEYER, P.; and VOGT R.: *Phys. Rev. Letters*, vol. 6, 1961, p. 193.
7. LINSLEY, J.: *Phys. Rev. Letters*, vol. 10, 1963, p. 146.
8. McDONALD, F. B.: *Phys. Rev.*, vol. 109, 1958, p. 1367.
9. WEBBER, W. R.; and McDONALD, F. B.: *J. Geophys. Res.*, vol. 69, 1964, p. 3097.
10. BROOKE, G.; HAYMAN, P. J.; KAMIYA, Y.; and WOLFENDALE, A. W.: *Nature*, vol. 198, 1963, p. 1293.
11. BARADZEI, L. T.; RUBTSOV, V. I.; SMORODIN, Y. A.; SOLOUYOV, M. V.; and TOLKACHEW, B. V.: *J. Phys. Soc. Japan*, vol. 17, Suppl. A-III, 433, 1962.
12. DELVAILLE, J.; KENOZORSKI, F.; and GREISEN, K.: *J. Phys. Soc. Japan*, vol. 17, Suppl. A-III, 76, 1962.
13. LINSLEY, J.; SCARSI, L.; and ROSSI, B.: *J. Phys. Soc. Japan*, vol. 17, Suppl. A-III, 91, 1962.
14. VERNOV, S. N.; KHRISTIANSEN, G. B.; ATRASHKEVICH, V. I.; DIMITRIEV, V. A.; FOMIN, YU.; KHRENOV, B. A.; KULIKOV, G. V.; NUCHIN, YU. A.; and SOLVIYEVA, V. A.: *J. Phys. Soc. Japan*, vol. 17, Suppl. A-III, 118, 1962.
15. McDONALD, F. B.; and LUDWIG, G. H.: *Phys. Rev. Letters*, 1964.
16. BALASUBRAHMANYAN, V. K.; and McDONALD, F. B.: *J. Geophys. Res.*, vol. 69, 1964, p. 3289.
17. FICHEL, C. E.; GUSS, D. E.; KNIFFEN, D. A.; and NEELAKANTAN, K. A.: *J. Geophys. Res.*, vol. 69, 1964, p. 3293.
18. FREIER, P. S.; and WADDINGTON, C. J.: *Phys. Rev. Letters*, vol. 13, 1964, p. 108.
19. ORMES, J.; and WEBBER, W. R.: *Phys. Rev. Letters*, vol. 13, 1964, p. 106.
20. CONFORTO, A. M.: *J. Phys. Soc. Japan*, vol. 17, Suppl. A-III, 144, 1962.
21. GREISEN, K.: *Progr. Cosmic Ray Phys.*, vol. 3, 1, 1956.
22. FORBUSH, S. E.: *Phys. Rev.*, vol. 70, 1946, p. 771.
23. BAILEY, D. K.: *J. Geophys. Res.*, vol. 62, 1957, p. 431.
24. REID, G.; and COLLINS, C.: *J. Atmospheric Terrest. Phys.*, vol. 14, 1959, p. 63.
25. *Solar Proton Manual* (Frank B. McDonald, ed.), NASA TR R-169, Dec. 1963.
26. FICHEL, C. E.; GUSS, D. E.; and OGIWIE, K. W.: *Solar Proton Manual*, NASA TR R-169, Dec. 1963.
27. McCracken, K. G.: *J. Geophys. Res.*, vol. 67, 1962, p. 447.
28. BISWAS, S.; and FICHEL, C.: *Astrophys. J.*, vol. 139, 1964, p. 941.
29. BISWAS, S.; FICHEL, C. E.; and GUSS, D. E.: *Phys. Rev.*, vol. 128, 1962, p. 2756.
30. FREIER, P. S.; and WEBBER, W. R.: *J. Geophys. Res.*, vol. 68, 1962, p. 1605.
31. BRYANT, D. A.; CLINE, T. L.; and McDONALD, F. B.: *Studies of Solar Protons with Explorers XII and XIV*. NASA Tech. Publ. X-611-64-217.
32. BRYANT, D. A.; CLINE, T. L.; DESAI, U. D.; and McDONALD, F. B.: *J. Geophys. Res.*, vol. 67, 1962, p. 4983.
33. PARKER, E. N.: *Interplanetary Dynamical Processes*. Interscience, 1963, p. 210.
34. HUFFMAN, D. J.; and WINCKLER, J. R.: *J. Geophys. Res.*, vol. 68, 1963, p. 2067.
35. GUSS, D. E.: *Phys. Rev. Letters*, vol. 13, 1964, p. 363.
36. WEBBER, W. R.: *AAAS-NASA Symp. on the Physics of Solar Flares* (W. Hess, ed.), NASA SP-50, 1964.
37. BAILEY, D. K.: *Planetary Space Sci.*, vol. 12, 1964, p. 495.

4—The Magnetosphere and Its Boundary Layer

NORMAN F. NESS

Goddard Space Flight Center, NASA

More than 30 years ago, in an attempt to explain the characteristic storm-time fluctuations of the geomagnetic field, a solar origin was postulated by Chapman and Ferraro (ref. 1). It was suggested that the sun, at times of solar disturbances such as flares, emitted a neutral but ionized gas referred to as a plasma. When this plasma reached the earth, it compressed the earth's magnetic field and contained it in a region of space surrounding the earth. The cavity in the solar plasma thus formed has been termed the Chapman-Ferraro cavity, and the mechanism of its formation has been reasonably successful in explaining the temporal characteristics of various geomagnetic sudden commencement and other storm phenomena. A naive representation of the interaction of the solar plasma with the earth's magnetic field is shown in figure 1. Here the individual particles are assumed to be specularly reflected at the boundary of the earth's magnetic field. The region within the boundary, the geomagnetic cavity, has been referred to as the *magnetosphere* since the dominant factor influencing charged particle motion within this region of space is the earth's magnetic field. In the remainder of this paper, the terminology will utilize magnetosphere rather than the Chapman-Ferraro cavity.

In an attempt to explain the fluctuations and characteristics of type I cometary tails, Biermann (ref. 2) early in the 1950's suggested that a continual flux of solar plasma was required. This was similar to that postulated by Chapman and Ferraro (ref. 1) in their theoretical studies. Subsequent to this, Parker (ref. 3) developed his hydrodynamic theory of the expansion of the solar corona referring to the phenomena as the "solar wind." This was

predicted to consist of ionized gas with the principal constituent being hydrogen and flowing radially from the sun with flux values of 10^7 to 10^{10} particles/cm²/sec. The energy of the particles was assumed to be approximately 1 keV. Direct measurements of this solar wind or plasma have recently been performed by means of satellite measurements conducted both by this country (refs. 4 and 5) and by the USSR (ref. 6). As a part of the overall NASA program investigating the characteristics of the interplanetary medium on a continuing basis, a series of interplanetary Explorer satellites has

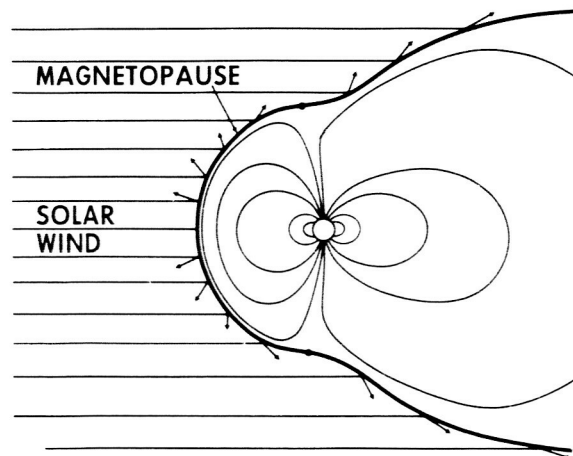


FIGURE 1.—Naive representation of the interaction of the solar plasma with the geomagnetic field. Direct impact of the plasma with the magnetic field is shown as being specularly reflected from the geomagnetic or Chapman-Ferraro boundary. The distance to the boundary at the subsolar point on this basis is given by $R_c = \left[\frac{B_o^2}{4\pi mn V_s^2} \right]^{1/6} R_e$ where R_e is the radius of the Earth, B_o the equatorial magnetic field strength, V_s the velocity of the solar plasma, and n the plasma density (m being proton mass). See Figure 7.

been developed. Figure 2 presents a photograph of the IMP-1 satellite, the first Interplanetary Monitoring Platform in this series which was successfully launched November 27, 1963. It transmitted information on the characteristics of magnetic fields, plasmas, and energetic particles in the region surrounding the earth for a period of more than six months. The apogee of the satellite was $31.7 R_e$ (earth radii) or 197 616 km, with an orbital period of 93 hours. The interaction of the solar wind with the earth's magnetic field leads to a distortion of the earth's magnetic field and also creates a disturbance in the flow field of the solar wind. This paper is concerned principally with the distortion of the earth's magnetic field and the resultant boundary layer region between the magnetosphere and the undisturbed interplanetary medium as measured by the IMP-1 satellite.

A broad complement of experiments in the measurement of energetic particles, low energy plasmas, and magnetic fields was instrumented for flight on the IMP-1 satellite. Table I presents a summary of the various instru-

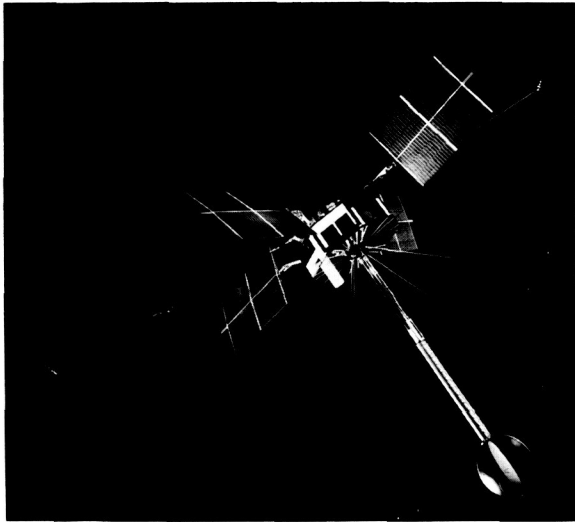


FIGURE 2.—Photograph of the first Interplanetary Monitoring Platform, IMP-1, launched November 27, 1963. The unique appendages extending from the spacecraft octagonal body support magnetometers at remote distances so that the magnetic fields of the electronic components do not contaminate the low field measurements. The satellite weighs 140 pounds and measures 14 feet from tip to tip of the fluxgate magnetometer booms.

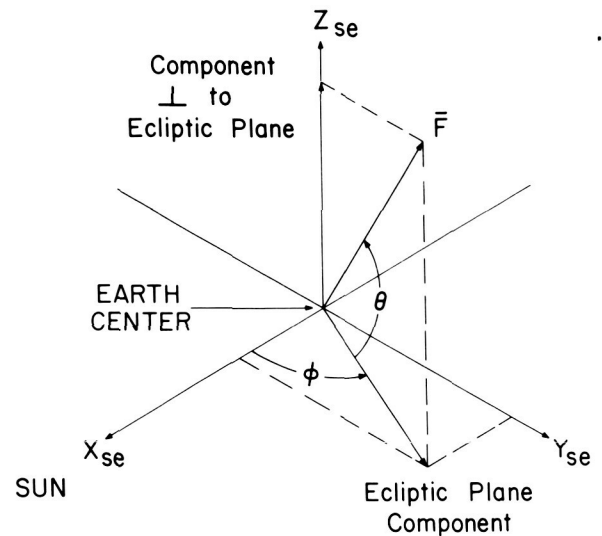


FIGURE 3.—Illustration of the solar-ecliptic coordinate system employed to study the characteristics of the interaction of the solar wind with the geomagnetic field. See text for an explanation of the specific parameters X_{se} , Y_{se} , Z_{se} , θ , and Φ .

ments with their measurement range and energy characteristics. Figure 3 presents the solar-ecliptic coordinate system appropriate for studying the interaction of the solar wind with the earth's magnetic field. In this coordinate system, the X-axis is directed at all times from the earth's center to the sun, the Z-axis is chosen to be perpendicular to the ecliptic plane, and the Y-axis forms a right-handed coordinate system. In addition, two angles are defined to represent a vector field: θ being the latitude, positive above the plane of the ecliptic and negative below; and Φ the longitude, being 0° directed to the sun and 180° when pointed away from the sun. The characteristics of the highly eccentric IMP-1 orbit are shown in figure 4 as projected on the ecliptic plane. The first four orbits are shown, with the figures adjacent to the trajectory indicating the time at which the satellite was at a particular position in space. Upon inspection of this figure, it is noted that, for approximately 60% of each orbit, the satellite is well beyond $20 R_e$ distance from the center of the earth. A corresponding view of the orbit projected on a plane perpendicular to the ecliptic plane is shown in figure 5. It is seen from these two figures that the orbit

TABLE I

IMP Experiment Repertoire

[The separate experiments were provided by both NASA and University laboratories including: Goddard Space Flight Center; Ames Research Center; and the Universities of Chicago, California, and MIT. Details of the various energy ranges and sensor techniques are included.]

Number	Study	Experiment	Characteristics
1	Cosmic rays.....	Range/Energy loss.....	100 keV < P < 200 MeV
2	Cosmic rays.....	Total energy/Energy loss.....	Energy, charge spectra
3	Cosmic rays.....	Neher ionization chamber.....	Total ionization
4	Cosmic rays.....	Orthogonal Geiger-Counter telescope.	Spatial isotropy CR events
5	Magnetic fields.....	Rubidium Vapor Scaler Mag.....	$ \vec{B} < 2000$ gammas
6	Magnetic fields.....	Fluxgate Vector Sensor Mag.....	$\vec{B} < 40$ gammas
7	Solar wind.....	Proton Flux—Electrostatic.....	200 eV < P < 20 keV
8	Solar wind.....	Proton Flux—Faraday Cup.....	10 k/s < Vp < 1000 k/s
9	Solar wind.....	Thermal Ion—Electrons (Charged—Particle Trap).	Few eV < electrons, ions

of IMP-1 is a very elongated ellipse. This paper shall utilize the experimental results obtained from the magnetometers (ref. 7) and the plasma probe (ref. 8) to illustrate the characteristics of the magnetosphere and its boundary region.

The results of the magnetic field measurements on the inbound portion of orbit No. 1 are shown in figure 6. The experimental data are presented as a magnitude \vec{F} and two angles θ and Φ . Each data point represents the av-

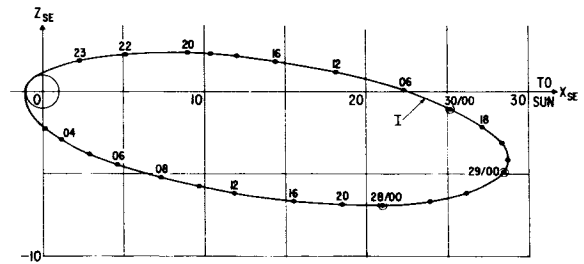


FIGURE 5.—Projection of the first orbit of the IMP-1 satellite as viewed on the X_{se} - Z_{se} plane. The positive Z_{se} axis points towards the north ecliptic pole.

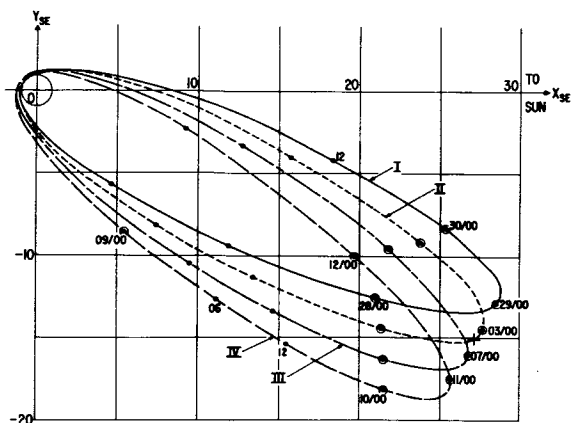


FIGURE 4.—Projection of the first four orbits of IMP-1 satellite as viewed on the X_{se} - Y_{se} plane, the ecliptic plane. The values adjacent to each trajectory orbit refer to the date and/or time in hours when the satellite was located at the indicated points.

verage of the vector magnetic field over a time interval of 5.46 minutes. The satellite is moving approximately 2 km/sec in this region of space so that over this time scale the satellite traverses a radial distance of approximately 660 kilometers. The measurements at geocentric distances beyond $10.7 R_e$ are seen to be highly variable in both magnitude and direction of the magnetic field. However, at a distance of $10.7 R_e$ the magnetic field abruptly increases in magnitude to a value of 60 gammas and assumes a stable configuration. The theoretical magnetic field to be measured in space, extrapolated by spherical harmonic analysis from surface measurements, is shown as dashed lines in this figure. The abruptness in both magnitude and direction, as well as the temporal characteristics of the magnetic field

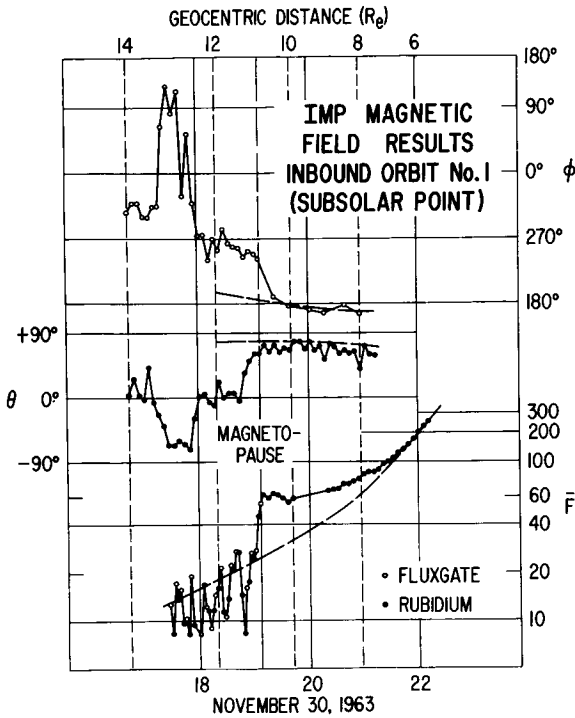


FIGURE 6.—Magnetic field measurements of the boundary of the magnetosphere from IMP-1 inbound orbit No. 1. The abrupt discontinuity in magnitude and direction of the field at $10.7 R_e$ is identified as the boundary. Theoretical values for \bar{F} , θ , and ϕ are shown as dashed curves and do not include any compression of the earth's field by the solar plasma.

at and beyond $10.7 R_e$, are identified as the boundary of the magnetosphere. It is seen that the observed magnitude is approximately twice that which would be theoretically predicted by considering the magnetic field in space to be only that caused by the earth's undistorted magnetic field.

The containment of the earth's field by the solar plasma essentially doubles the magnetic field strength at the boundary surface. This can be understood simply by viewing the plasma impacting the geomagnetic field as being represented by a plane boundary across which the normal component of magnetic field must be zero. This is related to the phenomenon that in a highly conducting plasma, such as the solar wind, the magnetic field is "frozen into" the plasma motion. Hence, as a plasma stream interacts with a magnetic field, it does so by compressing the lines of force ahead of it. Mathematically, this can be represented by

placing an image dipole on the sunward side of the earth at an equal distance from the boundary and, thus, the normal component of the field is zero. This can explain both the magnitude increase of the observed magnetic field as well as the preservation of its direction. This simplified viewpoint is not completely correct, but is substantially valid as long as the discussion refers only to the boundary near the subsolar or stagnation point.

Utilizing this simplified theoretical model of the solar plasma directly impacting the earth's magnetic field permits an interpretation of the solar stream properties on the basis of the size of the earth's magnetosphere. On the assumption that the subsolar radial distance to the magnetosphere boundary is $10.7 R_e$, it is seen in figure 7 that plasma density ranges from 1 to 10 protons per cubic centimeter for velocities between 200 and 600 km/sec. These plasma values are representative of those which have been measured on previous satellites and space

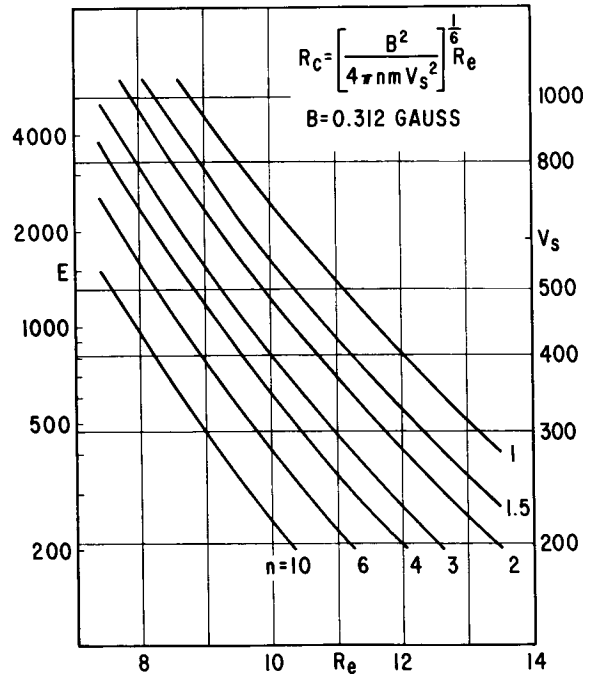
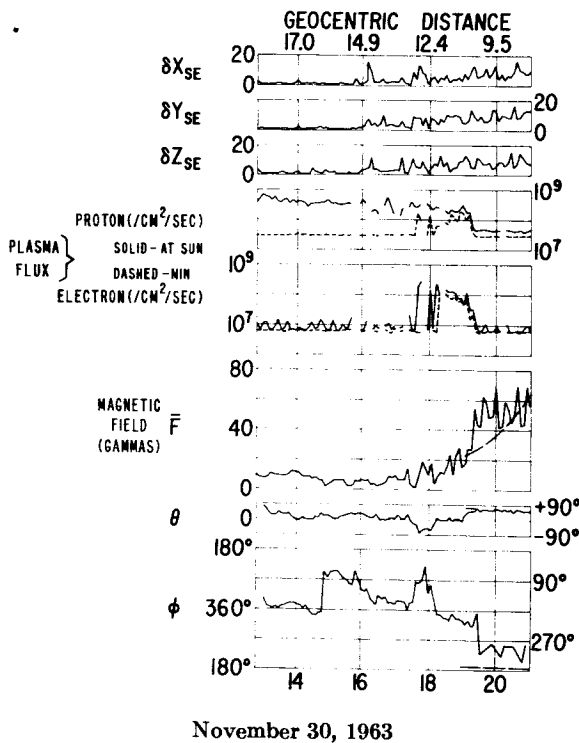


FIGURE 7.—Theoretical size of the magnetosphere at the subsolar point assuming normal impact of the solar plasma on the geomagnetic field. For a magnetosphere of $10.7 R_e$ and assumed velocity of 400 km/sec, the deduced plasma density is found to be 2 p/cm^3 .



November 30, 1963

FIGURE 8.—Time correlated MIT plasma and GSFC magnetic field measurements on IMP-1 inbound orbit 1. The root-mean-squared deviation or variance estimate of the magnetic field is shown as cX , cY , and cZ . The plasma flux values in both a solar and antisolar direction are shown for the plasma probe. Isotropic fluxes immediately outside the magnetosphere boundary terminate at 13.7 R_e . Directional fluxes are observed beyond this boundary, which is identified as a collisionless magnetohydrodynamic shock wave.

probes. Thus, it would appear that the general characteristics of the bounding of the earth's magnetic field by the solar plasma and the distance at which it occurs can be reasonably well understood on the elementary individual particle basis.

However, this is not the complete story on the characteristics of the magnetosphere and its boundary region. A correlated set of data from the MIT plasma probe and the GSFC magnetic field experiment is shown in figure 8. This included the same interval shown in greater detail in figure 6. The important feature of the MIT plasma detector, a Faraday cup, is that it is directionally sensitive to the flow of plasma. As the satellite rotates, the acceptance aperture of the detector scans the celestial sphere and includes orientations directly toward and away from the sun. Shown on this figure

are the plasma flux values when the detector is pointed almost directly toward the sun and directly away from the sun. The difference between these two measurements is a measure of the anisotropy of the plasma flow. It is seen that, at very large distances from the earth, greater than 16 R_e , the plasma flow is principally from the sun. However, at a distance of 13.6 R_e , the flow of plasma suddenly comes apparently from all directions, that is, the flux is isotropic. It is also at this point that the fluctuations in the magnetic field increase appreciably. These are measured by the root-mean-squared deviations shown in the topmost three curves illustrating the X, Y, Z components of the deviation of the magnetic field over the 5.46-minute time intervals. The fluctuating magnetic field and the isotropic plasma are observed until the distance at which the magnetic field abruptly increases to a very large value. This region of space surrounding the earth's magnetosphere in which a thermalized or isotropic plasma flux is observed to be correlated with fluctuating magnetic fields is termed the transition region of the magnetosphere boundary layer. This paper studies this boundary layer, discusses its characteristics, and attempts to present the current concepts related to its formation.

The first measurements, clearly suggesting a continual containment of the earth's magnetic field, were provided on the leeward side of the solar wind plasma flow by the Explorer X satellite in March, 1961 (ref. 9). Over an interval of 48 hours, the magnetic field and plasma were observed in a characteristic pattern in which strong fields directed radially from the earth were exchanged with periods during which radial plasma flow from the sun and fluctuating magnetic fields were observed. Conclusive experimental evidence for the bounding of the geomagnetic field by the solar wind was provided by the Explorer XII satellite measurements of the magnetic field and trapped particle fluxes as reported by Cahill and Amazeen (ref. 10) and Freeman, Van Allen, and Cahill (ref. 11). Subsequent to the Explorer XII, the Explorer XIV satellite provided additional information on these characteristics. Thus far, only limited summaries of the magnetic field in these regions have appeared, although

detailed discussions of the particle flux measurements have been presented in numerous articles. The plasma probes on board the Explorer XII and XIV did not reveal the isotropic fluxes observed on IMP-1.

Although the purpose of the IMP-1 satellite was primarily to investigate the characteristics of the interplanetary medium, the fact that the satellite is gravitationally anchored to the earth implies a traversal of the magnetosphere boundary region twice each orbit. The results of the IMP-1 satellite obtained in these traversals have substantially confirmed and extended our knowledge of the magnetosphere boundary layer. Our overall interpretation of the results is based upon an analogy with high speed aerodynamic flow. It is assumed that the magnetosphere acts as a blunt body which deflects the flow of the solar plasma. An important aspect of the rarefied solar plasma flow is that it contains a magnetic field. The average interplanetary magnetic field value has been accurately established by the IMP-1 satellite (ref. 12). For the average solar proton of 1 keV energy, this leads to a Larmor radius of approximately 500 kilometers. This small characteristic length permits the use of a fluid continuum approximation. This is also approximately the spatial resolution with which the boundaries of both the magnetosphere and the transition region are sampled. In this magnetized plasma, the propagation of disturbances is by magnetohydrodynamic waves as contrasted to the supersonic gas dynamic case when propagation is by acoustic waves. The appropriate propagation velocity, the Alfvén mode, is presented in figure 9 as a function of plasma density and magnetic field strength. The important feature of this diagram is that it shows that, for the interplanetary medium, the Alfvén velocity is characteristically less than 100 km/sec. The estimated velocity of the solar plasma is 385 km/sec from the interpretations of solar magnetic fields and the interplanetary magnetic field (ref. 12). Thus, the flow of the solar wind is supersonic in the magnetohydrodynamic sense. Actually, the flow is hypersonic since the equivalent Mach number or, more appropriately, the Alfvén number is greater than 4. Under such conditions, the well known phenomenon of a

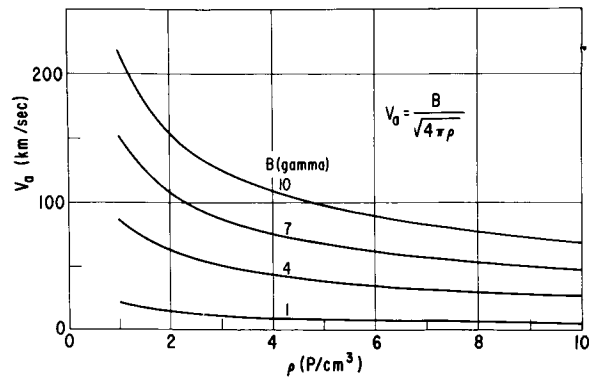


FIGURE 9.—The characteristic velocity of propagation of disturbances in the interplanetary medium is the Alfvén velocity. This magnetohydrodynamic mode is shown as a function of magnetic field strength, B , and plasma density, ρ .

detached shock wave develops in the gas dynamic case which encloses the disturbing body in a region of space with a boundary across which discontinuous changes in parameter values occur. At the present time, the detailed quantitative study of the physical properties of the boundaries as observed by the IMP-1 satellite has yet to be completed. A particular limitation to their detailed study will be the spatial and time resolution limitations inherent in the spacecraft orbit and telemetry system. The detached shock wave which is observed in gas dynamics has characteristics which closely resemble that of the earth's magnetic field interacting with the flow of the solar wind. The termination of the turbulent transition region observed as the satellite moves radially away from the earth is interpreted to be the collisionless magnetohydrodynamic shock wave associated with the interaction of the solar wind with the geomagnetic field. The IMP-1 data have provided the first accurate measurements of this phenomenon and indeed have mapped in detail its position relative to the earth-sun line. This is a most important feature of the boundary of the magnetosphere since it may provide mechanisms for acceleration of charged particles.

Within and adjacent to the transition region, satellite detectors have shown transient fluxes of energetic electrons having energies greater than 45 keV and total fluxes of 10^6 /cm²/sec, an order of magnitude greater than background (refs. 13 and 14). The IMP results suggest

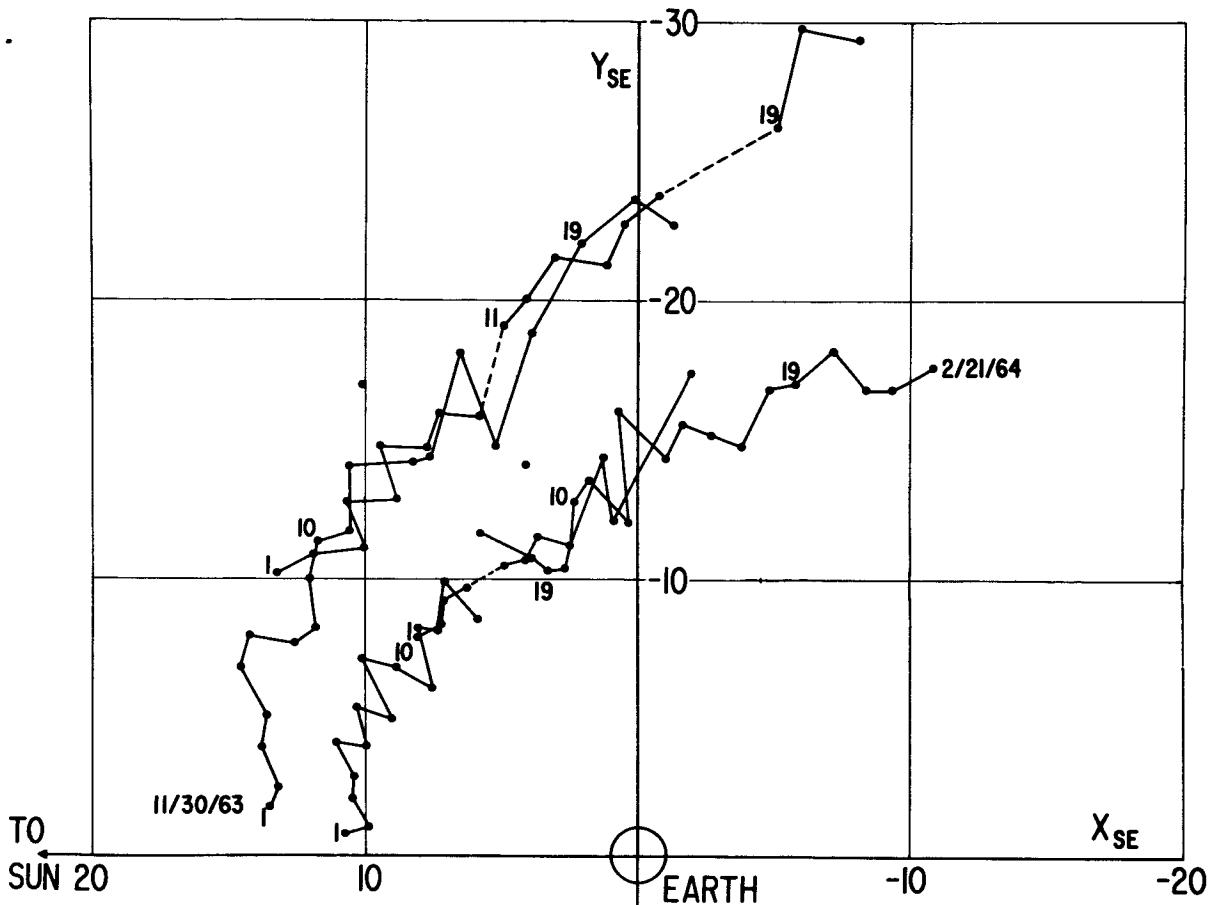


FIGURE 10.—Summary of the observed positions of the magnetosphere boundary and shock wave as determined by the magnetic field experiment on IMP-1. Successive traversals of the boundaries are connected by straight line segments. Orbits number 1 through number 23 are shown and are seen to be approximately parabolic in shape.

that these observations are related to the formation of the magnetosphere and the shock wave boundary. The experimental evidence is very recent, and the full theoretical significance of these data has yet to be completely evaluated. The particle fluxes which are observed are substantially less than those observed within the trapped particle belts within the earth's magnetic field. Hence it is not possible to consider these as hazards to manned space flight travel or to satellite hardware systems when one considers the more important contributions due to the Van Allen radiation belts.

A summary of the observed positions of the shock wave boundary and the magnetosphere boundary is shown in figure 10. In this presentation, the boundaries of the magnetosphere

and transition region as detected by the magnetic field experiment are illustrated. It is seen that the geocentric distance to the shock wave at the stagnation point is approximately $13.4 R_e$, but this distance increases away from the subsolar or stagnation point. This indicates an increase in the thickness of the transition region. The data also indicate that the magnetosphere is not closed, at least to the distance of 10 to 20 R_e behind the earth. The data are suggestive that the magnetosphere trails out far behind the earth in the fashion analogous to *cometary tails*. On this basis, it is reasonable to expect the moon to intersect the earth's magnetosphere once each month (ref. 15).

A comparison of the theoretical shape and position of the shock wave boundary and magnetosphere boundary with observations is

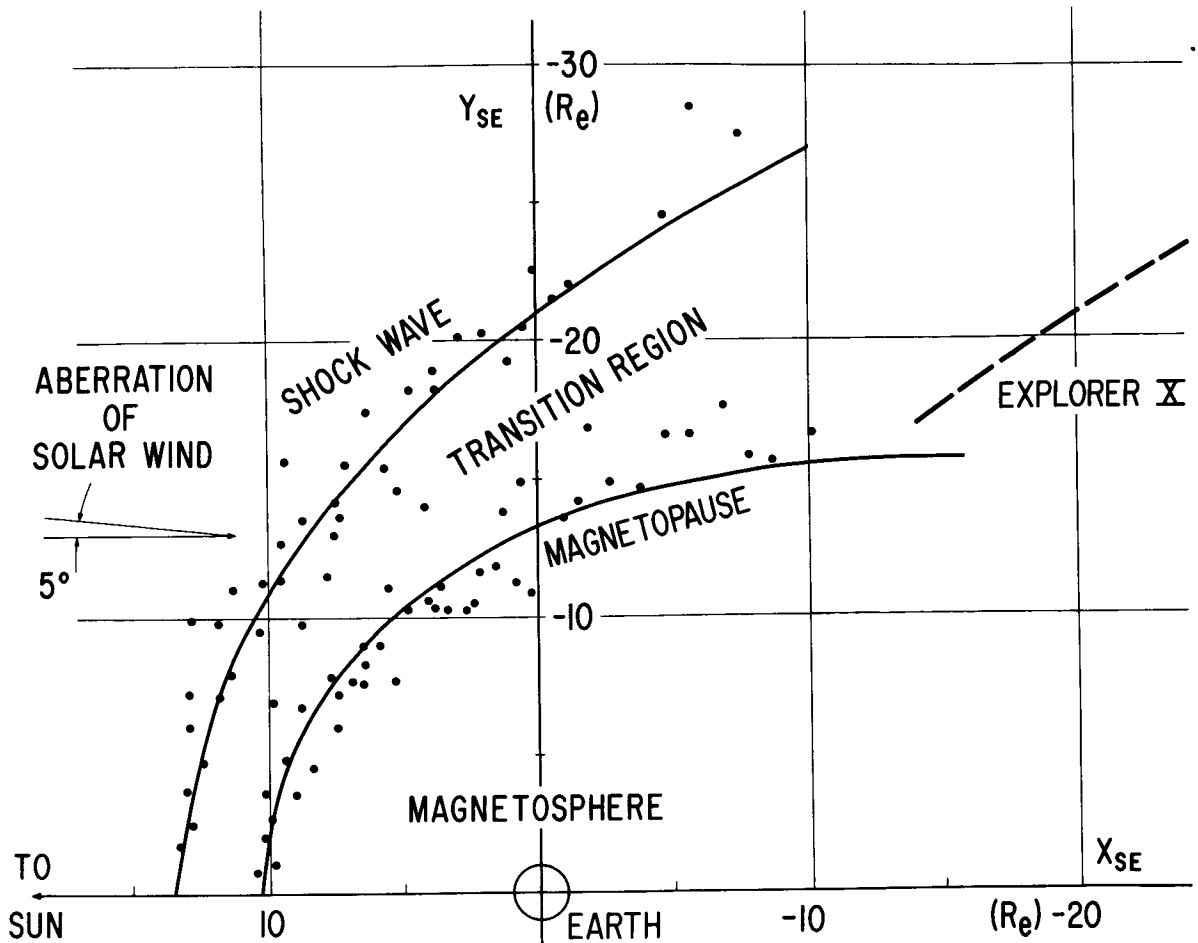


FIGURE 11.—Comparison of the observed positions of the boundary of the magnetosphere and shock wave with the theoretical positions according to Spreiter and Jones (ref. 16). Very good agreement is obtained by slightly modifying their treatment to accommodate the values of magnetosphere radius ($10.25 R_e$) and shock wave radius ($13.4 R_e$) actually observed.

shown in figure 11. Using a gas dynamic ratio of less than 2 but more than $5/3$ permits exact comparison of the data. The small scatter in the position of the boundary crossings is related to the variability of the solar plasma flow. The comparison with theory (ref. 16) is very good and indicates a fundamental characteristic of the interplanetary plasma near the stagnation point and on the scale on which the observations are made. The standoff ratio between the shock wave distance and the magnetosphere boundary is shown in figure 12 as a function of Mach number for two models of the shape of this magnetosphere. One is that of a sphere utilizing the theoretical results by Hida (ref. 17), and the other utilizes the various models

in generally good agreement as represented by Beard (ref. 18) and Spreiter and Jones (ref. 16). The observed value of $1.31 \pm 1\%$ is seen to be between the two limits. For the observed Mach numbers, the standoff ratio is reasonably insensitive to the exact value of Mach number. Hence, time variations in the characteristics of the solar plasma do not affect to first order the standoff ratio, as do the magnetosphere shape and specific heat ratio used in the gas dynamic analogy.

A summary of the description of the magnetosphere and its boundary layer as projected on the plane of the ecliptic is shown in figure 13. In this figure the interplanetary magnetic field is shown at an angle of 135 degrees to the

earth-sun line and in a sense which is positive with respect to flux lines extending from the sun into interplanetary space. The projected positions of the IMP satellite are shown for the first 19 orbits, and the positions of the magnetosphere boundary and shock wave are shown as average positions. Within the transition region is a turbulent plasma flow of very high temperatures with fluctuating magnetic fields. Within the magnetosphere a distorted geomagnetic field is observed, dependent upon the strength of the earth's magnetic field and the strength of the solar wind containing it. Present measurements do not indicate a termination of the magnetosphere on the leeward side of the solar wind flow. It is very possible that the earth's magnetic field trails out $100 R_e$ or more behind it, intersecting the orbit of the moon (ref. 15).

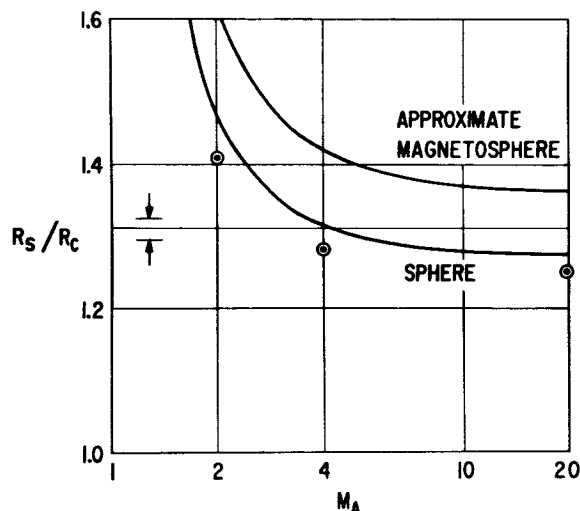


FIGURE 12.—Theoretical standoff ratios (R_s/R_c) for the magnetosphere assuming it to be a sphere or an extended blunt object as a function of Mach number. The observed value of 1.31 is shown intermediate to these two cases.

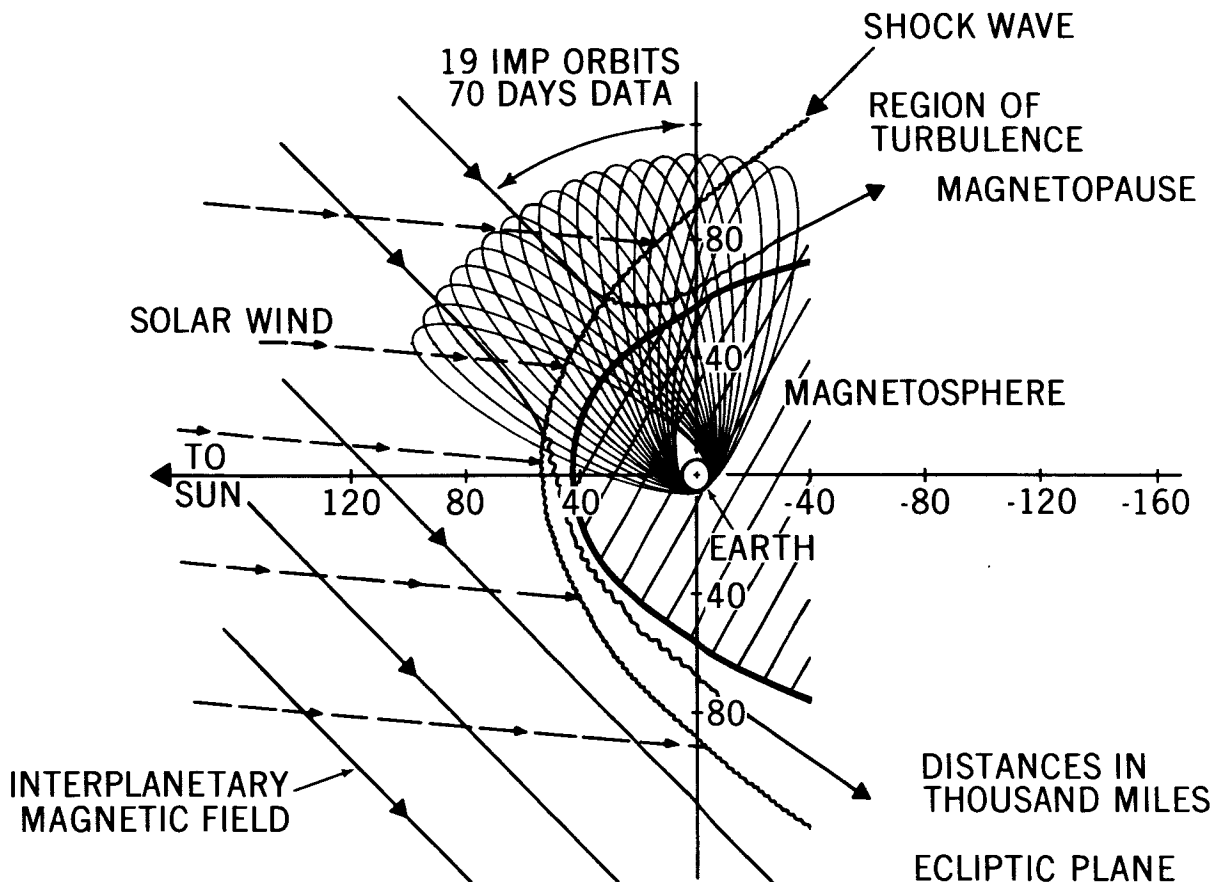


FIGURE 13.—Summary schematic illustration of the magnetosphere shape and boundary layer thickness as deduced from magnetic field measurements on the IMP-1 satellite. The flow of solar plasma, the solar wind, is taken to be aberrated by 5° west of the Sun because of the heliocentric orbital motion of the Earth.

REFERENCES

1. CHAPMAN, S.; and FERRARO, V. C. A.: A New Theory on Magnetic Storms. *Terr. Mag. and Atmos. Elec.*, no. 36, 1931, pp. 77-97, 171-186; no. 37, 1932, pp. 147-156, 421-429; no. 38, 1933, pp. 79-96.
2. BIERMANN, L.: Kometenschweife und solare Korpuscular Strahlung. *Z. Astrophys.*, vol. 29, 1951, pp. 274-286.
3. PARKER, E. N.: Dynamics of the Interplanetary Gas and Magnetic Fields. *Astrophys. J.*, no. 128, 1958, pp. 667-676.
4. BONETTI, A.; BRIDGE, H. S.; LAZARUS, A. J.; ROSSI, B.; and SCHERB, F.: Explorer X Plasma Measurements. *J. Geophys. Res.*, vol. 68, 1963, pp. 4017-4063.
5. SNYDER, C. W.; and NEUGEBAUER, M.: Interplanetary Solar Wind Measurements by Mariner II. *Space Res.*, IV, 1964, pp. 89-113.
6. GRINGAUZ, K. I.: Some Results of Experiments in Interplanetary Space by Means of Charged Particle Traps on Soviet Space Probes. *Space Res.* II, North Holland (Amsterdam), 1961, pp. 539-553.
7. NESS, N. F.; SCEARCE, C. S.; and SEEK, J. B.: Initial Results of the IMP-1 Magnetic Field Experiment. *J. Geophys. Res.*, vol. 69, 1964, pp. 3531-3570.
8. BRIDGE, H.; EGIDI, A.; LAZARUS, A.; LYON, E.; and JACOBSON, L.: Preliminary Results of Plasma Measurements on IMP-A. COSPAR Presentation (Florence, Italy), 1964.
9. HEPFNER, J. P.; NESS, N. F.; SKILLMAN, T. L.; and SCEARCE, C. S.: Explorer X Magnetic Field Measurements. *J. Geophys. Res.*, vol. 68, 1963, pp. 1-46.
10. CAHILL, L. J.; and AMAZEEN, P. G.: The Boundary of the Geomagnetic Field. *J. Geophys. Res.*, vol. 68, 1963, pp. 1835-1844.
11. FREEMAN, J. W.; VAN ALLEN, J. A.; and CAHILL, L. J.: Explorer XII Observations of the Magnetosphere Boundary and the Associated Solar Plasma on Sept. 13, 1961. *J. Geophys. Res.*, vol. 68, 1963, pp. 2121-2130.
12. NESS, N. F.; and WILCOX, J. M.: The Solar Origin of the Interplanetary Magnetic Field. *Phys. Rev. Letters*, vol. 13 (15), 1964, pp. 461-464.
13. ANDERSON, K. A.; HARRIS, H. K.; and PAOLI, R. J.: Energetic Electron Fluxes in and Beyond the Earth's Outer Magnetosphere. *J. Geophys. Res.*, vol. 70, 1965, pp. 1039-1050.
14. FAN, C. Y., GLOECKLER, G., and SIMPSON, J. A.: Evidence for >30 keV Electrons Accelerated in the Shock Transition Region Beyond the Earth's Magnetospheric Boundary. *Phys. Rev. Letters*, 13, 1964, pp. 149-153.
15. NESS, N. F.: The Magnetohydrodynamic Wake of the Moon. *J. Geophys. Res.*, vol. 70, 1965, pp. 517-534.
16. SPREITER, J. R., and JONES, W. P.: On the Effect of a Weak Interplanetary Magnetic Field on the Interaction Between the Solar Wind and the Geomagnetic Field. *J. Geophys. Res.*, vol. 68, 1963, pp. 3555-3565.
17. HIDA, K.: An Approximate Study on the Detached Shock Wave in Front of a Circular Cylinder and a Sphere. *J. Phys. Soc. Japan*, no. 8, 1963, pp. 740-745.
18. BEARD, D. B.: The Interaction of the Terrestrial Magnetic Field With the Solar Corpuscular Radiation. *J. Geophys. Res.*, vol. 65, 1960, pp. 3559-3568.

5—Solar Perturbations of the Space Environment

HENRY J. SMITH

NASA Headquarters

The sun's influence dominates the space environment of our planet. Fortunately its major effects on the lives of men are constant, and the transitory perturbations of solar influences are scarcely perceptible at ground level. However, *solar activity* generates a variety of major responses in the upper atmosphere, the magnetosphere, and the interplanetary medium. Other papers discuss these effects in detail; this review examines the different types of solar events which are significant to the study of the space environment.

At the outset, however, we should note that solar constancy dominates preponderantly over solar variability. The perturbations with which we shall be concerned are significant principally at the extremes of wavelength, relative to the wavelength of the monochromatic peak solar radiation which is attained at about 5000 Å, in the visible spectrum. The proportionally greatest variations of solar flux occur in the extreme ultraviolet and soft X-ray regions, and in the radio frequency portion at the other end of the electromagnetic spectrum. It is significant that the solar flux is distributed roughly according to the monochromatic transmission curve of the sun's atmosphere, so that the absorbed component of flux is very much less than the transmitted component. In consequence, the processes of attenuation of solar radiation show much more variation than ground observations of the sun would suggest. This indeed is the reason why the study of sun-earth relationships is so appealing; it is typically the pursuit of small unknown causes of very large observed defects. Hence, there is a real compulsion to pursue studies of solar-terrestrial phenomena with balloons, rockets, earth satellites, and deep space probes. Only by these

high altitude and extra-atmospheric techniques is it possible to make local measurements of the processes involved, or to observe the solar stimuli unaltered by the telluric attrition.

The solar constant must occupy some of our attention, even though our interest is principally in solar variation. Most of what we know about the constancy of the sun's integral radiated flux must be attributed to the classical work of Langley, Abbot, and their colleagues at the Smithsonian Institute between 1900 and 1950. Their well known technique combined measurements with the pyrhelimeter, a radiation calorimeter, with the spectrobolometer, a rather broad band spectrophotometer. The purpose of the spectrobolometer was to evaluate monochromatically the atmospheric losses, since it is necessary to extrapolate the pyrhelimeter measurements to zero air mass monochromatically. From these observations, the Smithsonian workers concluded that the most probable value of the constant is 1.94 cal/cm²/min. However, grave uncertainties remained due to the unknown effects of differential extinction, which is highly variable in time and place, and which was unknown outside the atmospheric transmission corridor. The modern discussion of the solar constant by Francis Johnson included Naval Research Laboratory rocket measurements of the ultraviolet radiant flux. Johnson's analysis suggested an improved value of the constant to be 2.00 ± 0.004 cal/cm²/min. It is true that modern technology would permit improved ground determinations of the solar constant. However, upper atmosphere or extra-atmospheric observations obviously would diminish the problem of extrapolating the pyrhelimeter measurements to zero air mass. At the time of writing, no experiments in the

United States' space program are committed to solar constant measurements. This reflects the formidable difficulty of such refined physical measurements, for several alternate procedures are currently under study.

The situation is equally obscure with respect to variations of the solar constant during the solar cycle and of short term. Abbot examined Smithsonian data from the period 1921 to 1952, and found an annual mean deviation of 0.23%. The extreme annual deviations from the 31-year mean occurred in 1922 (-0.9%) and 1948 (+0.4%). These magnitudes of course define an upper limit of the *sum* of the intrinsic variation plus the observational error, as Öpik has pointed out. Aldridge and Hoover correlated the solar constant with respect to the Wolf sunspot number *R*. They found the constant to be 0.6% higher at solar maximum (1948) than at solar minimum (1944). Öpik has found fluctuations in the annual means which cannot be described as random, and indeed are demonstrably larger than the atmospheric seasonal term. Hence, these fluctuations are likely to be intrinsic in the sun. The solar spectral radiance curve is, as well known, almost that of a blackbody. Therefore, since sunspots are cooler than the photosphere (4200° vs 5700°) one should expect the variation of the ultraviolet flux to be greater than the variation of visible or integrated radiation. Pettit, studying Mt. Wilson observations 1924 to 1931, found the ratio $I(3200 \text{ \AA}) : I(5000 \text{ \AA})$ ranged from 0.95 to 1.57. Moreover this variation correlated well with sunspot number (except for just one year). Thus it would appear that the ultraviolet variation is notably higher than the integrated flux variation. The idea of detecting long term variability of the sun by comparing the brightness of planets to selected stars is not a new one. It has most recently been implemented by the Lowell observers, who utilized modern stellar photoelectric techniques. Observations throughout Cycle 19 showed that Uranus and Neptune revealed no annual variation as large as 0.4%, the limit of measurement. Öpik has likewise discussed the short term variations in the Lowell data, and found deviations between 10-day means of about 0.6%.

Very long term changes of large magnitude have, as is well known, been invoked to explain

paleoclimatic changes. Such discussions are not relevant to this review. The average error of measurement of the solar constant is about 0.0023 stellar magnitudes for the annual means quoted above. In terms of stellar photometry this is extreme accuracy, exceeding by more than an order of magnitude the nominally quoted precision of best measurements. Stellar astronomers have found that "microvariability" ten times larger than .0023 magnitudes is commonplace among field stars. So we can say the sun is proved to be more constant than any known star.

Of foremost interest to any discussion of the sun's influence upon the earth's space environment is the expansion of the corona. Most of our knowledge in this area derives from the early discussions by Biermann, Chapman, and Parker. The existence of a solar wind was anticipated by Störmer's auroral theory of charged particles moving in the dipole magnetic field of the earth. The Chapman-Ferraro theory of sudden commencement (SC) geomagnetic storms recognized that these are the result of the impact of interplanetary plasma clouds on the magnetosphere. Forbush and Simpson discovered solar modulation of the galactic cosmic ray flux, which we conjecture is another result of solar interplanetary plasma clouds. Tangled magnetic fields inherent in these clouds possibly act as local diffusers of the galactic flux of cosmic rays.

Biermann's contribution was to show that solar radiation pressure was inadequate by large magnitude to account for the direction of comet tails of ionized gas. From these naive concepts, it is possible to deduce the interplanetary wind velocity, as from comet tail directions (about 500 km/sec), from SC storm delays after flares (1000 to 2000 km/sec), or from the delays in low energy magnetic disturbances assumed to issue from faculae (active regions on the sun) (150 to 400 km/sec). All of this conjecture was happily confirmed when Mariner II indicated a constantly flowing solar wind whose quiet time velocity ranged from 300 to 600 km/sec, with particle densities of 2 to 20 protons/cm²/sec on quiet days. A discussion of modern theories of origin of the solar wind can find no place in this review. We can note, however, that some net loss of material from the

sun follows inescapably from the very high thermal conductivity which prevails in the hot corona.

Perturbations of the wind have already been mentioned. The principal examples can be categorized as follows: (1) SC geomagnetic storms and/or 27-day recurrent disturbances are direct evidence of perturbations; (2) the nonuniformity visible in the low corona (streamers, hot spots over active regions) likewise indicates anisotropy of the driving mechanism; and (3) the high electrical conductivity of the plasma implies that magnetic fields in active regions will be dragged along into interplanetary space. The differential rotation characteristic of an extended gravitating gas mass dictates that the magnetic field will spiral in the sun's equatorial plane. A wind velocity of 500 kilometers per second would redirect the magnetic vector 45° to a radius at one AU. Moreover, a dipole field of 1 gauss at photospheric level would provide a residual field of 3γ at 1 AU. These data are roughly confirmed by the Mariner II observations. Flares are observed spectroscopically to heat the corona locally by factors of three to four times. Hence, the wind velocity and density will be enhanced for a few hours, as observed. The faster plasma overtaking the cooler, quiet time solar flux should produce aerodynamic phenomena which Parker calls a blast wave. There has been some conjecture that this indeed is the cause of the Forbush decreases.

Comet tails themselves serve as space probes to study the solar wind. Antract, Biermann, and Lüst have recently conducted a study of all cometary perihelion passages 1892-1957. Of 376 recorded cases, 44 exhibited tails of ionized gases which will be influenced by the solar wind. Such tails have small curvature and lie nearly along the solar vector, indicating they are subject to some force 50 times greater than solar gravitation. We conjecture that this force is momentum of the solar wind transferred to the cometary plasma by magnetic coupling. These investigators found statistically no dependence of the formation of these plasma tails upon the level of solar activity. (Thus, there were 20 cases when $R > 50$, 14 for $R = 25$ to 50, and 10 for $R < 25$, where R is sunspot number.) Nevertheless, there are several well documented

cases of tails perturbed by flares, by M-regions, and such. This points out that cometary tails permit us to study the solar wind well out of the ecliptic plane, and in regions not accessible to the current generation of interplanetary probe vehicles. For example, Comet Mrkos 1957 showed a tail one month after perihelion to heliographic latitude 40° . Outstanding examples of cometary activity were observed in Comet Morehouse in 1908, which for one month cast off a series of plasma sprays along its tail. Comet Humason 1961 exhibited a plasma tail when it was well beyond 3 AU from the sun.

Solar activity encompasses all aspects of the varying character of the sun. Recent theories recognize the central role of solar magnetism in these varying processes. Some mechanism, perhaps a combination of global circulation currents and turbulent gas motion, creates intense localized magnetic fields. We detect the fields by the Zeeman effect upon atomic spectral lines, or else infer them from perturbations of the the mass and temperature distributions in the sun's atmosphere. The large scale patterns of magnetic polarity and the heliographic distribution of these fields change cyclically in a total period of 22 years. During the 11-year cycle of sunspot incidence, the dominant polarity of magnetic fields remains constant in the northern or southern hemisphere, and reverses during the following cycle. Some evidence suggests that successive cycles may alternate between low and high degrees of activity. Superposed on this weaker trend is a stronger long period variation, of eight or more cycles, from low to high activity. These cycles are irregular, with wide dispersion in periods, phases, and amplitudes.

The basic episodes of solar activity are the active centers. The *chromosphere* is a thin layer dividing the cool, dense lower region (*photosphere*) from the hotter, tenuous upper region (*corona*) of the sun's atmosphere. The visible white light disk is the opaque photosphere, at a temperature of roughly 5000° ; at times of total eclipse the million degree corona becomes apparent, extending several solar radii above the photosphere. We can observe the chromosphere at any time through special filters which transmit only the narrow wavelength bands emitted by atoms abundant in

the chromosphere, like hydrogen, helium, or ionized calcium. An active center first appears as weak magnetization in a small area. In a short while the chromosphere brightens slightly in that position to form a *plage*. A few small sunspots emerge about this time, then grow and merge. The largest spots may attain a thousandth of the sun's surface area. Strong magnetization appears in and around the spots, amounting to a few thousand times the earth's magnetic field. Above an active center the corona may become compressed and heated twofold compared to adjacent quiet regions. Cool condensations of matter, the *prominences*, occur in the corona and persist for weeks. The total lifetime of a single activity center will range from a few days to a few months. Several can occur simultaneously, and there is a tendency for new centers to form in places previously active. Generally a region evolves smoothly, rising to maximum magnitude quickly and decaying more slowly.

Superposed on the slowly evolving pattern of the *plage* and spots are rapid dynamic events of impulsive energy release. Chromospheric flares are the most important examples of this class. A part of the *plage* will brighten (in hydrogen light, for example) to a few times normal intensity during the course of a few minutes, then fade gradually; typical durations range from 5 minutes for the smallest to 3 hours for the largest flares. Their areas range from 0.003 down to 0.00001 of the total surface of the visible sun. Despite their small fractional size, flares produce devastating perturbations on the space environment as you well know. We believe the chromospheric brightening to be a symptom of the passage of some violent disturbance through the atmosphere, as, for example, a hot plasma moving through the magnetic field, which can cause the observed intense bursts of radio noise. Flashes of ionizing radiation, particularly of soft X-rays, are emitted at the maximum phase of a flare. These are the cause of the well-known sudden ionospheric disturbances. A few flares eject streams of very hot plasma into the medium, at velocities ranging from a thousand kilometers per second up to a fraction of the velocity of light. These streams drag along some magnetic field, and distribute it broadly within the inner solar system. These fields

guide and scatter the faster charged particles, both those emitted by the sun and the galactic cosmic rays. The corona itself suffers deformation by the plasma ejections, and in this way modulates the low energy plasma streams causing geomagnetic disturbances. Less energetic impulsive phenomena in the sun's atmosphere provide gentler stimuli which are not so readily identifiable in the environmental response. Examples are radio noise storms, and hydromagnetic shocks in the corona which cause sudden disappearances of the prominences.

We cannot explain all of the solar perturbations by such obvious quantitative association of optical solar events. The M-regions are an outstanding example. Bartels' familiar time-correlation analysis reveals geomagnetically active days (when one of the indices Cp , Kp , or Ap exceeds specified thresholds) which define "recurrent storms" that return again and again at roughly 27 intervals. Bartels attributed these recurrent storms to "M-regions," otherwise unobservable solar disturbance regions. Several such storms are identifiable, for example in the 3½ years at the end of Solar Cycle 18. There is some recurrence tendency at all phases of solar cycles back to Cycle 11. However, the recurrent storms showing durations of 2 to 8 days are outstanding in their persistence, their magnitude, and their differentiation from contiguous activity. Their duration suggests that the sources, if uniformly distributed in solar longitude throughout the period of activity at the earth, must extend for 25° to 100° of longitude. Of course, some of this extent can be accounted for by velocity dispersion of fanning of plasma streams in transit from the solar source. Nevertheless, the typical lifetimes of 6 to 8 rotations are much longer than typical major solar centers of activity. There have been many efforts to associate them with different aspects of centers of activity, usually employing Chree's superposed epoch method. Thus sunspots, *plages*, bright coronal regions, indices of activity including flare incidence, and so forth, have all been tested to account for the recurrent geomagnetic phenomena. Universally these analyses reveal a geomagnetic activity minimum 3 days after central meridian passage (CMP) of one of these solar features. A maximum of geomagnetic activity occurs 6

days after CMP and a slight rise right at CMP. C. W. Allen points out that these phenomena permit two interpretations: either there is a zone of avoidance 3 days after CMP (with compensatory increase of flux either side); or else a particle arrives from the center of activity 6 days after CMP (requiring some controversial interpretation of the 3-day minimum in this case). Correlations like this are always found with solar activity features, but never so close that identification of a cause is secure. However, there is no doubt that the energetic behavior of the center of activity gravely influences M-regions.

Additional observational facts about M-regions increase our confusion. The sun-earth aspect obviously influences their incidence. According to Allen, there is a geomagnetic "culmination" in March and September. This could either be the result of the equinox (21st day of the month) or of the earth's arriving at maximum heliographic latitude (8th day of the month). The latter construction permits us to interpret this culmination as the intrusion of the earth into permanent northern hemisphere and southern hemisphere activity regions. Large M-regions generally disappear at sunspot minimum, suggesting that the renaissance of solar activity terminates the recurrent forms. Several authors have pointed to coronal streamers as the M-regions. Morphologically these streamers look like particle streams, they occur at the right part of the solar cycle, and they are a midlatitude phenomenon when most well developed. However, Saemundsson examined all streamers photographed at the eclipses between 1885 and 1962. He found no statistically significant connection between M-regions and identifiable streamers. This means that M-regions are not visible in integrated light in the regions observed at total eclipse; one can therefore set a rather low upper limit on the possible matter density in these streamers. Recent theories of solar magnetism suggest that the UM (magnetic) regions may be identified with M-regions. Babcock's analysis of Mt. Wilson observations supports this idea, but recent new understanding of the evolution of magnetic regions in centers of activity may diminish the attractiveness of this idea. UM regions are exceedingly difficult to identify,

when the data are sufficiently complete and continuous. Another idea which has attracted astronomers is the suggestion that quiescent prominences are M-regions. However, Dizer examined thirty-four years of Meudon prominence data, and found no statistical correlations. Waldmeier has recognized what he calls C-regions, which are strong 5303Å emission areas without attendant photospheric or chromospheric disturbances; possibly they are the situation of coronal brightening which has outlived its related photospheric effects. Statistically Bell has found that M-regions are, however, associated most closely with regions of weak 5303Å emission. The M-regions continue to mystify astronomers.

Spacecraft observations provide important new data on solar extreme ultraviolet radiation and its perturbations of the space environment. Early rocket surveys of the sun's extreme ultraviolet spectrum were made by various groups at the Naval Research Laboratory, Air Force Cambridge Research Laboratory, and the University of Colorado. These surveys provided maps and low precision estimates of fluxes in broad spectral regions. Orbiting satellites SR-1 (NRL) and OSO I (NASA) began a massive program of monitoring variations of the solar extreme ultraviolet on behalf of scientific research. (This is an important distinction: operational patrols, which yet remained to be justified, demand much greater continuity and uniformity than these basic research missions need.) The OSO I tape recorders provided unique continuity of data for several months after its launch in March 1962. These data permit study of quiet sun conditions, and of the slow variations of the extreme ultraviolet. J. Lindsay has summarized the principal results from this satellite:

(1) Plages on the quiet sun produce a slowly varying X-ray component which correlates well, but not perfectly, with 2800 megacycle flux variations.

(2) A lower limit can be established for the 1 to 8 angstrom X-rays of 4×10^{-5} ergs/cm²/sec; optical activity can be identified when the flux exceeds 0.6×10^{-3} ergs/cm²/sec and there is a sudden ionospheric disturbance when the flux exceeds 2×10^{-3} ergs/cm²/sec.

(3) A twofold increase in the flux of X-rays can occur within one second. Active prominences and bright limb events are known to produce distinct X-ray emission events.

(4) Flare X-ray spectra harden the plage region (pre-flare) spectrum.

(5) Extreme ultraviolet coronal emission lines (Fe XV 284Å and Fe XVI 335Å) were observed to increase fourfold, while He II 304 Å increased only 1.3 times when the sunspot number R rose from 75 to 125.

(6) The plage activity is much more effective in changing these extreme ultraviolet fluxes than were flares, even large ones.

(7) The average increase in the other extreme ultraviolet lines amounts to only 50 to 80%. These data, collected principally over just a 3-month period, reveal the vital importance of monitoring the solar input to the space environment from orbiting spacecraft.

To conclude, brief mention must be made of the observed solar influence upon the upper atmosphere. The top of our atmosphere merges gradually with the space environment, and much of what we call space operation is actually performed within what is essentially the earth's atmosphere. Jacchia has recently summarized our knowledge of the response of the top of the atmosphere to solar stimuli. The sun's

ultraviolet spectrum and the solar wind plasma are both important sources of thermal energy for the upper atmosphere. There is very close correlation between 2800 megacycle flux and the atmospheric density profile. Thus, 27-day recurrent processes are very apparent in satellite drag, as revealed by secular changes in satellite orbital parameters. There are also well known atmospheric perturbations of satellite orbits caused by magnetic storms. Since these storms endure only one to two days, their effects are hard to detect, but the phenomenon is well established. Bourdeau, Chandra, and Neupert have recently shown that the 27-day variation is caused by the sun's extreme ultraviolet flux variation (as revealed by OSO I data), rather than the solar wind. It is obvious that solar influences will be of primary importance in the emerging operational science of environment monitoring and forecasting. Many of the relations between the sun and the earth are not amenable to an intellectually gratifying causal relationship in basic physical terms. Nevertheless empirical relations, incontrovertible circumstantial associations of solar influences and environmental responses, are well enough known already that operational aspects of the sun's influence on the environment can be successfully pursued even now.

6—The Updating and Dissemination of the Knowledge of Trapped Radiation—Model Environments¹

JAMES I. VETTE

Aerospace Corporation

The purpose of this paper is to describe a program that is concerned with producing model environments of the trapped radiation for engineering and system planning uses that will be updated at suitable intervals. Past experience with the high intensity radiation trapped in the earth's magnetic field has shown the vulnerability of satellite systems to this environment and has forced the systems engineers and program planners to take full cognizance of the energetic particles in space.

Because the knowledge of space measurements and their meaning is no longer the sole province of the geophysicist and space scientist, it is necessary to provide these data in a form suitable for system uses. Although many satellite measurements of the trapped radiation have been made and will continue to be made, it is difficult to obtain the best picture of this complex phenomena unless a large body of these data is compared and digested. An individual satellite covers a restricted region of space and, in general, carries instruments which can make only some of the measurements necessary to describe trapped radiation in its entirety.

The individual experimenters recognized that an effort to integrate all of the measurements was needed to produce the model environments and have themselves been largely responsible for bringing the present program into existence. The program, as we envisioned it, was to consist of a six-man effort, with half of the funds provided by NASA and the remainder provided by the Air Force. At the present time only the

NASA funding has been provided, so the program described here is a three-man effort.

The program is concerned not only with producing model environments and with updating these environments at something like 6-month intervals, but also with developing programs for analyzing and displaying the environment. Another important aspect involves prediction of what the environment will be at some time in the future rather than what it was in the immediate past. The decay of the Starfish belt and the variation of the natural environment over the solar cycle are two examples of where prediction is needed.

The manner in which the program is being conducted will be described in some detail, and the first output of this program will be discussed briefly to illustrate some of the points.

The author is indebted to Dr. James Van Allen of the State University of Iowa, Dr. Carl McIlwain of the University of California at San Diego, Dr. William Imhof of the Lockheed Missile and Space Company, Dr. Harry I. West, Jr. of the Lawrence Radiation Laboratory, Dr. Walter L. Brown of the Bell Telephone Laboratories, John M. Mihalov of the Aerospace Corporation and Dr. Wilmot N. Hess of the Goddard Space Flight Center, NASA for supplying the data presented here and for discussions pertaining to the data. The author also thanks his colleagues at Aerospace, J. R. Stevens, A. L. Vampola, E. F. Martina, and K. W. Hubbard, who have contributed to this effort.

PROCEDURE

The initial step has been to contact each experimental group to discuss the program and

¹ Research supported by the National Aeronautics and Space Administration under Contract No. W-11, 683.

determine the proper time to receive data. In order to provide an environment that is not out of date, it is necessary to obtain the information as early as possible. On the other hand, processing preliminary data can be quite dangerous and the data are subject to change. The best compromise seems to be at that time when experimenters are ready to talk about their data at meetings or have prepared preprints or contractor reports. This seems to be the general consensus of opinion and has, in fact, been the time at which we have received data to date.

Discussions have been held with the experimenters to understand the data and, in particular, the instruments with which the data were obtained. In some cases it is necessary to know the energy spectrum from other measurements in order to convert the data to a meaningful form.

At the present time data are received in a wide variety of formats. Our procedure has been to convert this to a common format which can be stored on punched cards for future processing. After trying several formats, we have found the most useful one for our purposes to be the flux-magnetic field or F - B plots for those regions of space where B, L is a good coordinate system. A series of values of the flux and the field strength for given L values are punched on cards and stored according to these L values; enough points are stored so that, by interpolation, values of other points can be reproduced. Automatic plotting programs are in the process of development so that the data can be compared in all the important coordinate systems. Much of this comparison has been done by hand for the first environment produced. Hopefully, in the future, data can be provided to us in formats which are easy to reduce, or even provided on cards in our standard format. Such a procedure would result in a considerable saving of time in producing an environment and allow later data to be incorporated.

It is obvious that the representations and presentations of the data will differ as one attempts to make model environments farther out in the magnetosphere where time variations are quite important and redistributions occur in response to magnetic storms. However, for the

present paper our remarks will be confined to those regions below about $L=3.0$ where flux maps are a good way to represent a model environment over a time span of 6 months. It is true that the region between $L=2.0-3.0$ also shows response to magnetic storms, but the variations are smaller, or larger storms are required to produce changes.

The three main things that need to be determined by comparing the data are the flux distribution, the energy spectrum, and the absolute value of the flux.

If we represent the differential omnidirectional flux by

$$J(E, B, L)$$

then the integral omnidirectional flux is given by

$$J(>E, B, L) = \int_E^{\infty} J(E, B, L) dE$$

It is meaningful in most cases to represent this function as a product of two functions

$$J(>E, B, L) = F(B, L) N(>E, B, L)$$

F is the distribution function for some integral energy flux. If that energy is called E_1 , then

$$N(>E_1, B, L) = 1$$

This representation may have some advantage if many of the primary measurements are of integral fluxes near or at E_1 and, in the case of the electron measurements below $L=3.0$ which we have processed, the simplification is even greater. For that case, the energy spectrum is independent of B to the accuracy of the measurements and so

$$J(>E, B, L) = F(B, L) N(>E, L)$$

which breaks a function of three variables into a product of two functions of two variables.

When the data have been assessed to determine the best composite environment, the presentation of this environment can take many forms. It is our intention to put some of this information on punched cards and provide the other information by means of tables and graphs.

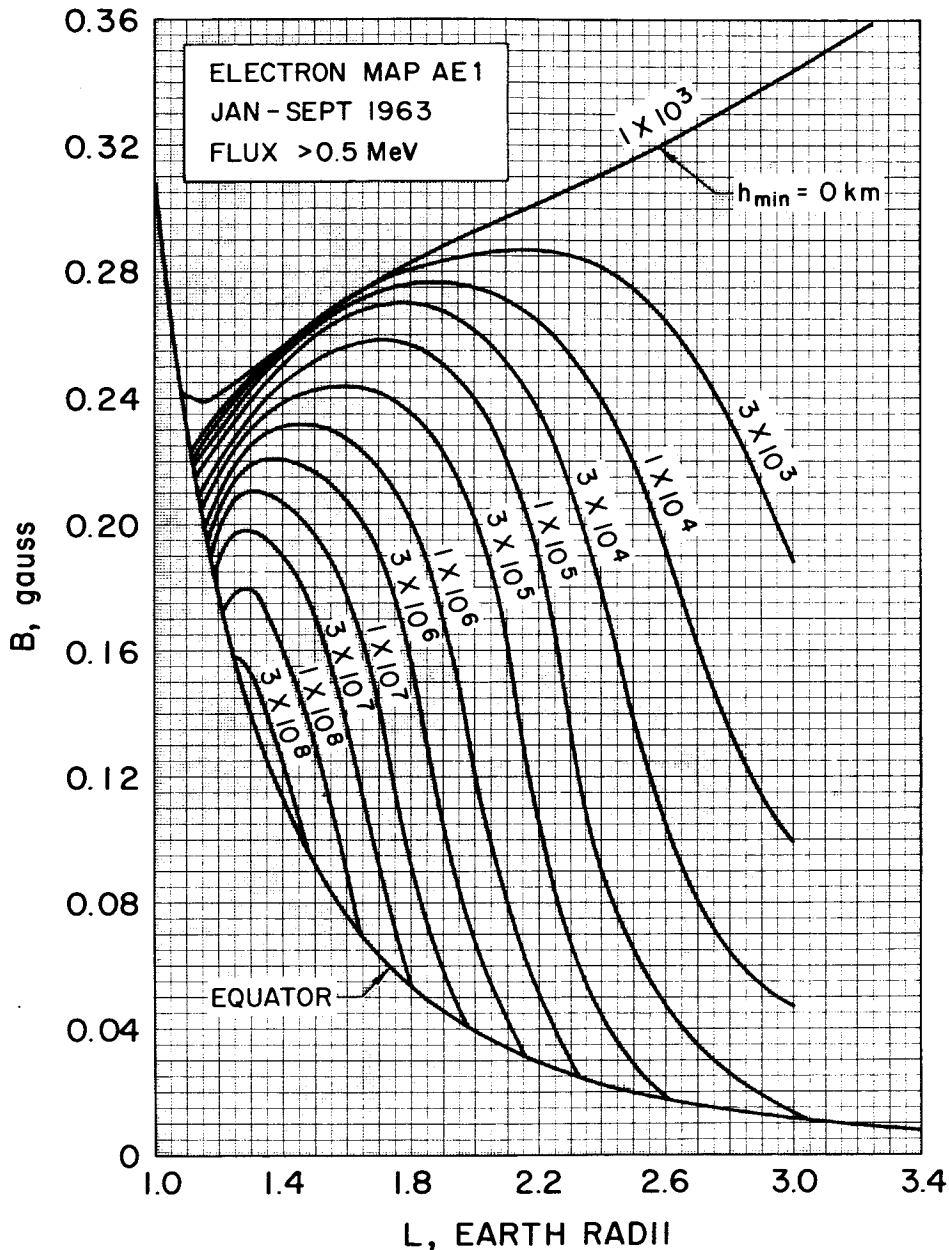


FIGURE 1.—A B-L flux map of the AE1 model environment.

The AE1 Environment

By taking the electron data made available to us by July 1964, we have determined a model environment for electrons above energies of 300 keV for the time epoch January through September 1963. We have designated this environment AE1, using the A to distinguish it from the series of flux maps produced by Dr. Wilmot Hess of the Goddard Space Flight Center.

The distribution function for electrons above 0.5 MeV is shown in figure 1 as a B, L flux map. We have bounded the map at the low altitudes by the line $h_{\min} = 0$ km and for $L > 1.3$ the 10^3 flux contour follows this line. Above this line in B, L space, the contours show a strong longitudinal dependence and represent both precipitated particles and particles redistributed by atmospheric scattering in the anomaly. It is true that this effect also takes place for

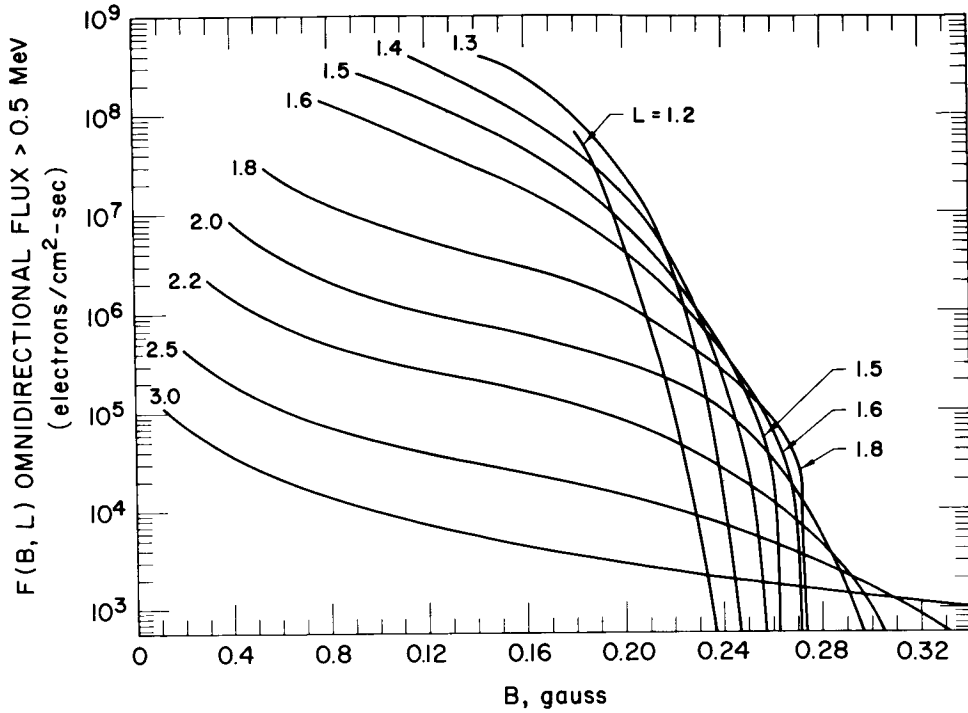


FIGURE 2.—A Flux-B plot of the AE1 model environment.

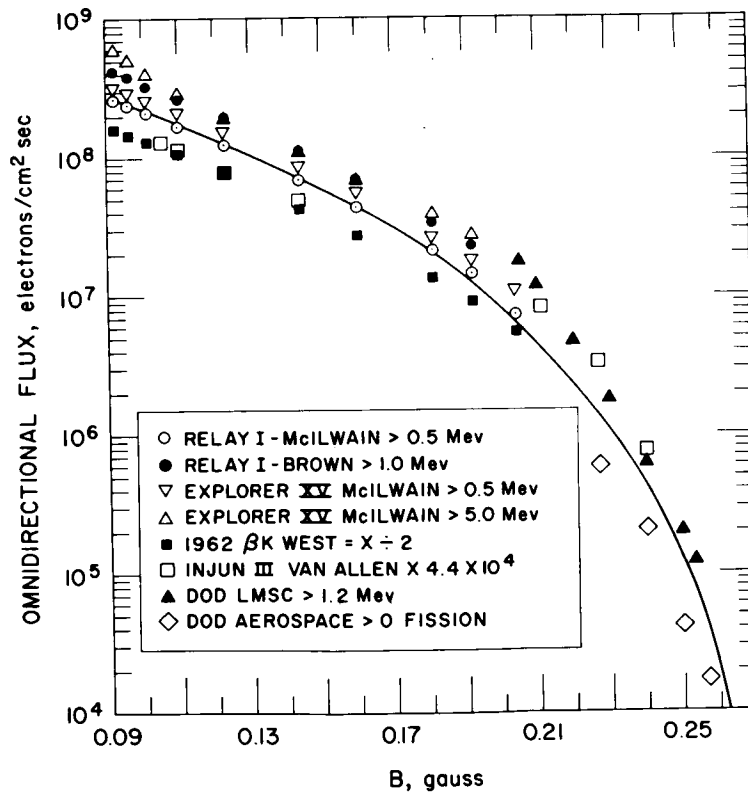


FIGURE 3.—A comparison of the experimental data and AE1 at $L=1.5$. The satellite and primary experimenter or organization for the coded points are given in the legend along with the threshold energy of the detector. The solid line is AE1.

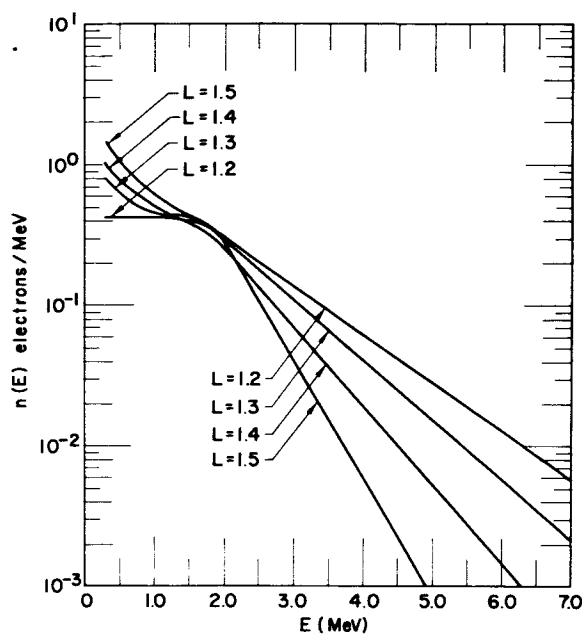


FIGURE 4.—The differential energy spectra at $L=1.2$, 1.3, 1.4, and 1.5 for AE1.

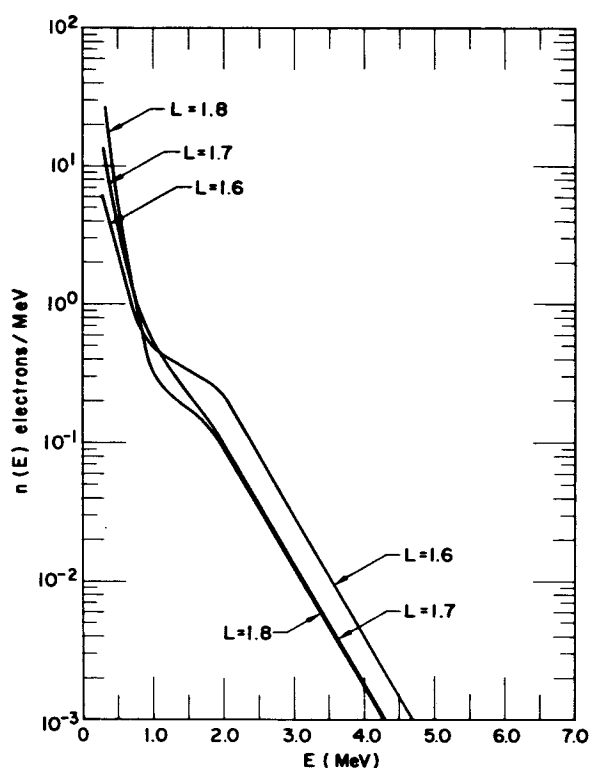


FIGURE 5.—The differential energy spectra at $L=1.6$, 1.7, and 1.8 for AE1.

$h_{\min} > 0$ km, but we have chosen this as the lower boundary of the trapped radiation for model environment purposes. The Flux- B presentation of this model is shown in figure 2. This is also stored on punched cards in the following manner. For each L value given by

$$L_i = 1.1 + 0.1i$$

$$i = 1, 2, \dots, 19.$$

there is a header card giving an alphanumeric description of the data. Behind each header card, there are a series of data cards on which are punched four coordinates of the form (B, F) . Enough points are taken off curves such as those shown in figure 2 to insure that linear interpolation of the log F versus B will provide accurate values at intermediate B values.

It is not the purpose of this paper to discuss the construction of the AE1 environment in detail or the comparison of the various input data. However, to illustrate the determination of the absolute value and to demonstrate the typical variation of the data, the model environment is compared with the input data at $L=1.5$ by means of figure 3. The various coded points do not represent the only B values where data

were available, but are used to show the extent of each experiment without drawing solid lines. All of the data are corrected by the model spectrum to give the omnidirectional flux above 0.5 MeV. The Van Allen data from Detector SpB on Injun III are multiplied by the arbitrary factor 4.4×10^4 , while the points representing the data of West from satellite 1962 $\beta\kappa$ are obtained by dividing the >0.5 MeV data from McIlwain's Flux Program by the factor 2. It can be seen that the data spread between about $F(B, L)/2$ and $2F(B, L)$, where F is the solid line describing the AE1 environment. This is a typical spread in the data for the various L values.

The differential spectra $n(E, L)$ for the model environment are shown in figures 4 through 7 and are normalized so that

$$N(>0.5, L) = \int_{0.5}^{\infty} n(E, L) dE = 1$$

This spectrum was derived mainly from the data of West and that of Imhof and Smith.

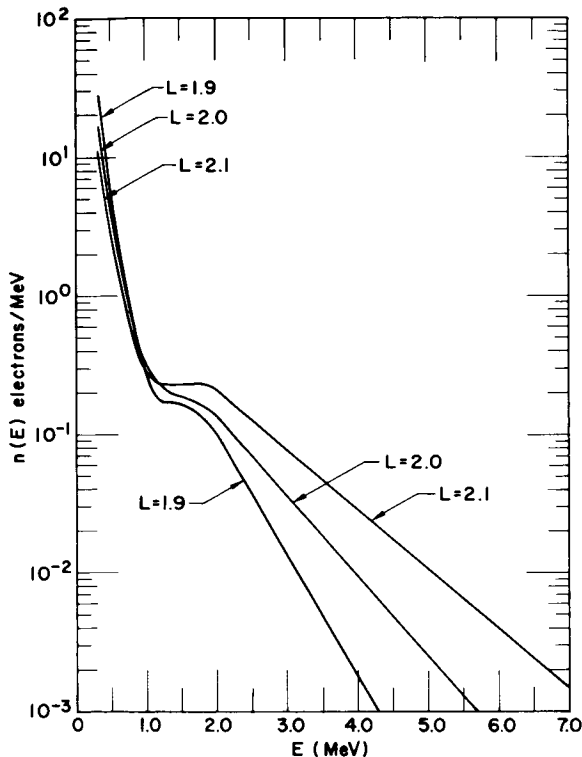


FIGURE 6.—The differential energy spectra at $L=1.9$, 2.0 , and 2.1 for AE1.

The comparison of AE1 with the E8 grid produced by Hess for November 1962 is shown in figures 8 and 9, where integrated orbital fluxes are given. The errors for AE1 are the \pm factor of 2 shown earlier. The spectral distribution of the integrated fluxes are given in table I and may be compared with that given by Hess for the E8 grid.

Dissemination of the Environments

The model environment will be sent to those requesting it from the author, in the form of the IBM punched card decks discussed earlier, in $B-L$ flux maps and orbital integration tables. It is planned to compute the orbital integrals for a series of circular orbits up to altitudes of about 6000 km for the four inclinations 0° , 30° , 60° , and 90° , and present the spectrum tables as given in table I for these integrations. The equatorial pitch angle distribution will be calculated and $R-\lambda$ maps will be constructed.

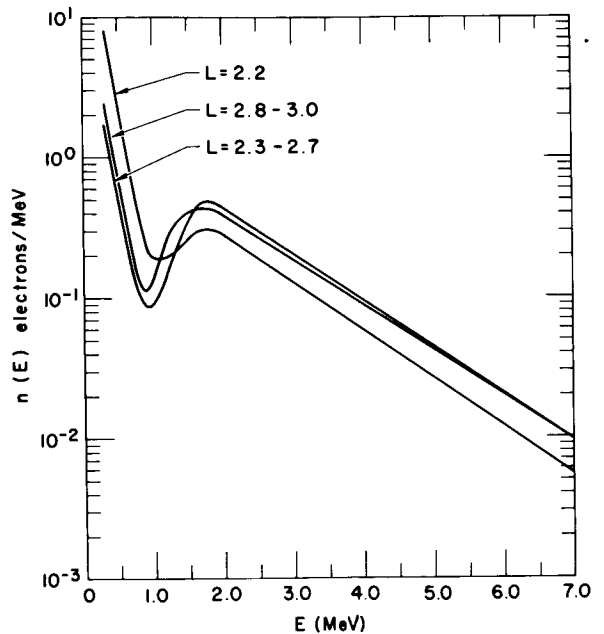


FIGURE 7.—The differential energy spectra at $L=2.2$, $2.3-2.7$, and $2.8-3.0$ for AE1.

A detailed discussion of the environments as they are produced will be published in the form of NASA Technical Notes and will be available for those desiring the detailed comparison of data.

Because the comments and questions concerning these environments can become quite time-consuming, Dr. Wilmot Hess has agreed to act as the contact point for all NASA activities and contractors, while the author will act as the contact point for all DOD activities and contractors. Although no funds exist at present for handling this, we are hopeful this will be corrected in the near future.

Uses of the Model Environments

After environments are produced, they will be discussed with the experimenters in order to assure that no misunderstanding of the data has occurred. By pointing out disagreements among various data and discussing them, it is felt that this program can also be of service to the experimenters. Certainly, satellite experiments are so time consuming and difficult that there is little opportunity for each individual

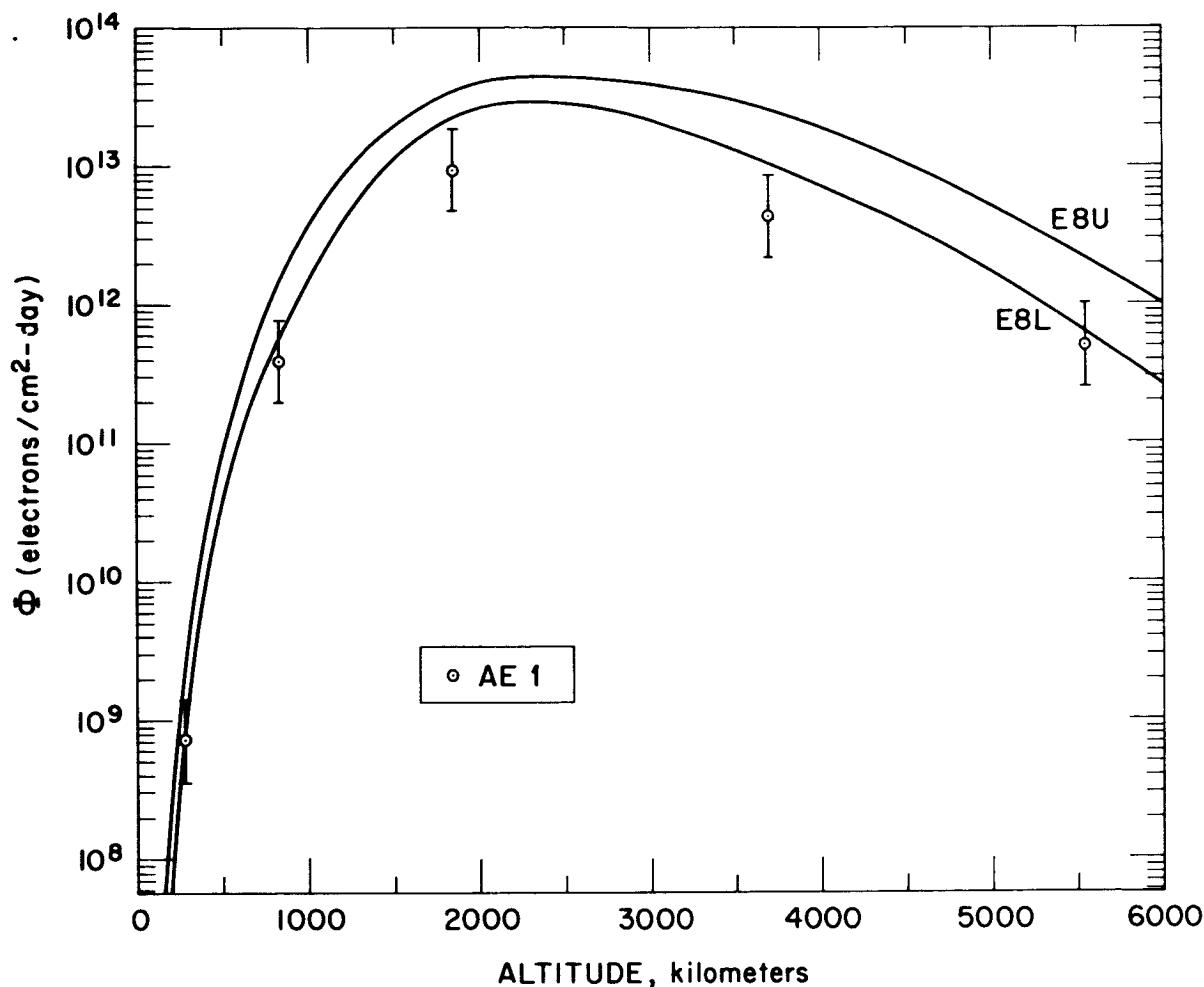


FIGURE 8.—Integrated electron fluxes for 30° inclination orbits for AE1 compared with E8L and E8U grids. The errors represent \pm factor of 2.

experimenter to do a detailed comparison of his data with those of all others. On the other hand it should be made clear that these environments do not necessarily bear the endorsement of those experimenters contributing data. The models will represent what we feel is the best compromise of available data for the specific purposes of satellite engineering and system planning.

In that sense they can be used in orbital integrations, dose calculations, radiation shielding studies, radiation damage problems, orbital maneuver studies, and similar types of endeavor. They should not be used in support of various

physical theories because they do not represent primary data. They represent only a smoothed version of many measurements, and, in regions where no data existed, the selection of contours may be guided by theory or intuitive judgment. Also, certain simplifications may be introduced to facilitate use of the models for practical purposes.

FUTURE ACTIVITIES

At the present time we are working on a proton environment for the L region below 3.0. This should be completed in about two months and is more difficult to construct than

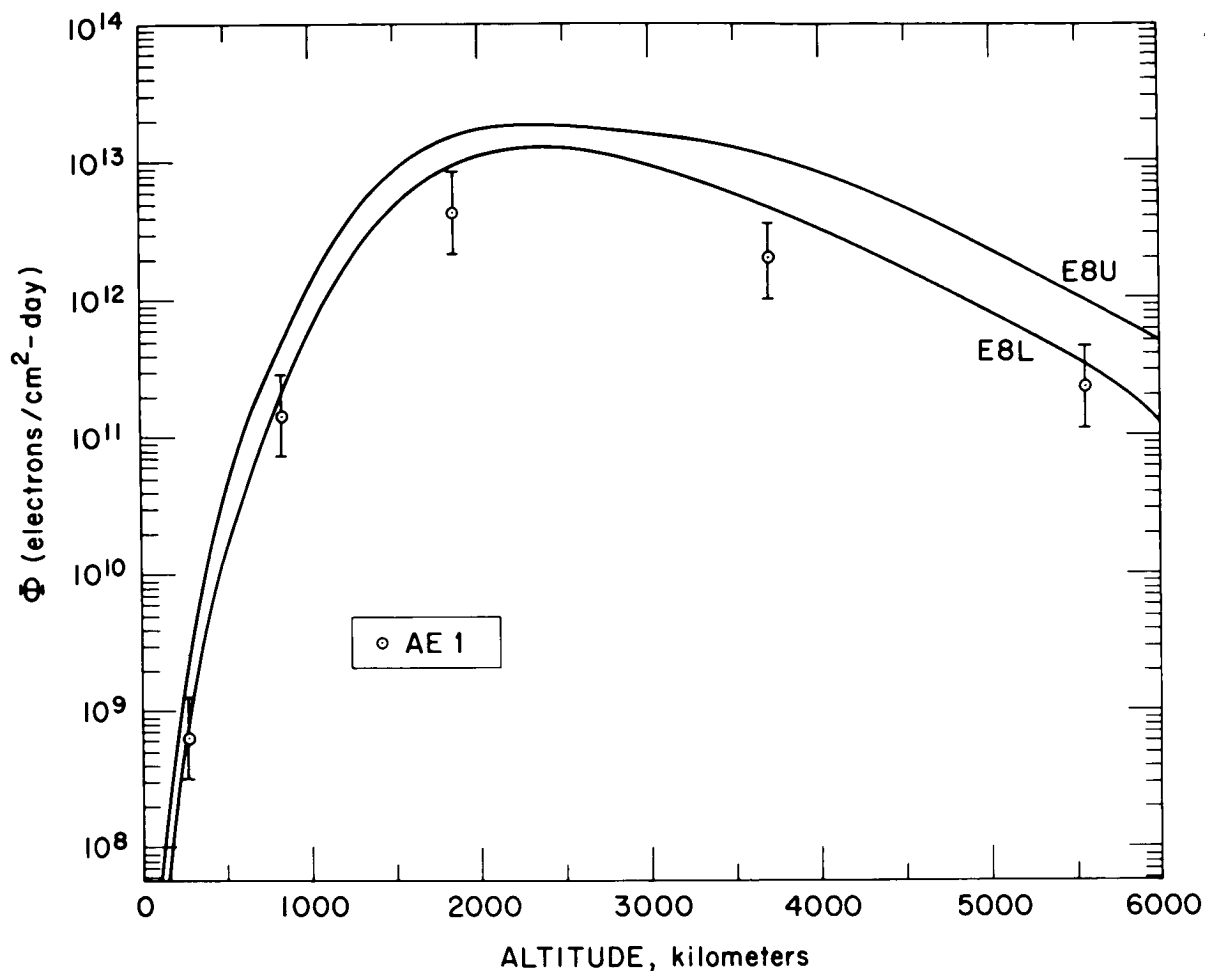


FIGURE 9.—Integrated electron fluxes for 90° inclination orbits for AE1 compared with E8L and E8U grids. The errors represent \pm factor of 2.

the electron environment discussed above because the energy spectrum is a strong function of B as well as L .

Another area of activity that will be pursued in the near future is the prediction of the future environment. In particular, the decay of the

Starfish belt can be handled, although the spectral changes are more difficult to determine. An outer belt radiation environment will be constructed at some later time in the program and, of course, the updating of the environments will remain a constant activity.

TABLE I

Fraction of Electrons in Various Energy Bands for Some of the Integrated Fluxes Given in Figures 8 and 9

$\frac{\Delta E}{h}$ (MeV) (n mi)	$i=30^\circ$				$i=90^\circ$			
	150	450	2000	3000	150	450	2000	3000
0.5-1	0.2778	0.2593	0.5413	0.7366	0.3440	0.2574	0.5401	0.7469
1-2	.4376	.4259	.3546	.1849	.4201	.4224	.3559	.1828
2-3	.1806	.1927	.0895	.0553	.1569	.1947	.0895	.0511
3-4	.0653	.0745	.0126	.0149	.0509	.0760	.0126	.0127
4-5	.0241	.0288	.0017	.0050	.0178	.0296	.0017	.0040
5-6	.0089	.0113	.0003	.0019	.0064	.0118	.0002	.0015
6-7	.0035	.0045	.0000	.0008	.0024	.0048	.0000	.0006
7- ∞	.0022	.0030	.0000	.0006	.0015	.0033	.0000	.0004

SESSION II

BIOLOGICAL EFFECTS OF SPACE RADIATION

Chairman: CORNELIUS A. TOBIAS

University of California

7—Methods in the Evaluation of Radiation Hazards in Manned Space Flight¹

DOUGLAS GRAHN

Argonne National Laboratory

and

WRIGHT H. LANGHAM

Los Alamos Scientific Laboratory

N65 34581

In many respects, this discussion will belabor the obvious—that radiation hazards in manned space flight operations should be evaluated from a viewpoint not inflexibly prejudiced by present-day occupational radiation safety standards. Manned space flight is a new occupation, totally different from those for which existing standards were established, and a fresh approach is required.

This position does not ignore the decades of accrued experience that have been used by many experts in the definition of good practices of radiation safety for the occupationally exposed individuals as well as for the general population. Rather, the position notes that the occupational standards reflect the considerations that radiation is the single outstanding risk, that large numbers (in excess of 200000 in the U.S.) will be in occupations involving radiation exposure, that an expanding nuclear energy industry and therefore threat of increased exposure is inevitable, and that the radiation sources or source materials are controllable.

In order to meet the objectives of large-scale radiation protection, “. . . to prevent or minimize somatic injuries and to minimize the deterioration of the genetic constitution of the population” (ref. 1), the concept of “permissible dose” became established. This dose is de-

finied by the ICRP (ref. 1) as “. . . that which involves a risk that is not unacceptable to the individual and to the population at large,” and which carries “. . . a negligible probability of severe somatic or genetic injury . . .” to the exposed individual. Although the objectives of space radiation protection are certainly the same as those noted above, the framework of historical reference in which the standards evolved must be sidestepped to avoid the application of permissible doses that may be unnecessarily restrictive.

Are there valid reasons to justify an independent review of the hazards and the setting of new standards if deemed appropriate? We believe there are at least these good reasons:

1. The radiation hazard is only one of many recognized and accepted serious potential hazards that could jeopardize the success of any flight mission.

2. The population-at-risk is extremely small and volunteer (the latter factor does not imply that a justification for relaxing controls exists, but that part of the burden of control is automatically apportioned to any volunteer).

3. The exact time, rate, duration, radiation quality, and frequency of exposure are largely unpredictable and uncontrollable, requiring inclusion of on-board protective means in the form of shielding. Since this can create an undesirable weight penalty, the radiation risks must be balanced against those invoked by the equipment capability traded for shielding weight.

¹ Work supported by U.S. Atomic Energy Commission.

4. Each flight may have a different profile and, therefore, a different risk versus benefit analysis sequence will be required.

These reasons and the experimental nature of present manned flight operations are obviously in conflict with the philosophy behind the occupational limits. Even the limit of 25 r for whole body exposure in unplanned emergencies is restrictive in magnitude and in the sense of the "once in a lifetime" permissiveness (ref. 2).

In spite of the clear differences in requirements for radiation safety between the average atomic energy employee and the astronaut, the ICRP-NCRP recommendations (refs. 1 and 2) have been utilized to form the basis of exposure limits for space flight operations (ref. 3). This was accomplished by assuming the astronaut could receive the equivalent of the occupational lifetime accumulated permissible dose within the briefer period of a 5-year flight career. This time scale compression along with other manipulations produced a set of exposure limits that by chance were partly sensible but were also quite arbitrary and devoid of flexibility.

The irony of it all is the simple fact that the Federal Radiation Council (FRC) position had been developed and quite clearly pointed out the flexible nature of the new look in protection standards (ref. 4). In fact, the FRC introduced the flexible concept of the Radiation Protection Guide (RPG) which is defined as ". . . the radiation dose which should not be exceeded without careful consideration of the reasons for doing so . . ." In addition, the FRC Report No. 1 states: in paragraph 7.7, ". . . there can be no single permissible or acceptable level of exposure, without regard to the reasons for permitting the exposure"; and further states, in paragraph 7.10, "There can, of course, be quite different numerical values for the Radiation Protection Guide, depending upon the circumstances" (ref. 4). Thus, the agencies are not rigidly bound to the recommended RPG. Although the same was true for the NCRP recommendations, flexibility of application was not an obvious trait of the NBS handbook presentations. In light of the FRC position, the agencies concerned with manned flight operations are clearly free to

derive their own radiation exposure limits, which may exceed the RPG, but which meet their own particular requirements.

EVALUATION OF HAZARDS

We recommend that the radiation hazards be evaluated from these viewpoints, in order of importance:

- a. Immediate or early (1 week to 1 month) incapacitation at any time during flight.
- b. Progressive incapacitation or serious decrementation of performance over long flight periods.
- c. Delayed or chronic injury as it may require intervention in a planned flight series and as a career limitation factor.

Early Incapacitation

This is the emergency or abort dose determination. Depending upon the penetrating quality, total dose, and intensity of the exposure, the limiting systemic and/or tissue responses are:

1. Acute gastrointestinal or prodromal symptomatology, i.e., nausea, vomiting, diarrhea. These may appear within an hour or two and subside within a day at any dose above about 75-100 r at the midline.

2. Acute hematopoietic symptomatology, i.e., thrombocytopenia, leukopenia, hemorrhage, intercurrent infection. These symptoms will appear within a few days to a week and can reach a clinically aggravating level at doses of 100-150 r or more to the marrow within several weeks to a month.

3. Widespread erythema and skin blistering. Under certain circumstances, such as extravehicular operations, high intensity surface exposure with little deep tissue dosage may occur. Depending upon the quality of the radiation, erythema will appear within a few hours to days following exposures of 500 r to 800 r (ref. 5). Severe damage will occur at doses above 1600-2000 r (ref. 6). Due to the restrictions and abrasive contacts of the space suit, even a partial body moderate erythema could become extremely uncomfortable and somewhat incapacitating.

4. Degradation of general operational skills through direct and indirect physiologic and neurologic injury, i.e., lassitude, fatigability.

The induction of acute systemic radiation injury is accompanied by nebulous symptoms of reduced performance capacity.

Wherever possible, the above responses should be examined in a probabilistic manner, and not all individuals may show the symptoms mentioned above at the stated dose levels. Dose-response relationships should be derived, and upper limit emergency doses defined for the several end points. The lowest limit will be the first determinant, but this will be a function of depth dose variation, total dose, and dose rate. For example, a high dose rate, whole body exposure to a penetrating radiation will undoubtedly cause the dose for prodromal responses to be determinant. A more protracted exposure will bring hematopoietic injury into the determining position, and, when moderate to high doses of very low energy radiations prevail under certain unshielded exposure conditions, skin injury will be determinant.

Progressive Incapacitation

This response category recognizes that most exposures will be at low levels where no early manifestations will occur, but where continued or periodic exposures can lead to a progressive emergence of principally hematopoietic injury expressed as a decrementation of performance necessary to maintain normal flight operations. This category also encompasses one of the most difficult areas for the prediction of biological effect—the situation following fractionated and protracted exposure.

Radiation injury has a comparatively slow time-course of expression and its manifestations will progressively emerge, then subside. Expression and recovery are concurrent. When the exposure is essentially continuous but at a low daily rate—perhaps 2 r/day or less for man—injury and recovery will probably equilibrate and a steady state will be maintained for long periods. Such observations have been made in experimental animal populations (ref. 7) and certainly would occur in man, but there are not yet sufficient data available to establish the kinetics of injury and recovery with any degree of confidence.

One theoretical approach to this problem has led to the evolution of the “equivalent residual

dose” (ERD) concept (ref. 8). This assumes a simple linear additive model for injury accumulation and concurrent recovery. The concept will not be discussed at length here, but it should be noted that the assumptions and constants employed in the ERD calculation have never been validated in man and are largely in conflict with much present day radiobiological data. The ERD concept is not based upon a correlation of physiological or cellular injury with lethality, and therefore it cannot determine in any realistic way a dose accumulation that can be related to an acute end point. Nevertheless, the ERD calculation may have some limited usefulness for single doses below 25 r and daily doses below 2 r/day where the level of injury may not, of itself, penalize recovery mechanisms.

At higher daily doses and fractionated exposures, a simple unweighted dose accumulation may be most realistic, since hematopoietic end points will probably be decisive. There are limited data on fractionated exposures in man to support this suggestion. Paired doses of 100 r to 400 r per fraction and at intervals of 3 to 7 days or two months indicated little or no recovery of the hematopoietic system during the first week and a super-normal sensitivity to second fractions even after the two-month interval (ref. 9). These observations are consistent with the Los Alamos accident case that demonstrated a prolonged hematopoietic depression of more than one year (ref. 10).

Prediction of man's response is difficult enough when a regular pattern of protracted or fractionated exposure obtains, but when the erratic pattern of exposure that would most likely occur under most projected flight profiles is acknowledged, the situation becomes virtually impossible. The prodromal symptoms and skin lesions will certainly benefit from dose protraction—the unanswered question is: To what extent will the hematopoietic system benefit and what are the significant time factors? We feel this is still largely unknown and emphasize the suggestion that all exposures of 50 r or more per fraction and protractions of 3 r/day or more be measured in terms of a straight exposure dose accumulation when evaluation of acute to subacute hematopoietic injury is under consideration. Small dose fractions of

less than 25 r may be managed by allowing for recovery during exposure-free intervals of at least several months duration. No particular recovery constant is recommended except that it should be no greater than the 2.5%/day employed in the ERD calculation, although it most certainly should be lower if it is to integrate all recovery processes acting over the first several months to a year (ref. 11).

Chronic Injury

As a general point of philosophy, chronic or long-term effects of radiation exposure appear to be of secondary importance in the evaluation of the hazards of manned flight. This should be the case for the foreseeable future, and this point is in sharp contrast to the evaluation of occupational hazards. In the latter, late effects are paramount and, among these, genetic effects are very influential.

Although the reasons for this relegation of late effects to a secondary role are several, the most quantitative argument is in the matter of population size. The astronaut population may be about 30 to 50; the occupational group may be 200 000 to millions. Chronic radiation injury is measured in probabilistic and actuarial statistical terms—an increase in an age-cause specific death rate, a reduction of the after-expectation of life, an increase in the sporadic incidence of a detrimental mutation. The end point is not identified with an individual; it is an entity of the population.

Among the different manifestations of chronic radiation injury, genetic damage always receives a little extra attention. This is justifiable for the case of the population-at-large under risk of exposure from fallout radiation or unnecessary medical or dental radiation sources. The gene pool of large populations is sufficient to cause the predictions for even very low probability mutational events to reach values of real concern. However, genetic hazards associated with manned space flight must be considered extremely small. The reasoning is entirely statistical—the small population of astronauts would have a virtually undetectable influence upon the mutational load of the general population. For example, if 50 astronauts receive 200 r apiece in a 10-year flight period, a total

of 10^4 man-roentgens will be accumulated. In the same time period, the actively reproducing portion of the U.S. population, about 10^8 persons, is permitted to receive 170 mr/year or 1.7 r in ten years to give a total of 1.7×10^8 man-roentgens. The sum, 170 010 000 man-roentgens, divided by 10^8 , is the per capita average exposure level. It is increased by 6 parts in 100 000 as a result of the astronaut exposures. Increases in genetic injury would be proportional.

The logic of the argument is simply that most modern populations are large interbreeding groups, and any contribution to the gene pool has a purely random chance of either elimination or transmission to the next generation. Since most new mutations are recessive and only mildly selected against in the heterozygote, they will persist in the population for many generations and thus randomly disseminate from the point of origin.

The above arguments should not be misconstrued as stating that the genetic damage should be of no concern to the individual exposed. Certain probability statements can be made concerning the individual, but the acceptance or rejection of these probabilities is somewhat a personal matter.

Nongenetic end points, as the induction of malignant diseases, cataracts, and nonspecific life shortening, must also be considered of secondary importance for this small population. Some reasonably acceptable probability statements can be generated for these responses, and certainly an awareness of these somatic manifestations of chronic injury must be maintained. It goes without saying that accurate records of the radiation history should be kept on all flight personnel. Since present prediction statements on these effects, in addition to the genetic effects, are always based on the observed total exposure dose, one requires only good record keeping.

It would seem important to be able to freely select from among the experienced personnel those crews that best meet specified mission requirements. This may entail periodic or repeated use of some astronauts and the possibility of dose build-up to an undesirable level as far as the individual's after-expectations are concerned. Long duration missions may then

be jeopardized if critical crew members should begin to develop manifestations of chronic injury when turn-around time may be many months. For this reason, the evaluation of late effects of radiation damage will progressively increase in its importance in the benefit-risk analysis. We feel, however, that these end points should be given very little weight in the present era of experimental manned space flights.

The next logical concern is the question of a "career dose." If we accept this as a necessity, then some value or set of organ-specific values must be established as acceptable "integrated annual dose increments." Are we sufficiently knowledgeable to do this now without being either too restrictive or not restrictive enough? Although one of the authors had previously discussed the matter (ref. 10), we now believe it is premature to dwell on the problem of career dosage, if for no other reason than to avoid setting an unrealistic figure for the annual increment. The latter is almost automatically derived when a career dose is established. In this regard, certain existing values for annual incremental dosage derived by manipulation of NCRP recommendations (ref. 3) provide, in our opinion, unrealistically low values that have no meaning or relationship to the biological effects they are designed to protect against.

One additional uncertainty needs to be noted. This concerns the problem area of combined stress. There is, at present, no information regarding the interaction of weightlessness, radiation, and other factors such as the subtle effects that may accrue from prolonged periods of demand for high operating performance. What influence, if any, concurrent physiological and psychological stresses may have upon the expression of radiation damage cannot be ascertained. Since any interaction is liable to influence the response in a negative way, an element of conservatism should be kept in all determinations.

In the meantime, flights will be programed for longer periods, and some limits will be sought for the 6-month, 1-year, and 2-year flights. How should accumulating dose be weighted for prediction of early incapacitation, progressive incapacitation, and chronic injury? Some suggestions have been made in this discussion. In recapitulation, for early incapacitation, one will almost invariably be dealing with a single brief exposure, and the estimated exposure dose at critical tissue levels will be determinant. For progressive incapacitation, unweighted accumulated dose under certain exposure patterns may be used for hematopoietic end points, with the cutoff being the abort dose. For chronic injury, again a straight forward dose accumulation may be used.

REFERENCES

1. International Commission on Radiological Protection: Recommendations. Pergamon Press, 1959.
2. Nat. Bur. Std. (U.S.) Handbook No. 59: Permissible Dose from External Sources of Ionizing Radiation, 1954.
3. GILL, W. L.: Shielding Requirements for Apollo. Proc. of Symp. on Protection Against Radiation Hazards in Space (Gatlinburg, Tenn.), Nov. 5-7, 1962, NASA TID-7652.
4. Federal Radiation Council: Staff Report No. 1; Background Material for the Development of Radiation Protection Standards. May 13, 1960.
5. BLOOM, W.; and BLOOM, M. A.: Histological Changes after Irradiation. Radiation Biology (A. Hollaender, ed.), McGraw-Hill Book Co., 1954, ch. 17, pp. 1091-1143.
6. LACASSAGNE, A.; and GRICOUROFF, G. (C. C. Lushbaugh and G. R. Riese, trans.): Action of Radiation on Tissues, an Introduction to Radiotherapy. Grune and Stratton (New York), 1958.
7. SACHER, G. A.: Late Effects of Continuous Irradiation: The Relation of Hematological Injury to Lethality. Laval Med., No. 34, 1963, pp. 163-168.
8. National Committee on Radiation Protection and Measurements: Rept. No. 29: Exposure to Radiation in an Emergency. Dept. of Pharmacology, Univ. Chicago, 1962.
9. TUBIANA, M.: Symp. on Physical Factors and Modification of Radiation Injury (L. D. Hamilton, ed.), Ann. N.Y. Acad. Sci., vol. 114, Art. 1, 1964, pp. 146-147.
10. LANGHAM, W. H.: Some Radiobiological Aspects of Early Manned Space Flight. Proc. Lunar and Planetary Exploration Colloq. 3(2), North American Aviation, Inc., Downey, Calif., 1963, pp. 117-134.
11. SACHER, G. A.; and GRAHN, D.: Survival of Mice Under Duration-of-Life Exposure to Gamma Rays. I. The Dosage-Survival Relation and the Lethality Function. J. Nat. Cancer Inst. vol. 32, 1964, pp. 277-321.

8—Lethal, Mutagenic, and Cytogenetic Effects of Fast Charged Particles on Various Biological Materials¹

G. E. STAPLETON

Oak Ridge National Laboratory

N 34582

Members of the Biology Division have participated in two general types of investigations related to the biological effects of space radiations: (1) attempts to detect the possible synergistic action of radiations and other flight parameters such as vibration, and weightlessness by use of sensitive systems in orbiting or probe vehicles; and (2) groundbased investigations of cellular response to high-energy protons and heavy particles, ranging in energy from 20 to hundreds of MeV. This paper will report results obtained from the second category of experiments. The concept that prompted these studies was that the changes in relative biological effectiveness (RBE) with increasing linear energy transfer (LET) of the particles might vary with different biological materials as well as the effects studied. Therefore, several materials were chosen as test objects, varying from microorganisms to human cells, and lethal, mutagenic, and cytogenetic responses were surveyed.

It was understood that similar work preceded and continued during our survey, in other laboratories, notably at the Lawrence Radiation Laboratory in Berkeley, California, and at Yale University. It was hoped that the results of the many experiments with widely varied test materials and end-points would fortify each other in helping us to understand this seemingly complicated interrelationship.

My own work was concerned with inactivation or lethality and induction of mutations in

the often used bacterium, *Escherichia coli* (refs. 1 and 2). The small size of these cells permits the irradiation of 10^9 or more cells in a very thin layer with any of the radiations of interest. Also, these cells respond to the presence or absence of oxygen in the atmosphere by a several fold change in their radiosensitivity. This change was studied as a function of the LET of the various radiations. The ability of the chemical protector β -mercaptoethylamine to reduce the radiosensitivity was also investigated in a limited number of irradiations. Mutation frequencies were estimated by use of a different strain of the same species.

The results of Drs. F. J. de Serres and B. B. Webber are based on lethality and forward mutations at specific loci in the fungus *Neurospora crassa* (ref. 3). The irradiated samples were asexual spores that contained two genetically different nuclei. This material allows the estimations of the types of genetic effects displayed by diploid cells. The techniques used permit the easy identification of all mutations at a specific locus by a color change from white to purple; therefore, tremendous numbers of irradiated and unirradiated cells can be screened for the mutations induced. Subsequent genetic analysis with well marked test strains allows the investigator to classify the genetic alterations ranging from single nucleotide changes to loss of entire chromosomes.

Dr. E. F. Oakberg's experiments are concerned with lethal effects on spermatogonia and oocytes in irradiated mice (ref. 4). The dynamics of gametogenesis in mice is now well enough understood to make a study of degeneration of certain cell types in the mouse

¹ Research sponsored by the National Aeronautics and Space Administration (NASA Order No. R-104, Task No. 3) under Union Carbide Corporation's contract with the U.S. Atomic Energy Commission.

ovaries and testes a reliable and sensitive measure of radiation damage incurred by whole body irradiation of these animals. The technique permits the amount of degeneration produced to be measured in the absence of any apparent repair by cell replacement. Since whole animals are irradiated, these experiments could not be performed with the short range protons and heavy ions.

Dr. M. A. Bender's experiments on production of chromosome aberrations in human cells (ref. 5) are carried out with samples of the blood of the investigator and, as one would guess, are "in vitro" experiments. These samples of whole heparinized blood are irradiated, the leukocytes are separated, by centrifugation, from the rest of the blood elements and cultured for 3 days in a tissue culture medium. The cells are stopped from further division, by addition of colchicine, in their first post-irradiation cell division, fixed, stained, and the number of aberrations is scored microscopically. Two easily identifiable types of chromosomal aberrations are scored.

The various radiations used are described in table I. The LET's quoted are taken from

the literature and track average values. As Randolph (ref. 6) has suggested, the composite average LET for all particles, primaries and secondaries, should be considered in critical LET calculations. This has not been done for the data reported here.

The types of dosimetry for the various radiations differed. The X-ray doses were measured in air with Victoreen "r" meter, with the thimble chambers placed in the position occupied by the biological sample. These dosimeters were calibrated against a standard instrument at the National Bureau of Standards. The Co^{60} gamma ray doses were measured by the system described by Conger et al. (ref. 7). The proton doses were determined either by measurement of the proton flux incident on the biological sample by activation of thin copper foils (ref. 8), or by activation of solid organic scintillators (ref. 9), or by ion-chambers interposed in the beam just upstream of the biological sample (ref. 6). The dosimetry used for the heavy particle irradiations was that adequately described by Brustad et al. (ref. 10).

When possible, we irradiated the different materials in sequence on the same day, after

TABLE I

Radiation Facilities Used

Facility	Radiation	LET, MeV cm ² /gm, track average
University of California— 184-in. Synchrocyclotron.....	750-MeV protons.....	^a 2.5
HILAC Accelerator.....	{ Carbon ions.....	^b ~2000
	{ Helium ions.....	180
University of Chicago— 170-in. Synchrocyclotron.....	450-MeV protons.....	^a 2.5
Harvard University— 160-in. Synchrocyclotron.....	50-MeV-100-MeV protons.....	^a 12-7
ORNL—86-in. Cyclotron.....	22-MeV protons.....	^a 2.5
ORNL—Maxitron 250 X-ray Machine.....	250-kVp X-rays.....	^c ~25
Co^{60} Gamma Source.....	1.2-1.4-MeV photons.....	^c ~2.6
ORNL—Health Physics Reactor.....	Fission neutrons.....	^c ~300
ORNL—Cockcroft-Walton Accelerator.....	14.1-MeV neutrons.....	^c ~300
	2.5-MeV neutrons.....	^c ~300

^a A. C. Birge et al. See reference 8.

^b T. Brustad. See reference 10.

^c Conger et al. See reference 7.

the beam had been characterized and the dosimetry performed. This was done in an effort to eliminate possible physical errors.

Figure 1 shows the type of inactivation data obtained for *Escherichia coli* B/r. It is clear that survival of this strain is not an exponential function of dose of X-rays or protons. This organism was chosen because of this characteristic, to determine if the shape of the curve would change, as a function of LET as is found for mammalian and other cells. It is clear that aerobic cells are equally sensitive to X-rays and protons of the indicated energies. The protection afforded by anaerobiosis is also similar for X-rays, 130, and 450 MeV protons. The uppermost curve indicates that β -mercaptoethylamine protects equally well against damage by X-rays and 130 MeV protons.

Table II shows the summary of data available for inactivation and mutation of *E. coli*. The inactivation coefficient for aerobic cells changes significantly only for the high LET carbon ions. Anaerobic cells show a significantly higher RBE for 22 MeV protons and the heavy carbon ions than for other radiations. Brustad (ref. 10) and others have shown similar data for *Shigella*, a closely related bacterium. The data for change in the ratio of sensitivities in aerobic and anaerobic conditions with radiations of

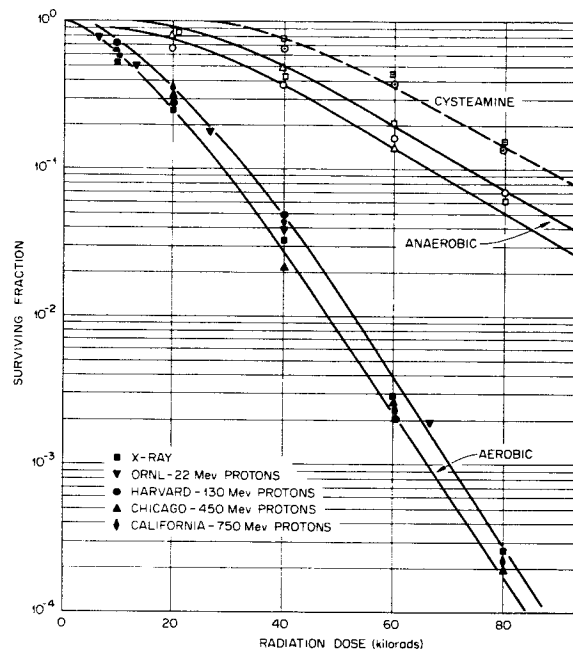


FIGURE 1.—Surviving fraction of *Escherichia coli* B/r as a function of dose (kilorads) for protons of various energies. Survival curves are for cells irradiated aerobically, anaerobically, and in the presence of cysteamine (0.12 M).

various LET's are similar also to those of Brustad. The data for mutation frequencies are far less complete than those for lethality but

TABLE II

Bacterial Inactivation and Mutation

Radiation	Inactivation coefficient ^a		Ratio, Aer./Anaer.	Mutation coefficient revertants per survivor per kilorad	
	Aerobic	Anaerobic		Proline	Galactose
750-MeV protons.....	0.14	0.043	3.0	10 × 10 ⁻¹⁰	20 × 10 ⁻¹⁰
430-MeV protons ^b15	.050	3.0	10	30
130-MeV protons.....	.13	.041	3.1	10	20
250-kVp X-rays.....	.125	.040	3.1	12	20
22-MeV protons.....	.13	.062	2.1	-----	-----
100-MeV carbon ions.....	.11	.078	1.4	-----	-----

^a The inactivation coefficient is the reciprocal of the e^{-1} dose (LD-37) determined from the exponential slope of the survival curves.

^b The data obtained with the 430-MeV proton beam are somewhat less reliable than the others because the uniform beam area was smaller and the dosimeter system was not cross-calibrated with the other radiations.

TABLE III

RBE's for Cellular Inactivation and Mutation in Neurospora

Radiations	Cellular inactivation		Mutation	
	Inactivation coefficients ^a	RBE	RBE for <i>ad-3^R</i> mutation (one-hit)	RBE for <i>ad-3^{IR}</i> mutation (two-hit)
750-MeV protons.....	0.1145	1.77	1.36	1.47
447-MeV protons.....	.0675	1.02	.87	1.00
442-MeV protons.....	.0839	1.30	1.24	1.30
250 kVp X-ray.....	^b .0648	1.00	1.00	1.00
39-MeV helium ions.....	.105	1.62	2.37	1.81
101-MeV carbon ions.....	.396	6.1	9.10	4.38

^a The inactivation coefficients are the reciprocals of the median lethal dose (e^{-1}) in kilorads.

^b Average of inactivation constants from four experiments is used for 250-kVp X-ray inactivation constant.

within experimental error do not indicate any difference in mutagenetic efficiency of protons of 100 to 750 MeV as compared with X-rays.

Table III is a compilation of the available data on inactivation and mutation of *Neurospora crassa*. The inactivation coefficients are the reciprocals of the median lethal dose (e^{-1}) in kilorads. The RBE's for the various radiations increase as a function of increased LET, as indicated by the coefficients for 39 MeV helium ions and 101 MeV carbon ions. The RBE's estimated for two different types of mutations are shown. They can be seen to increase likewise over the same range of LET, as does inactivation. The highest values of RBE, measured with carbon ion irradiation, ranged from 6 to 9. The data obtained with 750 MeV protons indicate an RBE significantly higher than 1 for the effects studied. It is not clear why the low LET, 750 MeV protons, yielded RBE's significantly greater than 1. The data obtained with the high LET radiations, however, indicate a very high RBE for heavy charged particles as high as 6 to 9 for the several effects studied. Such heavy particles can be produced at low frequency with these high-energy protons. Whether secondary particles with very high LET can account for this result cannot be judged on the basis of these experiments.

As far as they can be compared, the data shown here are in accord with the recent data

on lethal and mutagenic effects of radiations on a diploid strain of yeast, reported by Mortimer (ref. 11).

Dr. Oakberg's investigations of relative biological effectiveness of different radiations on gametogenesis in the mouse are less complete than the others as indicated in table IV. The RBE's for lethality are shown only for 130 and 750 MeV protons and for 14.1 MeV neutrons. Although the confidence intervals for RBE are quite large, the values for RBE of protons are not above 1 as compared with 250-kVp X-rays. It is clear that the values for 14.1 MeV neutrons are significantly greater than 1. Preliminary data from experiments with fission neutrons indicate an RBE of about 5. The peak or saturation RBE as a function of LET was not determined in these experiments, but the available data compare favorably with the data on cultured human cells of Barendsen (ref. 12) and Todd (ref. 13) which show the initial increase in RBE in the LET region of 100–200 MeV cm²/gm (10–20 keV/ μ of tissue). Dr. Bender's data on RBE for production of chromosome aberrations on human leukocytes can logically be considered together with Oakberg's. Bender's data, summarized in table V, for proton and neutron irradiations, include a large range of LET. The aberration frequencies include deletions as well as rings and dicentric. The frequencies of the former type increase linearly with dose

TABLE IV

RBE of Proton to X-Rays and 14.1-MeV Neutrons to Co⁶⁰ γ -Rays for Spermatogonial and Oocyte Killing

Radiation	Cell type	RBE		
		Lower 95% confidence limit	Point estimate	Upper 95% confidence limit
14.1-MeV neutrons ^a -----	Spermatogonia:			
	A-----	1.41	1.76	2.76
	Late A-----	2.19	2.52	2.89
	Late A + In-----	2.11	2.38	2.69
130-MeV protons-----	Spermatogonia:			
	A-----	0.28	0.47	0.70
	Late A-----	.41	.64	.95
	Late A + In-----	.27	.68	1.40
	Oocytes-----	.00	.28	.73
750-MeV protons-----	Spermatogonia:			
	A-----	0.64	0.84	1.10
	Late A-----	.52	.77	1.11
	Late A + In-----	.69	.96	1.34
	Oocytes-----	.20	.66	1.53

^a From Oakberg and Clark, 1961.

TABLE V

Coefficients of Chromosomal Aberration Production for Proton Irradiation of Human Leukocytes

Radiation	Coefficient of aberration production		RBE ^c
	Deletions ^a	Rings and dicentrics ^b	
750-MeV protons-----	0.6×10^{-3}	6.0×10^{-6}	0.7
450-MeV protons-----	.9	5.5	1.0
130-MeV protons-----	.9	6.0	1.0
100-MeV protons-----	.7	5.3	.8
50-MeV protons-----	.4	5.8	.4
250-kVp X-rays-----	$.9 \pm .03$	$6.0 \pm .5$	^d 1.0
14-MeV neutrons-----	$2.3 \pm .2$	(^e)	2.6
2.5-MeV neutrons-----	$2.8 \pm .2$	(^e)	3.1
1-MeV neutron-----	5.0	(^e)	5.6

^a From $Y = a + bD$; the coefficient is b , expressed in aberrations/cell/rad.^b From $Y = cD^2$; the coefficient is c , expressed in aberrations/cell/rad².^c Calculated from deletion coefficient only.^d By definition.^e For purposes of comparison, these coefficients would be meaningless because the kinetics of two-hit aberration production change in this LET range, becoming approximately linear for 2.5 MeV neutrons.

for low and high LET radiations and are presumed to result from one-hit events, while the frequencies of the latter type increase approximately with the square of the dose with low LET radiations and linearly with dose with high LET radiations.

The protons yield values for RBE not significantly above 1 as was found for all of the test systems used. This is the case for either type of aberration scored. With increasing LET above 60 MeV cm²/gm, the coefficient of deletion production increases, the RBE increasing to 5 or greater with the 1 MeV neutrons. It is of some interest that the change in kinetics of production of two-hit aberrations (rings and dicentrics) occurs in the same region of LET (~ 100 MeV cm²/gm) where overall efficiency in aberration production of two-hit aberrations per particle is reached. A more meaningful analysis could be made, however, if the complete LET response were known. Such data can be obtained only with very high LET particles such as those to be described by Dr. Todd in a later paper in this session.

It is clear from the data presented here for four cellular systems that each system responds to increasing LET with a change in RBE, and within the errors of the estimation of RBE and LET, it seems that the increase occurs within the same LET range, about 100–200 MeV cm²/gm. This is in good agreement with the data of Barendsen (ref. 12) and Todd (ref. 13) and others for lethality in mammalian cells. No attempt has been made in these studies to assess the effect of dose rate on the RBE versus LET relationship as has been investigated by the aforementioned authors.

The preliminary data obtained for inactivation and mutation of *Neurospora* conidia might suggest that high LET secondary radiation could be detectable with this system. We will need to know more about the maximum RBE as a function of LET to make any further statements about this phenomenon.

It is clear from the results discussed that large gaps exist in our present assessment of the role of LET in relative biological effectiveness of protons as well as other types of radiation. Although the different systems show different RBE's with the same radiation, there are reasonable consistencies among the responses of the various systems. Our data indicate that the maximum or peak RBE has not been obtained in any of the experiments so far performed. This is in apparent contrast to the data reported by Conger et al. (ref. 7) for production of chromosomal aberrations in *Tradescantia*, which show maximum RBE in the range of LET produced by 1.3 MeV neutrons.

The data are not inconsistent however, with those presented by Barendsen (ref. 12), nor with those of Tobias and Todd (ref. 13), Brustad (ref. 10), and Mortimer (ref. 11), which show maximum effectiveness per particle in the range of 2000 MeV cm²/gm for a number of effects on various types of living cells. We hope that more complete investigations with some of these systems will allow us to make more positive statements about this complicated interrelationship and ultimately about the hazards expected from space flights which will involve the encounter with radiations of the types studied here.

REFERENCES

1. HOLLAENDER, A.; STAPLETON, G. E.; and MARTIN, F. L.: *Nature*, vol. 167, 1951, pp. 103-104.
2. HOLLAENDER, A.; and STAPLETON, G. E.: *Peaceful Uses of Atomic Energy*, vol. 2, United Nations (New York), 1955, pp. 106-113.
3. DE SERRES, F. J.; and WEBBER, B. B.: *ORNL Space Biology Progress Annual Rept.*, ORNL TM-720, Jun. 30, 1963, pp. 6, 7, and 17.
4. OAKBERG, E. F.; and CLARK, E.: *J. Cellular Comp. Physiol.* vol. 58, (suppl. 1), 1962, pp. 173-182.
5. BENDER, M. A.; and GOOCH, P. C.: *Proc. Nat. Acad. Sci., U.S.*, vol. 48, 1962, pp. 522-532.
6. RANDOLPH, M. L.: *Ann. N.Y. Acad. Sci.*, vol. 114 (1), 1964, pp. 85-95.
7. CONGER, A. D.; RANDOLPH, M. L.; SHEPPARD, C. W.; and LUIPPOLD, H. J.: *Radiation Res.*, vol. 9, 1958, pp. 525-547.
8. BIRGE, A. C.; ANGER, H. O.; and TOBIAS, C. A.: In *Radiation Dosimetry* (G. J. Hines and C. L. Brownell, eds.). Academy Press (New York), ch. 14, 1957, pp. 623-665.
9. GIBSON, W. A.; STAPLETON, G. E.; and WEBBER, B. B.: ORNL TM 924, June 30, 1964.
10. BRUSTAD, T.: *Advan. Biol. Med. Phys.*, vol. 8, 1962, pp. 161-220.
11. MORTIMER, R. K.; BRUSTAD, T.; and CORMACK, D. V.: *Univ. of California Rept.*, UCRL-11387, 1964, pp. 35-53.
12. BARENDSEN, G. W.: *Ann. N.Y. Acad. Sci.*, vol. 114 (1), 1964, pp. 96-113.
13. TOBIAS, C. A.; and TODD, P. W.: *Univ. of California Rept.* UCRL-11387, 1964, pp. 25-34.

N65-34583

9—Biological Effects of Protons and Neutrons in Large Animals

S. TOM TAKETA

Ames Research Center, NASA

This report is concerned primarily with the biological effects of protons in large animals. Pertinent neutron data are also discussed. A review of the literature reveals only a limited number of large animal proton studies. This is not surprising because of the difficulties involved in exposing large animals to whole body proton irradiation in ground-based facilities.

Studies were undertaken, in collaboration with Drs. Tobias and Sondhaus of the University of California, Berkeley, to determine biological effects of high energy protons compared to Co^{60} gamma rays in whole body irradiated monkeys. The 730 MeV protons of the Berkeley 184-inch cyclotron were degraded to the desired 200 MeV energy level by multiple Coulomb scattering. In addition to causing angular divergence of the emergent beam, which provided the desired effective exposure field for whole body irradiation of large animals, the use of scatters allowed us to study the combined effects of the attenuated primary proton flux and the induced secondary radiations, hence simulating a more realistic situation which an occupant of a spacecraft may encounter. The exposure set-up employed was unique in that it provided omnidirectional exposure. This was accomplished by rotating the animal, strapped in a styrofoam holder, simultaneously around its longitudinal and vertical axes. Proton exposures ranged from 200 to 950 rads midpoint air dose, gamma exposures from 195 to 1065 rads. Dose rate for protons, 7 meters from the beam port, was about 20 rads per minute. A comparable dose rate for gamma rays was obtained at midpoint to source distance of 114 cm. Depth-dose profiles were determined in a frozen monkey, using LiF dosimeters.

The results of depth-dose measurements showed: (1) a dose falloff at midpoint in gamma exposures, but a dose build-up in proton exposures; (2) tissue doses at various loci varied, with respect to the midpoint dose, from 96 to 114 percent and 71 to 104 percent in gamma and proton exposures, respectively; and (3) the midpoint tissue dose (MTD) was 60 to 70 percent of midpoint air dose (MAD) in gamma exposures, and about 120 to 130 percent in proton exposures, indicating that, for a given MAD, the MTD for protons was about twice that for gamma rays.

The relative biological effectiveness (RBE) of protons was compared with gamma rays for lethality and white blood cell (WBC) depression. The RBE's were based on both MAD and MTD data for comparison with values in the literature, and to point out the discrepancies that could arise when data based on exposure (air) dose instead of tissue dose are used. It is suggested that a more accurate comparison, for the biological endpoints considered, might be based on average body dose (ABD). The minimal lethal doses for gamma- and proton-irradiated animals, based on MAD, MTD, and ABD, were 485 and 500 rads, 325 and 650 rads, and 340 and 565 rads, respectively, giving RBE's of 1, 0.5, and 0.6, respectively. The MAD's, MTD's, and ABD's to cause 80 percent WBC depression in gamma- and proton-irradiated animals were 290 and 200 rads, 190 and 250 rads, and 210 and 235 rads, respectively, for RBE's of 1.4, 0.7, and 0.9, respectively. The survival times of the decedents were essentially similar for the two types of radiation and ranged predominantly from the 10th to the 20th post-exposure days, which suggests prominence of the hematological syndrome.

The dose-response patterns of peripheral white blood cell (WBC) counts in animals given exposures of 500 rads and below were of interest. It was observed: (1) that the rate of depression appeared to be slower in proton animals even though the maximum level of depression was greater than in gamma animals; (2) the rate of recovery was fastest in both

proton and gamma animals given the highest dose, and slowest in those given the lowest dose; and (3) that a more permanent depression, maintained at about 50 to 75 percent of pre-exposure values, occurred from about the 50th to 60th post-exposure days in proton animals.

It is concluded on the basis of existing MTD data: (1) that for hematological effects, the effectiveness of high energy protons in large animals may be somewhat less than that of gamma rays, X-rays, or fast neutrons; and (2) that appropriate experimental data are lacking to even consider a maximum permissible emergency exposure for space explorers. The need to determine the effectiveness of protons, alpha particles, and other radiations prevalent in space on large animals, and, using sublethal doses, to study combined stress effects for establishing reasonably realistic exposure tolerance limits, is discussed.

INTRODUCTION

The hazard of radiation in space is of sufficient magnitude to require protective measures in manned spacecraft (refs. 1 to 3). The contributions of physicists, engineers, and life scientists are all essential in resolving this requirement. It is not an easy task because numerous uncertainties still persist, relating not only to environmental data and techniques for shielding calculations, but also to a permissible emergency exposure for man in space. The lack of pertinent experimental data precludes establishment of such a permissible dose level at present.

The biological effectiveness of protons—potentially the greatest radiation hazard known to exist in space—in man is unknown. It is unlikely that man himself will be purposely exposed to protons for assessment of their injurious effects. Consequently, the information must be derived from animal experimentation. Although extrapolation of animal data to man obviously has its limitations, past experience with other types of radiation has shown that valuable and useful information can be obtained from such animal studies (ref. 4).

This report is concerned primarily with the biological effects of protons in large animals. Pertinent neutron data will also be included. A review of the literature shows only a limited number of large animal proton studies. This is not too surprising because of the difficulties involved in exposing large animals to whole body proton irradiation in ground-based facilities. Relevant experimental proton data were presented at the Symposium on the Biological Effects of Neutron and Proton Irradiations (refs. 5 to 7).

The results presented in this report are from

the collaborative studies currently under way between NASA, Ames Research Center, and Lawrence Radiation Laboratory, University of California, Berkeley, to determine the biologic effectiveness of protons compared to other types of radiation in rhesus monkeys. They indicate that under our experimental conditions 200 MeV protons are less effective than 1.2 MeV Co^{60} gamma rays in causing lethality or white blood cell depression in whole body irradiated monkeys.

METHODS AND MATERIALS

Animals

Young adult male monkeys (*M. mulatta*) commercially imported from India and weighing about 4 to 6 kg at exposure time were used. The animals, which were quarantined for at least two months after arrival, underwent the usual routine treatment preparatory to their use (ref. 8). Blood for routine hematological studies (and occasional bacteriological cultures) was taken from the femoral veins. For pre-exposure hematological control values, blood samples were taken from each animal three to four times over a period of 1 month prior to irradiation. The frequency after irradiation was once every 3 to 4 days during the first post-exposure month and once every week or two thereafter. For exposure, the animals were sedated with thiamylal sodium, a short-acting anesthetic, strapped in a styrofoam animal holder, and placed on a rotator which turned the animal simultaneously around its longitudinal and vertical axes to provide an omnidirectional whole body exposure (refs. 9 and 10). The rates of rotation were 8 and 0.35 rpm, respectively. The animals were conscious throughout the exposure period, which lasted about 10 to 60 minutes, depending upon the

exposure dose. Nonirradiated control animals were treated similarly.

Exposure Set-up and Dosimetry

For proton exposure, the 730 MeV protons of the Berkeley 184-inch cyclotron were degraded to the desired 200 MeV energy level by multiple Coulomb scattering, which was accomplished by placing 42 inches of graphite between the path of the primary 730 MeV beam and the animal. This caused angular divergence of the emergent beam and provided the desired effective exposure field for whole body irradiation of monkeys. Dosimetric measurements indicated that the exposure dose at the perimeter of the effective 60 cm field at 7 meters from the beam port was about 70 percent of that at the center. Dose rate at the center was about 20 rads per minute. Figure 1 shows an animal positioned for exposure to protons. The Co^{60} radiation source at Berkeley was used for gamma exposure. A dose rate comparable to that of protons was obtained at a distance of 114 cm.

A reasonably flat, similar depth-dose profile for proton and gamma exposures was achieved by positioning the rotator in such a manner that the rate of vertical (sinusoidal) rotation (fig. 17, ref. 9) was minimal when the animal's longitudinal axis was parallel to the beam for exposure to protons, and perpendicular for exposure to gamma rays.

Surface doses were determined for each irradiated animal with dosimeters (polyethylene capsules filled with lithium fluoride) placed on the head, abdomen, arm, and leg. Depth-dose measurements were made in a frozen monkey cadaver in which dosimeters were placed on the surface and at varying depths at several loci. The exposure geometry of the cadaver was identical to that of live animals except, perhaps, for head movements of the latter. LiF dosimeters were used because of their convenience and reliability (refs. 11 to 13).

RESULTS

Dosimetry

The results of the depth-dose measurements are summarized in figure 2(a), in which the data are presented as percent of midpoint tissue

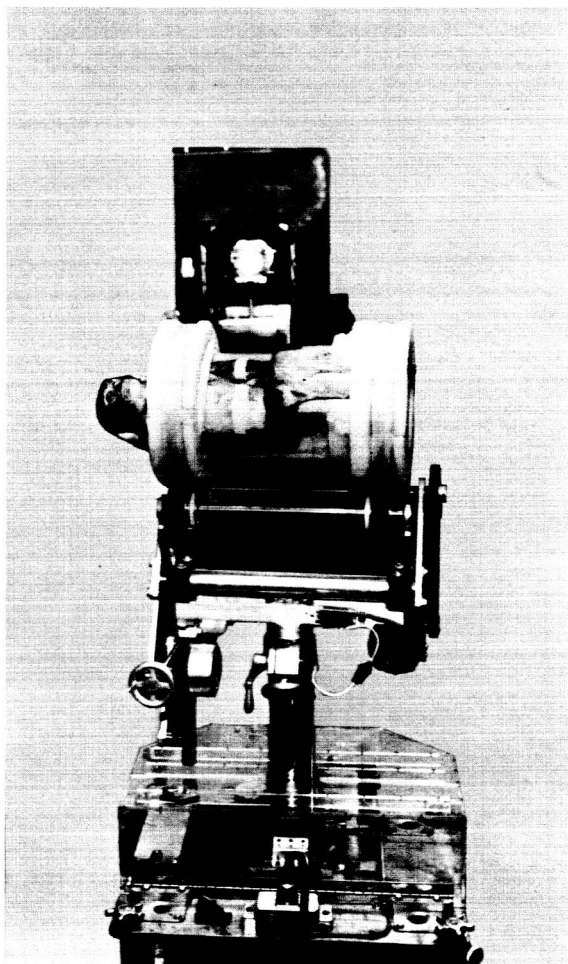
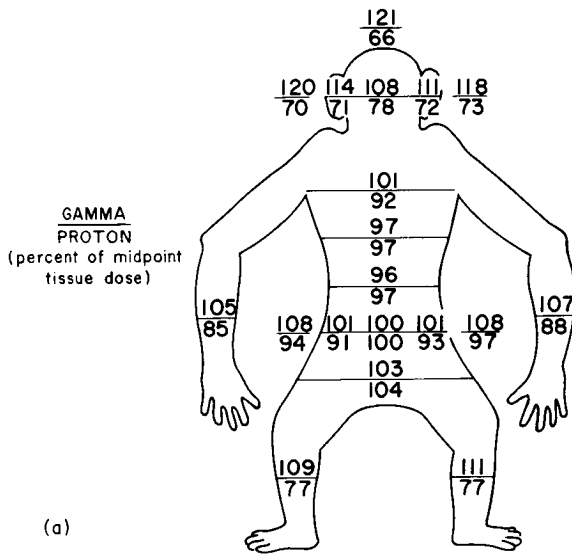


FIGURE 1.—Monkey positioned for omnidirectional exposure to protons from the Berkeley 184-inch cyclotron. The beam port is seen above the animal.

dose. The numerator at each point is the dose for gamma animals; the denominator is that for proton animals. The doses listed outside the animal are surface doses; those presented inside the animal immediately adjacent to the surface are doses at 1 to 2 cm depth; and those given in the center of the animal and in the limbs are midaxial doses. The midpoint dose is lower than in the extremities, including the head, in gamma animals, indicating a depth-dose fall-off; whereas, the midpoint dose is higher than in the extremities in the proton animals, indicating a dose build-up. The depth-dose profile shows that the tissue doses throughout the animal with respect to the midpoint dose varied from 96 to 114 percent in



(a)

(a) Whole body depth-dose profile.

FIGURE 2.—Depth-dose energy distribution profile in whole body irradiated monkeys: protons versus gamma rays.

gamma animals, and from 71 to 104 percent in proton animals.

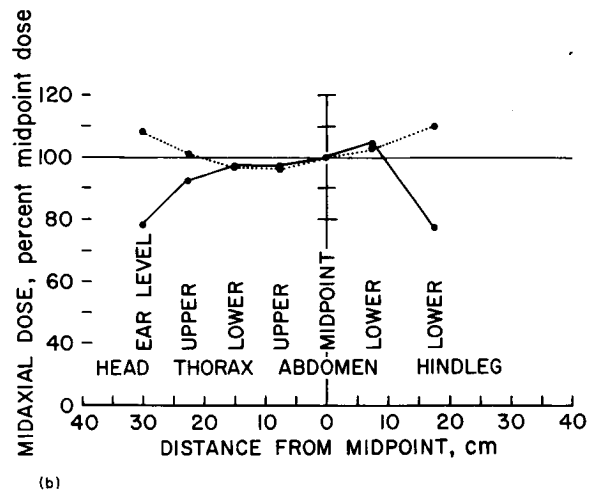
The midaxial dose profile is shown in figure 2(b). The midaxial trunk dose distribution was fairly uniform (or flat) for both gamma and proton animals. However, the doses in the head and in the lower hindlegs were about 10 percent higher than at the midpoint in gamma animals, and about 20 percent lower in proton animals.

The cross-sectional depth-dose profile at the midpoint level is illustrated in figure 2(c). It is evident that the MTD was about 8 percent lower than the dose at the surface in gamma animals, and about 3 to 6 percent higher in proton animals.

A comparison of MAD with MTD reveals that the latter is about 60 to 70 percent of the former in gamma animals, and about 120 to 130 percent in the case of proton animals. This means that for a given MAD, the MTD for protons is about twice that for gamma rays.

Mortality and Survival Time

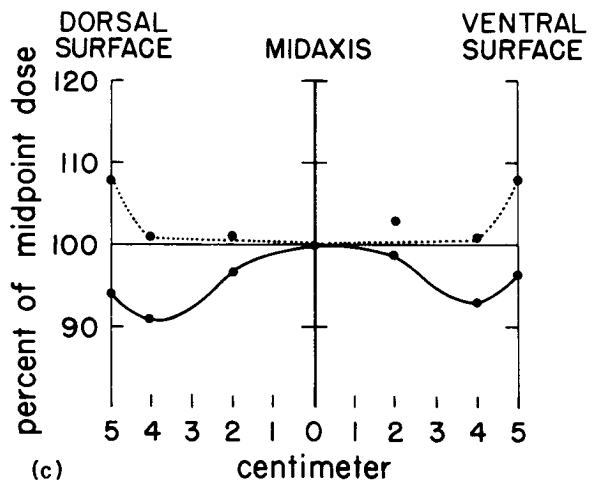
Table I summarizes the mortality and survival time data. When based on MAD, the minimal lethal doses for gamma and proton animals were essentially similar—485 and 500



(b)

(b) Midaxial dose profile. Solid line, protons; dotted line, gamma rays.

FIGURE 2.—Continued.



(c)

(c) Cross-sectional depth-dose profile at the midpoint level of the animal. Solid line, protons; dotted line, gamma rays.

FIGURE 2.—Concluded.

rads, respectively—giving an RBE of about 1. However, when based on MTD, the respective minimal lethal doses were 325 and 650 rads for an RBE of 0.5. The survival times of decedents were similar for the two types of radiation and ranged predominantly from the 10th to the 20th post-exposure days, which suggests prominence of the hematological syndrome (refs. 14 and 15).

White Blood Cell Response

Changes in peripheral white blood cell count, a fairly reliable and sensitive index of hemato-

TABLE I

Summary of Mortality and Survival Time Data

Type of radiation and experiment	Midpoint dose, rad	Survival time, days							
Gamma	Air -----	0	195	340	485	630	775	920	1065
	Absorbed---	0	125	225	325	425	525	625	725
63M2	Air -----						10		
	Absorbed---	S*		S	S	18	12	14	11
64M1	Absorbed---	S		S	S	16	12	15	11
64M4	Air -----		S	S	S				
	Absorbed---	S	S	S	29				
Proton	Air -----	0	200	350	500	650	800	950	
	Absorbed---	0	260	455	650	845	1040	1235	
64M2	Air -----	S	S	S	S	13	13	10	
64M3	Air -----	S	S	S	S	19	11	12	
64M5	Air -----		S	S	S				
	Absorbed---	S	S	S	18				

* 30-day period.

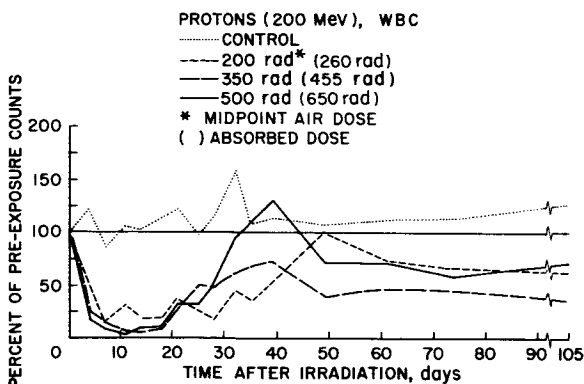


FIGURE 3.—Dose-response relationship of white blood cell count in whole body proton irradiated monkeys.

poietic tissue injury in whole body irradiated animals, were used to assess the effectiveness of protons compared to gamma rays. Figure 3 shows a radiation dose-WBC response pattern in our proton monkeys. Figures 4(a), 4(b), and 4(c) compare the WBC patterns in proton and gamma animals given 200, 350, and 500 rads air dose, respectively. Each line represents a single animal. As expected, the destructive

phase was dose dependent in both gamma- and proton-irradiated animals. Although the rate of WBC depression was faster in gamma- than in proton-irradiated animals at all three dose levels, the magnitude of the depression was greater in the proton animals (figs. 4(a), 4(b), 4(c)). WBC recovery in proton survivors was fastest in animals given the highest dose of radiation and slowest in those given the lowest dose (fig. 3). This was unexpected, since in general the rate of recovery is indirectly related to the magnitude of injury, which in turn is directly related to dose (refs. 16 and 17). This unexpected response was also seen in our gamma animals. A second, more permanent, WBC depression to about 50 to 75 percent of pre-exposure values occurred from about the 50th to the 60th post-exposure days in proton animals. This depression was not readily apparent in the gamma animals.

The relationship between radiation dose and magnitude of maximum WBC depression was determined for gamma and proton animals. The data are tabulated in table II and the mean

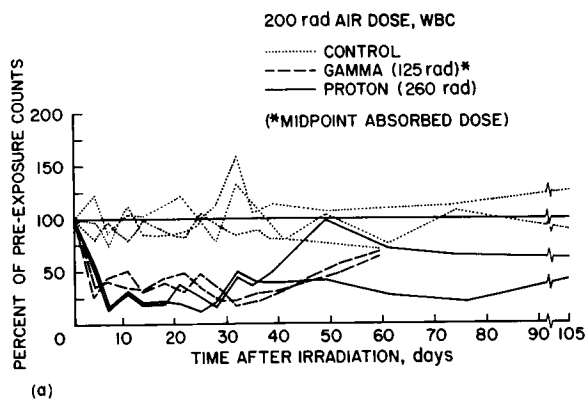


FIGURE 4.—Changes in white blood cell counts in whole body irradiated monkeys: protons versus gamma rays.

(a) 200 rad air dose.

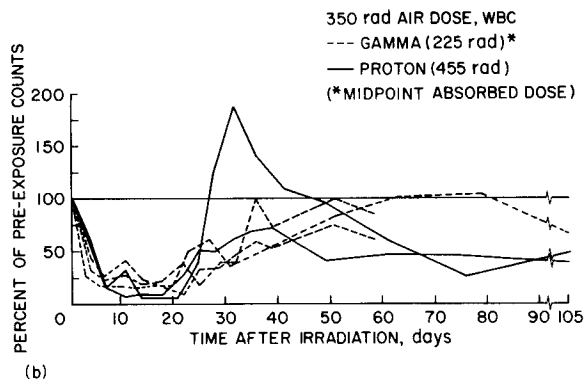


FIGURE 4.—Continued.

(b) 350 rad air dose.

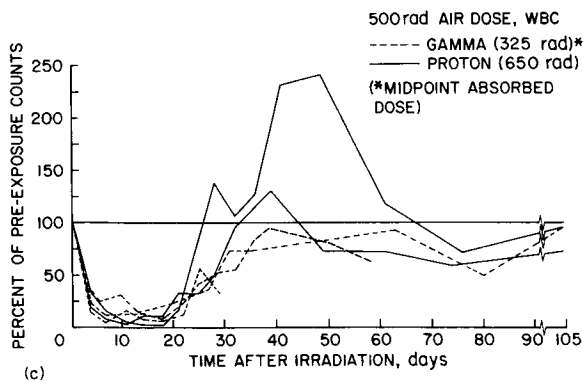


FIGURE 4.—Concluded.

(c) 500 rad air dose.

values are graphically presented as logarithmic probability plots in figures 5(a) and 5(b). The maximum WBC depression for each animal

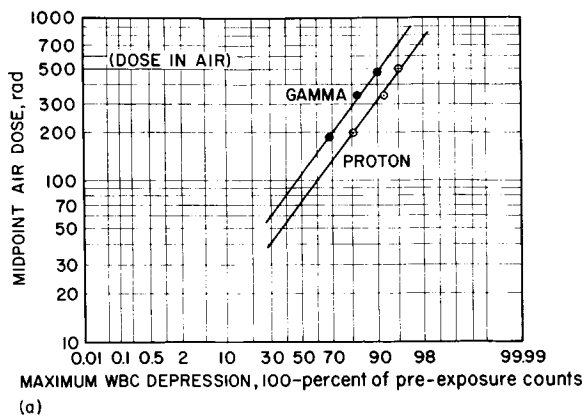


FIGURE 5.—Relationship between radiation dose and maximum depression of white blood cells in proton and gamma ray animals.

(a) Comparison based on air dose.

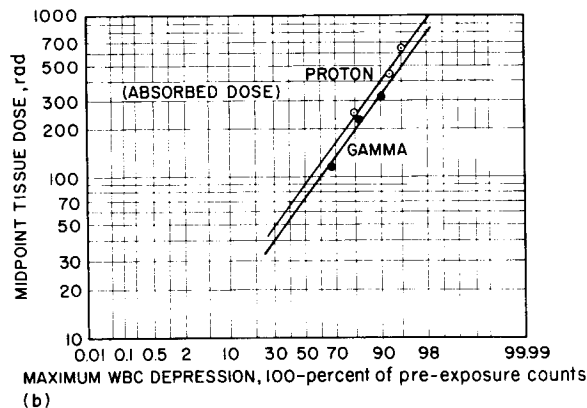


FIGURE 5.—Concluded.

(b) Comparison based on absorbed tissue dose.

was obtained by averaging several observations during the critical period, ranging from about the 6th to the 15th post-exposure days. The values given in the *Incidence* column of table II are the average depressions so obtained; each value represents the depression for a single animal. The values given in the *MEAN* column are the averages of the values given in the *Incidence* column. It is obvious that, when based on exposure dose (MAD), protons were more effective in causing WBC depression than gamma rays. However, when based on tissue dose (MTD), gamma rays were more potent than protons. For example, an exposure dose of 290 rads gamma rays compared to 200 rads proton was required to cause an 80 percent

depression in WBC (fig. 5(a)), giving an RBE of about 1.4. The respective tissue doses (MTD) were 190 and 250 rads (fig. 5(b)) for an RBE of about 0.7.

TABLE II

Relationship Between Radiation Dose and Magnitude of Maximum WBC Depression for Gamma and Proton Animals

Midpoint dose		Maximum WBC depression (100 % pre-exposure counts)	
Air, rad	Absorbed, rad	Mean	Incidence
Gamma radiation			
0	0	17	16, 18
195	125	68	68, 68
340	225	83	79, 87, 84
485	325	90	90, 93, 86
Proton radiation			
0	0	23	14, 15, 40
200	260	82	79, 84, 80, 87
350	455	92	95, 93, 86, 93
500	650	95	95, 92, 97, 95

Effectiveness of Protons and Neutrons in Large Animals

Table III (refs. 18 to 23 and 36) summarizes some of the pertinent proton and neutron studies in large animals. The three biological endpoints considered here have one thing in common—involvement of hematopoietic tissues. Hence, the RBE's apply primarily to hematologic effects of ionizing radiation. The effectiveness of fission neutrons, simulated fission neutrons, and protons have been compared with X-rays or gamma rays in dogs, monkeys, and in one case, goats. Acute, single exposure doses were used in all studies except by Baum (ref. 18), who compared the effect of four fractionated doses (150 rads per exposure, spaced 3 months apart) of simulated fission neutrons and gamma rays on erythropoietic recovery, as measured by Fe⁵⁹ uptake.

The studies of Alpen (ref. 19), Baum (ref. 18), Bond (ref. 20), and Grigor'ev (ref. 21) were similar in that they compared the effects of fast neutrons or protons with X-rays in dogs. The first three investigators reported RBE's of about 1 for neutrons, based on MTD data; the fourth, an RBE of 1 for protons. However, it was not clear whether the latter was based on air or tissue dose.

The studies of Pickering (ref. 22), Zellmer (ref. 23), and Taketa (this study) were comparable to the extent that they compared the effects of fast neutrons or protons with gamma rays in rhesus monkeys. Although it was not clear whether the first two based their RBE's on MAD or MTD data, it is known that they used the same basis, whichever it was. Their RBE values of 1.3 and 1.6 for neutrons and protons, respectively, suggest that protons may be as effective as neutrons. Taketa's RBE's of 1 and 1.4 for data based on MAD are not too different from those of Pickering (ref. 22) and Zellmer (ref. 23). However, Taketa's RBE's of 0.5 and 0.7, based on MTD, are lower by a factor of 2 to 3.

A comparison of the RBE values in table III based on MTD data (refs. 18 to 20 and Taketa, this study) indicates that high energy protons are less effective than gamma rays, X-rays, or fast neutrons for hematologic effects. The magnitude of the differences between protons and X-rays and neutrons is actually greater than is apparent here, when we consider that X-rays with which neutrons were compared are more effective than the proton-compared gamma rays (ref. 24).

DISCUSSION

The action of high energy protons, as used in this study, differs from commonly used lower energy gamma- and X-rays in that they induce dose build-up during passage through matter including tissue. This phenomenon, which was apparent in depth-dose measurements made in the present study, is particularly evident in large animals, since the dose build-up is related to the distance in tissue traversed by the primary protons. This increase in tissue dose is independent of the Bragg peak effect of the incident protons and is undoubtedly due to the production of secondary protons (elastic, cascade, and evaporation protons; in a

TABLE III
Relative Biological Effectiveness of Protons and Neutrons in Large Animals

Biological endpoint	Animal	Radiation: energy, MeV ^a	Dose, rads ^b	RBE and/or observations	Exposure geometry ^c	Investigator
Lethality	Dog	X: 0.25 vs SFN:9 1	MTD(252/289)	0.85(0.95)	BL	Bond, 1956 (ref. 20).
	Dog	X: 0.25 vs SFN:9 2	MTD(255/289)			
	Dog	X: 0.25 vs SFN:2	MTD(268/289)	0.9	BL	Alpen, 1960 (ref. 19).
	Monkey	G: 1.2 vs FN:14	MTD(212/239)	1.3	BL(?)	Zellmer, 1962 (ref. 23).
	Goat	G: 2.5 vs SFN:0.7	Air(?) (500/393)	0.7	BL	Batchelor, 1964 (ref. 36).
	Dog	X-ray	MAD(340/460)	1.0	?	Grigor'ev, 1964 (ref. 21).
			Air(?)	1.15	?	
			Air(?)	1.15	?	
			Air(?) (500/312)	1.6	UL(?)	Pickering, 1963 (ref. 22).
			MTD(325/650)	0.5	R	Taketa, This Study.
WBC depression	Monkey	G: 1.2 vs P:200	MAD(485/500)	1	R	Taketa, This Study.
	Monkey	G: 1.2 vs P:200	MTD(190/250)	0.7	R	
Erythropoiesis	Monkey	G: 1.2 vs P:200	MAD(290/200)	1.4		
	Dog	X: 0.25 vs SFN:2	MTD(150,4x)	1	X:R, N:BL	Baum, 1961 (ref. 18).

^a X = X-ray, N = neutron (S = simulated, F = fission), G = gamma ray, P = proton.

^b MTD = midline tissue dose, MAD = midline air dose.

^c BL = bilateral, UL = unilateral, R = rotation, X = X-ray, N = neutron.

subsequent paper by Wallace, Steward, and Sondhaus) and smaller numbers of other particles including electrons, mesons, recoil nuclei, and neutrons.

The importance of depth-dose measurements, particularly in large animals, cannot be over-emphasized (refs. 24 to 26). This is especially true when the degree of discrepancy between air and tissue dose differs greatly for the radiations being considered. For example, in the present study the MTD was 60 to 70 percent of MAD for gamma rays, and 120 to 130 percent for protons. Hence, for a given air dose (MAD), the tissue dose (MTD) in a proton animal was about twice that in a gamma animal. This difference was apparent in the RBE values for lethality and WBC depression, which differed by a factor of 2 when based on MAD (1 and 1.4) compared to MTD (0.5 and 0.7).

The discrepancy of 30 to 40 percent between MAD and MTD in our gamma animals is considerably larger than values reported by others. For instance, Baum (ref. 18) found midline tissue dose to be 17 percent lower than midline air dose in bilaterally irradiated dogs. Bond and Robertson (ref. 24) concluded that tissue dose is approximately equal to air dose in medium-sized species such as rabbit and monkey, given either bilateral exposure or lateral exposure with rotation along the long axis. The difference in ratio of air dose to tissue dose reported here compared to others could be explained, at least in part, by differences in exposure geometry, which is considered to influence greatly the relationship between air and tissue dose (refs. 24 and 25). It will be recalled that our exposure set-up was unique in that the animal was rotated simultaneously around its longitudinal and vertical axes for omnidirectional exposure.

Although we based our RBE values on both MAD and MTD data for a comparison with the values in the literature, and to point out the discrepancies that could arise when data based on air dose instead of tissue dose are used, a more meaningful comparison might have been based on average body dose (ABD). The reason for this is that tissue dose at midpoint was essentially the lowest for gamma rays and highest for protons. Hence, RBE's based on

MTD data were actually comparisons of extreme dose values, which were not necessarily representative of doses delivered to hematopoietic tissue—the tissue of interest in this study. Since hematopoietic tissue is found at various depths and loci, it seems that ABD may be a more realistic basis for RBE determination than MTD.

In order to compare the RBE's based on MTD data with those based on ABD, the ABD's for tissue doses listed in figure 2(a) were calculated. It was found that, for gamma exposures, ABD was about 5 percent higher than MTD, and for protons, about 13 percent lower. The minimal lethal ABD's for gamma and proton animals were 340 and 565 rads, respectively, for an RBE of 0.6 (compared to 0.5 based on MTD data). The ABD's required to cause 80 percent WBC depression in gamma and proton animals were 210 and 235 rads, respectively, for an RBE of about 0.9 (compared to 0.7 based on MTD data).

It is of interest that the RBE values of 0.5 to 0.6 for lethality and 0.7 to 0.9 for WBC depression found in this study were not too different from those given in a preceding paper by Stapleton for protons ranging in energy from a few MeV to 730 MeV on simple cellular systems, when the lower effectiveness of gamma rays to X-rays is taken into account.

Three observations involving WBC responses in proton and gamma animals are worthy of comment. The first concerns the observation that the rate of depression appeared to be slower in proton animals even though the maximum level of depression was greater than in gamma animals (figs. 4(a), 4(b), 4(c)). The latter response is apparently due to the higher tissue dose in proton than in gamma animals; however, this does not explain the slower rate of depression. The second concerns the observation that the rate of recovery was fastest in animals given the highest dose, and slowest in animals given the lowest dose (fig. 3). This phenomenon was also observed in gamma animals. The reason for this unexpected response is not known. Since it is apparently related to greater injury, it may involve infection, but not necessarily bacteremia. The third concerns the observation of a second, more permanent depression, main-

tained at about 50 to 75 percent of pre-exposure values, from about the 50th to 60th post-exposure day, especially in proton animals. The significance of this low WBC level is not known. Studies are in progress to determine the response of these animals to induced infection.

The data considered so far have been concerned with the effectiveness of highly energetic protons on hematological tissue in large animals. Now, let us consider the other biological effects of protons in large animals. Investigators at the USAF School of Aerospace Medicine, Brooks AFB, Texas, have undertaken studies to determine the biologic effects of monoenergetic protons ranging in energy from 14 MeV to 730 MeV in monkeys. In addition to the data presented in table III, Pickering (ref. 22) and Zellmer (ref. 27) reported RBE values of 1 for iridocyclitis and erythema, and 2 for epitation and desquamation in focal eye-irradiated monkeys exposed to 14, 39, 185, and 730 MeV protons (compared to Co⁶⁰ gamma rays). Rexford-Welch (ref. 28) reported that, in similarly irradiated animals, 730 MeV protons induced cataracts in 12 to 18 months at doses as low as 750 rads, whereas lower energy protons (14, 40, and 187 MeV) were ineffective even at doses as high as 2000 rads. This observation of cataractogenesis in high energy but not in low energy protons is of interest, since, for fast neutrons, damage to the lens is generally considered to be less pronounced with increasing energies (ref. 29). Rexford-Welch (ref. 28) also reported that death in the 187 MeV proton animals occurred in 100 to 200 days after exhibiting central nervous system (CNS) symptoms. Lindsay (personal communication) found that 6000 rads of 40 MeV protons to the whole body (given in two parts—upper and lower halves) caused convulsive seizures and death in about 48 hours following exposure, suggesting a CNS radiation effect. Admittedly the doses to produce the CNS effects were high, but the results are interesting and significant. Pickering (ref. 22) had expressed concern of possible latent or long-term effects based on his observation of a gradual onset of lethargy, anorexia, and ataxia exhibited among survivors of whole body proton-irradiated animals at 2½

to 5½ months post-irradiation. We have not observed these effects so far in any of our 5 to 6 month irradiated survivors.

A limited number of Russian reports involving large animal proton exposures have appeared. In addition to the data presented in table III, Grigor'ev (ref. 21) claimed that hemorrhage appeared earlier and was more severe in proton- than X-irradiated dogs. We have not observed any striking difference between proton- and gamma-irradiated monkeys at necropsy. A large animal (dog) exposure facility has been described by Afanas'yev (ref. 30) and the literature on the biological effects of neutrons and protons has been reviewed by Moskalev (ref. 26).

The existing MTD data suggest that, in general, the effectiveness of high energy protons in large animals may be less than that of gamma rays, X-rays, or fast neutrons. Whether this also applies to man is not known, since species differences are known to exist (refs. 15, 24, 31, and 32). Protons, like neutrons, have a preferential intestinal effect in whole body irradiated mice (ref. 33, and Sondhaus in a subsequent paper). It is clearly evident that additional data in several mammalian species are needed before extrapolation to man can even be considered.

Before proceeding with a discussion regarding the types of studies that are needed, let us first consider the criterion on which maximum permissible emergency exposure for man in space is to be based. It seems logical, as suggested by Schaefer (ref. 34) and expanded by Grahn in a preceding paper, that exposure should be kept below the level of acute injury and incapacitation effects which would impair performance. The criterion is, then, performance. The question remains, "What level of performance?" This is important, since success of a space mission may depend to a large extent upon the level of performance required of an astronaut. An example of the types of questions that should be considered is, "Would nausea impair the level of performance sufficiently to jeopardize the mission?"

Studies should be oriented to determine the exposure tolerance limits for the performance

capabilities required. It means studying sub-lethal as well as protracted dose effects, using both uniform and nonuniform (solar flare-type) depth-dose profiles. Biologic effects peculiar to ionizing radiations prevalent in space, particularly protons and alpha particles, should be determined and studied in detail to assess their significance. Examples of such effects observed in the present study have already been discussed: they involved apparent differences in the rates of WBC depression and recovery in proton compared to gamma animals. A realistic approach is to study in ground-based facilities

not only the effects of radiation, but also the combined effects of radiation and other stresses associated with space travel. (The influence of weightlessness as a variable would require studies in space.) Many of the nonradiation effects can be determined in man himself. However, chronic, long-term studies, and especially those involving ionizing radiation, require animal experimentation. Valuable data on radiation effects in man can be extracted from clinical radiation exposures (refs. 4 and 35). However, pertinency of the data so obtained will depend upon the performance required.

REFERENCES

1. FOELSCH, T.: Estimates of Radiation Doses in Space on the Basis of Current Data. Proc. Third Intern. Space Sci. Sym., (Washington, D.C.), Apr. 30-May 9, 1962, North-Holland Publ. Co. (Amsterdam), 1963, pp. 48-94.
2. McDONALD, F. B. (ED.): Solar Proton Manual. NASA TR R-169, 1963, p. 117.
3. FREIER, P.; and WEBBER, W. R.: Radiation Hazard in Space From Solar Particles. Science, no. 142, 1963, pp. 1587-1592.
4. BOND, V. P.; FLIEDNER, T. M.; and CRONKITE, E. P.: Evaluation and Management of the Heavily Irradiated Individual. J. Nucl. Med., vol. 1, 1960, pp. 221-238.
5. KOMAROV, E.: Biological Effects of Neutron Irradiations. Rept. on Intern. Symp. (Brookhaven Nat. Lab.), Oct. 1963. At. Energy Rev., no. 2, 1964, pp. 65-78.
6. IAEA (Vienna): Proc. Symp. Biological Effects of Neutron and Proton Irradiations, Oct. 7-11, 1963 (Upton, N.Y.), vol. I, Mar. 1964, p. 433.
7. IAEA (Vienna): Proc. Symp. Biological Effects of Neutron and Proton Irradiations, Oct. 7-11, 1963 (Upton, N.Y.), vol. II, May 1964, p. 446.
8. GISLER, D. B.; BENSON, R. E.; and YOUNG, R. J.: Colony Husbandry of Research Monkey. Ann. N.Y. Acad. Sci., no. 85, 1960, pp. 758-768.
9. SONDHAUS, C. A.: Biological Effects of High-Energy Protons. Proc. of Symp. Protection Against Radiation Hazards in Space, Nov. 1962, NASA TID-7652, Book 1, pp. 309-342.
10. SONDHAUS, C. A.; WALLACE, R. W.; LYMAN, J. T.; KASE, K. W.; and STEWARD, P. G.: Physical Parameters in Exposure of Large Animals to High-Energy Protons. Proc. Symp. Biol. Effects of Neutron and Proton Irradiations (Upton, N.Y.), vol. I, Intern. At. Energy Agency (Vienna), Mar. 1964, pp. 231-247.
11. CAMERON, J. R.; ZIMMERMAN, D.; KENNEY, G.; BUCH, R.; BLAND, R.; and GRANT, R.: Thermoluminescent Radiation Dosimetry Utilizing LiF. Health Phys., vol. 5, 1964, pp. 25-29.
12. MCCALL, R. C.; BABCOCK, L. E.; and FIX, R. C.: LiF Thermoluminescent Dosimeter System for Radiation Research. Radiation Res., vol. 19, 1963, p. 200.
13. TOCHILIN, E.; LYMAN, J. T.; ATTIX, F. H.; and WEST, E. J.: The Dose Response of Glass Thermoluminescent and Film Dosimeters to High Energy Charged Particles. Radiation Res., vol. 19, 1963, p. 200.
14. ALLEN, R. G., JR.; BROWN, F. A.; LOGIE, L. C.; ROVNER, D. R.; WILSON, S. G., JR.; and ZELLMER, R. W.: Acute Effects of Gamma Radiation in Primates. Sch. of Aviation Med., USAF (Randolph AFB), 1959. AFPS SA, Apr. 1960, 200 (59-41), pp. 1-23.
15. CRONKITE, E. P.; and BOND, V. P.: Effects of Radiations on Mammals. Ann. Rev. Physiol., vol. 18, 1956, pp. 483-526.
16. CRONKITE, E. P.; and BRECHER, G.: The Protective Effect of Granulocytes in Radiation Injury. Ann. N.Y. Acad. Sci., vol. 59, 1955, pp. 815-833.
17. SMITH, W. W.; ALDERMAN, I. M.; SCHNEIDER, C. A.; and CORNFIELD, J.: Radiation Dose-Response Characteristics of Leucocyte Recovery in the Mouse. Proc. Soc. Exp. Biol. Med., vol. 113, 1963, pp. 1016-1018.

18. BAUM, S. J.; DAVIS, A. K.; and ALPEN, E. L.: Effect of Repeated Roentgen or Neutron Irradiation on the Hematopoietic System. *Radiation Res.*, vol. 15, 1961, pp. 97-108.
19. ALPEN, E. L.; SHILL, O. S.; and TOCHILIN, E.: The Effects of Total Body Irradiation of Dogs with Simulated Fission Neutrons. *Radiation Res.*, vol. 12, 1960, pp. 237-250.
20. BOND, V. P.; CARTER, R. E.; ROBERTSON, J. S.; SEYMOUR, P. H.; and HECHTER, H. H.: The Effects of Total-Body Fast Neutron Irradiation in Dogs. *Radiation Res.*, vol. 4, 1956, pp. 139-153.
21. GRIGOR'EV, G.; DARENSKAYA, N. G.; DOMSHLAK, M. P.; LEBEDINSKII, A. V.; NEFEDOV, G.; and RYZHOV, N. I. (in Russian): Characteristics of the Biological Action and Relative Biological Effectiveness of High-Energy Protons. *Proc. Symp. Biol. Effects of Neutron and Proton Irradiations (Upton, N.Y.)*, vol. I, Intern. At. Energy Agency (Vienna), Mar. 1964, pp. 223-230. (English translation: AEC-Tr-6444, 1964.)
22. PICKERING, J. E.: Biological Effects of Whole Body Proton Irradiation. *Aerospace Med.*, vol. 34, 1963, pp. 942-943.
23. ZELLMER, R. W.; CULVER, J. F.; and PICKERING, J. E.: Proton Irradiation Effects in Primates. 2nd Intern. Cong. of Rad. Res. (Harrogate, England), 1962.
24. BOND, V. P.; and ROBERTSON, J. S.: Vertebrate Radiobiology (Lethal Actions and Associated Effects). *Ann. Rev. Nucl. Sci.*, vol. 7, 1957, pp. 135-162.
25. BOND, V. P.; CRONKITE, E. P.; SONDHAAUS, C. A.; IMIRIE, G.; ROBERTSON, J. S.; and BORG, D. C.: The Influence of Exposure Geometry on the Pattern of Radiation Dose Delivered to Large Animal Phantoms. *Radiation Res.*, vol. 6, 1957, pp. 554-572.
26. MOSKALEV, I. (in Russian): Some Results of the Study of the Biological Effect of Neutrons and Protons. *Proc. Symp. Biol. Effects of Neutron and Proton Irradiations (Upton, N.Y.)*, vol. I, Intern. At. Energy Agency (Vienna), Mar. 1964, pp. 181-193. (English translation: FTD-TT-63-1046, Foreign Tech. Div., AF Systems Command, Wright-Patterson AFB, Apr. 27, 1964.)
27. ZELLMER, R. W.; and ALLEN, R. G.: Cosmic Radiation-Laboratory Observations. *Proc. Symp. Aerospace Radiobiology, Aerospace Med.*, vol. 32, 1961, pp. 942-946.
28. REXFORD-WELCH, S. C.: Clinical Effects Consequent on the Exposure of Mammalian Ocular Tissues to High-Energy Protons. *Proc. Symp. Biol. Effects of Neutron and Proton Irradiations (Upton, N.Y.)*, vol. I, Intern. At. Energy Agency (Vienna), Mar. 1964, pp. 287-295.
29. LUSHBAUGH, C. C.: Vertebrate Radiobiology (The Pathology of Radiation Exposure). *Ann. Rev. Nucl. Sci.*, vol. 7, 1957, pp. 163-184.
30. AFANAS'YEV, V. P.; KEIRIM-MARKUS, I. B.; KUZNETSOVA, S. S.; LITVINOVA, E. G.; SOKOLOVA, I. K.; and STUKINA, L. YE. (in Russian): The Generation and Investigation of Field Doses for Irradiation of Experimental Animals with High-Energy Protons. *Proc. Symp. Biol. Effects of Neutron and Proton Irradiations (Upton, N.Y.)*, vol. I, Intern. At. Energy Agency (Vienna), Mar. 1964, pp. 71-90. (English translation: FTD-TT-63-1048, Foreign Tech. Div., AF Systems Command, Wright-Patterson AFB, Mar. 2, 1964.)
31. LEONG, G. F.; WISECUP, W. G.; and GRISHAM, J. W.: Effects of Divided Doses of X-Ray on Mortality and Hematology of Small and Large Domestic Animals. *USNRDL-TR-606*, Jan. 1963, p. 22.
32. PATT, H. M.; and MALONEY, M. A.: A Comparison of Radiation-Induced Granulocytopenia in Several Mammalian Species. *Radiation Res.*, vol. 18, 1963, pp. 231-235.
33. ASHIKAWA, J. K.; SONDHAAUS, C. A.; TOBIAS, C. A.; GREENFIELD, A. G.; and PASCHKES, V.: Difference in Injury Mode, Dose-Rate Dependence and RBE of 730-MeV Protons, 100-kVp X-rays, and 250-kVp X-rays. *Proc. Symp. Biol. Effects of Neutron and Proton Irradiations (Upton, N.Y.)*, vol. I, Intern. At. Energy Agency (Vienna), Mar. 1964, pp. 249-260.
34. SCHAEFFER, H. J.: Radiation Tolerance Criteria in Space Operations. U.S. Naval Sch. of Avia. Med., U.S. Naval Avia. Med. Ctr. (Pensacola, Fla.), Rept. No. 20, Sept. 1, 1961.
35. CRONKITE, E. P.; and BOND, V. P.: Radiation Injury of Man: Its Biological, Chemical, and Pathological Basis. C. C. Thomas Co. (Springfield, Ill.), 1960.
36. BATCHELOR, A. L.; and EDMONDSON, P. W.: Fast-Neutron Irradiation of Large Animals. *Proc. Symp. Biol. Effects of Neutron and Proton Irradiations (Upton, N.Y.)*, vol. II, Intern. At. Energy Agency (Vienna), May 1964, pp. 3-13.

10—The Radiobiological Consequences of Dose Distributions Produced by Solar-Flare-Type Spectra¹

ROBERT K. JONES

Lovelace Foundation for Medical Education and Research

and

DUANE E. ADAMS and IRVING J. RUSSELL

Air Force Weapons Laboratory

There are three situations in which ionizing radiations can pose a problem to crewmen on extended missions. These are: (1) prolonged orbiting in the trapped proton belts; (2) exposure to an Argus electron shell established by a high altitude nuclear explosion; and (3) encounter with a high energy charged particle event from the sun. Galactic cosmic rays, giving rise to whole body doses of approximately 10 rads per year, are considered to be of minor significance in the perspective of other mission risks (ref. 1). This paper will concern itself only with the solar flare question.

Solar flare particle radiations exhibit a characteristic which exercises a profound effect on their radiobiological significance: absorbed dose declines steeply with tissue depth because of the spectral character of the radiation.

Since there is no genuine counterpart on earth for the heterogeneous mixture of radiations which compose a solar particle event, biological effects must be deduced from analogous radiobiological experimentation in radiation environments which simulate, in some measure, the three dimensional depth dose and LET (LET, linear energy transfer, usually expressed as kilovolts of energy dissipated per micron of tissue) spectral patterns given by typical solar flares. Unfortunately, there are no experiments

to date in large animals which simulate, in any realistic sense, both depth dose and LET spectral profiles given by solar flares. The results to be reported here are for a high LET source (fission spectrum neutrons). The results are applicable to the solar flare situation on an *a fortiori* basis.

In the last two years considerable advances have been made, notably by the Minnesota group (refs. 2 and 3) in systematizing the descriptive features of solar flare particle events. Whereas but a few years ago dose estimates by different investigators might disagree by orders of magnitude for the same flare—ranging from supra-lethal to trivial—current estimates have converged. Although satellite and high altitude balloon data obtained during the 19th solar cycle are sketchy in many details, particularly with regard to compositional, spectral and temporal features, nonetheless a workable description of solar flares appears to be at hand. Freier and Webber's use of the exponential rigidity spectrum, and the classification of solar flares according to their characteristic rigidity, P_0 (the spectrum associated with a given flare at the time of maximum intensity), have greatly facilitated a standard calculational approach.

Most radiobiological data available have been obtained under carefully controlled conditions of whole body exposures to highly penetrating, homogeneous, electromagnetic radiations, possessing mean free paths long compared to the

¹ The views and conclusions expressed in this paper are those of the authors and are not intended to reflect official views of the United States Air Force.

bodily dimensions of the experimental subjects. Few studies have been performed for the express purpose of investigating the consequences of steep depth-dose profiles. Among the more relevant are data analyzed by Wilson and Caruthers (ref. 4) on dogs exposed to X-rays of different average energies. They show that the dose quantity of importance at the LD₅₀ level is that delivered to the bone marrow or to the tissue mid-line point. LD₅₀ for 250-kVp X-rays is 275 rad (mid-line air dose), giving a corresponding mean bone marrow dose of 165 rads. The mid-line air dose required for LD₅₀ was markedly elevated when less penetrating X-rays were employed. For example, a concomitant exposure of 3000 rads of 50 kVp and 250 rads of 250 kVp, delivering a mean bone marrow dose of 150 rads also corresponded to LD₅₀.

The most intriguing small animal experiment, to our knowledge, has been reported by Jackson (ref. 5). Using Co⁶⁰ and a wedge filter, he ingeniously produced a depth-dose pattern in the rat, which simulated that of the 16 June 1959 solar flare. The dose delivered at mid-line was 25% that at entry. The dose to produce LD₅₀ was elevated by a factor of three over the value obtained with unfiltered Co⁶⁰ irradiation. Most interestingly, he observed evidences of gastroenteric damage as a contributing cause of death.

These data bear upon the biological effectiveness of solar flare proton spectra because high energy protons exhibit a linear energy transfer (LET) in the majority of their interactions not too dissimilar from X-rays and gamma rays. In general, there will be a spectrum of LET. Without being too precise, it may be stated that up to some high value, cell-damaging potential increases with LET, although this microbiological effect may be difficult to discern in large and complex mammals, especially if depth-dose patterns are non-uniform. Calculations by Schaefer (ref. 6) have shown that LET spectra for 250-kVp X-rays for a filtered solar flare particle event are quite similar. Thus, it is not surprising that the relative biological effectiveness of *mono-energetic* protons in excess of 100 MeV, considering death as the end-point, is not too different than that obtained with hard electro-

magnetic radiations (Taketa and Sondhaus in other papers in this volume).

Unfortunately, there are few data extant on the effects of varying depth-dose profiles in animals similar in body mass to man. However, in the process of comparing the biologic effects of fission spectrum neutrons and 250-kVp X-rays on sheep, data were gathered by the Biophysics Branch of the Air Force Weapons Laboratory which provide some insight into this problem. Routine physiological and hematological observations were buttressed by post-mortem pathological examinations. The results of this work will be presented in a succeeding section. To provide a perspective on the solar flare problem, we shall first examine three selected flares more or less typical of a range of P_0 values.

The flares of 23 February 1956, 14 July 1959, and 12 November 1960, were chosen for this study. The proton fluxes in excess of 30 MeV for these three events were among the highest ever observed and, also, they represent a range of spectral types. It is assumed in these calculations that both the rise time and the decay time of each of these flares can be represented as an exponential. The parameters used by Webber (ref. 7) to describe these events are presented in table I.

In these calculations, the alpha component has not been considered. For the 14 July 1959

TABLE I

Parameters Describing Solar Particle Events

Date	Flux, $J > 30$ MeV	Spectrum, P_0 , MV	Rise time, t_R , hr ^a	Decay time, t_D , hr ^b
23 Feb 1956	1.0×10^9	195	6	30
14 Jul 1959	1.3	80	16	18
12 Nov 1960	1.3	124	10	18

^a t_R is the time interval at the earth from the first arrival of particles of a particular energy to the time at which the maximum intensity of these particles is attained.

^b t_D is the decay constant, where the intensity I of particles greater than some energy E at some time t after the maximum intensity of particles $I_{\max}(E)$ is: $I = I_{\max}(E) \exp(-t/t_D)$.

flare, a 1-1 proton-to-alpha flux ratio above a given rigidity was measured, and in the 12 November 1960 flare, there was a 2-1 proton-to-alpha flux ratio above a given rigidity. Behind 2 gm/cm² of shielding, the alpha dose to proton dose ratio in rads was 0.15 for the 14 July 1959 flare and 0.92 for the 12 November 1960 flare (ref. 2).

The dose due to secondary radiation is not included in these calculations; it is a rather small percent of the primary dose, with most of the secondaries being created in the body (ref.8).

It is assumed in these calculations that the protons arrive at the earth isotropically for the entire duration of the flare. Doses are calculated for both the free space environment and for near-earth orbits. In the near-earth orbits, the shielding provided by the earth's magnetic field has been taken into account. This has been accomplished by assuming that particles of a given energy can penetrate to a particular *L* shell (when *L* is defined as a line of force along which particles trapped in the earth's magnetosphere will travel) (ref. 8). It is assumed that during these larger events the accompanying geomagnetic storm causes a reduction in the magnetic field so that the effective *L* value at a given point is larger than normal (ref. 8).

There are two more parameters affecting the dose one will receive but which have not been included in the calculations. One is the shielding provided by the earth's mass. For a 200 n. mi. orbit, this shielding will reduce the dose by about one third. On the other hand, the albedo from reactions in the atmosphere may tend to increase the dose. To our knowledge, there have been no calculations and no measurements of this component of dose from a solar flare.

The Gemini vehicle and 2 gm/cm² and 5 gm/cm² aluminum spheres were used in the dose calculations. The Gemini was divided into 720 sectors to account for the heterogeneous shielding of the actual spacecraft. The astronauts are represented by Dye's 75 percentile model of man in the seated position (ref. 9), and the body self-shielding has been taken into account in these calculations.

The two dose points chosen were the chest

(skin dose) and a mid-line point 10 cm upward from the seat and 10 cm forward from the back of a seated man. These points were chosen because they represent the extremes in dose caused by the self-shielding of the human body. The second astronaut provides shielding to the occupant of the right-hand seat. The self-shielding effect is quite pronounced in the Gemini because there is a weak spot in the shielding above the astronaut's chest. Here the thickness of the Gemini capsule averaged over about 15% of the total solid angle is only 1.6 gm/cm². On the other hand, there is a region behind the astronauts subtending about 25% of the total solid angle where the average thickness is 6.8 gm/cm². This indicates that even the skin dose received in Gemini will be of a very non-uniform nature.

Figure 1 is a graph of the percent of skin dose as a function of tissue depth for the three

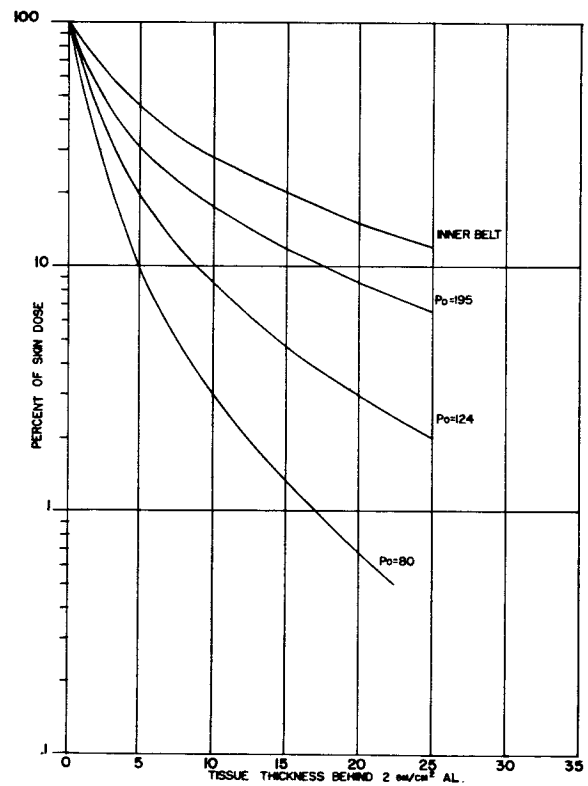


FIGURE 1.—Graph of the percent of skin dose as a function of tissue depth for the three solar flare spectra being considered.

solar flare spectra being considered. As can be seen, at a 5 cm depth, the solar flare dose is from 10 to 30 percent of the surface dose, being a function of the incident spectrum. It is to be emphasized that no critical organ is located at a discrete depth below the surface; since the body self-shielding is non-uniform, a more detailed analysis is necessary to determine the effect of a given radiation exposure on specific organs or organ systems.

The results of these calculations are summarized in table II. It is of interest to note that the doses obtained for the mid-line position in the Gemini suggest an effective shielding thickness somewhat in excess of 5 gm/cm². The skin doses obtained are more in consonance with the 2 gm/cm² results. There are weak spots in the Gemini's shielding where all protons above about 28 MeV can penetrate and contribute to the skin dose. This assumes 0.4 gm/cm² for space suit shielding. On the other hand, the 2 gm/cm² Al shield stops all particles below about 40 MeV.

Figure 2 is a graph of the LET spectra for $P_0=195$ at the mid-line and $P_0=80$ at the chest.

These values are comparable to those given by 250-kVp X-rays. Use of RBE versus LET curves given by Sondhaus (ref. 10) and others (ref. 11) would suggest an RBE near 1.

DEPTH-DOSE EXPERIMENTS IN SHEEP

The Sandia Godiva pulsed reactor delivers a source of fission spectrum neutrons in about 50 microseconds. At one meter from the reactor, first collision neutron doses of about 500 rads can be achieved for burst. The neutron to gamma rad dose ratio at this position is about 6.9. In connection with our studies of the effects of nuclear weapons radiations on large animals, we have performed a series of comparative effects studies with the Godiva and our 250-kVp X-ray source. A routine aspect of these experiments has been the documentation of neutron and gamma dose at entry, tissue-midline, and exit of the animal by surgically implanting dosimeters *in vivo*. Most of our data have been obtained using sheep (ref. 12).

Although a radiation source such as the Godiva may appear at first blush as a rather

TABLE II
Solar Flare Doses in Rads

	14 July 1959		12 November 1960		23 February 1956	
	Chest	Midline	Chest	Midline	Chest	Midline
	Free Space					
Gemini.....	145.0	2.5	128.0	8.9	92.0	16.0
2 gm/cm ²	158.0	4.0	148.0	12.0		
5 gm/cm ²	40.0	3.2	58.0	9.6		
	400 km circular orbit, 90° inclination					
Gemini.....	45.0	0.9	41.0	3.3	31.0	7.0
2 gm/cm ²	48.0	1.5	47.0	4.5		
5 gm/cm ²	14.0	1.1	20.0	3.5		
	400 km circular orbit, 60° inclination					
Gemini.....	17.0	0.4	17.0	1.7	13.0	4.0
2 gm/cm ²	18.0	0.7	19.0	2.3		
5 gm/cm ²	5.6	0.4	9.0	1.8		

TABLE III

Free Air and in vivo Dose Measurements in Sheep

	MAD	Subcutaneous entrance	Midline tissue	Exit
Neutrons-----	0.750	1.00 ± 0.07	0.117 ± 0.008	0.127 ± 0.008
Fission γ -----	.118	.134 ± .010	.190 ± .014	.080 ± .006

unlikely surrogate for a solar flare, the *in vivo* depth-dose pattern of the neutron dose component bears a strong resemblance to that of a solar flare. The average LET of fission spectrum neutrons (~ 100 keV/ μ) is considerably higher than it is for a solar flare proton spectrum (fig. 2). Hence, the cell-damaging potential of the neutron component will presumably be greater than if the pattern were produced by a solar flare spectrum. From this point of view the results derived from this comparative study may be considered to set a lower limit for the LD₅₀ of a large mammalian species subjected to a solar flare depth dose pattern. The ratio of mid-line tissue to entry dose in sheep, bilaterally exposed to 250 kVp X-rays filtered with 1.5 mm Cu, is about 0.85.

The results of the *in vivo* sheep measurements exposed to Godiva neutrons are summarized in table III. Enumerated are the mid-line free air dose (MAD), the sub-cutaneous entry dose, the mid-line tissue dose, and the exit dose for the first collision neutron and for gamma rays.

In figure 3 the depth-dose profiles obtained from bilateral exposures are depicted. The bilateral situation is more pertinent to the solar flare case since, apart from a brief period at the onset of the flare, the dose will be delivered essentially omnidirectionally. In table IV we list the calculated average relative doses delivered by the two components of the Godiva irradiations for the unilateral case, assuming an RBE of 4 for the neutron component in accordance with the indications of Sondhaus (ref. 10). This RBE corresponds to an average LET of about 50-75 keV/micron. The gamma component was assigned an average RBE=1. The variation of dose with depth was assumed to be as depicted in figure 3. The calculation

TABLE IV

Average Relative Doses of Neutron and Gamma Components

	Entry to mid	Mid to exit
Fast Neutron-----	0.682	0.198
Fission γ -----	.066	.054

was broken down from entry to mid-line and from mid-line to exit.

COMPARATIVE LD₅₀ MEASUREMENTS, X-RAYS AND FISSION NEUTRONS

The results of LD_{50/60} determinations in sheep with Godiva and with 250-kVp X-rays are summarized in table V.

TABLE V

Midline Air Dose

LD _{50/60} in sheep with neutrons and X-rays (bilateral)	
Godiva Neutrons-----	535 ± 11
250-kVp X-Rays-----	370 ± 15

Thus, in terms of lethality, the RBE for fission spectrum neutrons in sheep is ~ 7 . This value is considerably lower than the figure of 2-4 suggested by the National Committee on Radiation Protection and Measurement (ref. 13). As a result of work by Bond (ref. 14) and Pickering (ref. 15), it has been suspected for some time, however, that the recommended RBE for neutrons was unrealistically high. It is also apparent that the RBE, in terms of lethality, decreases with increasing body mass. We postulate that the value of 0.7 found in sheep is largely a reflection of the steep depth-

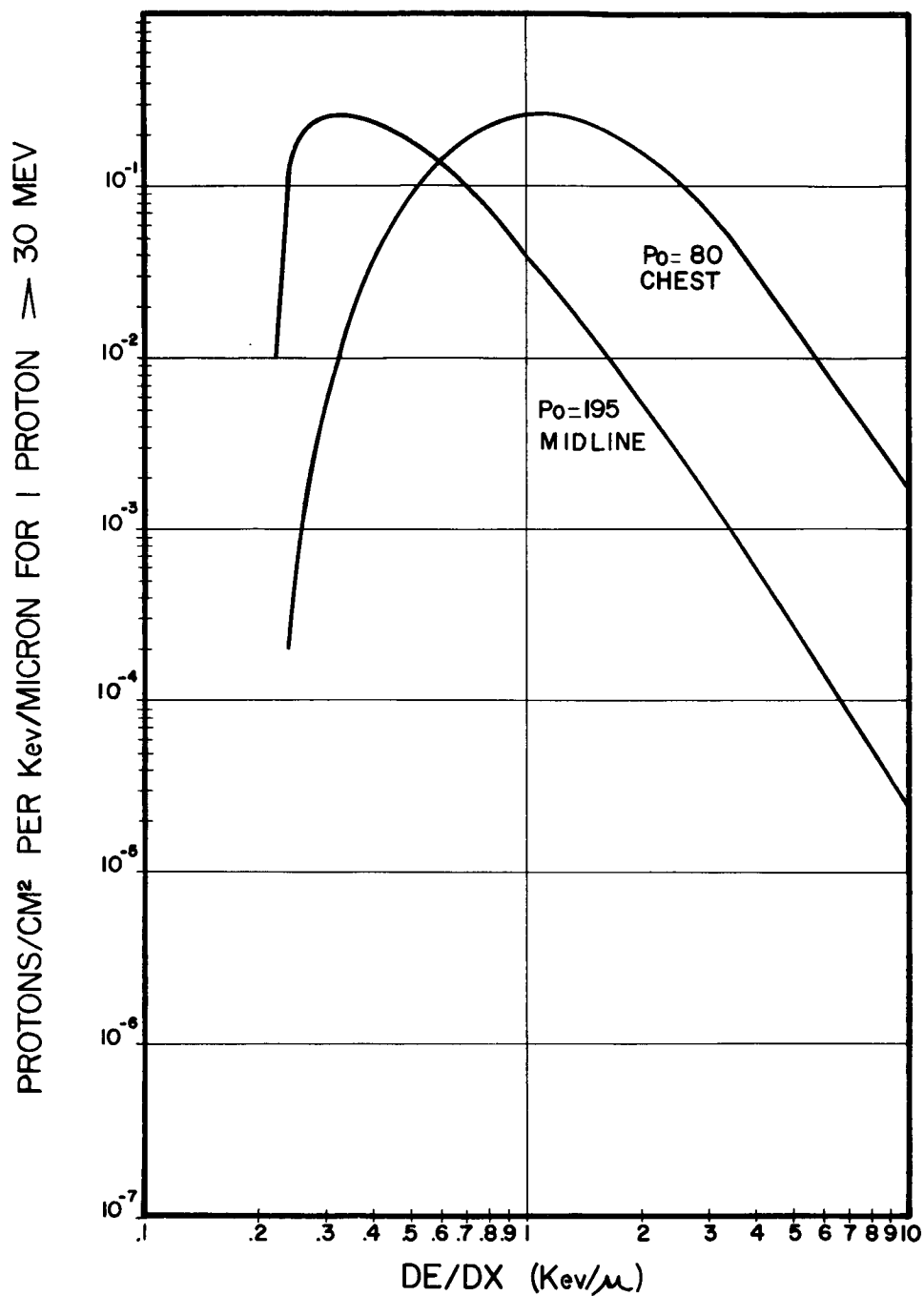


FIGURE 2.—Graph of the LET spectra for $P_0=195$ at the mid-line and $P_0=80$ at the chest.

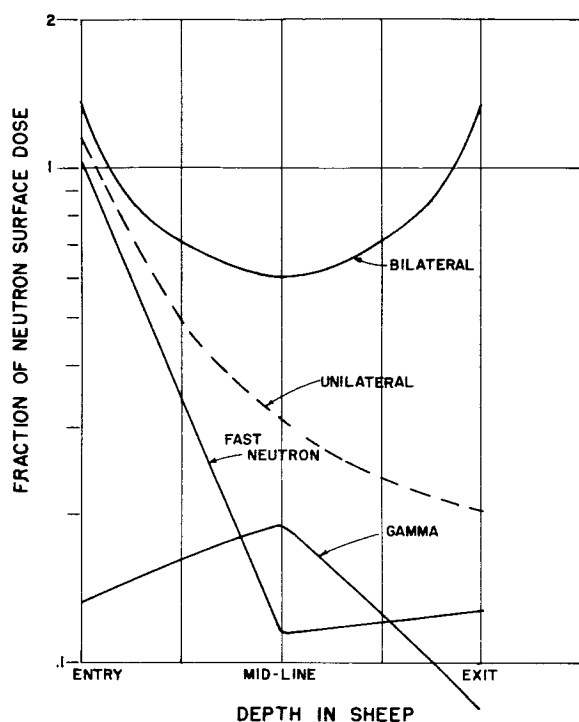


FIGURE 3.—Depth-dose profiles obtained from bilateral exposures.

dose profile exhibited by the neutron component. It does not imply that fast neutrons have an intrinsically lower RBE than gamma rays in large mammals, as the succeeding discussion of pathological observations will make clear.

A more extensive comparison of the effects of fission spectrum neutrons and 250-kVp X-rays on sheep was undertaken in collaboration with the Omaha Veterans Administration Hospital. Doses were delivered bi-laterally. Twelve sheep constituted each group consisting of four controls and eight experimental subjects for exposure. One group each was exposed to roughly 500, 400, 300, and 200 rads mid-line air dose of combined neutron-gamma from the Godiva. Similar groups were then exposed to matched total doses from a 250-kVp X-ray source at 10 R/minute. The dose rates delivered by these two sources differed markedly; therefore one cannot easily ascertain those differences in biologic response due to dose rate effect and those due to inherent differences in the two forms of radiation. However, the work of

Vogel (ref. 16) and Spalding (ref. 17) provides us with some assurance that dose rate effects are minimal in the case of neutrons, and therefore the following observations in all probability indicate differences in biologic response determined by the depth dose distribution and LET given by the Godiva and the X-ray source.

Figure 4 is a comparison of the death distribution derived from the three higher doses of fission spectrum neutrons and X-rays. One sees that neutron non-survivors die somewhat earlier than corresponding X-ray exposed animals. This is most evident in the $LD_{50/60}$ dose range where two animals died in the typical gastroenteric phase of the radiation syndrome. The other two animals died as a result of infection, as did the two non-survivors receiving 400 rad combined neutron-gamma radiation. Post-mortem examination on all non-survivors verified what had been suspected from the death distribution data. The gastroenteric tract was damaged more severely by neutrons than by a corresponding dose of X-ray and there appeared to be a threshold dose below which the enteric damage was not sufficient to lead to early death of the subject. The two animals that died on the fourth and fifth day, respectively, revealed marked desquamation of the enteric mucosa which assumed a peculiar, irregular distribution.

Two varieties of gastroenteric lesions were seen in neutron non-survivors dying between 11 and 14 days post-exposure. Multiple, distinct penetrating abomasal ulcers were present in two animals. These extended through the wall to involve the serosa and produced a striking peritoneal reaction.

Pseudomembranous enterocolitis was apparent in three animals. The proximal colon was involved to a greater extent than the small intestine or distal colon. In all cases the lesion assumed a skip type configuration with large areas of normal appearing tissue supervening between involved areas. Of perhaps most interest was the fact that these areas of involvement roughly corresponded with the areas of denudation observed in the animals that died on the fourth and fifth day post-exposure. This led to the premise that the affected loops of intestine represented segments which were in approximation to the lateral aspects of the

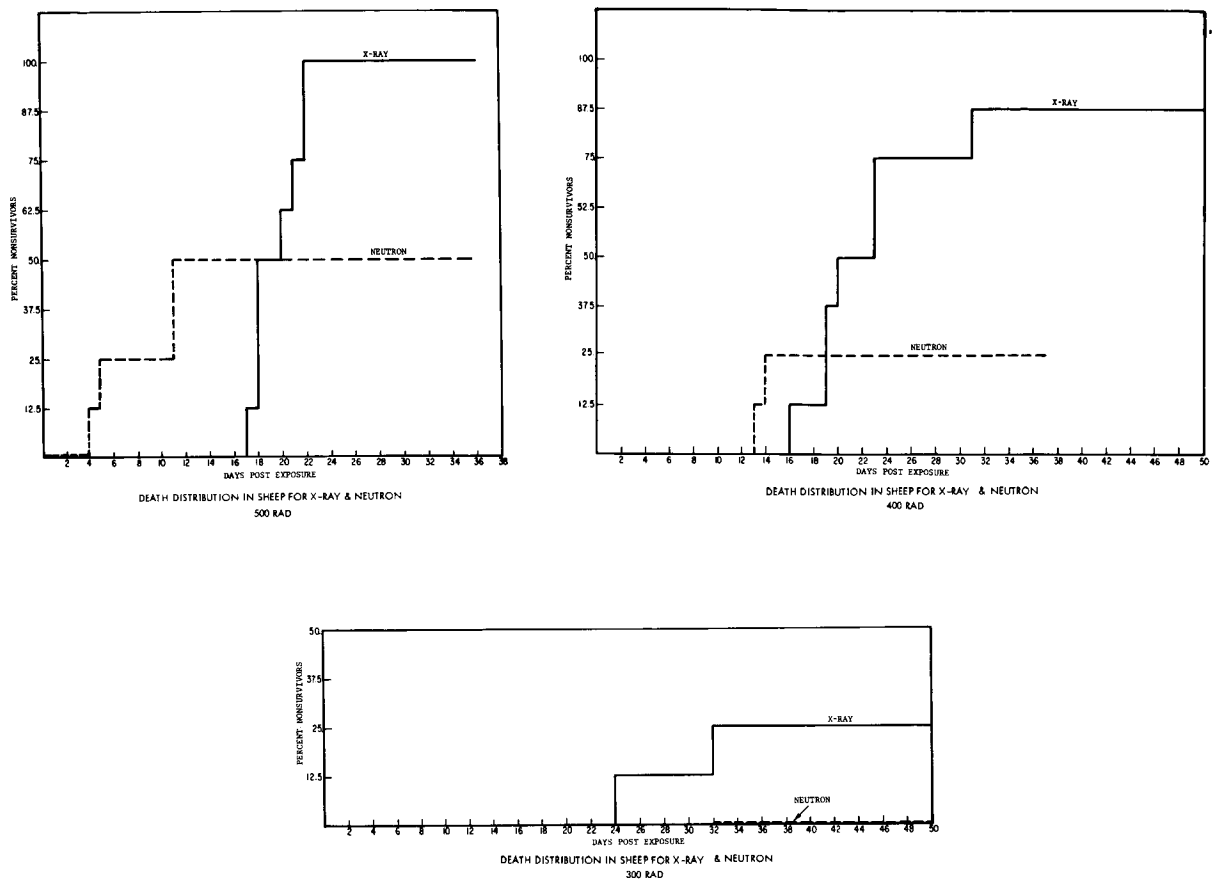


FIGURE 4.—Comparison of the death distribution derived from the three higher doses of fission spectrum neutrons and X-rays.

peritoneal cavity during exposure and therefore received an extremely high energy deposition. This postulate is most difficult to prove because of the inherent motility of the gastroenteric tract and the difference in position of sheep from the time of exposure to that assumed when assaulted by the pathologist's blade.

No similar enteric lesions were found in the X-ray exposed subjects, all of which died with typical signs of hemopoietic depletion and/or infection. Other than the aforementioned gastroenteric lesions, non-survivors from both groups showed no apparent grossly discernible differences.

The susceptibility of the enteric tract to neutrons has been observed in mice by Leshner and Vogel (ref. 18) who reported an RBE for gut damage of 6 in this species. It is interesting that Bond *et al.* (ref. 14) did not find early death in either rats or dogs exposed to neutrons;

it is possible that their highest dose, 475 rem, was below the threshold for injury severe enough to produce early death. Similar conclusions might have been drawn from this sheep study had the 500 rad dose group not been studied.

Figure 5 reveals another interesting difference in the biologic response of sheep to neutron and X-ray radiations. Although the initial fall in the peripheral platelets was similar for both forms of exposure, the neutron survivors demonstrate a remarkable recovery which began about 17 days post-irradiation. This response was most obvious in the higher dose groups, gradually becoming less evident until at 200 rad there is little difference in the response of sheep exposed to neutrons or X-rays. A similar but less pronounced difference in recovery was also observed in the total white count (fig. 6).

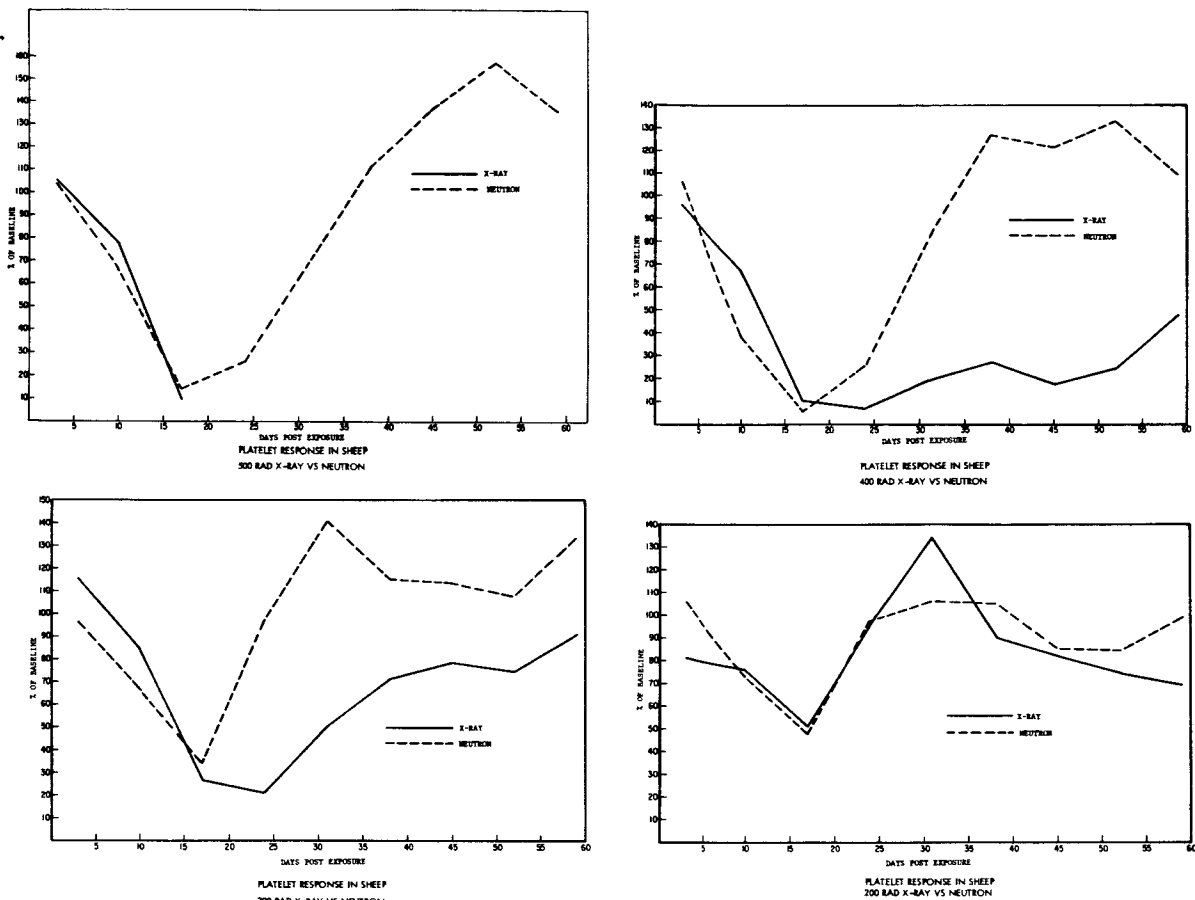


FIGURE 5.—Difference in the biologic response of sheep to neutron and X-ray radiations: platelet response.

This phenomenon has also been observed by Balm *et al.* (ref. 19) who found that repeated exposure of dogs to X-ray produced more severe leukocyte and platelet depletion than was seen in dogs exposed to neutrons. From this data it is evident that the bone marrow is less severely affected by neutrons than by X-ray. The explanation for this phenomenon probably lies in part in the difference in the percent of incident dose reaching mid-line marrow.

Striking disparities in response were also noted in the development of epilation and formation of cataracts.

Sheep receiving as little as 200 rads of neutrons showed complete epilation, whereas animals receiving the highest X-ray dose showed only patchy incomplete loss of wool. Thomas (ref. 20) working with burros also found a difference in the response of skin

appendages to these two forms of irradiation in this species.

Ocular changes resultant from exposure to fission spectrum neutrons were considerably more apparent than those resulting from a similar dose of X-ray. Although animals in this experiment have not survived long enough for cataracts to develop, a previous study has shown that doses as low as 500 rad combined neutron-gamma result in clinically significant uniform lenticular opacification within 10 months following exposure, whereas no cataracts were observed in X-ray exposed animals at this dose.

In applying these observations to solar flare radiation situations, one must carefully distinguish between those effects which are LET dependent and those which result from differences in depth dose profile. The average LET

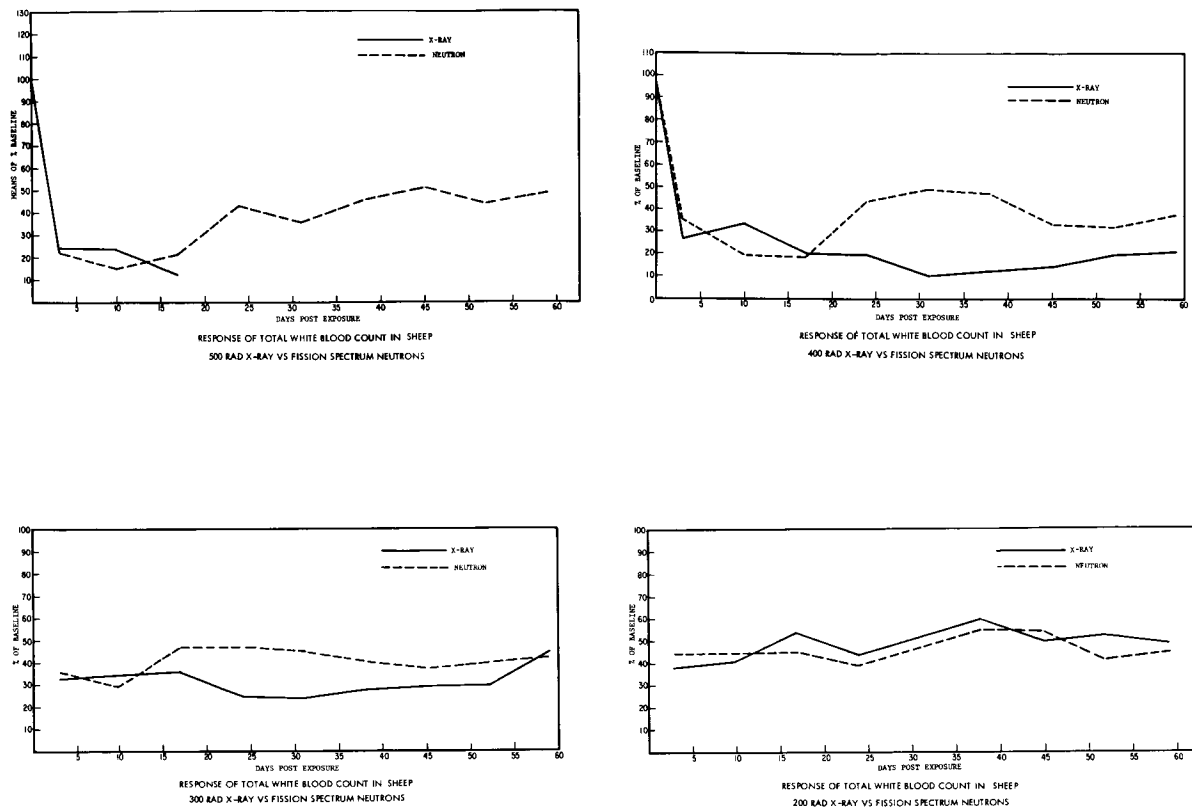


FIGURE 6.—Difference in the biologic response of sheep to neutron and X-ray radiations: white blood count response.

of fission spectrum neutrons responsible for the low threshold of epilation and cataract formation is perhaps 50 times that which is expected from solar flares. Even in the presence of a large alpha contribution, one might predict that the response of skin and lenticular structures to solar radiation would more closely approximate that seen consequent to X-irradiation.

The effect of solar flare protons on the gastroenteric tract will likewise to some degree be determined by these physical properties. Assuming a steep depth distribution profile and a low LET, one would suspect that the gastroenteric effects of such protons would be somewhere between those seen following X-ray and neutron exposure. The findings of Taketa and Sondhaus reported in other papers in this volume are of relevance. They find a hemopoietic picture and early death pattern in their proton irradiations delivered uniformly throughout the body strikingly similar in some respects to those we have found. This may imply that protons are more damaging to the gastroenteric system than are X-rays.

In any event, the steep depth distribution profile for solar flare protons should result in less hemopoietic damage than is seen following a corresponding dose of fission spectrum neutrons. Viewing this in a more practical manner, it would seem that total surface doses to the astronaut would have to be extremely high in order to deliver an effective dose to the deeper situated marrow cellular elements. The superficially orientated structures such as skin, eye, subcutaneous vessels, and even superficial loops of intestine would therefore assume the dominant role as critical areas for solar flare protons, and it is likely that our old standby the hemopoietic system may not prove to be the best biologic dosimeter in this situation.

CONCLUDING REMARKS

Based on information to date, it is concluded that no single one of the three high flux flares examined would have represented a serious radiation hazard to an astronaut in a polar orbit, even if he were to experience the full flux in a Gemini vehicle shielded only by the magneto-

sphere. This surmise should hold even if the alpha particle component were to lead to a doubling of the surface dose. The combination of relatively low surface dose (less than 100 rads); low LET (4 keV/ μ or less); steep depth dose profile (mid-line doses 7 rads or less); partial shielding provided by the Gemini vehicle (average 7 gm/cm² to the rear versus 1.6 gm/cm² from the front); and the protracted delivery of dose all lead to amelioration of the effect. According to Langham *et al.* (ref. 21), the threshold for the prodromal effect is about 100 rads, for penetrating whole body radiation, with higher thresholds likely for steeper depth dose distributions. Prudent measures can, of course, be adopted to provide partial body shielding to the eye, chest, and gonads with a minimum of weight penalty if further assurance is desired. For example, approximately 5 gm/cm² of shielding properly disposed about the astronaut will suffice to reduce his dose to the eyes, gonads, and chest by a factor of 3-10, depending on P_0 . Twenty pounds of shielding, distributed over two square feet, would give the desired 5 gm/cm².

The above analysis is based on ponderable evidence. No consideration has been given to such inponderables as synergisms between weightlessness, acceleration, vibrational, or psychological stresses. All would be expected on an intuitive basis to lead to an enhanced probability of personal indisposition, especially in the case of the prodromal syndrome. From a purely physical point of view, however, even allowing for a factor of two error in flux assessment and in the calculational program, the solar flare problem insofar as earth-orbiting vehicles

are concerned appears to be marginal at worst.

With respect to the physical parameters of solar flares requiring further definition, the next solar flare cycle should clarify these uncertainties. Of signal importance will be the characterization of the alpha particle component with respect to flux, depth dose, and LET spectrum. Direct verifications of calculational methods can be simply achieved by measurements of particle flux and simultaneously with spectrum, tissue equivalent depth dose, and LET during the life span of the solar flare.

Laboratory radiobiology research needs to become more mission oriented and to explore radiation environments peculiarly related to space: rate of dose application, LET of radiations, partially shielded configurations, and depth dose profiles. The finding that proton irradiated animals in the region of LD₅₀ display a propensity for gastroenteric death even when the dose distribution in the body is flat, as reported by Taketa and Sondhaus in other papers in this volume, calls for further investigation. This may have an important bearing on the acceptable threshold for the prodromal syndrome.

Jackson has pointed the way for exploring the consequences of steep depth dose profiles in animals as small as the rat. Imaginative extensions of this technique to other animals using protons is feasible. The important quantity to be simulated is not the proton spectrum *per se*, but the depth-dose and LET patterns in the experimental subject corresponding to those that would be produced in the body of a man by solar flare spectra.

REFERENCES

1. CURTIS, HOWARD J.: Some Specific Considerations of the Potential Hazards of Heavy Primary Cosmic Rays. Proc. Sym. on Protection Against Radiation Hazards in Space. Paper C-3, TID-7652, Atomic Energy Commission, 1962, pp. 291-308.
2. FREIER, P. S.; and WEBBER, W. R.: Science, vol. 142, Dec. 1963, p. 1587.
3. FREIER, P. S.; and WEBBER, W. R.: Exponential Rigidity Spectrums for Solar Flare Cosmic Rays. J. Geophys. Res., vol. 68, Mar. 1963, p. 1605.
4. WILSON, R.; and CARRUTHERS, J. A.: Health Phys., no. 7, 1958, p. 171.
5. JACKSON, K. L.: The Lethal Effectiveness of a Solar Flare-Type Dose Distribution Delivered to the Rat. Proc. Sym. on Protection Against Radiation Hazards in Space. Paper C-6, TID-7652, Atomic Energy Commission, 1962, pp. 375-392.
6. SCHAEFER, HERMANN J.: LET Spectrum and RBE of High Energy Protons. Proc. Sym. on Protection Against Radiation Hazards in Space. Paper C-7, TID-7652, Atomic Energy Commission, 1962, pp. 393-401.
7. WEBBER, W. R.: An Evaluation of the Radiation Hazard due to Solar Particle Events. Boeing Company Document D2-90469, Dec. 1963.
8. Computer Codes for Space Radiation Environment and Shielding. Technical Documentary Rept., No. WL TDR-64-71, vol. 1. Air Force Weapons Laboratory, Aug. 1964.
9. DYE, DAVID L.: Space Proton Doses at Points Within the Human Body. Proc. Sym. on Protection Against Radiation Hazards in Space. Paper D-8, TID-7652, Atomic Energy Commission, 1962, pp. 633-661.
10. SONDHAUS, C. A.: Biological Effects of High Energy Protons. Proc. Sym. on Protection Against Radiation Hazards in Space. Paper C-4, TID-7652, Atomic Energy Commission, 1962, pp. 309-342.
11. STORER, J.; HARRIS, P.; SURCHNER, J.; and LANGHAM, H.: Radiation Res., vol. 6, no. 2, 1957, p. 188.
12. ODLAND, L. T., ET AL.: Semi-Annual Report on Radiobiology Research. AFWL Rept., Aug. 1963.
13. PROTECTION AGAINST NEUTRON RADIATION UP TO 30 MILLION ELECTRON VOLTS: Nat. Bur. Std. (U.S.), Handbook 63.
14. BOND, V. P.; CARTER, R. E.; ROBERTSON, J. S.; SEYMOUR, P. H.; and HECHTER, H. H.: The Effects of Total Body Fast Neutron Irradiation in Dogs. Radiation Res., vol. 4, 1956, pp. 139-153.
15. PICKERING, J. E.: Biological Effects of Whole Body Proton Irradiation. Aerospace Med., no. 34, 1963, pp. 942-943.
16. VOGEL, H. H.; CLARK, J. W.; and JORDAN, D. L.: Radiology, vol. 68, 1957, pp. 386-398; and Radiation Res., vol. 6, 1957, p. 470.
17. SPALDING, J. F.; SAYEG, J. A.; and JOHNSON, O. S.: Dose Rate Effects on Lethality of Mice Exposed to Fission Neutrons. SM-44/13. Biological Effects of Neutron and Proton Irradiation, vol. 1.
18. LESHER, S.; and VOGEL, H. H.: A Comparative Histological Study of Duodenal Damage Produced by Fission Neutrons and Co⁶⁰ Gamma Rays. Radiation Res., no. 9, 1958, pp. 560-571.
19. BALM, S. J.; DAVIS, A. K.; and ALPEN, E. L.: Effect of Repeated Roentgen and Neutron Irradiation on the Hematopoietic System. USNRDL TR-474.
20. THOMAS, R. E.; and BROWN, D. E.: Response of Burros to Neutron-Gamma Irradiation. Health Phys., vol. 6, 1961, pp. 19-26.
21. LANGHAM, W. H.; BROOKS, P. M.; and GRAHN, D. (eds.): Radiation Biology and Space Environmental Parameters in Manned Spacecraft Design and Operations. Aerospace Med., vol. 36, no. 2, Feb. 1965, pp. 17-18.

11—Effect of High-Energy Protons and Alpha Particles on Small Mammals¹

CHARLES A. SONDHAUS

Lawrence Radiation Laboratory

Current studies indicate that the dose distribution produced in a mammal by exposure to high-energy protons is the most important parameter governing the type and degree of injury. For solar proton fluxes, average linear energy transfer (LET) is elevated significantly only at the ends of particle tracks, so that the high-LET component of a primary-plus-secondary proton dose remains small even with isotropic exposure of tissue volumes approaching the dimensions of the human body.

A review of experiments on small mammals (mouse, rat) in this country and abroad is presented. The results indicate a value of relative effectiveness about 0.7 to 0.8 times that of 250-kVp X-radiation for 50% mortality at 30 days, for protons at several energies above 50 MeV. In the small mammal, both the buildup of secondary particle dose and the gross nonuniformity of total dose distribution are minimal in this energy range, whether the exposure is unidirectional or isotropic. At energies below 50 MeV, the contribution of Bragg peak dose increases, since the dimensions of the animal exceed the particle range. Dose distribution in the tissue is thus nonuniform, and the apparent effectiveness of exposure dose increases.

Since recent experiments have shown a significant alpha-particle component in solar cosmic radiation, the effects of high-energy (910-MeV) alpha-particle irradiation of the mouse have also been investigated at this laboratory. A value of 720 rads for the LD₅₀ (30) dose has been found, which is identical to the value found for dose and, hence, for effectiveness of high-energy protons. This result is to be expected on the basis of dose uniformity and LET similarity between these radiations.

By use of a sufficiently large and well stabilized animal population, it can be shown that the relative effectiveness of high-energy proton and alpha radiation for acute mortality in the mouse is actually variable with time as well as dose, and depends on the time after irradiation at which mortality is evaluated. The effectiveness of both protons and alpha particles versus X-rays increases at shorter times post-irradiation, exceeding unity at 6 days. This effect, due presumably to temporal differences in the predominant injury modes constituting the acute radiation syndrome in these mammals, is discussed. The influence of dose rate is also considered.

INTRODUCTION

This symposium is largely concerned with the practical protection questions which have already arisen, mainly in regard to protons, in the planning phases of the space program. Recent experiments have shown that a significant alpha particle component exists in the solar flare radiation as well (ref. 1). During

the past 2 years, studies have been performed at Berkeley and elsewhere which may help us to draw some tentative conclusions in regard to the hazards of both of these radiations. Since the mammalian acute radiation syndrome has been studied extensively in small animal species, primarily the mouse and rat, exposed to X-, neutron, and gamma radiation, experiments with these animals enable us to relate our information to the vast body of radiobiological data which is available on these species and pertinent to human protection problems (refs. 2 and 3). The use of small animals also

¹ Research supported jointly by the National Aeronautics and Space Administration, under contract No. R-104, Task No. 2, and the U.S. Atomic Energy Commission.

permits us to investigate biological effects when no depth-dose variation pattern is present.

Some of the results of the first part of the Berkeley small animal program were reported on at the first Gatlinburg Symposium in 1962 (ref. 4) and at the IAEA Conference at Brookhaven in 1963 (ref. 5). Since that time, similar studies on proton effects were made here and abroad, and, by way of introduction, some of them will be mentioned briefly in this report.

Bonet-Maury and collaborators in Paris exposed both mice and bacteria to 157 MeV protons. In the mouse, they found a relative biological effectiveness of 0.77, for the ratio of median lethal doses at 8 days between protons and 250-kVp X-radiation (ref. 6). (This work was reported on fully at the Brookhaven Conference and is to be found in the recently published proceedings.) Subsequent to the French report, several Russian papers have appeared, describing studies with protons of several energies at 660 MeV and below, obtained by degrading the beam energy with absorbers; these are summarized here. No alpha particle studies appeared except our own.

At the highest energy, Kurlyandskaya and collaborators compared the effects of 660 MeV protons with those of X-rays in both mice and rats (ref. 7). They irradiated with a collimated beam 10 cm in diameter and determined the absorbed dose by calculation from flux density. The French and Russian investigators both determined the latter by measurement of induced activity in carbon plates exposed with the animals. Kurlyandskaya reports that the median lethal dose (LD_{50}) for mice exposed to X-rays was about 500 rad, and for protons, 1050 rad; these values were about 200 rad higher in rats. They concluded that the RBE of 660 MeV protons was about 0.5 to 0.6 for mice, and about 0.6 to 0.7 for rats. The same values were also indicated by blood changes, gonadal changes, and tumor induction ratios in the animals.

A somewhat different ratio was found by Shmakova and Yarmonenko, who studied the mitotic activity and the numbers of damaged cells in bone marrow removed from mice irradiated with 660 MeV protons (ref. 8). These workers reported that the number of

so-called "degenerate" cells was at least a factor of 2 less in the proton-irradiated mice than in the mice irradiated with cobalt 60 gamma radiation at the same dose level of 800 rads. They derived a value of RBE for protons of 0.3 compared to Co^{60} gamma radiation.

At lower proton energies, Grigoriev and collaborators irradiated rats with protons of 510, 240, and 126 MeV (ref. 9). They found 30-day LD_{50} values of 580 ± 40 rad at all three energies, while irradiation with X-rays produced an $LD_{50}(30)$ of 440 rad. The RBE value was thus between 0.7 and 0.8. Peak death rates were reported at 4, 8, and 10 days post-irradiation. In similar experiments with mice, they found an $LD_{50}(30)$ of 800 rad and an RBE of 0.7. These authors also report that two genetic effects showed the same value of RBE; these were the number of dominant lethal mutations produced in spermatogonial cells in the testis and the degree of weight loss in the testis as a whole.

Finally, Moskalev *et al.* irradiated white rats of the Wistar strain with 500 MeV protons and found an LD_{50} value of 710 rad at 15 days post-irradiation and a value of 600 rad at 30 days or beyond (ref. 10). They studied neutron effects more extensively than protons, and they report that fast neutrons in the energy range 0.2 to 14 MeV were found to be 1.5 to 1.7 times as effective as 500 MeV protons.

In this country, Plzcek, Doull and collaborators at the Air Force Radiation Laboratory in Chicago have studied the effects of protons on mice, at energies between 440 and 150 MeV (ref. 11). Their series of experiments was aimed mainly at investigating chemical protectant substances. They report somewhat higher RBE's approaching 1, the LD_{50} at 30 days being in the vicinity of 550 rads for all proton energies and for 250-kVp X-rays.

EXPERIMENTAL RESULTS

Randomly bred male Swiss mice have been used in all our experiments, and we have aimed at maintaining a well defined population by routinely selecting only those animals showing normal growth during a 2-week pre-irradiation period. All animals are caged individually throughout an experiment in pint-sized jars; the population is inoculated, checked frequently to assure freedom from pseudomonas and other

common pathogens, and well-standardized with respect to age and weight. Under these stable and isolated conditions, statistical variance among different experiments can be kept low.

In figure 1, mice are being loaded into irradiation tubes which are mounted on rotating disks in sets of six. This illustration also shows the individual caging technique. A disk loaded with animals is shown in figure 2 as it is positioned in the path of the particle beam. The disk is rotated during the exposure; the diameter of the collimated beam exceeds the disk diameter by a margin sufficient to insure an essentially flat intensity profile at the position of the animals. Three ion chambers are visible; one is a monitor chamber, and the other two are routinely used up and downbeam from the animals for control of the exposure dose. The beam emerges from the port in the shielding wall at the left. In addition to reading the dose in air, measurements of dose absorbed in the tissue have been made at points in the head, midline, and hindquarters of animals exposed anteroposteriorly to the beam in the manner shown. These absorbed dose measurements have been made by the newly developed method of thermoluminescent dosimetry (ref. 12). Small teflon capsules containing lithium fluoride are placed in the tissues of frozen mouse cadavers and the latter are exposed to the beam. Thermoluminescence produced in the LiF is proportional to energy absorbed from the beam; dose values are obtained by com-



FIGURE 1.—Loading individually caged mice on irradiation wheel.

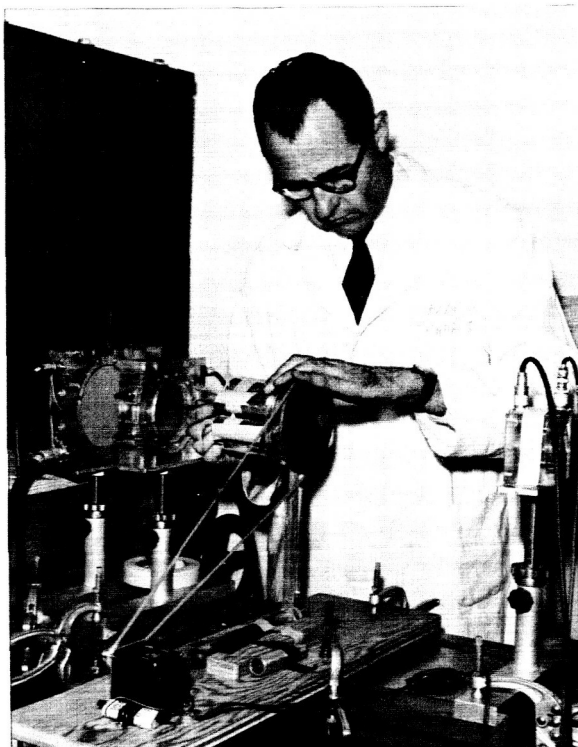


FIGURE 2.—Exposure set-up for irradiation of mice; medical cave of 184-inch cyclotron.

paring the integrated light output upon controlled heating of the powder samples with that from samples exposed to known doses in air. The response of the powder is proportional to dose and independent of dose rate and energy over a wide range.

Figure 3 illustrates the time course of mortality in mice exposed to 730-MeV protons and 910-MeV alpha particles from the 184-Inch Cyclotron, and to 250-kVp X-rays filtered with 0.5 mm Cu plus 1.0 mm Al. A marked difference in the time of peak death rate is immediately evident between the three radiations, although the doses chosen are such as to result in 97 to 99% death at 30 days in all three cases. The high incidence of early death at 4 to 6 days found here in the animals lethally irradiated with protons and alphas has been shown by much previous work (refs. 13 and 14) to be caused predominantly by the gastrointestinal injury syndrome, in which death results from damage to the rapidly dividing cells of the gut lining combined with bacterial infection and reduction in the numbers of circulating granulo-

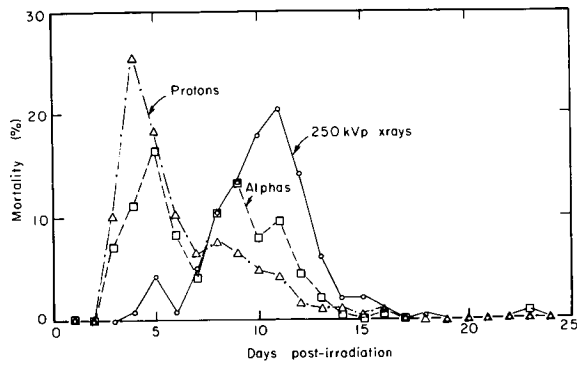


FIGURE 3.—Mortality vs time post-irradiation for mice exposed to 30-day 98% lethal doses of 730-MeV protons, 910 MeV-alpha particles, and 250-kVp X-rays.

cytes in the blood. The peak in death rate at 11 to 12 days in the X-irradiated animals is known to result from loss of cell production by the blood-forming tissues of bone marrow and spleen, producing the hematopoietic or bone marrow injury syndrome. These two injury modes are distinct and well separated in the mouse. It is apparent that the protons and alphas produce a high incidence of gut injury while the X-rays do not. There is thus a difference in the effectiveness of each radiation, with regard to either mode of injury.

Figure 4 shows these differences in another way, as dose-response curves or survival probabilities. Here the cumulative percent of deaths plotted on a probit scale for a given tissue dose in rads is shown for 6, 12, and 30 days after irradiation, the first two times corresponding to the characteristic times of peak death rate discussed above. For a proton exposure, three LD_{50} doses are thus defined; the 30-day tissue dose is 720 rad, while at the shortest time, 6 days, the median lethal dose is about 950 rad in tissue. These survival probability curves also illustrate that, for example, at a dose with 98% probability of death in 30 days, the probability of death at 6 days is already 50%, and similarly for other doses. This is what was shown for one level of mortality only in the previous figure. The curves reach about 300 rad at the 0.001–0.01% probability level, giving an estimate of the threshold lethal dose.

Figure 5 illustrates these relationships for 910 MeV alpha particles. Although the 30-

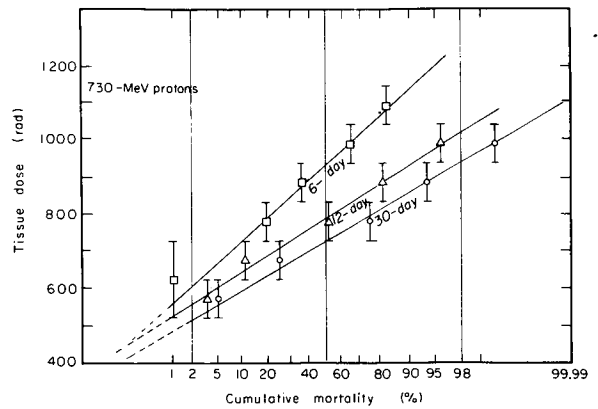


FIGURE 4.—Mortality vs dose at three times post-irradiation for mice exposed to 730-MeV protons (probit plot).

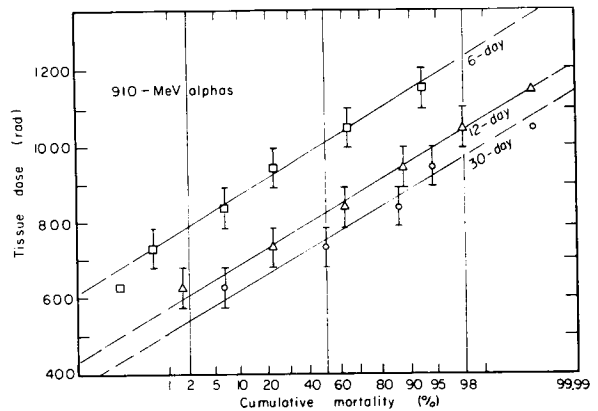


FIGURE 5.—Mortality vs dose at three times post-irradiation for mice exposed to 910-MeV alpha particles (probit plot).

day LD_{50} dose is essentially the same, the 6-day LD_{50} is higher, about 1000 rad; for a dose 98% lethal at 30 days, 30% or so of the lethality has occurred at 6 days. The estimated threshold dose for 30-day lethality is 400 rad.

Figure 6, showing cumulative mortality for different doses and times after X-ray exposure, illustrates that the 30-day LD_{50} value for X-rays is lower than for the particulate radiations, about 540 rads; that is, X-rays are more effective with respect to total mortality by 30 days. The threshold dose for this end point is about 200 rad. However, it is evident that for a dose which is, again, 98% lethal at 30 days, less than 5% of the deaths have occurred by 6 days. In other words, protons appear to be about 10 times as likely to produce intestinal

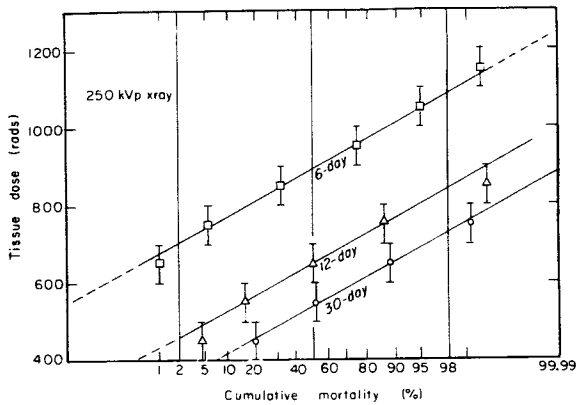


FIGURE 6.—Mortality vs dose at three times post-irradiation for mice exposed to 250-kVp X-rays (probit plot).

death as are X-rays for a given level of 30-day mortality in the mouse, and alpha particles fall between.

Figure 7 illustrates a further modifying effect, the dose rate. Although the point has not been extensively investigated, a higher proton dose rate, 1000 rad/min compared to 100 rad/min, appears to enhance early death at doses where the lower dose rate would produce relatively more late death. The average for both dose rates has been included; the previous graphs used the average values. It has been shown elsewhere for X- and gamma radiation that dose rate affects the 30-day LD_{50} , a higher rate increasing the effectiveness of the radiation (ref. 15), but no increase in the proportion of early death has been seen with increase in dose

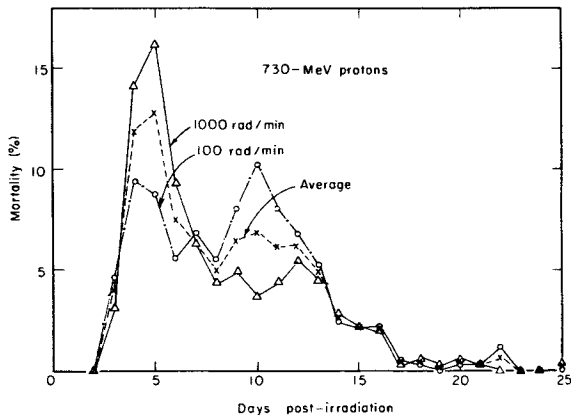


FIGURE 7.—Effect of dose rate on time course of mortality in mice exposed to the same total dose of 730-MeV protons.

773-446 O-65-8

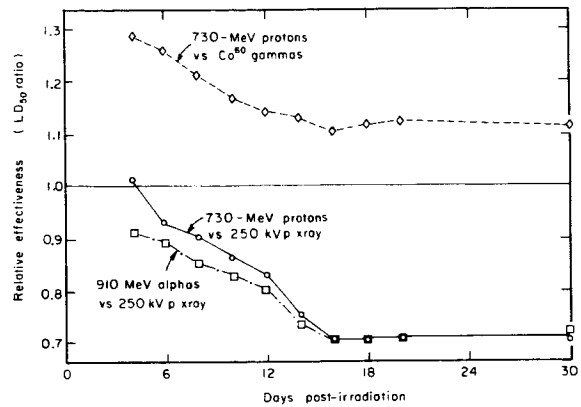


FIGURE 8.—Variability of relative effectiveness with time of median lethality for mice exposed to 730-MeV protons and 910-MeV alpha particles compared to X- and gamma radiation.

rate for X-rays. Further study at very low dose rates is presently impracticable but certainly needed with protons.

The relative effectiveness of proton and alpha radiation in regard to acute lethality is thus actually a variable, depending on the time after irradiation at which the lethality is evaluated. Figure 8 illustrates this effect; the ratios of LD_{50} dose are now plotted for each radiation against the post-irradiation time. Because of predominance of the different injury modes constituting the acute radiation syndrome, the effectiveness is near unity for protons at about the fourth day, and about 0.9 for alpha particles, but both decrease and converge to the value 0.7 from about day 16 onwards. The curve comparing protons with Co^{60} gammas is included for comparison; we have found a ratio greater than unity throughout the time interval.

Only a brief reference can be made here to the tissue dose characteristics, and to some preliminary experiments done with protons at energies below 50 MeV, at which energy the dimensions of the animal exceed the range of the particles in tissue. At the high energy, 730 MeV, no appreciable change in dose occurs with depth in the tissues, but instead, the production of secondary protons by intranuclear cascade, evaporation, and hydrogen recoil processes in the tissue results in a small and relatively uniform dose increase across the animal; this was found to be about 8% for protons. A similar process occurs for alpha particles and produces

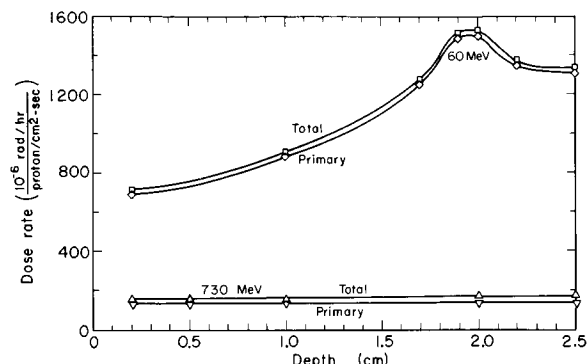


FIGURE 9.—Calculated primary and secondary proton doses in tissue equivalent sphere 2.5 cm in diameter, per unit isotropic proton flux.

about 12% increase in the tissue dose relative to air dose. These values, measured experimentally with LiF as described above, are in good agreement with calculations (see subsequent paper by Wallace, Steward, and Sondhaus). Figure 9, taken from these theoretical calculations, illustrates two cases. With protons of 730 MeV incident isotropically upon a 2.5 cm diameter tissue equivalent sphere, the small dose increase due to secondary protons is evident. When the calculations is carried through for 60 MeV protons, a smear of Bragg peaks near the ends of tracks produces a zone of high dose at some depths in the tissue because of cross contributions from the opposite side of the tissue volume. Superimposed upon this is the small secondary proton contribution. Since neither of these increases is indicated by the exposure dose values in air, the apparent effectiveness of the radiation increases relative to X-rays, in terms of the ratio of air doses. Preliminary experiments indicate that this increase is highly variable and depends on the tissue region in which the high dose is deposited, but so far, this ratio of effectiveness has not exceeded 1.5.

DISCUSSION

The results presented here confirm our previous experiments with protons, summarized earlier by Ashikawa (ref. 5). The difference in relative predominance of gut and bone marrow injury has now been found with alpha particle exposures as well, although the $LD_{50}(30)$ is found to be approximately the same for both radiations. It appears that the explanation of

the differences seen is to be sought in the microscopic dose distribution in bone marrow cavities and in soft tissue, since the LET of both radiations at high energy is similar to the X-ray controls.

It can be inferred from calculation, to be presented later (Wallace, Steward, and Sondhaus), that some tissue regions may receive one or two percent of the total dose from very low energy primary and secondary protons near the ends of their tracks. The relative biological effectiveness (RBE) of these particles may reach several times that of the primaries because of their higher LET, so that in some regions, depending on the dimensions of the animal and the energy distribution of the primary beam, the effectiveness of the dose may be increased by a few percent (ref. 16). This effect is small at high energies, but the differences observed between particulate and gamma radiation in the degree of acute injury produced in the mouse may result from such a factor, due either to proton cascade secondaries, neutron secondaries, or heavier particle production, neither of the latter two having been considered here. The differences in local dose are even greater in larger tissue volumes.

In bone, on the other hand, both calculation and experiment suggest that a gamma photon flux at ordinary X-ray energies will produce a high secondary electron flux in small cavities. This may therefore result in a dose to bone marrow which is higher than the average tissue dose (refs. 17 to 19). In the mouse, these cavity sizes may be smaller than in larger animals; the distribution of active blood-forming tissues in the marrow cavities of mammals needs to be investigated. In a 5 micron diameter cavity, for example, it is estimated that 250-kVp X-rays will produce a dose 1.3–1.8 times higher than in soft tissue. All the results observed with X-rays in the past would be influenced by this effect, whereas the high energy particle exposures would not be, regardless of their energy distribution.

In any case, it seems clear that the dose distribution, and probably the dose rate, factors are at least as important as the ionization density or LET in the practical problem of assessing relative effects of high energy particles on mammalian systems, and ultimately, on man.

REFERENCES

1. FRIER, P.; and WEBBER, W. R.: Radiation Hazard in Space From Solar Particles. *Science* 142, 1963, pp. 1587-1592.
2. CRONKITE, E. P.; and BOND, V. P.: Effects of Radiations on Mammals. *Ann. Rev. Physiol.* 18, 1956, pp. 482-526.
3. WHIPPLE, H. E., ED.: Physical Factors and Modification of Radiation Injury. *Ann. N.Y. Acad. Sci.*, 114, 1964, pp. 1-716.
4. SONDHHAUS, C. A.: Biological Effects of High Energy Protons. *Proc. Sym. on Protection Against Radiation Hazards in Space. Paper C-4, TID-7652, Atomic Energy Commission, 1962, pp. 309-342.*
5. ASHIKAWA, J. K.; SONDHHAUS, C. A.; TOBIAS, C. A.; GREENFIELD, A. G.; and PASCHKE, V.: Difference in Injury Mode, Dose-Rate Dependence, and RBE of 730 MeV Protons, 100 kVp X-rays and 250 kVp X-rays. In *Proc. Symp. Biol. Effects of Neutron and Proton Irradiations (Brookhaven), Oct. 1963. IAEA (Vienna), 1964.*
6. BONET-MAURY, P.; DEYSINE, A.; FRILLEY, M.; and STEFAN, C.: Relative Effectiveness of 157 MeV Protons. *C. R. Acad. Sci. (Paris)*, no. 251, 1960, p. 3087.
7. KURLYANDSKAYA, E. B.: Some Data on the Biological Effectiveness of Protons With Energies of 660 MeV. (Translation) *Joint Publ. Res. Service, JPRS-18395, pp. 363-368.*
8. SHMAKOVA, N. L.; and YARMONENKO, S. P.: A Cytological Analysis of the Effect of High Energy Protons. I. Cell Degeneration and Mitotic Activity of Bone Marrow in Mice Subjected to Whole Body Irradiation with 660 MeV Protons. *Radiobiologiya*, no. 3, 1963, pp. 291-293.
9. GRIGORIEV, G.; DARENKAYA, N. G.; DOMSHLAK, M. P.; LEBENDINSKII, A. V.; NEFEDOR, G.; and RYZHOV, N. I.: Characteristics of the Biological Action and Relative Biological Effectiveness of High Energy Protons. *Proc. Symp. Biol. Effects of Neutron and Proton Irradiations (Brookhaven), IAEA (Vienna), 1964. (Translation: AEC-TR-6444, 1964.)*
10. MOSKALEV, I.: Some Results of the Study of the Biological Effect of Neutrons and Protons. *Proc. Symp. Biol. Effects of Neutron and Proton Irradiations (Brookhaven), IAEA (Vienna), 1964. (Translation: FTD-TT-63-1046, Wright-Patterson AFB, 1964.)*
11. OLDFIELD, D. G.; PLZAK, V.; and DOULL, J.: U.S. Air Force Rad. Lab. Quart. Prog. Repts., 47-51, 1963-64.
12. CAMERON, J. R.; ZIMMERMAN, D.; KENNEY, G.; BUCH, R.; BLAND, R.; and GRANT, R.: Thermoluminescent Radiation Dosimetry Utilizing LiF. *Health Phys.*, vol. 10, 1964, pp. 25-29.
13. QUASTLER, H.; LANZL, E. F.; KELLER, M. E.; and OSBORNE, J. E.: Acute Intestinal Radiation Death. *Am. J. Physiol.*, vol. 164, 1951, pp. 546-556.
14. QUASTLER, H.: Effects of Irradiation on Intestinal Mucosal Cell Population. *Federation Proc.*, vol. 22, 1963, pp. 1330-1333.
15. BATEMAN, J. L.; BOND, V. P.; and ROBERTSON, J. S.: Dose Rate Dependence of Early Radiation Effects in Small Mammals. *Radiology*, vol. 79, 1962, p. 1008.
16. SCHAEFER, H. J.: Local LET Spectra in Tissue for Solar Flare Protons in Space and for Neutron Produced Recoil Protons. *Proc. Symp. Biol. Effects of Neutron and Proton Irradiations (Brookhaven), Oct. 1963, IAEA (Vienna), 1964.*
17. CHARLTON, D. E.; and CORMACK, D. V.: Energy Dissipation in Finite Cavities. *Radiation Res.*, vol. 17, 1962, p. 34.
18. WINGATE, C. L.; GROSS, W.; and FAILLA, G.: Experimental Determination of Absorbed Dose from X-rays Near the Interface of Soft Tissue and Other Material. *Radiology*, vol. 79, 1962, p. 984.
19. GEVANTMAN, L. H.; and CONNOLLY, E. B.: Absorbed Dose in a Ferrous Sulphate-Silica Analogue of a Tissue-Bone System. *USNRDL-TR-768, 1964.*

12—Biological Effects of Heavy Ions¹

PAUL TODD

Donner Laboratory

When one considers the magnitude of energy lost by high speed ions heavier than helium (or alpha particles), they loom large as a hazard wherever they are present. Particularly alarming are the early calculations presented by Schaefer (refs. 1 and 2) of the destructive ability of the densely ionizing tracks of the heavy-ion component of the primary cosmic radiation. The biological and experimental limitations of such calculations have been presented in detail by Tobias (ref. 3). Because of the high relative biological effectiveness of alpha particles, scientists have long been fascinated by the prospect of investigating the effects of heavier ions.

EXPERIMENTS WITH PRIMARY COSMIC RAYS

The discovery of high speed heavy nuclei in the primary cosmic radiation by Freier *et al.*, (ref. 4) led to some adventurous early research. It seemed reasonable to conduct high-altitude experiments with simple, but sensitive, test objects suspended in balloons. Seeds of genetically defined strains of plants can be evaluated for genetic and developmental aberrations and can withstand the rigors of balloon flight without careful protection. From the University of Chicago packets of seeds were flown at an altitude of 100 000 feet for 8 hours. Seedlings germinated from these seeds and their progeny were evidently without morphological abnormality (ref. 5). From our laboratory packages of commercial hybrid corn seeds were flown at 130 000 feet for 2 days, at 53° N latitude westward from Goose Bay, Labrador (Tobias and Slater, unpublished). A photo-

graph of one of the germinated seedlings is shown in figure 1. Streaked leaves were not observed in any of the control seedlings. It has not been possible to produce similar results with X-radiation. Table I shows the results of experiments with corn seeds. From these few data it appears that the total abnormality rate was around 8 percent for seeds exposed to the balloon-flight environment. It is estimated that the total dose received by the gondola was

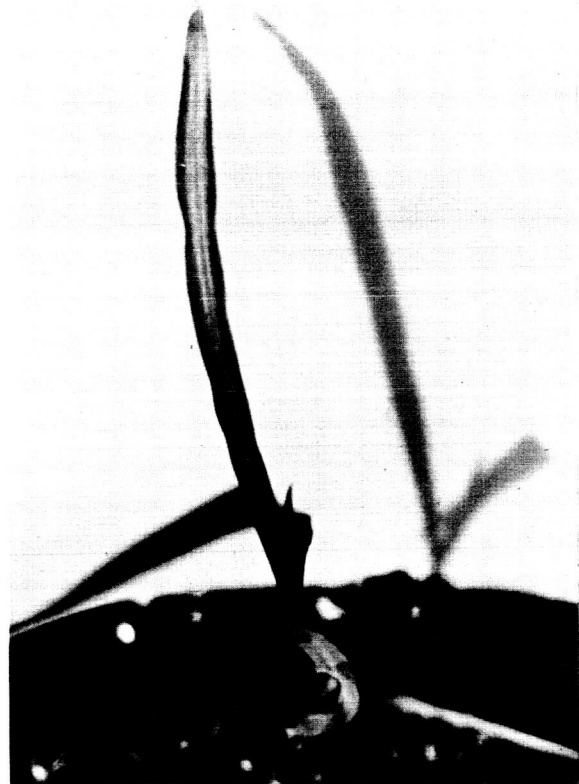


FIGURE 1.—An abnormal corn seedling germinated from a seed exposed to balloon-flight environment at 130,000 ft. (Tobias and Slater, unpublished).

¹ Research supported jointly by the National Aeronautics and Space Administration under NASA Order No. R-104, Task No. 2, and the U.S. Atomic Energy Commission.

in the neighborhood of 15 mrad. The 2300 r X-ray exposure resulted in many fewer abnormalities. Of particular note is the occurrence of cell-free streaks.

TABLE I

Developmental Defects Observed in Corn

	Number observed	Cell free streak	Spot bleaching
Control.....	36	0	0
Balloon Flight I....	49	3	1
Balloon Flight II....	67	2	3
X-ray Control.....	37	0	1

Curtis and Smith (ref. 6) have evaluated the frequency of somatic mutations from green to yellow in large numbers of genetically-defined corn seeds flown in artificial earth satellites. These experiments yielded results which are interpreted to be in accord with laboratory observations on the same genetic phenomenon.

Although these observations may be only remotely associated with effects in mammalian systems, they suggest that developmental processes in general are very sensitive to these radiations.

Some of the most definitive balloon experiments in this area have been performed with mice. Chase has reported what appear to be actual nuclear tracks in tissue; the amplifier in this case is the discolored hair which grew from follicles affected by cosmic-ray heavy nuclei (ref. 7). Further observations have been made on this phenomenon, an example of which is illustrated by the findings of Chase and Post (ref. 8) that the number of areas of discoloration may be related to the number of heavy-ion stops predicted by Schaefer, and that there is evidence for inhibition of hair replacement in damaged follicles. More recently, a team of workers headed by Haymaker performed similar experiments, in which the exposures were actually monitored by the nuclear-track methods of Yagoda, and pathological responses other than hair-graying were sought and not found (ref. 9).

Although the results are only qualitative, it is possible to conclude from the experiments

just cited that the major effects of heavy ions are upon *development*, and these effects probably stem from the inactivation of a large number of precursor cells by a single particle. That this is physically possible has been pointed out in the early calculations of Schaefer (ref. 2).

EXPERIMENTS WITH NEUTRON-INDUCED REACTIONS

Somewhat more quantitative results were obtained from deliberate radiation exposures due to nuclear reactions allowed to proceed *in vivo*. Specifically, the $B^{10}(n,\alpha)Li^7$ reaction has been used as a source of alpha particles and fast Li^7 ions simultaneously (ref. 10), and the thermal neutron induced fission of U^{235} has been used as a source of energetic ions in the 90-140 atomic weight range (ref. 11).

Results of the boron-disintegration experiments have been interpreted to indicate that a higher percentage of normal, tumor, or tissue-culture cells can be inactivated by thermal neutrons in the presence of B^{10} than can be inactivated in its absence (refs. 12 and 13).

In uranium fission experiments, mice injected with 2 mg of U^{235} -enriched UO_2 , and exposed to thermal neutrons, all died within 2 weeks, whereas mice exposed to the same neutron flux or the same amount of UO_2 all survived. The total neutron dose was one-half of the LD_{50} . It is interpreted that massive doses of high-LET radiation were delivered to the livers, spleens, and kidneys due to fission of the U^{235} nuclei. It originally appeared that fission was 27 times as effective as beta-emitting radioisotopes for the end-points observed. Because the fission effects were acute and the beta-emitting isotope effects were chronic, this effectiveness ratio should be reduced by a factor of approximately 3 (ref. 14).

Two clear generalizations arose from early quantitative studies on the effects of high-LET radiations (neutrons and alpha particles): sensitivity is increased and reversibility decreased if the response of the system to high-LET radiation is compared to the response to X-rays (ref. 15). Figure 2 illustrates that recovery of mice from the sublethal effect of neutron irradiation between fractionated doses is less than that which occurs between fractionated doses of X-rays. The residual injury

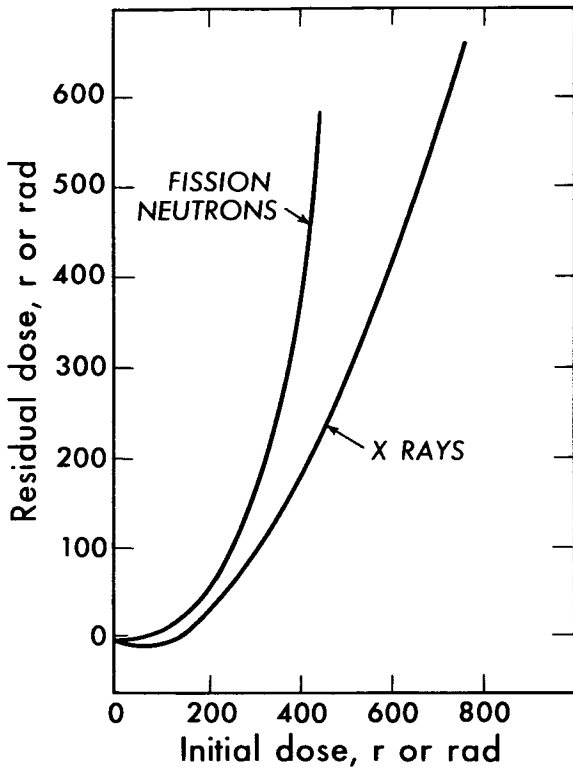


FIGURE 2.—Residual radiation injury in mice, following single acute exposures to X-rays and neutrons. (Grahn and Sacher, 1964.)

(measured in r or rads) is greater than that due to equivalent initial doses of X-rays (ref. 16).

EXPERIMENTS WITH ACCELERATED HEAVY IONS

In order to gain a quantitative approach to the problem of heavier-ion irradiation experiments, the help of large accelerators was sought by biophysicists at Yale and Berkeley. Figure 3 shows particle tracks and ionization (Bragg) curves for stripped ions of C, N, O, and Ne. These are among the more frequent nuclei in the primary cosmic radiation, due to their high cosmic abundance. They are called the *medium* nuclei. The ordinate presents total particle stopping power in MeV-cm²/g (or 0.1 keV/micron in unit density material), and these are the values that would apply to the corresponding cosmic-ray nuclei if they were stopped in tissue by ionization and if nuclear reactions were negligible. So far, nearly all elements up to and including argon, have been accelerated and used successfully in biological studies. Ele-

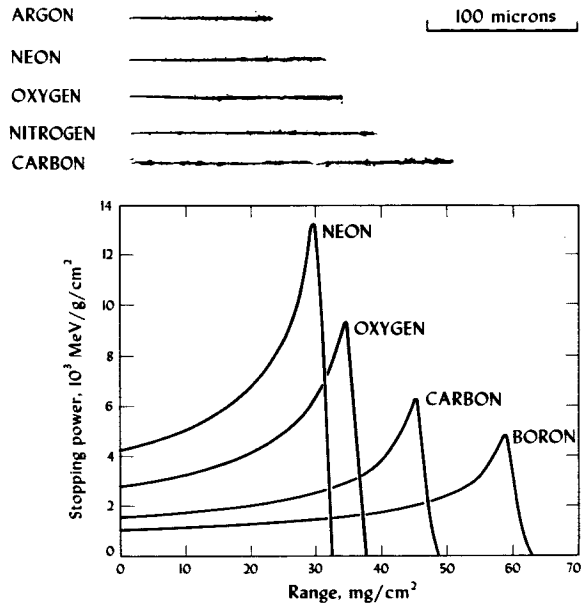


FIGURE 3.—Particle tracks and Bragg ionization curves of stripped ions of C, N, O, and Ne.

ments in the Fe-abundance (*heavy*) region are yet unavailable for radiobiological investigations.

In our experimental work, we have exposed small test objects by the track segment method, in which the specimen is sufficiently thin to leave the energy of the bombarding particle essentially unaltered upon passage through the specimen. Experiments generally determine inactivation as a function of dose, and the resulting inactivation curves are used to derive a probability of inactivation. The dose-response curves generally follow

$$N/N_0 = e^{-\sigma f}$$

if N/N_0 is the fraction of the sample (usually macromolecules or microorganisms) which escapes inactivation, f is the dose in particles per cm², and σ is the *inactivation cross section*, or probability, in reciprocal dose units (cm²/particle, in this case). We generally determine σ for particles of varying LET. From experiments on a large variety of test objects, interesting trends, which transcend phylogenetic boundaries, are beginning to emerge. Figure 4 shows plots of inactivation cross sections against total-particle stopping power for numerous test objects. The outstanding fea-

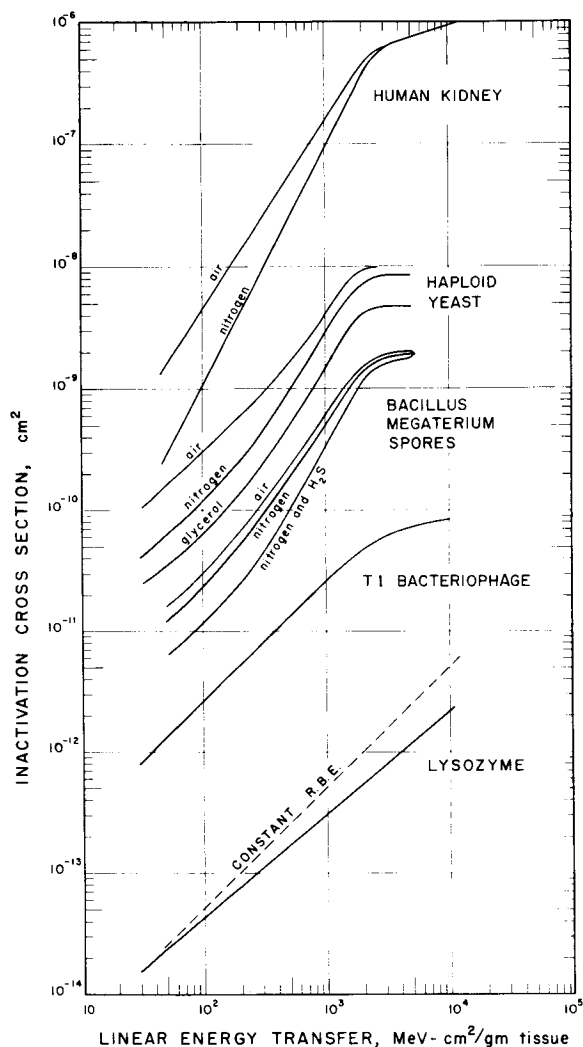


FIGURE 4.—Inactivation cross sections of biological test objects obtained from experiments using the Berkeley HILAC.

tures of this family of log-log plots are as follows:

1. The values of σ , in each case, become constant at about $3000 \text{ MeV-cm}^2/\text{g}$. This value of the cross section we have termed $\sigma(\infty)$, indicating that it applies at high LET.
2. The curves for small objects have a slope of 1, and those for large objects have a slope tending toward 2 at the intermediate values of the LET.
3. The shapes of all of the curves can be described by a function of the form

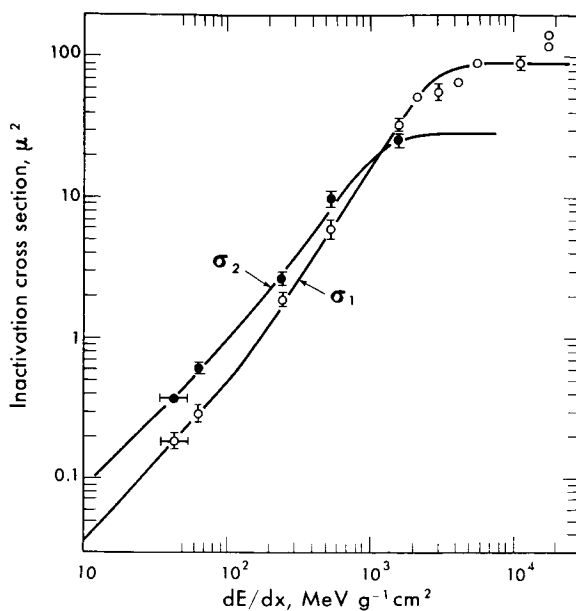


FIGURE 5.—Log-log plots of the inactivation cross sections of human kidney (T1) cells *in vitro*. The probability of irreversible inactivation is expressed by σ_1 , the initial slope of the "sigmoid" inactivation curves, and the probability of reversible inactivation (in which cells recover between fractionated doses) is expressed by σ_2 , determined from the final slope of the inactivation curves.

$$\sigma(E) = \sigma(\infty) [1 - \exp(-\alpha E - \beta E^2)]$$

in which E is LET and alpha and beta are coefficients which are constant for a given test object (ref. 17). This statement is also consistent with radiation chemical theory (ref. 18).

A more detailed version of this plot is given for human cells in figure 5. The upper curve corresponds to the initial slope of the survival curves, and the lower curve is an expression of the asymptotic (high-dose) slope of the survival curves. On the basis of dose-fractionation experiments, it can be said that σ_1 is the cross section for irreversible lethality and is probably dose-rate independent, and that σ_2 is the probability of reversible injury, which is probably negligible at extremely low doses and dose rates. Note that $\sigma_1(\infty)$ is about 90 square microns, the area of the cell nucleus.

Another expression of these statements is found in the original experimental data for the lethal effect of heavy ions on human cells in

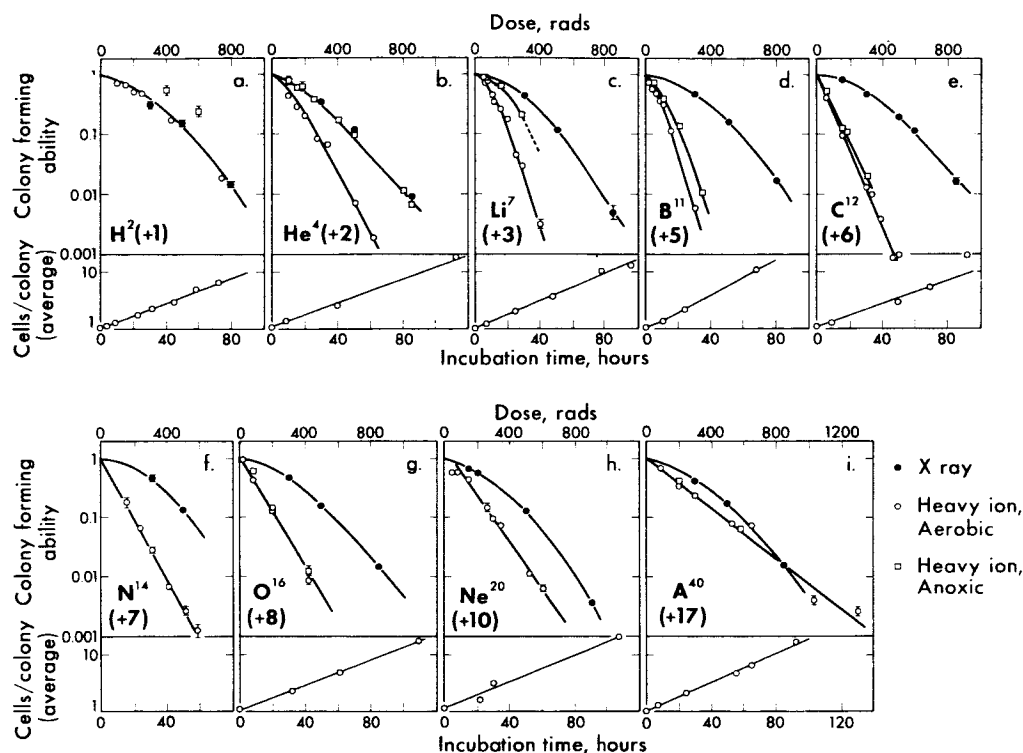


FIGURE 6.—Dose-response curves for the lethal effect of heavy ions upon human kidney T1 cells in the presence and absence of oxygen. Colony formation was the end-point.

tissue culture (ref. 19), figure 6. Each group of curves consists of the dose response of the colony forming ability of human kidney T1 cells (ref. 20) to X-radiation, and to heavy-ion irradiation under aerobic and anoxic conditions. The survival criterion is the ability of single cells to grow into visible colonies. The irreversible effect is very unimportant at low LET; that is, the initial slope of the curve is very slight by comparison to the final slope. At high LET, the curves become exponential and oxygen-independent. Apparently the lethal effect on human cells at high LET is irreversible and unalterable.

In passing, it is interesting to note that diploid yeast *can* recover from the lethal effects of very heavy ions if stored in distilled water and prevented from dividing (refs. 21 and 22).

The passage of a single ion (of LET 200 keV/micron) through the nucleus of a human cell suffices to inactivate it irreversibly. In

addition to this high relative efficiency, there is the further possibility that extremely densely ionizing particles may inactivate a cell by merely passing through the cytoplasm, thereby increasing $\sigma_1(\infty)$ by as much as a factor of 5 to 10. This conjecture requires further experimental substantiation, however, as it is based on the anomalously high experimental value of the A^{40} ion inactivation cross sections, for which the measurement of physical parameters in our system is still somewhat marginal.

Thus, it is not a simple matter to arrive at a means of predicting fractional cell lethalties for a mixture of heavy ions such as that which occurs in the primary cosmic radiation. As a first approximation, one might assume that $\sigma_1(E)$ is the nuclear area for ions in the C,N,O abundance group and that it is the total cell area for ions in the "iron abundance group". At the low doses which would be involved, it

is almost certain that cell lethality due to reversible injury can be neglected.

PREDICTED EFFECTS OF PRIMARY COSMIC RADIATION ON CELLS

The functional forms of these inactivation cross sections are employed by S. B. Curtis *et al.* in a subsequent paper in this symposium to estimate fractional cell lethalties due to solar flare particles from specific events with exponential rigidity spectra. In a crude way, we have investigated the relative importance of the three principal components of the primary cosmic radiation on the basis of these inactivation cross sections, and the assumption that a single ion in the heavy group inactivates a cell with probability 1.0.

Very roughly speaking, nearly all cells traversed by particles in the $Z=20$ to 30 range will be inactivated; about one-fifth of all cells traversed by particles with $Z=6$ to 10 will be inactivated; and about one-fiftieth of the cells traversed by particles with $Z \leq 2$ will be inactivated. In the primary cosmic radiation these particles occur with very approximate relative abundances of 0.2, 1.5, and 110, respectively (ref. 23). These abundance ratios give rise to relative hazards of 0.2, 0.3, and 2.2 for heavy, medium, and light nuclei, respectively, for each cell traversed by a primary cosmic ray.

The number of cells traversed by each type of particle depends upon the particle range. In numbers of cells, this can only be estimated very crudely, due to the very broad energy spectrum of all particles in the primary cosmic radiation. The ranges over which the above-

mentioned inactivation probabilities apply are roughly 300 cells for heavy nuclei, 200 cells for medium nuclei, and 20 cells for light nuclei. These ranges arise from calculations made at Boeing, assuming cells 30 microns in diameter and neglecting the effects of "star" events (ref. 24). Now, the relative hazards to the organism become 60, 60, and 45 for heavy, medium, and light nuclei, respectively. These approximations are summarized in table II. As Jones *et al.* point out in a preceding paper, this statement is applicable principally to the outer centimeter of tissue, so that blood-forming organs, for example, may not be involved, whereas the nervous system might.

It is important, at this point, to restate that the inactivation of a cell by a single heavy nucleus traversing its cytoplasm is an assumption yet to be verified, as such heavy particles are not currently available for laboratory research. It is interesting, however, that mouse spermatogonia respond to fast-neutron irradiation as if a single neutron passing through the cell suffices to inactivate it (ref. 25).

In any case, the distinguishing characteristic of heavy-ion radiation is its ability to kill large numbers of cells with very high probability. The mutagenic and physiological effects appear to be much less sensitive to large increases of the LET of ionizing radiations. This is indicated in part by the recent results due to Mortimer *et al.* of our laboratory, from which it has become evident that the maximum mutation cross section in yeast appears to be about 100 \AA^2 , or not much greater than a single nucleotide. Furthermore, for ions heavier than oxygen, this cross section appears to decrease

TABLE II

Relative Hazards of Components of the Primary Cosmic Radiation. All Columns are Approximate and Expressed in Arbitrary Units

Primary cosmic radiation	Approximate relative abundance	Estimated inactivation probability per particle per cell	Approximate number cells effectively traversed per average particle	Relative hazard to organism
H, He	110	0.02	20	44
C, N, O, Ne	1.5	.2	200	60
$Z=20-30$	0.2	1.0	300	60

in certain cases, for reasons not yet understood. Figure 7 illustrates the decreasing importance of mutation at high LET.

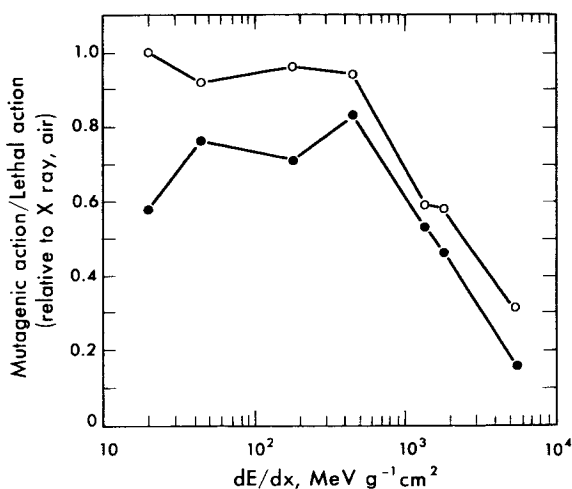


FIGURE 7.—Mutagenic efficiency (for histidine reversions) divided by lethal induction efficiency as a function of stopping power and oxygen tension.

This simple fact, that single heavy ions inactivate large numbers of cells with high probability, suffices to explain many effects found so far when biological test objects have been exposed to the primary cosmic radiation: The killing of several cells in a section of the cotyledon of a seed would logically result in a mature leaf with missing or depigmented cells; also, the inactivation of all, or nearly all, of the pigment-producing cells in a single hair follicle should give rise to discolored hair.

SOME PRECAUTIONS

It is at this point important to inject a few words of caution about the apparent simplicity of this interpretation. ("Seek simplicity and distrust it"—Whitehead.) In functioning tissue, the interaction between cells may be more important than the viability of single cells. One cell may or may not suffer from the death of its neighbor, and Curtis and others (ref. 26) have performed interesting experiments to demonstrate this by the irradiation of mouse brains with deuteron micro-beams of various sizes. The effects cited above are essentially those that result when a number of cells fail to

form clones. Formation of clones is not the task of most cells found in differentiated tissue; thus "cell lethality" may have an entirely different meaning *in vivo*. Whether cell lethality or other data are used in evaluating a hazard, they must be interpreted with great care, since many radiobiological phenomena in mammalian systems occur with an apparent "threshold", which may not exist when the phenomenon is brought about by heavy ions. Figure 8 compares inactivation curves in which there is a large threshold dose for the effect of one radiation (such as X-radiation), and no threshold for the other. If the "LD₅₀'s" are compared for these two radiations, they do not differ. For 5 percent lethality, on the other hand, X-rays may be as little as one-tenth as effective. This LD₅₀ deception is nearly as old as radiobiology and is of essentially no use when the effects of low doses are to be evaluated.

SUMMARY

In summing up, it is helpful to review some of the effects of heavy ions observed in intact living mammalian tissues: D'Angio *et al.* (ref. 27) found no apparent threshold for the erythema response of rabbit-ear skin irradiated with Li⁷ ions but a definite threshold for the same effect with deuterons; Li⁷ ions were 2 to 4 times as effective (fig. 9 and ref. 27). Bragg

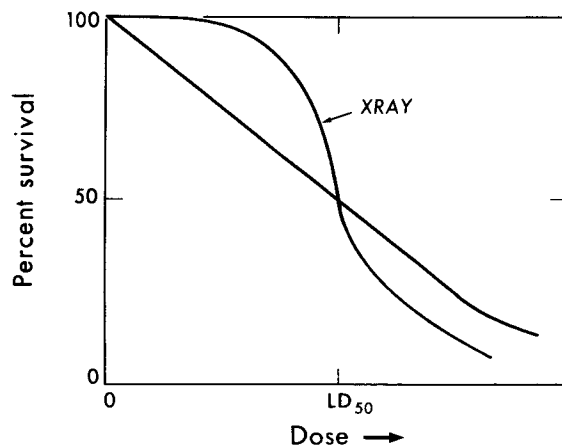


FIGURE 8.—Comparison of inactivation curves (linear plot), one of which has a large threshold dose (labeled X-ray) and one of which has no threshold, but the same LD₅₀. The RBE of this hypothetical radiation is very high at low doses and very low at high doses.

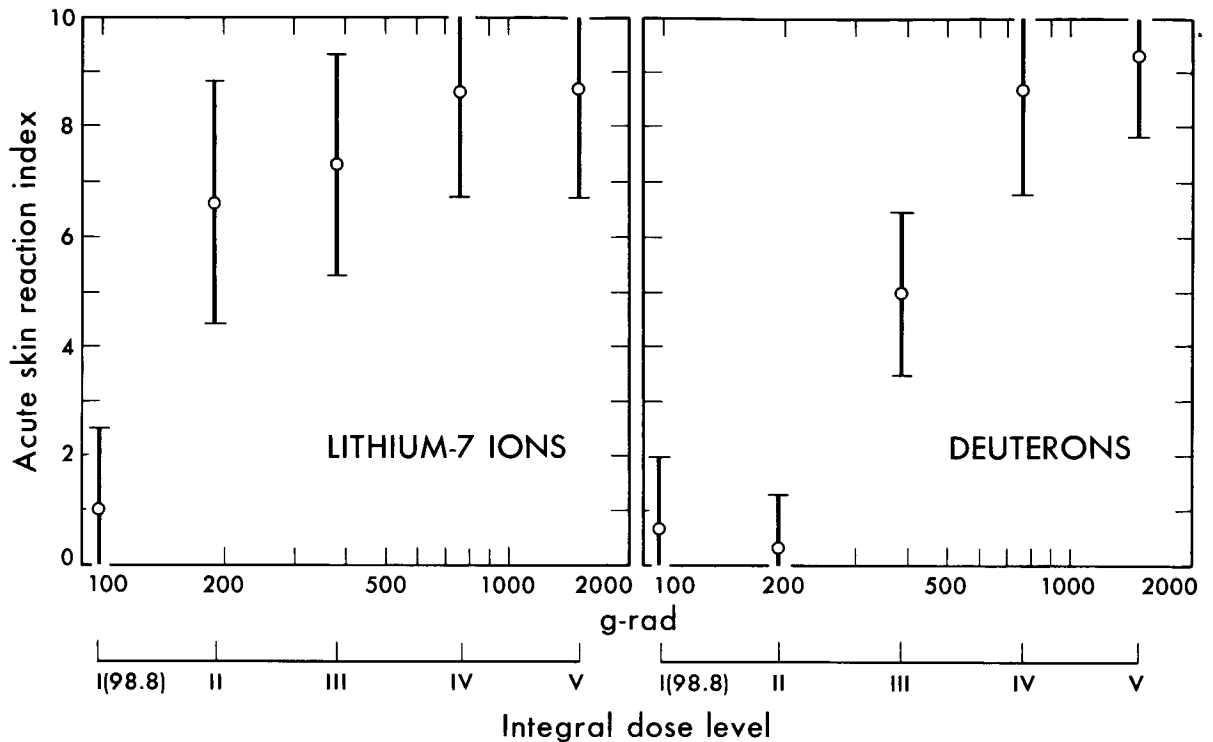


FIGURE 9.—Dose-response curves for the acute skin reaction of rabbit ears to Li^7 and H^2 ions, based upon pathological evaluation. (D'Angio *et al.*, 1964.)

peak alpha particles are about 4 times as effective as X-rays in producing cytopathological effects in the rabbit lens epithelium, in keeping with the effectiveness found for the inactivation of mammalian cells by radiations of similar LET's (ref. 28). Cosmic ray tracks and stars cause mouse hair graying, which occurs only after very high superficial doses of X-radiation (ref. 29). Rossi found that the passage of one fast neutron (on the average) through a mouse spermatogonial cell resulted in inactivation. The same follows for heavier ions. The high-LET portion of alpha-particle tracks neatly destroys cells in the cerebral cortex of mice, rats, cats, etc.; whereas X-rays cannot do so without concomitant involvement of the vascular system (ref. 30).

Although such radiosensitive processes as congenital malformations, life-span shortening, and carcinogenesis do not readily lend themselves to heavy-ion investigations, one might speculate that the first two would be sensitive to heavy-ion radiation, as they may be partly due to cell loss.

CONCLUSIONS

The conclusions of this discussion are:

1. The outstanding biological damage that results from heavy-ion irradiation is due to the lethal effects on large numbers of cells by a single particle with high probability.
2. Relative cell losses in a homogeneous biological system exposed to the primary cosmic radiation are expected to be about 1:1:0.7 for heavy, medium, and light nuclei, respectively, assuming that a heavy nucleus inactivates each cell it traverses.
3. It remains to be determined whether heavy nuclei inactivate all cells through which they pass, or only those cells which are struck in the nucleus.
4. Further research is needed to establish a quantitative relationship between fractional cell lethality and such radio-sensitive sequelae as cataract production, hair graying, congenital malformation, abnormal embryogenesis, life-span shortening, and carcinogenesis.

REFERENCES

1. SCHAEFER, H. J.: Further Evaluation of Present Day Knowledge of Cosmic Radiation in Terms of the Hazard to Health. U.S. Naval School of Aviation Medicine Rept. NM 001 059.13.02, Aug. 1951.
2. SCHAEFER, H. J.: Exposure Hazards from Cosmic Radiation Beyond the Stratosphere and in Free Space. J. Aviation Med., no. 23, 1952, pp. 334-344.
3. TOBIAS, C. A.: Radiation Hazards in High Altitude Aviation. J. Aviation Med., no. 23, 1952, pp. 345-372.
4. FREIER, P.; LOFGREN, E. J.; Ney, E. P.; Oppenheimer, F.; Bradt, M. L.; and PETERS, B.: Evidence for Heavy Nuclei in the Primary Cosmic Radiation. Phys. Rev., vol. 74, 1948, pp. 213-217.
5. BEAL, J. M.: Negative Results Following Exposure of Several Kinds of Seeds to Cosmic Rays and Other Radiations at High Altitudes. Botan. Gaz., vol. 112, 1951, p. 533.
6. CURTIS, H. J.; and SMITH, H. H.: Corn Seeds Affected by Heavy Cosmic Ray Particles. Science, vol. 141, 1963, pp. 158-160.
7. CHASE, H. B.: Cutaneous Effects of Primary Cosmic Radiation. J. Aviation Med., vol. 25, 1954, pp. 388-391.
8. CHASE, H. B.; and POST, J.: Damage and Repair in Mammalian Tissues Exposed to Cosmic Ray Heavy Nuclei. Aviation Med., vol. 27, 1956, pp. 533-540.
9. LEBISH, I. J.; SIMONS, D. G.; YAGODA, H.; JANSSEN, P.; and HAYMAKER, W.: Observations on Mice Exposed to Cosmic Radiation in the Stratosphere. Military Med., vol. 124, 1959, pp. 835-847.
10. BOND, V. P.; EASTERDAY, O. D.; STICKLEY, E. E.; and ROBERTSON, J. S.: The Relative Biological Effectiveness of Thermal Neutrons and of Heavy Particles from the $B^{10}(n, \alpha)Li^7$ Reaction for Acute Effects in the Mouse. Radiology, vol. 67, 1956, pp. 650-663.
11. TOBIAS, C. A.; WEYMOUTH, P. P.; WASSERMAN, L. R.; and STAPLETON, G. E.: Some Biological Effects due to Nuclear Fission. Science, vol. 107, 1948, pp. 115-118.
12. ARCHAMBEAU, J. O.; DREW, R. M.; and ROBERTSON, J. S.: Dose-Survival Curves for HeLa Cell Cultures Using Thermal Neutrons and the $B^{10}(n, \alpha)Li^7$ Reaction; in Biological Effects of Neutron and Proton Irradiations, vol. I, Intern. At. Energy Agency (Vienna), 1964, pp. 343-360.
13. ARCHAMBEAU, J. O.; ALCOBER, V.; CALVO, W. G.; and BRENNIS, J.: Biological Effects of Thermal Neutrons and the $B^{10}(n, \alpha)Li^7$ Reaction; in Biological Effects of Neutron and Proton Irradiations, vol. II, Intern. At. Energy Agency (Vienna), 1964, pp. 55-72.
14. BOND, V. P. (Chairman): Report of National Commission on Radiological Protection, Subcommittee M-4, Sept. 16, 1963.
15. STORER, J. B.; HARRIS, P. S.; FURCHNER, J. E.; and LANGHAM, W. H.: The Relative Biological Effectiveness of Various Ionizing Radiations in Mammalian Systems. Radiation Res., vol. 6, 1957, pp. 188-288.
16. GRAHN, D.; and Sacher, G. A.: The Measurement of Residual Acute Injury from Single Exposures by Survival Following Daily Irradiation. Ann. N.Y. Acad. Sci., vol. 114, 1964, pp. 158-168.
17. TOBIAS, C. A.; and TODD, P. W.: Analysis of the Effects of High-LET Radiation on Various Biological Test Objects. Univ. Calif. Radiation Lab. Rept., UCRL-11387, 1964, pp. 25-34.
18. KUPPERMAN, H.: Diffusion Kinetics in Radiation Chemistry; in The Chemical and Biological Actions of Radiations, vol. 5 (M. Haissinsky, ed.), Academic Press (New York), 1961, pp. 87-166.
19. TODD, P. W.: Reversible and Irreversible Effects of Ionizing Radiations on the Reproductive Integrity of Mammalian Cells Cultured *in vitro*. Univ. Calif. Radiation Lab. Rept., UCRL-11614, 1964, Ph. D. Thesis.
20. BARENDSEN, G. W.; BEUSKER, T. L. J.; VERGROESEN, A. J.; and BUDKE, L.: Effects of Different Ionizing Radiations on Human Cells in Tissue Culture. II. Biological Experiments. Radiation Res., vol. 13, 1960, p. 841.
21. KOROGODIN, V. I.: Some Regularities in the Post-Irradiation Changes in Resting Yeast Cells. Biofizika, no. 3, 1958, p. 703; or Biophysics (USSR), no. 3, 1958, p. 663.
22. LYMAN, J. T.; HAYNES, R. H.; and TOBIAS, C.: Recovery of Yeast Following Heavy Ion Irradiation. Radiation Res., vol. 19, 1963, p. 237.

23. MORRISON, P.: The Origin of Cosmic Rays. *Handbuch der Physik*, vol. 46/1, 1961, pp. 1-74.
24. SHELDON, W. R.; and DYE, D. L.: The Radiation Hazard at the Top of the Atmosphere. Boeing Co. Rept. No. D2-90529, Feb. 1964.
25. ROSSI, H. H.: Correlation of Radiation Quality and Biological Effect. *Ann. N.Y. Acad. Sci.*, vol. 114, 1964, pp. 4-15.
26. ZEMAN, W.; CURTIS, H. J.; and BAKER, C. P.: Histopathologic Effect of High-Energy-Particle Microbeams on the Visual Cortex of the Mouse Brain. *Radiation Res.*, vol. 15, 1961, pp. 496-514.
27. D'ANGIO, G. J.; LAWRENCE, J. H.; GOTTSCHALK, A.; and LYMAN, J. T.: The Relative Efficiency of High-LET Radiations (Bragg-Peak Lithium Ions) on Normal Rabbit Skin, Using Integral Dose as a Basis for Comparison. Univ. Calif. Radiation Lab. Rept., UCRL-11387 (Semiannual Rept., Biology and Medicine), 1964, pp. 127-139.
28. VON SALLMANN, L.; TOBIAS, C. A.; ANGER, H. O.; WELCH, G. P.; KIMURA, S. F.; MUNOZ, C. M.; and DRUNGIS, A.: Effects of High Energy Particles, X-rays and Aging on Lens Epithelium. *A.M.A. Arch. of Ophthalmol.*, vol. 54, 1955, pp. 489-514.
29. CHASE, H. B.: Irradiation Effects on Pigment, Hair Follicles, and Skin, with Relation to Cosmic Ray Heavy Ions, Microbeams, and the Oxygen Influence. *Second Intern. Conf. Peaceful Uses At. Energy*, no. 22, 1958, p. 252.
30. MALIS, L. I.; LOEVINGER, R.; KRUGER, L.; and ROSE, J. E.: Production of Laminar Lesions in the Cerebral Cortex by Heavy Ionizing Radiations. *Science*, vol. 126, 1957, p. 302.

SESSION III

THE EFFECTS OF SPACE RADIATION ON MATERIALS

Chairman: GEORGE F. PEZDIRTZ
Langley Research Center, NASA

13—A Summary of Radiation Effects Thresholds

DONALD J. HAMMAN

Battelle Memorial Institute

The information for this paper was taken from the files of the Radiation Effects Information Center (REIC) at Battelle Memorial Institute. The REIC was started at Battelle in 1957 by the United States Air Force in support of the radiation effects work being done for the Aircraft Nuclear Propulsion Program. Currently the REIC is sponsored by the Air Force and the National Aeronautics and Space Administration with additional support from the Atomic Energy Commission. The objectives of the REIC are:

- (1) To make available the pertinent data concerned with radiation and space environmental effects.
- (2) To assist the sponsoring agencies in defining those areas in which research should be initiated and to call attention to duplication of research efforts concerned with radiation and space-environmental effects.
- (3) To provide a source of coordinated information for those engaged in research and development in the field of radiation and space environmental effects.
- (4) To provide current information on the nature of facilities where radiation-effects and space-simulation research may be conducted.
- (5) To examine deficiencies existing in measuring and reporting radiation-effects data and recommend improved practices in experimental design, instrumentation, and dosimetry.

These objectives are to be achieved without-compromising the proprietary business-confidential information that may be supplied for Battelle's use or for further transmission to Government agencies.

The technical areas included within the scope of the REIC are:

- (1) Radiation environments including steady state, pulse, and space.
- (2) Electronic and semiconductor materials and devices.
- (3) Hydraulic, pneumatic, and mechanical systems and components.
- (4) Polymeric and other organic materials.
- (5) Ceramics.
- (6) Metals and alloys.
- (7) Propellants and explosives.
- (8) Miscellaneous materials.
- (9) Other areas such as radiation simulation facilities, dosimetry, and experimental methods and techniques.

Biological effects of radiation are specifically excluded from the scope of the REIC activities.

The purpose of the REIC is to collect, extract, and retain radiation-effects information on materials, components, and devices. The information collected is used for the preparation of state-of-the-art reports or technical memoranda in various areas and for answering technical inquiries from those interested in radiation effects.

The threshold values indicated by the figures in this paper are not, in general, the exposure levels where radiation effects first become evident or detectable. Rather, they are radiation values where some particular physical property or parameter has changed by some preset amount or percentage. Other points of importance are that these thresholds are, in many cases, heavily dependent on other environmental conditions, such as temperature or surrounding atmosphere, or on the method of application of the material or device. One other consideration to remember is that there

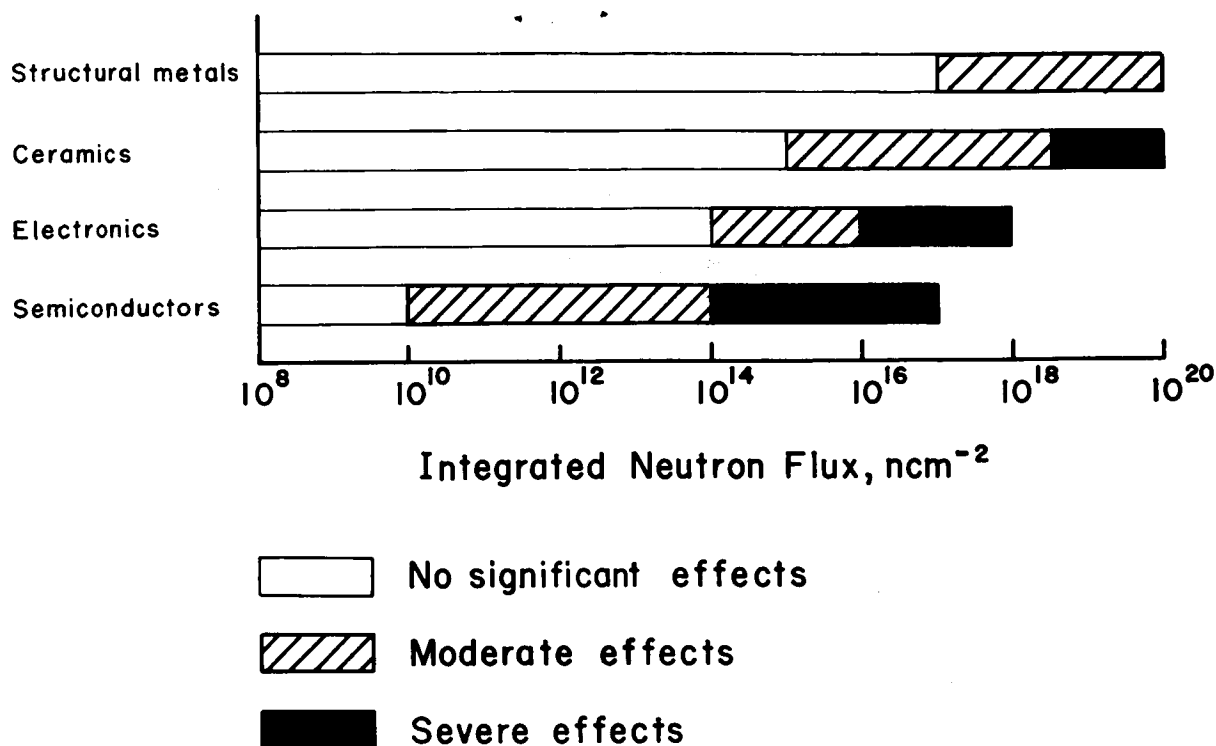


FIGURE 1.—Relative radiation effects.

are wide overlap regions for some of these thresholds.

Figure 1 presents the relative-radiation-effects thresholds for various classes of materials in a neutron environment. As may be expected, the structural metals are the most radiation-resistant materials, closely followed by ceramics, then the electronics, with semiconductors being the most sensitive of those shown. As previously stated, the various threshold regions will have wide areas of overlap. For instance, in the case of the semiconductors, there are some diodes that will not show any significant effects up to an exposure of as much as 10^{15} n cm^{-2} while there are other types of devices,

such as silicon-controlled rectifiers, that may show severe effects as low as 10^{11} n cm^{-2} .

Figure 2 presents the relative radiation resistance of various polymeric materials. The polymers are divided into three classes: elastomers that may be used for seals or shock mountings; thermosetting resins that may be used for potting compounds; and thermoplastic resins that may be used for insulators. This figure suggests that polyurethane rubber is one of the most resistant elastomers to radiation degradation. Natural rubber has about the same resistance as the polyurethane, while the polysulfide rubber is about the least resistant of the elastomers.

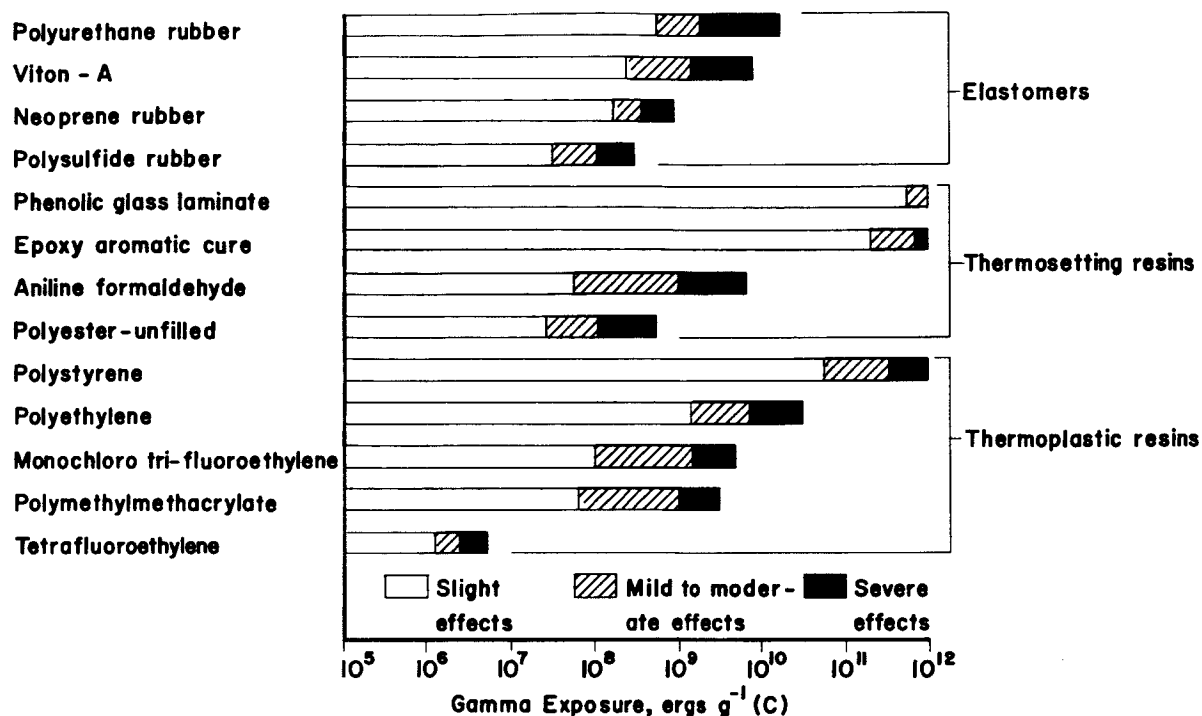


FIGURE 2.—Radiation resistance of polymers.

The filled phenolic and epoxy resins are probably the organic materials that are the most resistant to radiation damage, followed closely by polystyrene and even polyethylene. The tetrafluoroethylene is the most sensitive of the organics.

Figure 2 is designed to encompass all three classes of polymers shown. That is, all the elastomers will fall in between the polyurethane and polysulfide rubbers, all the thermosetting resins will fall between the phenolic glass laminate and the unfilled polyesters, and the other thermoplastic resins will be between polystyrene and tetrafluoroethylene.

Figure 3 is similar to figure 2 except that it is concerned with electronic materials and devices instead of organic materials. As may be seen

from the figure, the most radiation resistant of the electronic materials are the inorganic insulations and the magnetic materials that are normally not affected significantly until after an exposure of 10^{16} n cm⁻². The other items, in order of decreasing radiation resistance are: piezoelectric crystals; resistors, capacitors, and electron tubes; transducers; organic insulation; and semiconductors. Again, note that the various effects levels will have overlapping areas.

This paper has no intention of attempting to provide correlation factors for neutron-electron or neutron-proton effects. However, for figure 2, one may approximate that 2×10^{13} e/cm² is about the equivalent of 10^8 ergs g⁻¹ (C) for electrons having an energy of about 3 MeV.

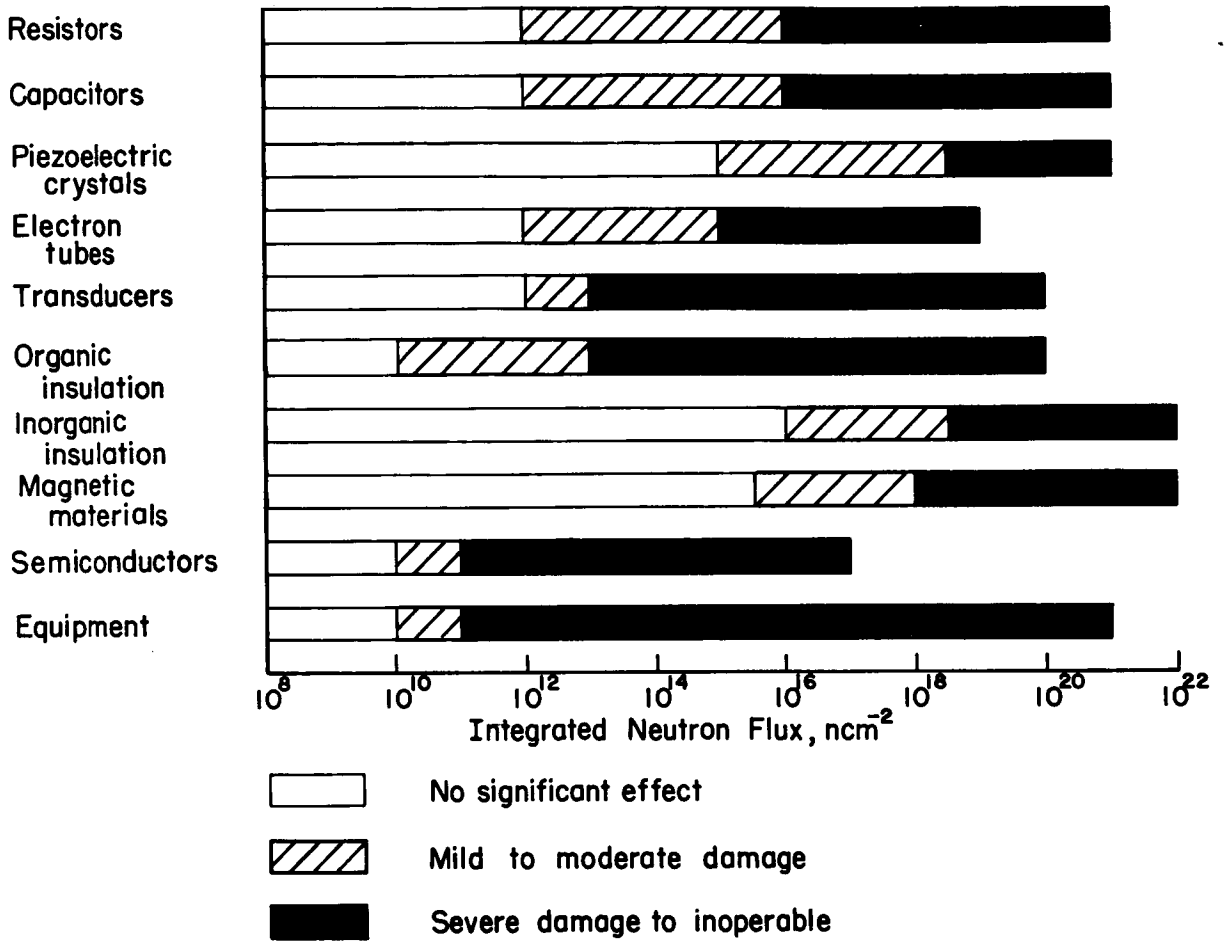


FIGURE 3.—Radiation resistance of electronics.

14—Radiation Effects on Semiconducting Materials

H. Y. FAN

Purdue University

N 65 - 34588

Irradiation with energetic particles produces lattice defects in semiconductors, displacing atoms from regular lattice sites by collision (refs. 1 and 2). The interstitial atoms and lattice vacancies migrate in the crystal and aggregate or associate with impurities in the material. Various defect centers are formed, depending on the temperature and the impurity content. Macroscopic disordered regions in the crystal lattice may also be produced, in case a large number of atoms are displaced as the result of a primary collision. Such regions in neutron-irradiated germanium have been revealed by electron microscopy (ref. 3) and X-ray studies (ref. 4).

Various properties of semiconductors are affected by irradiation, the electronic properties being especially sensitive (refs. 5 and 6).

(1) Certain defects act as donors or acceptors, and their introduction alters the concentration of charge carriers. With irradiation, a semiconductor may change its carrier concentration and electrical conductivity by orders of magnitude as in the case of Si and GaAs (refs. 7 and 8), and even the type of the semiconductor may be changed; for instance, *n*-type Ge is converted to *p*-type.

(2) Macroscopic disordered regions may have the type of conduction opposite to that of the rest of the semiconductor; for example, disordered regions produced by neutron irradiation represent *p*-type islands in *n*-type germanium. Such effect can play a dominant role in increasing the resistance of the specimen (ref. 9).

(3) Defect centers increase the scattering of charge carriers, thereby reducing the electrical conductivity (refs. 5 and 6).

(4) By acting as centers for electron-hole recombination, defects reduce the carrier life-

time, which may be much more sensitive to irradiation than the carrier concentration (refs. 6 and 10). Some defects act as traps for electrons or holes (refs. 5 and 6). These effects are important in semiconductor devices.

(5) The excitation and ionization of the defect centers give rise to infrared absorption bands and produce photoconductivity in new wavelength regions (refs. 11 and 12). New luminescence emission bands may appear. Additional absorption bands can be produced also by the influence of defects on lattice vibration (refs. 13 to 15).

(6) Paramagnetic resonance may be introduced by the defect centers. The resonance spectra can provide some detailed information on the structure of the defects. Fruitful studies have been carried out on irradiated silicon (ref. 16) from which the structures of several types of defects have been deduced.

(7) Thermal conductivity is reduced by irradiation (ref. 17). The effect is more pronounced at low temperature. Defects scatter the lattice waves which are responsible for heat conduction.

(8) The physical dimension of the specimen may change as the result of the strain introduced by the defect centers and macroscopic disordered regions. The effects produced by different kinds of irradiation have been studied for several semiconductors (ref. 18).

The temperature annealing of irradiation effects often shows complicated behavior (refs. 19 to 24). The annealing of one type of defect is accompanied sometimes by the formation of other types of defects. In some cases, the process is determined by the presence and the nature of chemical impurities. Annealing has

been found to depend on the concentration of charge carriers in the specimen which determines the charge state of the defects. There are usually several stages of annealing beginning at low temperatures and extending to several hundred degrees.

REFERENCES

1. SEITZ, F. C.; and KOEHLER, J. S.: in Solid State Phys. (F. Seitz and D. Turnbull, EDs.) vol. 2, Academic Press, 1956, p. 307.
2. DIENES, G. J.: in Effects of Radiation on Materials (J. J. Harwood, H. H. Hausner, J. G. Morse, and W. G. Rauch, EDs.), Reinhold Publ. Corp., 1958, p. 1.
3. BERTOLLOTTI, M.; PAPA, T.; SETTE, D.; GRASSO, V.; and VITALI, G.: Nuovo Cimento 29, 1963, p. 1200.
4. FUJITA, F. E.; and GONSER, U.: J. Phys. Soc. Japan, vol. 13, 1958, p. 1068.
5. FAN, H. Y.; and LARK-HOROVITZ, K.: In Effects of Radiation on Materials (J. J. Harwood, H. H. Hausner, J. G. Morse, and W. G. Rauch, EDs.), Reinhold Publ. Corp., 1958, p. 159.
6. BILLINGTON, D. S.; and CRAWFORD, J. H., JR.: Radiation Damage in Solids. Princeton Univ. Press, 1961.
7. AUKERMAN, L. W.; DAVIS, P. W.; GRAFT, R. D.; and SHILLADAY, T. S.: J. Appl. Phys., vol. 34, 1963, p. 3590.
8. AUKERMAN, L. W.; and GRAFT, R. D.: Phys. Rev., vol. 127, 1962, p. 1576.
9. CRAWFORD, J. H., JR.; and CLELAND, J. W.: Proc. Intern. Conf. on Semicond. Phys. (Prague), 1960, p. 299.
10. WERTHEIM, G. K.; CURTIS, O. L., JR.; LOFERSKI, J. J.; and RAPPAPORT, P.: Papers in J. Appl. Phys., vol. 30, no. 8, 1959.
11. FAN, H. Y.; and RAMDAS, A. K.: J. Appl. Phys., vol. 30, 1959, p. 1127.
12. VAVILOV, V. S.; and PLOTNIKOV, A. F.: J. Phys. Soc. Japan, vol. 18, supp. III, 1963, p. 230.
13. CORBETT, J. W.; WATKINS, G. D.; CHRENKO, R. M.; and MACDONALD, R. S.: Phys. Rev., vol. 121, 1961, p. 1015.
14. FAN, H. Y.; and RAMDAS, A. K.: Proc. of the Intern. Conf. on Semicond. Phys. (Prague) 1960, p. 309.
15. WHAN, R. W.; and STEIN, H. J.: Appl. Phys. Letters, vol. 3, 1963, p. 107.
16. WATKINS, G. D.: Proc. Symp. on Radiation Effects in Semiconductors, Intern. Conf. on the Phys. of Semiconductors (Paris), 1964.
17. VOOK, F.: Phys. Rev., vol. 135, 1964, pp. 1742 and 1750.
18. VOOK, F.: J. Phys. Soc. Japan, vol. 18, supp. II, 1963, p. 190.

For annealing in germanium, see:

19. BROWN, W. L.; AUGUSTYNIAK, W. M.; and WAITE, T. R.: J. Appl. Phys., vol. 30, 1959, p. 1258.
20. KLONTZ, E. E.; and MACKAY, J. W.: J. Phys. Soc. Japan, vol. 18, supp. III, 1963, p. 216.
21. ISHINO, S.; NAKAZAWA, F.; and HASIGUTI, R. R.: J. Phys. Chem. Solids, vol. 24, 1963, p. 1033.

For annealing in silicon, see:

22. BEMSKI, G.; and AUGUSTYNIAK, W. M.: Phys. Rev., vol. 108, 1957, p. 645.
23. SAITO, H.; HIRATA, M.; and HORIUCHI, T.: J. Phys. Soc. Japan 18, supp. III, 1963, p. 246.

For annealing in III-V Compounds, see:

24. EISEN, F. H.: Proc. Symp. on Radiation Effects in Semiconductors: Intern. Conf. on the Phys. of Semiconductors (Paris), 1964.

15—Radiation Effects in Optical Materials

W. E. SPICER

Stanford Electronics Laboratories

N65 3458

The purpose of this paper is to give a broad view of the mechanisms involved in radiation damage to optical materials, and the practical consequences of these mechanisms. Radiation damage to optical materials has not been studied in a systematic way in the past. In certain materials such as quartz (refs. 1 to 3), a reasonable first-order understanding of the mechanism of damage has been obtained. However, in complex systems such as thermal control surfaces, too little is known to make definitive statements as to the damage mechanisms. In dealing with these complex systems, it is important to avoid assuming models for the mechanisms of damage based on insufficient experimental evidence. In many cases, several mechanisms may be important in the production of damage. In this paper, certain possible mechanisms of damage in thermal control surfaces will be discussed; however, these must be treated as possible, and not established, mechanisms.

DEFINITION OF RADIATION DAMAGE TO OPTICAL MATERIALS

In most practical cases, the radiation damage of importance to optical materials consists of an increase in absorption in the material in a spectral range where this absorption is detrimental. The damage may give rise to new vibrational states in the solid which are optically active and absorb radiation; however, such absorption lies in the infrared region and is usually not of practical importance. For this reason, it will not be considered here. The optical damage due to the production of electronic states which absorb optical photons is of more practical importance and will be considered.

TYPES OF DAMAGE

In order to understand radiation damage to optical materials, it is useful to distinguish between three types of damage. These will be defined as: (1) direct electronic displacement damage; (2) direct atomic displacement damage; and (3) indirect atomic displacement damage.

Electronic displacement damage is that damage which results from the displacement of electrons alone, from the states they occupied before the material was subjected to radiation into other states which are displaced spatially from the original states. As an example, electrons in an insulator may be excited from a filled valence band into the conduction band. After such excitation, both the electron and hole may move through the lattice. If the electron and hole recombine, no damage is done by the radiation; however, if they are trapped at new centers, they are no longer free to move through the crystal and cannot recombine until they are again excited into the conduction and/or valence bands. In their new states, the electron and hole produce new absorption. Clearly, in the case of this type of damage, a governing factor is the presence of sites at which the charge carriers can be trapped. For example, consider the case in which a vacancy is present, and assume that under equilibrium conditions there is no charge trapped in this vacancy, so that it does not give rise to absorption in the optical range of interest. However, if radiation excites electrons into the conduction band, these electrons may move through the material and become trapped at the vacancies. The new system, consisting of the electron trapped in the vacancy, may give rise to undesirable optical absorption. Impurities as well as

usually correspond to the band gap in insulators or semiconductors, or to the minimum energy for charge transfer in organic materials. In case of high imperfection densities, it might correspond to the minimum energy necessary to excite carriers from the imperfections. For high energy particles, the threshold will not be of importance; instead, the quantity of importance will be the number of charge carriers produced per unit of incident energy.

Direct Damage Due To Atomic Displacements

Direct damage due to atomic displacements will have a threshold which usually lies in the range of 100 keV for electrons or γ rays. It will be lower for particle irradiation. Theories are available which give an estimate for the threshold of such damage due to particle irradiation (ref. 5).

Indirect Damage Due To Atomic And Electronic Displacements

Because of its indirect nature, this type of damage is much more complicated and much less generally understood. Two types of indirect damage will be discussed here; however, it should be recognized that this is not a comprehensive listing, but rather a representation of two mechanisms which are somewhat understood. There may be many other mechanisms which have not yet been identified.

1. *Creation of Color Centers in Alkali Halides Via the Varley Mechanism.* In this event, the threshold energy would be that necessary to twice ionize a halogen ion in the alkali halides. This energy would be expected to be of the order of thousands of electron volts and would vary from material to material.

2. *Surface Evolution of Oxygen from Zinc Oxide.* In this case, the threshold for damage has been shown to correspond to the band edge. It seems to be necessary only to produce free electrons and holes that can move to the surface, neutralizing oxygen ions that can then escape from the surface. Since holes and electrons can move through only relatively short distances in crystals, this mechanism will be important for only that radiation absorbed near the surface.

SPATIAL DISTRIBUTION OF DAMAGE

It is important to differentiate between surface and volume damage. If the damage is a bulk effect, then its spatial distribution will be determined solely by the spatial distribution of the energy loss of the incident particles. However, if the damage is a surface effect, the rate of energy loss near the surface will be of great importance. Comparing the effects that might be expected for high-energy gamma rays and ultraviolet radiation in zinc oxide, consider the case in which the surface-to-volume ratio is small. The high-energy gamma rays will deposit their energy and ionization uniformly throughout the crystal, and surface damage will probably not be important. However, if the same material is irradiated with ultraviolet absorbed quite close to the surface, the surface damage will be the dominant mechanism. For band-to-band absorption, the absorption coefficients are often between 10^5 and $10^6/\text{cm}$ corresponding to absorption depths of between 100 and 1000 Å.

IMPORTANCE OF PERFECTION OF THE SAMPLE

In bulk damage due to either direct electronic displacement or certain types of indirect atomic displacement, the perfection of the material clearly plays a dominant role. For example, if the damage is by direct electronic displacement, the probability of the damage is clearly directly proportional to the number of sites at which charge carriers may be trapped, producing optical absorption centers. Figure 2 indicates the effect of impurities on the damage produced in quartz. In many of the indirect atomic displacement processes, imperfections such as dislocations may produce sites at which damage occurs (refs. 8 and 9).

In considering imperfections, it is important to realize that it is impossible to make completely general statements. A given chemical impurity might be important in one material and not in another. A material completely free of foreign impurities might be damaged very easily if it contained a large number of structural imperfections such as vacancies, dislocations, or internal voids.

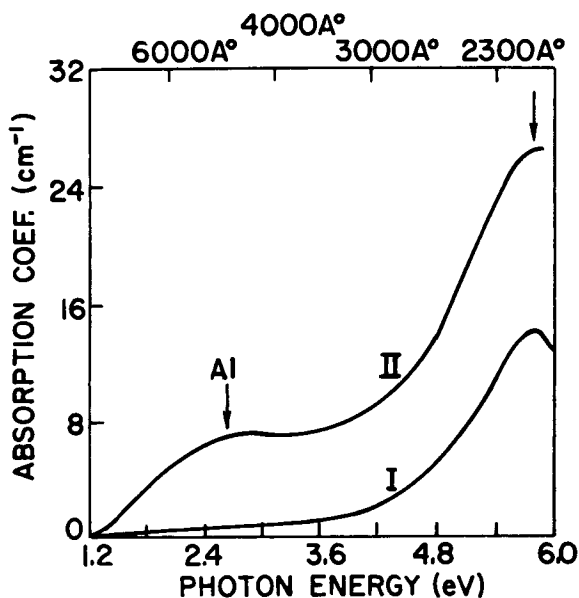


FIGURE 2.—Neutron irradiation damage to synthetic (curve labeled *I*) and Brazilian (curve labeled *II*) quartz (Ditchburn, *et al.*, ref. 1). The dosage given the Brazilian sample was slightly less than that given the synthetic quartz. The Brazilian samples studied contained 0.01 to 0.12 atomic percent aluminum impurity. Experimental evidence suggests that the difference between curves *I* and *II* is due to the difference in aluminum content.

DISCUSSION OF REAL MATERIALS

Real materials can be divided into two groups:

1. Simple, homogeneous materials such as quartz, CdS, and other compounds.
2. Complex, inhomogeneous materials.

An example of a complex, inhomogeneous material is a pigmented, thermal control surface. Such a material (fig. 3) is made up of particles of a pigment (such as TiO_2 or ZnO) suspended in a binder or vehicle (such as epoxy). In considering such an inhomogeneous material, it is necessary to consider possible damage mechanisms in: (1) the vehicle; (2) the pigment; and (3) the interface between the pigment and the vehicle.

Examples of Radiation Damage in Simple, Homogeneous Materials

Quartz (SiO_2). Only direct atomic and electronic displacement damage have been reported in SiO_2 . Figure 2 indicates damage produced by neutrons in two samples of SiO_2

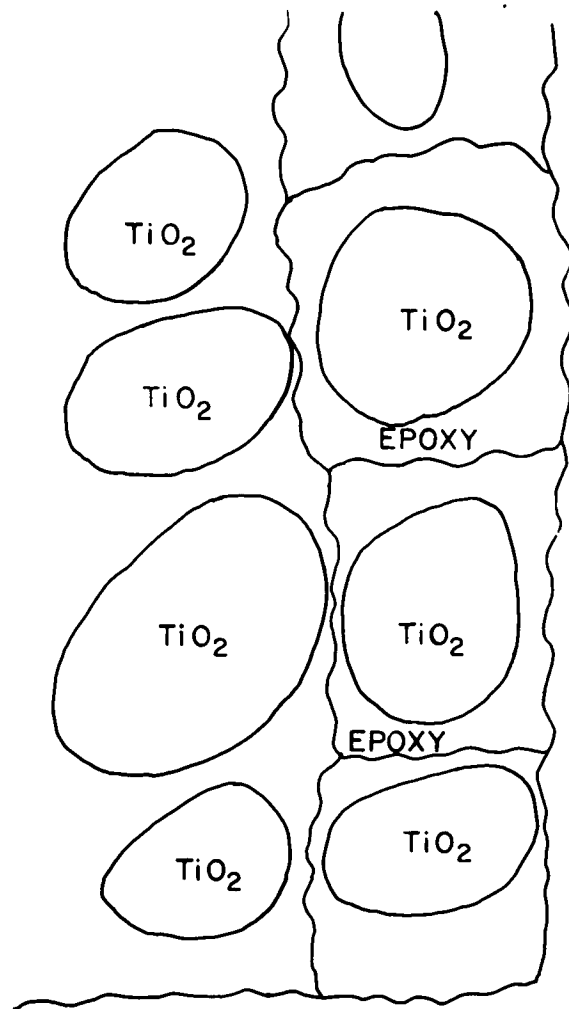


FIGURE 3.—An illustration of the composition of a pigmented thermal control surface. The particles of pigment are labeled TiO_2 . These are surrounded by the binder or vehicle (labeled Epoxy). The right-hand line indicates the external boundary of the paint. The paint will extend much further to the left than is indicated in the figure. The TiO_2 -epoxy system is one example among the many thermal control surfaces.

(refs. 1 to 3). The effect of an Al impurity can be clearly seen in this data. The damage which appears at longer wavelengths in the sample containing Al impurity is due to direct electron displacement. That, at the shorter wavelength independent of purity, is due to direct atomic displacement.

CdS. This material shows both direct and indirect atomic displacement damage (ref. 9). However, for radiation with energies and

momentum above the threshold for direct displacement, the direct process seems much more efficient than the indirect process. The efficiency of the indirect process in this material seems to depend on the past history of the sample. In particular, it seems to increase as the amount of mechanical damage (dislocation concentration) increases.

Because of its relatively small band gap (2.3 eV), damage due to direct electronic displacement will self-anneal relatively quickly (time constants between fractions of seconds and hours depending on sample conductivity). As a result, this type of damage will be of only secondary importance in insulating samples of CdS, and unimportant in conducting samples.

ZnO. This material is of particular interest because of the indirect atomic displacement damage produced by removal of oxygen from its surface (ref. 7). This evolution may be produced by photons with energy equal to or greater than the band gap energy. For this mechanism to be important, it is essential that relatively large amounts of energy from the damaging radiation be deposited near the surface. For example, since ultraviolet radiation near the band edge is absorbed fairly uniformly throughout the material, it is not nearly as effective in producing damage as is shorter wavelength ultraviolet, which is absorbed relatively close to the surface.

Alkali Halides. This class of compounds is notable because of the high efficiency with which damage may be produced by indirect atomic displacement. Various mechanisms of damage are discussed in the book *Color Centers in Solids* by Shulman and Compton (ref. 10). Damage produced by this process tends to saturate at a level of about $10^{18}/\text{cm}^3$ (corresponding to absorption coefficients of about $10^2/\text{cm}$), whereas that due to direct atomic displacement saturates at a much higher level.

COMPLEX, INHOMOGENEOUS MATERIALS

Pigmented thermal control surfaces (i.e., paints) provide a good example of a complex, inhomogeneous optical material which is of importance in space (ref. 11). An example of such a material is shown in figure 3. The surface is made of a pigment (TiO_2 in the example given) suspended in a vehicle or binder

(epoxy in the example given). The pigment and the binder have large emissivity (and, thus, large absorptance) in the middle and far infrared spectral regions, but a large reflectance (and, thus, small absorptance) in the near infrared spectral regions. Because of the large emissivity in the infrared, the paint emits its own characteristic blackbody radiation efficiently (characteristically, the space vehicle temperatures are several hundred degrees Kelvin). Because of the high reflectance in the visible and near infrared spectral regions, the absorption of solar radiation is minimized. Thus, by the use of thermal control surfaces, which balance the absorption of solar energy against the emission of thermal radiation, the temperature of a vehicle in space can be controlled.

The thermal control surfaces are subject to radiation damage which produces an increase in absorption of solar radiation without producing a significant increase in the emissivity of the paint. As a result of such damage, the temperature of the space vehicle is increased. It is this problem of radiation damage which is of interest here.

It is much more difficult to understand radiation damage in inhomogeneous materials such as the thermal control surface indicated in figure 3 than in the simple, homogeneous materials discussed previously. The increased complexity is due to several factors. First, one must consider the effects of damage in two materials, the vehicle and the pigment. The situation is further complicated by the fact that, in many cases, radiation effects are not understood in homogeneous samples of either material. Another complicating factor results from the processing necessary to produce a paint. For example, it is usual to ball mill the pigment. It is likely that this process introduces structural defects (ref. 12), such as dislocations, into the pigment particles. The presence of such defects may enhance direct electronic and/or indirect atomic displacement damage, as has been demonstrated in CdS (ref. 9) and the alkali halides (ref. 10). This is given as an illustration. There are many other possible implications of the fabrication process for the radiation damage in these complex materials.

Another important contributing factor to the complexity of the pigmented thermal control surfaces and similar materials is the interfaces between the pigment and the vehicle. If, as may be the case with ultraviolet radiation, absorption of energy near the surface is important, the increased surface (i.e., interface between vehicle and pigment) to volume ratio in the paints will enhance surface damage. In addition, reaction products may be released at the interfaces, diffuse into either vehicle or pigment, and react therein, producing another type of indirect atomic displacement damage.

It is possible to make some statements concerning the regions in a thermal control surface which are most likely to be damaged by various types of radiation. For example, relatively low-energy (hundreds of keV or less) heavy particles such as protons, alpha particles, or neutrons will have low penetration and probably produce most of their damage in the vehicle between the external surface and the first particles of pigment. Penetrating radiation should deposit its energy, and thus its damage, somewhat uniformly throughout the thermal control surface.

A principal source of radiation damage in thermal control surface is the solar ultraviolet radiation. The mechanism of damage in this case must be indirect atomic, or direct electronic, displacement because the photons have insufficient momentum to produce direct atomic displacement damage. An important factor in the damaging process is the spectral distribution of the optical absorption coefficient of the vehicle and the pigment. In order to produce an efficient thermal control surface, it is necessary for the indices of refraction of the vehicle and binder to be different. Consequently, the ultraviolet absorption of one will be much larger than that of the other, and the principal primary damage will occur in that material having the large ultraviolet absorption.

Solids are not often characterized by absolutely short absorption edges. Rather, the absorption often rises somewhat gradually. In such cases, the ultraviolet absorption near the band edge will be fairly uniform throughout a pigment particle. However, for radiation of shorter wavelengths, the absorption will be within 100 or 1000 Å of the surface. In this

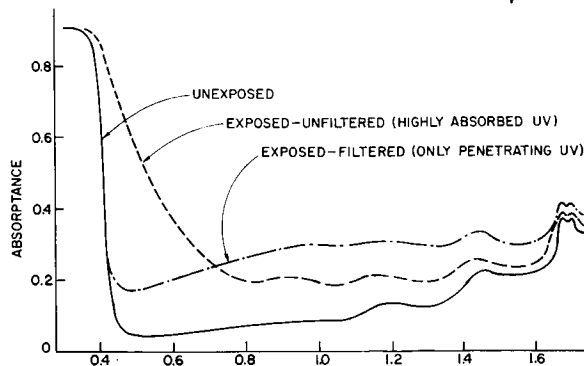


FIGURE 4.—This figure (ref. 13) illustrates the difference in radiation damage produced by penetrating (filtered) and nonpenetrating (unfiltered) ultraviolet. The damage due to the penetrating radiation should be principally bulk or volume damage, as opposed to that due to the nonpenetrating radiation, which should be principally surface damage. In this case, the surface of importance is probably that between the TiO_2 particles and the epoxy.

case, the damage will be localized near the pigment-binder interface, and surface process will become important.

Figure 4 shows data taken at the Lockheed Missiles and Space Company. Irradiation was done for identical periods of time on identical samples. However, for the sample labeled "Exposed-Filter," a filter was used to cut off the shorter wavelength ultraviolet so that only penetrating ultraviolet struck the sample; whereas, for the curve labeled "Exposed-Unfiltered," the short wavelength, highly absorbed ultraviolet struck the sample. The damage produced is quite different in the two cases. This difference must be a result of the difference between bulk and surface damage.

CONCLUDING REMARKS

Radiation damage mechanisms can be divided into three classes: (1) direct atomic displacement; (2) indirect atomic displacement; and (3) direct electronic displacement. Radiation damage in optical materials can be discussed in terms of these mechanisms. Whereas damage in some simple homogeneous materials such as quartz and the alkali halides is fairly well understood, damage in inhomogeneous materials such as thermal control paints is very complicated, and much additional work must be done before

it is understood. Caution must be taken in interpreting data from the complicated materials in terms of oversimplified models. Considerable work remains to be done before damage mechanisms can be conclusively established for these complicated materials.

REFERENCES

1. DITCHBURN, MITCHELL, PAIGE, CUSTERS, DYER and CLARK: Rept. of Conference on Defects in Crystalline Solids. Proc. Phys. Soc., (London), 1955, p. 92.
2. MITCHELL and PAIGE: Phil. Mag. vol. 1 (ser. 8), 1956, p. 1085.
3. SMOLUCHOWSKI, R.: Radiation Effects in Dielectric Solids. *In* The Effects of Radiation on Materials (Harwood, Hausner, Morse, and Rduch, eds.), Reinhold Publ. Co. (New York), 1958.
4. SCHULMAN, J.; and COMPTON, W.: Color Centers in Solids, ch. IV, Macmillan Co., 1962.
5. DIENES, G.; and VINEYARD, G.: Radiation Effects in Solids. Interscience Pub. Inc. (New York), 1957.
6. SCHULMAN, J.; and COMPTON, W.: Color Centers in Solids, ch. VII, Macmillan Co., 1962.
7. COLLINS, R.; and THOMAS, D.: Phys. Rev., vol. 112, 1958, p. 338.
8. SCHULMAN, J.; and COMPTON, W.: Color Centers in Solids, ch. VII, Macmillan Co., 1962, p. 222.
9. GARLICK, G.; BRYANT, F.; and COX, A.: Proc. Phys. Soc., (London), vol. 83, 1964, p. 967.
10. SCHULMAN, J.; and COMPTON, W.: Color Centers in Solids, ch. VII, Macmillan Co., 1962.
11. Proc. of Symp. on Thermal Radiation of Solids (S. Katzoff, ED.), NASA SP-55, 1965.
12. ZERLANT, G.; HARADA, Y.; and TOMPKINS, E.: Proc. of Symp. on Thermal Radiation of Solids (S. Katzoff, ED.). NASA SP-55, 1965.
13. OLSON, R. L.; MCKELLAR, L. A.; and STEWART, J. V.: Proc. of Symp. on Thermal Radiation of Solids (S. Katzoff, ED.) NASA SP-55, 1965.

16—Radiation-Induced Electrical Property Changes in Polymeric Solids

S. E. HARRISON AND E. A. SZYMKOWIAK

NO. 34590

Martin Company

The sources of photon and particle radiation which introduce changes in the electrical properties of polymeric insulating solids fall into two general categories. The first category is characterized by low dose rate, long duration nuclear radiation as found within isotopic power sources (odd numbered SNAP's), radiation inherent to systems with extended space missions, radiation as found in steady-state reactors, and radiation as encountered in cobalt-60 and spent reactor fuel irradiation facilities. The second category is characterized by high dose rate, short duration nuclear radiation as found in pulsed reactors (the TRIGA and Godiva types), in flash X-rays, in accelerators, and in the environment of a nuclear weapon. The electrical properties of prime concern in organic insulating solids include dielectric constant, dissipation factor, bulk conductivity, surface resistivity, electric strength, flashover strength, and microwave transmission properties (attenuation and phase shift). These properties are studied in the laboratory with frequency, temperature, pressure, ambient gas composition, and nuclear radiation dose and dose rate as controlled variables. It has been experimentally demonstrated that those electrical properties of organic insulating solids which demonstrate the largest incremental change as a function of dose and dose rate are "dissipation factor"¹ and "conductivity,"² respectively. Therefore, in this paper we discuss radiation induced changes in these two parameters and relate the changes to the mecha-

nism of damage where the state-of-the-art will permit.

TECHNICAL DISCUSSION

Dissipation Factor

To demonstrate the effects of dose on the bulk electrical characteristics of organic insulating solids, data on dissipation factor as a function of dose rate, temperature, and ambient gas composition have been chosen. The materials considered are TFE-7, FEP-100, and PF, which were studied by Frisco and Szymkowiak (refs. 1 and 2). These materials are of the tetrafluoroethylene (Teflon) family. TFE-7 is a polytetrafluoroethylene molding resin. FEP-100 is a copolymer of tetrafluoroethylene and hexafluoropropylene. PF was a Teflon resin which had been stored in the laboratory for about eleven years. The radiation source for this work was a 50-kVp continuous duty X-ray machine.

The effect of X-ray radiation in air and in vacuum on the 100 cps dissipation factor as a function of dose for TFE-7 at a temperature of 25° C is demonstrated in figure 1. The dissipation factor changes by greater than a factor of 100 in both air and vacuum at 10⁶ rads. With increased exposure to 6×10⁶ rads, the dissipation factor in air becomes asymptotic in nature and decreases in vacuum. The recovery behavior after exposure is demonstrated in figure 2. The significant observations in this illustration are: (1) the slow recovery in air from irradiation in air; and (2) the abrupt increase in dissipation factor when the specimen irradiated in vacuum was vented to air.

These data suggest that the presence or absence of oxygen, in a bulk material, will

¹ "Dissipation factor" (D) or "loss tangent" ($\tan \delta$) is the ratio of loss current to charging current in a capacitor.

² "Conductivity" (ohm-cm)⁻¹.

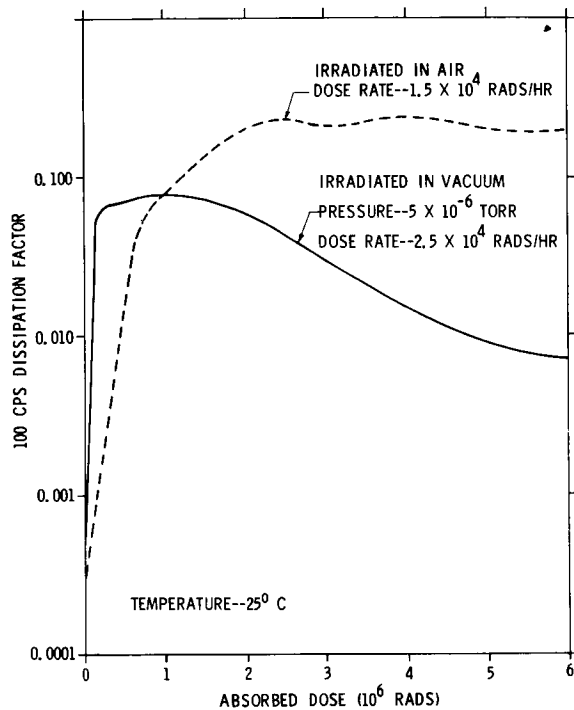


FIGURE 1.—Dissipation factor versus absorbed dose for TFE-7 at 25° C.

influence the measured dissipation factor of materials which fall in the Teflon family. This is demonstrated further in figure 3. TFE-7 and PF are essentially chemically equivalent. However, TFE-7 was sintered in air and PF in nitrogen during the manufacturing process. The copolymer of Teflon, FEP-100, demonstrated dissipation factor characteristics which differ significantly from those of TFE-7 and PF.

Measured changes in dissipation factor for TFE-7 as a function of dose at temperatures which range from 89° to 158° C are illustrated in figure 4. The data suggest a pronounced temperature effect. However, we believe that the small change in dissipation factor at the 158° C temperature is caused by the absence of trapped gas which is driven from the bulk material at the high temperature. Normally, this trapped gas contributes to large changes in dissipation factor.

In some instances, results of studies imply that there is a "dose rate effect" in organic insulating solids. Such an effect is measurable and is demonstrated by the data of figure 5. In this figure, the data show that at

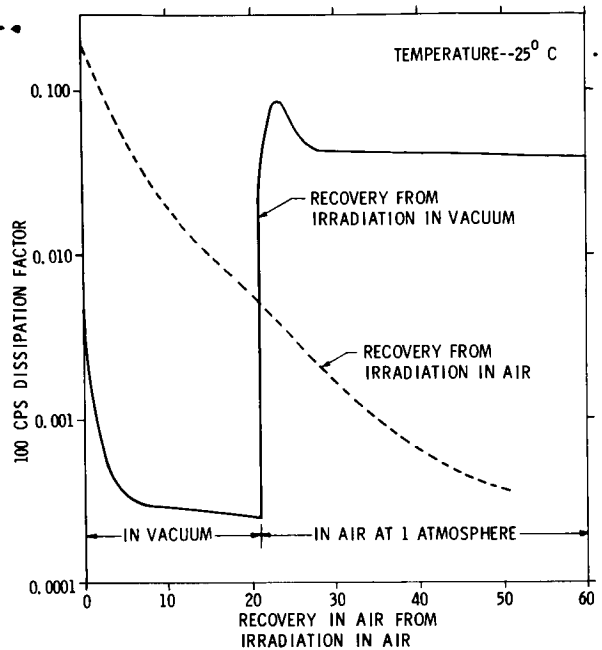


FIGURE 2.—Dissipation factor versus recovery time, in vacuum and in air, for TFE-7 at 25° C.

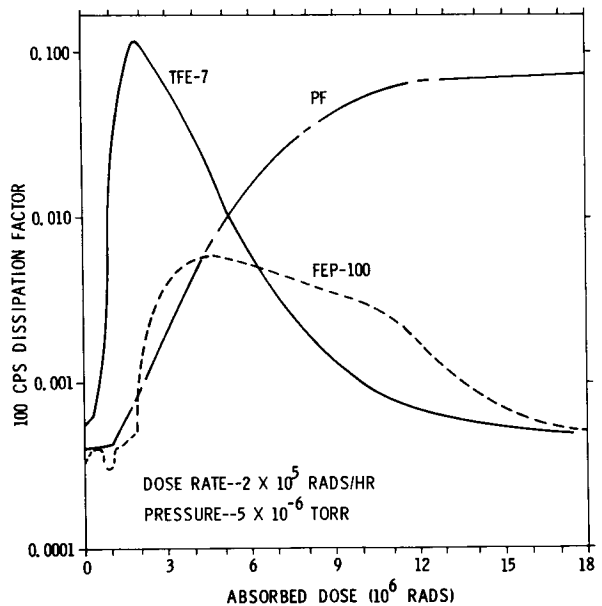


FIGURE 3.—Dissipation factor versus absorbed dose for TFE-7, PF, and FEP at 25° C.

the lower dose rate, the increase in dissipation factor is more abrupt than for the high dose rate. However, the peak changes are not much different. No explanation is offered for this difference at this time.

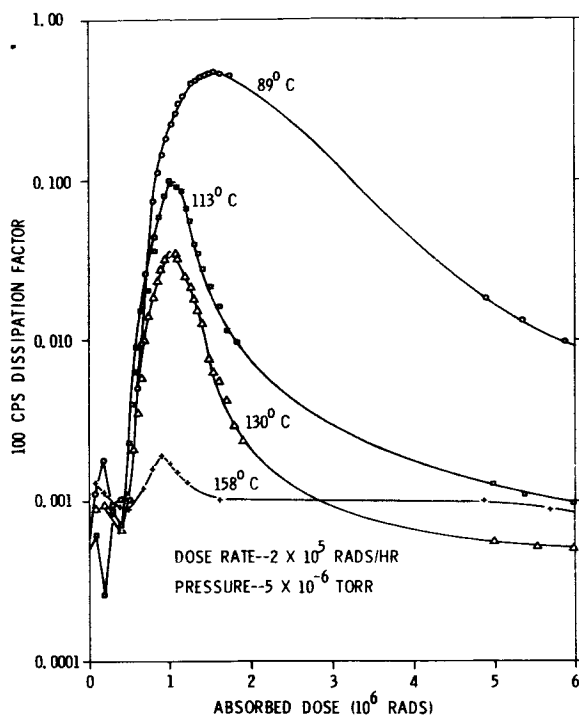


FIGURE 4.—Dissipation factor versus absorbed dose for TFE-7 at four temperatures.

It is well to emphasize that X-ray induced losses decreased rapidly with increased frequency for the materials discussed here. The losses are negligible at 100 kc. This condition at 100 kc would indicate either a dc conduction mechanism or a very low frequency dipole. Subsequent measurements of dc conductivity showed that conductivity (σ) in reality accounts for only about 10% of the ac losses. This leads one to believe that the ionizing radiation results in the formation of a relatively large number of dipoles, within the bulk material, which influence dissipation factor (D).³ The formation of peroxy radicals in Teflon has been studied by Ard and co-workers (ref. 3) and by Wall (ref. 4) as a function of dose. These radicals are believed to contribute to the formation of the referenced dipoles and therefore account for the measured changes in dissipation factor reported here.

³ ($D = \tan \delta = \epsilon''/\epsilon' = \sigma_{ac}/\omega\epsilon'$) where ϵ' is the real part and ϵ'' is the imaginary part of the complex dielectric constant, σ_{ac} is the total conductivity of the dielectric, and ω is equal to $2\pi f$.

Conductivity

The time-dependent behavior of induced conductivity in organic insulating solids, when exposed to high intensity, short duration ionizing radiation, has characteristics which can be broken down into three time intervals. The first of these intervals, as demonstrated in figure 6, is the response of the induced conductivity $[\sigma(t-a) - \sigma_0]$ extending to the plateau of the second time interval. This response has been reported to be exponential (ref. 5); i.e., it has the form:

$$[\sigma(t-a) - \sigma_0] = A\gamma[1 - \exp(-(t-a)/\tau_0)]\dot{\gamma}^\delta \quad (1)$$

where the time constant of the response, τ_0 , as a function of dose rate, is characterized by:

$$\tau_0 = \tau'_0 \dot{\gamma}^{-\mu} \quad (2)$$

From equations (1) and (2), μ , τ'_0 , δ , and $A\gamma$ are constants, and $\dot{\gamma}$ is the intensity or dose rate in rads/sec.

Measured data (ref. 6) for μ and τ'_0 are illustrated in figure 7 for Teflon. From this figure, μ is 0.85 and τ'_0 is 2.6 sec. In addition, μ and τ'_0 have been measured for polyethylene and polystyrene; μ is 0.5 for these two materials, and τ'_0 is 45 sec for polyethylene and 60 sec for polystyrene. Data for $A\gamma$ and δ have been reported by Fowler (ref. 7), by Wicklein (ref.

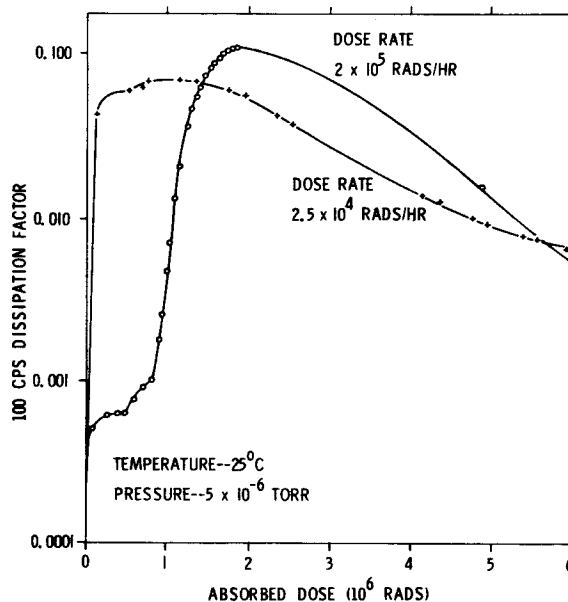


FIGURE 5.—Dissipation factor versus absorbed dose for TFE-7 at 25°C at two dose rates.

8), and by Harrison (ref. 5). In general, δ lies between 0.5 and 1 for organic insulating solids.

The third time interval of figure 6 includes the decay of induced conductivity after the irradiation is stopped. This decay has been measured (ref. 6) for nylon, polyethylene, polyvinylchloride, Kel-F, polystyrene, and Teflon,

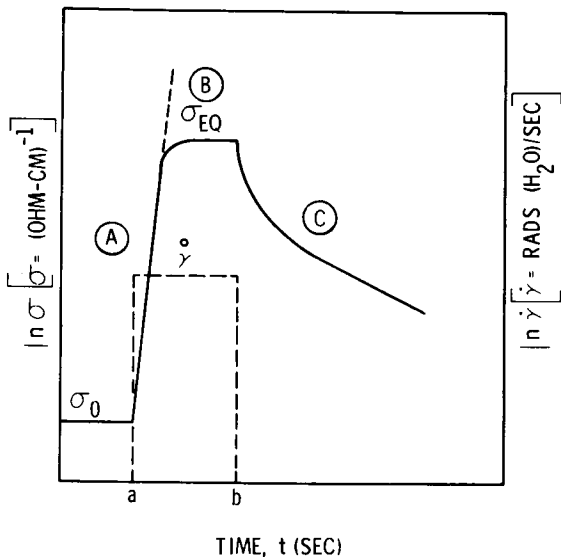


FIGURE 6.—Typical behavior of conductivity in response to a rectangular pulse of gamma ray intensity.

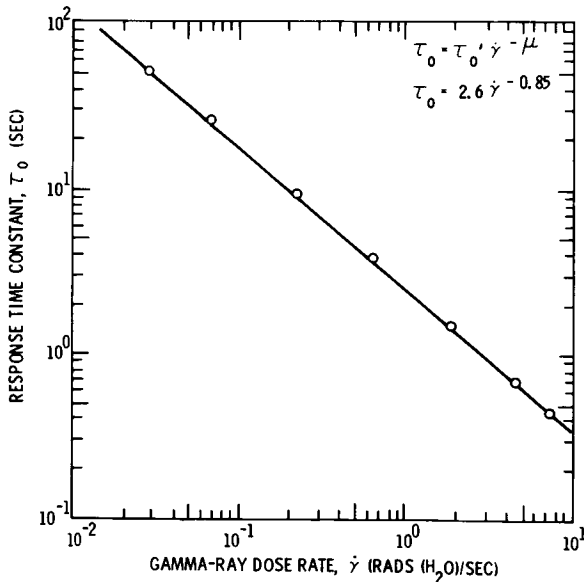


FIGURE 7.—Response time constant versus gamma-ray dose rate for teflon at 60° C.

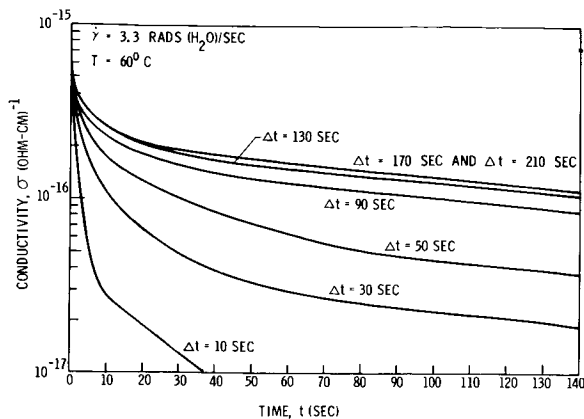


FIGURE 8.—Photoconductivity decay for teflon as function of exposure time (Δt) at 60° C.

and is characterized as obeying the relationship

$$\sigma(t-b) = \sigma(b) \sum_{i=1}^n k_i \exp(-(t-b)/\tau_i) \quad (3)$$

where the τ_i are time constants, the k_i weighing factors, and n the number of discrete time constants in the conductivity decay curve.

Decay data as a function of exposure time for Teflon are presented in figure 8. As the exposure time is increased from 10 to 210 sec, the magnitude of the decay conductivity also increases. The characteristic induced conductivity behavior just presented is consistent with a trap-controlled conduction process. The assumed model for conduction (ref. 9) then permits one to interpret n as the number of discrete trapping states, each of the measured τ_i as the mean time a carrier spends in the i th trapping state, and each of the k_i as a measure of the relative magnitude of the carrier contributions from the i th trapping level on decay. A summary of n and τ_i for six materials is presented in table I.

In addition to the work just discussed, where a trap-controlled model was used to interpret induced conductivity behavior, Davies (ref. 10) has made a study of the charge produced on the surface of organic insulating solids by electrical discharge. He presents data for polyethylene and polystyrene that, as a function of temperature, give direct evidence of a surface trapping process. This is not to imply that the surface traps are the same as the bulk traps, but to show that experimental evidence

TABLE I

Measured Values of n and τ_i

	n	τ_1 sec	τ_2 sec	τ_3 sec	τ_4 sec
Teflon.....	4	0.43	2.01	16.5	226
Polyethylene..	3	2.2	13	173	--
Polyvinyl- chloride.....	2	1.5	250	--	--
Kel-F.....	2	1.4	$>10^3$	--	--
Polystyrene....	2	0.47	875	--	--
Nylon.....	2	2.1	$>10^3$	--	--

also exists for surface trapping states in organic insulating solids.

If, indeed, conductivity behavior in organic insulating solids is a trap-controlled process as the work to date implies, then the questions still to be answered include: (1) are we dealing with a modified band model concept or a "hopping model" (refs. 11 and 12) concept for conduction; (2) what is the charge carrier in either conduction process; and (3) what magnitude of charge mobility is involved?

SUMMARY AND CONCLUSIONS

Significant changes are measured in the electrical properties of organic insulating solids as a function of nuclear radiation. The elec-

trical properties selected for discussion here include dissipation factor and conductivity. The dissipation factor changes by orders of magnitude as a function of dose. These changes, as a function of dose, are dependent upon temperature, pressure, ambient gas composition, and dose rate. Conductivity is particularly sensitive to dose rate, and the decay of photon-induced conductivity changes is considered to be controlled by a trapping process.

The significance or lack of significance of the nuclear radiation-induced changes in dissipation factor, conductivity, and other electrical properties of interest for organic insulating solids is very much dependent upon application. Thus, the significance must be determined by the electronics design engineer on an individual basis. For example, for low dose rate, long duration exposures dissipation factor changes are most significant, and for high dose rate, short duration exposures conductivity changes are most significant.

All questions relating to nuclear radiation and the induced changes in the electrical properties of interest in organic insulating solids are not answered. For these solids, the state-of-the-art of data acquisition in a nuclear radiation environment is a very significant limitation. This limitation compromises research activity which would tend to solve many of the unanswered questions.

REFERENCES

1. FRISCO, L. J.; and SZYMKOWIAK, E. A.: Investigation of the Behavior of Dielectric Materials at High Field Strengths in a High Vacuum Environment. The Johns Hopkins University, Dielectrics Laboratory, Tech. Rept., TR-15, June 1964.
2. FRISCO, L. J., *et al.*: Some Effects of Simulated Space Environment on the Electrical Properties of Dielectrics. Dielectrics and Space Symp., Westinghouse (Pittsburgh), June, 1963.
3. ARD, W. B., *et al.*: Paramagnetic Resonance of X-Irradiated Teflon—Effects of Absorbed Oxygen. J. Chem. Phys., vol. 23, 1955, p. 1725.
4. WALL, L. A.: Electron Spin Resonance Studies of Free Radicals in Irradiated Materials. ASTM Pub. 276, 1959, p. 208.
5. HARRISON, S. E.: Measured Behavior of Gamma-Ray Photoconductivity in Organic Dielectrics. IEEE Paper No. CP-62-1251, June 1962.
6. HARRISON, S. E., *et al.*: Neutron and Gamma-Ray Photoconductivity Behavior in Organic Insulating Solids. IEEE Dielectrics Conference (London), Apr. 1964.
7. FOWLER, J. F.: X-Ray Induced Conductivity in Insulating Materials. Proc. Roy. Soc. (London), 1956, p. 464.
8. WICKLEIN, H. W., *et al.*: IEEE Conference Paper, CP-63-1186.
9. HARRISON, S. E.: Gamma-Ray Photoconductivity Decay in Organic Dielectric Materials. IEEE Conference Paper CP-63-1143.
10. DAVIES, D. K.: Trapped Charges in Dielectrics. Nature, vol. 203, no. 4942, July 1964, pp. 290-291.
11. SEWELL, G. L.: Model of Thermally Activated Hopping Motion in Solids. Phys. Rev., vol. 129, no. 2, Jan. 1963.
12. GLARUM, S. H.: Electron-Lattice Interactions in Organic Semiconductors. Organic Crystal Symp. (Ottawa), Oct. 1962.

SESSION IV A

SHIELDING AGAINST SPACE RADIATION

Chairman: EDWARD D. HARNEY

USAF Space Systems Division

N65-345-1

17—Status Report on the Space Radiation Effects on the Apollo Mission

A SERIES OF FOUR PAPERS BY JOHN BILLINGHAM, DONALD E. ROBBINS, JERRY L. MODISETTE, AND PETER W. HIGGINS

Manned Spacecraft Center, NASA

The four papers in this status report present the current approach to the space radiation environment's effect on the Apollo lunar missions. As is apparent by the topics covered by each paper, this approach is based upon: (a) an analysis of the radiation dosages acceptable in a single emergency exposure by an astronaut during a lunar mission; (b) the accurate determination of the radiation environment to be encountered during the lunar missions; (c) the application of the probabilities of encountering this environment to the principles of good design; and finally, (d) the use of operational procedures to supplement spacecraft design to achieve the desired radiation protection. All of these factors should be considered together in order to describe in meaningful terms the radiation effects on Apollo.

17A—Apollo Dose Limits

JOHN BILLINGHAM

Radiation protection criteria for crew members in earth orbital and lunar Apollo missions have been specified by NASA. A summary of the radiation dose limits established is given in table I. The prime contractors for the Apollo spacecraft have been directed to use the criteria as guidelines for shielding calculations for the spacecraft.

The design dosages recommended by NASA were reviewed by the Working Group on Radiation Problems established by the Man in Space Committee of the National Academy of Sciences Space Science Board. A summary report of the group's review was issued on May 31, 1962 (ref. 1). In general, the limits described by NASA were considered to be "on the conservative side." In the case of the limit of 200 rad given as the maximum single acute exposure for the blood-forming organs (BFO), some of the committee members felt that the dose might be too high. The group noted that the limits (rad dose) were subject to change should further research in the radiobiological area indicate that

relative biological effectiveness (RBE) factors for the radiation flux within the vehicle were incorrect, and should the nature and magnitude of the flux anticipated differ from that predicted at the time the original limits were specified.

With regard to radiation, the nominal limits of exposure (the exposure received in transiting the regions of trapped radiation or other known sources of radiation for which the probability of exposure is 1) were not to exceed the average yearly exposures of table I. This requirement is unchanged. In practice it applies to earth-orbital Apollo missions passing through the trapped radiation belts. Any higher exposures were to be compensated for by grounding the astronaut until such time as his yearly average had fallen to the prescribed level. This specification also remains unchanged. The chances of exposures approaching the emergency limits given in table I are considered remote because spacecraft flying on currently planned missions in earth orbit have considerable geomagnetic shielding and, in any case, can

TABLE I

Radiation Exposure Dose Limits

Critical organ	Maximum permissible integrated dose, rem	RBE, rem/rad	Average yearly dose, rad	Maximum permissible single acute emergency exposure, rad	Location of dose point
Skin of whole body.	1600	1.4 (approx.)	250	^a 500	0.07-mm depth from surface of cylinder 2 at highest dose-rate point.
Blood-forming---	270	1.0	55	200	5-cm depth from surface of cylinder 2.
Feet, ankles, and hands.	4000	1.4	550	^b 700	0.07-mm depth from surface of cylinder 3 at highest dose point.
Eyes-----	270	^c 2	27	100	3-mm depth from surface on cylinder 1 along eyeline.

^a Based on skin erythema level.

^b Based on skin erythema level but these appendages are believed to be less radiosensitive.

^c Slightly higher RBE assumed since eyes are believed more radiosensitive.

under normal circumstances be returned to earth within an hour or two, should major solar flares occur.

In the case of lunar missions, the principal cause of concern is possible exposure of crew members to radiation emanating from solar flares. The dose limits of major interest in table I are the maximum permissible single acute emergency exposure figures. Succeeding papers will show that for a 14-day Apollo mission with a random starting date in relation to the development of a solar flare, with no operational procedures included for reducing exposure, and with a maximum length of exposure in the lunar excursion module and in spacesuits on the lunar surface, the probability of not exceeding the maximum permissible dose is 0.990. However, when it is considered that some advance warning of flare activity will be available, and that many different operational procedures can be employed to reduce the exposure of the crew, this probability increases to more than 0.995. It is emphasized, in addition, that the maximum permissible doses are probably conservative when considered in the light of the definition given above for emergency limits for other environmental variables; that is, those limits beyond which there is a high probability

of permanent injury, death, or incapacity to such an extent that the crew could not perform well enough to survive. The degree to which the limits are conservative is difficult to predict, particularly since the degree of incapacity which would preclude survival is a function of the phase of the mission. For example, fatal mistakes might be made if a radiation prodromal reaction peak were to occur in all three crew members at a time when some critical maneuver such as rendezvous and docking, or a mid-course trajectory correction, would be required. On the other hand, the prodromal reaction peak might occur over a period during which only a minimum amount of crew control over the vehicle would be required; and the mission plan might be altered so that such a period would be prolonged to give the crew chance to recover.

The arguments given above show that when all operational avoidance procedures are taken into account, the probability of no exposure to doses higher than the emergency limits of table I is greater than 0.995, and that the probability of serious injury or death is lower than 1 even if the doses should reach the limit. The author's best current estimate of the combined probability number for not reaching a fatal dose is better than 0.999.

Only one change is being made in table I. Recent evidence (ref. 2) has shown that α -particles may be present in greater numbers in large flares than was previously predicted. The maximum permissible single acute exposures in table I were given in rad on the assumption that the major constituents of the flare were protons. Since α -particles have a different RBE from protons, it now becomes logical to specify the biological limit in rem. Table II shows the maximum permissible single acute exposure in these units. The prime contractors for the Apollo vehicle are being apprised of this change and advised to use the relevant RBE factor for the α -component of the flare spectrum, and to consider that the shape of rigidity spectra of proton and α -particle fluxes are equivalent for flares having integrated fluxes of

greater than 5×10^8 protons/cm² (greater than 30 MeV). Further description of this change is given in a succeeding paper by Modisette.

TABLE II
Maximum Permissible Single Acute Emergency Exposure, REM

Critical organ	Maximum permissible single acute emergency exposure, rem
Skin of whole body	700
Blood-forming organs.....	200
Feet, ankles, and hands.....	980
Eyes.....	200

REFERENCES

1. Nat. Acad. Sci.—Nat. Res. Council: Man in Space Committee, Working Group on Radiation Problems. Summary Rept. Space Science Board (Washington, D.C.), May, 1962.
2. WEBER, W. R.; and FREIER, P. S.: Exponential Rigidity Spectrums for Solar Flare Cosmic Rays. J. Geophys. Res., vol. 68, Mar. 1963.

17B—Apollo Shielding Analysis

DONALD E. ROBBINS

The purpose of this paper is to present a status report on the shielding effectiveness of the Apollo spacecraft. Some of the calculational techniques used and general results obtained in the analysis of the space radiation doses inside the Apollo spacecraft will be discussed.

Two computer programs have been used at the NASA Manned Spacecraft Center for predicting dose from alphas and protons on the Apollo project. The workhorse has been a spherical geometry program which breaks the spacecraft into spherical solid angles with components homogenized for each solid angle. The physics of the program is fairly straightforward; a short discussion of the methods used is presented here. This program calculates only primary dose, utilizing the range energy relation for energy degradation; that is, a particle of kinetic energy T will have an energy T' after penetrating a distance t_i . The relation between T and T' is given by

$$R(T') = R(T) - t_i \quad (1)$$

where $R(T)$ and $R(T')$ are the ranges in the spacecraft material of a particle with kinetic energies T and T' , respectively. The energy deposited in an infinitesimal volume at the center point of a spherical shell of thickness t_i is the dose at that point and is given by

$$D(t_i) = 1.6 \times 10^{-8} \int_0^\infty \frac{dF}{dT'} \left(\frac{dE}{dx} \right)_{T'} dT' \quad (2)$$

where $\frac{dF}{dT'}$ is the differential flux at the point, $\left(\frac{dE}{dx} \right)_{T'}$ is the stopping power in the element of the infinitesimal volume of a particle with energy T' . All the particles in an energy integral dT about T are degraded to and contained in the energy interval dT' about T' , so substituting

$$\frac{dF}{dT} dT = \frac{dF}{dT'} dT' \quad (3)$$

into the equation for the dose, this result is obtained

$$D(t_i) = 1.6 \times 10^{-8} \int_{R^{-1}(t_i)}^\infty \frac{dF}{dT} \left[\frac{dE}{dx} \right]_{R^{-1}[R(T)-t_i]} \quad (4)$$

where $R^{-1}(t_i)$ and $R^{-1}[R(T)-t_i]$ are inverse ranges corresponding to energies whose ranges are t_i and $R(T)-t_i$, respectively.

For a solid-angle breakdown of the spacecraft which gives the size of a solid angle Ω_i in steradians versus its corresponding thickness t_i in gm/cm², the dose inside the spacecraft at the point where the breakdown is taken is

$$\text{Dose} = \sum_i \frac{D(t_i)}{4\pi} \Omega_i \quad (5)$$

The breakdown now being used for the Apollo Command Module (CM) is for 205 solid angles. The program is believed to be quite accurate for the exact geometry described by the solid-angle breakdown. However, the Apollo vehicle is not a spherical shell; therefore, it is necessary to homogenize components with different thicknesses, different chemical compositions, and different attenuating properties, thereby smearing them out over perhaps rather large solid angles. In short, the geometry description is not realistic. Since the solid-angle breakdown is for only one point, a survey of the spatial distribution of dose inside the spacecraft is possible only with another laborious breakdown.

To improve the reliability and versatility, it was necessary to improve the description of the geometry. This was done by writing a program which describes the spacecraft components both chemically and geometrically and places them in a vehicle coordinate system. Each component is described as a cone, cylinder, sphere, hemisphere, hexahedron, or any combi-

nation of one inside the other, to define cans or shells. A description of the Apollo CM, composed of about 5000 shells, has recently been completed.

The astronaut, of course, serves as a shield and is an effective one because of his comparatively large mass. When calculations were made of the skin dose received by the astronaut, it was found that his body serves as a good shield over about 2π steradians. For that reason, a definition of the astronaut and his placement into the space-craft is important. Provisions have been made for the description of up to three astronauts as a system of cylinders in the spacecraft. With the provisions for various shapes of components, plans are made to use a more realistic model of the astronaut.

The description of the geometry is independent of the dose point and is merely a three-dimensional system of bodies fixed in space. Any point in space can be chosen as a dose point from which all space is broken into 1280 solid angles by tracing rays. For each ray, the spacecraft components are examined, one by one, to see if an intersection is made with that component. When an intersection is made, the distance traversed by that ray through the component is calculated and converted to an equivalent thickness of aluminum. The physics of energy degradation and deposition in matter is handled in the same manner as the spherical solid-angle program.

Component location can be changed, others added or removed with a minimum of effort; i.e., adding two to four cards depending upon the geometrical shape. The resulting change in dose can then be obtained with a minimum of computer time, since dose contribution from each of the 1280 directions is stored on tape, making it necessary to run the problem for only the regions where the change in shielding occurs.

Using the programs above, some general results can be noted. First, a spatial variation of a factor of 2 has been found between points near the center of the spacecraft and the inside surface of the skin.

If a spectral variation of the form

$$N(>P) = N_0 \exp[-P/P_0] \quad (6)$$

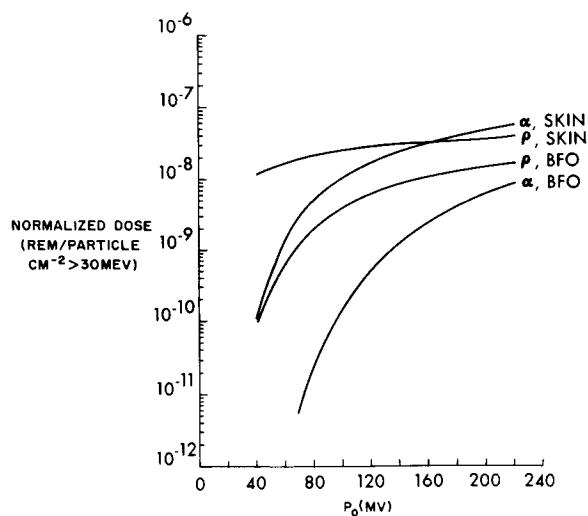


FIGURE 1.—Normalized dose versus characteristic rigidity for CM.

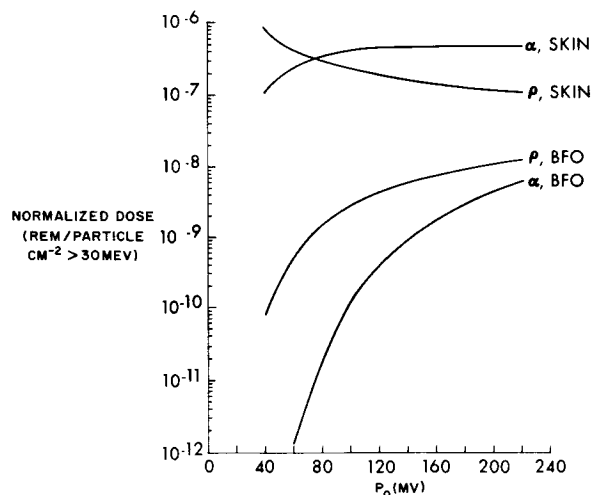


FIGURE 2.—Normalized dose versus characteristic rigidity for LEM. The curve includes effective shielding of moon.

is assumed, where $N(>P)$ is the integral flux, P is the magnetic rigidity in volts, P_0 is a characteristic rigidity denoting the spectral slope, and N_0 is a normalization constant, results are obtained like those in figures 1 and 2. Here are the normalized dose components at the center of the Apollo command module (CM) and lunar excursion module (LEM) in rem with respect to the characteristic rigidity P_0 in million volts. The range of P_0 during the last solar cycle is from 40–196 MV with an average around 100 MV.

The CM curves utilized the North American Aviation (NAA) solid-angle breakdown of the Apollo CSM19 with a dose point at the center of the CM. LEM curves utilize a crude solid-angle breakdown and include the space suit thickness as a shield. The dose point for the LEM curves is the center of the LEM. There is a rather large variation with P_0 for the BFO while the skin dose does not demonstrate quite as large a variation.

Using the maximum emergency dose limits presented by Dr. Billingham in the first part of this paper and the results in figures 1 and 2 for a spectrum with $P_0=100$ MV, the particles event sizes necessary to exceed the dose limits are

$$\begin{array}{l} \text{CM} \left\{ \begin{array}{l} 4.8 \times 10^{10}, \text{ BFO} \\ 2.0 \times 10^{10}, \text{ skin} \end{array} \right. \\ \text{LEM} \left\{ \begin{array}{l} 7.0 \times 10^{10}, \text{ BFO} \\ 1.2 \times 10^9, \text{ skin} \end{array} \right. \end{array}$$

Note that the LEM numbers include space-suit thickness and shielding by the moon. It can be seen from this that the skin dose limits will be reached before the BFO limits, and thus the skin limits become a limiting factor.

Figure 3 shows the percent of dose contribution from protons with energies greater than E for a spectrum with $P_0=100$ MV. The NAA solid-angle breakdown was used as geometry input so that the dose point was at the center of the CM. About 95 percent of the proton dose comes from particles with exterior energies in the range of 37 to 100 MeV.

Oak Ridge National Laboratory (ORNL) has

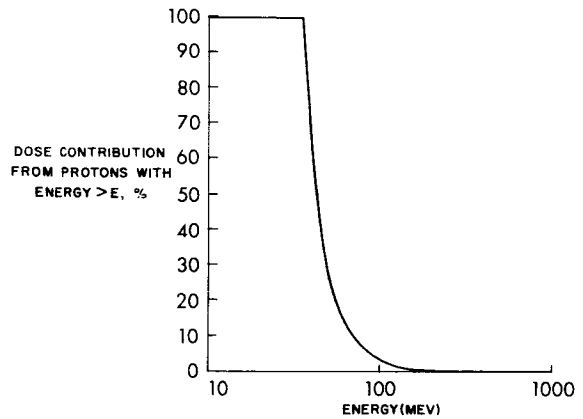


FIGURE 3.—Dose contribution in CM from protons with energy $>E$.

for the past few years been doing some very interesting work on secondary doses produced by high-energy protons. ORNL published data (ref. 1) were used by NASA to obtain some quantitative results relating to the secondary dose inside the Apollo spacecraft. These data were plots of the total, primary proton, secondary neutron, secondary pion, and secondary muon dose components as produced by typical solar-proton-event spectra plotted against the spherical shell thicknesses of aluminum.

The NAA solid-angle breakdown of the Apollo CM was used to obtain a comparison of total dose and secondary dose at the center of the spacecraft. For the hardest spectrum seen in the last solar cycle, the secondary-to-total ratio is about 0.08. For the average spectrum, the ratio of secondary dose to total dose is less than 1 percent.

REFERENCE

1. ALSMILLER, R. G.; and MURPHY, J. E.: Space Vehicle Shielding Studies (Part II): The Attenuation of Solar Flares by Aluminum Shields. ORNL 3520. Jan. 1964.

17C—Apollo Radiation Environment Analysis

JERRY L. MODISETTE

N65-34593

The analysis of the Apollo radiation environment concentrates on solar flare particle events. These particles are the major radiation hazard to Apollo. The flux of cosmic rays is too low to be significant, and the passage of the spacecraft through the Van Allen belts is fast enough to keep the dose to a low level.

The development of engineering solar particle environments appears much less straightforward than for cosmic or Van Allen radiation, largely because of the extreme and random temporal variation of the particle flux. It is useful to consider the engineering requirement in defining a model solar proton environment. For designing spacecraft shielding, one ultimately needs a model event, giving the total particle flux as a function of energy. The variation of the flux and spectrum with time are of lesser importance. Given the flux and spectrum of the model event, and the allowable dose limits, it is possible to design the spacecraft shielding that will keep the astronaut's dose below the allowable limit.

With an eye on the engineering requirements, the procedure for arriving at a model event early in the Apollo program was to select some large event, or composite of several such events, and call it a "typical," "largest," or "typical large" event. Such a procedure is commonly used when dealing with little-known phenomena. The treatment of reliability in such a procedure is rather crude, however, and is based entirely on implicit assumptions. It is implied that the model selected is of such severity that a larger event is improbable. In fact, it is assumed that the probability of no larger event is a satisfactory design reliability. Such a treatment of reliability is largely intuitive, and is subject to considerable error.

The early model solar particle events were considerably larger than the present one. The former intuitive approach involves a low con-

fidence, and as a result, safety factors tend to creep in. The present analytical approach shows the Apollo radiation hazard to be much less severe than was originally thought.

The Apollo radiation environment analysis is based on a compilation of solar particle events over the last sunspot cycle. The statistical nature of these events makes thoroughness of coverage critical. It is fortunate that there exist more or less continuous records from riometers and forward scatter systems, with a fair number of direct measurements for calibration. The Apollo compilation is based on material found in reference 1, and some unpublished data furnished by Central Radio Propagation Laboratory of the National Bureau of Standards.

In surveying the solar flare proton data, several things are immediately obvious. One is the apparent correlation of the data with the sunspot cycle. Another is the general irregularity of occurrence of proton events on any short term basis. It is also noted that the event size, or number of protons, ranges over four orders of magnitude. With the objective of obtaining a probability of encounter as a function of the number of protons, the obvious correlation to investigate is the effect of the sunspot cycle. Figure 1 shows the frequency of occurrence of solar proton events plotted against the sunspot number.

It is apparent that there is a correlation. A linear regression fit, resulting in the straight line shown in the figure, gives a correlation coefficient of 0.7. There is less than 1 chance in 2000 that this correlation is fortuitous.

It is also apparent that there is a lot of scatter. This scatter makes it impossible to determine the exact relationship between proton events and the sunspot number. The step function plotted on the figure gives a correlation coefficient of 0.7. A sine wave also gives 0.7. The

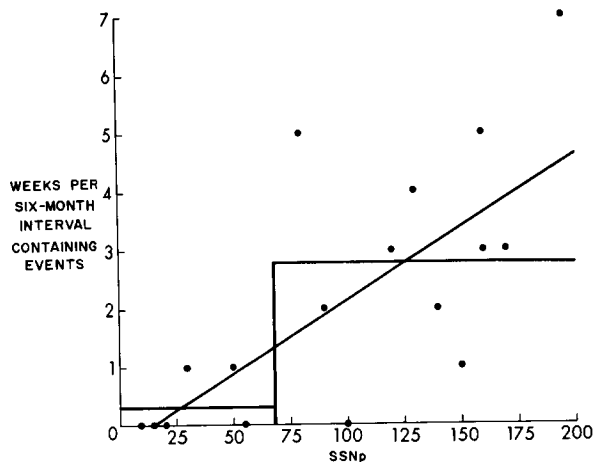


FIGURE 1.—Solar flare proton event frequency versus predicted smooth sunspot number.

conclusion is that there is definitely a relationship between the sunspot number and the number of protons, but all that can be said about the relationship is that there are many more protons during the upper half of the cycle than during the lower half. For this reason, and because Apollo missions will be conducted during the upper half of the next cycle, the analysis is based on the period 1956–61, the upper half of the 19th cycle, but no further consideration is given to sunspot number.

Another apparent correlation that should be taken into account is the tendency for proton events to occur in groups. However, there is a problem in determining the exact relationship. With the data giving thorough coverage for only one cycle, it is impossible to obtain analytical formulations of the grouping tendency in which one might have confidence. Consequently, a procedure has been adopted which factors the grouping effect into the result without explaining it, or even deriving explicit empirical relationships.

The procedure is to compile a calendar of proton events, listing each day in the period 1956–61 along with the corresponding number of protons (if any) seen on that day. Then each of the 2000 odd days in the time period is considered to be the launch date of a hypothetical mission. For a 2-week mission, all proton events encountered during the 14 days following the launch date are added together to give the total number of protons for that mis-

sion. In some 2000 missions, about 500 will encounter protons. At this point care must be taken, because not all of these missions are independent; there might be an overlap between successive missions. Very strange results can be obtained by trying to derive distribution functions directly from the 500 missions with protons. Still considering 14-day missions, there are obviously 500 divided by 14, or 33 independent missions in 500 days. By arranging the 500 missions in order of size, and grouping adjacent missions into 33 groups, the logarithmic normal distribution shown in figure 2 is obtained.

This distribution gives the probability of a mission encountering greater than N protons if any protons are encountered at all. There is a probability of 0.25 that some protons will be encountered, so that the overall probability of encountering more than N protons is $0.25 P(>N)$.

Alpha particles.—One simple assumption is made about alpha particles: that the number of alpha particles is equal to the number of protons over equal rigidity intervals. The available data indicate that this is the case for large events, although there is a lot of scatter. Since the large events determine the spacecraft design,

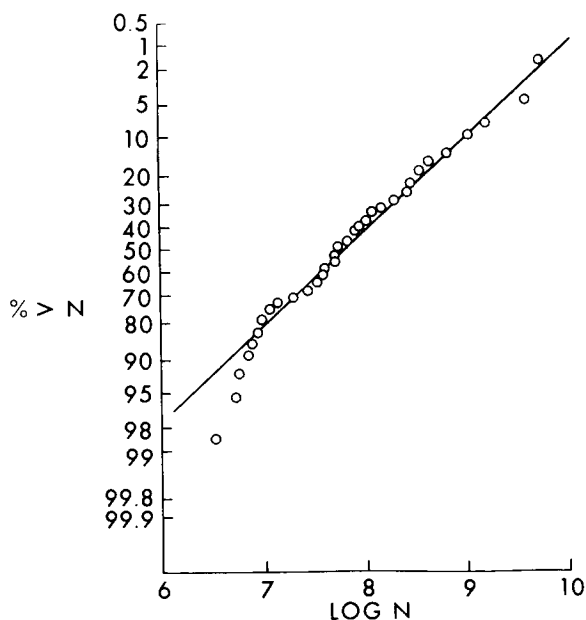


FIGURE 2.—Distribution of proton fluxes, two-week mission.

the 1-to-1 ratio is assumed and all of the analysis is based on the proton data.

Spectrum.—For Apollo, an average spectral parameter of 100 MV is used, where the spectral distribution is of the form

$$F(>P) = F_0 \exp(-P/P_0)$$

where P_0 is the parameter defining the spectrum. For the Apollo command module, the variation in the spectrum produces a variation of about a factor of 2 in dose for events having the same number of protons. For the more lightly shielded LEM and the space suit, the variation is less. When the variation in the spectrum is folded into the probability distribution for the number of protons, it makes an insignificant difference.

At present there exists a probability greater than 0.995 that the radiation exposure of the astronaut inside the CM will not exceed emergency dose limits during a 2-week mission, if a small amount of extra shielding can be provided for the astronaut's eyes in the form of a thick, transparent visor.

There is no radiation design goal for the LEM in the same sense as there is for the command module. This is because the length of time spent in the LEM is variable, depending on the particular mission under consideration. In addition, the preliminary analysis showed that for the early Apollo flights, it is more practical to return to the command module in case of a severe proton event. For the later mission, it may prove possible to set up temporary shielding on the moon, using local materials.

For operational procedures, an improved environment analysis is needed which would be capable of handling missions with part of the time in the heavily shielded command module, part of the time in the lightly shielded LEM, and some time on the lunar surface in a space suit. The importance of a detailed mission breakdown is shown by the fact that

a particle flux producing a 1-rem dose in the CM will produce a 17-rem dose in the LEM.

The approach for this "operations analysis" environment is very similar to that for the design environment. For this case, it is necessary to go into the variation of the events with time. These data are available in crude form for most events and, fortunately, in fair detail for most of the large events. The procedure is to construct an hour-by-hour table of proton fluxes and spectra for 1956-61, and to run missions starting on successive hours and broken down on an hourly basis. In the case of events for which some of the descriptive parameters such as spectrum, duration, et cetera, are missing, a model similar to Bailey's event is used, normalized to the total particle flux and adjusted to fit such parameters as were available.

It is obvious that there is little sophistication to the Apollo environment analysis. The procedure is straightforward, although tedious, especially in the case of the hour-by-hour operations analysis. The tedium is relieved considerably by the availability of computers. An hourly mission analysis requires about 10 minutes running time to derive a dose distribution. Dose distribution is used rather than flux in this case, because of the variation in shielding and spectrum over different parts of the mission.

The results of the above analysis, coupled with Robbins' shielding work described previously in this paper, show that there is less than 1 chance in 1000 that the emergency dose limits will be exceeded inside the command module on the first lunar mission. When the astronaut goes out on the lunar surface, this probability becomes about 1 chance in 100, if no operational procedures based on warning are instituted. The use of the warning system described by Higgins in the final section of this paper brings this probability down to about the same level as that for the CM.

REFERENCE

1. McDONALD, FRANK B. (ED.): Solar Proton Manual. NASA TR R-169, Dec. 1963.

N65-34574

17D—Operational Procedures for Apollo Dose Reduction

PETER W. HIGGINS

Dose reduction from solar proton radiation may be achieved through the intelligent use of operational procedures. This method has the same overall effect of increasing the mission reliability as does a further increase in vehicle shielding mass. The particular appeal in attacking the problems in this manner lies in avoiding both the exceptionally high cost of additional weight in the Apollo mission and the constraint imposed by carrying this additional weight, since it would be needed only a small percent of the time.

Operational procedures for Apollo radiation dose are centered primarily about the lunar-landing-exploration phase of the mission because, at this point, the astronauts are not protected by the well shielded command module but are exposed in the lightly shielded lunar excursion module or in the Apollo spacesuit. The dose reduction will be obtained by reducing this exposure time in the face of a solar proton event. The time reduction will be determined in relation to the expected size and severity of the event.

Notification of the approach of a solar proton event will be obtained by monitoring the birth of the event on the sun. Observation of the sun will be made by a world-wide network of solar hydrogen-alpha and radio frequency telescopes. These telescopes will record the intense solar flare emission and solar radio centimeter wave bursts that accompany the acceleration of the proton radiation from the sun, but being electromagnetic radiation, precede the arrival of these protons by minutes to hours. Seven optical telescope units and three radio telescope units are planned for the completed network to be in operation by the first Apollo flights at selected sites within the Apollo network. The Apollo network provides the facilities and communications necessary to transmit the solar-proton-event warning information to the Apollo Mission Control Center at Houston, where the flight directors will make the ultimate decision regarding the use of these operational procedures.

Initially, the Solar Particle Alert Network (SPAN) will be implemented as a development network in order to demonstrate its operational capabilities. This initial network will consist of three fully implemented sites using both the radio and optical solar telescopes. These locations will be in Australia; Houston, Texas; and Europe. Upon proving the operational goals of the SPAN early in this coming solar cycle, the full SPAN network will be installed. During the development period, extensive effort will be underway to advance the present warning criteria toward the goal of no false alarms. The major remaining problem to be solved is the solution to the physics of proton event transport through interplanetary space.

Operational procedures for dose reduction have evolved in the struggle to determine the best possible means to safeguard the Apollo astronauts from radiation overdose while performing a maximum of the mission objectives. The term "operational procedures," in this case, implies the use of mission modifications rather than an increase of shield thickness to achieve additional radiation protection. This technique looks particularly attractive considering the prohibitively high cost of additional spacecraft weight. This additional weight imposes an unnecessary mission constraint, because the weight must always be

carried on the spacecraft, even though the need for this extra protection arises only a small percent of the time. Both approaches, however, increase the probability of mission success or mission reliability. The use of operational procedures to account for radiation emergencies provides for more than simply increasing the Apollo design reliability. Operational procedures are the backup behind design uncertainties. For example, the design data are based on those taken during part of the last solar cycle; little or no proton event data exist for previous solar cycles. Furthermore, no one can say with complete confidence that the next

solar cycle (the one in which Apollo missions will be conducted) will be a carbon copy of the one upon which the design is based. Certainly, there is some probability that the present solar cycle will produce a more severe environment than the one just passed.

The probabilities that dictate good design do not and should not be carried over to limit efforts in dealing with emergency situations or in accounting for design unknowns. The Apollo lunar mission may expose three astronauts to solar radiation in one of three configurations: (a) inside the Apollo command module (CM); (b) inside the lunar excursion module (LEM); and (c) while wearing the spacesuit on the lunar surface outside the LEM.

The Apollo CM is an adequately shielded vehicle based on the current definition of the radiation environment. The Apollo LEM and the astronaut's spacesuit, however, afford very little radiation protection. During the period of LEM descent, landing, and lunar surface exploration, two Apollo astronauts (one of the astronauts will remain in the CM) will be exposed to possible solar radiation events.

The operational procedures employed for radiation protection will rely on warning of an impending solar proton event. With the knowledge of the size and intensity of the approaching event, the lunar exploration phase of the Apollo mission may be appropriately shortened so that the astronauts can rapidly return to the safety of the CM.

A solar proton event is born in a complex series of events which take place on the sun. The event begins in an enormous eruption on the sun known as a solar flare, which accelerates the particles in the proton event and ejects them into the interplanetary space. Not all solar flares eject earth-detectable solar protons, but those that do display these three phenomena:

- (a) Optical hydrogen-alpha emission characteristic of all flares.
- (b) Intense centimeter wave radio frequency (RF) bursts of long duration.
- (c) X-ray and ultraviolet (UV) bursts resulting in the sudden ionospheric disturbances.

Approximately an hour after the observation of the flare, the first arrival of solar protons is

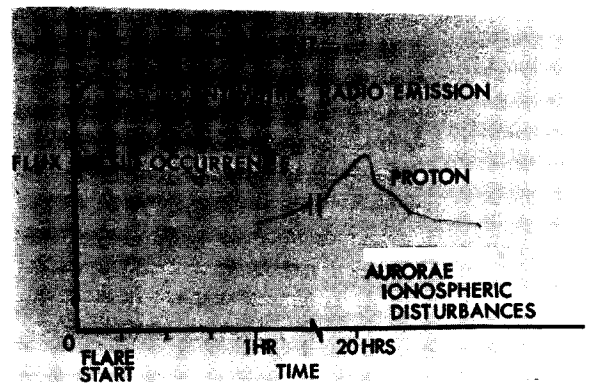


FIGURE 1.—A typical time sequence of a solar proton event.

detected, signifying the start of the polar cap absorption (PCA) event. The flux of particles increases and spreads throughout the energy spectrum to a peak flux some 24 hours later. At this point in the event, aurora and severe ionospheric disturbances are prominent. This sequence of events is summarized in figure 1.

The relationships between the three simultaneous electromagnetic radiation (EMR) phenomena and the resulting solar proton event have been pursued by numerous prominent investigators. Some of the principal results from an analysis performed during the 19th solar cycle may be summarized in the following statements:

1. Large solar proton events result from large intense solar flares. These flares are distributed so that slightly more proton events occur on the western hemisphere of the sun than on the eastern hemisphere.

2. Every large solar proton event for which simultaneous radio records were available displayed a centimeter wave burst characterized by a rapid rise, high peak intensity, and long decay. However, many of the similar RF bursts were not accompanied by a proton event. The ratio stands at three characteristic bursts to one earth-detectable proton event.

3. Proton events may be influenced in their passage through the interplanetary field by the geometry of this field. Therefore, many of the proton events may actually miss the earth-moon area by traveling to some other part of the solar system.

The planned warning system in support of Apollo will monitor two of the three simultaneous

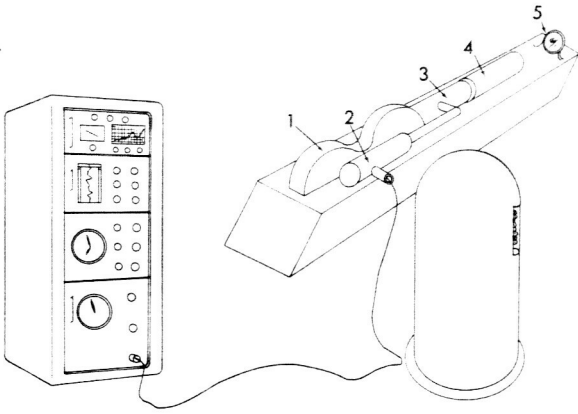


FIGURE 2.—Artist's sketch of small spar-type telescope employing a 4-inch objective lens and a Lyot birefringent filter.

solar flare phenomena, namely the hydrogen-alpha flare emission and the centimetric RF bursts. Analysis of the RF bursts has been shown to provide a definite correlation with the size of the ensuing solar proton event. The optical flare activity information will be used in conjunction with the RF burst analysis to provide warning with a lower false alarm rate than is possible using the RF burst analysis alone. The optical data will show the size and intensity of the parent solar flare as well as the flare position on the sun. Extensive analysis will also be performed using the optical data on the pre-flare solar activity which someday may well provide meaningful prediction indicators.

The instrument used to observe the sun in the light of neutral hydrogen is a small spar-type telescope employing a 4-inch objective lens and a Lyot birefringent filter. An artist's sketch of this telescope is shown in figure 2. The Lyot filter offers a bandpass of 0.5 angstrom, which may be manually shifted by that amount toward either end of the spectrum. This narrow bandpass allows a high degree of contrast to be obtained between the hydrogen-alpha continuum and the hydrogen-alpha emission of the solar flare.

The image of the sun taken in this manner will be monitored in three ways: (a) recorded on photographic film at a rate of approximately one frame every 10 seconds; (b) exposed to a vidicon tube for closed-circuit television moni-

toring and recording; and (c) observed with an eyepiece.

The instrument design allows it to be used in either real-time operation or as a data collection device. In real-time operation, an observer will report to the Apollo mission control center on the ongoing solar activity. During the non-mission intervals, the telescope will be constantly recording the sun's activity on film and on video tape. The centimeter radio bursts of the sun will be recorded by a small telescope of the type shown in figure 3. This instrument consists of an 8-foot parabolic dish antenna using a log-periodic array feed as an input to three fixed-frequency radiometers. The frequencies of operation have been chosen as centered about 1420 megacycles per second, 2695 Mc/sec, and 4995 Mc/sec, representing the wavelength interval of 6 to 21 centimeters. In addition to being centimeter wave frequencies, these particular frequencies have been set aside as cleared frequencies for radio astronomy by international agreement (International Telecommunication Union—Space Radio Communications Conference-General). The radiometers operate by comparing the input RF signal on the antenna to a calibrated RF noise source using a superheterodyne receiver system. The output of the radiometers is to be recorded on strip-chart recorders, magnetic tape, and in teletype format. The solar radio telescope is being built to have an accuracy range of 2-percent variation of the quiet sun

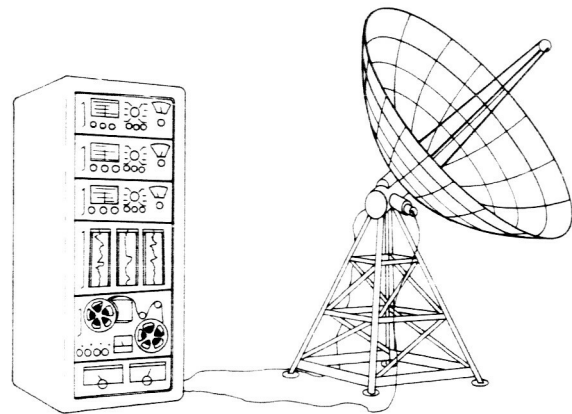


FIGURE 3.—Telescope used to record centimeter bursts of the sun. It consists of an 8-foot parabolic dish antenna using a log-periodic array feed as an input to three fixed-frequency radiometers.



FIGURE 4.—Solar Particle Alert Network.

RF flux to within 1 db of the signal strength of the largest recorded centimeter bursts.

Both the solar telescopes are being designed particularly for remote field service. The radio telescope is to be protected by a radome with a controlled interior environment. The antenna tracking will be automatic, with the antenna returning to the sunrise position automatically during the night. The optical telescope is housed in a small astronomical dome which opens automatically during the daylight hours and which will also close automatically under adverse weather conditions. The interior temperature of the dome will be controlled to prevent instrument freeze-up or damage due to extreme temperature variations.

The objectives behind site location of the optical and radio telescopes are as follows:

- (a) 24-hour coverage of the sun.
- (b) Access to a world-wide network of hard-line communications.
- (c) Availability of maintenance personnel.

Stations in the Apollo tracking and communications network were chosen as sites

because they can satisfy the above objectives. Figure 4 shows the position of the telescopes within the Apollo network with the lines indicating the cable and land-line communications available. The communications of this network are vitally important in the success of a real-time operation; that is, the observations can be instantaneously transmitted to the control center for Apollo (located in Houston) for analysis. Seven optical and three radio telescopes are planned to form the Solar Particle Alert Network (this network was called the Apollo Space Radiation Warning System). Radio telescopes are insensitive to cloud cover; consequently, three units will suffice. However, since optical units are extremely sensitive to weather conditions, it is necessary to use seven units instead of three. As indicated, the optical telescopes will probably be located at Carnarvon, Australia; Canberra, Australia; Hawaii, U.S.A.; Guaymas, Mexico; Houston, Texas; Madrid, Spain; and Tananarive, Republic of Malagasy. The radio telescopes



FIGURE 5.—Solar Particle Alert Network (SPAN) operational phases.

will probably be located at Canberra, Australia; Houston, Texas; and Madrid, Spain. In both cases, the Houston site will serve as both an operational and a training site. The training program conducted in Houston will develop scientific personnel to direct the field operations during the Apollo missions. The development phase of the warning system should be in operation by the spring of 1966. The development phase of the warning system will consist of three sites within the Apollo network using both radio and optical telescopes. These locations will be in Australia; Houston, Texas; and Europe. The development phase will test the principles behind early warning in order to prove the operational capabilities of the system. The data gathered in the interval before the first Apollo flight will be vitally important in extending knowledge of the solar events and should result in the improvement of warning criteria. During this period, attempts will be made to reduce the false-alarm rate and to establish further relationships between the

optical and radio characteristics with proton-event size. In this process, independent investigators will be encouraged by making NASA data available for their use.

The application of the Solar Particle Alert Network is a step toward the protection of the Apollo astronauts from hazardous and/or unnecessary dosages of particle radiation. Previously, it was mentioned that a warning of an approaching solar proton event would be used to instigate flight operational procedures aimed toward reducing the dose while still performing as much of the mission as possible. The majority of the Apollo mission will be performed with all crew members aboard the CM while they are either going to or from the moon. Figure 5 shows the vehicle trajectory, with this phase of the mission numbered 1. Although the CM is well shielded, additional protection is possible through either CM orientation or spot shielding. Orientation of the CM may gain dose reduction by pointing the thin regions of the CM away from the direction

of maximum particle flux in the proton event. The advantages of CM orientation are limited, however, because most solar events do not display particle anisotropy; and those that do, display anisotropy only during the first few hours of the event.

Spot shielding of the CM implies the erection of temporary shielding to cover the thin regions of the spacecraft, should this be necessary to hold the dose within safe limits. Spot shielding has a very definite appeal, since the thin regions of the CM cover a small accessible area near the apex of the vehicle. Serious consideration has been given to placing mylar water bags to cover this region, using available spacecraft water, and to the strategic placement of equipment such as the spacecraft air-purification tanks in this area.

As the spacecraft nears the moon, the critical period of the mission (from a radiation point of view) begins. Two astronauts must now leave the well-protected mother ship to enter the Apollo lunar excursion module for the descent and lunar-landing operation. From this point, until they reenter the CM, they will be virtually naked to solar proton radiation. The possibility of finding shelter on the moon during a solar proton event is limited by the fact that the oxygen supply (life support system) is sufficient for only 3 to 4 hours away from the LEM, which is not enough time to withstand an event which may last for a period of several days. The alternate solution to the problem of reducing the astronaut's dose is either to limit the lunar exploration phase of the mission in the face of a moderate solar

event or to return to the CM as quickly as possible before the arrival of a severe event.

Upon approaching the moon, the spacecraft achieves lunar orbit and, at this point, the decision is made to leave the CM in the LEM. If a proton event should be in progress at this point (no. 2 in fig. 5), the separation of the LEM could be delayed or cancelled. The mission would probably continue if the event proved to be moderate, using a revised lunar exploration schedule. Should the situation become worse, the LEM could return to the CM before touchdown (no. 3 in fig. 5).

In the normal Apollo mission, the crew is expected to stay on the lunar surface for approximately 1 day. During this period, a crew member will leave the LEM, explore the surface of the moon, and return to the LEM to replenish his oxygen supply, rest, make notes, et cetera, while the other crew member exits to explore. At other times, both members of the crew will be in the LEM, but at no time will they both be outside the spacecraft. Should a proton event occur during this period (no. 4 in fig. 5), the length of stay will be shortened proportionally to the event size. In this way, a compromise will be reached between the exploration objectives and the astronaut radiation dose. In the instance of a severe event, the astronauts will probably make immediate preparations to return to the CM. These decisions will be reached by the Apollo flight directors located in the Apollo control center in Houston and immediately communicated to the astronauts.

65-34595

18—Particles Emitted in the Forward Direction From High-Energy Nucleon-Nucleus Knock-On Reactions¹

H. W. BERTINI

Oak Ridge National Laboratory

Energy and angular distributions of emitted secondaries from nucleon-nucleus reactions can be obtained from an available intranuclear cascade calculation (ref. 1). The main assumption in this calculation is that high energy (~ 100 MeV) nucleon-nucleus reactions occur via a series of individual particle-particle reactions within the nucleus where the differential cross sections used in determining the scattering angles in the particle-particle reactions are the free-particle differential scattering cross sections.

Examples of the shapes of the curves for the n-p and p-p free-particle differential cross sections plotted versus the laboratory scattering angle for 40- and 160-MeV neutron-proton and proton-proton reactions are illustrated in figures 1 and 2. These data were derived from the center of mass cross sections presented in reference 2. It should be noted that all the curves peak at zero degrees in the laboratory system. On this basis alone one would expect the angular distribution of the particles knocked out of the nucleus in particle-particle reactions to be peaked at zero degrees, too. However, plots of these distributions (figs. 3 to 6) indicate that the distributions decrease for small forward angles as the angle approaches zero. (This decrease was predicted long ago when intranuclear-cascade reactions were first postulated (ref. 3), but to the author's knowledge has

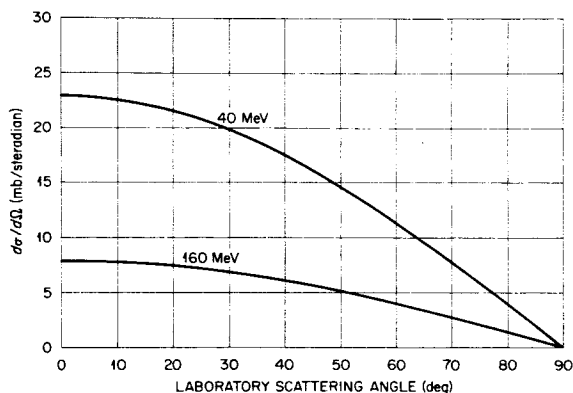


FIGURE 1.—The differential scattering cross section versus laboratory scattering angle for 40 and 160 MeV proton-proton collisions.

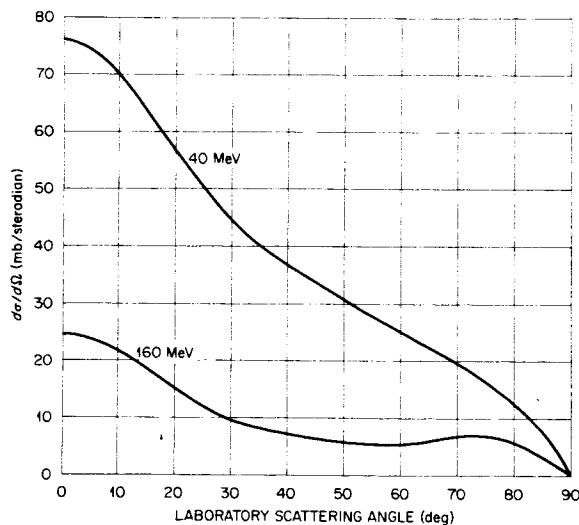


FIGURE 2.—The differential scattering cross section versus laboratory scattering angle for 40 and 160 MeV neutron-proton collisions.

¹ Research sponsored by the National Aeronautics and Space Administration (NASA Order R-104, Task No. 1) under Union Carbide Corporation's contract with the U.S. Atomic Energy Commission.

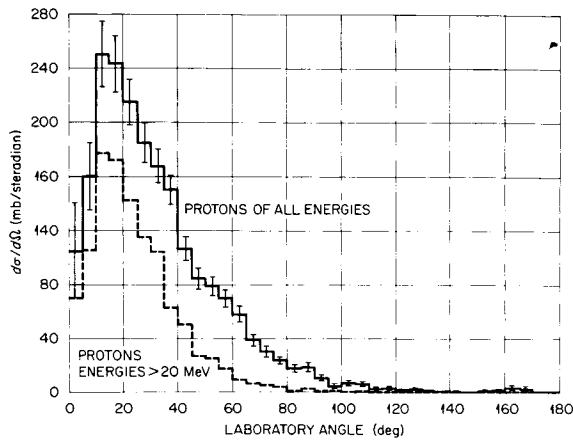


FIGURE 3.—The differential cross section versus laboratory angle for emitted knock-on protons for 50 MeV protons on cobalt. Solid line: knock-on protons of all energies. Dashed line: knock-on protons with energy greater than 20 MeV.

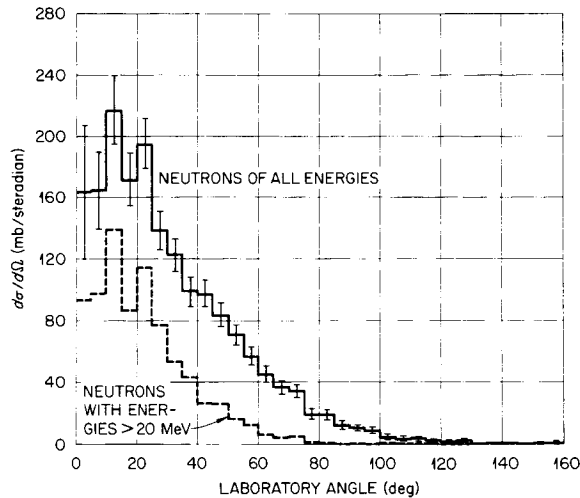


FIGURE 4.—The differential cross section versus laboratory angle for emitted knock-on neutrons for 50 MeV protons on cobalt. Solid line: knock-on neutrons of all energies. Dashed line: knock-on neutrons with energy greater than 20 MeV.

never been verified experimentally.) The decrease is attributable to the effect of the exclusion principle on the collisions which occur inside the nucleus.

To illustrate, consider a simple nonrelativistic scattering reaction where the struck particle is at rest. When the masses of the two particles are equal, the energy of the incident particle after scattering T is related to its initial energy

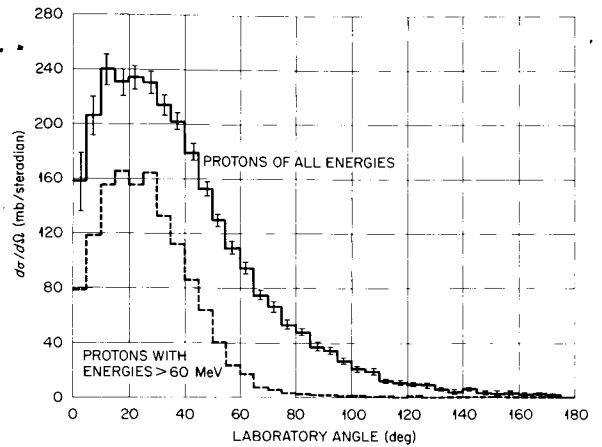


FIGURE 5.—The differential cross section versus laboratory angle for emitted knock-on protons for 160 MeV protons on cobalt. Solid line: knock-on protons of all energies. Dashed line: knock-on protons with energy greater than 60 MeV.

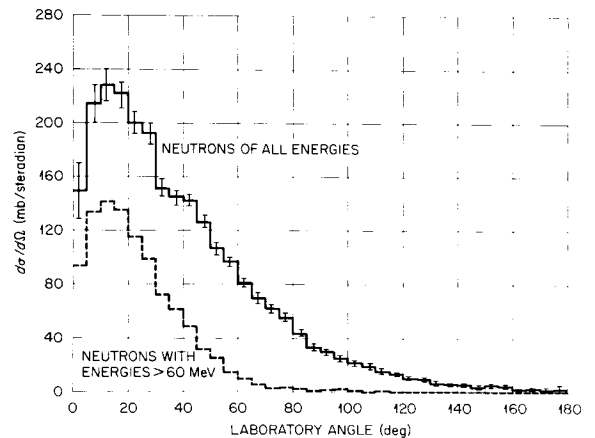


FIGURE 6.—The differential cross section versus laboratory angle for emitted knock-on neutrons for 160 MeV protons on cobalt. Solid line: knock-on neutrons of all energies. Dashed line: knock-on neutrons with energy greater than 60 MeV.

T_0 by the expression

$$T = T_0 \cos^2 \theta$$

where θ is the angle of scattering. The scattering angle determines the energy of the scattered particle and, hence, the energy transferred to the struck particle. When θ is small, the energy transferred to the struck particle is small. This is true even when the struck particle is moving.

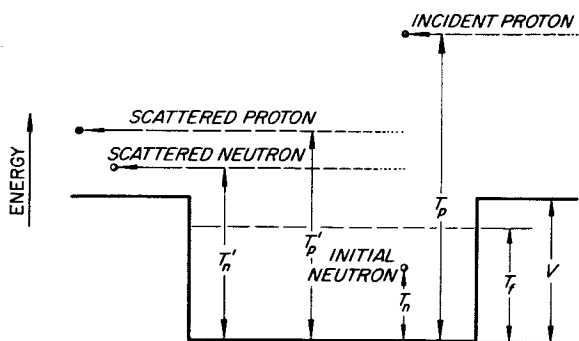


FIGURE 7.—Schematic energy diagram of a proton-nucleus knock-on reaction in which the proton collides with a neutron in the nucleus. V is the potential well of the nucleus and T_f is the Fermi energy of the nucleons in the nucleus.

Now consider the assumption that attempts to approximate the exclusion principle in the intranuclear cascade calculation. Figure 7 is a schematic energy diagram of a single proton-neutron reaction occurring inside the nucleus. The primes refer to quantities after scattering, while the T 's represent kinetic energies inside the nucleus. The assumption is that the energies of *both* particles after scattering must be greater than the Fermi energy, that is, that

$$T_n', T_p' > T_f$$

in order to be an "allowed" reaction. Otherwise, the reaction is not permitted to take place. Therefore, when the scattering angle is small, the energy transfer is small, and the only nucleons in the Fermi sea available for "allowed" reactions are those near the top of the sea, while reactions with all the other nucleons are "forbidden." This reduction in the nucleons available for small-angle scattering reactions reduces the nucleon-nucleus reaction

cross section for particles emitted at small forward angles.

Although only small energy transfers have been mentioned, the argument also holds for large energy transfer; that is, if the incident proton transfers energy to the struck neutron such that the neutron has the same energy that the proton had, the neutron will go off in exactly the same direction as the incident proton (equivalent to charge exchange scattering at zero charge exchange scattering angle), but the proton will assume the energy that the neutron had. Since the proton energy will then be below the Fermi Energy, this reaction will be forbidden.

From the expression

$$T = T_0 \cos^2 \theta$$

one can see that the higher the incident energy, the smaller this effect will be, because, although the fractional change in energy will be the same for a given scattering angle, the magnitude of the energy transfer will be larger; hence, more nucleons inside the nucleus will be available for "allowed" reactions. The effect is visible in figures 4 and 6.

The point of this paper, then, is to illustrate a potential pitfall for those doing shielding calculations. One must be careful in making simplifying assumptions with respect to the angular distribution of high energy secondary particles.

In the same vein, in figures 8 and 9 is illustrated the fraction of high energy particles emitted between zero and θ where θ varies in steps of 5° for the same reactions as before. In order to include 50% of the fast particles, one must use angular intervals from 0 to 25° or 0 to 45° depending on the case. The calculation predicts that less than 1% of the fast particles will be emitted in the first 5° cone.

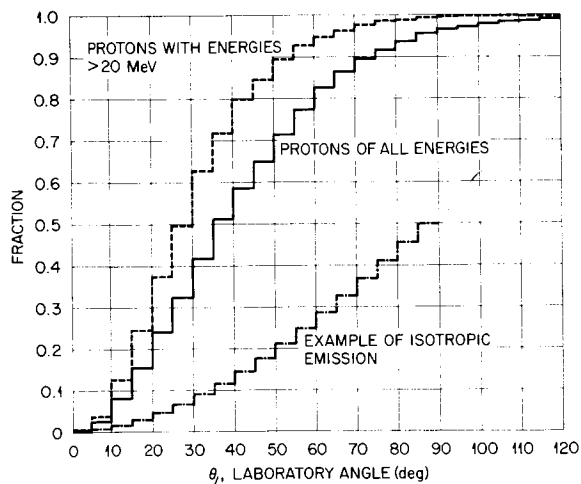


FIGURE 8.—Fraction of knock-on protons emitted between 0° and θ_L° for 50 MeV protons on cobalt. The value of the fraction is plotted only over the last five degrees of the interval, i.e., as an example, the fraction of knock-on protons emitted in the angular interval 0° to 50° is plotted from 45° to 50° (0.65 for “knock-on” protons of all energies).

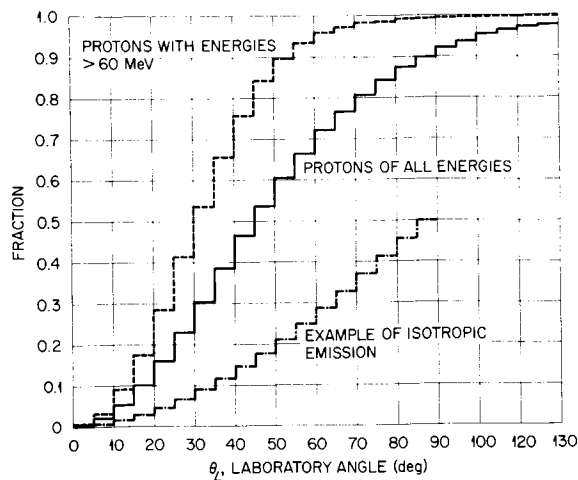


FIGURE 9.—Fraction of knock-on protons emitted between 0° and θ_L° for 160 MeV protons on cobalt. (See figure 8 for further explanation.)

REFERENCES

1. BERTINI, H. W.: Phys. Rev., vol. 131, 1963, p. 1801.
2. HESS, W. N.: Rev. Mod. Phys., vol. 30, 1958, p. 368.
3. SERBER, R.: Phys. Rev., vol. 72, 1947, p. 1114.

19—Calculated Tissue Current-to-Dose Conversion Factors for Nucleons of Energy Below 400 MeV¹

W. E. KINNEY

Oak Ridge National Laboratory

and

C. D. ZERBY

Union Carbide Research Institute

N65-34596

To assess the hazard to personnel encountering high-energy radiation in space or near accelerators, it is necessary to have a means of estimating the biological effects of these radiations. A useful and simple way of obtaining such an estimate is to multiply the current of a given type of incident particle by the appropriate current-to-dose conversion factor to obtain a measure of the dose received. Of course the physiological effects of radiation can be determined only by experiment, but in the past these effects have been correlated with the dose in the case of low-energy radiation. Hence, it is expected that the same situation will prevail at high energy although the correlation may be more complicated. To facilitate possible correlations, a series of Monte Carlo calculations were carried out to determine many details about the energy deposition in tissue as a function of depth. From these data, rad (1 rad=100 ergs/g) and rem (roentgen equivalent man) doses were calculated and current-to-dose conversion factors for the surface and 5-cm-depth doses and for the average whole-body and peak doses were extracted for hazard evaluation. Both incident neutrons and protons from 60- to 400-MeV incident energy were considered.

¹ Research sponsored by the National Aeronautics and Space Administration (NASA Order R-104, Task No. 1) under Union Carbide Corporation's contract with the U.S. Atomic Energy Commission.

Since the method of converting energy deposition to rem dose will be subject to change as additional data become available, the energy deposited by the protons as they passed through various energy ranges at the various depths was calculated separately. In this way, any preferred set of quality factors (QF) can be applied in the future with relative ease. In addition to the proton energy deposition data, information about energy deposition by heavy recoils and heavy charged particles was computed, and was reported separately for the same reason. A detailed breakdown of the energy deposition data is given elsewhere (ref. 1) for the depths and conditions corresponding to those for which the current-to-dose conversion factors were calculated.

Previous calculations by Neary and Mulvey (ref. 2) of the tissue dose from high-energy radiations estimated maximum permissible currents of nucleons in the 40- to 1000-MeV energy range on the basis of rather qualitative considerations. Gibson (ref. 3) performed calculations on energy deposition in tissue involving very conservative assumptions regarding the deposition processes. Turner *et al.* (ref. 4) recently performed more detailed Monte Carlo calculations of the tissue dose due to protons up to 400 MeV; the present calculation is an independent extension of this study. Detailed experiments of the tissue dose from high-energy radiation are very scarce. The experi-

ment of Shalnov (ref. 5) is an isolated example of the measurement of the dose from high-energy neutrons. His data include the dose as a function of depth in tissue-like material from approximately 140-MeV neutrons stripped from 280-MeV deuterons on Cu and from a broad spectrum from charge-exchange reactions of 480-MeV protons on Be.

The methods employed in the calculation will first be described and will then be followed by a comparison of these results with experiment and previous calculations. The current-to-dose data will then be presented and discussed.

METHODS

The interaction of a high-energy nucleon with matter initiates a complex avalanche of lower energy secondary particles which proceeds through the medium, increasing in population and decreasing in total energy as energy is deposited in the medium. In general, a non-elastic interaction with a nucleus produces, first of all, several secondary nucleons which are due to direct interactions of the incident particle with the nuclear constituents and which have energies ranging from a few MeV up to a large fraction of the incident particle energy. There is left a highly excited, recoiling nucleus which rids itself of most of its excess energy by evaporating nucleons and heavy particles of relatively low energy of the order of a few MeV. Any energy left after evaporation presumably goes into the production of electromagnetic radiation.

A series of Monte Carlo programs (ref. 6) for the IBM-7090 computer has been written to study the transport of nucleons of energies up to 400 MeV through quite arbitrary geometrical configurations. The intranuclear cascade is treated by a subroutine version of Bertini's code (ref. 7) which is itself a Monte Carlo nucleon transport calculation on an intranuclear scale and gives the velocities and types of particles resulting from direct interaction processes. The evaporation portion of the cascade is handled by Dresner's subroutine (ref. 8), which is essentially the same as Dostrovsky's calculation (refs. 9 to 11). Protons below 50 MeV were allowed to proceed to the

end of their range with no nuclear interaction, while neutrons below this energy were transported by an existing neutron transport code (ref. 12).

To apply the general-purpose nucleon transport code to the problem of the dose in tissue due to nucleons of energy less than 400 MeV, with the hope of arriving at some practical, usable current-to-dose conversion factors of sufficient generality of application, a 30-cm-thick infinite slab of tissue was chosen for study. The tissue was assumed to have a composition (ref. 13) of $C_{21}H_{140}O_{57}N_3$ with a density of 1 gm/cm³, assumptions which result in the nuclear densities given in table I. The average ionization potentials which were used in the stopping power formula for the computation of the range are also listed in table I.

TABLE I

Composition and Mean Excitation Potentials for Tissue

Element	Nucleon density, (nuclei/cm ³) × 10 ⁻²⁴	Mean excitation potential, eV
H	6.265 × 10 ⁻²	17.5
O	2.55075 × 10 ⁻²	99.0
C	9.3975 × 10 ⁻³	74.44
N	1.3425 × 10 ⁻³	86.0

In the application of the current-to-dose conversion factors, it is to be expected that widely varying angular distributions of nucleons incident upon the body will be encountered. In order to provide current-to-dose conversion factors which could be used to estimate upper and lower bounds on the doses for practical cases of interest, the nucleons were made to impinge on the tissue slab both normally in a broad beam and isotropically, with the expectation that these two extremes of incident angular distribution would represent the bounding cases. One can, of course, construct an angular distribution which results in a dose greater than the isotropic dose as, for example, a 400-MeV proton beam incident at such an angle as to be entirely stopped in the 30-cm-thick slab, and thus yield a higher average dose than the

isotropic case. It is felt, however, that such distributions would be most unrealistic. Generally, 10,000 monoenergetic source nucleons were introduced at each of the source energies of 400, 300, 200, 100 and 60 MeV, and for each angular distribution. The 30-cm-thick slab was divided into 30 subslabs of 1 cm thickness, and a print-out was then made of the energy deposited in each subslab due to primary protons, secondary cascade protons, secondary evaporated protons, evaporated heavy (mass >1) particles, and recoil nuclei resulting from both high-energy nuclear interactions and low-energy neutron elastic collisions. The residual nucleus excitation energy available for gamma-ray production was also recorded in each subslab.

The dose as a function of depth was calculated in units of rads and rems. For the purpose of converting the rad to rem units, the energy deposition resulting from protons as they passed through the energy ranges 0-1, 1-5, 5-10, 10-50, and >50 MeV was recorded separately. Average QF values, for each interval, of 8, 3, 1.25, 1, and 1, respectively, were calculated from the QF versus LET (linear energy transfer) curve shown in figure 1. The graphical data were derived from tabulated values in the National Bureau of Standards Handbook 59 (ref. 14), which agree very closely with the recommendations of the 1962 report of the RBE committee to the ICRP and ICRU (ref. 15). The values of the energy of the proton shown in figure 1 were correlated with the LET values by means of the stopping power formulas.

The constant value of 20 for the QF above an LET value of 1750 MeV/cm shown in figure 1 is not from Handbook 59, but constitutes a quite arbitrary assumption that a saturation effect takes place and can be represented by a constant QF at high LET values. It should be noted, that under all circumstances, the QF value of 20 is applied to the dose from the heavy evaporation particles and recoil nuclei in calculating the rem dose, since their LET value is generally above 1750 MeV/cm.

Because of the uncertainties connected with the QF versus LET curve, Schaefer (private communication) suggested that the dose data be recorded in energy intervals in a manner

similar to that described above so that any preferred set of QF's could be employed to calculate the rem dose with relative ease.

COMPARISON WITH OTHER WORK

In an attempt to establish the degree of reliability of the calculations, the results were compared with those obtained by other investigators, with particular interest given to a comparison with two neutron dose experiments. Both experiments were performed with multi-energetic neutrons and, rather than performing two lengthy calculations with neutrons introduced in an energy spectrum into a model of the experimental configuration, the results of our selected monoenergetic neutron dose calculations in the assumed tissue were applied as nearly as possible.

Shalnov (ref. 5) measured the dose as a function of depth in water and paraffin dummies due to neutrons which were incident in a broad beam and which resulted from the stripping reaction of 280-MeV deuterons on a thick copper target and also from the charge exchange of 480-MeV protons on beryllium. Serber (ref. 16) gives the energy spectrum of neutrons stripped from deuterons as

$$N(E)dE = \frac{\epsilon_a E_a}{\pi[(E - \frac{1}{2}E_a)^2 + \epsilon_a E_a]} dE$$

where

$N(E) dE$ = the number of neutrons in the energy range dE about E

E = neutron energy in MeV

E_a = the kinetic energy of the deuteron in MeV

ϵ_a = the binding energy of the deuteron = 2.18 MeV

This is a spectrum having a half width of $1.5(E_a \epsilon_a)^{1/2}$ which, for 280-MeV deuterons, is equal to 37 MeV.

The measured doses as a function of depth due to neutrons stripped from 280-MeV deuterons are compared in figure 2 with the calculated results for 100-MeV neutrons normally incident in a broad beam on an infinite slab of tissue. The results have not been

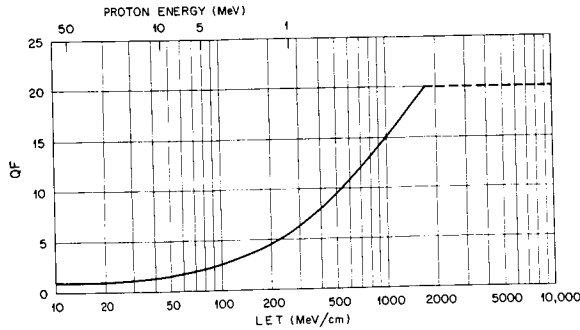


FIGURE 1.—QF versus LET.

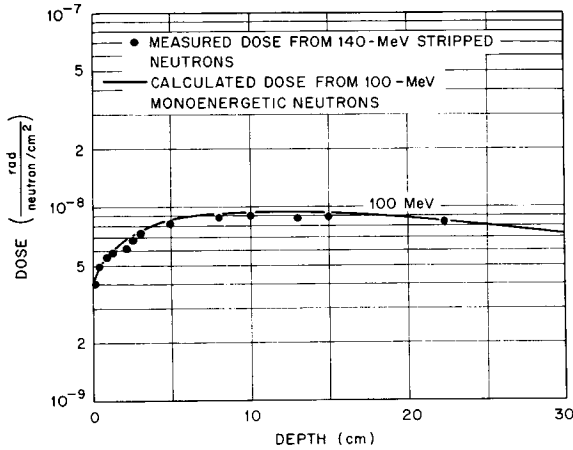


FIGURE 2.—Measured and calculated dose in tissue versus depth due to approximately 140-MeV neutrons.

normalized, and agreement is seen to be excellent.

The neutron spectrum from the charge-exchange reaction of 480-MeV protons on beryllium as measured by Dzheleпов *et al.* (ref. 17) is given in figure 3, where the extrapolation assumed for this work is indicated. The average neutron energy is roughly 380 MeV, with 30% of the neutrons lying between 350 and 480 MeV, 25% between 250 and 350 MeV, and 21% between 150 and 250 MeV.

In an attempt to compare the calculated doses due to monoenergetic sources with the measured dose from the charge-exchange neutrons, the calculated doses for normal incidence were weighted rather crudely with the spectrum. The 400-MeV neutron calculated doses were weighted with the integral of the spectrum above 350 MeV. Similarly, the 300-MeV results were

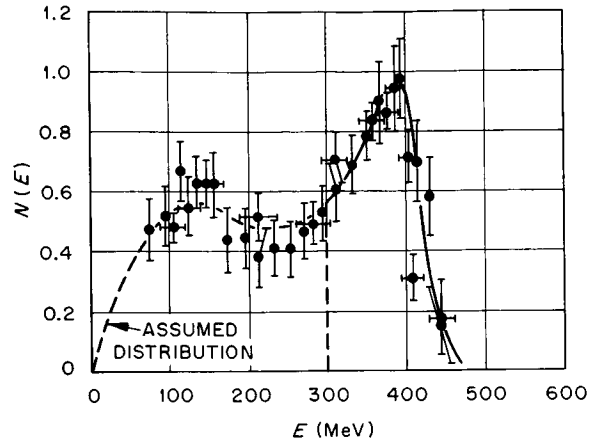


FIGURE 3.—Energy spectrum of neutrons resulting from the charge exchange of 480-MeV protons on beryllium.

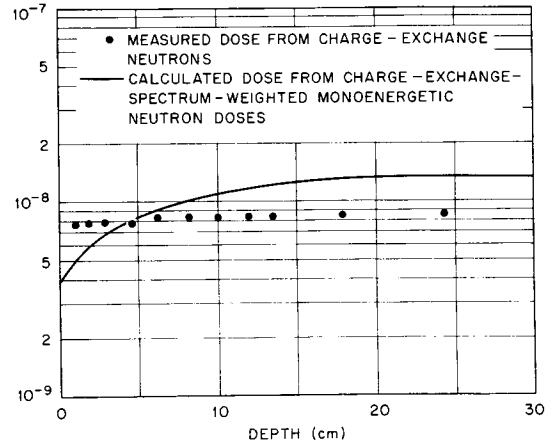


FIGURE 4.—Measured and calculated dose in tissue versus depth due to neutrons in a charge-exchange spectrum of mean energy 380 MeV.

weighted with the integral from 250 to 350 MeV, the 200-MeV results with the integral from 150 to 250 MeV, and the 100-MeV doses with the integral below 150 MeV. The resultant weighted dose as a function of depth is compared with measured values for the charge-exchange neutrons in figure 4. Again there has been no normalization; however, although the order of magnitude of the calculated and measured doses agrees approximately, the shape of the dose versus depth curves is not in the excellent agreement seen in the comparison in figure 2.

The experimental result in this case shows a flat behavior of the dose as a function of depth, while the calculated curve rises with increasing depth. Crude calculations show that a large number of low-energy neutrons could account in large measure for the flat behavior of the experimental results.

Neary and Mulvey (ref. 2) have estimated the permissible currents of incident nucleons of energy in the range of 40 to 1000 MeV which will produce a dose in a period of 40 hours equal to 0.3 rem, the value of maximum weekly dose recommended by the National Committee on Radiation Protection and Measurements (ref. 18). They estimated the relative biological effectiveness of the nucleons and assumed that all the energy was deposited within a distance equal to the range in the case of protons and within a mean free path in the case of neutrons. They then computed an average dose over these distances to arrive at the permissible incident current. Their results are compared in figure 5 with maximum currents based on the results of our calculations for both normally incident and isotropically incident nucleons. We determined the currents by computing average whole-body doses over the 30-cm slab for all the neutron calculations and for the protons of incident energy greater than 220 MeV, the energy at which the range of protons in tissue is 30 cm. For protons below 220 MeV, we averaged the doses over the range of protons. The differences are greatest in the case of neutrons, where our results indicate that currents higher by a factor of 2 to 4 may be permitted. The differences are chiefly due to the assumption by Neary and Mulvey that there was complete absorption of the neutron, while we considered a 30-cm-thick slab. The mean free path for neutrons in the 100- to 400-MeV energy range is approximately 80 cm, and so 70% of the primary neutrons at normal incidence pass through the slab without suffering interaction and, therefore, without depositing energy; many of the secondary neutrons also escape. The permitted currents of neutrons incident isotropically are, of course, less than those permitted at normal incidence since the former neutrons travel, on the average, twice as far as the latter in the slab. The permitted

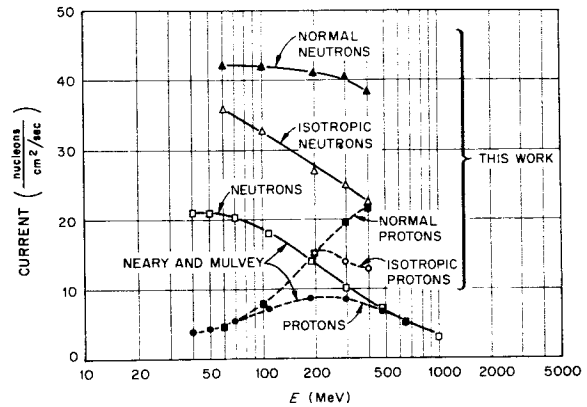


FIGURE 5.—A comparison of currents of nucleons to produce a dose of 0.3 rem per 40 hr versus incident energy.

proton currents resulting from our calculations are also higher than those of Neary and Mulvey. At low energies the permitted currents agree, but at round 70 MeV they start to diverge, the divergence increasing up to 220 MeV, the energy at which normally incident protons can just get through the slab. This is due to the fact that the effective QF for the incident proton from our calculations is lower than that assumed by Neary and Mulvey. Our effective QF, which is equal to the ratio of total rem to total rad dose, falls from 1.3 at 100 MeV to 1.1 at 200 MeV (see fig. 14), while the values of Neary and Mulvey rise from 1.24 at 70 MeV to 1.6 at 190 MeV. Above 220 MeV, our permitted current of normally incident protons increases since the primaries are now able to escape, as indicated in figure 8. The curve of permitted current for isotropically incident protons, however, turns over above 220 MeV and falls, since the higher energy protons produce more secondaries than do the lower energy ones, and while the average rad dose remains constant with increasing energy, the rem dose increases slightly, as shown in figure 9.

Gibson (ref. 3) computed the energy removed from primary nuclear beams by tissue, making the very conservative assumption that all the energy of nucleons absorbed is available and deposited locally. Actually, a considerable portion of the energy is expended in overcoming the binding energy of the nucleons within the nucleus and, also, much of it leaks

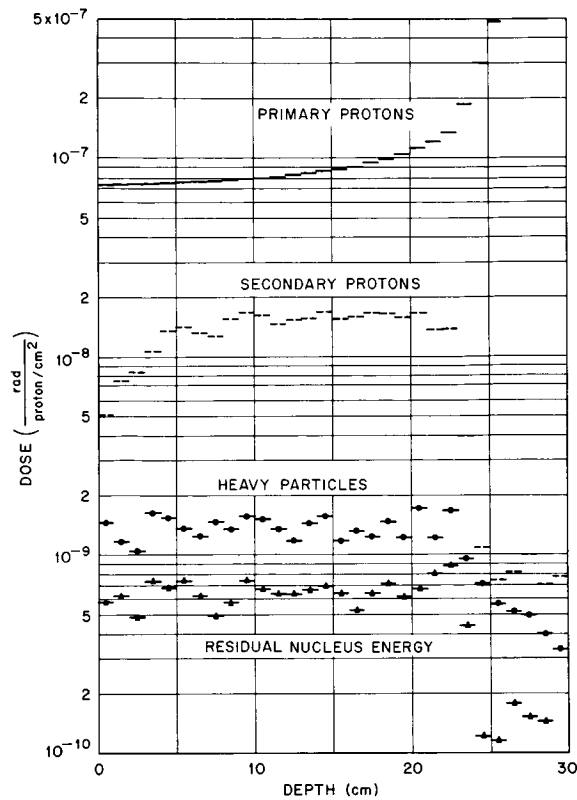


FIGURE 6.—Dose versus depth for 200-MeV normally incident protons.

out. The proton doses computed by Gibson are higher than ours by a factor of up to 2, while the neutron doses range from a factor of 3 higher at low energy to 4 higher than our average dose and 14 higher than our surface dose at 400 MeV.

RESULTS

As stated previously, Monte Carlo calculations were performed for both normally and isotropically incident protons and neutrons with energies of 60, 100, 200, 300, and 400 MeV. Ten thousand source particles were used for each case. The unsmoothed results from the case of normally incident 200-MeV protons presented in figure 6 indicate typical results and the statistical uncertainties associated with the data. Additional details and the remainder of the cases are presented in another report (ref. 1).

For the case of normal incidence, the dose from primary protons presented in figure 6

approximates, as expected, the stopping power curve for ionization energy loss as a function of depth in tissue. It is only an approximation because some of the protons are removed from the beam by nonelastic events and so the energy deposition falls below the stopping power curve. At 200-MeV incident energy, the increase in the stopping power with decreasing energy (and, hence, with depth) is sufficiently rapid to make up for the removal of particles by nonelastic events, thus causing the dose to increase initially as the depth increases. At about 400 MeV, the two effects almost balance and the energy deposition from the primary beam decreases slightly with depth, only to increase again near the end of the range as the stopping power increases. Of course, for normally incident 400-MeV protons, the rise at the end of the range is not experienced in our model of the body because their range is 84 cm.

The energy deposition by secondary protons indicated in figure 6 includes the contribution from cascade protons ejected in nonelastic events, nuclear evaporation protons, and protons from elastic scattering with hydrogen as a result of either neutron or proton interactions. Initially, the dose from the secondary protons increases with depth as the number of secondary particles builds up from cascades initiated by the primary beam. Near the end of the range of the primary beam (26.5 cm), where the particle energies are low, the contribution from secondary protons decreases rapidly as a result of the decrease in the number of nonelastic events creating secondary particles. Beyond the range of the primary beam, there is still a contribution from secondary protons ejected by neutrons that have migrated to that depth.

The dose from the heavy particles shown in figure 6 includes the contribution from the recoil of the residual nuclei after a nonelastic event, nuclear recoils (other than protons) from elastic scattering of low energy neutrons, and nuclear evaporation particles (other than protons). The dose from these particles is remarkably flat over most of the range of the primary beam, decreasing appreciably only near the end of the range, where contributions come only from neutron-initiated events. The dose from residual nuclei shown in figure 6 actually indicates the energy created in the

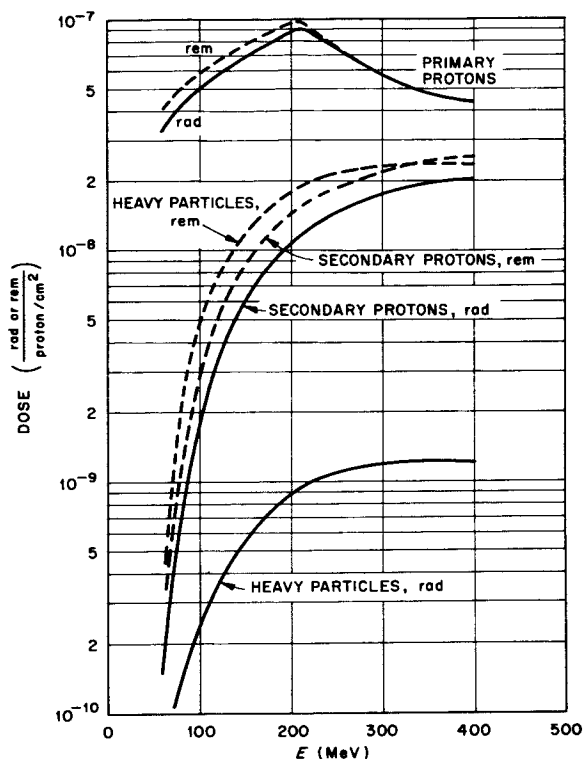


FIGURE 7.—Primary proton, secondary proton, and heavy-particle average whole-body rad and rem doses due to normally incident protons as a function of incident energy.

form of photons by transitions to the ground states of the residual nuclei after nonelastic events. The contribution to the dose from these radiations is usually so small for the cases considered that we did not calculate the migration of the photons; in fact, reference to the data is omitted in the remainder of the figures.

From the detailed depth-dose data of all the cases calculated, certain doses were extracted to establish current-to-dose conversion factors. The particular ones chosen were the average whole-body dose, the surface dose, the dose at a depth of 5 cm, which is the average depth of the blood-forming organs, and the peak dose. These data are presented in figures 7 through 14. The detailed results for normally incident protons are presented in figure 7 as an indication of the significance of the various contributions. Here the primary proton, secondary proton, and heavy particle rad and rem doses are presented separately.

In figure 7, the reason for the primary proton dose having a discontinuity at 215 MeV is that above this energy the proton beam penetrates 30 cm of tissue and some of the energy is not deposited. The decrease in dose with increasing energy above 215 MeV is accounted for by the decrease in stopping power with increasing energy in this energy range. Thus, less energy is deposited in the 30 cm of tissue as the energy increases. It is interesting to note that the rem dose of the primary or secondary protons in figure 7 is not appreciably different from the corresponding rad dose. This is because most of the protons are created with energies well above 1 MeV and they therefore deposit the greatest fraction of their energy with a QF close to unity. The heavy-particle rem dose, on the other hand, is exactly a factor 20 above the rad dose because the LET value of these particles is always above 1750 MeV/cm. This interesting situation, which admittedly depends on the *ad hoc* but perhaps reasonable assumption that the QF is 20 and constant at high LET values, causes the heavy-particle contribution to the total rem dose to be greater than the secondary proton dose for most energies. For instance, at 100 MeV the secondary proton rem dose is approximately 6% of the total dose, while the heavy-particle rem dose contributes 10%. At 400 MeV these percentages are each approximately 35%.

Figure 8 presents the total average whole-body rad and rem results for both normally incident neutrons and protons. Also shown is the average wholebody rad dose that would be received if the proton beam were totally absorbed. In comparison with the latter curve, it is easy to see that below 215 MeV little error would be introduced if the whole-body rad dose were calculated on the basis that all the energy is totally absorbed.

By dividing the rem dose by the rad dose, one obtains the average QF. In all cases presented, this average QF is significantly greater for incident neutrons in comparison with incident protons. The difference can be attributed to the fact that, in the case of incident protons, the dose from the primary protons with its associated QF which is near unity makes the most significant contribution to the total

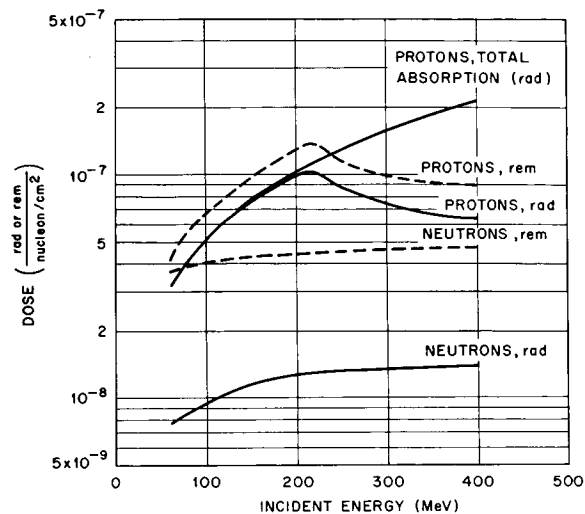


FIGURE 8.—Average total rad and rem doses versus incident energy for normally incident protons and neutrons.

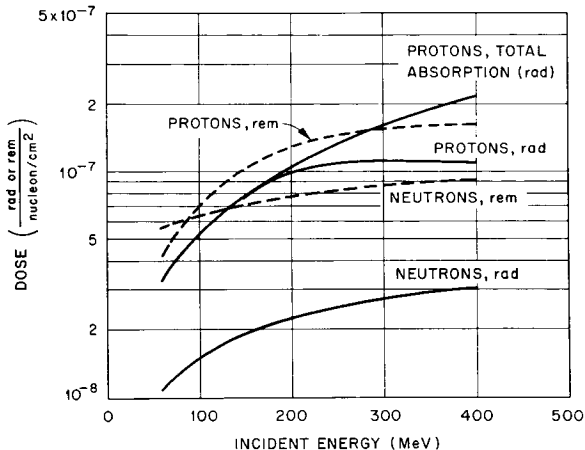


FIGURE 9.—Average total rad and rem doses versus incident energy for a unit current of isotropically incident protons and neutrons.

rad or rem dose. Thus the average QF would be expected to be close to unity. In the case of incident neutrons, approximately 11% of the rad dose is contributed by the heavy particles, but its associated QF of 20 makes it the most significant contributor to the rem dose (the QF associated with the secondary proton dose is close to unity). An approximate calculation indicates that under these circumstances the average QF should be close to 3 for the neutron cases. Indeed, the average QF for normally incident protons ranges from 1.3 at 100 MeV to

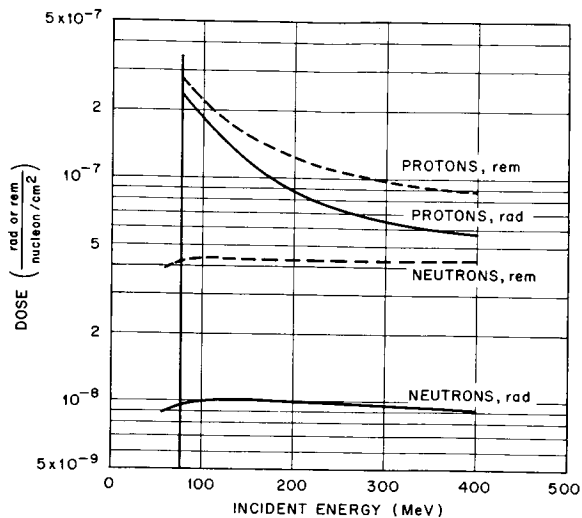


FIGURE 10.—The total dose at a depth of 5 cm versus incident energy for normally incident protons and neutrons.

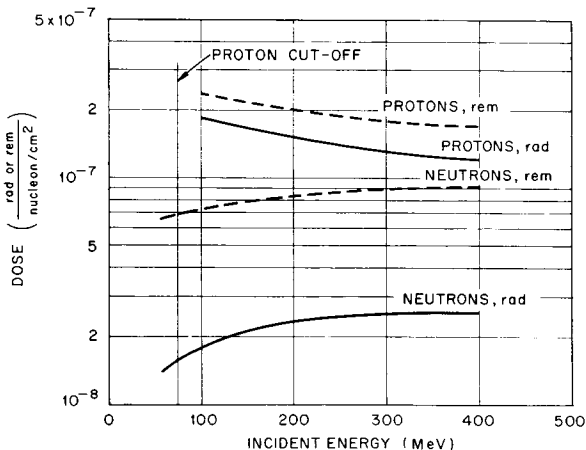


FIGURE 11.—The total dose at a depth of 5 cm versus incident energy for a unit current of isotropically incident protons and neutrons.

1.4 at 400 MeV, while for normally incident neutrons it ranges from 4.2 at 100 MeV to 3.4 at 400 MeV.

The curves for the average whole-body dose for isotropically incident particles shown in figure 9 are quite similar to the corresponding ones from the normally incident cases, and little need be said about them.

In figures 10 and 11, where the 5-cm-depth doses are reported, there is a definite cutoff at 80 MeV for incident protons. This is because protons in the range of approximately 80 MeV

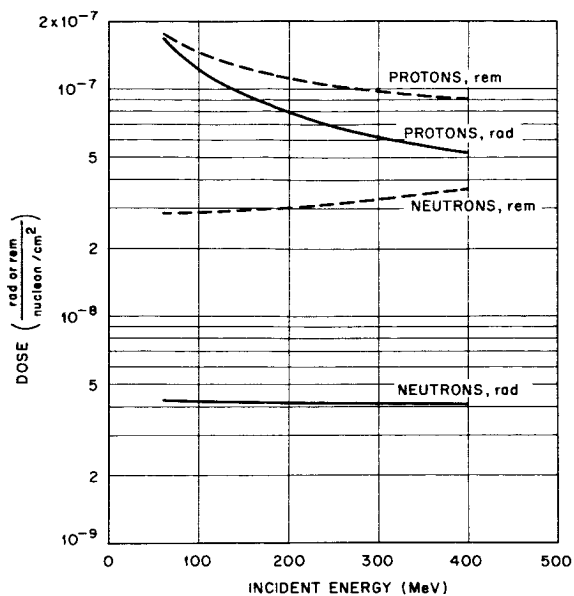


FIGURE 12.—The total dose at the surface versus incident energy for normally incident protons and neutrons.

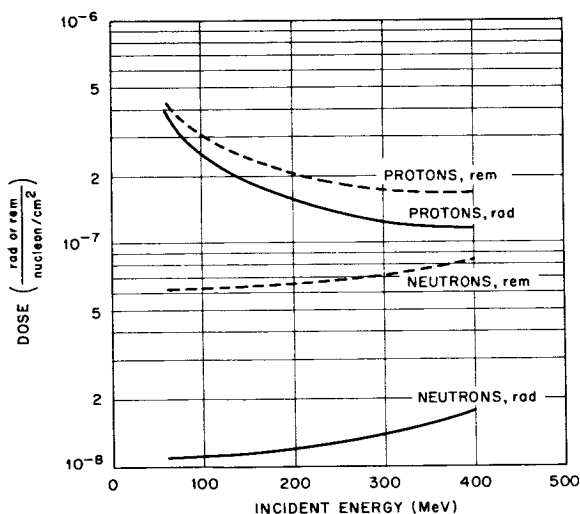


FIGURE 13.—The total dose at the surface versus incident energy for a unit current of isotropically incident protons and neutrons.

and below are less than 5 cm in tissue and cannot make a contribution at that depth.

The curves for the surface doses shown in figures 12 and 13 are not markedly different from the corresponding 5-cm-depth dose curves.

Figures 14 and 15 present the maximum dose curves for normally incident and isotropically

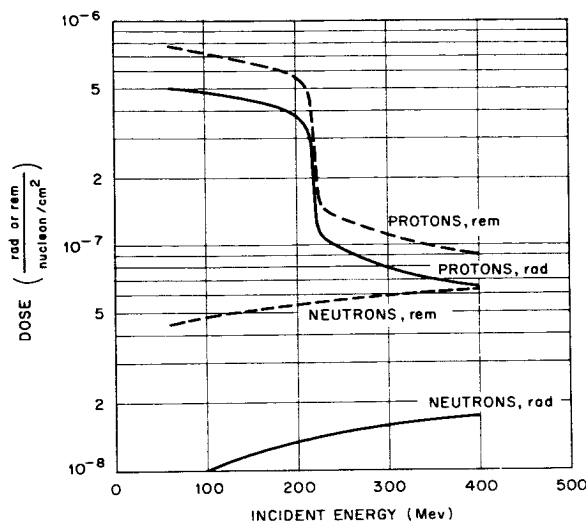


FIGURE 14.—Maximum total dose versus incident energy for normally incident protons and neutrons.

incident neutrons and protons. The depth at which these maximums occur is presented in table II. The apparent discontinuity in the normally incident proton curve shown in figure 14 is explained by the fact that, below 215-MeV incident energy, the maximum occurs at the end of the range of the protons where the stopping power is very high. Above 215-MeV incident energy, the range of protons is greater than 30 cm; therefore, the maximum in the body occurs at some intermediate proton energy where the stopping power is much less than that at the end of its range. The maximum doses for energies below 215 MeV were obtained by averaging the dose over the last centimeter of its range.

The current-to-rem dose conversion curves shown in figures 8 through 15 can be fit by an expression of the form

$$\log_{10} D = A + BE + CE^2$$

where D is the dose in rem per nucleon per cm^2 and E is the energy in MeV. Table III contains the values of the coefficients.

Space does not permit the inclusion of the partial rad doses as a function of depth so that arbitrary QF's may be applied in arriving at a rem dose. This detailed data may be found in reference 1.

TABLE II
Depth at Which Maximum Dose Occurs

Source	Depths (cm) for source energies of				
	400 MeV	300 MeV	200 MeV	100 MeV	60 MeV
Normal protons.....	30	30	24-25	6-7	
Normal neutrons.....	30	30	20-30	5-10	5
Isotropic protons.....	5	5	5	3	0
Isotropic neutrons.....	15-25	15-25	15	5-10	0

TABLE III
Coefficients of the Expansion for the Rem Dose Log D for Various Cases

<i>Normally incident protons</i>	
Average dose.....	$-7.72 + 6.4 \times 10^{-3}E - 1.1 \times 10^{-5}E^2$; $60 < E < 215$ $-6.20 - 4.3 \times 10^{-3}E + 5.5 \times 10^{-6}E^2$; $215 < E < 400$
5-cm-deep dose.....	$-6.27 - 4.6 \times 10^{-3}E + 6.4 \times 10^{-6}E^2$; $80 < E < 400$
Surface dose.....	$-6.64 - 2.2 \times 10^{-3}E + 2.9 \times 10^{-6}E^2$; $60 < E < 400$
Maximum dose.....	$-6.02 - 1.2 \times 10^{-3}E$; $60 < E < 215$ $-6.62 - 1.1 \times 10^{-3}E$; $215 < E < 400$
<i>Normally incident neutrons</i>	
Average dose.....	$-7.43 + 2.7 \times 10^{-4}E$; $60 < E < 400$
5-cm-deep dose.....	-7.38 ; $60 < E < 400$
Surface dose.....	$-7.59 + 3.7 \times 10^{-4}E$; $60 < E < 400$
Maximum dose.....	$-7.35 + 3.8 \times 10^{-4}E$; $60 < E < 400$
<i>Isotropically incident protons</i>	
Average dose.....	$-7.79 + 7.9 \times 10^{-3}E - 1.7 \times 10^{-5}E^2$; $60 < E < 215$ $-7.07 + 1.2 \times 10^{-3}E - 1.3 \times 10^{-6}E^2$; $215 < E < 400$
5-cm-deep dose.....	$-6.57 - 5.4 \times 10^{-4}E$; $80 < E < 400$
Surface dose.....	$-6.30 - 2.7 \times 10^{-3}E + 3.7 \times 10^{-6}E^2$; $60 < E < 400$
Maximum dose.....	$-6.26 - 2.9 \times 10^{-3}E + 4.1 \times 10^{-6}E^2$; $60 < E < 400$
<i>Isotropically incident neutrons</i>	
Average dose.....	$-7.26 + 5.6 \times 10^{-4}E$; $60 < E < 400$
5-cm-deep dose.....	$-7.18 + 3.9 \times 10^{-4}E$; $60 < E < 400$
Surface dose.....	$-7.26 + 4.5 \times 10^{-4}E$; $60 < E < 400$
Maximum dose.....	$-7.18 + 4.0 \times 10^{-4}E$; $60 < E < 400$

CONCLUDING REMARKS

The most striking feature of this calculation is the significant contribution that the heavy particle recoils makes to the rem dose for the

case of incident neutrons or protons. In the case of incident protons, the contribution is in general of the order of 10 to 20 percent, but for incident neutrons it constitutes the greatest

fraction of the total contribution. Unfortunately, the rad dose from the heavy particles was converted to rem dose by using a QF from the high LET and the most doubtful portion of the QF versus LET curve shown in figure 3—which points up the necessity of establishing the QF's with some degree of accuracy for high LET values if any reasonable degree of accuracy is to be expected in the current-to-rem dose conversion factors.

As a consequence of the significant contribution of the heavy particles and secondary protons to the rem dose, it is not reasonable to expect that the rem dose at any depth from incident protons can be calculated very accurately unless the secondary radiation created in the body is taken into consideration. For the case of incident neutrons this is obviously true, because only through secondary radiations is it possible for neutrons to deposit energy.

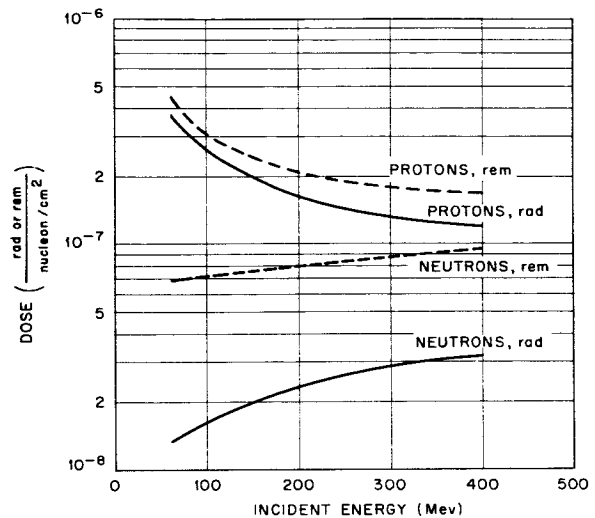


FIGURE 15.—Maximum total dose versus incident energy for a unit current of isotropically incident protons and neutrons.

REFERENCES

1. ZERBY, C. D.; and KINNEY, W. E.: Calculated Current-to-Dose Conversion Factors for Nucleons below 400 MeV. Oak Ridge National Laboratory Rept. ORNL-3706 (to be published).
2. NEARY, G. J.; and MULVEY, J.: Maximum Permissible Fluxes of High Energy Neutrons and Protons in the Range 40 to 1000 MeV. Med. Res. Council of Radiobiological Research Unit (Harwell) (unpublished).
3. GIBSON, W. A.: Energy Removed from Primary Proton and Neutron Beams by Tissue. Oak Ridge National Laboratory Rept. ORNL-3260, Sept. 6, 1962.
4. TURNER, J. E.; ZERBY, C. D.; WOODYARD, R. L.; WRIGHT, H. A.; KINNEY, W. E.; SNYDER, W. S.; and NEUFELD, J.: Calculations of Radiation Dose from Protons to 400 MeV. Health Phys., vol. 10, 1964, p. 783.
5. SHALNOV, M. I.: Tissue Doses of Fast and Ultra-Fast Neutrons. Soviet J. At. Energy, vol. 5, 1958, p. 735.
6. KINNEY, W. E.; COVEYOU, R. R.; and ZERBY, C. D.: A Series of Monte Carlo Codes to Transport Nucleons Through Matter. Proc. of Symp. on Protection Against Radiation Hazards in Space (Gatlinburg, Tenn.), Nov. 5-7, 1962, TID-7652, Book 2, p. 608; KINNEY, W. E.: The Nucleon Transport Code, NTC, ORNL-3610, Aug. 1964.
7. BERTINI, H. W.: Low-Energy Intranuclear Cascade Calculation. Phys. Rev., vol. 131, 1963, p. 1801.
8. DRESNER, L.: EVAP—A Fortran Program for Calculating the Evaporation of Various Particles from Excited Compound Nuclei. ORNL CF-61-12-30, Dec. 1961.
9. DOSTROVSKY, I.; FRAENKEL, Z.; and FRIEDLANDER, G.: Monte Carlo Calculations of Nuclear Evaporation Processes. III. Applications to Low-Energy Reactions. Phys. Rev., vol. 116, 1959, p. 683.
10. DOSTROVSKY, I.; FRAENKEL, Z.; and WINSBERG, L.: Monte Carlo Calculations of Nuclear Evaporation Processes. IV. Spectra of Neutrons and Charged Particles from Nuclear Reactions. Phys. Rev., vol. 118, 1960, p. 781.
11. DOSTROVSKY, I.; FRAENKEL, Z.; and ROBINOWITZ, P.: Monte Carlo Calculations of Nuclear Evaporation Processes. V. Emission of Particles Heavier than He⁴. Phys. Rev., vol. 118, 1960, p. 791.
12. COVEYOU, R. R.; SULLIVAN, J. G.; and CARTER, H. P.: The O5R Code: A General Purpose Monte Carlo Neutron Transport Code, ORNL-3622 (to be published).

13. Recommendations of the Intern. Commission on Radiological Protection, and of the Intern. Commission on Radiological Units, 1950, Nat. Bur. Std. (U.S.), Handbook 59, 1954.
14. Permissible Dose from External Sources of Ionizing Radiation. Nat. Bur. Std. (U.S.), Handbook 59, 1954.
15. Report of the RBE Committee to the Intern. Commissions on Radiological Protection and on Radiological Units and Measurements. Health Phys., vol. 9, 1963, p. 357.
16. SERBER, P. R.: The Production of High Energy Neutrons by Stripping. Phys. Rev., vol. 72, 1947, p. 1008.
17. DZHELEPOV, V. P., ET AL.: Izv. Akad. Nauk SSR. Ser. Fiz., no. 19, 1955, p. 573.
18. Protection Against Neutron Radiation up to 30 Million Electron Volts. Nat. Bur. Std. (U.S.), Handbook 63, 1957.

N65-34597

20—The Secondary-Particle Contribution to the Dose From Monoenergetic Proton Beams and the Validity of Current-to-Dose Conversion Factors¹

D. C. IRVING, R. G. ALSMILLER, JR., W. E. KINNEY, AND H. S. MORAN

Oak Ridge National Laboratory

The validity of the current-to-dose conversion factors reported in the preceding paper by Kinney and Zerby has been investigated for the case of monoenergetic protons isotropically incident on an infinite slab shield followed by a slab of tissue. The calculations were done by the Monte Carlo method using the Nucleon Transport Code (NTC) (ref. 1). We considered as shield materials carbon, aluminum, and copper in order to investigate any variation in atomic mass or number of the shield. For each shield material, we considered shield thicknesses of 10 and 30 g/cm². In all calculations, a 30-cm-thick slab of tissue followed the shield. Monoenergetic protons of energy 100 or 400 MeV were taken to be incident on the shield with the angular distribution of a current due to an isotropic flux.

The particle histories were tracked by Monte Carlo through the shield up to the shield-tissue interface. At this point the current into the tissue was divided into three parts: primaries, secondary protons, and secondary neutrons. The current-to-dose conversion factors were applied to these currents, and the average whole-body and 5-cm-depth doses were obtained in both rads and rems. To test the accuracy of these doses, the Monte Carlo calculation was continued, with the tracking of the particles through the tissue and the calculation of the actual doses in the tissue. Any particle that crossed from the tissue back into the shield was

tagged as a "backscattered" particle, and a separate account was kept of any dose resulting from such backscattered particles.

It is essential to the validity of current-to-dose conversion factors that the backscattered contribution be negligibly small. The calculation of the conversion factors was carried out in a geometry consisting of tissue alone with no shield present. Then the current leaving the shield was calculated as if no tissue were present, and the dose in the tissue was computed by means of the conversion factors. Any appreciable interaction between the shield and the tissue, in the form of particles passing from one to the other several times, would invalidate such an approach. Our calculations showed that the backscattered contribution is definitely negligible, amounting in general to less than 0.1% of the total dose in the tissue.

There is, however, one difficulty in using the current-to-dose factors. They have been calculated for only two types of incidence, normal and isotropic, whereas the actual angular distribution of the currents at the shield-tissue interface is, in general, neither normal nor isotropic. Consequently, we carried out the dose calculations twice, applying both conversion factors to the currents in the hope that this might provide upper and lower limits to the actual dose. This did not turn out to be true in all cases; however, in almost all cases the actual dose did not exceed the bounds provided by the two conversion factors by more than the statistical error of the Monte Carlo calculations. Standard deviations of 1 to 3% for the average dose and of 3 to 10% for the

¹ Research sponsored by the National Aeronautics and Space Administration (NASA Order R-104, Task No. 1) under Union Carbide Corporation's contract with the U.S. Atomic Energy Commission.

TABLE I

Doses Calculated for 400-MeV Protons Isotropically Incident on a 30-g/cm²-Thick Slab of Aluminum Followed by Tissue

	Actual dose	Calculated dose	
		With normal incidence conversion factor	With isotropic incidence conversion factor
Average dose (rads)			
Primary protons.....	0. 300×10 ⁻⁷	0. 235×10 ⁻⁷	0. 326×10 ⁻⁷
Secondary protons.....	. 444×10 ⁻⁸	. 416×10 ⁻⁸	. 447×10 ⁻⁸
Secondary neutrons.....	. 164×10 ⁻⁸	. 126×10 ⁻⁸	. 185×10 ⁻⁸
Total.....	. 361×10 ⁻⁷	. 289×10 ⁻⁷	. 389×10 ⁻⁷
Average dose (rems)			
Primary protons.....	0. 452×10 ⁻⁷	0. 316×10 ⁻⁷	0. 446×10 ⁻⁷
Secondary protons.....	. 614×10 ⁻⁸	. 543×10 ⁻⁸	. 594×10 ⁻⁸
Secondary neutrons.....	. 793×10 ⁻⁸	. 616×10 ⁻⁸	. 832×10 ⁻⁸
Total.....	. 592×10 ⁻⁷	. 432×10 ⁻⁷	. 588×10 ⁻⁷
5-cm-depth dose (rads)			
Primary protons.....	0. 338×10 ⁻⁷	0. 214×10 ⁻⁷	0. 409×10 ⁻⁷
Secondary protons.....	. 745×10 ⁻⁸	. 562×10 ⁻⁸	. 791×10 ⁻⁸
Secondary neutrons.....	. 201×10 ⁻⁸	. 140×10 ⁻⁸	. 230×10 ⁻⁸
Total.....	. 433×10 ⁻⁷	. 284×10 ⁻⁷	. 512×10 ⁻⁷
5-cm-depth dose (rems)			
Primary protons.....	0. 517×10 ⁻⁷	0. 314×10 ⁻⁷	0. 557×10 ⁻⁷
Secondary protons.....	. 104×10 ⁻⁷	. 732×10 ⁻⁸	. 104×10 ⁻⁷
Secondary neutrons.....	. 109×10 ⁻⁷	. 746×10 ⁻⁸	. 108×10 ⁻⁷
Total.....	. 730×10 ⁻⁷	. 462×10 ⁻⁷	. 768×10 ⁻⁷

doses at a 5-cm depth were obtained in these calculations.

Typical results for 400-MeV protons are shown in table I, which gives the average doses and the 5-cm-depth doses for incidence on a 30 g/cm² slab of aluminum. The first column gives the dose computed by tracking the particle histories through the tissue, while the second and third columns give the dose computed from the current-to-dose conversion factors. The headings at the left identify the current from which the dose was derived; i.e., lines marked "primary protons" include the doses

from primaries and from secondaries arising in the tissue from primaries, while the lines marked "secondary protons" are the doses from secondary protons born in the shield and entering the tissue. Similarly, table II shows the results for 100-MeV protons incident on 10 g/cm² of carbon. In these cases the primaries were stopped in the shield, and only secondary neutrons contributed to the dose. As may be seen from the tables, the current-to-dose conversions generally provide a fair estimate of the actual dose, and in most, but not all, cases, the actual dose is bracketed by the two esti-

TABLE II

Doses Calculated for 100-MeV Protons Isotropically Incident on a 10-g/cm²-Thick Slab of Carbon Followed by Tissue

	Actual dose	Dose calculated assuming	
		Normal incidence conversion	Isotropic incidence conversion
Average dose (rads)			
Primary protons.....	0	0	0
Secondary protons.....	0	0	0
Secondary neutrons.....	0. 109×10 ⁻⁹	0. 100×10 ⁻⁹	0. 126×10 ⁻⁹
Total.....	. 109×10 ⁻⁹	. 100×10 ⁻⁹	. 126×10 ⁻⁹
Average dose (rems)			
Primary protons.....	0	0	0
Secondary protons.....	0	0	0
Secondary neutrons.....	0. 784×10 ⁻⁹	0. 615×10 ⁻⁹	0. 752×10 ⁻⁹
Total.....	. 784×10 ⁻⁹	. 615×10 ⁻⁹	. 752×10 ⁻⁹
5-cm-depth dose (rads)			
Primary protons.....	0	0	0
Secondary protons.....	0	0	0
Secondary neutrons.....	0. 152×10 ⁻⁹	0. 135×10 ⁻⁹	0. 188×10 ⁻⁹
Total.....	. 152×10 ⁻⁹	. 135×10 ⁻⁹	. 188×10 ⁻⁹
5-cm-depth dose (rems)			
Primary protons.....	0	0	0
Secondary protons.....	0	0	0
Secondary neutrons.....	0. 105×10 ⁻⁸	0. 780×10 ⁻⁹	0. 105×10 ⁻⁸
Total.....	. 105×10 ⁻⁸	. 780×10 ⁻⁹	. 105×10 ⁻⁸

mates. In the cases considered, we found no significant variation with thickness of the shield or with atomic mass of the shield material. In no case did a current-to-dose conversion disagree with the actual dose by more than a factor of 2.

A secondary objective of our calculations was to determine the relative contribution of primary and secondary particles to the total dose and to estimate the error involved in a calculation which neglected secondary particles. In figures 1 and 2 respectively are shown the dose in rads and in rems as a function of depth

in tissue resulting from 400-MeV protons incident on 30 g/cm² of aluminum. The dose has been divided into five contributions:

1. The dose from ionization of primaries.
2. The dose from secondaries produced in the tissue by the primary protons.
3. The dose from secondary protons produced in the shield.
4. The dose from secondary neutrons produced in the shield.
5. The backscattered dose from particles which crossed from the tissue to the shield and back again.

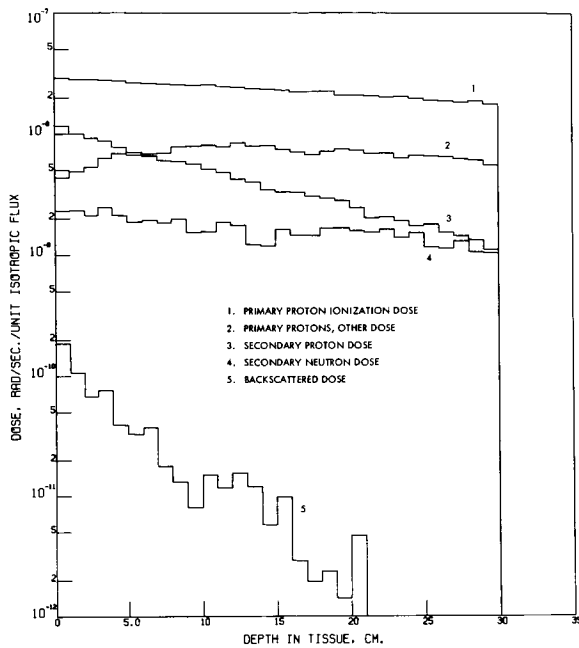


FIGURE 1.—Dose (in rads) for the case of 400-MeV protons isotropically incident on a 30-g/cm²-thick slab of aluminum followed by tissue.

It is readily evident from the figures that the backscatter is negligible, being a factor of 10 or more smaller than any other contribution. Ionization of the primary protons is the most important factor, and the secondaries produced in the tissue are next in importance. This is significant since one could account for tissue secondaries by means of current-to-dose conversion in a calculation that would otherwise neglect secondaries. The tissue secondaries certainly cannot be neglected in the rem dose where their contribution is

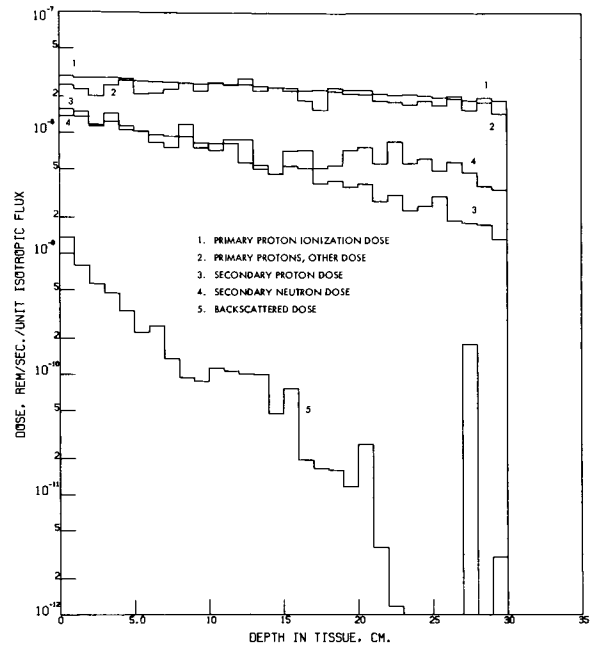


FIGURE 2.—Dose (in rems) for the case of 400-MeV protons isotropically incident on a 30-g/cm²-thick slab of aluminum followed by tissue.

approximately equal to that of the primary ionization. The dose from secondaries produced in the shields is of less importance. In fact, from table I, we can see that the "primary protons" (which here includes both ionization and tissue secondaries) constitute about 80% of the total rad dose and 70 to 75% of the rem dose, and that a calculation which had considered only the transport of primaries through the shield and used the larger of the current-to-dose conversions would have obtained more than 90% of the total rad dose.

REFERENCE

1. KINNEY, W. E.: The Nucleon Transport Code, NTC, ORNL-3610, 1964.

21—The Validity of the Straightahead Approximation in Space Vehicle Shielding Studies¹

R. G. ALSMILLER, JR., D. C. IRVING, W. E. KINNEY, and H. S. MORAN

Oak Ridge National Laboratory

Many of the shielding studies for manned space vehicles have been carried out in what is usually called the "straightahead approximation" (ref. 1). This approximation greatly simplifies the computation, but its use necessarily introduces inaccuracies. To test the validity of the approximation, calculations have been carried out and compared with results obtained with the angular distribution of the secondary particles properly taken into account.

To define the approximation as it is used here, we note that, in general,

$$F_{ij} = F_{ij}(E', E, \vec{\Omega}' \cdot \vec{\Omega}) \quad (1)$$

where F_{ij} = the number of particles of type i per unit energy range per unit solid angle possessing kinetic energy E and direction given by the unit vector $\vec{\Omega}$ after a particle of type j with kinetic energy E' and direction $\vec{\Omega}'$ undergoes either an elastic or a nonelastic collision. In the straightahead approximation, the quantity F_{ij} is approximated by

$$F_{ij}(E', E, \vec{\Omega}' \cdot \vec{\Omega}) = f_{ij}(E', E) \frac{\delta(\vec{\Omega}' \cdot \vec{\Omega} - 1)}{2\pi} \quad (2)$$

where

$$f_{ij}(E', E) = \int_0^\pi \int_0^{2\pi} F_{ij}(E', E, \vec{\Omega}' \cdot \vec{\Omega}) d\Omega \quad (3)$$

The delta function in equation (2) ensures that all emergent particles have the same direction as the incident particle, and equation (3) follows from integrating equation (2) over all solid angles. It must be carefully noted that,

¹ Research sponsored by the National Aeronautics and Space Administration (NASA Order R-104, Task No. 1) under Union Carbide Corporation's contract with the U.S. Atomic Energy Commission.

as defined here, the straightahead approximation applies to both elastic and nonelastic collisions. Furthermore, all emergent particles are assumed to go in the forward direction; that is, no attempt is made to discriminate against those particles which are emitted in the backward quadrant.

To ensure that any differences which exist between the approximate and the exact calculation are due to the approximation being considered and not to differences in nuclear data, the straightahead calculations presented here have been carried out using the Nucleon Transport Code (NTC) with which the exact calculations were done (ref. 2). The only change made in the code was in the angular distribution of the scattered particles.

In figure 1 the results of the approximate and exact calculations are compared for the case of a 400-MeV proton beam isotropically incident on a slab of aluminum followed by a 30-cm-thick slab of tissue. The solid curves are the results of the exact calculations (see the preceding paper by Irving *et al.*), while the plotted points are the results of the approximate calculations. The primary proton, secondary proton, and secondary neutron fluxes incident on the tissue are defined to be those fluxes which would emerge from the aluminum if the tissue were absent. The dose as a function of depth in the tissue is broken into five contributions:

1. The primary proton ionization dose.
2. The dose from secondary particles produced by primary protons in the tissue.
3. The secondary proton dose.
4. The secondary neutron dose.
5. The backscattered dose; that is, the dose from all particles which are produced in the tissue and cross into the aluminum.

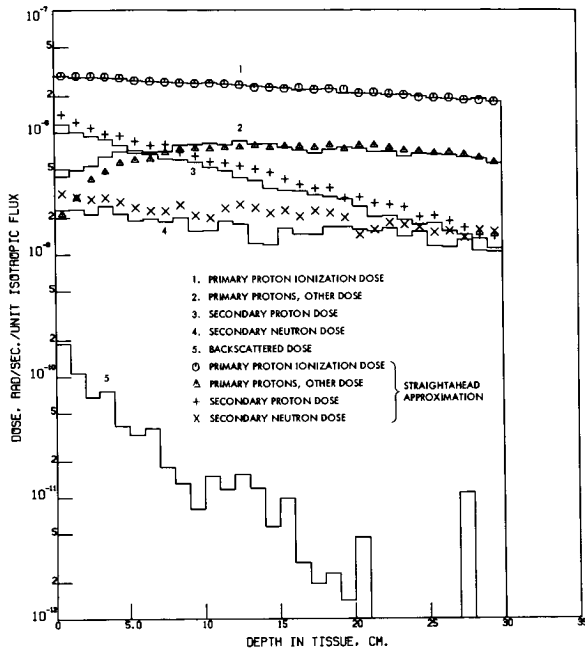


FIGURE 1.—Comparison of straightahead dose results with exact results (in rads) for the case of 400-MeV protons isotropically incident on a 30-g/cm²-thick slab of aluminum followed by tissue.

Since the primary protons travel in a straight line (multiple Coulomb scattering was not included in the calculation), the exact and approximate calculations are the same for the primary proton ionization dose. The approximate secondary proton dose and secondary neutron dose are slightly too large, particularly in the first few centimeters of tissue, while the approximate primary proton secondary dose is too small in the first few centimeters. There is, of course, no approximate backscattered dose.

The same calculations are compared again in figure 2, but this time the dose is given in rems rather than rads. The rem calculation was carried out in the same manner as that described in a preceding paper by W. E. Kinney and C. D. Zerby. The agreement between the exact and approximate calculations is roughly the same as in figure 1.

In figure 3, the results for 100-MeV protons isotropically incident on a 10-g/cm² slab of aluminum followed by a 30-cm-thick slab of tissue are given. In this case, the primary protons do not penetrate the shield, and so we have exact doses only from secondary protons,

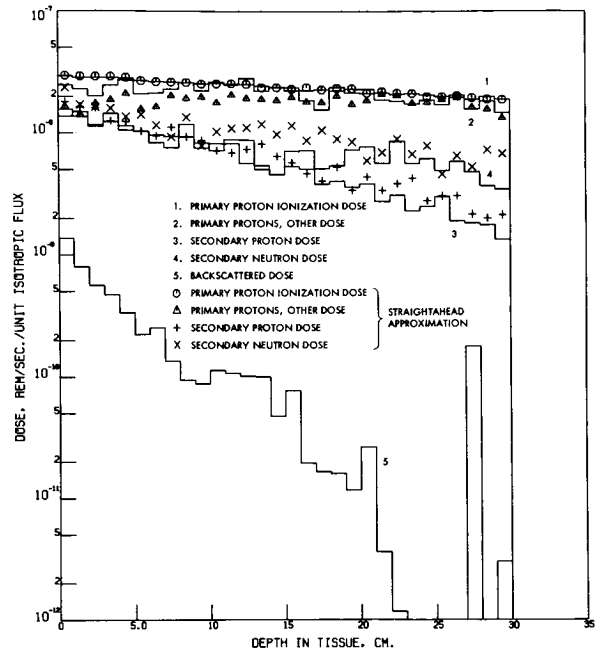


FIGURE 2.—Comparison of straightahead dose results with exact results (in rems) for the case of 400-MeV protons isotropically incident on a 30-g/cm²-thick slab of aluminum followed by tissue.

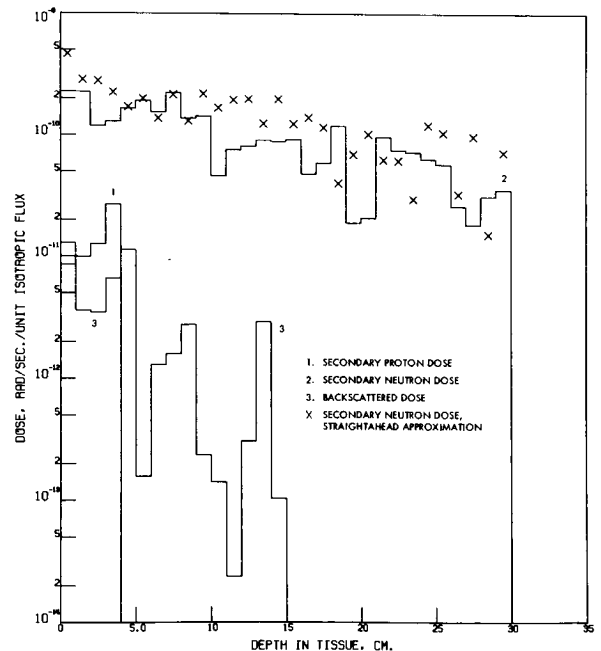


FIGURE 3.—Comparison of straightahead dose results with exact results for the case of 100-MeV protons isotropically incident on a 10-g/cm²-thick slab of aluminum followed by tissue.

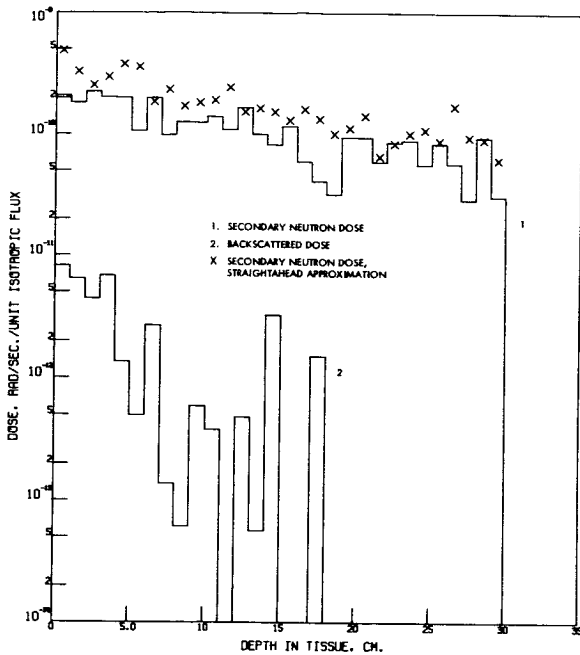


FIGURE 4.—Comparison of straightahead dose results with exact results for the case of 100-MeV protons isotropically incident on a 10-g/cm²-thick slab of carbon followed by tissue.

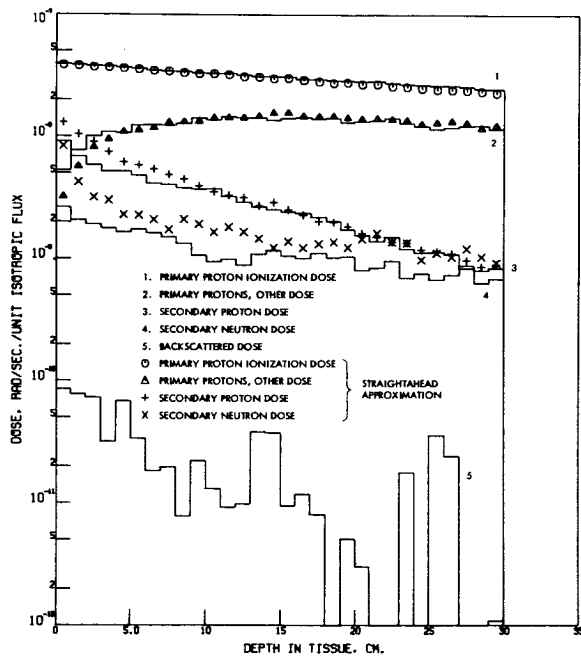


FIGURE 5.—Comparison of straightahead dose results with exact results for the case of 400-MeV protons isotropically incident on a 10-g/cm²-thick slab of copper followed by tissue.

secondary neutrons, and backscattered particles. In fact, the approximate secondary proton dose is zero within the statistics; therefore, only the secondary neutron doses can actually be compared. The approximate secondary neutron dose is somewhat too large in this case, as it was in figure 1.

Figures 4 and 5 give results for two additional cases: 100-MeV protons incident isotropically on 10 g/cm² of carbon followed by tissue, and 400-MeV protons incident isotropically on 10 g/cm² of copper followed by tissue. These results are not appreciably different from those obtained in the previous cases.

In the cases presented here, the straightahead approximation appears to be quite good. The approximation usually overestimates the dose and appears to have approximately the same validity for elements between carbon and copper. One must, however, avoid drawing very general conclusions on the basis of so few computations. It must be remembered that the low-energy region (<100 MeV) is still to be treated and may be important when one considers typical flare spectra.

In the results just discussed, the dose in tissue was calculated directly. An alternate procedure is to calculate the straightahead approximation current at the shield tissue interface and apply current-to-dose conversion factors to this current. Because of the approximation, one has no information about the angular distribution of particles at the interface, but one may carry through the computation assuming either isotropic or normal incidence, since conversion factors for these cases are available (see the preceding paper by Kinney and Zerby). The results of this procedure are shown in table I for the case of a 400-MeV proton beam isotropically incident on a 30-g/cm² slab of tissue followed by a 30-cm-thick slab of tissue.

The first column in the table gives the doses obtained by exact calculation, while columns 2 and 3 give the approximate doses obtained by applying the conversion factors. The isotropic conversion gives an overestimate of both the 5-cm-depth dose and the average dose. The normal conversion underestimates the primary proton and total dose, but overestimates the secondary proton and secondary

TABLE I

Doses Calculated for 400-MeV Protons Isotropically Incident on a 30-g/cm²-Thick Slab of Aluminum Followed by Tissue

	Actual dose	Dose calculated	
		With normal incidence conversion factor	With isotropic incidence conversion factor
Average dose (rads)			
Primary protons.....	0.300×10^{-7}	0.236×10^{-7}	0.327×10^{-7}
Secondary protons.....	$.444 \times 10^{-8}$	$.484 \times 10^{-8}$	$.518 \times 10^{-8}$
Secondary neutrons.....	$.164 \times 10^{-8}$	$.190 \times 10^{-8}$	$.264 \times 10^{-8}$
Total.....	$.361 \times 10^{-7}$	$.303 \times 10^{-7}$	$.405 \times 10^{-7}$
Average dose (rems)			
Primary protons.....	0.452×10^{-7}	0.317×10^{-7}	0.446×10^{-7}
Secondary protons.....	$.614 \times 10^{-8}$	$.633 \times 10^{-8}$	$.689 \times 10^{-8}$
Secondary neutrons.....	$.793 \times 10^{-8}$	$.966 \times 10^{-8}$	$.124 \times 10^{-7}$
Total.....	$.592 \times 10^{-7}$	$.477 \times 10^{-7}$	$.640 \times 10^{-7}$
5-cm-depth dose (rads)			
Primary protons.....	0.338×10^{-7}	0.217×10^{-7}	0.412×10^{-7}
Secondary protons.....	$.745 \times 10^{-8}$	$.641 \times 10^{-8}$	$.905 \times 10^{-8}$
Secondary neutrons.....	$.201 \times 10^{-8}$	$.222 \times 10^{-8}$	$.346 \times 10^{-8}$
Total.....	$.433 \times 10^{-7}$	$.303 \times 10^{-7}$	$.537 \times 10^{-7}$
5-cm-depth dose (rems)			
Primary protons.....	0.517×10^{-7}	0.318×10^{-7}	0.561×10^{-7}
Secondary protons.....	$.104 \times 10^{-7}$	$.835 \times 10^{-8}$	$.118 \times 10^{-7}$
Secondary neutrons.....	$.109 \times 10^{-7}$	$.121 \times 10^{-7}$	$.167 \times 10^{-7}$
Total.....	$.730 \times 10^{-7}$	$.523 \times 10^{-7}$	$.846 \times 10^{-7}$

neutron dose. In considering these results, it must be remembered that, since the calculations were carried out using Monte Carlo methods, there are statistical errors associated with each of the numbers in the table. Roughly speaking, a standard deviation of about 10% is to be associated with each entry.

Results are given in table II for 100-MeV protons isotropically incident on 10 g/cm² of aluminum followed by tissue. In this case, essentially the only contribution comes from secondary neutrons, and both the normal and isotropic conversion overestimates this contribution.

TABLE II

Doses Calculated for 100-MeV Protons Isotropically Incident on a 10-g/cm²-Thick Slab of Aluminum Followed by Tissue

	Actual dose	Dose calculated	
		With normal incidence conversion factor	With isotropic incidence conversion factor
Average dose (rads)			
Primary protons.....	0	0	0
Secondary protons.....	0.193×10^{-11}	0	0
Secondary neutrons.....	$.977 \times 10^{-10}$	0.169×10^{-9}	0.195×10^{-9}
Total.....	$.996 \times 10^{-10}$	$.169 \times 10^{-9}$	$.195 \times 10^{-9}$
Average dose (rems)			
Primary protons.....	0	0	0
Secondary protons.....	0.238×10^{-11}	0	0
Secondary neutrons.....	$.735 \times 10^{-9}$	0.103×10^{-8}	0.117×10^{-8}
Total.....	$.738 \times 10^{-9}$	$.103 \times 10^{-8}$	$.117 \times 10^{-8}$
5-cm-depth dose (rads)			
Primary protons.....	0	0	0
Secondary protons.....	0	0	0
Secondary neutrons.....	0.178×10^{-9}	0.235×10^{-9}	0.309×10^{-9}
Total.....	$.178 \times 10^{-9}$	$.235 \times 10^{-9}$	$.309 \times 10^{-9}$
5-cm-depth dose (rems)			
Primary protons.....	0	0	0
Secondary protons.....	0	0	0
Secondary neutrons.....	0.129×10^{-8}	0.139×10^{-8}	0.173×10^{-8}
Total.....	$.129 \times 10^{-8}$	$.139 \times 10^{-8}$	$.173 \times 10^{-8}$

REFERENCES

1. SHEN, S. P.: Astronaut. Acta, vol. 9, no. 28, 1963 (includes an extensive list of references).
2. KINNEY, W. E.: The Nucleon Transport Code. NTC, ORNL-3610, 1964.

22—Cosmic-Ray Shower Production in Manned Space Vehicles—Copper

K. A. MORE and O. L. TIFFANY

The Bendix Corporation

N65-34599

In previous work (refs. 1 and 2), we calculated the generation of cosmic ray showers in an aluminum-walled spacecraft by a three-dimensional Monte Carlo technique using intranuclear cascade data furnished by Friedlander (private communication). This work has been extended to the case of a spacecraft composed of copper in order to determine the effect of Z on shielding. As before, data on neutron and pion production are of particular interest, since only a model including shower production can give an estimate of these products. The proton results are compared with the simpler calculations using ionization only or ionization and exponential absorption.

authr

INTRODUCTION

In the First Symposium on Protection Against Radiation Hazards in Space, we presented a comparison of computed radiation dose inside an aluminum-walled spacecraft for three computational methods. The first method was Monte Carlo, which accounts for cosmic ray shower production; the second was proton attenuation by ionization losses, which assumes no nuclear collisions; and the third was proton attenuation by both ionization losses and exponential absorption due to nuclear collisions, but no shower production.

The purpose of the comparison was to determine whether calculation methods that are simpler and more amenable to complex geometries than Monte Carlo would give nearly the same results as a Monte Carlo calculation. The results showed that for thin spacecraft (less than about 10 cm thick) both approximations, attenuation by ionization losses and attenuation by ionization losses and exponential attenuation, gave nearly the same results as Monte Carlo and bounded the Monte Carlo results (the ionization loss was higher but within 10 percent of the Monte Carlo, and the ionization loss plus exponential attenuation was lower but within 20 percent of the Monte Carlo results for spacecraft walls less than 5 cm thick). Even for thick spacecraft (up to

50 cm thick), the approximate methods always bounded the Monte Carlo and gave results that were within a factor of 3 of the Monte Carlo results.

We have repeated the Monte Carlo calculations for a copper-walled spacecraft and made similar comparisons with the same approximate calculation methods. Copper was chosen for the spacecraft walls since copper was the closest material to steel for which intranuclear cascade data were available (ref. 3). The major purpose of this comparison was to determine the effect of increased cascade secondary particle production in higher atomic weight material.

The reasons for the choice of input proton spectra and the details of the method of calculation are reported in our previous paper (ref. 2; paper E-2, in figs. 4, 5, 8, and 9, the points plotted at 55 cm should be plotted at 85 cm). These were unchanged to permit direct comparison between the previous Monte Carlo results for aluminum and the results presented here for copper. The input proton spectra shown in figure 1 are for yearly averages of the proton flux near the earth but outside the proton belts during solar maximum and solar minimum.

The Monte Carlo calculation is the same as was previously used for aluminum. The code

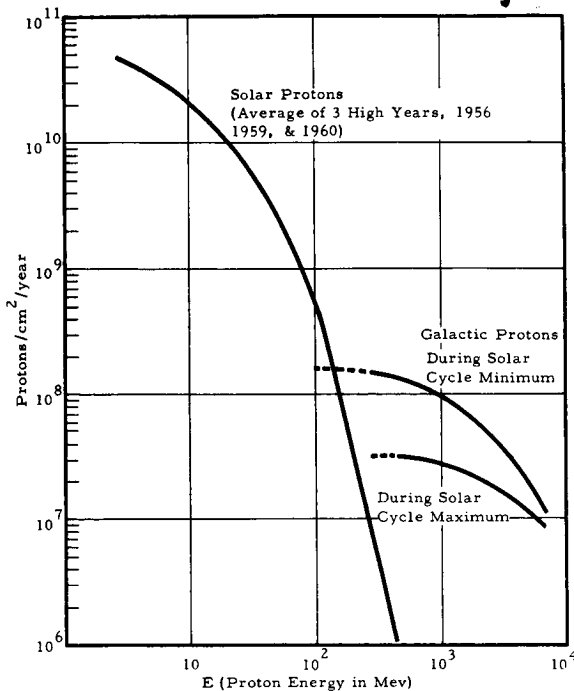


FIGURE 1.—Omnidirectional integrated proton flux—number of protons having an energy greater than E .

was written for a one-material, spherical-shell spacecraft. The dose in the interior of the spacecraft was computed by assuming that the interior was homogeneously filled with tissue and by determining the amount of energy removed from the particle beams as they traversed the spacecraft interior. The rate of energy removed from the primary and secondary protons and evaporation neutrons was based on the values computed by Gibson (ref. 4). These energy removal rates include both ionization and nuclear collision mechanisms. The energy removed by secondary pions used ionization losses in plexiglas (assumed to be tissue equivalent). Since the energy removed from the particle beam is not necessarily deposited in the tissue, our results give only an approximate value for the absorbed dose. In order to avoid any confusion on this subject, we have labeled our results as energy removal dose (in units of 100 ergs/gm of tissue) and we define the energy removal dose as the energy removed from a beam of particles by a gram of tissue.

Two spacecraft models were used in the calculation. The first was a spherical shell spacecraft with inside dimensions comparable to

those of the Apollo command module (inside diameter: 9 feet). The mass of tissue was taken to be 225 kg, which is roughly equivalent to the weight of three astronauts. This gives a density of 0.021 gm/cm³ for the homogeneous tissue. Since this tissue density is thin and does not fully account for self shielding by the astronaut and partial shielding of one astronaut by the other two astronauts, a second model was used which consisted of a spherical copper shell surrounding the same mass of tissue that had unit density. This gave an inside radius of 37.33 cm for the second model. These two models can be assumed to bound the self shielding effects of the astronauts. As will be shown, both models give the same qualitative results.

All three methods of computation used the multi-group approximation. The incident proton spectra were divided into 18 energy groups for the thin tissue model calculations and into 10 energy groups for the unit density tissue model. The incident energies for these groups ranged from 10 MeV to 4000 MeV. The spacecraft walls were considered to be solid copper and the wall thicknesses were varied from 0.6 cm to 13.5 cm in steps that corresponded to the equivalent thicknesses of aluminum in gm/cm² used in our previous calculation.

DISCUSSION OF RESULTS

The results are discussed in two parts: (1) the shielding properties of copper and a comparison of the different approximations used for computing these shielding properties; and (2) a comparison of the Monte Carlo results for copper with those for aluminum.

The computed dose as a function of spacecraft thickness inside the two spacecraft models during solar maximum and solar minimum are shown in figures 2 through 5. Two general conclusions, which also were shown by our aluminum calculations, can be drawn: (1) for very thin spacecraft, the computed energy removal dose is nearly the same whether calculated by proton attenuation by ionization loss (curves referenced as ionization loss in the figures) or by Monte Carlo; and (2) for moderately thick-walled spacecraft, the energy removal dose for missions longer than a year was predicted to be higher during periods of solar minimum than

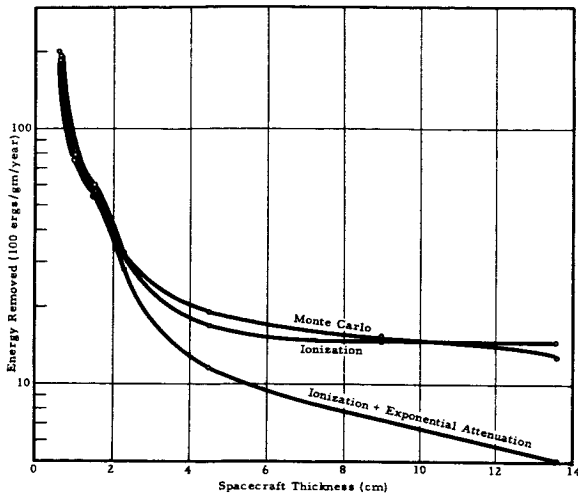


FIGURE 2.—Comparison of Monte Carlo and ionization results for copper-walled spacecraft during solar maximum, thin tissue ($\rho = .021$).

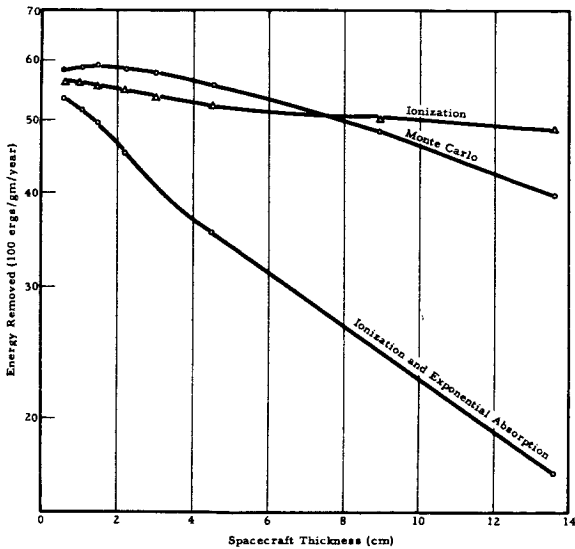


FIGURE 3.—Comparison of Monte Carlo and ionization results for copper-walled spacecraft during solar minimum, thin tissue ($\rho = .021$).

solar maximum. A third conclusion drawn from our aluminum results was that the ionization loss calculations always computed a higher dose than the Monte Carlo calculations. Our copper results do not show this same conclusion.

The first conclusion—that ionization loss and Monte Carlo should give nearly equal results for thin spacecraft—was expected because the probability of a nuclear collision in thin space-

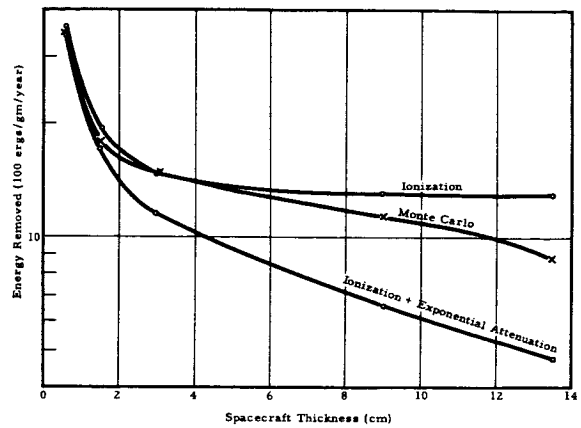


FIGURE 4.—Comparison of Monte Carlo and ionization results for copper-walled spacecraft during solar maximum, thick tissue ($\rho = 1.0$).

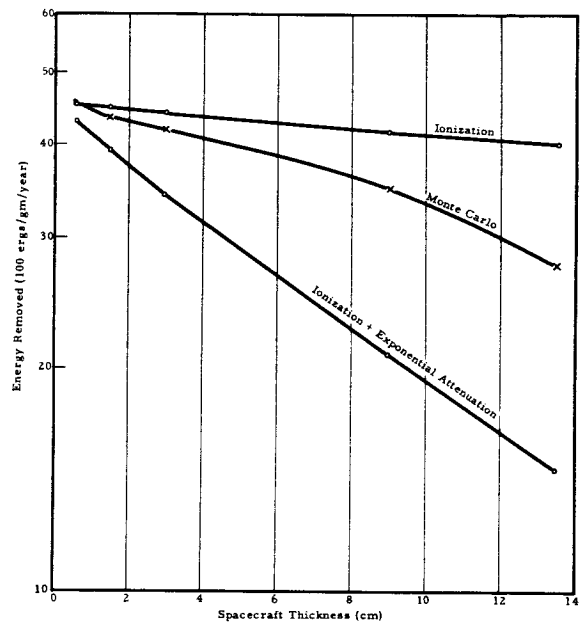


FIGURE 5.—Comparison of Monte Carlo and ionization results for copper-walled spacecraft during solar minimum, thick tissue ($\rho = 1.0$).

craft is small; thus, the dominant shielding mechanism is ionization loss. The second conclusion, that the yearly dose for moderately thick spacecraft would be lower during solar maximum than solar minimum, can be explained by the Forbush decrease argument given in our previous paper. That is, there are fewer galactic protons during solar maximum than solar minimum (see fig. 1) because of the Forbush decreases, and this causes a lower dose

during solar maximum inside those spacecraft which are sufficiently thick (greater than 1.5 cm of copper or 5 cm of aluminum—approximately 13 gm/cm²) to remove most of the dose from solar flare protons.

The major reason for performing Monte Carlo calculations on copper was to determine whether the increase in secondary particle production with atomic number caused an increase or decrease in the computed energy removal dose. In our aluminum calculations, the effect of secondary particle production caused a decrease in the computed energy removal dose compared to the dose computed by proton attenuation by ionization loss alone. The effects of secondary particle production on the computed dose yield some mechanisms that increase the dose and some that decrease the dose. Most of the secondary particles are of low energy, and the dose from these low-energy secondaries may be greater than if the original particle had passed through the tissue. Also, because of the energy difference between the parent particle and the secondary particles, the parent and secondaries fall on different regions of the energy removal curve. Because of the nature of this curve, a high-energy proton may lose more energy in tissue than low energy secondaries. However, this effect may be compensated for by the larger number of secondaries. Some of the secondaries are protons which, because of their lower energy, are more readily absorbed in the spacecraft walls, which reduces the dose. However, some of the secondaries are neutrons and pions, which produce a lower dose per unit path length than protons, but, because neutrons and pions are more penetrating than protons, they will cause a dose increase inside thick spacecraft.

Thus, with all of these mechanisms varying the energy removal dose, the only way to determine whether Monte Carlo results would be higher or lower than ionization results was to carry out the calculations.

The comparison of the Monte Carlo results with the ionization loss and ionization loss plus exponential attenuation can be seen in figures 2 through 5. In all cases, the ionization loss approximation gave nearly the same results as the Monte Carlo calculation even for thick

spacecraft. This is a major difference between the equivalent results for aluminum where the Monte Carlo results were always less than the ionization loss calculations, and the two results were comparable only for thin spacecraft. The relatively higher doses predicted by the Monte Carlo computations in copper are attributed to the increase in secondary particle production.

A part of the results of a Monte Carlo calculation is the neutron and pion dose. As with aluminum, the pion dose was about two orders

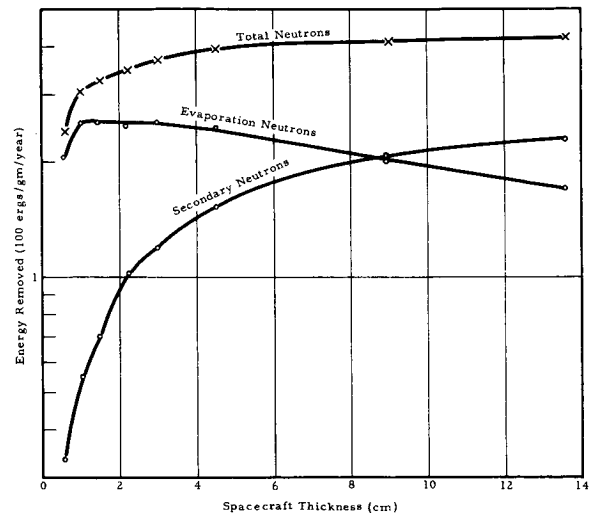


FIGURE 6.—Neutron energy removal dose inside copper-walled spacecraft during solar maximum, thin tissue ($\rho = .021$).

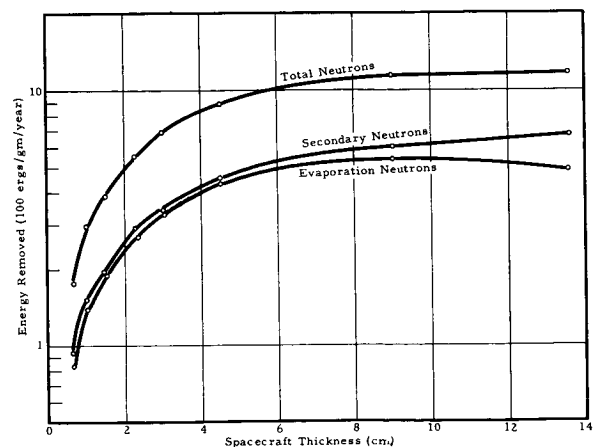


FIGURE 7.—Neutron energy removal dose inside copper-walled spacecraft during solar minimum, thin tissue ($\rho = .021$).

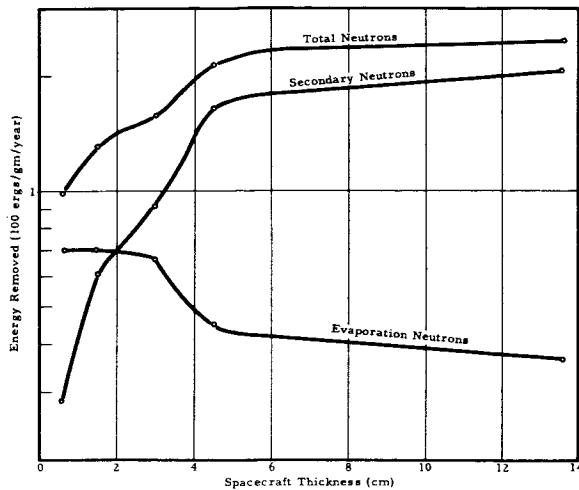


FIGURE 8.—Neutron energy removal dose inside copper-walled spacecraft during solar maximum, unit tissue ($\rho=1.0$).

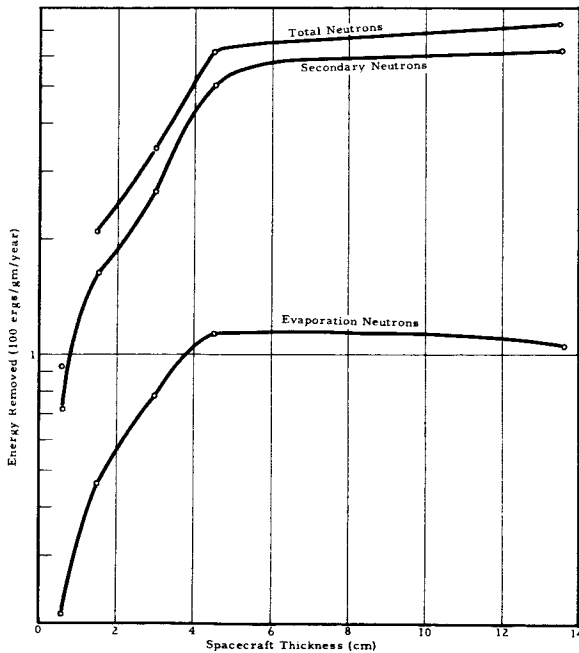


FIGURE 9.—Neutron energy removal dose inside copper-walled spacecraft during solar minimum, unit tissue ($\rho=1.0$).

of magnitude below that of the total dose and is therefore of little interest. The neutron energy removal dose was an appreciable fraction (15 to 30 percent) of the total for all but the thin spacecraft and was about twice the amount calculated for aluminum having the same thick-

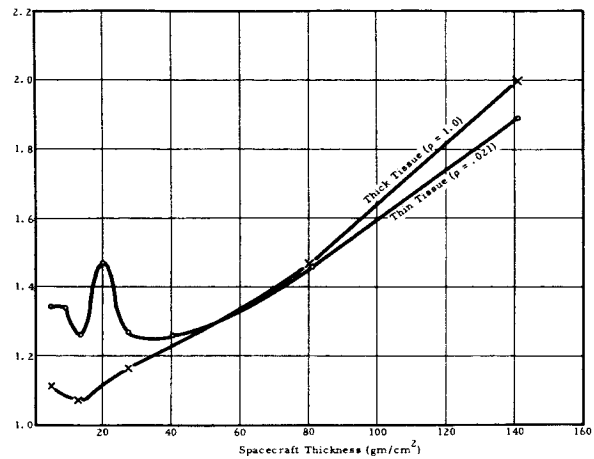


FIGURE 10.—Ratio of total dose inside copper-walled to inside aluminum-walled spacecraft—Monte Carlo results for solar maximum.

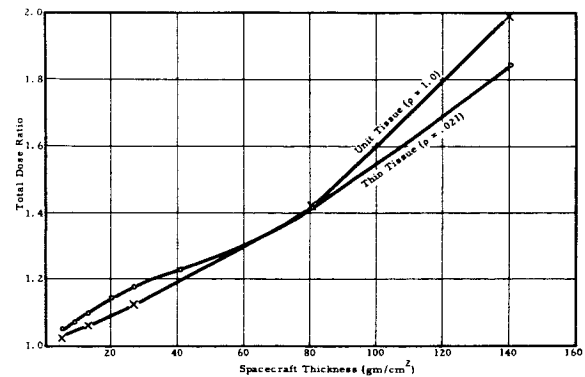


FIGURE 11.—Ratio of total dose inside copper-walled to inside aluminum-walled spacecraft—Monte Carlo results for solar minimum.

ness in gm/cm². The neutron energy removal doses for the different spacecraft models are shown in figures 6 through 9.

The second part of our results was the comparison between the aluminum and copper Monte Carlo calculations. This comparison is shown in figures 10 and 11 where the ratio of the total energy removal dose for copper-walled to aluminum-walled spacecraft is plotted against spacecraft thickness (in units of gm/cm²). For spacecraft thicker than 40 gm/cm², the ratios are the same for solar maximum and solar minimum input spectra and are nearly the same for either the thin tissue or thick tissue models. As can be seen, this ratio predicts twice the dose behind a thick copper-walled spacecraft com-

pared to an aluminum-walled spacecraft. We speculate that the oscillation in the thin tissue model for thin spacecraft and solar maximum input spectra is produced by the different copper and aluminum thicknesses required to cause low energy solar flare protons to have their Bragg peak in the tissue. We attribute the lack of this oscillation in the thick tissue model to

calculating too few points to show it. These two figures also show that, for shields thicker than 40 gm/cm^2 , the ratios are the same for solar maximum and solar minimum input spectra. For shield design purposes, these ratios can be used to estimate the increase in dose that can be expected if copper (or steel) is used instead of aluminum.

REFERENCES

1. MORE, K. A.; TIFFANY, O. L.; and WAINIO, K.: Cosmic Ray Shower Production in Manned Space Vehicles. Medical and Biological Problems of Space Flight, ch. 8. Academic Press, Inc. (New York), 1963.
2. MORE, K. A.; and TIFFANY, O. L.: Comparison of Monte Carlo and Ionization Calculations for Spacecraft Shielding. Proc. Sym. on Protection Against Radiation Hazards in Space. Paper E-2, TID-7652, Atomic Energy Commission, 1962, pp. 682-697.
3. METROPOLIS, J., ET AL.: Summary Data. Phys. Rev., Nos. 110, 185, and 204, 1958.
4. GIBSON, W. A.: Energy Removed from Primary Proton and Neutron Beams by Tissue. ORNL-3260, Oak Ridge National Laboratory, 1962.

N65-34600

23—The Application of the Liouville Theorem to Magnetic Shielding Problems

A. D. PRESCOTT, E. W. URBAN, and R. D. SHELTON

Marshall Space Flight Center, NASA

The approach to magnetic shielding, with few exceptions, may be divided into two parts, one dealing with the experimental problem of establishing appropriate magnetic fields with large currents flowing in superconductors (refs. 1 and 2) and the other dealing with the theoretical problems of charged particle motion in electromagnetic fields (refs. 2 to 6). For our purposes here, we will assume that the distribution of particles and fields is time independent and axially symmetric about a localized current distribution in the neighborhood of the coordinate origin, that the field is unconfined (that is, extending to infinity), that there are no collisions between particles, and that the particle distribution at large distances is spatially uniform and isotropic. In the space composed of the six coordinates of position and velocity, the particle distribution is described by a density function $N(\vec{r}, \vec{v})$ which, by the Liouville theorem, is constant along a particle trajectory in this space. In a form more common to cosmic ray applications, the Liouville theorem requires that the directional flux be constant in the direction of and along a particle trajectory. This latter statement of the theorem is possible because the speed of a charged particle is constant in a magnetostatic field.

Let us suppose that a particle of velocity \vec{v} passes through a point P located by the position vector \vec{r} and finally goes to infinity, where by definition the flux is uniform, isotropic, and normalized to unity. By virtue of the Liouville theorem,

$$\Phi(\vec{r}, \vec{v}) = N(\vec{r}, \vec{v})v = \frac{1}{4\pi} \quad (1)$$

where we have equated the directional flux at

\vec{r} along the particle trajectory to the value of the directional flux assigned to large distances. By integrating $\Phi(\vec{r}, \vec{v})$ over all directions of \vec{v} associated with particle orbits connecting to infinity, the total flux is expressed as

$$\Phi(\vec{r}) = \left(\frac{1}{4\pi}\right) \iint d\omega \quad (2)$$

where $d\omega$ is the element of solid angle to be defined later.

To determine the directions of \vec{v} associated with particle trajectories connecting to infinity, we write in spherical coordinates the relativistic Lagrangian for a charged particle in a magnetostatic field with rotational symmetry about the z axis. Because of the symmetry, the azimuthal angle, ϕ , is cyclic, and its conjugate angular momentum, as determined from the Euler-Lagrange equations, is a constant of the motion expressible in terms of two position coordinates r and θ and two velocity coordinates v and α , defined in figure 1. The equation for the conservation of the angular momentum conjugate to ϕ may be viewed as an equation of constraint involving four of the six variables of (\vec{r}, \vec{v}) space and may be used to define the solid angle for the integration of equation (2).

Assuming that the axially symmetric magnetostatic field arises from a dipole situated at the origin and oriented along the z axis, we follow the historical development of Störmer and write the equation for the conservation of the angular momentum conjugate to ϕ as

$$-Q + \frac{qA_\phi(r, \theta)}{p} + \frac{2\bar{\gamma}}{\rho \sin \theta} = 0 \quad (3)$$

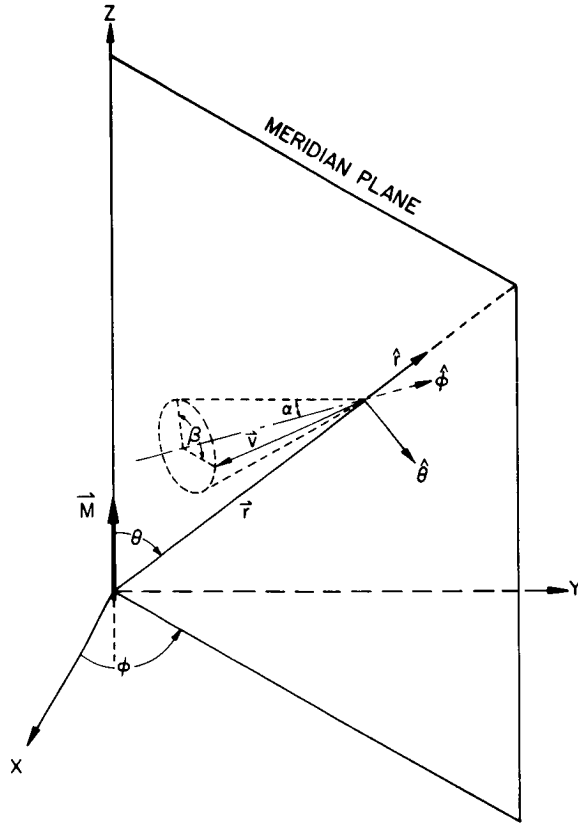


FIGURE 1.—Reference coordinate system.

or

$$-Q + \frac{\sin \theta}{\rho^2} + \frac{2\bar{\gamma}}{\rho \sin \theta} = 0 \quad (4)$$

where we have defined the Störmer parameters:

$$Q \equiv -\frac{v_\phi}{v} = -\hat{v} \cdot \hat{\phi} \equiv -\cos \alpha \quad (5)$$

$$2\bar{\gamma} \equiv -P_\phi / pR \quad (6)$$

$$R \equiv (qM/4\pi p)^{1/2} \quad (7)$$

$$\rho \equiv r/R \quad (8)$$

In these equations, q is the particle charge, assumed to be positive, p is its linear mechanical momentum, P_ϕ is the constant angular momentum conjugate to ϕ , M is the dipole moment, A_ϕ is the vector potential, and the remainder of the variables are defined in figure 1.

Of the six variables of the equations of motion, only two are absent from equation (4). The azimuthal angle ϕ is absent because of the assumption of rotational symmetry about the z axis. The angle β of figure 1 is absent also,

and this means that the integral of equation (2) can be reduced to the form

$$\Phi(\vec{r}) = \frac{1}{4\pi} \int_0^{2\pi} \int_{\alpha_1}^{\alpha_2} \sin \alpha \, d\alpha \, d\beta = \frac{1}{2} \int_{\alpha_1}^{\alpha_2} \sin \alpha \, d\alpha \quad (9)$$

which by the definition of equation (5) can be written as

$$\Phi(\vec{r}) = \left[\frac{Q_1 - Q_2}{2} \right] \quad (10)$$

ESTABLISHING THE LIMITS ON Q

Evidently the problem of calculating $\Phi(\vec{r})$ from equation (10) depends on establishing the proper limits on Q . Equation (4) obviously permits all values of Q , for $-1 < Q < 1$, because we can send particles from the point \vec{r} in any direction we choose. However, some of these particles would travel on bound orbits, and some would travel on unbound orbits connecting to infinity at both ends, if we rule out impacts with solid bodies. By requiring that all the variables be real and consistent with their geometric definition, and by using equation (4) as an equation of constraint for four of the six variables of phase space, outer limits for the range of Q can be established. For example, if \vec{r} is considered to be a parameter, equation (4) can be reduced to a three-dimensional surface on which the particle must move. The projection of this surface on the (ρ, θ) plane results in patterns such as shown in figures 2 to 4. The unshaded regions are regions of permissible motion and the shaded regions are forbidden to particle motion. It turns out that figure 3 divides (ρ, θ) space into regions quite convenient for discussion. The important feature of figure 3 is that it defines the circumstances when, with $\bar{\gamma}$ increasing, the inner and outer regions of permissible particle motion become connected at a point $(\rho_c, \theta_c, \bar{\gamma}_c)$, referred to as a critical point, and thereby defines the minimum $\bar{\gamma}$ for access into the inner region. The assumption of an isotropic homogeneous distribution at infinity means that $-\infty \leq \bar{\gamma} \leq \infty$. Since, from equation (4),

$$\frac{\partial Q}{\partial \bar{\gamma}} = \frac{2}{\rho \sin \theta} \geq 0 \quad (11)$$

we know that Q calculated from equation (4)

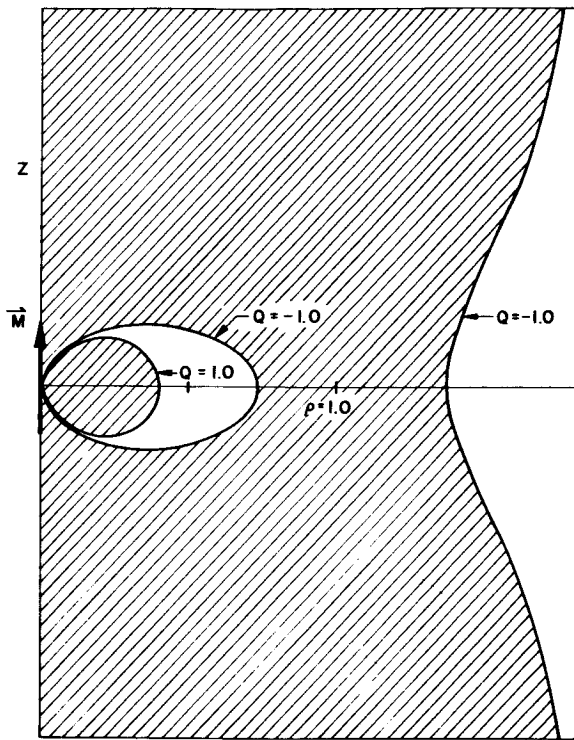


FIGURE 2.—Allowed and forbidden regions in the (ρ, θ) plane of an infinitesimal dipole for $\bar{\gamma} = -1.05$.

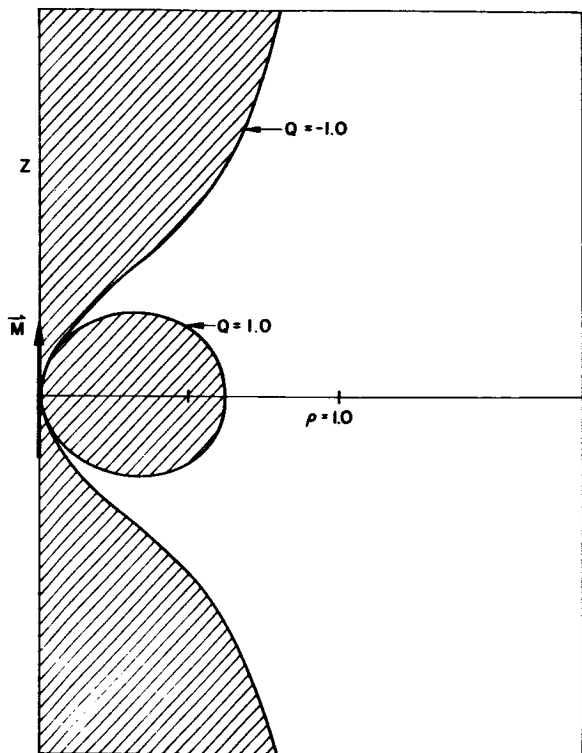


FIGURE 4.—Allowed and forbidden regions in the (ρ, θ) plane of an infinitesimal dipole for $\bar{\gamma} = -0.5$.

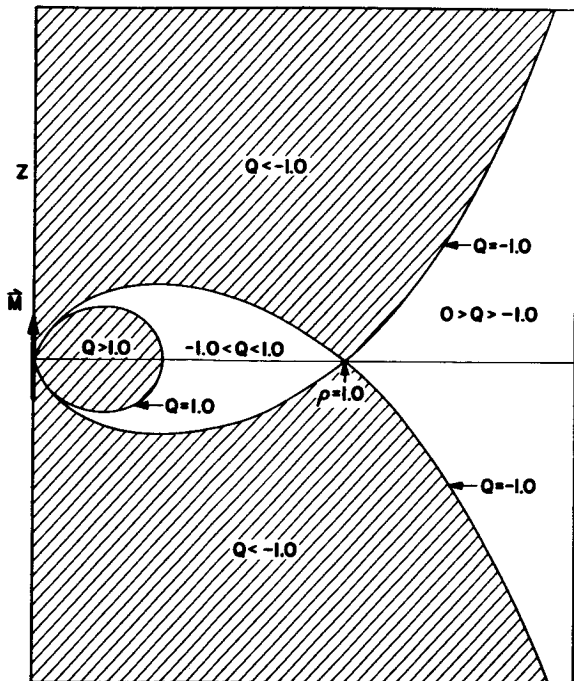


FIGURE 3.—Allowed and forbidden regions in the (ρ, θ) plane of an infinitesimal dipole for $\bar{\gamma} = -1.0$.

with $\bar{\gamma} = \bar{\gamma}_c$ for points in the inner region for the situation of figure 3 is the minimum Q that a particle coming from infinity can have. From the analytical viewpoint, figure 3 occurs when equation (4) is viewed as a three-dimensional surface in Q, ρ , and θ with $\bar{\gamma}$ as a parameter and the value of $\bar{\gamma}$ is such that an extremum in Q occurs at a point for $Q = -1$. By taking the differential of equation (4) and equating the coefficients of $d\rho$ and $d\theta$ to zero, two equations in ρ, θ , and $\bar{\gamma}$ are obtained; these, together with equation (4), are sufficient to determine the value of ρ, θ , and $\bar{\gamma}$ for which a critical point occurs. Using the value of $\bar{\gamma}_c$ obtained, equation (4) can be used to compute the minimum value of Q , referred to as Q_c , at any point (ρ, θ) in the inner allowed region of figure 3.

Figure 5 shows typical $(Q, \bar{\gamma})$ curves for three points in the inner region of the (ρ, θ) plot. The different shadings correspond to regions from which the $(Q, \bar{\gamma})$ curves are prohibited by virtue of different physical requirements which can be expressed in equation form.

From the Störmer theory and a study of the

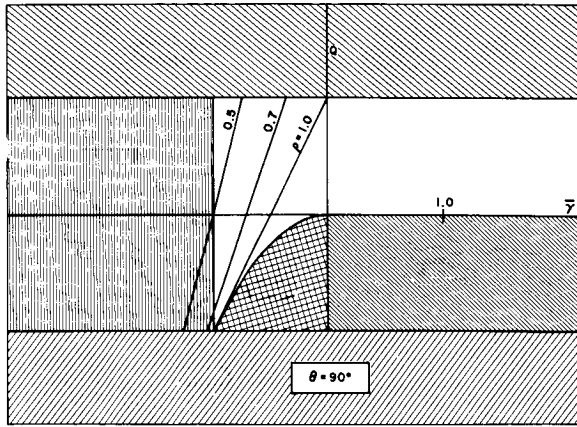


FIGURE 5.— $(Q_c, \bar{\gamma})$ plot in an infinitesimal dipole field at points (ρ, θ) within the inner allowed region where some directions can be connected to infinity.

$(Q_c, \bar{\gamma})$ plots, point (ρ, θ) can be shown to be:

$$\text{shielded if } Q_c \geq 1.0 \quad (12)$$

$$\text{unshielded } \begin{cases} \text{if } Q_c \leq -1.0 \\ \text{or} \\ \text{if } -1 < Q_c < 0 \text{ and } \frac{\partial Q_c}{\partial \rho} > 0 \end{cases} \quad (13)$$

$$\text{partially shielded if } -1 < Q_c < 1 \text{ and } \frac{\partial Q_c}{\partial \rho} < 0 \quad (14)$$

Thus, equation (10) can be written:

$$\Phi(\vec{r}) = 0 \text{ if } Q_c \geq 1.0 \quad (15)$$

$$\Phi(\vec{r}) = 1.0 \begin{cases} \text{if } Q_c \leq -1.0 \\ \text{or} \\ \text{if } -1 < Q_c < 0 \text{ and } \frac{\partial Q_c}{\partial \rho} > 0 \end{cases} \quad (16)$$

$$\Phi(\vec{r}) = \frac{[1 - Q_c]}{2} \text{ if } -1 < Q_c < 1 \text{ and } \frac{\partial Q_c}{\partial \rho} < 0 \quad (17)$$

where

$$Q_c = \frac{qA_\phi(r, \theta)}{p} + \frac{2\bar{\gamma}_c}{\rho \sin \theta} \quad (18)$$

PRESENTATION AND DISCUSSION OF THE CALCULATIONS

Following the procedure outlined, calculations of the flux were made at points in several magnetic field configurations (figs. 6 and 7). In all cases, the range of Q included all values

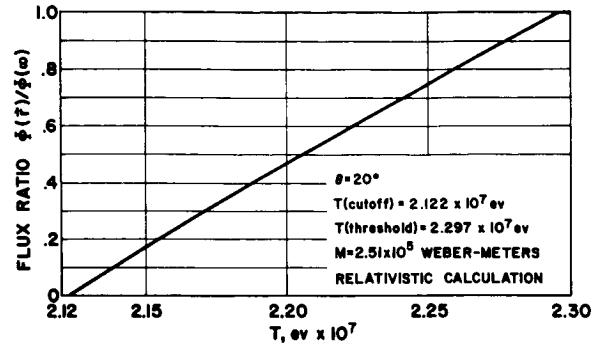


FIGURE 6.—Relativistic proton flux ratio 10 meters from an infinitesimal dipole at a magnetic co-latitude of 20° , with a dipole moment = 2.51×10^5 Weber meters.

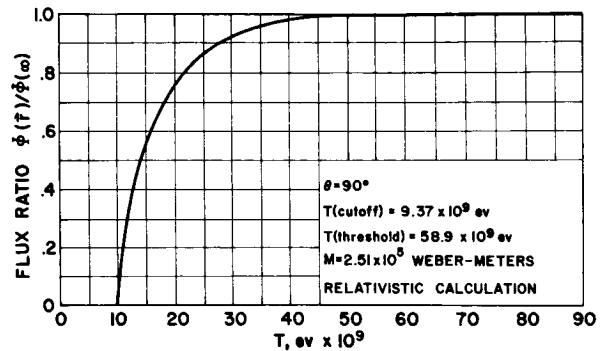


FIGURE 7.—Relativistic proton flux ratio 10 meters from an infinitesimal dipole at a magnetic co-latitude of 90° , with a dipole moment = 2.51×10^5 Weber meters.

not positively excluded by known physical constraints, so that the curve presented represents an absolute upper limit for the particle flux as a function of energy under the assumption that the flux at infinity is isotropic, uniform, and normalized to unity. For example, an arbitrary flux spectrum at infinity, multiplied by the ordinates of figure 7, yields the flux spectrum at the point $r = 10$ meters, $\theta = \pi/2$, in the dipole field.

Constant Q_c curves shown in figure 8 for the dipole are isoflux curves (compare equation (17)) in the partially shielded region. The volume of the partially shielded region of the dipole (defined by equation (14)) is 5.5 times the volume of the shielded region, independent of particle energy. The volume of the partially shielded region over which the flux is at most one-half of the flux at infinity is approximately

equal to the volume of the shielded region. From these considerations, the partially shielded regions in a magnetic field would seem to be important in optimizing the design of the magnetic shield.

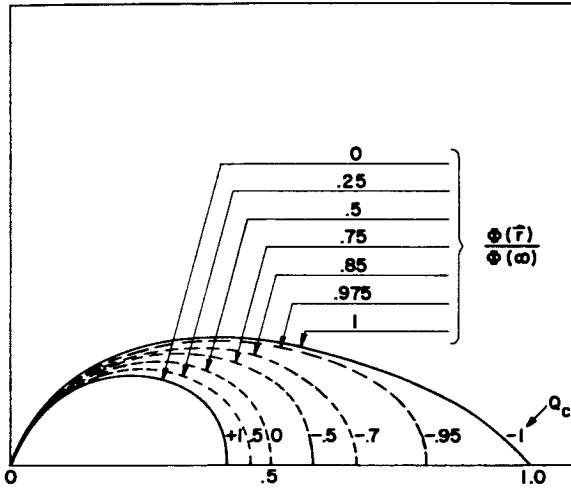


FIGURE 8.—Isoflux curves in (ρ, θ) coordinates in an infinitesimal dipole field and their relation to the constant Q_c curves in the partially shielded region.

Figure 9 shows a series of (ρ, θ) plots in an infinitesimal quadrupole field. Of the higher infinitesimal multipole fields, this is the first appearance of two critical points off the equatorial plane and the first appearance of a critical point for which $Q=1.0$. Equations for the flux similar to equations (15) through (18) can be written down for each shielded and partially shielded region defined by a critical point.

Figure 10 shows the behavior of the (ρ, θ) plots in an infinitesimal octopole field. This is the first appearance of two critical points for the same value of $\bar{\gamma}$. The three shielded and three partially shielded regions defined by the three critical points provide radiation protection in the vicinity of the origin over more directions than the single shielded and partially shielded region of the dipole. This is a feature of the higher multipole fields, and is of importance to magnetic shielding problems.

The number of critical points, their coordinates, and properties of the (ρ, θ) plots of

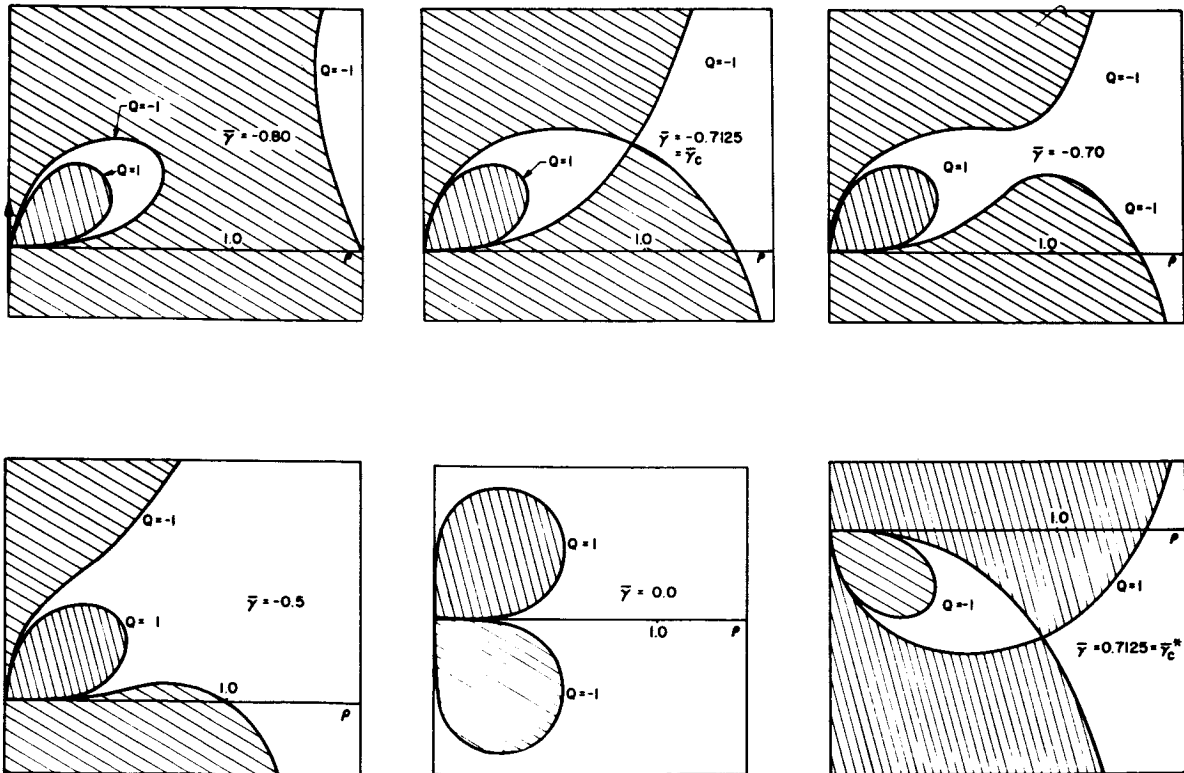
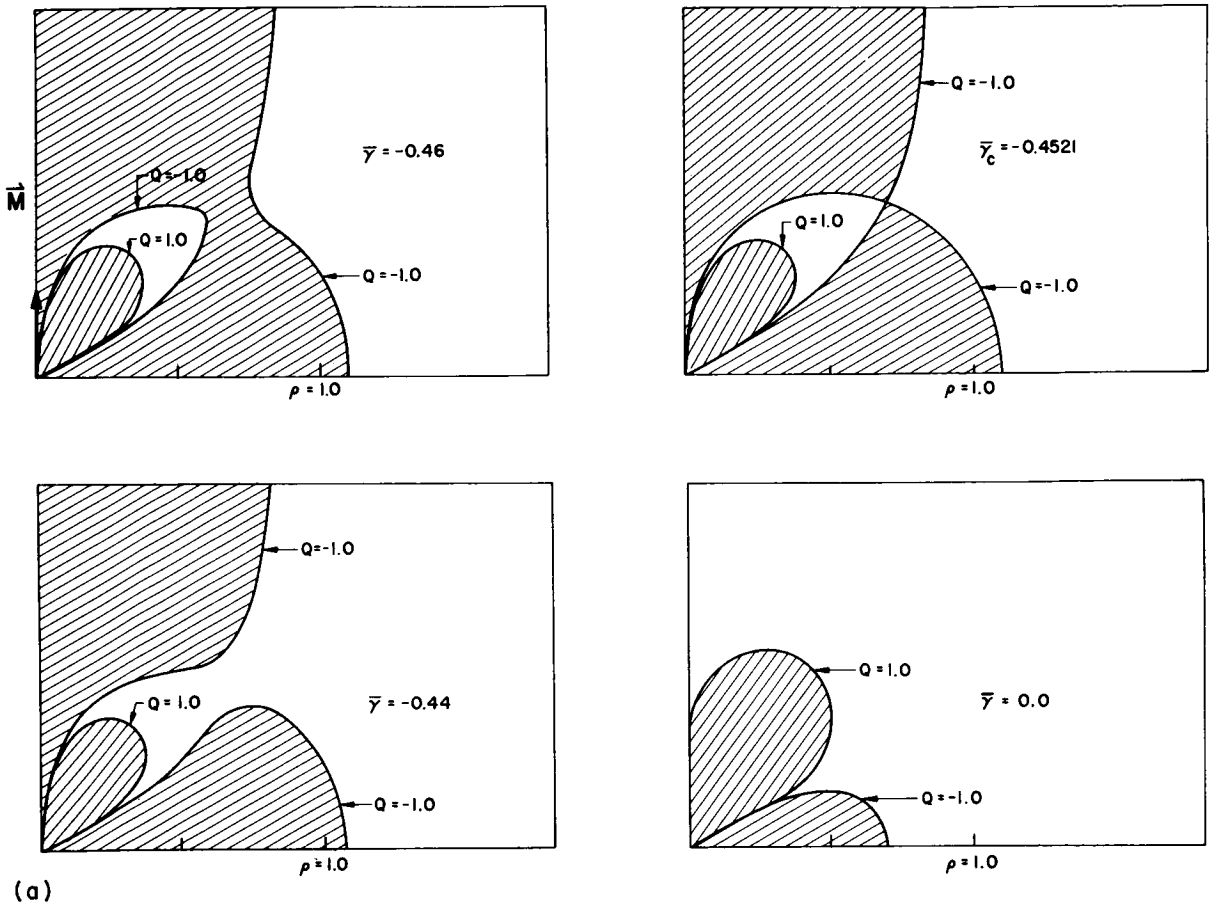


FIGURE 9.—Allowed and forbidden regions in the (ρ, θ) plane of an infinitesimal quadrupole.



(a)

FIGURE 10(a).—Allowed and forbidden regions in the (ρ, θ) plane of an infinitesimal octopole.

higher multipole fields are listed in tables I and II.

Consider two current loops of equal, finite radii, located symmetrically above and below the equatorial plane and centered on the z axis. The current loop array is termed parallel or antiparallel, depending on whether the currents are in the same or opposite directions, respectively. Figure 11 shows typical (ρ, θ) plots for an antiparallel array with a particular loop separation and loop radius. The (ρ, θ) plots resemble those of the quadrupole, and in the case of the quadrupole, two critical points define two shielded and two partially shielded regions surrounding the loops. The (ρ, θ) plots for any combination of loop separation distance

follow this same simple quadrupole-type behavior.

By studying the gradient of the Q curves in a (ρ, θ) plot, it can be shown that a critical point is a saddle point in (ρ, θ, Q) space (paper entitled "Critical Stormer Conditions in Quadrupole and Double Ring Current Fields" by E. W. Urban to be published in *J. Math. Phys.*, Nov.-Dec. 1965). For a critical point to be a saddle point, the additional sufficiency condition

$$\left[\frac{\partial^2 Q}{\partial \rho \partial \theta} \right]^2 - \left[\frac{\partial^2 Q}{\partial \rho^2} \right] \left[\frac{\partial^2 Q}{\partial \theta^2} \right] > 0 \quad (19)$$

must be satisfied. A critical point must be a saddle point, but the converse is not necessarily

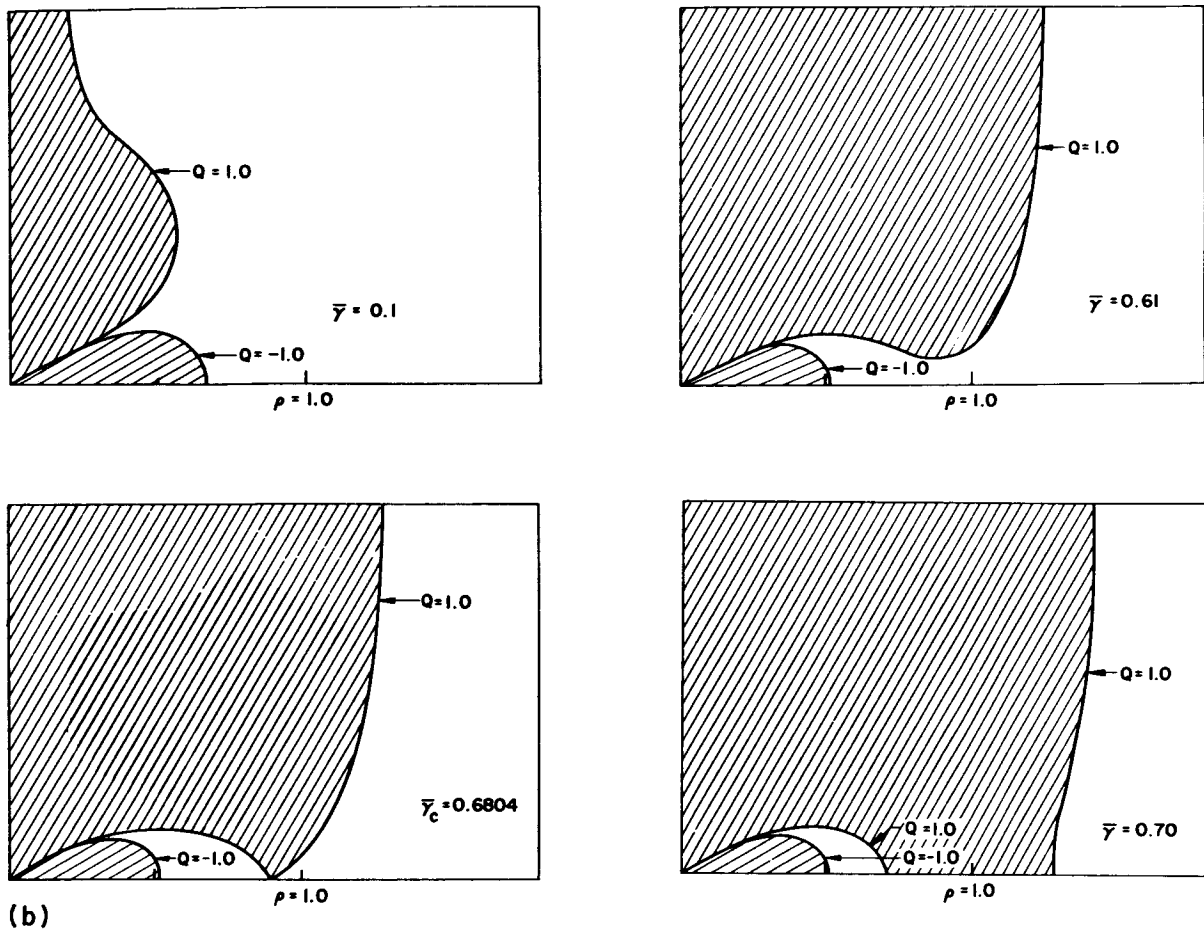


FIGURE 10(b).—Allowed and forbidden regions in the (ρ, θ) plane of an infinitesimal octopole.

TABLE I

Number of Critical Points and Symmetry Properties in Infinitesimal Multipole Magnetic Fields

Field	Number of critical points for $Q = -1.0$	Number of critical points for $Q = 1.0$	Are critical points symmetric w/resp. to $\bar{\gamma}_c$?	Are (ρ, θ) plots symmetric in xy plane for any $\bar{\gamma}$?
Dipole.....	1	0	No	Yes
Quadrupole.....	1	1	Yes	No
Octopole.....	2	1	No	Yes
Hexadecapole.....	2	2	Yes	No
32-pole.....	3	2	No	Yes
64-pole.....	3	3	Yes	No

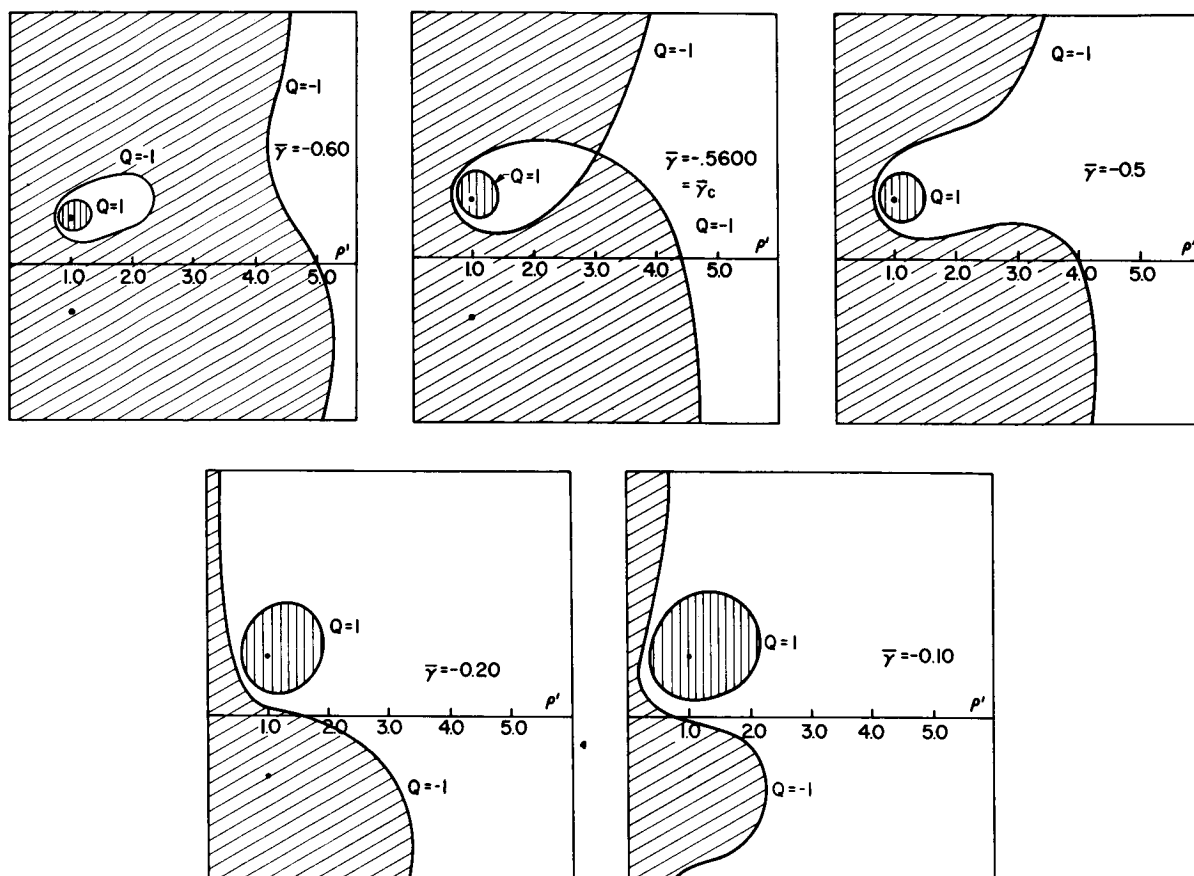


FIGURE 11.— Allowed and forbidden regions in the (ρ, θ) plane of a double loop system with antiparallel magnetic moments. $\rho' = \rho/\lambda$.

TABLE II

Coordinates of the Critical Points in Infinitesimal Multipole Magnetic Fields

Field	Type of critical point, Q	γ_c	θ_c	ρ_c
Dipole.....	-1	-1.0	90°	1.0
Quadrupole.....	-1	-.7125	63° 26'	1.063
Quadrupole.....	1	.7125	116° 34'	1.063
Octopole.....	-1	-.4521	49° 6'	.8972
Octopole.....	1	.6204	90°	.9306
Octopole.....	-1	-.4521	130° 54'	.8972
Hexadecapole.....	-1	-.2987	40° 5'	.7422
Hexadecapole.....	1	.4633	73° 26'	.7734
Hexadecapole.....	-1	-.4633	106° 34'	.7734
Hexadecapole.....	1	.2987	139° 55'	.7422

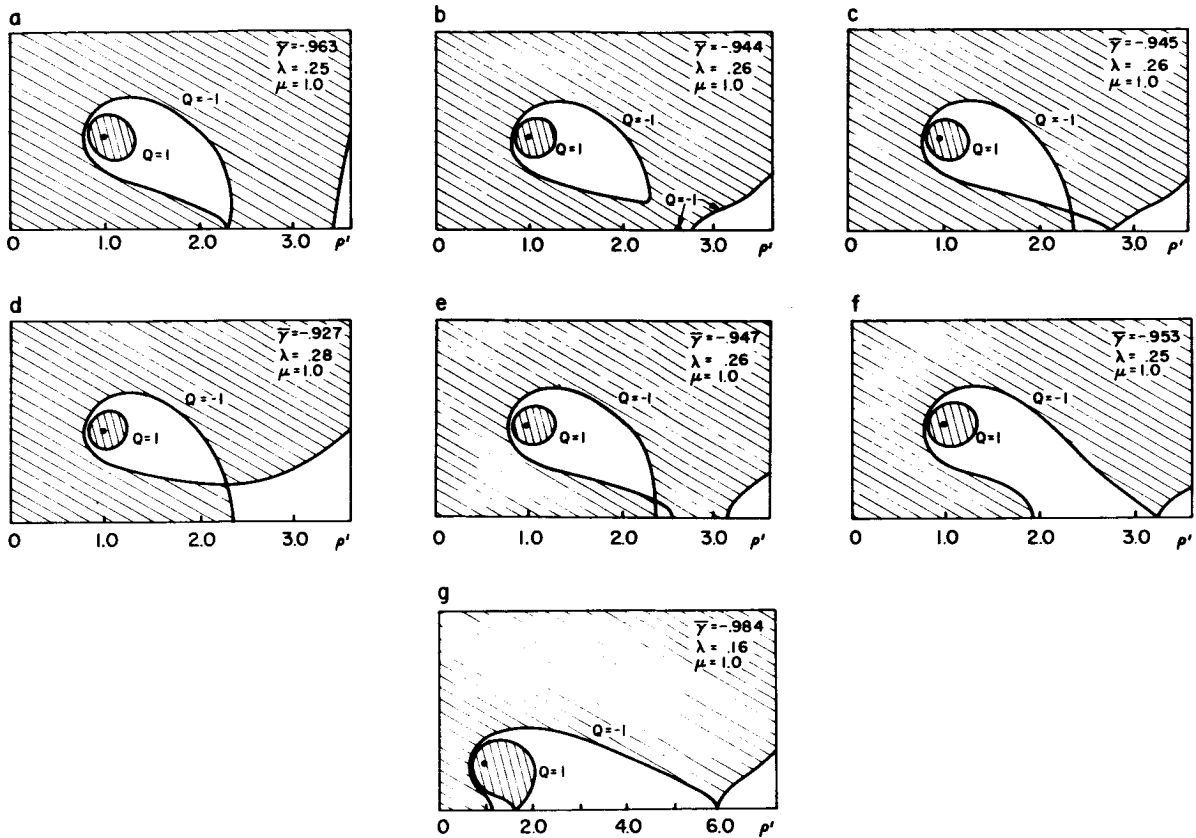


FIGURE 12.—Saddle points in the (ρ, θ) plane of a double loop system with parallel magnetic moments. $\rho' = \rho/\lambda$.

true, as we shall see. Figure 12 illustrates the different types of saddle points in the field of a parallel array for various combinations of loop radius and loop separation parameters, λ and μ . These (ρ, θ) plots are symmetric in the equatorial plane. The saddle point in figure 12(a) does not define a shielded or a partially shielded region whereas the three saddle points in figure 12(c) define two shielded and two partially shielded regions surrounding the loops and an isolated triangular-shaped partially shielded region astride the equatorial plane. This is the first appearance of a partially shielded region which does not contain a shielded region. Figure 12(b) shows a point which satisfies the necessary conditions for the existence of a saddle point but not the sufficiency condition.

773-446 O-65-14

In conclusion, we have considered the problem of specifying the flux of unbound particles at a point in an axially symmetric magnetic field, assuming an isotropic, homogeneous distribution at infinity. We have seen that the flux can be calculated in each shielded and partially shielded region defined by a critical point provided the critical point can be found. We have demonstrated the technique of finding the critical points in infinitesimal multipole fields and in the fields of two finite parallel current loops and have shown the complex behavior of the saddle points in the double current loop system. Finally, we have illustrated the problem with a number of examples and have emphasized the role of the partially shielded regions in the application of magnetic fields to shield space vehicles.

REFERENCES

1. HOAG, E.: Superconducting Strip and Its Use in Magnets. Annual Rept., Contract NAS 8-5279, AVCO Everett Res. Lab., Sept. 1964.
2. ANON.: Feasibility of Magnetic Orbital Shielding System. Tech. Rept., Contract AF 04(695)-252, Lockheed Missiles and Space Co., May 1964.
3. BERNERT, R. E.; and STEKLEY, Z. J. J.: Systems Analysis of Superconducting Magnets for Space Radiation Shielding. Tech. Rept., Contract NAS 8-5278, AVCO Everett Res. Lab., Mar. 1964.
4. BERNERT, R. E.: Design of a Mars Class Radiation Shield Using a Superconducting Magnet. Tech. Rept., Contract NAS 8-5278, AVCO Everett Res. Lab., Sept. 1964.
5. TOOPER, R. F.: Electromagnetic Shielding Feasibility Study. Contract ASD-TDR-63-194, Wright-Patterson AFB, May 1963.

N65-346J1

24—Magnetic Radiation Shielding Using Superconducting Coils¹

R. E. BERNERT and Z. J. J. STEKLY

Avco-Everett Research Laboratory

34601

The two present choices of shielding against space radiation are passive bulk shields and active magnetic shields. This paper presents an analysis of superconducting magnetic shield systems to determine the total weight of this type of active shield. The major components of the superconducting magnet considered are superconducting wire, support structure, and cryogenic environment.

From this analysis, an optimum system mass is determined as a function of shielded volume and shielding level. Of three magnetic field geometries analyzed, the best configuration on the basis of weight was found to be a spherically shaped shield consisting of a set of nested toroidal windings having a confined magnetic field and a field free shielded cavity in the center of the sphere. The empirical weight of this shield is:

$$M_s = 22.6 (E)^{0.572} (V)^{0.439} \text{ kg}$$

for $200 < E < 700$ MeV

and $10 < V < 1000$ m³

Because of a difference in the shielding mechanism of magnetic and passive shields, the dose rate behind shields of equal threshold levels differs, in general being lower for the magnetic shields. Accordingly, the shielding values of magnetic and passive shields are compared on a dose rate basis rather than on a threshold energy basis. The general results of this comparison show that as shielded volumes and shielding levels increase, the advantage of using magnetic shields also increases.

A preliminary study of mission requirements was also conducted and is summarized by presenting a design of a Mars class solar flare storm cellar. The study shows that the system is feasible and compatible with the spacecraft and that, with design improvements, the indicated weight savings of 4000 kg for the 10-man 200-MeV equivalent threshold storm cellar may be exceeded.

The overall conclusion is that early Mars voyages, or perhaps extended flights within the Van Allen belts, will present the earliest opportunity for using this type of shielding to advantage.

author
Z. J. J. Stekly

INTRODUCTION

The relative shielding value of space radiation shields may be determined by comparing the weights of shield material required to limit the dose rate within a given volume to a specified level. To obtain a realistic weight of a superconducting magnet system, the major components which must be considered are:

- (1) Superconducting wire, which carries the field producing current.
- (2) Support structure, which is necessary to contain the energy stored in the coil.
- (3) Cryogenic environment, required to maintain the low temperatures for superconductor operation. The cryogenic environment consists of insulation, refrigeration machinery, power supply, and waste heat radiator.

¹ Research supported by the George C. Marshall Space Flight Center, NASA, under contract NAS-8-5278.

By deriving general expressions for the weight of each of these components, an opti-

imum systems mass can be determined as a function of proton shielding level and shielded volume (ref. 1). This analysis permits a comparison of the stopping power (active) or threshold level (passive) of the two types of shields versus shield mass. However, because there is a difference in the shielding mechanism of the shields (ref. 2), direct comparison by dose rate for a given proton spectrum is necessary. Accordingly, a determination of the dose rates behind both passive and magnetic shields for expected proton spectra is necessary.

MAGNETIC FIELD REQUIREMENT

It is well known that a charged particle moving under the influence of a magnetic field has a force exerted on it which is perpendicular to the velocity vector of the particle. Of significance are the stopping power equations which provide the basic field design information. The shielding mechanism for the two types of magnetic fields considered, namely, confined and unconfined dipole, have been analyzed by Levy (refs. 3 and 4).

For a confined field, the "design" condition is given by

$$\Delta = \frac{2mv}{q} \times \frac{1}{B} \quad (1)$$

where Δ is equal to one proton Larmor diameter as shown in figure 1, mv/q is the particle momentum to charge ratio, and B is the magnetic field intensity. In this analysis, particle drift caused by gradients and curvature in the magnetic fields have not been considered. Elimination of the potential leakage of protons through the field by this mechanism may require that some increase in the calculated mass be made to maintain the dose rates as calculated by "design" condition.

For an unconfined field, the proton path or stopping power is not as easily illustrated.

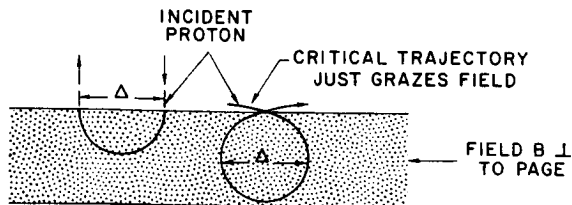


FIGURE 1.—Effect of magnetic field on charged particle path.

Levy (ref. 4) has shown, however, that the shielded volume V for an unconfined field generated by a single turn circular coil is approximated by a toroid and is defined by

$$V = \frac{1}{2} \pi^2 a^3 (\Delta S)^2 \quad (2)$$

where ΔS is a function of the nondimensional ratio r_0/C . Values for ΔS are given in table I. For r_0 the coil radius and C the Störmer radius, we also have

$$r_0/C = \frac{mv}{q} \frac{r}{\mu_0 I} \quad (3)$$

where I is the coil current. This geometry requires no correction for leakage due to drift.

Since these expressions relate proton mass to charge ratio and field requirements, field designs can be carried out for any volume and given proton energy.

FIELD GEOMETRIES

Three field geometries have been analyzed to determine the effect of geometry on mass. Two arrangements have confined magnetic fields while the third has an external field.

Unconfined Field Dipole

The unconfined field dipole is toroidal in shape, similar to a ring shaped hollow conductor. Placing the windings at the outer limit of the shielded region formed by the dipole field produces a desirable region of relatively low field. This low field can be eliminated if required. The extent of the shielded region, according to Levy (ref. 4), is given by equations (2) and (3). These equations define a region which is shielded from all particles below the design energy. There is, however, increased shielding effectiveness against higher energy particles approaching from other than a certain critical direction. This effect has not been considered in the dose rate calculations.

The mass of superconductor is calculated using the total coil current determined from equation (3). An analysis similar to that of Stekly (ref. 5) for a toroidal conductor was used to determine the mass of structure required to contain the energy in the magnetic field. In general, considering the geometry

TABLE I
Tables of ΔS vs the Ratio r_o/C

r_o/C	ΔS	r_o/C	ΔS
0.005000	82.74	0.144522	2.451
.006666	62.02	.155932	2.231
.010000	41.28	.169327	2.009
.010526	39.21	.185286	1.786
.011111	37.13	.204641	1.561
.011765	35.06	.228636	1.334
.012501	32.98	.259229	1.105
.013334	30.91	.299708	.8733
.014287	28.83	.320000	.7700
.015386	26.75	.340000	.7000
.016669	24.67	.356107	.6390
.018185	22.60	.400000	.5000
.020004	20.52	.441061	.4045
.022228	18.44	.500000	.3000
.025008	16.35	.540000	.2400
.028584	14.27	.587262	.1810
.033354	12.18	.650000	.1300
.040036	10.09	.700000	.0950
.050070	7.996	.750000	.07000
.066833	5.886	.800000	.0510
.100566	3.754	.850000	.0370
.105924	3.538	.900000	.0260
.111890	3.323	.924251	.02073
.118572	3.106	1.061049	.007301
.126111	2.888	1.261800	.001309
.134684	2.670	1.598634	.0000437

on figure 2, the $J \times B$ force on the windings require that they be supported with a surface structure. The stresses in the windings are tensile in the tangential direction (current direction) and compressive in the meridional direction (perpendicular to the current, tangent to the surface).

In this geometry there will be some magnetic field "leakage" into the shielded region. Should the intensity prove detrimental to the crew, additional windings may be provided which would eliminate it, since a field will not penetrate a closed superconducting circuit.

To maintain the coil at superconducting temperatures, the winding would be refrigerated via refrigeration coils and insulation applied to both the exterior and interior surface of the torus.

Confined Field Geometries

Double Torus. The confined field double torus consists of two toroidal windings, one

inside the other. The general arrangement is shown in the lower left of figure 2. Current direction on the inner winding is opposite to that on the outer winding, confining the magnetic field in the annular space formed between the windings and providing a field free shielded region within the inner torus.

The equation for the field strength B for a toroid is given as

$$B = \frac{\mu_0 I}{2\pi r} \quad (4)$$

indicating that the field intensity decreases with distance from the origin. This field variation requires that the two windings be eccentric with respect to each other in order to shield from all directions all particles up to the specified design energy. Thus the Larmor radius for a given proton energy is greater on the outer portion where the field intensity is lowest.

The mass of superconductor for each winding may be determined using the total current

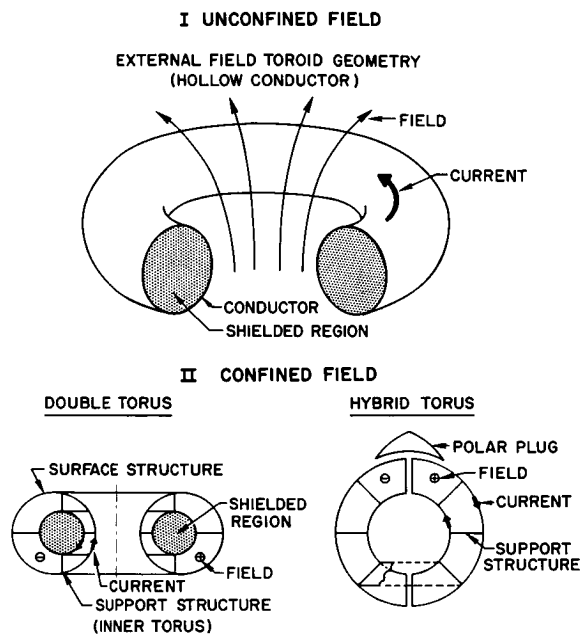


FIGURE 2.—Magnetic field configurations.

calculated by combining equations 1 and 4 and allowing for the field variation with r .

The confined magnetic field between the inner and outer winding exerts a force normal to the winding surface. On the outer winding the force is outward, tending to expand the system, and on the inner winding the force is inward, tending to collapse the shielded volume. Using the force per unit area P_m defined by the "magnetic pressure" relationship,

$$P_m = B^2/2\mu_0 \quad (5)$$

it can be shown (ref. 1) that the total outward force on the outer winding is greater than the total inward force acting on the inner winding. This being the case, it is possible to support the inner winding as a "force-free" coil from the outer winding by tying the two coils together via a system of tension members or membranes shown as the support structure on figure 2. The outer winding must also be provided with structural support wherever the magnetic forces result in stresses above the allowable of the wire. A constant-stress surface structure has been calculated which yields a toroid of variable shell thickness. The total structure is taken as the sum of the tension members and outer winding support.

To maintain the windings at superconducting temperature, refrigeration is supplied between the windings and insulation applied on the outer surface of the outer winding and the inner surface of the inner winding.

Hybrid Torus. The second confined field geometry can be generated by deforming a toroidal winding, as shown on the lower right of figure 2. The shielded region is spherical in shape and is located in the center of the geometry. For this configuration, it is necessary to add a polar plug of passive shielding material to prevent proton leakage at the field interface.

The field is generated by a single toroidal winding indicated in the figure and is confined within the winding providing a field free shielded region. To eliminate field variation at a given radius from the center of the sphere, a winding of constant radial thickness is provided by crossing wire through the field in such a way that the total conductor cross-section is greatest at the equator and essentially zero at the poles. This procedure eliminates high fields at the poles. It also permits the field depth to be constant for a given design proton energy.

The mass of superconductor and structure is determined in a manner similar to that used for the double torus. An important difference, however, is that the total force acting to expand the outer winding is equal and opposite to the force tending to compress the inner winding. This being the case, a support structure comprising a system of tension hoops or membranes can be provided between the inner and outer windings, shown as support structure in figure 2. Additional support is required for the crossover wire.

At the poles of the shield, particles are either curved toward or away from the pole centerline. When the particle is curved toward the centerline, there is the possibility that particles of lower than design energy can penetrate the field. If particles of a given charge are curved toward one pole of the shield, they will be curved away from the opposite pole. Since the shield is designed primarily for positively charged protons, it is necessary to cap (plug) only one pole of the shield.

The geometry of the plug has been calculated

to prevent leakage of all protons up to the design energy. The general shape is shown on figure 2. It has a thickness along the pole centerline sufficient to completely stop the design proton and tapers to zero at a distance from the centerline equal to slightly less than one Larmor diameter. Polyethylene has been used in the calculations as the plug material.

Maintaining the windings at superconducting temperature is accomplished in the same manner as for the double torus.

CRYOGENIC ENVIRONMENT

Superconductors must be maintained at temperatures near 4.2° K. For a space radiation shield utilizing superconductors, the mass required to provide this low temperature environment consists of insulation and a source of refrigeration. The refrigeration may be furnished by either an open loop liquid helium system (helium boils at 4.2° K under 1 atm pressure) or a closed loop mechanical refrigeration system. Because of the extended mission times anticipated, (that is, over one year), a closed loop will be lighter than an open loop system (ref. 6).

The heat load is due primarily to radiation through the vacuum insulation since, under persistent operation of the coil and zero gravity conditions, thermal conduction and joule heating are eliminated. An optimum weight relationship between refrigeration and insulation therefore exists.

A closed loop refrigeration system to operate in space will include refrigerator machinery, shaft power, and heat rejection radiator. A schematic for such a system is shown in figure 3. The mass requirement of each of these components is proportional to the rate of work of the refrigerator.

After determining the specific mass of each of these components with respect to refrigerator power, an optimum subsystem mass is determined, with respect to the refrigeration requirement. The main variable is radiator temperature.

With this determined, a second optimum is found between insulation and refrigeration, with respect to heated area (winding surface). The variable is heat load to the cryogenic en-

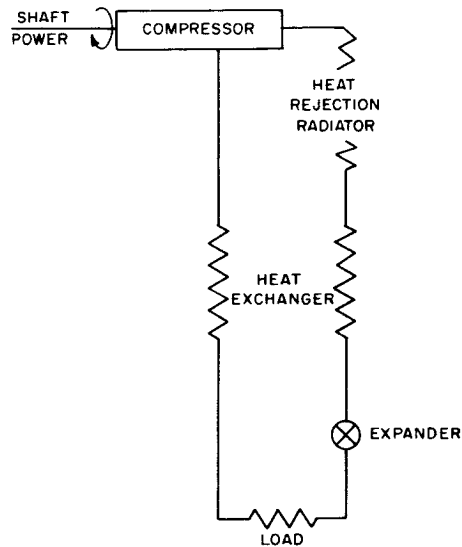


FIGURE 3.—Simple closed loop refrigeration cycle.

vironment. The results of this optimization are presented as figure 4. Other variables included in the analysis were the variation with refrigerator work of refrigerator specific mass, refrigerator efficiency, and space nuclear power source. It should be pointed out that these results are based on advanced refrigerators now in the component development stage and on the present or anticipated performance of space-power systems (ref. 7), radiators (refs. 8 and 9), and insulations (ref. 10), reported in the literature.

MASS OPTIMIZATION PROCEDURE

With expressions derived for the mass of the major components of the shield system, i.e., superconductor, structure, and cryogenic environment, optimization calculations can be made for each of the three geometries studied. After selecting material properties such as superconductor critical current and structure strength to weight ratio, the system mass is determined with respect to magnetic flux density for a given shielded volume and magnetic "stopping power." Note that the structure is at superconducting temperatures when under stress; thus the higher allowable values at these temperatures may be used. Figure 5 illustrates this procedure for the hybrid geometry and shows also the mass variation of each major

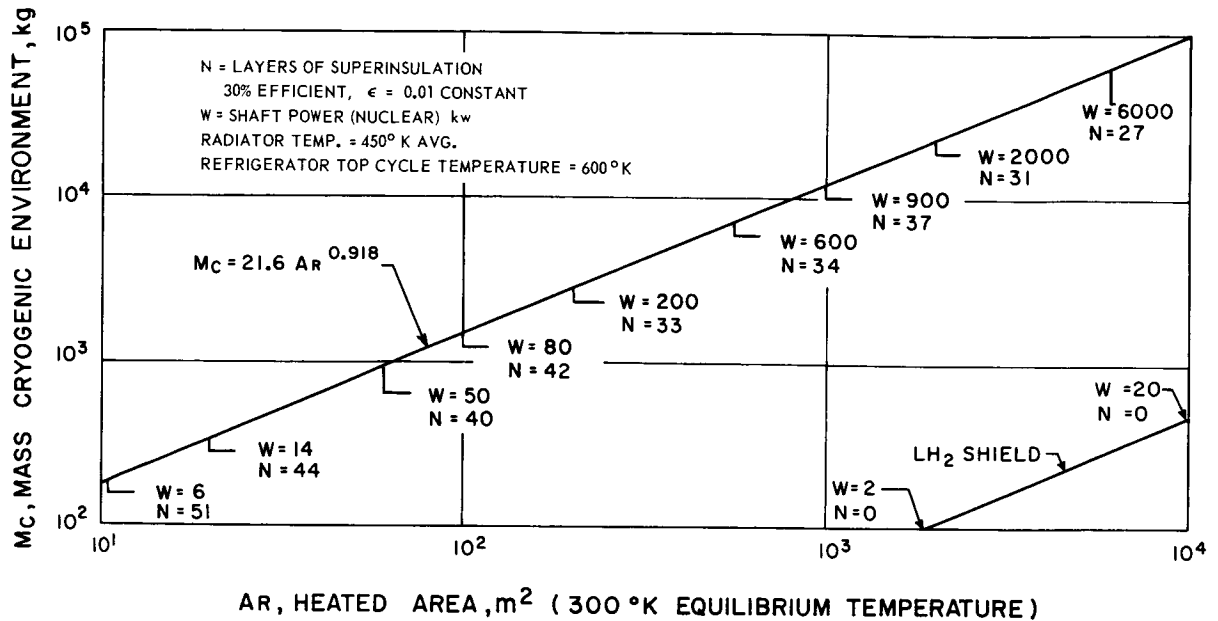


FIGURE 4.—Plot showing the mass requirement to maintain 4.2°K in space. The system consists of insulation, refrigerator, power source, and heat rejection radiator. Also shown is the requirement if a liquid hydrogen radiation barrier is available.

component. For the hybrid, note that the polar plug must be included. Figure 6 compares the three geometries studied, indicating that the hybrid geometry is the lightest. This conclusion holds for all energy levels and volumes of current interest. Also shown is the weight of a spherical polyethylene shield of equal threshold level.

DOSE RATE ANALYSIS

The difference in shielding mechanism of passive and magnetic shields requires that the dose rates for each be calculated in slightly different ways. Passive shields absorb energy from all particles, so that those which penetrate the shield have a reduced energy governed by range-energy laws. With a magnetic shield, however, particles penetrating the field suffer no loss of energy (if winding mass is neglected). Hence for equal threshold (or cutoff) level, the target sees the same number of protons, but at different energy levels. The effects of the two types of shields are shown in figure 7(a).

The effect of a magnetic shield on proton spectra is illustrated in figure 7(b). The figure shows that the low energy end of the spectrum is cut off, and those protons penetrating are of high energy. Note the effect of winding mass

on increased cutoff level ($E_M + \Delta E_1$) and decreased energy ($E_M - \Delta E_2$ minimum) of the penetrating spectrum. ΔE_1 and ΔE_2 refer to the energy losses suffered by a proton passing through the outer and inner windings, respectively. Thus for a magnetic "stopping power" E_M equal to a passive threshold energy ΔE_p , different dose rates will result. A preliminary analysis of the dose rates for passive (polyethylene) and magnetic shields was therefore made to determine the significance of this difference. More thorough calculations should be undertaken at a later time.

The basic approach used was that of Madey (ref. 2) employing the following assumptions: all particles strike normal to passive material and tangential to magnetic fields; no particle leakage due to field curvature and gradients; range-energy material constants for aluminum and water used for magnetic and passive shield materials respectively.

The above analysis has shown that, of the field geometries studied, the hybrid geometry yields the lowest dose rate for a given magnetic cutoff energy. Since this geometry is also the lowest in mass, it has been selected for comparison with passive shields. The comparison is presented as the shield mass ratio (magnetic/

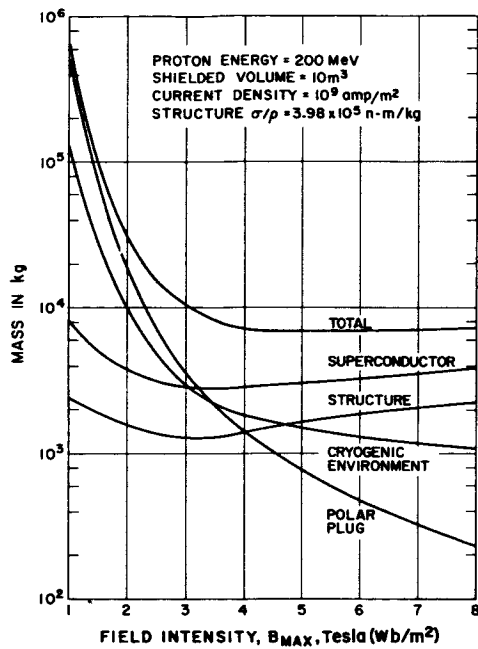


FIGURE 5.—Plot showing the relation among component weights for a hybrid torus geometry magnetic shield.

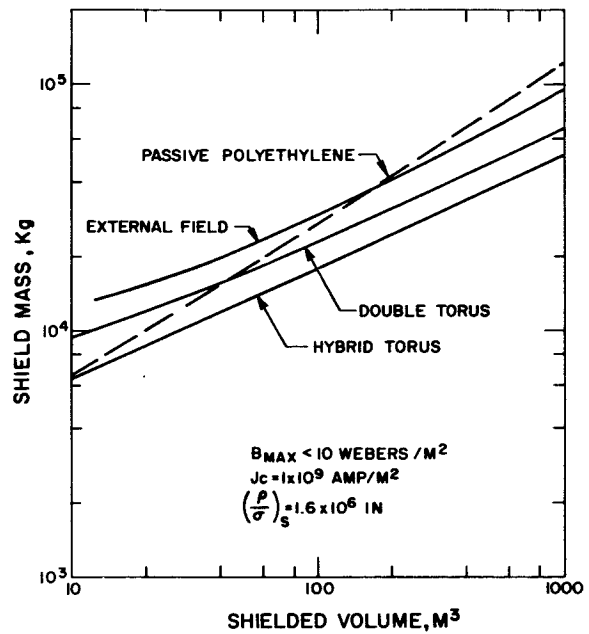


FIGURE 6.—Plot comparing passive and magnetic shield weights versus shielded volume for a shielding level of 200 MeV.

passive) versus shielded volume for several passive threshold levels on figure 8. The figure was constructed from a plot of shield mass versus primary dose rate calculated for the proton spectrum of the 3 high year flare average (1956, 1959, 1960) (ref. 11). Figure 8 shows that for shielding levels around 150 MeV (passive threshold) and shielded volumes above 30 m³, the magnetic shield approach appears competitive. As mission duration and crew size increase with increasing space activity, the magnetic approach becomes more competitive.

Consideration of secondary dose rates indicates generally that it will be more of a problem with passive shields than with magnetic shields. Further, should the secondary dose rate become a limiting design factor, the external magnetic field design should be considered further since secondaries are formed mainly by the high intensity, low energy end of the flare spectrum.

MARS CLASS SHIELD DESIGN

An investigation of mission considerations on the design of a magnetic shield was undertaken to determine compatibility of this concept

with spacecraft design (ref. 12). Considering a typical Mars Class mission of 2 to 3 years (refs. 6 and 13) a crew of 10 is deemed reasonable based upon crew functions and reliability (ref. 14). For this mission, total flare exposure time should be not more than 5% of the total trip, with a maximum of 7 days for any given flare (ref. 15). For this case, a 30 m³ shielded volume having an equivalent passive threshold level of 200 MeV (170 MeV magnetic cutoff energy) would be adequate, using current estimates of crew space requirements (ref. 16), exposure standards, and flare information (ref. 17).

To meet this design, magnetic shielding appears attractive since, from figure 8, a hybrid geometry storm cellar would yield a shield mass ratio of 0.71 for a potential savings of 4000 kg. The shield design results are summarized in table II and figures 9 and 10. An artist's concept of the shield is shown on figure 11.

The design illustrated in figures 9 and 10 incorporates several changes from the analytic model used to determine the optimum weight. First, the superconductor is crossed through the field at 17 "stations." This provides a

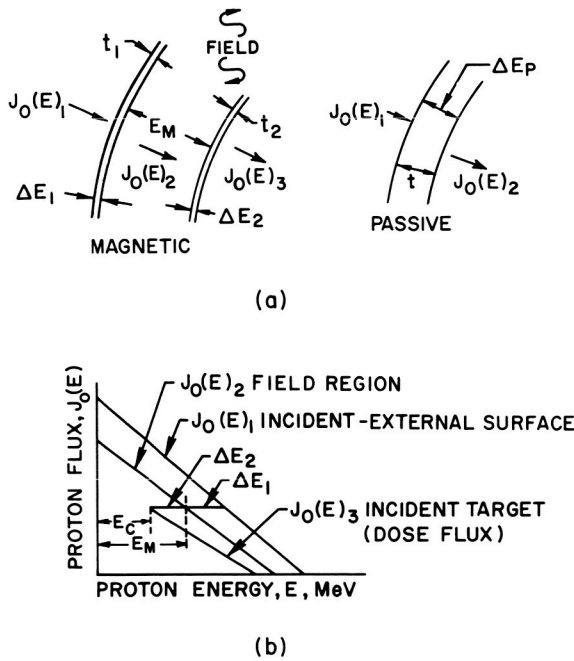


FIGURE 7.—Energy degradation of flux by magnetic and passive proton shields.

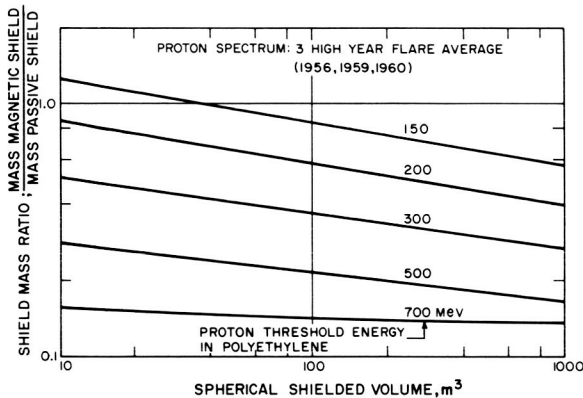


FIGURE 8.—Plot of shield mass ratio, magnetic/passive, versus shielded volume for several dose rates.

maximum field variation of +10% over the optimum of 4 tesla. Little or no mass increase is required; however, a field gradient is produced which will increase drift leakage. The magnitude of the drift has not been evaluated. We should note here that the optimum field of 4 tesla is within the present state of the art; however, coils of this size performing at the design current density of 10^9 amp/m² have yet to be produced commercially (ref. 18).

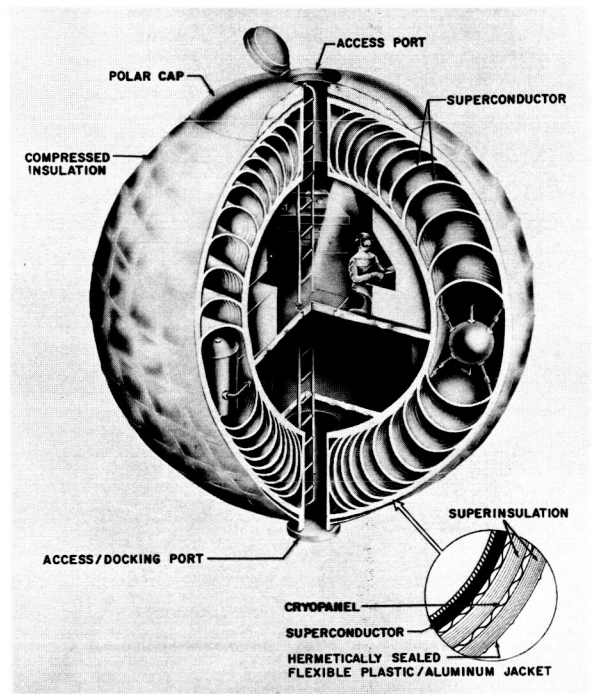


FIGURE 9.—Cross-section of superconducting magnetic hybrid geometry solar flare shelter, shielded volume: 30 m³, equivalent passive shielding level: 25 g/cm².

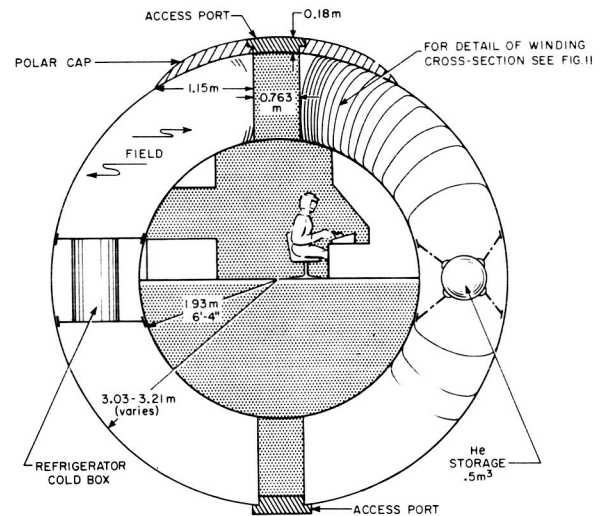


FIGURE 10.—Detail of winding cross-section, hybrid magnetic shield.

A second design alternative is the structural support. Of several alternatives investigated, the structural enhancement of the superconductor itself using structural adhesives (ref. 19) appears the best approach. Maximum benefit

is obtained using strip superconductor (ref. 20) since the full allowable stress of the superconductor may be developed in two axes of the strip. This method simplifies coil fabrication as well as reducing the system mass by as much as 22%.

TABLE II

Magnetic Shield Design Requirements and Weights

A. Requirements	
Shielded Volume.....	30 m ³ .
Passive Threshold Level.....	200 MeV.
Equivalent Magnetic Stopping Power.....	170 MeV.
B. Component Weights	
Superconductor.....	4.13 × 10 ³ kg.
Structure.....	2.65 × 10 ³ kg.
Cryogenic Environment.....	2.40 × 10 ³ kg.
Polar Plug.....	0.655 × 10 ³ kg.
C. Total Shield Weight.....	9.835 × 10 ³ kg.
D. Shield Mass Ratio, Magnetic/Passive.....	0.71.
E. Optimum Field Flux Density.....	4T (Wb/m ²).

A most important consideration is the reliability of this system. Admittedly, an active shield can never be as reliable as a passive shield. However, the potential weight savings for equal shielding value may be used to increase the reliability of the overall space vehicle which would be worthwhile. For the active shield, only the refrigerator is subject to mechanical failure. Based upon present planning studies (refs. 6, 13, and 14) the reliability of machinery may be increased to an acceptable degree with a nominal weight increase of 20 to 30%. Since the machinery is but a small percentage of the overall system, an overall weight increase of only 2.4% might be necessary to meet mission reliability criteria.

Other design and operational aspects and their estimated effect on system mass are summarized in table III. The result of this design

TABLE III

Effect of Design Alternatives on System Mass Ratio

Item	System weight, % change	Comment
Field Design.....	-----	Allowing +10% variation of field intensity <i>B</i> to simplify fabrication.
Cryogenic System.....	0.9	Compressed superinsulation on inner surface of shield.
Access Hatches.....	7	Fabrication at poles is simplified. May be decreased by further design analysis.
Stand-by Liquid Helium.....	0.5	Permits 8-hour coolant supply during refrigerator shutdown.
Reliability.....	2.4	An early estimate. Demonstrates that system reliability requirements can be met.
Total Required Increase.....	+10.8	
Structural Support Alternates		
(a) Separate spherical supports.....	-----	Simpler to fabricate.
(b) Same as alternate a, using structural adhesives.	-4.5	Requires strip shaped superconductor for maximum benefit.
(c) All surface loaded structure using structural adhesives.	-22	Easiest to fabricate, requires strip conductor for maximum benefit.
Intermittent Operation.....	< -2	Does not appear practical. Integration of total auxiliary power requirements with shield power may result in some savings.
Potential Reduction.....	>22	

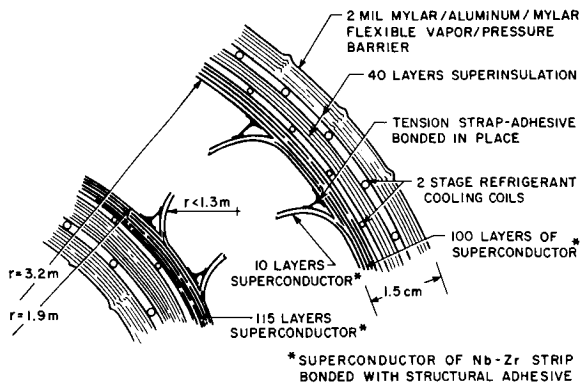


FIGURE 11.—Artist's Concept—Superconducting magnetic hybrid geometry solar flare shelter for an early Mars mission. Equivalent shielding level: 25 g/cm² polyethylene (200 MeV proton threshold); shielded volume: 30 m³ (10-man crew); weight ratio magnetic/passive: 0.71 or a potential savings of 4000 kg.

study is that shield mass ratios presented in figure 8, while based on an idealized model, may be considered to be representative of the state of the art 5 to 10 years from today. The primary advances required are experience in large coil fabrication and stable operation at current densities presently attainable on short samples of superconductors.

CONCLUDING REMARKS

As a result of this study, it has been shown that magnetic shielding becomes more competitive as the shielding volume and shielding level are increased. Early Mars exploration or extended trips within the Van Allen belts appear to be the earliest applications for this method of proton shielding.

REFERENCES

1. BERNERT, R. E.; STEKLY, Z. J. J.: Systems Analysis of Superconducting Magnets for Space Radiation Shielding. Avco-Everett Research Lab. Final Rept., Contract NAS 8-5278, Mar. 1964.
2. MADEY, R.; and DUNEER, A. JR.: Proton Dose Rates in Manned Space Vehicles. AAS Preprint 62-22, Jan. 1962.
3. LEVY, R.: Prospects of Active Shielding. Avco-Everett Research Lab. AMP 95, Nov. 1962.
4. LEVY, R.: Radiation Shielding of Space Vehicles by Means of Superconducting Coils. Avco-Everett Research Lab. Rept. 106, Apr. 1961.
5. STEKLY, Z. J. J.: Magnetic Energy Storage Using Superconducting Coils. Avco-Everett Research Lab. AMP 102, Jan. 1963.
6. Douglas Aircraft Corporation: Manned Mars Exploration in the Unfavorable (1975-1985) Time Period, vol. II, Summary, Rept. SM-45576, Jan. 1964.
7. BERNATOWICZ, T. T. ET AL.: Space Powerplant Needs and Selection. Astronaut. Aerospace Eng. I, 22-26, May 1963.
8. CALLINAN, J. P.; and BERGGREN, W. P.: Some Radiator Design Criteria for Space Vehicles. Trans. ASME, Series C. J. Heat Transfer, vol. 81, Aug. 1959, pp. 237-244.
9. ROSE, D. ET AL.: Heat Rejection from Space Vehicles. AAS Preprint No. 60-39, Jan. 1960.
10. HNILICKA, M. P.: Engineering Aspects of Heat Transfer in Multilayer Reflective Insulation and Performance of NRC Insulation. Advan. Cryog. Eng. vol. 5 (K. D. Timmerhaus, ED.), Plenum Press (New York) 1960, pp. 199-208.
11. MORE, K.; and TIFFANY, O.: Comparison of Monte Carlo and Ionization Calculations for Spacecraft Shielding. Proc. Sym. on Protection Against Radiation Hazards in Space. Paper E-2, TID-7652, Atomic Energy Commission, 1962, pp. 682-697.
12. BERNERT, R. E.: Design of a Mars Class Radiation Shield. Avco-Everett Research Lab. Final Rept., Contract NAS8-5278.
13. GENERAL DYNAMICS (Fort Worth): A Study of Manned Mars Exploration in the Unfavorable Time Period (1975-1985). Vol. II, Summary, FZM-4039-2, Jan. 1964.
14. EHRIKKE, K. A.: A Study of Early Manned Interplanetary Missions (Empire Follow-On). General Dynamics/Astronautics, GD/A-AOK 64-002, Jan. 1964.
15. BAILEY, D. K.: Time Variations of the Energy Spectrum of Solar Cosmic Rays in Relation to the Radiation Hazard in Space. J. Geophys. Res., vol. 67, Jan. 1962, pp. 391-396.
16. SANDERS, H. C.: The Effects of Man on the Weight of a Manned Space Vehicle. AAS Preprint 62-12, Jan. 16, 1962.

17. LOCKHEED MISSILES AND SPACE COMPANY: Manned Interplanetary Missions. Summary, vol. 1, 8-32-63-4. Jan. 28, 1964.
18. STEKLY, Z. J. J.: The Feasibility of Large Superconducting Coils. Avco-Everett Research Lab. Rept. 160, Sept. 1963.
19. HERTZ, J.: Epoxy-Nylon Adhesives for Low-Temperature Applications. Adv. Cryog. Eng., vol. 7 (K. D. Timmerhaus, ED.), Plenum Press, 1962, pp. 336-342.
20. HOAG, E.: Experimental Investigation of Advanced Superconducting Magnets. Avco-Everett Research Lab. Final Rept., Contract No. NAS 8-5279, Sept. 1964.

NG5-34602

25—Plasma Radiation Shielding¹

RICHARD H. LEVY and G. SARGENT JANES

Avco-Everett Research Laboratory

It has been recognized for some time that energetic protons constitute a serious radiation hazard in space, especially for trips lasting longer than a week or two. An important attribute of the radiation shielding problem is that very few methods are available to us for dealing with it. This note describes an approach to the problem which has not to our knowledge been suggested before. At this stage the new approach indicates the possibility of a substantial reduction in the weight of a space radiation shield.

Three methods of shielding are currently available. First, of course, there is solid shielding. Second, pure magnetic shielding has been shown to have substantial advantages over solid shielding, but only for very large vehicle sizes (refs. 1 to 4). Third, there is electrostatic shielding, in which the space vehicle to be protected must be kept at a positive potential of one or two hundred million volts relative either to an outer part of the space vehicle or to "infinity." Maintaining a potential difference of this order of magnitude between two solid conductors is well beyond the limit of present-day technology using heavy ground equipment. On the other hand, the electrons present in the interplanetary plasma would rapidly discharge any positive potential of the whole space vehicle relative to infinity. The power required to maintain a potential of 2×10^8 volts against this loss is estimated to be about 10^7 kilowatts.

If it were possible to reduce very substantially the flow of electrons from space to the vehicle,

electrostatic shielding might after all be feasible. Our suggestion is based on the fact that under suitable conditions electrons do not flow across magnetic field lines. Thus, in the presence of a magnetic field strong enough to control the electron motions, a space vehicle might be maintained at a very high potential relative to infinity. The magnetic field necessary to control electrons of modest energy is far less than that required to control very energetic protons, as in the pure magnetic shielding scheme. As a result, the device as a whole is far lighter than the pure magnetic shield. A preliminary comparison of the weights of the various systems is given in figure 1. This scheme, which we call plasma radiation shielding, shows an even greater advantage over pure magnetic shielding at lower values of the design proton energy. Plasma radiation shielding has two principal physical requirements. The first requirement is for a lightweight means of charging the vehicle. The second requirement is for an effective mechanism of "containing" electrons away from the vehicle. Fortunately, our containment mechanism also provides the basis for a remarkably simple charging scheme. As a consequence of this, primary consideration must be given to containment problems.

The way in which the electrons are restrained from flowing to the vehicle requires that the shape of the magnetic field be such that no field line which extends a long way from the vehicle should intersect the surface of the vehicle. This consideration drives us to the toroidal shape illustrated schematically in figures 2 and 3. There is, however, some latitude in the design of the cross section and the four-coil arrangement shown is no more than a suggestion.

¹ This work was supported by the Air Force Office of Scientific Research, Office of Aerospace Research, United States Air Force, under Contract No. AF 49(638)-659.

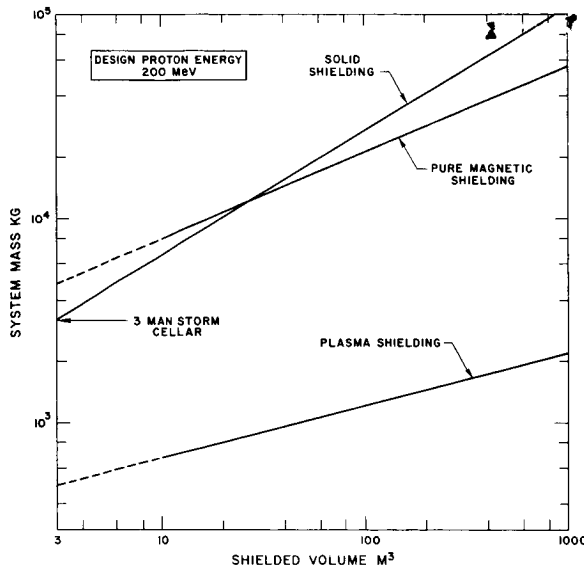


FIGURE 1.—Comparative weights for different shielding systems. The weights of the pure magnetic shield are taken from references 3 and 4. The Plasma Radiation Shield weight includes an allowance for a high energy electron accelerator which may not be necessary. At lower design proton energy, plasma shielding shows an even greater advantage over pure magnetic shielding.

In the presence of crossed electric and magnetic fields, electrons acquire a drift motion with the velocity $(\vec{E} \times \vec{B})/B^2$ provided that the magnitude of this quantity is less than the speed of light. Since E is determined by the design proton energy and the over-all size of the space vehicle, the condition $E/B < c$ gives a lower limit to the strength of the magnetic field, namely E/c . If B is much greater than E/c , we approach a pure magnetic shield and could dispense with the electric field. We do not at present know how close to this minimum value of B we can design, but we have assumed provisionally that we can work with $B \approx 2E/c$. The direction of the electron drift is azimuthally around the space vehicle. In addition to the drift motion, the electrons can be expected to have thermal motions; a typical thermal motion is illustrated in figure 2.

Knowledge of the required magnetic and electric fields allows us to calculate all those quantities appropriate to the Plasma Radiation Shield which are independent of the magnitude of the losses in the device, and do not pertain to the starting of the shield. Rather than do this

by means of a series of formulae, we present in table I a list of design parameters of the type referred to, based on a design proton energy of 200 MeV and a major radius for the shield of 5 meters. The derivation of all the quantities given in the table follows from these two design numbers, and the assumption that $E/B = c/2$. The total positive charge on the vehicle is obtained by integrating the normal component of the electric field over the surface area of the vehicle. The electron cloud, which is distributed on the magnetic field lines in the neighborhood of the shield, must have an equal and opposite negative charge. This observation allows us to calculate the electron density in the neighborhood of the shield.

We observe that no ions can be trapped in the magnetic field since their Larmor radii would typically be larger than the size of the magnetic field, and they are therefore promptly ejected by the electric field. The absence of ions together with the relatively large electron density leads to the very striking observation that we are dealing here with a "one-component plasma." The use of the word plasma is justified by noting that the electric field in which each electron moves is determined by the instantaneous positions of all the other electrons, so that the electrons cannot be considered

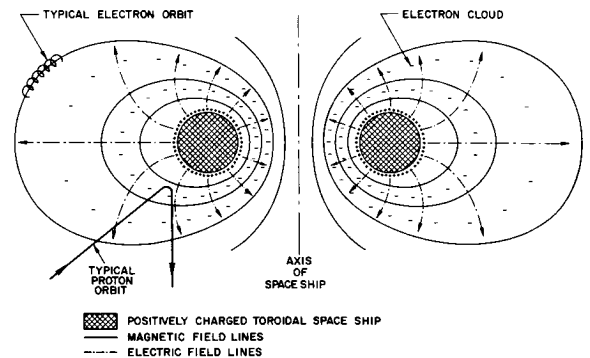


FIGURE 2.—Principle of the Plasma Radiation Shield.

The shield is basically electrostatic and repels protons by virtue of being positively charged. Electrons, attracted by the positive charge, cannot cross the magnetic field lines and discharge the vehicle. Instead they drift azimuthally around the vehicle as shown in figure 3. Viewed in a frame moving with the drift velocity, they also execute helical (thermal) motions around the field lines as shown here. The total charge in the electron cloud is equal and opposite to the charge on the vehicle.

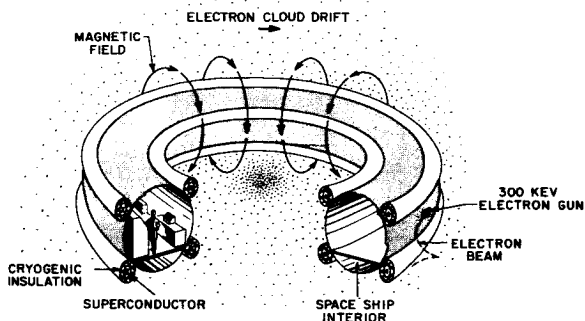


FIGURE 3.—Schematic diagram of a space vehicle using a Plasma Radiation Shield. The four-coil superconducting magnet system shown here is no more than a suggestion. The charge ejection system shown utilizes the inductive mechanism associated with the turning on of the magnet in order to transport electrons away from the vehicle. Ejection from the vehicle must be accomplished at a velocity greater than E/B velocity, or about 300 keV.

as following independent trajectories in fixed external fields, but must be treated as strongly correlated. The available body of theoretical and experimental knowledge regarding this type of one-component plasma is extremely limited. Indeed, for our application, the requisite control of such a plasma appears feasible only in the rather special geometry under consideration. We do not propose to discuss the properties of this plasma here, but two observations are of particular interest. First, each electron moves in such a way as to satisfy roughly the equation

$$\vec{E} + \vec{V}_e \times \vec{B} = 0$$

for motions having characteristic frequencies less than cyclotron frequency. Multiplying this equation by $n_e e$ we find:

$$n_e e \vec{E} = \vec{j} \times \vec{B}$$

In other words, the plasma is in equilibrium under the opposing electric and magnetic body forces. The electron pressure is less than both these forces by a factor on the order of kT/eV_o , where kT is the mean electron energy measured in a frame moving with the drift velocity and V_o is the design electrostatic potential of the shield. This equilibrium is to be contrasted with the more usual situation in plasma physics in which charge neutrality prevails, \vec{E} is small,

TABLE I

Typical Plasma Radiation Shield Quantities Independent of the Magnitude of the Losses

<i>Assumed Quantities</i>	
Overall Voltage, V_o -----	2×10^8 volts
Size, R -----	5 meters
<i>Derived Quantities</i>	
Electric Field, E -----	4×10^7 volts/meter
Magnetic Field, B -----	2660 gauss
Cyclotron Frequency, $\omega_c/2\pi$ -----	7 k Mc
Circumferential Drift Velocity, v_{Drift} -----	1.5×10^8 m/sec
Total Charge, Q -----	0.3 coulomb
Number of Electrons, N_e -----	2×10^{18}
Electron Density, n_e -----	2×10^9 cm ⁻³
Plasma Frequency, $\omega_p/2\pi$ -----	400 Mc
Magnetic Field Energy, U_M -----	1.2×10^8 joules
Electric Field Energy, U_E -----	3×10^7 joules
Power Required to Charge Both Fields in 5000 Sec-----	30 kw
Electron Drift Energy-----	80 keV
Electron Flux-----	3×10^{19} cm ⁻² sec ⁻¹
Momentum Flux-----	4×10^2 dynes/cm ²
Energy Flux-----	4×10^5 watts/cm ²
Magnet Current, I_{magnet} -----	2×10^6 amp
Mass of Superconductor, M_{sc} -----	550 kg
Cryogenic Area, A_{cry} -----	10 sq m
Cryogenic Mass, M_{cry} -----	180 kg
Cryogenic Power, P_{cry} -----	6 kw

and the Lorentz force is balanced by the plasma kinetic pressure. In connection with the electron plasma, we also note that we can calculate a Debye length h , but that the interpretation of this length is not the usual one. It is now the size of the region which contains sufficient electrons to make a potential kT/e at its surface. From this definition, we find that the ratio of h to R , the size of the shield, is:

$$\frac{h}{R} \approx \sqrt{kT/eV_o} \ll 1.$$

It is this observation which ultimately justifies our description of the electron cloud as a plasma.

As in all machines which, in the steady state, have charged particles moving in trapped orbits, injection is a problem. In our case, two alternative methods of injection are suggested. Of these, the more desirable consists simply of injecting the electrons onto field lines close to the vehicle while the magnetic field is being built up. As the magnetic field increases, field

lines initially near the space vehicle move away from it, carrying with them any electrons which happen to be on them. The resulting separation of charge sets up the electric field. This scheme suffers from the limitation that if, for any reason, losses occur which reduce the electrostatic potential of the device (and therefore the energy in the electric field), they can be made good only by increasing the strength of the magnetic field. Therefore, the scheme is usable only if the losses are so low that the electric field does not leak away in a time shorter than the time for which shielding is needed. If we are thinking in terms of solar flares, the electric field should stay on by itself for a day or two. If the losses are somewhat greater than this, it will be necessary to eject electrons continuously during a solar flare in order to maintain the electric field. This could be done with an electron linear accelerator emitting a beam of electrons at the design energy. These electrons could be expected to escape through the magnetic field on account of the relativistic increase in their mass. An allowance for this linear accelerator has been made in the weights quoted in figure 1. However, on account of the greater simplicity and negligible weight of the inductive charge ejection scheme, it is to be hoped that the accelerator would be unnecessary.

It can be seen from the above discussion that the magnitude of the losses we can expect are at present unknown. Losses take the form of motion of electrons toward the space vehicle or positive ions away from the vehicle, in either case at the expense of the energy of the electric field. Taking first the losses due to positive ions, we note that, since there are no trapped ions in the system, and since ions coming from outside the system (including the solar flare ions) are reflected without loss, the only source is from the ionization of neutral atoms in the electric field region. Following such an ionization, the electron that is born is retained on the magnetic field line where it is, but the ion is simply ejected. The worst case is if ionization takes place at the surface of the vehicle, for then each ion ejected carries with it an energy eV_0 acquired from the electric field. Two possible sources of neutral atoms are outgassing from the surface and micro-

meteorites. Assuming pessimistically that each ionization is at the surface of the vehicle, table II shows the permissible outgassing rates for two values of the power consumed by the ion current. The outgassing can be seen to represent a serious problem, but is probably not insuperable since conditions in space are very favorable to achieving a good bakeout of exposed surfaces. The micrometeorite rate near the earth is given by Whipple (ref. 5) as about 10^{-6} gm/cm² yr, but evidence obtained in deep space by Alexander (ref. 6), using an instrument aboard Mariner II, showed flux rates 10^4 times lower than corresponding rates near the earth.

The remaining source of loss arises from the possibility of diffusive motion of the electrons toward the space vehicle. This source of loss is at present, by many orders of magnitude, the least certain aspect of the whole device. We are attempting here to confine a plasma with a magnetic field; experience gained in the field of controlled thermonuclear fusion prompts us to comment on this problem with extreme caution. We can, however, point out that our configuration having the magnetic field "inside" and the plasma "outside" does fulfill the so-called minimum B requirement presently thought to contribute to stability (ref. 7). Furthermore, certain types of instabilities which might have been expected to contribute to substantial rates of diffusion across the magnetic field (ref. 8), and which are thought to be basically caused by the difference between the masses (and hence mobilities) of electrons and ions, will, in our case, be absent. We can also show that electron-electron collisions will give rise to a classical diffusion which can be shown to be negligibly small. On the other hand, the confinement has to be very good indeed for our device to work. In the lower part of table II we list the requirements on the containment process. We note that each electron is required to circle the device some 10^{12} times in the drift (azimuthal) direction before diffusing across the magnetic field. The maximum permissible temperature is calculated by assuming that the loss power heats the electron gas and that the heat thus gained is lost by cyclotron radiation.

These remarks on losses lead us to conclude

on this note: the Plasma Radiation Shield, as presently conceived, violates no principle of physics. On the other hand, it requires a degree of plasma containment greatly in excess of anything hitherto achieved. Although the

configuration and other factors appear favorable, no definite answer will be possible without experimental verification. The range of uncertainty is at present so great that marginal operation seems unlikely.

TABLE II

Typical Plasma Radiation Shield Quantities Dependent on the Magnitude of the Losses

Assumed Loss:	500 w ^a	10 kw ^b
Corresponding radial leakage current.....	2.5×10^{-6} amp.....	5×10^{-5} amp
Corresponding radial leakage current density...	6×10^{-13} amp/cm ²	1.25×10^{-11} amp/cm ²
(1) If these losses are due entirely to outgassing: ^c		
Acceptable outgassing rate.....	$< 1.5 \times 10^{13}$ atoms/sec.....	$< 3 \times 10^{14}$ atoms/sec
Average outgassing rate.....	$< 5 \times 10^4$ atoms/cm ² sec.....	$< 10^8$ atoms/cm ² sec
Acceptable surface vapor pressure.....	$< 5 \times 10^{-14}$ mm Hg.....	$< 10^{-12}$ mm Hg
(2) If these losses are due entirely to micrometeorites: ^c		
Acceptable flux (iron).....	$< 1.5 \times 10^{-8}$ gm/cm ² yr.....	$< 3 \times 10^{-7}$ gm/cm ² yr
(3) If these losses are caused by any form of diffusion in the electron gas:		
Electron containment time = $Q/I_{leakage}$	$> 1.2 \times 10^5$ sec.....	$> 6 \times 10^3$ sec
Radial Drift Velocity, $v_{ E}$	$< 4 \times 10^{-5}$ m/sec.....	$< 8 \times 10^{-4}$ m/sec
Drift Angle = $(1/\omega \epsilon r)_{eff} = j_{ E}/j_{\perp E}$	$< 3 \times 10^{-12}$	$< 6 \times 10^{-12}$
"Effective" Collision Time with Fixed Centers.....	> 80 sec.....	> 4 sec
Electron Temperature (thermal energy).....	< 80 keV.....	< 1 MeV
Electron Gyro Radius.....	< 3 mm.....	< 1 cm
Debye Length.....	< 4 cm.....	< 15 cm

^a Initial inductive charge ejection, no further charge ejection necessary after start-up.

^b Needs continuous operation of linac during flares.

^c Assuming worst case, that is, each atom ionized at the surface.

REFERENCES

1. LEVY, R. H.: Radiation Shielding of Space Vehicles by Means of Superconducting Coils. Avco-Everett Research Lab. Rept. 106, Apr. 1961. ARS J., vol. 31, Nov. 1961, p. 1568.
2. LEVY, R. H.: The Prospects for Active Shielding. Proc. Sym. on Protection Against Radiation Hazards in Space. Paper F-1, TID-7652, Atomic Energy Commission, 1962, pp. 794-801.
3. BERNERT, R. E.; and STEKLY, Z. J. J.: Magnetic Radiation Shielding Systems Analysis. Avco-Everett Research Lab. AMP 134, July 1964.
4. FELTON, J. E.: Feasibility of Electrostatic Systems for Space Vehicle Radiation Shielding. J. Astronaut. Sci., no. 11, 1964, pp. 16-22.
5. WHIPPLE, F. L.: Dust and Meteorites. Astronautics, vol. 7. Aug. 1962, pp. 40-42.
6. ALEXANDER, W. M.: Cosmic Dust. Science, vol. 138, Dec. 1962, pp. 1098-1099.
7. GOTT, Y. V.; IOFFE, M. S.; and TELKOVSKY, V. G.: Some New Results on Confinement in Magnetic Traps. Nuclear Fusion, Suppl. Pt. 3, 1962, pp. 1045-1047.
8. JAMES, G. S.; and DOTSON, J.: Experimental Studies of Oscillations and Accompanying Anomalous Electron Diffusion Occurring in DC Low Density Hall Type Crossed Field Plasma Accelerators. Fifth Symp. on Engineering Aspects of Magnetohydrodynamics. Mass. Inst. Technol., Apr. 1-2, 1964, pp. 135-148.

SESSION IVB

SHIELDING AGAINST SPACE RADIATION

Chairman: PHILLIP MITTELMAN

United Nuclear Corporation

N65-34603

26—Fractional Cell Lethality Approach to Space Radiation Hazards

S. B. CURTIS, D. L. DYE, and W. R. SHELDON

The Boeing Company

34603

A method of radiation hazard evaluation has been introduced in which the fractional number of cells of an organ killed or inactivated is calculated. This Fractional Cell Lethality or FCL depends only on the particle energy spectrum and the probability of cell inactivation. Recent data on inactivation cross sections of human kidney cells have been used to calculate the contribution of protons, alpha particles, and M-group particles to the FCL of the kidney. The results indicate that the proton and alpha particle contributions would have been the same order of magnitude for the 12 November 1960 giant flare and that their relative contribution does not vary much with shielding thickness. For a seated astronaut, the FCL values are on the order of 5 percent under reasonable shielding at points 4 and 6 cm inside the body at the waist. When data on inactivation cross sections become available on more critical organs, containing cells not replaced by the body, this approach may yield a realistic evaluation of the hazard from high LET radiation on extended space missions.

The authors are indebted to Dr. Paul Todd for his permission to use his experimental data on inactivation cross sections of kidney cells before publication.

authr

The greatest radiation hazard to astronauts on extended missions beyond the magnetosphere is from large solar particle events. There is strong experimental evidence published by Webber and Freier (refs. 1 to 3) and Fichtel and Guss (ref. 4) that alpha particles make up a considerable fraction of the particle flux above a given rigidity in the larger events, and it is true that the more energetic of these will penetrate the spacecraft and deposit a significant dose in the astronaut's body (ref. 5). These alpha particles and the stopping protons (the so-called "proton enders") cause a sizable fraction of the dose to be deposited at high LET.

It has been recognized in a preceding paper by Grahn and Langham that the radiation hazard to astronauts must be approached independently from the considerations which dictate the Maximum Permissible Dose (MPD) levels for occupational exposure. We are not concerned here with whether the astronaut has exceeded his MPD, but rather with the functional degradation of his critical body organs and his overall task performance over an ex-

tended period of time. The Quality Factor (QF) has been introduced by the RBE committee of the ICRP (ref. 6) as the low dose or dose rate limit of the RBE and has been recommended for use in evaluating the biological effectiveness of various types of ionizing radiation. The calculation, however, of a rem dose from an assumed QF versus LET relationship may be very misleading in the evaluation of the radiation damage to specific body organs. Little is known from direct experiment at low dose or dose rate about the appropriate values of QF to be used for the various organs of the body. This is especially true for the sub-lethal effects of interest here which will affect the astronaut's performance, thus jeopardizing mission success and his safe return. Therefore, we feel that the QF concept, though useful in a limited way to give a gross picture of the radiation danger, will not yield meaningful results when applied specifically to consequences that astronauts may face upon encountering one or more solar particle events in space.

THE FCL CONCEPT

We have, therefore, approached the problem from a slightly different point of view. Instead of either a rem or rad dose, we calculate the fraction of cells of a given organ damaged or inactivated. This Fractional Cell Lethality, or FCL, is a well-defined, calculable quantity and depends only on the particle energy spectrum at the cell in question and the probability for damage as a function of LET (ref. 7.) The latter quantity is conveniently expressed as a cross section, analogous to the nuclear cross sections encountered in scattering experiments in nuclear physics. It is a function of particle energy, but otherwise depends only on the biological aspects of the irradiated tissue, not on type of incident particle, depth-dose distribution, or other physical aspects. This approach appears valid for those organs which contain non-reproducing cells or cells which are not replaced by the body, such as neural or retinal cells. Rapidly dividing cells, such as those making up the intestinal lining, are known to be more radiosensitive, but they divide so quickly that large doses must be deposited in a short period of time before tissue malfunction becomes evident. For the purposes of the calculation below, and as an example of the use of the concept, we have used experimental inactivation cross sections on human kidney cells.

DERIVATION OF INACTIVATION HITS PER CELL PER UNIT FLUX

Let the probability be $\phi(x)$ that a cell or sensitive site at depth x has not been hit. The change in this probability, $-d\phi$, in a time, dt , is

$$-d\phi = J(x, t)\phi(x)dt$$

where $J(x, t)$ is the number of inactivation hits per site per second. Integrating, we have the familiar exponential dependence,

$$\phi(x) = \exp[-J(x)]$$

where $J(x)$ is now the time integrated number of inactivation hits per site:

$$J(x) = \int_0^T J(x, t)dt$$

where T is the event duration. For a single hit

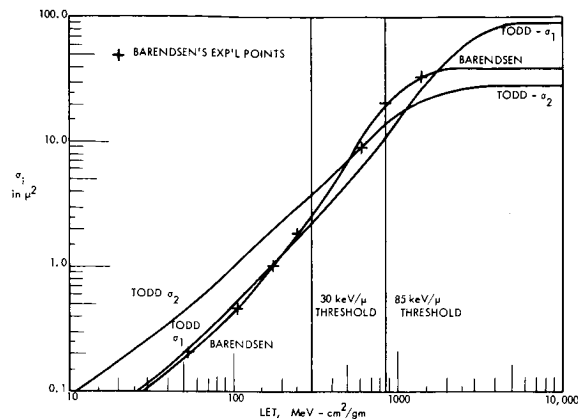


FIGURE 1.—Inactivation cross sections.

damage mechanism, the Fractional Cell Lethality (FCL) is just the probability that a cell has been hit:

$$\text{FCL}(x) = 1 - \phi(x).$$

We assume a time integrated exponential rigidity spectrum for the solar particle events as measured by Freier and Webber (ref. 1) of the form

$$\frac{dJ}{dP} = (J_0/P_0) \exp(-P/P_0)$$

where J_0 and P_0 are characteristic constants of the event and P is the rigidity or momentum per charge of the particle. We now write

$$J(x) = J_0 N(x)$$

and calculate $N(x)$, the number of inactivations per site per incident particle/cm²:

$$N(x) = \int_0^\infty \frac{\exp(-P/P_0)}{P_0} \frac{dP}{dE_1} \frac{dE_1}{dE_2}(x) \sigma_i(E_2) dE_2$$

where P and E_1 are the particle rigidity and energy in free space, E_2 is the particle energy at depth x , and σ_i is the inactivation cross section. The various forms of σ_i that we have assumed are shown as a function of LET in figure 1. The vertical lines indicate the threshold LET values of 30 and 85 keV/ μ . The 30 keV/ μ value seems consistent with the maximum of the RBE curve of Storer et al. (ref. 8) for complete mammalian systems; the 85 keV/ μ value appears reasonable from the experimental probability of injury curve (ref.

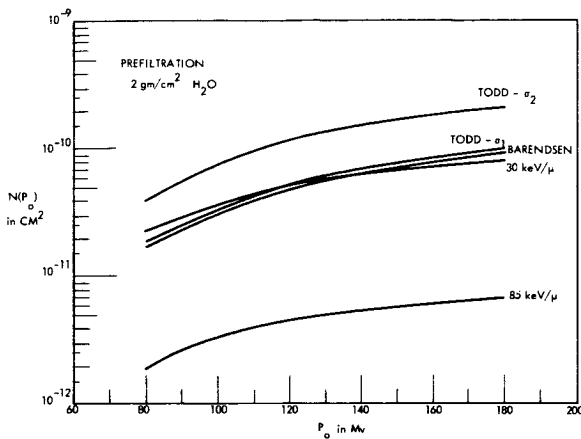


FIGURE 2.—Inactivation hits per cell per incident proton/cm².

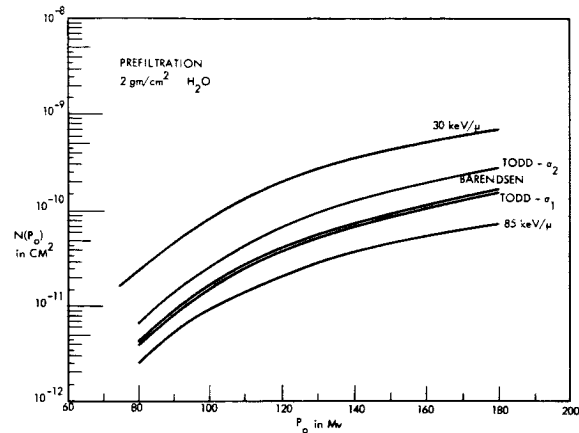


FIGURE 3.—Inactivation hits per cell per incident alpha/cm².

9) for human kidney cells of the strain, T_1 . The assumption made here is that the probability for inactivation is zero until the particles are slowed to an energy such that their LET reaches the threshold value. Then the probability of inactivation jumps to unity. The area of the sensitive region in these cases is assumed to be $100\mu^2$. The Barendsen curve is a smooth curve drawn through the experimental points of "effective cross section" taken from his work (ref. 9) with human kidney cells. The Todd curves are the analytical expressions taken from his work (private communication) on the same strain of kidney cells. The two expressions correspond to the two types of damage mechanisms described by him in a preceding paper in these proceedings.

RESULTS

The function, $N(x)$, has been calculated for various depths, x (1, 2, 5, 10, 20 gm/cm² water), as a function of P_0 . The results for 2 gm/cm² depth of water-equivalent shielding are shown in figures 2 to 4 for protons, alpha particles, and M-group particles. The latter are CNOF nuclei ($6 \leq Z \leq 9$), also found in solar particle events. They are represented here by oxygen, ($Z=8$). The functions, $N(x)$, are probabilities per incident flux expressed in inactivation hits per cell per incident particle/cm², thus giving them the dimension of an area. For a given particle event, with measured P_0 and J_0 , the $N(P_0)$ at a given x is multiplied by J_0

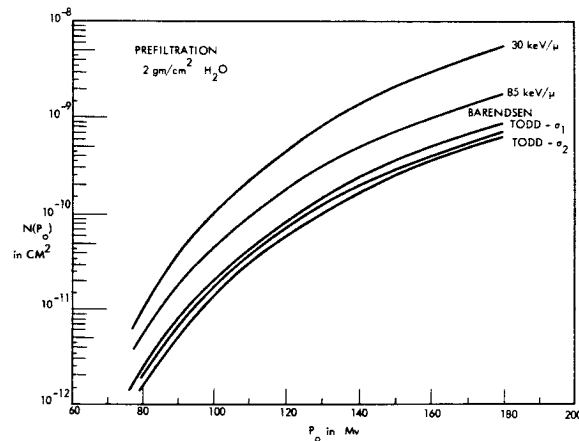


FIGURE 4.—Inactivation hits per cell per incident M-particle/cm².

yielding $J(x)$, the number of inactivation hits per site at depth x .

It should be noted that for large P_0 , the M-particle contribution per particle dominates the alpha and proton contributions. At low P_0 the reverse is true as might be expected, since low P_0 implies fewer high energy particles present relative to low energy particles. Low energy M-particles have very short ranges, and are strongly absorbed in the 2 gm/cm² water shielding.

The experimental data compiled by Webber (ref. 3) on the integral particle spectra for the large solar particle event on 12 November 1960 have been used to yield a J_0 for this event by extrapolation of the exponential dependence

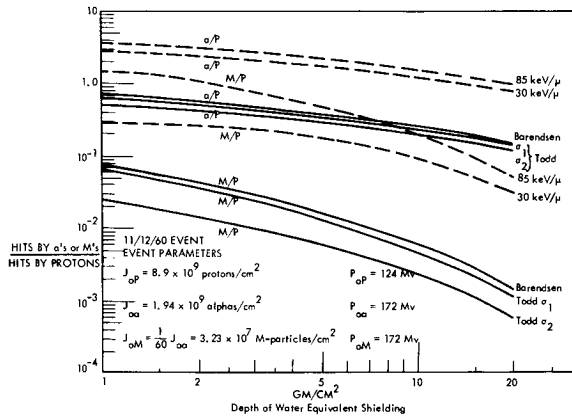


FIGURE 5.—Relative contribution to inactivation hits/cell of alphas and protons and of M-group particles and protons.

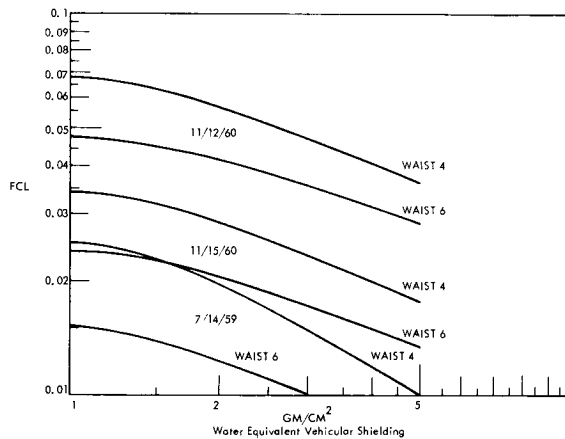


FIGURE 6.—Fractional Cell Lethalities to a seated astronaut during several solar particle events of cycle 19.

on rigidity to zero rigidity. The P_0 is obtained from the slope of the spectrum. If thicknesses less than 1 gm/cm² are considered, the exponential form assumed above may become invalid, as there is some evidence that the flux of very low energy particles exceeds that predicted by an extrapolation of an exponential form (ref. 5). The M-particle spectrum was assumed to have a J_0 one sixtieth the alpha particle J_0 , and a P_0 equal to the alpha particle P_0 (ref. 3).

With the above data, the inactivation hits per cell are calculated as a function of shielding thickness for the 12 November 1960 event. The relative contributions of the alpha and M-group particles to the protons are shown in figure 5. It is seen that for the threshold LET

assumptions, the alpha particle contribution dominates that of the protons. For the more realistic Barendsen and Todd curves, the proton contribution dominates, although both are of the same order of magnitude and remain so even at large shielding thicknesses. The M-group contribution is seen to be down by an order of magnitude from the alpha contribution.

FCL CALCULATION OF A SEATED ASTRONAUT

Calculations of FCL have been made at two body points in a seated astronaut for three of the solar particle events of solar cycle 19. Here the body self-shielding of the astronaut has been considered. We write the number of inactivation hits per site at a body point for the j th particle type as

$$J_j(\text{body point}) = \sum_i f(x_i) J_j(x_i)$$

where $f(x_i)$ is the fractional solid angle that is seen from the body point through a thickness, x_i . These weighting factors have been calculated by Dye (ref. 10) for various points within the seated 75 percentile man. Calculations of FCL at two body points, 4 cm and 6 cm into the body at the waist (right side, 25 cm up from the seat level, on mid-sagittal line), are shown in figure 6 as a function of vehicular shielding for three particle events. We have used the Todd curves here, and his expression for survival S :

$$\begin{aligned} \text{FCL} &= 1 - S \\ &= 1 - \exp(-J_{\sigma_1}) \{1 - [1 - \exp(-J_{\sigma_2})]^n\} \end{aligned}$$

where

$$J_{\sigma_1} = \sum_{j=1}^3 J_j(\text{body point})$$

for Todd's single hit damage mechanism, and J_{σ_2} has a similar form for the multi-hit mechanism. The three terms in this summation are the proton, alpha particle, and M-particle contributions. The exponent, n , may be interpreted as the number of hits necessary to inactivate the cells by the multi-hit mechanism. We have set $n=3$ and have compared the results to those obtained with $n=6$. There is negligible difference since the flux is low and the dominant damage is from the single-hit mechanism at these depths. It is seen from figure 6 that up

to 7 percent of the kidney cells would have been killed had an astronaut experienced one of these events.

The above calculation utilizing the experimental results on kidney cells has been presented simply as an example of the use of the FCL concept. Other organs may well be more critical to the astronaut's health and performance. We make a plea, therefore, for more

experiments like that of Todd, where the probability of damage to cells of other organs is measured as a function of LET. Finally, experiments are needed to relate loss of function to fraction of cells killed.

It is from experiments such as these that the necessary information will be obtained to make a more realistic evaluation of the hazard from the high-LET component of the solar radiation.

REFERENCES

1. FREIER, P. S.; and WEBER, W. R.: J. Geophys. Res., vol. 68, 1963, p. 1605.
2. FREIER, P.: J. Geophys. Res., vol. 68, 1963, p. 1805.
3. WEBER, W. R.: An Evaluation of the Radiation Hazard Due to Solar-Particle Events. Boeing Document D2-90469.
4. BISWAS, S.; FICHEL, C. E.; and GUSS, D. E.: Phys. Rev., vol. 128, 1962, p. 2756.
5. FREIER, P.; and WEBER, W. R.: Science, vol. 142, 1963, p. 1587.
6. Report of the RBE Committee to the ICRP and ICRU, Health Phys. vol. 9, 1963, p. 357.
7. DYE, D. L.; and SHELDON, W. R.: SAE paper 683C, Apr. 1963, or Boeing Document D2-90391, 1963.
8. STORER, J. B.; HARRIS, P. S.; FURCHNER, J. E.; and LANGHAM, W. H.: Radiation Res., vol. 6, 1957, p. 188.
9. BARENDSEN, G. W.; WALTER, H. M. D.; FOWLER, J. F.; and BEWLEY, D. K.: Radiation Res., vol. 18, 1963, p. 106.
10. DYE, D. L.: Health Phys. vol. 9, 1963, p. 749.

N65-346J4

27—Synthesis of Spherical Minimum-Weight Proton Shields¹

J. CELNIK, A. D. KRUMBEIN, and F. R. NAKACHE

United Nuclear Corporation

A systematic method has been developed for minimizing spherical shield weights for protection against proton radiation, including secondary neutron production, subject to various specified dose constraints. Variational methods are applied to a radiation model yielding the choice of optimum shielding materials and their mixtures, together with a prescription for their disposition in a multi-layer spherical shield.

The radiation attenuation model, and its justification, was discussed in reference 1. An extension of the general synthesis theory, described therein, shows that, neglecting secondary neutron production, the optimum materials are polyethylene, carbon, nickel, and tungsten. Analytical expressions for several types of primary dose rates are derived in a subsequent paper by F. R. Nakache. These include average body dose, skin dose, depth dose, and local dose. For example, the constraint that the average body dose must be less than, or equal to, a specified value, \bar{D} , can be written as

$$f(K_0 K_m) = \frac{e}{c} \bar{D} = \bar{f}, \quad (1)$$

where e is the phantom radius and c is a constant which depends only on the characteristics of the incident proton spectrum and aluminum stopping power fits. The function f is an analytic expression in K_0 and K_m , the minimum and maximum equivalent aluminum thicknesses of the shield. These are given by equations (2) and (3).

$$K_0 = \sum_{i=1}^j (A_i - A_{i+1}) r_i - A_j r_0 \quad (2)$$

and

$$K_m = \sum_{i=1}^j (A_i - A_{i+1}) (r_i^2 - e^2)^{1/2} - A_j (r_0^2 - e^2)^{1/2} \quad (3)$$

where r_0 is the inner shield radius, r_i is the outer radius of the i^{th} shield layer, and A_i is the relative proton stopping power of the material in the i^{th} layer to that for aluminum.

To optimize the shield, then, for the average body dose, we construct the Lagrangian given by equation (4).

$$\begin{aligned} L = & \frac{W}{4\pi} + \mu [\bar{f} - f(K_0, K_m)] \\ & + \nu' \left[K_0 - \sum_{i=1}^j (A_i - A_{i+1}) r_i + A_j r_0 \right] \\ & + \eta \left[K_m - \sum_{i=1}^j (A_i - A_{i+1}) (r_i^2 - e^2)^{1/2} \right. \\ & \left. + A_j (r_0^2 - e^2)^{1/2} \right] \quad (4) \end{aligned}$$

where W is the shield weight and μ , ν' and η are Lagrange multipliers.

The minimum weight shield is achieved if equations (1), (2), and (3) are satisfied with μ , ν' and η all positive and $\frac{\partial L}{\partial K_0}$, $\frac{\partial L}{\partial K_m}$ and $\frac{\partial L}{\partial r_i}$ are all set equal to zero. As the optimum materials and their disposition are given by the Young diagram (ref. 1) the optimum proton shield is obtained by solving the variational equations for the r_i . The appropriate optimization equations for various types of dose constraints have been programmed for the CDC-1604A computer.

¹ Research sponsored by George C. Marshall Space Flight Center, NASA, under Contract NAS 8-5277.

For cases in which the man (at the void center) occupies only a small fraction of the inner void volume, so that one can assume a normal incident proton spectrum, the optimization problem is greatly simplified. Once one determines the normal shielding attenuation, K_0 , corresponding to the specified dose constraint of the problem, the shielding materials to be used are given by table I.

TABLE I

K_0/r_0	Shield materials
$K_0/r_0 \geq 1.35$	CH ₂ , C, Ni, W
$1.35 \geq K_0/r_0 \geq 0.15$	CH ₂ , C, Ni
$0.15 \geq K_0/r_0 \geq 0.078$	CH ₂ , C
$0.078 \geq K_0/r_0$	CH ₂

Once the number of materials, j , is known from table I, the layer thicknesses can be readily computed from equation (5)

$$r_i = \frac{K_0 + r_0 A_i}{\sum_{i=1}^j \frac{(A_i - A_{i+1})^{3/2}}{(\rho_i - \rho_{i+1})^{1/2}}} \times \left(\frac{A_i - A_{i+1}}{\rho_i - \rho_{i+1}} \right)^{1/2};$$

$$A_{j+1} = \rho_{j+1} = 0 \quad (5)$$

where ρ_i is the material density of the i^{th} layer.

Another case of particular interest is the case for which the phantom completely fills the void. For this case it can be shown that *all* the materials available on the Young diagram must be used in the minimum weight shield. This result is important in the design of space suits where the astronaut completely fills the "shielded void." In addition, even for a space vehicle, if the man moves around inside the crew compartment, he can be viewed as being uniformly distributed in the available space.

To include the production and subsequent attenuation of secondary neutrons in the variational method, we assume, for simplicity, that the protons are incident normally on the shield. The neutron production cross sections used included production of isotropic evaporation neutrons and of straightahead cascade neutrons. The values used came from the literature and were supplemented by Bertini's calculations at ORNL. Typical curves of neutron production versus equivalent aluminum thickness for the May 10, 1959 solar flare, the February 23, 1956 giant flare, and the Van Allen belt are shown in figures 1 and 2. The curve represents

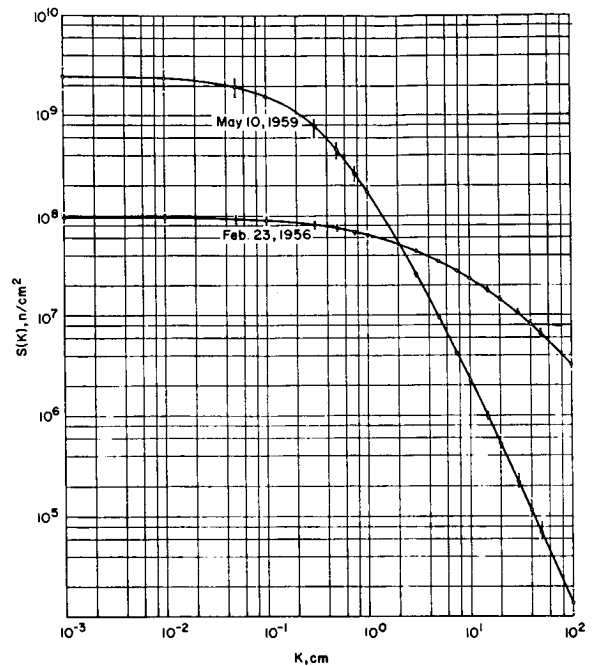


FIGURE 1.—Secondary neutron production in several materials as a function of equivalent aluminum thickness for two solar flare spectra.

aluminum, while the spread shows the deviation for the normalized curves for carbon, copper, tungsten, polyethylene, and phenol formaldehyde (used as an ablative material in heat shields). These curves show that the neutron production in these materials can be assumed to be proportional to the production in aluminum, the proportionality factor, z , being a function of material only. A neutron attenuation factor, y , which is likewise assumed to be a function of material only, is included in the model.

Whereas for the pure proton case a material was completely described by the two parameters A (the proton relative stopping power) and ρ (the density), when secondary neutrons are included there are the two additional parameters z and y (the neutron production and attenuation factors). Thus the "Young diagram" is now generalized to the four-dimensional A, y, z, ρ coordinate system. The materials, and their mixtures (whereas only pure materials are to be used for a pure proton shield, mixtures may be included in a minimum weight shield when secondaries are considered),

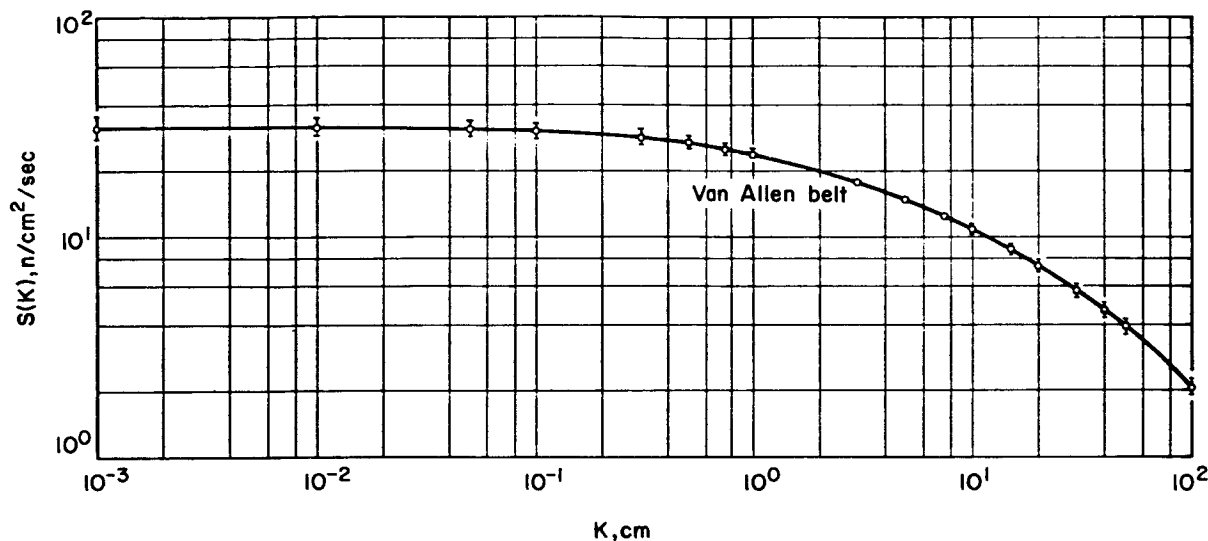


FIGURE 2.—Secondary neutron production in several materials as a function of equivalent aluminum thickness for the Van Allen belt spectrum.

which are to be considered in an optimum shield, together with their disposition, are governed by their location in the generalized Young diagram.

The projection in two dimensions of the hypersurface generated by the six materials, Al, C, Cu, W, CH₂, and C₇H₆O, is shown in figure 3.

The following conclusions can be drawn from figure 3:

1. Phenol formaldehyde is not an optimum shielding material, as it does not appear on the hypersurface.

2. Of the materials considered, only polyethylene may be at the outside of the shield, as it is the only material adjacent to vacuum.

3. Tungsten can only be adjacent to a pure region of copper, or to a mixed region of tungsten and copper. This stems from the synthesis technique, which shows that all materials in adjacent regions must lie on the same tetrahedron. In this case the tetrahedron has decayed into the straight line Cu-W.

4. Three-material mixtures can consist only of combinations of CH₂, C, Al, and/or Cu. (Four-material mixtures are excluded on theoretical grounds.) This stems from the theoretical fact that three-material mixtures must consist of materials lying on the same triangle or tetrahedron of the hypersurface. We note, however, that three-material regions can occur

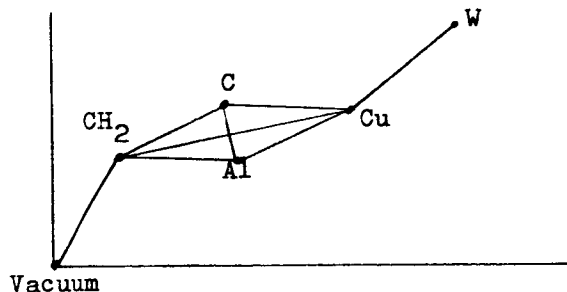


FIGURE 3.—Projection in two dimensions of the four-dimensional Young diagram.

only in relatively complex shields containing five or more regions (inasmuch as in joining two regions it is permissible to add or delete only one material, and the innermost and outermost regions must be composed of pure materials).

The increased reliability of the present cross section data permitted us to optimize more accurately several multilayer shields. The optimization equations are derived in UNC-5049. Some results for two-layer shields are given in table II.

Note that substantial weight savings can be attained for small void shields against relatively hard incident proton spectra. A Cu-CH₂ shield results in a 44% weight saving over an all CH₂ shield. Additional savings can be expected when more materials and more complex shield designs are considered.

Another important contribution of the synthesis technique is that it indicates how one may select the relative size of the void and crewman, and the proper placement of equipment in order to increase the shield effectiveness for a given radiation environment. The technique may also lead to materials, and mixtures,

which might otherwise be neglected by the shield designer.

The methods outlined in this paper can also be expanded to include other primary and secondary radiations, as well as more sophisticated dose and material constraints (e.g., the requirement for a heat shield).

TABLE II

Total Central Dose Constraint: $\bar{D}=25$ rem

Materials		Void Radius, cm.	Outer Radius, cm, of Material		Proton Dose, rem	Neutron Dose, rem	Weight, kg
Inner	Outer		Inner Layer	Outer Layer			
<i>May 10, 1959, Solar Flare</i>							
Al	-----	20	30.71	-----	4.51	20.49	237.0
C	-----	20	31.17	-----	4.81	20.19	206.0
CH ₂	-----	20	33.12	-----	12.57	12.43	109.8
Al	CH ₂	20	20.39	32.70	12.57	12.43	107.5
C	CH ₂	20	21.20	32.19	12.14	12.86	106.0
<i>February 23, 1956, Giant Flare</i>							
Al	-----	20	66.06	-----	16.32	8.68	3170
C	-----	20	68.69	-----	16.52	8.48	2940
Cu	-----	20	38.65	-----	14.29	10.71	1861
CH ₂	-----	20	92.38	-----	22.11	2.89	3009
Al	CH ₂	20	44.60	80.90	18.08	6.92	2616
C	CH ₂	20	49.80	78.60	18.17	6.83	2466
Cu	CH ₂	20	34.15	55.10	15.12	9.88	1688

REFERENCE

1. KRUMBEIN, A. D. ET AL.: Synthesis of Minimum Weight Proton Shields. Proc. Sym. on Protection Against Radiation Hazards in Space. Paper E-9, TID-7652, Atomic Energy Commission, 1962, pp. 773-793.

28—Quality Factors for Degraded Proton Spectra

RICHARD MADEY and THOMAS E. STEPHENSON

Republic Aviation Corporation

Quality factors for degraded proton spectra may be obtained by evaluating the ratio of the dose equivalent (rem) to the absorbed dose (rad). For a monoenergetic proton, the dose equivalent is given by the product of the absorbed dose and a monoenergetic quality factor.

For a spectral distribution of protons incident omnidirectionally on a spherical shell shield, the quality factor for the proton dose absorbed at the center of the shield may be represented by the following analytic formula:

$$QF \text{ (rem/rad)} = 1 - \frac{B_x(q, p)}{B(p, q)} + Q_z \frac{B_x(s, r)}{B(p, q)}$$

where B is a beta function and B_x is an incomplete beta function with the following arguments

$$p = (\gamma + \alpha_0 - 2)/\alpha$$

$$q = (1 + \alpha - \alpha_0)/\alpha$$

$$r = p + b(\alpha_0 - 1)/\alpha$$

$$s = q - b(\alpha_0 - 1)/\alpha$$

The quantity γ is the spectral exponent in a power-law representation of the incident omnidirectional differential energy flux:

$$j \text{ (p/cm}^2\text{-sec-MeV)} = 4\pi C E^{-\gamma}$$

The quantity α is the exponent in a power-law representation of the range-energy relation for protons in the material of the shield:

$$R \text{ (g/cm}^2\text{)} = K E^\alpha$$

For tissue, $\alpha = \alpha_0 = 1.80$.

The quantity b is the exponent in a power-law representation of the relationship between the quality factor for a monoenergetic particle and the linear energy transfer (LET):

$$QF = a \text{ (LET)}^b \quad (\text{LET} \geq 35 \text{ MeV/gm-cm}^{-2} \text{ H}_2\text{O})$$

$$QF = 1 \quad (\text{LET} \leq 35 \text{ MeV/gm-cm}^{-2} \text{ H}_2\text{O})$$

From the recommendation of the RBE Committee (ref. 1) to the International Commissions on Radiological Protection and on Radiological Units and Measurements, we obtain $a = 0.060 \text{ (gm/cm}^2 \text{ H}_2\text{O-MeV)}^b$ and $b = 0.80$. From range-energy tables of Rich and Madey (ref. 2), we find that the LET value of 35 MeV/gm-cm⁻² H₂O corresponds to a 14.3 MeV proton that has a range of 0.226 gm/cm² H₂O. The quantity Q_z in the first equation denotes the value of $a \text{ (LET)}^b$ for a monoenergetic proton that has a range equal to the shield thickness $z \text{ (gm/cm}^2\text{)}$; that is,

$$Q_z = a \text{ (LET)}^b$$

Note that Q_z takes on values less than unity for shield thicknesses z such that $(\text{LET})_z$ is less than 35 MeV/gm-cm⁻² H₂O. For shield thicknesses that stop protons below 14.3 MeV so that $(\text{LET})_z$ is greater than 35 MeV/gm-cm⁻² H₂O, the quantity Q_z is numerically equal to the monoenergetic quality factor.

The parameter x in the incomplete beta functions is

$$x = \frac{R_1}{R_1 + z}$$

where R_1 is the range in the material of the shield of a 14.3 MeV proton.

INTRODUCTION

The RBE Committee Report (1963) to the International Commission on Radiological Protection (ICRP) and to the International Commission on Radiological Units and Measurements (ICRU) introduced the concept of dose equivalent for use in radiation protection (ref. 1). The purpose of the dose equivalent concept is to provide a radiation protection scale that expresses numerically for all ionizing radiations the irradiation incurred by exposed persons. The concept of dose equivalent involves equivalence of the biological effect, or the probability of biological effect rather than equivalence of absorbed energy. The unit of the dose equivalent is the rem. For an external radiation source, the dose equivalent is numerically equal to the absorbed dose in rads multiplied by the quality factor (QF) for the radiation averaged over the absorbed dose in tissue. The quality factor is a function of the linear energy transfer (LET). If the maximum permissible dose (MPD) is viewed as that radiation dose which gives a "just acceptable risk," then the quality factor is the ratio of such maximum permissible doses for two radiations of different qualities. This value of the QF ensures that the risk from a maximum permissible dose of high LET radiation never exceeds the risk from an MPD of the low LET reference radiation. The difficulty with defining the QF as the ratio of MPD's for two radiations of different qualities lies in assigning values to the QF because of lack of data on appropriate risk limiting effects for many body organs.

DERIVATION

We want to derive an analytic expression for the quality factor averaged over the dose of protons absorbed in tissue at the center of a spherical shell shield bombarded by a spectral distribution of omnidirectionally incident protons. The dose-equivalent rate $d(DE)/dt$ is

given by the following integral:

$$\begin{aligned} \frac{d(DE)}{dt} &= \int_0^{\infty} \text{QF}(R) S_0(R) j'(R, z, t) dR \\ &= \overline{\text{QF}} \int_0^{\infty} S_0(R) j'(R, z, t) dR \end{aligned}$$

where $j'(R, z, t)$ represents the omnidirectional differential (in range) flux of protons emerging from the shield of thickness z at any time t , $S_0(R)$ is the stopping power of tissue expressed as a function of the proton range R , and $\overline{\text{QF}}$ is the mean absorbed-dose quality factor at any given instant of time. As defined by the right-hand member of equation (1), the mean quality factor is given by the ratio of the dose-equivalent rate to the absorbed dose rate.

As described in the Report of the RBE Committee (1963) to the International Commissions on Radiological Protection and on Radiological Units and Measurements (ref. 1), the dose-equivalent formulation was introduced for use in radiation protection. The monoenergetic quality factor (QF) is a function of the linear energy transfer (LET). For the determination of permissible tissue doses in rads from external radiation sources, the RBE Committee (1963) to the ICRP and the ICRU has recommended that the monoenergetic quality factor (QF) be related to the LET in water in accordance with table I. Table I implies that the QF for X- and gamma-rays is in practice close to unity and for electrons is greater than unity only at very low energies. It is of interest to note that the recommended QF values in table I imply a QF of unity independent of energy for protons above 14.3 MeV. From the stopping power tabulation of Rich and Madey (1954), the LET_{∞} for a 14.3 MeV proton is 35 MeV/gm-cm⁻² of water (ref. 2); in table I, this LET_{∞} value corresponds to a unity quality factor. Similarly, the LET_{∞} for a 6 MeV proton, for example, is 7.0 keV per micron of water; in table I, this LET_{∞} value is associated with a recommended QF value of 2. Similarly, a

TABLE I

Relationship Between Linear Energy Transfer (LET) and Quality Factor (QF)

[LET_∞ is the same as the "stopping power." The "restricted stopping power" would be indicated by a numerical subscript; e.g., LET₁₀₀ refers to the LET when tracks from secondary particles with energies greater than 100 eV are counted as separate tracks]

LET _∞		QF
(MeV/gm-cm ⁻² H ₂ O)	(keV/μ in water)	
35 or less.....	3.5 or less.....	1
35-70.....	3.5-7.0.....	1- 2
70-230.....	7.0-23.....	2- 5
230-530.....	23-53.....	5-10
530-1750.....	53-175.....	10-20

2 MeV proton has a LET_∞ of 16.7 keV/μ (H₂O) and an associated QF of 3.8.

In figure 1, we have constructed a log-log plot of the monoenergetic quality factor as a function of LET (in units of MeV/gm-cm⁻² H₂O). As shown by the solid lines, we find that these data may be well represented by the following relationship:

$$QF = a S_0^b \quad (\text{for } S_0 \geq S_{01}) \quad (2a)$$

$$QF = 1 \quad (\text{for } S_0 \leq S_{01}) \quad (2b)$$

where $b = 0.80$, $a = 0.060 \text{ (gm/cm}^2\text{-MeV)}^b$, and S_{01} denotes the value of S_0 corresponding to a quality factor of unity. Since S_{01} equals 35 MeV/gm-cm⁻² H₂O, the corresponding proton kinetic energy T_1 equals 14.3 MeV and the corresponding proton range R_1 equals 0.226 gm/cm² H₂O.

Based on this power-law representation of the quality factor for a monoenergetic particle, we may rewrite equation (1) for the dose-equivalent rate:

$$\frac{d(DE)}{dt} = a \int_0^{R_1} S_0^{b+1} j'(R, z) dR + \int_{R_1}^{\infty} S_0 j'(R, z) dR \quad (3)$$

The emergent spectrum j' is related to the incident spectrum j through the differential

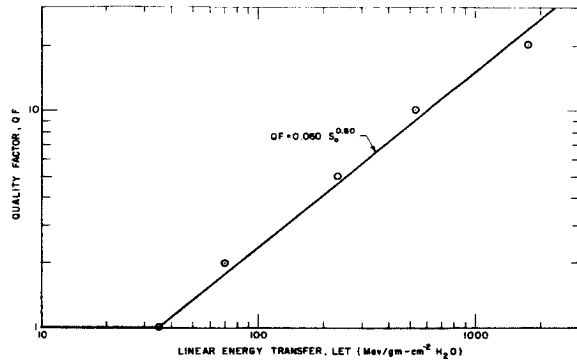


FIGURE 1.—The monoenergetic quality factor versus the linear energy transfer.

relationship

$$j'(R, z) = j(R + z) \quad (4)$$

provided that attenuation of protons by nuclear collisions can be neglected, and provided also that the direction of motion of the protons is unchanged by the slowing down process by electronic collisions. This differential relationship is a consequence of the fact that the number of protons $j'(R, z)dR$ emerging from a shield thickness z (gm/cm²) with a residual range between R and $R + dR$ must be equal to the number of protons incident with a residual range between $z + R$ and $z + R + dR$. Hence, equation (3) may be rewritten:

$$\frac{d(DE)}{dt} = a \int_0^{R_1} S_0^{b+1} j(R + t) dR + \int_{R_1}^{\infty} S_0 j(R + t) dR \quad (5)$$

We shall evaluate the integrals in equation (5) on the basis of the following approximations:

(1) The differential flux spectrum of the omnidirectionally incident protons is representable by a power law of the form:

$$j(p/cm^2\text{-sec-MeV}) = 4\pi CT^{-\gamma} \quad (\text{for } T > T_c) \quad (6)$$

where the coefficient C (cm⁻²-sec⁻¹-steradian⁻¹-MeV^{-γ}) and the differential spectral exponent γ may be functions of time. Since the power-law representation, equation (5), diverges as the proton kinetic energy approaches zero, we note that this representation is valid above some cutoff energy T_c .

(2) The range-energy relation for protons in matter is representable by a power law of

the form

$$R \text{ (gm/cm}^2\text{)} = KT^\alpha \quad (7)$$

where the constants K (gm/cm²-MeV ^{α}) and α depend on the material.

On the basis of the power-law representations, equations (6) and (7), the incident omnidirectional differential range spectrum is given by

$$j(R) = \bar{j}[T(R)]dT/dR = 4\pi C\alpha^{-1}K^\beta R^{-(\beta+1)} \quad (\text{for } R > R_c) \quad (8)$$

where R_c is the cutoff range corresponding to the cutoff energy T_c , and

$$\beta \equiv (\gamma - 1)/\alpha \quad (9)$$

In view of equation (4), we may now write down the following expression for the emergent spectrum:

$$j'(R) = j(R+z) = 4\pi C\alpha^{-1}K^\beta (R+z)^{-(\beta+1)} \quad (\text{for } z > R_c). \quad (10)$$

In order to perform the integration over the residual range variable in equation (5), we first convert the specific ionization S_0 in tissue into the equivalent specific ionization in material of the shield. From equation (7), we may write

$$T = (R/K)^{1/\alpha} = (R_0/K_0)^{1/\alpha_0} \quad (11)$$

where the zero subscripts denote values in tissue. Hence

$$S_0 \equiv dT/dR_0 = (\alpha_0 K_0)^{-1} (R_0/K_0)^{-(\alpha_0-1)/\alpha_0} \\ = -(\alpha_0 K_0)^{-1} (R/K)^{-(\alpha_0-1)/\alpha} \quad (12)$$

Thus, substitution of equations (10) and (12) into equation (5) gives for the dose-equivalent rate

$$\frac{d(DE)}{dt} = \frac{a4\pi CK^{\beta+\epsilon}}{\alpha(\alpha_0 K_0)^{\beta+1} z^{\beta+1}} \int_0^{R_1} \frac{dR}{R^\epsilon [1+(R/z)]^{\beta+1}} \\ + \frac{4\pi CK^{\beta+\nu}}{\alpha_0 K_0 \alpha z^{\beta+1}} \int_{R_1}^\infty \frac{dR}{R^\nu [1+(R/z)]^{\beta+1}} \quad (13)$$

where

$$\epsilon \equiv (\alpha_0 - 1)(\beta + 1)/\alpha = \nu(\beta + 1) \quad (14)$$

and

$$\nu \equiv (\alpha_0 - 1)/\alpha \quad (15)$$

$$\epsilon - \nu = b\nu = b(\alpha_0 - 1)/\alpha \quad (16)$$

Let

$$R/z \equiv y \quad (17)$$

Then

$$\frac{d(DE)}{dt} = \left[\frac{4\pi C}{\alpha\alpha_0 K_0} \left(\frac{K}{z}\right)^\nu \right] \left[\frac{a}{(\alpha_0 K_0)^\beta} \left(\frac{K}{z}\right)^{\beta\nu} \right. \\ \left. \int_0^{R_1/z} \frac{y^{\nu-1} dy}{(1+y)^{\epsilon+\nu}} + \int_{R_1/z}^\infty \frac{y^{\nu-1} dy}{(1+y)^{\epsilon+\nu}} \right] \quad (18)$$

where

$$p \equiv \beta + \nu = (\gamma + \alpha_0 - 2)/\alpha \quad (19)$$

$$q \equiv 1 - \nu = (1 + \alpha - \alpha_0)/\alpha \quad (20)$$

$$p + q = \beta + 1 = (\gamma + \alpha - 1)/\alpha \quad (21)$$

$$r = p + b\nu \quad (22)$$

$$s = q - b\nu \quad (23)$$

$$r + s = p + q = \beta + 1 \quad (24)$$

We shall now show that the common factor in equation (18) is proportional to the dose rate of protons absorbed in tissue at the center of the spherical shell shield. The omnidirectional integral flux spectrum of protons incident on the shield is

$$J(>z) \equiv \int_z^\infty j(R) dR \\ = \frac{4\pi C}{(\gamma-1)} \left(\frac{K}{z}\right)^{(\gamma-1)/\alpha} = \frac{4\pi C}{\beta\alpha} \left(\frac{K}{z}\right)^\beta \quad (25)$$

Hence, the factor

$$\frac{4\pi C}{\alpha\alpha_0 K_0} \left(\frac{K}{z}\right)^\nu = \beta(S_0)_z J(>z) \quad (26)$$

where we see from equation (12) that $(S_0)_z$ is the specific ionization energy loss in tissue for a monoenergetic proton of kinetic energy T_z that can just penetrate the shield of thickness z (gm/cm²).

Equation (18) may now be rewritten:

$$\frac{d(DE)}{dt} = \beta(S_0)_z J(>z) [Q_z I_1 + I_2] \quad (27)$$

where

$$Q_z \equiv \frac{a}{(\alpha_0 K_0)^\beta} \left(\frac{K}{z}\right)^{\beta\nu} = a(S_0)_z^2 \quad (28)$$

$$I_1 \equiv \int_0^{R_1/z} \frac{y^{\nu-1} dy}{(1+y)^{\epsilon+\nu}} \quad (29)$$

and

$$I_2 \equiv \int_{R_1/z}^{\infty} \frac{y^{q-1} dy}{(1+y)^{q+p}} \quad (30)$$

Note that Q_z takes on values less than unity for shield thicknesses z such that $(S_0)_z$ is less than S_{01} ($=35$ MeV/gm-cm² H₂O). For shield thicknesses that stop protons below T_1 ($=14.3$ MeV) so that $(S_0)_z$ is greater than S_{01} ($=35$ MeV/gm-cm² H₂O), the quantity Q_z is numerically equal to the monoenergetic quality factor given by equation (2a).

In the integrals I_1 and I_2 , let

$$y \equiv x/(1-x) \quad (31)$$

Then

$$I_1 = \int_0^{x_1} x^{s-1}(1-x)^{r-1} dx \equiv B_{x_1}(s, r) \quad (32)$$

and

$$I_2 = \int_{x_1}^{\infty} x^{q-1}(1-x)^{p-1} dx = B(q, p) - B_{x_1}(q, p) \quad (33)$$

where

$$x_1 \equiv \frac{R_1/z}{1+R_1/z} = \frac{R_1}{R_1+z} \quad (34)$$

and equation (32) defines the incomplete beta function, denoted by B_x . The complete beta function denoted simply by B is the value of the integral in equation (32) when the upper limit x is infinite. Note that $B(q, p) = B(p, q)$ but that $B_x(q, p) \neq B_x(p, q)$.

In view of equations (32) and (33), equation (27) may now be rewritten:

$$\frac{d(DE)}{dt} = \frac{dD}{dt} \left[1 - \frac{B_{x_1}(q, p)}{B(p, q)} + Q_z \frac{B_{x_1}(s, r)}{B(p, q)} \right] \quad (35)$$

where, as Madey (1963) has shown in a previous paper (ref. 3), the dose rate of protons absorbed in tissue at the center of the spherical shell shield is

$$\begin{aligned} \frac{dD}{dt} &\equiv \int_0^{\infty} S_0 j'(R, z) dR = \bar{S}_0 J(>z) \\ &= \beta(S_0)_z B(p, q) J(>z) \end{aligned} \quad (36)$$

with

$$\begin{aligned} \beta(S_0)_z B(p, q) &= \bar{S}_0 \\ &= \int_0^{\infty} S_0 j'(R, z) dR / \int_0^{\infty} j'(R, z) dR \end{aligned} \quad (37)$$

Hence, combining equations (1) and (35), we obtain the following result:

$$\overline{QF} = 1 - \frac{B_{x_1}(q, p)}{B(p, q)} + Q_z \frac{B_{x_1}(s, r)}{B(p, q)} \quad (38)$$

INTERPRETATION

We have calculated from equation (38) and plotted in figure 2 for typical proton spectra found in space the quality factor at the center of a water sphere for omnidirectionally incident proton spectra as a function of the size of the sphere expressed in terms of the kinetic energy of a proton that comes to rest after penetrating a distance equal to the radius of the sphere. It is necessary to multiply the absorbed dose (in rads) by the quality factor averaged over the absorbed dose to obtain the dose-equivalent (in rems) of the proton radiation reaching the center of the sphere.

Equation (3) expresses the dose-equivalent rate as the sum of two terms. The first term gives the contribution to the dose-equivalent rate from that portion of the degraded proton spectrum with residual ranges less than R_1 , whereas the second term gives the contribution from protons with residual ranges greater than R_1 . The high residual range portion of the degraded spectrum corresponds to the low LET fraction of the degraded spectrum. Since the dose rate absorbed in tissue is identical with the dose equivalent rate for the portion of the residual range spectrum above R_1 , the quality factor for the low LET fraction so defined is identically equal to unity. The portion of the residual range spectrum below R_1 gives the high LET fraction of the degraded spectrum. The mean quality factor for this high LET fraction is given by

$$\overline{QF}_h = a \int_0^{R_1} S_0^{h+1} j'(R, z) dR / \int_0^{R_1} S_0 j'(R, z) dR \quad (39)$$

$$\overline{QF}_h = \frac{(dD/dt) Q_z B_{x_1}(s, r) / B(p, q)}{(dD/dt)_h} \quad (40)$$

where the integral in the numerator of equation (39) has been evaluated previously, and the integral in the denominator of equation (39) is the absorbed dose for the high LET fraction,

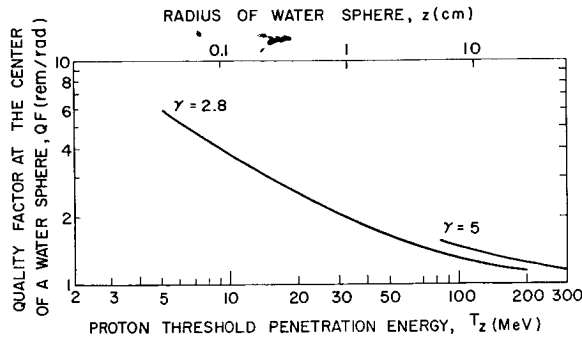


FIGURE 2.—Quality factor at the center of a water sphere for omnidirectionally incident proton spectra in space (with $\gamma=2.8$ and $\gamma=5$) versus the threshold proton energy for penetration to the center of the sphere.

namely,

$$\begin{aligned} \left(\frac{dD}{dt}\right)_h &= \int_0^{R_1} S_0 j(R+z) dR \\ &= \beta(S_0)_z J(>z) B_{x_1}(q, p) \quad (41) \\ &= \bar{S}_0 J(>z) \frac{B_{x_1}(q, p)}{B(q, p)} = \left(\frac{dD}{dt}\right) \frac{B_{x_1}(q, p)}{B(q, p)} \end{aligned} \quad (42)$$

Hence

$$(\overline{QF})_h = Q_z B_{x_1}(s, r) / B_{x_1}(q, p) \quad (43)$$

Let us now calculate the relative contributions to the total dose rate of the high and low LET fractions of the degraded proton spectra.

$$\dot{D} = \dot{D}_h + \dot{D}_l \quad (44)$$

$$\frac{\dot{D}_l}{\dot{D}} = 1 - \frac{\dot{D}_h}{\dot{D}} = 1 - \frac{B_{x_1}(q, p)}{B(q, p)} \quad (45)$$

The right-hand member of equation (45) follows from equation (42).

In view of equations (43) and (45), we may rewrite equation (38) for the mean quality factor as follows:

$$\overline{QF} = \frac{\dot{D}_l}{\dot{D}} + (\overline{QF})_h \frac{\dot{D}_h}{\dot{D}} \quad (46)$$

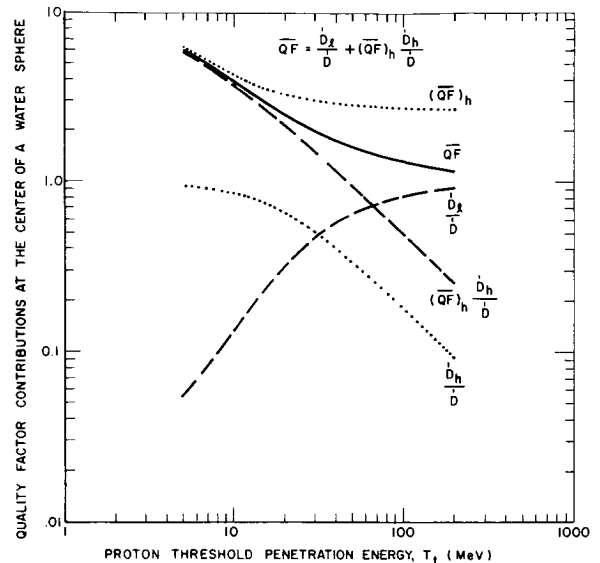


FIGURE 3.—Relative contributions to the quality factor at the center of a water sphere for an omnidirectionally incident proton spectrum (with $\gamma=2.8$) versus the threshold proton energy for penetration to the center of the sphere.

Hence, the mean quality factor has been decomposed into contributions from the low LET and the high LET portions of the degraded proton spectra. The low LET contribution to the mean quality factor is just the fraction of the absorbed dose rate contributed by the low LET portion which has been chosen to have a unity quality factor. The high LET contribution to the mean quality factor is the fraction of the absorbed dose rate contributed by the high LET fraction multiplied by the mean quality factor for the high LET fraction of the degraded spectrum.

The relative contributions to the mean quality factor from the high LET and low LET portions of a degraded spectrum at the center of a water sphere bombarded by a solar proton flux with a spectral exponent $\gamma=2.8$ are plotted in figure 3 as a function of the sphere radius z measured in terms of the proton threshold penetration energy T_z .

REFERENCES

1. Report of the RBE Committee to the ICRP and ICRU. Health Phys., vol. 9, 1963, p. 357.
2. RICH, MARVIN; and MADEY, RICHARD: Range-Energy Tables, Univ. Calif. Radiation Lab. Rept. UCRL-2301.
3. MADEY, RICHARD: A Useful Formula for Calculating Space Proton Dose Rates. Trans. Am. Nucl. Soc., no. 60 (1), 1963, p. 194.

65-34606

29—Radiation Spectrometry in Space: Requirements for Accurate Dose Determinations¹

BENTON C. CLARK

Air Force Weapons Laboratory

Calculating radiation dose levels in space has been an engaging pastime for a large number of groups ever since Van Allen's discovery of the extra-atmospheric radiation zones. Undoubtedly, a strong motivation in studying the energetic particles in these zones is to elucidate the nature of the hazard posed to manned space travel. But although scores of instruments have been flown on satellites, there appears to have been little attempt to design these instruments with quantitative optimization procedures aimed at maximizing the usefulness of collected data as inputs to dose calculations. The marked increase in sophistication which can now be realized allows one to do this. In this paper, an analysis is performed to find relationships between dose-calculation errors and radiation measurement errors. Throughout, it is assumed that the dose calculation itself is without error (a strong assumption indeed!) in order to isolate the requirements on the basic data itself. It is found, in general, that errors in critical experiment parameters are magnified considerably because of the functional form of the dependence of dose on energy spectrum and on parameters such as count-rate and energy threshold.

ERROR DEPENDENCIES OF DOSE UPON SPECTRUM PARAMETERS

Recently, a group of excellent data has been published on the flux levels and energy spectra of the particles in space: geomagnetically trapped electrons (ref. 1), trapped protons (refs. 2 and 3), and solar flare protons (ref. 4). A very convenient factor common to all these

¹ The views and conclusions expressed in this paper are those of the author and are not intended to reflect official views of the U.S. Air Force.

data is that in each case the experimental spectra are best fitted analytically by an exponential function. These functions may be written in the form:

$$N(E)dE = N_0 \exp(-E/E_0)dE \quad \text{for trapped particles} \quad (1)$$

$$N(P)dP = N_0 \exp(-P/P_0)dP \quad \text{for solar protons} \quad (2)$$

where

E = particle energy

P = particle rigidity (momentum-to-charge ratio)

P_0 and E_0 = a characteristic constant defining the slope of the spectrum

N_0 = number of particles per unit energy (or rigidity) at zero energy

$N(E)dE$ = number of particles having energy E to $E+dE$

Whence, the total flux of particles, Φ , is given by

$$\begin{aligned} \Phi &= \int_0^{\infty} N(E)dE \\ &= N_0 E_0 \quad \text{for trapped particles} \\ &= N_0 P_0 \quad \text{for solar protons} \end{aligned}$$

At this time there is no known physical basis for a *a priori* prediction of exponential spectra. The experimental facts suggest that such bases may be found. However, it is to be noted that the exponential form generally holds only for a portion which contributes the dose in shielded space vehicles.

The problem we wish to address ourselves to is determining the dependence of the calculated dose, S , upon the critical parameters E_0 and Φ (or $N_0 E_0$). If, for a spacecraft of given geometry and for a specified dose point within the body, the dose for one particle/cm² of energy

E is described by the function $s(E)$, then

$$S(E_0, N_0E_0) = \int_0^\infty s(E)N(E)dE \quad (3)$$

By substituting equation (1) for $N(E)$, and then differentiating both sides of (3) with respect to E_0 and N_0E_0 , and dividing by (3), one obtains

$$\frac{dS}{S} = \frac{d(N_0E_0)}{N_0E_0} + \frac{dE_0}{E_0} \left[\frac{1}{E_0} \int_0^\infty Es(E)N(E)dE - E_0 \int_0^\infty s(E)N(E)dE \right] \quad (4)$$

and we see that the error in calculated dose, dS/S , is equal to the error in the measured flux, $d(N_0E_0)/N_0E_0$ plus a weighted value of the error in e -fold constant, dE_0/E_0 . One reason for carrying out the analysis below is that the quantity in brackets generally turns out to be greater than one. For future reference, we shall call the bracketed quantity the "shape magnification factor," and denote it by m :

$$\frac{dS}{S} = \frac{d(N_0E_0)}{N_0E_0} + m \frac{dE_0}{E_0} \quad (4a)$$

DOSE CALCULATIONS

Since the shape factor, m , is a measure of the ultimate accuracy to be obtained in a given dose calculation, it is of interest to calculate $s(E)$, and thence m , for a number of typical cases. The dose calculation itself is not without error, for the interaction models must necessarily be simplifications of the real situation. However, the calculations are conducted with sufficient sophistication to yield useful values of m . Wherever possible, experimental data are used to supplement or supplant the calculations.

Bremsstrahlung

The dose-rate from bremsstrahlung radiation (X-rays produced by electrons stopping in a material) is very high in the low-central region of the inner belt. A formulation of the bremsstrahlung dose calculation, using experimental results of thick-target studies, is given in reference 5. For simplicity, we shall calculate the dose, $s(E)$, for an electron of energy E by

performing

$$s(E) = 2kKZ \int_0^E (E-E') \exp[-u'(E', Z)T] u(E') dE' \quad (5)$$

where k and K are constants (ref. 5)

E' = energy of bremsstrahlung photon

T = shield thickness

u' = attenuation or absorption coefficient of photons in the absorber (ref. 6)

u = absorption coefficient of photons in human muscle tissue

Z = atomic number of the absorber

Since the angular distributions of the incident electrons and the secondary photons are not considered, this calculation applies only for the dose at the center of spherical shell absorbers with the assumption that the bremsstrahlung radiation is all produced "straight-ahead."

In figures 1 and 2, calculated values of $s(E)$ are compared with experimental measurement (ref. 5, data revised), in which electrons were incident from all angles. Calculations were performed for both pure attenuation and pure photo-electric effect, to try to allow for the effects of photon scattering. An interesting result is that the values plot an almost straight line on the log-log graph, especially the experimental values. This was found to hold for all cases considered, which means

$$s(E) \approx gE^\gamma \quad (6)$$

where g and γ depend on T and Z only. If this relation is substituted for $s(E)$ in the brackets in (4), and the integration performed, the following result is obtained

$$m = \frac{\Gamma(\gamma+2)}{\Gamma(\gamma+1)} - 1 \quad \text{for } \gamma > 0$$

where Γ is the standard Gamma Function. Hence,

$$m = \gamma$$

Thus, for the special relationship of equation (6), the shape factor m is independent of E_0 . In figures 3, 4, and 5, computed values of m are

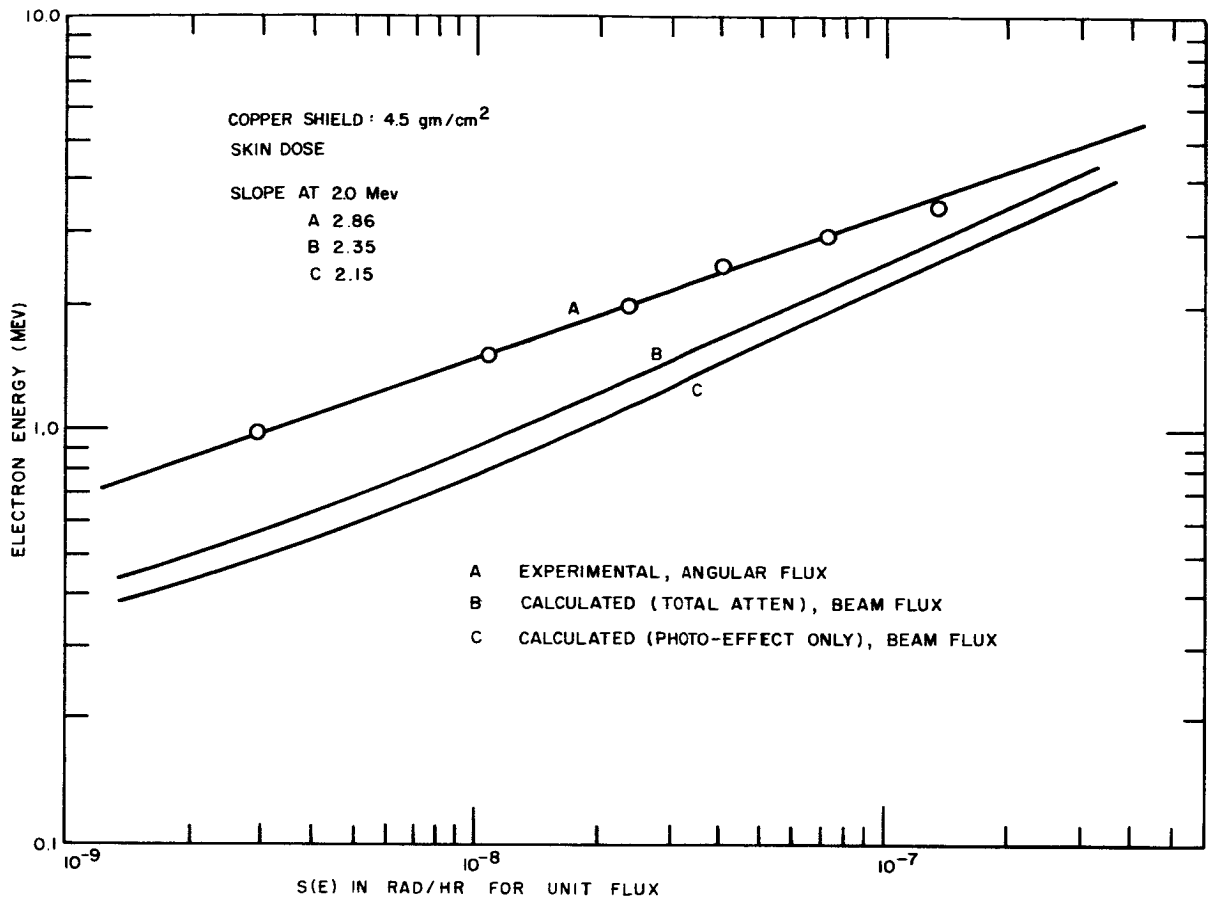


FIGURE 1.—Bremsstrahlung radiation: comparison of calculated values of skin dose $s(E)$, using copper shield 4.5 gm/cm² (beam flux), with values obtained by experimental measurement (angular flux).

presented and it is seen that for bremsstrahlung radiation, m is indeed not very sensitive to the value of E_0 .

A second important result can be obtained by manipulating equation (4). Replacing the brackets by γ (the value of m), and integrating,

$$\ln S = \ln N_0 E_0 + \gamma \ln E_0 + \ln c$$

where $\ln c$ is a constant of integration. Thus,

$$S = c(N_0 E_0)(E_0)^\gamma \quad (7)$$

Penetrating Electrons

For shield thicknesses below a few gm/cm², energetic electrons may penetrate and produce serious skin burns. The model for calculating electron doses is simply to assume that there

is a cut-off energy, E_c , above which all electrons produce an equal dose, regardless of energy, and below which the electrons cannot penetrate. The value of E_c is the energy of the electron whose maximum range is the shield thickness, T . For E_c above a few hundred keV,

$$E_c \text{ (MeV)} \approx 2T \text{ (gm/cm}^2\text{)}$$

In spite of its simplicity, this model has proved to be quite satisfactory for low- Z absorbers and an electron spectrum with E_0 about 1200 keV (ref. 5). Thus, assuming

$$s(E) = \text{const} \quad E > E_c \\ = 0 \quad E < E_c$$

and performing the integration to find m from

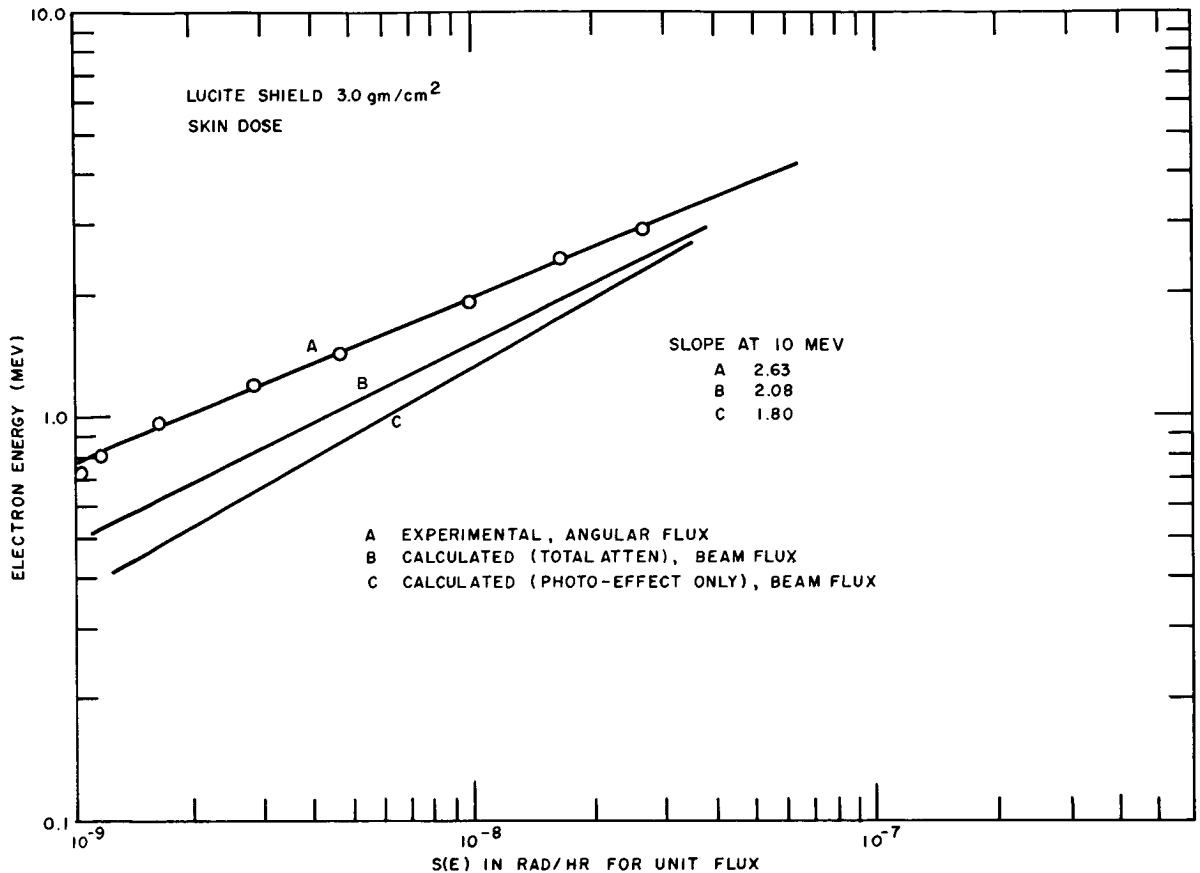


FIGURE 2.—Bremsstrahlung radiation: comparison of calculated values of skin dose $s(E)$, using lucite shield 3.0 gm/cm² (beam flux), with values obtained by experimental measurement (angular flux).

the bracketed expression of equation (4),

$$m = \frac{E_c}{E_0} \quad (8)$$

Note that when $E_c < E_0$, m can actually be less than one. The maximum observed value of E_0 for electrons in space is about 1500 keV (ref. 1), so that for shielding thicknesses above 0.75 gm/cm², m will always be greater than one. At 1.5 gm/cm², the shape magnification factor has a value of at least 2 for penetrating electrons in all regions of space.

Placing the result of equation (8) into equation (4a) and integrating, the relation between penetrating electron dose and the spectral parameter E_0 is obtained:

$$S = c\Phi \exp(-E_c/E_0)$$

Protons

The proton dose in tissue behind a shield of thickness T can be calculated from the value of the stopping power, dE/dx , in tissue and the shield material (the stopping power formula is available in almost any text on nuclear physics) from the relation,

$$s(E) = k \frac{dE}{dx} (E', \text{ tissue})$$

$$E' = E - \int_0^T \frac{dE}{dx} (E, \text{ shield material}) dx$$

where k is a constant whose value depends upon the units. In figure 6, $s(E)$ is plotted for a plane-slab calculation in which the radiation was assumed to be normal to the slab (this is equivalent to the spherical shell geometry where the dose-point is at the center of a tissue

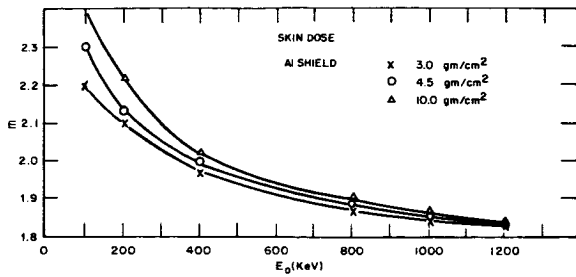


FIGURE 3.—Bremsstrahlung radiation: computation of 'shape magnification factor' m , for Al shield 3.0, 4.5 and 10.0 gm/cm².

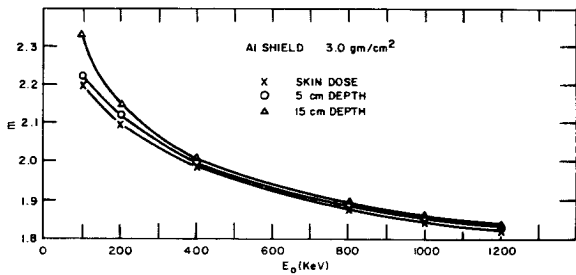


FIGURE 4.—Bremsstrahlung radiation: computation of 'shape magnification factor' m , with Al shield 3.0 gm/cm²; for skin dose, dose at 5 cm depth, and dose at 15 cm depth.

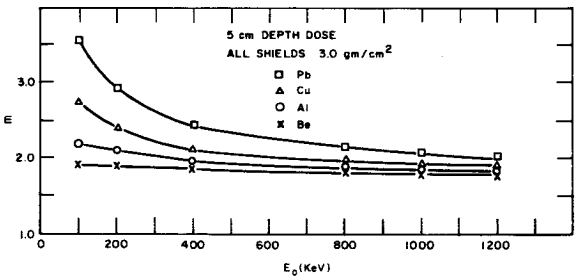


FIGURE 5.—Bremsstrahlung radiation: computation of 'shape magnification factor' m , for 5 cm depth dose, with all shields at 3.0 gm/cm².

sphere of radius equal to the quoted depth). It turns out that $s(E)$ has no convenient analytic fit. Figure 7 plots $s(E)N(E)$ for two values of E_0 . It is apparent that the dose, S , is not appreciably different at the skin for the two spectra. However, at 15 cm depth, S is strikingly dependent upon E_0 . This points out the fact that m will generally be a strong function of shield thickness and geometry.

In viewing the relatively complex problem of calculating the dose field inside a man who

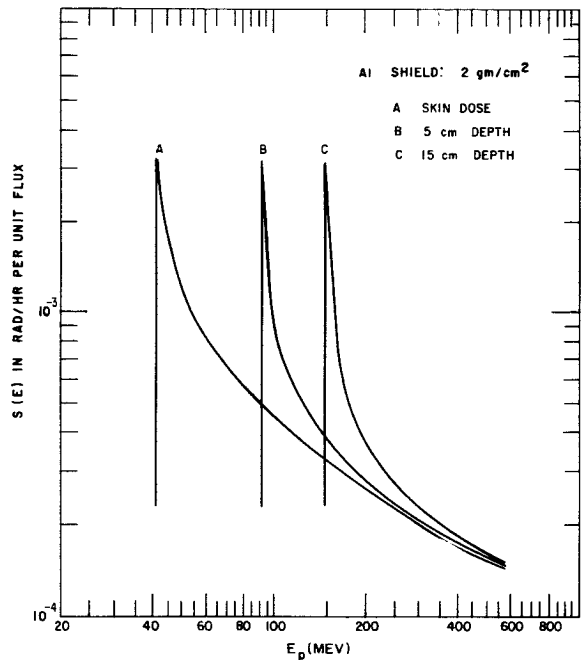


FIGURE 6.—Proton radiation: dose, $s(E)$ plotted for a plane-slab calculation in which radiation is assumed to be normal to the slab.

in turn is inside an odd-geometry shield, it is obvious that it is difficult to obtain generalized solutions. This was possible to an extent in treating bremsstrahlung and penetrating electron doses. However, calculations of proton doses using the geometry described above yield markedly different results than calculations based upon the detailed geometry of body self-shielding and external shields (private communication with D. A. Adams). It is therefore of little use to calculate m for simple cases. Determinations must be made with sophisticated computer runs on the complicated geometries of interest by varying E_0 and comparing results.

The value of $(m+1)$ as given by equation (4) is just \bar{E}/E_0 , where \bar{E} is the first energy moment of the distribution $s(E)N(E)$. Now, since a given shield stops all protons below a critical energy, E_c , the value of \bar{E} must be in any case greater than E_c . We can say, then

$$m > \frac{E_c}{E_0} - 1$$

From this relation, we can compute minimum values of m for given depths in the human

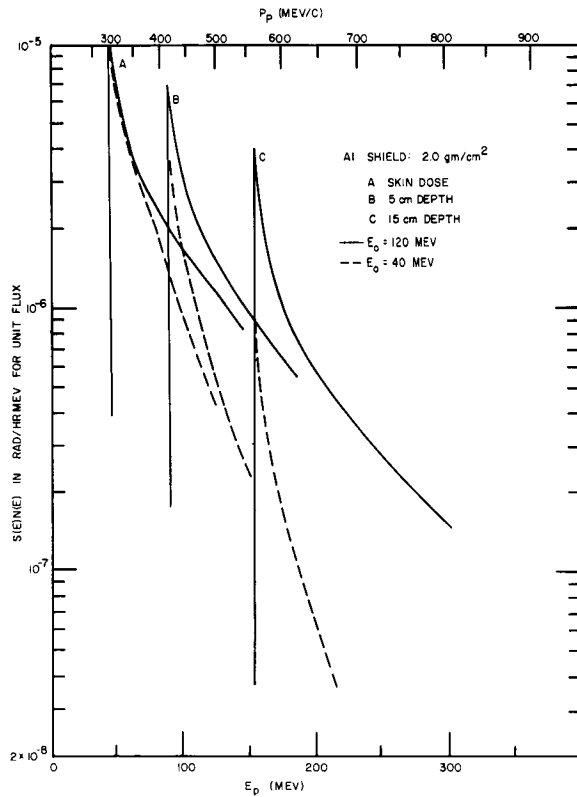


FIGURE 7.—Proton radiation: computation of $s(E)N(E)$ for two values of E_0 .

body and given E_0 's. Table I presents such results, which, it is to be noted, are independent of the detailed geometry of the external shields. A similar analysis can be carried out for solar proton beams, with $(m+1)$ greater than P_c/P_o . Since P_o 's are usually quite small, the shape magnification factors will be high for solar proton events.

The data on the inner-belt proton spectrum parameter, E_0 , are best fitted by the equation

$$E_0 = aL^{-b} \tag{9}$$

where L is the geomagnetic shell on which E_0 is measured and a and b are constants (refs. 2 and 3). Taking the logarithm of (9) and differentiating,

$$\frac{dE_0}{E_0} = \frac{da}{a} - db \ln L - b \frac{dL}{L} \tag{10}$$

From reference 3, the data fits only within $da/a = \pm 11\%$ and $db = \pm 20\%$. When using

TABLE I

Minimum Shape Magnification Factors in the Human Body for Inner Belt Proton Fluxes

Depth in body, cm	Minimum value of m for E_0 (MeV) equals—		
	40	80	120
2	0.2	0	0
5	.95	0	0
10	1.9	.45	0
15	2.6	.8	.2

equation (9) for dose calculations, E_0 is uncertain by at least $\pm 19\%$ at $L=1.5$ earth radii (the heart of the inner belt). The uncertainty is, in actual fact, probably much greater since the experiment reported in reference 3 did not establish E_0 for high energies. Data from reference 2 cover somewhat higher energies, but likewise indicate a higher value for a .

ERROR DEPENDENCES OF SPECTRUM PARAMETERS UPON INSTRUMENT PARAMETERS

The measurement of energy spectrum may be made with either a differential spectrometer or with threshold counters. Typically, the parameters most likely to be sources of error are the count-rate and the energy width, in the first case, and the count-rate and threshold energy, in the second case.

Threshold Detectors

Consider two detectors with count-rates C_1 and C_2 , each counter measuring all particles of a given type with energies above E_1 and E_2 respectively. Then,

$$C_1 = \int_{E_1}^{\infty} N(E)dE = N_0 E_0 \exp(-E_1/E_0)$$

$$\ln C_1 = \ln N_0 E_0 - E_1/E_0$$

Differentiating,

$$\frac{dC_1}{C_1} = \frac{d(N_0 E_0)}{N_0 E_0} = \frac{dE_1}{E_0} + \frac{E_1}{E_0} \frac{dE_0}{E_0} \tag{11}$$

Writing a similar equation for dC_2/C_2 and solving

the two simultaneous equations,

$$\frac{dE_0}{E_0} = \frac{E_0}{E_2 - E_1} \left[\frac{dC_2}{C_2} - \frac{dC_1}{C_1} \right] + \frac{E_2}{E_2 - E_1} \frac{dE_2}{E_2} - \frac{E_1}{E_2 - E_1} \frac{dE_1}{E_1} \quad (12)$$

and

$$\frac{d(N_0 E_0)}{N_0 E_0} = \frac{E_2}{E_2 - E_1} \left[\frac{dC_1}{C_1} - \frac{E_1}{E_2} \frac{dC_2}{C_2} \right] + \frac{E_1}{E_0} \frac{E_2}{E_2 - E_1} \left[\frac{dE_1}{E_1} - \frac{dE_2}{E_2} \right] \quad (13)$$

Since all errors are plus or minus values, the errors actually add, and the minus signs inside the brackets of the two equations above have no significance.

It is seen from equations (12) and (13) that the error in E_0 can never be less than dE_2/E_2 and that the error in $N_0 E_0$ can never be less than dC_1/C_1 . From equation (12), it is apparent that for dE_0/E_0 to be small, $(E_2 - E_1)$ must be greater than E_0 . And from equation (13), the minimization of errors in flux requires that E_2 be much greater than E_1 and that E_0 be greater than E_1 . Combining these results, the following criteria for a well-designed threshold detector pair is obtained:

$$\begin{aligned} E_2 &\gg E_1 \\ E_2 &> E_0 + E_1 \\ E_0 &> E_1 \end{aligned} \quad (14)$$

Differential Spectrometer

Consider a two-channel spectrometer measuring the fluxes at energies E_1 and E_2 within narrow energy ranges, w_1 and w_2 , respectively. If the count-rates are C_1 and C_2 ,

$$C_1 = N_0 \exp(-E_1/E_0) w_1$$

$$\frac{dC_1}{C_1} = \frac{d(N_0 E_0)}{N_0 E_0} - \frac{dE_0}{E_0} \left[1 - \frac{E_1}{E_0} \right] - \frac{dE_1}{E_0} + \frac{dw_1}{w_1} \quad (15)$$

and writing the second equation, for C_2 , and solving,

$$\frac{dE_0}{E_0} = \frac{E_0}{E_2 - E_1} \left[\frac{dC_2}{C_2} - \frac{dC_1}{C_1} + \frac{dw_2}{w_2} - \frac{dw_1}{w_1} \right] + \frac{E_2}{E_2 - E_1} \frac{dE_2}{E_2} - \frac{E_1}{E_2 - E_1} \frac{dE_1}{E_1} \quad (16)$$

and

$$\frac{d(N_0 E_0)}{N_0 E_0} = \frac{E_2 - E_0}{E_0 - E_1} \left[\frac{dC_1}{C_1} + \frac{dE_1}{E_0} - \frac{dw_1}{w_1} \right] + \frac{E_0 - E_1}{E_2 - E_1} \left[\frac{dC_2}{C_2} + \frac{dE_2}{E_0} - \frac{dw_2}{w_2} \right] \quad (17)$$

where the signs of the error terms, as before, have no practical consequence and should all be considered positive.

From equations (16) and (17), we obtain the criteria for a well-designed differential spectrometer, which turn out to be the same as the criteria listed in equation (14).

It is interesting that equation (16) shows that the minimum attainable error in E_0 is dE_2/E_2 , while equation (17) proves the error in flux can be reduced to an arbitrarily low value by simply emphasizing the conditions of equation (14).

Errors in E_1 , E_2 , w_1 , and w_2 are intimately related to the design of a given instrument and the care with which it is calibrated. Basically, it is a problem in applied physics. On the other hand, the errors in C_1 and C_2 are related to a host of problems: interference from unwanted particles, noise, statistical fluctuations in the random-counting process, stability of the electronics system, and accuracy of the data link. It is of interest to look at the data transmission problem area since it is one that can be generalized and often is the major source of error.

An analog telemetry system conventionally processes signal levels between 0 and 5 volts, with a reproduction accuracy of ± 0.05 to ± 0.2 volts (depending on the system and sometimes on who you talk to). Since flux levels in space vary by as much as eight orders of magnitude, it is desirable to have a large dynamic range while maintaining accuracy. To this end, an electrical circuit is often employed which produces a voltage level proportional to the logarithm of the count-rate. Hence, the relation

$$V = 5 \frac{\ln(C/C_0)}{\ln(C_5/C_0)}$$

where

- V = voltage output
- C = count-rate to give voltage V
- C_5 = count-rate at 5 volts
- C_0 = count-rate at 0 volt

Differentiating,

$$\frac{dC}{C} = \frac{dV}{5} \ln(C_5/C_0) \quad (18)$$

Now $dV/5$ is from 1% to 4%, and the transmission error introduced into the count-rate will depend upon the number of decades spanned. If f is the decade span (i.e., C_5/C_0 equals 10^f), then

$$\frac{dC}{C} = 2.3f \frac{dV}{5} \quad (18a)$$

In some cases, an analog signal is converted into a set of n digital pulses, representing a binary code of n bits and $2^n - 1$ voltage levels. The error $dV/5$ will then be plus or minus 3.4%, 1.6%, and 0.8% for n equal to 4, 5, and 6 bits, respectively.

ADDITIONAL SOURCES OF ERROR

Angular Resolution

Many spectrometers, especially the differential type, measure particles only in one narrow direction. An advantage of this technique is that it allows a determination of the pitch-angle distribution, $n(\theta)$, of trapped particles (here, θ is the angle between the direction of observation and the magnetic line of force). The count-rate, $C(\theta)$, of an instrument with geometric factor G (that is, the product of detector effective area and solid angle of viewing) is

$$C(\theta) = n(\theta)G \quad (19)$$

And the total flux to be determined is

$$\Phi = 2\pi \int_0^\pi n(\theta) \sin \theta d\theta \quad (20)$$

where the factor $2\pi \sin \theta$ is the solid angle at θ . Combining equation (19) with equation (20) and differentiating,

$$\frac{d\Phi}{\Phi} = -\frac{dG}{G} + \frac{\int_0^\pi dC \sin \theta d\theta}{\int_0^\pi C \sin \theta d\theta} + f d\theta \quad (21)$$

where f is a complicated integral involving $C(\theta) \cos \theta$ and $\sin \theta dC(\theta)/d\theta$, and dC denotes an error in the value of C which has θ dependence other than $\sin \theta dC/d\theta$. An example of this

would be counting statistics: $dC(\theta) = \sqrt{C(\theta)}$. Of these sources of error, probably the most significant is the error in geometric factor. It is very difficult in practical situations to accurately determine G . The most satisfactory method is by experimental calibration, but this is usually a very involved experiment.

One would expect some dependence of S upon the form of $C(\theta)$. This problem has been considered in other papers by Mar, and Fortney and Duckworth, in this volume.

Spatial Resolution

Position in space may be determined quite accurately with the advanced tracking techniques of today. Since flux levels can change by $\sim 10\%$ in about 0.01 L, the position should be accurate to 60 km. At the near-earth edge of natural and artificial radiation belts, flux levels can change much faster than this, so that extremely good positional resolution is required for dose-estimation purposes.

Considerable scatter is in evidence for most flux data organized on the B, L system. It is not yet entirely clear whether this is due to instrument recording accuracies or to inaccuracies in the mathematical description of the geomagnetic field from which B and L are calculated. In the South Atlantic anomaly region, the geomagnetic field is not well known and likewise neither are the flux levels.

Temporal Resolution

Proton fluxes in the inner belt are inherently quite stable, although recent data show that infrequent, catastrophic alterations can occur. There is also reason to expect a modulation of inner belt intensities with the solar cycle.

The outer belt, on the other hand, appears to be quite unstable, with exceedingly drastic changes occurring in less than one day. In view of the relatively small hazard of the outer belt and the virtual impossibility of predicting flux levels, there is little interest in performing dose calculations for this region.

Solar proton events are as yet unpredictable with a reasonable degree of confidence, especially as concerns fluxes and spectra. Measurements of proton events do not require time resolution of more than 1 minute to quite accurately determine the integrated flux.

Artificially-formed radiation belts exhibit very strong transient effects in the first 2 to 3 hours—so much so that it is probably a practical impossibility to completely characterize this time behavior experimentally. Subsequent to reaching a modicum of stability (\sim few days), such belts continue to exhibit strong decay for weeks to months to years (depending on the manner of formation and the spatial location of flux measurement).

EXPERIMENT DESIGN

Any spectrometer should accurately determine the energy spectrum for those particle energies which contribute to the dose. Series of calculations show that 90% of the dose is caused (for realistic shielding geometries) in the inner zone by

0.5 to about 6 MeV electrons
30 to about 300 MeV protons

Several energy channels should be employed (perhaps a half dozen) to determine shape accurately; the energy channels should be linearly spaced in energy for electrons and more or less logarithmically spaced for protons, because of the form of $s(E)N(E)$ for the two cases. The high and low channels should be somewhat outside the end-points given above. It is to be pointed out that for protons and penetrating electrons, it is only necessary to accurately know the flux for energies above the critical energy, E_c , since below this $s(E)$ is zero. Equations (13) and (17) can therefore be modified to calculate $d\Phi(>E_c)/\Phi(>E_c)$ by replacing $d(N_0E_0)/N_0E_0$ with this quantity and replacing E_2 and E_1 everywhere by $(E_2 - E_c)$ and $(E_1 - E_c)$, respectively. This fact can greatly improve accuracies possible. The criteria of equation (14) remain unchanged except for the additional criteria of

$$E_1 < E_c$$

In any spectrometer design, efforts should be made to keep the percentage uncertainty in E_0 at least three times smaller than the uncertainty in N_0E_0 (or $\Phi(>E_c)$) because of the shape magnification factor in dose calculations. Unidirectional spectrometers should be designed with particular care in regard to collimators so as to reduce dG/G . This is usually best accomplished by using multiple, knife-edge collimators. On the other hand, a trade-off analysis should be performed to determine the maximum value of G (to minimize statistical errors in count, \sqrt{C}/C) consistent with maintaining energy resolution, dE/E . Omnidirectional spectrometers should be designed to minimize variations of the threshold energy with the angular distribution of the external flux, $n(\theta)$. Finally, when using logarithmic count-rate circuits, no more than two or three decades should be read out on each telemetry channel. All experimental data should be reported with accompanying accuracy limits.

CONCLUDING REMARKS

There are several sources of error in particle measurements. A good spectrometer must cover a large range in both energy and particle flux level. Within present technology, this can probably be accomplished accurately only by a large, sophisticated instrument (weighing perhaps 15 to 30 pounds). It is now appropriate to conduct such experiments, with the aim of obtaining 10 to 20% data. Priority should be given to the large, well-designed spectrometers rather than a number of different instruments originated by different research groups.

It appears impractical to obtain particle environment data to better than 10%. Since relatively simple dosimetric devices are already available which have this accuracy over five decades or more of intensity, these should also be flown to obtain supplemental data.

REFERENCES

1. WEST, MANN, and BLOOM: Proc. Fifth Intern. Space Sci. Symp. (Florence, Italy), May 1964.
2. IMHOF, W. L.; and SMITH, R. V.: Proton Intensities and Energy Spectrum in the Inner Van Allen Belts. *J. Geophys. Res.*, vol. 69, 91, 1964.
3. McILWAIN, D. E.; and PIZZELLA, G.: On the Energy Spectrum of Proton Densities in the Earth's Inner Van Allen Zone. *J. Geophys. Res.*, vol. 68, 1963, p. 1811.
4. FREIER, P.; and WEBBER, W. R.: Radiation Hazards in Space From Solar Particles. *Science*, vol. 142, Dec. 20, 1963, p. 1587.
5. CLARK, B. C.; and ADAMS, D. A.: Proc. Fifth Intern. Space Sci. Symp. (Florence, Italy), May 1964.
6. GRODSTEIN, G. W.; and MCGINNIES, R. T.: X-Ray Attenuation Coefficients From 10 keV to 100 MeV. *Nat. Bur. Std. Circ. 583*, 1957, and Suppl. to Circ. 1959.

NS 34607

30—An Application of the Generalized Concept of Dosimetry to Space Radiations¹

H. A. WRIGHT, G. S. HURST, and E. B. WAGNER

Oak Ridge National Laboratory

34607

We wish to illustrate the application of the generalized concept of dosimetry to the dosimetry of high-energy protons. Calculations have been made of the distribution of energy losses in an array of silicon detectors exposed to an isotropic flux of monoenergetic protons. The array consists of a main crystal of dimensions $1 \times 1 \times 1$ cm bounded on each of its six faces by a crystal of dimensions $0.1 \times 1 \times 1$ cm. A computer code has been used to plot the distribution of energy losses for several selected energies up to 400 MeV. An energy loss operator is defined which transforms an energy loss distribution function into a dose function. This operator can be used to calculate the rem dose accurately at selected energies and to within a given tolerance at intermediate energies. An electronic circuit is described which selects energy loss signals from the detector and routes them to the appropriate section of a data processor, thus permitting the calculation of the dose received from radiation by high-energy protons of arbitrary energy spectrum.

author

It is the purpose of this investigation to describe conceptually a high-energy proton dosimeter which illustrates the use of the generalized concept of dosimetry as described by Hurst and Ritchie (ref. 1). The particular illustration given here was chosen quite arbitrarily and is intended to describe the technique which might be employed in designing an instrument to use this principle. It is expected that the particular dimensions of the detector, selection of energy loss channels, etc., chosen here quite arbitrarily would very likely be modified in a specific application. The detector chosen for this illustration consists of an array of lithium drift silicon detectors. The particular geometry used is a main crystal in the shape of a cube with dimensions $1 \times 1 \times 1$ cm and bounded on each of its six faces by a side crystal of dimensions $0.1 \times 1 \times 1$ cm.

Protons entering the detector array can penetrate the entire array or can stop within the array. Since the dimension of the array is

approximately equal to the range (1.18 cm) in silicon of a 50-MeV proton, it is convenient to separate the protons into two energy groups: the high-energy group (group 1) of energy greater than 50 MeV, and the low-energy group (group 2) of energy less than 50 MeV.

Figure 1 shows a cross-sectional view of the detector array and various kinds of paths that can be traversed by the protons. Some of the protons in group 1 can enter one face of the array and exit through the opposite face, as shown by the path numbered 1. Some of the protons in group 2 can enter the array and stop within the side crystal from which they enter, as shown by the path numbered 3, or can stop within the main crystal, as shown by the path numbered 4. However, some protons in either group 1 or group 2 can enter one face and exit through an adjacent face as shown by the path numbered 2. The electronic circuitry to be described subsequently will count a proton with a trajectory similar to that in path 1 in the high-energy group, count a proton with a trajectory similar to that in path 3 or 4 in the low-energy group, and reject a proton with a trajectory similar to that in path 2, since such a proton may be in either energy group.

¹ Research sponsored by the National Aeronautics and Space Administration (NASA Order R-104, Task No. 3) under Union Carbide Corporation's contract with the U.S. Atomic Energy Commission.

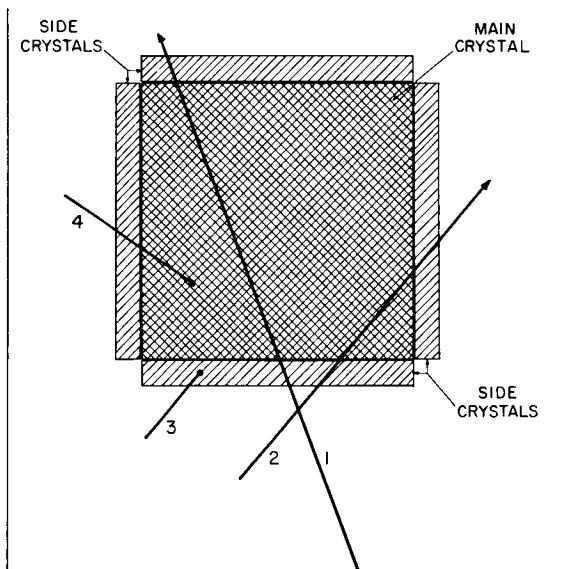


FIGURE 1.—Cross-sectional view of the detector array showing different types of particle trajectories.

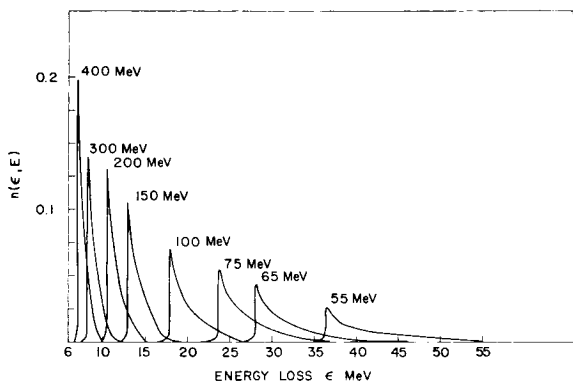


FIGURE 2.—The distribution $n(\epsilon, E)$ of energy losses ϵ in the detector per unit flux of protons with incident energy E .

The energy lost by protons in traversing the detector array can be calculated from the relativistic stopping power formula (ref. 2). Although a few nuclear collisions (less than 1%) can be expected to occur within the detector, they will usually be rejected by the electronic circuitry, and have been neglected in the calculation of energy losses within the array.

A Fortran program has been written for the CDC 1604 computer which will calculate the distribution of energy losses that will result from radiation of the above array of silicon detectors by isotropically incident monoenergetic protons.

The history of each incident proton is generated randomly, and recorded as it is generated. The information recorded for each history consists of:

- (1) The point of penetration
- (2) The direction of travel
- (3) Whether the proton stopped within the detector array
- (4) The component of the array in which the proton stopped, if it indeed did stop
- (5) Whether the proton penetrated opposite side crystals, adjacent side crystals, or neither
- (6) The amount of energy lost by the proton in each component of the detector array

The calculations are performed for isotropically incident protons. If the incidence of protons is not isotropic, an adjustment can be made by rotating the detector.

Consider those protons in group 1 which enter one face and exit through an opposite face. Let E be the energy of the incident proton and let ϵ be the total energy lost by the proton in passing through the detector array, i.e., the sum of the energy lost in the main crystal and the two opposite side crystals penetrated by the proton. Let $n(\epsilon, E)d\epsilon$ be the fractional number per unit isotropic fluence² of protons of incident energy E having total energy losses within the detector array between ϵ and $\epsilon + d\epsilon$. Thus the number of losses in the high-energy group per unit isotropic fluence of protons with incident energy E

is given $\int_0^{\infty} n(\epsilon, E)d\epsilon$. The computer program

was run for each of eight incident energies 400, 300, 200, 150, 100, 75, 65, and 55 MeV. Figure 2 shows a graph of $n(\epsilon, E)$ as a function of ϵ for each of these energies. Each of the eight curves is labeled with the appropriate energy E .

Consider now protons in the low-energy group. The only protons counted in this group are those which lose all their energy within the detector array. Therefore, for monoenergetic incident particles there will not be a spread of energy losses such as shown in figure 2.

Figure 3 is a graph of rem dose per proton/cm² as a function of incident energy. It is not the

² The term "fluence" has been recommended by the ICRU (ref. 3) to denote the time integral of flux.

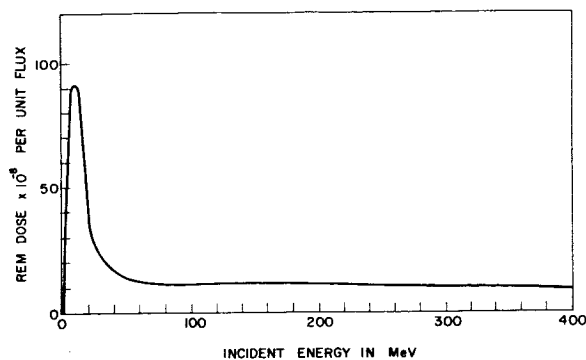


FIGURE 3.—The dose in rem per unit flux as a function of incident proton energy.

purpose of this investigation to justify this particular dose curve as being the "best" in any sense but just to illustrate how any dose curve whatsoever can be approximated by the dosimeter to be described here. This particular dose curve was obtained from information in a paper by Turner et al. (ref. 4). In this paper a man was approximated by a rectangular parallelepiped of tissue of dimensions 20 x 30 x 60 cm. This "man" was irradiated by an isotropic flux of monoenergetic protons and the dose in various parts of the body was calculated. For incident energies of 200 MeV and above, the dose was found to be approximately uniform throughout the body. However, for energies of 100 and 150 MeV the dose near the surface was substantially higher than the dose within the body.

The dose curve in figure 3 was constructed by drawing a smooth curve through points obtained in the following manner. Since the dose was found to be approximately uniform for each of the incident energies 200 MeV, 250 MeV, 300 MeV, 350 MeV, and 400 MeV, the point used in figure 3 for each of these energies was taken to be the average dose in the whole parallelepiped of tissue. However, at 100 MeV and 150 MeV the dose was higher near the surface and, therefore, the point used in figure 3 for each of these energies was taken to be the average dose in the outside 5 cm of tissue in the parallelepiped, as given in reference 4. For energies between 10 MeV and 50 MeV the dose was averaged over the range of the proton in tissue. The range of a 10-MeV proton is approximately 0.1 cm, which is the average thickness of the skin as

given in the description of the standard man (ref. 5). No average was taken over ranges less than the skin thickness. Thus for energies less than 10 MeV the dose was taken to be the average over 0.1 cm.

This dose curve will be approximated by the response of the dosimeter to be described here. However, any other curve could be approximated equally well. The curve could be for rad dose, or rem dose, or the dose which contributes to a specific effect such as cataract production, etc. In fact, the output from a single exposure of the dosimeter can be used to fit any number of curves and thus to determine the dose received for a given exposure as related to any number of different effects.

The fundamental principle involved in the generalized concept of dosimetry is based on an operator $O(\epsilon)$ which will transform an energy loss distribution function $n(\epsilon, E)$ such as given in figure 2 into a dose function $D(E)$, such as given in figure 3. An operator of the matrix element weighting type is particularly suited to the present illustration.

Consider protons in the high-energy group. Eight channels of energy losses ϵ were selected. These channels are indicated at the top of table I. The computer program described above was run for eight selected incident proton energies E_i , and numbers N_{ij} (which represent the number of pulses/proton/cm² counted in channel j when the incident energy was E_i) were calculated. The results are shown in table I,³ the numbers N_{ij} being located in the body. The dose $D_i = D(E_i)$ in rem per unit flux at each incident energy E_i is obtained from the dose curve in figure 3 and recorded at the right of the table opposite the energy. Finding the required operator $O(\epsilon)$ then consists of computing weighting coefficient a_j for channel j in

³ The calculations performed to obtain these numbers did not take into account the fact that a proton in the high energy group may penetrate a side detector while travelling nearly parallel to a face of the main detector. Such a proton would deposit energy only in this one side detector. Therefore, the signal would be routed to the low energy portion of the data processor as though it resulted from a low energy proton which entered and stopped in this side detector. More accurate numbers could be obtained by reducing the thickness of the side detectors or by revising the calculations to take into account this effect.

TABLE I

The Number N_{ij} of Pulses per Unit Flux in Each High-Energy Channel j at Each Incident Energy E_i

Channel no.	1	2	3	4	5	6	7	8	
Energy span (MeV)	6-8	8-10	10-12	12-17	17-23	23-27	27-35	35 up	
Incident energy E_i MeV									Dose D_i rem per unit flux
400	0.1116	0.0544	0.0004	0	0	0	0	0	8.9×10^{-8}
300	.0009	.1417	.0224	.0001	0	0	0	0	10.0
200	0	.0002	.1161	.0548	0	0	0	0	11.3
150	0	0	0	.1662	.0048	0	0	0	11.5
100	0	0	0	.0004	.1506	.0167	.0001	0	11.0
75	0	0	0	0	.0012	.1047	.0599	.0006	11.0
65	0	0	0	0	0	.0012	.1324	.0328	11.5
55	0	0	0	0	0	0	.0849	.0736	12.5
a_i Rems $\times 10^7$ per pulse	5.0466	5.9754	6.5545	6.7238	6.7752	6.6088	6.6185	8.1358	

such a way that

$$\sum_{j=1}^8 a_j N_{ij} = D_i \quad (1)$$

for each value of $i=1, 2, \dots, 8$. This simply consists of solving the eight equations given in (1) for the eight unknowns a_j . The weighting coefficients a_j were calculated for this particular illustration and are given along the bottom of table I. When the detector is irradiated by high-energy protons, the dose curve in figure 3 will be accurately fitted if the incident proton energy is one of the eight energies selected above. The dose curve will be approximately fitted if the incident proton energy is different from the above. In principle, any number of channels can be selected and, therefore, it is possible to obtain any desired degree of accuracy.

If the detector is placed in a field of unknown proton energies, a number of pulses will be experienced in each of the eight channels. Then, by simply multiplying the number of pulses in channel j by the coefficient a_j and summing on j , the total dose according to the dose curve in figure 3 is obtained. It is noted that the total information received from the detector as a result of exposure to radiation

consists of a number of pulses in each of the selected channels. Consequently, k different dose curves could be used and k sets of coefficients $a_j^{(k)}$ calculated to compute the dose resulting from the dose curve k . Therefore, in order to compute the total dose $D^{(k)}$ received according to the response of dose curve k , it is simply necessary to weight the channels by the coefficients $a_j^{(k)}$. For example, dose curves representing a maximum estimate of dose and a minimum estimate of dose might be used, and an estimate of both can then be determined from the information received by the detector.

It must be emphasized that except for the total energy range being considered (0 to 400 MeV in the present case) no previous information as to the energy spectrum of the incident radiation is needed to determine the dose $D^{(k)}$.

Consider now protons in the low-energy group. Since only protons that lose all their energy in the detector are counted, losses by protons of a given incident energy will be confined to only one channel. Therefore, the matrix of numbers N_{ij} will be diagonal and the calculation of the weighting coefficients will be much simpler than for the high-energy case. For the purpose of this illustration, nine low-

TABLE II

The Number N_{ij} of Pulses per Unit Flux in Each Low-Energy Channel j at Each Incident Energy E_i

Channel no.	Energy span, MeV	Incident energy E_i , MeV	Dose D_{ij} , rem $\times 10^8$ per unit flux	Number N_{ij} of pulses per unit flux	a_j , Rem $\times 10^8$ per pulse
1	< 7.5	5	70	1.4999	46.7
2	7.5-12.5	10	90	1.4987	60.1
3	12.5-17.5	15	75	1.4924	50.3
4	17.5-22.5	20	35	1.4381	24.3
5	22.5-27.5	25	26	1.3445	19.3
6	27.5-32.5	30	21	1.2084	17.4
7	32.5-37.5	35	18	1.0478	17.2
8	37.5-42.5	40	15.8	.8648	18.3
9	> 42.5	45	14.2	.6654	21.3

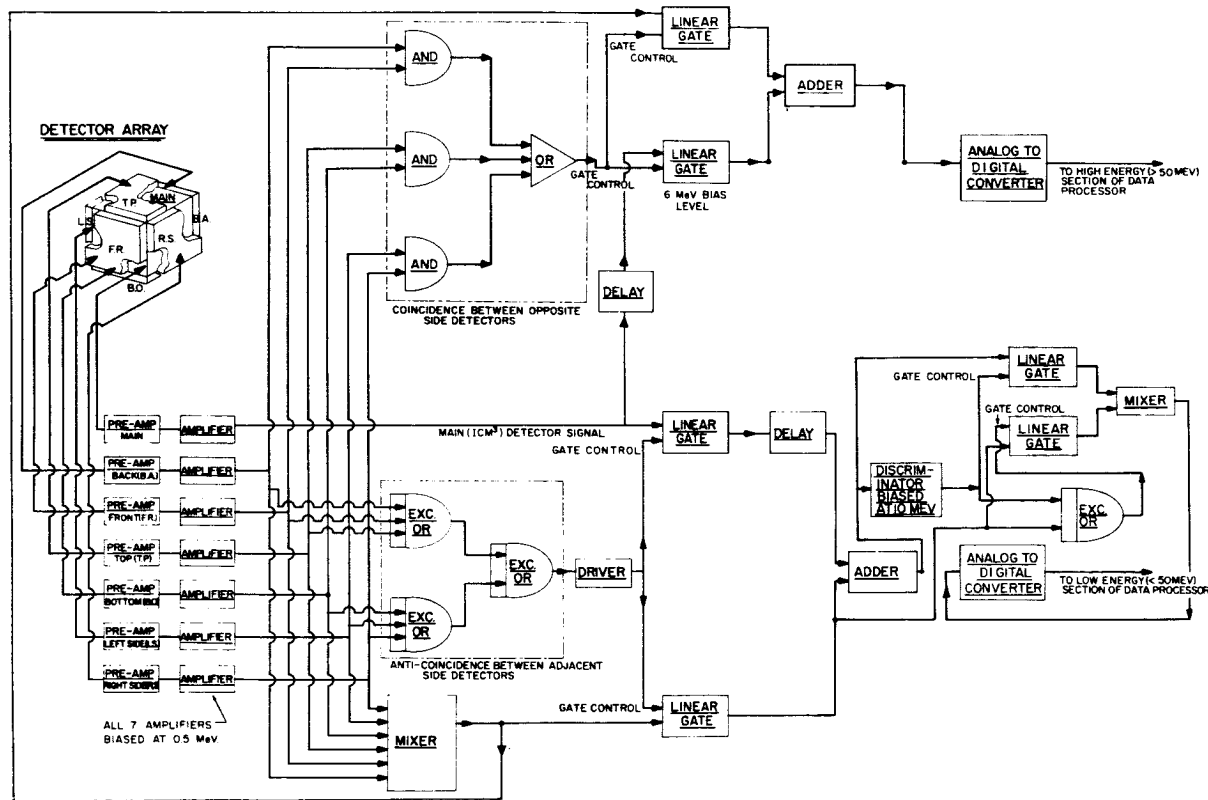


FIGURE 4.—Electronic circuitry which performs the appropriate energy selection and signal routing.

energy channels were selected and an energy in each channel was chosen for use in computing the weighting coefficients a_j . The pertinent information for this selection is given in table II. It is noted that any pulse received in channel j will be assigned the dose a_j in rem/pulse as

though the proton had incident energy E_j . For example, from table II it is seen that any proton with energy between 22.5 MeV and 27.5 MeV which would have a loss in channel 5 would be assigned the weighting value of 19.3×10^{-8} rem/pulse. This, in effect, assumes the

dose curve to be a step function with the height of the steps being the values of the dose curve in figure 3 at the nine selected energies E_i shown in column 3 of table II. The width of each step is the width of the corresponding energy channel as given in table II. It is easy then to determine the maximum error that might result from the given approximation to the curve. More channels could be chosen if the approximation is not adequate.

An electronic circuit which will perform the above energy selection and pulse routing is shown in figure 4. The pulses corresponding to the high-energy proton data are routed to the

proper section of the data processor by means of circuitry that senses coincidence between opposite side detectors and then routes the output to a linear gate that passes this output only when the gate is activated simultaneously by a signal from the main detector. The pulses corresponding to the low-energy proton data are routed to the proper section of the data processor by means of a unit which senses anti-coincidence between all six side detectors, and if this circuit shows an output in only one side detector this output is added linearly (by means of a linear mixer and linear gates) to any signal that may be present in the main detector.

REFERENCES

1. HURST, G. S.; and RITCHIE, R. H.: Health Phys., vol. 8, 1962, p. 117.
2. FANO, U.: Penetration of Protons, Alpha Particles and Mesons. Ann. Rev. Nucl. Sci., vol. 13, 1963, p. 1.
3. Radiation Quantities and Units, ICRU Report 10a, Nat. Bur. Std. (U.S.) Handbook 84, 1962.
4. TURNER, J. E.; ZERBY, C. D.; WOODYARD, R. L.; WRIGHT, H. A.; KINNEY, W. E.; SNYDER, W. S.; and NEUFELD, J.: Health Phys., vol. 10, 1964, p. 783.
5. Report of ICRP Committee II on Permissible Dose for Internal Radiation, 1959, with Bibliography for Biological, Mathematical, and Physical Data. Health Phys., vol. 3, 1960, p. 151.

NO. 24608

31—Proton Flux, Dosage, and Damage Estimates in the Van Allen Belt

S. RUSSAK and K. RICHARDSON

Martin Company

~~34608~~ 34608

Proton fluxes and spectrums have been obtained for a number of near earth circular and elliptical orbits. From these, radiation dose versus absorber thickness and solar cell damage estimates have been made.

The environmental model to obtain flux uses McIlwain's empirical data (refs. 1, 2, and 3) from Explorer XV. The distribution of protons with energy as used in the calculation varies with position in the geomagnetic field in accordance with the relationship derived by Imhof and Smith (ref. 4). These have been combined into a single IBM 7094 program which determines flux and composite incident spectrum at various points along the orbit and calculates emergent spectrum and dose within simple or complex configurations. The results obtained are compared with earlier dosage estimates based upon the Freden and White spectrum (ref. 5) and a flux model derived from Explorer IV data.

Richardson

INTRODUCTION

The initial measurements of geomagnetically trapped particles provided little detail for the evaluation of dosages that would be absorbed by the crews of spacecraft traversing the belts of trapped particles. In the case of the electron constituent, particularly, the ambiguity of the response of the early particle detectors used in the first satellites resulted in a number of interpretations of the flux and spectrum of those particles. An evaluation of the radiation doses from electrons based upon some of these estimates of the trapped electrons is given in reference 6.

With regard to geomagnetically trapped protons, most dosage evaluations were based upon the spectral data developed by Freden and White (1960) (ref. 5) from emulsions recovered from a missile nose cone. We have been using a segmented power law fit to the Freden and White data in our dosage calculations over the last 3½ years. These were by no means the only spectral data available and were not universally accepted by all researchers and experimentalists in trapped particles. For the

first calculations we defined the flux of particles by a contour chart developed from fluxes measured by some of the early Pioneer and Explorer satellites. The flux of particles was assumed to follow the magnetic field strength and dip latitude in accordance with the relationship found by Yoshida, Ludwig, and Van Allen (1960) (ref. 7). Dosage calculations using these models were reported elsewhere by us (Beck, Divita, and Russak, 1961) (ref. 8).

PROTON FLUX CONTOURS

Subsequently, McIlwain reported on Explorer IV proton measurements showing that the flux contours could be organized in an orderly fashion in a coordinate system comprising the scalar intensity of the magnetic field (B) and a parameter (L) related to the field strength and the integral invariant of particle motion (ref. 1). Data from two Geiger counters of Explorer IV were plotted in this system. The data were applicable to proton detection thresholds of 31 and 43 MeV. We found that the relative count rates fit the shape of Freden and White relationship quite

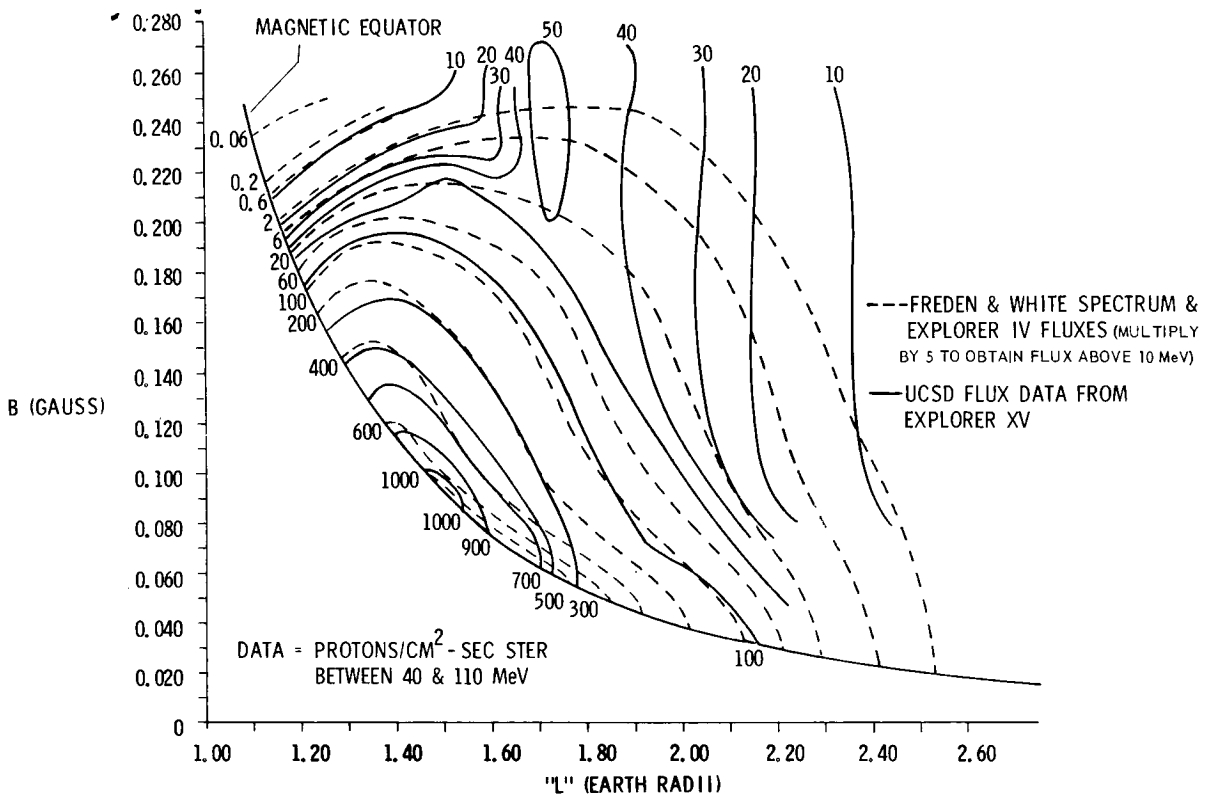


FIGURE 1.—Van Allen belt protons in B, L coordinates.

well and extrapolated the data in energy and in space to the plot shown in figure 1. The peak flux, $6600 \text{ cm}^{-2} \text{ sec}^{-1} \text{ steradian}^{-1}$ with $E > 10 \text{ MeV}$, was considerably greater than that we had used in our previous representation of the proton belt ($2460 \text{ cm}^{-2} \text{ sec}^{-1} \text{ steradian}^{-1}$) and the dosage estimates therefore increased accordingly.

McIlwain (ref. 2) has presented new data from Explorer XV on trapped particles which show two distinct maximums of energetic proton flux (40 to 110 MeV).

The greater maximum of approximately $1100 \text{ cm}^{-2} \text{ sec}^{-1} \text{ steradian}^{-1}$ occurs at 1.5 earth radii. In the same energy interval (40 to 110 MeV) the maximum flux of the Explorer IV B, L plot extrapolated with the Freden and White spectrum was about $1300 \text{ cm}^{-2} \text{ sec}^{-1} \text{ steradian}^{-1}$.

The Explorer XV data was put in the form of an IBM computer routine and Dr. McIlwain kindly furnished us with a copy of this routine called FLUX for our use. Unidirectional flux contours plotted from FLUX points are

shown over the older Explorer IV derived contours in figure 1.

Basic differences in the two maps are in the location of the regions of maximum flux, a ridge of relatively high flux on the new data at $L=1.75$ and $B \geq 0.200$. The older data are also seen to fall off much more rapidly at high values of B and low values of L .

PROTON ENERGY SPECTRUMS

Although most estimates of dosages from trapped protons used a constant energy spectrum, there was no evidence that the spectrum was temporally and spatially constant. On the contrary, there was both theoretical and experimental evidence that the energy spectrum did vary with position. However, there was little if any basis on which to extend or extrapolate the spectral variations indicated over the entire trapped particle region or even over significant portions of it.

Early last year McIlwain and Pizzella (ref. 2) showed that there was a dependence of the energy spectrum of 30 to 50 MeV protons (as

measured by Explorer IV) upon the parameter L such that

$$dN/dE = I_0 e^{-E/E_0}$$

$$\text{with } E_0 = 306L^{-5.2}$$

This relationship was shown to be consistent also with the experimental data from a number of sources.

More recently Imhof and Smith (ref. 4) have analyzed proton fluxes above three energy levels obtained with scintillators flown on three satellites and an Atlas pod. They found that the data could be well fit by a relationship very similar to that given in the last cited reference. Specifically, they found

$$dN/dE = I_0 e^{-E/E_0}$$

$$\text{with } E_0 = 460L^{-4.8}$$

Since this relationship had been developed from data over a wider range of energies (59 to 148 MeV) than the previously cited relationship (31 to 43 MeV), it was decided to use it to determine the flux of particles at energies above and below the 40 to 110 MeV available from the FLUX routine. A new IBM 7094 computer routine was developed at the Martin Company for this purpose, incorporating also the dose determination subroutine from one of our other programs as well as FLUX and the INVAR subroutine (of Dr. McIlwain's group) for the determination of B , L coordinates.

Input data in the new program include the trajectory coordinates of the orbit (as determined from another program) together with data on the absorber materials and geometric shape. The B , L coordinates of each trajectory point are determined, and from these the unidirectional proton flux in the interval 40 to 110 MeV at each point is determined. E_0 is determined from the calculated value of L , and the flux of protons in each of 249 energy groups is determined from the equation relating N and E_0 .

The number of protons encountered at each trajectory point is determined from the flux and time interval to the next trajectory point. These values are saved and cumulated to the end of the trajectory or orbit and are used in an energy-to-range-to-residual range-to-residual

energy determination through the input absorber materials and configuration. A dose calculation is then made from the residual energy spectrum.

Arbitrary limitations have been put into the portion of the program which determines and stores the number of protons at each trajectory point. This has been done because of the nature of the exponential flux relation to give impossibly high values of flux at lower energies relative to the flux between 40 to 110 MeV. Therefore, no 1 MeV wide group of particles is allowed to contain more particles than the total between 40 and 110 MeV. Furthermore, the 40 to 110 MeV flux, as determined from the FLUX subroutine, is set equal to zero at values of B and L where the FLUX accuracy is poor. This occurs at L values greater than 4 or L values less than 4 and R values less than 1.1.

The effect of the first of these limitations is to change the residual energy spectrums and dosages at absorber thicknesses up to the range of particles for which the adjustment is made. Therefore, at absorber thicknesses in excess of 1.5 to 2 gm cm⁻² this limitation does not have any effect upon the residual energy spectrum and dose. The second limitation causes the incident flux to be read as zero. FLUX gave these regions an arbitrary value of 10 cm⁻² sec⁻¹ even though neighboring trajectory points might have lower values. However, it seemed more reasonable to set these equal to zero.

The incident integral proton energy spectrum (normalized to unity) as calculated from the new program is plotted on figure 2 for three different orbits. Also shown for comparison is the Freden and White spectrum. The new spectrums are all softer than the older version. Furthermore, as would be expected from the relationship between E_0 and L , they become increasingly softer as L increases (as altitude increases). Note that the spectrums are based upon 24 hours of flight in order to minimize the orbit-to-orbit variations that would result from the geographic asymmetries of the trapped particles.

RADIATION HAZARD DATA

Whole body entrance doses were determined for a number of earth satellite orbits under

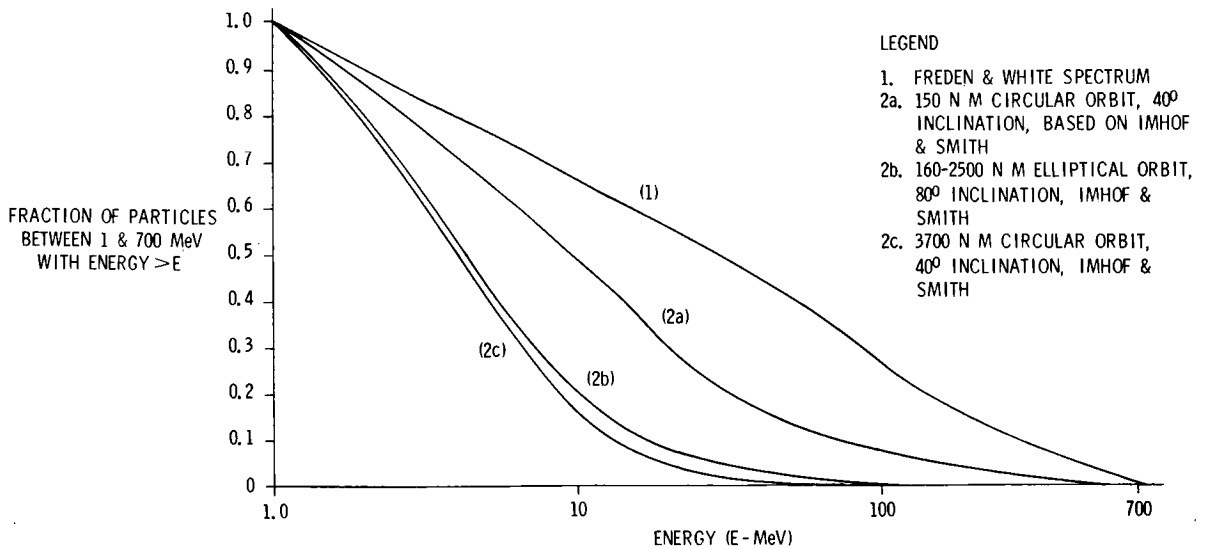


FIGURE 2.—Comparison of proton energy spectra based on Freden and White, and Imhof and Smith.

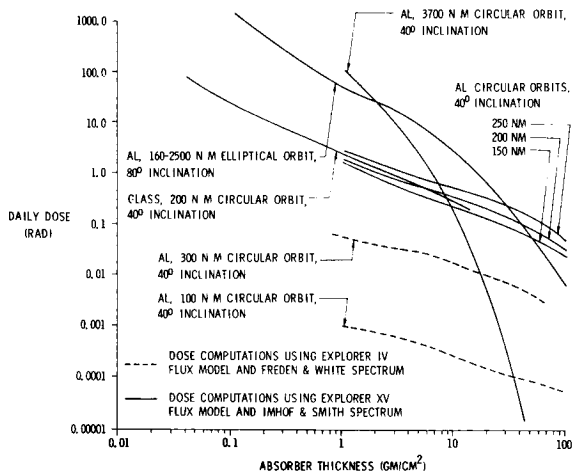


FIGURE 3.—Daily proton dose versus absorber thickness for various spacecraft orbits through the Van Allen belt.

varying thicknesses of aluminum and glass. These are shown in figure 3. Since there is no evidence of an abrupt change in slope on any of the curves near 1 gm cm^{-2} , it can be reasonably concluded that the effect of the limitation on the particle flux imposed at energies below 40 MeV is insignificant. This is further indicated by those two curves for which the calculation has been extended to thicknesses below 1 gm cm^{-2} .

The increasing effectiveness of shielding as the orbital altitude increases is due, of course, to the softening of the incident and therefore

of the residual energy spectrum. A significance of this trend would be that a high altitude orbit would require less proton shielding than a low orbit for an equal number of particles. However, as will be shown, the RBE will increase because of the softer spectrum at higher altitudes.

Also shown (in fig. 3) are the daily orbital dosages determined from the Freden and White spectrum and the proton flux contours based upon Explorer IV data. Very large differences exist in the dosages obtained from the two models. Although the new spectrums were shown to be considerably softer, the major difference in the dosages in the 100 to 300 n. mi. interval arises from differences in the 24-hour flux. For example, at 100 and 300 n. mi. and 40° inclination the old data gave a total flux of 5.80×10^2 and 3.01×10^4 protons cm^{-2} steradian $^{-1}$, respectively. Using the new models, 9.14×10^5 protons cm^{-2} steradian $^{-1}$ were seen in 24 hours at 150 n. mi. and 40° inclination. The ratio of the new flux at 150 n. mi. to the old flux at 100 n. mi. is 1.57×10^3 . This compares to a ratio of 1.54×10^3 of the doses at an absorber thickness of 1 gm cm^{-2} aluminum. Similarly, the new flux at 150 n. mi. is 30.4 times the old flux at 300 n. mi. and the dose ratio is 29.7.

Since the flux contours shown on figure 1 do not appear to differ by so great an amount, the

flux histories were examined. It was seen that even at 300 n. mi. the old model had long periods (in excess of 1 hour and up to more than 6 hours) when no particles were encountered. This occurred generally at L values in excess of 1.1 and B values in excess of 0.24. The new model had definable fluxes over a good part of this region. This difference should become less significant at higher altitudes; however, the low altitude region is of considerable importance to manned space flight, and the new data obtained from Explorer XV clearly indicate to us that the radiation dosages will be much higher than we had anticipated based upon our earlier calculations.

Since the new proton spectrums are softer, the relative biological effectiveness or RBE will be somewhat higher. This is shown in figure 4 for the residual spectrums of three orbits calculated with the new program and for the older Freden and White spectrum. RBE's in excess of 3 are indicated with absorber thicknesses under 0.1 gm cm^{-2} . At 1 gm cm^{-2} the Freden and White spectrum gives an RBE of 1, but the new data show RBE values from about 1.5 to 2. These continue in excess of 1 at absorber thicknesses up to 100 gm cm^{-2} .

Solar cell performance degradation from the absorption of energetic particles has become of concern particularly since the detonation of Starfish. In view of the increased flux of protons indicated at low altitudes by the new proton data, we evaluated the remaining maximum power output after six months exposure under glass cover slips of different thicknesses. This is shown on figure 5 for 1 ohm cm N/P silicon cells of 150 micron initial minority carrier diffusion length. Damage estimates were based upon the degradation of minority carrier diffusion length (Cooley and Janda, ref. 9).

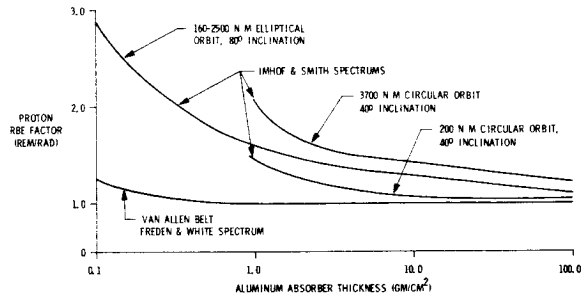


FIGURE 4.—Proton RBE versus aluminum absorber thickness.

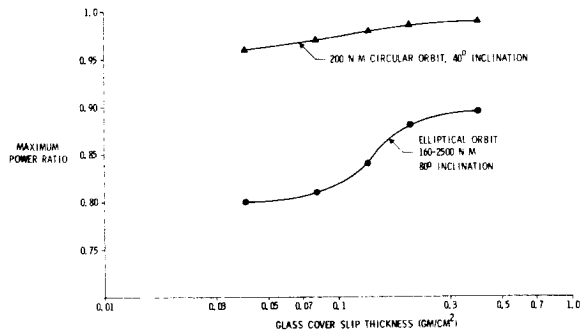


FIGURE 5.—N/P Silicon solar cell proton damage versus cover slip thickness for 150μ original diffusion length 1 ohm-cm cell exposed to space sunlight for 6 months.

The points plotted on figure 5 correspond to glass thicknesses of 6, 12, 20, 30, and 60 mils. The S-shaped curve arises from the shape of the damage effectiveness factor versus energy relationship. It can be seen that significant damage is indicated for the elliptical orbit at the end of six months. These proton damage estimates may be compared with electron damage estimates from the undegraded Starfish spectrum that we made for the same elliptical orbit. The residual powers in that environment are 0.75, 0.758, 0.76, 0.77, and 0.775, respectively, for the cover slip thicknesses shown on figure 5.

REFERENCES

1. McILWAIN, C. E.: Coordinates for Mapping the Distribution of Magnetically Trapped Particles. *J. Geophys. Res.*, vol. 66, no. 11, 1961, p. 3681.
2. McILWAIN, C. E.; and PIZZELLA, G.: On the Energy Spectrum of Protons Trapped in the Earth's Inner Van Allen Zone. *J. Geophys. Res.*, vol. 68, no. 7, 1963, p. 1811.
3. McILWAIN, C. E.: The Radiation Belts, Natural and Artificial. *Science*, vol. 142, 18 Oct. 1963, p. 355.
4. IMHOF, W. L.; and SMITH, R. R.: Proton Intensities and Energy Spectrums in the Inner Van Allen Belt. *J. Geophys. Res.*, vol. 69, no. 1, 1964, p. 91.
5. FREDEN, S. C.; and WHITE, R. S.: Particle Fluxes in the Inner Radiation Belt. *J. Geophys. Res.*, vol. 65, no. 5, 1960, p. 1377.
6. RUSSAK, S. L.: Radiation Dosages From Electrons and Bremsstrahlung in the Van Allen Belts. *Proc. Sym. on Protection Against Radiation Hazards in Space. Paper E-8, TID-7652, Atomic Energy Commission, 1962, pp. 760-772.*
7. YOSHIDA, S.; LUDWIG, G. H.; and VAN ALLEN, J. A.: Distribution of Trapped Radiation in the Geomagnetic Field. *J. Geophys. Res.*, vol. 65, no. 3, 1960, p. 807.
8. BECK, A. J.; DIVITA, E. L.; and RUSSAK, S. L.: Evaluation of Space Radiation Safety Procedures in the Design and Operation of Some Early Manned Lunar Vehicles. *Proc. Sixth Symp. on Ballistic Missile and Aerospace Technol. (C. T. Morrow, L. D. Ely, and M. R. Smith, eds.)*, vol. III, Academic Press (New York), 1961, pp. 365-426.
9. COOLEY, W. C.; and JANDA, R. J.: Handbook of Space-Radiation Effects on Solar Cell Power Systems. NASA SP-3003, 1963.

No 5-34609

32—A Gamma-Ray Probe System for Determining the Shielding Effectiveness of the Apollo Vehicle¹

A. D. KRUMBEIN, R. C. ROSS, and C. BEAULIEU

United Nuclear Corporation

34609

A gamma-ray probe technique to determine the shielding effectiveness of any given material configuration against proton radiations likely to be encountered in space has been devised and tested. The essence of the technique is the use of gamma ray attenuation measurements to determine the areal electron densities along a great many paths through the configurations to be tested. A computer code is then used to calculate the proton dose received behind these configurations from typical space proton spectra.

The basis of the gamma probe technique is reviewed, and a semiautomatic system designed to determine the shielding effectiveness of the Apollo Command and Service Modules is described. This system is capable of obtaining data at as many as 10 dose points inside the module simultaneously. Additional applications of the gamma probe technique are mentioned.

author

INTRODUCTION

The suggestion to use a gamma probe to test the effectiveness of a proton shield was made several years ago as a result of an Apollo preliminary design effort. It was apparent that most, if not all, of the radiation shielding for the Apollo vehicle would have to be provided by structure and on-board equipment. While this equipment is relatively massive, its heterogeneity and distribution is such that its shielding effectiveness is greatly reduced. Furthermore, it is very difficult to determine the shielding effectiveness of a complex array of equipment analytically with any degree of confidence. An experimental verification of the shield effectiveness was strongly recommended.

We were also able to show that gamma transmission measurements would be nearly as definitive and a great deal simpler than actual proton measurements. Following preliminary development work, United Nuclear Corporation was awarded a contract by NASA to evaluate the feasibility of the gamma probe

method for testing the shielding effectiveness of the Apollo vehicle (ref. 1). This paper will first review briefly the basis of the gamma probe technique, then describe the application of the gamma probe method to the Apollo command module, and finally mention other related gamma probe applications.

ANALYSIS

The basis of this shield verification method is that the primary attenuating constituent of matter for both protons and gammas in suitable energy ranges is electrons. Hence, by making gamma transmission measurements along a great many paths from the outside of a shield to points of interest inside, one can determine the electron density along these paths. This permits calculation of proton attenuation along these paths, and from this the dose received at these points from any specified radiation environment outside the shield. By using automated equipment with the readings recorded directly in a form suitable for input to a computer program, the verification program becomes quite manageable.

It is also worth noting that, since alpha particles also attenuate by ionization, the gamma probe technique is applicable to veri-

¹ This paper is based in part on work performed under contract No. NAS 8-5252 with George C. Marshall Space Flight Center, NASA.

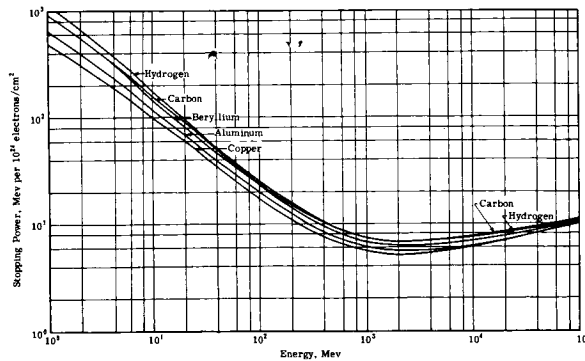


FIGURE 1.—Stopping power for protons in terms of electron density.

fication of shield effectiveness against alpha radiation as well.

Figure 1 shows the stopping power of various materials for protons in terms of electron density rather than mass density, as is usually given. The closeness of the curves shows that electron density is a more uniform measure of proton attenuation than is mass alone. For mixtures of materials, one can use either a composite stopping power curve or the curve for a typical material, such as aluminum or carbon. For typical space vehicle materials, the use of a composite curve should not introduce errors greater than a few percent.

Next we consider the use of gamma attenuation to give us electron density. The most convenient gamma emitters for this use are Cs^{137} , with an energy of 0.67 MeV, and Co^{60} , with energies of 1.17 and 1.33 MeV. At these energies, for the materials likely to be used in space vehicles ($z \leq 30$), the Compton process accounts for more than 98% of the gamma cross section. In the Compton scattering process, the photon scatters from an atomic electron, changes direction, and loses an amount of energy related to the deflection. A transmission measurement in which one measures the number of transmitted photons which have not suffered Compton scattering thus gives the areal electron density from the relationship

$$\int_0^t N_e dt = \frac{1}{\mu_e} \ln \frac{I_0}{I}$$

where I_0 is the number of gamma ray photons incident on a portion of the shield and I is the number transmitted without scattering. In

practice, the ratio of I_0 to I is determined by two separate measurements with the same source and detector location, one with and one without the shield being present. In the former measurement, the unscattered portion of the transmitted beam can be determined either by collimation or by energy discrimination, or by a combination of both techniques. The published value of μ_e for Cs^{137} is 0.254×10^{-24} cm²/electron, and for Co^{60} the average value is 0.186×10^{-24} cm²/electron. These values were checked experimentally on a 3/4-inch-thick aluminum sample using simultaneously good collimation and energy discrimination. The number of electrons/cm² indicated from the transmission measurements were within 1% of those actually present (ref. 1).

Experimental Method

In application, the use of collimation is inconvenient. Since the source is to be moved over the shield surface and a number of detectors may be used simultaneously, neither source nor detector is easily collimated. Therefore, the effectiveness of using energy discrimination alone was investigated. Ideally, if the pulse height analyzer were set to record only those gamma pulses in the full energy peak of the pulse height spectrum, it would detect to a high degree of accuracy only the unscattered gamma rays. However, since the energy peak has a finite width, a finite "window" size must be used. In practice, the discriminator of the system must be set at the lower end of the peak, at a value where changes in discriminator level caused by noise or drift will have the least effect on the observed counting rate. When Co^{60} was used as the source, the discriminator was set at the minimum of the lower peak, thus including counts from both peaks.

Setting the discriminator below the energy peak leads to the acceptance of some scattered gamma rays by the counting system. Since there is no collimation to block these scattered gamma rays, they result in spuriously high transmitted counting rates, making it appear that the shielding material is thinner than it actually is. For the Co^{60} source, where $E_{\gamma_1} = 1.17$ MeV and $E_{\gamma_2} = 1.33$ MeV, the discriminator

was set at 1.07 MeV, and gamma rays scattered through angles of 17° and 25° , respectively, were accepted by the counting system. For Cs^{137} , where $E_\gamma=0.67$ MeV, the discriminator setting was 0.58 MeV, and gamma rays scattered through as much as 27° were accepted.

One can largely compensate for this in-scattering effect by determining experimentally an effective Compton cross section, μ_{eff} , which will lead to the correct areal electron density when used with the observed gamma ray transmission. To test this approach, transmission measurements were made on slabs of a number of different materials, with results shown in table I. These results show that up to about $Z=30$, a single value of μ_{eff} can be used for transmission measurements even without collimation. The effective value of 0.150×10^{-24} cm²/electron for Co^{60} is substantially smaller than the theoretical value of 0.186×10^{-24} used with a collimated source, showing the effect of scattered radiation in increasing the observed transmission.

TABLE I

The Effective Compton Cross Section as Measured for a Number of Materials for Co^{60} Gamma Rays

Material *	Atomic No.	μ_{eff} , cm ² /electron
Paraffin.....	-----	0.147×10^{-24}
Al.....	13	.150
Ni.....	28	.148
Cu.....	29	.152
W.....	74	.187
Pb.....	82	.193
U.....	92	.222

* The thicknesses used are equivalent to 2 cm of Al (5.58 g/cm²).

A similar set of transmission measurements was made through thicknesses of aluminum varying from 0.25 inches to 4.0 inches, as indicated in table II. The value of μ_{eff} increased only very slightly to about 0.156×10^{-24} for the thickest piece tested.

TABLE II

The Effective Compton Cross Section as Measured for a Number of Aluminum Thicknesses for Co^{60} Gamma Rays

Aluminum		μ_{eff} , cm ² /electron
in.	g/cm ²	
0.25	1.77	0.152×10^{-24}
.50	3.54	.150
1.0	7.09	.154
1.5	10.6	.151
2.0	14.2	.155
3.0	21.3	.157
4.0	28.4	.156

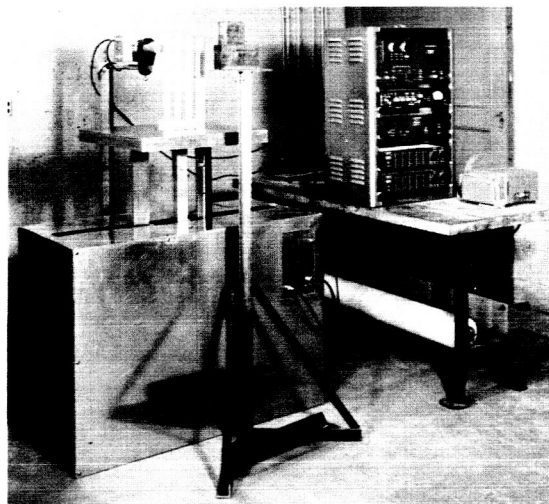


FIGURE 2.—Experimental apparatus.

The experimental apparatus used in these measurements is shown in figure 2. This particular setup shows a fixed source and detector and a movable shield array. This arrangement is useful for calibration and test purposes, but for most applications it is preferable to move either the source or detector, keeping the shield fixed. The apparatus can of course be used in that way also.

In operation, the scanning table moves uniformly in a horizontal direction, counts being accumulated continuously, for a preset distance or time. At predetermined intervals the accumulated count is recorded directly onto

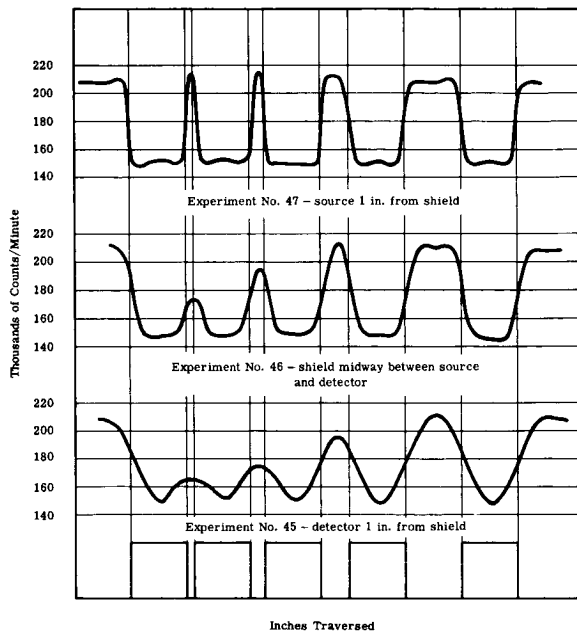


FIGURE 3.—Results of a gamma-ray scan of a 1-inch Al cube array spaced $\frac{1}{8}$, $\frac{1}{4}$, $\frac{1}{2}$, and 1 inch. A 1-inch \times 1-inch crystal and a 5-mc Co^{60} source were used.

paper tape, together with position data if necessary, and the next count interval is begun. After a horizontal traverse is completed, the scanning table is moved vertically a preset amount and another horizontal scan is begun. In this way, the horizontal scan motion is continuous and the vertical is in increments. An alternative technique is to scan in increments in both directions.

A number of parameters were investigated, including detector size, mesh size, source and detector locations, etc. Figure 3 shows the observed counting rate as a shield with discrete holes was scanned with three different source-detector locations. The shield consisted of one-inch blocks of aluminum spaced $\frac{1}{8}$ inch, $\frac{1}{4}$ inch, $\frac{1}{2}$ inch, and 1 inch apart. Source and detector were kept 20 inches apart, and positions relative to the shield were varied as shown. Because the source is small, good resolution is achieved when the source is near the shield. Much poorer resolution is shown when the source is not near the shield.

A more serious consideration is the effect of source and detector location on inferred proton shield effectiveness. Table III shows the result of assuming a particular flare proton spectrum

to be incident on this particular shield, and a simplified dose model (a 10-cm thick slab of water) to be behind the shield.

TABLE III

Effect of Source and Detector Locations on Calculated Dose (Discrete Slab Shield)

Geometry	Dose, MeV
Ideal calculation.....	9.1×10^{11}
Source near shield.....	8.9
Shield at midpoint.....	6.8
Detector near shield.....	7.0

The spectrum used was that of the May 10, 1959 flare, whose large component of low energy protons makes its dose particularly sensitive to shield irregularities. With this geometrically simple shield, we can calculate directly the dose received by the dose model as 9.1×10^{11} MeV. The calculated dose with no shield present was 2.2×10^{12} MeV, so that this partial shield gave an attenuation of a little more than a factor of 2. The gamma probe traverse with the source near the shield gave an inferred dose of 8.9×10^{11} MeV, a value within 3% of the analytical result. With the source far from the shield, however, the inferred doses were substantially lower, because the larger detector ($1'' \times 1''$) partially averaged over the gaps and did not give full effect to gap streaming. We concluded from this test that the source should be kept as close to the shield as possible.

A final measurement that should be mentioned was made on a piece of electronic equipment supplied by NASA, designated NASA Equipment Box, SA 105. The results of this measurement are shown in table IV.

TABLE IV

Shield Effectiveness of Electronic Component (NASA Unit SA 105)

Average Density, gm/cm ²	5.50
Calculated Dose if Homogenized, MeV.....	1.44×10^{11}
Calculated Dose from Gamma Scan	
Collimated geometry.....	3.95×10^{11}
Uncollimated geometry.....	4.2 to 5.2×10^{11}

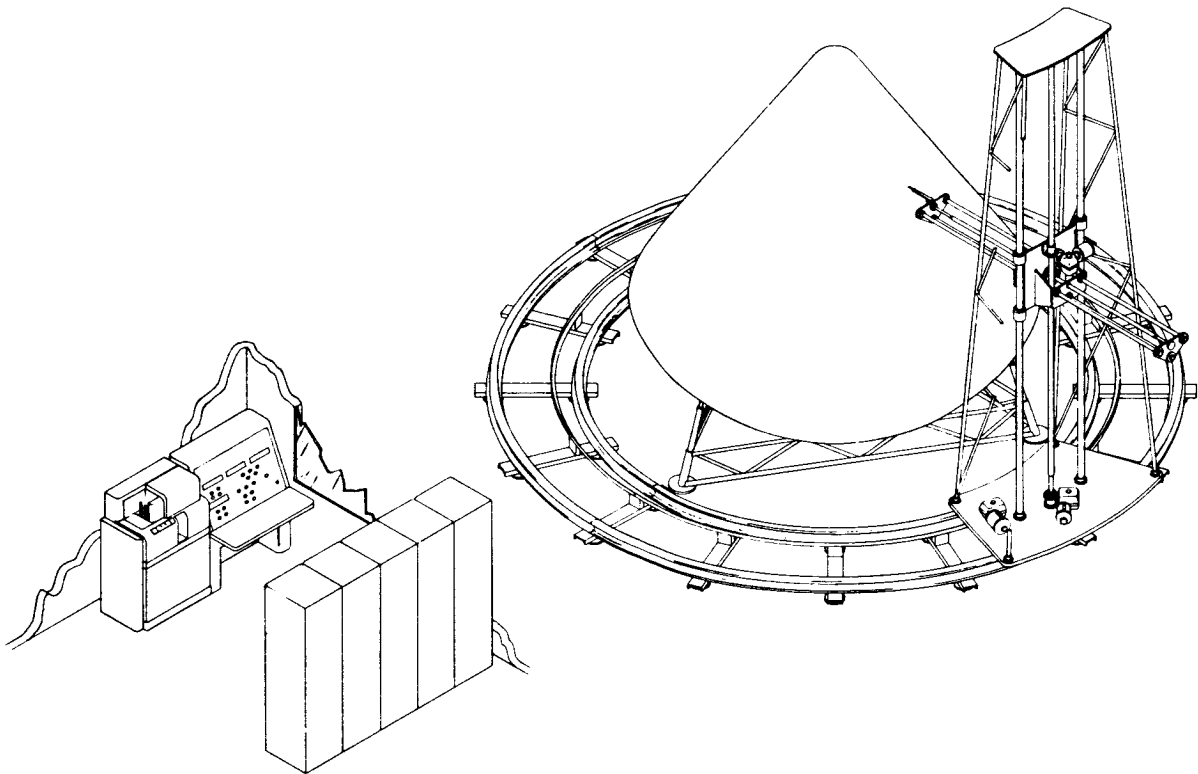


FIGURE 4.—Apollo gamma probe—semiautomatic machine—general arrangement—control and mechanical systems.

The equipment had an average areal density of 5.5 gm/cm^2 . If treated as a homogeneous and uniform aluminum layer, the dose calculated behind it (for the same flare spectrum as in the previous example) would be 1.44×10^{11} MeV. However, the results of the gamma scan on this piece of equipment indicate considerable effects of inhomogeneity. With collimated geometry and a close mesh, the inferred proton dose was 3.95×10^{11} MeV. Several measurements with uncollimated geometry and various mesh intervals gave even higher dose calculations. If we accept the collimated geometry result as accurate, the homogeneous approximation is shown to give a dose in error by more than a factor of 2.5. The homogenization of individual pieces of equipment such as this is characteristic of existing shield analysis methods. Where the equipment comprises only part of the total shielding, however, the error in dose will be less than shown in this example.

The disagreement between uncollimated and collimated results in this case implies that

gamma scattering is more important in a heterogeneous sample such as this than in the homogeneous samples from which μ_{eff} was determined. In a practical situation, it would be possible to make a number of comparison collimated and uncollimated measurements at various points on a shield to determine appropriate values of μ_{eff} for the particular configurations involved. Following this, the comprehensive scans could be made with uncollimated geometry.

As a result of this program, the feasibility and usefulness of the gamma probe technique have been demonstrated, and we have recommended performing a complete gamma scan and associated shield analysis of an Apollo command module. Figure 4 shows a gamma probe design which can be used for the Apollo vehicle. The design also offers considerable flexibility in the geometry that can be treated. The source is mounted on a moving carriage, and up to 10 fixed detectors are located within the module. The y and z coordinates of the

source are positioned remotely but manually. A circumferential traverse is then made automatically around a full revolution, with all detector channels read at predetermined angular locations. Then the y and z coordinates are repositioned manually, and a second circumferential traverse is made in the reverse direction. This is continued until the entire lateral surface is scanned. A somewhat more complex procedure is required to scan beneath the module. The equipment is also capable of scanning the combined command and service modules.

Detector readings and source position data are recorded automatically either on punched cards or magnetic tape. Following the complete scan, the count data are compared with previously determined I_0 values, and all of the data are automatically analyzed in a computer program to permit direct evaluation of shield design calculations.

Another application of the gamma ray probe which is of considerable interest is in the analysis of data obtained by scientific satellites. Many of the detectors used are omnidirectional, and their readings will be strongly influenced by self shielding from other equipment on the

satellite. Consideration is being given to the use of our gamma probe equipment to probe the detector locations of the WL-412 satellite. The results will be used to predict the reading to be expected from the detectors when exposed to a specified omnidirectional proton spectrum. The results could also be correlated to give complete calibration curves for the detectors in terms of proton energy and angle if the program warranted the additional computational effort.

Still other applications of the gamma probe technique for which interest has been expressed include:

1. Probing anthropomorphic man models to determine proton dose to specific organs for various environments. This can easily be done for various positions and with protective clothing or other devices to determine quickly the resulting dose variation.

2. Probing individual equipment components to determine their shielding effectiveness. This can be useful in the design of equipment for maximum shielding effect or in determining the effect on the shield when individual components are moved or replaced.

REFERENCE

1. KRUMBEIN, A. D., and JOHNSON, F.: The Use of Gamma Probing to Determine the Shielding Effectiveness of Space Vehicles. UNC-5075, Feb. 18, 1964.

SESSION IVC

SHIELDING AGAINST SPACE RADIATION

Chairman: R. G. ALSMILLER, Jr.

Oak Ridge National Laboratory

65-34610

33—The Effect of Charged-Particle Environments on Manned Military Space Systems

F. L. KELLER and R. G. PRUETT

Aerospace Corporation

The charged-particle radiation environments in space, both natural and man-made, have recently been receiving the attention of more and more space program planners and system designers. For future space missions, especially those which will be manned, the threat posed by the charged-particle environment could impose certain restrictions on either the vehicle and/or its mission. This paper presents an evaluation of these radiation threats and discusses those which could have a marked influence on future manned space systems.

Many people active in related areas have contributed to this work, including people from the AFWL, AFAMD, The Boeing Company, and, of course, a group of people from SSD/Aerospace headed by Lt. Col. Edward Harney, Dr. F. L. Keller, and Dr. James Vette. The values of internal radiation dose presented in this paper are considered to be best estimates for the environments specified. However, the confidence levels in the environmental data and the dose computation techniques are not considered high and, therefore, these estimates could be in error by factors of two or three or more. Work has continued in all associated fields by a great many people in an effort to improve these data and bring about a more accurate method of predicting the internal radiation dose to the crews of vehicles like Apollo, Gemini, and the MOL.

For convenience of discussion, the charged particle environments have, in this paper, been grouped into three types. These are:

1. Galactic Cosmic Rays.
2. Solar Flares.
3. Geomagnetically Trapped Radiation.

The first section discusses the threat from cosmic rays and the second section presents the most recent data on the nature of solar flares and their effects. The third section describes the geomagnetically trapped belts, their effects on man and equipment, the importance of shielding, and an estimate of internal radiation dose to the crews behind various shielding.

GALACTIC COSMIC RAYS

The steady-state primary galactic cosmic radiation consists mainly of high energy protons (approximately 80 percent) and alphas (approximately 20 percent). They arrive isotropically and have an average energy of several BeV per nucleon. The flux, however, is generally quite small, being on the order of a few particles per square centimeter per second in free space. The problem of galactic cosmic rays and associated RBE values is still an unresolved area; however, their contribution is considered negligible when compared to the dose due to trapped protons. Negligible in this case is defined as a few millirad/day.

SOLAR FLARES

Since the arrival of solar protons at the earth has been studied in detail only since 1956, it has been difficult to obtain a complete picture of this phenomenon and its implications to manned space flight. In addition, there has been some confusion associated with the data gathered, in that measurements made by two or more groups have been shown to be incompatible. However, recent studies, employing a wide variety of techniques, have begun to provide a reasonably complete picture of these solar

proton events. This knowledge is reflected in the work of McDonald (ref. 1) and Webber (ref. 2). Most of the basic solar flare flux data presented in this paper was taken from these references, and the reader is referred to them for a more complete discussion.

The detailed features of solar proton events, that is, energy spectra, intensity-time profiles, and so forth, may vary considerably from event to event and should be cataloged individually for each important event. However, it is useful to define first certain general characteristics which are common to all events in order to aid in understanding these events. The discussion of these general characteristics which follows has been taken directly from Chapter I of reference 1.

A typical event will have a set of intensity-time profiles, one for each energy, such as those shown in figure 1. Certain times characterize each profile:

Onset-Delay Time

The onset-delay time t_o is defined as the time from the maximum of the visual flare intensity to the arrival of the first particles at the earth. This time is variable from event to event and is strongly energy-dependent, the higher energies arriving first. Onset-delay times may vary from a few minutes for high energy particles in some events to many hours for low energy particles in other events.

Rise Time

The rise time t_r is defined as the time interval from the first arrival at the earth of particles of a particular energy to the time at which maximum intensity of these particles is attained. This time also varies from event to event and is strongly energy-dependent, the higher energies reaching maximum intensity first. These times are usually related to the onset times in a particular event, and may range from a few minutes for high energy particles in some events to many hours for low energy particles in other events.

Decay Time

A growing body of evidence indicates that the decay of the intensity of the particles is an exponential at most times for the most energies.

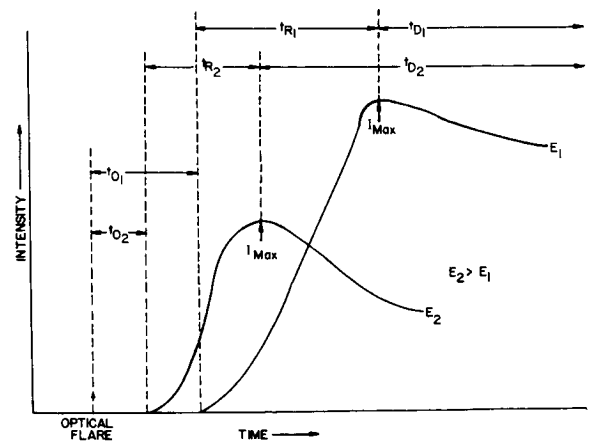


FIGURE 1.—Intensity-time profiles for a typical event.

Thus, we may define a characteristic decay time t_D and write the following equation for the intensity of flare particles with energy greater than some energy E at some time t after the maximum intensity $I_{\max}(E)$ has been attained:

$$I = I_{\max}(E)e^{-t/t_D}$$

the time t_D is a function of energy and is variable from event to event. It may be changed during the course of an event by the arrival at the earth of a changed interplanetary field configuration, such as might be evidenced by a magnetic storm or other magnetic activity. The decay time may range from 3 to 4 hours for high energy particles in some events to 2 to 3 days for low energy particles in other events.

Using particle counters and emulsions in balloons, satellites, and space probes, and through the use of riometer data, approximately 50 solar proton events were recorded during the period from 1956 through 1961. In addition, from a reexamination of old records of ionospheric data taken before 1956, it appears that approximately 17 events can now be identified as having occurred during the period from 1949 through 1955. Therefore, approximately 80 solar proton events which occurred between 1949 and 1962 have been detected. This is not necessarily all of the events which occurred during this time period, of course, but merely the number detected. A larger percentage of all events is probably detected each year as the sensitivities of the detection methods improve.

Some detailed characteristics of the 30 largest events (minimum integrated intensity of 10^6 particles/cm² with $E > 30$ MeV observed at the earth) which were detected during the six-year period 1956 to 1961 are given in table I. These characteristics were obtained from a tabulation given in reference 1.

The study of these 30 events has indicated that, when a flare occurs in the western hemisphere of the sun, on the average a larger fraction of the solar protons which are produced are received at the earth. A *large*, important solar proton event, however, is almost equally likely to arise from a flare in either the eastern or western hemisphere. On the other hand, the majority of these events appears to occur in the northern hemisphere of the sun.

Without going into a detailed discussion of the physical processes involved in the passage of protons through matter, it can be stated that accurate parametric dose calculations can be performed rather simply for protons having a simple power-law energy spectrum incident on a uniform spherical shield of reasonable thickness (~ 1 to 10 g/cm²).

$$\phi(E)dE = kE^{-N}dE$$

are incident on the outside of a uniform spherical shield of thickness t (g/cm²). Next, let

E = initial proton energy, in MeV

E' = proton energy after penetrating shield of thickness t

E_c = initial energy of proton whose range is just equal to the shield thickness (E_c = the "cutoff" energy).

The dose in a small tissue sample located at the center of the spherical shield is then given by

$$\text{Dose (rad)} = k_1 \int_{E_c}^{\infty} \left[\phi(E) \left(-\frac{1}{\rho} \frac{dE'}{dX} \right)_{\text{tissue}} \right] dE$$

where $k_1 = 1.6 \times 10^{-8}$ rad/MeV/g and $\left(-\frac{1}{\rho} \frac{dE'}{dX} \right)_{\text{tissue}}$

is the stopping power of tissue (MeV/g/cm²) for a proton of energy E' .

Included in table I are values for the integrated fluxes of particles with energies greater than 30 to 100 MeV.

In order to estimate the total integrated dose inside shields of various thicknesses, it is necessary to assume a spectrum for the integrated flux of particles. It is obvious from the previous discussion that, if the integrated fluxes of particles with energies greater than 30 and 100 MeV are given, then approximate values for the doses inside shields of 1 g/cm² ($E_c = 30$ MeV) and 10 g/cm² ($E_c = 100$ MeV) can be obtained without an exact knowledge of the spectrum. However, some assumptions regarding spectrum must be made in order to estimate the doses for intermediate shield thicknesses. Therefore, for the purpose of these calculations, it has been assumed that the differential energy spectrum of the integrated flux follows a simple power law. Although this is probably not a true representation of the spectral dependence, it should yield results which are reasonably correct in the region of principal interest (30 to 100 MeV).

For a detailed discussion of how the exponent, N , of the power-law spectrum for each case was determined, the reader is referred to reference 3.

Using this procedure, it was possible to calculate skin doses which would have been accumulated inside shields of 1, 2, 4 and 10 g/cm² thicknesses. Table II presents a summary of these data for the 26 largest solar proton events which occurred during the six-year period 1956 to 1961 (the four smallest events from table I have been omitted in this table).

It may be noted that most of the events which would have produced the largest doses occurred during just three months of the six-year period, namely: February 1956; July 1959; and November 1960 (all of these events were associated with just three active centers on the sun). An inspection of table II shows that severe skin doses would have been acquired inside very thin shields (~ 1 to 2 g/cm²) from a number of the events. On the other hand, because of the steep energy spectra of solar protons, none of the events would have resulted in a serious skin dose inside a 10 g/cm² shield. This rapid decrease in dose with shield thickness also makes it obvious that skin dose is the important quantity to consider for the range of shield thicknesses considered here. However, since the

TABLE I
A Summary of Characteristics of the 30 Largest Solar Proton Events During the Years 1956-1961^a

Date of flare	Importance	Onset and rise time, hr		Decay time, hr		Peak intensity, protons/cm ² /sec		Spectrum at peak intensity	Integrated intensity ^b	
		>30MeV	>100MeV	>30MeV	>100MeV	>30MeV	>100MeV		>30MeV	>100MeV
1956 Feb. 23 Aug. 31	3+ 3	10-16	>100MeV	36	>100MeV	5×10 ⁴	1×10 ⁴	E-4	8×10 ⁹ ~3×10 ⁷	8×10 ⁸ -----
1957 Jan. 20 July 03 Aug. 29-31 Oct. 20	3+ 3+ ----- 3+	-----	-----	No Detailed Estimate Possible	-----	2-5×10 ⁸ ----- 2-3×10 ²	1-3×10 ² ----- ~10 ¹	-----	~3×10 ⁸ ~1×10 ⁷ 5×10 ⁷ 1×10 ⁷	10 ⁷ ----- ----- -----
1958 Feb. 09 Mar. 23 July 07 Aug. 16 Aug. 22 Aug. 26	2+ 3+ 3+ 3+ 3 3	-----	-----	No Detailed Estimate Possible	-----	1.5-2.0×10 ³ 2-3×10 ⁸ 2×10 ² 5×10 ² 1.1×10 ⁸	----- ~5×10 ¹ ~8×10 ¹ ----- 2×10 ¹	-----	~5×10 ⁸ 4×10 ⁸ 5×10 ⁸ 2×10 ⁷ 5×10 ⁷ 5.3×10 ⁷	----- 5×10 ⁶ 7×10 ⁶ ----- 1×10 ⁶ -----
1959 May 10 July 10 July 14 July 16	3+ 3+ 3+ 3+	18-22 30-40 16-20 12-14	12-18 18-20 12-18 4-5	22 40 18 30	10-14 20 9-12 18	1.0-1.2×10 ⁴ 3×10 ³ 1.5-2.0×10 ⁴ 1.2-1.8×10 ⁴	1.5×10 ³ 1.2×10 ³ 2×10 ³ 5×10 ³	E-6 E-4.5 E-4.5 E-4.5	1.2×10 ⁹ 8×10 ⁸ 2.0×10 ⁸ 3.0×10 ⁸	7.5×10 ⁷ 1.2×10 ⁸ 1.2×10 ⁸ 2.0×10 ⁸
1960 Apr. 01 Apr. 05 Apr. 28 May 04 May 06 Sept. 03 Nov. 12 Nov. 15 Nov. 20	3 2+ 3 3+ ----- 3 3+ 3+ 3'	2-3 ----- 8-10 2-3 ----- 12-16 12-16 10-16 3-4	<1 ----- 3-4 <1 ----- 7-9 8-10 3-5 ~1	12 12 18-24 8 32 18-24 16-20 10-16	4-6 ----- 8 4 26 14-18 8-12 4-6	5×10 ¹ 4×10 ¹ 3×10 ² 2×10 ² 0.5-1.0×10 ² 2.4×10 ² 2.4×10 ⁴ 1.5-2.0×10 ⁴ 1×10 ³	6×10 ⁰ ----- 2×10 ¹ 4×10 ¹ ----- 6×10 ¹ 2.5×10 ³ 2.4×10 ³ 3×10 ²	E-4 E-5 E-4.5 E-4 ----- E-3.5 E-4 E-4 E-4	2.7×10 ⁶ 2×10 ⁶ 2.5×10 ⁷ 7×10 ⁶ 7×10 ⁶ ----- 4×10 ⁷ 2.7×10 ⁹ 2×10 ⁹ 6×10 ⁷	1.5×10 ⁶ ----- 7×10 ⁵ 7×10 ⁵ ----- 7×10 ⁶ 2.4×10 ⁸ 1.5×10 ⁸ 6×10 ⁶
1961 July 11 July 12 July 18 July 20 Sept. 28	3 3+ 3+ 3+ 3	8-10 8-12 6-10 4-6 -----	4 6 2-3 1.5 -----	22-26 16-20 24 6-8 -----	18 12 12 3 -----	2×10 ¹ 1.2×10 ² 2.5×10 ³ 3×10 ²	3×10 ⁰ 1.5×10 ¹ 6×10 ² 7×10 ¹	E-4 E-4.5 E-4 E-3.3 -----	2×10 ⁶ 1×10 ⁷ 2.5×10 ⁸ 9×10 ⁶ -----	3×10 ⁵ 1.6×10 ⁶ 3×10 ⁷ 1.2×10 ⁶ -----

^a Some of the values presented in this table have been revised in the Solar Proton Manual, NASA TR R-169, Dec. 1963.
^b Total integrated intensity of protons in event with energies greater than 30 and 100MeV, protons/cm².

TABLE II

Summary of Doses for the Largest Solar Proton Events During 1956-1961

Date of flare		Integrated skin doses (rads) for various shield thicknesses (free space)			
		$t=1\text{g/cm}^2$	$t=2\text{g/cm}^2$	$t=4\text{g/cm}^2$	$t=10\text{g/cm}^2$
1956	Feb. 23	280	180	100	48
	Aug. 31	9.5	2.6	.74	.13
1957	Jan. 20	100	25	5.9	.84
	July 03	3.2	.88	.25	.04
	Aug. 29-31	16	4.4	1.2	.22
	Oct. 20	3.2	.88	.25	.04
1958	Feb. 09	1.6	.44	.12	.02
	Mar. 23	170	29	4.9	.47
	July 07	210	37	6.5	.64
	Aug. 16	6.3	1.7	.49	.09
	Aug. 22	20	3.9	.77	.09
	Aug. 26	17	4.7	1.3	.23
	May 10	360	110	31	5.8
1959	July 10	190	72	28	7.7
	July 14	610	180	50	9.2
	July 16	890	270	78	15
	July 16	890	270	78	15
1960	Apr. 28	9.1	2.1	.46	.06
	May 04	1.8	.62	.21	.05
	May 06	1.6	.44	.12	.02
	Sept. 03	8.8	3.6	1.5	.44
	Nov. 12	740	240	78	18
	Nov. 15	580	180	55	11
	Nov. 20	16	5.3	1.8	.43
1961	July 12	2.6	.89	.31	.07
	July 18	62	23	8.2	2.0
	July 20	2.2	.82	.30	.08

decrease in dose per unit shield thickness decreases with increasing shield thickness, the depth dose becomes relatively more important for thicker shields.

The doses inside a 4 g/cm² shield are of particular interest because of high-energy trapped electrons in the geomagnetic field. For these particles, there is an abrupt change in the curve of total dose versus shield thickness at approximately 4 g/cm² for medium low-Z materials. In this case, it is seen that the only events which would have produced skin doses large enough to cause serious concern were those which occurred during the three months mentioned above (February 1956; July 1959; and

November 1960). If the events which occurred during these three months are neglected, it is seen that the largest dose which would have been acquired inside a 4 g/cm² shield from any of the remaining events was only 30 rad (May 10, 1959), and the sum of the doses from all of the remaining events over the six-year period would have been less than 70 rad (the addition of the smaller events not listed individually would result in only a slight increase). It may be noted that this is probably less than the dose which would be accumulated from galactic cosmic rays over a similar period of time. Hence, it is seen that, with a 4 g/cm² shield, the problem of radiation hazard from solar proton

events reduces to a study of only the very largest events (that is, events such as occurred during February 1956; July 1959; and November 1960).

In the case of the February 23, 1956 event, it is seen that the skin dose inside a 4 g/cm² shield in free space would have been approximately 100 rad. From the rise and decay times, given in table I, it is seen that this dose would have been accumulated over a time period of one to two days.

From table II, it is seen that none of the events which occurred during the other important months of July 1959, and November, 1960, would have resulted in doses of more than approximately 80 rad inside a 4 g/cm² shield in free space. A skin dose of ~80 rad accumulated over a period of one day falls in a region where there are, probably, no statistically demonstrable effects. However, it should be noted that, although no more than ~80 rad would have been accumulated from any one of these events, several closely spaced events occurred during each of these months. Hence, during a period of a week, more than one of these events could have been encountered. The maximum skin dose inside a 4 g/cm² shield from any two adjacent events in these months was ~135 rad. On the other hand, there was sufficient time between the events to allow spacecraft in near-earth orbits to de-orbit and avoid encountering more than one such event.

It should also be pointed out that the doses given in table II are free space doses. If a spacecraft is in a near-earth orbit, then the earth's geomagnetic field (and the earth itself) provides a large amount of additional shielding. The exact amount of additional shielding provided by this means depends, of course, on the orbit inclination, being a maximum (essentially complete) for near-earth equatorial orbits and decreasing to a minimum for near-polar orbits.

In summary, from the above discussion, it appears that a 4 g/cm² shield offers a rather attractive compromise between shield weight and radiation protection from solar events for military spacecraft. With a shield of this thickness, there were no single events during the six-year period 1956 to 1961 which would probably have produced acute radiation effects, and only ~5 events occurred which would have

resulted in skin doses as large as 50 to 100 rad in free space.

It is always tempting to consider providing sufficient shielding to insure that *none* of the observed events would have produced serious effects. However, such a decision should be tempered by the fact that the one event mentioned above was about one-third larger than any of the others observed during this time period and, even if additional material were added to provide protection against a relatively rare event of the size which occurred on February 23, 1956, there would be no assurance that the next rare event would not be even larger.

GEOMAGNETICALLY TRAPPED RADIATION

Trapped Radiation Environment

In order to study the problems imposed by radiation doses accumulated by men and equipment in various orbits, it is first necessary to establish a suitable model for the trapped radiation environment. To be useful, this model must be simple enough to make calculations tractable and yet must represent reality close enough that the results are essentially correct.

The environmental model which was used in this study is typical of conditions which existed around November of 1962, one reason for this choice being the great amount of experimental information which was obtained during the period from July through December of 1962. This environmental model does contain contributions from the fission electrons which were injected as a result of the Starfish nuclear detonation of July 1962. However, since a recent analysis by Van Allen has indicated that the decay time of the artificially injected electrons is of the order of 16 months, conditions at later time periods can be estimated by decreasing the contribution from the fission electrons consistent with this time constant.

The trapped radiation environment consists of electrons ranging in energy from zero up to several MeV and protons ranging from zero up to several hundred MeV. For this study, separate B-L flux maps were constructed for the natural trapped radiation which gave omnidirectional flux contours for low-energy protons, high-energy protons, and two electron spectra.

It was, of course, necessary to assume that the spectrum associated with each of the flux maps remained constant over the whole region covered by the map; therefore, care was taken to establish a most representative spectrum for each of the components. The spectra actually used in this study, normalized to one particle per square centimeter, were the following:

Low-energy protons:

$$\begin{aligned}\phi_1(E)dE &= 4.47 \times 10^2 E^{-4.5} dE & 4 \leq E \leq 15 \text{ MeV} \\ &= 2.29 \times 10^{-3} dE & 15 \leq E \leq 20\end{aligned}$$

High-energy protons:

$$\begin{aligned}\phi_2(E)dE &= 8.7 \times 10^{-3} dE & 20 \leq E \leq 40 \\ &= 1.4 \times 10^{-2} e^{-E/84} dE & 40 \leq E \leq 150 \\ &= 7.8 \times 10^{-3} e^{-E/125} dE & 150 \leq E\end{aligned}$$

Soft electrons:

$$\phi_3(E)dE = 1.724 e^{-E/0.58} dE \quad 0 \leq E$$

Fission electrons:

$$\phi_4(E)dE = 0.71 \exp[-0.575E - 0.055E^2] dE \quad 0 \leq E$$

The choices of spectra and the construction of the B-L flux maps were based primarily on the results of measurements reported from Explorers XII, XIV, and XV, and Telstars I and II.

The quantity of interest in assessing the effects of the environment on satellite systems is the total flux of particles of a given energy spectrum intercepted by satellites in various orbits. Hence, having established the B-L flux maps, the next step was to perform flux interpretations for orbits of various altitudes and inclinations. Machine calculations were performed using a computer code which, first, calculated the B-L values at close intervals around an orbit, then obtained the appropriate flux values at these points from the B-L flux maps, and, finally, integrated the results over time to yield the total number of particles of each given spectrum that intercept 1 cm² of surface area per day on orbit. These calculations were performed for a wide variety of circular orbit altitudes and inclinations, and the results obtained are shown in figures 2 through 6,

where the number of particles of a given spectrum accumulated per cm² per day is plotted versus orbit inclination with orbit altitude as a parameter. It should be mentioned that, for altitudes below ~600 n. mi., almost all of the flux is accumulated during the short interval of time while the satellite is in the region of the South Atlantic anomaly, which is centered at approximately 30 degrees south latitude and has its longest dimension in an east-west direction. Satellites in low-altitude equatorial orbits tend to miss the anomaly entirely, whereas satellites in orbits with inclination of approximately 30 to 40 degrees spend more time per day, on the average, in the region of the anomaly than satellites in higher inclination orbits. This gives a qualitative explanation for the shapes of the flux curves for low altitude orbits. At higher altitudes, the effects of the anomaly disappear and the satellite intercepts appreciable fluxes over a large part of the orbit, causing the curves to have a considerably different shape. From figures 2 through 6, it is seen that the accumulated fluxes can be quite high in some regions of space. Therefore, the next item which should be investigated is the effect of these radiation fluxes on components and materials and the resultant tolerance values.

Radiation Effects and Tolerance Levels

An investigation was made of the radiation effects of each of the types and spectra of particles discussed earlier on typical spacecraft internal and external materials and components. Some of the results of this investigation are summarized in table III in the form of practical external radiation flux tolerance levels for sensitive spacecraft materials and components, assuming that each of the components is located behind an amount of shielding which might be typical of its location in a well designed vehicle. The tolerance level represents the maximum acceptable external flux level, using the specified shielding thicknesses, for each of the four reference spectra given previously. It should be noted that the damage criteria which were used to establish the tolerance levels are given at the bottom of the table and are necessarily different for the different types of materials and components.

From table III, it is seen that photographic film is by far the most sensitive of the internally carried spacecraft materials and components, exclusive of the crew itself. The damage criterion which was used for photographic film was serious fogging, which occurs in typical films at dose levels of ~ 2 to 200 rad. This range of maximum dose levels for film also brackets the region of maximum acceptable dose levels generally assumed for man. Acceptable dose levels established by NASA for its Apollo crews have been in the neighborhood of ~ 50 rad with a maximum emergency dose of ~ 150 to 200 rad. It is possible, of course, that in a crucial situation man could accept considerably larger doses and still accomplish a mandatory military mission, particularly if the dose were accumulated over a relatively long time period such as weeks; however, for the purpose of this paper, it is assumed that the range of tolerance levels given for photographic films also brackets the maximum acceptable tolerance levels for man. Hence, since films can be selected which have tolerance levels at the upper end of this range, it appears that, in a properly designed manned vehicle, the crew

itself should represent the most sensitive internally carried item.

External to the spacecraft, some types of unshielded solar cells could be employed which could exceed acceptable dose levels while the crew inside the vehicle was still within safe tolerances. However, if the same attention is given to the selection of external components and shields as is given to crew shielding, then the crew should continue to be over-all the most sensitive to the radiation environment. For example, this is true for the type of solar cells and shield thicknesses given in table III. This situation could reverse, of course, if crews are rotated and other hardware is not; however, in such cases, the problem merely reverts to an unmanned satellite case. In addition, it is possible to increase the effective radiation tolerance levels of items such as solar cells and transistors by merely over-designing the systems in which they are used. For example, if the capacity of a solar cell system is increased by ~ 25 percent, the tolerance levels increase by approximately an order of magnitude. Similar techniques can be applied to electronic systems by over-designing to allow a larger margin

TABLE III

Practical Radiation Tolerances for Some Typical Sensitive Materials and Components

Material	Tolerance ^a			
	Low energy protons, ϕ_1 , protons/cm ²	High energy protons, ϕ_2 , protons/cm ²	Natural electrons, ϕ_3 , electrons/cm ²	Fission electrons, ϕ_4 , electrons/cm ²
Photographic film ^b with 4 g cm ⁻² shield ----	Large	10 ⁸ -10 ¹⁰	>10 ¹⁴	10 ¹² -10 ¹⁴
N on P silicon solar cells: ^c				
with 20 mils silica shield -----	5 × 10 ¹¹	5 × 10 ¹¹	2 × 10 ¹⁵	5 × 10 ¹⁴
with 100 mils silica shield -----	Large	5 × 10 ¹¹	3 × 10 ¹⁵	5 × 10 ¹⁴
High frequency transistors and diodes: ^d				
with 1 g cm ⁻² shield -----	Large	10 ¹³ -10 ¹⁵	10 ¹⁶ -10 ¹⁸	10 ¹⁵ -10 ¹⁷
with 4 g cm ⁻² shield -----	Large	10 ¹³ -10 ¹⁵	large	>10 ¹⁸
Teflon: ^e with 4 g cm ⁻² shield -----	Large	10 ¹² -10 ¹³	>10 ¹⁷	10 ¹⁶ -10 ¹⁷
Plastics (general) ^e : with 4 g cm ⁻² shield --	Large	10 ¹³ -10 ¹⁶	>10 ²¹	10 ¹⁷ -10 ²¹

^a Maximum acceptable external radiation level using the specified shield thickness for each of the four reference spectra.

^b The damage criterion for given flux tolerances is serious film fogging.

^c The damage criterion is 25% reduction in power output.

^d The damage criterion is 25% reduction in gain.

^e The damage criterion is loss of structural strength.

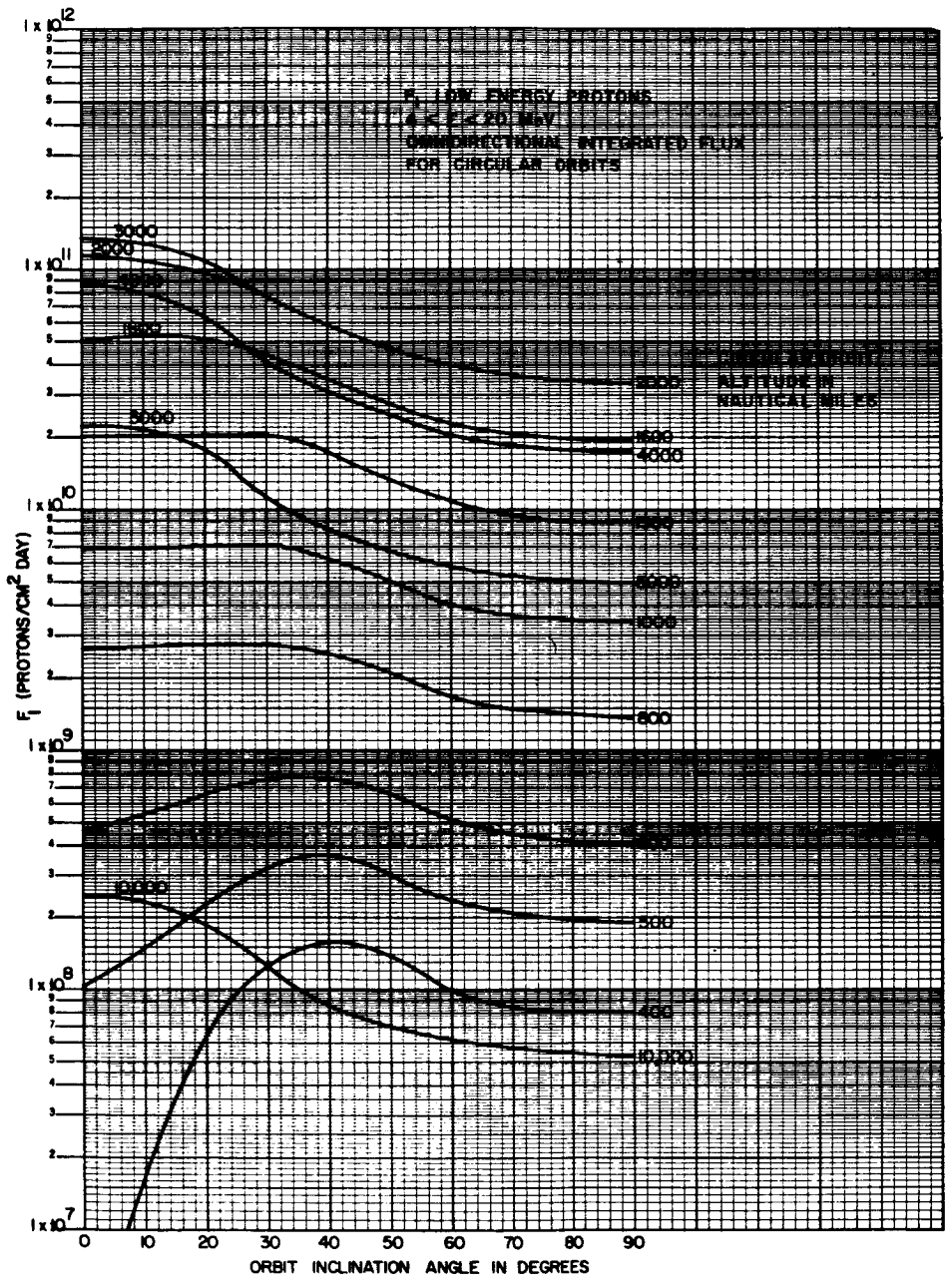


FIGURE 2.—Total flux of particles intercepted by satellites in circular orbit (F_1 , low energy protons, $4 < E < 20$ MeV).

of transistor degradation before a malfunction occurs. On the other hand, material shielding represents the only practical means, at present, of providing radiation protection for the crew. In view of the above facts, the remainder of this paper is concerned only with astronaut dose sensitivity.

The determination of dose levels inside a

spacecraft and the amount of protection which may be provided through the use of material shielding are discussed in the next section.

Shielding

The requirement for providing radiation protection for personnel and equipment in manned space vehicles can result in severe restrictions

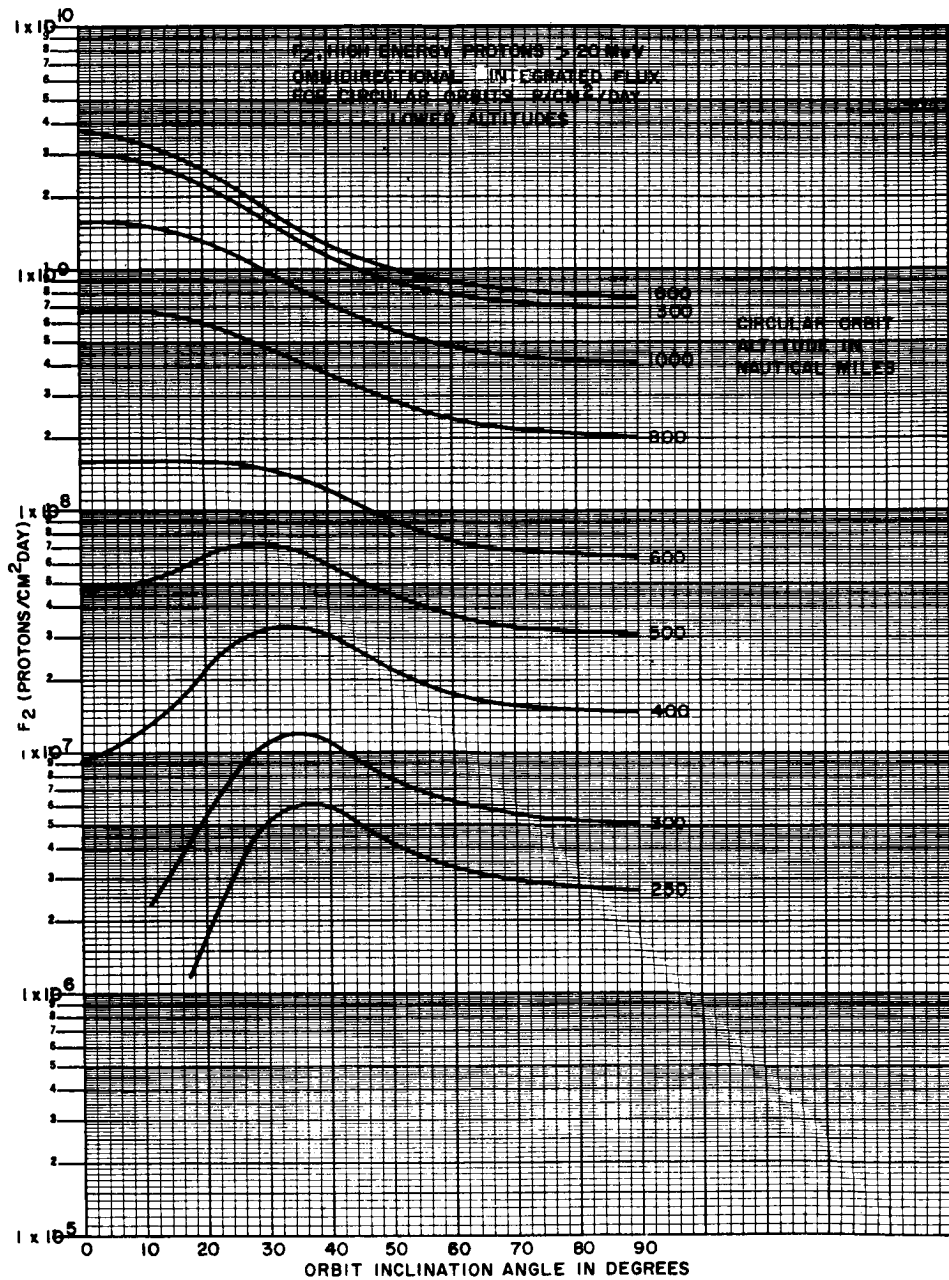


FIGURE 3.—Total flux of particles intercepted by satellites in circular orbit at lower altitudes (F_2 , high energy protons, > 20 MeV).

on vehicle design, mission planning, and payload capability. Therefore, it is important to investigate the degree of protection which may be provided by various combinations and configurations of shielding materials in order that trade-off studies may be performed.

As indicated previously, all of the B-L flux maps used in this investigation were con-

structed to yield omnidirectional flux contours, that is, they did not specify the angular distribution of the radiation as a function of position in space. Therefore, the orbital flux integrations which were performed merely gave integrated omnidirectional fluxes of particles encountered in various orbits. If the effect of spacecraft shielding is to be included and

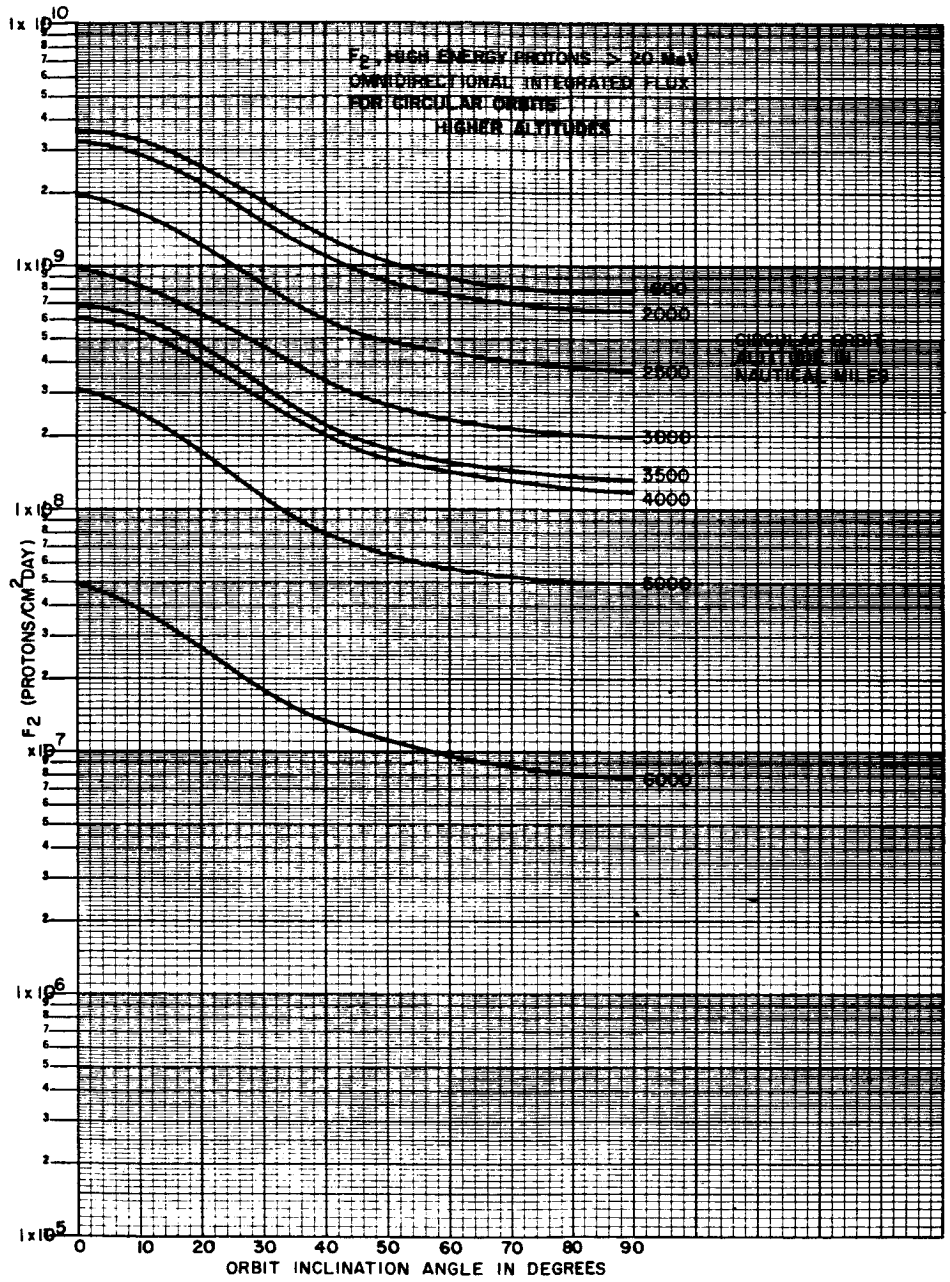


FIGURE 4.—Total flux of particles intercepted by satellites in circular orbit at higher altitudes (F_2 , high energy protons, > 20 MeV).

internal doses calculated, it is necessary to specify an external angular distribution for the incident radiation (except for the special case of dose at the center of a uniform spherical shield). Due to the lack of detailed, reliable information concerning angular distributions, an isotropic distribution of incident particles is usually assumed in performing shielding calculations.

This leads to no error in the special case of a spherical shield, mentioned above, and is probably a fairly good assumption for the integrated flux in more general cases. If the integrated flux is assumed to be isotropic, then the shielding calculations can be performed independent of the orbital integrations. That is, the dose per unit isotropic flux of particles having a

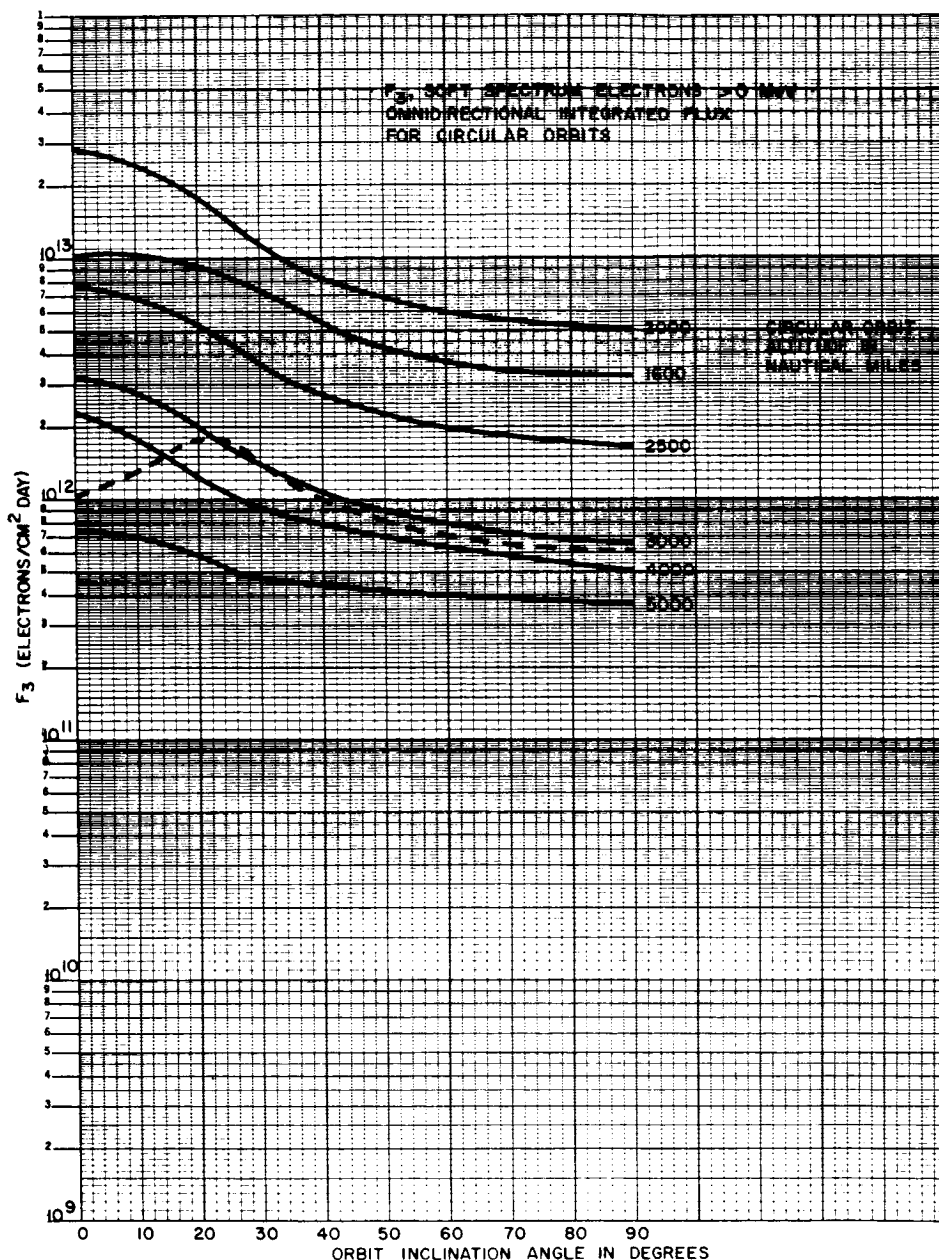


FIGURE 5.—Total flux of particles intercepted by satellites in circular orbit (F_3 , soft spectrum electrons, > 0 MeV).

particular spectrum is calculated only once for a given shield configuration. The integrated dose for any mission is then obtained by merely multiplying the integrated external flux obtained from the orbital calculation by this "unit flux dose."

This section is primarily concerned with the results of calculations which were performed to

determine "unit-flux doses" which would result inside uniform spherical shields of various thicknesses and types of material, for each of the particle spectra given in the section entitled "Trapped Radiation Environment" (with the exception of the low-energy protons). Protons with energies of ~ 20 MeV, or less, are stopped by approximately 0.5 gm/cm^2 of most materials.

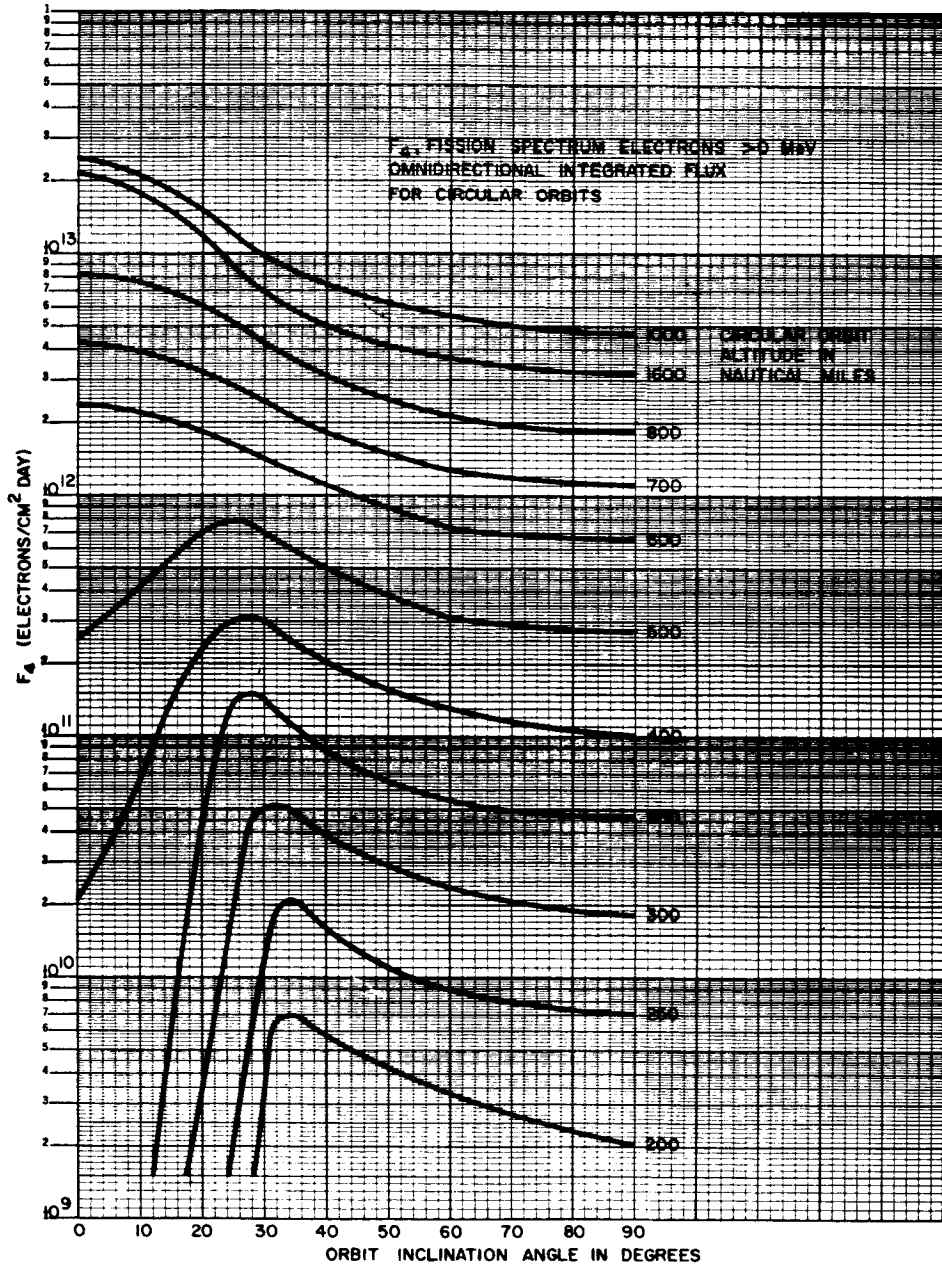


FIGURE 6.—Total flux of particles intercepted by satellites in circular orbit (F_4 , fission spectrum electrons, > 0 MeV).

Therefore, since any reasonable manned space vehicle (or space suit) would be expected to provide at least ~ 0.5 gm/cm² of shielding in any direction, dose calculations have not been performed for the low-energy proton spectrum, ϕ_1 . It should be mentioned that shielding codes developed by the Boeing Company were used

to obtain most of the electron and electron bremsstrahlung dose results in this paper.

In figure 7, the unit-flux dose (rad/unit external flux) from high-energy protons, ϕ_2 , is plotted versus shielding thickness, t (gm/cm²), for various shielding materials. The high-energy proton dose should be approximately the

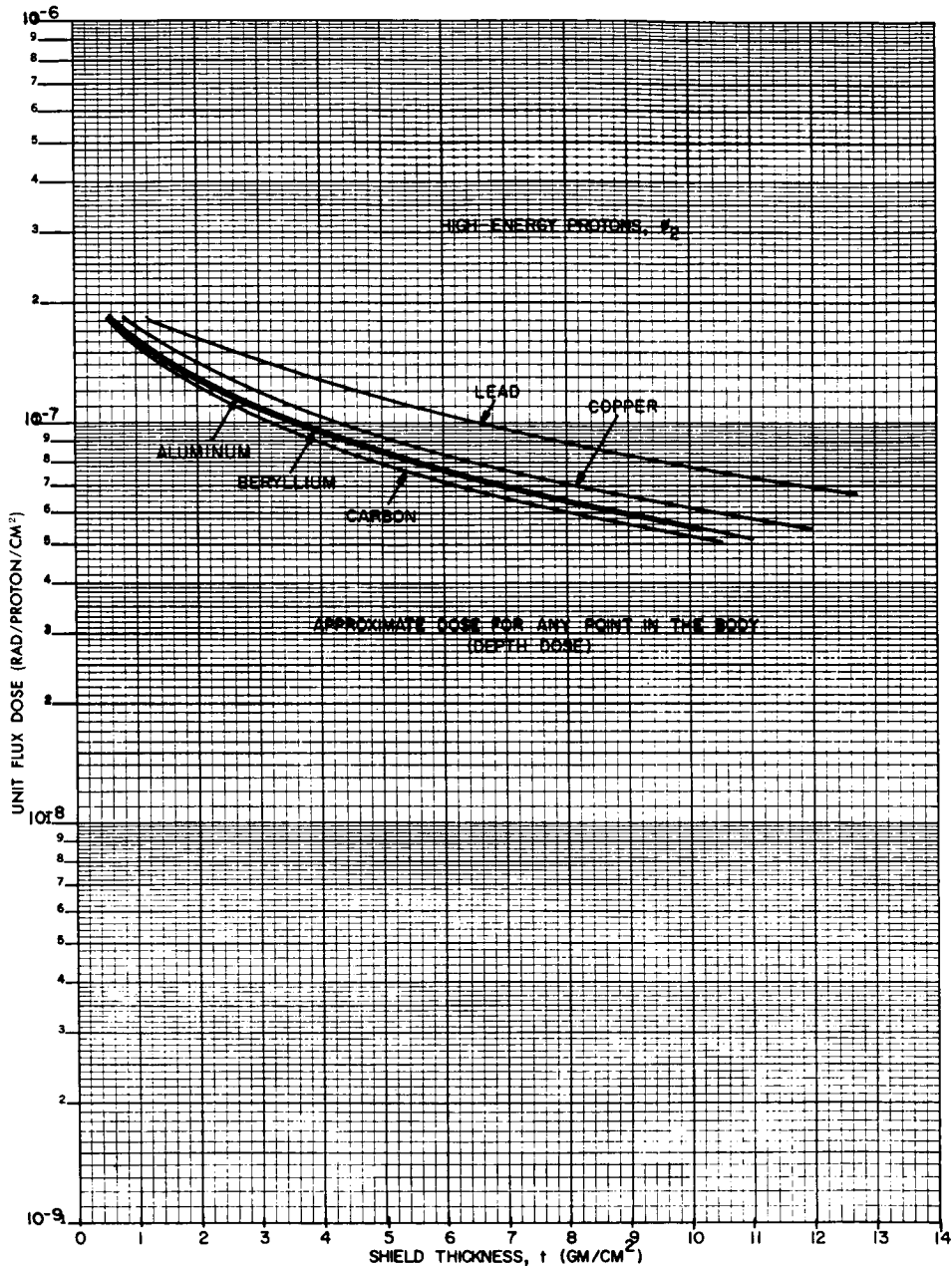


FIGURE 7.—Dose at any body point from high-energy protons.

same at any point in the body. From figure 7, it is seen that the unit-flux dose from high-energy protons decreases very slowly with increasing shield thickness and is not strongly dependent upon the type of shielding material employed. To within a factor of approximately two, it appears that the dose behind 0.5 to 10 gm/cm² of any of these materials is approximately the same. Hence, it is obvious that very large shielding thicknesses, implying

enormous spacecraft weights, would be required to make major changes in the high-energy proton dose. As a result, the high-energy proton dose at any point in the body should be approximately equal to 10⁻⁷ rad/unit external flux for any vehicle of reasonable weight (to within a factor of 2 or 3).

Curves are presented in figure 8 for unit-flux doses from both direct penetrating electrons and electron bremsstrahlung, for incident electrons

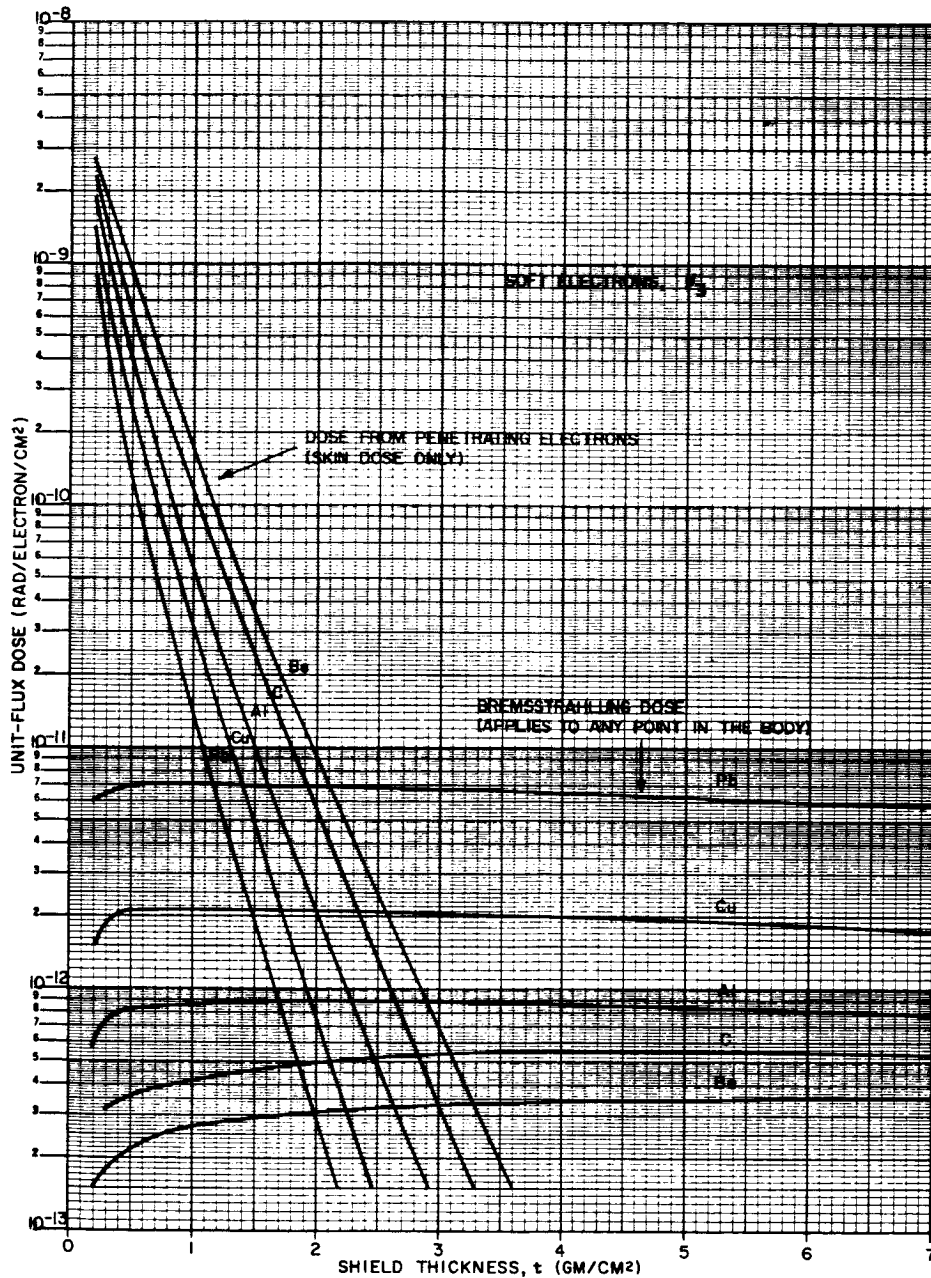


FIGURE 8.—Electron and bremsstrahlung body doses for incident electrons having the soft spectrum, ϕ_3 .

having the soft spectrum, ϕ_3 . The dose from direct penetrating electrons represents a unit-flux dose which would be expected at the surface of the body (skin dose); whereas, the bremsstrahlung dose should be approximately the same at every point in the body. Similar curves are presented in figure 9 for incident electrons having the fission spectrum, ϕ_4 . Plotted in this manner, the curves allow one to make the following observations:

- (1) The first few gm/cm² of shielding material are extremely effective in reducing the crew dose from incident electrons because of the very rapid attenuation of the skin dose which results from penetrating electrons.
- (2) After the first few gm/cm² of material have reduced the skin dose from penetrating electrons to a value which is comparable to the bremsstrahlung dose (~ 4 to 5 gm/cm² for fission electrons), there is very little advantage

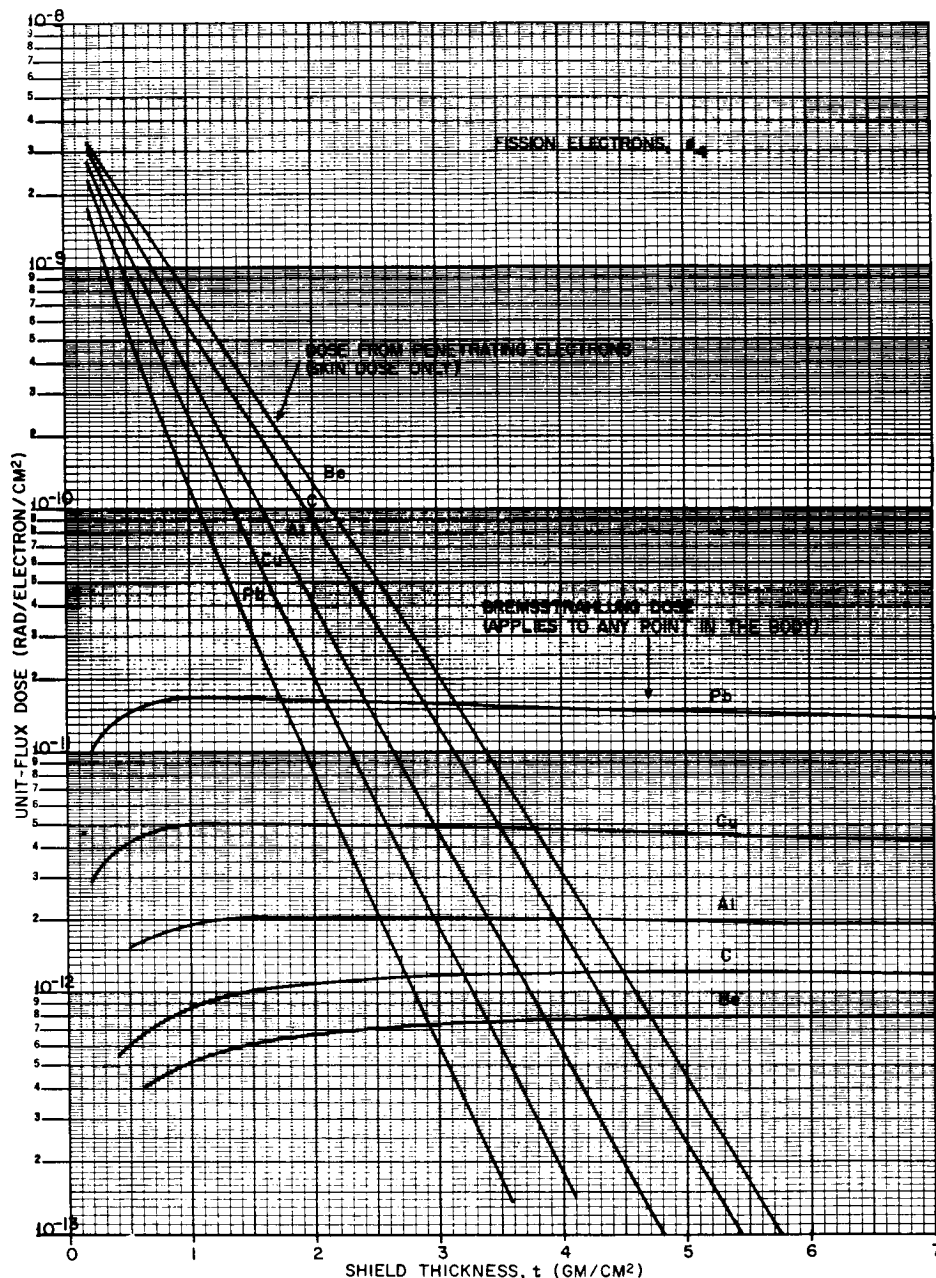


FIGURE 9.—Electron and bremsstrahlung body doses for incident electrons having the fission spectrum, ϕ_1 .

in adding additional shielding material since very large thicknesses are required to produce a major change in this bremsstrahlung gamma dose.

(3) The bremsstrahlung dose is approximately proportional to the atomic number of the stopping material. Therefore, it is desirable to have several gm/cm² of low-Z materials on the outside of the shield. On the other hand, since

essentially all the materials which are used in spacecraft construction have effective atomic numbers which lie between 4 and 40, the bremsstrahlung dose inside any reasonable vehicle should lie within a factor of approximately 3 of the value for a shield of pure aluminum ($Z=13$).

From the above comments it is clear that, if a crew shield must provide protection in high electron fluxes, an effort must be made to

provide at least a few gm/cm² of relatively low-Z material in all directions. One must be very careful to insure that there are no very thin regions, or "windows," in the shield since it is obvious, from the very rapid increase of penetrating electron dose with decreasing shield thickness, that the dose contribution from a "window" region can completely negate the effect of the rest of the shield. After a few gm/cm² of shielding has been provided in all directions, however, the addition of more material has a relatively minor effect on the resultant dose because of the difficulty in attenuating the bremsstrahlung gammas.

In summary, it appears that the following general statements can be made. To within a factor of approximately three, the unit-flux doses at any point in the body from high-energy protons and electron bremsstrahlung should have the following values inside any spacecraft of reasonable weight:

Protons (high energy, ϕ_2) : 10^{-7} rad/unit external flux.

Electron bremsstrahlung (soft electrons, ϕ_3) : 8×10^{-13} rad/unit external flux.

Electron bremsstrahlung (fission electrons, ϕ_4) : 2×10^{-12} rad/unit external flux.

If a minimum of 4 or 5 gm/cm² of shielding is provided in all directions, then the doses from penetrating electrons may be neglected compared with the doses given above for the electron bremsstrahlung. On the other hand, if the shielding in some directions is considerably smaller than this, then the skin dose from penetrating electrons can be the most important contribution, and a detailed shielding calculation for the specific vehicle configuration is required in order to establish its value.

It should, perhaps, be mentioned that shielding calculations, based on detailed sector analyses, were performed for the NASA Gemini and Apollo vehicles in order to obtain some feeling for the radiation protection provided by specific manned vehicles which have already been designed. For both vehicles, the calculated unit-flux doses from high-energy protons and electron bremsstrahlung were consistent with the approximate values given above (within a factor of ~ 2), the unit-flux bremsstrahlung doses for Gemini being somewhat higher than those for Apollo because of

the large amount of relatively high-Z material, René 41 ($Z \approx 28$), which is used on the outside surface of Gemini. On the other hand, it was found that, because of "thin" spots in the hatch or window regions of both of these vehicles, the unit-flux doses from direct penetrating electrons were considerably greater (a factor of ~ 10) than the unit-flux bremsstrahlung doses. For both vehicles, the results of the detailed sector calculations gave unit-flux doses from direct penetrating electrons which were approximately equivalent to the values shown in figures 8 and 9 for the case of $1\frac{1}{2}$ to 2 gm/cm² aluminum shield. Hence, it is obvious that the addition of shielding material in the "thin" spots could increase significantly the radiation protection provided against trapped electrons by both of these vehicles. Calculations indicate that the careful addition of a few hundred pounds of shielding material in these regions would reduce the doses from direct penetrating electrons below those from bremsstrahlung in both of these vehicles (≈ 4 gm/cm² effective shielding in all directions). Further major dose decreases would then, of course, require enormous weight increases.

Dose Calculations

Using the environment outlined in the section entitled "Trapped Radiation Environment" and the shielding techniques of the preceding section, total dose estimates behind various shield thicknesses can be made for a wide range of orbit altitudes and inclinations. Since the first manned military space flights will probably occur in the 1968 to 1970 time period, the contributions from the fission electrons have been adjusted (using a ~ 16 month decay time) to yield results for this paper which should be typical of ~ 1968 . Representative curves are presented in figures 10 and 11 which yield total biological dose accumulated per day behind various shield thicknesses as a function of circular orbit altitude for orbit inclinations of 30 and 90 degrees, respectively. These inclinations were chosen as being typical of those commonly associated with launches from the Eastern Test Range and the Western Test Range, respectively. Aluminum shield thicknesses of 0.5, 1.0, 2.0, and 4.0 g/cm² were selected on the basis that: (a) 0.5 g/cm² is

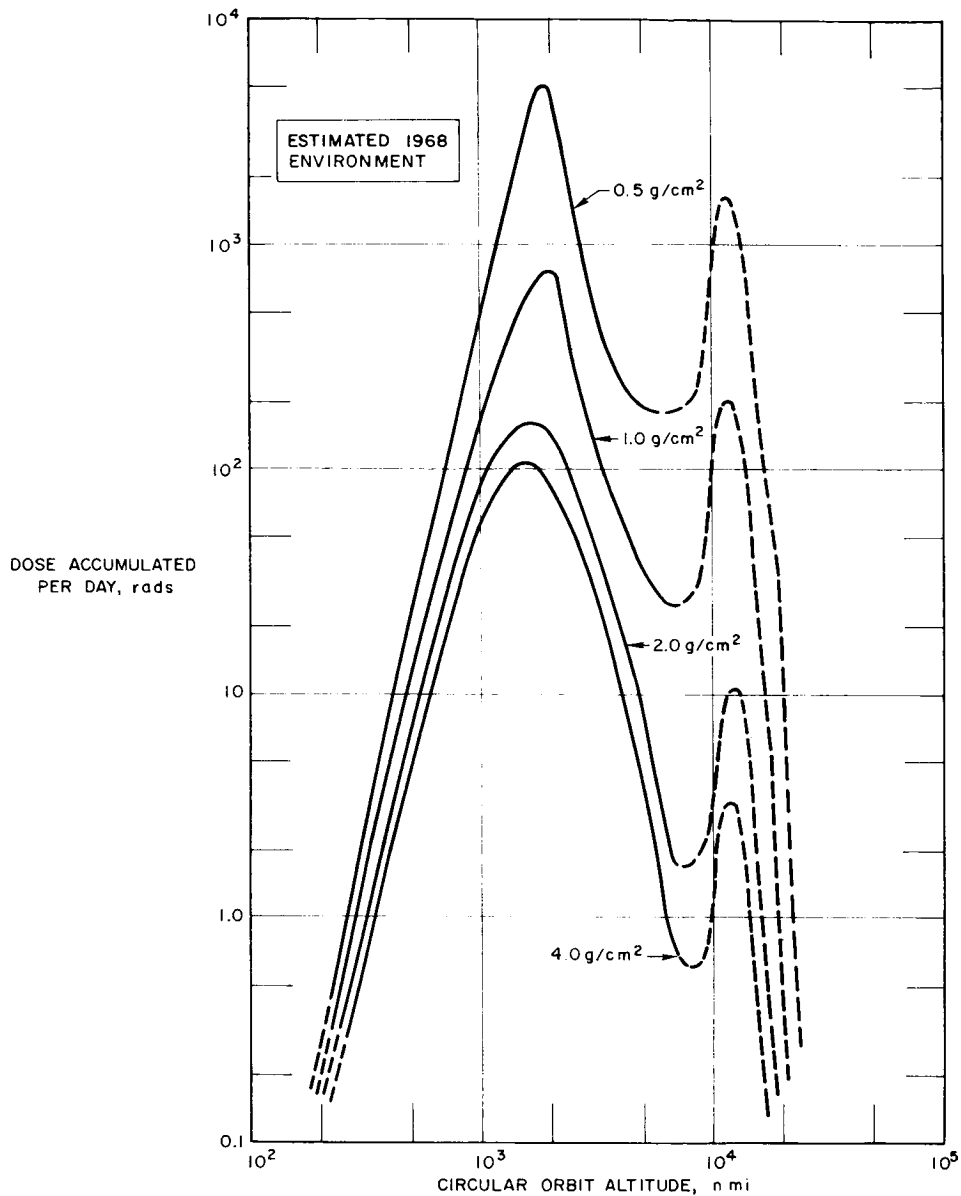


FIGURE 10.—Biological dose due to trapped radiation environment (30 degree inclination).

typical of the shielding provided by astronaut space suits; (b) 1.0–2.0 g/cm² represents thicknesses which are typical of normal spacecraft construction where minimum weight is a prime objective; and (c) 4 g/cm² is typical of a well-shielded vehicle (that is, much greater thicknesses are required to make further significant dose decreases).

From figures 10 and 11, it is seen that the shapes of the curves for the two inclinations are very similar, the curves for 30 deg inclination

generally being a factor of approximately two greater than those for 90 deg inclination. It should perhaps be mentioned that, if curves were drawn for equatorial orbits, they would be slightly higher than those shown in figure 10 for altitudes greater than ~ 600 n. mi.; however, at lower altitudes the doses accumulated in equatorial orbits would be much lower since these orbits would miss the intense region of the South Atlantic anomaly.

As mentioned above, the curves shown in

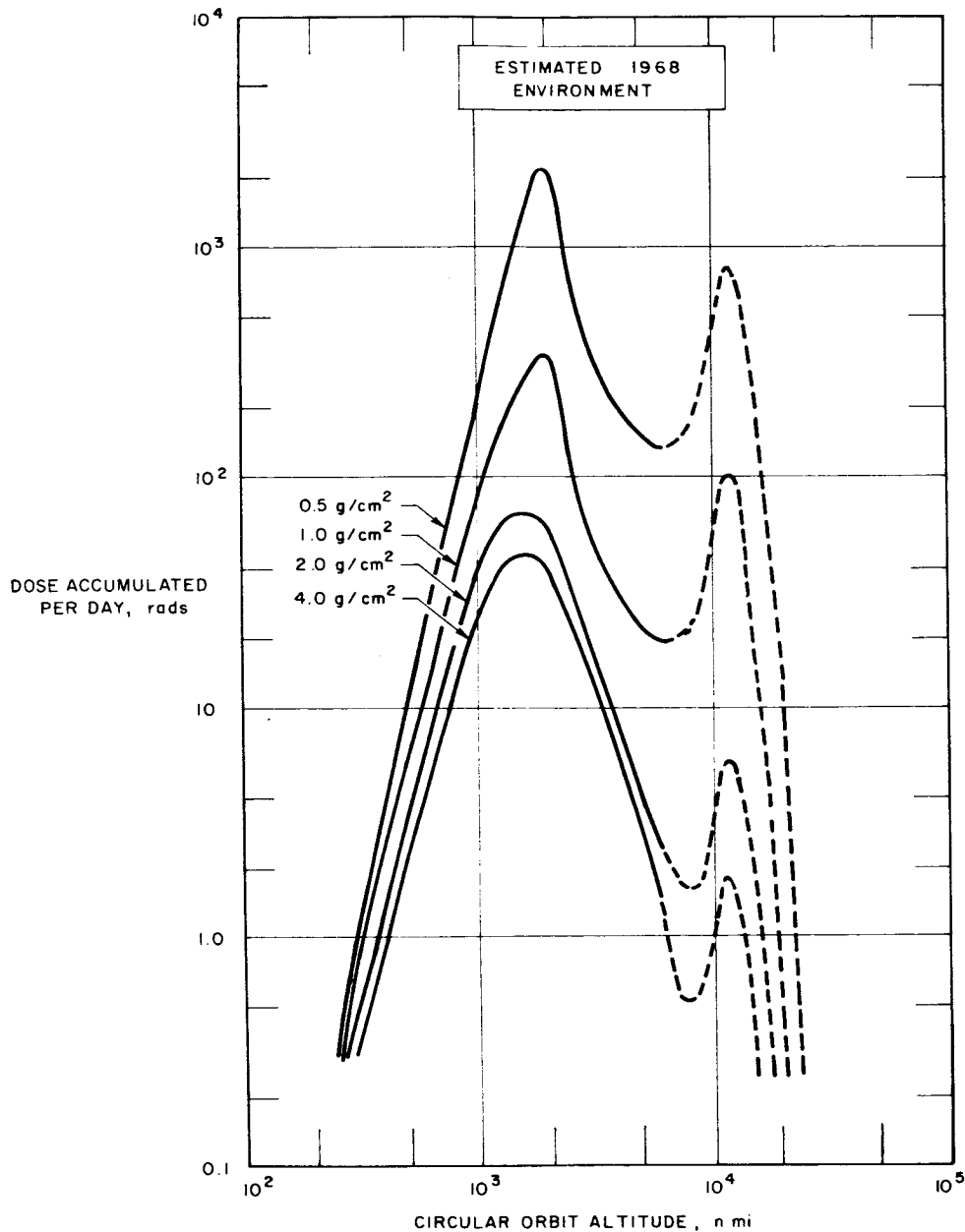


FIGURE 11.—Biological dose due to trapped radiation environment (90 degree inclination).

figures 10 and 11 represent total doses accumulated per day, that is, they include the contribution from both protons and electrons. In the case of the curves for 4 g/cm² of shielding, it is obvious from the discussion of shielding in the preceding section that the accumulated dose represents a whole body depth dose from either high-energy protons or electron bremsstrahlung. For altitudes below ~7000 to 8000 n. mi. the dose behind a 4 g/cm² shield is

almost entirely due to high-energy protons, the heart of the inner proton belt being located at an altitude of ~1500 n. mi. At altitudes above ~8000 n. mi. the dose behind a 4 gm/cm² shield is due to bremsstrahlung from outer belt electrons, the peak occurring at an altitude of ~12 000 n. mi. As the shielding thickness is decreased, the major reason for the increase in dose is the increased contribution from direct penetrating electrons. (There is a slight in-

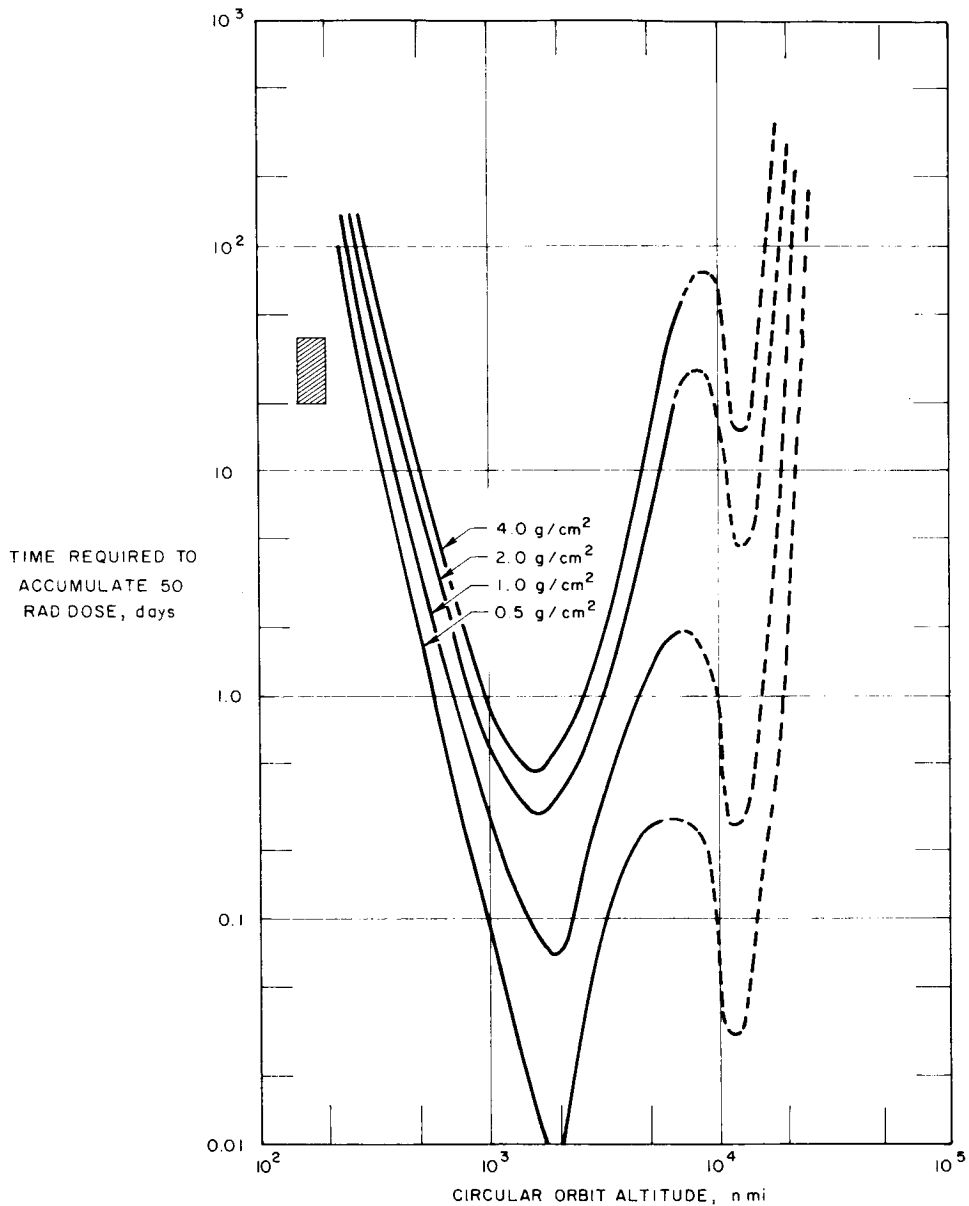


FIGURE 12.—Allowable mission duration for 50 rad dose (30 degree inclination).

crease in the high energy proton dose; however, it changes by less than a factor of two going from 4.0 to 0.5 gm/cm².) Therefore, the increase in dose which occurs as one goes to smaller shield thicknesses is primarily an increase in the surface, or skin, dose due to direct penetrating electrons, the depth dose remaining approximately the same as for the 4 g/cm² shield.

From figures 10 and 11, it is seen that very large radiation doses can be accumulated in relatively short periods of time over a large

altitude range. Hence, for a given dose tolerance level, the radiation environment imposes a restriction on the allowable mission time at any altitude. The data shown in figures 10 and 11 have been re-plotted in figures 12 and 13 to give directly the time required to accumulate a dose of ~50 rads behind various shielding thicknesses as a function of altitude, for orbit inclinations of 30 and 90 degrees, respectively. For example, from figure 12 it is seen that, for an accumulated dose tolerance level of 50 rad,

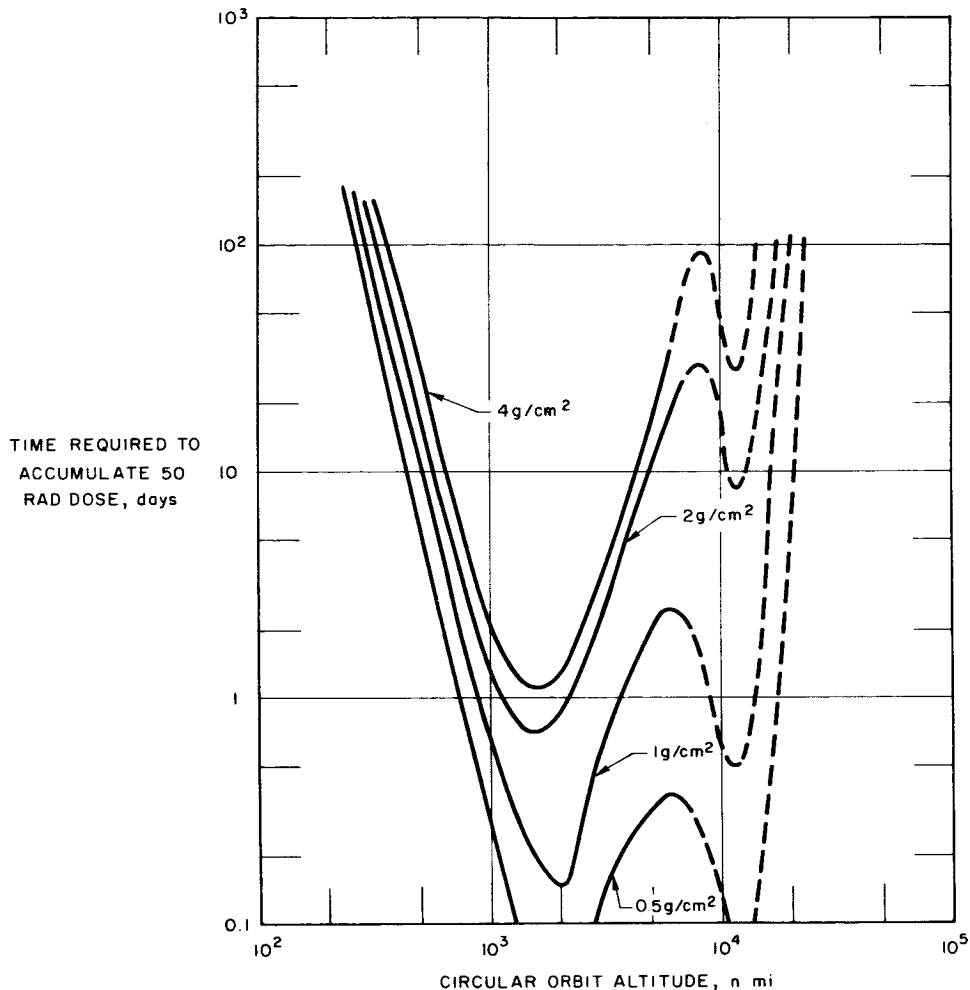


FIGURE 13.—Allowable mission duration for 50 rad dose (90 degree inclination).

even with a 4 g/cm² shield, missions involving a crew duration of 90 days would be restricted to altitudes of less than ~300 n. mi. or greater than ~15 000 n. mi. Similarly, doses of greater than 50 rad would be accumulated behind a 4 g/cm² shield for missions as short as one day at altitudes of ~900 to 2500 n. mi. Hence, it is obvious that the effects of the trapped radiation environment and the possible shielding trade-offs must be carefully considered in mission planning for manned military space flight.

It is not the purpose of this paper to become involved in a discussion of potential manned military space missions; however, some comments should, perhaps, be made regarding the first manned military space flights which will probably occur in the 1968 to 1970 time period

in connection with the Manned Orbiting Laboratory (MOL) Program.

The primary objective of the MOL Program is to provide an in-space testing capability which will qualitatively and quantitatively assess the military usefulness of man in space. In order to fulfill this objective, a flight program is envisioned which will involve launches from the Eastern Test Range into orbits with ~30 degree inclination and altitudes of ~125 to 200 n. mi. The orbiting vehicle will probably consist of the Laboratory Vehicle and a Gemini B Spacecraft. The MOL mission duration is to be of the order of one month with re-entry to be accomplished with the Gemini vehicle. The approximate MOL operating regime is indicated by the shaded area on

figure 12. From figures 10 and 12, it is seen that even at the high end of the possible MOL altitude range, the allowable mission time to accumulate 50 rads in a vehicle with an effective shielding thickness of no more than ~ 1 g/cm² is hundreds of days. Hence, at the high end of the possible altitude range, the astronauts would not be expected to receive more than a few rads in 30 days; whereas, at the lower end of the possible altitude range, the accumulated dose should be considerably less than 1 rad. In view of these facts, the trapped radiation environment is expected to have little influence on the MOL vehicle design. On the other hand, as pointed out previously, the trapped radiation environment could have a dramatic influence on the planning of other higher altitude or longer duration potential manned military space missions.

CONCLUSIONS

From the foregoing discussions, the following general conclusions regarding radiation effects on manned military space systems can be drawn.

(1) The earth's trapped radiation belts constitute a definite threat to manned satellites orbiting for extended periods between a few hundred nautical miles and several thousand nautical miles.

(2) For earth orbit altitudes out to a few thousand miles and inclinations up to about 50°, the threat from solar flares is generally negligible compared with the threat from the geomagneti-

cally trapped radiation. Polar orbiting satellites could conceivably encounter solar proton bursts which would make a quick de-orbit or a descent to lower altitudes desirable.

(3) For the altitude range and inclination currently planned for the MOL, the 30-day radiation dose to the crew is expected to be no more than a few rads, even at the highest altitudes considered. This conclusion is based on the assumption that no further nuclear detonations occur in near-earth space (few earth radii).

(4) Vehicle shield thicknesses greater than about 4 to 5 g/cm² are not considered worthwhile from an added radiation protection standpoint.

(5) Where electrons and the accompanying bremsstrahlung make a large contribution to the total dose, and when cost and other factors permit, low-Z materials should be used to form the spacecraft's outermost surface.

(6) For Gemini and Apollo, the addition of a few hundred pounds could afford the crews the protection of about 4.5 g/cm² over the entire 4π steradian solid angle. Were these vehicles to be used in either a high electron flux environment or for long periods in a relatively low flux electron environment, this added shielding might prove desirable.

(7) A better definition of the space radiation environment and a more accurate method of calculating internal dose are needed. Progress in both these areas is being made.

REFERENCES

1. McDONALD, FRANK B. (ED.): Solar Proton Manual. GSFC Doc. X-611-62-122, Revised Jan. 25, 1963.
2. WEBBER, W. R.: An Evaluation of the Radiation Hazard Due to Solar-Particle Events. Boeing Company Rept. D2-90469, Dec. 1963.
3. ANON.: The Effect of Charged Particle Environments on Military Space Flight. SSD-TDR-63-244, Sept. 1963 (SRD).

Revised
1165-18921
✓

34—The Ionizing Radiations in Supersonic Transport Flights

TRUTZ FOELSCHÉ

Langley Research Center, NASA

Commercial supersonic transport planes are envisioned to cruise at altitudes up to 23 km or 75 000 feet. The exposure to crew and passengers from galactic and solar cosmic rays at these altitudes on polar routes is estimated and compared with the maximum permissible dose rates (MPD) cited in the guidelines of the Federal Radiation Council or the International Commission for Radiation Protection.

The dose equivalent in rem from galactic cosmic radiation at cruise altitudes on polar routes is estimated as ≤ 2 mrem/hr. This implies that the crew should experience ≤ 20 percent of the MPD for radiation workers (5 rem/year), at 20 hours/week flight duty or 10 hours in 23 km altitude, if evasive measures during intense and energetic solar flare events are taken. The above dose rate from Galactic Cosmic Rays is considered as an upper limit because the fast neutron flux and the buildup factors of secondaries in the airplane are assumed conservatively high.

Estimates of dose rates for the most important intense and energetic flare events (solar cosmic radiation) show that in cruise altitudes at high latitudes and in impact zones, e.g., during the February 23, 1956 event, 1 to 4 rem/hr might have been reached. Such doses are undesirable for the crew and especially for passengers, even if their occurrence is very rare.

If evasive measures are carried out in these cases, such as descending to 40 000 feet (12 km), the radiation doses received by passengers from solar and galactic cosmic rays appear negligible (≈ 10 percent of the MPD of 0.5 rem/year at 2 polar flights/month) except for the effects of certain characteristic biological effective components of galactic cosmic rays which appear only in high altitudes, i.e., heavy primaries and stars. These components and also the fast neutron fluxes as they occur in the human body in the passenger plane are not well known in their intensity except that this intensity is very low (e.g., heavy primaries ≈ 1 hit/g/day; stars ≈ 1000 hits/g/day) and will not produce a significant ionization dose. More research appears necessary on their fluxes and on their effects at the very low doses, which would be encountered at a reasonable amount of flying, to determine more closely the risk involved for especially sensitive persons such as pregnant passengers and children.

INTRODUCTION

Supersonic commercial airplanes as they are envisioned for the near future are planned to cruise in altitudes up to about 75 000 feet or 23 km. At this altitude there is only 36 g/cm², or 3.6 percent of the mass of the atmosphere above the airplane, which protects against space radiations if their energy is not too high.

This air layer suffices, for instance, to shield against the soft belt radiations and aurora radiations that reach the uppermost atmosphere during magnetic storms; however, it does not suffice to protect against galactic cosmic rays

(G.C.R.) which penetrate deep into the atmosphere, down to sea level and below sea level, or against energetic solar cosmic rays, which are observed in some cases also at sea level. In estimating the effects of space radiations on crew and passengers of SST airplanes, one is, therefore, mainly concerned with G.C.R. and energetic solar cosmic rays (S.C.R.).

It might be well to recall in the beginning the maximum permissible exposure levels for normal peacetime operations, as listed in the protection guidelines of the International Commission for Radiation Protection (ICRP) or of the Federal Radiation Council.

TABLE I

Type of exposure	Condition	Dose, rem
Radiation worker:		
(a) Whole body, head and trunk, active blood forming organs, gonads, or lens of eye.	Accumulated dose-----	5 times number of years beyond age 18.
	$\left(\frac{5 \text{ rem}}{\text{year}} = \frac{100 \text{ mrem}}{\text{week}} = \frac{15 \text{ mrem}}{\text{day}} = \frac{0.625 \text{ mrem}}{\text{hour}}\right)$	
(b) Bone-----	Body burden-----	0.1 microgram of radium 226 or its biological equivalent.
Population:		
(a) Individual-----	Year-----	0.5 (whole body).
(b) Average-----	30 years-----	5 (gonads).

These low permissible doses for continuing peacetime operations—low in comparison to the standards for space crews in the present pioneer period—are the reason that the low level G.C.R. might have to be taken into consideration in commercial supersonic transport flights, especially since the G.C.R. and their secondaries at SST altitudes have different characteristics from the radiations at sea level.

It might be emphasized, that the dose values presented in the following are estimates with emphasis on upper limits. Since not all components and their biological effects are accurately known, a safety factor is included.

GALACTIC COSMIC RAYS

We might recall first some quantitative data on G.C.R. Figure 1 (ref. 1) shows the decrease

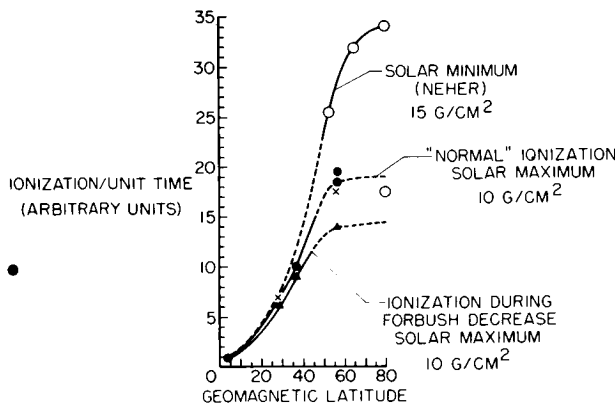


FIGURE 1.—Total ionization at atmospheric depth of 10 g/cm² as a function of geomagnetic latitude at solar minimum and maximum (ref. 1)

of dose rate toward the equator, or the shielding effect of the earth's magnetic field according to balloon measurements of Neher and Winckler and coworkers (ref. 1). It decreases by a factor of 20 during solar maximum years (at an altitude of about 30 km). A second fact is indicated by this figure, namely that the ionization is higher by a factor 2 during solar minimum years than during solar maximum years in latitudes above ≈ 55°.

We derive from the figure, that the dose rate is highest near the poles and about constant above 50° magnetic latitude during solar activity years. We are, therefore, mainly concerned with the radiation on polar routes.

Figure 2 (ref. 2) shows the variation of the particle flux with altitude, especially the transition peak at about 60 g/cm² atmospheric depth

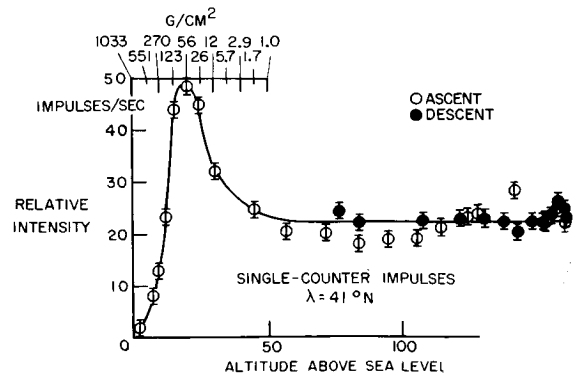


FIGURE 2.—Total intensity up to ν measured by unshielded sing' latitudes (ref. 2)

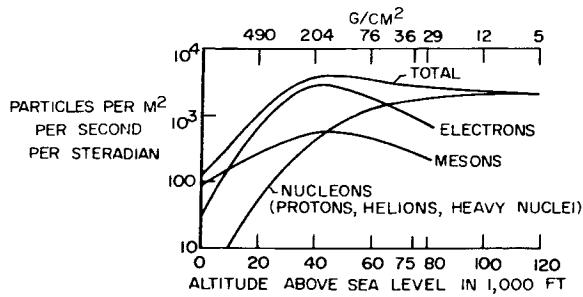


FIGURE 3.—Altitude profile of particle transition of cosmic ray beam in the atmosphere (ref. 3)

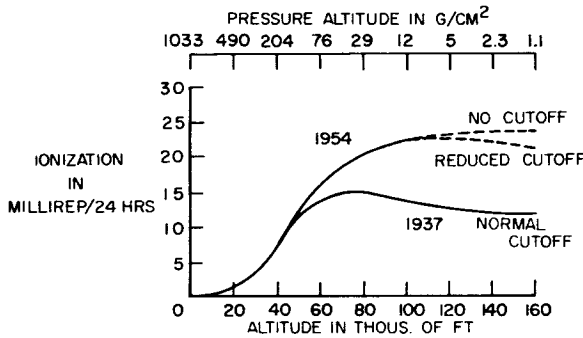


FIGURE 4.—Altitude profile of the total ionization in a year of high (1937) and low (1954) solar activity. (ref. 3).

according to the famous first rocket measurements of Van Allen and Tatel up to altitudes of 160 km.

Figure 3 (ref. 3) shows the change of the composition of the G.C.R. beam penetrating through the atmosphere. Down to 36 g/cm² from above the nuclear component is prevalent (protons, helions, heavy nuclei, and neutrons, which latter are not included on the figure). At sea level mainly the hard and lightly ionizing component, namely, μ -mesons, are left. We derive from this figure that at SST altitudes we have mainly protons, α and neutrons, which produce in tissue particles with a high linear energy transfer (LET), or ion density along their track if their energy is in the 0.5 to 10 MeV range. The radiation at high altitudes will therefore have a higher biological effectiveness than the lightly ionizing radiations in low altitudes. Figure 4 (ref. 3) shows the increase of total ionization with altitude in high latitudes during maximum and minimum years according to balloon measurements of Neher over a period

of 20 years. We derive from these measurements two important numbers as basis of our estimates of the exposure at SST altitudes, namely, the overall ionization at 36 g/cm² atmosphere depth:

(1) During solar activity years

$$\approx 15 \frac{\text{mrad}}{\text{day}} \text{ or } \approx 100 \frac{\text{mrad}}{\text{week}} = 0.625 \frac{\text{mrad}}{\text{hr}}$$

and

(2) During solar minimum years

$$\approx 20 \frac{\text{mrad}}{\text{day}} \text{ or } 140 \frac{\text{mrad}}{\text{week}} \approx 0.84 \frac{\text{mrad}}{\text{hr}}$$

The number for activity years is easy to remember—100 mrad/week is the same number as the MPD (maximum permissible dose rate) for radiation workers in rem, namely, $100 \frac{\text{mrem}}{\text{week}} = 0.625 \frac{\text{mrem}}{\text{hr}}$, or $5 \frac{\text{rem}}{\text{year}}$.

The above numbers are rad doses measured in a small ionization chamber. In an SST airplane the surrounding masses of higher Z number and the human body itself produce additional secondaries in nuclear collisions, which increase the rad dose absorbed in tissue. On the basis of measurements of the increase of secondaries under thick layers of material, Van Allen suggested a factor of 2 to 3 for the dose increase at these altitudes below shields of several cm thicknesses of aluminum or steel. If we adopt the factor 2 we would obtain thus as rad dose rates for continuous exposure at 75 000 feet $200 \frac{\text{mrad}}{\text{week}}$ or $280 \frac{\text{mrad}}{\text{week}}$ in solar maximum or solar minimum years, respectively, or in rad two to three times the MPD.

For the crew of SST the average dose rate remains substantially below the MPD for their professional life, because they are at these altitudes only 1/16.8 of the time (10 hours/week flight time at 75 000-ft altitude). At 80 hours/month flight duty, as is usual today, about 40 hours would be spent in cruising altitudes.

To estimate the rem dose rate or "dose equivalent" (ref. 4), we have to remember that the radiation in 23-km altitude consists mainly of nuclei especially protons, neutrons, and

α -particles. The biologically most effective components are the slow evaporation protons, α 's and other nuclei (≈ 10 MeV energy), which originate in nuclear collisions in the human body, and the energetic neutrons which produce heavy ionizing recoil protons in the hydrogen containing tissue.

Schaefer, Krebs, and especially Van Allen (ref. 5) estimated the biological effects in the human body of the heavy prongs of cosmic ray induced stars by comparison with equivalent amounts of incorporated radium. The star components of low energy, being of short range and high specific ionization, resemble closely in energy and ionizing characteristics the α -particles and recoil nuclei from the radioactive decay of radium and its follower products. The number of stars in tissue was estimated by Van Allen, on the basis of measurements in nuclear emulsions at high altitudes, to be 850 per gram of biological material per day. This number of stars is equivalent, with respect to energy deposition, to 0.035 μ Ci radium within the human body. This would be $\frac{1}{2}$ of the maximum permissible burden of Ra²²⁶, at continuous stay at 75 000 feet altitude. If we intend to assess the radiation exposure of the crew, both numbers, that for the ionization rad dose and that for the radium equivalent have to be divided by 16.8 because the crew is in 75 000 feet only about 10 hours/week. (The dose rate in mrad/hr must be multiplied by 10 to obtain the dose per week.) Thus we obtain, as approximate exposure for the crew from G.C.R. at high latitudes,

	<i>Fraction of MPD</i>
Overall ionization:	
$2 \times (0.625 - 0.84) \frac{\text{mrad}}{\text{hr}} \times 10$	
$= 12.5 - 16.4 \text{ mrem}/10 \text{ hours (week)}$	$\approx 15\%$
Nuclear stars:	
$0.035 \mu\text{Ci Ra}^{226}/16.8$	
$= \frac{1}{2} \text{ MPD}/16.8$	$\approx 2\%$
	$\approx 17\%$

As was already emphasized by Van Allen, this estimate of the "rem" dose or of the biological effect contains large uncertainties. The distribution of stars is uniform throughout the body, while the radium accumulates to 97 per cent or more within the bones. Thus the bio-

logical effect of the stars may be lower or higher than that of an equivalent body content of Ra²²⁶, dependent on whether the concentration near the bone marrow or a uniform distribution over other sensitive organs is more effective.

Furthermore, the number of stars seems to be higher in tissue if one includes 1- and 2-prong stars, which are difficult to observe in photo-emulsions. Also the effect of secondary neutrons in tissue is not included except in the factor 2 which was attached to the rad dose. Their energy deposition (recoil protons) is not measured adequately in the ion chambers of Neher, which were filled with argon. The energy deposited by fast secondary neutrons in the human body by means of heavily ionizing recoil protons is substantially higher than the energy imparted to heavy argon atoms. Although the contribution of these neutron recoils to the rad dose is low, the recoils from a fast neutron have a high LET (linear energy transfer) or quality factor.

A more comprehensive approach to estimate the dose equivalent or the rem dose is, to compile measurements and theoretical calculations on the biologically most effective components especially on the neutrons and on charged heavily ionizing particles, and on their spectra, and to multiply their flux in the different energy ranges with their dose conversion and quality factors for this energy range.

On the basis of neutron data of Hess et al. (ref. 6), Sobermann (ref. 7), Lingenfelter (ref. 8), Lal et al. (ref. 9), Korff, Haymes et al. (ref. 10), and the calculations of Patterson et al. (ref. 11), S. P. Shen (ref. 12) comes in this way to the result that the neutrons in air would produce a rem dose¹ of at most equal the rad dose measured in an argon ionization chamber at SST altitudes and high latitudes. The primaries and secondaries in air produce in tissue about 850 to 1 000 stars/g/day as mentioned before. If each star deposits locally about 50 MeV on the average, the resulting physical dose would be 0.03 mrad/hr. If a quality factor of 10 for the heavy ionizing components and

¹ The neutron flux to dose conversion factors are taken from "Protection Against Neutron Radiation up to 30 Million Electron Volts," Nat. Bur. Std. (U.S.) Handbook 63, Nov. 1957.

recoils is assumed, the dose equivalent in rem would then be 0.3 mrem/hr or ≈ 40 percent of the ionchamber dose rate in rad/hr. Because of the implied conservative assumptions on fast neutron flux, and energy deposit and quality factor of stars, we assume here, that the dose equivalent in rem from neutrons and stars combined is equal to the ion chamber dose in rad. Taking again into account by a factor of 2 the secondaries produced in the environmental masses of the airplane of higher Z -number than air, the dose balance in the airplane at 75 000 feet and at high latitudes would be, at most, about three times the ion chamber dose rate.

Rad dose from charged particles (ion chamber).

$$100-140 \frac{\text{mrad}}{\text{week}} = 0.625 - 0.84 \frac{\text{mrad}}{\text{hr}}$$

Maximum neutron and star rem dose (including that produced by secondaries from the airplane).

$$200-280 \frac{\text{mrem}}{\text{week}} = 1.25 - 1.67 \frac{\text{mrem}}{\text{hr}}$$

$$\text{Total} \dots\dots\dots 1.9 - 2.5 \frac{\text{mrem}}{\text{hr}}$$

The high contribution from neutrons is based on the assumption that the fast neutron flux in these altitudes corresponds to the spectrum calculated by Hess in $\approx 40 \text{ g/cm}^2$ atmospheric depth from data in (ref. 6) and that the flux of secondaries is doubled by the aircraft. Unfortunately while the approximate shapes of the neutron spectra are fairly well known, the absolute flux values are still uncertain. More recently direct measurements with detectors that are highly selective to fast neutrons (1 to 10 MeV), by Mendell and Korff (ref. 13) gave neutron intensities in these altitudes that were lower by a factor of about 3.

On the basis of the more conservative assumptions the exposure of the crew at 10 hours/week duty in 75 000 feet on high latitude routes would then be about 19 to 25 percent of the MPD; corresponding additions have to be made for ascent and descent. The exact values depend on the contribution of neutrons which is uncertain by a factor of 3

and the contribution of secondaries from the airplane which is difficult to calculate and may have to be measured for different types of aircraft.

At altitudes of 10 to 11 km (30 to 35 000 ft) where our subsonic jets of today cruise, the ion chamber dose rate in high latitudes and the neutron flux are lower by about a factor of 3. The number of stars is, however, at least smaller by a factor of 4.

The ion chamber dose is (fig. 4):

$$\approx 5 \text{ mrad/day} = 0.21 \text{ mrad/hr}$$

Because the radiation in these lower altitudes contains fewer nucleons and nuclei the production rate of secondaries in the structure of the airplane and of stars and recoils in the human body is smaller than in high altitudes. We allow therefore only a factor of 2 to the ion chamber dose rate as the quality and buildup factor and obtain about 0.4 mrem/hr as a rough approximation for the less biological effective radiation at 30 to 35 000 feet or 9 to 10.5 km altitude in high latitudes.

HEAVY PRIMARIES

With respect to heavy primaries I might add here only a short remark on their frequency at 75 000 feet in high latitudes.

The compilation of balloon flight measurements of Yagoda in figure 5 (ref. 14) shows that in 75 000 feet about 1 hit/cm³/day is obtained. Furthermore from the comprehensive theoretical studies of H. Schaefer (ref. 3) it can be seen that the heavier primaries ($Z > 20$) can penetrate only very seldom to these relatively low altitudes.

Thus the above number of hits is mainly produced by the lighter nuclei C, N, O—up to Ne (more data on heavy primaries and on considerations of their effects are given in references 15 and 22 and references therein).

SOLAR COSMIC RAYS

In figure 6 (ref. 1) dose rates actually measured within the atmosphere at a low energy event of extreme size (July 14, 1959) are given. By "low energy" event is understood an event in

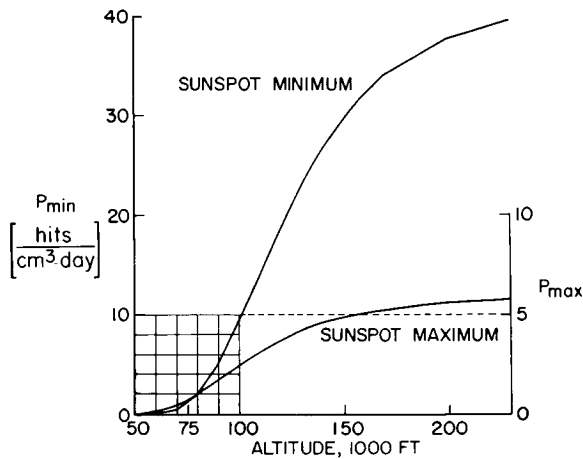


FIGURE 5.—Variation of thin-down intensity with altitude for seasons of maximum and minimum sunspot activity. (ref. 14).

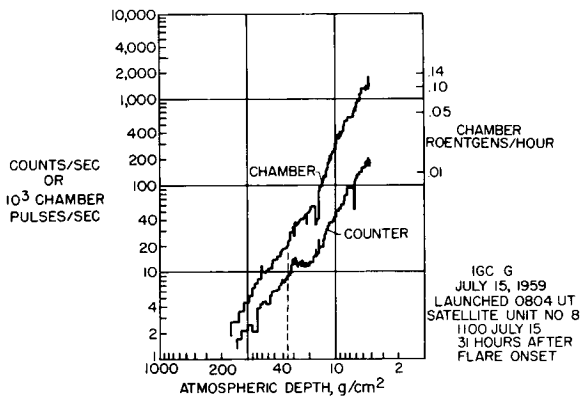


FIGURE 6.—Altitude dependence during a period of high intensity. This flight ascended between 0800 and 1100 universal time on July 15, 1959. (ref. 1).

which the particle spectra fall off steeply with energy and no relativistic particles are measured ($E \lesssim 300$ MeV). Such extreme events occurred with a frequency of 1 to 3 per year during the 3 years of maximum activity of the last solar cycle. At a depth of 5 g/cm² about 0.14 rad/hr was measured, and at a depth of 36 g/cm² about 1 mrad/hr is estimated. These dose rates were valid 29 hours after onset of the solar event in the decreasing phase of the event and may have been higher by a factor of 10 at the peak of the event, i.e., 10 mrad/hr. Because of this low dose rate it seems justifiable, therefore, to consider the low energy events as a minor hazard, even though the dose contribution from neutrons was not measured in the nitrogen chamber

and is not included. Three such events occurred in 1959. (May 12, July 10, and July 14.)

A fourth extreme event, on July 16, 1959, called "medium energy event" was of greater significance. An increase of neutrons at sea level was observed which implied particles with energies above 500 MeV, which penetrate much deeper into the atmosphere and produce energetic secondaries which reach sea level. Its spectra were similar in intensity and energy to those of the November 12 (and November 15) event in 1960, which are more completely known.

We consider here the spectra on November 12, at 23³⁰ U.T., and on November 13, 16⁰³ U.T. (fig. 7) 10 and 27 hours, respectively, after the particle flux onset. The two spectra are determined from measurements with rockets in Fort Churchill launched by Goddard scientists, from the measurements of Winckler with balloons and from the measurements of Van Allen and Lin with Explorer VII. Furthermore, the neutron measurements at Deep River by Carmichael, Steljes, and McCracken are taken into consideration (ref. 15, and references therein cited).

By far the highest doses at SST altitudes are produced by "high energy" events such as that of February 23, 1956. In this case the sea level monitors recorded a neutron increase of 3600 to 5000 percent in high latitudes or in impact zones, respectively. During the November 1960 "medium energy" events the neutron monitor in Deep River (Canada) recorded a maximum increase to 225 percent only. In the same figure 7 approximate prompt spectra of the February 23, 1956 high energy event are shown. The intensities in the 700 MeV range were of the same order of magnitude as those of medium energy events in the 70 MeV range (about 500 to 1000 particles/cm² sec sterad). Because of the large flux of high energy particles this would have been the most important event of the last cycle with respect to implications to the SST. Unfortunately its fluxes between 100 and 1000 MeV are not as well known as the intensities of the November 12 event; however, based on the spectra of Simpson, measured 1 to 10 hours after onset (ref. 16), and on the balloon measurements of Van Allen and Winckler (refs. 17 and 18) and the estimates of Fowler and Perkins, Bristol,

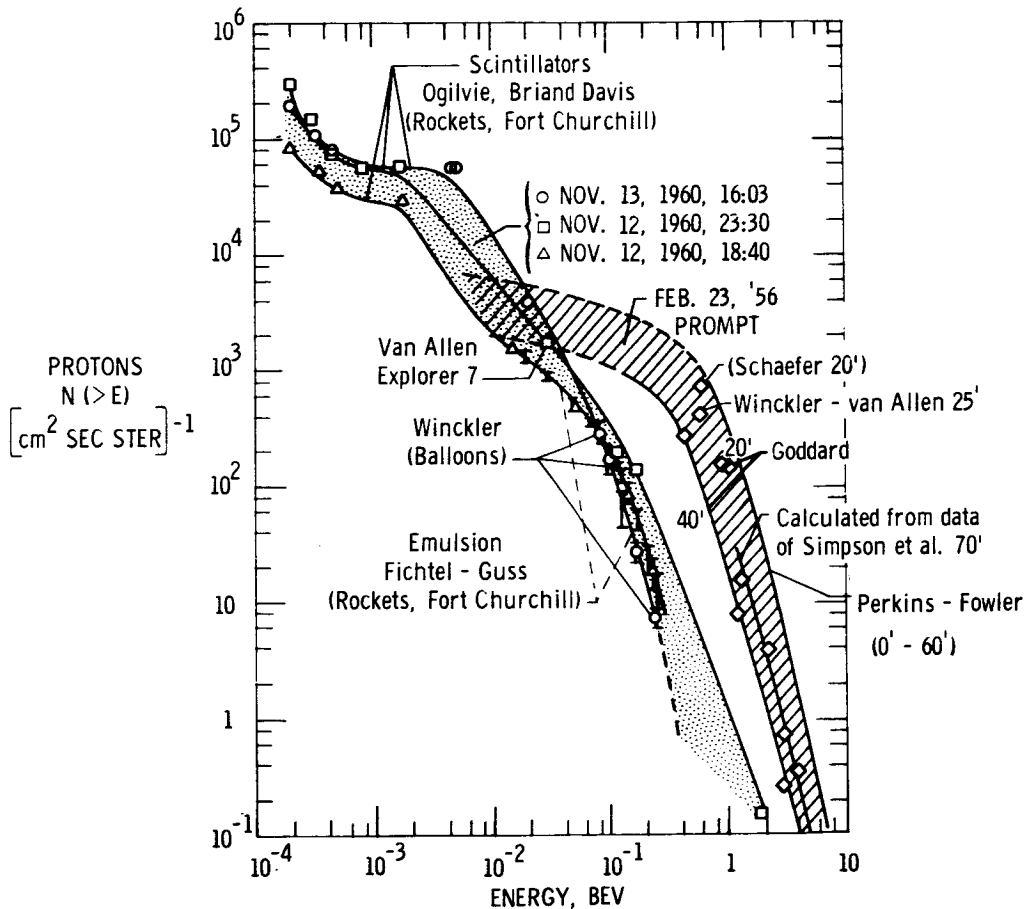


FIGURE 7.—Flare-particle spectra. The numbers 20', 25', . . . , are the minutes after solar cosmic ray onset, observed on Earth at 0350.

Great Britain (ref. 19) derived from the 50-fold increase of neutrons in Leeds, England, the spectra for the first hours lie in the broad strip indicated in figure 7. The measurements are extrapolated to lower energies by the dashed lines.

We see the Simpson 0500 U.T. Spectrum 70' after C.R. onset (flare max 0342), the estimate of the Goddard group for 0430, the extrapolation back to the time of the maximum of the Chicago monitor (0415) on the basis of balloon measurements about 19 hours later by Van Allen and Winckler, and estimate from H. Schaefer based on the 3600 percent neutron increase in the Durham monitor. The estimates of the Bristol group are substantially higher in the low energy range and are only used down to ≈ 900 MeV.

The dose rates within the atmosphere derived from these spectra for the 12 November 1960

medium energy event and the February 1956 high energy event are shown in figure 8. At 36 g/cm² altitude are obtained: on November 12, 1960: $50 \frac{\text{mrad}}{\text{hr}}$, on February 23, 1956: 0.5 to $2 \frac{\text{rad}}{\text{hr}}$ in the early phases.

One sees that about 10 1-hour trips during medium energy events are needed to obtain the same dose as that produced by the February 1956 event in one of its first hours in 75 000-foot altitude.

It may be mentioned that nuclear collisions and their secondaries, especially neutrons, are not taken into account in these calculations. For medium energy events like that of November 12 in a recent paper Lingenfelter and Flamm (ref. 20) estimate the contribution of neutrons to the rem dose in approximate calculations.

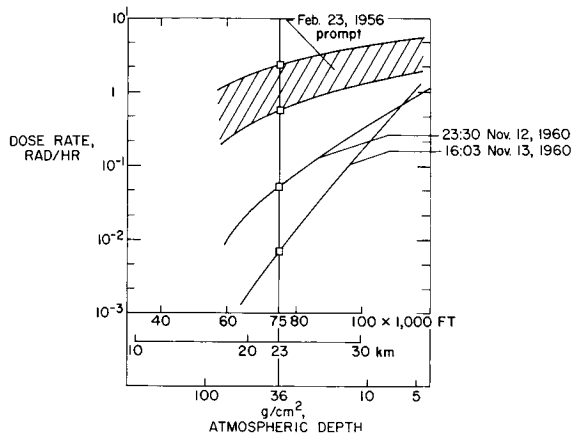


FIGURE 8.—Dose rates within the atmosphere from solar flare particles (high magnetic latitudes).

For an atmospheric depth of 30 g/cm² the result is obtained that the rem neutron dose is of the same magnitude as the dose produced by the primary protons. In higher altitudes the primary dose exceeds the n-dose, in lower altitudes the neutron rem dose is the larger. The February 1956 event with its much higher intensities in the high energy range is not treated in reference 20. The rad doses in 36 g/cm² of 1/2 to 2 rad/hr would have to be multiplied by a factor of about 2 to account for the secondaries. Thus, as a rough upper estimate, 1 to 4 rem/hr are obtained from the prompt spectra of figure 8. Events comparable to the February 1956 event in intensity and energy occurred only one or two times per cycle during the last three 11-year periods. They occur apparently during the rising or descending phases of the sunspot cycles, as figure 9 indicates.

More information about these events is contained in figure 10 (ref. 21). The figure shows the increase of C.R. intensity at sea level and at mountain level measured in ionization chambers covered by 10 cm lead, indicative of the meson and electron components produced mainly by primaries of very high energy. Unfortunately neutron monitor data are not available for these earlier high-energy events. Thus a comparison with respect to spectra in the low BeV and hundreds MeV range with the February 1956 event cannot be made. The meson and electron increase in these ion chambers is a measure of the more energetic

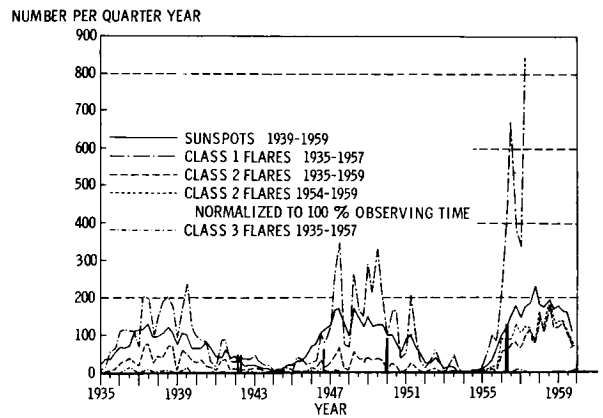
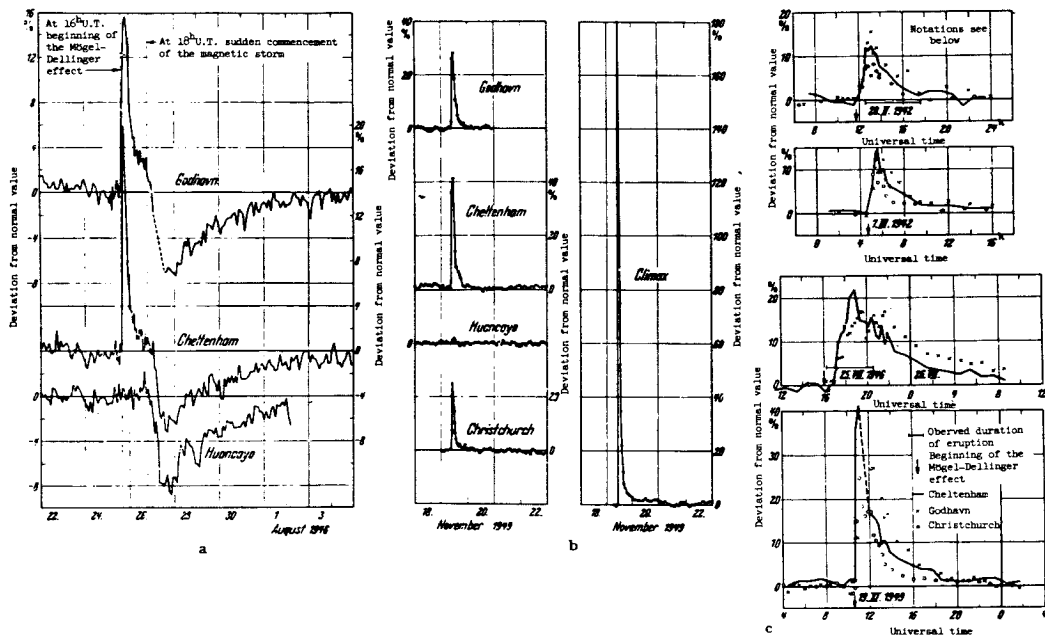


FIGURE 9.—Frequencies of sunspots and flares in the last solar periods and high-energy proton events. (Courtesy J. W. Evans, Sacramento Peak Observatory, New Mexico.)

particles in the multi BeV range and not, as the neutron increase in pile monitors, of the lower energy particles, which are of most interest in SST altitudes. Nevertheless it is interesting to note that during the November 1949 event the increase within the ion chamber at Cheltenham (50° N. magn. latitude) was 40 percent in comparison to 80 percent in February 1956. This indicates that the spectra in the high-energy range were of comparable magnitude. It may be mentioned also that the intensity in impact zones may have been higher than at the medium latitudes where G.C.R. monitors were located.

SUMMARY ON EXPOSURE OF CREW AND PASSENGERS ON POLAR ROUTES

In table II the exposure of the crew under extreme conditions, i.e., on polar routes, averaged over the 11-year solar cycle is summarized according to these rough estimates. The crew flight time is assumed to be 80 hours/month of which 40 hours are at 23 km (75 000 ft) altitude. Exposure during ascent and descent is disregarded. The frequency, durations, and spectra of flare events important in SST altitudes are taken as those of the last solar cycle, which was the most active cycle of this century. No evasive measures such as diving to lower altitudes, if a flare event is in progress, are assumed. There is no indication that events of larger size (larger intensity and duration of the penetrating components) than the February



- (a) Increase of cosmic ray intensity on 25.VII.1946.
 (b) Increase of cosmic ray intensity on 19.XI.1949.
 (c) Increase of cosmic ray intensities during the sun eruptions of 28.II.1942, 7.III.1942, 25.VII.1946, and 19.XI.1949 at different stations.

FIGURE 10.—Intense high energy solar events 1942 to 1949, observations with ionization chambers on different stations (ref. 21).

1956 event cannot occur; however, they should be very rare.

From table II it is seen, that the average rem dose rate from Galactic and solar C.R. would amount to about 30 percent of the MPD of 5 rem/year, i.e., ≈ 1.5 rem/year. For the crew the main contribution, i.e., 21 percent of the MPD comes from G.C.R. It is difficult to say how trustworthy this number is, since the contribution from additional secondaries originating in the airplane and especially the contribution of neutrons is not well known. It should be, however, at most, too high by a factor of 2. Furthermore, since the crew will probably be on duty for a maximum of 25 years the MPD for radiation workers referring to 50 years duty is not directly applicable and is cited here only to have a rough comparison with the maximum permissible radiation exposure in other professions. Taking evasive measures in case of energetic flare events the exposure of the crew on polar routes would be $\lesssim 20$ percent of the MPD of 5 rem/year at flight duty time as usual at present.

The exposure of passengers under extreme conditions and without evasive measures in case of solar events is given in table III. We assume here two flights = 2 hours/month, that is 24 hours flight time per year at 23 km altitude on polar routes. For such short periods the overall ionization dose in rem from G.C.R. is small and may be neglected. With respect to the question, first discussed by Hermann Schaefer, concerning pregnant passengers, we mention the number of heavy-primary hits/cm³. The foetus is most sensitive to irradiation in the early differentiation stage between 14 days and 6 weeks and has in this period a volume of ≈ 0.5 to 1.2 cm³. If we assume a sensitive volume of (3 mm)³, the 2.3×10^{-3} hits/(3 mm)³/month would afflict 2.3 of 1000 passengers pregnant in the second month who fly two times in this period. Furthermore, the number of stars of 850 to 1000/cm³ tissue/24 hours would be equivalent to an average of two stars/(3 mm)³/month for the same passengers. Because of the uncertainties with respect to the size of the sensitive volume, which is assumed rather

TABLE II
Crew, Without Precautions

[Upper limits of exposure, polar routes 40 hour/month duty at 75 000-foot (23-km) altitude (not including ascent and descent)]

(1) G.C.R.	Continuous stay		10 hr/week duty at 75,000 ft		Average for 11-year cycle	Fraction of maximum permissible (5 rem/yr)	
	Sol min	Sol max	Sol min	Sol max			
Ion chamber.....	0.84	$0.625 \frac{\text{mrad}}{\text{hr}}$					
Dose equivalent produced by primaries, secondaries (also from the air-plane), and their collisions in tissue (stars, neutron recoils).	$2.5 \frac{\text{mrem}}{\text{hr}}$	$1.9 \frac{\text{mrem}}{\text{hr}}$	$1.3 \frac{\text{rem}}{\text{yr}} \times \frac{2}{11}$	$1.0 \frac{\text{rem}}{\text{yr}} \times \frac{9}{11}$	$1.06 \frac{\text{rem}}{\text{yr}}$	21 percent	
Heavy primary hits.....	$1 \frac{\text{hit}}{\text{cm}^2 \text{ day}}$		$0.4 \frac{\text{hit}}{\text{cm}^2 \text{ week}}$		$20 \frac{\text{hits}}{\text{cm}^2 \text{ year}}$?	
(2) SOLAR EVENTS Medium energy: = 1/year (4 yrs)	During activity years 2 round trips per event (4 hrs) $1 \frac{\text{event}}{\text{year}} \times 4 \text{ hours} \times < 100 \frac{\text{mrem}}{\text{hour}} \times 4 \text{ years}$ or $0.4 \times < 4 \text{ rem} < 1.6 \text{ rem}$						
High energy: [1 extreme event or 2 to 3 major events 11 years]	$1 \text{ trip (1 hr)} \times < 4 \frac{\text{rem}}{\text{hr}}$ $< \frac{5.6 \text{ rem}}{11 \text{ years}}$ =					$< 10 \text{ percent}$	
Maximum permissible dose rate for radiation workers.	} = 5 rem/yr					Total $< 1.6 \text{ rem/yr}$	$< 31 \text{ percent}$

TABLE III
Passengers, Without Precautions

[Upper limits of exposure (polar routes) = 0.5 rem/yr; MPD maximum permissible dose rate for population (one-time exposure) = 1 to 4 rem in 1 hr]

(1) G.C.R.	Continuous in 75 000 feet	Level for two flights per month of 1 hour each	Fraction of MPD
Stars.....	stars 850 to 1000 $\frac{\text{cm}^3 \text{ tissue/day}}$	$\approx 75 \frac{\text{stars}}{\text{cm}^3 \text{ month}} = 2 \frac{\text{stars}}{(3 \text{ mm})^3 \text{ month}}$	
Heavy primaries.....	hit 1 $\frac{\text{cm}^3 \text{ tissue/day}}$	1 hit $12 \text{ cm}^3 \text{ month} = 2.3 \times 10^{-8} \frac{\text{hit}}{(3 \text{ mm})^3 \text{ month}}$?
(2) SOLAR EVENTS	Encountering all energetic events of solar cycle	During 11 years	
Medium energy: 1/yr (4 yrs).....	1 trip per event (1 hr) $\frac{1}{\text{yr}} \times 1 \text{ hr} \times < 100 \frac{\text{mrem}}{\text{hr}} = 100 \frac{\text{mrem}}{\text{yr}} \times 4 \text{ yrs} \dots\dots\dots$	< 0.4 rem	
High energy: 1 extreme event or 2 to 3 major events 11 years	1 trip (1 hr) $\times < 4 \frac{\text{rem}}{\text{hr}}$ per 11 yrs.....	< 4 rem	
	Total.....	$\frac{< 4.4 \text{ rem}}{11 \text{ yrs}}$ < 0.40 rem/yr	< 80 percent

arbitrarily, the uncertainties in the number of heavy primary hits and the effectiveness of heavy primaries and stars, there is no proof as yet that their effects on these passengers can be completely neglected.

Without evasive measures the doses for passengers from solar events are estimated as high as 4.5 rem per 11 years, if we make the extreme assumption that this passenger encounters all major energetic events of the solar cycle. This would be an average dose rate of 0.4 rem/year or 80 percent of the maximum permissible dose rate of 0.5 rem/year for a small part of a population pool. This fact is therefore considered as of no genetic significance, especially since such heavy freight schedules would hardly continue through 30 years of procreation age. More pertinent is the fact that the main part of the flare event doses would occur in a very short time, that is in about 1 hour. A dose of 1 to 4 rem in 1 hour appears not desirable especially for pregnant passengers and children. Such exposure can be avoided by evasive measures, e.g., of diving down to lower altitudes of about 40,000 feet in case of such major events and by continuation of the flight to its destination under a protective air cover of about 200 g/cm². The dose values given here are lower by a factor of approximately 2 than the numbers given by this author in references 22. Higher multiplication factors for the influence of the airplane and very conservatively extrapolated flare particle spectra based on early data were used in those articles. The factor of 3, which is

lower than that of the previous studies, used herein to obtain the dose equivalent in rem of G.C.R. from the ionchamber dose is still considered as conservative, since the fast neutron flux is apparently lower than previously assumed and a factor of 2 for buildup of secondaries by structural elements of an airplane having a titanium wall thickness of ≈ 1 g/cm² appears highly conservative.

In conclusion, if appropriate precautions are taken by the airplane during an energetic solar proton event—such as diving down to sufficiently low altitudes or rerouting to lower geomagnetic latitudes—the ionization exposure of passengers and crew in supersonic flights lies significantly below the maximum permissible dose rates, as defined by the Federal Radiation Council or ICRP for the commonly known more lightly ionizing radiations (protons, neutrons, and even alphas). However, no permissible dose for protection purposes is stated for heavy primaries, recoils, and certain components of stars which are uniformly distributed through the human body. Indications are that these heavy ionizing components are very effective in germinating tissue. On the other hand, their intensities at SST altitudes up to 23 km is very low and not well known. The question if and to what extent these components constitute a risk for sensitive passengers can be most satisfactorily answered by investigations of their intensities *in situ* and of their biological effects in animal experiments.

REFERENCES

1. WINCKLER, J. R.: Primary Cosmic Rays. Proc. Conf. Radiation Problems in Manned Space Flight (George J. Jacobs, ED.). NASA TN D-588, 1960, pp. 72-93. Also published in Radiation Res., vol. 14, no. 5, May 1961, pp. 521-539.
2. VAN ALLEN, J. A.; and TATEL, H. E.: The Cosmic-Ray Counting Rate of a Single Geiger Counter From Ground Level to 161 Kilometers Altitude. Phys. Rev., vol. 73, no. 3, second ser., Feb. 1948, pp. 245-251.
3. SCHAEFFER, HERMANN J.: Radiation and Man in Space. Advances in Space Science (Frederick I. Ordway III, ED.), vol. 1, Academic Press, Inc., 1959, pp. 267-339.
4. Nat. Bur. Std. (U.S.) Handbook 85: Physical Aspects of Irradiation, Recommendations of the International Commission on Radiological Units and Measurements.
5. VAN ALLEN, J. A.: The Nature and Intensity of the Cosmic Radiation. Physics and Medicine of the Upper Atmosphere (Clayton S. White and Otis O. Benson, Jr., EDs.), ch. XIV, Univ. New Mexico Press (Albuquerque), 1952, pp. 239-266.
6. HESS, WILMOT N.; PATTERSON, H. WADE; WALLACE, ROGER; and CHUFFP, EDWARD L.: Cosmic-Ray Neutron Energy Spectrum. Phys. Rev., vol. 116, Oct. 1959, p. 445.
7. SOBERMAN, ROBERT K.: High-Altitude Cosmic-Ray Neutron Intensity Variations. Phys. Rev., vol. 102, June 1956, p. 1399.
8. LINGENFELTER, R. E.: Production of Carbon 14 by Cosmic-Ray Neutrons. Reviews of Geophysics, vol. 1, no. 1, Feb. 1963, p. 35.
9. LAL, D.; MALHOTRA, P. K.; and PETERS, B.: On the Production of Radioisotopes in the Atmosphere by Cosmic Radiation and Their Application to Meteorology. J. Atmospheric Terrest. Phys., vol. 12, 1958, p. 306.
10. HAYMES, R. C.; REIDY, W. P.; and KORFF, S. A.: The Cosmic Ray Neutron Density at High Altitudes. J. Phys. Soc. Japan, vol. 17, Suppl. AII, 115, 1962.
11. PATTERSON, H. W.; HESS, W. N.; MOYER, B. J.; and WALLACE, R. W.: The Flux and Spectrum of Cosmic-Ray Produced Neutrons as a Function of Altitude. Health Phys., vol. 2, 1959, pp. 69-72.
12. SHEN, S. P.: Space Radiation and the Hypersonic Transport. Gen. Elec. Co. Rept. R-64 SD1, Jan. 1964.
13. MENDELL, R. B.; and KORFF, S. A.: Fast Neutron Flux in the Atmosphere. J. Geophys. Res., vol. 68, Oct. 1963, pp. 5487-5495.
14. YAGODA, HERMAN: Cosmic-Ray Monitoring of the Manned Stratolab Balloon Flights. GRD Res. Notes No. 43 (AFCL-TN-60-640), Air Force Res. Div., Sept. 1960.
15. FOELSCHKE, T.: Estimates of Radiation Doses in Space on the Basis of Current Data. Proc. Third Intern. Space Sci. Symp. April-May 1962. Also: Specific Solar Flare Events and Associated Radiation Doses. Symp. Space Radiation Effects, Proc. 66th Annual Meeting, Am. Soc. Testing Mater. (Atlantic City), June 1963. ASTM Spec. Tech. Publ. No. 363.
16. MEYER, P.; PARKER, E. N.; and SIMPSON, J. A.: Solar Cosmic Rays of February 1956 and Their Propagation Through Interplanetary Space. Phys. Rev., vol. 104, no. 3, second ser., Nov. 1, 1956, pp. 768-783.
17. VAN ALLEN, J. A.; and WINCKLER, J. R.: Spectrum of Low-Rigidity Cosmic Rays During the Solar Flare of February 23, 1956. Phys. Rev., vol. 106, no. 5, June 1957, pp. 1072-1073.
18. WINCKLER, J. R.: Cosmic-Ray Increase at High Altitude on February 23, 1956. Phys. Rev., vol. 104, No. 1, second ser., Oct. 1956, p. 220.
19. FOWLER, P. H.; and PERKINS, D. H.: Cosmic Radiation and Solar Particle Radiation at Aircraft Altitudes. Alt. Registration Board, Supersonic Aeroplane Airworthiness Committee, SAA C/20, Sept. 25, 1962.
20. FLAMM, E. J.; and LINGENFELTER, R. E.: Neutron and Proton Dosages in the Upper Atmosphere from Solar Flare Radiation. Science, vol. 144, June 1964, pp. 1566-1569.
21. HEISENBERG, W.: Kosmische Strahlung; Zeitliche Schwankungen, by Biermann, L., and Schlueter, A. Springer Verlag, Berlin, Goettingen, Heidelberg, 1953.
22. FOELSCHKE, T.: Radiation Exposure in Supersonic Transports. NASA TN D-1383, 1962; and Foelsche, T. and Graul, E. H.: Atompraxis 8, Oct. 1962, pp. 365-379.

65-34611

35—Primary- and Secondary-Proton Dose Rates in Spheres and Slabs of Tissue¹

ROGER WALLACE, PALMER G. STEWARD, and CHARLES SONDHAUS

Lawrence Radiation Laboratory

A code has been developed for the depth-dose relation in spheres of tissue due to primary protons and to cascade, evaporation, and hydrogen elastically scattered secondary protons. Hydrogen elastically scattered protons are assumed to be emitted in the forward direction, as also, on the basis of Metropolis's calculations, are cascade protons. Evaporation protons are assumed to deposit their dose locally. It is shown that the dose rate at a depth d in a slab due to a normally incident parallel broad beam of protons is the same as the dose rate at the center of a sphere of radius d when an isotropic flux is incident upon the sphere.

The depth-dose results are checked by experiments using 730-MeV protons, and compared with Monte Carlo calculations performed at Oak Ridge for 400-MeV protons. The results show that the depth-dose pattern varies widely with proton energy and sphere size. For certain intermediate proton energies, the primary protons cause a peak dose rate at a predictable depth in the sphere. The secondary proton dose rate increases with increasing incident proton energy, sphere size, and depth. Protons of 730 MeV cause a secondary proton dose at the center of a 2.5-cm-radius sphere which is 14% of the total dose, 35% for a 10-cm radius, and 48% for a 25-cm radius.

INTRODUCTION

During recent years depth-dose distributions in tissue due to incident high-energy proton fluxes have been under investigation in order to determine the space radiation hazards to biological organisms. Simple methods of calculating these depth-dose curves are of limited value, since they yield only the effect due to primary protons incident usually upon slabs (refs. 1 and 2). It is now clear that neither the effect of secondary protons nor the effect of the geometrical deviation of animals from slabs is negligible when considering incident protons of energy greater than 100 or 200 MeV.

The work presented in this paper is part of a research effort centering around experiments using the Lawrence Radiation Laboratory's cyclotrons to irradiate animals in a simulated space radiation field. The radiation field to be

simulated is an isotropic flux of high-energy protons (say 20 to 730 MeV) in an energy spectrum depending upon the solar flare conditions.

Depth dose due to an incident isotropic flux of monoenergetic protons, including the effect of primary and first-generation secondary protons, was determined in spheres of arbitrary size containing tissue-equivalent material. The sphere was chosen because it is, for present purposes, the simplest reference solid useful in showing the effects of the variables. Throughout most of the development of the equations presented here, the tissue-equivalent material is water. The effect of a continuous spectrum of proton energies can be approximated by summing at each dose point the dose rate due to each of several energies of arbitrary relative intensity.

One of the results of this effort is a fast-running IBM 7044 computer code which calculates the depth-dose curves described above. In later sections of this paper, each of the equations solved by this code is developed (Section III). Emphasis is placed upon several approxi-

¹ This research was supported in part by the Atomic Energy Commission (AEC Contract No. W-7405-eng-48) through its Special Fellowship Program in Health Physics, which is administered by the Oak Ridge Institute of Nuclear Studies, and in part by the National Aeronautics and Space Administration.

mations incorporated into the equations (Section IV), although comparison of results from this code with experiment and other calculations indicate that very little accuracy has been sacrificed (Section V). Results of the code calculation are presented in some detail in Section VI.

Dose rate due to primary protons and three classes of proton secondaries are treated by the code. The treatment of primary protons is simplified by neglecting straggling, and approximating the range-energy relation by $R = pE^q$, where p and q are constants over each of five energy intervals, and E and R are respectively the energy and corresponding range of the protons. The author feels that straggling is only a second-order effect when the flux is isotropic, and that the Bragg peaks are therefore already dispersed in the medium.

The first class of secondary protons is the cascade protons. Using a Monte Carlo code based upon a nuclear model, Metropolis et al. (refs. 3 and 4) have estimated the energy spectrum and number of cascade protons created. Functions that approximate these nuclear data are the basis of the present calculations. Since the angular distribution of cascade protons is peaked in the forward direction and the primary flux is isotropic, it is assumed that all cascades are emitted in the direction of the incident primary, thus eliminating angular dependence.

The second class of secondary protons considered is the evaporation protons. Again, functions approximating Metropolis's data are the basis of the calculation. A Maxwell-Boltzmann energy spectrum is used, which gives almost entirely low-energy protons, so that it is assumed all the energy of the evaporation protons is deposited locally.

The third class of secondary protons consists of those which have undergone elastic collisions between hydrogen nuclei and primary protons. The code treats both the scattered primary proton and the recoiling hydrogen nucleus. The angular distribution in the lab system is again peaked in the forward direction, so that angular dependence is removed by the forward scattering assumption. However, the energy spectrum of these protons is calculated by applying conservation of energy and momentum to the p - p elastic-scattering differential cross section.

The dose rate contributed by each of the

proton classes described above is tabulated as a function of depth in the sphere. At each depth, the dose rate deposited by protons in each of eight energy intervals (0-1, 1-2, 2-5, 5-10, 10-20, 20-40, 40-80, and 80- ∞ MeV) is tabulated separately for each energy interval and each class of protons. On the IBM 7044 computer, approximately 0.12 minute is required per dose point for this entire calculation.

II. THE EQUIVALENCE OF MONODIRECTIONAL CURRENT INCIDENT UPON A SLAB AND AN ISOTROPIC FLUX INCIDENT UPON A SPHERE

At the outset we wish to present an analysis which is a very powerful tool relating the results presented later in this paper with a convenient experiment. (See Section V.)

The flux at the center of a sphere of radius r_0 due to an isotropic monoenergetic proton flux $\Phi(E_0)$ at the surface is

$$\phi(r_0) = \frac{\Phi}{4\pi} d\Omega d\sigma \exp\left(-\int_0^{r_0} \Sigma_R dr\right)$$

where $d\Omega$ is the number of steradians subtended by one square centimeter of area at the center of the sphere, $d\sigma$ is the elemental area at the surface of the sphere, and the last factor is an exponential proton-removal probability (fig. 1). Since $d\Omega = 1/r_0^2$ and $d\sigma = 2\pi r_0^2 d\beta$, we see that the flux at the center of a sphere of radius r_0 due to an isotropic flux of protons at its surface is

$$\phi(r_0) = \frac{\Phi}{2} \exp\left(-\int_0^{r_0} \Sigma_R dr\right) \int_{-1}^1 d\beta = \Phi \exp\left(-\int_0^{r_0} \Sigma_R dr\right) \quad (1)$$

The flux at depth d in a slab due to an incident monoenergetic collimated beam of protons of $\Phi(E_0)$ protons per $\text{cm}^2\text{-sec}$ is

$$\phi(d) = \Phi \exp\left(-\int_0^d \Sigma_R dr\right) \quad (2)$$

which is identical to equation (1) for $r_0 = d$.

This shows that the flux at the center of a sphere of radius d due to an isotropic flux at its surface is identical to the flux at depth d in a slab due to an incident collimated beam of protons. Since the protons travel the same distance in the sphere and in the slab, they arrive at the dose point with the same energy

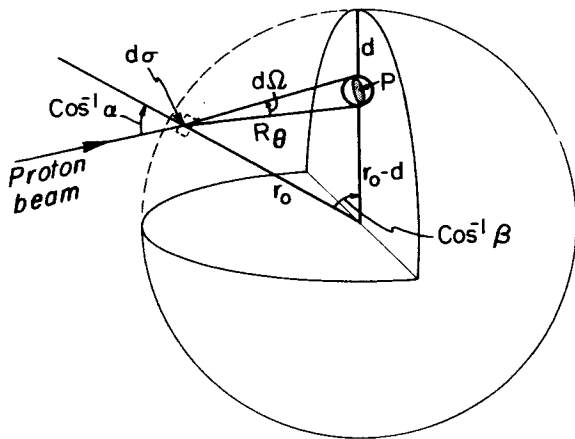


FIGURE 1.—Calculation of primary proton dose rate.

in each case. Thus the flux and energy are identical, which leads to the conclusion that the dose rate deposited in the two cases is identical.

The above analysis is rigorous only for primary protons, of course. A less trivial development, not presented here, shows that this same conclusion holds for the secondary protons, because the assumption is made that they are all emitted in the forward direction.

This important equivalence, pointed out above, can be used in two ways. First, by running the simple experiment of a broad beam of monodirectional protons incident upon a slab of tissue, the results presented in this paper for dose rates due to isotropic fluxes when the dose point is at the center of a sphere can be verified by experiment. Second, if (as assumed) the depth-dose profiles are correct, the results presented here can be transformed into semi-empirical results by normalizing the central dose rates to experimental results by using the simple experiment described above.

III. DERIVATION OF EQUATIONS

In order to achieve an analytic expression for the various proton dose-rate contributions which can be incorporated into a fast-running computer code, many approximations are necessary. The usefulness of the results depends largely upon the skill with which the approximations are chosen and how they are incorporated into the expressions. This section presents the detail of the calculation. A summary of the approximations is presented later.

A. Derivation of the Equation for the Dose-Rate Contribution From Ionization Due to Primary Protons

It is assumed that an isotropic flux of protons, $\Phi(E_0)$, at energy E_0 , is incident upon a sphere of radius r_0 (fig. 1). The flux of protons at the dose point P due to protons entering the sphere through the surface element $d\sigma$ is

$$\frac{\Phi}{4\pi} ad\Omega d\sigma = \frac{\Phi}{4\pi} a \frac{1}{R_\theta^2} 2\pi r_0^2 d\beta \frac{\text{protons}}{\text{cm}^2\text{-sec}} \quad (3)$$

where $d\Omega$ is the number of steradians subtended by 1 cm^2 of area at the dose point P .

From the law of cosines,

$$R_\theta = [r_0^2 + (r_0 - d)^2 - 2r_0(r_0 - d)\beta]^{1/2} = R(E_0) - R(E_{pp}) \quad (4)$$

where $R(E_0)$ and $R(E_{pp})$ are the ranges of a proton of energy E_0 and E_{pp} (the proton energy at the dose point P).

Differentiating (4) gives

$$d\beta = \frac{R_\theta}{r_0(r_0 - d)} \frac{dR}{dE} \Big|_{E_{pp}} dE_{pp} \quad (5)$$

where $\frac{dR}{dE} \Big|_{E_{pp}}$ is the inverse of the stopping power of a proton with energy E_{pp} .

Again, using the law of cosines, we have

$$\alpha = -\frac{(r_0 - d)^2 - r_0^2 - R_\theta^2}{2R_\theta r_0} \quad (6)$$

Substituting (4), (5), and (6) into (3) gives

$$\frac{\Phi}{4(r_0 - d)} \left[\frac{r_0^2 - (r_0 - d)^2}{[R(E_0) - R(E_{pp})]^2} + 1 \right] \frac{dR}{dE} \Big|_{E_{pp}} dE_{pp} = \frac{\text{protons}}{\text{sec}}$$

striking P at energy E_{pp} from the surface element $d\sigma$.

If we include an exponential removal probability, the flux of protons at P becomes

$$\phi(E_{pp}) dE_{pp} = \frac{\Phi(E_0)}{4(r_0 - d)} \left[\frac{r_0^2 - (r_0 - d)^2}{[R(E_0) - R(E_{pp})]^2} + 1 \right] \frac{dR}{dE} \Big|_{E_{pp}} \exp \left[-\int_{E_{pp}}^{E_0} \Sigma_R(E) \frac{dR}{dE} dE \right] dE_{pp} \quad (7)$$

where $\Sigma_R(E)$ is the macroscopic removal cross section. Integrating (7) gives the total flux at P ,

$$\phi = \frac{\Phi(E_0)}{4(r_0-d)} \int_{E[R(E_0)-r_0-(r_0-d)]}^{E[R(E_0)-d]} \left[\frac{r_0^2 - (r_0-d)^2}{[R(E_0) - R(E_{pp})]^2} + 1 \right] \frac{dR}{dE} \Big|_{E_{pp}} \exp \left[- \int_{E_{pp}}^{E_0} \Sigma_R(E) \frac{dR}{dE} dE \right] dE_{pp} \quad (8)$$

where $E[R(E_0)-d]$, for instance, is the energy of a proton with a range of $R(E_0)-d$.

The dose rate is given by

$$D(E_{pp})dE_{pp} = \phi(E_{pp})dE_{pp} \frac{1}{\rho} \frac{dE}{dR} \Big|_{E_{pp}} \frac{\text{MeV}}{\text{g-sec}} \\ = \frac{5.75 \times 10^{-5}}{\rho} \phi(E_{pp}) \frac{dE}{dR} \Big|_{E_{pp}} \frac{dE_{pp}}{\text{hr}} \frac{\text{rad}}{\text{hr}} \quad (9)$$

where ρ is the density of the sphere material at p . Equations (9) and (7) give the dose rate at P due to protons of energy between E_{pp} and $E_{pp} + dE_{pp}$,

$$D(E_{pp})dE_{pp} = \frac{1.44 \times 10^{-5}}{\rho(r_0-d)} \Phi(E_0) \\ \left[\frac{r_0^2 - (r_0-d)^2}{[R(E_0) - R(E_{pp})]^2} + 1 \right] \\ \times \exp \left[- \int_{E_{pp}}^{E_0} \Sigma_R(E) \frac{dR}{dE} dE \right] dE_{pp} \quad (10)$$

and the total dose rate at P is

$$D = \frac{1.44 \times 10^{-5} \Phi(E_0)}{\rho(r_0-d)} \int_{E[R(E_0)-r_0-(r_0-d)]}^{E[R(E_0)-d]} \left[\frac{r_0^2 - (r_0-d)^2}{[R(E_0) - R(E_{pp})]^2} + 1 \right] \\ \exp \left[- \int_{E_{pp}}^{E_0} \Sigma_R(E) \frac{dR}{dE} dE \right] dE_{pp} \quad (11)$$

The range-energy relationship for protons in water (which is, for purposes of this paper, a tissue-equivalent material) is approximated by the function

$$R(E) = pE^q \quad (12)$$

where R and E are the residual range and corresponding energy respectively; and p and q are constants. Inverting and differentiating equation (12) give other forms of the function:

$$E(R) = \left(\frac{R}{p} \right)^{1/q} \quad (13)$$

$$\frac{dR(E)}{dE} = pqE^{q-1} \quad (14)$$

and

$$\frac{dE(R)}{dR} = \frac{1}{pq} \left(\frac{R}{p} \right)^{1/q-1} \quad (15)$$

Substituting the functions into equations (8) and (11) gives

$$\frac{\phi}{\Phi(E_0)} = \frac{1}{4(r_0-d)} \int_{\left[\frac{pE_0^q - r_0 - (r_0-d)}{p} \right]^{1/q}}^{\left[\frac{pE_0^q - d}{p} \right]^{1/q}} \\ \left[\frac{r_0^2 - (r_0-d)^2}{[pE_0^q - pE_{pp}^q]^2} + 1 \right] pqE_{pp}^{q-1} \\ \times \exp \left[- \int_{E_{pp}}^{E_0} \Sigma_R(E) pqE^{q-1} dE \right] dE_{pp} \quad (16)$$

where $\frac{\phi}{\Phi(E_0)}$ is the primary proton flux at depth d in a sphere of radius r_0 per unit incident isotropic proton flux at energy E_0 . The corresponding expression for dose rate is

$$\frac{D}{\Phi(E_0)} = \frac{1.44 \times 10^{-5}}{r_0-d} \int_{\left[\frac{pE_0^q - r_0 - (r_0-d)}{p} \right]^{1/q}}^{\left[\frac{pE_0^q - d}{p} \right]^{1/q}} \\ \left[\frac{r_0^2 - (r_0-d)^2}{[pE_0^q - pE_{pp}^q]^2} + 1 \right] \\ \times \exp \left[- \int_{E_{pp}}^{E_0} \Sigma_R(E) pqE^{q-1} dE \right] dE_{pp} \quad (17)$$

where $\frac{D}{\Phi(E_0)}$ is the primary proton dose rate at depth d in a sphere of radius r_0 per unit incident isotropic proton flux at energy E_0 . The units of

$\frac{D}{\Phi(E_0)}$ are $\frac{\text{rads/hr}}{\text{protons/cm}^2 \text{ sec}}$.

When P is at the center of the sphere it is clear that no integration is required, since all protons of energy E_0 at the surface reach P with the same energy, implying that E_{pp} is a constant. Returning to figure 1 and equation (1), recognize that $R_0^2 = r_0^2$ and $\alpha = 1$. When one integrates β from -1 to $+1$ and includes the exponential removal probability, the fraction of the surface flux at P becomes

$$\frac{\phi}{\Phi(E_0)} = \exp \left[- \int_{E_{pp}}^{E_0} \Sigma_R(E) pqE^{q-1} dE \right] \quad (18)$$

for $d=r_0$. The proton energy at P is $E\{R(E_0) - r_0\}$, or, from equations (12) and (13),

$$E_{pp} = \left(\frac{pE_0^q - r_0}{p} \right)^{1/q}$$

Substituting this into the above equation yields

$$\frac{\phi}{\Phi(E_0)} = \exp \left[- \int_{\frac{(pE_0^q - r_0)^{1/q}}{p}}^{E_0} \Sigma_R(E) pq E^{q-1} dE \right] \quad (19)$$

for the special case when $d=r_0$.

From equations (9) and (15) (let $\rho=1.0$ g/cc for tissue) the dose-rate equation becomes

$$\frac{D}{\Phi(E_0)} = \frac{5.75 \times 10^{-5}}{pq \left(\frac{pE_0^q - r_0}{p} \right)^{1-1/q}} \exp \left[- \int_{\frac{(pE_0^q - r_0)^{1/q}}{p}}^{E_0} \Sigma_R(E) pq E^{q-1} dE \right] \frac{\text{rad/hr}}{\text{proton/cm}^2\text{-sec}} \quad (20)$$

for the case when $r_0=d$.

B. Derivation of the Equation for the Dose-Rate Contribution Due to First-Generation Cascade Protons

Table I gives the energies the protons have, in terms of the energy variables, at specific locations in figure 2.

TABLE I
Definition of Energy Variables

Location on figure 2	Corresponding proton energy	
	Secondary	Primary
$d\sigma$ -----	-----	E_0 (a constant)
S -----	E_s	E_p
P -----	$E\{R(E_s) - [R(E_p) - R(E_{pp})]\}$	E_{pp}

The major assumption of the calculation which is to follow is that all cascade secondary protons are emitted in the direction of the parent primary proton. This is a reasonable assumption for high-energy primary protons, since the lab system angular distribution is peaked in this direction (ref. 3). However, one

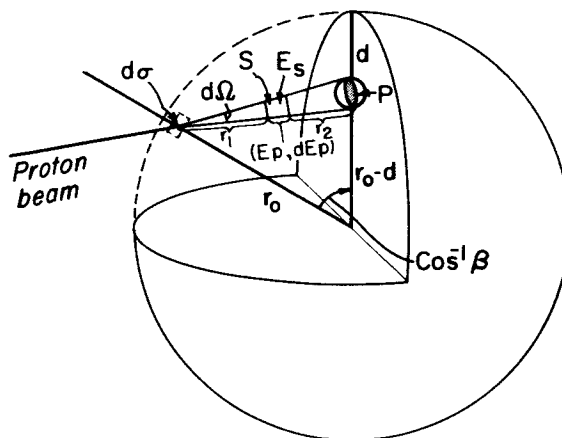


FIGURE 2.—Calculation of secondary proton dose rate.

should recall this assumption when evaluating the significance of the results presented in this paper.

This assumption makes it convenient to define a function $F(E_p, E_s)$ such that $F(E_p, E_s)dE_s dE_p$ is the number of cascade protons in the energy interval dE_s , about E_s , henceforth denoted as (E_s, dE_s) , emitted per incident primary proton in the energy interval (E_p, dE_p) . This definition is more easily understood if it is realized that the primary proton energy interval (E_p, dE_p) is identical to a primary proton path segment (r, dr) at the point S in figure 2. Thus the function $F(E_p, E_s)dE_s dE_p$ represents the number of cascade protons at energy (E_s, dE_s) emitted at S as a result of primary proton nuclear collisions in (E_p, dE_p) .

We may now write the flux of cascade protons moving toward P (the dose point) from S as

$$\begin{aligned} \phi_c(E_{pp}, E_p, E_s) dE_{pp} dE_p dE_s \\ = \phi_p(E_{pp}) dE_{pp} F(E_p, E_s) dE_s dE_p \quad (21) \end{aligned}$$

where $\phi_p(E_{pp}) dE_{pp}$ is the primary proton flux reaching P in the energy interval (E_{pp}, dE_{pp}) to which the exponential removal probability factor is applied only over the path segment r_1 . The expression for $\phi_p(E_{pp}) dE_{pp}$, which will later be substituted in equation (21), is given in equation (7).

We must determine the permissible values of E_s , E_p , and E_{pp} in order to find the limits of integration of equation (21). One reasonable assumption is that no secondary proton is

emitted with an energy greater than the primary causing it.² Thus

$$E_{s_{\max}} = E_p \quad (22)$$

Three factors determine the minimum energy that the secondary proton may have. The first is that 4.6 MeV (the Coulomb barrier potential) is assumed the minimum energy that a cascade must have for emission. This 4.6-MeV figure is actually for aluminum, but we will use it here for oxygen with, we hope, negligible error. The second is that a secondary proton emitted at S must have enough energy to reach the dose point P or it clearly will not contribute to the dose rate at P . The third is that at an energy of about 0.025 MeV the proton will pick up an electron and become neutral hydrogen. Since only dose rate due to ionization energy loss is considered here, the neutral hydrogen cannot contribute to this dose rate. The second and third minimum energy criterion yield (eqs. (12) and (13)):

$$E_{s_{\min}} = [E_p^q - E_{pp}^q + 0.025^q]^{1/q}$$

Combining this with the first minimum energy criterion gives

$$E_{s_{\min}} = \text{MAX} \{ [E_p^q - E_{pp}^q + 0.025^q]^{1/q}; 4.6 \} \quad (23)$$

Notice that the integration over this variable, E_s , is in effect an integration over the energy spectrum of cascade secondaries emitted at some source point S .

The minimum energy that the primary proton can have and still contribute secondaries that can reach P is limited in part by the assumption that secondaries can be emitted only in the forward direction. Thus no $E_p < E_{pp}$ can be allowed. Also, it is assumed that no primaries with energy less than 16.5 MeV can cause secondary protons. The yield of secondaries for low-energy primaries is very small, and, in fact, usually such data are not given for primary energies less than 25 MeV (refs. 3 and 5). The reason for choosing 16.5 MeV as the cutoff

² Secondary protons of higher energy can be created by nuclear bombardment by secondary neutrons, which are not subject to ionization energy loss. These protons, however, are beyond the scope of the present calculation, since secondary neutrons are neglected.

energy in this case is that the mathematical function (derived later) which approximates the cascade proton yield goes negative when the primary proton energy is less than 16.5 MeV. Thus, the minimum permissible primary proton energy is

$$E_{p_{\min}} = \text{MAX} \{ E_{pp}; 16.5 \} \quad (24)$$

The maximum energy of this primary proton causing the cascade is the energy at which it enters the sphere. Thus

$$E_{p_{\max}} = E_0 \quad (25)$$

The integration over this variable, E_p , is in effect an integration over the path $R(\theta)$ (fig. 1) or $r_1 + r_2$ (fig. 2).

The variable E_{pp} is the variable that represents the direction of approach of the primary and secondary proton, since, given an incident proton energy E_0 , E_{pp} uniquely defines a path length in the sphere and thus an angle (fig. 2). An integration over the variable is thus an integration over the surface of the sphere, which is just what we performed in deriving the dose-rate contribution from primary protons alone. The limits of integration over this variable are the same as in this earlier derivation, for exactly the same reasons as outlined in the previous section. Thus (see equation 16),

$$E_{pp_{\min}} = \left[\frac{pE_0^q - r_0 - (r_0 - d)}{p} \right]^{1/q} \quad (26)$$

and

$$E_{pp_{\max}} = \left[E_0^q - \frac{d}{\eta} \right]^{1/q} \quad (27)$$

We can now write the total cascade proton flux reaching P , from equations (21) through (27), as

$$\phi_c = \int_{\left[\frac{pE_0^q - r_0 - (r_0 - d)}{p} \right]^{1/q}}^{\left[\frac{E_0^q - d}{p} \right]^{1/q}} dE_{pp} \int_{\text{MAX} \{ E_{pp}; 16.5 \}}^{E_0} dE_p \int_{\text{MAX} \{ [E_p^q - E_{pp}^q + 0.025^q]^{1/q}; 4.6 \}}^{E_p} dE_s \phi_p(E_{pp}) F(E_p, E_s) \quad (28)$$

The task of calculating the dose rate due to this flux is straightforward. The energy of

the secondary at P is the energy corresponding to the range $R(E_s) - r_2$, which is equivalent to the expression in table I. Using equations (12) and (13), we can write the energy of the secondary protons at P as $[E_s^q - E_p^q + E_{pp}^q]^{1/q}$. Equation (15) gives the corresponding stopping power as $[1/pq][E_s^q - E_p^q + E_{pp}^q]^{1/q-1}$. Since the dose rate due to ionization energy loss is just $\phi(E)(1/\rho)(dE/dx)$, as in equation (9), we can write the dose rate at P due to cascade protons as

$$D_c = \frac{5.75 \times 10^{-5}}{\rho} \int \left[\frac{E_0 - d}{p} \right]^{1/q} \left[\frac{pE_s^q - r_0 - (r_0 - d)}{p} \right]^{1/q} \phi_p(E_{pp}) dE_{pp} \times \int_{\text{MAX}\{E_{pp}, 16.5\}}^{E_s} dE_p \times \int_{\text{MAX}\{(E_s^q - E_p^q + .025^q)/q, 4.6\}}^{E_p} \frac{F(E_p, E_s) dE_s}{pq[E_s^q - E_p^q + E_{pp}^q]^{1-1/q}} \quad (29)$$

To find the function $F(E_p, E_s)$ we use the data presented in figures 3 (ref. 3) and 4 (ref. 4). Note from figure 4 that, over the primary proton energy range 0.4 to 1.8 BeV, the slope on log log graph paper of the cascade proton energy spectrum from aluminum is approximately constant. This slope is not far from that for uranium (ref. 4). In the absence of better data when this work was begun, this slope has been assumed valid for tissue. The function $E_s^{-10/11} dE_s$ approximates the slope

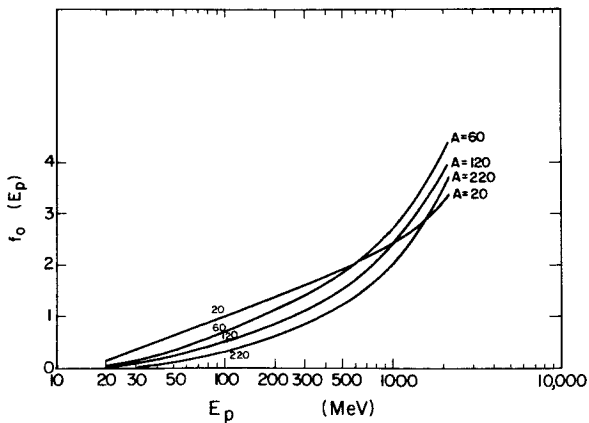


FIGURE 3.—The number of cascade protons per incident primary proton per inelastic collision, $f_0(E_p)$, as a function of primary proton energy, E_p , and atomic weight of the target.

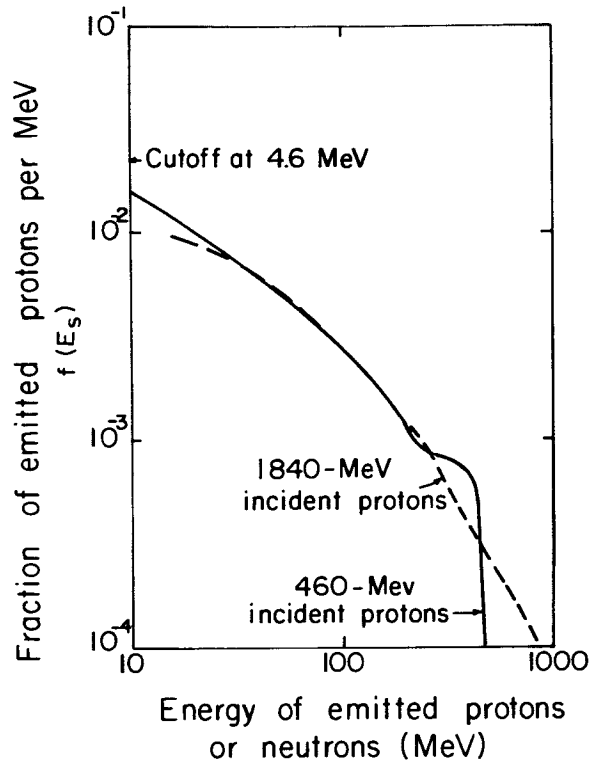


FIGURE 4.—The cascade proton energy spectrum. The fraction of the cascade protons emitted into unit MeV interval, $f(E_s)$, as a function of cascade energy.

of figure 4. We want the integral overall possible E_s of this differential energy spectrum to be the number of cascade protons emitted per incident primary proton per inelastic scattering. Thus we write

$$N_0(E_p) \int_{4.6}^{E_p} E_s^{-10/11} dE_s = f_0(E_p) = \frac{\text{cascades}}{\text{primary-inelastic collision}} \quad (30)$$

where the limits of integration are the same as the ones discussed earlier, $N_0(E_p)$ is a normalizing function, and $f_0(E_p)$ is defined by equation (30).

Note that $f_0(E_p)$ is the functional representation of the curve plotted in figure 3. This curve for $A=20$ is approximated by the function

$$f_0(E_p) = \frac{1}{1.76} \ln \frac{E_p}{16.5} \quad (31)$$

and it is assumed that this curve is approximately valid for tissue.

What will finally be needed to obtain $F(E_p, E_s)$ is the number of cascades per primary per dE_p interval. This simple conversion is indicated in the following steps:

$$f_0(E_p)\Sigma_{in}(E_p) = \frac{\text{cascades}}{\text{primary}-dR},$$

where $\Sigma_{in}(E_p)$ is the macroscopic inelastic cross section;

$$f_0(E_p)\Sigma_{in}(E_p) \frac{dR}{dE_p} = \frac{\text{cascades}}{\text{primary}-dE_p}$$

where $\frac{dR}{dE_p} = pqE_p^{q-1}$ from equation (14).

Thus equation (30) can be written

$$N_1(E_p) \int_{4.6}^{E_p} E_s^{-10/11} dE_s = \frac{pqE_p^{q-1}\Sigma_{in}(E_p)}{1.76} \ln \frac{E_p}{16.5} \quad (32)$$

where

$$N_1(E_p) = pqE_p^{q-1}\Sigma_{in}(E_p)N_0(E_p)$$

By the previous definition of $F(E_p, E_s)$ (the number of cascade protons at energy E_s per dE_s interval emitted per incident primary proton of energy E_p per path segment corresponding to the energy degradation dE_p) it is apparent that

$$F(E_p, E_s) = N_1(E_p)E_s^{-10/11} \quad (33)$$

Solving equation (32) for $N_1(E_p)$ and substituting this into equation (33) gives

$$F(E_p, E_s) = \frac{1}{11 \times 1.76} \frac{pqE_p^{q-1}\Sigma_{in}(E_p) \ln \frac{E_p}{16.5}}{E_s^{10/11}(E_p^{1/11} - 4.6^{1/11})} \quad (34)$$

Finally, substituting equations (7) and (34) into (29) and letting $\rho = 1.0$ for tissue gives

$$\begin{aligned} \frac{D_c}{\Phi(E_0)} = \frac{7.42 \times 10^{-7}}{r_0 - d} & \left\{ \int_{\left[\frac{pE_0^q - r_0 - (r_0 - d)}{p}\right]^{1/q}}^{\left[\frac{E_0 - d}{p}\right]^{1/q}} \left[\frac{r_0^2 - (r_0 - d)^2}{(pE_0^q - pE_{pp}^q)^2} + 1 \right] pqE_{pp}^{q-1} \right. \\ & \times \left[\int_{\text{MAX}[E_{pp}; 16.5]}^{E_0} \frac{pqE_p^{q-1}\Sigma_{in}(E_p) \ln \frac{E_p}{16.5}}{E_p^{1/11} - 4.6^{1/11}} \exp \left[- \int_{E_p}^{E_0} \Sigma_R(E) pqE^{q-1} dE \right] \right. \\ & \left. \left. \times \left(\int_{\text{MAX}[(E_0^q - E_{pp}^q + .025^q)^{1/q}; 4.6]}^{E_p} \frac{dE_s}{E_s^{10/11} pq[E_s^q - E_p^q + E_{pp}^q]^{1-1/q}} dE_p \right) dE_{pp} \right] \right\} \quad (35) \end{aligned}$$

This equation gives the dose rate in rads/hr per proton/cm²-sec for cascade protons at a depth d in a sphere of radius r_0 due to an isotropic flux of protons of energy E_0 incident upon the sphere. Notice that the primary protons have been exponentially attenuated (removal due to nuclear reaction), but that this removal is neglected for the secondaries. This is an approximation that significantly decreases the computer time needed to solve the equation,

and it tends to cancel the error introduced by neglecting second- and third-generation cascade protons. Including this exponential attenuation in the simple case of a collimated primary beam incident upon a slab decreased the cascade dose rate at a depth of 25 cm by about 10%.

For the special case when P is at the center of the sphere, the integration over the variable E_{pp} disappears, as it did for the primary protons. To treat this special case substitute equations

(18) and (34) into (29) to get

$$\frac{D_c}{\Phi(E_0)} = 2.96 \times 10^{-6} \left[\int_{\text{MAX}}^{E_0} \left[\left(E_0^q - \frac{r_0}{p} \right)^{1/q}; 16.5 \right] \frac{pq E_p^{q-1} \Sigma_{\text{in}}(E_p) \ln \frac{E_p}{16.5}}{E_p^{10/11} - 4.6^{1/11}} \right. \\ \left. \times \exp \left[- \int_{E_p}^{E_0} \Sigma_R(E) pq E^q dE \right] \right. \\ \left. \times \int_{\text{MAX}}^{E_p} \left[\left(E_p^q - E_0^q + \frac{r_0}{p} + .025^q \right)^{1/q}; 4.6 \right] \frac{dE_s}{E_s^{10/11} pq \left[E_s^q + E_0^q - \frac{r_0}{p} - E_p^q \right]^{1-1/q}} \right] dE_p \quad (36)$$

This equation gives the cascade proton dose rate (rads/hr per proton/cm²-sec) at the center of a sphere of radius r_0 due to an isotropic incident flux of protons of energy E_0 . In this equation, as with the similar equation for primary protons, E_{pp} of equation (35) has become a constant whose value is

$$E_{pp} = \left(E_0^q - \frac{r_0}{p} \right)^{1/q} \quad (37)$$

C. Derivation of the Equation for the Dose-Rate Contribution From Scattered and Recoil Protons Resulting From Elastic Interactions Between Primary Protons and Hydrogen Nuclei

The assumption can again be made that all the scattered and recoil protons are emitted in the same direction as the incident primary, since scattering in the center-of-mass system is not far from isotropic (ref. 6), and the center of mass is in rapid motion in the direction of the primary. However, the energy spectrum of these secondaries is derived by applying conservation of energy to the angular dependence of the differential elastic scattering cross section.

The forward scattering approximation makes all the equations derived in the preceding section for cascade secondaries valid here also for the elastically scattered protons, with the exceptions that the function $F(E_p, E_s)$ becomes a different function, $F_H(E_p, E_s)$, and the limits of integration will differ in some cases. See table I and figure 2 for the definition of the variables.

Let us first derive the expression for $F_H(E_p, E_s)$, which is defined to be exactly analogous to the corresponding function of the preceding section. That is, $F_H(E_p, E_s) dE_p dE_s$ is the number of scattered protons in the energy interval (E_s, dE_s) emitted per incident primary proton in the energy interval (E_p, dE_p) (see the previous verbal expansion on this definition at the beginning of section B). Since the p-p elastic scattering cross section has the units

$$\Sigma_{e_i}(E_p, \eta) d\Omega dR \\ = \frac{(\text{scattered} + \text{recoil}) \text{ protons in } (\eta, d\Omega)}{\text{incident primary in } (R, dR)}$$

the function $F_H(E_p, E_s) dE_p dE_s$ is given by

$$F_H(E_s, E_p) dE_p dE_s \\ = \Sigma_{e_i}(E_p, \eta) \frac{d\Omega}{d\eta} \frac{d\eta}{dE_s} dE_s \frac{dR}{dE_p} dE_p \quad (38)$$

where η is the cosine of the center-of-mass scattering angle, and E_s and E_p are the secondary and primary energies, respectively, in the lab system.

The required solid angle relationship is the familiar $d\Omega/d\eta = \pm 2\pi$, where the plus sign is for the scattered proton and the minus sign for the recoil proton. Differentiating the relativistically correct function (ref. 7) $E_s = 1/2 E_p (1 \pm \eta)$ gives

$$\frac{d\eta}{dE_s} = \pm \frac{2}{E_p}$$

where the plus sign is again used when E_s is the scattered proton energy and the minus sign

when it is the recoil energy. The stopping-power expression of equation (14) gives

$$\frac{dR}{dE_p} = pqE_p^{q-1}$$

Thus we can write

$$F_H(E_s, E_p)dE_p dE_s = \Sigma_{ei}(E_p, \eta) \frac{4\pi pq}{E_p^{2-q}} dE_p dE_s \quad (39)$$

To set a function to the elastic scattering cross section we divide it into an isotropic and an anisotropic part. The scattering due to the nuclear potential is not isotropic in the center-of-mass system at high primary proton energies, though the assumption is made that it is. Experimental data indicate that the scattering is peaked in the forward direction and that the solid angle included in this peak is a small fraction of the total solid angle (ref. 6). So the author feels that if we include Rutherford scattering, which is the dominating anisotropic component of the cross section in the limit of low-energy recoils (and thus the most significant biologically), no major error is encountered by neglecting the anisotropic scattering component of the nuclear potential. This reasoning leads to the conclusion that we can write

$$\Sigma_{ei}(E_p, \eta) = \Sigma_{ei}(E_p) + \Sigma_c(E_p, \eta)$$

where the second term is the Rutherford formula

$$\Sigma_c(E_p, \eta) = \frac{N_H}{4} \frac{e^4}{E_p^2} \frac{1}{\sin^4 \frac{\theta}{2}} \text{ cm}^{-1}$$

which is identical to

$$\Sigma_c(E_p, \eta) = \frac{N_H e^4}{E_p^2} \frac{1}{(1-\eta)^2}$$

where E_p is here in units of ergs, η is the cosine of the scattering angle in the c.m. system, and N_H is the hydrogen atom density. We allow this Rutherford cross section to represent only the recoil proton, which is of low energy, so the primary, which is only slightly degraded in energy, may continue unaltered as an approximation in this development. This means that the Rutherford cross section will be excluded from the removal cross section used in the exponential attenuation factor applied to the

primaries. Thus, considering E_s to be the recoil proton energy, we use the expression $2E_s = E_p(1-\eta)$ to give

$$\Sigma_c(E_p, E_s) = 5.2 \times 10^{-27} \frac{N_H}{E_s^2} \text{ cm}^{-1}$$

where appropriate constants have been employed so that E_s is now in units of MeV. The atom density of hydrogen in tissue is approximated by using $C_7H_{70}O_{32}N_2$ as tissue-equivalent material with a density of

$$N_H = 6.09 \times 10^{22} \text{ atoms/cc}$$

Data from reference 6 for the isotropic component of the elastic cross section is approximated by the function

$$\Sigma_{ei}(E_p) = N_H \sigma_{ei}(E_p) = bE_p^m \quad (40)$$

where

$$\begin{aligned} b &= 0.00584, \quad m=0 \text{ for } E \leq 5 \text{ MeV,} \\ b &= 0.00292, \quad m=-1 \text{ for } 5 \leq E \leq 125, \\ b &= 0.000234, \quad m=0 \text{ for } E \geq 125 \end{aligned}$$

Therefore we write the total differential elastic scattering cross section as

$$\Sigma_{ei}(E_p, E_s) = bE_p^m + \frac{0.000316}{E_s^2} (\text{cm-steradian})^{-1} \quad (41)$$

and $F_H(E_s, E_p)$ becomes

$$\begin{aligned} F_H(E_s, E_p)dE_p dE_s &= \frac{4\pi pq}{E_p^{2-q}} \left(bE_p^m + \frac{0.000316}{E_s^2} \right) dE_p dE_s \quad (42) \end{aligned}$$

This expression and the limits of integration of the variables E_s and E_p represent the only differences between the equations being developed here and those developed in the preceding section for cascade secondary protons. In a manner exactly analogous to the development of the preceding section, the criterion that the secondary must reach the dose point with an energy of 0.025 MeV yields

$$E_{s_{\min}} = [E_p^q - E_{pp}^q + .025^q]^{1/q}$$

The maximum energy of the recoil or scattered proton is the energy of the primary itself

at that point, thus

$$E_{s_{\max}} = E_2$$

Since there is no backscattering, the minimum energy that the primary can have and still contribute secondaries to the dose point is the energy of the primary at the dose point, or

$$E_{p_{\min}} = E_{pp}$$

The maximum primary energy is clearly

$$E_{p_{\max}} = E_0$$

The limits on the E_{pp} variable are the same as before:

$$E_{pp_{\max}} = \left[E_0^q - \frac{d}{p} \right]^{1/q},$$

and

$$E_{pp_{\min}} = \left[\frac{pE_0^q - r_0 - (r_0 - d)}{p} \right]^{1/q}$$

Now substitute equation (7), $F_H(E_s, E_p)$, and the new limits of integration into equations (28) and (29); this gives the hydrogen recoil and scattered proton flux,

$$\phi_H = \int_{E_{pp_{\min}}}^{\left[\frac{E_0 - d}{p} \right]^{1/q}} \left[\frac{pE_0^q - r_0 - (r_0 - d)}{p} \right]^{1/q} \phi_p(E_{pp}) dE_{pp}$$

$$\int_{E_{pp}}^{E_0} dE_p \int_{[E_p^q + E_{pp}^q - .025]^{1/q}}^{E_p} dE_s F_H(E_p, E_s) \quad (43)$$

and the hydrogen recoil and scattered dose rate,

$$\frac{D_H}{\Phi(E_0)} = \frac{1.81 \times 10^{-4}}{r_0 - d} \int_{\left[\frac{pE_0^q - r_0 - (r_0 - d)}{p} \right]^{1/q}}^{\left[\frac{E_0 - d}{p} \right]^{1/q}} \left[\frac{r_0^2 - (r_0 - d)^2}{(pE_0^q - pE_{pp}^q)^2 + 1} \right] p q E_{pp}^{q-1}$$

$$\times \int_{E_{pp}}^{E_0} \frac{\exp \left[- \int_{E_p}^{E_0} \Sigma_R(E) p q E^{q-1} dE \right]}{E_p^{2-q}} \int_{[E_p^q - E_{pp}^q + .025]^{1/q}}^{E_p} \frac{\left(b E_m^2 + \frac{.000316}{E_s^2} \right)}{(E_s^q - E_p^q + E_{pp}^q)^{1-1/q}} dE_s dE_p dE_{pp} \quad (44)$$

in units of rads/hr per incident proton/cm²-sec at a depth d in a sphere of radius r_0 due to an isotropic flux of protons of energy E_0 incident upon the sphere.

For the special case when the dose point P is at the center of the sphere, the E_{pp} integral disappears as before. Equations (18), (29), (37), and (42), and the new limits of integration, give

$$\frac{D_H}{\Phi(E_0)} = 7.25 \times 10^{-4} \int_{\left(E_0^q - \frac{r_0}{p} \right)^{1/q}}^{E_0} \frac{\exp \left[- \int_{E_p}^{E_0} \Sigma_R(E) \eta q E^{q-1} dE \right]}{E_p^{2-q}}$$

$$\times \int_{\left[E_p^q - E_0^q + \frac{r_0}{p} + .025 \right]^{1/q}}^{E_p} \frac{\left(b E_m^2 + \frac{.000316}{E_s^2} \right)}{\left(E_s^q - E_p^q + E_0^q - \frac{r_0}{p} \right)^{1-1/q}} dE_s dE_p \quad (45)$$

for the dose rate when P is at the center of the sphere ($r_0 = d$) in units of rads/hr per proton/cm²-sec.

D. Derivation of the Equation for the Dose-Rate Contribution From First-Generation Evaporation Protons

The major simplifying assumption of this derivation is that each evaporation secondary proton deposits all its energy at its point of

formation. This is a valid assumption, since 70 to 100% of the evaporation protons always have a range of less than 1 mm. (ref. 8). Thus the variable E_p is eliminated, since now only those secondaries created at the dose point contribute to the dose.

It is useful to define a function $S(E_s, E_{pp})$ such that $S(E_s, E_{pp}) dE_s$ is the number of evaporation protons in (E_s, dE_s) emitted per

unit length of travel of a primary proton per primary proton. Thus the dose rate is

$$D_E = \frac{5.75 \times 10^{-6}}{\rho} \int_{E_{pp\min}}^{E_{pp\max}} \phi_p(E_{pp}) dE_{pp} \int_{E_{s\min}}^{E_{s\max}} E_s S(E_s, E_{pp}) dE_s \quad (46)$$

Two further approximations are used to derive $S(E_{pp}, E_s)$. The first is that one evaporation proton is emitted per inelastic collision. The data in reference 3 indicate that this is approximately correct. The second approximation is that the evaporation protons are emitted with the Maxwell-Boltzmann energy spectrum. This gives

$$S(E_s, E_{pp}) dE_s = [1.0] [\Sigma_{in}(E_{pp})] \left[\frac{E_s}{\tau^2(E_{pp})} \exp[-E_s/\tau(E_{pp})] dE_s \right] \quad (47)$$

where $\Sigma_{in}(E_{pp})$ is the macroscopic inelastic cross section and $\tau(E_{pp})$ is the effective nuclear temperature, in units of MeV, required to give the proper Maxwell-Boltzmann energy distri-

bution. We approximate the data of reference 3 for $\tau(E_{pp})$ by

$$\begin{aligned} \tau(E_{pp}) &= 2.41 \ln(0.1 E_{pp}) & \text{for } E_{pp} \leq 50 \text{ MeV} \\ \tau(E_{pp}) &= 0.29 \ln(1.222 \times 10^4 E_{pp}) & \text{for } E_{pp} \geq 50 \text{ MeV} \end{aligned} \quad (48)$$

The first of these functions requires that there be no evaporations emitted when the incident primary has an energy less than 10 MeV. This is probably not unreasonable anyway, since evaporation proton emission is bound to be unlikely, if not energetically impossible, for low primary proton energy.

Incorporating this requirement into the limits of integration of E_{pp} from the previous sections of this paper gives

$$E_{pp\max} = \left[E_0^q - \frac{d}{p} \right]^{1/q}$$

and

$$E_{pp\min} = \text{MAX} \left\{ \left[\frac{pE_0^q - r_0 - (r_0 - d)}{p} \right]^{1/q}; 10.0 \right\}$$

Now we can write, from equations (7) and (46),

$$\begin{aligned} D_E &= \frac{5.75 \times 10^{-6} \Phi}{4\rho(r_0 - d)} \int_{\text{MAX} \left\{ \left[\frac{pE_0^q - r_0 - (r_0 - d)}{p} \right]^{1/q}; 10.0 \right\}}^{\left[E_0^q - \frac{d}{p} \right]^{1/q}} \left[\frac{r_0^2 - (r_0 - d)^2}{(pE_0^q - pE_{pp}^q)^2} + 1 \right] p q E_{pp}^{q-1} \frac{\Sigma_{in}(E_{pp})}{\tau^2(E_{pp})} \\ &\quad \times \exp \left[- \int_{E_{pp}}^{E_0} \Sigma_R(E) p q E^{q-1} dE \right] \left[\int_{E_{s\min}}^{E_s} E_s^2 \exp[-E_s/\tau(E_{pp})] dE_s \right] dE_{pp} \quad (49) \end{aligned}$$

where $\tau(E_{pp})$ is defined in equation (48).

Performing the integration over the variable E_s and letting $\rho = 1.0$ gives, for the dose rate due to evaporation protons of energy between $E_{s\min}$ and $E_{s\max}$,

$$\begin{aligned} D_E &= \frac{2.88 \times 10^{-5}}{r_0 - d} \int_{\text{MAX} \left\{ \left[\frac{pE_0^q - r_0 - (r_0 - d)}{p} \right]^{1/q}; 10.0 \right\}}^{\left[E_0^q - \frac{d}{p} \right]^{1/q}} \left[\frac{r_0^2 - (r_0 - d)^2}{(pE_0^q - pE_{pp}^q)^2} + 1 \right] \\ &\quad \times \left[\left(\frac{E_{s\min}^2}{2\tau(E_{pp})} + E_{s\min} + \tau(E_{pp}) \right) \exp[-E_{s\min}/\tau(E_{pp})] - \left(\frac{E_{s\max}^2}{2\tau(E_{pp})} + E_{s\max} + \tau(E_{pp}) \right) \right. \\ &\quad \left. \exp[-E_{s\max}/\tau(E_{pp})] p q E_{pp}^{q-1} \Sigma_{in}(E_{pp}) \right] \times \exp \left[- \int_{E_{pp}}^{E_0} \Sigma_R(E) p q E^{q-1} dE \right] dE_{pp} \quad (50) \end{aligned}$$

in units of rads/hr per protons/cm²-sec, where

$$E_{s_{\min}}=0, \text{ and} \\ E_{s_{\max}}=\infty$$

Owing to the shape of the Maxwell-Boltzmann energy distribution, the exact lower and upper limits of integration of E_s are not crucial so long as they are very small and very large respectively. Thus zero and infinity serve perfectly well.

For the special case in which the dose point is at the center of the sphere, E_{pp} becomes a constant given by equation (37). So, from equations (18), (46), and (47), the dose rate from evaporation protons at the center of the sphere of radius r_0 simplifies to

$$D_R = \frac{5.75 \times 10^{-5}}{\rho} \Phi \exp \left[- \int_{(E_0^q - r_0/p)^{1/q}}^{E_0} \Sigma_R(E) p q E^{q-1} dE \right] \\ \times \int_{E_{s_{\min}}}^{E_{s_{\max}}} \Sigma_{\ln}(E_{pp}) \frac{E_s^2}{\tau^2(E_{pp})} \exp[-E_s/\tau(E_{pp})] dE_s$$

Carrying out the integration and letting $\rho=1.0$ gives

$$\frac{D_R}{\Phi(E_0)} = 1.15 \times 10^{-4} \Sigma_{\ln}(E_{pp}) \exp \left[- \int_{(E_0^q - r_0/p)^{1/q}}^{E_0} \Sigma_R(E) p q E^{q-1} dE \right] \\ \times \left[\left(\frac{E_{s_{\min}}^2}{2\tau(E_{pp})} + E_{s_{\min}} + \tau(E_{pp}) \right) \exp \left[-E_{s_{\min}}/\tau(E_{pp}) \right] - \frac{E_{s_{\max}}^2}{2\tau(E_{pp})} + E_{s_{\max}} + \tau(E_{pp}) \right] \\ \times \exp[-E_{s_{\max}}/\tau(E_{pp})] \quad (51)$$

where $E_{pp} = \left(E_0^q - \frac{r_0}{p} \right)^{1/q}$ for the dose rate at the center of the sphere due to evaporation protons.

E. The Breakdown of Dose Rate Into Energy Groups

To determine the LET of the protons at the dose point one must know the energy at the dose point of the protons contributing to the dose rate. This knowledge is easily obtained

for the primary protons by integrating equation (17) in steps. For example, integrating equation (17) from

$$\left[\frac{pE_0^q - r_0 - (r_0 - d)}{p} \right]^{1/q}$$

to 20 MeV gives the primary proton dose rate which is deposited by protons between an energy

$$\left[\frac{pE_0^q - r_0 - (r_0 - d)}{p} \right]^{1/q}$$

and 20 MeV. Then integrating from 20 MeV to

$$\left[\frac{pE_0^q - d}{p} \right]^{1/q}$$

gives the remaining dose rate resulting from primary protons with an energy at the dose point greater than 20 MeV.

Similar information is obtained for cascade protons by integrating the E_s integrand in equation (35) in steps. A cascade proton with energy 0.025 MeV at the dose point has energy $(E_p^q - E_{pp}^q + 0.025^q)^{1/q}$ at the source point S (see eq. (35) and fig. 2). Thus setting the upper limit of E_s at $(E_p^q - E_{pp}^q + 1.0^q)^{1/q}$, instead of E_p , gives the dose rate contributed by cascade protons within an energy range of 0.025 to 1.0 MeV at the dose point. This type of consideration yields the information that will be found in table III.

The same limits on the E_s variable are used for the hydrogen recoil and scattered protons as for the cascade protons.

To obtain the dose rate due to evaporation protons in any energy interval just replace $E_{s_{\min}}$ and $E_{s_{\max}}$ in equations (50) and (51) by the lower and upper limits respectively of the interval.

The proton energy intervals for which the computer program is presently designed to calculate dose rates are 0-1, 1-2, 2-5, 5-10, 10-20, 20-40, 40-80, and 80- ∞ MeV. These dose rates do not reflect the energy deposited at the dose point (LET), but rather the energy lost by the protons at the dose point (stopping power). The difference between these two values is normally small (ref. 9), and an estimate of the energy lost at the dose point can be obtained by multiplying the dose from each

interval by a factor (which is different for each interval)

$$\langle \text{LET} \rangle / \langle dE/dx \rangle,$$

where $\langle \text{LET} \rangle$ is the average LET for the particular energy interval and $\langle dE/dx \rangle$ is the average stopping power for the same interval.

F. The Zero-Range Approximation for Recoil and Scattered and Cascade Protons With Energy Less Than 1 MeV

In order to simplify finding the solution to equations (35), (36), (44), and (45) for the lowest-energy group (i.e., when the protons causing the dose rate have an energy less than 1 MeV), all secondary protons of less than 1 MeV are considered to have zero range so that all their energy is deposited locally.

To satisfy this approximation we scan, at the source point, all secondary proton energies E_s , pick the value of E_s for which the secondary proton reaching the dose point has an energy of 1 MeV, and require that it deposit this 1 MeV at the dose point. So, in effect, we are eliminating the E_s integral from the equation that gives the dose-rate contribution from the 0–1.0-MeV energy group.

A mathematical trick which gives us the required equation for the 0–1.0-MeV energy group is to make a change of variables from E_s to E_{sd} , where E_{sd} is defined as the secondary proton energy at the dose point, then multiply the E_{sd} integrand by a delta function defined as $\delta(E_{sd}-1.0)=0$ for $E_{sd}=1.0$ MeV and

$$\int_{-\infty}^{\infty} \delta(E_{sd}-1.0) dE_{sd} = 1.0 \text{ MeV}$$

The secondary proton energy at the dose point is (see table I)

$$E_{sd} = (E_s^q - E_p^q + E_{pp}^q)^{1/q}$$

When we make the indicated change of variables and multiply by $\delta(E_{sd}-1.0)$, the E_s integral of equations (35) and (36) becomes

$$\frac{1.0}{pq(1.0^q + E_p^q - E_{pp}^q)^{1-1/q}}$$

for the 0–1.0-MeV group. Similarly, the E_s integral for equations (44) and (45) becomes

$$\frac{bE_p^m - \frac{3.16 \times 10^{-4}}{(1.0^q + E_p^q - E_{pp}^q)^{2/q}}}{(1.0^q + E_p^q - E_{pp}^q)^{1-1/q}}$$

for the 0–1.0-MeV group.

G. The Inelastic Scattering Cross Section

The inelastic cross section, $\Sigma_{in}(E)$, is chosen as the inelastic cross section for protons in oxygen. It is approximated by the function

$$\Sigma_{in}(E) = N\sigma_{in}(E) = gE^h, \quad (52)$$

where

$$g = 0.0347, h = 0, \text{ for } E \leq 0.5 \text{ MeV},$$

$$g = 0.06405, h = -0.381, \text{ for } 5 \leq E \leq 125,$$

$$g = 0.01019, h = 0, \text{ for } E \geq 125, \text{ and}$$

N = atom density of nonhydrogenous elements in tissue.

The basic cross-section data come from references 5 and 10 and are presented below.

E (MeV)	σ (mb)	Reference
25	524	5
50	407	5
100	316	5
200	283	5
400	281	5
3.0 BeV	314	10

The following approximations are made in finding the atom density of oxygen in tissue:

(a) The molecule $C_7H_{70}O_{32}N_2$ is representative of tissue.

(b) Tissue has the density of 1.0 g/cc.

(c) Carbon, oxygen, and nitrogen are all considered to be oxygen. Thus $N = 3.56 \times 10^{22}$ atoms/cc.

H. The Removal Cross Section

The removal cross section, $\Sigma_R(E)$, used in the exponential attenuation factor is considered to be the sum of the inelastic and the elastic scattering cross sections. However, the Coulomb (Rutherford) component of the elastic cross section is not included, since the resulting angular deviation and energy loss would be negligible.

The inelastic cross section is identical to the one of the preceding section. The elastic scattering cross section includes only proton-

hydrogen events. The reason for including this as a removal cross section at all is that hydrogen recoil protons and elastically scattered primary protons are treated as one of the sources of secondary protons. Thus the hydrogen-scattered primary protons must be removed to prevent duplication in the calculation.

The differential elastic scattering cross section is taken from reference 6 and is approximated by the following functions:

$$\Sigma_{ei}(E)d\Omega = N_H \sigma_{ei}(E) d\Omega = b E^m \frac{d\Omega}{dE'} dE' \quad (53)$$

where

$$b = 5.845 \times 10^{-3}, m = 0 \text{ for } E \leq 5 \text{ MeV,}$$

$$b = 2.92 \times 10^{-3}, m = -1 \text{ for } 5 \leq E \leq 125,$$

$$b = 2.43 \times 10^{-4}, m = 0 \text{ for } E \geq 125,$$

E is the energy of the incident proton, and

E' is the energy of the scattered proton.

The relation $E' = 1/2E(1 + \eta)$ is used with $d\Omega/d\eta = 2\pi$ to give

$$\frac{d\Omega}{dE'} = \frac{4\pi}{E'}$$

where E is the primary proton energy in the lab system, E' is the scattered proton energy in the lab system and η is the cosine of the scattering angle in the center-of-mass system.

Now we can write the total elastic cross section as

$$\int_0^\pi \Sigma_{ei}(E) d\Omega = b E^m \frac{4\pi}{E} \int_{0.025}^{\pi} dE' = 4\pi b E^m \left(1 - \frac{0.025}{E}\right) \quad (54)$$

Note we have assumed the differential cross section to be isotropic in the c.m. system.

A peculiarity of the proton-proton differential cross section is that it reflects the probability of finding both the scattered and the recoil proton in $d\Omega$. Thus for our purposes here we must take one-half of equation (54). The removal cross section becomes

$$\Sigma_R(E) = g E^h + 2\pi b E^m \left(1 - \frac{0.025}{E}\right) \quad (55)$$

I. The Range-Energy Relation

Range-energy data for water are used throughout and they are found to follow closely

the function $R = pE^q$. The range-energy data from reference 11 are represented by the following function (where R is the range in centimeters and E the energy in MeV),

$$R = pE^q, \quad (56)$$

where the values of p and q are:

E	p	q
< 5 MeV	0.002245	1.698
5-100	0.001903	1.800
100-300	0.002640	1.729
300-500	0.005207	1.610
> 500	0.01192	1.477

In order to minimize the computation time for the cascade and recoil secondaries, when the triple integral must be evaluated, the range energy relation is limited to

$$R = 0.0027 E^{1.729} \text{ for all } E$$

in the E_p and E_s integrands only. This expression fits the data very well in the interval 40 to 400 MeV, and holding p and q constant greatly simplifies the computation. The more accurate step function defined in the above table is always used in the E_{pp} integrands.

IV. SUMMARY OF APPROXIMATIONS

Before any results of the calculations are presented it may be wise to have well in mind the assumptions implicit in the code.

A. Approximations in the Primary Proton Calculation

1. No flux intensity gradient is maintained in the region of space outside the sphere.
2. The range-energy relationship of protons in the sphere material is $R = pE^q$, where R is distance in cm, E is energy in MeV, and p and q are given in equation (56).
3. Straggling is neglected.
4. The density of the sphere material is 1.0 g/cc.
5. The removal cross section of the primary protons is

$$\Sigma_R = g E^h + 2\pi b E^m \left(1 - \frac{0.025}{E}\right)$$

[See eqs. (52) and (53).]

6. Only interactions resulting in ionization energy loss contribute to the dose rate.

B. Approximations in the Cascade Proton Calculation

1. All the above assumptions given for primary protons are also used in the cascade proton calculation.

2. All cascade protons are emitted in the forward direction.

3. The number of cascade protons emitted per incident primary proton per inelastic collision is given by

$$\frac{1}{1.76} \ln \left(\frac{E_p}{16.5} \right)$$

4. The energy spectrum of these cascade protons has the functional behavior $E_s^{-10/11} dE_s$ for all incident primary proton energies.

5. A primary proton of less than 16.5 MeV cannot cause the emission of a cascade proton.

6. A primary proton cannot cause the emission of a cascade proton with energy greater than that of the primary.

7. The only interaction of cascade protons with the sphere is ionization energy loss. That is, no second-generation secondary protons are considered, and exponential attenuation of the cascade is included only in figures 5 and 6.

8. The inelastic scattering cross section is given by

$$\Sigma_{in} = gE^h$$

[See eq. (52).]

9. No cascade proton can be emitted with an energy less than 4.6 MeV.

10. The range-energy relation $R = 0.0027 E^{1.739}$ is used in the E_s and E_p integrals (i.e., p and q are constant for all energies in these two integrals).

11. A cascade proton at 0.025 MeV captures an electron, becomes neutral hydrogen, and no longer contributes to the dose rate.

C. Approximations in the Hydrogen Scattered and Recoil Proton Calculation

1. All assumptions used for primary protons are continued.

2. All scattered and recoil protons resulting from elastic interactions between primary protons and hydrogen nuclei travel in the same direction as the incident primary.

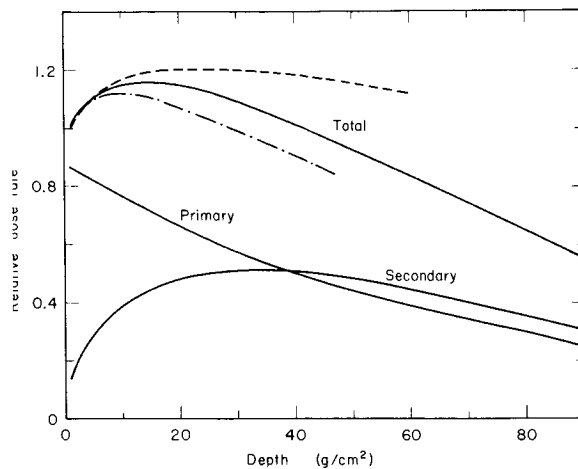


FIGURE 5.—Code-calculated depth dose (—) from a collimated beam of 730-MeV protons incident normally upon a slab of tissue-equivalent material (H_2O) compared with experimental values for copper (---) and Lucite (-.-.-). Total dose rates have been normalized to unity at 1 cm depth. Note that Lucite ($C_5H_8O_2$), tissue (H_2O), and copper have effective atomic weights of 13, 16, and 63.5 respectively (neglecting hydrogen, which does not contribute to the production of cascade protons).

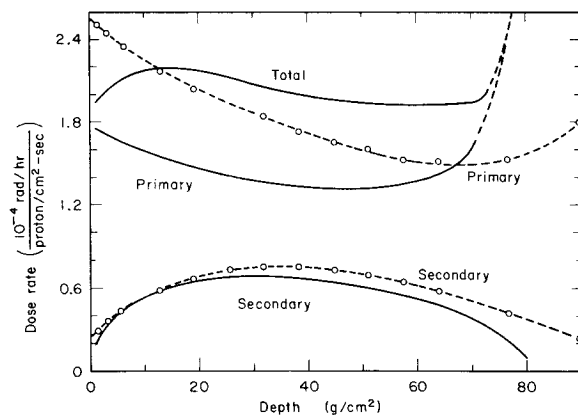


FIGURE 6.—Code-calculated depth dose (—) from a collimated beam of 400-MeV protons incident normally upon a slab of tissue-equivalent material compared with the Oak Ridge Monte Carlo code calculation for the beam incident upon aluminum (---).

3. The only interaction of recoil and scattered protons with the sphere is ionization energy loss.

4. The range-energy relation $R = 0.0027 E^{1.739}$ is used in the E_s and E_p integrals.

5. The p-p differential elastic scattering cross section is represented by an isotropic nuclear

potential component plus Rutherford scattering:

$$\Sigma_{ei}(E_p, \eta)d\Omega = \left(bE_p^m + \frac{0.00126}{E_p^2(1-\eta)^2} \right) d\Omega$$

where η is the cosine of the c.m. scattering angle. [See eq. (40).]

6. A recoil or scattered proton at 0.025 MeV captures an electron and becomes neutral hydrogen.

D. Approximations in the Evaporation Proton Calculation

1. All assumptions used for primary protons are continued.

2. All the energy of an evaporation proton is deposited at its point of formation.

3. One evaporation proton is emitted per primary proton per inelastic scattering.

4. The inelastic scattering cross section is given by

$$\Sigma_{in} = gE^h$$

[See eq. (52).]

5. Evaporation protons are emitted with a Maxwell-Boltzmann energy distribution; no skewing due to Coulomb repulsion is considered.

6. The integration over the evaporation proton energy spectrum can be extended from zero to ∞ without significant error.

7. The nuclear temperature needed to give the correct spectrum is (in units of MeV)

$$\tau(E_{pp}) = 2.41 \ln(0.1E_{pp}) \text{ for } E_{pp} \leq 50 \text{ MeV}$$

$$\tau(E_{pp}) = 0.29 \ln(1.222 \times 10^4 E_{pp}) \text{ for } E_{pp} \geq 50 \text{ MeV}$$

8. No evaporation protons are emitted if the incident primary proton energy is less than 10 MeV.

9. Only first-generation evaporation protons are included.

V. AGREEMENT OF THE CODE WITH EXPERIMENT AND OTHER CALCULATIONS

The literature contains very few data, experimental or calculated, with which calculated results of the code can be compared. Unfortunately, no depth-dose data in a sphere, due to an isotropic flux of protons at its surface, which includes the effect of secondary protons, could be found with which to compare the code

calculations. Thus all attempts to compare the results of the part of the code that calculates the effect of secondary protons must be limited to collimated primary protons incident upon a slab.

The first such comparison is with a cyclotron experiment in which the beam of 730-MeV protons incident upon an ionization chamber was interrupted by various thicknesses of Lucite and copper (ref. 12). Since in the code the approximation is made that all secondary protons travel in the forward direction, depths in the slab which are greater than the depth of the dose point cannot contribute secondaries to the dose point. Thus the code calculation at depth d in an infinite slab can be compared to the experimental result obtained with an interrupting slab of thickness d . This comparison is given in figure 5. The code, of course, calculates dose rate only in water (a tissue-equivalent material). However, the Lucite and copper experimental results form an envelope for the code-calculated water result in a way one would expect them to. Note that only the shape of the depth-dose curve is compared, since the absolute experimental dose rate is not known.

In the second comparison we illustrate the code's capability to calculate depth-dose curves due to secondary protons. We compare a calculation by the present code with a calculation performed at the Oak Ridge National Laboratory (ref. 13). The calculation at Oak Ridge utilized a complex Monte Carlo code which includes the angular distribution of the secondary protons, uses a nuclear model itself to calculate the number of secondaries and their energy spectrum rather than functions approximating the results of a nuclear model, and includes not only first-generation secondaries, but also all proton generations. Thus one would expect that the Oak Ridge calculation serves to check the general validity of the present simpler calculation. Unfortunately, Oak Ridge calculations for water are not available, so that the comparison given in figure 6 is for an Oak Ridge calculation for aluminum with the present code calculation for water. Both calculations assume a collimated 400-MeV proton beam incident upon a slab. One would expect the secondary-proton depth-dose curve for

aluminum to deviate from a similar water curve in much the same way as the Oak Ridge calculation deviates from the present calculation.

The third comparison is a confirmation of the code's capability to calculate primary-proton depth-dose curves due to an isotropic incident proton flux. In the limit of large sphere radius or low proton energy (or both), the sphere depth-dose curve becomes identical to that of a slab. The primary proton depth-dose curves in a 50-cm-radius sphere with incident isotropic fluxes of 60 MeV (range equals 6% of the radius) and 100 MeV (range equals 15% of the radius) are compared to depth-dose curves in a slab due to isotropic proton fluxes of the same energies. The slab calculations were done by hand, using an approximate method described in reference 2. We see in figure 7 (ref. 2) that the 60-MeV curves agree well in shape and magnitude, and the 100-MeV curves reflect a small effect due to the curvature of the sphere.

Finally, we compare depth-dose curves, in a sphere, due to a solar flare spectrum of an isotropic flux of protons. An estimate by Schaefer (ref. 14) of the relative depth dose 4

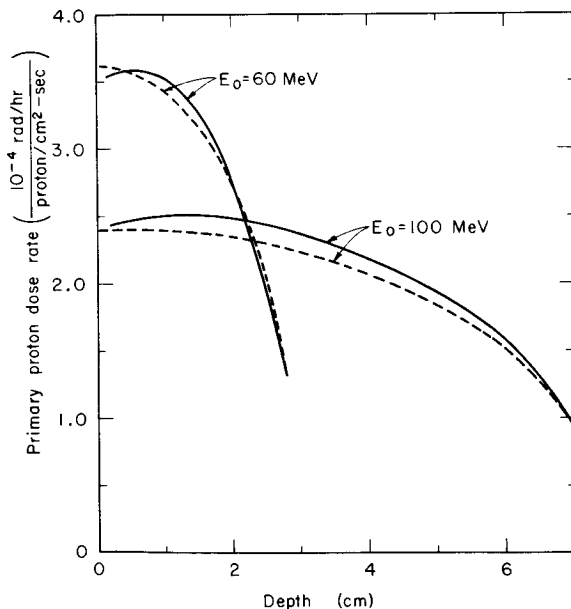


FIGURE 7.—Code-calculated depth dose (—) from an isotropic flux of 60- and 100-MeV protons incident upon a 50-cm-radius sphere compared with the depth dose calculation, using the method of reference 2, for the same fluxes incident upon a slab (-----).

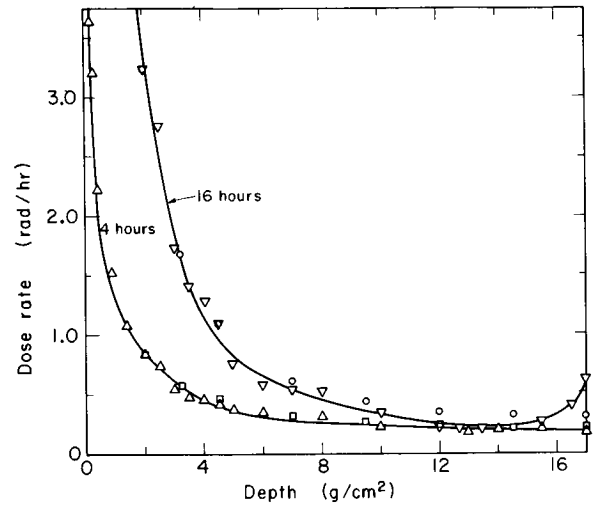


FIGURE 8.—Depth dose in tissue-equivalent material using Bailey's estimated solar flare spectrum. Code-calculated points for 4 (Δ) and 16 (∇) hours after onset of the radiation surge are compared with Schaefer's depth-dose estimate in a 15-cm-radius sphere with 2 g/cm² of shielding for 4 (\square) and 16 (\circ) hours after onset of the radiation surge. The effect of Schaefer's 2 g/cm² of shielding is approximated by normalizing Schaefer's surface dose in the 15-cm-radius sphere to the code calculation at 2 cm depth in a 17-cm-radius sphere. The depth-dose pattern for code-calculated points is irregular because the code approximates the continuously varying solar flare energy spectrum in discrete energy groups.

and 16 hours after onset of the radiation surge, using Bailey's solar flare spectrum (ref. 15), is compared with similar code calculations. Schaefer's curves were for a 15-cm-radius sphere with 2 g/cm² of shielding. Simulating this situation with the code, Schaefer's data at zero depth is normalized to the code at a 2-cm depth in a 17-cm-radius sphere. Figure 8 indicates good agreement.

VI. RESULTS AND DISCUSSION

We now put the code to its intended use and concentrate on depth-dose calculations in spheres of tissue-equivalent material irradiated by an isotropic flux of high-energy protons. Calculations have been performed for a large number of sphere sizes ranging from 1.0 to 50 centimeters in radius, each of which is irradiated with protons of several energies between 20 and 730 MeV. Three sphere sizes which give representative depth-dose patterns for varying sphere size and proton energy are

chosen for study in this paper. The 2.5-cm-radius sphere (fig. 19 and tables X and XII) is chosen for its similarity in mass to the rodent that is widely used in radiation experiments. The 25-cm-radius sphere (fig. 20 and tables XI and XIII) is chosen for its similarity in mass to man. The 10-cm-radius sphere (figs. 9 to 18 and tables II to IX) is chosen for a detailed examination of depth-dose patterns, since it has been used as a reference in beam-degradation experiments at the Lawrence Radiation Laboratory, and also because it approximates the size of the small primates that are used in radiation experiments.

Figure 9 contains the three basic types of primary proton depth-dose patterns. Type 1, represented by the 40-MeV curve, drops to zero before reaching the center of the sphere,

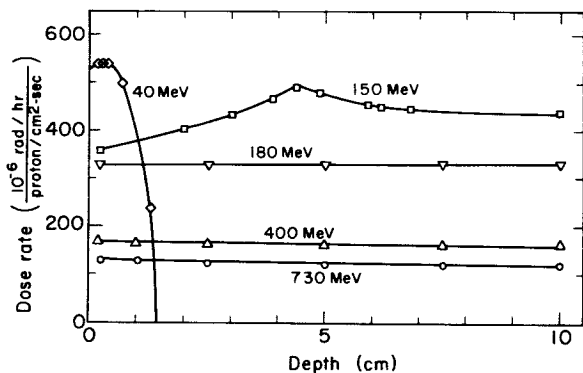


FIGURE 9.—Primary proton depth-dose patterns due to monoenergetic isotropic fluxes of protons of indicated energies incident upon a 10-cm-radius sphere of tissue-equivalent material.

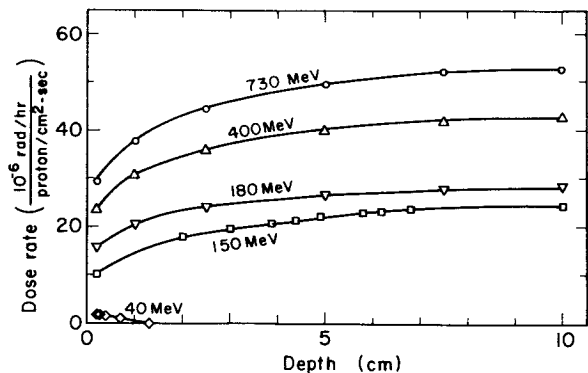


FIGURE 10.—Cascade secondary-proton depth-dose patterns due to monoenergetic isotropic fluxes of protons of indicated energies incident upon a 10-cm-radius sphere of tissue-equivalent material.

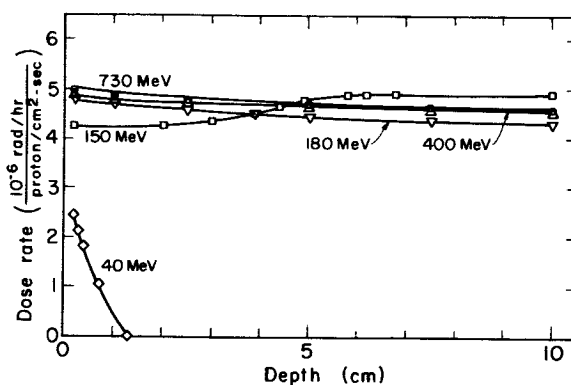


FIGURE 11.—Evaporation secondary-proton depth-dose patterns due to monoenergetic isotropic fluxes of protons of indicated energies incident upon a 10-cm-radius sphere of tissue-equivalent material.

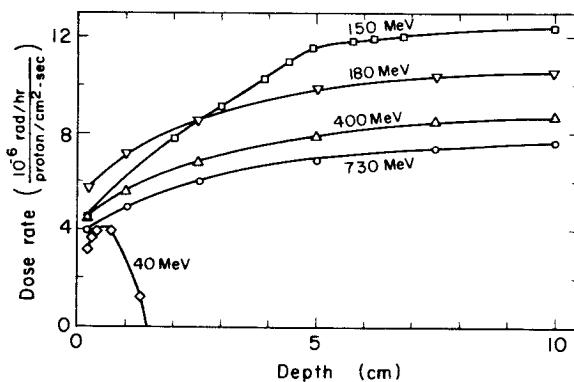


FIGURE 12.—Recoil secondary-proton depth-dose patterns due to monoenergetic isotropic fluxes of protons of indicated energies incident upon a 10-cm-radius sphere of tissue-equivalent material.

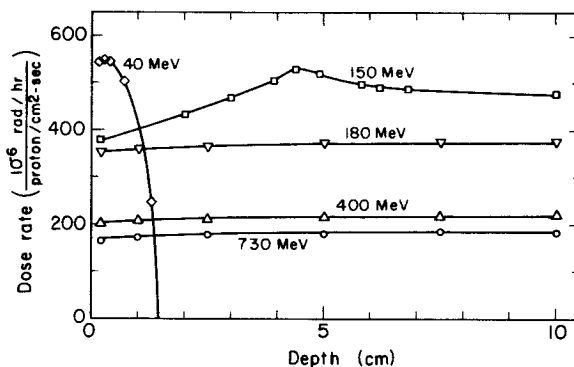


FIGURE 13.—Total (primary plus secondary) proton depth-dose patterns due to monoenergetic isotropic fluxes of protons of indicated energies incident upon a 10-cm-radius sphere of tissue-equivalent material.

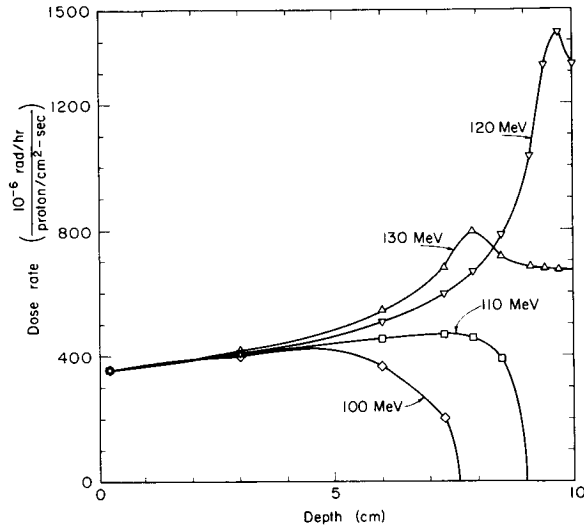


FIGURE 14.—Primary proton depth-dose patterns due to monoenergetic isotropic fluxes of protons of indicated energies incident upon a 10-cm-radius sphere of tissue-equivalent material.

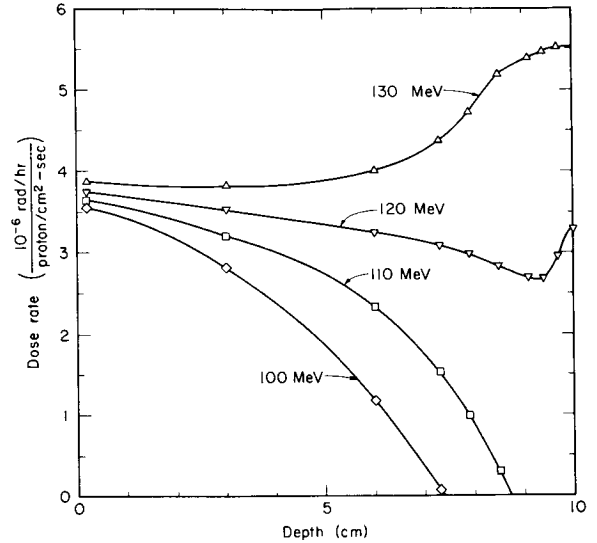


FIGURE 16.—Evaporation secondary-proton depth-dose patterns due to monoenergetic isotropic fluxes of protons of indicated energies incident upon a 10-cm-radius sphere of tissue-equivalent material.

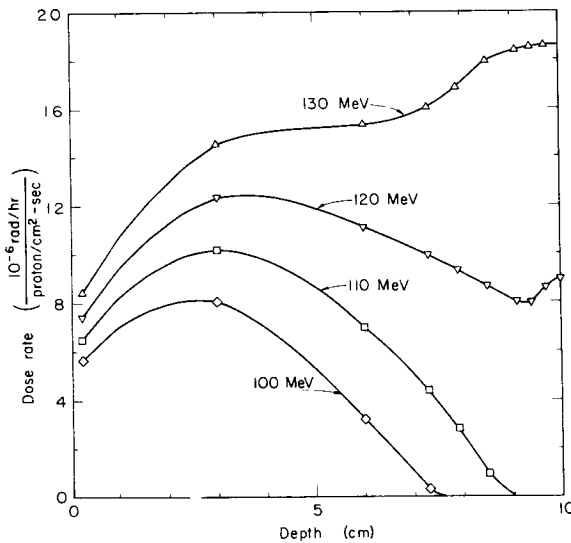


FIGURE 15.—Cascade secondary-proton depth-dose patterns due to monoenergetic isotropic fluxes of protons of indicated energies incident upon a 10-cm-radius sphere of tissue-equivalent material.

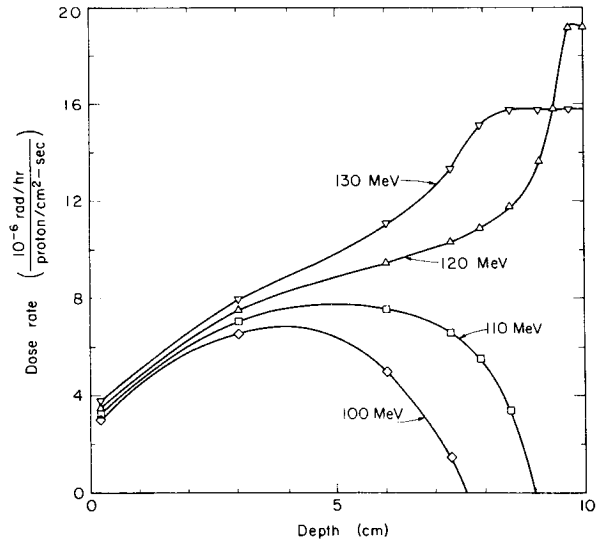


FIGURE 17.—Recoil secondary-proton depth-dose patterns due to monoenergetic isotropic fluxes of protons of indicated energies incident upon a 10-cm-radius sphere of tissue-equivalent material.

since the range of these protons is less than the radius of the sphere. Increasing dE/dx and decreasing flux compete, and usually form a slight maximum before the curve drops to zero. The major effect that decreases the flux with depth for the Type 1 curve is that the surface area of the sphere for which the dose

point is within the range of the protons decreases rapidly with increasing depth. The 100- and 110-MeV curves of figure 15 are other examples of the Type 1 curve.

The Type 2 curve, represented by the 150-MeV curve of figure 9, is produced by protons of sufficient energy to penetrate to the center

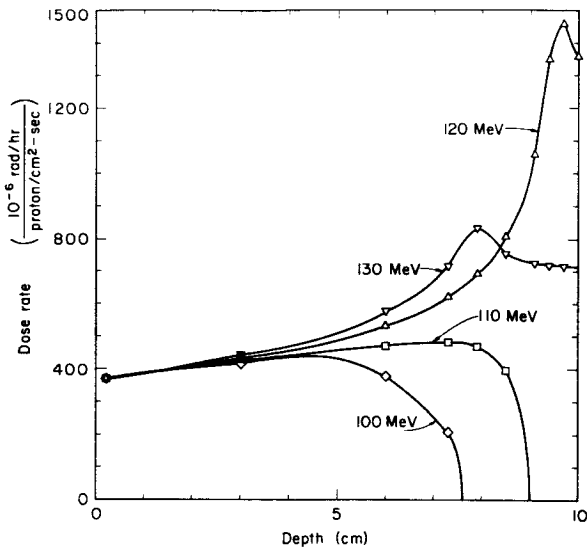


FIGURE 18.—Total (primary plus secondary) proton depth-dose patterns due to monoenergetic isotropic fluxes of protons of indicated energies incident upon a 10-cm-radius sphere of tissue-equivalent material.

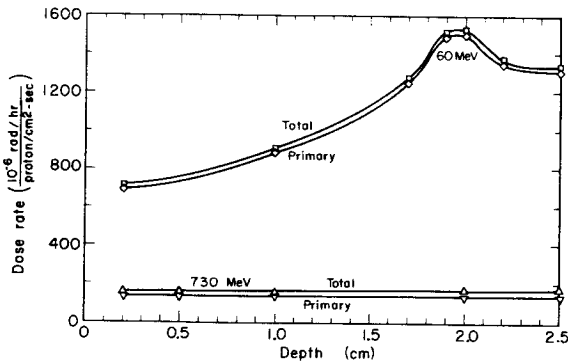


FIGURE 19.—Primary and total (primary plus secondary) proton depth-dose patterns due to monoenergetic isotropic fluxes of protons of indicated energies incident upon a 2.5-cm-radius sphere of tissue-equivalent material.

of the sphere, but not to penetrate the diameter. A large fraction of the protons enter the sphere and pass near its center, producing maximum ionization density near a depth of $2r_0 - R_0$ where r_0 and R_0 are the radius of the sphere and the proton range respectively. A maximum in the depth-dose curve resulting from the superposition of these Bragg peaks thus occurs at this depth. As this peak approaches the center of the sphere, the peak becomes better defined, the maximum becoming greater in magnitude. Had straggling been included in these calcula-

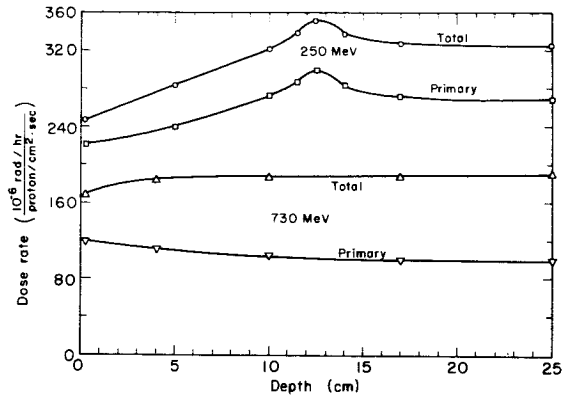


FIGURE 20.—Primary and total (primary plus secondary) proton depth-dose patterns due to monoenergetic isotropic fluxes of protons of indicated energies incident upon a 25-cm-radius sphere of tissue-equivalent material.

tions it would have had the effect of slightly broadening and lowering these peaks, but only in the cases in which the peaks occur near the center of the sphere. See figures 14, 19, and 20 for further examples of the Type 2 curve.

The Type 3 curve is represented in figure 9 by the 180-, 400-, and 730-MeV curves. These curves are produced by protons with range greater than the diameter of the sphere. They are fairly flat curves and may increase slightly with depth if the energy of the proton is small enough so that the dE/dx increase with depth can overcome the effect of the exponential attenuation of the proton flux. However, these nearly flat curves usually decrease monotonically with depth owing to the exponential proton removal probability. Figures 19 and 20 include other examples of this Type 3 depth-dose pattern.

Although the above discussion has been limited entirely to primary proton depth-dose patterns, it can also be applied to the total proton dose. The total depth-dose pattern is very similar except that for large spheres and very high proton energies, the secondary protons become more important and may even contribute sufficiently to transform a monotonically decreasing Type 3 primary curve into an increasing total curve. See figure 20 for an example of this. However, the secondary proton depth-dose pattern is always such that the total curves can easily be recognized as

TABLE II

Primary Proton Depth-Dose Data for 730-MeV Protons Incident Upon the 10-cm-Radius Sphere of Tissue-Equivalent Material

Depth, cm	Energy interval, MeV	Dose, $\frac{10^{-6} \text{ rad/hr}}{\text{proton/cm}^2\text{-sec}}$
0.2-----	681-730	131
1.0-----	683-728	129
2.5-----	687-724	126
5.0-----	693-718	124
7.5-----	699-712	122
10-----	705	122

Type 1, 2, or 3. See figures 13 and 18 to 20 for examples.

The depth-dose pattern of each type of secondary proton is governed by more complicated factors than for primary protons, so the secondaries display a greater variety of depth-dose profiles. Nevertheless, the profiles from secondaries produced by each of the three types of primaries can usually be distinguished easily from one another. The Type 1 secondary pattern is defined as the pattern due to secondary protons that are produced by Type 1 primaries. Type 2 and Type 3 secondary patterns are defined similarly.

TABLE III

Cascade Secondary Proton Depth-Dose Data for 730-MeV Protons Incident Upon the 10-cm-Radius Sphere of Tissue-Equivalent Material

Depth, cm	Total dose rate	Dose rate per energy interval, $\frac{10^{-6} \text{ rad/hr}}{\text{proton/cm}^2\text{-sec}}$							
		Energy interval, MeV							
		0.02-1	1-2	2-5	5-10	10-20	20-40	40-80	80-∞
0.2-----	29.8	0.478	0.480	1.44	2.05	3.03	4.10	4.96	13.3
1.0-----	38.0	0.600	0.597	1.79	2.59	3.92	5.39	6.47	16.6
2.5-----	44.6	0.648	0.645	1.93	2.83	4.39	6.25	7.74	20.2
5.0-----	49.9	0.677	0.671	2.01	2.96	4.68	6.82	8.70	23.4
7.5-----	52.3	0.688	0.681	2.03	3.01	4.79	7.05	9.12	24.9
10-----	52.9	0.690	0.682	2.04	3.01	4.82	7.11	9.23	25.3

TABLE IV

Evaporation Secondary Proton Depth-Dose Data for 730-MeV Protons Incident Upon the 10-cm-Radius Sphere of Tissue-Equivalent Material

Depth, cm	Total dose rate	Dose rate per energy interval, $\frac{10^{-6} \text{ rad/hr}}{\text{proton/cm}^2\text{-sec}}$							
		Energy interval, MeV							
		0.02-1	1-2	2-5	5-10	10-20	20-40	40-80	80-∞
0.2-----	5.01	0.007	0.042	0.429	1.36	2.20	0.939	0.042	0
1.0-----	4.92	0.007	0.041	0.421	1.33	2.16	0.921	0.041	0
2.5-----	4.81	0.007	0.040	0.412	1.30	2.11	0.900	0.040	0
5.0-----	4.70	0.007	0.039	0.403	1.27	2.06	0.879	0.039	0
7.5-----	4.65	0.007	0.039	0.399	1.26	2.04	0.868	0.039	0
10-----	4.62	0.007	0.038	0.397	1.25	2.03	0.863	0.038	0

TABLE V

Recoil Secondary Proton Depth-Dose Data for 730-MeV Protons Incident Upon the 10-cm-Radius Sphere of Tissue-Equivalent Material

Depth, cm	Total dose rate	Dose rate per energy interval, $\frac{10^{-6} \text{ rad/hr}}{\text{proton/cm}^2\text{-sec}}$							
		Energy interval, MeV							
		0.02-1	1-2	2-5	5-10	10-20	20-40	40-80	80-∞
0.2-----	4.04	0.017	0.017	0.050	0.079	0.148	0.265	0.445	3.02
1.0-----	4.99	0.022	0.021	0.063	0.100	0.188	0.336	0.558	3.71
2.5-----	6.02	0.025	0.025	0.073	0.118	0.223	0.402	0.674	4.48
5.0-----	6.98	0.028	0.028	0.082	0.133	0.252	0.459	0.777	5.22
7.5-----	7.46	0.029	0.029	0.086	0.140	0.266	0.486	0.828	5.60
10-----	7.62	0.030	0.030	0.088	0.142	0.271	0.495	0.844	5.72

TABLE VI

Primary Proton Depth-Dose Data for 120-MeV Protons Incident Upon the 10-cm-Radius Sphere of Tissue-Equivalent Material

Depth, cm	Total dose rate	Dose rate per energy interval, $\frac{10^{-6} \text{ rad/hr}}{\text{proton/cm}^2\text{-sec}}$							
		Energy interval, MeV							
		0.02-1	1-2	2-5	5-10	10-20	20-40	40-80	80-∞
0.2-----	355	1.24	1.28	3.84	6.42	13.0	28.2	56.4	245
3.0-----	409	2.47	2.54	7.63	12.8	26.1	63.4	144.	150
6.0-----	507	5.22	5.36	16.1	27.1	55.6	127.	270.	0
7.3-----	595	8.09	8.30	25.0	42.0	86.2	189.	237.	0
7.9-----	666	10.6	10.8	32.6	54.8	112.	245.	199.	0
8.5-----	783	14.9	15.3	46.1	77.5	159.	347.	123.	0
9.1-----	1032	25.1	25.7	77.3	130.	267.	507.	0	0
9.4-----	1321	37.7	38.7	116.	196.	401.	532.	0	0
9.7-----	1426	0	0	0	63.6	804.	559.	0	0
10-----	1328	0	0	0	0	1130.	0	0	0

The cascade and recoil proton Type 1 pattern passes through a maximum and then to zero (figs. 10, 12, 15, and 17). The Type 1 evaporation proton pattern decreases monotonically to zero (figs. 11 and 16).

The Type 2 cascade profile may be recognizable as Type 2 only because of a very slight inflection (fig. 10), or it may have a very marked inflection or minimum (fig. 15). Similarly, a Type 2 evaporation curve is

distinguished by an inflection or minimum (figs. 11 and 16). A Type 2 recoil curve increases monotonically to the depth $2r_0-R_0$, where it becomes fairly flat and is so until it reaches the center of the sphere. In every case, the irregularity in the secondary proton depth-dose pattern which marks it as Type 2 occurs at a depth near $2r_0-R_0$.

The Type 3 secondary depth-dose profiles are characterized by a monotonic rise for cascades

TABLE VII

Cascade Secondary Depth-Dose Data for 120-MeV Protons Incident Upon the 10-cm-Radius Sphere of Tissue-Equivalent Material

Depth, cm	Total dose rate	Dose rate per energy interval, $\frac{10^{-6} \text{ rad/hr}}{\text{proton/cm}^2\text{-sec}}$							
		Energy interval, MeV							
		0.02-1	1-2	2-5	5-10	10-20	20-40	40-80	80-∞
0.2.....	7.38	0.281	0.283	0.856	1.16	1.53	1.70	1.31	0.271
3.0.....	12.3	0.399	0.399	1.20	1.72	2.54	3.19	2.63	0.252
6.0.....	11.1	0.393	0.392	1.17	1.70	2.57	3.15	1.68	0
7.3.....	9.90	0.387	0.387	1.15	1.68	2.52	2.89	0.879	0
7.9.....	9.28	0.387	0.386	1.15	1.68	2.50	2.69	0.486	0
8.5.....	8.61	0.391	0.391	1.16	1.69	2.50	2.35	0.132	0
9.1.....	8.02	0.415	0.414	1.22	1.78	2.55	1.65	0	0
9.4.....	7.96	0.452	0.451	1.33	1.93	2.65	1.15	0	0
9.7.....	8.57	0.521	0.521	1.54	2.34	3.06	0.592	0	0
10.....	8.93	0.539	0.541	1.59	2.41	3.89	0	0	0

TABLE VIII

Evaporation Secondary Proton Depth-Dose Data for 120-MeV Protons Incident Upon the 10-cm-Radius Sphere of Tissue-Equivalent Material

Depth, cm	Total dose rate	Dose rate per energy interval, $\frac{10^{-6} \text{ rad/hr}}{\text{proton/cm}^2\text{-sec}}$							
		Energy interval, MeV							
		0.02-1	1-2	2-5	5-10	10-20	20-40	40-80	80-∞
0.2.....	3.74	0.010	0.050	0.449	1.20	1.55	0.465	0.011	0
3.0.....	3.52	0.012	0.057	0.467	1.17	1.42	0.391	0.009	0
6.0.....	3.24	0.017	0.070	0.506	1.13	1.21	0.299	0.006	0
7.3.....	3.08	0.022	0.084	0.551	1.11	1.07	0.235	0.004	0
7.9.....	2.98	0.027	0.096	0.591	1.10	0.970	0.190	0.003	0
8.5.....	2.82	0.035	0.117	0.660	1.09	0.805	0.121	0.001	0
9.1.....	2.68	0.051	0.160	0.785	1.06	0.578	0.054	0	0
9.4.....	2.68	0.071	0.206	0.907	1.03	0.437	0.027	0	0
9.7.....	2.95	0.125	0.328	1.20	1.01	0.278	0.008	0	0
10.....	3.29	0.082	0.339	1.54	1.15	0.179	0.001	0	0

and recoils and a monotonic fall for evaporations (figs. 10 to 12 and 15 to 17).

Now we briefly consider the biological significance of each of the three types of depth-dose profiles. Type 1 protons are responsible for heavy surface doses. Generally they have

comparatively low energy, and the lowest energies may have high LET. The secondary protons are usually insignificant.

Type 2 protons can localize a heavy dose at the maximum of the pattern. However, to produce this maximum the incident protons

TABLE IX

Recoil Secondary Proton Depth-Dose Data for 120-MeV Protons Incident Upon the 10-cm-Radius Sphere of Tissue-Equivalent Material

Depth, cm	Total dose rate	Dose rate per energy interval, $\frac{10^{-6} \text{ rad/hr}}{\text{proton/cm}^2\text{-sec}}$							
		Energy interval, MeV—							
		0.02-1	1-2	2-5	5-10	10-20	20-40	40-80	80-∞
0.2-----	3.46	0.109	0.106	0.290	0.419	0.668	0.891	0.794	0.182
3.0-----	7.50	0.223	0.218	0.607	0.893	1.46	2.03	1.87	0.194
6.0-----	9.45	0.357	0.348	0.956	1.38	2.17	2.74	1.50	0
7.3-----	10.3	0.461	0.448	1.22	1.72	2.60	2.97	0.891	0
7.9-----	10.9	0.540	0.523	1.41	1.96	2.89	3.00	0.529	0
8.5-----	11.8	0.666	0.644	1.72	2.3	3.31	2.91	0.157	0
9.1-----	13.6	0.926	0.891	2.34	3.08	4.02	2.35	0	0
9.4-----	15.8	1.22	1.17	3.04	3.88	4.70	1.82	0	0
9.7-----	19.2	1.34	1.31	3.67	5.46	6.33	1.07	0	0
10-----	19.2	1.21	1.19	3.35	5.05	8.46	0	0	0

TABLE X

Total (Primary Plus Secondary) Proton Depth-Dose Data for 60-MeV Protons Incident Upon the 2.5-cm-Radius Sphere of Tissue-Equivalent Material

Depth, cm	Total dose rate	Dose rate per energy interval, $\frac{10^{-6} \text{ rad/hr}}{\text{proton/cm}^2\text{-sec}}$							
		Energy interval, MeV—							
		0.02-1	1-2	2-5	5-10	10-20	20-40	40-80	80-∞
0.2-----	711	6.84	7.06	21.6	36.0	70.5	150	419	0
1.0-----	907	13.4	13.7	41.7	70.0	143.0	364	261	0
1.7-----	1275	27.6	28.4	85.6	144.0	300.0	690	0	0
1.9-----	1519	37.2	38.3	115.0	194.0	406.0	728	0	0
2.0-----	1526	1.70	1.85	41.0	234.0	490.0	757	0	0
2.2-----	1374	1.50	1.71	5.50	7.40	492.0	866	0	0
2.5-----	1337	1.45	1.65	5.49	7.46	9.70	1310	0	0

must be monoenergetic and the proton beam cannot be contaminated with neutrons or gamma rays (a situation often not realized in practice). Also, it is not known how deviations from an exact sphere will affect this maximum, and animals are not spheres. Nevertheless, the Type 2 pattern may be useful in indicating that a heavy dose may occur in a

shell within, and symmetric with, the volume being irradiated if a segment of the surface of this volume approximates the curvature of a sphere. The significance of secondary protons in the Type 2 pattern increases with sphere size (figs. 19 and 20). The detail of a particular Type 2 pattern is presented in tables VI through XI.

TABLE XI

Total (Primary Plus Secondary) Proton Depth-Dose Data for 250-MeV Protons Incident Upon the 25-cm-Radius Sphere of Tissue-Equivalent Material

Depth, cm	Total dose rate	Dose rate per energy interval, $\frac{10^{-6} \text{ rad/hr}}{\text{proton/cm}^2\text{-sec}}$							
		Energy interval, MeV—							
		0.02-1	1-2	2-5	5-10	10-20	20-40	40-80	80-∞
0.2-----	247	0.81	0.86	2.79	4.92	8.22	11.9	19.4	198.0
5.0-----	283	1.18	1.23	3.96	6.73	11.7	18.5	30.7	209.0
10.0-----	322	1.51	1.56	4.95	8.40	15.0	24.9	43.0	223.0
11.5-----	338	1.65	1.70	5.38	9.09	16.3	27.4	48.0	229.0
12.5-----	352	1.75	1.81	5.71	9.65	17.4	29.5	52.0	234.0
14.0-----	338	0.82	0.86	2.87	4.92	7.93	19.0	60.5	241.2
17.0-----	328	0.81	0.84	2.80	4.83	7.83	10.6	32.9	268.0
25.0-----	325	0.80	0.83	2.74	4.73	7.71	10.6	15.2	283.0

TABLE XII

Total (Primary Plus Secondary) Proton Depth-Dose Data for 730-MeV Protons Incident Upon the 2.5-cm-Radius Sphere of Tissue-Equivalent Material

Depth, cm	Total dose rate	Dose rate per energy interval, $\frac{10^{-6} \text{ rad/hr}}{\text{proton/cm}^2\text{-sec}}$							
		Energy interval, MeV—							
		0.02-1	1-2	2-5	5-10	10-20	20-40	40-80	80-∞
0.2-----	161	0.44	0.47	1.74	3.22	4.75	3.90	2.98	144
0.5-----	165	0.52	0.55	1.98	3.57	5.26	4.53	3.62	144
1.0-----	167	0.55	0.58	2.08	3.73	5.57	5.03	4.20	145
2.0-----	169	0.58	0.61	2.16	3.87	5.81	5.42	4.71	146
2.5-----	169	0.58	0.61	2.17	3.93	5.82	5.46	4.75	146

The Type 3 pattern gives a fairly flat depth-dose profile. It is the pattern usually used in laboratory experiments. The penetrating and secondary-particle-producing ability of the Type 3 protons make them the most difficult to shield against. Since secondary proton production increases with increasing primary energy and increasing sphere size, we expect the Type 3 pattern in large spheres to exhibit the greatest secondary proton component, which is indeed the case. Figure 20 shows

that almost half the total dose at the center of a 25-cm-radius sphere from 730-MeV incident protons is due to secondary protons. Secondary protons in the Type 3 depth-dose pattern have special significance, not only because of the magnitude of their contribution, but also because they are in general the only source of low-energy high-LET protons. Detail of the Type 3 depth-dose pattern is presented in tables II through V, XII, and XIII.

TABLE XIII

Total (Primary Plus Secondary) Proton Depth-Dose Data for 730-MeV Protons Incident Upon the 25-cm-Radius Sphere of Tissue-Equivalent Material

Depth, cm	Total dose rate	Dose rate per energy interval, $\frac{10^{-6} \text{ rad/hr}}{\text{proton/cm}^2\text{-sec}}$							
		Energy interval, MeV—							
		0.02-1	1-2	2-5	5-10	10-20	20-40	40-80	80-∞
0.2-----	170	0.50	0.53	1.86	3.37	5.31	5.70	6.66	146
4.0-----	184	0.68	0.71	2.38	4.16	6.80	8.42	10.7	151
10.0-----	189	0.70	0.73	2.41	4.20	6.97	9.08	12.2	152
17.0-----	190	0.69	0.73	2.40	4.17	6.97	9.28	12.8	153
25.0-----	190	0.69	0.72	2.37	4.15	6.94	9.32	13.0	153

VII. SUMMARY OF RESULTS

Following are some conclusions concerning isotropic fluxes of protons incident upon spheres of tissue-equivalent material which may be drawn from this work.

The depth-dose patterns for both primary and secondary protons fall into three main categories, each with very distinct characteristics:

Type 1. The primary protons cannot penetrate to the center of the sphere.

Type 2. The primary protons can penetrate to the center, but cannot penetrate the whole diameter.

Type 3. The primary protons can penetrate through the diameter of the sphere.

Type 1 primary protons cause high surface doses, are easily shielded against, and do not normally cause a significant secondary dose rate.

Type 2 primary protons cause a heavy dose rate localized at a depth $2r_0 - R_0$, where r_0 and R_0 are the radius of the sphere and range of the primaries respectively. Secondary protons usually are not very significant, since primaries are present in much larger quantities.

Type 3 primary protons create significant quantities of secondary protons, since they are present in large numbers and they are the only source of low-energy high-LET protons. For Type 3 primary protons, the secondary proton dose rate increases with increasing incident

proton energy, sphere size, and depth in the sphere. For the case of 730-MeV protons incident upon the sphere, the percent of the total dose rate at the center of the sphere which is contributed by secondary protons is 14% for 2.5-cm radius, 35% for 10-cm radius, and 48% for 25-cm radius.

APPENDIX

The Computer Code

The methods and approximations used by the computer program to solve the foregoing equations is summarized below.

In the E_s and E_p integrands of the formulas for the dose rate due to the cascade and recoil secondaries [eqs. (35), (36), (44), and (45)], the range-energy relation [eq. (56)] is approximated by letting $p=0.0027$ and $q=1.729$ for all energies. This approximation is also used in the exponent of the exponential attenuation factor wherever it appears in each dose-rate formula.

All integrals are evaluated by Simpson's rule. The integration process is terminated for each integral when the results of the i th iteration, I_i , differs from the preceding iteration, I_{i-1} , by less than 1%. That is, the integral is given the value I_i when

$$|I_{i-1} - I_i| < 0.01.$$

However, to prevent excessive running time, an arbitrary maximum number of iterations, N , is set. That is, the integral is given the value

I_N whenever

$$|I_{i-1} - I_i| \leq 0.01$$

for any $i \leq N$. The value of N is chosen so that the integration usually converges. But when it does not, $|I_N - I_{N-1}|$ is never larger than 10% and almost always less than 5%.

Integration by parts was performed on the E_s integrals of the cascade and recoil proton secondary formulas. This eliminates numerical integration of a pole, and produces greater numerical integration accuracy, since the magnitude of the resulting boundary term predominates over the remaining integral. The E_s integral in the cascade proton formula can be written as

$$I_c = \int_{E_m}^{E_M} E_s^{-\alpha} (E_s^q - K)^{1/q-1} dE_s = \int u dv$$

Let

$$u = E_s^{1-\alpha} E_s^{-\alpha} = E_s^{1-\alpha-q}$$

Thus

$$dv = (E_s^q - K)^{1/q-1} E_s^{q-1} dE_s$$

The integration then yields

$$I_c = E_s^{1-\alpha-q} (E_s^q - K)^{1/q} \Big|_{E_m}^{E_M} - (1-\alpha-q) \int_{E_m}^{E_M} E_s^{-(\alpha+q)} (E_s^q - K)^{1/q} dE_s$$

Similarly, the E_s integral in the recoil proton formula can be written as

$$I_R = \int_{E_m}^{E_M} \left(bE_p^m + \frac{3.16 \times 10^{-4}}{E_s^2} \right) (E_s^q - K)^{1/q-1} dE_s = \int u dv$$

Let

$$u = E_s^{1-\alpha} (bE_p^m + 3.16 \times 10^{-4}/E_s^2)$$

Thus

$$dv = (E_s^q - K)^{1/q-1} E_s^{q-1} dE_s$$

The integration then yields

$$I_R = (bE_p^m E_s + 3.16 \times 10^{-4}/E_s) \frac{(E_s^q - K)^{1/q}}{E_s^q} \Big|_{E_m}^{E_M} + \int_{E_m}^{E_M} \left[\frac{(1+q)3.16 \times 10^{-4}}{E_s^2} + (q-1)bE_p^m \right] \frac{(E_s^q - K)^{1/q}}{E_s^q} dE_s$$

The remaining integrals are evaluated by Simpson's rule, as described above.

Difficulty in evaluating the E_p integrals for the cascade and recoil proton formulas was due to a very rapid increase in the magnitude of this integrand as E_p approached its lower limit of integration. Experimentation showed that the rate of convergence of this integral was greatly improved by the change of variables,

$$E_s = E_{pp} \exp \left[\frac{\tau^3}{3} \right]$$

where E_{pp} is the variable in the third integral [(see eqs. (35), (36), (44), and (45)]. Thus, the E_s integral was rewritten as

$$I_s = \int_{\bar{m}}^{\bar{M}} f(E_s) dE_s = \int_{\bar{m}}^{\bar{M}} f \left\{ E_{pp} \exp \left[\frac{\tau^3}{3} \right] \right\} \frac{dE_p}{d\tau} d\tau$$

or

$$I_s = \int_{\bar{m}}^{\bar{M}} f \left\{ E_{pp} \exp \left[\frac{\tau^3}{3} \right] \right\} \tau^2 E_{pp} \exp \left[\frac{\tau^3}{3} \right] d\tau$$

where \bar{M} and \bar{m} are defined by

$$M = E_{pp} \exp \left[\frac{(\bar{M})^3}{3} \right]$$

and

$$m = E_{pp} \exp \left[\frac{(\bar{m})^3}{3} \right]$$

Running time of the program was greatly reduced by preliminary evaluation of the E_s and E_p integrals for the cascade and recoil protons and tabulation of the result as a function of E_{pp} in 1-MeV intervals. Such a table was produced for each of thirty values of E_0 (the energy of protons incident upon the sphere) ranging from 20 to 730 MeV. Now, in calculation of the cascade or recoil proton dose rate, parabolic interpolation is used on this table, eliminating the necessity of repeated evaluation of the E_s and E_p integrals.

This computer program has been written by Anthony Schaeffer, and the techniques developed in this appendix are due to him.

REFERENCES

1. EVANS, ROBLEY D.: Principles for the Calculation of Radiation Dose Rates in Space Vehicles. Technical Report to NASA, July 1961 (unpublished).
2. GOLDSTEIN, RUBIN: Analytical Method for the Calculation of Radiation Dose Rates Due to Protons. Lawrence Radiation Laboratory Rept., UCRL-10988 Rev., Jan. 1964 (unpublished).
3. METROPOLIS, N.; BIVINS, R.; STORM, M.; TURKEVICH, ANTHONY; MILLER, J. M.; and FRIEDLANDER, G.: Monte Carlo Calculations on Intranuclear Cascades. I. Low-Energy Studies, *Phys. Rev.*, no. 110, 1958, p. 185.
4. METROPOLIS, N.; BIVINS, R.; STORM, M.; MILLER, J. M.; FRIEDLANDER, G.; and TURKEVICH, ANTHONY: Monte Carlo Calculations on Intranuclear Cascades. II. High-Energy Studies and Pion Processes. *Phys. Rev.*, no. 110, 1958, p. 204.
5. ZERBY, CLAYTON, D.: Material Requirement for Shielding Against Space Radiation. Oak Ridge National Laboratory Rept. ORNL-TM-552, May 1963 (unpublished).
6. HESS, WILMOT N.: A Summary of High-Energy Nucleon-Nucleon Cross Section Data. Univ. of Calif. Radiation Laboratory Rept., UCRL-4639 Rev., Dec. 1956 (unpublished).
7. MORRISON, PHILIP: A Survey of Nuclear Reactions. *In Experimental Nuclear Physics* (E. Segrè, ed.), vol. II, John Wiley & Sons, Inc. (New York), 1953, p. 1.
8. WALLACE, ROGER; and SONDHAUS, CHARLES: Techniques Used in Shielding Calculations for High-Energy Accelerators: Applications to Space Shielding. Lawrence Radiation Laboratory Rept., UCRL-10439, Oct. 1962 (unpublished).
9. HOWARD-FLANDERS, P.: Physical and Chemical Mechanisms in the Injury of Cells by Ionizing Radiation. *In Advances in Biological and Medical Physics* (C. A. Tobias and J. H. Lawrence, eds.), vol. 6, Academic Press Inc. (New York), 1958, p. 553.
10. LONGO, M. J.; and MOYER, B. J.: Nucleon and Nuclear Cross Sections for Positive Pions and Protons Above 1.4 BeV. Lawrence Radiation Laboratory Report UCRL-9497 Rev., Aug. 1961 (unpublished).
11. RICH, MARVIN; and MADEY, RICHARD: Range-Energy Tables. Univ. of Calif. Radiation Laboratory Rept., UCRL-2301, Mar. 1954 (unpublished).
12. SONDHAUS, C. A.: Biological Effects of High Energy Protons. Proc. Sym. Protection Against Radiation Hazards in Space. Paper C-4, TID-7652, Atomic Energy Commission, 1962, pp. 309-342.
13. KINNEY, W. E.; COVEYOU, R. R.; and ZERBY, C. D.: A Series of Monte Carlo Codes to Transport Nucleons Through Matter. Proc. of Symp. on Protection Against Radiations in Space (Gatlinburg, Tenn.), Nov. 1962, NASA TID-7652, Book 2, p. 608.
14. SCHAEFER, HERMANN J.: Time Profile of Tissue Ionization Dosages for Bailey's Synthetic Spectrum of a Typical Solar Flare Event. Project MR 005. 13-1002 Subtask 1, Rept. No. 22 (Pensacola, Fla.). U.S. Naval School of Aviation Medicine, Apr. 1962.
15. BAILEY, D. K.: Time Variations of the Energy Spectrum of Solar Cosmic Rays in Relation to the Radiation Hazard in Space. *J. Geophys. Res.*, no. 67, 1962, p. 391.

NS 24612

36—Differential Cross Sections by Flight-Time Spectroscopy for Proton Production in Reactions of 160-MeV Protons on Nuclei¹

R. W. PEELLE, T. A. LOVE, N. W. HILL, AND R. T. SANTORO

Oak Ridge National Laboratory

First we would like to review why it is that we are concerned with cross sections of protons on nuclei in the 100-MeV region, then discuss briefly what the general view is of reactions in this energy region, and, finally, discuss some of the results from an experiment designed to yield additional quantitative information in this field.

As we have seen, sometimes there are substantial primary proton fluxes for energies as high as a few hundred MeV. If these charged primaries penetrate to the astronaut, surely direct energy loss in electromagnetic collisions will ever be the most important type of event to consider. However, secondary particles or gamma rays from nuclear reactions in the surroundings produce a correction which we need to be able to estimate with confidence. So that we may be sure of ourselves as various missions develop, we must have a grasp of the behavior of the relevant nuclear cross sections perhaps more precise than that we have now.

What are the things that we think we know about nucleon reactions with nuclei in the 100-MeV region (ref. 1)? We believe that the nuclei show reasonable transparency to a relatively small or localizable incident particle, and that this transparency does not depend on exclusion effects. Thus, this case is distinguished from low-energy nuclear physics where surface regions seem to be the most important for reactions, and where the incident proton cannot be so localized. The 100-MeV region is different from that at much higher energy in that below

300 MeV or so meson production is impossible or unlikely.

Conceptually, reactions in the ~ 100 -MeV energy region are generally divided into three groups, which almost correspond to the energy regions of the emerging nucleons. All three types of reactions have been verified qualitatively by detailed experiments.

(a) The first group includes elastic scattering of the incident nucleon from the aggregate Coulomb repulsion and nuclear attraction of the bundle of nucleons, together with diffraction effects caused by absorption reactions with these nucleons. Elastic reactions can be estimated theoretically as though they were at lower energy, but since they have little effect on the incident nucleon, they are not very important for space shielding. Also in this group are nearly elastic reactions in which there is one emerging nucleon with the nucleus remaining only weakly excited. This type of reaction is of great interest to nuclear structure physicists because it represents a low-energy experiment that is moved up the energy scale and thus requires fewer corrections. However, these reactions are thought to be relatively rare and probably are not important for our purposes except for the gamma rays which are produced.

(b) The second group includes reactions in which a target nucleon is struck sufficiently hard so that both it and the incident nucleon retain considerable momentum. If both nucleons escape the nucleus, the reaction is termed quasi-elastic scattering. Otherwise it is considered to be some other "intranuclear cascade" event of the type that Bertini (ref. 2) tries to estimate by Monte Carlo. One of these cascade

¹ Research sponsored by National Aeronautics and Space Administration (NASA Order R-104, Task No. 1) under Union Carbide Corporation's contract with the U.S. Atomic Energy Commission.

nucleons can participate in a pickup reaction, perhaps to form a deuteron, on its way out of the nucleus. This last reaction is not included in present intranuclear cascade computations. Our hope of understanding the reactions of this group is based largely on the applicability or near-applicability of information from free two-nucleon scattering.

(c) The third group includes reactions that occur following an event of type b, after which there will generally be enough nuclear excitation energy to allow liberation of one or more evaporation nucleons.

We believe that nucleons from reactions of types b and c may be of importance to this conference, together with the gamma rays produced by reactions of types a and c. The results obtained in this paper, and a subsequent paper by Gibson et al., are dominated by the cascade and quasi-elastic (type b) reactions. Our experimental resolution was inadequate to observe any definite level structure which might otherwise show in the elastic and near-elastic regions of the particle spectra obtained. However, this lack of resolution should not impair the usefulness of the data very much in studying type b reactions. The hope is to provide fresh quantitative information about the bulk of the reaction products, whereas studies conducted elsewhere have concentrated on relatively rare events which have cleaner interpretations.

The experimental arrangement used for the experiment (ref. 3) is shown in figure 1. (Although flight-time spectroscopy has been used to measure both secondary proton and secondary neutron spectra, our discussion is limited to the results for protons.) The 160-MeV proton beam from the Harvard Synchrocyclotron penetrated the A and A' timing counters before striking the target, the beam intensity being turned so low that pulses from individual protons were not confused. The B' and C' coincidence counters required that the secondary particle be charged, while the particle velocity was measured from the time of passage between A and B' counters. The targets used were about 0.6 g/cm² thick.

A typical raw flight-time distribution obtained in this experiment for protons is shown by the open circles in figure 2. The time scale is reversed as is customary in such experiments.

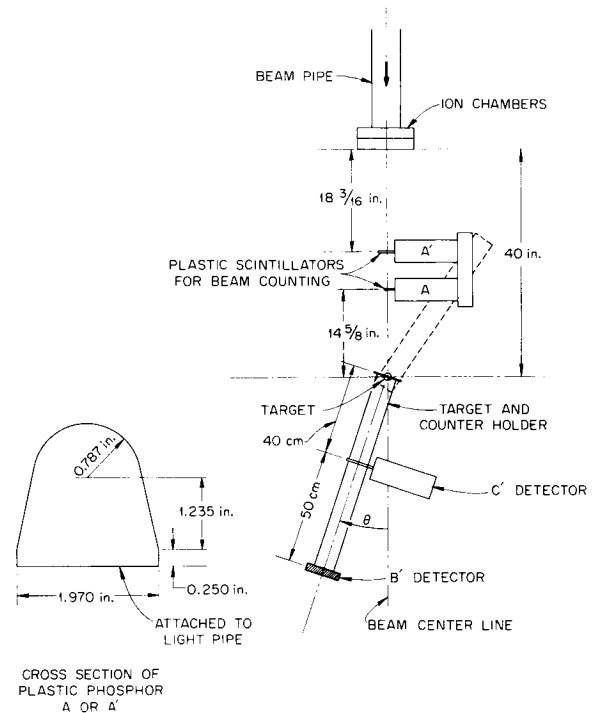


FIGURE 1.—Experimental geometry for proton flight-time experiments, including cross section of the 1-mm-thick A and A' Beam scintillators. A thin edge of the A, A', and C' counters is viewed in each case by a 56 AVP multiplier phototube, while a flat side of the B' counter is viewed by a 58 AVP.

The resolution curve for full energy protons is the solid line, and the solid points are a target-out background which was subtracted. A few approximate energies are marked to show the rather poor energy resolution afforded by the 1-nsec time resolution.

The overall energy resolution is illustrated directly by the calculated energy response of the various bins shown in figure 3, applicable to the data at 30° for various targets. Each bin combines the experimental counts from several adjacent time channels. At low energies the energy resolution is dominated by the target thickness and at high energies it is dominated by the time resolution. Bins were chosen to have moderately overlapping energy response.

Figure 4 demonstrates the spectrometer on proton-proton scattering from water at 60°. The expected hydrogen scattering would be at 40 MeV were it not for the angular and energy resolution of the B' counters. The expected distribution including these effects is shown.

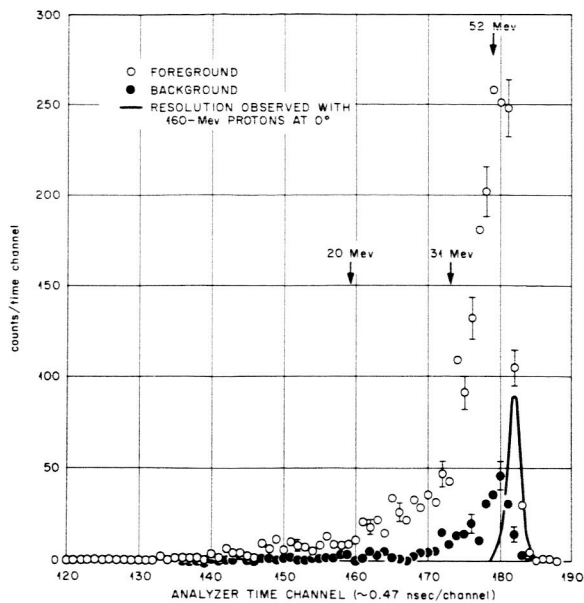


FIGURE 2.—Raw flight-time spectrum from secondary protons observed at 30° using a Co target. The solid points represent a target-out background, and the solid curve shows the resolution function for full energy protons.

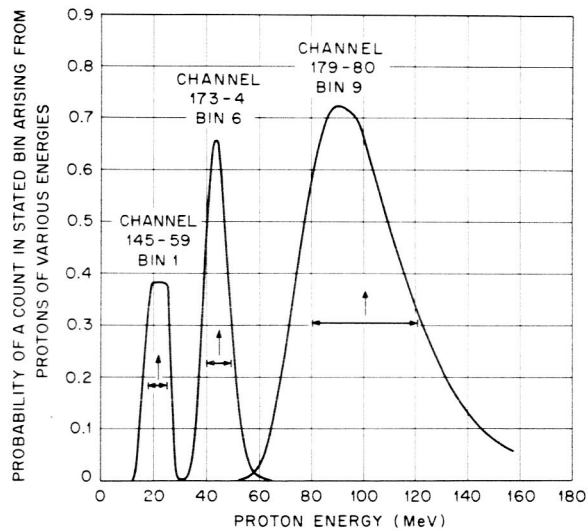


FIGURE 3.—Typical birth energy distribution for 1963 flight-time proton spectrometer (90-cm flight path).

The expected proton scattering does not subtract quite smoothly from the whole, suggesting an energy calibration error commensurate with the 2-MeV error estimated for the 40-MeV energy region.

Differential cross sections measured at 30° for targets ranging from Be to Bi are shown in

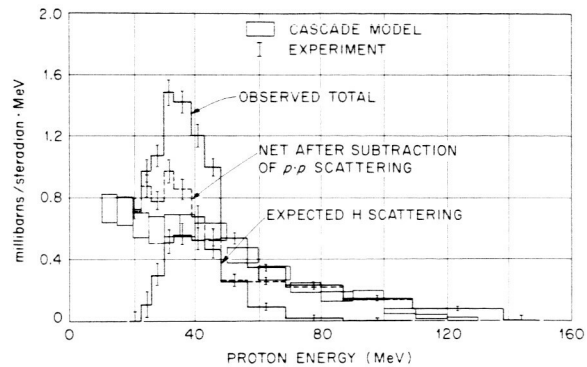


FIGURE 4.—Cross section for the scattering of 160-MeV protons at 60° from water.

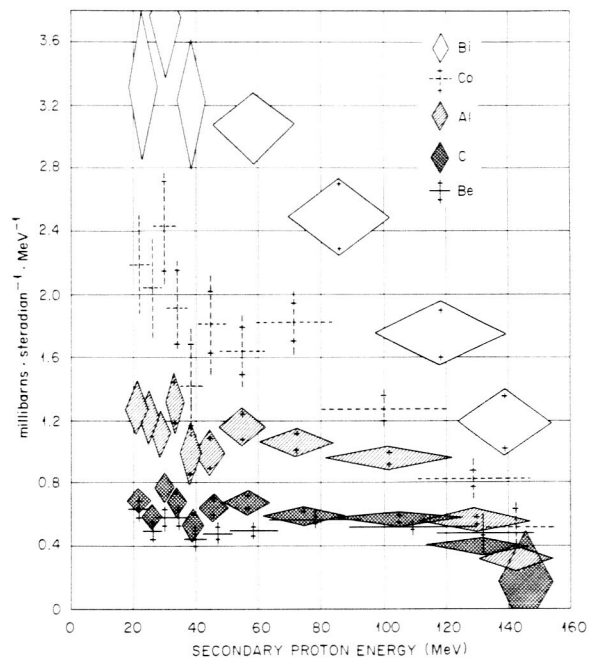


FIGURE 5.—Cross sections for the production of secondary protons at 30° in various targets.

figure 5. The magnitude is monotonic with mass number, but the shape, as expected, is less flat for heavier elements where fewer quasi-elastic particles may escape the nucleus. The primary feature of these data is probably a generally smooth dependence on mass number.

Figure 6 shows a similarly smooth dependence on angle for reaction products from Co. The importance of higher energy reaction products diminishes smoothly as the angle from the original beam direction increases, just as would

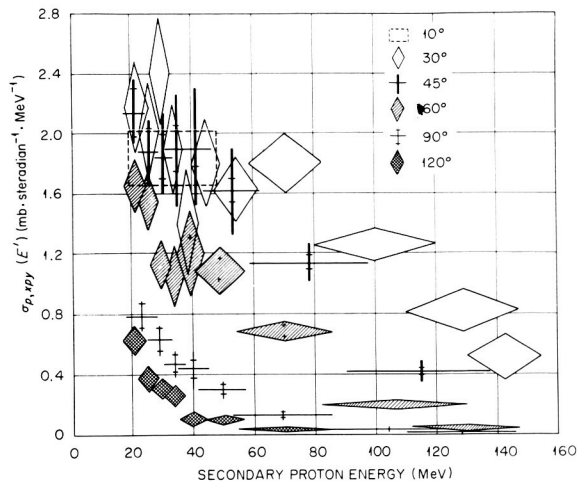


FIGURE 6.—Cross sections for the production in cobalt of secondary protons at various angles.

be expected from a nuclear cascade approach based on quasi-elastic scattering.

Results of the type shown here presently can only be compared against the predictions of Monte Carlo nuclear cascade models, in which repetitive nucleon-nucleon collisions are followed through a model nucleus. Bertini's estimates (ref. 2), based on a three-step nuclear density, are the most complete available. In table I the angle differential laboratory cross sections for the production of secondary protons above 20 MeV by 160-MeV protons on various nuclei are compared with Bertini's estimates. For all angles below 90°, agreement is excellent except for O, C, and Bi at 30°, the last disagreement being very wide. At wide angles the observed cross sections are much larger than expected, though still small and rather sensitive to assumptions made concerning the evaporation process.

Figure 7 shows a typical comparison of an energy distribution against Bertini's estimates for secondary protons observed at 30° from a Co target. At forward angles the expected differential cross section shows too much of a quasi-elastic peak. This result seems general at small angles throughout our results unless the shape of the model nucleus is changed to improve this particular situation. Bertini (private communication) has found that such

TABLE I

Laboratory System Angle-Differential Cross Sections for the Production of Secondary Protons of Energy >20 MeV

Target	Integrated Cross Section, mb/steradian	
	Experimental	Calculated
Scattering Angle=30° (24°-35°) ^a		
H ₂ O-----	152 ± 7	128 ± 4 ^b
D ₂ O-----	157 ± 7	102 + x ^c
Be-----	70 ± 2	70 ± 2
C-----	75 ± 2	87 ± 3
Al-----	124 ± 4	125 ± 3
Co-----	187 ± 7	(188 ± 5) + 0.7 ^d
Bi-----	330 ± 14 ^e	254 ± 7
Scattering Angle=45° (40°-50°) ^a		
Al-----	80 ± 3	85 ± 2
Co-----	129 ± 5	(129 ± 3) + 1.8 ^d
Scattering Angle=60° (56°-64°) ^a		
H ₂ O-----	54 ± 3	47 ± 2 ^f
Al-----	43 ± 1.5	45 ± 2
Co-----	70 ± 3	(67 ± 3) + 1.8 ^d
Scattering Angle=90° (85°-95°) ^a		
Al-----	11.4 ± 0.6	8.0 ± 0.7
Co-----	21.2 ± 1.1	(12.5 ± 0.9) + 1.4 ^d
Scattering Angle=120° (110°-131°) ^a		
Co-----	9.7 ± 0.7	(2.5 ± 3) + 1.5 ^d

^a Values in parentheses give angular interval for calculation.

^b A contribution of 26 mb/steradian is included for hydrogen scattering.

^c x is unknown contribution from scattering in deuterium.

^d This is a contribution predicted from evaporation proton spectrum smeared by instrument response.

^e Estimated contribution from elastic scattering is less than 10 mb/steradian.

^f A contribution of 15 mb/steradian is included for hydrogen scattering.

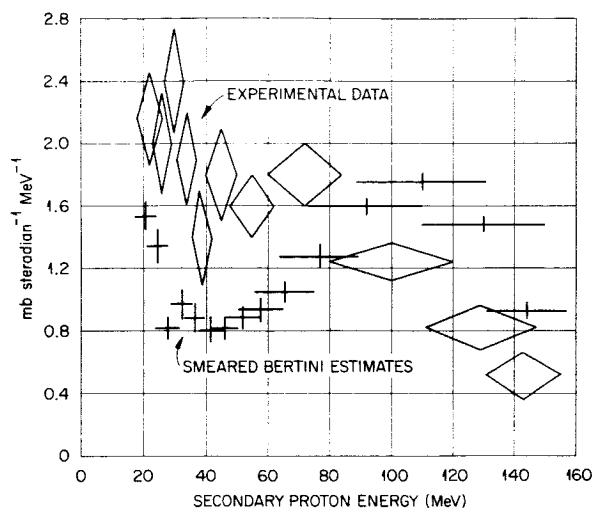


FIGURE 7.—Experimental results and smeared theoretical predictions for secondary protons at 30° from cobalt.

changes give a rather ambiguous result for other characteristics of the computed estimates; in general the changes tended to worsen comparisons with experiment.

Figure 8 shows a more favorable comparison, namely the cross section for energies above 50 MeV from Al at 60° . Here reasonable agreement is demonstrated between the Bertini predictions, the results of this experiment, and the results of the experiment described by Gibson *et al.* in a subsequent paper. This figure, then, rather than the previous one, is in most accord with the tentative general

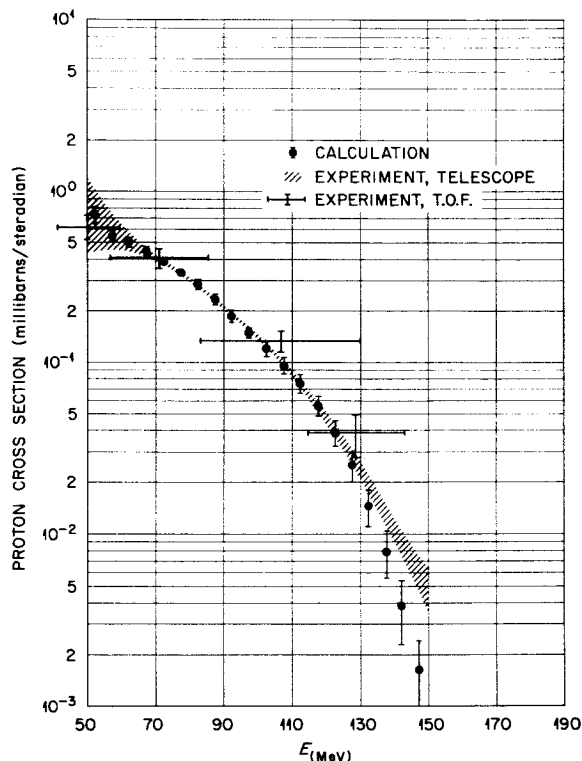


FIGURE 8.—Cross sections for the production of secondary protons at 60° in a 0.549-g/cm-thick aluminum target.

conclusion from this work; except at small and wide angles, the estimates at 160 MeV for secondary protons from Bertini's standard calculation, using a three-step nucleus, are quite good.

REFERENCES

1. STRAUCH, KARL: Measurements of Secondary Spectra from High-Energy Nuclear Reactions. Proc. of Symp. on Protection Against Radiation Hazards in Space, Nov. 1962. NASA TID-7652, Book 2, p. 409.
2. BERTINI, H.W.: Phys. Rev., vol. 131, 1963, p. 1801.
3. PELLE, R.W. ET AL.: Neutron Phys. Div. Ann. Progr. Rept., ORNL-3499, vol. II, 1963, p. 73.

No. 54613

37—Comparison of Measured Neutron and Proton Spectra With Calculated Spectra in the Energy Region Between 50 and 160 MeV¹

W. A. GIBSON, W. R. BURRUS, W. E. KINNEY, and J. W. WACHTER

Oak Ridge National Laboratory

and

C. F. JOHNSON

General Dynamics/Forth Worth

A principal objective of the experimental program at ORNL to measure the secondary proton and neutron spectra from targets bombarded by high-energy protons is to generate data to compare with the theoretical Monte Carlo calculations of Bertini (ref. 1) and Kinney (ref. 2).

The energy spectra of secondary protons and neutrons emerging from targets bombarded by a collimated beam of 160-MeV protons were obtained with a proton recoil spectrometer (refs. 3 and 4) covering the energy range between 50 and 160 MeV.

The following two types of comparisons for secondary neutron production are presented for the energy region between 50 and 160 MeV:

Cross Sections.—Since the targets used in making these measurements were thin, the incident proton beam lost less than 10% of its energy in traversing the target. Furthermore, the probability of secondaries produced undergoing additional nuclear interactions was small. Comparisons of proton production will also be made for this case.

Transport.—In this case, targets which completely stopped the incident protons were considered.

Two factors must be considered in making direct comparisons between the calculations and the measurements: (1) the resolution of the spectrometer causes mixing of adjacent regions of the spectrum, an effect which is especially significant in cases where the energy spectrum changes rapidly, such as in the case of proton cross sections; and (2) the calculational model must correctly simulate the experimental conditions. (Thus angular data calculated without regard to the point of interaction are not comparable since for thick-target measurements a particle emitted at a given angle in the target may pass through the spectrometer, whereas a particle emitted at the same angle but at a point farther from the spectrometer may not enter the spectrometer.)

The resolution effect was included by smearing the calculated spectrum with a Gaussian resolution function which closely approximates the resolution function of the experimental results analyzed by the SLOP (ref. 5) code. The correct computational model was obtained by writing a Monte Carlo analysis code to consider only those particles which correspond

¹ Research sponsored by the National Aeronautics and Space Administration (NASA Order R-104 task No. 1) under Union Carbide Corporation's contract with the U. S. Atomic Energy Commission.

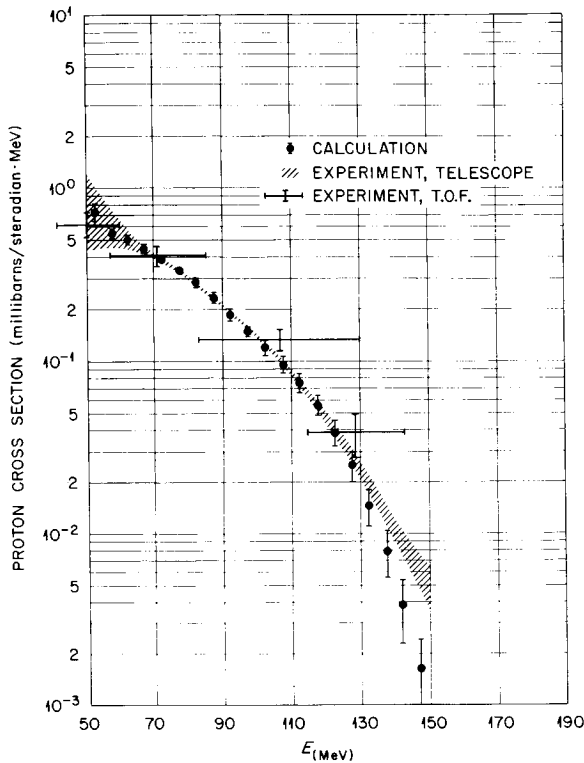


FIGURE 1.—Secondary proton cross section at 60° for 160-MeV protons incident on a 0.549-g/cm²-thick Al target. (Note: the experimental data labeled "T.O.F." are time-of-flight results discussed in a paper by R. W. Peelle *et al.*, these proceedings.)

to particles entering the spectrometer under actual experimental conditions. Figures 1 and 2 are cross-section comparisons for protons and neutrons at 60° and 45° , respectively, and figures 3 and 4 show the yield spectra for neutrons from thick targets. The shaded band in the figures is the 68% confidence interval for the experimental data analyzed by the SLOP code. The errors on the calculated data of Bertini and Kinney are also the 68% confidence limits. In both cases the errors represent the statistical error only. Comparisons with additional targets and configurations are continuing.

The theoretical and experimental cross sections, in general, agree favorably. In most cases the differential cross sections at 45° and 60° integrated with respect to energy from 50

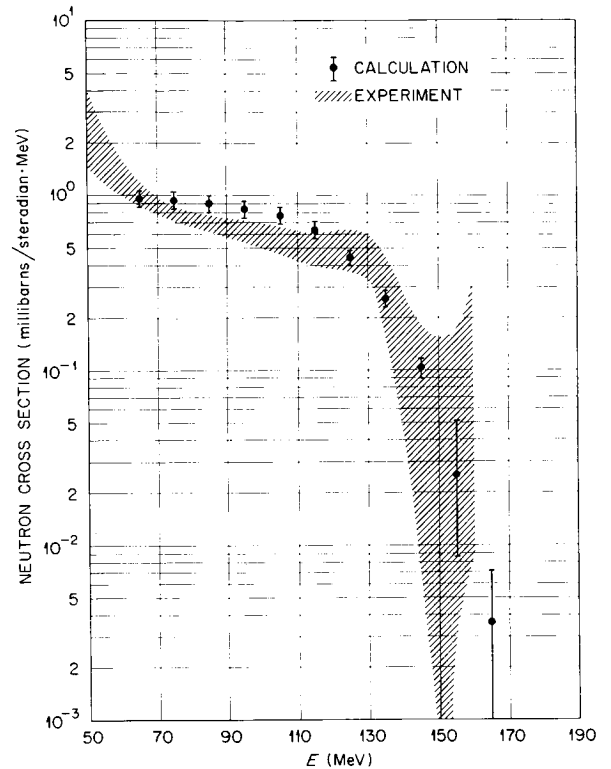


FIGURE 2.—Secondary neutron production cross section at 45° for 160-MeV protons incident on a 3.224-g/cm²-thick Co target.

to 160 MeV agree within expected error, and in a few cases agreement within expected error over the entire energy range above 50 MeV is found. In order to find improved fits, the calculations were done with three different potential well shapes, with those presented here judged as the ones giving the best overall agreement with experiment.

The disagreement between the experimental results and the transport-code calculations seems to be more serious; in all cases the calculation predicts yields which are too large. Little possibility exists for changes in this code since the only variable parameters occur in the input data obtained from the cross-section code. Such effects as Coulomb scattering of the incident protons have been included, and other factors are being investigated which might improve comparisons with experiments.

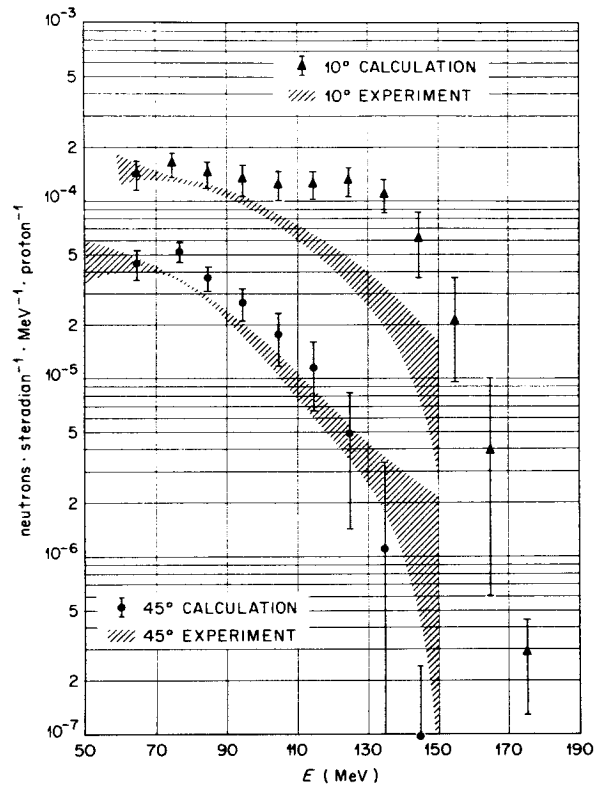
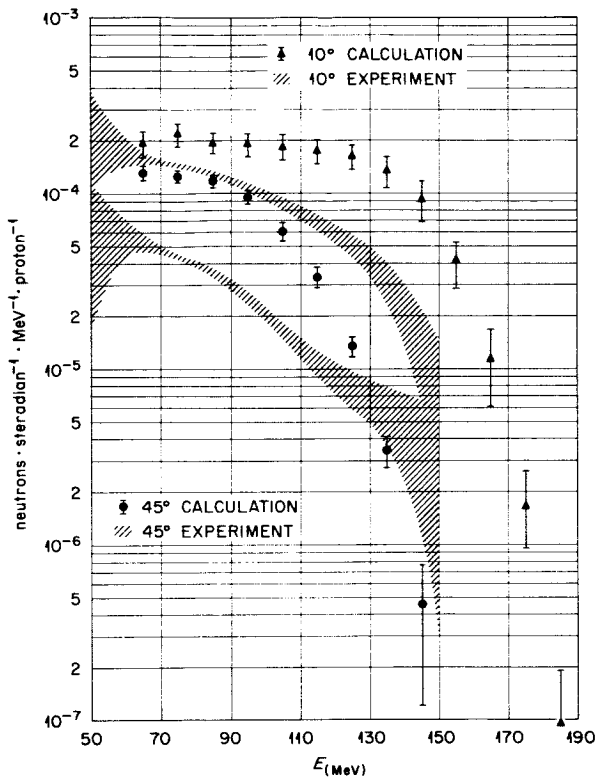


FIGURE 3.—Secondary neutron yield from a 26.89-g/cm²-thick Al target at 10 and 45° to the incident 160-MeV proton beam. The incident beam was completely stopped in the target.

FIGURE 4.—Secondary neutron yield from a 44.33-g/cm²-thick Bi target at 10 and 45° to the incident 160-MeV proton beam. The incident beam was completely stopped in the target.

REFERENCES

1. BERTINI, H. W.: Monte Carlo Calculations on Intranuclear Cascades. ORNL-3383, Apr. 23, 1963.
2. KINNEY, W. E.: The Nucleon Transport Code, NTC, ORNL-3610, Aug. 1964.
3. GIBSON, W. A.; BURRUS, W. R.; WACHTER, J. W.; and JOHNSON, C. F.: Neutron Phys. Div. Ann. Progr. Rept. for Period Ending Aug. 1, 1963. ORNL-3499, vol. II, p. 109.
4. WACHTER, J. W.; GIBSON, W. A.; BURRUS, W. R.; and JOHNSON, C. F.: Neutron Physics Div. Ann. Progr. Rept. for Period Ending Aug. 1, 1963. ORNL-3499, vol. II, p. 89.
5. BOGERT, V. D.; and BURRUS, W. R.: Neutron Phys. Div. Ann. Progr. Rept. for Period Ending Sept. 1, 1962. ORNL-3360, p. 22.

N65-34614

38—Spectra of Gamma Rays Produced by Interaction of ~160-MeV Protons With Be, C, O, Al, Co, and Bi¹

W. ZOBEL, F. C. MAIENSCHN, and R. J. SCROGGS

Oak Ridge National Laboratory

The nuclear secondaries produced by the interaction of high-energy protons with nuclei are of interest since protons are the most abundant of the charged particles present in space which present a hazard to manned space travel. Spacecraft shields that are presently envisaged as necessary for protection on interplanetary flights are of such thickness that nuclear interactions in the shield become important with respect to ionization produced by the primary protons. The secondaries may be uncharged, making them more penetrating than the primaries, and they may produce a greater biological damage. Thus their production and transport in the spacecraft shield or structure must be carefully assessed.

As part of a larger effort to study secondaries (ref. 1), measurements were made of the gamma rays produced in several materials by 160-MeV protons from the Harvard University Synchrocyclotron. The targets were chosen to cover a wide range in Z and included Be, C, H₂O, Al, Co, and Bi. Their specifications are given in table I.

Previous measurements include an extensive set by the Oxford group (refs. 2 to 5) who used the Harwell Synchrocyclotron. A single NaI(Tl) crystal spectrometer was used to study the gamma-ray spectra obtained with targets ranging from Li to Ca. Unresolved backgrounds were ascribed to neutron effects, and cross sections were determined for specified gamma-ray energies. Typical cross sections are a few millibarns.

¹ Research sponsored by the National Aeronautics and Space Administration (NASA Order R-104, Task No. 1) under Union Carbide Corporation's contract with the U.S. Atomic Energy Commission.

For the measurements described in this report, the gamma-ray spectrometer requirements were considered to include ascertainable absolute efficiency, high neutron rejection, and an adequate response function (peak-to-total ratio). Multiple-crystal spectrometers were chosen in spite of their attendant complexities and the requirement for experimental efficiency calibration. A three-crystal pair spectrometer was used above 2.0 MeV and an anticoincidence spectrometer below 2.5 MeV in order to meet the last two requirements. In addition, a time-of-flight requirement was established in

TABLE I

Target Specifications

Material	Diameter, cm	Thickness, g/cm ²	Energy loss in target, MeV
Be-----	7.6	6.055 ± 0.030	27.4 + 1.2 ^a - 1.6
C-----	7.6	6.002 ± 0.030	30.1 ± 1.4 ^a
H ₂ O-----	7.6	5.10 ± 0.05	30.0 ± 2 ^b
Al-----	7.6	6.808 ± 0.034	29.1 + 1.1 ^a - 1.6
Co-----	7.6	3.224 ± 0.016	11.16 + 0 ^c - 0.56
Bi-----	7.6	4.505 ± 0.023	11.36 ± 0.11 ^d

^a Calculated from difference in range, using linear interpolation of data given by R. M. Sternheimer, *Phys. Rev.* 115, 137 (1959).

^b Calculated from difference in range, using curves by M. Rich and R. Madey, *Range Energy Tables*, UCRL-2301 (1954).

^c Calculated using $dE/\rho dx$ data of Sternheimer (see footnote *) for Cu.

^d Calculated using $dE/\rho dx$ data of Sternheimer (see footnote *) for Pb.

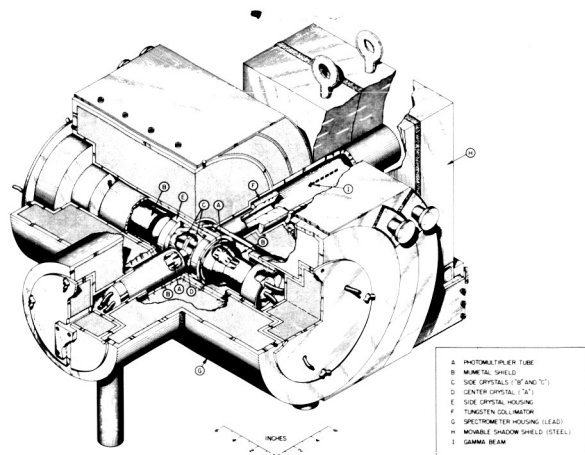


FIGURE 1.—Three-crystal spectrometer assembly and housing.

order to discriminate against neutron-induced effects. The spectrometer is shown in figure 1.

The output of the spectrometer is, of course, a pulse-height spectrum which must be "unscrambled" to obtain the corresponding photon spectrum. The unscrambling method used on our data is that of Burrus (ref. 6). It yields an

upper and lower bound to the 68% confidence interval connected with the "true" value.

The data were divided by the fractional solid angle subtended by the detector, the number of incident protons, and the target thickness. The effect of chance coincidences in the pair spectrometer runs were subtracted by measuring the total number of chance coincidences and assuming that their distribution was similar to that of the foreground spectrum. Neutron contributions to the total absorption spectrometer runs were measured by closing the collimator with 12¾ inches of lead and subtracting the resulting spectrum from the one obtained with the open collimator. Corrections of $\leq 1.19 \pm 0.09$ for variations in the spectrometer efficiency were applied to the data.

A constant correction of 0.94 ± 0.02 for the efficiency of the fast coincidence circuit was made. It was discovered later that this correction varies rather strongly with energy due to the "walk" of the fast signal in the "A" channel. Since the exact energy dependence was not measured, the correction is not made in the spectra presented here. An additional uncer-

TABLE II

Measured Energies and Cross Sections of Gamma Rays From a Beryllium Target Bombarded by ~ 160 -MeV Protons

E_γ , keV, Measured	σ , mb, Measured	Spectrom- eter ^a	Possible transition	
			Reaction	Energy
987 ± 10	1.69 ± 0.63	T	${}^9_4\text{Be}(p,2p){}_3^8\text{Li}$	987
1447 ± 10	.18 ± .10	T		
1536 ± 10	.15 ± .10	T		
1718 ± 15	.28 ± .14	T	${}^9_4\text{Be}(p,3pn){}_2^6\text{He}$	1710
1878 ± 15	.27 ± .15	T		
2069 ± 15	.24 ± .13	T	${}^9_4\text{Be}(p,\alpha){}_3^6\text{Li}$	2184
3575 ± 15	2.02 ± .91	P	${}^9_4\text{Be}(p,\alpha){}_3^6\text{Li}$	3560
4390 ± 38	.72 ± .34	P		
5225 ± 30	.40 ± .20	P	${}^9_4\text{Be}(p,\alpha){}_3^6\text{Li}$	5350
5675 ± 25	.42 ± .25	P		
6250 ± 35	.46 ± .22	P	${}^9_4\text{Be}(p,\alpha){}_3^6\text{Li}^b$	6190

^a In this and the following similar tables, T=total absorption mode and P=pair mode.

^b Denotes transition between excited states.

tainty of $\pm 30\%$ must be ascribed to the results from this cause. Also not shown in the spectra is a correction for the absorption of the gamma rays in the target itself; however, this correction was applied to the cross sections calculated from the data. A correction for the count losses existing in the pair mode of the spectrometer, amounting to $\leq 2.14 \pm 0.73$, is included in the spectra presented. An analogous correction for the data taken in the total absorption mode was not attempted. Counts lost in the side channels would result in a gain of anticoincidence counts, but the spectrum of these counts is distorted to lower energies with respect to the true spectrum. Counts lost in the center channel do not introduce such a spectrum shift. The governing loss, however, is not in the electronics of the center channel but in the multi-channel analyzer. It is difficult to obtain a good correction for this loss. Only an approximate correction (1.0 ± 0.2) could be obtained. This was not applied to the spectra shown, but is included in the cross-section calculations.

Data taken at 136° to the direction of the incident proton beam, with a separation distance of 104.1 ± 0.5 cm between the center of the central crystal and the target center, are presented in figures 2 to 7. Since the unscrambling program only gives the bounds of the 68% confidence interval, only this confidence band is shown.

Tables II to VI summarize the results for the different targets. They include the measured energy of the photon, the cross section for its production, corresponding data from the Oxford group where such data have been reported, and possible transitions giving rise to the gamma rays observed. In some entries, two values are shown for the same transition. These represent measurements made with the spectrometer both in the total absorption mode and in the pair mode. Since there is essentially no line structure noticeable in the data from a Bi target, no cross sections were determined for this case.

TABLE III

Measured Energies and Cross Sections of Gamma Rays From a Carbon Target Bombarded by ~ 160 -MeV Protons

E_γ , keV, Measured	σ , mb, Measured	Spectrom- eter	Oxford group	Possible transition	
				Reaction	Energy
695 \pm 17	7.13 \pm 2.60	T	4.5 \pm 0.5	$^{12}_6\text{C}(p,2pn)^{10}_5\text{B}$	717
980 \pm 18	3.55 \pm 1.33	T	1.8 \pm 0.2	$^{12}_6\text{C}(p,4pn)^8_3\text{Li}$	980
1982 \pm 27	8.51 \pm 3.12	T}	3.9 \pm 0.4	$^{12}_6\text{C}(p,pn)^{11}_6\text{C}$	1990
2014 \pm 40	5.44 \pm 1.99	P}			
2872 \pm 35	1.72 \pm 0.63	P	0.9 \pm 0.4	$^{12}_6\text{C}(p,2pn)^{10}_5\text{B}^b$	2870
3335 \pm 36	2.00 \pm 1.37	T}	6.6 \pm 1.0	$^{12}_6\text{C}(p,3p)^{10}_4\text{Be}$	3368
3370 \pm 30	1.64 \pm 0.61	P}			
4480 \pm 50	10.9 \pm 4.1	T}	2.3 \pm 1.0	$^{12}_6\text{C}(p,p')^{12}_6\text{C}$	4433
4470 \pm 15	11.4 \pm 4.1	P}			
4930 \pm 35	4.08 \pm 1.46	P	2.1 \pm 0.7	$^{12}_6\text{C}(p,2p)^{11}_5\text{B}$	4460
6750 *	3.03 \pm 1.09	P		$^{12}_6\text{C}(p,2p)^{11}_5\text{B}$	5030
8795 \pm 50	0.37 \pm 0.15	P		$^{12}_6\text{C}(p,2p)^{11}_5\text{B}$	8920

* Average energy for several gamma rays; not resolved.

^b Denotes transition between excited states.

TABLE IV

Measured Energies and Cross Sections of Gamma Rays From a Water Target Bombarded by ~ 160 -MeV Protons

E_γ , keV, Measured	σ , mb, Measured	Spec- trometer	Oxford group	Possible transition	
				Reaction	Energy
727 ± 10	3.25 ± 1.24	T	3.9 ± 1.0	$^{16}_8\text{O}(p, \alpha 2pn)^{12}_5\text{B}$	717
1668 ± 10	4.4 ± 1.8	T	1.7 ± 0.5	$^{16}_8\text{O}(p, 2pn)^{14}_7\text{N}^*$	1634
2060 ± 10	1.7 ± 1.3	T		$^{16}_8\text{O}(p, 2p)^{15}_7\text{N}^*$	2034
2392 ± 10	2.5 ± 1.4	T	2.9 ± 0.8	$^{16}_8\text{O}(p, 2pn)^{14}_7\text{N}$	2311
2320 ± 25	6.7 ± 3.0	P			
3720 ± 30	2.8 ± 1.3	P		$^{16}_8\text{O}(p, 3pn)^{13}_6\text{C}$	3680
4430 ± 30	15.8 ± 5.7	P	8.3 ± 1.7	$^{16}_8\text{O}(p, p\alpha)^{12}_6\text{C}$	4433
5260 ± 25	12.0 ± 4.9	P	2.6 ± 0.7	$^{16}_8\text{O}(p, pn)^{16}_8\text{O}$ $^{16}_8\text{O}(p, 2p)^{15}_7\text{N}$	5240
6290 ± 35	55.6 ± 19.7	P	22.7 ± 3.0		5276
7100 ± 50	12.3 ± 4.4	P	2.8 ± 0.7	$^{16}_8\text{O}(p, 2p)^{15}_7\text{N}$ $^{16}_8\text{O}(p, p')^{16}_8\text{O}$	6328 7120

* Denotes transition between excited states.

TABLE V

Measured Energies and Cross Sections of Gamma Rays From an Aluminum Target Bombarded by ~ 160 -MeV Protons

E_γ , keV, Measured	σ , mb, Measured	Spec- trometer	Oxford group	Possible transition	
				Reaction	Energy
845 ± 10	12.4 ± 5.3	T	11 ± 2	$^{27}_{13}\text{Al}(p, pn)^{26}_{13}\text{Al}^*$	830
1026 ± 10	14.0 ± 7.7	T	14 ± 3	$^{27}_{13}\text{Al}(p, pn)^{26}_{13}\text{Al}^*$	1010
1392 ± 10	30.4 ± 11.4	T	31 ± 4	$^{27}_{13}\text{Al}(p, \alpha)^{24}_{12}\text{Mg}$	1369
1677 ± 10	21.9 ± 8.8	T	18 ± 3.5	$^{27}_{13}\text{Al}(p, pn)^{26}_{13}\text{Al}^*$	1640
1877 ± 10	13.2 ± 6.4	T		$^{27}_{13}\text{Al}(p, pn)^{26}_{13}\text{Al}$	{1850 1880*
2250 ± 25	7.3 ± 9.2	P	7.1 ± 1.7	$^{27}_{13}\text{Al}(p, p')^{27}_{13}\text{Al}$	2219
2560 ± 35	7.3 ± 7.7	P	8.8 ± 2.2	$^{27}_{13}\text{Al}(p, pn)^{26}_{13}\text{Al}$	2540
2770 ± 50	10.7 ± 8.4	P		$^{27}_{13}\text{Al}(p, \alpha)^{24}_{12}\text{Mg}^*$	2753
3400 ± 20	2.2 ± 5.1	P		$^{27}_{13}\text{Al}(p, 2pn)^{25}_{12}\text{Mg}$	3410
3975 ± 25	6.4 ± 6.2	P		$^{27}_{13}\text{Al}(p, 2pn)^{25}_{12}\text{Mg}^*$	3920
4630 ± 35	7.0 ± 6.2	P		$^{27}_{13}\text{Al}(p, pn)^{26}_{13}\text{Al}^*$	{4600 4620
5165 ± 50	3.1 ± 4.1	P		$^{27}_{13}\text{Al}(p, pn)^{26}_{13}\text{Al}^*$	5120 5140
6140 ± 50	5.8 ± 4.5	P		$^{27}_{13}\text{Al}(p, pn)^{26}_{13}\text{Al}^*$	6190

* Denotes transition between excited states.

TABLE VI

Measured Energies and Cross Sections of Gamma Rays From a Cobalt Target Bombarded by ~160-MeV Protons

E _γ , keV, Measured	σ, mb, Measured	Spectrom- eter	Possible transition	
			Reaction	Energy
857 ± 12	153 ± 60	T	⁵⁹ ₂₇ Co(p, n) ⁵⁹ ₂₈ Ni	870
1264 ± 10	169 ± 65	T	⁵⁹ ₂₇ Co(p, p') ⁵⁹ ₂₇ Co	1289
1452 ± 15	86 ± 33	T	⁵⁹ ₂₇ Co(p, p') ⁵⁹ ₂₇ Co	1479
1745 ± 20	28 ± 15	T	⁵⁹ ₂₇ Co(p, p') ⁵⁹ ₂₇ Co	1743

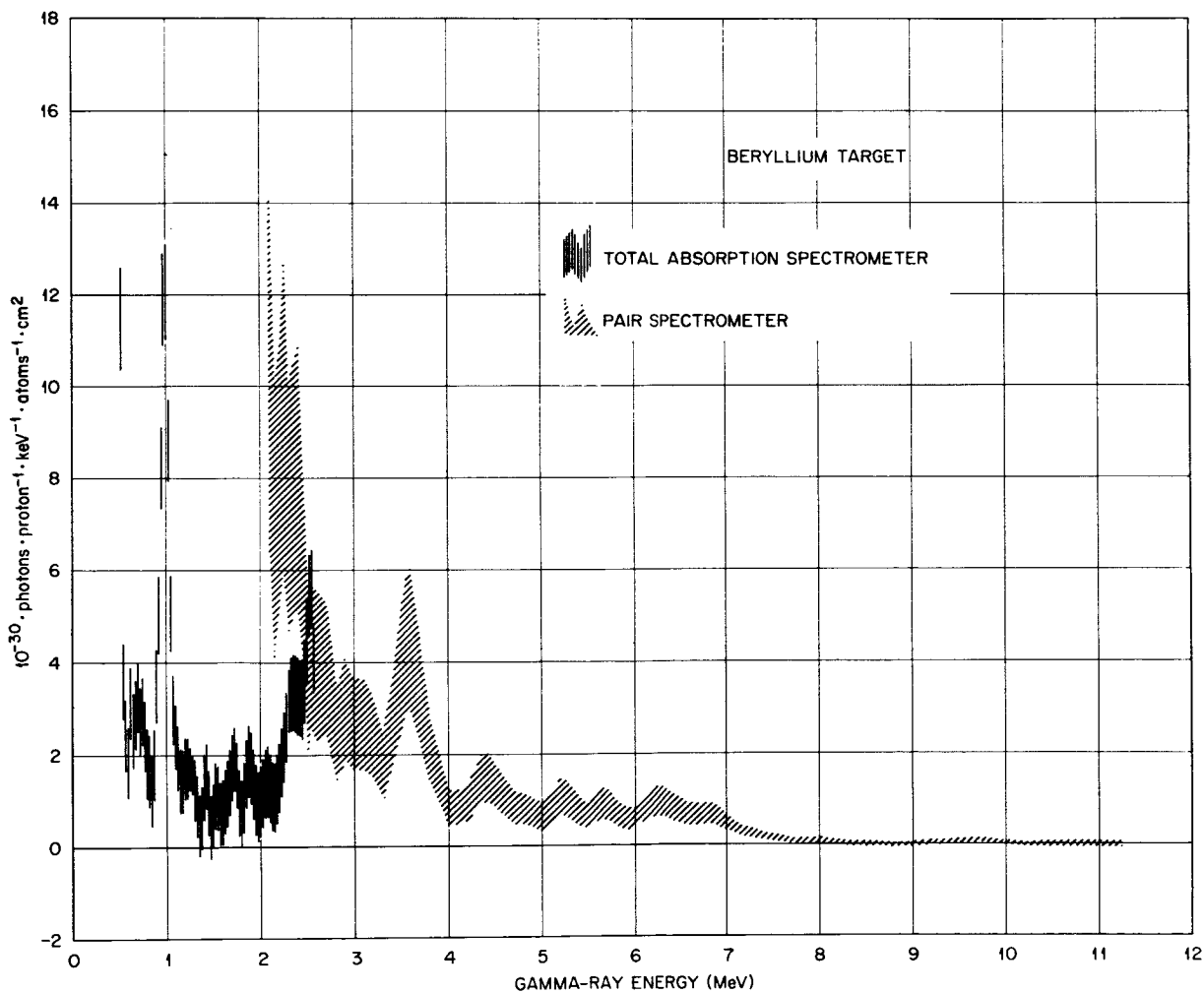


FIGURE 2.—Absolute gamma-ray yield as a function of gamma-ray energy due to the bombardment by 160-MeV protons of a 29-MeV-thick beryllium target.

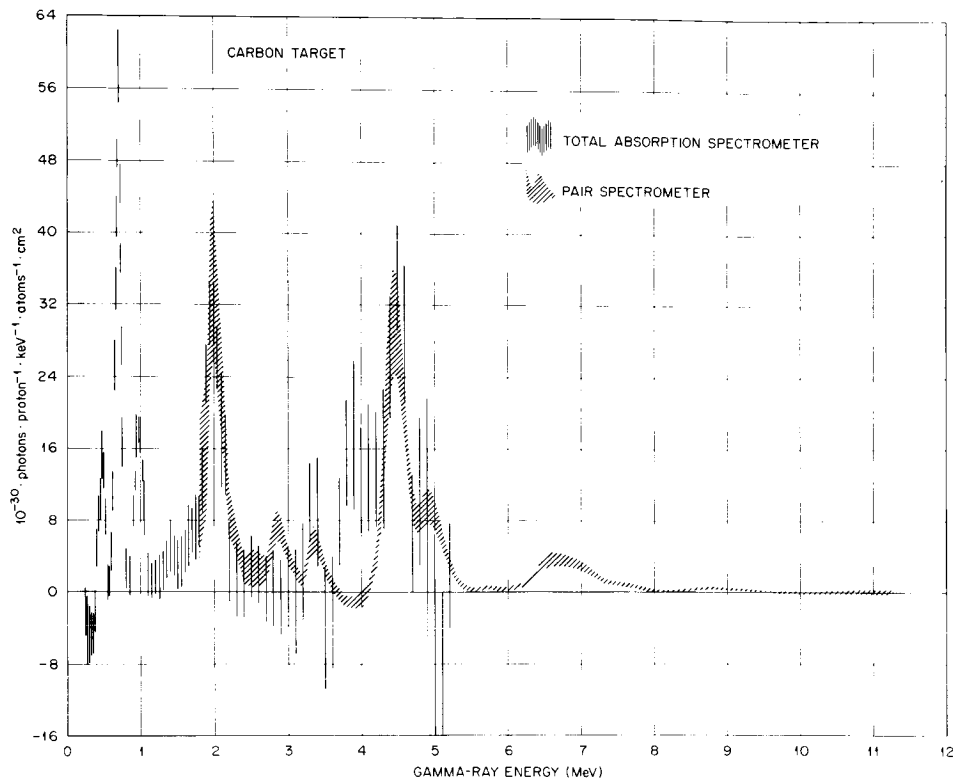


FIGURE 3.—Absolute gamma-ray yield as a function of gamma-ray energy due to the bombardment by 160-MeV protons of a 29-MeV-thick carbon target.

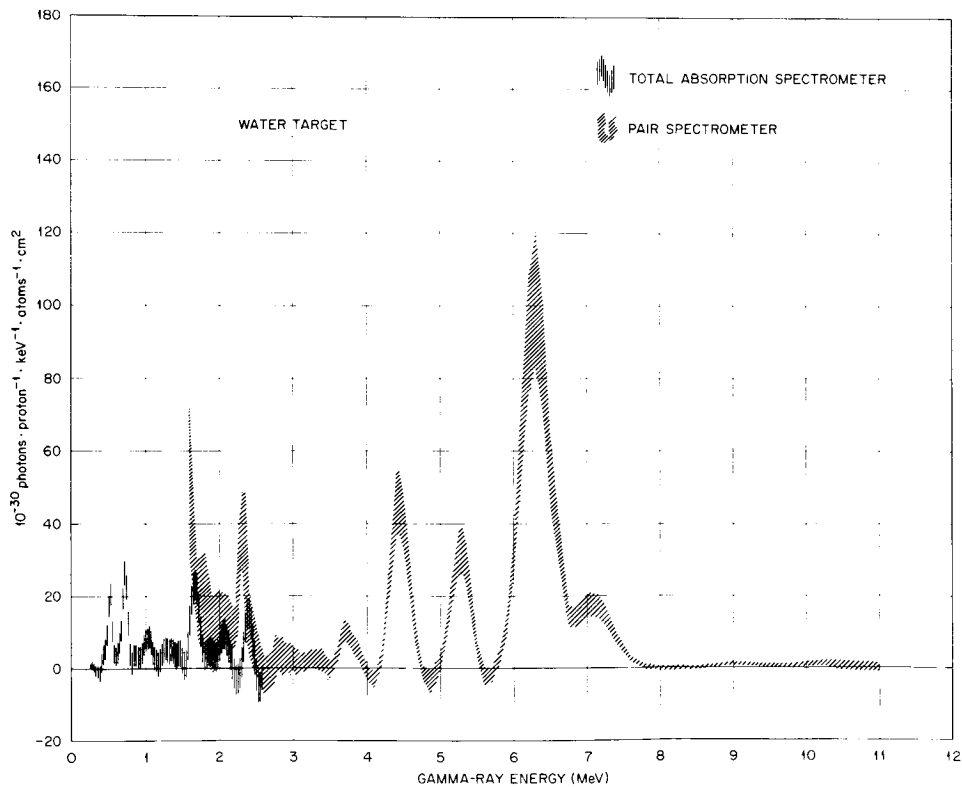


FIGURE 4.—Absolute gamma-ray yield as a function of gamma-ray energy due to the bombardment by 160-MeV protons of a 29-MeV-thick water target.

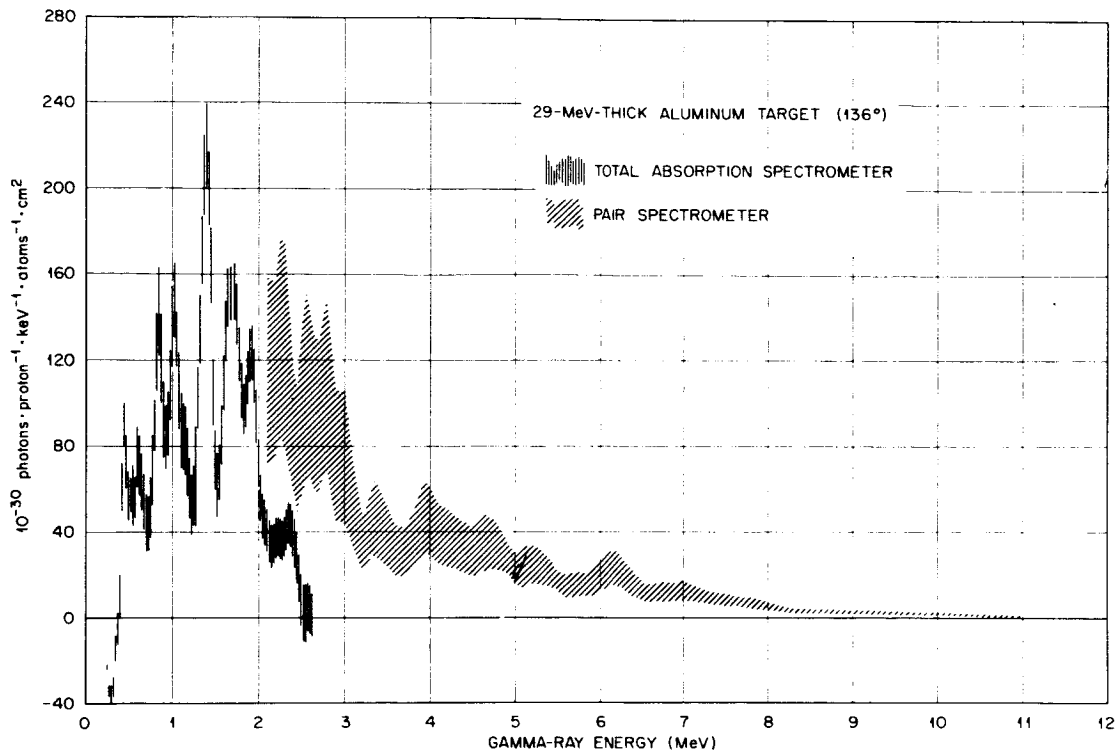


FIGURE 5.—Absolute gamma-ray yield as a function of gamma-ray energy due to the bombardment by 160-MeV protons of a 29-MeV-thick aluminum target.

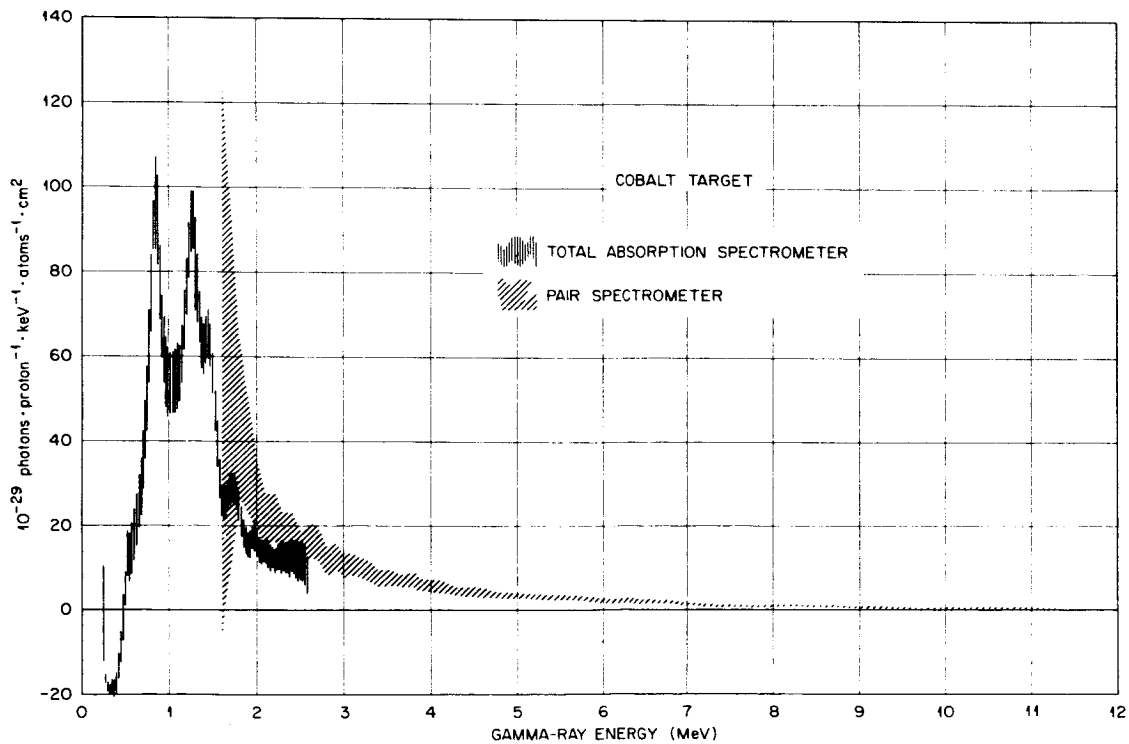


FIGURE 6.—Absolute gamma-ray yield as a function of gamma-ray energy due to the bombardment by 160-MeV protons of a 12-MeV-thick cobalt target.

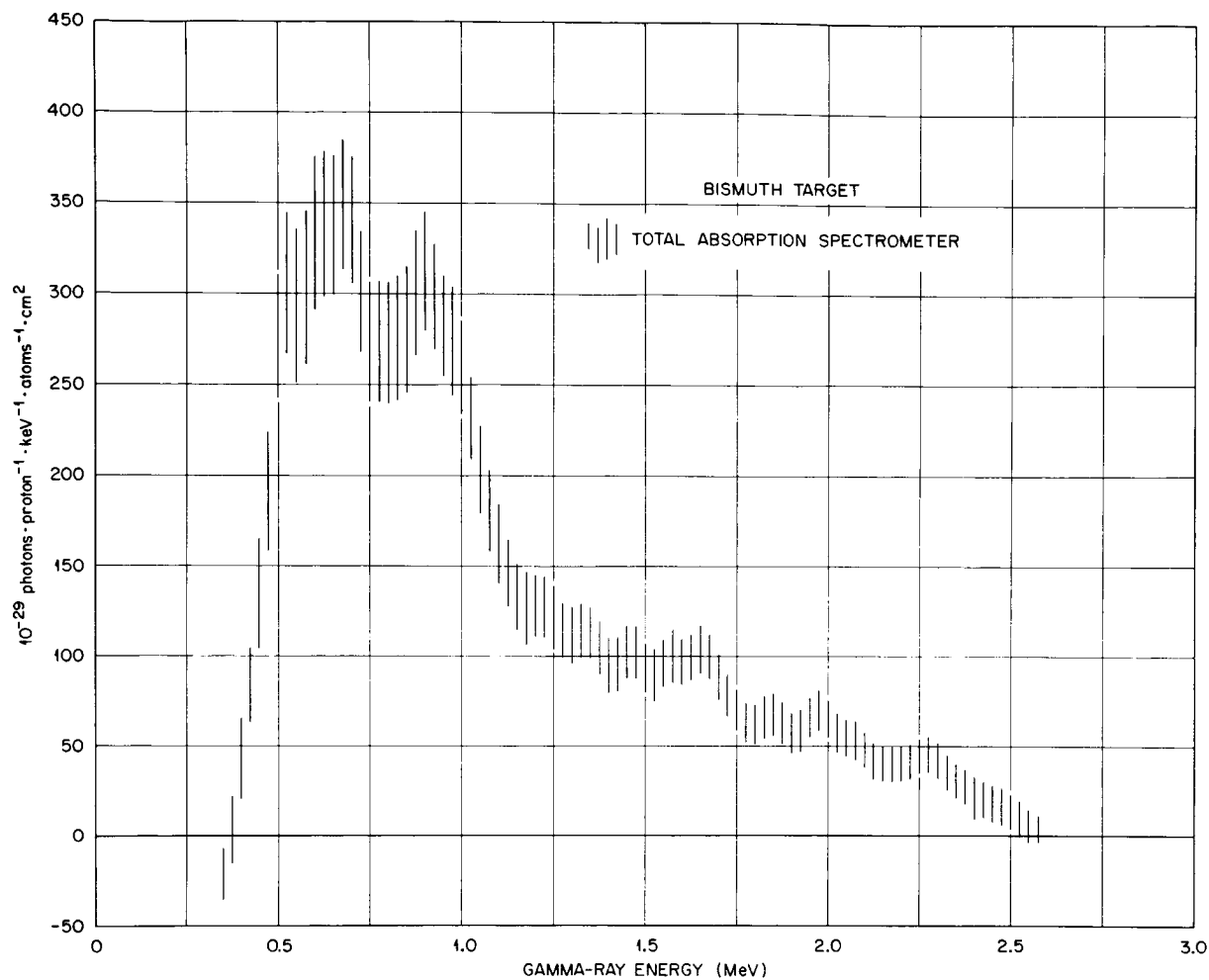


FIGURE 7.—Absolute gamma-ray yield as a function of gamma-ray energy due to the bombardment by 160-MeV protons of a 12-MeV-thick bismuth target.

TABLE VII

Measured Cross Sections for the Production of Gamma Rays Above 600 keV Compared to Calculated Total Nonelastic Cross Sections

Material	Cross section, mb	
	Measured	Calculated ^a
Be.....	6.8 ± 1.3	196 ± 2
C.....	41.4 ± 6.3	233 ± 4
O.....	115 ± 22	296 ± 3
Al.....	434 ± 97	427 ± 4
Co.....	1050 ± 220	732 ± 5

^a H. W. Bertini, private communications.

Table VII shows a comparison of calculations by Bertini (private communication) of the total nonelastic cross section with our measured cross sections for the production of photons with energy in excess of 600 keV.

We also made some measurements, using only the Al target and the spectrometer in the total absorption mode, at 44° with a separation distance of 102.8 ± 0.5 cm, and at 20.5° with a separation of 155.9 ± 0.5 cm. The results, together with those from the run at 136° , are shown in figure 8. It is seen that there is essentially no difference in the three spectra, indicating isotropic emission of the prominent gamma rays.

Preparations are currently in progress for similar experiments in which the incident protons will have (nominal) energies of 70, 35, and 15 MeV.²

² Since the presentation of this paper, data have been obtained with ~ 34 -MeV protons incident on Be, C, H₂O, Mg, and Al targets. Analysis of these data is in progress.

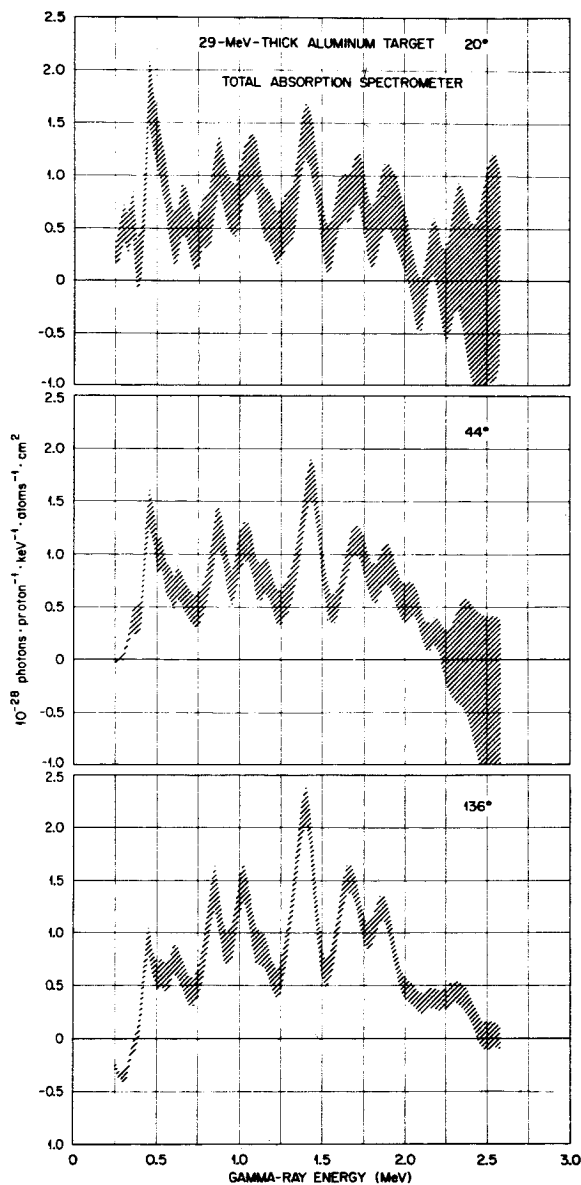


FIGURE 8.—Measurements using only the Al target and the spectrometer in the total absorption mode.

REFERENCES

1. NEUTRON PHYS. DIV.: Space Radiation Shielding Res. Ann. Progr. Rept., Aug. 31, 1962, ORNL-CF-62-10-29, rev.
2. CLEGG, A. B. ET AL.: Proc. Phys. Soc. (London), vol. 78, 1961, p. 681.
3. FOLEY, K. J. ET AL.: Nucl. Phys., vol. 31, 1962, p. 43.
4. FOLEY, K. J. ET AL.: Nucl. Phys., vol. 37, 1962, p. 23.
5. SALMON, G. J. ET AL.: Nucl. Phys., vol. 41, 1963, p. 364.
6. BOGERT, V. D.; and BURRUS, W. R.: Neutron Phys. Div. Ann. Progr. Rept., Sept. 1, 1962, ORNL-3360, p. 22.

NS-34615

39—Calculation of Proton-Induced Gamma-Ray Spectrum and Comparison With Experiment

C. W. HILL and K. M. SIMPSON, JR.

Lockheed-Georgia Company

A number of investigations have estimated the gamma ray secondary dose produced by solar flare protons interacting in aluminum shields. Madey, Duneer, and Krieger (ref. 1) have extrapolated the 10 and 14 MeV proton experimental data of Wakatsuki et al. (ref. 2) to higher energies in order to obtain estimates. Dye (ref. 3) has used the same data plus the 17 MeV proton data of Schrank et al. (ref. 4) to predict upper and lower bounds for the gamma ray dose. Alsmiller, Alsmiller, and Truby (ref. 5) have taken the theoretical neutron data of Troubetzkoy (ref. 6) up to 18 MeV, applied Coulomb corrections, and extrapolated to higher bombarding energies. The Lockheed group has programmed the LIGHT (ref. 7) code for the George C. Marshall Space Flight Center, NASA, using Troubetzkoy's model, and recalculated the gamma spectrum, but again it was necessary to make an empirical correction above low bombarding energies, say 10 MeV. Each of these attempts to evaluate the gamma ray problem has suffered from major uncertainties for bombarding energies above 10 or 15 MeV. The secondary gamma dose estimates for solar flares vary by more than a factor of 10 depending upon the assumptions made. This paper reports the results of a new attempt to predict secondary gamma rays arising from energetic proton reactions with nuclei. The predictions are compared to the 150 MeV proton data reported by Zobel, Maienschein, and Scroggs in the preceding paper. The new data above 25 MeV are combined with the Troubetzkoy data below 25 MeV in order to estimate secondary gamma ray dose due to a solar flare.

The processes which take place after proton-nucleus inelastic collisions may be represented

approximately by a sequence of de-excitation events as illustrated in figure 1. Knock-on particles emerge first, leaving the residual nucleus in an excited state. A fraction or all of the excess energy may be removed by the emission of evaporation particles. After evaporation is terminated, gamma ray emission is the dominant energy removal mechanism. The existence of metastable levels or the formation of unstable nuclei may lead to beta emission and electron conversion processes, possibly followed by further gamma emission. This simplified picture ignores competition between decay modes.

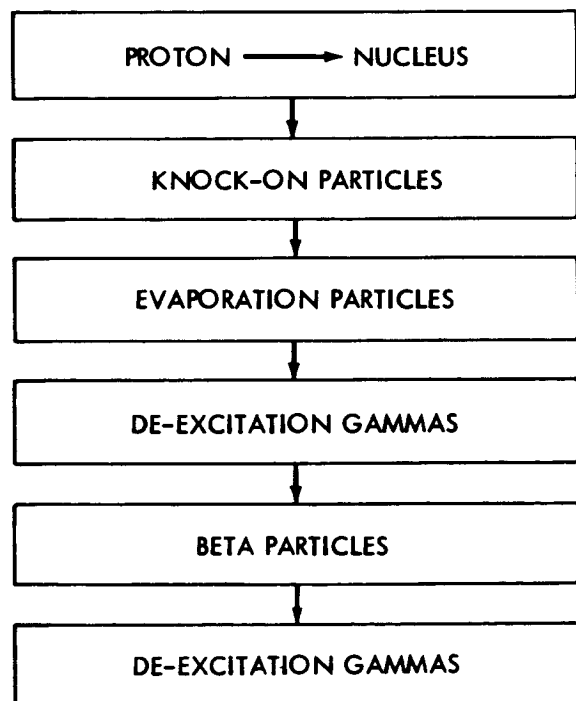


FIGURE 1.—Proton-nucleus processes.

The original LIGHT code is not capable of treating highly excited nuclei because particle emission removes the nucleus from the calculation. Gamma rays following cascade and evaporation are lost. This difficulty is avoided in the present study by treating gamma emission only after the cascade and evaporation phases are completed. Data on residual nucleus distributions are taken from the Monte Carlo results of Bertini and Dresner (private communication). This method of treatment required revision of the LIGHT code. The new version is called DLIGHT, an acronym for Diversified Lockheed Inelastic Gammas from High Energy Transitions.

The DLIGHT code is basically similar to the LIGHT code. However, the new code treats gamma ray emission from up to twenty residual nuclei rather than from the parent nucleus only. The discrete gamma ray lines are broadened to match the resolution available in experimental data. Further, the ground state of each nucleus may have an initial non-zero population following evaporation.

A representation of the energy levels of nuclei is shown in figure 2. Values for the low-lying levels are taken from the Nuclear Data Sheets (ref. 8). At higher energies, a continuum is assumed with level density given by Varshni's (ref. 9) fit to the Bethe equation. These data are tabulated for each significant residual nucleus in the Bertini-Dresner results. An initial distribution of excited state populations is estimated using a statistical model. This estimate is somewhat arbitrary, but the results are not excessively sensitive to reasonable variations.¹ The nuclei in excited states cascade down to ground state by emitting gamma rays. Electric dipole transition probabilities are assumed for all transitions. The transitions are computed and the resulting gamma rays are summed over the residual nucleus distribution.

¹ Recent calculations have shown that gamma ray yield is sensitive to the initial nuclear level population assumptions for low energy protons bombarding carbon and oxygen. Some spectral lines may be enhanced by a factor of 10 for 33 MeV protons. The revised data are in fair agreement with preliminary experimental results.

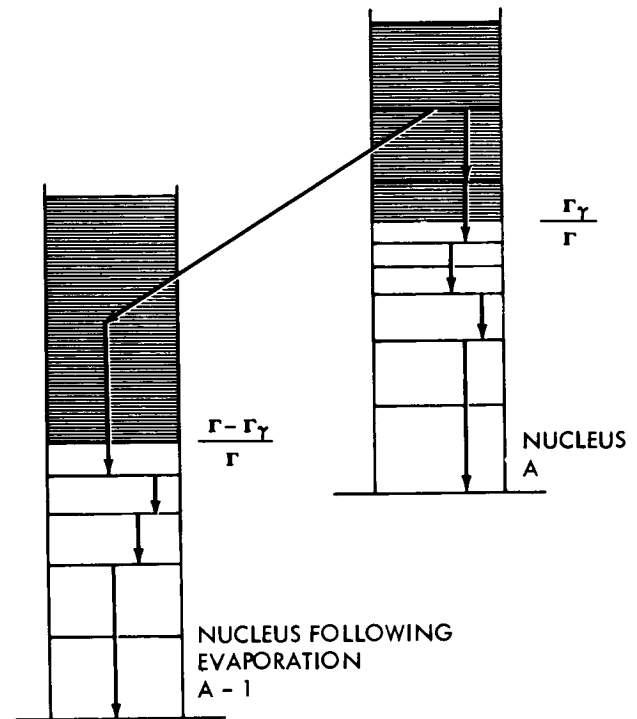


FIGURE 2.—De-excitation scheme for residual nucleus.

There are six principal sources of uncertainty in this calculation. First, gamma ray emission is the third step in the decay process. Inadequacies in the cascade and evaporation calculation should be reflected in the gamma spectrum. Indeed, the present calculation offers an indirect check on the validity of the Bertini-Dresner results. Second, the assumed initial population of excited states is an educated guess. Third, the values of some energy level parameters are uncertain. Fourth, transition probabilities between all levels are assumed to be electric dipole in nature. This assumption should lead to erroneous branching ratios in many cases. Fifth, the competition offered by evaporation may not be adequately accounted for at high excitation energies. Sixth, inelastic cross sections are not accurately known in some energy regions.

A comparison of the calculated spectrum with experimental data reported in the previous paper is shown in figure 3 for 150 MeV protons bombarding carbon-12. Eight residual nuclei are considered in this calculation. The solid line is the calculated spectrum and the band is an error corridor of the experimental spectrum.

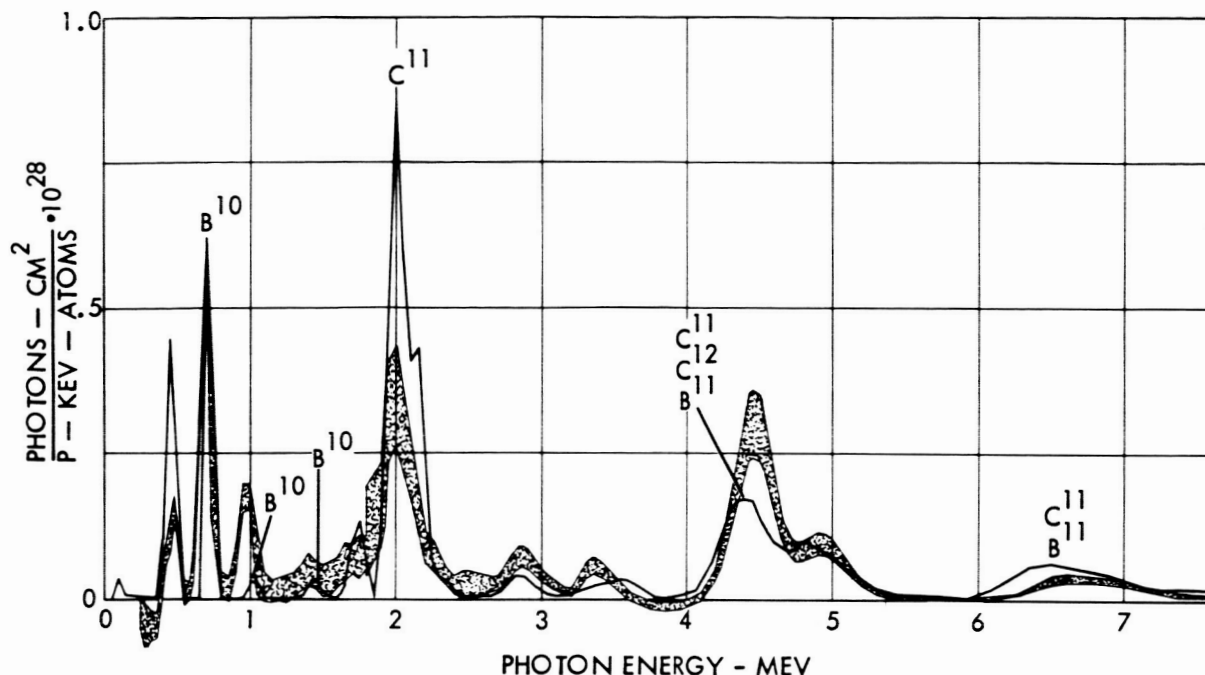


FIGURE 3.—Carbon-12 150 MeV protons.

The calculated curve has been multiplied by Bertini's estimate of the total inelastic cross section in order to make units agree. No other normalization has been performed.

Despite the possible uncertainties in the calculation, the agreement is surprisingly good. Peaks are slightly displaced at the higher energies, possibly due to difficulties in calibrating the pair spectrometer. R. W. Peelle of ORNL suggests that the low value at 4.43 MeV may be due to the fact that Bertini's calculation underestimates direct excitation of the target nucleus. This anomaly will also be seen in the oxygen-16 data but not in the aluminum-27 data. Below about 0.6 MeV, the disagreement could conceivably be caused by the sliding bias applied to the total absorption spectrometer.

Figure 4 shows a similar comparison for oxygen-16. Twelve residual nuclei are considered in this calculation. Here, the agreement is excellent over most of the spectrum. The low value near 6 MeV may again be caused by underestimation of direct excitation.

Figure 5 shows a similar comparison for aluminum-27. Eighteen residual nuclei are

considered in this calculation. The agreement is good over most of the spectrum. The spectrum above 2.1 MeV has a smeared appearance. This impression is confirmed by the theoretical data which show that the contribution from each residual nucleus is generally less than 30 percent of the total. Between 0.6 and 2 MeV, the discrete experimental peaks are reproduced fairly well. The calculated aluminum-26, sodium-23 peak at 0.42 MeV goes to 4.9 and the magnesium-25, sodium-22 peak at 0.58 MeV goes to 4.75. The comparison is unreliable for these and lower energy peaks because of the sliding bias used in the spectrometer.

Theoretical gamma ray spectra were calculated for bombarding energies of 25, 50, 100, 150, and 200 MeV. For aluminum targets, the spectrum is constant from 50 MeV to 200 MeV. The total gamma energy per inelastic collision varies by only 4 percent over this range of bombarding energies. It would be interesting to check this result experimentally. At 25 MeV the spectrum is softer, and the gamma energy yield increases 25 percent. It

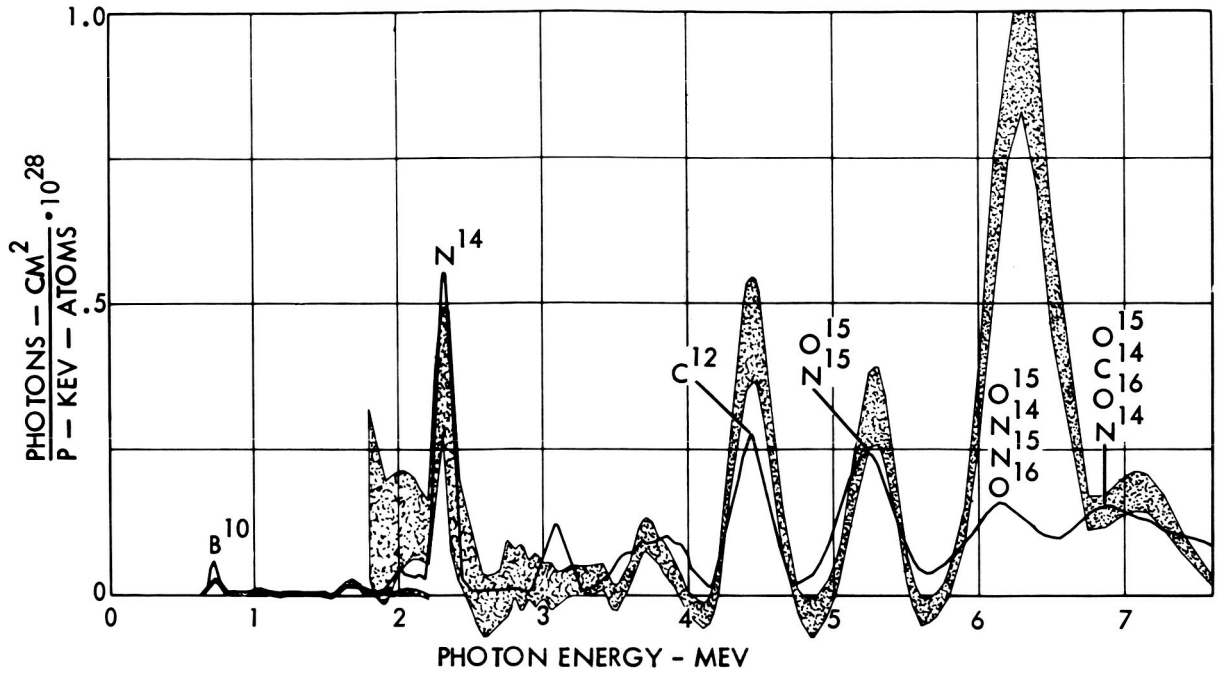


FIGURE 4.—Oxygen-16 150 MeV protons.

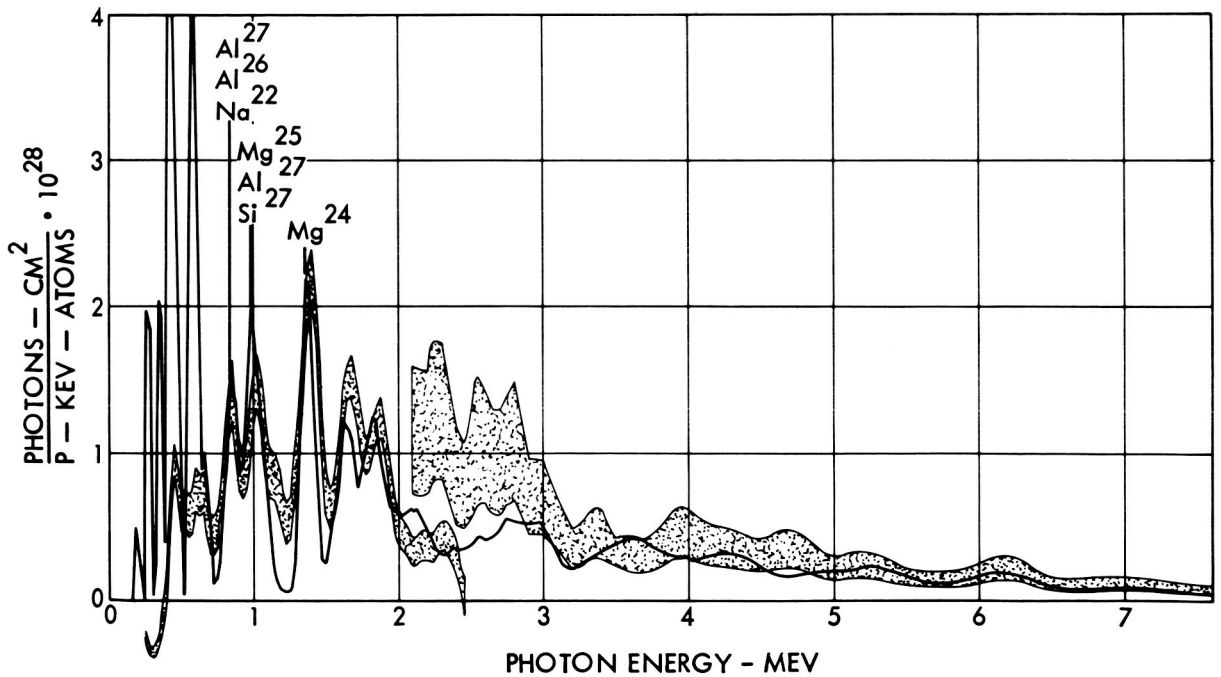


FIGURE 5.—Aluminum-27 150 MeV protons.

is essential to check these low energy yields experimentally because the inelastic cross section is large and the DLIGHT data are uncertain here. The possible range of error is

illustrated by the fact that the gamma yield predicted by the Troubetzkoy data for 22 MeV protons is 2.2 times larger than the yield predicted by the present calculation for 25

MeV protons. The spectra are also radically different in shape.

The gamma ray yields computed by the DLIGHT code for protons above 25 MeV are combined with the Troubetzkoy yields with Coulomb correction below 25 MeV in order to estimate the gamma ray secondary component within an aluminum shield for a solar flare. This estimate, shown in figure 6, is compared to the primary proton dose and to previous estimates. In order to simplify the calculation, the high bombarding energy gamma ray spectrum has been used for all proton energies despite the fact that the DLIGHT code predicts a softer spectrum and the Troubetzkoy data predicts a harder spectrum for low proton energies. The contributions of positron annihilation gammas and gammas following beta decay have been included here.

In figure 6, the lower Alsmiller curve assumes that gamma production does not take place for proton inelastic collisions above 22 MeV. The upper curve assumes a cutoff at 50 MeV, using the Troubetzkoy 22 MeV yield above 22 MeV. The Lockheed curve dips below the 22 MeV curve because a softer spectrum is assumed. The gradual change in slope of the Lockheed curve at large shield thicknesses is due to the contributions of cascade protons and neutrons. The sharp peak

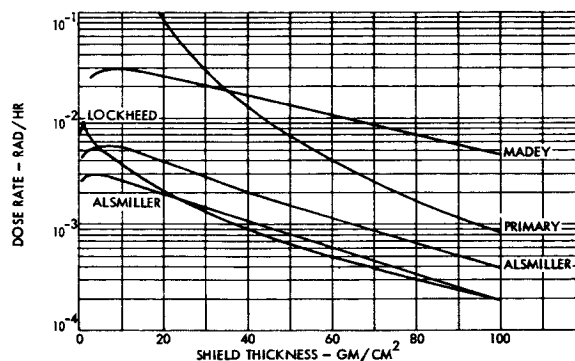


FIGURE 6.—Primary proton and gamma dose rate aluminum shield.

at small shield thicknesses is due to the large source strength within 0.5 gram per square centimeter from the entry face.

The present estimate of gamma ray secondaries shows that this component is relatively small even for fairly thick aluminum shields. However, uncertainties in the calculation could lower the estimate by a factor of two or raise the estimate by a factor of four. Furthermore, the possible existence of an intense proton flux below 15 MeV mentioned by D. K. Bailey, NBS, could double or triple the gamma component for some solar flares. The resolution of the gamma ray problem awaits accelerator experiments below 30 MeV and solar flare flux measurements below 15 MeV.

REFERENCES

1. MADEY, R.; DUNEER, A. G., JR.; and KRIEGER, T. J.: Gamma Dose from Solar Flare Protons Incident on an Aluminum Shield. Paper presented at meeting of American Nuclear Society (Boston), June 1962.
2. WAKATSUKI, T. ET AL.: Gamma Rays from Several Elements Bombarded by 10 and 14 MeV Protons. *J. Phys. Soc. Japan*, vol. 15, 1960, p. 1141.
3. DYE, D. L.: Space Proton Doses at Points Within the Human Body. The Boeing Company, DZ-90106, 1962.
4. SCHRANK, G. ET AL.: Inelastic Scattering of 17 MeV Protons. *Phys. Rev.*, vol. 127, 1962, p. 2159.
5. ALSMILLER, F. S.; ALSMILLER, R. G., JR.; and TRUBEY, D. K.: Comparison of Primary Proton Dose with the Dose from Gamma Rays Produced by Inelastic Scattering of Solar Flare Protons. TID-7652, Book 2, 1963.
6. TROUBETZKOY, E. S.: Fast Neutron Cross Sections of Iron, Silicon, Aluminum, and Oxygen. NDA 2111-3, vol. C, 1959.
7. HILL, C. W.; DOUGLASS, C. C., JR.; RITCHIE, W. B.; and SIMPSON, K. M., JR.: Computer Programs for Shielding Problems in Manned Space Vehicles. Lockheed-Georgia Company, ER-6643, 1964.
8. Nuclear Data Sheets. Nat. Acad. Sci.-Nat. Res. Council (Washington, D.C.).
9. VARSHNI, Y. P.: Comparison of Three Equations for the Spacing of Nuclear Levels. *Il Nuovo Cimento XXII*, 145, 1961.

N65-34616

40—Some Experimental Data on the Nuclear Cascade in Thick Absorbers¹

B. S. P. SHEN

New York University

A series of survey experiments on the passage of high-energy protons in solid absorbers have been conducted at the Brookhaven Cosmotron. Some raw data suitable for comparison with nuclear-cascade calculations are given.

INTRODUCTION

The past few years have seen an increase of interest in the nuclear cascade produced in dense media such as solids and liquids. By nuclear cascade, we mean the chain of nuclear interactions which takes place in a thick absorber when bombarded by an incident high-energy particle, itself not necessarily strongly interacting. Component processes of the nuclear cascade are: the collisions within absorber nuclei during the direct-interaction stage of the Serber model; the subsequent particle evaporation from the excited nuclei; other nuclear collisions in the absorber including low-energy processes; electromagnetic interactions linking one nuclear collision with another; etc.

Interest in the nuclear cascade in dense media was kindled by increased interest in: (a) the production of nuclides by cosmic rays in meteorites and the Moon; (b) the depth dosimetry of high-energy particles in the cosmic radiation and from accelerators; and (c) the physics of shielding against these high-energy particles. The nuclear cascade, together with its dosimetric, shielding, and astrophysical significance, has recently been reviewed at length in another paper (ref. 1), where relevant references can also be found.

We summarize for this symposium some results from a series of survey experiments on nuclear cascades induced in solid absorbers by

monoenergetic protons of 1 and 3 GeV. Preliminary results of some of these experiments were given at the first symposium (ref. 2). These experiments form part of a continuing program to study the passage of high-energy radiation in matter.

These experiments were conducted during a series of cooperative irradiations at the Cosmotron. We thank Dr. R. Davis, Jr., Dr. J. P. Shedlovsky, and Dr. R. W. Stoenner for invaluable help during and immediately following the irradiations. The cooperation of the Cosmotron staff is also much appreciated.

THE BROOKHAVEN SURVEY EXPERIMENTS

A narrow beam (in most cases <4 cm² in cross-sectional area) of monoenergetic protons from the Brookhaven Cosmotron was aimed at the central axis of a thick target (absorber), as shown in figure 1. The target was a rectangular parallelepiped. At various depths inside the target were sandwiched very thin aluminum foils normal to the beam direction. After the irradiations, the foils were removed and the fluorine-18 and sodium-24 activities produced in them during the irradiation were assayed, using calibrated counters. Some of the foils were cut into small pieces, which were individually assayed. In this way, we determined the distribution in the irradiated target of the F¹⁸ and Na²⁴ activities produced in aluminum. Figures 2 to 10, to be discussed presently, give such distributions for the five cases studies. These data are suitable for

¹ Work supported in part by the National Aeronautics and Space Administration and the U.S. Atomic Energy Commission.

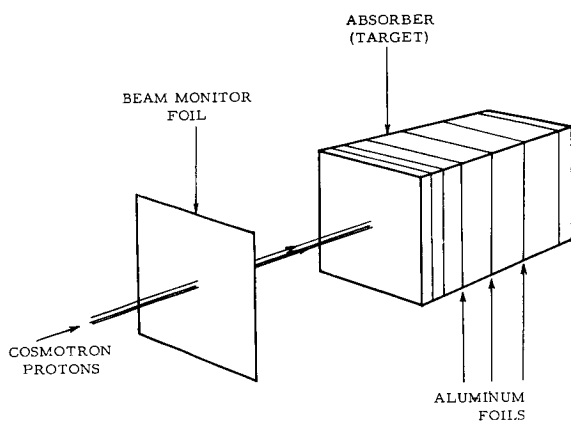


FIGURE 1.—Schematic sketch of the irradiation arrangement.

comparison with nuclear-cascade calculations tailored to the particular geometries of these experiments.

It is known that F^{18} is producible from aluminum only by strongly-interacting particles above about 50 MeV, whereas Na^{24} is producible from aluminum both by these particles and by neutrons below 50 MeV (particularly neutrons around 15 MeV) by the (n, α) reaction. As a result, it is possible to interpret the measured F^{18} and Na^{24} activities in terms of particle fluxes in the cascade. This flux interpretation is not very useful for direct comparison with calculations, and will not be discussed here.

The five cases studies are: 3-GeV protons on an iron absorber ("3GeV Fe"), 1-GeV protons on an iron absorber ("1GeV Fe"), 3-GeV protons on a chondritic absorber² ("3GeV Ch"), 1-GeV protons on a chondritic absorber³ ("1GeV Ch"), and 1-GeV protons on a Plexiglas absorber ("1GeV Pl"). The symbols in parentheses are abbreviations for the five cases, to be used in the sequel.

TRANSITION CURVES

Figures 2 to 6 give the experimental Θ_F and Θ_{Na} (the thick-target production cross sections of F^{18} and Na^{24} , respectively, from aluminum) as a function of depth x in the absorber. Θ_F , in the

² Composition by weight: 37% O; 28% Fe; 27% Si; 9% Mg+Na.

³ Composition by weight: 37% O; 27% Fe; 20% Si; 15% Mg+Na.

usual cross-section units, is defined such that

$$R_F = mJ_0\Theta_F$$

where R_F is the number of F^{18} nuclei produced per unit time in an aluminum foil of a particular shape and size and placed, *normal* to the incident beam direction, at a particular location inside the absorber. R_F is obtained from measurements. J_0 is the number of primary protons per unit time incident on the absorber surface. m is the number of aluminum nuclei per unit foil area; the value of m in the definition of Θ_F is thus fixed, regardless of the directional distribution of the local F^{18} -producing flux at the foil. Θ_{Na} is similarly defined for Na^{24} . The ratio Θ_F/Θ_{Na} is given in the lower halves of figures 2 to 6; this quantity is not of interest in the present context.

The size of the aluminum foils in which the Θ 's were measured is given in the legend. The cross-sectional area of the absorber is equal to the foil size, except in "3GeV Ch" as noted in the legend. The arrow on the abscissa of figures 2 to 6 marks the total thickness of the absorber.

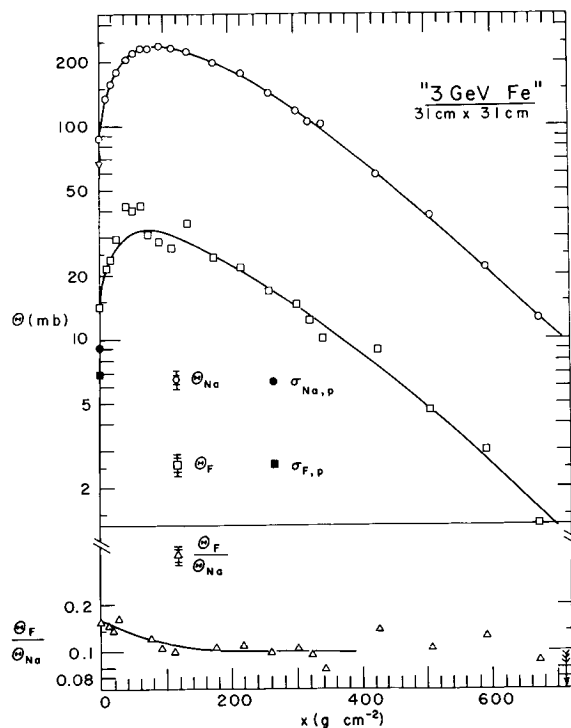


FIGURE 2.—Transition curves for 3-GeV protons on iron.

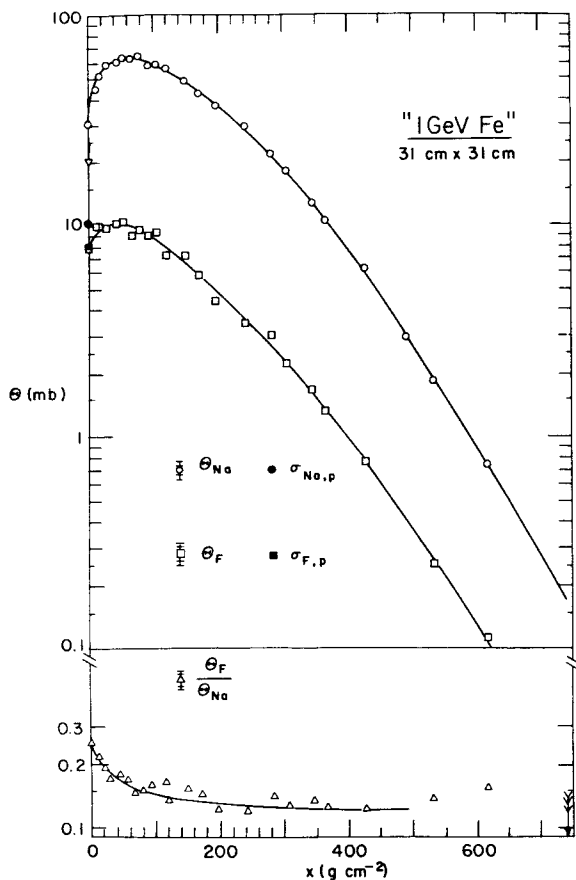


FIGURE 3.—Transition curves for 1-GeV protons on iron.

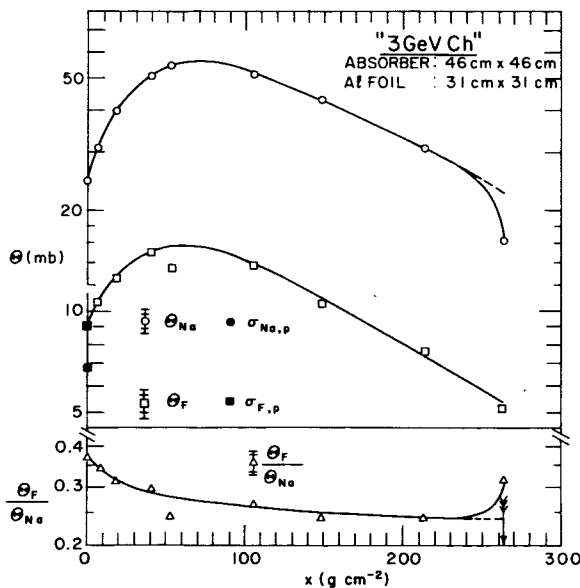


FIGURE 4.—Transition curves for 3-GeV protons on chondritic absorber.

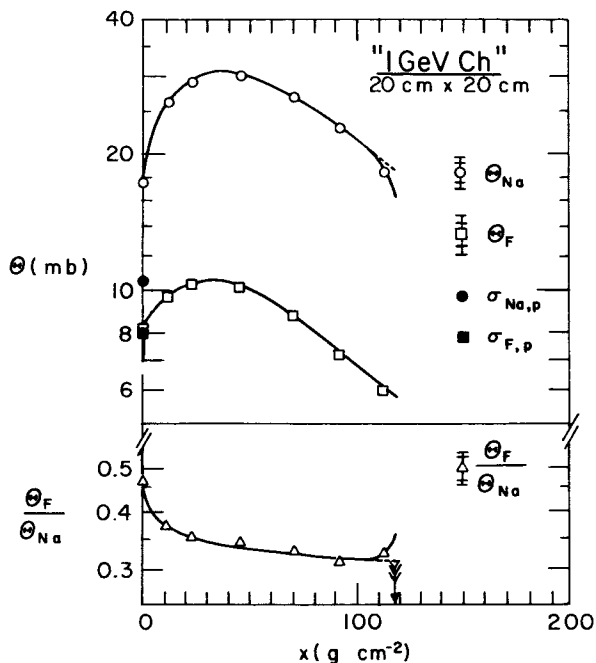


FIGURE 5.—Transition curves for 1-GeV protons on chondritic absorber.

For example, in "3GeV Fe" the absorber was 713 g cm^{-2} thick and had a cross-sectional area of $30.5 \text{ cm} \times 30.5 \text{ cm}$, which was also the area of the aluminum foils used. Absolute and relative errors are given respectively by the outer and inner error bars in the legend.

In figures 4 and 5, if the absorbers were longer, the curves would follow the dashed versions. Thus, the actual curves exhibit an "exit loss," which is due to the lack of albedo (upstream-moving) particles near the absorber's end. Since F^{18} is not producible by MeV neutrons as is Na^{24} , the exit loss is not seen in the Θ_F curves.

Table I gives the Θ_F and Θ_{Na} for "1GeV Pl" already plotted in figure 6. This case is of particular interest here since the absorber used can be regarded as a human phantom, in first approximation. In figure 6, it is seen that Θ_F and Θ_{Na} both exhibit a broad maximum. Unlike the usual transition maximum (for example those in figures 2 to 5), this "premature" maximum is apparently caused by the lack of albedo particles near the downstream end of the $\sim 30 \text{ g cm}^{-2}$ phantom. In other words, it results from the superposition of the initial buildup and the exit loss mentioned earlier. Such a "premature" maximum is

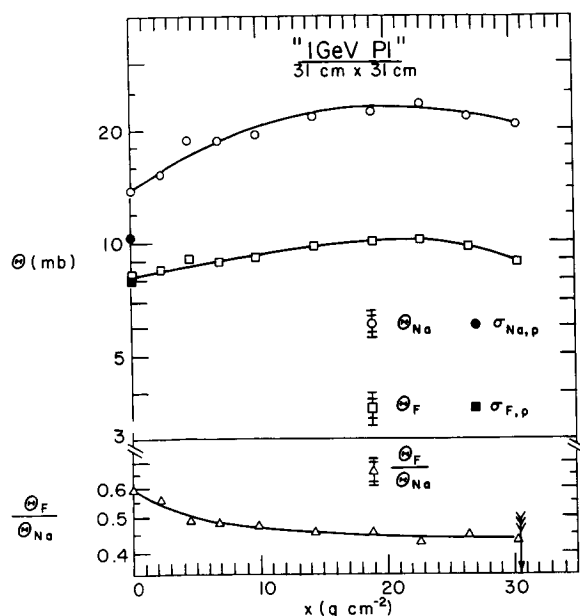


FIGURE 6.—Transition curves for 1-GeV protons on Plexiglas.

probably characteristic of small phantoms such as the one used when irradiated by GeV particles.

LATERAL DISTRIBUTION CURVES

Figures 7 to 10 give the lateral distributions of Na^{24} and, in one case ("3 GeV Ch"), also that of F^{18} . Length r is the lateral distance measured radially from the cascade axis (absorber axis). The depth x is the parameter. The lateral distribution function $\rho_{Na}(r)$ is defined as

$$\rho_{Na}(r) = \Theta_{Na}(r)/A$$

where $\Theta_{Na}(r)$ is the thick-target cross section (as defined above) for producing Na^{24} in a small aluminum foil sample of area A , placed normal to the incident beam direction at some given depth x and at a lateral distance r . Similarly, we define $\rho_F(r)$, for F^{18} .

The lateral-distribution curves in figures 7 to 10 are relative ones; they are all normalized to unity at $r=3.8$ cm. The values of ρ for $r=0$ cm are not given in the figures; they are given separately in table II, because we consider these values to be lower limits only. The arrow on the abscissa marks the edge of the absorber. Unless otherwise indicated by error bars, counting statistical errors do not exceed $\pm 6\%$.

TABLE I

Depth Dependence of Θ_{Na} and Θ_F for the Case of 1-GeV Protons on Plexiglas ($\text{C}_5\text{H}_8\text{O}_2$)

Depth, g cm^{-2}	Θ_{Na}, mb^a	Θ_F, mb^b
0	13.9	8.2
2.3	15.3	8.6
4.5	18.8	9.2
6.9	18.7	9.0
9.9	19.5	9.3
14.4	21.7	9.9
19.0	22.2	10.1
22.8	23.4	10.2
26.6	21.8	9.9
30.4	20.7	9.0

- ^a Absolute errors $\pm 8\%$; relative errors $\pm 5\%$.
- ^b Absolute errors $\pm 10\%$; relative errors $\pm 6\%$.

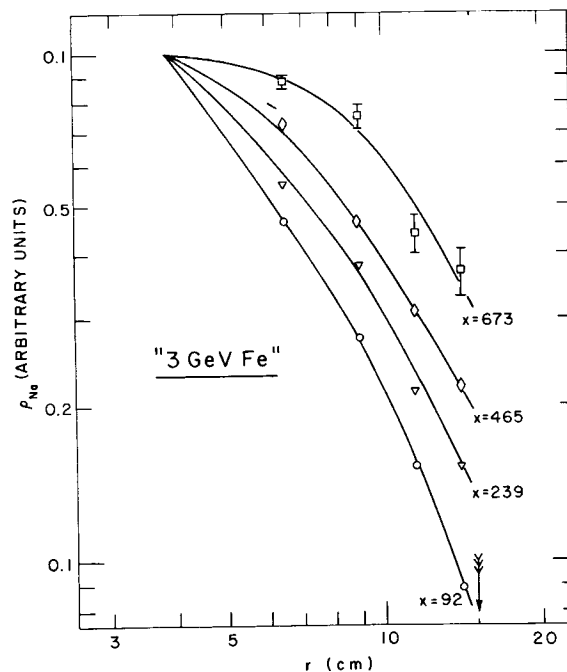


FIGURE 7.—Lateral distribution functions for 3-GeV protons on iron.

SENSITIVITY OF EXPERIMENTAL TESTS OF CALCULATIONS

Several procedures now exist for calculating the nuclear cascade in thick absorbers as reported in papers by Alsmiller et al., Irving et al., Kinney, More et al., and Wallace et al., elsewhere in this volume. However, experi-

TABLE II

Values of Lateral Distribution Functions $\rho_{Na}(r)$ and $\rho_F(r)$ at $r=0$ cm, for Various Depths x .

[These values should be regarded as lower limits. All values are normalized so that, at $r=3.8$ cm, $\rho_{Na}(r)=\rho_F(r)=1$ as in figures 7 to 10]

"3GeV Fe"		"1GeV Fe"		"3GeV Ch"			"1GeV Ch"		"1GeV Pl"	
$x, \text{g/cm}^2$	$\rho_{Na}(0)$	$x, \text{g/cm}^2$	$\rho_{Na}(0)$	$x, \text{g/cm}^2$	$\rho_{Na}(0)$	$\rho_F(0)$	$x, \text{g/cm}^2$	$\rho_{Na}(0)$	$x, \text{g/cm}^2$	$\rho_{Na}(0)$
		18	5.2						23	25
92	3.3	93	4.3	53	6.2	12				
				105	4.6	8.5	92	9.9		
239	2.1	242	2.6	213	3.1	4.7				
		366	2.1	263	2.2	3.2				
465	1.7	491	1.1							
673	1.3	679	1.1							

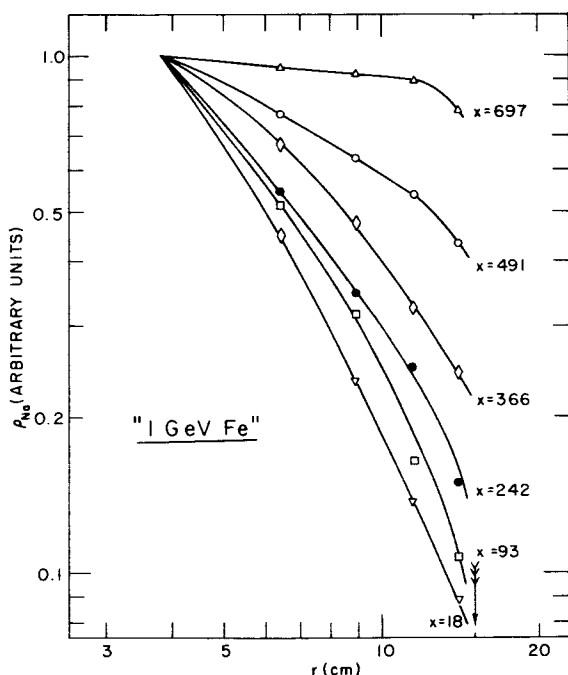


FIGURE 8.—Lateral distribution functions for 1-GeV protons on iron.

mental data suitable for comparison with calculations are still scarce. The curves in figures 2 to 10 furnish some such data for incident protons of a few GeV.

In a complete nuclear-cascade calculation, there are several types of data (e.g., particle spectra; doses) that can be used to compare

with the corresponding data from experiments. However, some types of data are able to provide more sensitive tests for the calculation than others. In general, one would expect that, the more "distant" the data are from the starting point of the cascade calculation (i.e., the more numerous the physical processes and mathematical operations interposed between the starting point and the data), the less sensitive would be the test that these data can provide. (By an insensitive test is meant one in which a relatively large change in the initial values and assumptions of the calculation affects only slightly the calculated results being tested.) The spectrum of neutrons above 20 MeV at a given depth in the cascade, for example, is less "distant" than the spectrum of neutrons below 20 MeV at the same depth, since the latter depends on the evaporation stage in addition to the direct-interaction stage. The integral yield of neutrons of all energies at that depth is a still more "distant" type of data, as are the production rates of specific spallation products at that depth. However, the production rates at depth 3 cm is less "distant" than the production rates at depth 30 cm. Among the most "distant" types of data is the dose in the cascade, especially the dose at large depths. Often, the more "distant" the data, the more extensive is the test they can provide, i.e., the greater is the fraction of the calculation that can be tested at a time. This advantage,

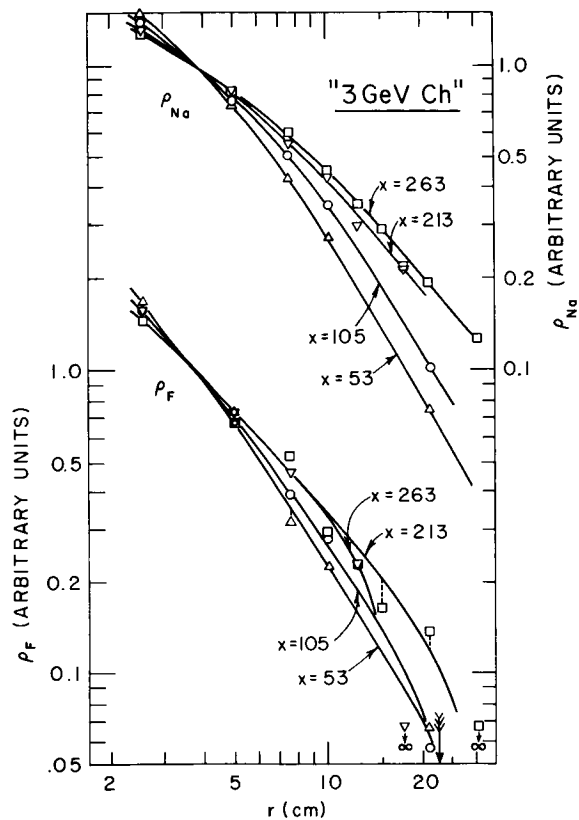


FIGURE 9.—Lateral distribution functions for 3-GeV protons on chondritic absorber.

however, may be offset by the lesser sensitivity of the test. Reverting to our experiments, an interesting question yet to be answered is: how sensitive a test can the spallation products F^{18} and Na^{24} provide for nuclear-cascade calculations? One would expect F^{18} to provide a more sensitive (and less extensive) test than Na^{24} , since Na^{24} can be produced by MeV neutrons and F^{18} not.⁴

⁴ If one utilizes in the calculation the (thin-target) production cross-sections of F^{18} or Na^{24} from aluminum, which are either well measured (refs. 3 to 5) or can be plausibly inferred, then the data become slightly less "distant" and the test slightly more sensitive.

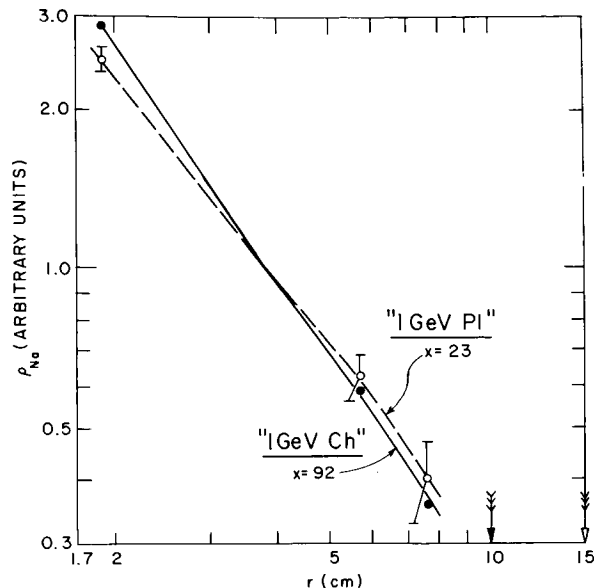


FIGURE 10.—Lateral distribution functions for 1-GeV protons on chondritic absorber and 1-GeV protons on Plexiglas.

Although an insensitive test may not be particularly interesting from the standpoint of the physics of the cascade, the calculational scheme thus tested can still be very useful in practical applications if it can predict, even though only roughly, such experimental data as the dose in an absorber. In fact, if the Na^{24} distribution in the cascade can be predicted, then one should not be too far from being able to predict also the absorbed dose (but not necessarily the LET spectra) in the cascade.

Ultimately, one looks forward to the time when the average outcome of individual nuclear reactions are so accurately known that a test of the nuclear-cascade calculation need not also be an inevitable test of the calculation of processes taking place inside the nucleus. At that time, one may well wonder whether there is still anything left worth calculating about the nuclear cascade.

REFERENCES

1. SHEN, S. P.: *Astronaut. Acta*, vol. 9, 1963, p. 211.
2. SHEN, S. P.: Some Experiments on the Passage of High-Energy Protons in Dense Matter. *Proc. Sym. on Protection against Radiation Hazards in Space*. Paper F-5, T1D-7652, Atomic Energy Commission, 1962, pp. 852-865.
3. CUMMING, J. B.: *Ann Rev. Nucl. Sci.*, vol. 13, 1963, p. 261.
4. POSKANZER, A. M.; and REMSBERG, L. P.: *Phys. Rev.*, vol. 134, 1964, B779.
5. BUTLER, J. P.; and SANTRY, D. C.: *Can. J. Phys.*, vol. 41, 1963, p. 372.

SESSION IVD

SHIELDING AGAINST SPACE RADIATION

Chairman: NORMAN M. SCHAEFFER

Radiation Research Associates, Inc.

N65-34617

41—Apollo Spacecraft Nuclear Radiation Protection Status Report

FREDERICK RAYMES

North American Aviation, Inc.

Since the initiation of the Apollo program, considerable discussion has taken place with regard to the radiation protection requirements of the astronauts during a typical lunar mission. It stands, of course, to reason, that the overall radiation protection needs of the Apollo mission must include consideration of protection available in the Command/Service Modules (CSM), in the Lunar Excursion Module (LEM), and during the time spent on the lunar surface. Consequently, to speak realistically of probable lunar mission radiation doses and resulting protection requirements, one must include total mission considerations, that is to say, total exposure time of the astronaut in the various mission modes.

Because of time limitation, the present paper is restricted to a discussion of space radiation protection considerations with regard to the Command/Service Module only, although some remarks will be made concerning total mission radiation reliability considerations. In addition to the above constraints, the paper is further limited to discussions of shielding and dose calculations for particular environments in comparison to allowable dose limits which have been set by the NASA. Although NAA has had substantial interaction with the NASA regarding both the environment to be utilized and the interpretation of the allowable doses, this paper will not discuss the pro's and con's of these important design elements; reliance will be placed instead on a preceding paper by Modisette et al. to provide the background for the selection of both the design environment and allowable dose limits which are being utilized.

METHOD OF ATTACK

Before proceeding with a determination of the degree of protection offered by the spacecraft, one must define a method of attack to perform the task at hand. The approach utilized by NAA was as follows:

1. It was felt that environmental criteria for design purposes should be selected to be consistent with the overall mission success reliability criteria goals which are being designed into other subsystems of the spacecraft.

2. The allowable emergency dose limits are considered as lower threshold limits where radiation sickness symptoms may appear. In other words, these limits are not considered to be lethal, but rather are limits, which if reached, could impair the optimum functioning of the astronauts and thus potentially reflect in the overall mission success reliability.

3. With items 1 and 2 as a basis, the next step was to determine the inherent spacecraft shielding capability; that is, the shielding effectiveness of the inherent structure, equipment, and other subsystems without considering additional weight specifically for shielding purposes.

4. Methods of dose reduction were investigated by determining the feasibility and effectiveness of spot shielding, through the utilization of movable equipment and materials within the spacecraft which could be utilized to improve the inherent shielding capability of the spacecraft.

5. Additional considerations for dose reduction were to be investigated by resorting to operational procedures through warning and preferred orientation and, if necessary, mission

modification in order to prevent the dose from exceeding stated limits.

The above rationale will serve as an outline for the subsequent discussion.

SHIELDING EFFECTIVENESS OF SPACECRAFT

For clarification purposes, let us briefly review the Apollo mission radiation environments of interest. The preceding paper of Modisette et al., provides details of environment selection for Apollo mission utilization. Figure 1 shows a simplified representation of the Apollo mission radiation profile in the event that a solar flare should take place during the mission. Insofar as the Command/Service Module (CSM) dose picture is concerned, the earth geomagnetically trapped radiations represent 9% of the total, galactic cosmic radiation 1% of the whole, and solar radiation (proton and alphas) 90% of the Apollo radiation dose. The paper will concentrate primarily on the solar radiation aspects, although a few words will be said about the trapped radiation picture.

If one considers only the lunar mission during which the spacecraft slices through the more intense regions of the trapped radiation belts for a duration in the order of 20 minutes, the belts present no serious problem to the astronauts as long as they are residing in the CSM. Calculations have been performed for various mission modes which require CSM-LEM docking during transition through the trapped radiation belts. It was found that the astronauts could not be permitted to enter the LEM adapter, nor the LEM, for 10 to 20 minutes after injection into the translunar phase. Mission operational procedures have been worked out which will not require the astronauts to leave the CSM for at least that time period after injection into the translunar trajectory.

It may be of interest to point out that, in spite of the large number of measurements in the trapped radiation environment, gross uncertainties continue to exist for detailed application to design tradeoff studies. These uncertainties require us to be more conservative in our estimates than we would normally be if we really knew the value of the actual environment.

Returning to the solar radiation aspects of the CSM shielding effectiveness, I want to

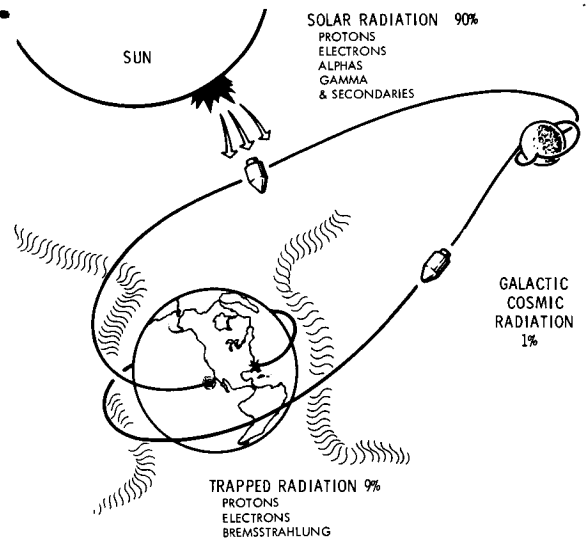


FIGURE 1.—Apollo mission radiation profile.

briefly discuss the computer program which is being utilized to calculate astronaut dose. Anyone who has performed shielding calculations in detail will attest to the fact that the reliability in such calculations is only as good as the input data which have been provided. The input data of relevance in this case are, of course, the spacecraft geometry.

Geometry is defined as a description of the dimensions (weight and volume) and the material composition of the structure and subsystems which constitute the spacecraft in question. It is obvious that the more detailed such description, the better the evaluation of shielding effectiveness. Unfortunately, one is faced with an anachronistic situation as follows. In the early steps of any spacecraft development, the geometric details as previously defined are fluid and consequently not well known; it is at this time, however, that one wants to determine the need for extra shielding requirements. On the other hand, as the spacecraft becomes better defined, its weight and general configuration are "cast in concrete," so to speak, and any attempt in changing the design meets with loud protestations. It is at this latter time period that detailed calculations can be performed; the problem is to determine the geometric detail required upon which to base reliable conclusions.

In order to strike a reasonable compromise between these two requirements, NAA selected

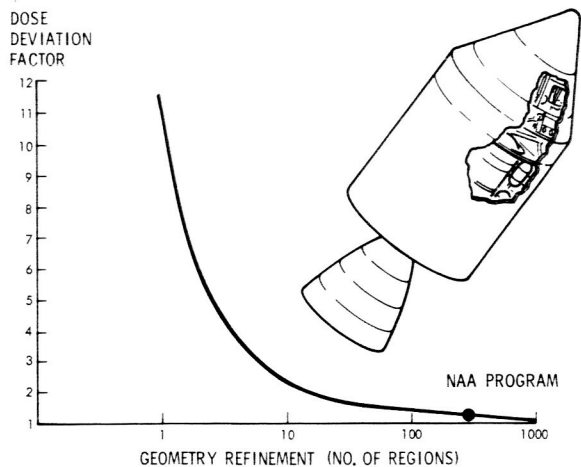


FIGURE 2.—Effect of spacecraft geometry refinement on computed dose.

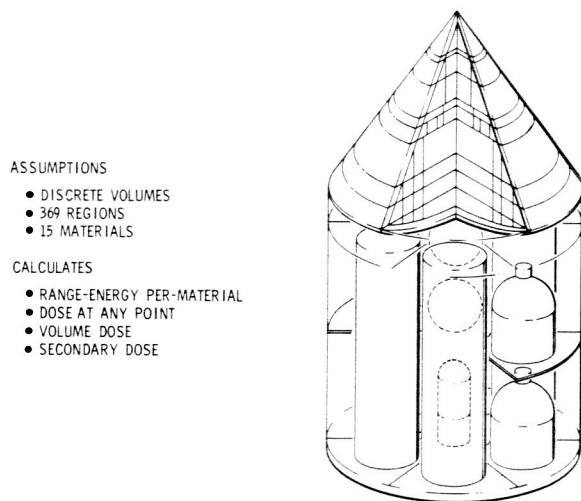


FIGURE 3.—Apollo master shielding code.

a program which divides the spacecraft into approximately 370 regions (figs. 2 and 3). This program permits geometry evaluations for input into calculation procedures at a reasonably early time, without having to wait for the detailed "nut and bolt" design definition. It also offers the advantage that, as the design evolves and progresses, one can easily update these regions without spending an inordinate effort. It is believed at this time that the geometry input yields dose results accurate to within 20%. This factor has been taken into consideration in the dose evaluation which will be discussed subsequently. The general characteristics of the program are such as to allow the

description of the CSM in discrete volumes with approximately 370 regions and 15 materials. The program will calculate the range—range energy for each material, the dose at any point in the CSM, dosimetric volume, and secondary doses as desired. The astronauts are represented by means of standard phantoms.

Utilizing the above mentioned program, and based upon the environments and allowable doses discussed in a preceding paper by Modisette et al., the Apollo dose picture as presently understood is as shown in figure 4. Figure 4 shows the comparison of astronaut doses within the Apollo CSM. The doses shown are to the eyes, the skin, and the blood forming organs at 5 centimeter depth. It can be seen that the allowable doses are exceeded only in the case of the eyes, which will be protected by means of goggles for a very nominal weight. It is evident, that for the skin and blood forming organs, the expected doses are substantially below the allowable levels for the design environment.

It may be of interest to discuss briefly the elements which went into the comparison. As illustrated for the skin doses, the proton contribution is approximately 31% of the total expected dose, the alphas approximately 35% of the total, the trapped radiations 10%, the secondaries approximately 10%, and an uncertainty factor of 20% for the previously discussed geometry considerations. Since alpha and proton doses are being added, the relative

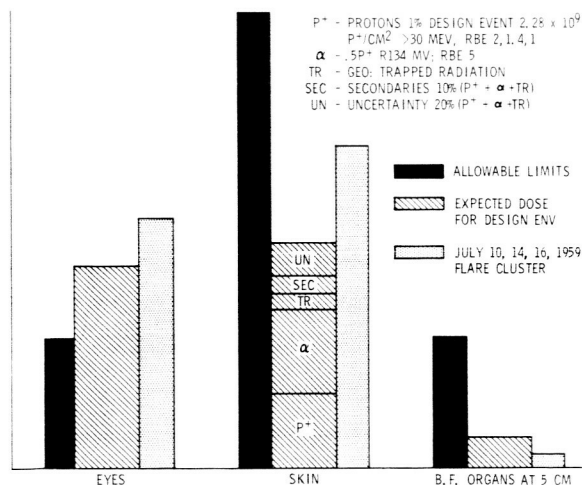


FIGURE 4.—Apollo CSM dose status.

biological effectiveness for protons and alphas had to be determined. The calculations assume an RBE of 5 for alphas regardless of region, and an RBE of 2, 1.4, and 1 for protons for the eyes, skin, and blood forming organs, respectively.

The alpha model utilized for these calculations has an alpha population of 50% of the number of protons in the design event with a rigidity of 131 MV. The substantial alpha dose is significant. It is pointed out, however, that the discussion concerns the skin dose only, which signifies that only the CSM attenuation considerations come into play. In addition, the alphas have been given a 5/1.4 importance. In contrast to the skin dose, the alpha contribution to the blood forming organ dose, because of tissue attenuation, is practically nil.

During the investigation for alpha RBE, it became evident that no systematic research had been performed to assess a proper value for human tissue and the spectra of interest. Added research is required to determine actual values. The RBE of 5 used herein is believed to be conservative.

It is well understood, of course, that the environment that really matters is that which is encountered during a two-week period in the case of Apollo, rather than a discrete flare which is used for design purposes. In order to underline the validity of the design environment utilized for Apollo, a comparison has been performed by assuming a CSM lunar flight during the worst possible two-week solar activity period during the last solar cycle. On July 10, 14, and 16, 1959, one of the largest flare clusters was observed containing both proton and alpha particles. Had a mission taken place during that particular time, the astronauts would have received the doses shown in figure 4. Although in some cases the doses would have been slightly higher than those calculated for the design environment, both the skin and blood forming organ doses are well below the allowable limits. This is not to imply that these doses are trivial. It must be remembered, however, that the probability of encountering these levels is less than 1 out of 100 flights, and are of the same order as other risks that the astronaut may have to face. Additional precautions are being taken to re-

duce this level further, as will be discussed subsequently. In general, it can be stated that the astronauts are provided with substantial protection in the Apollo CSM for the nuclear radiation environments which they may encounter on a two-week mission.

It may be of interest to take a closer look at the microscopic dose picture with the astronaut in the reclining position within the CSM as shown in figure 5. The figure shows the relative proton dose distribution both in depth and on the surface of the phantom. The depth distribution is through the astronaut from the navel to the spine; the surface distribution is on the skin surface from the eye to the lower abdomen. Such calculations have been performed for various rigidities of which the 158 MV and 80 MV rigidities are shown. With regard to the depth distribution through the astronaut, it is evident that a very rapid decrease in dose takes place. It will be remembered that the previous blood forming organ doses were specified at 5 centimeters depth. The depth distribution shown here indicates a decrease of a factor of approximately 5 between the outer skin and the 5-centimeter position. Some experts consider the radiation level of the gastro-intestinal tract region (2 cm) more relevant insofar as radiation sickness is concerned compared to the blood forming organ level. Since the G.I. tract dose levels are substantially higher than the blood forming organ levels, consideration should be given to allowable limits at that point as well.

One further remark about the depth distribution; it is seen that the dose near the spine is substantially less than that on the chest of the astronaut. The reason for this is the much heavier shielding provided by the service module which tends to protect the back of the astronaut from irradiation in that region. The chest area, on the other hand, is exposed to the relatively thinner region of the conical surface of the command module, resulting in higher dose levels.

Insofar as the surface dose distribution is concerned, the lower abdominal region has a slightly higher dose compared to the eye level because of the interaction of the previously discussed geometry considerations and the solid angle view factors which interplay with the

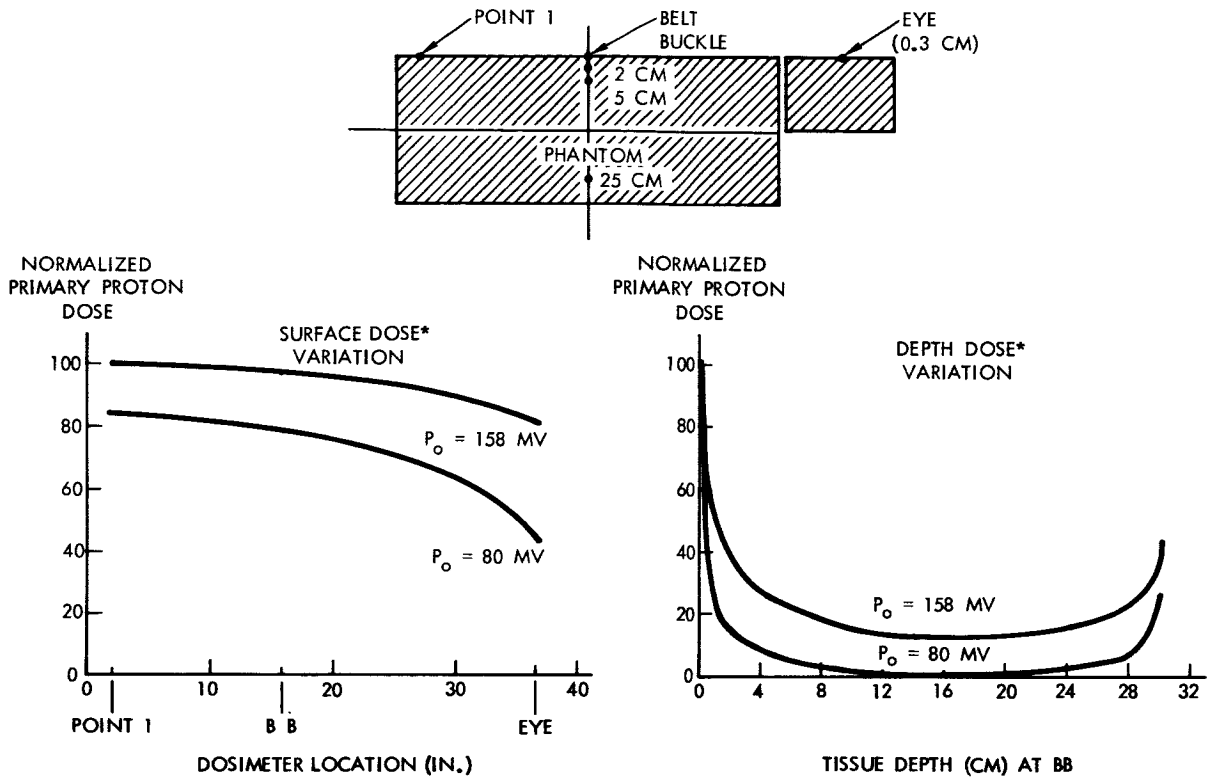


FIGURE 5.—Surface and depth dose variation for a phantom in CSM.

geometry at various dose point calculation positions.

The real point of interest in figure 5 is the nonhomogeneous dose distribution which the astronauts can expect to receive as a result of the geometry variations of the spacecraft. This, of course, raises a question with regard to our research in determining the effects of radiation on the human body, which, in general, considers whole body irradiation of experimental animals in a homogeneous fashion.

DOSE REDUCTION METHODS

It may be of interest to discuss briefly the source of the doses which were shown on the previous chart. Figure 6 shows the distribution of CSM surface area and dose as a percent of total, plotted against area density. The figure vividly portrays the fact that regions on the spacecraft representing 5 grams/cm² or less cover only 9% of the surface area on the spacecraft; through this 9% region one obtains approximately 60% of the total doses which were previously shown. This relatively thin region

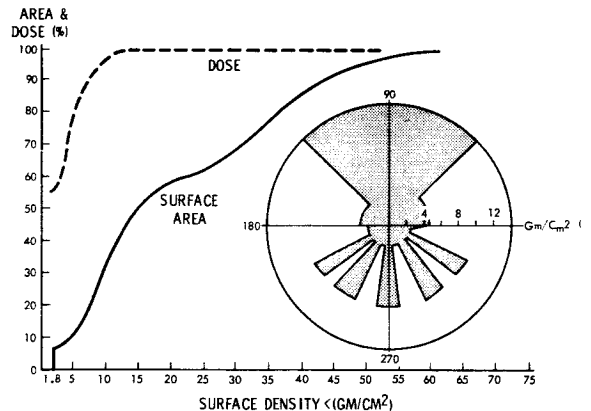


FIGURE 6.—Apollo geometry—dose relationship.

is located behind the astronaut's head primarily between the 5 windows. A cross-sectional distribution of the thickness through the window region is shown as an inset in figure 6. Figure 6 is important because it demonstrates that, if the need ever arises to reduce the dose below that which was previously discussed, added protection could be placed in a fairly restricted

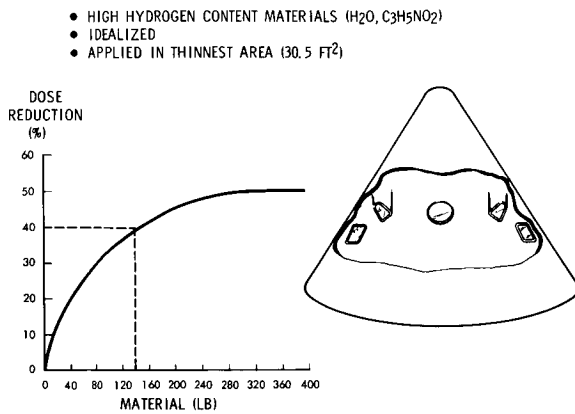


FIGURE 7.—Apollo CM weight—dose reduction relationship.

region providing for an effective means of dose reduction. This point is demonstrated in figure 7.

A trade-off study was performed in terms of percent dose reduction in comparison to the amount of material required, if this material were placed in the thin region previously described. This region represents approximately 30 square feet, against which various thicknesses of a high hydrogen content material such as water were placed. It is stressed that this is an idealized representation, no penalties having been assigned for the required means of retention of the material in the location indicated. It can be seen that approximately 140 pounds of material in this thin region could reduce the dose by 40%. The reason for the rapid flattening of the curve near the 50% point is the dose contribution from other regions of the spacecraft.

Based on the results of the previous figure, a search was initiated for materials and/or equipment items already onboard the spacecraft which could be positioned against the thin region during an emergency, if it were desired to reduce the dose below the levels previously shown. Since water is a near optimum shielding material, a detailed investigation was performed in terms of water available on the spacecraft from the fuel cells for the total mission profile. The amount of water available from this source, is of course, a function of the electric power requirement which varies throughout the mission. This meant that, from a protection standpoint, one could count only

on the minimum amount of water available consistent with other mission water requirements. The amount of dose reduction which could be obtained by that method was approximately 18%. Other equipment items were investigated, a few of which are shown in table I. The most attractive of these are the LiOH canisters, of which 24 are available. These canisters are utilized for CO₂ removal in the spacecraft and have dimensions of 7 inches by 7 inches by 5 inches. If we were to use these canisters in their present shape, a dose reduction of approximately 15% could be achieved. If, however, they could be redesigned into a more pancake shape so that they would cover a larger surface area, a dose reduction of 35% would result. The LiOH canisters provide a good illustration of the interaction between the spacecraft designer, and the shielding specialist's requirements. Redesign of the canisters would have a strong impact on the environmental control hardware. Since at present the need for added protection has not been made evident, the environmental control system's design has not been modified.

The previous discussion has demonstrated that, if ever required, relatively simple methods are available which could be utilized to reduce previously discussed dose levels by a substantial amount without imposing significant weight penalties on the CSM.

DYNAMIC PROTECTION METHODS

In conjunction with dose reduction, it has been our feeling that dynamic protection methods are superior to static means for space trips of a few weeks in terms of weight effectiveness. Dynamic methods refer to instrumentation either on the ground or in the spacecraft, such as a warning system and other means of radiation detection. These would give the astronaut the information required to permit him to take appropriate action, particularly for extra CSM activities, i.e., in LEM or the lunar surface. Such instrumentation is light in weight compared to the more conventional static protection such as shields which are permanently built into the spacecraft. Fixed shields would, of course, be carried on every mission, regardless of whether a solar event took place, with resulting increased booster require-

TABLE I

Dose Reduction with Spot Shielding in Window Region of CSM

Shielding methods	Percent of unshielded dose
No spot shielding.....	100
Minimum H ₂ O available.....	82
Maximum H ₂ O available.....	70
Redesigned LiOH canister.....	65
Polyurethane panel.....	60
Maximum shielding in window region..	50

ments. The radiation instrumentation has been designed to provide the astronaut with the degree of flexibility required to permit intelligent modification of the mission as may be desirable. As was previously discussed, the probability of receiving a particular dose on a typical lunar mission is a function of the mission profile and the astronauts' residence in both the CSM, LEM, and lunar surface. If one could develop a warning system, for example, which would alert him prior to entry into LEM and to postpone, if necessary, this particular mission phase for some hours, a substantial improvement would result in terms of total mission success reliability.

The dynamic protection methods referred to earlier are two-fold:

1. A warning system to be installed on earth which will alert the astronaut of an impending solar event and permit him to initiate protective action; this installation is presently being implemented by the NASA.

2. A radiation system onboard the spacecraft which will detect the environmental level exterior and interior to the command module, and permit the astronaut to orient the spacecraft in a preferred direction with respect to the sun, if such orientation does not interfere with other mission requirements. Preferred orientation will allow the utilization of the maximum protection available from the spacecraft by interposing the heavily shielded service module between the radiation and astronaut, if the event is anisotropic.

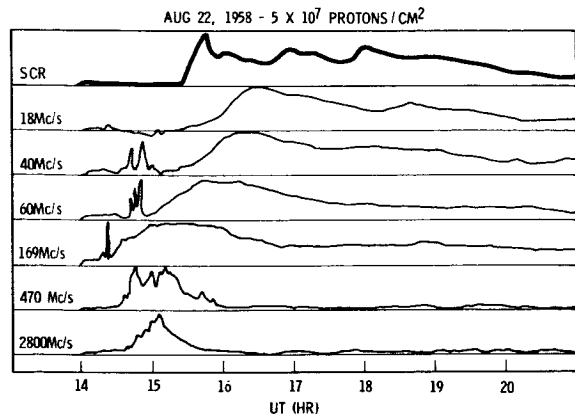


FIGURE 8.—Typical proton event and RF emission relationship.

NAA has investigated a whole series of warning phenomena including:

1. Solar RF Emission
2. Solar X-Rays
3. Solar Ultra-Violet Rays
4. Solar Flares (Visible)
5. Solar Magnetic Field Distribution
6. Ionospheric Disturbances

The most attractive of these presently appears to be the RF emission from the sun at approximately 2800 Mc/s as shown in figure 8. Such RF emissions result in an average of a 2-hour warning period before solar particle arrival.

When dealing with warning requirements, the problem is two-fold. One must determine (1) whether the signal represents proton events in general, and (2) if the information is to be useful in taking corrective action, what size solar event the particular signal represents. In order to develop the required confidence in the RF warning system, a thorough search and study was performed of the available RF data for known solar proton events during the past solar cycle. The details of these studies are the subject of a previously presented paper (ref. 1).

A systematic analysis was performed utilizing relevant signature characteristics, as shown in figure 9, to determine whether the particular signal represented a proton or non-proton flare. These results are shown in figure 10, which compares the reliability of known RF signals to proton event sizes as obtained from the Goddard proton manual (ref. 2). It is evident that, for the larger events, the proper analysis of the RF

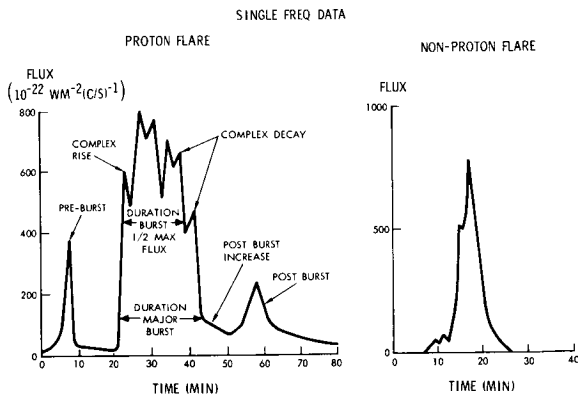


FIGURE 9.—Model RF signatures.

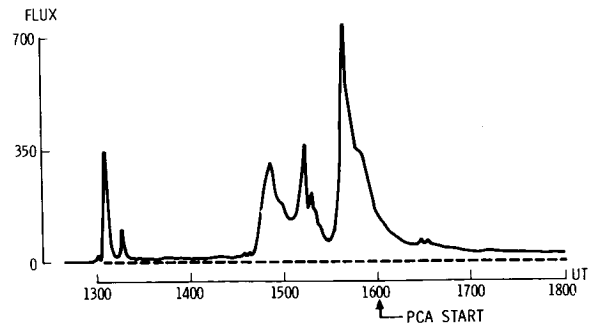


FIGURE 11.—Proton event, 16 September 1963.

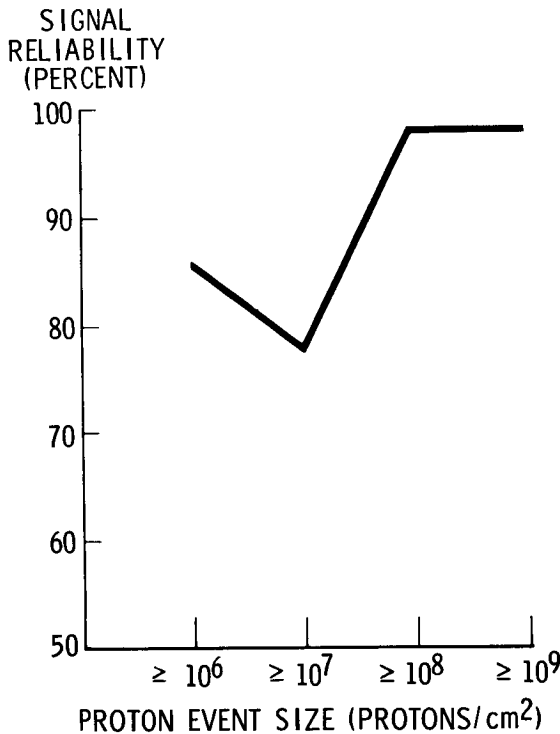


FIGURE 10.—Reliability for predicting solar proton events for 2800 Mc/s RF emissions. (Probability of warning success is 100%.)

signal provides intelligence which is approximately 96% reliable, whereas for the smaller events, this reliability is in the order of 70%. Insofar as the Apollo mission is concerned, only events in the order of $10^9 p^+/cm^2 > 30$ MeV cm^2 size are meaningful in terms of dose.

One is always reluctant to draw conclusions from past history and project these into the future. The warning analysis results were

tested in a small way recently. On September 16, 1963, a very active series of solar events took place, during which RF signals were noted. Through the courtesy of Dr. Covington of the National Research Council of Ottawa, Canada, the RF signature as illustrated in figure 11 was received. This signature was analyzed through the methods previously discussed to determine: (1) if it represented a proton event; and (2) the size of the event. It was concluded that this RF signal did represent a proton event in the low $10^7 p^+/cm^2 > 30$ MeV size. Several months later it was learned from the Douglas Aircraft Company, which had a riometer located on the South Pole, that their calculations indicated that this event was in the order of 10^6 to $10^7 p^+/cm^2 > 30$ MeV. This check in our methods gave us added confidence that the RF method of proton detection, even for short warning time periods, can be a useful tool and of particular importance for LEM and lunar surface operations.

With regard to dose reduction by means of spacecraft orientation during an anisotropic event, one must, first, postulate orientation modes for the spacecraft and, second, synthesize a model for the anisotropic behavior of the solar event. Figure 12 shows some of the orientation modes considered in the studies. These assumed that the radiation would be intercepted by the heavily shielded service module and/or the relatively thin window region previously described, in order to compare the relative effectiveness of these extreme orientations. Figure 13 shows an example of the degree of anisotropy considered in the model. It is seen that for the first 60 minutes of this

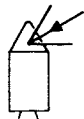
SOURCE	S C ORIENTATION
• ANISOTROPIC	THIN REGION (C/M) 
• ANISOTROPIC	THICK REGION (S/M) 
• ISOTROPIC	RANDOM

FIGURE 12.—CSM orientation modes.

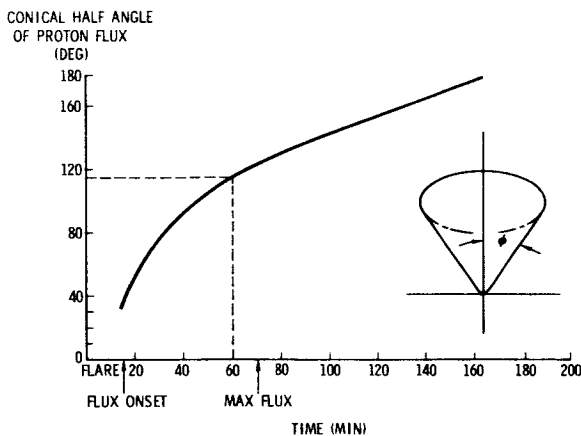


FIGURE 13.—Anisotropy model. Time dependent distribution, 4 May 1960.

event, for example, the total flux is contained in a cone of approximately 110° half angle, whereas complete isotropy is represented by 180° . It is evident that the degree of anisotropy is strongly time dependent. It was assumed that various levels of anisotropy were present up to the time of peak flux and thereafter assumed that the event was completely isotropic for the remainder of the event's duration. A previous paper has discussed this model in detail (ref. 3). Figures 14 and 15 show the results of the dose calculations. Comparison was made of the anisotropic model previously discussed to an event containing the same number of particles but having no directional characteristics, i.e., total isotropy. It is seen from figure 14 that the ratio of anisotropic to isotropic dose is a strong function of the region of penetration of the radiation field. With

regard to the extreme positions when the beam is assumed to enter through the thin region, figure 15 shows a potential increase of the dose by 45% in comparison to isotropic dose levels, whereas the optimum shielding position through the service module would reduce the dose approximately 20%. Although dose reduction by means of orientation does not appear too significant, particularly when other spacecraft orientation requirements are considered, its value resides chiefly in avoiding the exposure of the relatively thinner regions of the spacecraft to the anisotropic radiation field.

Returning briefly to the reliability considerations which were discussed earlier concerning the radiation dose picture, NAA has developed a computer program using Monte Carlo techniques which permits the assessment of the effective reliability of the "radiation system" of the spacecraft. The total capabilities of the program cannot be treated in this paper. Briefly stated, however, consideration is given in a random fashion to the occurrence of 1, 2, 3, or more flares based on the past solar cycle, including the random occurrence of the flares in the mission, the mission phase in question, and the assessment of the dose for various operational modes. NAA has flown 21 000 Apollo missions to the moon and return with this program during which assessment has been made, for example, of the effects of various mission modification criteria, assuming that modification decisions are made as a function of the radiation dose received at any time during the mission. This is illustrated in figure 16, which shows the percent of total missions during which the various decision criteria would have been exceeded; i.e., had the various decision criteria been implemented, the ordinate shows the percent of missions which would have been affected both in terms of total missions, and in terms of mission phase (Command Service Module, Lunar Excursion Module, and Lunar Surface), during which the decisions would have taken place. For example, if the mission were to be modified after the dose reaches 50 rads, 9 percent of all missions would be affected, of which 4 percent of the occurrences are in the CSM, 4 percent in LEM, and 1 percent on the lunar surface.

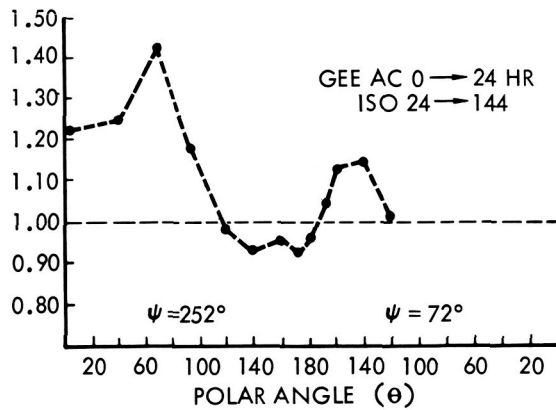
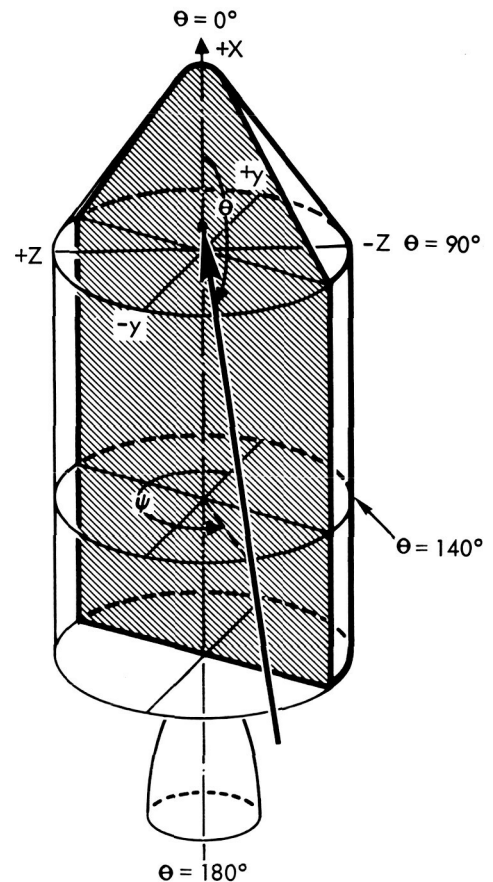
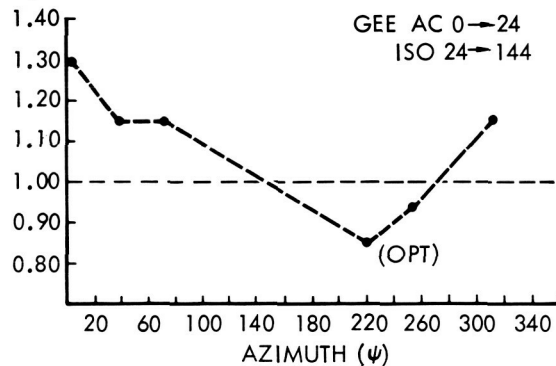
ANISOTROPIC/ISOTROPIC
(DOSE)ANISOTROPIC/ISOTROPIC
(DOSE)

FIGURE 14.—Effect of spacecraft orientation on dose.

If one resorts to mission modification in order to reduce the dose, the next question is how much dose saving can be realized by means of this type of operation. Figure 17 shows a typical output from the program. For a mission termination criteria of 50 rads, for example, 10 to 20 percent of dose reduction would have been achieved for 8 percent of the missions, 40 to 50 percent dose reduction for 12 percent of the missions, and so on. The aforementioned examples are typical of the type of information which can be obtained.

*EFFECT OF RADIATION ENVIRONMENT OF
MATERIALS AND SUBSYSTEMS*

In addition to the radiation protection activities on Apollo for the astronaut, NAA is actively involved in assuring the reliable performance of

materials and subsystems with regard to the nuclear radiation environment.

The windows, heat protection system, coatings, RCS fuel gage system, and high-gain antenna are a few of the materials and subsystems which have been analyzed with respect to radiation damage. In general, it may be stated that materials used on Apollo can easily withstand the worst environment which can be contemplated during a 2-week mission. In the case of the windows, for example, a fused silica glass was selected after proton irradiation tests on several materials indicated that fused silica was superior for design purposes. Concern was expressed earlier in the program with regard to the deterioration of the ablative heat protection system due to the high exterior radiation flux levels. The irradiation of heat protection

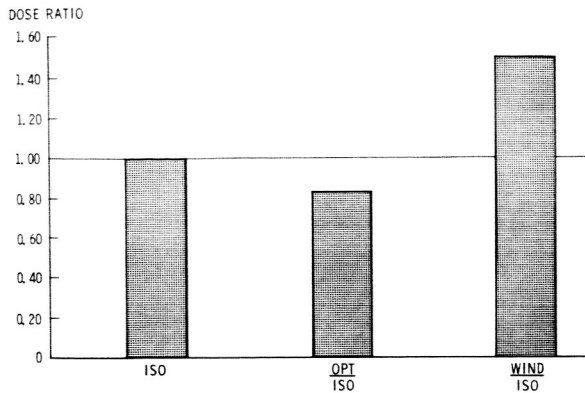


FIGURE 15.—Effect of orientation on dose.

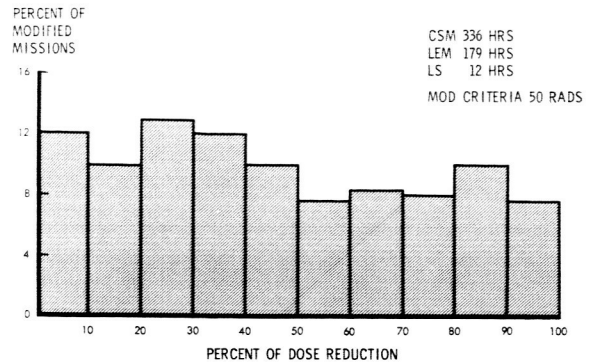


FIGURE 17.—Effect of mission modification on dose reduction. 21 000 missions IGY.

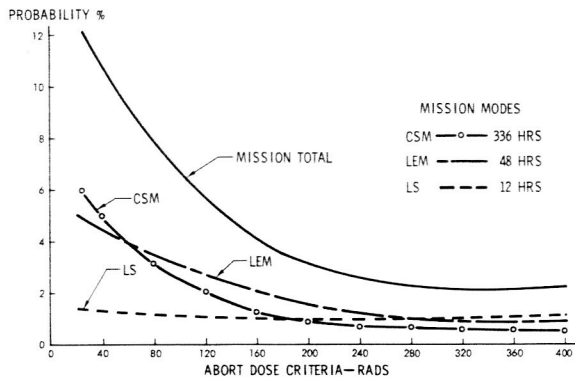


FIGURE 16.—Probability of exceeding abort criteria during a lunar mission. 21 000 missions IGY.

material samples, and ablative tests before and after irradiation with protons, showed no effect on material performance for the material which will be utilized on the Apollo vehicle. With regard to the other systems listed above, NAA is actively working with the subcontractors of the systems to avoid any deterioration. Let me cite for example, the Reaction Control System fuel gage. This gage consists of a nucleonics system utilizing a cobalt 60 source, which, as a result of its attenuation through the fuel tank, will measure the amount of fuel available. The original detection system for this design was sensitive to protons from a solar flare event which would have resulted in an

erroneous fuel quantity reading. In conjunction with the subcontractor, a method was worked out which will prevent such erroneous readings from taking place.

In general, it may be stated that materials and methods are available which can withstand the Apollo radiation environment. Intelligent awareness must, however, be shown during the early development in making proper choices if expensive redesign is to be avoided.

CONCLUDING REMARKS

In summary, it is our present feeling that based on the expected environment and allowable doses, the degree of protection to the astronauts available in the Command/Service Modules is adequate. It is also felt that a reasonable cushion against surprises is available, in the event that the coming solar cycle is substantially more active than the past, through the utilization of the warning system, spacecraft orientation, and various levels of dose reduction by means of spot shielding.

It is evident, of course, that efforts of this scope, in part previously presented, can never be the contribution of a single individual. Grateful acknowledgment is extended to the staff members of the Apollo Nuclear Radiation Protection Unit for their imaginative contributions in this pioneering effort.

REFERENCES

1. FLETCHER, J. D.: Solar Radio Emission as Criteria for Solar Proton Event Warning. Proc. of Am. Inst. Aeron. Astronaut. (New York), Jan. 1964.
2. McDONALD, FRANK B. ed.: Solar Proton Manual, NASA TR R-169, Dec. 1963.
3. STAZER, A. K.: A Model Anisotropic Solar Proton Event, AIC. Proc. of Am. Inst. Aeron. Astronaut. (New York), Jan. 1964.

N65 34618

42—Optimum Solar Cell Shielding for the Advanced Orbiting Solar Observatory

HOWARD WEINER

Republic Aviation Corporation

The National Aeronautics and Space Administration, as a continuation of its Solar Physics Program, has established the requirement for an Advanced Orbiting Solar Observatory (AOSO). Republic Aviation Corporation was selected as prime contractor for AOSO, under the cognizance of the NASA Goddard Space Flight Center.

The AOSO will be required to point accurately at any position on the sun to within ± 5 arc-seconds and be able to provide continual solar observations for many months. This pointing accuracy permits the location and observation, in fine detail, of centers of X-ray, ultra-violet ray, and gamma-ray portions of the spectrum that cannot penetrate the earth's atmosphere. Long-term continuous observation of the sun is obtained by orbiting the AOSO at 300 nautical miles and an inclination of 97.6° . The near-polar retrograde orbit will provide continuous solar illumination of the observatory for periods of up to nine months, since at this inclination, the earth's oblateness provides a mechanism of progressing the orbit plane in synchronism with the revolution of the earth around the sun. Total operational period of AOSO is one year.

The basic AOSO structure is that of a cylinder with one end (forward) pointed continuously at the sun. This cylinder is approximately 125 inches long with a diameter of 48 inches. Solar experiments are housed at the forward end of the spacecraft, while controls and electronics are aft. At the aft end are also located eight solar paddles which are fixed, after erection in orbit, since the spacecraft is solar-oriented. Up to 100 square feet of solar cell area will be accommodated by these paddles.

During the operational lifetime of the AOSO, the spacecraft will be exposed to both the particles in the Trapped Radiation Belts and solar flare protons over the polar caps. These radiations could severely degrade the solar cells, unless shielding is provided for their protection. Cover-glass shielding, however, will add weight to the satellite. This weight might be more useful in the form of an additional solar cell allowance for radiation degradation rather than as shielding. A proper trade-off, described below, between shielding and solar paddle area is therefore necessary to obtain the minimum weight penalty.

SOLAR PADDLE DESIGN PARAMETERS

The pertinent material layers in a solar paddle are shown in figure 1.

If the solar paddles are normal to the incident light, the net thermal power reaching the surface of the cells is:

$$h_s = h_0 \left\{ e^{-\left(\frac{\mu}{\rho}\right)_s \tau_s} \right\} G_s \quad (1)$$

where: h_s = Net thermal power reaching cell surface, watts/ft²

h_0 = Normally incident light intensity on paddle, watts/ft²

τ_s = Effective areal density of solar cell shield, lb/ft²

$(\mu/\rho)_s$ = Mass absorption coefficient of shield for light, ft²/lb

G_s = Interfacial reflection loss factor in shield

The effective shield thickness is made up of the cover glass and transparent adhesive

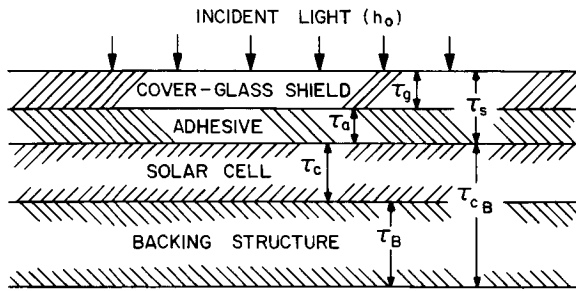


FIGURE 1.—Solar paddle material layers.

layers, that is:

$$\tau_s = \tau_g + \tau_a \tag{2}$$

where: τ_g = Cover glass areal density, lb/ft²
 τ_a = Adhesive areal density, lb/ft²

While the mass absorption coefficient of the shield is defined as:

$$\left(\frac{\mu}{\rho}\right)_s = \frac{1}{\tau_s} \left[\left(\frac{\mu}{\rho}\right)_g \tau_g + \left(\frac{\mu}{\rho}\right)_a \tau_a \right] \tag{3}$$

where: $(\mu/\rho)_g$ = Mass absorption coefficient of cover glass, ft²/lb

$(\mu/\rho)_a$ = Mass absorption coefficient of adhesive, ft²/lb

The light finally reaching the solar cells is converted to electrical energy with an efficiency:

$$\eta_e = p_e / h_s \tag{4}$$

where: p_e = Specific power output of solar cells, watts/ft²

η_e = Solar cell conversion efficiency

Combining equations (1) and (4), the cell output at any time is given by:

$$p_e = \eta_e h_0 G_s e^{-(\mu/\rho)_s \tau_s} \tag{5}$$

While the total power output of a solar paddle is:

$$P_e = \eta_e A_p h_0 G_s e^{-(\mu/\rho)_s \tau_s} \tag{6}$$

where: P_e = Solar paddle electrical output, watts

A_p = Solar paddle area for power conversion, ft²

A schematic of the solar paddle is shown in figure 2.

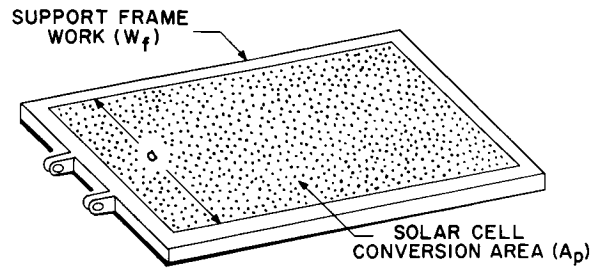


FIGURE 2.—Solar paddle.

The total weight of the solar paddle is:

$$W_p = W_f + W_c \tag{7}$$

where: W_p = Total weight of paddle, lb
 W_f = Weight of support framework, lb
 W_c = Weight of conversion section, lb

Examination of figure 1 shows that the weight of the conversion section is given by:

$$W_c = A_p (\tau_c + \tau_B + \tau_s) \tag{8}$$

where: τ_c = Areal density of solar cells, lb/ft²
 τ_B = Areal density of cell backing, lb/ft²

For simplicity in analysis, we define:

$$\tau_{CB} = \tau_c + \tau_B \tag{9}$$

where: τ_{CB} = Areal density of paddle behind shield, lb/ft²

Combining equations (7) to (9), the total paddle weight is:

$$W_p = W_f + A_p (\tau_s + \tau_{CB}) \tag{10}$$

Since the weight of the framework is dependent on the perimeter of the solar paddle, it can be shown that

$$W_f = \left(\frac{2d_f}{a}\right) (a^2 + A_p) \tag{11}$$

where: a = Paddle width, ft
 d_F = Lineal density of support framework, lb/ft

Substituting for W_F in equation (10), the total paddle weight is:

$$W_p = (2ad_F) + A_p \left(\tau_s + \tau_{CB} + \frac{2d_F}{a} \right) \quad (12)$$

Rearranging equation (6), we may obtain an expression for solar paddle conversion area. Substituting this expression into equation (12), we have for the total paddle weight at any time during the mission:

$$W_p = (2ad_F) + \left(\frac{P_e}{\eta_e G_s h_0} \right) \left(\tau_s + \tau_{CB} + \frac{2d_F}{a} \right) e^{\left(\frac{\mu}{\rho} \right)_s \tau_s} \quad (13)$$

In terms of the power requirements and solar cell and cover glass qualities at the end of the mission:

$$W_p = (2ad_F) + \left(\frac{P_{ef}}{\eta_{ef} G_s h_0} \right) \left(\tau_s + \tau_{CB} + \frac{2d_F}{a} \right) e^{\left(\frac{\mu}{\rho} \right)_{ef} \tau_s} \quad (14)$$

where: P_{ef} = Solar paddle electrical output at the end of the mission, watts
 η_{ef} = Solar cell conversion efficiency at the end of the mission
 $(\mu/\rho)_{ef}$ = Mass absorption coefficient of shield, for light, at the end of the mission, ft²/lb

During the mission, the solar cell conversion efficiency is degraded by interaction with the space environment. This degradation is given by:

$$\lambda_c = 1 - \frac{\eta_{ef}}{\eta_{ei}} \quad (15)$$

where: λ_c = Solar cell degradation factor
 η_{ei} = Solar cell conversion efficiency at the start of the mission

In like manner, the cover glass shielding and adhesive are degraded by the space environment and absorb more of the incident light. The form of this degradation factor is given by:

$$\lambda_s = 1 - \left\{ \frac{e^{-(\mu/\rho)_s \tau_s}}{e^{-(\mu/\rho)_{st} \tau_s}} \right\} \quad (16)$$

where: λ_s = Shielding transmission degradation factor

$(\mu/\rho)_{st}$ = Shield mass absorption coefficient, for light, at the start of the mission, ft²/lb

Substituting equations (15) and (16) into equation (14), the total solar paddle weight is:

$$W_p = (2ad_F) + \left(\frac{P_{ef}}{\eta_{ef} G_s h_0} \right) \frac{\left(\tau_s + \tau_{CB} + \frac{2d_F}{a} \right)}{(1-\lambda_c)(1-\lambda_s)} e^{\left(\frac{\mu}{\rho} \right)_{st} \tau_s} \quad (17)$$

Defining the overall power degradation factor as:

$$\lambda_p = 1 - \frac{P_{ef}}{P_{ei}} \quad (18)$$

where: P_{ei} = Power output at start of mission, watts

λ_p = Overall power degradation factor

it can be shown that:

$$(1-\lambda_p) = (1-\lambda_c)(1-\lambda_s) \quad (19)$$

and hence the total weight of the solar paddle, in terms of its pertinent design parameters, is given by:

$$W_p = (2ad_F) + \left(\frac{P_{ef}}{\eta_{ef} G_s h_0} \right) \frac{\left(\tau_s + \tau_{CB} + \frac{2d_F}{a} \right)}{(1-\lambda_p)} e^{\left(\frac{\mu}{\rho} \right)_{st} \tau_s} \quad (20)$$

OPTIMIZATION OF SOLAR CELL SHIELDING

The necessary and sufficient conditions for an optimum shielding thickness may be obtained by taking successive derivatives of equation (20) with respect to this thickness. Thus, the first derivative of (W_p) with respect to (τ) is:

$$\frac{dW_p}{d\tau_s} = \frac{P_{ef}}{\eta_{ef} G_s h_0} \left[\frac{e^{(\mu/\rho)_{st} \tau_s}}{(1-\lambda_p)} \right] \left\{ 1 + \left(\tau_s + \tau_{CB} + \frac{2d_F}{a} \right) \left[\left(\frac{1}{1-\lambda_p} \right) \frac{d\lambda_p}{d\tau_s} + \left(\frac{\mu}{\rho} \right)_{st} \right] \right\} \quad (21)$$

while the expression for the second derivative of (W_p) with respect to (τ_s) is:

$$\begin{aligned}
& \left\{ \left(\frac{\eta_{ei} G_s h_0}{P_{ef}} \right) \frac{(1-\lambda_p)}{e^{(\mu/\rho)_{st} \tau_s}} \right\} \left(\frac{d^2 W_p}{d\tau_s^2} \right) \\
& = \left[\left(\frac{-1}{1-\lambda_p} \right) \left(\frac{d\lambda_p}{d\tau_s} \right) + (\mu/\rho)_{st} \right] + \dots \\
& + \left(\tau_s + \tau_{CB} + \frac{2d_F}{a} \right) \left[\left(\frac{1}{1-\lambda_p} \right) \left(\frac{d\lambda_p}{d\tau_s} \right) \right]^2 \\
& + \left(\frac{\tau_s + \tau_{CB} + \frac{2d_F}{a}}{1-\lambda_p} \right) \left(\frac{d^2 \lambda_p}{d\tau_s^2} \right) + \dots \\
& + \left[\left(\frac{\mu}{\rho} \right)_{st} + \left(\frac{1}{1-\lambda_p} \right) \left(\frac{d\lambda_p}{d\tau_s} \right) \right] \\
& \left\{ 1 + \left(\tau_s + \tau_{CB} + \frac{2d_F}{a} \right) \right. \\
& \left. \left[\left(\frac{1}{1-\lambda_p} \right) \left(\frac{d\lambda_p}{d\tau_s} \right) + \left(\frac{\mu}{\rho} \right)_{st} \right] \right\} \quad (22)
\end{aligned}$$

To obtain a relative extremum we set $\frac{dW_p}{d\tau_s} = 0$ and hence a necessary condition for an optimum shield thickness (from eq. (21)) is:

$$\begin{aligned}
& \left\{ 1 + \left(\hat{\tau}_s + \tau_{CB} + \frac{2d_F}{a} \right) \right. \\
& \left. \left[\left(\frac{1}{1-\lambda_p} \right) \left(\frac{d\lambda_p}{d\tau_s} \right) + \left(\frac{\mu}{\rho} \right)_{st} \right] \right\} = 0 \quad (23)
\end{aligned}$$

where: $\hat{\tau}_s$ = Optimum shield thickness, lb/ft²

If we consider minimum weight of solar paddle as an optimum situation, then a sufficient condition for this occurrence is:

$$\left(\frac{d^2 W_p}{d\tau_s^2} \right)_{\tau_s = \hat{\tau}_s} > 0 \quad (24)$$

Substituting equation (23) into equation (22) we note that:

$$\begin{aligned}
\left(\frac{d^2 W_p}{d\tau_s^2} \right)_{\hat{\tau}_s} & = \left[\left(\frac{P_{ef}}{\eta_{ei} G_s h_0} \right) \frac{e^{(\mu/\rho)_{st} \tau_s}}{(1-\lambda_p)} \right] \left\{ 2 \left(\frac{\mu}{\rho} \right)_{st} \right. \\
& + \left(\frac{\mu}{\rho} \right)_{st}^2 \left(\hat{\tau}_s + \tau_{CB} + \frac{2d_F}{a} \right) + \dots \\
& \left. + \left(\frac{\hat{\tau}_s + \tau_{CB} + \frac{2d_F}{a}}{1-\lambda_p} \right) \left(\frac{d^2 \lambda_p}{d\tau_s^2} \right)_{\hat{\tau}_s} \right\} \quad (25)
\end{aligned}$$

Since all the known terms in equation (25) are positive, then the sufficient condition for an

optimum shield thickness reduces to:

$$\left(\frac{d^2 \lambda_p}{d\tau_s^2} \right)_{\hat{\tau}_s} > 0 \quad (26)$$

Taking note of equation (19), we then have:

$$\begin{aligned}
\frac{d^2 \lambda_p}{d\tau_s^2} & = (1-\lambda_c) \left(\frac{d^2 \lambda_s}{d\tau_s^2} \right) + (1-\lambda_s) \left(\frac{d^2 \lambda_c}{d\tau_s^2} \right) \\
& - 2 \left(\frac{d\lambda_c}{d\tau_s} \right) \left(\frac{d\lambda_s}{d\tau_s} \right) \quad (27)
\end{aligned}$$

Defining a light extinction coefficient as:

$$\delta_s = \frac{(\mu/\rho)_{st}}{(\mu/\rho)_{sf}} \quad (0 \leq \delta_s \leq 1) \quad (28)$$

where: δ_s = Radiation-induced extinction coefficient

we obtain a new expression for the shielding, light-transmission degradation factor (eq. (16)), that is:

$$\lambda_s = 1 - \exp \left\{ - \left[\left(\frac{\mu}{\rho} \right)_{st} \tau_s \right] \left(\frac{1}{\delta_s} - 1 \right) \right\} \quad (29)$$

Taking successive derivatives of (λ_s) with respect to (τ_s) and substituting into equation (27) we have

$$\begin{aligned}
\frac{d^2 \lambda_p}{d\tau_s^2} & = (1-\lambda_s) \left(\frac{d^2 \lambda_c}{d\tau_s^2} \right) \\
& - 2(1-\lambda_s) (\mu/\rho)_{st} \left(\frac{1}{\delta_s} - 1 \right) \left(\frac{d\lambda_c}{d\tau_s} \right) + \dots \\
& - (1-\lambda_s)(1-\lambda_c) (\mu/\rho)_{st}^2 \left(\frac{1}{\delta_s} - 1 \right)^2 \quad (30)
\end{aligned}$$

Hence, if we are to fulfill the sufficient conditions for an optimum shielding thickness to exist (eq. (23)) it is required that the following inequality hold:

$$\begin{aligned}
\left(\frac{d^2 \lambda_c}{d\tau_s^2} \right) & > \left[\left(\frac{\mu}{\rho} \right)_{st} \left(\frac{1}{\delta_s} - 1 \right) \right] \\
& \left\{ (1-\lambda_c) \left[\left(\frac{\mu}{\rho} \right)_{st} \left(\frac{1}{\delta_s} - 1 \right) \right] + 2 \left(\frac{d\lambda_c}{d\tau_s} \right) \right\} \quad (31)
\end{aligned}$$

While the optimum shield thickness (eq. (23)) reduces to:

$$\hat{\tau}_s = \left[\frac{(1-\lambda_c)}{\left(-\frac{d\lambda_c}{d\tau_s} \right) - \left(\frac{1-\lambda_c}{\delta_s} \right) \left(\frac{\mu}{\rho} \right)_{st}} \right] - \left(\tau_{CB} + \frac{2d_F}{a} \right) \quad (32)$$

Relations between solar cell degradation and shield thickness are discussed in the sections following.

RADIATION EFFECTS ON SOLAR CELLS

Space radiations will cause a reduction in the power output of a solar cell array via either damage to the photovoltaic cell or darkening of the cover-glass shielding. A solar cell degradation factor was defined in equation (15), which indicates the dependency of the degradation factor on cell conversion efficiency.

The relation between cell conversion efficiency and minority carrier diffusion length in the cell base may be given by an expression of the type:

$$\left[\frac{l_f/l_i - B_2}{1 - B_2} \right] = e^{-[B_1(1 - \frac{\eta_f}{\eta_i})]} \equiv e^{-B_1\lambda} \quad (33)$$

where: l_f = Final minority carrier diffusion length, cm

l_i = Initial minority carrier diffusion length, cm

B_1, B_2 = Empirical constants dependent on solar cell material

For blue-shifted silicon solar cells, the table below gives values of B_1 and B_2 . These values are believed to hold (ref. 1) under the following conditions:

- $10 \leq l \leq 200$ microns
- $100 \leq l_i \leq 200$ microns
- $1 \leq \text{base resistivity} \leq 10$ ohm-cm

The data, from which the constants in table I are obtained, are shown graphically in figure 3.

Experimental data on radiation damage to solar cells have been correlated by an expression of the form (ref. 2):

$$\frac{1}{l_f^2} = \frac{1}{l_i^2} + \nu_c \quad (34)$$

where: ν_c = solar cell radiation damage factor, cm^{-2}

Equation (34) may be rearranged to yield a more useful expression:

$$l_f/l_i = (1 + \nu_c l_i^2)^{-1/2} \quad (35)$$

TABLE I
Silicon Solar Cell Constants

Cell type	B_1	B_2
N/P-----	7.85	0.025
P/N-----	10.27	0.0185

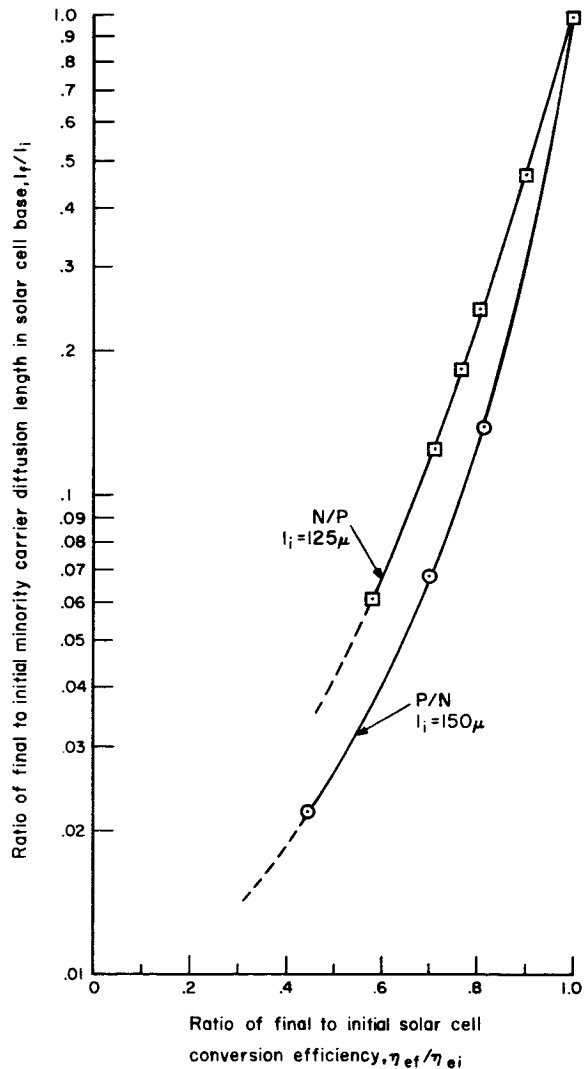


FIGURE 3.—Solar cell conversion efficiency as a function of minority carrier diffusion length. Corrected for space sunlight. Base resistivity equals 1 ohm-cm.

The initial minority carrier diffusion length for 10 Ω -cm N/P silicon solar cells is (based on private communications with R. A. Hoffman, Hoffman Electronics Corp.; and J. G. Leisenring,

Spectrolab):

$$l_i \cong 150\mu \cong 1.5 \times 10^{-2} \text{ cm} \quad (36)$$

In a field of mixed radiations, radiation damage factors are additive and hence:

$$\nu_c = \sum_j \nu_{cj} \quad (37)$$

where

$$\nu_{cj} = \text{Solar cell damage factor for the } j^{\text{th}} \text{ type of radiation, cm}^{-2}$$

For a given type of charged particle, the solar cell radiation damage factor is:

$$\nu_{cj} = \int_t \int_\Omega \int_{E_j} \{ [k_j(E_j)] [F_j(E_j, \Omega)] \} dE_j d\Omega dt \quad (39)$$

where: E_j = Energy of the j^{th} type of charged particle entering sensitive cell volume, MeV

k_j = Radiation damage coefficient for the j^{th} type of charged particle, particles $^{-1}$

F_j = Unidirectional, differential flux of particles of the j^{th} type entering the sensitive volume, particles/cm 2 -sec-MeV-steradian

Ω = Solid angle, steradians

t = Time of exposure to radiation, sec

As indicated in equation (39) above, the cell radiation damage factor (ν_{cj}) may be reduced by two approaches. First, we may reduce the radiation damage factor (k_j) by using more radiation-resistant cells. This is accomplished by using N/P rather than P/N silicon cells and by using a 10 ohm-cm rather than a 1 ohm-cm cell base-resistivity. The second method of reducing damage is to suppress the flux term (F_j) via the use of a cover-glass shield.

Data have been obtained (ref. 1) for the variation of electron damage coefficients with electron energy. These data have been plotted against residual range in the sensitive volume (fig. 4), yielding an expression of type:

$$k_e(\xi_e) = \sum_{m=1}^2 K_{em} \xi_e^{\alpha_{em}} \quad (40)$$

where: ξ_e = Residual range of electrons in silicon, gm/cm 2

K_{em}, α_{em} = Material constants

The variation of (k_e) with base sensitivity of the cell is shown in figure 5. These data were also obtained from reference 1.

The constants in equation (40) are given in table II below:

TABLE II
N/P Silicon Solar Cell Electron Damage Constants

1 ohm-cm base resistivity		
m	α_{em}	K_{em} (1 ohm-cm) \sim (electrons $^{-1}$)
1	2.019	2.43×10^{-9}
2	2.070	-2.00×10^{-9}

while from figure 5 we obtain

$$\frac{K_e(10 \text{ ohm-cm})}{K_e(1 \text{ ohm-cm})} \cong 0.509 \quad (41)$$

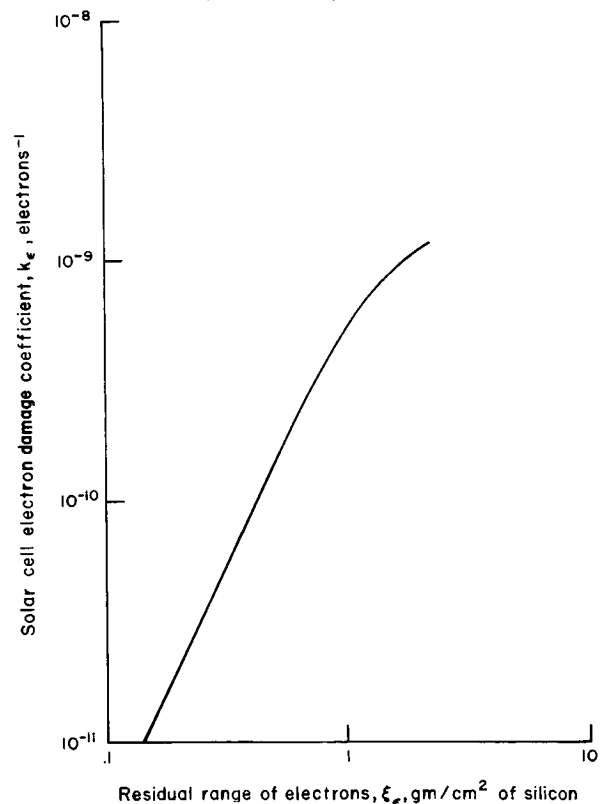


FIGURE 4.—Silicon solar cell electron damage coefficients for N/P silicon solar cells with 1 ohm-cm base resistivity.

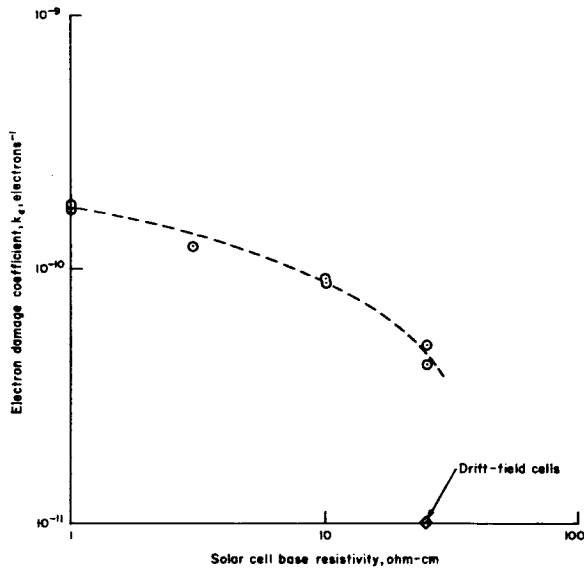


FIGURE 5.—The effect of solar cell base resistivity on electron damage, N/P silicon cells. $E_e=1$ MeV.

Data have been obtained from references 1, 3, 4, 5, and 6 (figs. 6 to 8) which indicate that the variation of proton damage coefficient with residual range is given as:

$$k_p(\xi_p) = K_p \xi_p^{\alpha_p} \quad (42)$$

where: ξ_p = Residual range of protons in silicon \sim gm/cm²

K_p, α_p = Material constants

Table III shows the variation of the above constants, with cell material.

TABLE III

Solar Cell Damage Constants (Protons)

Cell type	Cell material	Base resistivity (ohm-cm)	K_p	α_p
N/P	Silicon	1	7.714×10^{-7}	-0.272
		10	2.62×10^{-7}	-0.480

AOSO RADIATION ENVIRONMENT

Within the constraints of its 300 n-mile, circular, near-polar orbit, the major sources of radiation which can affect the solar cells are:

- Trapped radiation belts
- Solar flare protons

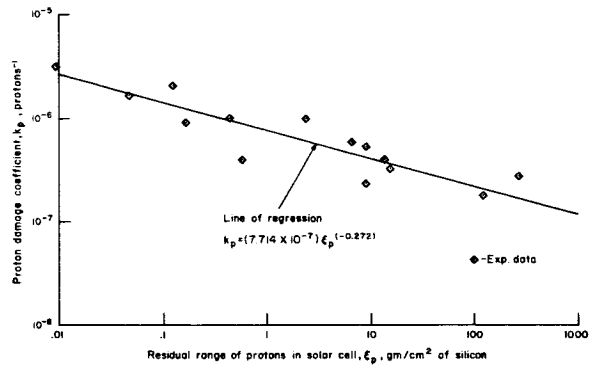


FIGURE 6.—Silicon solar cell proton damage coefficients, N/P cells; base resistivity = 1 ohm-cm.

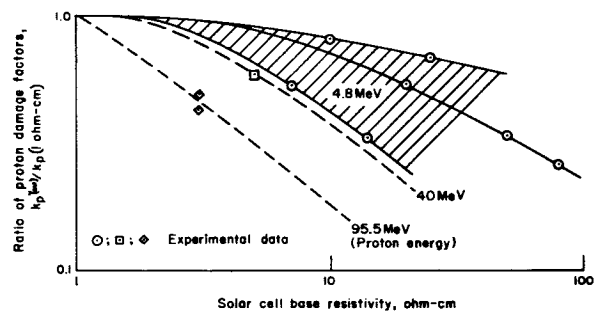


FIGURE 7.—The effect of solar cell base resistivity on proton damage, N/P silicon cells.

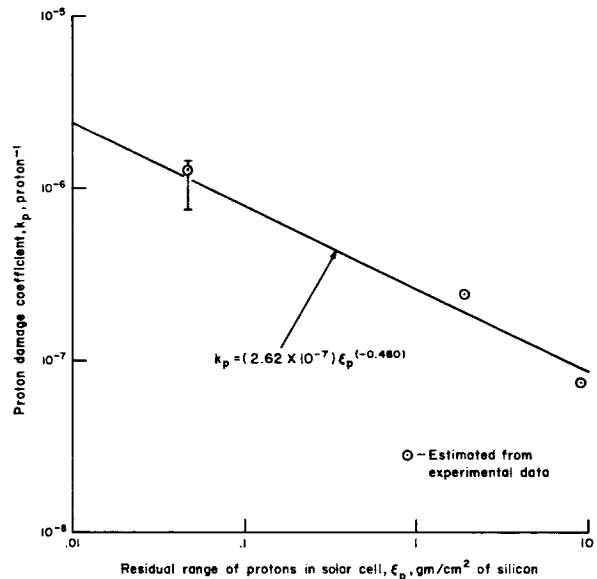


FIGURE 8.—Silicon solar cell proton damage coefficients, N/P cells; base resistivity = 10 ohm-cm.

Trapped Radiation Belts

The terrestrial trapped radiation belts consist of the natural Van Allen proton and electron belts and the artificial electron belt created by the July 9, 1962, high altitude nuclear explosion ("Starfish").

Trapped Electron Flux. Decay of the electron component in the trapped radiation belts has been observed since the "Starfish" explosion. The new data on electron intensities has been estimated by Hess (private communication) for a near AOSO orbit (300 nautical miles—90° inclination). These data correspond to the epoch November 1962. The lower and upper limits of the electron flux above 0.5 MeV are:

$$\Phi_{se}(>0.5)_{upper} = 7.8 \times 10^{10} \text{ electrons/cm}^2\text{-day} \quad (43)$$

$$\Phi_{se}(>0.5)_{lower} = 2.8 \times 10^{10} \text{ electrons/cm}^2\text{-day} \quad (44)$$

where:

$$\Phi_{se}(>E_{se}) = \text{Integral, omnidirectional electron flux above } E_{se}, \frac{\text{electrons}}{\text{cm}^2\text{-sec}}$$

$$E_{se} = \text{Electron energy, MeV}$$

Uncertainties in these fluxes are about a factor of two.

The approximate distribution of electrons in various energy levels, for the November 1962 epoch, are given in table IV.

TABLE IV

Trapped Radiation Belt Electron Spectrum
(300 n miles ~ 90° inclination—Nov. 1962)

ΔE_{se} , MeV	% electrons in ΔE_{se}
0.5-1	37.4
1-2	19.3
2-3	30.4
3-4	11.1
4-5	1.24
5-6	.42
6-7	.14
7-8	.03

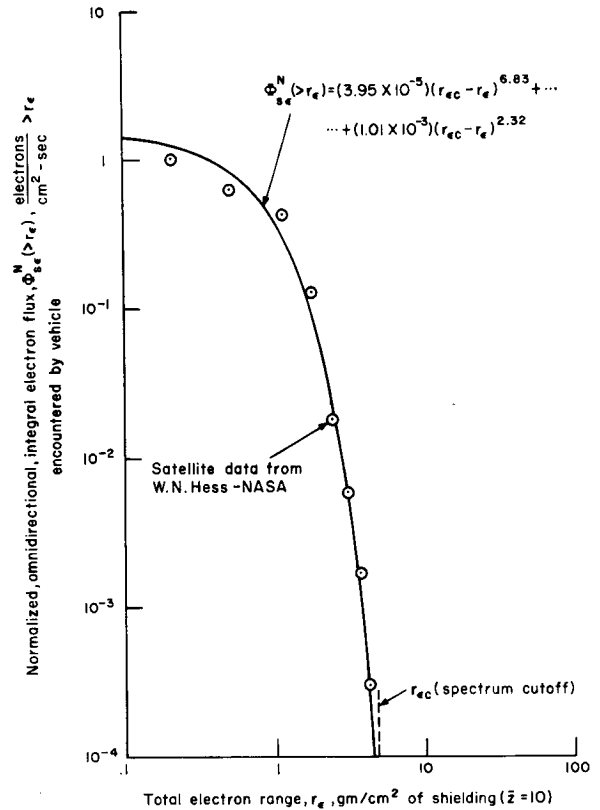


FIGURE 9.—Trapped radiation belt electron spectrum for the epoch, November 1962. Polar orbit; 300 n. mile altitude.

The data in table IV are shown in figure 9 in terms of total electron range in SiO₂ shielding, rather than electron energy. Using the upper limit of the total electron flux (eq. (42)), the spectrum in figure 9 may be closely approximated by an expression of the type:

$$\Phi_{se}(>r_e) = \sum_{n=1}^2 Q_{sen} (r_{ec} - r_e)^{\gamma_{en}} \quad (45)$$

where:

Q_{sen}, γ_{en} = Constants depending on time of exposure to electron flux and orbital altitude

r_e = Range of electron of energy E_{se} in shield material, gm/cm²

r_{ec} = Range of maximum energy electron in vehicle encountered spectrum, 4.85 gm/cm²

Constants for use in equation (45) are given in table V.

TABLE V
Trapped Electron Belt Constants

<i>n</i>	γ_{en}	Q_{en} electrons/cm ² -day
1	6.83	2.55×10^6
2	2.32	6.52×10^7

Trapped Proton Flux. Republic has utilized the "BL+Flux Codes," obtained from Dr. W. N. Hess, NASA-Goddard Space Flight Center. These computer codes describe the spatial variation of particle fluxes trapped in the geomagnetic field. The proton flux is obtained from Explorer VI data. Computer runs, equivalent to 60 orbits, have been made with this program. The resulting AOSO trapped proton flux is:

$$\Phi_{sp}(>30 \text{ MeV}) = 2.66 \times 10^6 \frac{\text{Protons}}{\text{cm}^2\text{-day}} \text{ above } 30 \text{ MeV} \quad (46)$$

where:

Φ_{sp} = Omnidirectional integral proton flux above E_{sp} , (protons/cm²-day above E_{sp})
 E_{sp} = Proton energy, MeV

McIlwain's formulation for the trapped proton spectrum (ref. 7) is:

$$\Phi_{sp}(>E_{sp}) = Q_{sp} e^{-E_{sp}/E_{p0}} \quad (5 \leq E_{sp} \leq 700 \text{ MeV}) \quad (47)$$

where:

Q_{sp} = Normalization factor dependent on total vehicle encountered flux, proton/cm²-sec

The exponential coefficient E_{p0} is given by (ref. 7):

$$E_{p0} (\text{MeV}) = (306 \pm 28) L^{-(5.2 \pm 0.2)} \quad (48)$$

where:

L = McIlwain parameter

The flux-weighted average McIlwain parameter has been determined by examination of the output data from the IBM program described above. The resulting value of this parameter, for AOSO, is

$$\bar{L} = \frac{\int_0^T \Phi_{sp} L dt}{\int_0^T \Phi_{sp} dt} = 1.366 \quad (49)$$

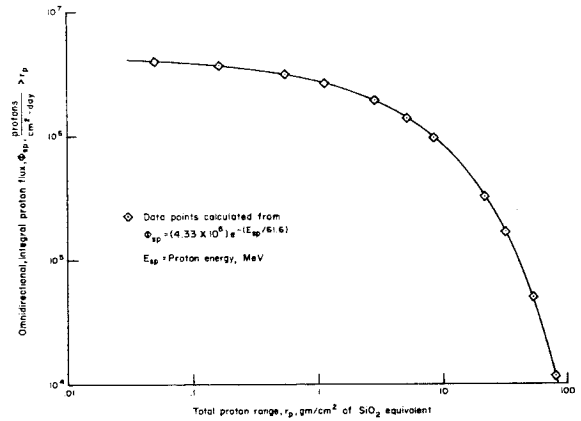


FIGURE 10.—Trapped radiation belt proton spectrum. AOSO orbit 97.6° inclination; 300 n. mile altitude.

Combining equations (45) to (48), the expression for the spectral distribution of trapped protons is obtained; that is:

$$\Phi_{sp} = (4.33 \times 10^6) e^{-(E_{sp}/61.6)} \text{ protons/cm}^2\text{-day} \quad (5 \leq E_{sp} < 700 \text{ MeV}) \quad (50)$$

This spectrum of trapped protons has been plotted as a function of total proton range in figure 10. The data in figure 10 may be expressed in the form:

$$\Phi_{sp}(>r_p) = \sum_{n=1}^4 Q_{spn} e^{-\beta_{pn} r_p} \quad (51)$$

where:

Φ_{sp} = Total proton flux, protons/cm²-day above r_p

r_p = Total proton range in SiO₂ shielding, gm/cm²

Q_{spn}, β_{pn} = Constants depending on mission orbit and exposure time to trapped protons

Values of the flux constants in equation (50) are given below:

TABLE VI

AOSO Trapped Proton Spectrum Constants

<i>n</i>	Q_{spn}	β_{pn}
1	1.09×10^6	2.66
2	1.75×10^6	0.276
3	1.16×10^6	0.081
4	2.92×10^5	0.0038

TABLE VII
Solar Cosmic Ray Proton Flux Above 30 MeV

Year	No. of events	$N_{sps}(>30)$, protons/cm ² -year	Major event	$N_{sps}(>30)$, protons/cm ² -flare
1956.....	2	8×10^9	Feb. 23, 1956	8×10^9
1957.....	4-5	4×10^8		
1958.....	6	1×10^9	July 10, 14, 16, 1959	5.8×10^9
1959.....	4	7×10^9	May 10, 1959	1.2×10^9
1960.....	8	5×10^9	Nov. 12, 15, 20, 1960	4.7×10^9
1961.....	5	2.7×10^8	~	~

Solar Flare Protons

During the past solar cycle, there were a number of major solar flares of high intensity (refs. 8 and 9). These flares are listed in table VII along with total yearly solar cosmic ray flux.

The above flux data contain an uncertainty factor of 2.

On the basis of the data above, Shulte (ref. 8) described a model solar flare having the following characteristics:

$$N_{sps}(>30 \text{ MeV}) = 6 \times 10^9 \text{ Protons/cm}^2\text{-Flare} \\ (\text{Uncertainty Factor of 2}) \quad (52)$$

Probability of flare occurrence 1% in 10 days.

Unidirectional Spectral distribution: (Protons/cm²-flare-steradian)

$$\frac{dN_{sps}}{d\Omega} (>E_{sp}) = (2.6 \times 10^{10}) E_{sp}^{(-1.33)} \\ (5 < E_{sp} < 100 \text{ MeV}) \quad (53)$$

$$\frac{dN_{sps}}{d\Omega} (>E_{sp}) = (1.9 \times 10^{17}) E_{sp}^{(-4.77)} \\ (E_{sp} > 100 \text{ MeV}) \quad (54)$$

McDonald (ref. 9) indicates that the frequency of occurrence of large events (which control the yearly proton flux) is one every 18 months to 2 years. Table VIII below compares the probability of flare occurrence, using both Shulte's and McDonald's criteria. The probabilities of occurrence are based on the Poisson distribution:

$$P_n(T) = \frac{(\lambda_F T)^n}{n!} e^{-(\lambda_F T)} \quad (55)$$

TABLE VIII
AOSO Solar Flare Probabilities

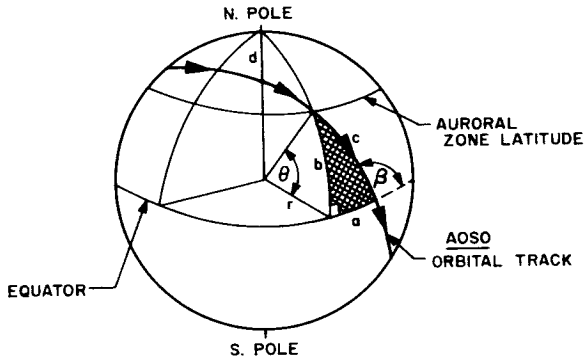
Rate of flare occurrence	Schulte model (1% in 10 days) $\lambda_F = 0.365/\text{yr}$	NASA models	
		(1 per 2 years) $\lambda_F = 0.500/\text{yr}$	(1 per 18 months) $\lambda_F = 0.667/\text{yr}$
No. of flares	Probability of flare occurrence		
0.....	69.4	60.6	51.2
1.....	25.2	30.3	34.1
2.....	4.61	7.57	11.4
3.....	0.565	1.26	2.53
Cumulative Probability.....	99.88	99.73	99.23

where:

- $P_n(T)$ = Probability of occurrence of (n) flares during period (T)
- T = Mission time ~ (1 year)
- n = Integers (0, 1, 2, . . .)
- λ_F = Rate of flare occurrence, flares/year

The information, in table VIII, indicates that by designing the solar cell shielding to withstand three flares, better than 99 percent of all situations are covered—over a fairly wide range of flare occurrence rates.

Terrestrial geomagnetic field cut-off of the solar flare protons must also be accounted for in the estimation of the AOSO radiation environment. A schematic of the AOSO orbital track on the earth's surface is shown below:



Since the AOSO would be exposed to solar flare protons above the auroral zone latitude, the schematic above indicates that the fraction of solar flare protons reaching the vehicle is approximated by the ratio:

$$\frac{N_{sp}}{N_{spo}} = \frac{d}{d+c} = \frac{d}{\pi/2} \quad (56)$$

where:

- N_{sp} = Cut-off proton flux due to geomagnetic field, proton/cm²-flare
- N_{spo} = Solar flare proton flux in interplanetary space, protons/cm²-flare
- d = Arc of AOSO orbital track above auroral zone latitude
- c = Arc of AOSO orbital track between equator and auroral zone latitude.

Since the Law of Sines for a right spherical triangle is:

$$\sin c = \frac{\sin b}{\sin(\pi - \beta)} = \frac{\sin \theta}{\sin \beta} \quad (\text{for unit earth radius}) \quad (57)$$

Then equation (56) becomes:

$$\frac{N_{sp}}{N_{spo}} = 1 - \left(\frac{2}{\pi}\right) \arcsin \left(\frac{\sin \theta}{\sin \beta}\right) \quad (58)$$

Noting, that for AOSO

$$\beta = 97.6^\circ \quad (\text{Orbital Inclination}) \quad (59)$$

$$\theta \approx 60^\circ \quad (\text{Auroral Zone Latitude}) \quad (60)$$

Then:

$$\frac{N_{sp}}{N_{spo}} = 0.321 \quad (\text{Uncertainty Factor of 2}) \quad (61)$$

Combining equations (52) and (61), the AOSO encountered proton flux from a single model flare is:

$$\begin{aligned} N_{sp}(>30) &= (0.321)(6 \times 10^9) \\ &= 1.93 \times 10^9 \text{ protons/cm}^2\text{-flare above 30 MeV} \end{aligned} \quad (62)$$

The uncertainty factor in this intensity is 3-4.

On the basis of the data in table VIII and equation (62) we will consider the "design" solar flare proton flux for the observatory to be:

$$\Phi_{sp} = 2 \times 10^{10} \text{ protons/cm}^2\text{/year} > 30 \text{ MeV} \quad (63)$$

This "design" flux includes the above-mentioned uncertainty factors. Normalizing the flare spectrum (eqs. (53) and (54)) to the "design" flux, we obtain the spectral distribution:

$$\Phi_{sp}(>E_{sp}) = (1.84 \times 10^{12}) E_{sp}^{(-1.33)} \quad (5 \leq E_{sp} \leq 100 \text{ MeV}) \quad (64)$$

$$\Phi_{sp}(>E_{sp}) = (1.39 \times 10^{19}) E_{sp}^{(-4.77)} \quad (E_{sp} > 100 \text{ MeV}) \quad (65)$$

The AOSO solar flare spectrum is plotted in figure 11 as a function of proton range in SiO₂

shielding. Using the same expression as equation (51), the constants for the AOSO Solar Flare environment are given in table IX.

TABLE IX

AOSO Solar Flare Proton Spectrum Constants

n	Q_{spn}	β_{pn}
1	3.57×10^{11}	23.1
2	1.08×10^{11}	3.72
3	2.20×10^{10}	0.491
4	6.02×10^9	0.0489

ENVIRONMENTAL PROTECTION ANALYSIS

Protection against solar cell damage, by the use of cover-glass shielding, is discussed in this section.

Solar Cell Damage Factors—Trapped Electron Belt

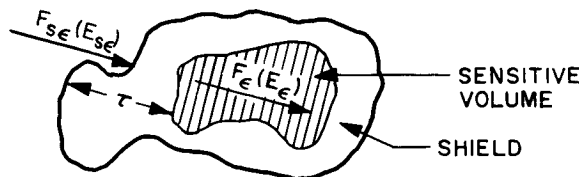
Following equation (39) the Solar Cell Electron Damage Factor is defined as:

$$\nu_{ce} = \int_0^T \int_{\Omega} \int_{E_e} \{ [k_e(E_e)] \cdot [F_e(E_e, \Omega)] \} dE_e d\Omega dt \tag{66}$$

where:

- ν_{ce} = Electron damage factor, cm^{-2}
- E_e = Energy of electron entering the sensitive volume of a solar cell, MeV
- k_e = Electron damage coefficient, electrons^{-1}
- F_e = Unidirectional differential flux of electrons entering the sensitive volume of the solar cell, $\text{electrons}/\text{cm}^2\text{-sec-MeV-steradian}$
- Ω = Solid angle, steradians
- t = Time, sec
- T = Time of exposure to electron flux, sec

The relation between the electron flux entering the sensitive volume of the solar cell material and the electron flux in space outside the shield is indicated in the schematic below:



A beam of electrons, having initial energy (E_{se})

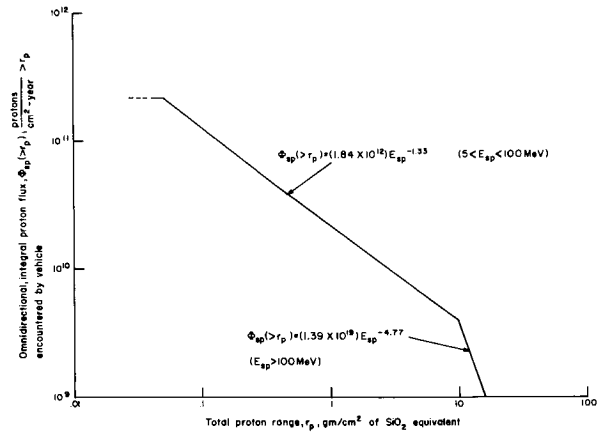


FIGURE 11.—Solar flare proton spectrum. AOSO orbit 97.6° inclination; 300 n. mile altitude.

and initial direction (Ω), will enter the material surrounding the sensitive volume. While traversing a thickness (τ) of this material, the electrons will undergo scattering as well as energy degradation by ionization and excitation of the surrounding atoms. The beam will then emerge from the outer layers (and enter the sensitive volume) with an average energy (E_e) and with a direction vector, on the average, the same as the initial direction. If the above interactions are the only ones occurring, and if the number of electrons scattered into the beam equals the number scattered out, no electrons will be lost to the beam. (This latter assumption will yield conservative damage estimates.) Hence we may write:

$$F_{se}(E_{se}, \Omega) dE_{se} = F_e(E_e, \Omega) dE_e \tag{67}$$

where:

- E_{se} = Energy of electron in space, MeV
- F_{se} = Unidirectional, differential flux of electrons in space impinging on shield material, $\text{electrons}/\text{cm}^2\text{-sec-MeV-steradians}$

As the electrons penetrate material they gradually lose energy and are finally stopped. The maximum penetration is defined as the total range. Thus:

$$r_e = \int_0^{E_e} \frac{dE}{\left(-\frac{dE}{d\tau}\right)} \equiv r_e(E_{se}) \tag{68}$$

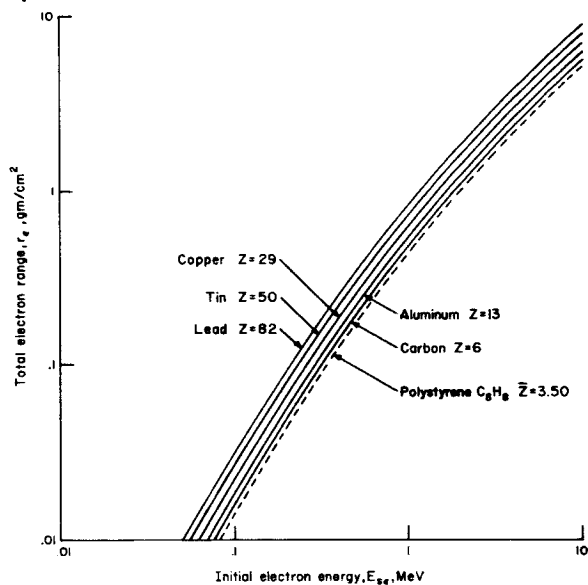


FIGURE 12.—Range of electrons in various materials. Ref: NBS Monograph 1. Z=atomic number.

where:

r_e = total range of electron, gm/cm²

$\left(-\frac{dE}{d\tau}\right)$ = rate of energy loss of electrons in shielding, MeV/gm/cm²

The range-energy relation for electrons in various materials has been obtained (ref. 10) and is shown in figure 12. Since range is interchangeable with energy, one may also write:

$$F_{se}(E_{se}, \Omega) dE_{se} = F_{se}(r_e, \Omega) dr_e \quad (69)$$

where:

$F_{se}(r_e)$ = unidirectional differential flux of electrons in space impinging on shield, electrons/gm-sec-steradian

Noting that the residual range of an electron entering the sensitive volume, analogous to total range is:

$$\xi_e = \int_0^{E_e} \frac{dE}{\left(-\frac{dE}{d\xi}\right)} = \xi_e(E_e) \quad (70)$$

where:

ξ_e = residual range of electrons in sensitive volume, gm/cm²

$\left(-\frac{dE}{d\xi}\right)$ = rate of energy loss of electrons in sensitive volume, MeV/gm/cm²

The electron damage coefficient is:

$$k_e(E_e) \equiv k_e[E_e(\xi_e)] \equiv k_e(\xi_e) \quad (71)$$

Combining equations (66) to (71), the cell electron damage factor now becomes:

$$\nu_{ce} = \int_0^T \int_{\Omega} \int_{r_e} \{ [k_e(\xi_e)] \cdot [F_{se}(r_e, \Omega)] \} dr_e d\Omega dt \quad (72)$$

The electron-range integral (eq. (68)) may be written as:

$$\int_0^{E_{se}} \frac{dE}{\left(-\frac{dE}{d\tau}\right)} = \int_0^{E_e} \frac{dE}{\left(-\frac{dE}{d\tau}\right)} + \int_{E_e}^{E_{se}} \frac{dE}{\left(-\frac{dE}{d\tau}\right)} \quad (73)$$

If the electron residual range in shield material is defined as:

$$\xi_{se} = \int_0^{E_e} \left(\frac{dE}{-\frac{dE}{d\tau}} \right) \quad (74)$$

while the "lost" range due to traversal of shielding material by the electron is:

$$\tau = \int_{E_e}^{E_{se}} \frac{dE}{\left(-\frac{dE}{d\tau}\right)} \quad (75)$$

Then we may write, for the over all range-energy relation:

$$r_e(E_{se}) = \xi_{se}(E_e) + \tau(E_{se}, E_e) \quad (76)$$

The ratio of residual range in shield material to that in cell material is given by:

$$f_{se} = \frac{\xi_{se}}{\xi_e} = \frac{\int_0^{E_e} \frac{dE}{\left(-\frac{dE}{d\tau}\right)}}{\int_0^{E_e} \frac{dE}{\left(-\frac{dE}{d\xi}\right)}} \quad (77)$$

Combining equations (76) and (77):

$$r_e = \tau + f_{se}\xi_e \quad (78)$$

Since both (τ) and (f_{se}) are constant under the range integral (in eq. (72)), we may write the expression for the electron damage factor as:

$$\nu_{ce} = f_{se} \int_0^T \int_{\Omega} \int_{\xi_e} [k_e(\xi_e)] \cdot \{ F_{se}[(\tau + f_{se}\xi_e), \Omega] \} d\xi_e d\Omega dt \quad (79)$$

The relation between total, omnidirectional, and differential, unidirectional fluxes is given by:

$$\Phi_{se}(>r_e) = \int_{\Omega} \int_0^{(r_{ec}-r_e)} [F_{se}(r_e, \Omega)] d(r_{ec}-r_e) d\Omega \quad (80)$$

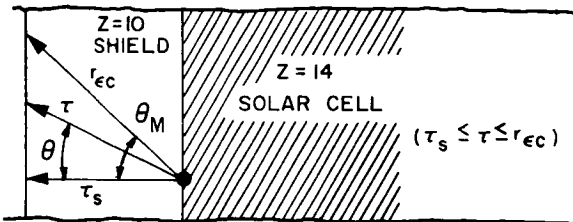
Hence, for an isotropic flux of trapped electrons, the differential, unidirectional flux, using equations (45) and (80), is:

$$F_{se}(r_e, \Omega) = \sum_{n=1}^2 \frac{\gamma_{en} Q_{sen} K_{em}}{4\pi} (r_{ec}-r_e)^{(\gamma_{en}-1)} \quad (81)$$

Using the expression for electron damage coefficient as a function of residual range (eq. (40)) as well as equation (81), the electron damage becomes:

$$\nu_{ce} = \frac{1}{4\pi} \sum_{m,n=1}^2 \int_0^T \int_{\Omega} \int_{\xi_e} (\gamma_{en} Q_{sen} K_{em}) [r_{ec}-r-f_{se}\xi_e]^{(\gamma_{en}-1)} [\xi_e^{(\alpha_{em})}] d\xi_e d\Omega dt \quad (82)$$

The solution to equation (82) is dependent on the geometrical properties of the solar cell shielding. Since we are dealing with a solar paddle array, the equivalent shield geometry is that of an infinite slab—shown in the schematic diagram below:



For a semi-infinite half-space, the differential solid-angle is given by:

$$d\Omega = 2\pi \sin \theta d\theta \quad (83)$$

Combining equations (82) and (83), we have:

$$\nu_{ce} = \left(\frac{1}{2}\right) \sum_{m,n=1}^2 \int_0^T \int_0^{\theta_M} \int_{\xi_e} (\gamma_{en} Q_{sen} K_{em}) [r_{ec}-r-f_{se}\xi_e]^{(\gamma_{en}-1)} [\xi_e^{(\alpha_{em})}] \sin \theta d\xi_e d\theta dt \quad (84)$$

The maximum angle of entry for the electrons is determined by the spectrum cut-off range

(r_{ec}) and thus:

$$\cos \theta_M = \frac{\tau_s}{r_{ec}} \quad (85)$$

Performing the integrations indicated in equation (85), the expression for electron damage factor is then:

$$\nu_{ce} = \left(\frac{T}{2}\right) \left\{ \sum_{m,n=1}^2 \left[\frac{\gamma_{en} Q_{sen} K_{em}}{f_{se}^{(\alpha_{em})}} \right] \left[\frac{\Gamma(1+\alpha_{em})\Gamma(\gamma_{en})}{\Gamma(1+\alpha_{em}+\gamma_{en})} \right] [(r_{ec}-\tau_s)^{(\alpha_{em}+\gamma_{en})}] \left[1 - \left(\frac{T_s}{r_{ec}}\right) \sum_{\beta=0}^{\infty} \left(\frac{\alpha_{em}+\gamma_{en}}{\alpha_{em}+\gamma_{en}+\beta}\right) \left(1-\frac{\tau_s}{r_{ec}}\right)^{\beta} \right] \right\} \quad (86)$$

where:

$\Gamma(g)$ = Gamma Function of Argument (g)

Examination of figure 12 shows little difference, in the range-energy relation, between the shielding and solar cell materials, hence:

$$\bar{f}_{se} = 1.00 \quad (87)$$

Using the data in tables II and V, as well as in equation (41), the electron damage factors may be estimated with equation (86). The results are shown graphically in figure 13 for both 1Ω-cm and 10Ω-cm solar cells for a mission time of 365 days.

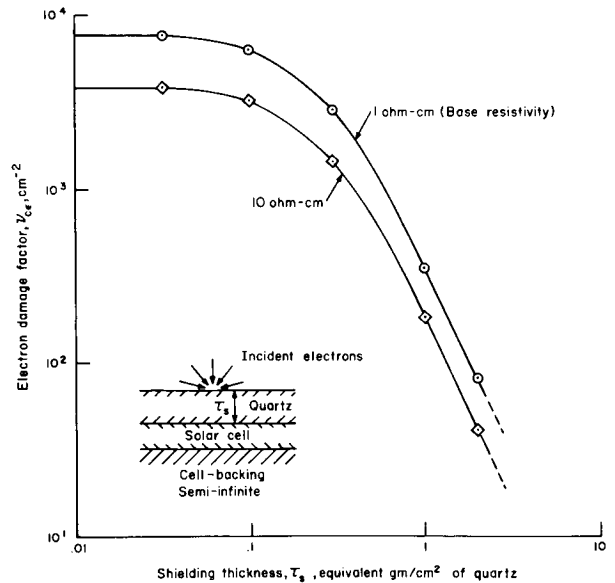


FIGURE 13.—Solar cell damage factors ~trapped electron belt. Epoch ~November 1962. N/P silicon cells, circular polar orbit; 300 n. mile altitude.

Solar Cell Damage Factors—Trapped Proton Belt

In a manner analogous to the derivation of equation (79) for electrons, it may be shown that the solar cell proton damage factor is:

$$\nu_{cp} = (f_{sp}) \int_0^T \int_{\Omega} \int_{\xi_p} [k_p(\xi_p)] \{F_{sp}[(\tau + f_{sp}\xi_p), \Omega]\} d\xi_p d\Omega dt \quad (88)$$

where:

- ν_{cp} = Proton damage factor, cm^{-2}
- k_p = Proton damage coefficient, protons $^{-1}$
- Ω = Solid angle, steradians
- T = Time of exposure to proton flux, sec
- t = Time, sec
- F_{sp} = Unidirectional, differential flux of protons in space encountered by vehicle, Protons/gm-sec-steradian
- τ = Thickness of shield along proton path, gm/cm 2
- f_{sp} = Ratio of proton residual range in shield material to that in cell material
- ξ_p = Proton residual range, gm/cm 2

(Note—Proton-range energy relations are shown in figure 14—based on data from references 11 and 12.)

The relation between total, omnidirectional flux and differential, unidirectional flux is given by:

$$\Phi_{sp}(>r_p) = \int_{\Omega} \int_{r_p}^{r_{pc}} F_{sp}(r_p, \Omega) dr_p, d\Omega \quad (89)$$

where

- r_{pc} = Total proton range corresponding to maximum energy of proton spectrum, gm/cm 2
- r_p = Total proton range, gm/cm 2

For an isotropic flux of trapped protons, the unidirectional differential proton flux is obtained by combining equations (51) and (82) to yield:

$$F_{sp}(r_p, \Omega) = \sum_{n=1}^4 \left(\frac{\beta_{pn} Q_{spn}}{4\pi} \right) \epsilon^{-\beta_{pn} r_p} \quad (90)$$

Combining equations (42), (88), and (90), the proton damage factor is:

$$\nu_{cp} = \left(\frac{K_p}{4\pi} \right) \sum_{n=1}^4 (f_{sp}) \int_0^T (\beta_{pn} Q_{spn}) \int_{\Omega} \epsilon^{-\beta_{pn} \tau} \int_0^{(\frac{r_{pc}-\tau}{f_{sp}})} [\epsilon^{-(\beta_{pn} f_{sp} \xi_p)}] [\xi_p^{\alpha_p}] d\xi_p d\Omega dt \quad (91)$$

It may be shown (ref. 13) that the last integral in equation (91) is an incomplete gamma function given by:

$$\int_0^{r_{pc}-\tau} [\xi_p^{\alpha_p}] [\epsilon^{-(\beta_{pn} f_{sp}) \xi_p}] d\xi_p = C_{\gamma} \left[\frac{\beta_{pn} (r_{pc} - \tau)}{\sqrt{1 + \alpha_p}} \right] [\alpha_p] \left\{ \frac{\Gamma(1 + \alpha_p)}{(\beta_{pn} f_{sp})^{(1 + \alpha_p)}} \right\} \quad (92)$$

where:

- $\Gamma(1 + \alpha_p)$ = A complete gamma function of argument (α_p)
- $C_{\gamma} \{ \}$ = Correction factor to the γ -function

Combining equations (51) and (52) we have:

$$\nu_{cp} = \frac{K_p}{4\pi} \sum_{n=1}^4 \int_0^T \frac{Q_{spn} \Gamma(1 + \alpha_p)}{\beta_{pn}^{\alpha_p} f_{sp}^{(1 + \alpha_p)}} \int_{\Omega} C_{\gamma} \{ r_{pc} - \tau \} \epsilon^{-\beta_{pn} \tau} d\Omega dt \quad (93)$$

If we make the very reasonable assumption that the maximum proton range is much greater than any shield thickness we are examining, we can write:

$$r_{pc} \gg \tau \rightarrow (r_{pc} - \tau) \cong r_{pc}$$

and remove the gamma function correction factor (c_{γ}) from under the geometry integral.

Using equation (83) for the geometry integral, we find:

$$\int_{\Omega} \epsilon^{-\beta_{pn} \tau} d\Omega = (2\pi) \int_0^{\pi/2} [\epsilon^{-(\beta_{pn} \tau_s) \sec \theta}] \sin \theta d\theta \quad (94)$$

and letting:

$$y_n = \beta_{pn} \tau_s \sec \theta \quad (95)$$

then by substitution:

$$\int_0^{\pi/2} [\epsilon^{-(\beta_{pn} \tau_s) \sec \theta}] \sin \theta d\theta = (\beta_{pn} \tau_s) \int_{(\beta_{pn} \tau_s)}^{\infty} \frac{e^{-y_n}}{y_n^2} dy_n \equiv \tilde{E}_2(\beta_{pn} \tau_s) \quad (96)$$

where:

$\tilde{E}_2(\beta_{pn} \tau_s)$ = Second order exponential integral function of argument ($\beta_{pn} \tau_s$)

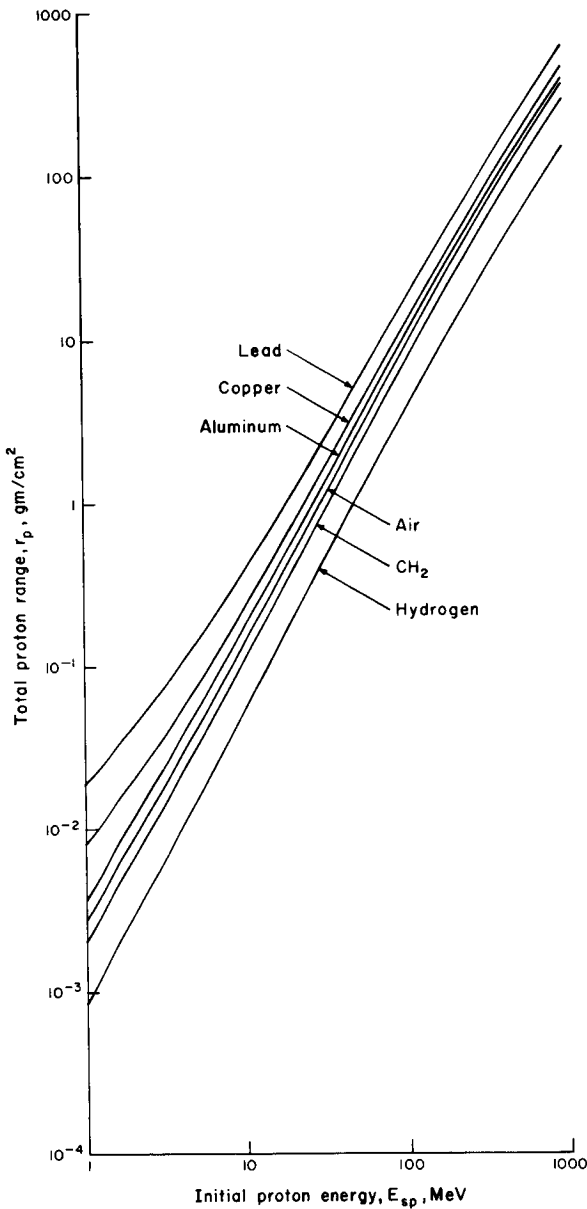


FIGURE 14.—Range of protons in various materials.

Tables of $\tilde{E}_2(\beta_{pn}\tau_s)$ may be found in reference 14.

Combining equations (93), (94), and (96), and integrating over a complete mission, the trapped proton damage factor is:

$$\nu_{cp} = \left[\frac{K_p T \Gamma(1 + \alpha_p)}{2 f_{sp}(\alpha_p)} \right] \sum_{n=1}^4 \left[\frac{Q_{spn} \tilde{E}_2(\beta_{pn}\tau_s)}{\beta_{pn}(\alpha_p)} \right] C_r \left\{ \frac{\beta_{pn} r_{pc}}{\sqrt{1 + \alpha_p}}, (\alpha_p) \right\} \quad (97)$$

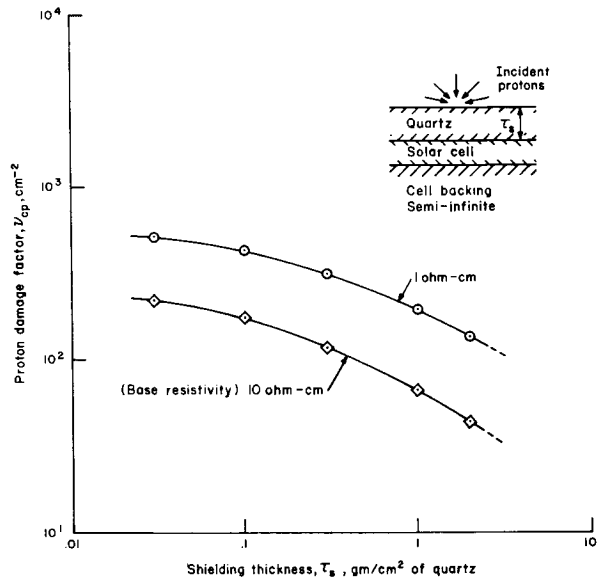


FIGURE 15.—Solar cell damage factors—trapped proton belt. N/P silicon cells; 300 n. mile circular orbit; 97.6° inclination.

Estimates of trapped proton damage using equation (97) are shown in figure 15. These estimates are based on the data in tables III and VI as well as a value of:

$$\bar{f}_{sp} \approx 1.00 \quad (98)$$

Solar Cell Damage Factors—Solar Flare Protons

We may utilize the solar cell damage factors derived for the trapped proton belt for solar flare protons as well (eq. (92)). Solar cell proton damage constants may be obtained from table III. The spectrum of solar flare protons may also be expressed in the form of equation (43). Using the data in table IX, for the yearly solar proton flux, an estimate of cell damage factors may be obtained. This estimate is shown in figure 16.

OPTIMUM AOSO SOLAR CELL SHIELDING

The solar cell degradation factor is dependent upon the damage induced by the several vehicle encountered radiations. In a field of mixed radiations, this damage is additive, as indicated by equation (37). Combining the electron and proton damage factors (from figs. 13, 15 and 16) we obtain the overall solar cell damage factor (ν_c) shown in figure 17.

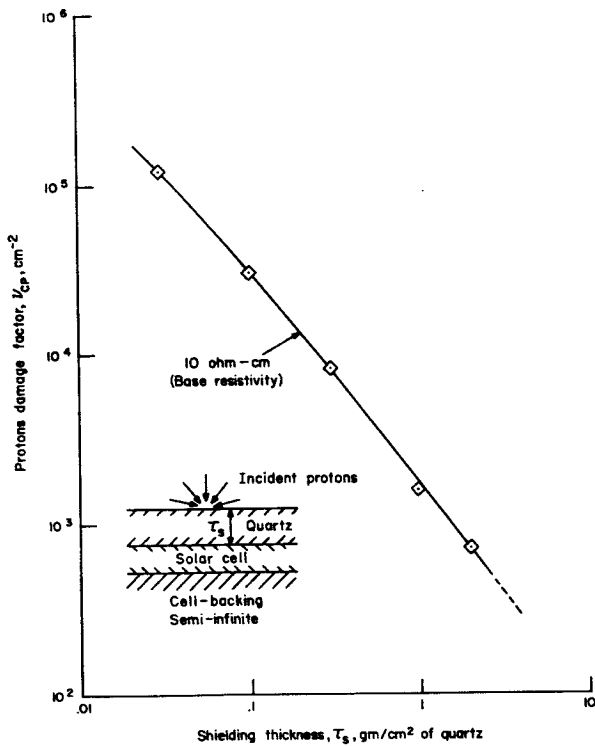


FIGURE 16.—Solar cell damage factors—solar flare protons. N/P silicon cells; 300 n. mile circular orbit; 97.6° inclination.

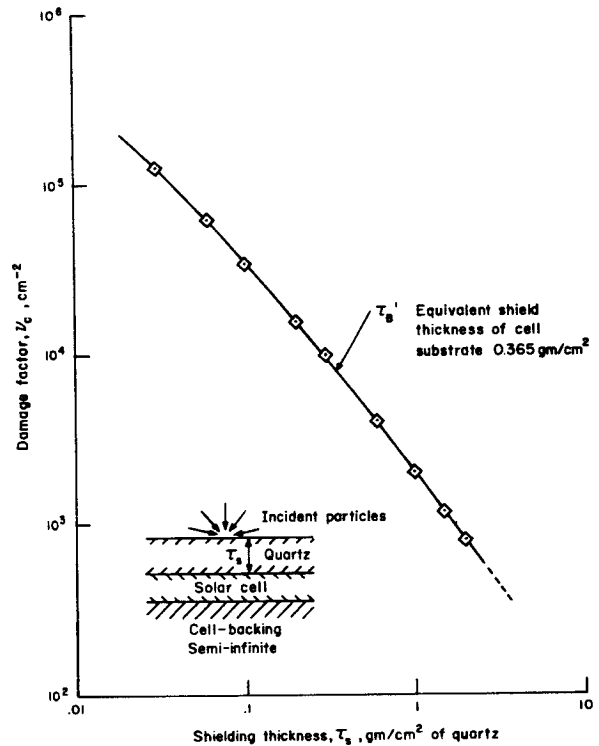


FIGURE 17.—AOSO solar cell damage factors; N/P silicon cells; 10 ohm-cm base resistivity; 300 n. mile circular orbit; 97.6° inclination; 1 year exposure at solar maximum.

Using the data in figure 17, the ratio of initial to final diffusion length may be estimated with equations (35) and (36). These ratios are given in table X below:

TABLE X
AOSO Solar Cell Diffusion Length Ratios
[$l_1 = 150$ microns]

T_s (gm/cm ²)	l_f/l_i
0.03	0.185
.06	.259
.10	.338
.20	.468
.30	.555
.60	.723
1.00	.830
1.50	.890
2.00	.920

The relationship between solar cell conversion efficiency and minority carrier diffusion length (fig. 3), together with the data in figure 17 and table X, may be used to obtain the

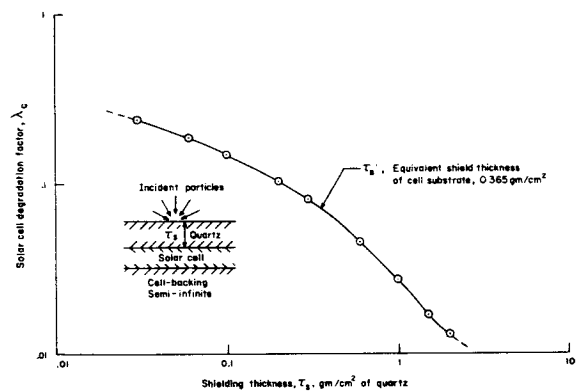


FIGURE 18.—AOSO solar cell degradation factors. N/P silicon cells; 10 ohm-cm base resistivity, $l_i = 150$ microns; 300 n. mile circular orbit; 97.6° inclination; 1 year exposure at solar maximum.

change in solar cell efficiency with shield thickness. Applying the resulting data to equation (33), this efficiency estimate is shown in figure 18.

The necessary and sufficient conditions for an optimum solar cell shield thickness are given by

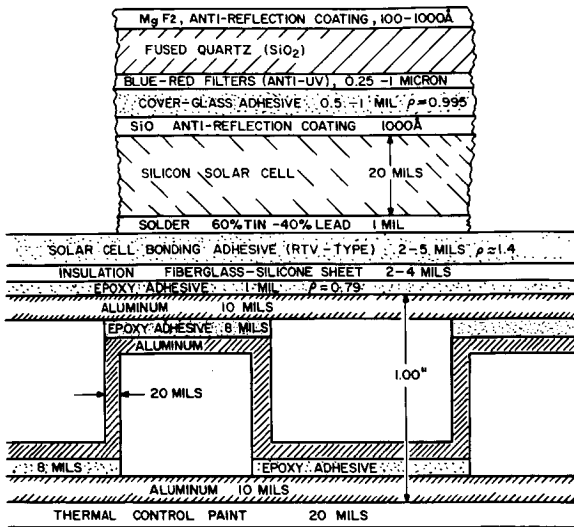


FIGURE 19.—Typical solar cell and paddle assembly.

equations (31) and (32). However, in the case of AOSO the solar cells are mounted to the edge of the paddle. Hence:

$$d_F = 0 \tag{99}$$

Using Corning 7940 (UV Grade) Fused Quartz—or equivalent—reduces the radiation-induced darkening to negligible levels. Hence:

$$\delta_s = 1 \tag{100}$$

Finally, in the thicknesses of cover glass used for shielding, absorption of light is negligible. Thus:

$$(\mu/\rho)_{st} \approx 0 \tag{101}$$

Substituting equations (99) to (101) into equations (31) and (32) we find that the necessary condition for an optimum shield thickness is:

$$\hat{\tau}_s = \left[\frac{(1-\lambda_c)}{\left(\frac{-d\lambda_c}{d\tau_s} \right)} \right] - \tau_{cB} \tag{102}$$

while the sufficient condition is:

$$\frac{d^2\lambda_c}{d\tau_s^2} > 0 \tag{103}$$

The value of (τ_{cB}) can be obtained by examination of a typical solar cell and paddle assembly—an example of which is given in figure 19. From this schematic we determine that the total weight of solar cell and substrate is

given by:

$$\tau_{cB} = 0.498 \text{ gm/cm}^2 \tag{104}$$

The degradation of cells is due to particles incident on both the quartz shield and cell backing. Examination of figure 19 further indicates that the equivalent (Quartz) thickness of cell backing and nonsensitive portion of the cell base is:

$$\tau'_B = 0.365 \text{ gm/cm}^2 \tag{105}$$

Hence, the degradation due to particles incident on the backside of the cell is (from fig. 18):

$$\lambda'_c = 0.070 = 7\% \tag{106}$$

The data in figure 18 may be correlated by the expression:

$$(\lambda'_c + 0.2) = (0.05)(\tau_s + 0.04)^{(-0.612)} \tag{107}$$

and since the total degradation is given by:

$$\lambda_c = \lambda'_c + \lambda''_c \tag{108}$$

we may write:

$$\lambda_c = (0.05) + (0.05)(\tau_s + 0.04)^{(-0.612)} \tag{109}$$

$$(1 - \lambda_c) = (0.95) - (0.05)(\tau_s + 0.04)^{(-0.612)} \tag{110}$$

and taking derivatives:

$$(d\lambda_c/d\tau_s) = (-0.0306)(\tau_s + 0.04)^{(-1.612)} \tag{111}$$

$$\frac{d^2\lambda_c}{d\tau_s^2} = (+1.612)(+0.0306)(\tau_s + 0.04)^{(-2.612)} > 0 \tag{112}$$

Since equation (112) fulfills the sufficient condition (eq. 103), an optimum value of the shield thickness exists.

Substituting equations (110) and (111) into equation (102), and rearranging, we obtain the polynomial:

$$\hat{\tau}_s = (11.80)(\hat{\tau}_s + 0.4)^{(1.612)} - (0.214) \tag{113}$$

Solving equation (113), by trial and error, we obtain the optimum shield thickness as:

$$\hat{\tau}_s = 0.055 \text{ gm/cm}^2 (\approx 9.9 \text{ mils of Corning 7940 UV Grade}) \tag{114}$$

...the corresponding solar cell degradation is:

$$\lambda_c = 0.070 + (0.005)(0.055 + 0.04)^{(0.612)} - (0.02) = 0.257 \approx 25.9\% \quad (115)$$

These optimum shield estimates have been made for other thicknesses of paddle substrate. The results are shown in table XI below as well as in figure 20.

TABLE XI
Optimum Solar Cell Shield Thickness

Substrate τ_{CB} , gm/cm ²	Cover Glass τ_s (7940 Quartz)		λ_c Solar Cell Degradation, percent
	gm/cm ²	mils	
0.498	0.055	9.9	25.9
0.687	.0745	13.3	22.8
0.887	.090	16.2	19.8

These data show that, as the substrate density increases, the optimum cover-glass shield thickness increases, while the solar cell degradation factor decreases. The comparatively low ratio of optimum cover-glass thickness to substrate density ($\approx 1/10$) indicates that

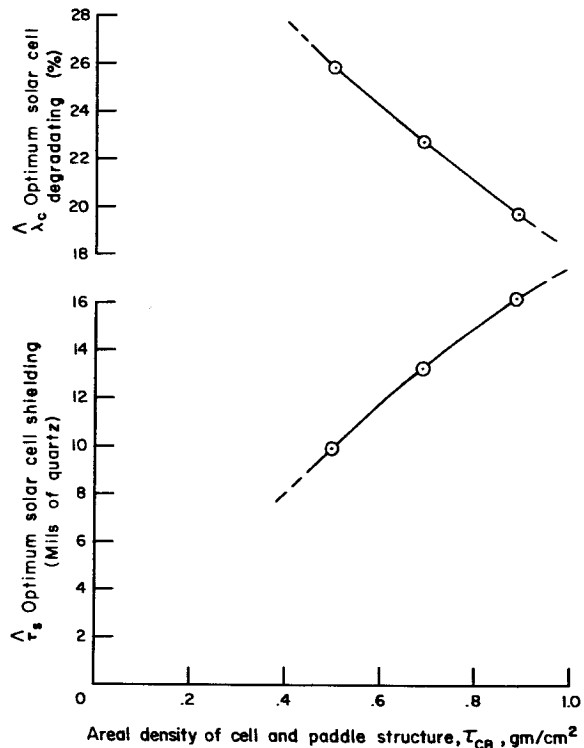


FIGURE 20.—The effect of paddle structure on optimum solar cell shielding.

where paddle area is unconstrained, minimum paddle weight is achieved by increasing the number of solar cells rather than by adding cell shielding.

REFERENCES

1. COOLEY, W. C.; and JANDA, R. J.: Handbook of Space-Radiation Effects on Solar Cell Power Systems. NASA SP-3003, 1963.
2. ROSENZWEIG, W.: Diffusion Length Measurements by Means of Ionizing Radiation. Bell System Tech. J., no. 4, Sept. 1962, p. 1573.
3. DOWNING, R. G.: STL Radiation Damage Experiments. Photovoltaic Specialists Conference (Washington, D.C.), Apr. 1963. Rept. No. PIC-SOL 209/3, July 1963.
4. WELLER, J. F.; and STATLER, R. L.: Low Energy Proton Damage to Solar Cells. IEEE Trans. Nucl. Sci., NS-10, no. 5, Nov. 1963.
5. CHERRY, W. R.; and SLIFER, L. W.: Solar Cell Radiation Damage With 1-MeV Electron and 4.6-MeV Protons. NASA X-636-63-110, May 27, 1963.
6. Nuclear Electronic Effects Program. 7th Tri-Annual Report, ASD-TN-61-137, July 15, 1961, AD-264121.
7. McILWAIN, C. E.; and PIGELLA, C.: On the Energy Spectrum of Protons Trapped in the Earth's Inner Van Allen Zone. J. Geophys. Res., vol. 68, no. 7, 1963, p. 1811.
8. SHULTE, H. J.: Models for Space Environment Hazards. Bellcomm, Inc. (Washington, D.C.), Jan. 21, 1963.
9. McDONALD, FRANK B., ED.: Solar Proton Manual. NASA TR R-169, Sept. 1963.
10. SPENCER, L. V.: Energy Dissipation by Fast Electrons. Nat. Bur. Std. Monograph 1, Sept. 10, 1959.
11. STERNHEIMER, R. M.: Phys. Rev., vol. 115, 1959, p. 137.
12. ARON, W. A., ET AL.: Univ. Calif. Radiation Laboratory Rept., UCRL-121, 1951.
13. PEARSON, K.: Tables of the Incomplete Gamma Function. Cambridge Univ. Press (London, England), 1946.
14. Reactor Shielding Design Manual (T. Rockwell, ED.): US AEC TID 7004, Mar. 1956.

N65-34619

43—A Space Radiation Protection System for Near-Earth Manned Orbital Space Stations

FRANK L. BOUQUET, JR.

Lockheed-California Company

It is rapidly becoming clear that Man, as he ventures on typical extended missions into space, will require appreciable protection from the hazards of the environment. The primary hazards have been identified as high-speed meteoroids and high-energy nuclear radiation. Considerable scientific effort in recent years has been expended to define and evaluate these hazards. It is the purpose of this paper to discuss a space radiation protection system for near-earth manned space vehicles in general, and for large orbital space stations in particular. The space radiation protection system is defined to include the following four basic elements:

1. Portable crew shielding including helmets and goggles.
2. Shielding around sleeping areas.
3. Space radiation monitoring and warning system.
4. Individual personnel dosimeters.

The radiation protection requirements are approached from a system viewpoint. The feasibility of shielding single or multiple modules and the use of storm cellars as well as portable personnel shielding are investigated.

THE SPACE STATION CONFIGURATION

This paper is primarily concerned with the space radiation shielding requirements for a large, three-radial spoke space station, as shown in figure 1.

In a typical design configuration, as shown here, the living quarters are quite large, 15.2 feet in diameter and approximately 47.5 feet in length. Consequently, if the entire living quarters are shielded, considerable area is involved.

Possible locations of nuclear power sources, if used, are in the spin plane on the end of one of the spokes, or on the spin axis.

In this study, we are concerned with the shielding requirements in low-altitude circular orbits, of 100 to 400 n. mi., and low inclinations in the 1968 time period. The general types of radiation sources that are of concern in space are shown in table I.

TABLE I

Penetrating Radiation Sources in Near-Earth Space Station

Space environment sources

- Artificial belt of the Earth
- Natural belt of the Earth
- Solar flare events
- Cosmic rays
- Miscellaneous radiation components

Nuclear power sources

- Reactors
- Radioisotopes

THE SPACE RADIATION SHIELDING PROBLEM

The protection requirements for personnel and/or equipment may vary widely, depending upon the particular space mission under consideration. For certain missions, involving short duration, low orbit altitudes or low inclination orbits, it is conceivable that no radiation shielding will be required other than the meteoroid and pressurization structure. For the majority of near-earth space flights of interest, however, radiation shielding is required to reduce the personnel exposure to tolerable biological levels. Local shielding for sensitive equipment (instruments, experiments, etc.) may be required, depending upon the exact

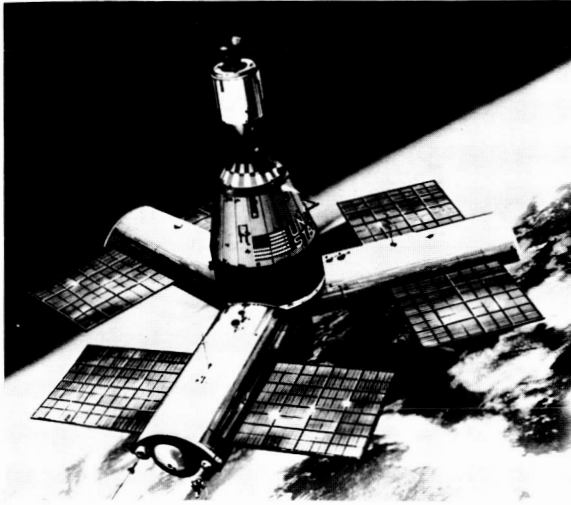


FIGURE 1.—Large orbital manned space station.

level of sensitivity and/or location (for example exterior to the space vehicle). In general, however, personnel are much more sensitive than equipment to the energetic space radiation. Therefore, the emphasis in the remainder of this paper will be on the personnel shielding problem.

The design analysis in this study involves eight basic steps as follows:

1. Determination of the "model" environment, including the space radiation components. These include the characteristics of solar proton events, the radiation belts of the earth, cosmic rays, and the miscellaneous space radiations (X-rays, γ -rays, albedo neutrons, and so forth). The required characteristics of each of the above should include the types of particles, intensities, energy spectra, time dependence, and angular distributions. Because space environment knowledge is limited at the present time, is changing with improved measurements, and varies with measurement instruments, the data to be used in a given study must be "frozen" on the best available information at the beginning of the study.

2. Determination of the mission trajectory profile. This will define the spatial location of the space vehicle as a function of time.

3. Determination of the integral fluxes in the space environment to be encountered on the space mission in a given interval of time.

This will include the shielding effect due to the presence of the earth.

4. Determination of the biological nuclear radiation dosage limits for the total body and/or the various critical body organs.

5. Determination of a mathematical model to represent the space vehicle. Geometrical effects must be included to properly compute the internal energy transport.

6. Determination of the dimensions, composition, and characteristics of the man-model to be assumed, as well as its location within the space station.

7. Determination of the material attenuation characteristics for the elements used. These characteristics are required for the assumed basic vehicle structure, the shield materials, and the vehicle equipment.

8. Determination of the method of shielding to be used. Alternatives are the shielding of the entire space station, the shielding of one or more modules, the use of storm cellars, and local body shielding.

Inclusion of an additional sub-problem is required if on-board nuclear power systems are used, either for primary nuclear propulsion or for auxiliary electrical power generation. The intense, penetrating radiation fields from these units require powerplant shielding as well as an increase in the space biological radiation shielding if the allowed personnel dose limit criteria are to remain unchanged over the mission time.

THE SPACE RADIATION ENVIRONMENT MODEL

Much scientific information concerning the nature of the space environment has been accumulated in recent years from NASA and USAF satellites. The space radiation is found to be dynamic and, at the present time, no "model" as such exists. However, for the purposes of this design study, model assumptions are required in order to proceed with the system optimization. The components of the radiation flux that are treated are the natural components shown in table I. Extrapolation of the space radiation components into the future as far as 1968 is risky in view of the limited amount of data available in near-earth orbits. Therefore, the values of the main

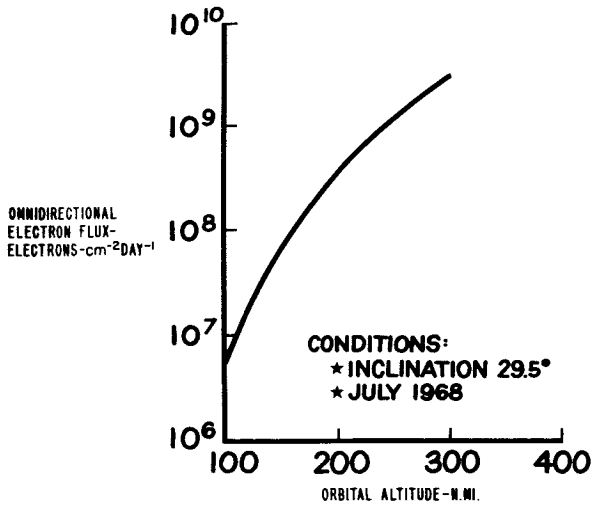


FIGURE 2.—Electron flux versus altitude.

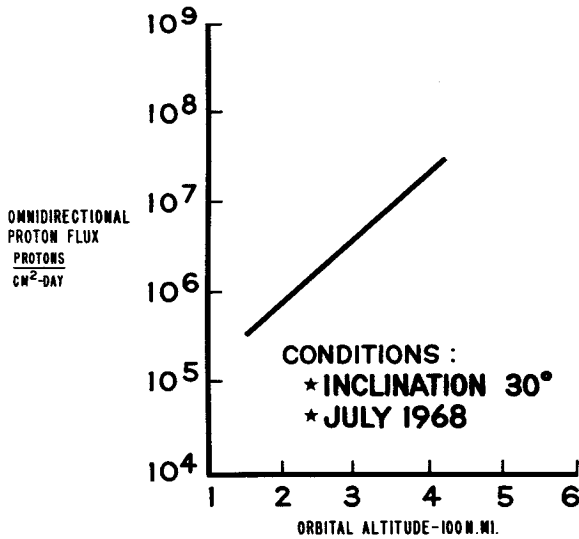


FIGURE 3.—Trapped proton flux versus altitude.

components (trapped electrons, trapped protons, and solar protons) that are actually used are treated in detail below.

The trapped electron omnidirectional flux distribution assumed in the study is shown in figure 2 versus the circular orbit altitude. This estimate of the trapped electron flux was obtained using the data of Hess (ref. 1) and the decay rate from the observations of Van Allen (ref. 2) on *L* shell 1.15 extrapolated to 1 year after the formation of the artificial belt.

The flux intercepted at a typical altitude of interest, 260 n. mi., is 1.75×10^9 electrons/cm²-

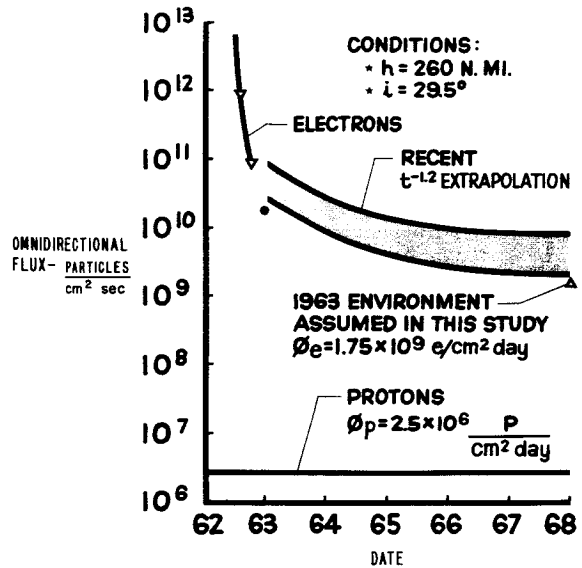


FIGURE 4.—Geomagnetically trapped particle flux versus time.

day. At low altitude, the electron flux is reduced many orders of magnitude.

The trapped proton omnidirectional flux distribution that was assumed is shown in a similar fashion in figure 3. At 260 n. mi., the flux intercepted is 2.5×10^6 protons/cm²-day.

Both these particle fluxes increase rapidly with altitude. This is also true of many of the miscellaneous flux components, including the cosmic ray flux.

The artificial electron belt is known to be decaying with time at the low altitudes of interest in this study, namely near 260 n. mi. altitude. A curve of the omnidirectional electron fluxes assumed for 1968 is shown in figure 4; also shown is the recent data from a computer program based on the data of McIlwain (Personal communication from W. H. Harless, Lockheed Missiles and Space Co., Data based on work of Drs. R. V. Smith, E. E. Gaines, R. A. Glass of LMSC; Dr. W. N. Hess, Goddard Space Flight Center).

The assumptions used in this study show good agreement with the lower bound of this more recent data.

INTEGRATED SPACE RADIATION DOSE

The space radiation dose depends on the type of dosimeter that is used. In this case we are

interested in the absorbed dose to the human body organs. The biological dose limits are treated briefly under the section on dose criteria. However, if a typical body organ is selected as an example, the integrated dose to the eye, in rads per year, can be plotted as a function of altitude (fig. 5). This is the dose to be expected inside a space station with the shielding effect of the man-model and the space station walls (1.8 lb/ft²) present.

The absorbed radiation dose increases rapidly with altitude as the center of the inner electron and proton belts is approached. It is seen that the eye dose criterion (27 rad/year) is exceeded at an orbital altitude of approximately 125 n.mi. Therefore, eye shielding is required above that altitude if the mission is to last one year.

It should be recognized that these results refer only to the environmental radiation model used. For further information concerning general nature of the space radiation, see reference 3. The use of a different environment model for the time period of interest would raise or lower the threshold eye dose altitude.

The permissible orbit time in days, if dose criteria are not to be exceeded within the station, is also shown in figure 5.

A breakdown of the dose components included for the particular orbital conditions of 260 n.mi. altitude, 29.5° inclination, are shown in table II.

TABLE II

Unshielded Eye Dose Rates for the 1968 Time Period

[260 n. mi. altitude; 29.5° orbital inclination; inside space station walls of 0.9 g/cm² Al equiv.]

<i>Radiation Dose Component</i>	<i>Dose Rate (Rad-Yr⁻¹)</i>
Geomagnetically trapped electrons.....	1136.0
Geomagnetically trapped protons.....	23.78
Solar protons.....	0
Cosmic rays.....	1.0
Bremsstrahlung.....	20.2
Cascade protons.....	0.332
Evaporative neutrons.....	0.0078
Excitation gammas.....	0.00594
Cascade neutrons.....	0.00475
Total.....	* 1181.34049

* Only first 2 digits are significant.

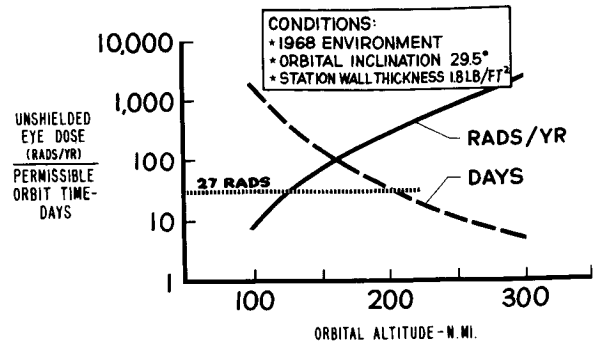


FIGURE 5.—Unshielded eye dose and permissible orbit time versus altitude.

It is seen that the geomagnetically trapped electrons, trapped protons, and the bremsstrahlung contribute the major portion of the unshielded eye dose.

The secondary radiations are found to be finite, but small, contributions compared to the primary radiations for thin-skinned vehicles. If internal equipment and shielding are added, the secondary radiations will increase.

DESCRIPTION OF THE OPTIMIZATION ANALYSES

A generalized nuclear radiation shield optimization program has been formulated. A high-speed computer (IBM-7094) has been programmed in FORTRAN IV language to compute the optimum shield materials, geometrical placement of the materials, and the thickness and weights for a given crew dose limit. Special input provisions are included as an option to accept the space environment input data in a form of probability distributions.

Exterior as well as interior dose rates may be computed for arbitrary slab, cylindrical, or spherical geometrical configurations. In addition, self-shielding effects and cargo and equipment placement can be computed. Laminar construction of both space station walls and shielding materials may also be included. The biological dose rate per unit solid angle can be computed with this program.

THE RADIATION SHIELDING COMPUTER PROGRAM

A simplified schematic of the computer program used for the assessment of the space radiations is shown in figure 6.

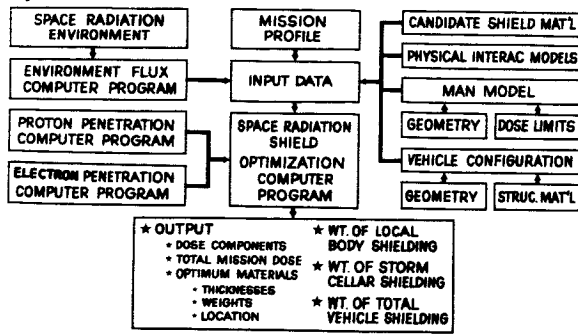


FIGURE 6.—Schematic representation of the space radiation analysis computer program.

The method of computation used in this study is essentially that of marginal or incremental analysis. Definition of the optimum is accomplished by the addition of successive layers of shielding materials. The basic equations used in the program are given as follows:

$$D_i = \int_{E, \theta, \varphi} K_i I_{r_i} \prod_{j=0}^i A_{ij} dE dt d\Omega$$

D_i = Absorbed dose per unit time to the body organ under consideration from the i th particle component
 $d\Omega$ = Differential solid angle
 r, θ, φ = Polar coordinates
 I_{r_i} = Flux per unit solid angle
 $A_{ij} = A_{ij}[E, x, A_{j-1}, \dots, A_1, d\Omega]$. Relative attenuation function of the j th material
 K_i = Flux-to-dose conversion factor for the i th type or particle
 dE = Differential element of particle energy
 $D_{tot} = \sum_m \sum_i D_i$
 D_{tot} = Total radiation absorbed dose over the mission time
 i = Index for summation over the particles in a particular radiation source
 m = Index for summation over the radiation flux sources

A computer program that is successful in the analysis of the high-energy space radiations must account for the increase of ionization with depth.

As the velocity of a heavy charged particle approaches zero, the ionization increases rapidly. For instance, figure 7 shows the Bragg effect for 140 MeV protons incident

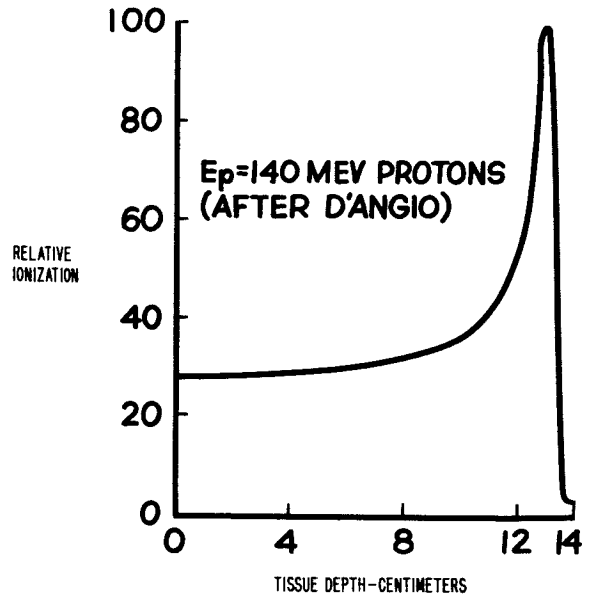


FIGURE 7.—Relative ionization versus depth in tissue.

upon tissue (ref. 4). It is seen that, near the end of the particle path, almost four times the ionization per unit path length occurs relative to the surface ionization. The depth of occurrence of the peak depends on the type of particle as well as the absorber material. These effects are included in this method of analysis.

The man-model used in this study is shown in figure 8. The man-model location was assumed to be in the center of one of the modules, facing at right angles to the length of the module. The relative depth dose attenuation functions were obtained from a number of sources. The depth doses for the particular radiation components under consideration were computed by means of separate Lockheed-generated dose depth machine programs. Two curves are shown in figure 9 for the trapped protons, representing the differences in relative penetrability depending on the lower energy threshold. The more penetrating curve represents protons, with a lower energy spectra limit of 30 MeV, while the rapidly attenuated curve represents a lower energy limit of 10 MeV. The penetrating nature of the radiations from fission sources is also shown.

The relative depth dose is much larger for the nuclear heat sources. Therefore, the depth

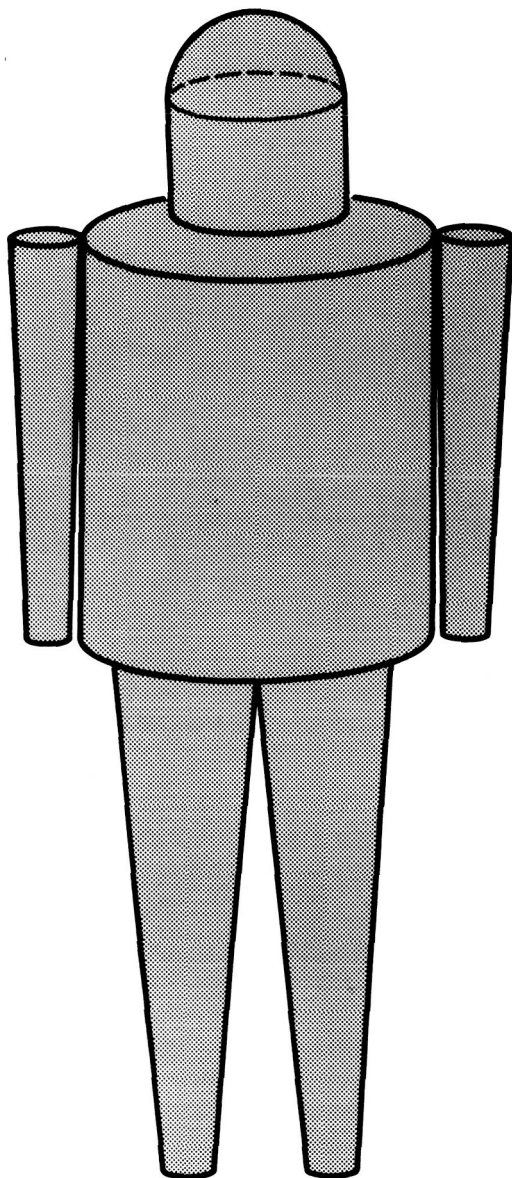


FIGURE 8.—Typical man-model composed of ellipsoids and truncated cylinders.

dose distribution of fission energy gammas and neutrons becomes of major importance if nuclear reactor on isotropic power sources are used on board future space stations.

The attenuation functions for relativistic electrons used in this study were based on the measured ion chamber response measurements in MA-8 spacecraft (ref. 5). The geomagnetically trapped proton attenuation functions

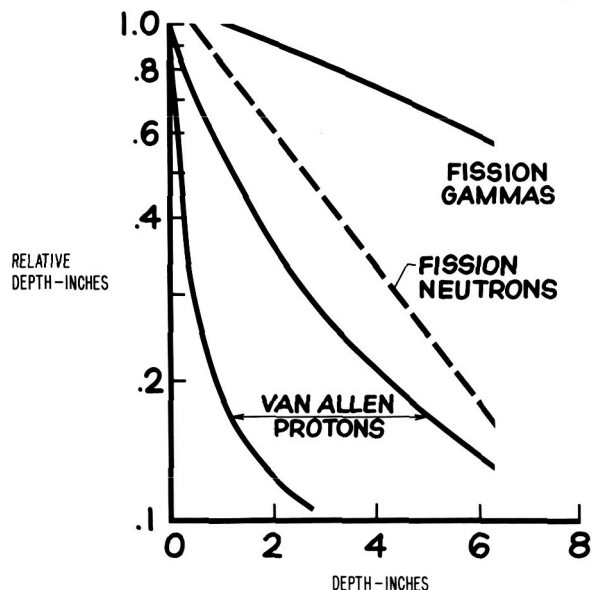


FIGURE 9.—Relative dose versus depth.

were based upon recent calculations (Personal communication: W. L. Gill, NASA Manned Space Flight Center).

ALLOWABLE RADIATION DOSE CRITERIA

Formal critical radiation dose limits for man are not established at the present time. Nonetheless, data from many sources make possible the estimation of approximate dose limits for the purposes of design. The yearly radiation dose limits that have been used in a typical analysis for near-earth space stations are shown in table III in order of decreasing importance. These various organ limits are assumed to include the energy deposition from all environmental radiation sources.

TABLE III

Allowable Dose for Crew

Critical body organ	Average dose Rad
Eyes	27
Blood forming organs.....	54
Skin of whole body.....	233
Feet, ankles, and hands.....	559

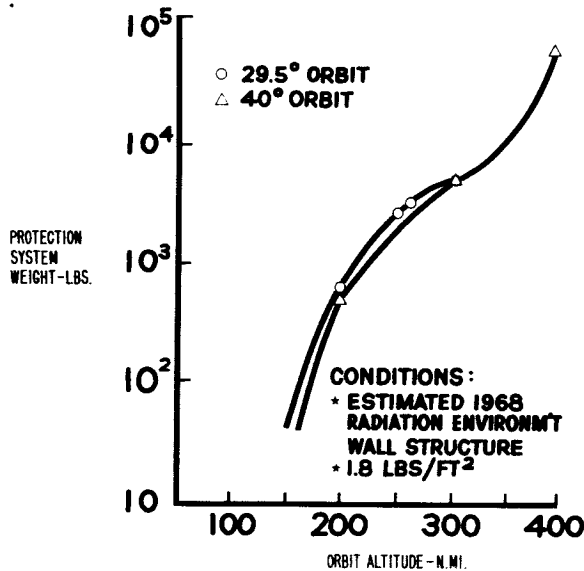


FIGURE 10.—Protection shield weights versus orbit altitude: 29.5 degree and 40 degree orbits.

The eyes constitute the most sensitive part of the human body considered in this analysis. If the eyes are shielded during solar storms or other space radiation activity by goggles, then, of course, the blood-forming organs become the critical organs.

PROTECTION REQUIREMENTS FOR LOW INCLINATION ORBITS

The radiation protection weights for the large 24-man space station for low inclinations are shown in figure 10. All shield weights are shown in pounds.

These weights include shielding on the bunks for 8 of the 24 men that are sleeping. The remaining awake personnel don portable body shielding, in the form of tunics and helmets, whenever the space station passes through the earth's radiation belts. At 29.5°, the space station passes through the intense radiation regions at altitudes greater than 150 n. mi. At 260 n. mi., the station is in the radiation fields and body shielding must be used for a period of 15 to 20 minutes per orbit on approximately 7 out of 15 orbits per day.

In all cases, the shield thicknesses were computed assuming the doses shown in table III. The radiation shielding is in addition to meteoroid and thermal protection, which consists of

an exterior meteoroid bumper of 0.025-in. Al, followed by 2-in. insulation and finally 0.067-in. Al interior pressure shell. For the 260 n. mi. case cited above, the thicknesses of the shielding materials to be used are 1.6 in. of hydrogenous material followed by 0.08 in. of heavy metal (such as lead) on the bunks and helmets, but only 0.35 in. of equivalent hydrogenous material on the suits. Of the 3226 lb of total radiation shielding required, approximately 66 percent is on the double bunks. If it is required that the entire space station be shielded, the weight penalties shown will increase by at least an order of magnitude, because of the greater area involved.

PROTECTION REQUIREMENTS FOR HIGH INCLINATION ORBITS

The shielding weights vs altitude for the 60 and 90° orbital inclination cases are shown in figure 11.

Under the assumptions used in this study, the shield weights in polar orbits are slightly lower than those in lower equatorial orbits, for the same probability of not exceeding a given dose. This is primarily because the numbers of protons and electrons intercepted during passage through the belts are reduced because of the shorter amount of time spent in them. Also,

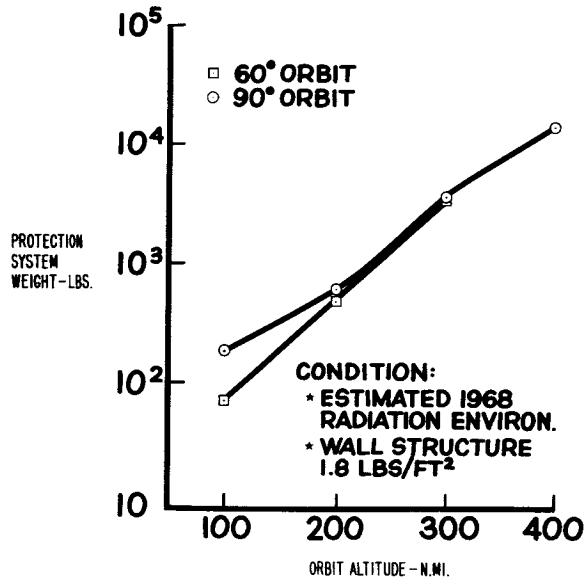


FIGURE 11.—Protection shield weights versus orbit altitude: 60 degree and 90 degree orbits.

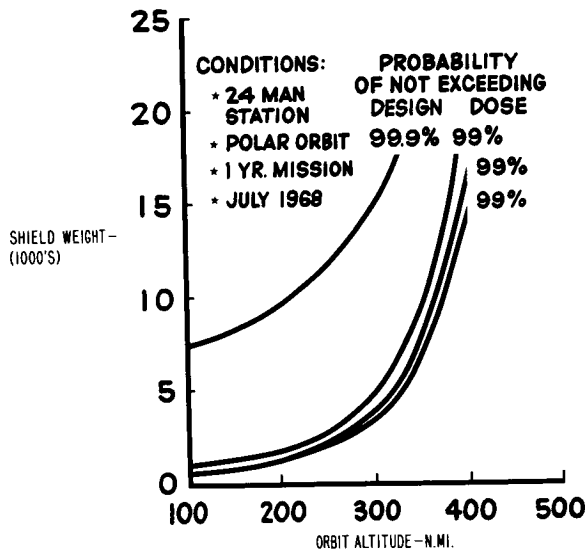


FIGURE 12.—Radiation shield weights versus altitude in polar orbit.

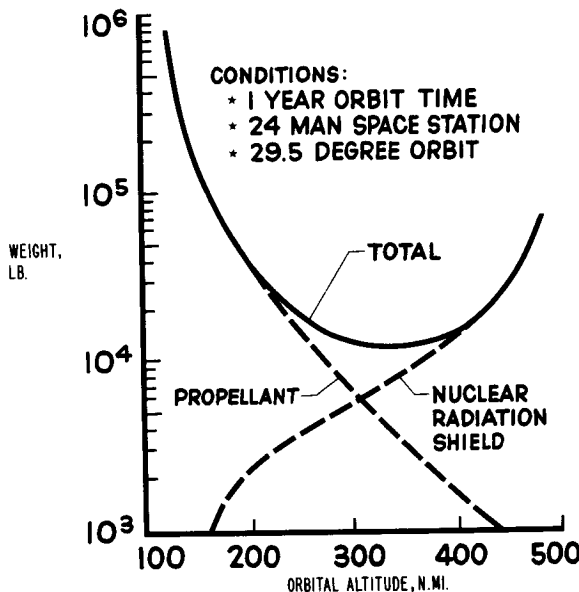


FIGURE 13.—Propellant and shield weights.

the solar proton fluxes are assumed to be received essentially independently of temporal effects. Further work is under way to determine the magnitude of the increase in the polar shield weights, if any, when these effects are included.

All the previous curves have been computed assuming a 90 percent probability of not exceeding the biological dose limits. A further

parametric study, varying this probability from 90 to 99.9 percent, was performed. The results are shown in figure 12. It is seen that weights increase rapidly as one designs to higher probabilities of not exceeding a given absorbed dose from the sun.

Inclusion of the propellant weight required to maintain orbit altitude gives the curve shown in figure 13.

It is seen that a broad optimum appears near the 250 to 400 n. mi. orbital altitude region. This shows that the orbital altitude should be selected in consideration of factors other than nuclear radiation shielding alone. Inclusion of heavier shielding, such as storm cellars or complete station shielding, would shift the location of the optimum to lower altitudes.

SPACE RADIATION MONITORING AND WARNING SYSTEM

At altitudes greater than 150 n. mi., the near-earth space station will be traversing the radiation belts and the polar regions periodically. Because protection is mandatory for times of exposure if design limits are not to be exceeded, a warning system is required to supply the space station commander with information concerning the status of the space environment. He needs to know in advance when the space station will be exposed, so the crew can don protective garments or seek shelter in a storm cellar. Also, information concerning the decreasing particle fields is required to ascertain if it is safe to remove protective garments or leave the radiation shelter. Complete reliance on space radiation field data from ground communication links will probably be unsatisfactory because of a number of potential problems, such as communication blackout.

The measurement equipment may be divided into essentially two groups: (1) external monitoring equipment; and (2) internal monitoring equipment. Since the space radiations exhibit energies, masses, and intensities which may vary over wide ranges, no single detector will satisfy the measurement requirements adequately. It is suggested that a series of external monitors may be required for the exterior environment, while the internal radiation levels may be measured continuously by portable meters. Cumulative exposure records

can best be obtained by the use of individual personnel photographic badges. The external monitoring systems in typical three-spoke stations are estimated to consist of six detectors weighing a total of 20 lb. Because of the tremendous variation in the anisotropy, energy, intensity, and types of particles in the near-earth space, considerable effort is required to define the optimum characteristics and detector location for the system.

SPACE RADIATION DOSIMETERS

The continuous monitoring of the amount of absorbed dose that space station crewmen receive can be performed by pocket dosimeters. Readings should be made inside the space suit shielding in order to get a true estimate of the body-absorbed dose. There appears to be no reason why this cannot be performed using conventional radiological dosimetric devices, such as photographic film badges, which have been successfully used for many years in AEC laboratories. Analysis of the dosimeter data will permit the radiation effects to be predicted. The evaluation of an individual absorbed dose could be performed periodically, either on the space station or at ground installations.

CONCLUDING REMARKS

Space stations operating in the near-earth environment over the next decade will require protection for personnel from the hazards of high-speed meteoroids and high-energy particles. The thicknesses and weights required for protection for a large three-spoke space station in 1968 have been computed by means of computer analysis for circular orbits and one-year missions. Although little or no shielding is required at orbital altitudes of less than 110 to 125 n. mi., shielding weights increase rapidly with altitude. The helmet, suit, and bunk shielding used are determined, under the assumptions of this study, to be minimum weight.

In low-altitude, low-inclination orbits, the shielding requirements are nominal, being of the order of 3226 lb at 260 n. mi., 29.5°. A broad optimum in the propellant and shield weight is found between 250 and 400 n. mi. altitude. Therefore, it is concluded that the radiation fields in space during this time period will not prohibit the successful operation of near-earth space stations in low-altitude, low-inclination orbits.

REFERENCES

1. HESS, W. N.: The Artificial Radiation Belt Made on July 9, 1962. *J. Geophys. Res.*, vol. 68, no. 3, 1963, pp. 667-683.
2. VAN ALLEN, J. A.: Spatial Distribution and Time Decay of the Intensities of Geomagnetically Trapped Electrons From the High Altitude Burst of July 1962. Research Rept. No. 63-11, State Univ. Iowa.
3. BOUQUET, JR., FRANK L.: The Radiation Hazard of Space. *Space/Aeronautics*, vol. 39, no. 5, 1963, pp. 72-77.
4. D'ANGIO, GUILIO J.; and LAWRENCE, JOHN H.: Medical Research With High Energy Heavy Particles. *Nucleonics*, vol. 21, no. 11, 1964, 56.
5. WARREN, CARLOS S.; and GILL, WILLIAM L.: Radiation Dosimetry Aboard the Spacecraft of the Eighth Mercury-Atlas Mission (MA-8). NASA TN-D-1862, Aug. 1964, p. 42.

105-34620

44—The Importance of Space Radiation Shielding Weight

E. R. BEEVER and D. H. RUSLING

North American Aviation, Inc.

34620

The shielding weights required to protect astronauts against space radiation should be considered in relation to the weights of the meteoroid shielding and the life support systems. Comparisons have been carried out for a variety of crew sizes and mission durations.

The radiation shield weights were based upon a 1% probability and were obtained from Webber's data on solar proton events. A mission dose of 100 rad was used as the allowed limit. The doses allowed from solar events were reduced by 45 mrad/day due to galactic radiation and by the amount of radiation expected for two high thrust trips through the earth's trapped radiation belts. In the calculation of the shield weights, the "storm cellar" concept was employed, allotting 50 ft³ per man.

The meteoroid shield weights were based upon the work of Bjork and the NASA-Ames Research Center criterion. The single shield thicknesses calculated were modified to take into account the reduced penetration where two facing sheets with space between them are used as the meteoroid shield. A 1% probability of penetration was assumed in the calculations.

The weights of the life support system are dependent upon the assumptions made regarding the particular subsystems to use for a specific mission. Two systems were used for this comparison. The system selected for the 30-day mission provides for body waste storage rather than reprocessing. Each system assumes a cabin leakage rate of 10 lbs/day and a power penalty weight of 320 lbs/kWe.

autho

INTRODUCTION

Historically, the shield designer has worked under two rather divergent forces. First of all, there is the pressure to design a minimum weight shield which derives from the realities of total weight, power, and costs. At the same time, the shield designer has the pressures of conservatism which evolve from considerations of reliability and crew safety. As a result, the problem is approached in a deliberate and iterative manner.

In the early phases of design, the total radiation protection requirements for the crew are determined. The bookkeeping for these requirements is in the form of thickness or weight. The actual shield weight, which must be included strictly for radiation protection, becomes known progressively as the inherent shielding effectiveness of the vehicle is understood.

The importance of the radiation protection weight, then, is best understood when placed in the context of its relation to other spacecraft

necessities. Two systems of particular interest are the meteoroid protection and life support (or ecological) system. These systems not only offer potential weight savings, but are also amenable to weight and volume analysis in the conceptual and preliminary design phases.

For the purposes of this study the spacecraft was assumed to be a cylinder, the length of which was two times the diameter, sized on the basis of 700 ft³ per man internal volume.

LIFE SUPPORT SYSTEMS

Life Support Systems comprise those assemblies of subsystems which provide for atmospheric control, food, and water. They range in degree of closure from essentially open to almost full ecological systems. Of particular importance to the shield designer is the fact that these systems contain substantial amounts of storables for which there is a measure of flexibility in the location of storage.

Several life support systems have been analyzed at S&ID (ref. 1). These were

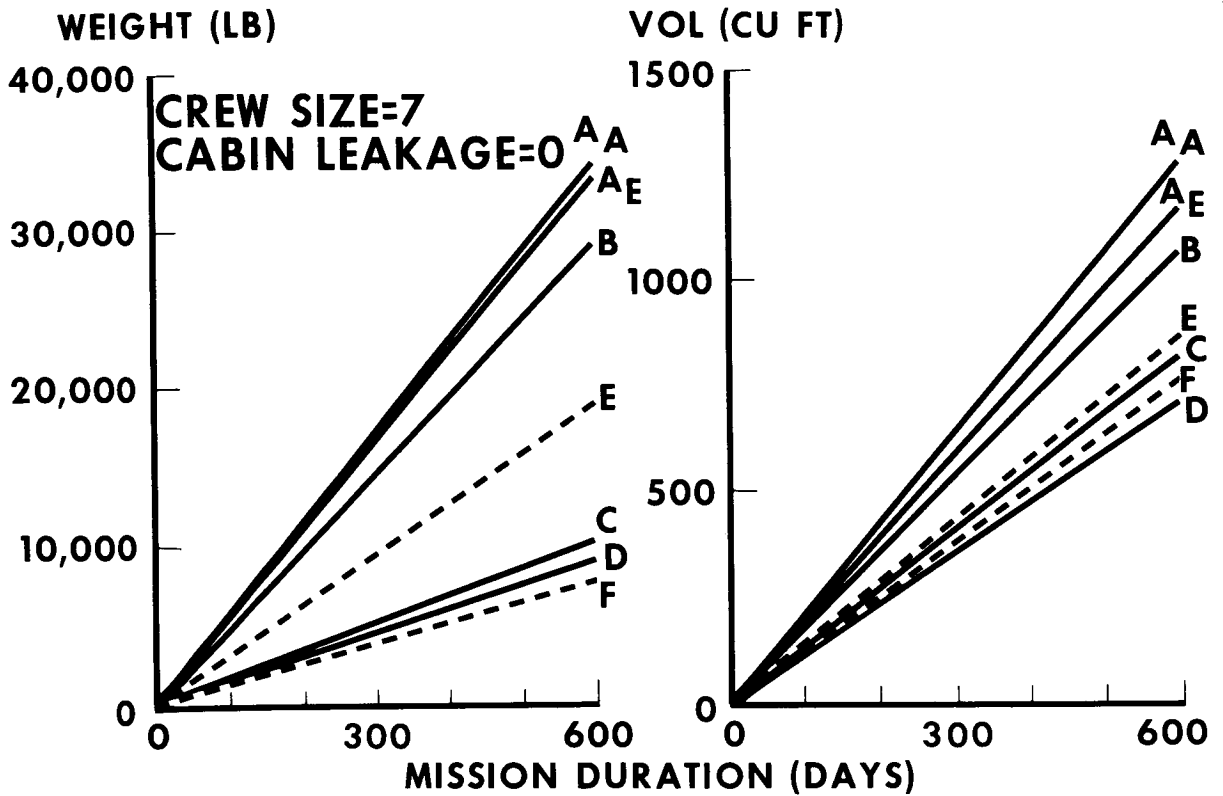


FIGURE 1.—Degree-of-closure results.

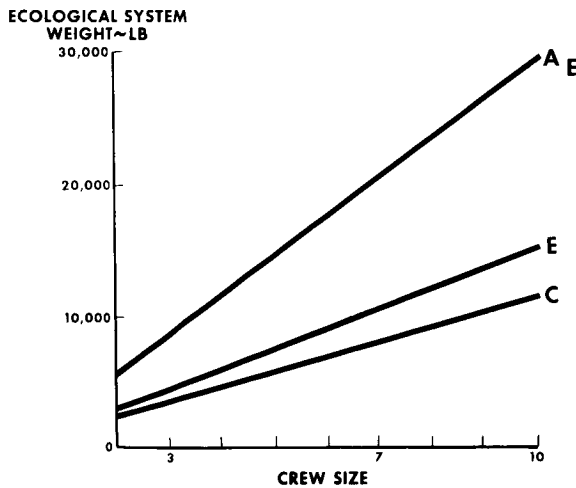


FIGURE 2.—Ecological system weight: 440-day mission; zero leakage.

reviewed during this study for trends in total weight and volume. Table I is a description of the various systems studied. Table II shows their degree of closure and the makeup requirements for each. Systems "A_A" and "A_E" are

practical "open" type systems, and the makeup requirements are high. System "C" is considered to be a state-of-the-art closed ecological system and the makeup requirements are down by a factor of 3. Table III shows the weight, power, and volume of the subsystems involved as a function of crew size and mission duration. The subsystems do not combine in a strictly additive manner to make up a system, since ecological balances must be accounted for. Table IV shows the resupply weights and volumes for the various systems. Figure 1 shows the weights and volumes for the various systems as a function of mission duration for a 7-man crew. Figure 2 shows the effect of crew size on the ecological system weight. Here, the mission duration has been fixed at 440 days. In these two figures, it was assumed that there was no cabin leakage, and no power penalty was estimated for externally generated heat loads.

The effects of cabin leakage are shown in figure 3 for three of the systems. Figure 4 shows system weights for two sizes of crews as a

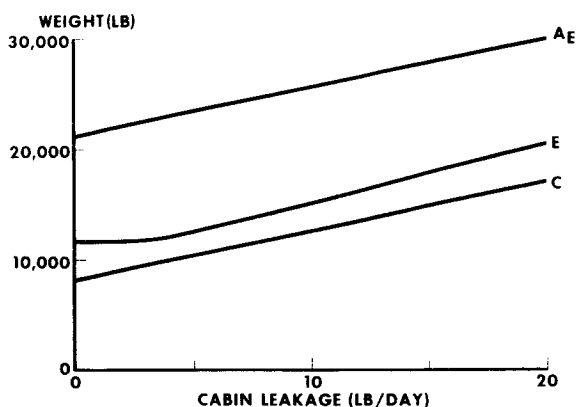


FIGURE 3.—Leakage study results: 440-day mission; 7-man crew.

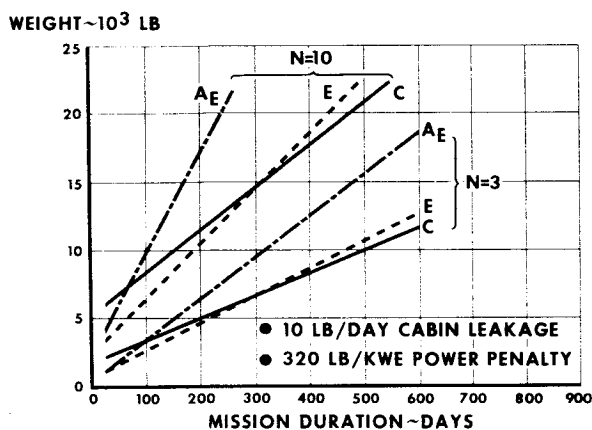


FIGURE 4.—ECS plus power penalty.

function of mission duration assuming a reasonable cabin leakage of 10 lbs/day and a power penalty of 320 lbs/kWe.

METEOROID PROTECTION

Meteoroid protection is of prime importance to the radiation shield designer because it constitutes a mass envelope which is fully effective in radiation protection.

Meteoroids appear to be of two types. The first type has a high density (3-8g/cm³) and is believed to be related to the asteroidal belt which largely lies between Mars and Jupiter. The second type is believed to have a low density ($\lesssim 1$ g/cm³) and is believed to be cometary in origin. Both types have velocities lying between 10 km/sec (earth escape velocity) and 70 km/sec (sun escape velocity). Both types have flux distributions which increase as the

TABLE I

Life Support Systems Description

System	Description
A _A ----- Base Point----- "Open"-----	(1) Heat rejected by radiators using recycle coolant. (2) CO ₂ removal by adsorption. (3) Wash water reclaimed. (4) Materials stored are food, O ₂ , water, and N ₂ . (5) Perspiration and respiration water reclaimed.
A _E -----	Same as System A _A except change (2): (2) CO ₂ removal by electrodi- alysis.
B-----	System A _E with (6) added: (6) O ₂ regenerated by hydrogen- ation.
C-----	System B with (7) added: (7) Urine water reclaimed.
D-----	System C with (8) added: (8) Feces water reclaimed.
E----- (Alternative to B).	System A _E with (6b) added: (6b) Partial urine water recla- mation for water bal- ance.
F----- (Alternative to D).	System C with (6) changed: (6) O ₂ regenerated by direct conversion.
"Closed" ECS.	System D or F with feces and other waste products recon- verted to food.

mass decreases, with no mass-velocity correlation being apparent. Both types apparently tend to occur in showers, most of which have annual periodicities. This may be due to the inability of measurements to determine the type of meteoroid encountered.

From a space meteoroid shielding standpoint, the important parameters are the mass and velocity distributions. The measurements, however, do not provide such information directly, and therefore, it must be inferred. Bjork obtained an m^{-10/9} dependence, with a velocity distribution from 15 km/sec (m < 10⁻⁷

TABLE II
ECS Makeup Requirements

[Wash water and vapor reclaimed in all systems: Zero leakage compartment]

Percent closure	System	Subsystems	Makeup lb/man-day			
			Food	Water	Oxygen	Total
68.5	A _A	CO ₂ removed—MOL sieve	1.4	2.33	1.80	5.53
68	A _E	CO ₂ removed—electrodialysis	1.4	2.90	1.30	5.60
73	B	Reduce CO ₂ methanation → Produce O ₂ H ₂ O electrolysis	1.4	3.34	0	4.74
84	E	Reclaim urine	1.4	0	1.30	2.70
90	C	Reclaim urine	1.4	0.35	0	1.75
91	D	Reclaim fecal water	1.4	0.13	0	1.53
92	F	O ₂ from direct reduction CO ₂	1.4	0	0	1.40

gm) to 28 km/sec ($m > 3 \times 10^{-2}$ gm) (ref. 2). By using this meteoroid environment and the laboratory data available from impact studies, the thickness of aluminum or steel required to prevent puncture by a projectile of the same material was obtained.

Other studies have been carried out along similar lines by Whipple (ref. 3), Opik (ref. 4), and Eickellenger and Gehring (ref. 5). While the theoretical approaches were different, the results predicted are quite similar. Perhaps the most widely used information is the NASA-Ames Research Center criterion. This criterion is discussed in relation to the other studies in a Bellcom report, "The Meteoroid Environment for Project Apollo" (ref. 6). The result is:

$$t^2 N = 2 \times 10^{-17} \quad (1)$$

where:

t = meteoroid shield thickness, m
 N = meteoroid flux, meteoroids/m²-sec

Another relationship required is:

$$P = NE \quad (2)$$

where:

N = exposure, m²-sec
 $E = AT$

where:

A = area of spacecraft surface, m²
 T = duration of exposure in space, sec

TABLE III
Subsystem Weight, Power, and Volume

Subsystem	Weight lb ¹	Power ¹ watts	Heat load, q ¹ Btu/hr	Volume ¹ Cu Ft
1. Temperature control.....	8.07N+0.0091q+43...	30N.....	102.5N...	0.113N
2. CO ₂ removal				
2a. Molecular sieve.....	0.111Nτ+26.33N+17...	97N.....	331N.....	0.0222Nτ+1.125N
2b. Electrolysis.....	91.0N+27.75.....	160N.....	60.3N.....	0.444N
3. CO ₂ reduction				
3a. Electrolysis+methana- tion.....	77.65N.....	340N.....	390N.....	1.0N
3b. Direct CO ₂ conversion....	10N.....	182.6N...	345N.....	1.0N
4. Wash water reclamation.....	0.107Nτ+10.....	3.983N...	13.6N.....	0.128N+0.10
5. Urine reclamation.....	0.2356Nτ+25.....	5.0N.....	17.1N.....	0.051N+0.10
6. Urine sources container.....	0.32Nτ.....	0.0513Nτ
7. Feces water recovery.....	0.02356Nτ+2.5.....	6.48N.....	22.1N.....	0.0032N+0.01
8. Waste storage container.....	0.033Nτ.....	0.0066Nτ
9. Trace contaminant removal....	2.4N+4.....	10N.....	34.2N.....	0.5N
10. Personal cleanliness.....	N+20.....	2N.....	6.48N.....	2.0
11. Ducting and blower.....	N+10.....	66N.....	225.72N...	0.044N+0.20
12. Cabin atmosphere.....	24.71N.....	(700N)

¹ N=crew size; τ=mission duration, days; q=process heat load, Btu/hr.

Combining equations (1) and (2) yields

$$t = \left[\frac{2 \times 10^{-17} AT}{P} \right]^{0.33}$$

$$= 2.7 \times 10^{-6} \left(\frac{AT}{P} \right)^{0.33} \quad (3)$$

It is seen that in this form the Ames criterion looks like Bjork's formula

$$t = 2.5 \times 10^{-6} K v^{0.33} \left(\frac{A\tau}{-\ln p'} \right)^{0.31} \quad (4)$$

where

K =constant=1.64 for Al on Al
=0.908 for steel on steel
 v =velocity of meteoroid, km/sec
 p' =probability of no hits

Table V shows single and double sheet thicknesses of aluminum meteoroid shielding calculated using Bjork's formulation and the Ames criterion.

RADIATION SHIELDING

Calculating the radiation thickness needed for a mission in space requires some knowledge of the mission profile. If trapped radiation

belts around planets with magnetic fields are avoided, the remaining sources of radiation are galactic (cosmic) particles and solar event particles.

To a first approximation, the galactic radiation is constant in time and space, and the dose rate is almost independent of shield thickness (for thicknesses up to a few tens of gm/cm²). The dose rate varies from ~30 mrad/day during periods of maximum solar activity to ~45 mrad/day when the sun is quiet. For purposes of this study, a constant value of 45 mrad/day was used.

The major sources of radiation in space are solar events (flares). Only gross probabilities of flare occurrence can be predicted, as flares tend to occur in 11-year cycles with the most recent minimum in 1964 to 1965. During solar maxima, flares are 5 to 10 times as probable as during solar minima. Unless the actual year in which the mission will take place is specified, one can use the solar cycle average only for estimating the solar event radiation environment. For the purpose of this study, this assumption was made with Webber's tabulation of the 1956 to 1961 data being used as a basis (ref. 7).

TABLE IV

Ecological Systems Atmosphere and Food Resupply Weight and Volume

Item	System	Subsystems—Items from table III	Weight, ^{a b c} lb	Volume, ^{a b c} cu ft	Comments
1	A	1, 2, 4, 6, 8, 9, 10, 11, 12-----	-----	-----	Molecular sieve 30 day Resupply
1a	A _A	Molecular sieve CO ₂ removal-----	6. 007N τ	0. 208N τ	
1b	A _F	Electrodialysis CO ₂ removal-----	6. 048N τ	0. 048N τ	
2	B	1, 2b, 3a, 4, 6, 8, 9, 10, 11, 12-----	5. 143N τ	0. 196N τ	
3	C	1, 2b, 3a, 4, 5, 8, 9, 10, 12-----	1. 8539N τ	0. 1459N τ	
4	D	1, 2b, 3a, 4, 5, 7, partial 8, 9, 10, 11, 12	1. 612N τ	0. 1425N τ	
5	E	1, 2b, 4, partial 5 & 6, 8, 9, 10, 11, 12	2. 860N τ	0. 1607N τ	Complete water bal- ance
6	F	1, 2b, 3b, 4, partial 5 & 6, 8, 9, 10, 11, 12	1. 47N τ	0. 140N τ	Complete oxygen and water balance

^a N=Crew size, No. men; τ =mission duration, days.

^b Container and hardware weights and volumes are included.

^c N₂ and O₂ are stored at 150 psia, subcritical, cryogenic with boil-off equal to usage rate.

TABLE V

Single and Double Sheet Thicknesses of Aluminum Meteoroid Shielding

Crew size	Mission duration, days	Meteoroid protection weight, lb			
		Bjork		Ames Criterion	
		Single	Double	Single	Double
3	30	8500	2380	4038	1130
	100	12 200	3410	6020	1686
	300	17 250	4815	8680	2430
	1000	24 250	6780	12 950	3630
7	30	17 800	5000	8600	2410
	100	25 200	6980	12 840	3600
	300	35 600	10 000	18 500	5200
	1000	51 000	14 400	28 800	8050
10	30	24 300	6780	12 500	3495
	100	35 400	9920	17 650	4940
	300	48 200	13 500	25 500	7120
	1000	69 300	19 400	38 100	10 660

The radiation shield thicknesses were constructed using the probability of encountering an integrated flux as a function of mission duration in conjunction with the calculated point doses within a spherical aluminum shield. Figure 5 shows the probability of encountering a total flux above 30 MeV for mission durations

from three months to two years. A summary of the calculated point doses for shield thicknesses of 1 g/cm² and 10 g/cm² (corresponding to proton cut-off energies of 30 MeV and 100 MeV) is shown in figure 6. Straight line fits have been applied to these data. From these two plots the total dose probabilities can

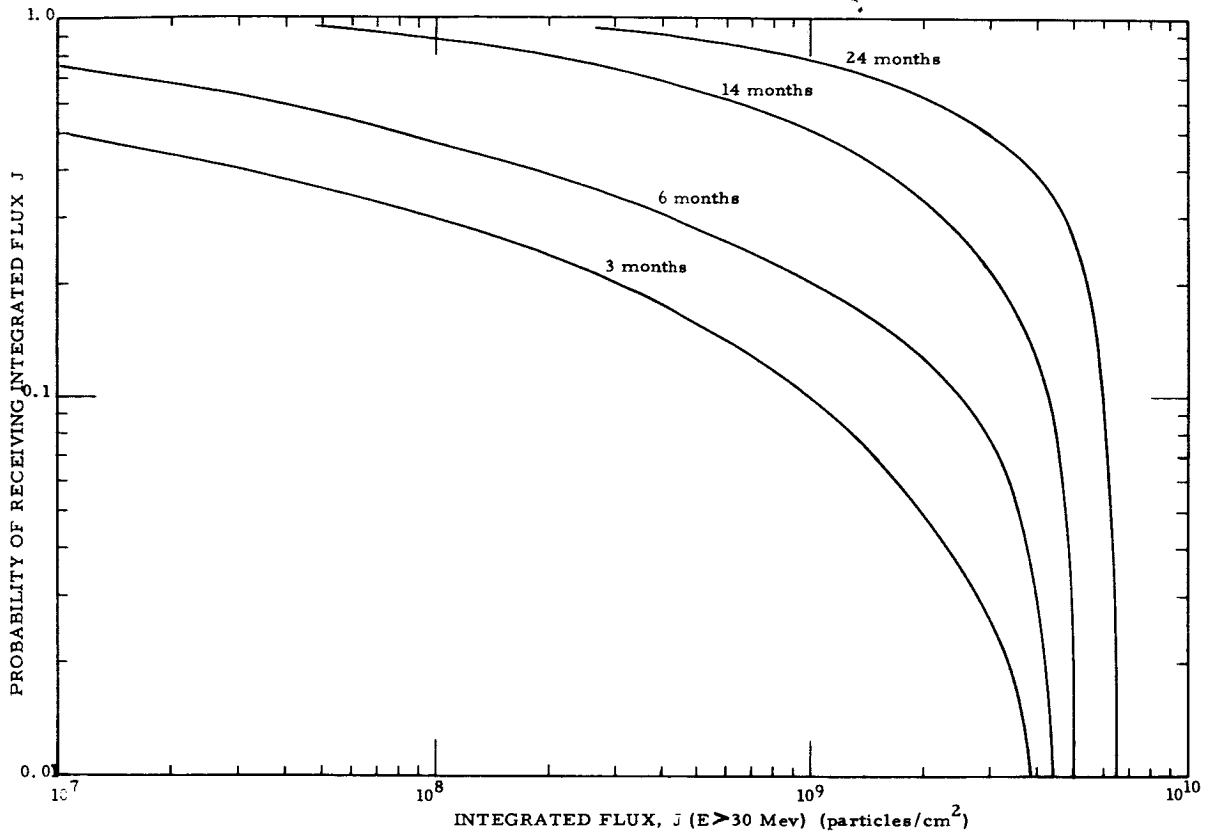
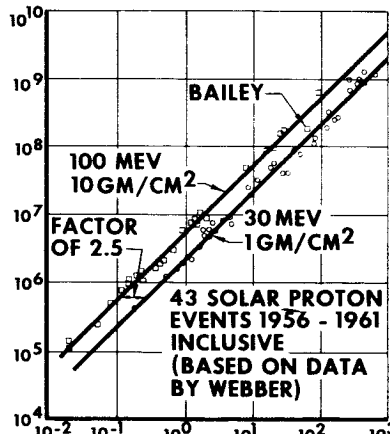


FIGURE 5.—Cumulative probability-flux curves for various mission durations.

PROTONS/CM²



DOSES INSIDE SPHERICAL ALUMINUM SHIELD ~ RADS

FIGURE 6.—Summary of flare proton flux.

be constructed for various mission durations; an example for a 400-day mission is shown in figure 7. Interpolations for other shield thicknesses were made using the dose as a function

PROBABILITY ~ %

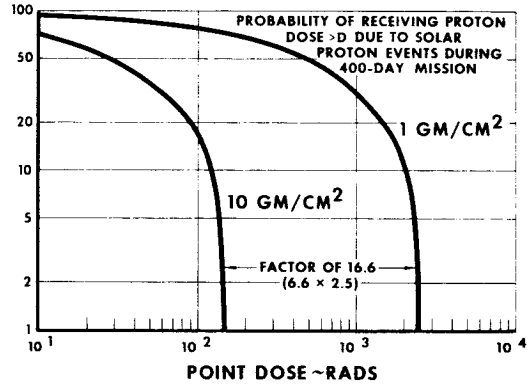


FIGURE 7.—Total dose probability.

of shield thickness calculated for the Bailey Model Event, figure 8. Weight calculations were based upon using a minimal volume storm cellar of 50 ft³ per man. The dose criteria applied was 100 rad/mission to the blood forming organs.

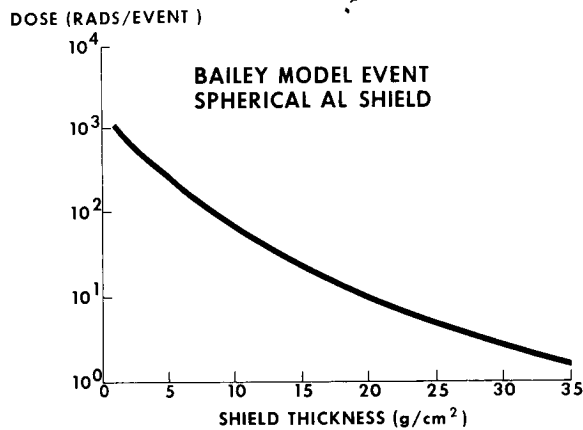


FIGURE 8.—Solar proton integrated dose.

SUMMARY

Table VI shows a summary of the system weights for the life support systems, meteoroid shielding, and the radiation shielding. The radiation shielding weights have been reduced by the protection afforded by the meteoroid protection, but do not include any allowances for the shielding effectiveness of the life support systems. In this regard, it is interesting to note that the resupply needs of system "C" exceed the shielding requirements of a 10-man crew for 300-day missions. While not

TABLE VI

System Weights

Mission duration, days	Life support system "C"	Meteoroid shielding (Ames Criterion single sheet)	Net radiation shielding (radiation shield-meteoroid shield)
3-Man Crew			
30	1500	4038	1890
100	3300	6020	2200
300	6700	8680	2440
1000	18 200	12 950	2530
7-Man Crew			
30	4100	8600	3100
100	5700	12 840	3520
300	10 600	18 500	3810
1000	27 600	28 800	3520
10-Man Crew			
30	6100	12 500	3530
100	8300	17 650	4190
300	14 500	25 500	4440
1000	36 000	38 100	4180

all these storables can be used as shielding—and there are some consumables included—the advantages and possible weight savings are apparent.

REFERENCES

- HONEA, F. I.: Life Support Systems. Manned Mars Landing and Return Mission Study North American Report SID 64-619-3, Sec. 3.1.1
- BJORK, R. L.: Meteoroids versus Space Vehicles ARS J., June, 1961.
- WHIPPLE, F. L.: Vistas in Astronautics (Morton Alperin, Marvin Stein, eds.), Pergamon Press (New York), 1958.
- OPIK, E. J.: Irish Astronomical Journal, no. 5, 1958, pp. 14; also, Physics of Meteor Flight in the Atmosphere. Interscience, 1958.
- EICHELBERGER, R. J.; and GEHRING, J. W.: ARS J., Oct. 1962, p. 1583.
- The Meteoroid Environment for Project Apollo, Annex C, Bellcom Rept., Jan. 31, 1963.
- WEBBER, W. R.: An Evaluation of the Radiation Hazard Due to Solar-Particle Events. D2-90469, The Boeing Co.
- HAFFNER, J. W.; and BEEVER, E. R.: Effective Mars Mission Radiation Doses. North American Report SID 64-1298.

N65-34621

45—Shielding Requirements for Manned Orbiting Space Stations

T. M. JORDAN, E. F. KOPROWSKI, and R. W. LANGLEY

Douglas Aircraft Company

A detailed parametric investigation of radiation shielding requirements was performed for first generation manned orbiting space stations. Two specific space station designs were studied; the results of the shielding analysis are based on the actual geometry of the vehicles, onboard equipment, and supplies. Results are presented for circular orbits ranging from 100 to 600 nautical miles and from 29° to 90° inclination. The effects of the geometry of the space stations, the use of personal shielding, and the use of particular shielding materials are discussed.

INTRODUCTION

One of the major considerations affecting the design and orbit selection of manned orbiting space stations is the shielding required for protecting the crew against the space radiation environment. In order to evaluate the shielding requirements for early extended orbital missions, two specific space station configurations were selected for analysis: one is a nominal 260 inch diameter, 6-man vehicle, the other a nominal 120 inch diameter, 2-man vehicle. Both of these systems have been defined in detail as to vehicle size, amount and location of equipment and supplies, structural design, etc.

The mission duration contemplated for these systems is on the order of one year. The orbits selected for study are circular and vary in altitude from 100 to 600 nautical miles, and in inclination from 29° to 90°. The altitude limits were chosen on the basis of excessive orbit decay and excessive shielding requirements, and the inclination limits were chosen to vary from a maximum payload launch at Cape Kennedy to polar orbit.

In order to account for the shielding effectiveness of the space stations with the onboard equipment and supplies, and the self-shielding

of the crew members to various biological organs, the space stations, including a simple man model, were analytically simulated by plane and quadratic surfaces to facilitate the detailed point kernel dose integrations required for each case.

The space radiations that were considered include trapped protons, trapped natural and artificially injected electrons, and solar cosmic rays; estimates were made of the state of the space radiation environment during the projected operational period of 1968 to 1974.

SPACE STATION CONFIGURATIONS

The two specific space station configurations chosen for this study represent typical first generation systems that could be made operational between 1968 and 1974. These systems have been studied in detail to determine the vehicle configuration and the amount of onboard equipment and supplies that are required. The systems were sized for a two-man vehicle and a six-man vehicle. The radiation dose received from isotopic or fission reactor auxiliary power sources is not included because the design dose for these systems is only a few rads per year and does not directly affect the space station shielding.

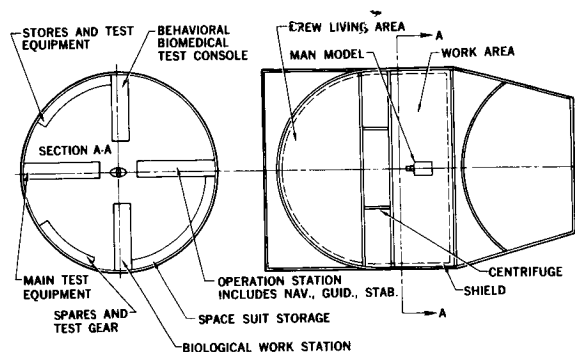


FIGURE 1.—Six-man space station calculational model.

Six-Man Space Station

Figure 1 presents the vehicle design of the 260 inch diameter, six-man space station. A total of 45 surfaces defining 49 regions were necessary to adequately describe this system. The shield indicated on the figure has a uniform thickness surrounding the work area, the rest area, and the centrifuge. The centrifuge is the artificial gravity system onboard the vehicle. In the center of the work area, a simplified version of a man model is shown. This radiobiological model is used to simulate the biological self-shielding. This model consists of two elliptical cylinders representing the trunk and the head, and is composed of water to approximate the composition of tissue. The organs for which the dose was calculated are the lens of the eye, the blood-forming organs, and the skin. The blood-forming organs were assumed to be located 5 cm inside the surface of the large cylinder which represents the trunk.

Two-Man Space Station

The two-man space station shown in figure 2 has a nominal diameter of 120 inches. For this space station configuration, a total of 59 surfaces were used to define 54 regions. In addition, a docked Gemini capsule was included since it will remain in this position almost continuously providing some shielding. The same biological model was used in this configuration as described previously, and the indicated shield has a uniform thickness.

METHOD OF ANALYSIS

The shielding analysis was performed in three steps: (1) definition of the integrated space

radiation environment; (2) calculation of the dose attenuation data in idealized geometry; and (3) an angular dose integration over the space station configuration for each dose point. The data and methods used in each step are discussed below.

Space Radiation Environment

The space radiation sources which are important to manned orbiting space stations are geomagnetically trapped protons and electrons (natural and artificially injected), and solar cosmic rays. Galactic cosmic rays also contribute to some extent, but are generally of a much lower magnitude; for low altitude orbits, from <1 to 4 rads/yr during solar minimum, depending on the orbit inclination.

The Douglas computer program OGRE was used to calculate the time integrated trapped proton and electron radiation and solar cosmic ray protons which a space station will encounter in various orbits and mission times. This is accomplished by transforming the geographic coordinates of a given trajectory into the B-L coordinate system of McIlwain, in which terms the radiation fields are expressed, and summing the time-weighted particle fluxes over the mission profile. Reference 1 gives a detailed description of OGRE and the sources of all data included in it; a brief discussion follows.

OGRE has four modes of operation: (1) a table of geographic positions can be specified, and the fluxes at those positions printed out; (2) for trajectories which are not elliptical or circular, the position versus time for a vehicle can be specified, and the fluxes at these positions and the total time integrated fluxes versus energy produced; (3) the elements of an ellipti-

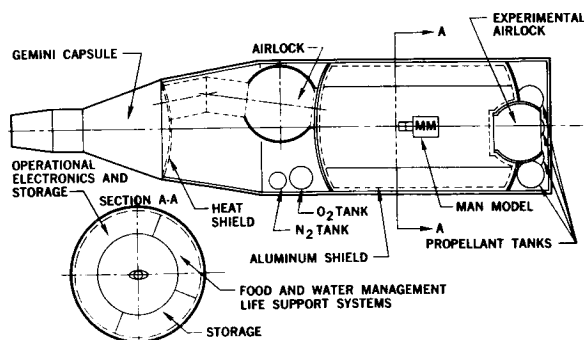


FIGURE 2.—Two-man space station calculational model.

cal trajectory can be specified and the total flux and energy spectra produced; and (4) for the special case of circular orbits that sufficiently cover the region of space accessible to them, a more efficient calculation is used which amounts to integrating the flux region within the orbit bands with a simple harmonic weighting factor. For most cases involving orbiting space stations, the latter option is used, which greatly reduces computer time requirements over the method of orbit tracing, while improving the accuracy of the results for relatively long missions (>2 weeks).

The following is a brief description of the data and assumptions used in this study.

Protons. The most accurate and recent data used were those from Explorer XV as reported by McIlwain, and those from an Air Force polar orbiting satellite reported by Freden and Paulikas. The fluxes at other positions were obtained by normalizing other data to that above, taking into account the distribution changes with time since the measurements were made. These time changes, explicitly included in the program, are caused by changes in atmospheric density which is a function of the solar cycle. The most useful data for evaluating this effect were from Explorer VI, Explorer VII, Holly's rocket experiments, other Air Force Satellites, and Sputniks II and III.

The best available proton energy spectrum is due to McIlwain and Pizzella, which takes into account the softening of the spectrum with increasing L . This spectrum is:

$$\phi_p(E)dE = K_e e^{-E/E_0} dE$$

where

$$E_0 = (306 \pm 28)L^{-(5.2 \pm 0.2)} \text{ MeV}$$

The above data, plus that from Explorer IV and various other sources, were used to form a consistent flux map in B - L coordinates.

In general, when interpolations and extrapolations were made to produce the flux maps, the data indicating the highest fluxes were used, and similarly the type of extrapolation which gave the highest fluxes in regions where no data were available was used. This technique was based on the philosophy that it is more desirable to overestimate the flux than to underestimate it.

A preliminary examination of recent published measurements from Cosmos 3 and Cosmos 5 agree rather well with these maps, which includes extensive coverage of protons with energies greater than 75 MeV.

Natural Electrons. For $L < 2$, there is very little data available on the natural, or pre-Starfish electron flux. The Starfish was a nuclear device detonated on July 9, 1962, at an altitude of about 400 km over Johnston Island, on the $L=1.12$ geomagnetic line. Beta decay of the radioactive material created an artificial electron belt in that region of the geomagnetic field. Data taken since Starfish include both natural and artificial electrons and are in themselves of very limited usefulness for determining the natural electron flux. However, previous studies indicate that the variation of natural electron intensity with altitude is not greatly different from the variation of total electron intensity as measured by Explorer XV. The variation of natural electron flux with position is similar enough to that of the total flux (as well as can be determined from the data) that the total flux distribution curves can be used for the natural flux distribution when they are normalized to the proper magnitudes. An upper limit for the natural electron flux can be obtained by assuming that, in this inner zone region, it has a space independent integral spectrum of the form:

$$\phi_e(>E) = K_1 E^{-0.5}; 30 < E < 200 \text{ keV}$$

$$\phi_e(>E) = K_2 E^{-4}; 0.2 < E < 5 \text{ MeV}$$

and that the natural electron flux with energy greater than 180 keV is numerically equal to the total flux greater than 0.5 MeV (as of January 1, 1963).

For $L > 2$, lack of good data and the existence of sporadic, short-term variations prohibit estimates of electron fluxes better than an order of magnitude.

Artificial Electrons. The Starfish nuclear device injected some 10^{25} electrons with energies between 0.5 and 10 MeV into trapped orbits in the geomagnetic field. The peak flux at $L=1.2$ to 1.3 on the equator was over $10^9 \text{ cm}^{-2} \text{ sec}^{-1}$, and significant fluxes were found at altitudes as low as 100 km.

The most complete artificial electron data available to date are from Explorer XV and Discoverer satellites 29 and 31. The Explorer XV data for electrons with energy greater than 0.5 MeV and 5 MeV were compared with Discoverer 29 and Discoverer 31 data, along with that from rockets, Injun I, Alouette, Explorer XIV, Explorer XII, and polar-orbiting Air Force satellites. According to McIlwain, the integral energy spectrum between 0.5 MeV and 5 MeV is exponential within about 50%. For electrons above 5 MeV, a fission spectrum has been assumed, which is consistent with Paulikas and Freden's low, high-energy fluxes.

The time decay of the artificial radiation is uncertain. The measurements of McIlwain on Explorer XV showed no measurable change in fluxes at L values between 1.25 and 1.7, near the equator, over a period of about three months at the end of 1962. An analysis of electron decay at the L and B values of most interest has been made by Walt, Crane, and MacDonald and compared to data from Injun I and III. In general, the results for positions in the South Atlantic anomaly are in fair agreement and indicate that the flux, even at these low altitudes, although it has decreased significantly from the initial value to the January 1, 1963, value, decreased at a decreasing rate, and that the rate is not a strong function of B .

Various data and decay rate estimates have been compared, and the present estimate is that the decay is of the form:

$$\phi_e = \phi_{e0} t^{-\gamma}$$

with the typical value of γ being 0.9 for $20 < t < 100$ days, and 0.7 ± 0.20 for $t > 100$ days where t is the time after the Starfish test. In addition to this decay factor, there is another factor which affects the time dependence of all trapped particles; this is the change in the low altitude fluxes due to the expansion and contraction of the atmosphere caused by variations in the solar activity. For the natural radiation, this dependence is assumed to follow the eleven-year solar cycle and is included in OGRE; it is based on a comparison of proton data. For the artificial electrons,

it is assumed that there will be no significant decay after the reduction occurs due to the next solar maximum. That is, the artificial electron flux will remain approximately constant during the 1968-1974 time period considered in this study.

A procedure very similar to that used to determine the proton flux distributions in B - L coordinates was followed for the electrons, again based on Explorer XV data. However, no additional set of data comparable in amount to the Explorer IV data for protons is available, so each set of data used for the electron flux extrapolations was corrected to the proper energy range, insuring that the spectrum did vary regularly with L and B .

Solar Cosmic Rays. A space vehicle near the earth will be partially shielded by the geomagnetic field which alters the trajectories of the incoming charged particles in such a way that all particles with less than a certain cutoff energy cannot penetrate the field. The vertical cutoff energy shows a dependence on L which is very nearly independent of position. According to calculations based on measurements by Explorer VII, the cutoff energy can be expressed as

$$E_c = 2.5 \times 10^5 e^{-L/0.35} \text{ MeV}$$

for the November 12, 1960, event. This equation is included in the computer program, and each time L is computed at the satellite position, the cutoff energy is calculated and the fluxes at higher energies (using the November 12, 1960, event spectrum) accumulated. In this way, the flux spectrum which would be seen by a space vehicle during an identical event is determined.

Dose Attenuation Calculations

The Douglas program CHARGE provides a straight-ahead approximation solution to the radiation-penetration problem for primary electrons with their associated bremsstrahlung, and primary protons with their associated secondary nucleons and gamma rays, for geometrically simple shields. The attenuation of primary charged particles is governed primarily by ionization. The primary-radiation dose rates, D_p , are computed by a numerical

evaluation of the integral

$$\dot{D}_\beta(x) = C \int_{E_i(x)}^{E_n} \phi(E) e^{-\int_0^x \Sigma_{ne}[E'(E, x')] dx'} \frac{dE'(E, x)}{dx} dE$$

where

$E'(E, x)$ is the degraded energy at shield depth x corresponding to the incident energy E , and is calculated from the range-energy relation, (MeV)

C is the flux to dose-rate conversion factor, (rad/hr)/(MeV/cm²-sec)

$\phi(E)$ is the incident primary particle flux, (particles/MeV-cm²-sec)

$\Sigma_{ne}[E'(E, x')]$ is the macroscopic cross-section for nonelastic collisions, (cm⁻¹)

E_n is the maximum energy of the incident particles, (MeV)

$E_i(x)$ is the energy which has range x in the shield material, (MeV)

The incident spectrum is divided into energy groups and the shield materials into layers, for the penetration analysis. The approximate spectrum shape is retained within each energy group when performing the dose integral. The incident group of charged particles is attenuated through the shield by an integration of $\frac{dE'(E, x)}{dx}$, determining the group boundary energies as a function of x . Electrons and protons are treated in a slightly different manner to account for their different range-energy characteristics.

The electron energy-loss rate is computed by the formula of Bethe and Ashkin (ref. 2). The integration of this expression is simplified through recognizing the approximate linear dependence of E on x for energies greater than 0.5 to 1.0 MeV. Bremsstrahlung production is of little importance as an energy-loss mechanism for electron energies normally encountered; however, it can be a significant contributor to radiation dose.

Several formulations of the bremsstrahlung production cross sections are presently used to calculate the source of this dose component. The empirical treatment by Evans (ref. 3) is the simplest model and yields results which

agree reasonably well with a combination of Bethe-Heitler nonscreened cross sections and various cross sections compiled by Koch and Motz (ref. 4). The photons thus generated are transported from the source point to the detector location by exponential attenuation with buildup. The calculated photon spectra, transmitted through the shield, bracket the experimental spectra of Edelsack (ref. 5) for 1.0 to 2.0 MeV electrons.

The secondary particle dose rates are represented by the integral

$$\dot{D}_\beta(x) = \int_{E_i(x)}^{E_n} dE \int_0^{E_n} dE_\beta \int_0^x dx' \phi_\alpha(E) \Sigma_{\alpha\beta}[E'(E, x), E_\beta] e^{-\int_0^x \Sigma_{ne}[E_\pm(E, x')] dx'} \times T_\beta(x-x', E_\beta) R[E'_\beta(E_\beta, x-x')]$$

where

$\Sigma_{\alpha\beta}(E_\alpha, E_\beta)$ is the cross section for production of secondary particle type β with energy E_β from primary type α with energy E_α (cm⁻¹)

$T_\beta(x-x', E_\beta)$ is the transport function for particle type β , created with energy E_β at position x' , to the detector at x (dimensionless)

$R[E'_\beta(E_\beta, x-x')]$ is the flux to dose-rate conversion for particle type β at degraded energy E_β (rad/hr)/(MeV/cm²-sec)

The production cross sections $\Sigma_{\alpha\beta}$, dependent on both primary and secondary energy, for (p, p') , (p, n) , (n, p) and (n, n') reactions are included in the CHARGE program by an empirical treatment of Monte Carlo calculations and experimental data. The transport and dose conversion functions for secondary protons are identical to those for primary protons at the same energy. For neutrons, the transport function is obtained from multigroup removal theory.

Detailed Geometry Calculations

The detailed geometry calculations consist of utilizing basic dose attenuation data, like that generated in CHARGE, to perform an angular integration over the detailed geometry

of the system, for each dose point. The integration is performed by the Douglas program SIGMA. Basically, program SIGMA calculates the dose received at specified points inside a system of arbitrary configuration. The system geometry is described by a series of material regions with one or more boundaries which are defined by equations of the form:

$$A_0 + A_1x + A_2y + A_3z + A_4x^2 + A_5y^2 + A_6z^2 + A_7xy + A_8yz + A_9xz = 0$$

The dose $D(\vec{r})$ received at the point \vec{r} is calculated by a numerical Simpson's rule integration of the equation

$$D(\vec{r}) = \frac{1}{4\pi} \int_{-1}^1 \int_0^{2\pi} K(\vec{r}, \vec{\Omega}) d\theta d\mu$$

where

μ = the cosine of the polar angle

θ = the azimuthal angle

$$\vec{\Omega} = \sqrt{1-\mu^2} (\cos \theta \vec{i} + \sin \theta \vec{j}) + \mu \vec{k}$$

(a unit vector in the direction defined by μ and θ)

The kernel, $K(\vec{r}, \vec{\Omega})$, represents the dose that would be received at \vec{r} if the material thickness encountered along a ray from \vec{r} in the direction of $\vec{\Omega}$ were spherically symmetric about \vec{r} . The number of intervals in the μ and θ integrations are variable, with systems of pronounced asymmetry requiring a larger number of intervals.

Two options, which can be used concurrently, are provided for the calculation of the dose received through various outer sections of the vehicle. The first provides a dose breakdown according to specified geometrical regions through which the radiation enters the vehicle, and the second limits the ranges of integration of the angular variables.

Program SIGMA incorporates several features to facilitate parametric studies. For example, multiple orbits are treated simultaneously during the geometric calculations. Each orbit may entail several radiation sources and the dose received from each primary and secondary radiation component is printed out. Multiple material sets are allowed, and, as a result, each material region can have several

different densities, which allows a determination of the variable shielding effects of equipment, supplies, etc., and facilitates parametric studies on shield thickness where geometric effects are negligible and changes in shield thickness can be approximated by changes in material density. This also allows one to take advantage of the fact that it is sometimes possible to express with sufficient accuracy the dose attenuation data in various materials, for a given radiation component, in terms of equivalent densities of a single material, as for example, protons, electrons, and X-rays or gamma rays when the materials are not very dissimilar and the attenuation is not too great. For large parametric studies, it has been found that this can save a great deal of computer time without appreciably affecting the accuracy of the results. The multiple material sets are treated concurrently with the multiple orbits for a given vehicle and dose point. The dose received from each element of solid angle may be calculated by several alternate methods including a basic transport calculation for each solid angle element. These calculations may also include the effects of anisotropic source distributions.

For this study, the radiation source was assumed to be isotropic and the radiation transport was treated by using tabular dose attenuation data generated with CHARGE. A power-law or exponential interpolation on material thickness was used to calculate doses at intermediate material thicknesses.

RESULTS

The parametric data presented in this report represents a brief synopsis of the total shielding attenuation data generated during various studies on the shielding requirements for manned orbiting space stations (ref. 6). The results presented are for circa 1974 unless otherwise noted.

Parametric Shielding Calculations

Figure 3 presents the total expected yearly dose for the six-man space station for circular orbits of 100 nautical miles altitude. The curves show the dose received by the three body dose points (E indicates the lens of eye, B indicates blood-forming organs, S indicates

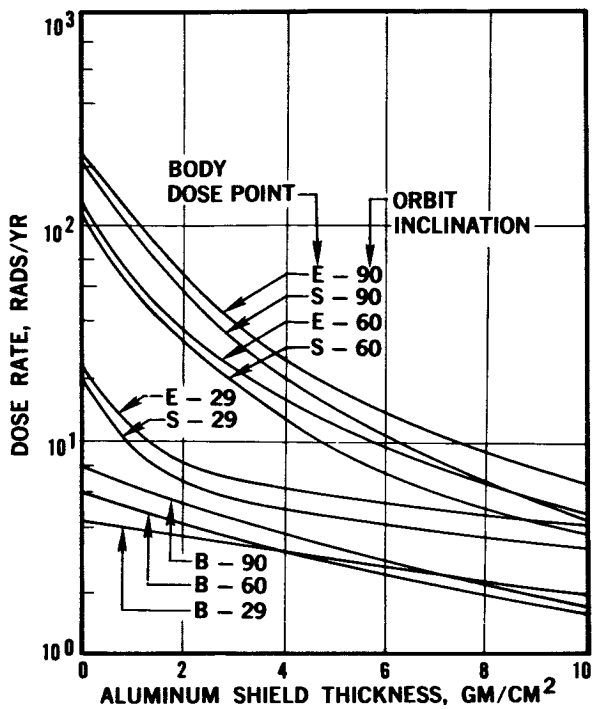


FIGURE 3.—Total dose rate (six-man space station): 100 n. mi. orbits.

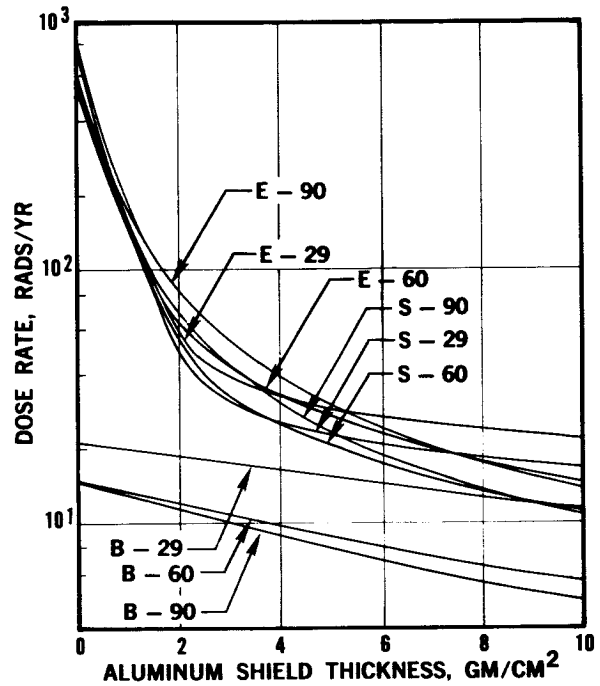


FIGURE 4.—Total dose rate (six-man space station): 200 n. mi. orbits.

skin) for three orbit inclinations, 29° , 60° , and 90° , as a function of aluminum shield thickness, for the body location indicated in figure 1. Included in these doses are contributions from trapped protons, trapped natural and artificial electrons, and solar flare protons for one flare event of the November 12, 1960 type. This flare event was chosen because it is one of the largest events observed, is well documented, and its spectrum is similar to other large events. The expected frequency is assumed to be one per year. Mission reliability was not considered for this analysis; therefore, no attempt was made to calculate the probability of encountering more than one solar flare event for the mission.

Figures 4 and 5 present similar data for the six-man vehicle for 200 and 400 nautical miles. Figures 6, 7, and 8 present results for the same situations involving the two-man space station with the location of the man model as indicated in figure 2.

Various work-rest cycles were used to determine the dose received by a crew member

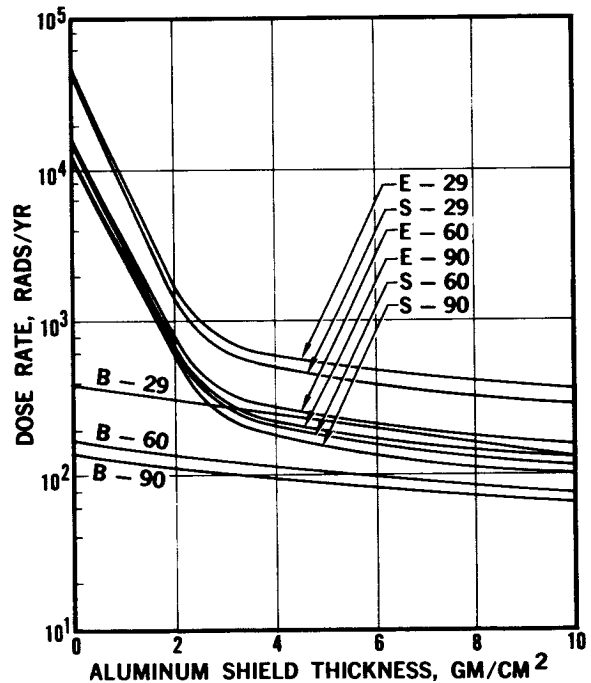


FIGURE 5.—Total dose rate (six-man space station): 400 n. mi. orbits.

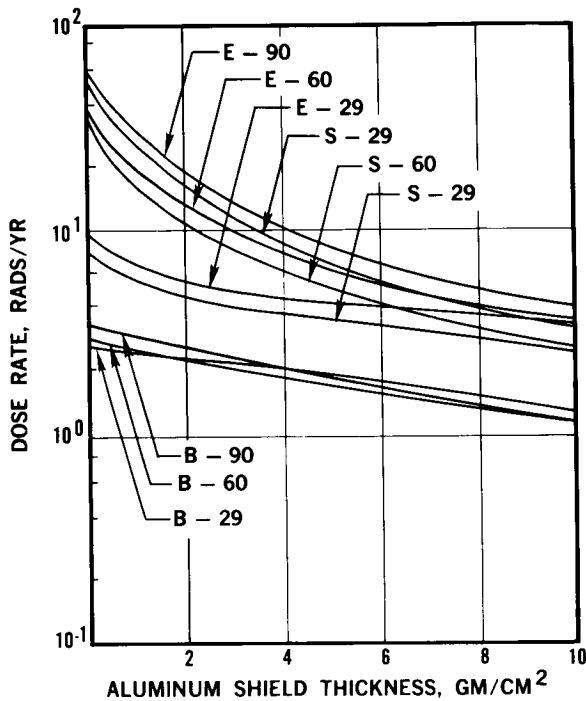


FIGURE 6.—Total dose rate (two-man space station):
100 n. mi. orbits.

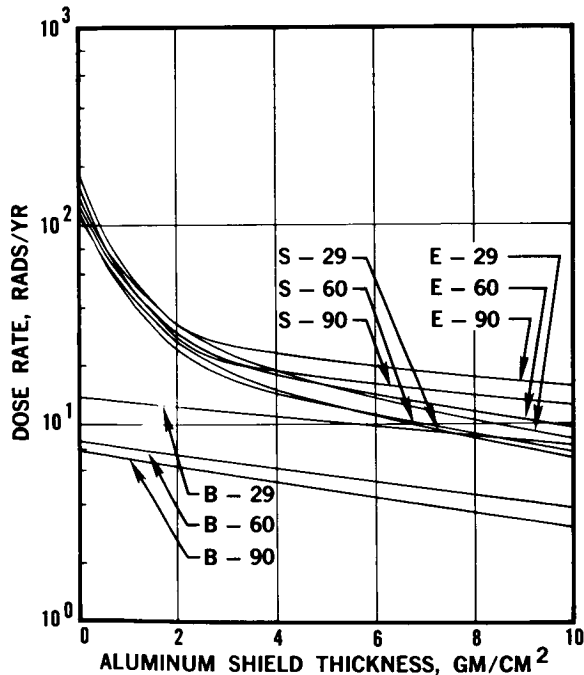


FIGURE 7.—Total dose rate (two-man space station):
200 n. mi. orbits.

during various residence times in particular vehicle locations. Little difference in dose was found ($<10\%$) between the results for the work-rest cycles and the centrally located positions shown in figures 1 and 2, for a simple unit shield. However, the use of localized shielding surrounding specific areas is advantageous. For example, for the case of an allowable dose of 27 rads/yr to the eyes in a 200 nautical mile, 29° inclination, orbit, shown in figure 4, a reduction of aluminum shield weight from 20 300 lb to 14 100 lb is realized assuming that $\frac{1}{3}$ of the crew's time is spent in the bunk and that the bunks are more heavily shielded than the rest of the vehicle. Greater advantage of localized shielding can be realized if the mobility of the crew is restricted during the intermittent periods of high dose rate occurring during a solar flare event, or during the relatively short periods spent in the high-flux region of the trapped radiation belts. Figure 9 indicates, for the 200 nautical mile altitude, the extent of the trapped proton radiation localization. The trapped electrons have approximately the same spatial distribution.

Personal shielding can also be very effective in reducing the shield weight requirements to meet a given set of dose criteria. The weight of any reasonable amount of personal shielding is comparatively small. The extent to which it can replace the space station shielding is determined by acceptable compromise of mobility, physical dexterity, and convenience of the crew members. Once these criteria have been established in terms of shield weight or thickness, the corresponding space station shield requirements can be obtained from the parametric shielding data. The dose to the lens of the eye is usually the most restrictive and the dose to the skin the least restrictive. Therefore, personal shielding requirements will usually begin with eye shielding in the form of goggles or helmet followed by a vest-type shield to protect the trunk, and finally by a heavy outer garment to protect the skin. A moderate amount of personal shielding can mean a substantial increase in useful payload. For example, peripheral shielding for the six-man vehicle weighs approximately 3500 lbs per gm/cm^2 . The desirability of this approach to radiation

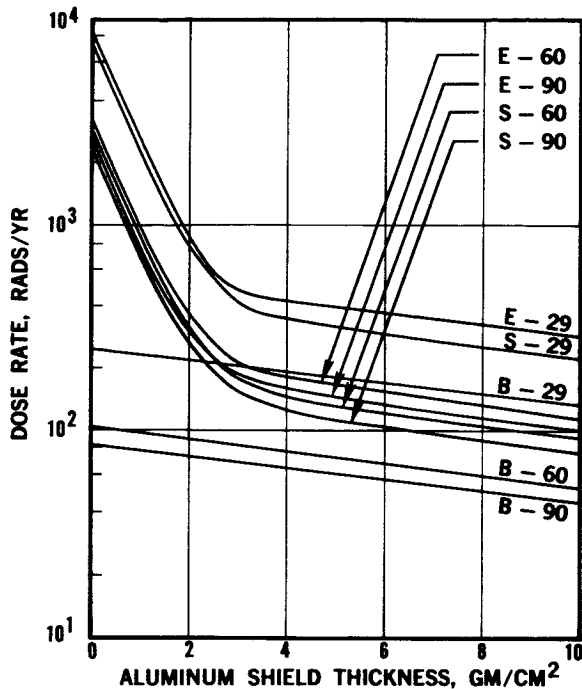


FIGURE 8.—Total dose rate (two-man space station): 400 n. mi. orbits.

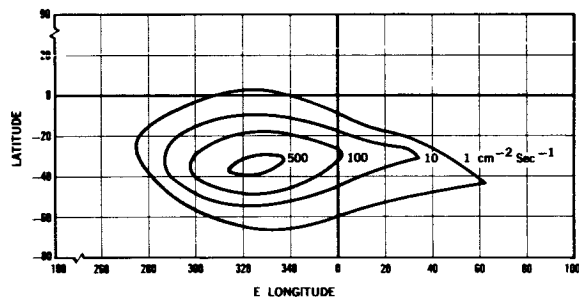


FIGURE 9.—Omnidirectional proton flux ($40 < E < 110 \text{ MeV}$): iso-flux contours; 200 n. mi. altitude.

protection is dictated by general design philosophy concerning the physical mobility and dexterity criteria, radiation tolerance criteria, etc.

For approximate calculations of biological self-shielding, the assumption of 2π shadow shielding was found to be a good approximation when calculating the dose to the skin and the blood forming organs. For the dose to the eyes, this assumption underestimates the dosage by approximately 10% to 30% because the head is not as effective as a shadow shield as is the trunk of the body.

There is no consistent way to express the radiation protection worth of the unshielded space stations because of the non-uniform mass distribution causing "streaming", and the different dose attenuation characteristics of each radiation component. However, for the sake of comparison, the approximate worth of the equipped six-man space station is 2.2 gm/cm^2 of aluminum, and that of the two-man space station is 3.2 gm/cm^2 of aluminum. To obtain consistent and accurate results, each situation has to be evaluated by a detailed geometry treatment.

Tables I and II indicate for each system the aluminum shielding requirements in terms of gm/cm^2 at 29° inclination as a function of altitude for two sets of dose criteria. The more conservative criteria of 27, 54, and 233 rads per year to the lens of the eyes, blood forming organs, and skin of whole body, respectively, correspond to the project Apollo criteria. The other set of allowable doses are suggested by Kelton (ref. 7) as appropriate for manned orbiting space stations. It is obvious from the tables that the shielding requirements become prohibitive somewhat above 200 nautical miles for the Apollo criteria, and slightly above 400 nautical miles for the less conservative criteria unless shielded compartments are used during the intermittent periods of high dose rate. At 400 nautical miles, the design dose is approximately divided between electron bremsstrahlung and trapped protons; at 600 nautical miles, the electron bremsstrahlung constitutes about two-thirds of the design dose.

It is interesting to note that at 200 nautical miles and 29° inclination, the skin is more restrictive to the shield design than the blood forming organs in the six-man space station. This is due to the biological self-shielding of the rapidly attenuating electron dose in this case.

Variation of Radiation Sources

The figures discussed in the previous section present total radiation doses which enables one to determine shielding requirements for specified dose criteria. These total doses are composed of the different radiation sources whose individual importance varies with time and mission.

TABLE I

Shielding Requirements (Six-Man Space Station) 29° Orbit Inclination

Orbit altitude, n. mi.	Aluminum thickness for listed criteria, gm/cm ²					
	Suggested criteria			Apollo criteria		
	250 rads to eyes	150 rads to BFO	500 rads to skin	27 rads to eyes	54 rads to BFO	233 rads to skin
100	0	0	0	0	0	0
200	0.8	0	0.3	5.8	0	0.8
400	19.1	8.9	3.6	67.7	29.6	14.8
600	56.1	45.9	34.4	105	66.6	51.8

TABLE II

Shielding Requirements (Two-Man Space Station) 29° Orbit Inclination

Orbit altitude, n. mi.	Aluminum thickness for listed criteria, gm/cm ²					
	Suggested criteria			Apollo criteria		
	250 rads to eyes	150 rads to BFO	500 rads to skin	27 rads to eyes	54 rads to BFO	233 rads to skin
100	0	0	0	0	0	0
200	0	0	0	2.8	0	0
400	12.5	7.9	2.6	61.1	28.7	9.6
600	49.5	44.9	29.8	98.1	65.7	46.6

With the assumed artificial electron fluxes, the electron dose is initially dominant (<2 gm/cm² shielding) for low inclinations and for altitudes from 200 nautical miles to >600 nautical miles. Next, the single solar flare event is dominant above 60° inclination and below 300 nautical miles, with the range of shield thickness over which it is important decreasing with altitude. Below 60° inclination and 400 nautical miles, the trapped proton dose is dominant for >3 gm/cm² shielding with the bremsstrahlung being dominant above 600 nautical miles for >3 gm/cm² shielding and all inclinations. Figure 10 shows the individual dose contributions to the

eyes for the six-man space station at 200 nautical miles and 90° inclination.

Figure 11 indicates the variation of trapped proton dose rate with orbit inclination and solar activity, and figure 12 shows the effects of the variation of the solar flare proton flux and spectrum with orbit inclination, for 200 nautical mile orbits.

Shielding Materials

Figure 13 is for a 400 nautical mile, 90° inclination orbit. It demonstrates the effectiveness of using shielding materials other than aluminum. For each case, 2 gm/cm² of alumi-

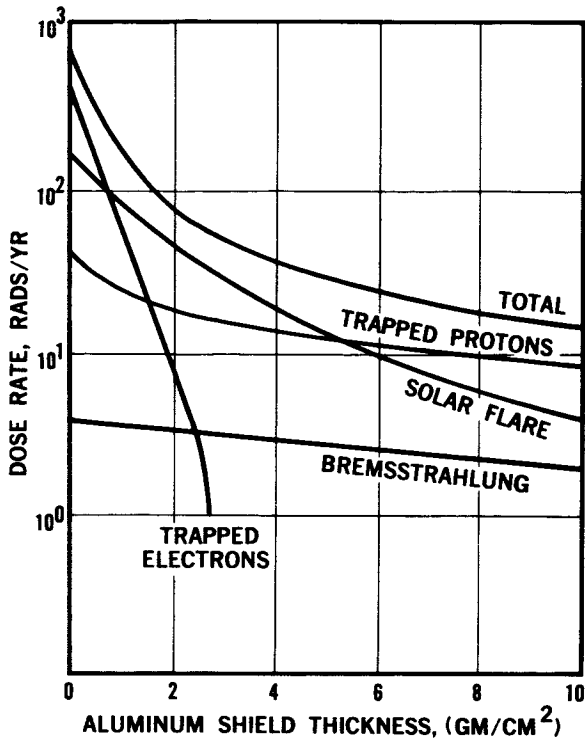


FIGURE 10.—Lens of eye dose rate (six-man space station): 200 n. mi. 90° incl. orbit.

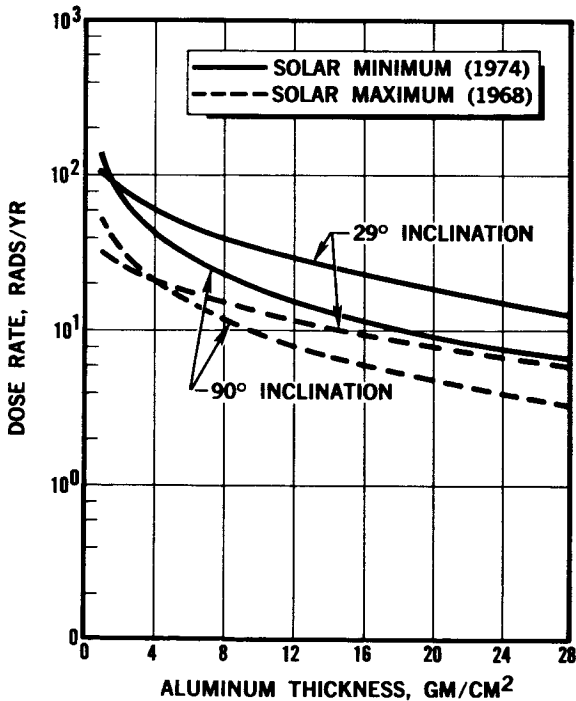


FIGURE 11.—Trapped proton dose rate (spherical geometry): 200 n. mi. orbits.

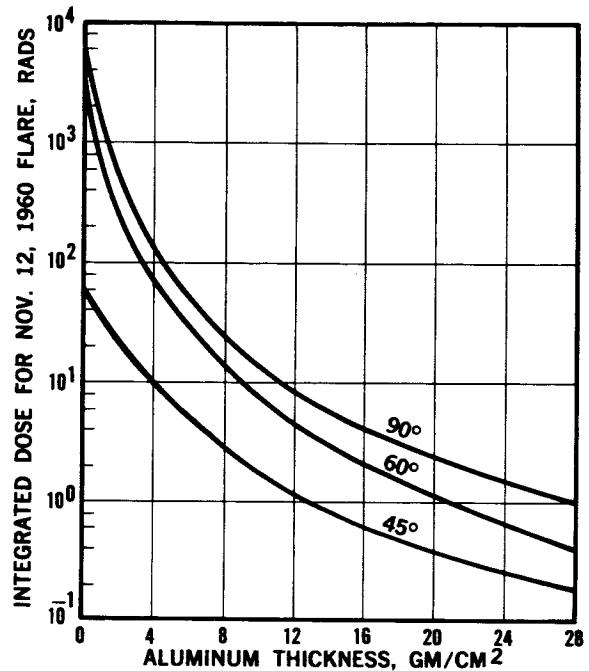


FIGURE 12.—Solar flare proton dose (spherical geometry): 200 n. mi. orbits.

num represents the basic vehicle structure. It can be seen from these curves that polyethylene (CH_2) is a superior shielding material for attenuating protons, and for reducing bremsstrahlung production if it can be successfully placed outside the pressure shell. Polyethylene also has the advantage of relative ease and flexibility of installation. This is important for allowing for non-interference shield modifications in case of contingencies such as additional hazardous, high-altitude nuclear tests, and for allowing for leak tests and repair of the pressure shell in case of meteoroid puncture.

One gm/cm² of lead is very effective in reducing the bremsstrahlung dose by about 50% because of its effectiveness in absorbing the low-energy X-rays. In the case^s where proton dose is dominant, it is better to use additional polyethylene shielding after this reduction is accomplished; however, in the case where bremsstrahlung is dominant, additional shielding would be more effective if composed of a material of high atomic number such as sheet lead. The optimum shield material combination is dependent on the radiation environment.

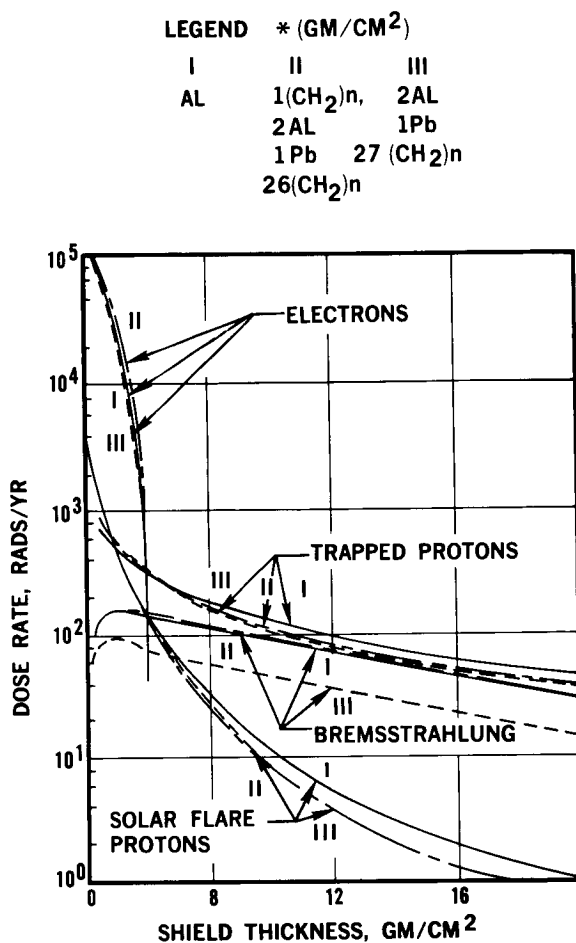


FIGURE 13.—Dose rates in laminated shields: 400 n. mi.—90° incl. spherical geometry.

CONCLUSIONS

The following summarizes the conclusions concerning shielding requirements of manned orbiting space stations.

1. The shielding requirements for manned orbiting space stations are low for orbits with altitudes less than about 200 nautical miles and inclinations less than about 45°.

2. Shielding requirements become prohibitive somewhat above 200 nautical miles for the Apollo dose criteria and slightly above 400 nautical miles for the less conservative criteria unless specially shielded compartments are used

during the intermittent periods of high dose rate.

3. Shielding requirements are sensitive to orbit altitude because of the strong dependence of the trapped radiation environment on altitude.

4. The assumed decay of the artificial electron belt indicates the electron dose is dominant for the first one or two gm/cm² of shielding for orbits with low altitudes and inclinations. Between approximately 300 and 600 nautical miles, the electron bremsstrahlung and trapped proton doses have about the same magnitude around 1974, during solar maximum, but the bremsstrahlung dose dominates around 1968, during solar minimum.

5. The trapped proton dose at 200 nautical miles is reduced by a factor of 2 to 3 in going from solar minimum to solar maximum, depending on the orbit inclination.

6. Shielding calculations based on the actual geometry of a space station are necessary to obtain estimates of the dose with accuracy comparable to that of the space radiation environment.

7. Shielding requirements can be very effectively reduced by the use of personal and localized shielding. Taking advantage of the intermittency of the received dose can greatly reduce shield weight by the use of specially shielded compartments.

8. The degree of conservatism expressed in the dose criteria can drastically affect the shield weight for some orbits because of the large surface areas involved.

9. Obviously, any additional high-altitude nuclear tests may seriously affect the operation of a manned orbiting space station. If a contingency requires that additional shielding be provided after hardware development, or that, because of booster capabilities, shielding must be installed in orbit, then the ease of installation, design flexibility, and requirements for pressure shell accessibility make a plastic material like polyethylene attractive as a shielding material.

REFERENCES

1. BAKER, M. B.: Geomagnetically Trapped Radiation. Douglas Rept., SM-47635, Sept. 1964.
2. BETHE, H. A.; and ASHKIN, J.: Passage of Radiation Through Matter. Experimental Nuclear Physics, vol. 1 (E. Segrè, ED.). John Wiley & Sons, Inc. 1953.
3. EVANS, R. D.: The Atomic Nucleus. McGraw-Hill, 1955.
4. KOCH, H. W.; and MOTZ, J. W.: Rev. Mod. Phys., vol. 31, 1959, p. 920.
5. EDELSACK, E. A.; KREGER, W. E.; MALLET, W.; and SCOFIELD, N. E.: Experimental Investigation of Thick Target Bremsstrahlung Radiations From Electrons of 1.0, 1.5, and 2.0 MeV. Health Phys., vol. 4, Jan. 15, 1960.
6. JORDAN, T. M.; KOPROWSKI, E. F.; and LANGLEY, R. W.: Radiation Protection for Manned Orbiting Space Stations. Douglas Rept., SM-46257, Sept. 1964.
7. KELTON, A. A.: Radiation Guidelines for Manned Space Vehicles. Douglas Rept., SM-47749, Oct. 1964.

N 65-34622

46—Solar Flare Hazard to Earth-Orbiting Vehicles¹

E. KUHN, F. E. SCHWAMB, and W. T. PAYNE

Republic Aviation Corporation

Procedures are developed for calculating approach cones for solar flare particles at points on the orbit of an earth satellite, taking into account the effects of the geomagnetic field and also the magnetic effects of the solar flare. The purpose is to provide information for optimum shielding design for satellites. Three models are considered for the geomagnetic field: (1) a pure dipole field, treated by simple Störmer theory; (2) a dipole field with a superposed time-dependent uniform field to simulate the effects of the magnetic storm, treated by a modified Störmer theory; and (3) same as model (2) but with shadowing effects of the earth considered in an approximate way. Computer programs have thus far been constructed for the first two of these models.

INTRODUCTION

This paper deals with the calculation of the particulate radiation environment at points inside the magnetosphere during a solar flare, taking into account the effects due to the geomagnetic field, and also the magnetic effects of the solar flare itself. The ultimate purpose of the work is to provide essential information for optimum shielding design for earth satellites. Accordingly, it is desired to get a complete description of the particle flux at each point of the satellite orbit, including both the number flux and also the directional distribution of the flux at every orbit point. Computer programs have been developed, based on different available models of the geomagnetic field, that are used in combination with existing trajectory codes and dose codes for the purpose of calculating the dose rates received by a satellite during a solar flare.

The physical basis for the solution is the calculation of the size and shape of the allowable approach cone, at each orbit point, for particles of a given rigidity (or energy). Then all the required results follow at once, since from Liouville's theorem the total particle flux can be found by multiplying the solid angle of the approach cone by the unidirectional flux

per unit solid angle incident on the magnetosphere; and also the directional properties of the particle flux are completely described, this flux being isotropic within the approach cone and zero outside the approach cone, which again follows from Liouville's theorem (ref. 1).

The models used for the geomagnetic field are as follows: (1) a pure dipole field, treated on the basis of simple Störmer theory, with the Störmer cone used for the allowable approach cone; (2) a dipole field with a superposed time-dependent uniform field that is either parallel or antiparallel to the dipole moment vector, to simulate the magnetic effects of the different phases of the magnetic storm associated with a solar flare (refs. 2 and 3)—this will be called a modified Störmer model; (3) same as model (2), but with the shadowing effects of the solid earth taken into account, in an approximate way.

INPUT DATA REQUIRED

It is necessary to have certain data on the solar flare, and also to have specifications of the satellite orbit.

The solar flare data required are the specifications of the particle flux and the solar flare magnetic field. For the first of these, it is necessary to know the differential particle flux (per unit rigidity) as a function of rigidity and time. The exponential rigidity formulation

¹ Research sponsored by Langley Research Center, NASA, under Contract NAS 1-3601.

of Freier and Webber for solar flare spectra was used (ref. 4), namely,

$$\frac{dJ}{dP} = (J_0/P_0) \exp(-P/P_0) \quad (1)$$

where dJ/dP is the differential unidirectional flux in number of particles per $\text{cm}^2\text{-sec-MV-steradian}$, P is the rigidity, and J_0 and P_0 are the intensity and characteristic rigidity parameters depending on time only. As for the solar flare magnetic field, it is only necessary to know the deviation from the quiet value of the horizontal component of the geomagnetic field, averaged around the geomagnetic equator and given as a function of time. This will be taken, in the modified Störmer model, to be equal to the intensity of the superposed uniform field.

The satellite orbit specifications needed are the geomagnetic coordinates of the satellite given as functions of the time, or a machine code that will enable these to be computed from other data. If the code computes geographic rather than geomagnetic coordinates, these must be transformed to geomagnetic coordinates. This involves a translation from the geographic to the geomagnetic origin and a rotation of the coordinate axes to align the z -axis with the dipole axis.

SIMPLE STÖRMER MODEL

From the Störmer integral, one can derive the equation (refs. 1 and 5)

$$\cos \omega = \frac{2\gamma}{r \cos \lambda} - \frac{\cos \lambda}{r^2} \quad (2)$$

where ω = approach angle measured from the easterly direction, γ = Störmer constant, r = radial coordinate in Störmer units, λ = geomagnetic latitude. To calculate the half-angle (ω_c) of the forbidden Störmer cone at any point (r, λ), one sets $\gamma=1$ and calculates ω from equation (2) (ref. 6). This is done, of course, for one particular rigidity value. Then the solid angle Ω of the allowed Störmer cone for the given location and the given rigidity value can be found from the equation,

$$\Omega = 2\pi(1 + \cos \omega_c) \quad (3)$$

The Störmer allowed cone is a right circular cone with axis along the east-west line, opening toward the west, as shown in figure 1.

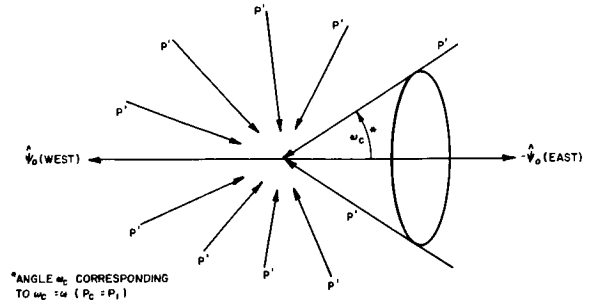


FIGURE 1.—Störmer cone, showing allowed directions of approach.

Thus for each value of particle rigidity (or energy), Ω can be calculated at any point of the satellite trajectory. For a given location in space, there is some rigidity value below which $\Omega=0$, and another rigidity value above which $\Omega=4\pi$ steradians; these values will be called $P_{c \text{ min}}$ and $P_{c \text{ max}}$. In constructing a computer program for calculating the Störmer cone, it is important to know these values for each orbit point, so that the machine can be told at what rigidity values to begin and end its calculations for the allowed Störmer cone. The formulas for these quantities appear in the literature (ref. 6). They are:

$$P_{c \text{ min}}^{\text{max}} = \frac{Q \cos^4 \lambda}{[1 + (1 \mp \cos^3 \lambda)^{1/2}]^2} \quad (4)$$

where $Q=59.4Z/R^2$ BeV/c and R = radial coordinate in earth radii.

A computer program for the IBM 7094 has been constructed that accomplishes the above calculations and yields the cone description and the differential flux at any point of the satellite orbit. The general program layout is shown in figure 2. The computer program has been applied to the case of a circular orbit of altitude 200 miles and inclination 70° (geographic), for the purpose of illustrating geomagnetic effects on dose rates during the flares of 23 February 1956 and 12 November 1960. For this orbit, the geomagnetic inclination ranges between 58° and 82° . It proved

MODIFIED STÖRMER MODEL

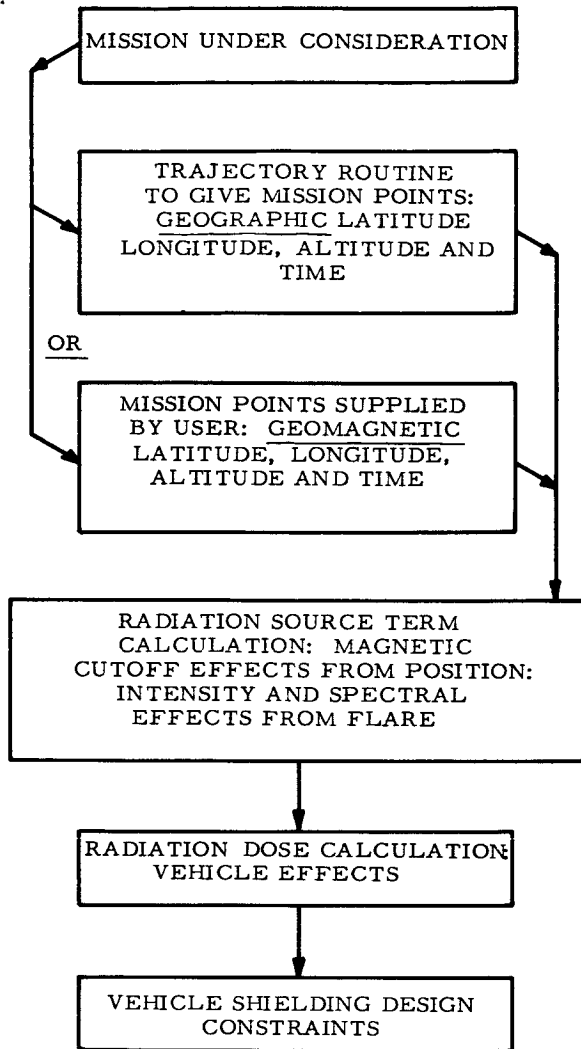


FIGURE 2.—General program layout.

to be convenient to make the dose rate calculation for the two extremal orbits having geomagnetic inclinations of 58° and 82°, respectively, rather than for the given orbit; the dose rate curves (i.e., dose rate against time) thus obtained are lower and upper bounds of the actual dose rate curve. These are shown in figures 3 and 4, which also show the dose rate curve with no geomagnetic field present. The figures show that the geomagnetic field produces a reduction by 2 to 3 orders of magnitude below the no-field case.

During the initial phase of a magnetic storm, the resultant horizontal magnetic intensity at the geomagnetic equator is greater than the quiet value; during the main phase, it is less than the quiet value. In the modified Störmer model to be used here, these phenomena are accounted for by assuming that a uniform magnetic field of external origin is superposed on the geomagnetic dipole field, and that this uniform field varies in time to correspond with the observed changes in the resultant magnetic field. The intensity of the superposed uniform field at any instant may be taken to be equal to the average deviation (from the quiet value) of the resultant horizontal intensity, averaged around the geomagnetic equator. Thus in the equatorial plane the superposed field is parallel to the dipole field during the initial phase and anti-parallel to it during the main phase (ref. 2).

The presence of the superposed uniform field requires that equation (2) be modified by adding to the right side the vector potential (in dimensionless form) of the uniform field; a suitable expression for such a vector potential is a constant times the quantity $r \cos \lambda$, where the constant (here dependent on the time) measures the intensity of the uniform field. Thus equation (2) is to be replaced by an equation that can be written in the form (ref. 7):

$$\cos \omega = \frac{2\gamma}{r \cos \lambda} - \frac{\cos \lambda}{r^2} + \frac{r \cos \lambda}{r_0^2} \quad (5)$$

where $(1/r_0^2)$ denotes the above-mentioned constant, with r_0 positive for the initial phase and negative for the main phase. During the initial phase, the resultant field is assumed to extend out only to $r=r_0$ (in Störmer units) where it is terminated by a Chapman-Ferraro current (ref. 3); this assumption requires that equation (5) shall be valid only for $r \leq r_0$; for $r > r_0$, equation (5) is to be replaced by the equation,

$$\cos \omega = \frac{2\gamma}{r \cos \lambda} \quad (5a)$$

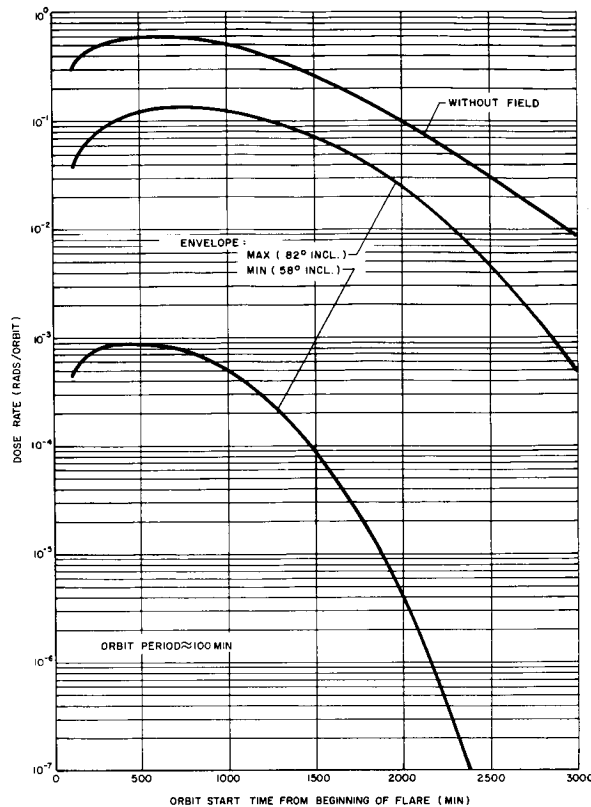


FIGURE 3.—Extremal envelope for 23 February 1956 Flare.

The effect of the solar wind on the geomagnetic field can also be taken into account by this model, within the limitations imposed by the axial symmetry of the model. To accomplish this, one assumes that equations (5) and (5a), with r_0 taken equal (in Störmer units) to 10 earth radii, are valid for the quiet field. The quiet magnetosphere is then represented as spherical in shape; the well-known elongation of the real magnetosphere of the dark side does not appear in this simple description.

Thus the quiet magnetosphere has radius $r_0=10$ earth radii. During the initial phase of a magnetic storm, r_0 becomes smaller than this quiet value and, as the storm progresses, it becomes larger, approaches infinity, and finally becomes negative.

To calculate the half-angle of the Störmer cone at a given location and at a given time, one must put into equation (5) the appropriate value of r_0 , as calculated from magnetic records, and then one must find the limiting value of γ

in equation (5), by setting $\cos \omega = \cos \lambda = 1$ and finding the γ value that gives a real double root for the resulting cubic. For the initial phase it can be done only for $r_0 > \sqrt{3}$; for smaller r_0 values, one can show that a one-point pass is formed when the inner allowed region of the Störmer diagram becomes tangent to the spherical surface $r=r_0$, and that the limiting value of γ in this case is simply $\frac{1}{2}r_0$. A routine (which will be called the "cubic routine") has been constructed for finding the limiting γ values for different values of r_0 . Figure 5 shows Störmer diagrams for two cases. One can show from these diagrams that the Störmer cone at a given point is reduced in size during the initial phase and enlarged during the main phase.

Having found the limiting γ value, one proceeds as in simple Störmer theory, by inserting this value into equation (5), putting in the given values of r_0 , r , and λ , and calculating $\cos \omega$.

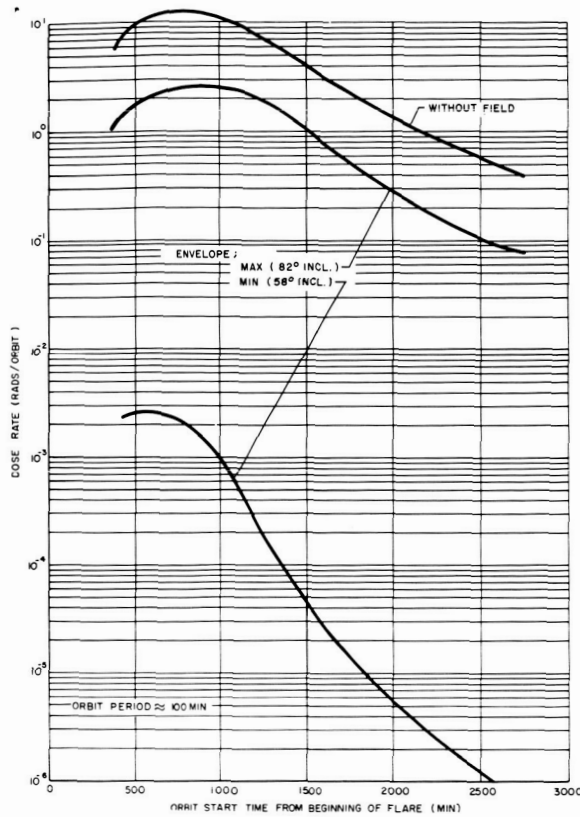


FIGURE 4.—Extremal envelope for 12 November 1960 Flare.

The solid angle of the allowed Störmer cone is then found by equation (3).

A computer program has been constructed for calculating the solid angle of the Störmer cone and the particle flux at any point of a satellite orbit. Because of the greater complexity of the modified Störmer model, the program is different from the program for the pure Störmer model. First, r_0 must be calculated as a function of time, using data from magnetic records and normalizing in such a way that $r_0=10$ earth radii for the quiet field, as mentioned above. Next the above-mentioned cubic routine is applied to the results to get γ_{lim} as a function of time. Since all quantities appearing in equation (5) are now known as functions of time, ω_c , and consequently Ω can also be calculated as functions of time. The particle flux on the satellite at a given time can be calculated in the usual way, that is, by multiplying the value of Ω just calculated by the unidirectional particle flux, which is given as a function of time. All the above calculations are carried out, of course, for one value of the particle rigidity at a time.

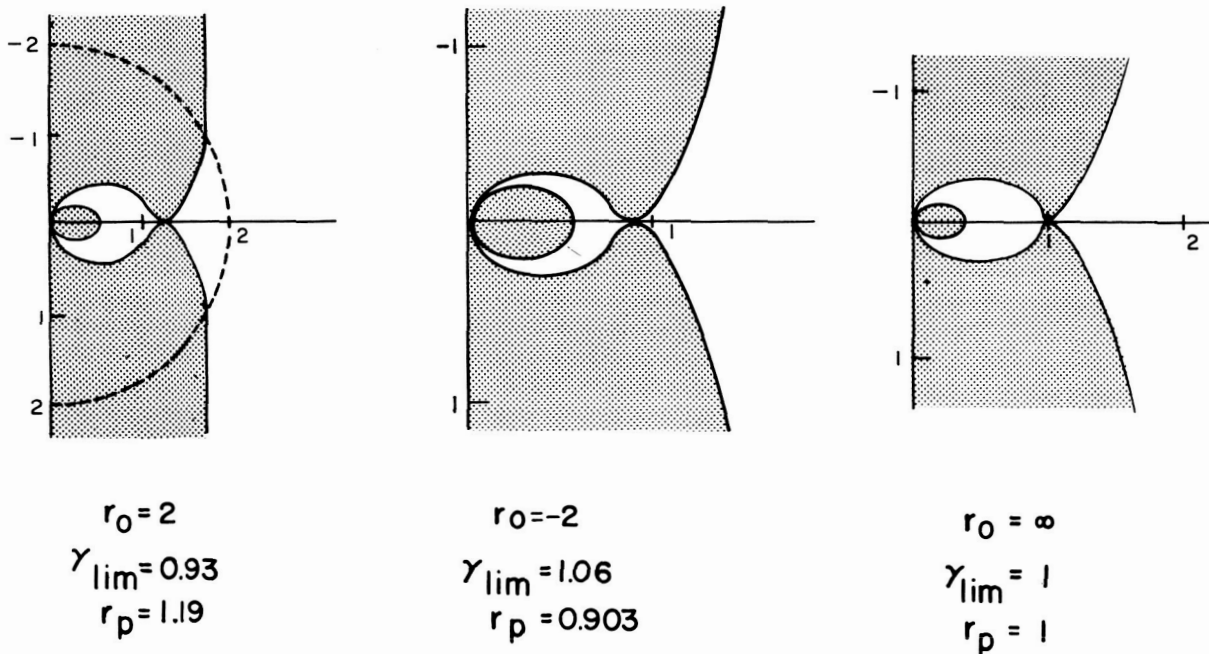


FIGURE 5.—Störmer diagrams. From left, initial phase for modified Störmer model, main phase for modified Störmer model, simple Störmer model.

SHADOWING EFFECTS OF SOLID EARTH

It is immediately evident that, in some cases, the solid earth will block some directions of approach lying within the allowed Störmer cone. For example, if the observation point is at zero altitude, all approach directions lying below the horizontal are blocked. Thus on the earth's surface, at least 50% of the allowed Störmer cone solid angle contributes nothing to the incident flux.

For low but nonvanishing altitudes, one can calculate approximately the blocked part of

the Störmer cone by assuming that the particle trajectories are nearly straight lines in the region between the earth's surface and the observation point; the problem then reduces to a calculation of the optical shadow of the earth. Simple calculations on this basis show that, at 200 miles, 35% of the Störmer cone is blocked for rigidities whose Störmer cone fills up 4π steradians, and a larger fraction for lower rigidities. At 2700 miles, the corresponding percentage is 10%. More complete calculations can be carried out by relatively simple means.

REFERENCES

1. VALLARTA, M. S.: Theory of the Geomagnetic Effects of Cosmic Radiation. *Handbuch der Physik*, vol. XLVI/1, Springer-Verlag (Berlin), 1961.
2. OBAYASHI, T.; and HAKURA, Y.: Enhanced Ionization in the Polar Ionosphere and Solar Corpuscular Radiation. *Space Research, Proc. First Intern. Space Science Symp. (Nice)*, 1960. Interscience Publ. (New York), 1960.
3. KELLOGG, P. J.; and WINCKLER, J. R.: Cosmic Ray Evidence for a Ring Current. *J. Geophys. Res.*, vol. 66, 1961, p. 3991.
4. FREIER, P. S.; and WEBBER, W. R.: Exponential Rigidity Spectrums for Solar-Flare Cosmic Rays. *J. Geophys. Res.*, vol. 68, 1963, p. 1605.
5. CHAMBERLAIN, J. W.: Motion of Charged Particles in the Earth's Magnetic Field. *Geophysics, Lectures Delivered at Les Houches*. Gordon and Breach (New York), 1963.
6. ALPHER, R. A.: Theoretical Geomagnetic Effects in Cosmic Radiation. *J. Geophys. Res.*, vol. 55, 1950, p. 437.
7. AKASOFU, S. I.; LIN, W. C.; and VAN ALLEN, J. A.: The Anomalous Entry of Low-Rigidity Solar Cosmic Rays into the Geomagnetic Field. *J. Geophys. Res.*, vol. 68, 1963, p. 5327.

SESSION IV E

SHIELDING AGAINST SPACE RADIATION

*Chairman: TRUTZ FOELSCHE
Langley Research Center, NASA*

N 24623

47—Results of Some Recent Transport Calculations for Electrons and Bremsstrahlung¹

M. J. BERGER and S. M. SELTZER

National Bureau of Standards

Illustrative results are given for three types of problems: (1) the transmission of electrons through thin and thick foils, with emphasis on the effect of energy loss straggling; (2) the energy dissipation by electrons in a semi-infinite water phantom, for an incident broad beam (depth dose distribution), and for an incident pencil beam (distribution as function of two spatial variables); (3) the production of bremsstrahlung in thick targets. The data presented for the first two problems are entirely theoretical and result from a Monte Carlo calculation. Similar calculations for the third problem are compared with recent experiments.

INTRODUCTION

During the past two years, with the support of NASA (Contract R-80), we have investigated a number of charged-particle and photon transport problems. These problems were selected because of their relevance to the shielding of spacecraft against electrons and associated bremsstrahlung in the Van Allen belts. The purpose of this work has been to provide basic radiation penetration data, and to make pilot calculations for situations which are reasonably realistic but simple enough to allow an accurate treatment. It has not been our intention to treat the very complicated shielding configurations that arise in engineering practice. Rather, it is hoped that the pilot calculations will eventually provide a yardstick for gaging the accuracy of the necessarily much more approximate techniques that must be used in engineering calculations.

A family of computer programs (FORTRAN, IBM 7094) has been developed, by means of which the transport of charged particles, and of the bremsstrahlung photons emitted by them, can be followed by Monte Carlo techniques. Typically, these programs fall into two categories: (a) numerous data preparation programs which manipulate the required single-

scattering cross sections and multiple-scattering distributions into a form suitable for rapid table look-up; (b) the actual Monte Carlo programs for tracing, scoring, and analyzing particle histories.

The Monte Carlo programs must take into account various aspects of penetration and diffusion: angular deflections, energy losses, and spatial propagation. For photons, these can be followed by random sampling more or less in direct analogy to the physical processes. For charged particles, the large number of interactions (running into the ten-thousands), which an electron may undergo in a thick target, makes it necessary to resort to more sophisticated schemes in which many successive collisions are grouped into a single step of an artificial random walk (refs. 1 to 5). The transition probabilities for this random walk are then obtained from pertinent analytical multiple scattering distributions governing angular deflections and energy losses. The rules according to which the random walk is sampled in the work described here have been described in some detail in reference 4. Multiple scattering angular deflections are determined according to the Goudsmit-Saunderson (ref. 6) distribution evaluated with the use of the Mott (ref. 7) single-scattering cross section. The latter was modified to take into account screening according to the prescription of Molière (ref. 8). In

¹ Research supported by the National Aeronautics and Space Administration under Contract No. R-80.

regard to collision energy loss, the computer programs have been developed on three levels of complexity. The crudest version treats the loss in the continuous-slowng-down approximation and disregards bremsstrahlung. (In this approximation, fluctuations of the collision loss are disregarded, and the electron is assumed to have, at each point along its path, an energy loss equal to the mean loss given by Bethe's theory of stopping power.) The second version, which is the current production model, includes the mean bremsstrahlung loss, and treats fluctuations of collision losses according to the theory of Landau (ref. 9), as modified by Blunck and Leisegang (ref. 10). The third version, now being developed, will in addition include the effect of bremsstrahlung loss fluctuations, and the production of secondary knock-on electrons.

PRELIMINARY RESULTS

The grouping of collisions (construction of artificial electron random walks) can be done in various ways, and obviously may involve a systematic error superimposed on the statistical error associated with random sampling. We have done a certain amount of numerical experimentation, and have been guided by intuition and experience, but a comprehensive error analysis is difficult and has not yet been undertaken. In connection with problems involving the production of bremsstrahlung, the pertinent cross sections, particularly in the energy region up to a few MeV, are poorly known (experimentally as well as theoretically) so that one must resort to a certain amount of guessing and empirical correction. In view of these facts, the results presented in this talk must therefore be regarded as preliminary.

Transmission of Electrons Through Foils

The introduction of collision loss fluctuations makes transmission calculations both more difficult to program and more time-consuming to run. It is therefore interesting to see how much, and under what conditions, this refinement changes transmission data. Pertinent results, for 1-MeV electrons incident perpendicularly on aluminum foils of various thicknesses, are summarized in figures 1, 2, and 3. These results are based on the analysis of 1000 Monte Carlo histories generated by a

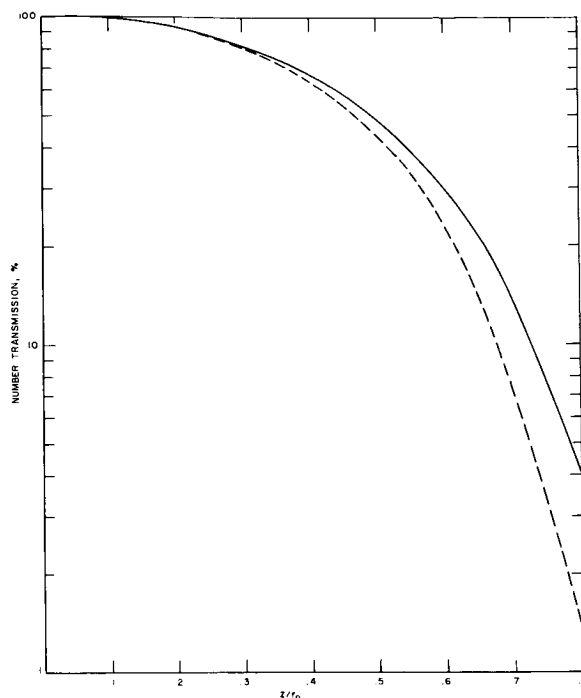


FIGURE 1.—Percent number transmission of 1-MeV electrons incident perpendicularly on aluminum foil. Solid curve includes effects of energy loss straggling; dotted curve is based on continuous-slowng-down approximation. Foil thickness is indicated by z , mean electron range by r_0 ($=0.549$ g/cm²).

program which used the technique of splitting particle histories. This was done in such a manner that approximately 1000 particles (including the original particle and descendants) penetrated to each depth considered. Splitting increased the required computation time by a factor of four over that required otherwise. In the figures, the foil thickness is expressed as the ratio of the actual thicknesses z to the mean range r_0 .² When expressed as function of the variable z/r_0 , the shape of the transmission curve is quite insensitive to the value of the source energy, so that the 1-MeV results given here are quite representative of conditions for source energies as low as 0.1 MeV.

² The mean range r_0 is defined as the rectified path-length which an electron would travel if its energy loss at each point of the trajectory were equal to the mean loss. In other words, the mean range is obtained by integrating the reciprocal of the stopping power with respect to energy. Of course, r_0 depends on the initial electron energy; at 1 MeV in aluminum, $r_0 = 0.55$ g/cm².

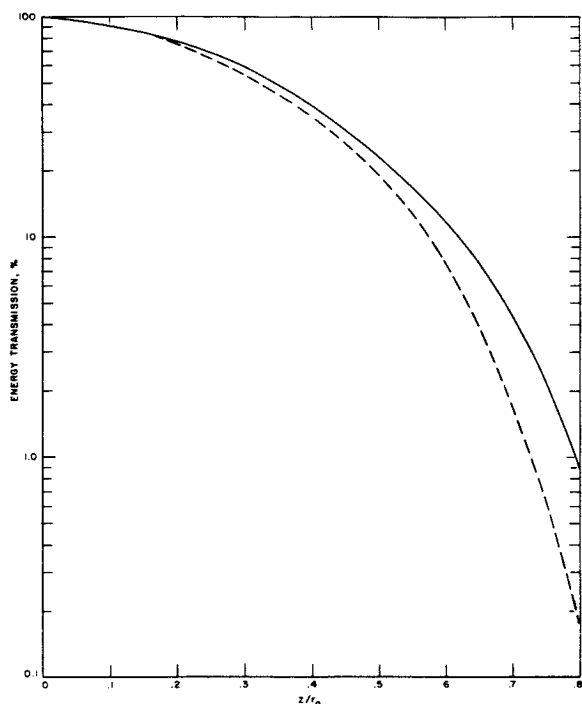


FIGURE 2.—Percent energy transmission of 1-MeV electrons incident perpendicularly on aluminum foil. Solid curve includes effects of energy loss straggling; dotted curve is based on continuous-slowing-down approximation. Foil thickness is indicated by z , mean electron range by r_0 ($=0.549$ g/cm²).

Inspection of figures 1 and 2 indicates that energy loss straggling has the effect of raising the transmission. The fractional increase is greater for energy than for number transmission, and is an increasing function of foil thickness. Figure 3 indicates the corresponding effect of energy loss straggling on the spectra of the transmitted electrons. As expected, straggling broadens the spectra, allowing both slower and faster electrons to emerge from the foil than would be possible in the continuous-slowing-down approximation.

Energy Dissipation by Electrons in a Water Phantom³

The biological damage done by electron irradiation depends, in first approximation, on the energy dissipation per unit mass (absorbed dose), and it is of interest to calculate this for simple conditions, namely, for a semi-infinite

water phantom that might approximately represent a human body.

A method of calculating the energy dissipation in an unbounded medium has been developed earlier by Spencer (ref. 11). His method does not involve random sampling, but rather the numerical calculation of spatial moments of the energy dissipation distribution through solution of a transport equation, followed by construction of the distribution from its moments. Spencer's method has been applied almost entirely to problems involving only one space variable (distance from a plane-perpendicular, or point-isotropic source). An extension to two-dimensional problems is difficult and has been attempted so far only in an isolated instance (ref. 12).

Our Monte Carlo program can be considered an extension of Spencer's work in the following respects: (a) The restriction to unbounded media is removed; for example, the leakage of electrons from the entrance face of a water phantom can be taken into account; (b) it is relatively easy to calculate the energy dissipation distribution as a function of more than one spatial variable, and the choice of variables can be made in many ways, depending upon practical requirements; (c) it is possible to calculate not only the energy dissipation as it would be recorded by a water-equivalent detector placed in a water phantom, but also the corresponding reading of an air-equivalent detector (e.g. an ionization chamber) placed in the same environment. As will be shown below, for source energies greater than a few MeV, the ratio of two such readings obtained with different detectors will significantly vary from point to point in the medium. Knowledge of this variation should be useful to experimenters who want to make a precise conversion of ionization-chamber readings into an energy dissipation distribution; (d) the current version of the Monte Carlo program is similar to Spencer's method in that it is based on the continuous-slowing-down approximation. However, an extension to include energy loss straggling, analogous to that used in the transmission problem, is under consideration.

The results presented here are based on the analysis of 5000 Monte Carlo histories, pertaining to 1-MeV and 10-MeV electrons incident

³ This part of the work was also supported by the U.S. Army Natick Laboratories.

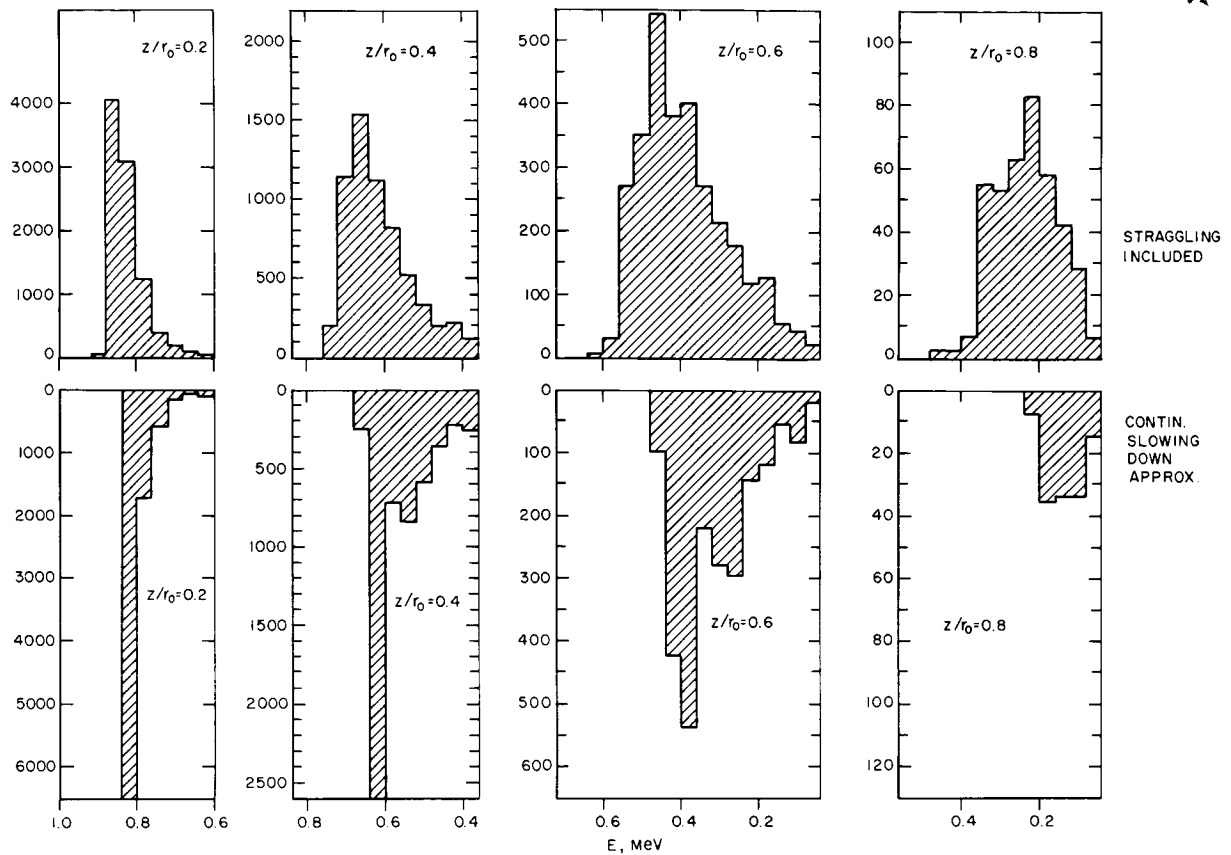


FIGURE 3.—Energy spectra of 1-MeV electrons transmitted through aluminum foil. Results are normalized to an incident beam of 10 000 electrons.

perpendicularly on semi-infinite water medium. The histories were analyzed: (a) to obtain energy dissipation as a function of depth for a broad incident beam; and (b) to obtain energy dissipation as a function of specific location for a narrow incident ray of electrons (gun source). In the two-dimensional problem, case (b), the variables are the length R of the vector from the point of incidence of the electron beam to the point of interest P , and the angle θ between this vector and the direction of incidence (fig. 4). Thus the angle θ lies between 0° and 90° , and R is no greater than the mean range r_0 (in the continuous-slowng-down approximation).

Table I gives the energy dissipation as a function of depth, i.e., mean values of this quantity in successive plane-parallel layers, each of which has a thickness equal to 5% of r_0 . In addition to the energy dissipation in MeV/g (normalized to one incident electron),

the fraction of the incident energy that is dissipated in each layer is given. It is to be noted that the sum of this fractional value adds up to a value somewhat less than unity, because some energy escapes from the semi-infinite medium through leakage of electrons, and the escape of energy in the form of bremsstrahlung. Finally, the column labeled "air-water ratio" gives the relative magnitude of the readings that would be obtained with air-equivalent or water-equivalent detectors. The air-water ratio decreases the deeper that one goes into the medium. The explanation for this is that the air-water stopping power ratio decreases with electron energy, and that the mean electron energy decreases, of course, with depth in the medium.

Tables II and III pertain to the energy dissipation problem in two dimensions. The entry in the i th row and j th column pertains to a spherical volume element (integrated over

TABLE I

Distribution of Energy Dissipation as Function of Depth in a Semi-Infinite Water Phantom

[$r_0 = 4.88 \text{ g/cm}^2$ at 10 MeV, 0.430 g/cm^2 at 1 MeV]

Depth, as percent of mean range r_0	Source energy 10 MeV			Source energy 1 MeV		
	Energy dissipation		Air-water ratio	Energy dissipation		Air-water ratio
	MeV/g	Percent of incident energy		MeV/g	Percent of incident energy	
0-5	1.99	4.9	0.934	2.04	4.4	0.874
5-10	2.03	5.0	.933	2.22	4.8	.873
10-15	2.04	5.0	.931	2.44	5.2	.872
15-20	2.08	5.1	.930	2.76	5.9	.871
20-25	2.12	5.2	.928	3.10	6.7	.870
25-30	2.18	5.3	.925	3.41	7.3	.869
30-35	2.29	5.6	.922	3.64	7.8	.869
35-40	2.34	5.7	.919	3.81	8.2	.868
40-45	2.44	6.0	.916	3.79	8.1	.867
45-50	2.52	6.1	.911	3.74	8.0	.866
50-55	2.65	6.5	.906	3.46	7.4	.866
55-60	2.76	6.7	.901	3.15	6.8	.865
60-65	2.80	6.8	.895	2.76	5.9	.864
65-70	2.66	6.5	.889	2.28	4.9	.864
70-75	2.38	5.8	.883	1.66	3.6	.863
75-80	2.00	4.9	.877	1.05	2.3	.862
80-85	1.33	3.2	.872	.51	1.1	.861
85-90	.61	1.5	.868	.12	.3	.860
90-95	.11	1.3	.867	.01	.0	.858
95-100	-----	-----	-----	-----	-----	-----

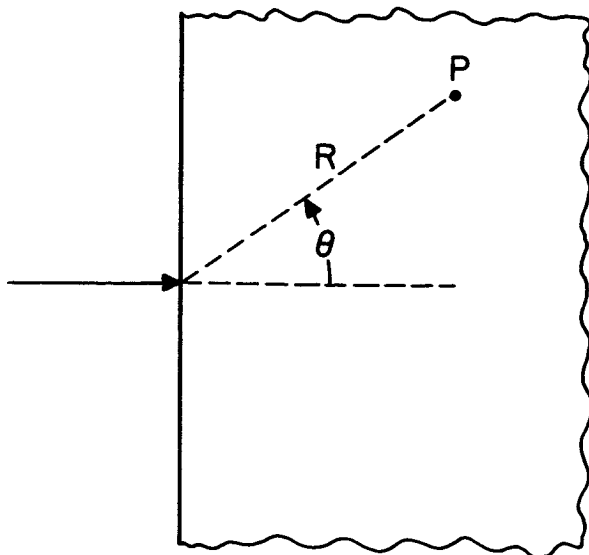


FIGURE 4.—Definition of variables R and θ .

azimuths between 0 and 2π) such that θ lies between $5(i-1)$ and $5i$ degrees ($i=1, 2, \dots, 18$), and such that R lies between $r_0(j-1)/20$ and $r_0j/20$ ($j=1, 2, \dots, 20$). The values given represent fractional energy dissipation normalized such that the values in any column (summed over all values of i from 1 to 18) add up to 100.0. The absolute normalization is provided by the bottom row, marked T_R , which contains, for each region $r_0(j-1)/20 \leq R < r_0j/20$, the percentage of the incident energy which is dissipated in that region. Finally, the column on the extreme right marked T_θ indicates the percentage of the incident energy that is dissipated in each angular region $5(i-1) \leq \theta < 5i$ degrees. The general characteristics of the two-dimensional distribution are as expected. At shallow depths the distribution is concentrated around the axis of incidence because

TABLE II
Energy Dissipation Distribution for a 10-MeV Pencil Beam of Electrons, Incident Perpendicularly on Semi-Infinite Water Phantom, as Function of Coordinates R and θ

$\frac{j}{i}$	1	2	3	4	5	6	7	8	9	10	11	12	13	14	15	16	17	18	19	20	T_0
1	99.9	87.9	60.8	40.7	29.6	23.2	18.0	14.7	12.3	10.4	9.1	7.8	6.9	5.6	4.9	4.4	5.1	5.8	8.5	0.	22.4
2	0.1	10.8	33.5	43.3	43.6	39.0	35.1	30.7	26.8	23.2	19.9	17.7	15.2	13.6	12.1	12.3	12.9	16.4	20.2	25.0	21.1
3	—	0.9	4.5	12.1	19.0	24.3	26.9	27.3	26.6	25.9	24.0	21.7	19.3	17.1	16.4	17.4	18.0	20.2	25.1	75.0	17.3
4	—	0.2	0.7	2.5	5.2	9.0	12.4	16.2	18.2	19.9	19.9	19.0	19.6	18.7	17.6	18.1	18.6	18.7	20.8	—	12.9
5	—	0.1	0.3	0.6	1.5	2.5	4.5	6.3	8.5	10.0	12.2	14.2	14.9	15.4	16.2	15.9	16.8	17.6	16.1	—	8.8
6	—	—	0.2	0.3	0.6	1.0	1.7	2.4	3.7	5.3	6.5	8.0	10.0	11.5	11.8	12.3	12.3	10.7	6.1	—	5.6
7	—	—	0.1	0.2	0.2	0.4	0.6	1.2	1.8	2.4	3.7	4.4	5.8	7.6	9.0	8.5	7.9	6.4	2.0	—	3.5
8	—	—	0.1	0.1	0.2	0.2	0.3	0.4	0.8	1.2	1.8	2.7	3.6	4.3	5.6	5.5	4.3	2.6	1.2	—	2.0
9	—	—	—	0.0	0.1	0.2	0.2	0.4	0.4	0.6	1.1	1.5	2.1	2.8	3.2	2.7	2.6	1.2	—	—	1.1
10	—	—	—	0.0	0.1	0.1	0.2	0.1	0.4	0.4	0.7	1.0	1.1	1.6	1.6	1.3	0.9	0.3	—	—	0.6
11	—	—	—	0.1	—	—	—	0.1	0.1	0.4	0.5	0.9	0.8	0.9	0.8	0.7	0.2	0.1	—	—	0.3
12	—	—	—	—	—	—	—	—	0.2	0.1	0.3	0.6	0.6	0.6	0.4	0.4	0.2	0.1	—	—	0.2
13	—	—	—	—	—	—	—	—	—	0.1	0.2	0.2	0.2	0.2	0.1	0.3	0.1	—	—	—	0.1
14	—	—	—	—	—	—	—	—	—	0.1	0.0	0.2	0.1	0.2	0.1	—	—	—	—	—	0.0
15	—	—	—	—	—	—	—	—	—	—	0.1	0.1	—	—	0.1	—	—	—	—	—	0.0
16	—	—	—	—	—	—	—	—	—	—	—	—	—	—	—	—	—	—	—	—	0.0
17	—	—	—	—	—	—	—	—	—	—	—	—	—	—	—	—	—	—	—	—	0.0
18	—	—	—	—	—	—	—	—	—	—	—	—	—	—	—	—	—	—	—	—	0.0
T_R	4.8	4.9	4.9	4.9	4.9	4.9	5.0	5.0	5.1	5.2	5.3	5.6	5.8	6.3	6.6	6.6	5.6	3.5	0.8	0.0	0.0

TABLE III
 Energy Dissipation Distribution for a 1-MeV Pencil Beam of Electrons, Incident Perpendicularly on Semi-Infinite Water Phantom, as Function of Coordinates R and θ

$\frac{R}{r_0}$	1	2	3	4	5	6	7	8	9	10	11	12	13	14	15	16	17	18	19	20	T_0	
1	100.0	70.1	27.0	14.7	10.0	7.4	5.2	4.0	3.4	2.5	2.0	2.1	2.2	2.0	2.0	2.4	3.3	4.3	5.4	—	11.5	
2	—	22.6	40.4	31.1	23.1	16.9	13.7	10.8	8.7	7.2	6.1	5.5	5.7	5.8	5.8	7.0	8.3	14.0	11.5	—	11.3	
3	—	—	5.0	19.3	23.7	20.6	17.6	14.5	12.4	9.9	9.1	8.6	8.0	8.3	8.0	9.4	12.5	15.5	15.0	—	11.7	
4	—	—	—	1.0	7.7	14.0	17.8	15.1	13.5	12.3	10.3	9.6	9.4	9.8	11.5	12.3	14.1	17.4	27.5	—	11.3	
5	—	—	—	—	0.4	2.8	7.1	10.2	13.4	14.9	13.7	12.7	12.1	11.5	10.9	12.1	13.0	13.7	14.6	21.7	—	10.4
6	—	—	—	—	—	0.3	1.0	3.2	6.2	8.3	9.8	11.5	11.4	11.3	10.9	11.8	12.9	11.1	13.6	—	9.0	
7	—	—	—	—	—	—	0.6	1.7	3.6	5.5	6.8	8.8	9.3	10.0	10.4	11.2	11.4	9.5	8.1	2.7	7.7	
8	—	—	—	—	—	—	—	0.3	0.8	1.8	3.2	4.5	6.5	7.4	8.6	10.9	11.3	6.2	2.7	—	6.8	
9	—	—	—	—	—	—	—	—	0.2	0.5	1.0	1.9	3.5	4.4	5.2	7.5	5.2	3.8	—	—	5.3	
10	—	—	—	—	—	—	—	—	—	0.4	0.9	1.2	2.1	2.9	4.0	5.1	4.4	2.1	—	—	4.0	
11	—	—	—	—	—	—	—	—	—	—	0.1	0.4	1.1	1.4	2.3	3.2	3.8	1.7	—	—	3.1	
12	—	—	—	—	—	—	—	—	—	—	—	0.2	0.2	0.3	0.5	1.2	2.4	0.5	—	—	2.2	
13	—	—	—	—	—	—	—	—	—	—	—	—	0.1	0.2	0.3	0.6	1.0	0.5	—	—	1.6	
14	—	—	—	—	—	—	—	—	—	—	—	—	—	0.1	0.2	0.4	0.7	0.1	—	—	1.1	
15	—	—	—	—	—	—	—	—	—	—	—	—	—	—	0.2	0.2	0.4	0.1	—	—	0.7	
16	—	—	—	—	—	—	—	—	—	—	—	—	—	—	—	0.2	0.3	0.1	—	—	0.5	
17	—	—	—	—	—	—	—	—	—	—	—	—	—	—	—	—	0.4	0.2	—	—	0.4	
18	—	—	—	—	—	—	—	—	—	—	—	—	—	—	—	—	—	—	—	—	0.3	
T_R	4.0	4.2	4.3	4.4	4.5	4.7	5.1	5.4	6.0	6.5	7.3	7.8	8.2	8.3	7.4	6.0	3.4	1.1	0.1	0.0	—	

the electrons have not yet had time to be deflected in a sideways direction. At intermediate depths the distribution broadens. Finally, at depths approaching the mean range, the distribution again constricts around the axis of incidence, because electrons can penetrate very deeply only if their entire track lies close to their initial direction.

Bremsstrahlung from Thick Targets

The solution of this problem required the combination of electron and photon Monte Carlo programs, in order to take into account correctly the motion of the electrons prior to producing bremsstrahlung (allowing for the escape of the electron from the target), and the scattering and absorption of the bremsstrahlung photons before emerging from the target. The target was assumed to have the shape of a plane-parallel slab unbounded in the other two directions. In the results presented here, the direction of incidence of the electrons was taken to be perpendicular.

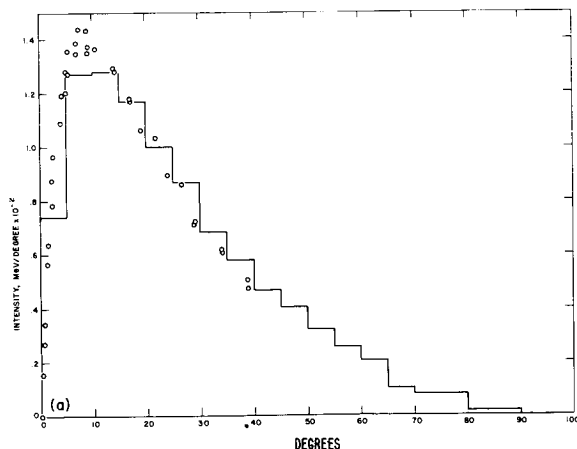
The electron part of the calculation was done by a Monte Carlo model based on the continuous-slowing-down approximation as outlined in reference 4. The photon part involved straight-forward random sampling combined with use of the method of expected values (refs. 13 and 14). The chief uncertainty of the entire calculation resulted from the lack of reliable theoretical or experimental information about the differential bremsstrahlung cross section. For the results shown here, we have used a cross-section package suggested in Table V of a review paper by Koch and Motz, (ref. 15) which consists of a suitable combination of low-energy and high-energy approximation results of the Bethe-Heitler theory, together with empirical corrections. The latter take into account departures at low energies of the experimental cross section from the theoretical (Born approximation) results.

Being primarily interested in electron source energies below 10 MeV, and in low-Z materials, we have for the time being limited the treatment to two stages of the cascade process (initial electron stage, secondary photon stage), and have ignored bremsstrahlung-produced photoelectrons, Compton electrons and pair electrons, and the bremsstrahlung in turn produced by

these particles. Auxiliary calculations are now in progress to estimate the error incurred thereby; it is expected to be quite small for our conditions. The current model of the program takes into account only the continuous bremsstrahlung spectrum. The next version will also allow us to include characteristic X-rays which are important in high-Z materials at very low energies.

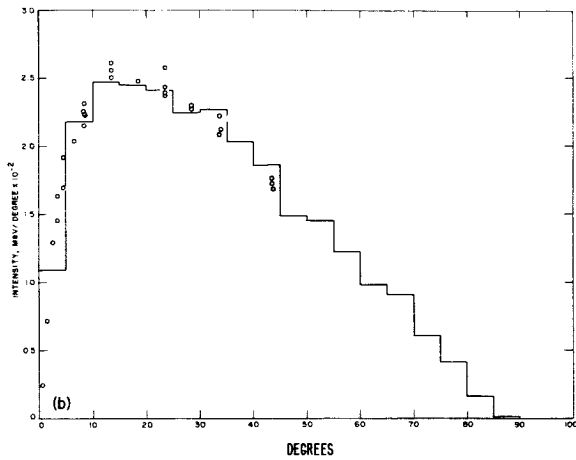
The random sampling procedures were arranged such that the ratio of the number of sampled photon histories to electron histories could be adjusted arbitrarily, and a subsequent weighting was used to make allowance for the correct value of the ratio. Guided by our experience, derived from numerical experimentation, we have in general kept the sample size for electrons rather small (200 to 1000 histories), and the sample size for photons large (10,000 to 70,000 histories).

Figures 5(a) and 5(b) compare the calculated angular distribution of bremsstrahlung with measurements by Jupiter, Hatcher, and Hansen (ref. 16 and private communication) for 10-MeV electrons incident on thick aluminum and tungsten (tantalum) targets. The experimental points result from measurements with a Victoreen ionization chamber covered with an $\frac{1}{8}$ -inch lead cap. The calculated quantity is the angular distribution of the intensity (spec-



(a) 11.7 g/cm² aluminum target. Points (o) from experiment of Jupiter et al.; histogram from Monte Carlo calculation.

FIGURE 5.—Angular distribution of bremsstrahlung intensity for 10-MeV electrons incident on thick target.

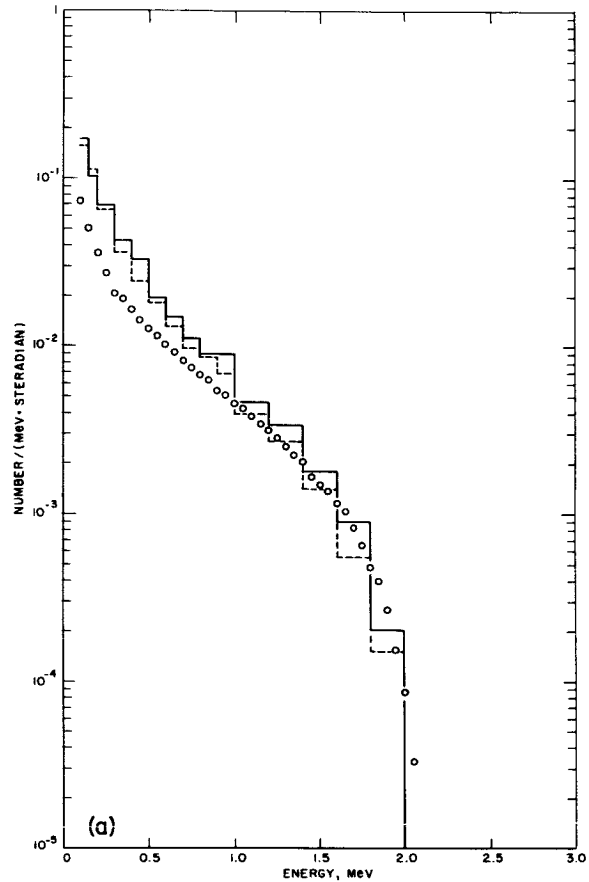


(b) Points (o) from experiment of Jupiter et al for 8.3 g/cm² tantalum target ($Z=73$). Histogram from calculation for 8.3 g/cm² tungsten target ($Z=74$).

FIGURE 5.—Concluded.

trum of photon current emerging from target, weighted by photon energy, integrated over all spectral energies and normalized to one incident electron). The normalization of the experiment is not absolute, and has been adjusted so that the area under the experimental and theoretical distribution in the region $0 \leq \theta \leq 40$ degrees is the same. (The angle θ is measured with reference to the direction of incidence.) It can be seen that for both low- Z and high- Z material there is good agreement between experiment and calculation. What this proves is primarily the correctness of the electron part of the calculation, which largely determines the angular distribution of the bremsstrahlung. Because of a lack of absolute normalization, the results are insensitive to errors in the assumed bremsstrahlung cross sections.

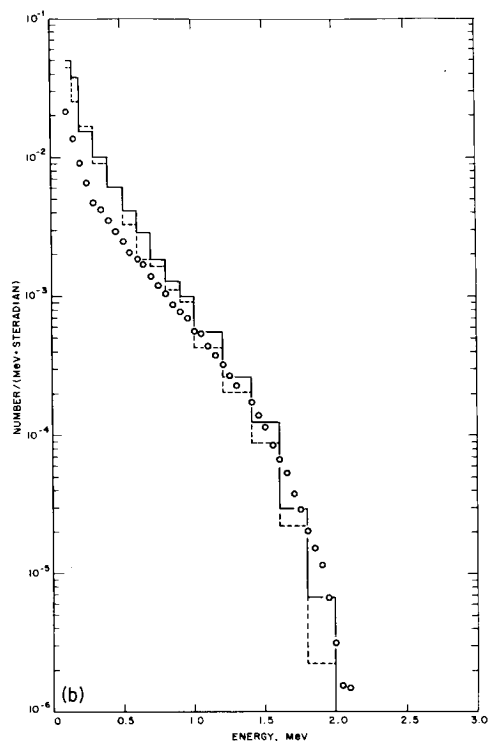
Figure 6 contains comparisons between calculated thick-target bremsstrahlung spectra for aluminum and corresponding measurements by Baggerly, Dance, Farmer, and Johnson (private communication, and a subsequent paper in this volume) at 2 MeV and 0.5 MeV. The spectra are shown at various angles with respect to the incident beam of electrons (angles smaller than 90° indicate transmission spectra; those greater than 90° indicate reflection spectra). The comparisons are absolute. On the whole,



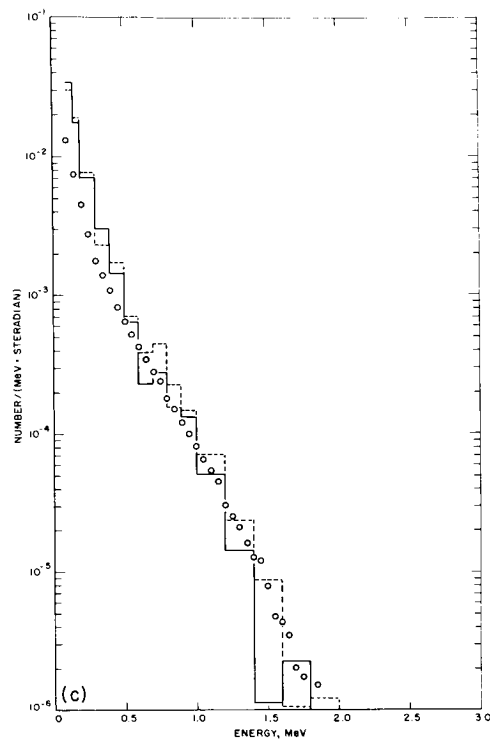
(a) 2-MeV, 1.878 g/cm² target; experimental: 15°, solid histogram: 10–15°, dashed histogram: 15–20°.

FIGURE 6.—Thick-target bremsstrahlung spectra from aluminum target. Comparison with experiment of Baggerly et al. Points (o) are experimental; histograms from Monte Carlo calculation.

the agreement is reasonably good, in fact even better than might be expected in view of the uncertainty of the bremsstrahlung cross section values used as input for the calculations. There is a definite tendency for the calculated spectra to lie above the experimental results at low spectral energies. It is possible that this discrepancy might be reduced if the effect of screening on the bremsstrahlung cross section at low energies were better known. Figure 7 contains similar comparisons with experimental results of Placious (private communication) at 50 keV. It should be noted that here the plotted quantity is not the emergent photon spectrum but the intensity (spectrum multiplied by photon energy). Again the agreement is good.



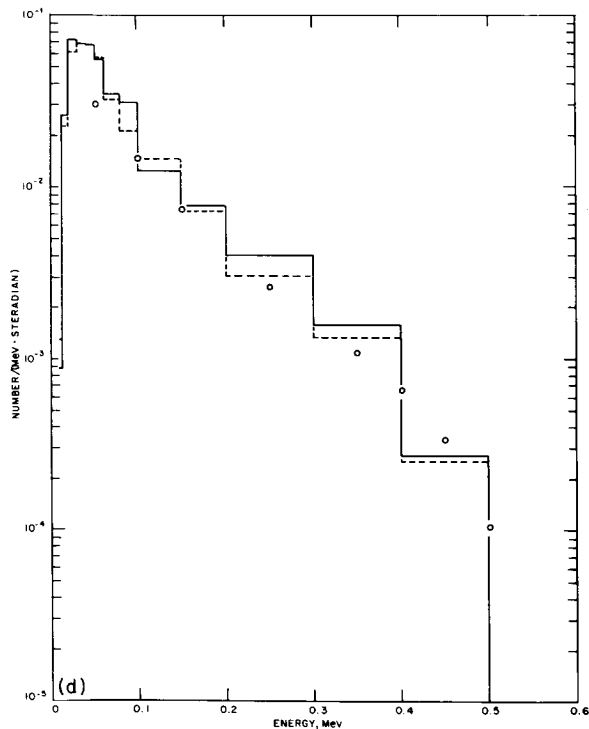
(b) 2 MeV, 1.878 g/cm² target; experimental: 60°, solid histogram: 55–60°, dashed histogram: 60–65°.



(c) 2 MeV, 1.878 g/cm² target; experimental: 120°, solid histogram: 120–125°, dashed histogram: 115–120°.

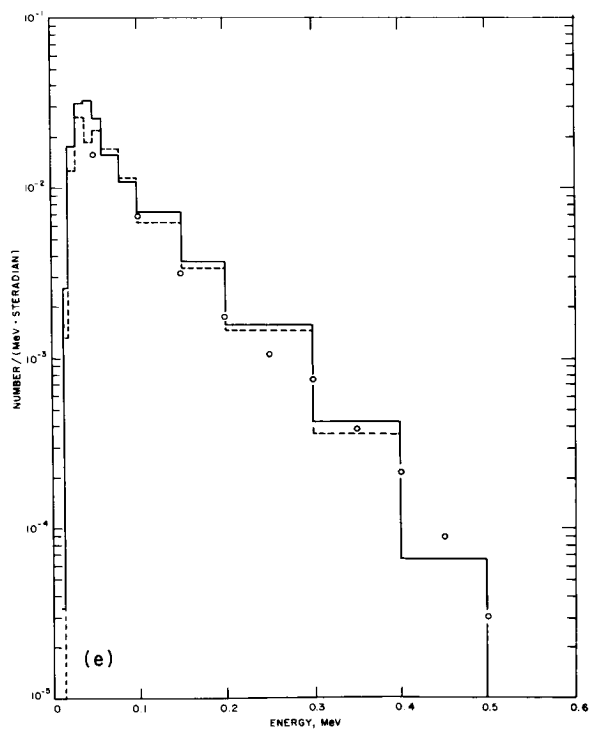
FIGURE 6.—Continued.

FIGURE 6.—Continued.



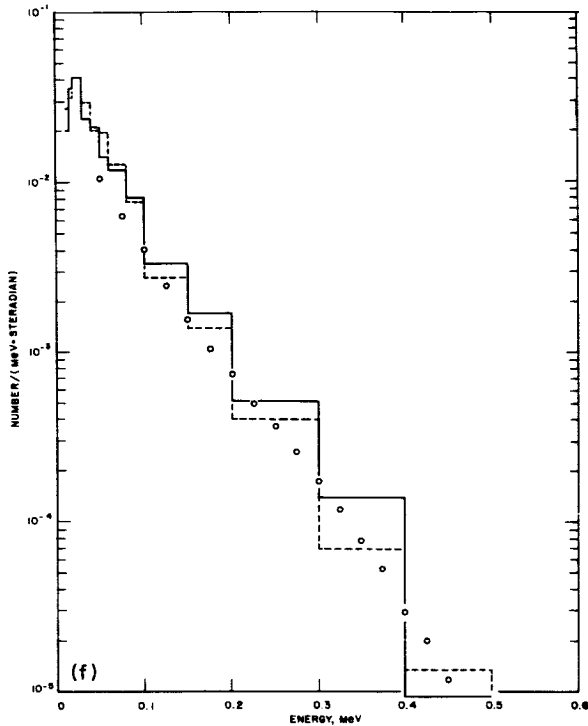
(d) 0.5 MeV, 0.5484 g/cm² target; experimental: 15°, solid histogram: 10–15°, dashed histogram: 15–20°.

FIGURE 6.—Continued.



(e) 0.5 MeV, 0.5484 g/cm² target; experimental: 60°, solid histogram: 55–60°, dashed histogram: 60–65°.

FIGURE 6.—Continued.

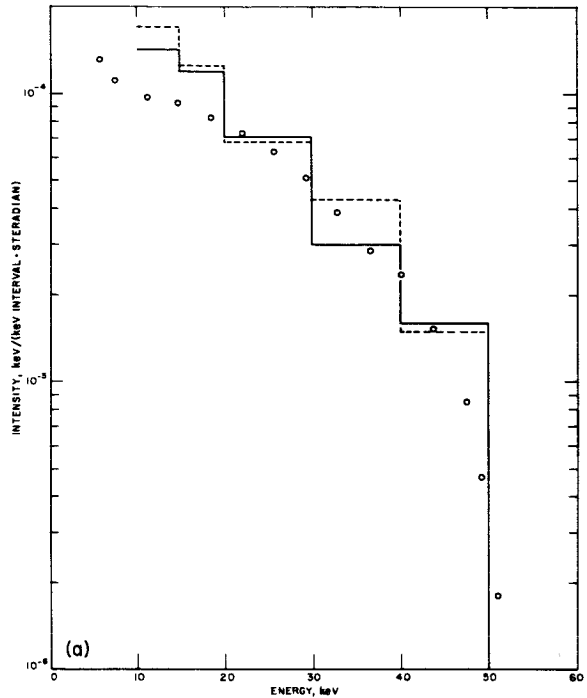


(f) 0.5 MeV, 0.5484 g/cm² target; experimental: 120°, solid histogram: 115-120°, dashed histogram: 120-125°.

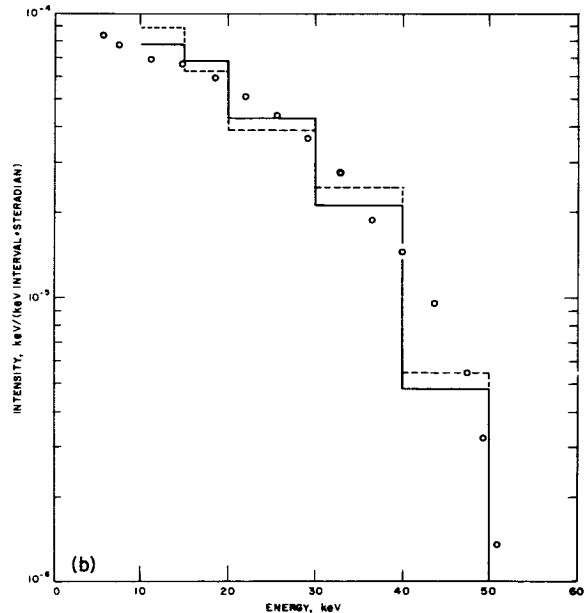
FIGURE 6.—Concluded.

Our tentative conclusion is that for electron energies from a few MeV down to very low energies, and for low-Z materials, the available procedures for calculating thick-target spectra are adequate for engineering applications, but that improved cross section input data are highly desirable.

Figure 8 shows calculated estimates of the external bremsstrahlung efficiency for aluminum and tungsten slabs, as a function of the incident electron energy and slab thickness. This external efficiency is the fraction of the incident electron energy that is converted to bremsstrahlung and emerges from the exit face of the slab, i.e. the face opposite the one where the electrons enter the target. The absorption of bremsstrahlung photons in the target is thus accounted for, whereas the efficiency (or internal efficiency), as usually defined and quoted in the literature (refs. 15 and 17), does not take this absorption into account. The results of figure 8 pertain to electrons incident perpendicularly on the target. It should be emphasized that the efficiency estimates are tentative, and are sensitive to changes of the bremsstrahlung cross sections.



(a) Experimental, 30°, solid histogram: 25-30°, dashed histogram: 30-35°.



(b) Experimental, 110°, solid histogram: 105-110°, dashed histogram: 110-115°.

FIGURE 7.—Thick-target bremsstrahlung intensity spectra from aluminum target. Comparison with experiment of Placius. 50 keV electrons incident on 0.003776 g/cm² target. Points (o) are experimental, histograms from Monte Carlo calculation.

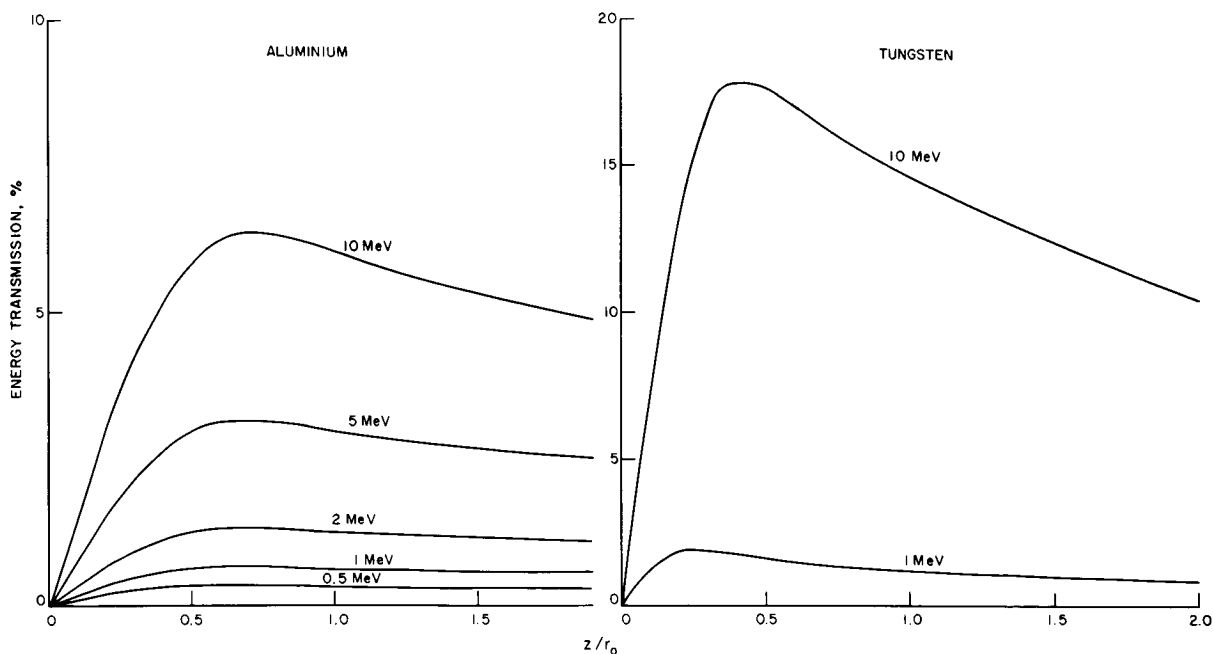


FIGURE 8.—External bremsstrahlung efficiency for aluminum and tungsten targets. For aluminum, r_0 , g/cm², =0.224 for $E=0.5$ MeV; 0.549 for 1 MeV; 1.21 for 2 MeV; 3.08 for 5 MeV; 5.84 for 10.0 MeV. For tungsten, r_0 , g/cm², =0.748 for 1 MeV; 5.94 for 10 MeV.

REFERENCES

1. SIDI, T.; HIGASIMURA, T.; and KONOSITA, K.: Mem. Fac. Eng., Kyoto Univ., no. 19, 1957, p. 22.
2. LEISS, J. E.; PENNER, S.; and ROBINSON, C. S.: Phys. Rev., vol. 107, 1957, p. 1544.
3. PERKINS, J. F.: Phys. Rev., vol. 126, 1962, p. 1781.
4. BERGER, M. J.: Methods in Computational Physics, vol. I, Academic Press (New York), 1963.
5. MAR, B. W.: Rept. D2-90414, The Boeing Company, 1963.
6. Goudsmit, S.; and Saunderson, J. L.: Phys. Rev., vol. 57, 1940, p. 24.
7. MOTT, N. F.: Proc. Roy. Soc., no. A124, 1929, p. 475.
8. MOLIÈRE, G.: Z. Naturforsch., vol. 2a, 1947, p. 133; vol. 3a, 1948, p. 78.
9. LANDAU, L.: J. Phys., USSR, no. 8, 1944, p. 201.
10. BLUNCK, O.; and LEISEGANG, S.: Z. Physik, vol. 128, 1950, p. 500.
11. SPENCER, L. V.: Phys. Rev., vol. 98, 1955, p. 1507; Nat. Bur. Std. Monograph, no. 1, 1959.
12. CREW, J. E.: J. Res., Nat. Bur. Std., vol. 65A, 1961, p. 113.
13. FANO, U.; SPENCER, L. V.; and BERGER, M. J.: Encyclopedia of Physics, vol. XXXVIII/2, Springer (Berlin), 1959.
14. BERGER, M. J.: An Application of the Monte Carlo Method to a Problem in Gamma Ray Diffusion. Symp. on Monte Carlo Methods (H. A. Meyer, ed.), John Wiley & Sons, 1956.
15. KOCH, H. W.; and MOTZ, J. W.: Rev. Mod. Phys. vol. 31, 1959, p. 920.
16. JUPITER, C. P.; HATCHER, C. R.; and HANSEN, N. E.: Proc. of Am. Phys. Soc. Meeting (Washington), Apr. 1964.
17. EVANS, R. D.: The Atomic Nucleus. McGraw-Hill Co., 1955.

N65-34064

48—Bremsstrahlung Production in Thick Aluminum and Iron Targets by 0.5- to 3.0-MeV Electrons¹

L. L. BAGGERLY, W. E. DANCE, B. J. FARMER, and J. H. JOHNSON

LTV Research Center

The intensity of bremsstrahlung produced by bombarding thick targets of the important structural materials, aluminum and iron, has been measured as a function of incident electron energy, photon energy, and angle of photon emission. The energy of the incident electrons ranged from 0.5 to 3.0 MeV. The electron beam from a 3 MeV Van de Graaff accelerator was incident normally on targets of sufficient thickness to stop the electrons. The total integrated intensities have been computed from these measurements, and the results from aluminum and iron will be compared.

INTRODUCTION

I shall describe an experimental laboratory study to investigate the production of bremsstrahlung, and report some of the initial results from this study, now in progress at the LTV Research Center (of Ling-Temco-Vought, Inc.) in Dallas. The objective of this program is to determine the production of continuous X-rays, or bremsstrahlung, by monoenergetic electrons incident on various materials. This information will ultimately be used in making dose calculations. In this paper we shall consider bremsstrahlung absolute intensities from thick targets. By thick targets here we mean targets which are thick enough to stop the electrons completely. We shall report results for the two materials, aluminum and iron. The energy range covered to date is 0.5 to 3.0 MeV, which is of the same order as the rest energy of the electron—a range for which the present knowledge of bremsstrahlung is less satisfactory than that for the non-relativistic range on the one hand, and the highly relativistic range on the other hand. It is thus important to accumulate systematic experimental data in this "in-between" energy range. The accelerator used in these measurements is a 3.0 MeV Van de Graaff, an effective instrument for supplying

monoenergetic electrons with these energies. In the present study bremsstrahlung spectra were accumulated for 10 different values of θ , the photon emission angle, varying from 0 degrees to 150 degrees to the incident beam direction, and 6 different values of T_0 , the electron incident energy.

EXPERIMENTAL METHOD

At this point let us turn briefly to the experimental arrangement by which the data to be presented were obtained. The arrangement is shown schematically in figure 1. The electron beam from the Van de Graaff accelerator impinges at normal incidence on the target, positioned at the center of an evacuated cylindrical chamber, 12 inches in diameter and approximately 14 inches high. The bremsstrahlung radiation produced at the target and emerging at an angle θ to the incident beam direction passes through a thin window in the chamber wall, through a lead collimator, and then through a defining aperture in a 3-inch thick lead sheath which encloses the scintillation spectrometer. In front of the detector a permanent magnet is provided for the purpose of sweeping out any electrons which are scattered into the solid angle of acceptance of the detector.

The target chamber is isolated electrically from the electron beam tube and from the

¹ Research supported by the National Aeronautics and Space Administration under contracts NASw-647 and NASw-948.

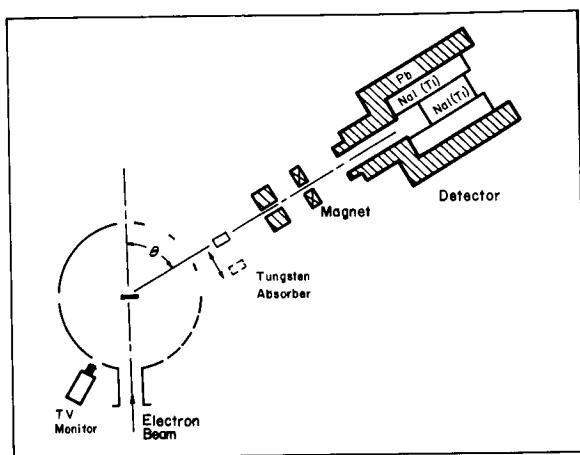


FIGURE 1.—Schematic representation of the experimental arrangement. The tungsten absorber is shown in position for taking a background spectrum.

chamber support stand, to enable one to integrate the total electron current delivered to the target and the chamber and thus to determine the number of electrons incident on the target during a run. The target is mounted on a $\frac{1}{2}$ -inch shaft which can be remotely driven vertically for positioning either the target or a viewer into the beam. During operation, the target or the beam viewer is observed by a television monitor. Target thicknesses in each case were chosen so as to present to the electron beam a thickness of material equal to or greater than the maximum range of the electrons.

The target-to-detector distance is 98.1 cm, so that with a $\frac{1}{2}$ -inch defining aperture, the detector subtends a solid angle of 1.31×10^{-4} steradian. The scintillation detector is a 2.32-inch diameter by 6-inch long NaI(Tl) crystal surrounded by an annulus of NaI(Tl), the annulus being operated in anticoincidence with the center crystal. We thus accept for analysis only those pulses from the center crystal which are not accompanied by coincident pulses in the surrounding annulus. This dual crystal arrangement effectively removes a substantial portion of the low-energy part of the detector line shape which is due to Compton scattering and other partial absorption processes in the center crystal. The response of the detector to monoenergetic gamma rays in the energy range of interest is well approximated by a Gaussian photopeak and a trapezoidal low-

energy tail. This response was unfolded from the pulse height distributions to yield the spectra to be presented in this paper. The energy calibration and the efficiency of the detector were determined experimentally using various standard gamma ray sources having energies ranging from 0.279 MeV (Hg^{203}) to 2.754 MeV (Na^{24}). The photopeak efficiency is about 0.94 at 200 keV and decreases to approximately 0.25 at 3.00 MeV.

The procedure used in making a typical data run to obtain a bremsstrahlung spectrum for a given electron energy T_0 and photon angle θ involves the following steps:

(1) *Accumulation of the main pulse height distribution.* Pulses corresponding to photons absorbed in the center crystal are amplified and fed to a 256-channel pulse height analyzer. The amplified signal from the annulus serves to gate off the analyzer for maximum reduction in background. The analyzer live time is determined by the ratio of the number of pulses stored in the memory to the number arriving at the analyzer with pulse height between the lower and upper level discriminator levels, as counted by two fast scalars. In each run, counts are accumulated for a fixed total charge of electrons on target, consistent with reasonable counting statistics.

(2) *Background run.* A background spectrum is accumulated by inserting a remotely operated tungsten absorber between the target and the detector and observing the counts for one-half the total fixed charge of the main spectrum. The diameter of the absorber was chosen so as to shield only the target from the detector, leaving exposed to the detector all background producing areas within its acceptance angle.

(3) *Background subtraction.* The background data are subtracted from the main pulse height data after correcting each group of data for analyzer live time and normalizing the background run to the total charge of the main spectrum.

Several times during each day of runs, a detector energy calibration spectrum is accumulated and recorded as a part of each run in order to allow a correction for gain shift in the spectrometer during the day. This calibration spectrum, along with the main

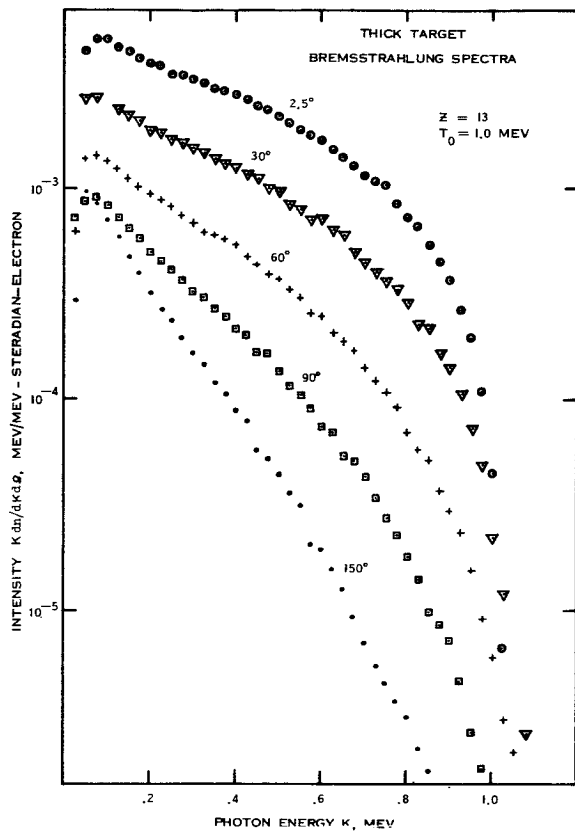


FIGURE 2.—Bremsstrahlung intensity from a thick aluminum target at various photon angles, for 1.00 MeV electrons incident on the target.

spectrum, the background spectrum, the total charge, and the live time correction factor, are input data peculiar to each individual run, for the 7090 computer program used to calculate the spectral intensities.

It should be noted that the spectra to be reported here are those observed from the particular thickness of target material used without corrections for photon absorption in the target.

RESULTS

The 7090 computer program was used to compute the following quantities:

(1) Bremsstrahlung spectral intensities differential in photon energy and solid angle, $K \, dn/dK \, d\Omega$, for each value of θ and each electron energy, T_0 .

(2) Spectral intensities integrated over photon angle θ , giving $K \, dn/dK$, for each energy T_0 .

(3) Total intensities (integrated over photon angle and energy) $\int K \, dn$, for each electron energy T_0 .

The intensities differential in photon energy and angle, resulting from bombarding an aluminum target with 1.0 MeV electrons, are presented in figure 2. Of interest here is the change in magnitude (approximately 2 orders) of the intensity, as well as the significant change in shape of the spectra as the photon angle θ increases from the forward to the backward direction. The bending over of the spectra at $K=0.1$ MeV is attributed to photon absorption in the target. Figure 3 shows the comparative data for an iron target for 1.00 MeV electrons.

The results of integrating, over angle θ , the intensities of figures 2 and 3 are shown in figure 4. The lower set of points is for aluminum, the

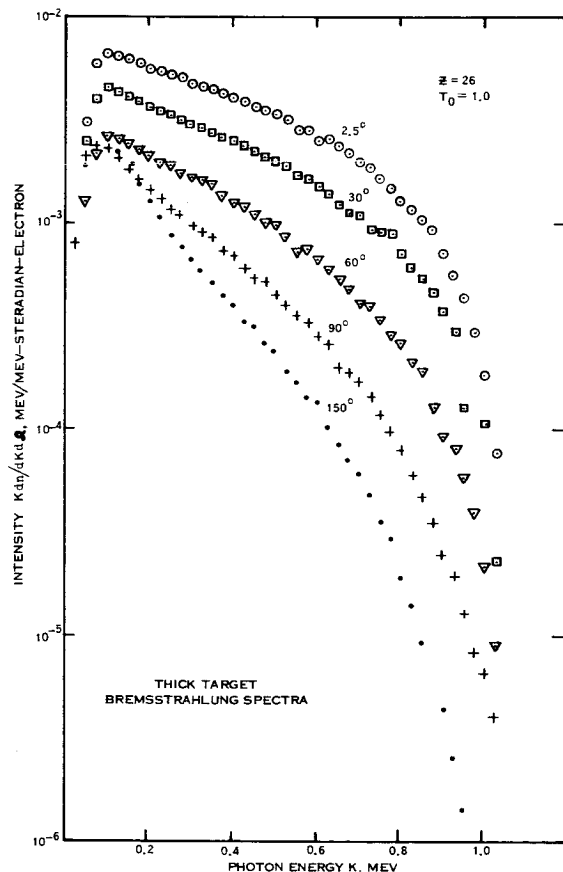


FIGURE 3.—Bremsstrahlung intensity from a thick iron target at various photon angles, for 1.00 MeV electrons incident on the target.

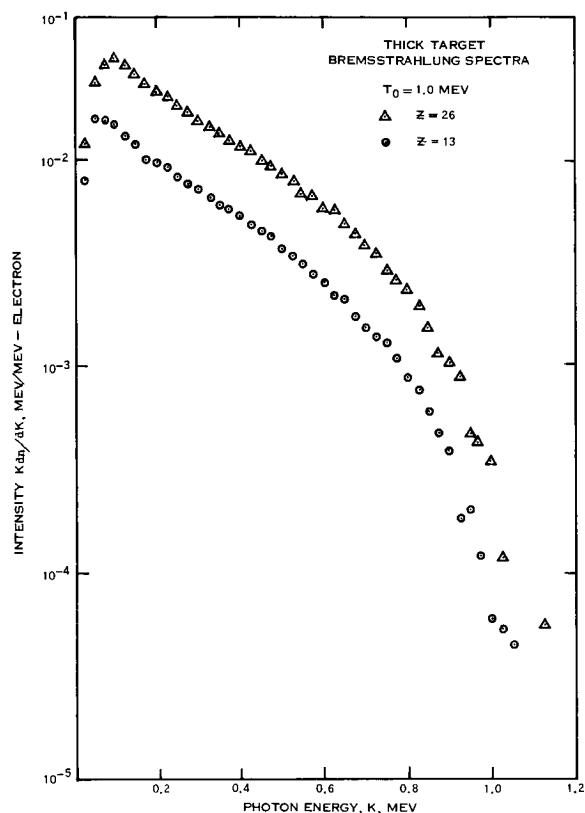


FIGURE 4.—Comparison of the bremsstrahlung intensities, integrated over solid angle Ω , for aluminum and iron. These spectra were obtained from 1.00 MeV electrons incident on the targets.

upper set for iron. In each case $T_0=1.00$ MeV. The spectra are approximately exponential in shape over most of the range, until the photon energy approaches the maximum T_0 where the intensity rapidly approaches zero. The intensity curves for the entire electron energy range, 0.5 to 3.00 MeV, are given in figure 5 in the case of aluminum, and in figure 6, for iron. They are plotted here as a function of K/T_0 . It is seen from these curves that, as the electron energy is increased, the spectral shape is generally preserved, although the intensity at $K/T_0=0.200$ for 3.00 MeV electrons is several times that at 0.5 MeV. In aluminum, for example, the intensity at $K/T_0=0.200$ for 3.00 MeV electrons is approximately 5 times that for 0.5 MeV. The corresponding ratio for iron is approximately 4.5.

The results of integrating the bremsstrahlung intensities over both photon energy and angle are shown in figure 7. In this figure, the total intensity in MeV/electron is plotted as a function of the electron energy T_0 . The lower set of points is the data for aluminum, the upper set for iron. The straight solid lines are approximate fits of the integrated form of the bremsstrahlung intensity given by Kramers' empirical relation (ref. 1)

$$I = CZT_0^2$$

to the experimental data. Thus our experiment indicates that the total integrated intensity is directly proportional to Z and to T_0^2 , in good agreement with the Kramers relation.

The average value of C determined from these data is $C = (0.40 \pm 0.04) \times 10^{-3} \text{ MeV}^{-1}$,

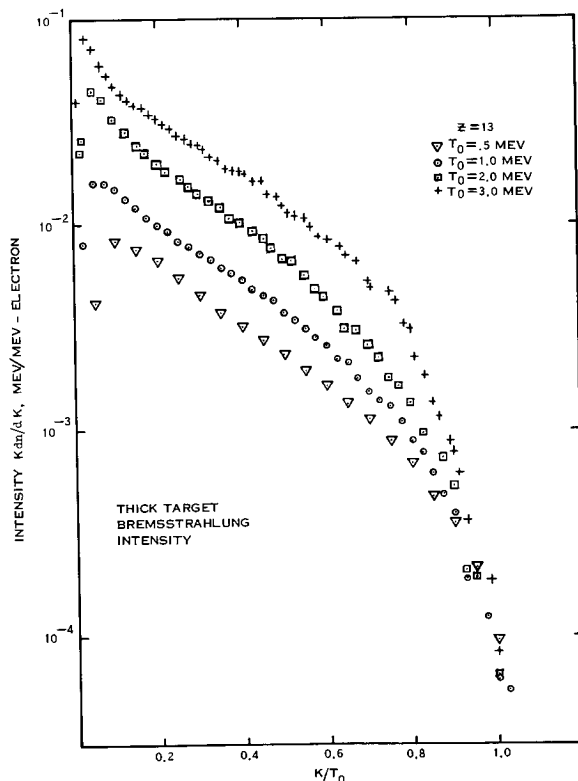


FIGURE 5.—Comparison of the bremsstrahlung spectra integrated over solid angle Ω for various values of the incident electron energy, T_0 , for thick aluminum targets. The photon energy in each case is normalized to the electron incident energy, and thus is plotted as K/T_0 .

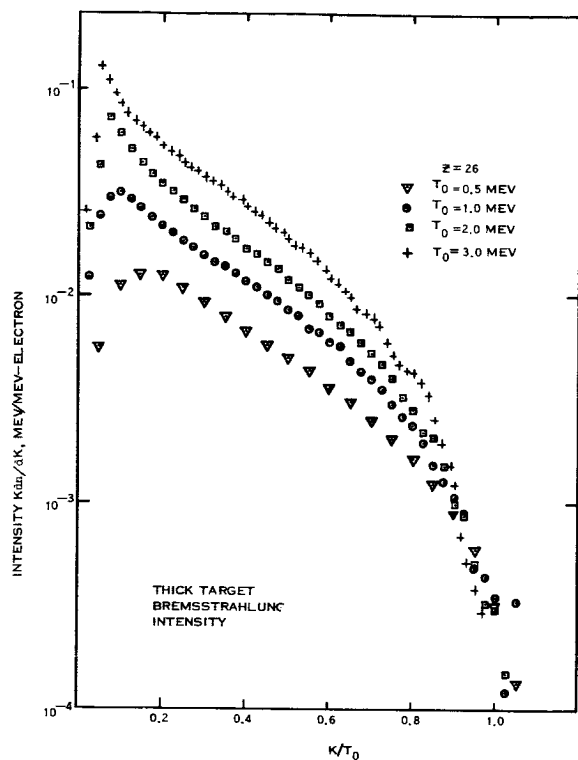


FIGURE 6.—Comparison of the bremsstrahlung spectra integrated over solid angle Ω for various values of the incident electron energy T_0 , for thick iron targets. The photon energy in each case is normalized to the electron incident energy, and thus is plotted as K/T_0 .

for the energy range $0.5 \leq T_0 \leq 3.0$ MeV. This is in close agreement with the value $C=0.4 \times 10^{-3}$ MeV $^{-1}$ estimated from the data of Buechner, et al. (ref. 2), who measured total bremsstrahlung intensities for electrons in the range 1.25 to 2.35 MeV using an ionization chamber. Evans (ref. 3) gives the value $C=(0.7 \pm 0.2) \times 10^{-3}$ MeV $^{-1}$, and Koch and Motz (ref. 4) suggest $C=1 \times 10^{-3}$ MeV $^{-1}$, within a factor of two, as averages from a wide range of theoretical and experimental evaluations of this constant over a wide energy range. (Note that Koch and Motz write T_0 in units of mc^2 rather

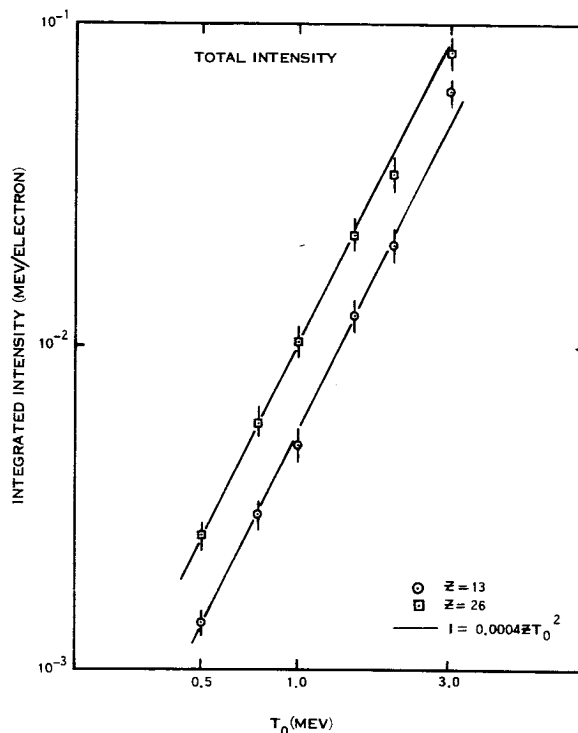


FIGURE 7.—Total absolute bremsstrahlung intensity, integrated over photon energy and angle, as a function of incident electron energy, for aluminum (lower curve) and iron (upper curve). The solid lines are approximate fits of Kramer's empirical relation $I=CZT_0^2$ to the present experimental data.

than MeV.) At very low energies (below 0.1 MeV), Kulenkampff and Schmidt (ref. 5) find $(1 \leq C \leq 1.5) \times 10^{-3}$ MeV $^{-1}$. Each of these latter values is corrected for absorption in the target.

Plans for future work in this laboratory include measurements of bremsstrahlung intensities from other materials, as well as measurement of thin target cross sections for the same materials. In addition, a program is underway to measure electron scattering cross sections for targets of various thicknesses.

REFERENCES

1. KRAMERS, H. A.: Phil. Mag., no. 46, 1923, p. 836.
2. EVANS, ROBLEY D.: The Atomic Nucleus. McGraw-Hill, 1955, pp. 616-617.
3. BUECHNER, W. W.; VAN DE GRAAFF, R. J.; BURRILL, E. A.; and SPERDUTO, A.: Phys. Rev., vol. 74, 1948, p. 1348.
4. KOCH, H. W.; and MOTZ, J. W.: Rev. Mod. Phys., vol. 31, 1959, p. 955.
5. KULENKAMPPF, H.; and SCHMIDT, L.: Ann. Physik, no. 43, 1943, pp. 494-512.

NO. 34625

49—Space Electron Radiation Shielding—Bremsstrahlung and Electron Transmission

G. D. MAGNUSON and A. W. McREYNOLDS

General Dynamics/Astronautics

The manned space missions so far have been restricted to a relatively radiation-safe region, altitudes low enough to avoid the trapped radiation belts, and latitudes low enough to provide geomagnetic shielding against energetic solar flare protons and partly against more energetic galactic radiation. In the next phase of the manned space flight program, more extended orbital missions at higher altitudes, the first major radiation hazard to be encountered arises from electron bombardment in the trapped radiation belts, representing a composite of the natural Van Allen belts and, particularly, the low altitude trapped electrons added by the fission product beta decays from the 1962 nuclear detonations. An accurate evaluation of the radiation hazard, and the design of optimum shielding against it, for any specified mission, would require detailed knowledge of both the electron environment and its interaction with the spacecraft materials.

Considering the quite recent discovery and creation of the radiation belts and development of satellite instrumentation, it is to be expected that the knowledge of the intensity, space distribution, and energy spectrum is rapidly increasing, but far from complete. The present status has been summarized by Freeman, and by Vette, in other papers in this volume. For present purposes it is sufficient that the flux generally has a broad maximum somewhere in the 1–3 MeV range, and drops rapidly with increasing energy, to negligible values above 10 MeV. Figure 1 shows 1962 data of West, Mann, and Bloom (ref. 1).

It might also be expected, from the long history of electron bombardment of materials to produce X-rays, that data on electron

interactions with materials would be quite complete, and both transmission and bremsstrahlung generation would be known with precision. Such is not the case. First, the low mass of the electron leads to large angular and energy straggling effects, which render computation from microscopic cross sections much more difficult than for heavy ion penetrations. This is particularly true for material thicknesses approaching the maximum electron range. Second, there has been neither

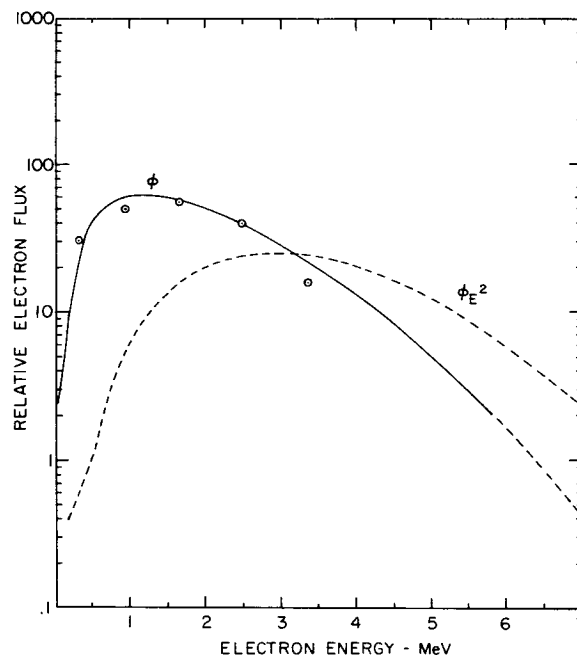


FIGURE 1.—Typical energy spectrum of electrons in the trapped radiation belts, according to West, Mann, and Bloom. Curve ϕE^2 represents bremsstrahlung energy generated as a function of incident electron energy.

the incentive of fundamentally significant physical data, nor the practical need for engineering data, to study those cases which are of importance for space electron shielding: light elements, energies of several MeV, large angles of electron incidence, thicknesses near maximum range, and composites of several materials.

To meet this need for fundamental data for radiation shielding, an extensive program of experimental measurements has been undertaken, using beams of monoenergetic electrons from the General Dynamics/Astronautics Dynamitron accelerator to bombard light metals, plastics, and other potential shielding materials. The angular distribution, intensity, and energy distribution of both transmitted electrons and bremsstrahlung X-rays are measured as a function of incident angle and energy. Since a preceding paper by Baggerly et al. discusses bremsstrahlung, the present paper describes primarily our results on electron transmission.

DEFINITION OF THE ELECTRON SHIELDING PROBLEM

Spacecraft in the radiation belt area are subjected to omnidirectional bombardment of electrons. Except for the unlikely case that orientation is controlled with respect to the earth's magnetic field lines, its motion also tends to average out any directional properties of the electron flux, so that the flux may be assumed as approximately isotropic. The purpose of present experiments is to get data from which the dosage of electrons and X-rays inside the hull can be computed. As illustrated in figure 2, the parameters concerned are the energy and angle of an incident electron, E, θ , the thickness r_1, r_2 and atomic numbers z_1, z_2 of one or more layers of shielding material, and the statistical distribution of the energies and angles of emergence E', θ' and E'', θ'' of transmitted electrons and transmitted X-rays, respectively. The radiation dosage at the internal point is determined by integrating over the entire hull and over all values of the variables $E, E', E'', \theta, \theta', \theta''$. Qualitatively, the incident energy distribution is as shown in figure 2, with negligible low energy flux and a maximum in the range 1 to 3 MeV. Also shown

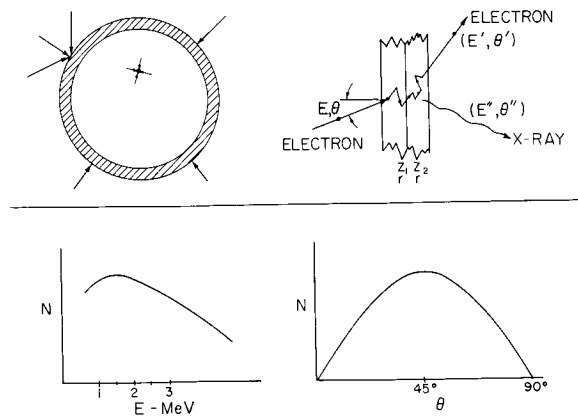


FIGURE 2.—The problem of space electron radiation shielding is to determine the radiation intensity at a point inside a hull bombarded by an omni-directional flux of electrons. The curves $N(E)$ and $N(\theta)$ indicate qualitatively the energy distribution and angular distribution (assuming isotropic flux) of incident electrons. Data on intensity of electrons and bremsstrahlung as functions of $E, \theta, E', \theta', E'', \theta''$ are required, particularly in the range $\theta=30$ to 60° .

in figure 2 is the number of incident electrons as a function of angle, assuming isotropic flux. It is worth noting that, from purely geometrical considerations, the distribution follows $N(\theta) = \sin \theta \cos \theta$, such that most of the incident electrons are at angles in the 30 to 60 degree range, and none are at normal (0 degree) angle of incidence, where most of the existing electron penetration measurements have been made.

The total radiation dose at an internal point is the sum of two components—transmitted electrons and bremsstrahlung—either of which may predominate, according to the relation of the external flux to the tolerance level. Generally, for very low external flux, only very thin shielding will be required and bremsstrahlung production is a small fraction of the total dose; for high external flux, the shield will necessarily be thick enough to stop nearly all of the electrons, and bremsstrahlung will constitute most of the dosage; at intermediate external flux levels, the two components may be comparable. Their ratio is, of course, influenced also by the nature of the shield, since bremsstrahlung production increases linearly with atomic number. Assuming that an orbit has been selected, that the radiation environment is known well enough to predict the integrated electron flux, and that a radiation tolerance level has been specified,

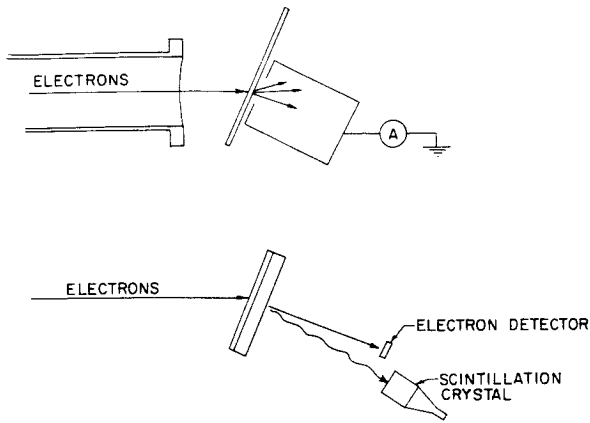


FIGURE 3.—Schematic experimental arrangement using electron beams from the Dynamitron accelerator to measure fraction of electrons transmitted (above) and energy and angular distributions of electrons and bremsstrahlung transmitted (below) through shield panels.

the problem of design of an optimum, that is, minimum weight, shield subject to various other design considerations, requires selection of materials and thicknesses such that the sum of the electron and the bremsstrahlung dosages is minimized. This design may vary rather sensitively with selection of the arbitrary parameters, such that the weight requirements depend strongly on the mission definition or the tolerance. The objective of the experiments, as extended by theoretical extrapolation and interpolation, is to provide a complete and accurate enough set of data to serve as input for shield computation programs.

EXPERIMENTS

The two types of experiments are schematically indicated in figure 3. The electron beam from the Dynamitron 0 to 3 MeV accelerator was brought out through a thin titanium window and further defined by a thin lead collimator, to eliminate angular spreading in the exit window. To measure the number transmission coefficient for electrons

$$T_N = \frac{\text{number of electrons transmitted}}{\text{number of electrons incident}}$$

incident current and the current collected in a Faraday cup immediately behind the sample panel were measured by electrometers. A col-

lection system was arranged in front of the panel such that both electrons stopped in the panel and those back-scattered from the front face were counted, and the Faraday cup was placed to collect all electrons transmitted.

The more detailed measurements of energy and angular distribution were also carried out in air, with a 4×5 inch NaI (TI) scintillation crystal as detector for gamma spectra, a thin plastic scintillator to measure total X-ray ionization, and a silicon lithium drifted electron detector. The scintillation and lithium drifted detectors were used with a 400-channel pulse height analyzer.

The qualitative form of the electron transmission and bremsstrahlung relations studied is summarized in figure 4. Beginning with the upper portion of the figure, the number transmission coefficient, T_N , is zero at a critical energy for which the target thickness represents the extreme range. T_N rises more or less linearly with increasing energy, finally approaching $T_N=1$ asymptotically as E goes to infinity. The energy distribution $N(E')$ is zero at an energy $E' = (\text{incident energy, } E - \text{minimum energy loss in transmission})$; below this value of E' the transmitted electrons are distributed in a broad peak as indicated. The total transmitted energy from an incident spectrum $\theta(E)$ is therefore given by $\int_0^\infty \theta(E) T_N(E) \int_0^E N(E') dE'$.

At very high incident electron energy, E_1 , there is little angular scattering in transmission, and the angular distribution of the emergent electrons is very closely grouped about the incident direction θ . At lower incident energies, where an appreciable fraction of the initial energy is lost in transmission, the emergent angular distribution is broader, approaching a cosine distribution after traversal of material equivalent to roughly half of the maximum range.

The bremsstrahlung generated by stopping of an electron of energy E in material of atomic number Z is proportional to ZE^2 to a good approximation. As indicated, the number of photons emitted is highest at low energy and decreases monotonically, dropping rapidly to zero as the incident electron energy E is approached. As in the case of electron transmission, the photon emission for high energy

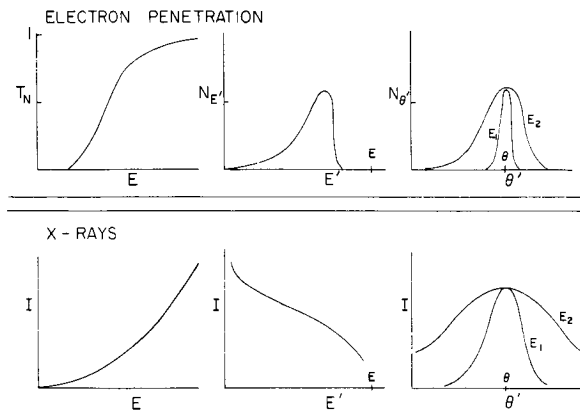


FIGURE 4.—Qualitative form of the electron transmission coefficient (T_N), energy spectrum ($N_{E'}$) and angular distribution ($N_{\theta'}$) for transmitted electrons, and form of the total intensity and energy and angular distributions of bremsstrahlung X-rays generated in a thick target. The transmitted radiations are forward peaked for high incident energy E_1 but diffuse for lower energy E_2 .

incident electrons is in the forward direction of electron propagation, but at lower energies becomes much broader, approaching an isotropic distribution in the energy range below ~ 0.5 MeV.

ELECTRON BREMSSTRAHLUNG EXPERIMENTS

The total bremsstrahlung radiation was measured behind a composite panel, the composition of which is shown in figure 5. The detector used in these measurements was a Pilot B plastic scintillation crystal 1.0 in. in diameter and 0.060 in. thick. The crystal was placed in contact with a 1.0 in. diameter lucite light pipe about 8 in. in length, with a silicone diffusion pump oil at the interface for optical coupling. The light pipe was placed in direct contact with a Dumont 6447 photomultiplier, again with silicone oil at the interface. A 0.001 in. aluminum foil was placed over the front face of the crystal and the entire unit made light tight by wrapping with black 0.007 in. vinyl tape.

Calibration of the crystal was carried out using an NBS calibrated Co^{60} source of strength 7.94 mc. The output current from the photomultiplier tube was measured as a function of the distance from the standard source. Knowing the radiation field in mr/hr from the standard

source, one can then relate the photomultiplier current to the radiation field.

Since the ultimate purpose of these measurements was to obtain information on the bremsstrahlung received by an astronaut behind a typical space station panel, the crystal detector was mounted at the front face of a phantom consisting of a rectangular parallelepiped of paraffin 12 in. by 12 in. on a face and 6 in. deep. Hence, the radiation received and measured by the plastic scintillation crystal includes that radiation scattered by the torso back to the point at which the measurements were made. By using a tissue equivalent crystal as the detector, and the phantom, it was hoped to obtain a reasonable approximation of the radiation received by an astronaut behind the panel. The light pipe was inserted through a hole in the phantom with the crystal at the center of the front face of the phantom. A 2-in. Pb shield surrounded the photomultiplier housing at the rear of the phantom.

The entire phantom and detector assembly was mounted on a rotating arm powered by a selsyn motor remotely controlled from the accelerator control room. The arm could rotate in polar angle, as measured from the beam axis, from -45° to $+90^\circ$. In this way the

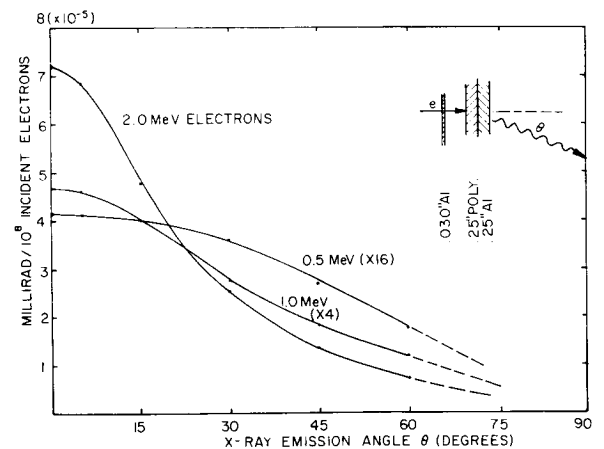


FIGURE 5.—Bremsstrahlung intensity as a function of angle behind hypothetical laminar aluminum and polyethylene spacecraft hull. Curves for 0.5 and 1.0 MeV have been multiplied by 16 and 4 respectively, for direct comparison with the 2.0 MeV curve, since total bremsstrahlung production is approximately proportional to E^2 .

spatial distribution of the bremsstrahlung behind the panel could be measured. In practice it was only possible to make measurements at polar angles less than 60° due to the finite size of the panels.

Background measurements were taken with a 2-in. Pb shield placed so as to completely block the direct line of sight from the detector to the panel. The gamma ray background in all cases was less than about 8% of the measured bremsstrahlung.

The results of the measurements for different electron energies are shown in figure 5. The curves show the absorbed dose in the plastic scintillator in millirads/ 10^8 electrons as a function of the polar angle. The 0.5 MeV curve was multiplied by 16 and the 1.0 MeV curve by 4 in order to make a comparison with the 2 MeV results, since bremsstrahlung generation goes as E^2 . Peaking of the radiation in the forward (beam) direction is quite noticeable with increasing electron energy. An integration of the distribution in figure 5 was made to determine the fraction of the total energy incident upon the panel that appears as bremsstrahlung behind the panel. These fractions were 0.28%, 0.40%, and 0.67% for 0.5, 1.0, and 2.0 MeV, respectively

ELECTRON TRANSMISSION EXPERIMENTS

Using the Faraday cup arrangement shown in figure 3, electron transmission measurements were made on polyethylene and aluminum. Figure 6 shows the transmission T_N for electrons normally incident on different thicknesses of Al, plotted as a function of the incident electron energy. Figure 7 shows the same type of plot for polyethylene. To obtain the polyethylene data, it was necessary to wrap the target sheets in 0.0005 in. Al foil to prevent build-up of charge in the polyethylene.

Some measurements were also made on the effect of incident angle on T_N . Figures 8 and 9 show T_N for Al with electrons incident at angles 30° and 60° , respectively. Identical sets of measurements were made for the polyethylene samples.

The effects on the transmission curve of variation in the angle of incidence, and in the atomic number of the material, are best seen

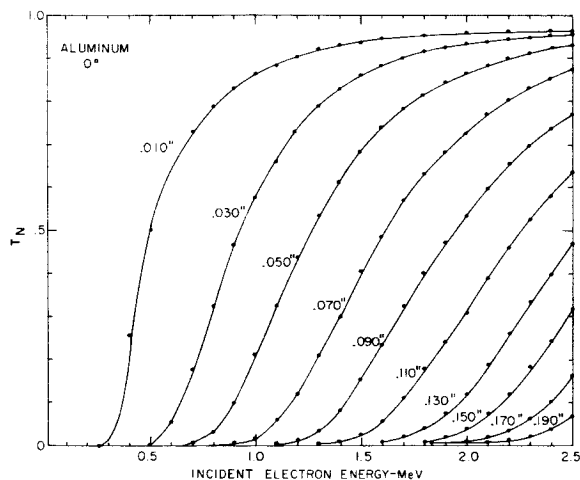


FIGURE 6.—Number transmission coefficient $T_N = \frac{\text{transmitted electrons}}{\text{incident electrons}}$ incident at 0° on various thicknesses of aluminum.

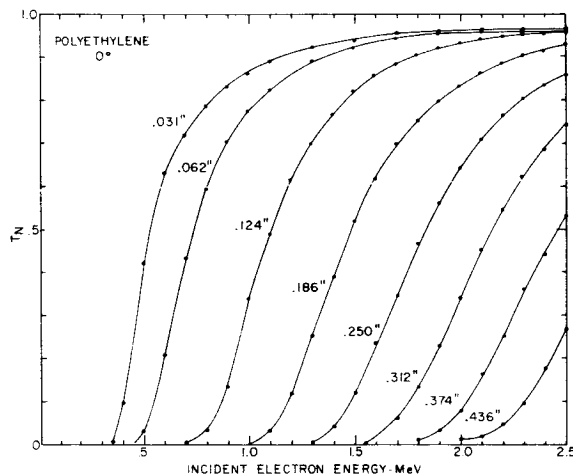


FIGURE 7.—Number transmission coefficient $T_N = \frac{\text{transmitted electrons}}{\text{incident electrons}}$ incident at 0° on various thicknesses of polyethylene. Curves are steeper than for aluminum.

by comparing curves for the same material thickness in units of mass per unit area. Figure 10 shows the curves for 0.410 g/cm^2 of aluminum and polyethylene at 0° incident angle. Although the energy at which transmission begins is higher for polyethylene, the transmission curve then rises more steeply, crossing the aluminum curve in the vicinity of 50% transmission and remaining higher as the energy

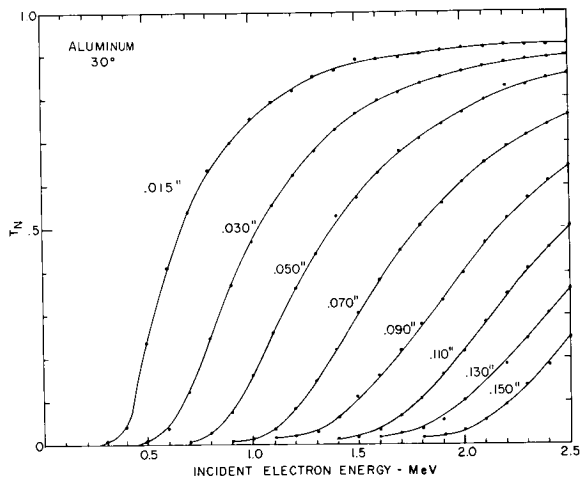


FIGURE 8.—Number transmission coefficient T_N for electrons incident at 30° on various thicknesses of aluminum.

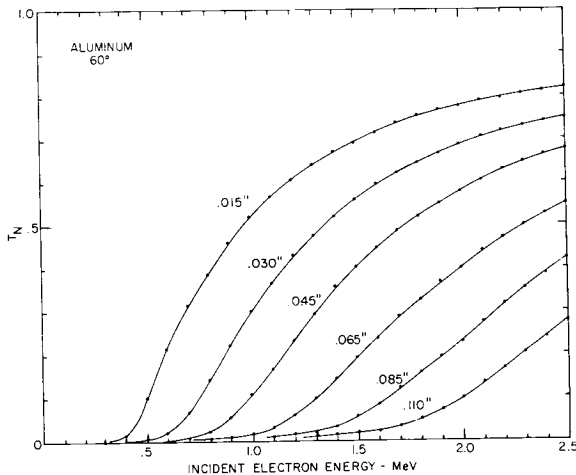


FIGURE 9.—Number transmission coefficient T_N for electrons incident at 60° on aluminum. Curves are less steep than for 0° incident because of angular spread of the electron beam in transmission.

increases. Thus polyethylene is more effective for low energies, less effective for high energies, and roughly equal for a broad incident energy distribution. Figure 10 also shows data for 0.205 g/cm^2 of aluminum at 60° incident angle. Since the thickness in the direction of incidence is equal to the 0.410 g/cm^2 0° case, the curves would be identical in the absence of angular spreading of the electron beam. The effect of angular spread is that some electrons are scattered toward the normal, shortening the transmission path and causing transmission to

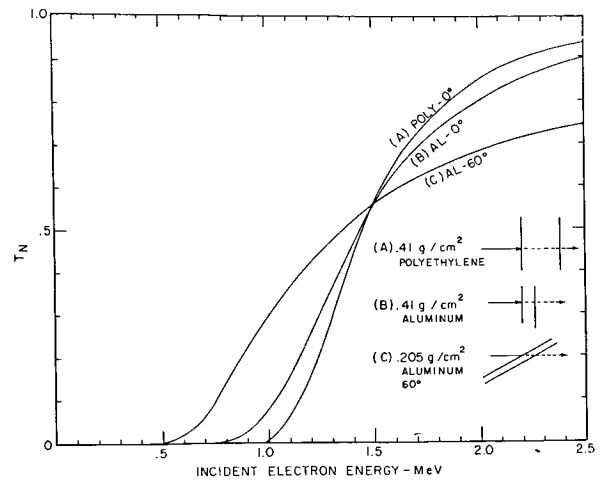


FIGURE 10.—Comparison of number transmission coefficients for electrons incident on (A) $0.180''$ polyethylene at 0° angle, (B) $0.060''$ aluminum at 0° angle, and (C) $0.030''$ aluminum at 60° angle, all representing 0.41 g/cm^2 of material in the direction of electron incidence.

begin at lower energy, while some are scattered away from the normal, lengthening the path and decreasing the transmission at higher energies.

DISCUSSION OF ELECTRON TRANSMISSION RESULTS

The families of transmission versus energy curves, as shown in figures 6, 7, 8, and 9, could be directly used to determine the fraction of an arbitrary incident spectrum which is transmitted through a hull, simply by integrating the product of the incident spectrum and the transmission curve for the appropriate hull thickness. It was the intent, however, to obtain data more generally applicable to other shielding computation codes set up for different types of input data. The families of curves are therefore at close enough thickness intervals to allow other types of analysis. Figure 11 shows the same data plotted in the more usual form of transmission versus shield thickness in grams/cm² for fixed incident energies of 1.5 and 2.0 MeV. These show that, although the maximum range (or the extrapolated range) is significantly lower for polyethylene than for aluminum, it cannot be concluded that polyethylene is a superior electron shield. The greater transmission at thicknesses less than about 0.6 to 0.7 times maximum range approximately compen-

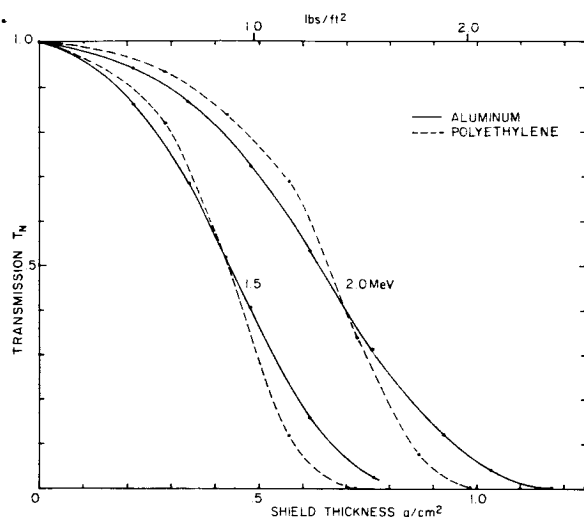


FIGURE 11.—Transmission of 1.5 and 2.0 MeV incident energy electrons as a function of thickness of aluminum and polyethylene, derived from the data in figures 6 and 7. The maximum range is lower in polyethylene, but for thin sheets, transmission is greater through polyethylene than through aluminum.

sates for the lesser maximum range. The observed difference between aluminum and polyethylene is a consequence of the lesser angular spread of the beam in lower atomic number elements, allowing penetration to greater depths before the unidirectional incident beam is changed to a cosine angular distribution.

Generally, it is clear from figure 11 that electron range is not a sufficient parameter to characterize the shielding effectiveness of a particular material. The shape of the transmission versus thickness curve must also be considered, although the *S* shape seen here is much less pronounced for 30° and 60° angles of electron incidence.

Comparison of the present experimental data with theory can best be accomplished by plotting in the form of families of curves of transmission versus incident angle, for fixed electron energy. Figure 12 shows the case of polyethylene and 2.0 MeV electrons. Curves have been extended only as far as the 60° data points, since they do not extrapolate to zero even at 90° (grazing) incidence, where angular scattering still allows significant transmission. For aluminum, Berger (ref. 2) has made Monte Carlo calculations for angles of 0, 45, 60, 75, and 90°, as shown in figure 13. Our experimental

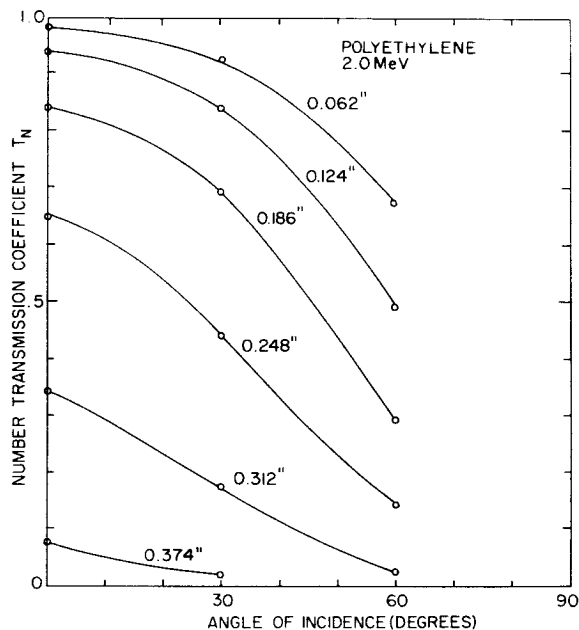


FIGURE 12.—Experimental number transmission coefficient T_N for 2.0 MeV electrons incident at various angles on polyethylene of various thicknesses.

data, shown in the same figure, are points obtained by interpolation between the actual measurements, in order to apply to the same aluminum thicknesses used in the Monte Carlo calculations. Agreement is very good up to $0.3r$ (Berger used a maximum range of $r=1.214$ g/cm²). At greater thicknesses, the deviation between experiment and theory increases rapidly, the experimental values being about 20% higher at thickness $0.5r$, beyond which computations were not made. This deviation is not unexpected, because of the rapidly increasing difficulty of the statistical theory as the thickness approaches maximum range. In a preceding paper, Berger and Seltzer report the inclusion of further correction terms in their recent electron penetration computations, with which our experiments may be in much closer agreement.

TRANSMITTED ELECTRON ENERGIES

The number of transmission measurements reported so far are only part of the data needed for shielding computations. The need for experimental data on energy transmission is illustrated in figure 14, derived entirely from Berger's Monte Carlo computations (ref. 2) of the energy transmission coefficient, $T_E=$

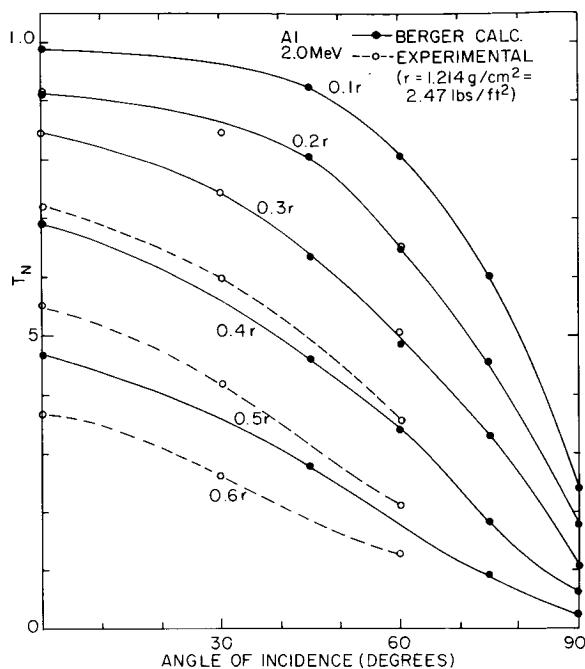


FIGURE 13.—Experimental number transmission coefficient for 2.0 MeV electrons incident at various angles on aluminum, compared with Monte Carlo calculations by Berger. Experimental points have been interpolated in order to compare directly with the aluminum thicknesses computed. Agreement is good up to $0.3r$, but divergence increases rapidly with larger thicknesses.

transmitted electron energy/incident electron energy. The points shown represent the fraction of the energy of an isotropic flux of 2.0 MeV electrons which penetrates to depths of 0.1 to $0.5r$ in aluminum, where r = maximum range for a 2.0 MeV electron at normal incidence. They were computed as transmitted fraction = $\int_0^{90^\circ} T_E \sin 2\theta d\theta$. The important part of the curve for shielding purposes is the region $0.5r$ to $1.0r$, where only a small fraction—from 5% to 0%—of the incident energy is transmitted. The significant point is that accurate computations in this region are extremely difficult because of the energy and angular straggling effects, and that the nature of the curve is such that, regardless of the accuracy of the computed points for thicknesses 0 to $0.5r$, extrapolation to greater thicknesses cannot be made with any certainty. It is therefore necessary to make experimental measurements in this region.

Measurements of the energy spectrum and angular distribution of the transmitted electrons have been initiated, using a lithium drifted 2 mm thick silicon solid state detector, with suitable low noise amplifiers and 400 channel pulse height analyzer.

Figure 15 shows typical data, for electrons at normal incidence, 0° , on 0.030 inch aluminum. The upper curve represents a transmission versus energy curve as already shown in figure 6. Points *A*, *B*, *C*, and *D* on the curve correspond to the measured energy spectra behind the aluminum panel, as shown in the lower half of the figure. *D* represents electrons of sufficiently high energy that only a small fraction of the incident energy is lost in transmission, and almost the entire incident beam is transmitted. In this case the transmitted beam is only slightly broadened. At the intermediate point *C*, where roughly half of the electrons are transmitted, the upper energy limit of the transmitted beam is shifted downward an amount equal to the minimum energy loss (that is, an electron with no angular straggling), and, in addition, the energy distribution is appreciably broadened. At point *B*, there is a further downshift and broadening

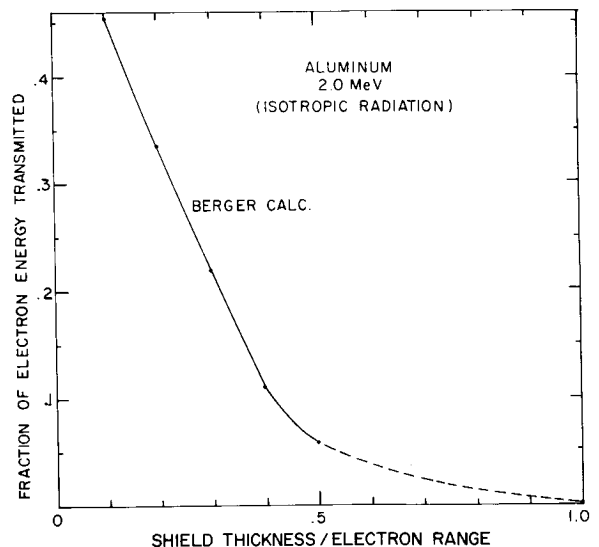


FIGURE 14.—Energy fraction of 2.0 MeV isotropic electron flux penetrating to various depths in aluminum, as derived by integration of Berger Monte Carlo calculation. Experimental data are required to extend the curve into the region of shield thickness 0.5 to 1 , for which transmitted energy is small, as necessary for shielding.

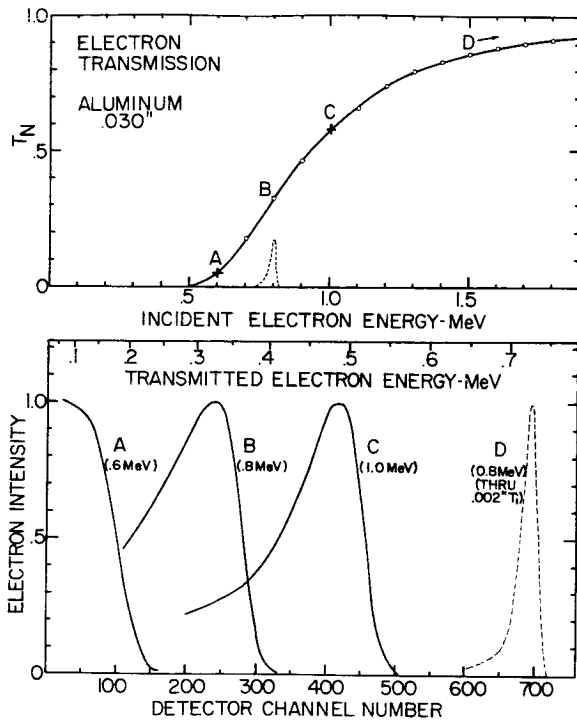


FIGURE 15.—Experimental energy distributions of electrons transmitted through 0.030'' of aluminum, for incident energies of 0.6, 0.8, and 1.0 MeV corresponding to points A, B, and C respectively, on the upper curve, which represents transmission versus incident energy. Curves measured by solid-state detector and pulse height analyzer have been normalized to same peak height.

by straggling. Finally, at point A, where only a small fraction of the incident beam is transmitted, the transmitted electrons are, of course, predominantly of very low energy. The curves shown each represent some 300 points of about 1 to 2% statistical accuracy, too closely spaced to be indicated in the figure. The curves, A, B, C, and D, have been normalized to the same peak height, and represent only the relative shape, not the total intensity. Similar curves have been measured on other materials. A later publication is intended to include data on other materials, thicknesses, angles of incidence, and angles of emergence.

SUMMARY

1. Curves of transmission versus incident electron energy have been measured over the energy range 0.2 to 2.5 MeV for a number of thicknesses of aluminum and polyethylene from about 0.07 to 1.3 g/cm².

2. Generally, for equal g/cm², transmission starts at higher energy for polyethylene but the curve rises more steeply, crossing the aluminum transmission curve. Thus, the relative shielding effectiveness depends on the incident energy.

3. At larger angles of incidence, for either material, the curves rise less steeply, as a result of angular deviations of the electrons in transmission. For equal g/cm² measured along the incident direction, transmission starts at lower energy for larger angle of incidence, and the transmission curve crosses the curve for normal incidence.

4. Transmission coefficient versus angle of incidence curves for aluminum are in good quantitative agreement with the Monte Carlo calculations of Berger up to material thicknesses of about 0.3 maximum range, but diverge substantially from the calculations at greater thicknesses.

5. Bremsstrahlung intensities have been measured behind laminar aluminum-polyethylene-aluminum structures and show a broad angular distribution at 0.5 MeV incident energy, increasingly forward peaked at 1.0 and 2.0 MeV in accordance with theory.

6. Energy distributions of the transmitted electrons have been measured behind the target panels by solid state detectors.

7. In order to make adequate shielding analyses for spacecraft in the trapped electron belts, there is need for a considerable quantity of experimental data for the relevant cases: incident electron energies up to several MeV, large angles of incidence, thicknesses near maximum range, light elements, and composite structures.

REFERENCES

1. WEST, H.; MANN, L.; and BLOOM, S.: Some Electron Spectra in the Radiation Belts in the Fall of 1962. UCRL-7659, Apr. 13, 1964.
2. BERGER, M. J.: Transmission and Reflection of Electrons by Aluminum Foils. Nat. Bur. Std. Tech. Note 187, Apr. 1, 1963.

N65-34626

50—Errors from Geometric Approximations Introduced in Three Computational Models for Space Vehicle Electron Dose Prediction

R. P. MOSHOFSKY

The Boeing Company

Evaluation of shield designs for space vehicles is a complex problem involving the coupling of radiation transport to difficult geometries. Various approximations are made regarding both geometry and physical interactions in order to shorten computation time. It is desirable to know the significance of error introduced by geometric approximations. Using the idea that simplified models should be most nearly valid for simple geometries, three models for electron dose calculation are compared in cases involving spherical shell shields. The explicit differences in these models relate mainly to the treatment of the radiation angular distributions and the shield geometry. Relatively accurate calculations are possible for spherical shell cases so that error estimates are made for the various computational procedures.

INTRODUCTION

Present methods for evaluating space electron radiation hazards inside space vehicles vary from consideration of depth dose curves to calculations accounting in some detail for the difficult geometric configurations of the vehicles. Because of the short penetration range of electrons in the trapped radiation belts, contributions to electron doses are chiefly due to the thinly shielded sections of a vehicle wall.

Over these sections, electron penetration may be found by a one-dimensional analysis. Nevertheless, it would be quite convenient if vehicle geometry could be handled similarly for both electrons and protons. For proton radiation, a conventional "sector analysis" is valid in which the slant thicknesses through material volumes are the important quantities (ref. 1). A fundamentally more accurate model has been devised which employs the thickness of the wall measured on the normal to the wall surface and directly involves the angular distribution of the penetrating radiation. This method has been used in a following paper by Mar with different assumptions than are used here. Finally, a structured wall is considered by a thickness averaging model and the results

compared to a two-sector approach, in order to set limits on the error introduced by the use of an average wall thickness for a structured wall.

In order to provide satisfactory estimates of the errors involved in these three methods, test problems were set up with the idea that the models should work satisfactorily for simple geometries. Consequently, four basic situations with spherical shell shielding have been considered. Dependence of accurate results on electron angular distributions has been emphasized, since this is the property of the radiation which is most directly tied to the geometry. The angular dependence has been separated from the energy dependence of the radiation fluxes. However, such assumptions have been applied consistently for all the computational models. Crude estimates of the contributions from particles reflected inside the shell have been made simply to assign limits to the error from neglect of such reflections.

ASSUMPTIONS AND RELATIONS

For the purposes of this study, several simplifying assumptions have been made which do not affect significantly the validity of the

results. A free-space environment is defined to have a time-integrated isotropic electron flux of magnitude ϕ_0 . The energy spectrum of this radiation is assumed to be similar to that of fission electrons. The shield material will be aluminum. These three conditions are combined and are implicitly contained in a net transmission function for the radiation. The axial symmetry of the shielding has been used such that angular dependence is upon only a single polar angle.

At any point, the current distribution is related to the flux distribution by

$$I(E, \theta) = \phi(E, \theta) \cos \theta \frac{\text{Particles}}{\text{cm}^2 \cdot \text{MeV} \cdot \text{steradian}} \quad (1)$$

where

$I(E, \theta)$ = the number of particles crossing a 1 cm² area per MeV per steradian at energy E and angle θ , with the plane of the unit area fixed perpendicular to the line $\theta = 0$

$\phi(E, \theta)$ = differential particle flux in the same units as the current distribution

θ = an angle measured from some convenient symmetry axis which is normal to the plane specifying the current

It is assumed that the energy dependence of the radiation may be effectively separated from the angular dependence at any point in the geometries considered in this study.

The current at any point may then be defined by

$$I(E, \theta) = \phi_m n(E) f(\theta) \cos \theta \quad (2)$$

or

$$= I_m n(E) g(\theta)$$

where

$n(E)$ = fraction of particles per MeV at energy E , normalized to unity

$f(\theta)$ = fraction of particles per steradian at an angle θ , normalized to unity over the possible range of θ

$g(\theta)$ = fraction of particles per steradian crossing a fixed planar surface of unit area, normalized to unity

and

$I_m = 2\pi\phi_m \int_{\theta} |f(\theta) \cos \theta| \sin \theta d\theta$ = magnitude of an omnidirectional current with ϕ_m = magnitude of the omnidirectional flux at the point.

Using this separation of variables, absorbed dose at any point may be calculated by

$$D = 2\pi \frac{K}{\rho} I_m \int_{\theta'} g(\theta') \frac{\sin \theta'}{\cos \theta'} d\theta' \int_E n(E) \left[\frac{dE}{dx}(E) \right] dE \text{ rads} \quad (3)$$

where

K = conversion from MeV/gm to rads

ρ = specific gravity of the absorber

I_m = magnitude of current at the point in particles/cm²

$\frac{dE}{dx}(E)$ = linear energy transfer for particles of energy E in $\frac{\text{MeV} \cdot \text{cm}^2}{\text{gm}}$

$g(\theta')$ = angular distribution of the omnidirectional current at the point of interest

TRANSPORT RELATIONS

Applying the separation of the angular dependence from energy dependence to the current penetrating a plane slab shield, a transmission function may be defined which relates the incident current to the penetrating current. Both the energy distribution function and the angular distribution function may change in form with slab thickness, but they remain normalized to unity. Furthermore, it is possible to define an effective transmission function which includes the linear energy transfer as

$$T_D(t) = \frac{\bar{D}(t)}{\bar{D}_0} = \frac{\frac{K}{\rho} I_m(t) \int_{E'} n_t(E') \left[\frac{dE}{dx}(E') \right] dE'}{\frac{K}{\rho} I_0 \int_E n_0(E) \left[\frac{dE}{dx}(E) \right] dE} \quad (4)$$

where

$I_m(t)$ = magnitude of current penetrating a plane slab of thickness t in particles/cm²

$n_i(E')$ = energy distribution of the penetrating radiation in MeV^{-1} , normalized to unity

I_0 = magnitude of the incident current in particles/cm²

$n_0(E)$ = energy distribution of the incident radiation in MeV^{-1} , normalized to unity

E' = energy of penetrating particles

E = energy of incident particles

$\overline{D}(t)$ = value of the numerator

\overline{D}_0 = value of the denominator

From various data, particularly that shown by Mar (ref. 2), it was seen that this transmission function has an exponential form for a fission spectrum incident on aluminum. That is, for aluminum thicknesses from about 0.2 gm/cm² to about 2.0 gm/cm², the transmission function may be written as

$$T_D(t) = A \exp(-Bt) \quad (5)$$

where

A = a constant

B = the exponential slope, which is about 3 cm²/gm

For the geometries considered, a required relation is depicted in figure 1. With the aid of figure 1 the angular dependent current at a point inside a spherical surface is easily related to the current distribution on the surface.

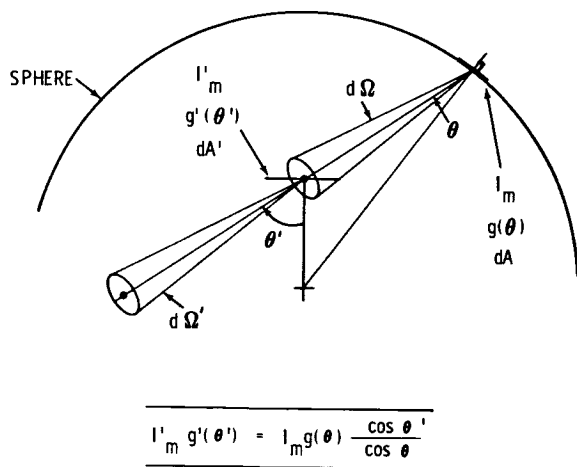


FIGURE 1.—Relation between angular distribution functions.

If the angular distribution of current on the surface is symmetric about the normal to the surface, the current measurement at the point of interest is through a small surface increment which lies perpendicular to a symmetry axis through the point, and only an inward current is considered on both surfaces, then

$$I_m' g'(\theta') = I_m g(\theta) \frac{\cos \theta'}{\cos \theta} \quad (6)$$

where

I_m' = magnitude of the inward current at the point of interest in particles/cm²

$g'(\theta')$ = angular distribution of the inward current at the point of interest, in steradian⁻¹, normalized to unity for $\theta' = 0, \Pi/2$

I_m = magnitude of the inward current on the surface in particles/cm²

$g(\theta)$ = angular distribution of the inward current on the surface, in steradian⁻¹, normalized to unity for $\theta = 0, \Pi/2$

CASE A

In order to estimate the error introduced in a conventional sector analysis, as the point of interest is moved about inside a vehicle, a single spherical shell is considered. The distance of the receiver point from the center of the shell is varied. Referring to the geometry shown in figure 2, only the contribution from the portion of the shell lying above the receiver will be considered. It may be noted, however, that the remainder of the surface contributes an equal amount to the dose. The calculation is performed two ways. The first method evaluates the transmission through the normal thickness of the shell and considers the fraction of the radiation scattered to the receiver according to the angular distribution of the penetrating radiation. Neglecting backscatter effects, this method is accurate for this case. The calculation is also made using the transmission through the slant thickness of the shell. This corresponds to a conventional sector analysis.

Using equations (4) and (6), the defining equation for dose (eq. (3)) and neglecting backscatter, the dose at a point may be calculated

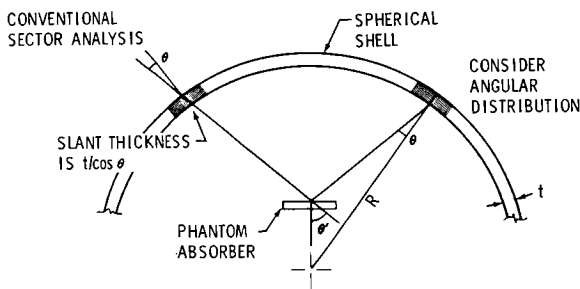


FIGURE 2.—Geometry for Case A.

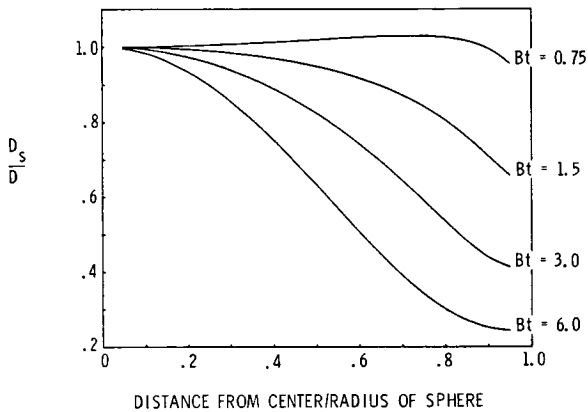


FIGURE 3.—Results for Case A.

from

$$D = 2\pi\bar{D}_0 T_D(t) \int_0^{\pi/2} g(\theta) \frac{\sin \theta'}{\cos \theta} d\theta' \quad (7)$$

where

$g(\theta)$ = angular distribution of the penetrating current in steradian⁻¹

The equivalent expression using a conventional sector analysis is

$$D_s = 2\pi\bar{D}_0 g(0) \int_0^{\pi/2} T_D\left(\frac{t}{\cos \theta}\right) \sin \theta' d\theta' \quad (8)$$

On the basis of data of Frank (ref. 3), it was decided to approximate the angular distribution by

$$g(\theta) = \frac{3}{2\pi} \cos^2 \theta, \quad 0 \leq \theta \leq \pi/2 \quad (9)$$

The results from equation (7) were evaluated analytically, whereas equation (8) was evaluated by a numerical integration using 100 equal increments on the cosine of the angle θ' . The ratio of the conventional sectoring results

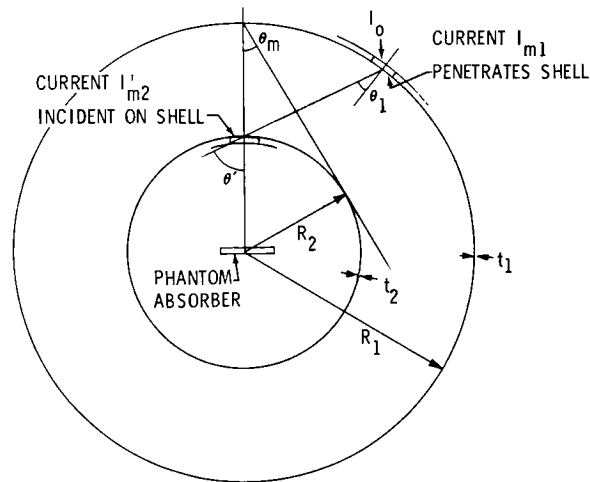


FIGURE 4.—Geometry for Case B.

to the results from equation (7) are shown in figure 3.

The increase in dose from particles trapped in the shell by reflection from the walls can be estimated by considering a repetitive reflection process. However, because of the small reflection coefficients for electrons in the energy range of 0.1 to 10 MeV, the first reflection is all that need be considered. From data presented by Price, Horton, and Spinney (ref. 4), it is seen that the albedo may range from ~0.05 to 0.25 for this energy range.

It is seen from equation (6) that the outward current on the inner surface of the shell will be just equal to the penetrating current for the first reflection. Therefore, the dose may be enhanced by the factor $1 + \beta$, where β is an effective reflection coefficient.

CASE B

In order to determine the effect of neglecting separation between material layers or volumes, as is done in a conventional sector analysis, a concentric shell geometry has been considered with the receiver at the center. The main difference between assuming a single multi-layer shell, and two concentric shells, arises from the fact that not all the radiation penetrating the outer shell impinges on the second layer or shell. The geometry for this case is shown in figure 4.

The key to calculating dose accurately for this case is finding the current, I'_m2 incident

on the inner shell from the current I_{m1} penetrating the outer shell. However, a conventional sector analysis for a receiver at the center depends only on the transmission through the two layers of thickness t_1 and t_2 . There is no dependence on the radii of the two shells. Backscattering is more involved in this case, but the results do not merit a detailed analysis since reflection factors are typically small.

Neglecting backscatter, and using equation (4) repetitively, the dose at the center of the configuration may be given by

$$D = 2\bar{D}_0 T_D(t_1) F(\theta_m) T_{D2}(t_2) g_2(0) \quad (10)$$

where

\bar{D}_0 = as defined in equation (4)

$T_D(t_1)$ = effective transmission through outer shell

$F(\theta_m)$ = ratio between magnitudes of that current incident on the inner shell and that penetrating the outer shell

$$= \frac{I'_{m2}}{I_{m1}}$$

θ_m = defined in figure 4

$T_{D2}(t_2)$ = effective transmission through the inner shell thickness t_2

$g_2(0)$ = value of the angular distribution of radiation penetrating the inner shell evaluated at $\theta_2 = 0$

If the transmission through the inner shell is not significantly altered by the variation of g' with R_2 , and if g_2 is identical to g_1 , the ratio between the dose calculated from equation (10) and that from a conventional sector analysis (one sector) is just $F(\theta_m)$.

The function $F(\theta_m)$ may be found using equation (6). If $g_1(\theta_1)$ is equal to $\frac{3}{2\pi} \cos^2 \theta_1$, then from the geometry in figure 4

$$F(\theta_m) = 2\pi \int_0^{\pi/2} \frac{3}{2\pi} (1 - \sin^2 \theta_m \sin^2 \theta') \cos \theta' \sin \theta' d\theta'$$

or

$$F(\theta_m) = \frac{1}{\sin^2 \theta_m} (1 - \cos^3 \theta_m) \quad (11)$$

where

$$\theta_m = \arcsine \left(\frac{R_2}{R_1} \right)$$

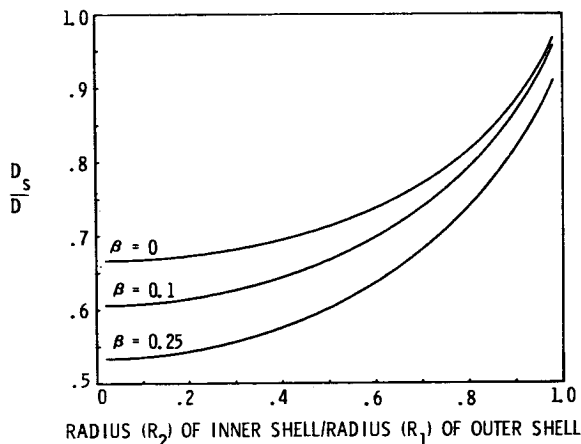


FIGURE 5.—Results for Case B.

The reciprocal of the function $F(\theta_m)$ has been plotted versus the ratio R_2/R_1 in figure 5.

A rough estimate of the contribution from reflecting radiation for this case can be made by considering the outward current incident on the inner surface of the outer shell in one reflection from the outer shell. A single reflection inside the inner shell may also be considered as in Case A. The inwardly reflected current will be assumed to have the same distributions as the principal current. Ignoring the transmission of particles from inside the inner shell, the outward current on the outer shell arises from the particles reflected from the inner shell and those transmitted directly from the outer shell surface which are not intercepted by the inner shell. This backward current is then

$$I_B = I_{m1} \left[\beta F(\theta_m) \frac{4\pi R_2^2}{4\pi R_1^2} + 2\pi \int_{\theta_m}^{\pi/2} \frac{3}{2\pi} \cos^2 \theta \sin \theta d\theta \right] \quad (12)$$

Substituting from equation (11), and integrating, yields the ratio between the effective current incident on the inner shell and I_{m1} :

$$F_\beta(\theta_m) = F(\theta_m) \{ 1 + \beta[\beta(1 - \cos^3 \theta_m) + \cos^3 \theta_m] \} \quad (13)$$

where

β = an effective reflection coefficient assumed to be constant for all reflections

As in Case A, the reflection inside the inner shell yields an additional factor of $1 + \beta$. Also shown in figure 5 is the plot of the reciprocal of F_β for values of β equal to 0.1 and 0.25.

CASE C

Calculations for a single shell shield have been done with the angular distribution of the penetrating radiation artificially varied with shell thickness. Such a variation would be expected with thin shells where the angular distribution may vary from that of the incident radiation to that obtained with thick shells. A valid estimate of the dose at points inside the shell has been found using the procedure involved in Case A. Results for more conventional sector analyses have been obtained by two methods. The first method treats the angular distribution as varying with slant thickness by the same relation used for the valid estimate. The second method considers the distribution to be fixed at either of two functions of the angle.

The angular distribution of penetrating current was arbitrarily assigned the form

$$g(\theta, t) = h(t) \frac{\cos \theta}{\Pi} + [1 - h(t)] \frac{3}{2\Pi} \cos^2 \theta \quad (14)$$

where

$$h(t) = \exp(-Bt)$$

Bt = thickness of the shell in number of e-folds of the transmission

The reference dose calculations were made using equation (7) with substitution from equation (14) in place of $g(\theta)$. Calculations for the first

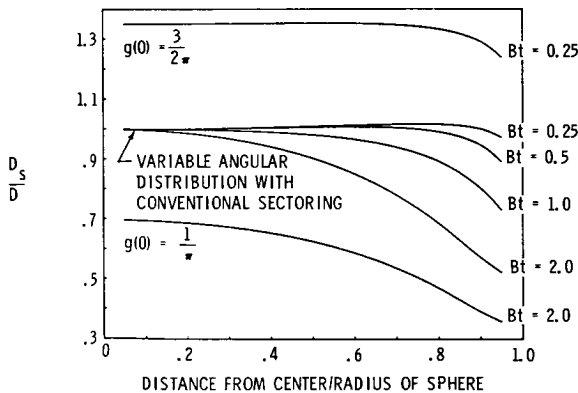


FIGURE 6.—Results for Case C.

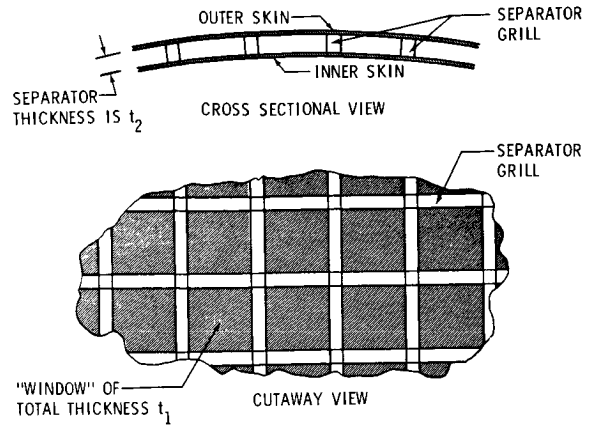


FIGURE 7.—Geometry for structured wall, Case D.

sectoring method were performed using

$$D = 2\Pi \bar{D}_0 \int_0^{\Pi/2} T_D \left(\frac{t}{\cos \theta} \right) g \left(0, \frac{t}{\cos \theta} \right) \sin \theta, d\theta \quad (15)$$

For the second sectoring method, equation (8) was used with $g(0) = \frac{1}{\Pi}, \frac{3}{2\Pi}$. The results obtained as a function of receiver position parameterized by shell thickness are shown graphically in figure 6. Note that the transmission slope B is only symbolic in this case.

CASE D

It is frequently convenient, where "structured" walls are involved, to use an average wall thickness in dose calculations. In this study the case considered involves two concentric thin shells attached to separators of some form (fig. 7). The separators serve some purpose, such as strengthening or insulating. The separator grill was simply represented by an added shield layer in some fraction of the shell surface. Thus, an estimate of dose at points inside the shell which are not close to the wall may be found from a weighted sum of transmissions through the two effective wall thicknesses. These results are compared to those found using the transmission through an average wall thickness. The ratio of the results is then

$$\frac{D_{ave}}{D_s} = \frac{T_D [Gt_1 + (1-G)(t_1+t_2)]}{GT_D(t_1) + (1-G)T_D(t_1+t_2)} \quad (16)$$

where

G = fraction of surface having total thickness t_1
 t_1 = total thickness of the shells without separators

t_2 = thickness of separators measured normal to the shell surface

The ratio defined in equation (16) is shown graphically in figure 8 as a function of t_2/t_1 with G and t_1 treated as parameters.

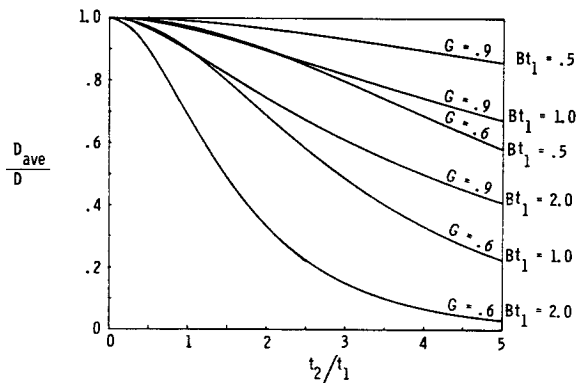


FIGURE 8.—Results for Case D.

CONCLUDING REMARKS

The results show that for highly scattered radiation such as electrons, the conventional sectoring approach has significant error in some cases. For small angular scattering the errors would be insignificant. It is most important to note that the errors in conventional sectoring vary strongly with receiver position and wall thickness. From the results of Case B it is seen that neglecting separation between material volumes may also be serious. To obtain more accurate results in complex configurations would require an accurate calculation of the radiation currents incident on material volumes. This in turn requires consideration of the scattering of radiation from one material surface to another.

Fortunately, for the problem of electron dose, only the thinly shielded segments of a vehicle are important. Since interior component volumes will frequently totally stop penetrating electrons, a more accurate calculation may be made with important "windows" being represented by portions of single layer shells. The method used for the reference calculations in this paper would be suitable in such cases.

REFERENCES

1. DYE, D. L.: Space Proton Doses at Points Within the Human Body. Proc. of Symp. on Protection Against Radiation Hazards in Space, NASA TID 7652, Nov. 1962.
2. MAR, B. W.: Electron Shielding Codes for Evaluation of Space Radiation Hazards. Boeing Document D2-90414, June 4, 1963.
3. FRANK, H.: On the Multiscattering and Back-Diffusion of Fast Electrons After Passage Through Thick Layers. Z. Naturforsch., vol. 14a, 1959, pp. 247-261.
4. PRICE, B. T.; HORTON, C. C.; and SPINNEY, K. T.: Radiation Shielding. Pergamon Press (New York), 1957.

165-24627

51—An Evaluation of Radiation Shielding by Vehicle Orientation

B. W. MAR

The Boeing Company

An elementary analysis was performed to determine the decrease in shield weight obtained by selective orientation of a vehicle in an anisotropic flux of geomagnetically trapped charged particles. Study results indicate a minor decrease in proton shield weight and electron shield weight. The study was limited to cylindrical and conical geometries; the energy spectra were assumed to be independent of pitch angle, whereas angular distribution was a function of pitch angle (maximum cutoff angle of 60 degrees).

INTRODUCTION

The angular distribution of geomagnetically trapped particles is generally assumed to be isotropic for shielding calculations. This approximation is valid because the continuous random reorientation (tumbling and spinning) of the vehicle smears the incident flux so that the angular distribution appears isotropic. Because the equilibrium distribution of trapped particles obeying the adiabatic invariance condition along any line of force is not commonly isotropic, a study was made of the possible advantages in orienting a vehicle with the line of force and varying the shield thickness for each portion of the vehicle.

An analysis of the results of this study are presented with the mathematical model used to describe the angular distribution of trapped particles, the model for transport of electrons and protons through a shield, and the geometric analysis of these particles penetrating a vehicle.

ANGULAR DISTRIBUTION OF TRAPPED PARTICLES

The steady-state angular distribution of trapped particles (fig. 1) can be shown to be uniform in the azimuth angle measured about the field line and dependent only upon the pitch angle α measured between the velocity vector and the field line. Confining the analysis to the region where the adiabatic invariant provides a working description of the particle

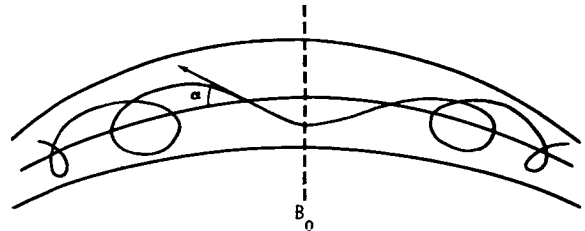


FIGURE 1.—Geometry for description of angular distribution.

motion, Thomas (ref. 1) has computed the unidirectional intensity from omnidirectional flux data. Figure 2 contains some typical results from his study. The angular distribution is characterized by a cutoff angle and symmetry about the normal to the field line. For this study, a mathematical expression of the form

$$f(\alpha)d\Omega = A \sin(\alpha - \alpha_0)d\Omega \text{ for } \alpha \geq \alpha_0; = 0 \text{ for } \alpha < \alpha_0$$

was assumed for the angular distribution. The angle α is the pitch angle and the angle α_0 is the cutoff angle below which no particles can enter. Several values of α_0 were used in the above equation, but no detailed analyses of the variation of α_0 with the magnetic field strength were made.

PROTON SHIELDING

The penetration of protons through a shield can be described by a "straight ahead" model used by Dye (ref. 2). As shown in figure 3,

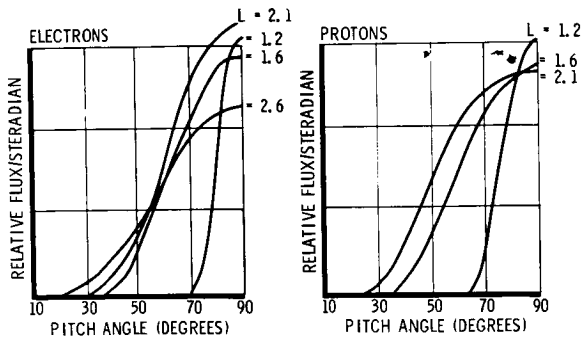


FIGURE 2.—Equatorial pitch angle distributions.

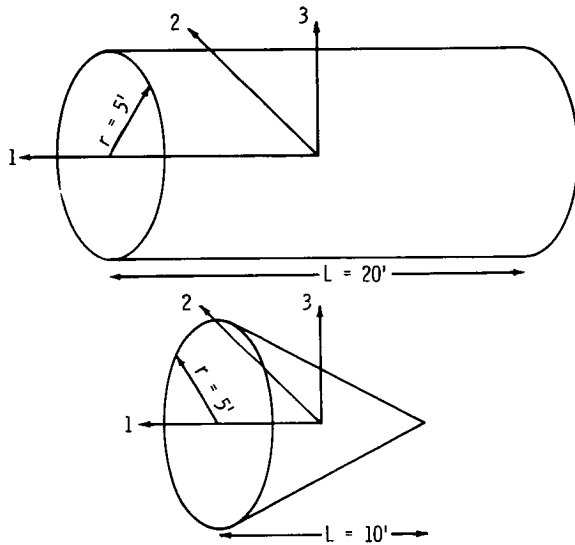


FIGURE 3.—Vehicle orientation and geometry.

there is only one proton velocity vector penetrating each unit area capable of reaching the receiver. The vehicle orientation problem for protons is approached in the following manner: (1) a reference axis is selected on the vehicle; (2) the orientation between the reference axis and the field line is established; (3) the vehicle is sectored (the slant path through each area increment is defined); (4) the product of the unidirectional flux and the transmission for each increment is computed; and (5) this product is summed over 4π solid angle to obtain the dose entering the vehicle.

This procedure was followed for three vehicle orientations as shown in figure 4, using cutoff angles of 30, 45, and 60 degrees. The sector analysis used 146 sectors of equal solid angle.

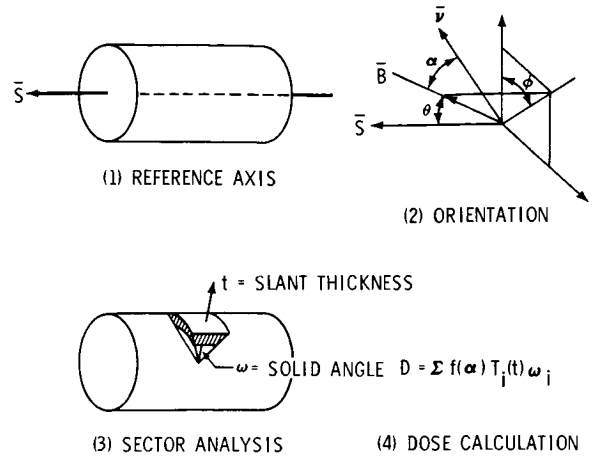


FIGURE 4.—Shielding procedure.

The vehicle was a cylinder 20 feet long and 10 feet in diameter. The results for this vehicle are shown in table I. As expected, the results indicate the penetrating dose per particle increases as the flux becomes monodirectional. The improvement observed for this configuration did not indicate that the vehicle orientation can be an effective shielding technique unless the cutoff angle is larger than 60 degrees.

ELECTRON SHIELDING

Electrons cannot be described by a straight-ahead model because they suffer many scatters in traversing a shield. In thick shields, the electron motion can be described by a diffusion model. The electron transport will differ from the proton transport analysis in Step 4. Previously, the unidirectional flux directed toward the receiver was computed; for electrons, the fraction of the omnidirectional flux crossing a unit area is required. (Omnidirectional and isotropic are not synonymous.) Evans (ref. 3) has shown that the fraction of an isotropic flux that crosses a unit area is 0.25. This fraction was computed by integrating the contribution from the half space above the unit area as shown in figure 5. When an angular distribution other than isotropic is used, an additional factor ω (the angle between the normal to the unit area and the field line) is required to express α in terms of θ . Table II is a tabulation of the fraction of flux entering a unit area versus ω and α_0 . As ω approaches 90 degrees, more

TABLE I

Dose Transmission of Protons in Cylinder (rad per proton/cm²)

Side shield (gm/cm ²)	End shield (gm/cm ²)	Orientation with reference axis	α_0		
			30°	45°	60°
1	1	parallel	7.9×10^{-9}	7.8×10^{-9}	8.1×10^{-9}
1	1	45°	8.1×10^{-9}	8.1×10^{-9}	8.0×10^{-9}
1	1	normal	8.2×10^{-9}	8.1×10^{-9}	7.5×10^{-9}
1	1	isotropic		7.7×10^{-9}	
2	2	parallel	6.9×10^{-9}	6.8×10^{-9}	7.1×10^{-9}
2	2	45°	7.2×10^{-9}	7.1×10^{-9}	7.0×10^{-9}
2	2	normal	7.1×10^{-9}	7.0×10^{-9}	7.0×10^{-9}
2	2	isotropic		6.6×10^{-9}	
0	1	parallel	1.3×10^{-8}	1.2×10^{-8}	1.3×10^{-8}
0	1	45°	1.3×10^{-8}	1.3×10^{-8}	1.3×10^{-8}
0	1	normal	1.3×10^{-8}	1.1×10^{-8}	1.0×10^{-8}
0	1	isotropic		1.2×10^{-8}	
1	2	parallel	7.9×10^{-9}	7.8×10^{-9}	8.1×10^{-9}
1	2	45°	8.0×10^{-9}	8.0×10^{-9}	8.0×10^{-9}
1	2	normal	8.1×10^{-9}	7.8×10^{-9}	7.8×10^{-9}
1	2	isotropic		7.6×10^{-9}	

TABLE II

Particle Fraction Entering Vehicle

(a) Cylinder

θ_0 (deg)	α_0			
	0°	30°	45°	60°
0	0.268	0.286	0.295	0.305
45	0.256	0.260	0.262	0.264
90	0.246	0.273	0.231	0.227

(b) Cone

θ_0 (deg)	α_0			
	0°	30°	45°	60°
0	0.246	0.238	0.231	0.221
45	0.251	0.249	0.247	0.248
90	0.256	0.260	0.261	0.265

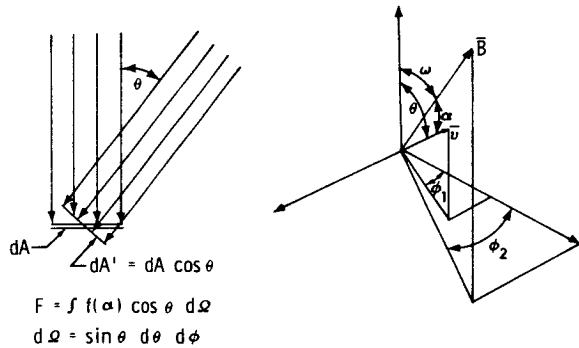


FIGURE 5.—Geometry used to compute F .

particles enter at small θ values so that higher fractions are observed.

The penetration of electrons was computed with the following technique: (1) establish a reference axis on the vehicle; (2) sector the vehicle and compute the fraction of flux entering each sector; (3) select the orientation between the reference axis and field line; (4) compute the incident electron flux and transmission through each sector; and (5) sum the dose from each sector. The calculation was performed

TABLE III
Particles Crossing Unit Area

ω (deg)	α_0				
	0°	30°	45°	60°	85°
0	0.209	0.156	0.124	0.085	0.025
30	0.226	0.192	0.175	0.165	0.157
45	0.243	0.229	0.221	0.219	0.19
60	0.258	0.265	0.266	0.266	0.33
75	0.270	0.292	0.302	0.312	-----
90	0.275	0.300	0.314	0.329	0.54

for a cylinder and cone as shown in figure 4. In each case, a uniform wall was considered and the transmission was normalized to unity. Under these conditions, the result should be

1.0 for an isotropic flux. As can be seen from the results in table III, there is little variation from this number due to vehicle orientation and angular distribution. Only when the angular distribution becomes almost monodirectional is a large difference observed.

CONCLUSION

An angular distribution that is symmetric about a field line and dependent on the sine of the pitch angle was observed to behave similarly to an isotropic flux for shield analyses if the cut-off angle is less than 60 degrees. The observed error in dose when an isotropic distribution is used for the shield analysis is less than 30 percent. The orientation of a vehicle is not important unless highly directional fluxes are encountered.

REFERENCES

1. Computer Codes for Space Radiation Environment and Shielding. Air Force Weapon Lab., Document WL TDR 64-71, 1964.
2. DYE, DAVID L.: Space Proton Dose at Points Within the Human Body. Proc. Sym. on Protection Against Radiation Hazards in Space. Paper D-8, TID-7652, Atomic Energy Commission, 1962, pp. 633-661.
3. EVANS, R. D.: Principles for the Calculation of Radiation Dose Rates in Space Vehicles. Arthur D. Little, Inc., Report No. 63270-05-01, July 1961.

NS-34628

52—The Importance of Radiation Anisotropy in Dose Calculations

R. E. FORTNEY and G. D. DUCKWORTH

Northrop Space Laboratories

Geomagnetically trapped charged particles are highly anisotropic in their directional distribution. When a space vehicle provides uniform shielding about a detector point, or the vehicle has a tumble which results in a uniform exposure to the radiative environment, the directionality of the charged particles is not important. However, most experimental satellites and manned spacecraft such as Gemini and Apollo do not provide uniform protection against space radiation and are not oriented to uniformly sample the radiative environment. Then, how important is radiation anisotropy in dose calculations?

The interaction of radiation anisotropy and vehicle orientation for a wide range of material distributions has been investigated in detail. The basis for this study has been a space experiment which has three solid state detectors located at different depths in a sphere of aluminum (ref. 1). The sphere, the other experiments, and the components of the satellite establish extremes of material distribution about the three detectors. The material distributions seen by these three detectors and various orientations of the satellite relative to the earth's lines of magnetic force are utilized to assess the importance of radiation anisotropy in dose calculations.

PARTICLE ANGULAR DISTRIBUTION AND WEIGHTING FACTORS

Pitch angle distributions of protons trapped in the so-called inner Van Allen zone have been calculated based upon data from Relay I (ref. 2). Equatorial pitch angle distributions can be calculated from the omnidirectional particle intensities along magnetic lines of force (refs. 3 and 4). This was accomplished utilizing a computer program developed by

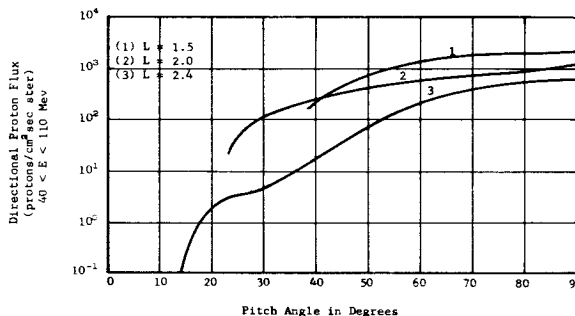
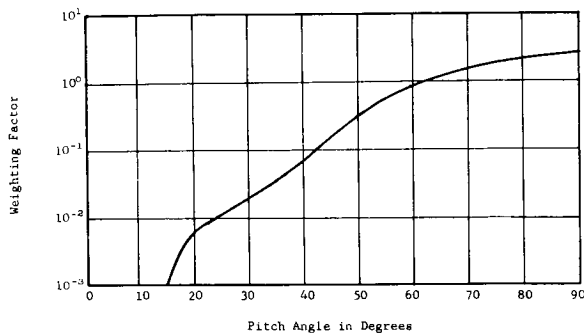


FIGURE 1.—Equatorial pitch angle distributions for various L values.

T. A. Farley for several L values of the McIlwain B, L coordinate system (ref. 5). Equatorial angular distributions of trapped protons for L shells of 1.5, 2.0, and 2.4 are illustrated in figure 1. The steepest of the three curves ($L=2.4$) was utilized to assess the importance of radiation anisotropy because, in general, pitch angle distributions become steeper with increasing magnetic latitude.

In order to assess the importance of radiation anisotropy, three basic computer programs were used: MAVRAC, MWFP, and CAD. MAVRAC (Model Astronaut and Vehicle Radiation Analysis Code) was developed for the Aerospace Medical Research Laboratory under contract AF33(657)-8762, and was utilized to calculate normalized isotropic dose rates per steradian (ref. 6). The second program, MWFP (Mean Weighting Factor Program), was used to determine pitch angles for all look directions for any satellite orientation and compute corresponding weighting factors. The function of the third program, CAD (Calculation of Anisotropic Dose), was to combine the results of MAVRAC and MWFP to obtain the weighted-anisotropic dose values.

FIGURE 2.—Weighting factor for $L=2.4$.

These computer programs calculate the normalized isotropic dose rate for each solid angle and weight this with the fraction of the omnidirectional flux incident with the respective pitch angle. This fraction or weighting factor, WF , was obtained using a normalized polynomial expression representing the pitch angle distribution for $L=2.4$. This weighting factor function is illustrated in figure 2. Mathematically this was obtained using

$$WF(\alpha) = \exp \sum_{i=0}^n A_i \alpha^i \quad (1)$$

with A_0 chosen so that

$$\int_0^{\pi/2} WF(\alpha) \sin \alpha d\alpha = 1 \quad (2)$$

Based upon the straightahead assumption for the penetration of protons, the dose rate per unit solid angle as a function of thickness, $D(t)$, is calculated per unit directional flux ($E > 40$ MeV) and the total normalized dose rate is expressed as

$$D_T = \sum_{i=0}^n WF(\alpha_i) D(t_i) \Delta\Omega_i \quad (3)$$

In this expression $\sum_{i=0}^n WF(\alpha_i) \Delta\Omega_i = 4\pi$ steradians due to equation (2).

The angle between the proton velocity vector directed toward the detector and the magnetic field vector corresponds to the pitch angle, α . The coordinate system utilized in this study is illustrated in figure 3. Vehicle orientation is specified by the components of a unit magnetic field vector, B_x , B_y , and B_z . These then are the direction cosines of the magnetic field

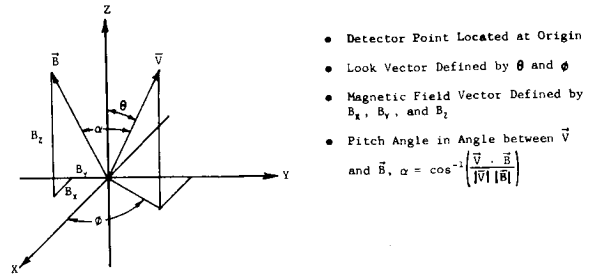


FIGURE 3.—Coordinate system.

vector with respect to X , Y , and Z axes of the spacecraft coordinate system.

An error analysis was made of the method used in calculating pitch angle weighting factors. A comparison was made between mean weighting factors, $\overline{WF}(\alpha)$, and the weighting factors, $WF(\alpha_c)$, where α_c is the angle between the vector through the center of the solid angle and the magnetic field vector. Mean weighting factors were obtained by calculating $\frac{\int WF(\alpha) d\Omega}{\int d\Omega}$ over the solid angle.

First the error was established for various values of α_c for a solid angle of 0.15 steradian. These results, shown in table I, show an increasing error with decreasing α_c . It can be seen that when α_c is 40° , the error is nearly 64%. The errors tabulated in table I are too great to tolerate even when the errors tend to cancel each other. In fact, preliminary computer results utilizing large solid angles produced erroneous results due to this error. Weighting factor errors were then determined for a given α_c (40°) using various sizes of solid angles. These results are listed in table II and show that even the error for $\alpha_c=40^\circ$ can be reduced

TABLE I

Mean Weighting Factors for Constant Solid Angle ($\Delta\Omega=0.15$)

α_c (Center)	$\overline{WF}(\alpha)$	$WF(\alpha_c)$	% Error
90	2.30	2.45	6.5
50	.374	.320	14.5
48	.318	.245	23.0
45	.222	.154	30.6
40	.115	.070	63.9

TABLE II

Mean Weighting Factors for Constant Pitch Angle ($\alpha_c=40^\circ$)

Solid angle	$\overline{WF}(\alpha)$	$WF(\alpha_c)$	% Error
0.15	0.115	0.0704	63.9
.1	.0999	.0704	41.9
.05	.0848	.0704	20.6
.01	.0732	.0704	4.05
.005	.0718	.0704	2.00
.001	.0706	.0704	.38

significantly by using solid angles as small as 0.0015 steradian. Based upon these results, the maximum capability of the computer program (7200 solid angles) was utilized to minimize the error in assuming $\overline{WF}(\alpha) = WF(\alpha_c)$.

MATERIAL DISTRIBUTIONS

The vehicle configuration selected for consideration in this study was a satellite which will be used in a future space radiation experiment (ref. 1). The vehicle is essentially a right cylinder (27 inches in diameter and 30 inches in length) with hemispherical domes on each end. A spherical aluminum phantom of 16.0 g/cm² radius is located at the center of the vehicle. The satellite support equipment is housed in the hemispherical domes so that the space between the phantom and the sides of the vehicle is essentially void. Three detectors are positioned in the phantom on a line perpendicular to the side of the vehicle at depths of 0.0 g/cm² (surface of sphere), 4.0 g/cm², and 16.0 g/cm² (center of sphere). It is at these three points (A, B, and C, respectively) that dose calculations were made. The satellite's longitudinal axis is the X axis of the coordinate system (fig. 3) with the line through the three detectors forming the Z axis. The surface detector, A, is the positive Z direction.

Material distributions about the three detector points A, B, and C are given in figure 4. Each distribution includes the contribution of the aluminum sphere and equivalent aluminum thicknesses of the satellite equipment and vehicle structure. The material distribution about point A is seen to peak sharply at a small

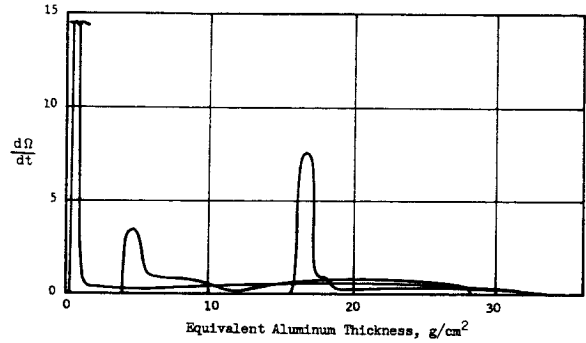


FIGURE 4.—Material distribution.

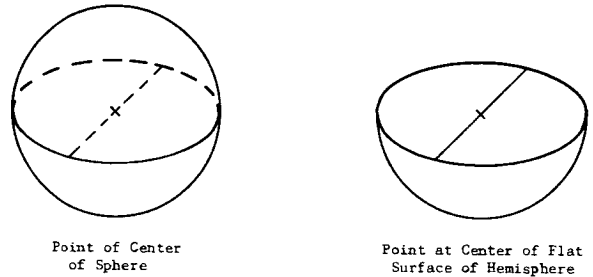


FIGURE 5.—Material distributions where dose is independent of particle anisotropy.

thickness corresponding to the vehicle skin thickness. This is due to the fact that much of the space in the 2π steradians above the sphere is enclosed only by the vehicle skin. The material distribution about point B exhibits a combination of spherical phantom and vehicle material with a minimum value of 4.0 g/cm² plus the vehicle skin thickness. The distribution about point C is 16.0 g/cm² plus contributions from the satellite. Integration of each of these curves results in 4π steradians.

For certain material distributions, the proton dose at a point is independent of the trapped radiation distribution. Two such material distributions exhibiting this quality are illustrated in figure 5. Due to the symmetry of trapped radiation about magnetic field lines, a hemisphere will always sample half of the radiative environment and, therefore, the doses at the indicated points of figure 5 will be independent of orientation in space. In reality, these distributions will rarely, if ever, be encountered; however, they serve as limiting cases which aid in understanding some of the results of this study.

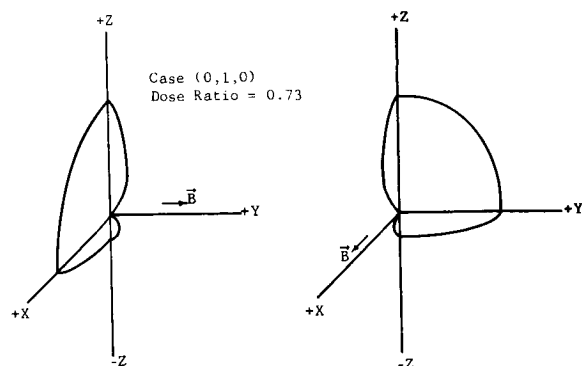


FIGURE 6.—Coupling of radiation anisotropy and material distribution for Detector A (sphere only).

RESULTS

Anisotropic and isotropic dose calculations were made for seven different vehicle orientations and the results are presented in table III. For each orientation, anisotropic dose rates are ratioed to the isotropic dose rate to indicate the relative importance of radiation anisotropy in dose calculations. The experimenter, M. C. Chapman, states (personal communication) that the accuracy of the experimental measurements will be within $\pm 10\%$. Therefore, it can be seen that vehicle orientation must be considered for detectors *A* and *B*, but not for *C*. Detector *C* has no shielding less than 16.0 g/cm² and, therefore, a flat portion of the dose versus thickness curve is utilized; hence, the results are insensitive to radiation anisotropy. Detector *C* approaches the case of a point at the center of a homogeneous sphere which was earlier stated to be independent of orientation.

A comparison of results for detectors *A* and *B* shows that the dose rate at detector *B* will be influenced by radiation anisotropy more than the surface detector. While at first this seems surprising, it can be seen that detector *A* approaches the case of the detector at the center of the flat surface of a hemisphere. This is a plausible explanation of why detector *B* is influenced more by anisotropy than detector *A*.

To aid in the understanding of the coupling of radiation anisotropy and material distribution, figure 6 is presented to qualitatively represent the results considering only the sphere and detector *A* for the first two cases in table III. The curved lines in figure 6 represent

TABLE III

Anisotropic Dose Results (Ratioed to Isotropic Dose)

Direction cosines	Point A (Surface)	Point B (4 gm/cm ²)	Point C (16 gm/cm ²)
0, 1, 0	0.73	1.12	0.96
1, 0, 0	1.44	1.50	1.08
0, 0, 1	.83	.31	.95
.707, .707, 0	1.10	1.34	1.03
.707, 0, .707	1.14	.92	1.03
0, .707, .707	.74	.83	.95
.5, .5, .707	.94	.87	.99

magnitudes of radius vectors from the origin which are proportional to the dose per steradian from that direction. First consider the case (0, 1, 0) and the +*X*, +*Z* quadrant. This curve represents the unattenuated dose with α always 90° for a uniform maximum dose rate per steradian. In the +*Y*, +*Z* quadrant, radiation is also unattenuated; however, in rotating from the +*Z* axis toward the +*Y* axis, α decreases and so does the directional flux until the dose rate per steradian becomes zero at the α defining the loss cone. Consider next the +*X*, -*Z* quadrant. The pitch angle, α , is always 90° and the peak directional flux is present all along the curved line, but the amount of shielding increases from zero at the +*X* axis to 32.0 g/cm² at the -*Z* axis. The shielding reduces the dose rate per steradian as the curve goes from +*X* to the -*Z* axis. Finally in the +*Y*, -*Z* quadrant, both the pitch angle distribution and the shielding interact to produce the small dose rate per steradian illustrated. Due to the symmetry of the material about detector *A* relative to the *Z* axis, the other diagram for case (1, 0, 0) is very similar, and the dose at detector *A* would be the same in either case.

Now consider the shielding contribution of the satellite, recalling that the hemispherical domes are located on the *X* axis. For case (0, 1, 0) the satellite materials tend to suppress a high dose rate, while in case (1, 0, 0) they interact with a small dose rate. This explains why the anisotropic dose rate for case (0, 1, 0)

is less than that for an isotropic flux, while case (1, 0, 0) results in a higher dose rate.

CONCLUSIONS

1. The anisotropy of space radiation must be considered for detectors *A* and *B*, but need not be considered for detector *C*.

2. There is likely to be some location between *A* and *C* where the dose rate would be most influenced by radiation anisotropy.

3. The dose at specific points in an astronaut, such as the eyes and localized critical organs, should be investigated considering the anisotropy of the trapped radiation.

REFERENCES

1. CHAPMAN, M. C.; BRATT, R. W.; and COOP, W. H.: A Space Flight Experiment to Assess Radiation Shielding Calculations. Paper for AIAA Unmanned Spacecraft Meeting (Los Angeles), Mar. 1-4, 1965.
2. McILWAIN, C. E.; FILLIUS, R. W.; VALERIO, J.; and DAVE, A.: Relay I Trapped Radiation Measurements. Univ. Calif. (San Diego), Mar. 1964.
3. RAY, ERNEST C.: On the Theory of Protons Trapped in the Earth's Magnetic Field. *J. Geophys. Res.*, vol. 65, no. 4, Apr. 1960, pp. 1125-1134.
4. FARLEY, T. A.; and SANDERS, N. L.: Pitch Angle Distributions and Mirror Point Densities in the Outer Radiation Zone. *J. Geophys. Res.*, vol. 67, no. 6, June 1962, pp. 2159-2168.
5. McILWAIN, CARL E.: Coordinates for Mapping the Distribution of Magnetically Trapped Particles. *J. Geophys. Res.*, vol. 66, no. 11, Nov. 1961, pp. 3681-3691.
6. DUCKWORTH, G. D.: Model Astronaut and Vehicle Radiation Analysis Code (MAVRAC), NSL-63-159, Northrop Space Laboratories, Sept. 1963.

SESSION IVF

SHIELDING AGAINST SPACE RADIATION

Chairman: CHARLES W. HILL
Lockheed—Georgia Company

65-34629

53—Analytical Formulation of Proton Dose Rates Behind Spherical Multilayer Shields¹

F. R. NAKACHE

United Nuclear Corporation

34629

As a part of the studies on spherical minimum-weight proton shields made at United Nuclear Corporation (ref. 1), analytical expressions were derived for calculating several types of primary proton dose rates, such as average body doses, skin doses, depth doses, and local doses. These expressions are believed to be more general and capable of wider application than those heretofore found in the literature (refs. 2 and 3). In addition, they eliminate the need of numerical integration. The only restrictions to their application are that the shield layers and the crew man model must be spherical, and the incident proton spectra must have an isotropic angular distribution.

author
BASIC ASSUMPTIONS

The proton attenuation model is based on the following assumptions:

(a) The ratio of the proton stopping power in any material to that in aluminum A_i is a constant, independent of the proton energy.

(b) The shield consists of concentric shells of a radii r_0, r_1, \dots, r_j , where r_0 is the radius of the void region to be shielded, containing materials with proton relative stopping powers, A_1, A_2, \dots, A_j .

(c) The proton energy range can be subdivided into an arbitrary number of intervals, L , in each of which the energy distribution of the incident proton flux and the proton stopping power in aluminum are well represented by power functions of the proton energy.

¹ Research sponsored by the George C. Marshall Space Flight Center, NASA, under contract NAS 8-5277.

$$P_l(E) = C_l E^{-m_l} \quad (1)$$

$$\left(\frac{1}{\rho} \frac{dE}{dr}\right)_l = \alpha_l E^{-n_l} \quad (2)$$

with $l=1, 2, \dots, L$; C, α, m , and n are constant in each energy interval l .

(d) The crew man is represented by a sphere of density ρ_c , relative stopping power A_c , and radius $e (e \leq r_0)$. Use is made of the fact that the energy deposited in a spherical phantom is greatest if its center coincides with the void center. In our analysis it is then possible to consider only phantoms which are concentric with the void.

The geometry of the dose constraint model is presented in figure 1.

EQUIVALENT ALUMINUM THICKNESS OF THE SHIELD AND THE PHANTOM

The equivalent aluminum shield thickness seen by a ray penetrating the shield at angle φ with the normal direction at the phantom surface is

$$K = \sum_{i=0}^j (A_i - A_{i+1}) (r_i^2 - e^2 \sin^2 \varphi)^{1/2} \quad (3)$$

with the convention that $A_0 = A_{j+1} = 0$. The minimum and maximum attenuation are given when $\varphi=0$ and $\varphi=\pi/2$ respectively.

$$K_0 = \sum_{i=0}^j (A_i - A_{i+1}) r_i \quad (4)$$

$$K_m = \sum_{i=0}^j (A_i - A_{i+1}) (r_i^2 - e^2)^{1/2} \quad (5)$$

If K is expanded in series in the form

$$K = K_0 + K_1 \sin^2 \varphi + K_2 \sin^4 \varphi + \dots,$$

it can be shown that the coefficient K_i decreases

rapidly, particularly when $e \ll r_0$ and therefore a good approximation to K is

$$K = K_0 + K_1 \sin^2 \varphi \quad (6)$$

with

$$K_1 = \frac{e^2}{2} \sum_{i=0}^j \frac{A_{i+1} - A_i}{r_i} \quad (7)$$

The equivalent aluminum thickness at angle φ through both the shield and the phantom is given by

$$K_T = K + 2A_T e \cos \varphi \quad (8)$$

where A_T is the phantom relative stopping power.

The behavior of K_T versus φ is not obvious, since as φ increases from 0 to $\pi/2$, $2A_T e \cos \varphi$ decreases while K increases. It can be shown, however, that if $\frac{K_0}{r_0} \leq 2A_T \approx 1$, then K_T is a nonincreasing function of φ . K_T decreases from $K_T(0) = K_0 + 2A_T e$ to K_m given in equation (5).

A good approximation to K_T can be shown to be

$$K_T = K_m + (K_T(0) - K_0) \cos \varphi - (K_m - K_0) \cos^2 \varphi \quad (9)$$

AVERAGE BODY DOSE

The dose or dose rate per unit mass of the spherical crew man per unit proton flux for an isotropic proton flare incident on the shielded void is given by

$$D_V = \int_0^\infty F_V(E) P(E) dE \quad (10)$$

where $F_V(E)$ is the energy deposition per unit mass of the spherical phantom by an incident proton of energy E .

$$F_V(E) = \frac{3}{2e\rho_T} \int_0^{\pi/2} (E' - E'') \sin \varphi \cos \varphi d\varphi \quad (11)$$

Here, E' is the energy of the proton incident on the proton after penetrating the shield at angle φ .

E'' is the energy of the proton after penetrating both the shield and the phantom.

ρ_T is the phantom density (≈ 1).

If $F_V(E)$ is expressed in MeV/g per unit flux, the units of D_V are in MeV/g-sec if a time-

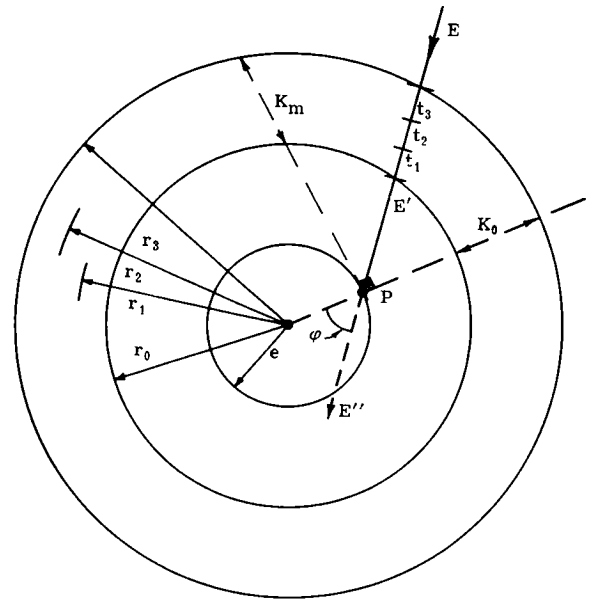


FIGURE 1.—Geometry of the dose constraint model.

dependent proton flux is given and in MeV/g if a time-integrated proton flux is given.

Let us assume that single power fits represent well the incident proton spectrum and the stopping power in aluminum for incident proton energies which give a range in aluminum higher than K_0 .

Then the range of protons incident and emerging from the phantom as a function of the range in aluminum of incident protons, $R(E)$, and incident angles, φ , is given in table I.

The average body energy deposition rate per unit mass of tissue, $F_V(E)$, is given in table II as a function of $R(E)$.

Numerical results for a typical case ($K_0 = 10$ g/cm² of Al, $r_0 = 26$ cm) are given in figure 2. Then the average body dose per unit proton flux (in MeV/g) is given by

$$D_V = \frac{\beta B(a, b)}{e} \left\{ \frac{K_0^{-b} - K_m^{-b}}{K_m - K_0} - \frac{K_m^{-b} - (K_0 + 2A_T e)^{-b}}{K_0 + 2A_T e - K_m} \right\} \quad (12)$$

where

$$\beta = \frac{3}{4} \frac{C}{\rho_T} \frac{[\alpha(n+1)]^{-(b+1)}}{n+2} \quad (13)$$

$$b = \frac{m-n-3}{n+1} \quad (14)$$

TABLE I

Range of Protons Incident and Emerging From the Phantom as a Function of R and φ

Range of protons incident on the shield, R	Range of protons incident on the phantom, R'	Range of protons emerging from phantom, R''	Comments
$R \leq K_0$ $K_0 \leq R \leq K_m$ $K_m \leq R \leq K_T(0)$ $R > K_T(0)$	0 $R' = R - K(\varphi), 0 < \varphi \leq \varphi_0$ $R' = 0 \quad \varphi_0 < \varphi$ $R' = R - K(\varphi), 0 < \varphi \leq \pi/2$ $R' = R - K(\varphi)$	0 0 for $0 < \varphi \leq 1/2$ $R'' = R - K_T(\varphi), \varphi_1 < \varphi < \pi/2$ $R'' = 0 \quad 0 < \varphi \leq \varphi_1$ $R'' = R - K_T(\varphi)$	For all incidence angles $R = K_0 + K_1 \sin^2 \varphi_0$ $R = K_m + [K_T(0) - K_0] \cos \varphi_1 - (K_m - K_0) \cos^2 \varphi_1$ For all incidence angles

TABLE II

Average Body Energy Deposition Rate per Unit Mass of Tissue per Unit Proton Flux as a Function of Range in Aluminum of the Incident Protons

Proton range, R(E)	$F_V(E)$	Comments
$R(E) \leq K_0$	0	$R = \frac{E^{n+1}}{(n+1)\alpha}$
$K_0 < R < K_m$	$\epsilon \frac{E_0 R_0'}{K_m - K_0}$	$R'_0 = R - K_0$
$K_m < R < K_T(0)$	$\epsilon \left[\frac{E_0 R_0' - E_m R_m'}{K_m - K_0} - \frac{E_m R_m'}{K_T(0) - K_m} \right]$	$R'_m = R - K_m$
$R > K_T(0)$	$\epsilon \left[\frac{E_0 R_0' - E_m R_m'}{K_m - K_0} - \frac{E_m R_m' - E'_0 R'_0}{K_T(0) - K_m} \right]$	$R'_0 = R - K_T(0)$
	where $\epsilon = \frac{3}{4e\rho_T} \left(\frac{n+1}{n+2} \right)$	

$$a = \frac{2n+3}{n+1} \tag{15}$$

$$B(a, b) = \int_0^\infty \frac{y^{a-1}}{(1+y)^{(a+b)}} dy$$

is the complete Beta function.

For $b \rightarrow 0$,

$$D_0 = \frac{\beta}{e} \left[\frac{\log K_m/K_0}{K_m - K_0} - \frac{\log K_T(0)/K_m}{K_T(0) - K_m} \right] \tag{16}$$

These relationships have been applied to the calculation of the average body dose for particular flare spectra as a function of shield thickness and void radius. Results are shown in figures 3 and 4.

The first flare considered is that of May 10, 1959. Two different spectra have been postulated for this flare. The NASA integral

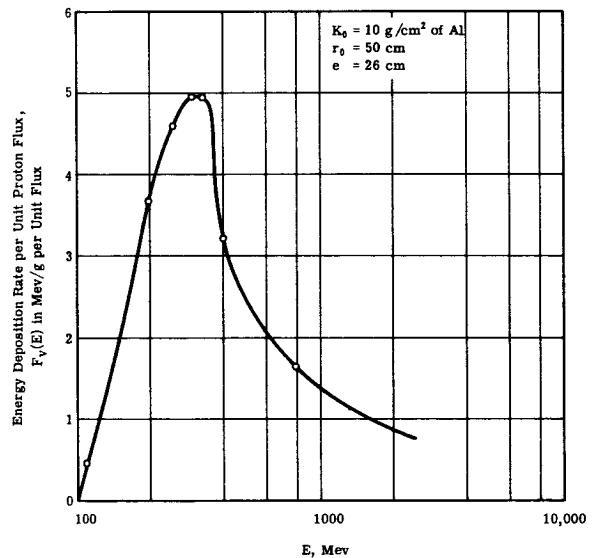


FIGURE 2.—Energy deposition rate versus energy of incident protons.

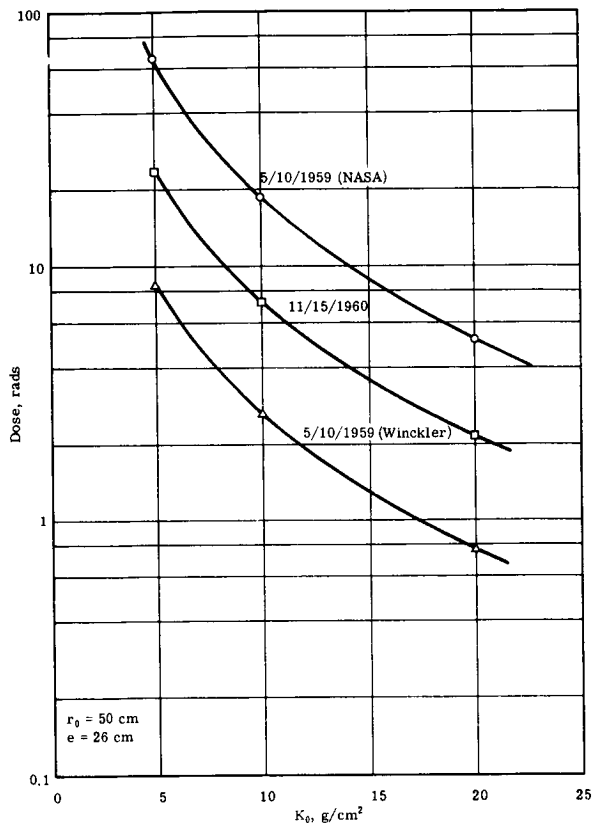


FIGURE 3.—Average body dose versus aluminum, equivalent shield thickness, K_0 . Flares of May 10, 1959, and November 15, 1960.

spectrum is matched suitably by

$$\begin{cases} 1.90 \times 10^{11} E^{-1.5} & 10 < E < 60 \text{ MeV} \\ 3.19 \times 10^{17} E^{-5} & 60 < E < 780 \text{ MeV} \end{cases}$$

The Winckler spectrum is given by a single power fit for $30 < E < 1000$ MeV, namely

$$P(E) = 1.672 \times 10^6 E^{-4.5}$$

A phantom of radius $e = 26$ cm is used. This represents approximately an average man, since the weight of the model is about 73.5 kg or 162 lb.

For a void radius, r_0 , of 50 cm, the average body dose versus aluminum shield thickness in g/cm^2 is plotted in figure 3 for the NASA and Winckler spectra. A similar plot for the November 15, 1960, flare is also given. These results have been compared to other numerical dose calculations performed at United Nuclear

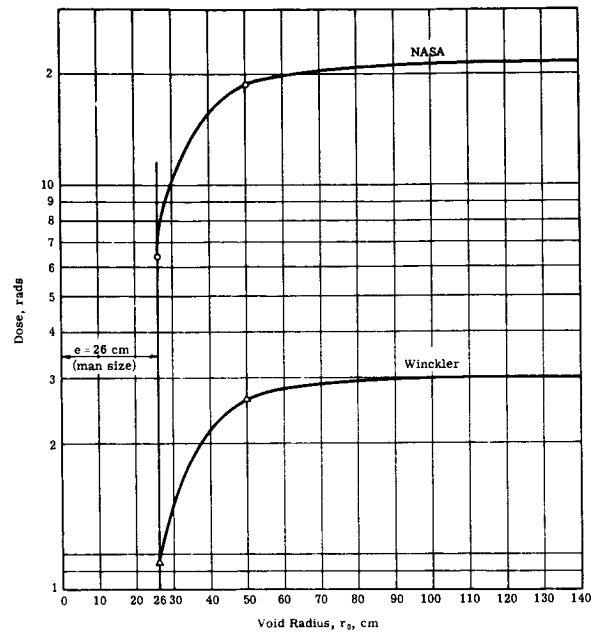


FIGURE 4.—Average body dose versus void radius, r_0 , for a shield of $10 \text{ g}/\text{cm}^2$ of Al—flare of May 10, 1959.

by E. Greuling et al., in which protons were assumed to be isotropically incident on the phantom (rather than on the shield). The agreement is very good because the man-to-void size ratio is small ($\approx 1/2$). As the ratio e/r_0 increases, the average body dose becomes smaller because many of the protons which reach the phantom now penetrate the shield at a flatter angle and thus have a large path length through the shield.

In figure 4, the average body dose versus the void radius is shown, assuming an aluminum shield thickness of $10 \text{ g}/\text{cm}^2$. When r_0 becomes very large, all protons which contribute to the energy deposition in the body can be considered as normally incident on the shield. Note that the average body dose increases rather rapidly when r_0 increases from $r_0 = e = 26$ cm to $r_0 = 50$ cm, and then increases very slowly to the asymptotic value given when all protons are normally incident on the shield.

OTHER TYPES OF PRIMARY DOSES

The dose or dose rate per unit flux at the void center for a point detector is given by:

$$D = D(0) = b(b+1) A_T \frac{C}{K_0^{b+2}} \quad (17)$$

The dose or dose rate per unit flux at the center of the spherical phantom is given by

$$D(\text{center}) = b(b+1)\beta A_T \frac{B(a, b)}{(K_0 + A_T e)^{b+2}} \quad (18)$$

If we compare the values of dose obtained by use of this equation to those shown in figures 3 and 4, we find that the dose at the phantom center, when self-shielding is taken into account, is small compared to the average body dose for a phantom 26 cm in radius. Most of the average body dose is contributed by radiation deposited in the outer portion of the phantom.

The proton energy per gram of tissue deposited in an infinitesimally thin tissue shell at a given depth in the spherical man model is of special interest. Since the energy deposited will depend on the location of the shell with respect to the surface of the man, it is called depth dose. In particular, the energy per gram of tissue deposited in a shell located at the phantom surface is called the skin dose.

It is likely that, for shielding purposes, a depth dose constraint rather than an average body dose constraint will be imposed because the permissible dose to certain vital organs such as eyes, kidneys, and such is smaller than the permissible average body dose.

The energy deposited or rate of deposition per unit flux per gram of tissue in a shell of thickness de' located at radius e' in the phantom is given by

$$D_p(e') = \frac{A_T C}{3} \left\{ \left[\frac{K_0'^{-b} - K_m'^{-b}}{(K_m' - K_0')^2} - \frac{K_m'^{-b} - (K_0' + 2A_T e')^{-b}}{(K_0' + 2A_T e' - K_m')^2} \right] + b \left[\frac{K_0'^{(b+1)} - 2K_m'^{(b+1)}}{K_m' - K_0'} + \frac{2K_m'^{(b+1)} - (K_0' + 2A_T e')^{-(b+1)}}{K_0' + 2A_T e' - K_m'} \right] \right\} \quad (19)$$

where K_0' and K_m' are now defined for both the shield and the tissue layer of thickness $(e - e')$.

The particular case of $e' = e$ is of interest since, in this case, equation (19) reduces to $D_p(e)$, the skin dose. In figures 5 and 6, the depth dose distribution versus e' is plotted for the NASA and Winckler spectra of the flare of

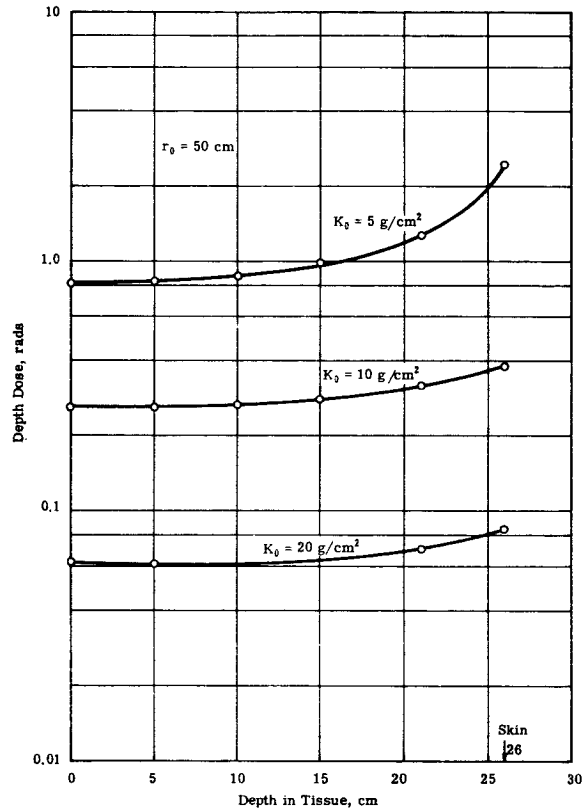


FIGURE 5.—Depth dose versus depth in tissue for a 52-cm diameter sphere—NASA spectrum of flare of May 10, 1959.

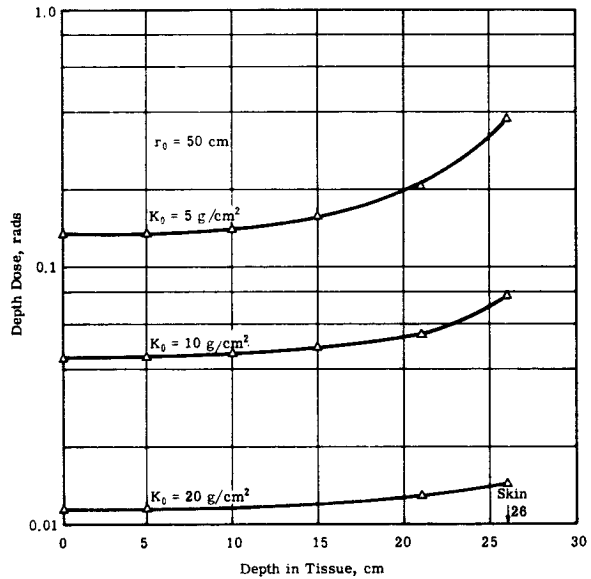


FIGURE 6.—Depth dose versus depth in tissue for a 52-cm diameter sphere—Winckler spectrum of flare of May 10, 1959.

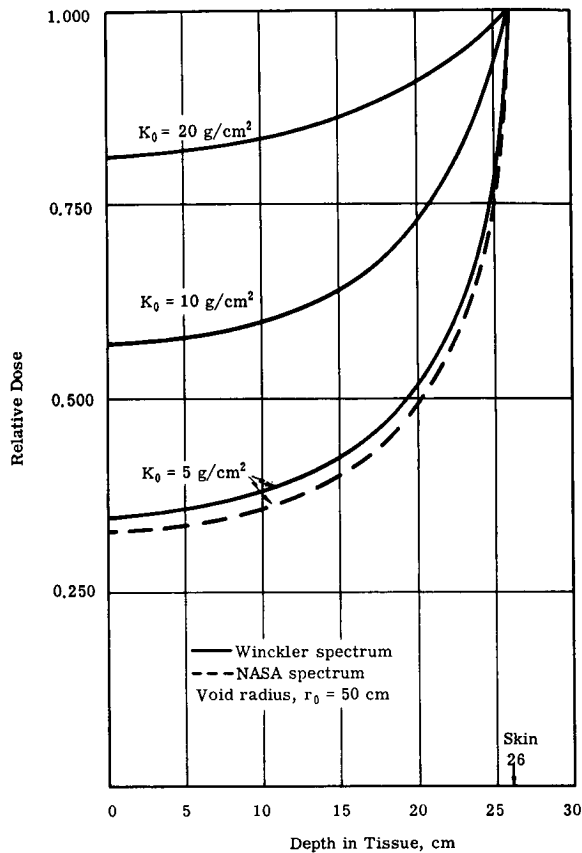


FIGURE 7.—Relative proton depth dose versus depth in tissue for a 52-cm diameter tissue sphere for various Al shields for the flare of May 10, 1959.

May 10, 1959. The parameters used are

$$e = 26 \text{ cm}$$

$$r_0 = 50 \text{ cm}$$

$$K_0 = 5 \text{ g/cm}^2, 10 \text{ g/cm}^2, 20 \text{ g/cm}^2 \text{ of aluminum}$$

As the depth in tissue increases (that is, as e' decreases), the depth dose decreases from a maximum on the skin to a minimum at the center of the spherical man. For relatively thin shields, D_p decreases rapidly near the skin. As the thickness of the shield increases, the reduction in dose becomes less important and the dose remains practically constant.

In figure 7, the doses are normalized to the skin dose. Thus, for $K_0 = 5 \text{ g/cm}^2$ of aluminum, the relative dose decreases from 1.0 on the skin to 0.347 at the center, while for $K_0 = 20 \text{ g/cm}^2$ of aluminum, it decreases only from 1.0 to 0.81. The curves of figure 7 have the same

shape and otherwise compare very well with the single curve given by Schaefer (ref. 4).

GENERAL CASE

It may be necessary to divide the energy range into several portions in each of which the energy distribution of the incident protons can be represented by a power function of the energy. This would be the case if one considers protons from the Van Allen belt or the February 23, 1956, flare as being incident on the shield. Hence, a general solution for the average body dose is of interest.

Assume that the energy distribution of the incident proton flare can be represented by L power fits as follows:

$$P_i(E) = C_i E^{-m_i} \quad (20)$$

when $E_{i-1} < E \leq E_i$ (or $R_{i-1} < R < R_i$ if the proton range in aluminum is used as a variable), $i = 1, 2, \dots, L$; $E_0 = R_0 = 0$, and E_L and R_L are infinite.

Then, in each energy range, the following quantities can be defined:

$$b_i = \frac{m_i - n - 3}{n + 1}$$

$$\beta_i = \frac{3C_i [\alpha(n+1)] \frac{m_i - 2}{n + 1}}{4\rho_T n + 2}$$

$$a = \frac{1}{n + 1} + 2$$

and

$$B_x(a, b) = \int_0^x u^{(a-1)} (1-u)^{(b-1)} du$$

By convention, when $x \geq 1$, $B_x(a, b)$ equals the complete beta function $B(a, b)$ and when $x < 1$, it becomes the incomplete beta function often found in mathematical statistics. When $x = 0$, $B_x(a, b) = 0$. Numerous approximations to the incomplete beta function $B_x(a, b)$ are available. Most tables use the "standardized" form which is called the incomplete-beta-function ratio.

$$I_x(a, b) = \frac{B_x(a, b)}{B(a, b)}$$

Then, the average body dose is given by

$$D = \frac{1}{e} \sum_{i=1}^L \beta_i f_i(K_0, K_m) \quad (21)$$

where

$$f_i(K_o, K_m) = \frac{1}{K_m - K_o}$$

$$\left\{ K_o^{-b_i} \left[\frac{B_{K_o}}{R_{l-1}}(a, b_i) - \frac{B_{K_o}}{R_l}(a, b_i) \right] - K_m^{-b_i} \left[\frac{B_{K_m}}{R_{l-1}}(a, b_i) - \frac{B_{K_m}}{R_l}(a, b_i) \right] \right\}$$

$$\frac{1}{K_T(0) - K_m} \left\{ K_m^{-b_i} \left[\frac{B_{K_m}}{R_{l-1}}(a, b_i) - \frac{B_{K_m}}{R_l}(a, b_i) \right] - K_T(0)^{-b_i} \left[\frac{B_{K_T(0)}}{R_{l-1}}(a, b_i) - \frac{B_{K_T(0)}}{R_l}(a, b_i) \right] \right\}$$

Equation (21) reduces to equation (12) if a single power fit for the energy spectrum is valid when $R \geq K_o$.

REFERENCES

1. KRUMBEIN, A. D.: Proc. of Symp. on Protection Against Radiation Hazards in Space, TID-7652, AEC, Nov. 1962, p. 773.
2. MADEY, R.: Trans. Am. Nucl. Soc., vol. 6, June 1963, p. 194.
3. HAFNER, J. W.: Trans. Am. Nucl. Soc., vol. 7, June 1964, p. 16.
4. SCHAEFER, H. J.: A Note on the Influence of Shield Geometry on Air Dose and Tissue Dose From Protons Within a Space Vehicle. Figure 6, NASA-CR-50780, Apr. 1963.

54—The Calculation of Proton Penetration and Dose Rates

MARTIN O. BURRELL

Marshall Space Flight Center, NASA

There have been several calculational methods developed to determine the proton energy degradation and flux attenuation as a function of penetration depth in various materials, the ultimate purpose being to estimate the energy deposition or dose rate at a given depth or on the surface of a shielded target such as a man. The methods range from fairly simple approximations to complex and tedious numerical methods. However, most of the methods are essentially the same in that they assume the so-called "straightahead model." In this model, the assumption is made that energetic protons lose energy by ionization losses associated with the removal of bound electrons in the shield materials,¹ with no subsequent change in particle direction. Elastic scattering is assumed to be strongly in the forward direction with a negligible energy loss and hence is ignored as a slowing-down mechanism. However, in most of these models, an attenuation correction is made for nonelastic collisions that completely remove the primary proton. The degree of sophistication in the nonelastic collision calculation is usually a function of the shield thickness and the subsequent treatment of the secondary particles liberated.

The methods introduced by the writer are in the same category as those discussed above. It is hoped that the innovations presented will help in obtaining reliable solutions in a simpler manner than is now available.

ENERGY SPECTRA OF PRIMARY PROTONS

It seems to follow that, regardless of the methods or models used, the slowing-down energy loss of the primary protons is assumed to be dependent only on the ionization loss

from bound electrons which is given by various modifications of the Bethe-Bloch formula for stopping power:

$$S(E) = -\frac{dE}{dX} = \frac{4\pi e^4}{mV^2} N \left[Z \left(\ln \frac{2mV^2}{I} - \ln(1-\beta^2) - \beta^2 \right) - C \right] \quad (1)$$

where E is the kinetic energy of the proton, Z is the atomic number, $V = \beta C$ is the proton velocity, m is the electron mass, N is the number of atoms of the material per cm^3 , I is the average ionization potential of the material, and C is a correction term for electron-shell binding.

A quantity of greater utility in many of the computational schemes is the range of a proton which is given by

$$R(E) = \int_0^E \frac{dE'}{S(E')} \quad (2)$$

The dimensions of stopping power, $S(E)$, are usually $(\text{MeV}\cdot\text{cm}^2/\text{gm})$ and, therefore, for the range, the dimensions are (gm/cm^2) from equation (2). In order to see how the above quantities enter into the calculation of proton penetration, the following development is presented. Figure 1(a) illustrates the parameters of the problem, where E denotes the incident energy of a proton and E^* the energy at depth X .

Now if certain liberties are granted, it can be seen that the proton energy in going from E to E^* might be represented by an analytical relationship such as

$$E = g(E^*) \quad (3)$$

where, obviously, E^* is a function of X . Hence, the proton differential energy flux at depth

¹ Hydrogen shields should probably be excepted.

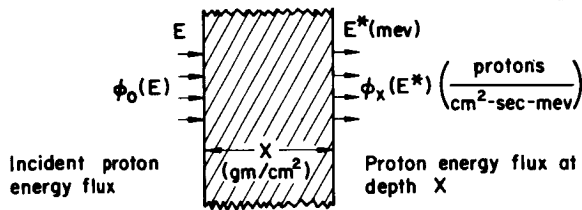


FIGURE 1(a).—Relationship of proton flux to penetration depth.

$X > 0$ may be related to the flux at depth $X = 0$ by a simple change of variable technique denoted by

$$\phi_x(E^*)dE^* = \phi_0 \left\{ g(E^*) \right\} \left| \frac{dg(E^*)}{dE^*} \right| dE^* \quad (4)$$

Of course, the practicality of representing the flux at depth X , as shown in equation (4), depends on the ability to find a usable relationship between the energy E and E^* . However, the ability to write equation (3) in a nice mathematical expression does not follow from direct application of the Bethe-Bloch formula. In order to arrive at a practical solution to the problem, one can resort to the following exercise in functional manipulation.

The proton range is assumed to be represented by an empirical curve fit, or even as a tabulated set of numbers, in the case of a pure numerical approach. Thus, if

$$R = F_Z(E) \text{ [gm/cm}^2\text{]} \quad (5)$$

is used to denote the range of a proton of energy E incident on a material denoted by the subscript Z , then at the depth X (gm/cm²) in material " Z ," the energy of the proton is reduced by an amount ΔE associated with an equivalent reduction in range given by $\Delta R = X$. Thus we can write

$$R - X = F_Z(E - \Delta E) \quad (6)$$

Now $E - \Delta E = E^*$, the energy of the proton at depth X , and since $R = F_Z(E)$, we write

$$F_Z(E) = X + F_Z(E^*)$$

and

$$E = g(E^*) = F_Z^{-1}[F_Z(E^*) + X] \quad (7)$$

Thus, equation (7) provides the relationship required by equation (3). However, there are some obvious restrictions to the functional form

which the approximation of $R(E)$ can assume. For this reason, use is often made of the numerical approaches to finding the proton differential energy flux at a depth X . However, it should go without saying that the number of functional forms which are amenable to the manipulations indicated in equation (7) are, mathematically speaking, without limits. The most popular attempt to arrive at a simple solution to the proton penetration problem is that given by assuming that the range of a proton in a material " Z " can be represented simply by

$$R = aE^r \quad (8)$$

where the coefficient " a " is dependent on the material, and the power " r " only slightly dependent on the " Z " number. (See ref. 1.) In fact, a value of $r \cong 1.78$ will suffice for $Z = 6$ to 30. This choice of range formula is usually considered valid from about 10 to 250 MeV with a maximum error of $\pm 5\%$ in approximating the various n integrations for range based on the Bethe-Bloch formula for stopping power. As an illustration of the techniques that can be used to arrive at a simple formula for primary proton penetration, the following is presented:

Assume that the incident proton energy spectrum is given by

$$\phi_0(E) = HE^{-a} \left[\frac{\text{protons}}{\text{cm}^2 - \text{MeV}} \right] \quad E_1 \leq E \leq E_2 \quad (9)$$

and that for the slab thickness and energy spread the range is sufficiently well approximated by equation (8); then, from equation (7), we write

$$E = g(E^*) = \left(E^{*r} + \frac{X}{a} \right)^{1/r} \quad (10)$$

from which it is readily seen that

$$E^* = \left(E^r - \frac{X}{a} \right)^{1/r} \quad \text{if } E > \left(\frac{X}{a} \right)^{1/r}$$

and

$$E^* = 0 \quad \text{if } E \leq \left(\frac{X}{a} \right)^{1/r} \quad (11)$$

From equation (11), it follows that if the slab thickness is exactly $X = aE_0^r$, the incident proton of energy E will just reach zero energy at depth X .

Next we find

$$\frac{dg(E^*)}{dE^*} = \frac{E^{*r-1}}{\left(E^{*r} + \frac{X}{a}\right)^{\frac{r-1}{r}}} \quad (12)$$

Substituting the appropriate results of equations (9) to (12) into equation (4), we obtain

$$\phi_x(E^*) = \frac{HE^{*r-1}}{\left(E^{*r} + \frac{X}{a}\right)^{\frac{r+q-1}{r}}} \left(E_1^r - \frac{X}{a}\right)^{1/r} \leq E^* \leq \left(E_2^r - \frac{X}{a}\right)^{1/r} \quad (13)$$

where equation (11) must be satisfied for the limits. Figure 1(b) depicts the general appearance of the transformations between equations (9) and (13).

Equation (13) gives the proton differential energy spectrum at depth X for the incident spectrum given in equation (9), if we consider only ionization losses and the range energy equation, $R = aE^r$. At the present, the above formulation will be terminated and the improvisations developed by the writer will be undertaken.

The main improvement by the writer is the introduction of an approximation for the proton range which represents the theoretical data, such as presented in Sternheimer's article (ref. 2), with an accuracy of $\pm 4\%$, or better, for energies from around 5 MeV to over 1200 MeV. Also, the algebraic manipulation is essentially as elementary as that for the relationship, $R = aE^r$. The new empirical formula for the range is

$$R(E) = \frac{a}{2b} \ln(1 + 2bE^r) \quad (14)$$

where a , b , and r are determined by fitting the range data of reference 3 with the requirement to minimize the maximum relative error from 10 to 1000 MeV. If, in equation (14), $2bE^r \ll 1$, then $R \cong aE^r$.

Figure 2 depicts an error analysis of the approximating function of equation (14) compared to data presented in reference 3 for two different coefficients of r . In general practice, it appears that for $Z < 20$, a value of $r = 1.78$ is adequate, and for $Z > 20$, $r \leq 1.75$ should be

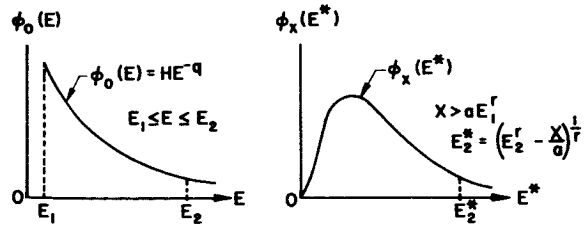


FIGURE 1(b).—Variation of spectrum shape as protons penetrate a shield.

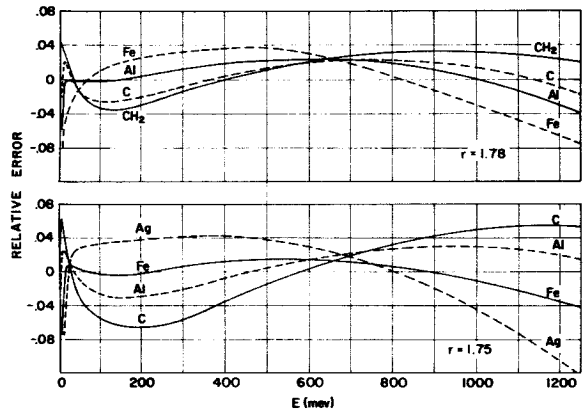


FIGURE 2.—The relative error in approximating proton range using equation (14).

used. However, in the case of mixed materials of medium and low Z , it seems that a compromise may be made and that, for a given calculation, one choice of r be adhered to, perhaps 1.78. Table I provides a summary of different values of a and b for different materials with r of 1.75 and 1.78. It should be noted that a value of $r = 1.8$ is also given for tissue; this will be discussed in the development of the methods used by the writer for dose calculations. Figure 3 is a comparison of the error in the range for aluminum when using equation (14) to the error in range when using $R = aE^r$.

Reverting to the original problem of this section, we develop the following relationships using equation (14) for the proton range. From equation (7),

$$\frac{a}{2b} \ln(1 + 2bE^r) = X + \frac{a}{2b} \ln(1 + 2bE^{*r})$$

or

$$\ln\left(\frac{1 + 2bE^r}{1 + 2bE^{*r}}\right) = \frac{2bX}{a} \quad (15)$$

TABLE I
Coefficients for the Range Equation

Material	r=1.75		r=1.78	
	a	b	a	b
Carbon.....	2.58×10 ⁻³	1.2×10 ⁻⁶	2.33×10 ⁻³	2.0×10 ⁻⁶
Aluminum.....	3.10	1.9	2.77	2.5
Iron.....	3.70	2.6	3.26	3.0
Copper.....	3.85	2.7	3.40	3.25
Silver.....	4.55	3.7	-----	-----
Tungsten.....	5.50	4.2	-----	-----
Polyethelene.....	2.15	1.1	1.95	1.7
Tissue ^a	2.32	1.2	2.11	2.0
Water.....	2.32	1.2	2.10	2.0
Air.....	2.68	1.4	2.41	2.1
SiO ₂	2.87	1.7	2.58	2.5
Glass.....	3.17	2.1	2.83	2.8

^a For stopping power in tissue: r₀=1.80, a₀=1.943×10⁻³, b₀=2.273×10⁻⁶.

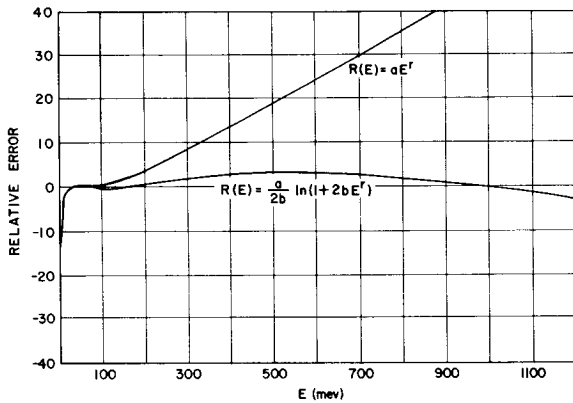


FIGURE 3.—Comparison of relative error in proton range using equation (8) and equation (14).

Solving for E, we obtain

$$E = g(E^*) = (A + BE^{*r})^{1/r} \tag{16}$$

where

$$B = \exp\left(\frac{2bX}{a}\right) \text{ and } A = \frac{1}{2b}(B-1)$$

From equation (16) it follows that

$$E^* = \left(\frac{E^r - A}{B}\right)^{1/r}$$

if $E > A^{1/r}$ and

$$E^* = 0 \text{ if } E \leq A^{1/r} \tag{17}$$

It is worth noting that if $\frac{2bX}{a} \ll 1$, then $A \approx X/a$ and $B \approx 1$. (See equation 10.) For example, with carbon, $2bX/a = 1.717 \times 10^{-3} X$ and for $X \leq 10$ gm/cm², the above approximation is quite valid. The foregoing analysis demonstrates why the simple range formula ($R = aE^r$) gives good results when X is not too large ($X \leq 20$ gm/cm² and $E \lesssim 250$ MeV). Next, the differentiation of $g(E^*)$ gives

$$\frac{dg(E^*)}{dE^*} = \frac{BE^{*r-1}}{(A + BE^{*r})^{r-1/r}} \tag{18}$$

Substituting the above into equation (4), we obtain

$$\phi_X(E^*) = \frac{\phi_0\{g(E^*)\}BE^{*r-1}}{(A + BE^{*r})^{r-1/r}} \tag{19}$$

There are two choices of the incident differential energy spectrum in vogue at present; the first is that given by equation (9) or else a family of N such curves given by

$$\phi_i(E) = H_i E^{-\alpha_i}, \quad E_i \leq E \leq E_{i+1} \tag{20}$$

where $i = 1, 2, 3, \dots, N$. The second choice of representation is given by the integral rigidity spectrum

$$N(>p) = N_0 e^{-p/p_0} \text{ (protons/cm}^2\text{)} \quad p > p_0 \tag{21}$$

where p and p_0 are in rigidity units of MV (millionvolts). From equation (21) the differential rigidity spectrum becomes

$$\phi(p)dp = -dN(>p) = \frac{N_0}{p_0} e^{-p/p_0} dp, \quad p > p_1 \quad (22)$$

In order to represent the above momentum rigidity units in energy (MeV) units, it is sufficient to use the relativistic relationship between variables given by

$$(pze)^2 = E^2 + 2Em_0$$

or

$$p = \sqrt{E^2 + 1876E} \quad (23)$$

where $(ze) = 1$ electron charge for protons, $m_0 = 938.23$ (the rest mass of the proton in MeV units), p is in MV, and E is in MeV. (Note that $\Delta V = \text{work}/q$; in basic physics the potential difference is thus defined and, hence, eq. (23) is dimensionally valid.) Next, using a change of variable technique, we obtain

$$\phi(E)dE = -dN(>p(E)) = \frac{N_0}{p_0} e^{-\frac{p(E)}{p_0}} \left| \frac{dp}{dE} \right| dE, \quad p > p_1 \quad (24)$$

where

$$\frac{dp}{dE} = \left(\frac{E + m_0}{\sqrt{E^2 + 2m_0E}} \right)$$

Substituting dp/dE into equation (24), we obtain

$$\phi(E)dE = \frac{N_0(E+938)}{p_0\sqrt{E^2+1876E}} \exp \left(-\frac{\sqrt{E^2+1876E}}{p_0} \right) dE, \quad E > E_1 \quad (25)$$

where

$$E_1 = \sqrt{p_1^2 + (938)^2} - 938$$

and $\phi(E)$ has the units of protons/cm² MeV. The validity of the above transformation follows from elementary probability theory of distribution functions or else elementary calculus, depending on the reader's academic orientation.

Referring to equation (19) it is of interest to obtain the proton differential energy spectrum at a depth X using the incident spectrums of

equations (20) and (21). Using the incident spectrum of equation (20) we obtain:

$$\phi_x(E^*) = \frac{H_i B E^{*r+1}}{(A + B E^{*r})^{\frac{r+q_i-1}{r}}} \left(\frac{E_i^r - A}{B} \right)^{1/r} \leq E^* \leq \left(\frac{E_{i+1}^r - A}{B} \right)^{1/r} \quad (26)$$

where equation (17) must be satisfied; $B = \exp(2bX/a)$ and $A = (B-1)/2b$. Using the rigidity spectrum of equation (21) we obtain (from equation (25)):

$$\phi_x(E^*) = \frac{N_0(s+938) B E^{*r-1} \exp(-\sqrt{s^2+1876s/p_0})}{p_0 s^{r-1} \sqrt{s^2+1876s}} \quad (27)$$

where

$$s = (A + B E^{*r})^{1/r}; \quad E^* > \left(\frac{E_i^r - A}{B} \right)^{1/r};$$

and

$$E_i = \sqrt{p_i^2 + 879,844} - 938$$

The use of s was simply to shorten the size of the expression in equation (27). Examples of typical differential energy spectra as a function of depth X in aluminum are given in figures 4 and 5 illustrating the evaluation of equations (26) and (27).

MULTILAYER SHIELDS

The above discussion is equally well applied to stratified layers of different materials. Figure 6 illustrates the parameters involved. In order to see the nature of the derivation for multiple layers of different materials, two layers will be considered initially. Referring to equation (16) let us define

$$A_1 = \frac{1}{2b_1} [B_1 - 1] B_1 = \exp \left(\frac{2b_1 X_1}{a_1} \right)$$

and consequently,

$$E_0^r = A_1 + B_1 E_1^r \quad (28)$$

where a_1 and b_1 are the material coefficients of equation (14); X_1 refers to the thickness of the first layer with E_0 and E_1 denoting the energies respectively incident on the first layer and

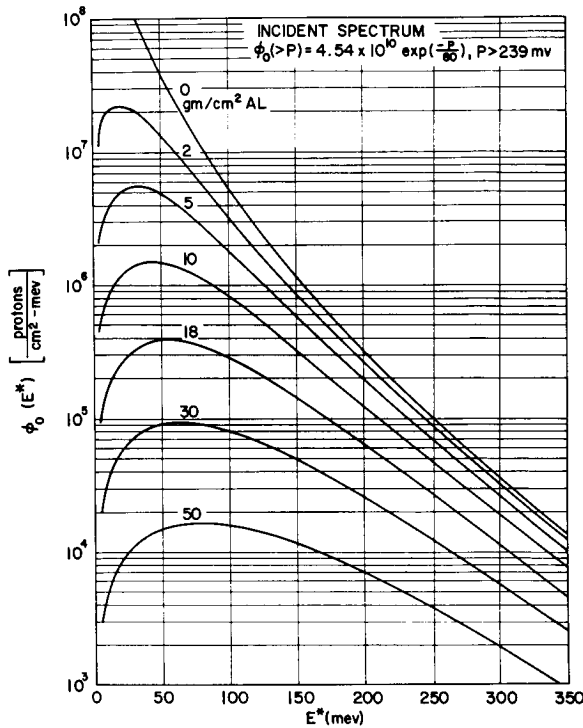


FIGURE 4.—Proton differential energy spectrum at different depths in aluminum.

transmitted through the first layer. Now applying the relationship of equation (7) to the second layer, we obtain

$$\frac{a^2}{2b_2} \ln(1 + 2b_2 E_1^r) = X_2 + \frac{a_2}{2b_2} \ln(1 + 2b_2 E_2^r)$$

Simplifying,

$$E_1^r = A_2 + B_2 E_2^r \tag{29}$$

where

$$B_2 = \exp\left(\frac{2b_2 X_2}{a_2}\right)$$

and

$$A_2 = \frac{1}{2b_2} [B_2 - 1]$$

Substituting E_1^r of equation (29) into equation (28), we obtain

$$E_0^r = A_1 + B_1(B_2 E_2^r + A_2) = (A_1 + B_1 A_2) + B_1 B_2 E_2^r \tag{30}$$

Equation (30) expresses the energy at a depth of X_2 in the second layer in terms of the energy incident on the first layer. If this is repeated

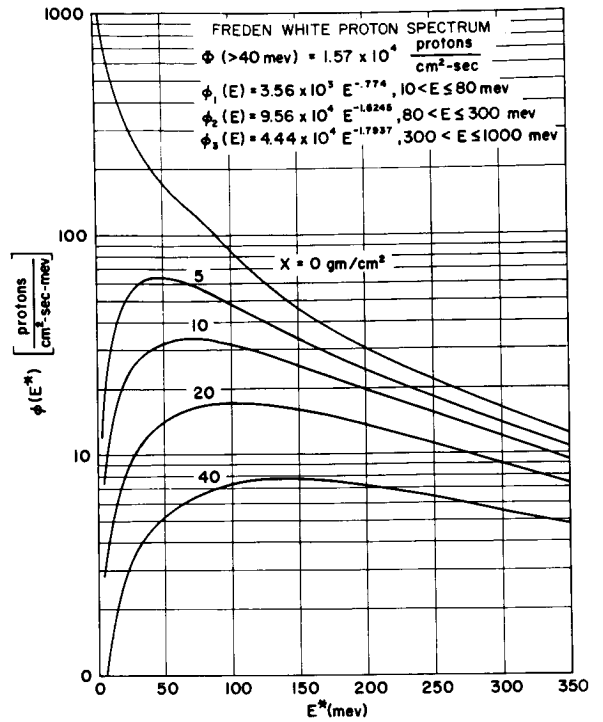


FIGURE 5.—Proton differential energy spectrum at different depths in aluminum, Freden and White proton spectrum.

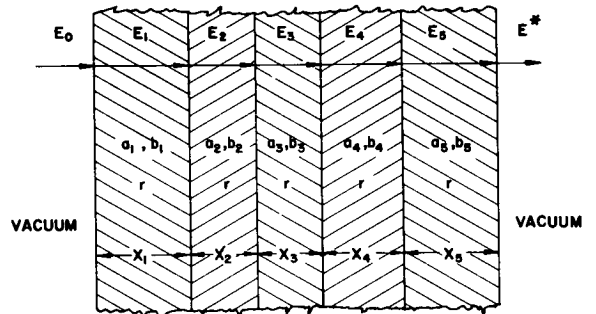


FIGURE 6.—Multilayer shields and associated parameters.

for N layers one obtains:

$$E^r = A^* + B^* E^{*r} \tag{31}$$

where E is the incident energy on the first layer and E^* is the energy at the end of the N th layer; and,

$$A^* = A_1 + A_2 B_1 + A_3 B_1 B_2 + \dots + A_N B_1 B_2 B_3 \dots B_{N-1}$$

$$B^* = B_1 B_2 B_3 \dots B_N \tag{32}$$

where $B_i = \exp\left(\frac{2b_i X_i}{a_i}\right)$, $A_i = (B_i - 1)/2b_i$, and $i = 1, 2, \dots, N$. This fairly simple representation of the energy as a function of depth and layer thicknesses of different materials is brought about by the fact that r is assumed to be constant for all materials considered. In shield optimization techniques, such a representation should be promising. Since equation (31) has the same form as equation (16), it follows that the coefficients A , B may be replaced by A^* , B^* whenever multilayer shields are considered. Thus, all results obtained in the preceding or subsequent sections can be extended to multiple layers by using A^* , B^* for A , B . In the special case where $2bX/a \ll 1$, that is, ($R \cong aE^r$) then for the i th layer $B_i = 1$, $A_i = X_i/a_i$ and for N layers

$$E^r = E^{*r} + \sum_{i=1}^N \left(\frac{X_i}{a_i}\right) \quad (33)$$

NONELASTIC PROTON COLLISIONS AND SECONDARIES

It was pointed out in the introduction to this paper that elastic scattering off a nucleus by high energy protons (>20 MeV) is highly forward with trivial reduction in energy. This assumption is not as valid for proton collisions in hydrogen, but this problem will not be treated here. It is worth mentioning that the so-called range straggling associated with energetic protons is an effect mainly due to elastic collisions with electrons. However, this type of error is usually quite small and can be represented approximately for protons by

$$\sigma_R \cong 0.015R \quad (34)$$

where σ_R is the standard deviation of a Gaussian distribution depicting the statistical fluctuation of the range about a mean range R (p. 662, ref. 4). This can be interpreted as meaning that 95% of monoenergetic protons should have a measured range within about $\pm 3\%$ of the theoretical range calculated from ionization losses only. This is not a bad error for shielding calculations since the proton energy spectrum always contains uncertainties of a much greater order of magnitude. This error is also in keeping with the use of the approximation for the

range introduced by the writer (eq. (14)). Examination of the error curves in figure 2 shows that for energies from less than 10 MeV to over 1000 MeV, the coefficients (a , b , r) can be chosen to maintain a maximum variation of less than 4% from an accurate theoretical calculation.

In the treatment of nonelastic cross sections the writer has represented the cross section as a function of energy and mass number using an empirical expression which is amenable to obtaining closed form solutions in the mathematical operations necessary to obtain transmitted flux and dose rates. The greatest constraint in obtaining an accurate expression for cross sections is the lack of adequate experimental nonelastic cross sections in the range of 5 MeV to 50 MeV for protons. There are a few values at widely separated energies. However, the low-energy cross section seems to resemble that of neutrons to some extent, and for energies from 5 MeV to 18 MeV the nonelastic cross section of neutrons taken from Troubetzkoy (ref. 5) were used for the protons with a Coulomb correction in energy. Then the low-energy cross sections were blended into the proton nonelastic cross section at higher energies. For proton energies in the range of 200 to 2000 MeV, the nonelastic cross section is fairly well represented by

$$\sigma_{ne} = 0.38 \left(\frac{A}{27}\right)^{0.73} [\text{barns}] \quad (35)$$

The reason for choosing the ratio ($A/27$) in equation (35) is that the nonelastic cross sections for aluminum ($A=27$) will be the basis for the empirical formulas which are developed below. The requirements for such a formula are that the values of the cross section should be zero at zero energy, have a maximum between 5 and 25 MeV, and be approximately a constant (asymptote) as the energy exceeds, say, 200 MeV. Equation (36) satisfies these requirements with some degree of success, in addition to being tailored for further mathematical operations:

$$\sigma_{ne}(E) = \frac{0.38 \left(\frac{A}{27}\right)^{0.73} E^{2r} + dE^r}{E^{2r} + fE^r + g} \quad (36)$$

where d , f , g are constants to be determined by curve fitting techniques and $r (=1.78)$ is the

same power as used in the range equation (14). Details of the methods used to treat the above cross sections and the conclusions of the analysis are given in reference 6.

PROTON DOSE RATE CALCULATIONS

The next step in this development is to derive expressions for the primary proton tissue dose or dose rate as a function of shield thickness and/or depth dose in tissue. This is obtained as follows. For the general case after penetrating a depth x in a shield, the dose rate is simply given by

$$D_x = \bar{F} \int_{E_1^*}^{E_2^*} e^{-\int_0^x \Sigma_{E(x)} dx} \phi_x(E^*) S(E^*) dE^* \quad (37)$$

where the energy E^* is taken at the penetration depth x . The $S(E^*)$ is the stopping power in tissue and is given by equation (1). The \bar{F} is a flux-to-dose conversion factor depending on units of flux. The stopping power formula for tissue can be made compatible with the approximating range equation, (14), in the following manner. Using the definition of equation (2), we see that

$$S(E) = -\frac{dE}{dR} = \frac{1}{\frac{d}{dE} \left[\frac{a_0}{2b_0} \log_e (1 + 2b_0 E^{r_0}) \right]}$$

or

$$S(E) = \left(\frac{1}{a_0 r_0} \right) E^{1-r_0} + \frac{2b_0}{a_0 r_0} E \quad (38)$$

where a_0 , b_0 , r_0 are corresponding range coefficients for tissue (fig. 7). Using the approximations suggested in reference 6 for the non-elastic cross sections, we can write the proton dose rate after transmitting several layers including tissue in the last layer in the following way:

$$D_x = \bar{F} \int_{E_1^*}^{E_2^*} \left(\frac{E_2^* - A^*}{B^*} \right)_{1/r} e^{-(\Sigma_1 X_1 + \Sigma_2 X_2 + \dots)} \phi(E^*) \left\{ \frac{E^{*1-r_0}}{a_0 r_0} + \frac{2b_0 E^*}{a_0 r_0} \right\} dE^* \quad (39)$$

The flux $\phi(E^*)$ is given by either equation (26) or equation (27) with the constants A^* , B^* defined for multiple layers as shown in equation (32). Also, it should be noted that the r power

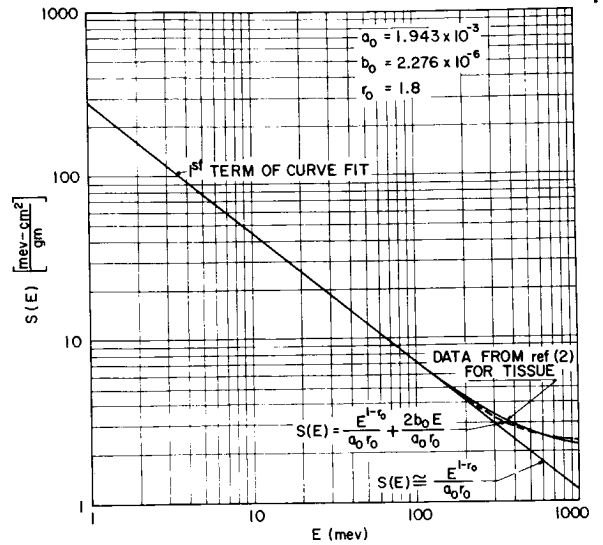


FIGURE 7.—Stopping power of protons in tissue using approximation methods.

used in equation (32) is constant for all layers; however, the r_0 power used in the stopping power may be different. In fact, in all calculations presented in this paper for dose the r is chosen to be 1.78 for the shielding materials, but r_0 is 1.80 for the stopping power in tissue. This flexibility permits a small increase in accuracy with little loss in computational speed when numerical integration methods are employed. It should be pointed out that if equation (26) is used for the energy flux, then for each energy sector of the spectrum confined between two energies E_{i+1}^* and E_i^* , another integral analogous to equation (39) is required, but the integration limits change with the H_i , q_i for each sector. However, this is conveniently carried out in a numerical integration process by using the coefficients H_i , q_i which are necessary to satisfy the limits of equation (26) at the energy E^* . Very often it is useful to examine the integrand as a function of E^* . In this manner, a feeling is obtained for the important energy regions in terms of dose. Also, the slope of this curve should indicate the width of energy intervals necessary for an accurate numerical calculation. Thus, the differential proton dose is calculated as follows:

$$\frac{dD_x}{dE} = \bar{F} e^{-(\Sigma_1 X_1 + \Sigma_2 X_2 + \dots)} \phi(E^*) S(E^*) \frac{\text{rads}}{\text{MeV}} \quad (40)$$

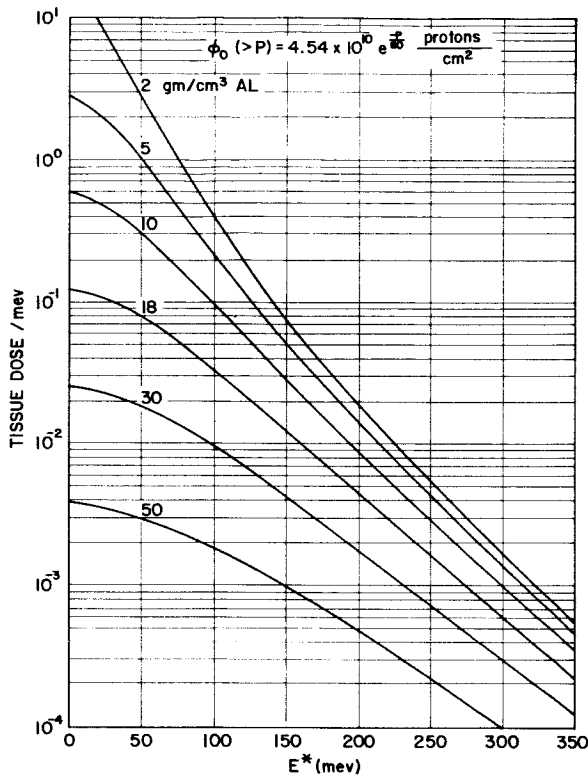


FIGURE 8.—Differential proton dose in aluminum.

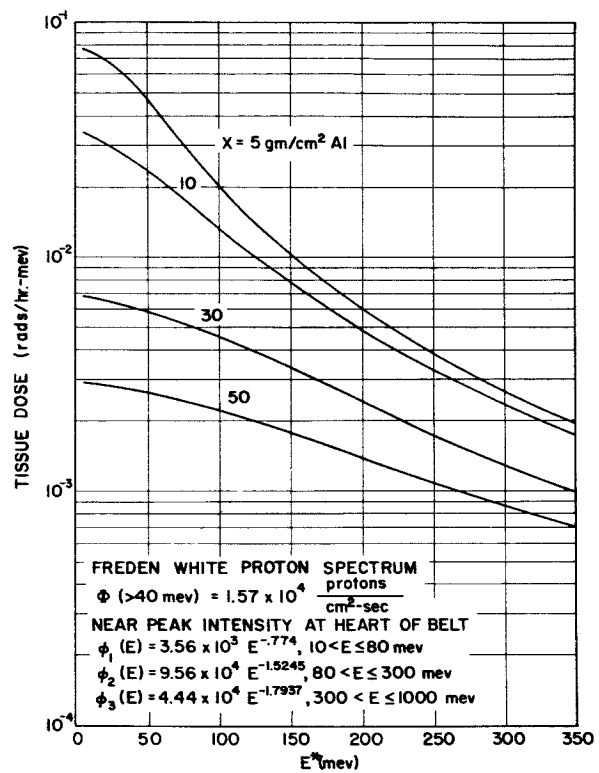


FIGURE 9.—Differential proton dose in aluminum, Freden and White proton spectrum.

Examples of equation (40) are shown in figures 8 and 9. The proton dose as a function of depth, calculated from equation (39), is shown in figures 10 and 11. In the latter two figures, there is a curve labeled "Total Estimated Dose"; this refers to an approximation of dose in rads which corrects for the secondary protons and neutrons generated by nonelastic collisions. The correction is based on the observation that for a shield of low-*Z* materials the number of secondary protons and neutrons per nonelastic collision at energies below around 200 MeV is less than one cascade particle of each kind (protons and neutrons). With the above observation and other considerations, it became plausible to conjecture that if the non-elastic attenuation factor $\exp(-\Sigma_{ne}X)$ is omitted in the dose calculation, then a correction is made for the secondary particles. The foregoing is the correction made in this paper for the calculations of the "Total Estimated

Dose." Thus,

Total Estimated Dose=Primary Proton Dose

$$\times \exp(\Sigma_1 X_1 + \Sigma_2 X_2 + \dots) \quad (141)$$

Of course such an approximation is valid only within certain fixed limits of shield thickness, *Z* number of target, and energy of colliding protons. However, to lend validity to the above assumption, figure 12 is presented. The secondary data in figure 12 were generated by C. W. Hill of Lockheed (ref. 3). The interesting result is that the approximation of equation (41) is rather accurate for dose in rads for the thicknesses of aluminum shown. The approximation will probably become less dependable at greater thicknesses, but at these greater depths the total dose is substantially smaller, and even a fairly large error in estimating secondary contributions may be unimportant from a practical point of view. Table II provides an analysis of figure 12.

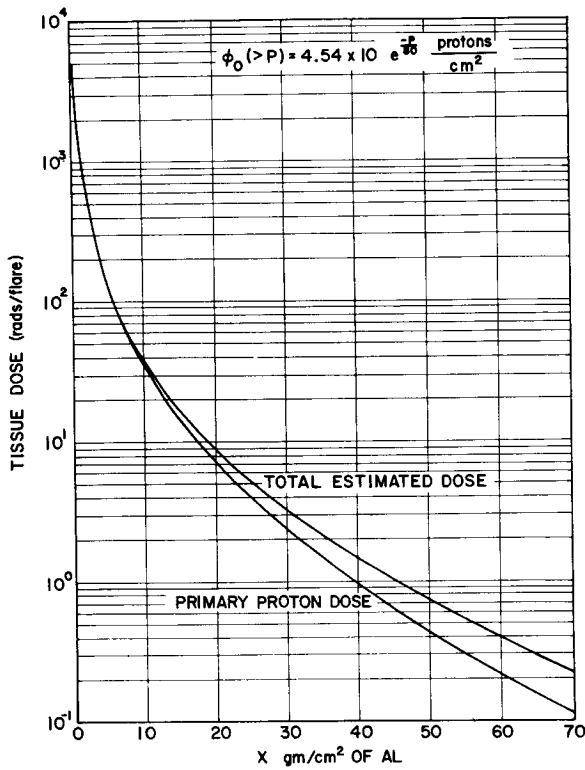


FIGURE 10.—Proton dose at center of sphere.

Some useful simplifications in equation (39) can be made if a power law input spectrum (eq. (26)) is used. Thus, the dose rate is represented by

$$D_x = F \exp [-\Sigma_1 X_1 - \Sigma_2 X_2 - \dots] \int \frac{(E_{i+1} - A^*)^{1/\tau}}{(E_i - A^*)^{1/\tau}} \frac{H_i B^* E^{*r-1}}{(A^* + B^* E^{*r})^{\tau + q_i - 1}} \left(\frac{E^{*1-r_0}}{a_0 r_0} + \frac{2b_0 E^{*r}}{a_0 r_0} \right) dE^* \quad (42)$$

where A^* , B^* are defined for multiple layers in equation (32). If we make the change of variables indicated by

$$E^{*r} = \left(\frac{A^*}{B^*} \right) \left(\frac{t}{1-t} \right)$$

or

$$t = \frac{B^* E^{*r}}{A^* + B^* E^{*r}} \quad dE^* = \left(\frac{A^*}{B^*} \right)^{1/\tau} \frac{t^{\frac{1}{\tau}-1} dt}{r(1-t)^{\frac{r+1}{\tau}}} \quad (43)$$

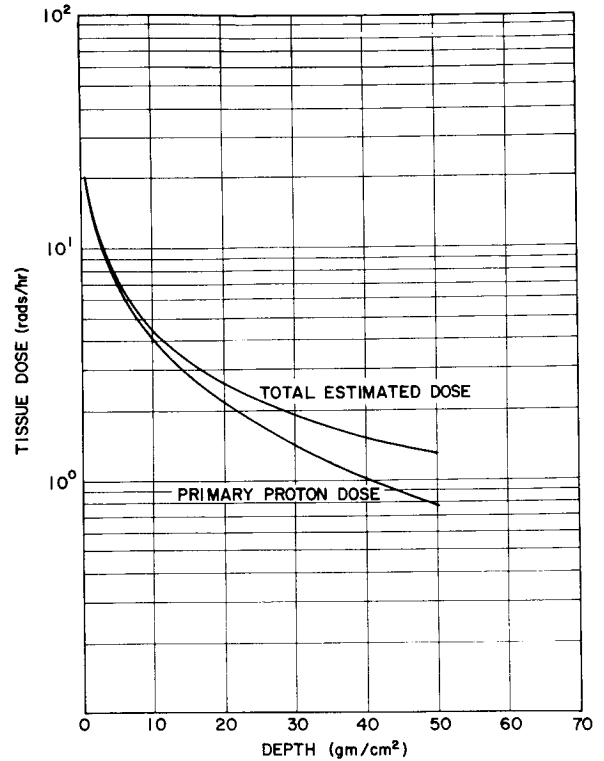


FIGURE 11.—Proton dose at center of sphere, Freden and White proton spectrum.

and

$$m = \frac{1+r-r_0}{r}, \quad n = \frac{r_0 + q_i - 2}{r} \quad (44)$$

$$m^* = \frac{r+1}{r}, \quad n^* = \frac{q_i - 2}{r}$$

we obtain, after some simplification,

$$D = \frac{F \exp (-\Sigma_1 X_1 - \Sigma_2 X_2 - \dots) H_i}{a_0 r_0 r A^* \frac{q-2}{r} B^{*1/\tau}} \left\{ \left(\frac{B^*}{A^*} \right)^{\frac{r_0}{r}} \int_{1-A^* E_i^{-r}}^{1-A^* E_{i+1}^{-r}} t^{m-1} (1-t)^{n-1} dt + 2b_0 \int_{1-A^* E_i^{-r}}^{1-A^* E_{i+1}^{-r}} t^{m^*-1} (1-t)^{n^*-1} dt \right\} \quad (45)$$

where the lower limit is set to zero if $A^* \geq E_i^{*r}$. This condition is met when the minimum proton energy E_i has a range equal to or less than the minimum shield thickness. For example, if $E_i = 30$ MeV, then any aluminum thickness greater than 1.175 gm/cm² would cause the lower limit to be zero. Thus, one can always

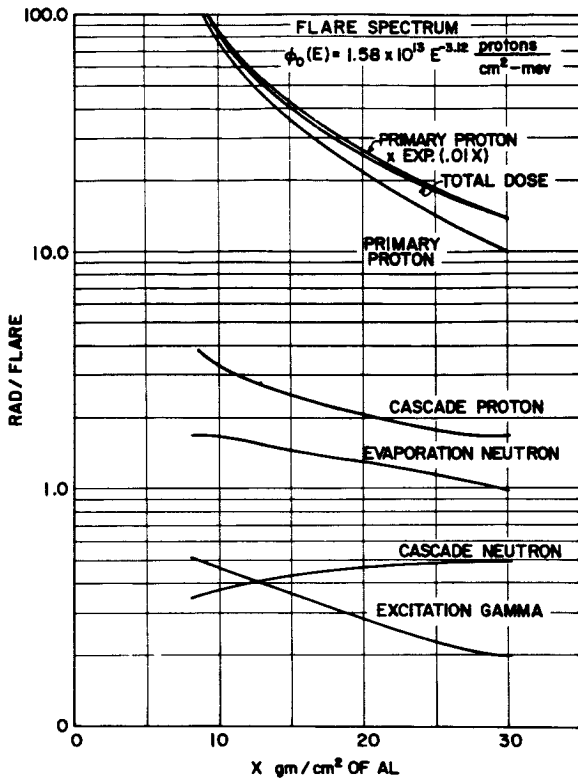


FIGURE 12.—Comparison of approximation method for total dose to detailed calculation of total dose.

choose a thickness of shield so that the integral of equation (45) may be written as:

$$D = \phi \left\{ \psi \int_0^\alpha t^{m-1}(1-t)^{n-1} dt + 2b_0 \int_0^\alpha t^{m^*-1}(1-t)^{n^*-1} dt \right\} \quad (46)$$

where

$$\phi = \frac{F \exp(-\Sigma_1 X_1 - \Sigma_2 X_2 - \dots) H_i}{a_0 r_0^2 A^* \frac{q-2}{r} B^{*1/r}}$$

$$\psi = \left(\frac{B^*}{A^*} \right)^{\frac{r_0}{r}}, \text{ and } \alpha = 1 - A^* E_{i+1}^{-1/r}$$

However, the integrals are now recognized as incomplete beta functions. Thus, one may

write the dose as simply

$$D = \phi \{ \psi \beta_\alpha(m, n) + 2b_0 \beta_\alpha(m^*, n^*) \} \quad (47)$$

Now, if the assumption is made that the initial upper energy limit E_{i+1} is sufficiently large, then the value of α approaches 1. Thus, the further simplification in terms of gamma functions is made:

$$D = \phi \left\{ \psi \frac{\Gamma(m)\Gamma(n)}{\Gamma(m+n)} + 2b_0 \frac{\Gamma(m^*)\Gamma(n^*)}{\Gamma(m^*+n^*)} \right\}, \quad q > 2 \quad (48)$$

If the stopping power coefficient b_0 for tissue is set to zero, we get simply:

$$D = \phi \psi \frac{\Gamma(m)\Gamma(n)}{\Gamma(m+n)}, \quad q > 2 - r \quad (49)$$

Equation (49) should be used when $n^* \leq 0$, ($q \leq 2$). Finally, if all b_i are set to zero for the range coefficients, then $B^* = 1$ and $A^* = X_1/a_1 + X_2/a_2 + \dots$; and if $r_0 \equiv r$ we obtain the version of the simplest feasible model for proton dose rate calculations (see eq. (13)),

$$D = \frac{FH \exp(-\Sigma_1 X_1 - \Sigma_2 X_2 - \dots)}{a_0 r^2 \left(\frac{X_1}{a_1} + \frac{X_2}{a_2} + \dots \right)^{\frac{r+q-2}{r}}} \frac{\Gamma\left(\frac{1}{r}\right) \Gamma\left(\frac{r+q-2}{r}\right)}{\Gamma\left(\frac{r+q-1}{r}\right)} \quad (50)$$

The above equations have the defect that the incident proton energy spectrum is represented by only one power function $\phi_0(E) = HE^{-q}$, $E > E_0$ and in equation (50) the range is depicted by the simple relation $R = aE^r$. However, the results obtained by using equation (48) are quite impressive as is demonstrated in figures 13, 14, and 15 by comparison to Alsmiller (ref. 7) and Hill (ref. 3). For greater details in both methods and results, see reference 6.

TABLE II

Data Analysis of Figure 12

Z, gm/cm ²	Dose of primary protons	Total dose of secondaries	Total dose	Primary dose × exp (.01Z)	% Diff.
10	73.5	5.8	78.8	80.6	2.3
15	36.0	4.7	40.7	41.8	2.7
20	21.5	4.2	25.7	26.2	2.0
25	14.2	3.7	17.9	18.2	1.7
30	10.0	3.4	13.4	13.5	.75

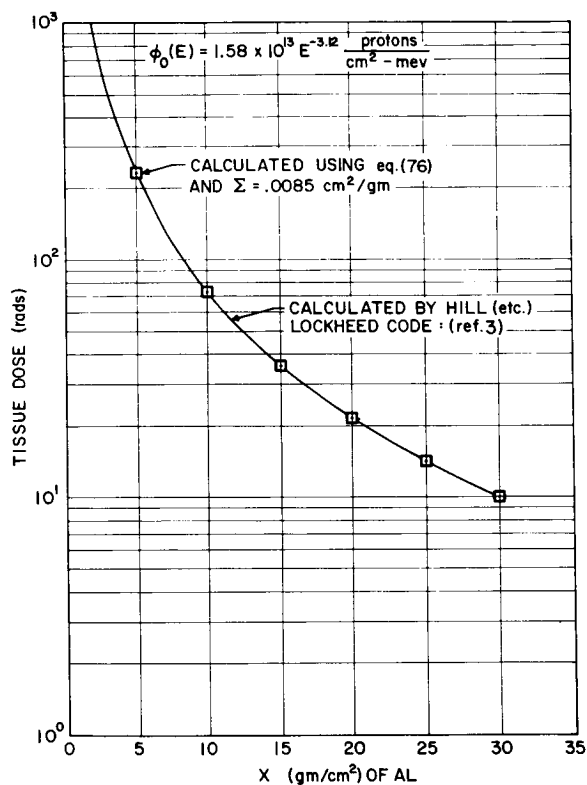


FIGURE 13.—Comparison of analytical calculation of dose to numerical methods.

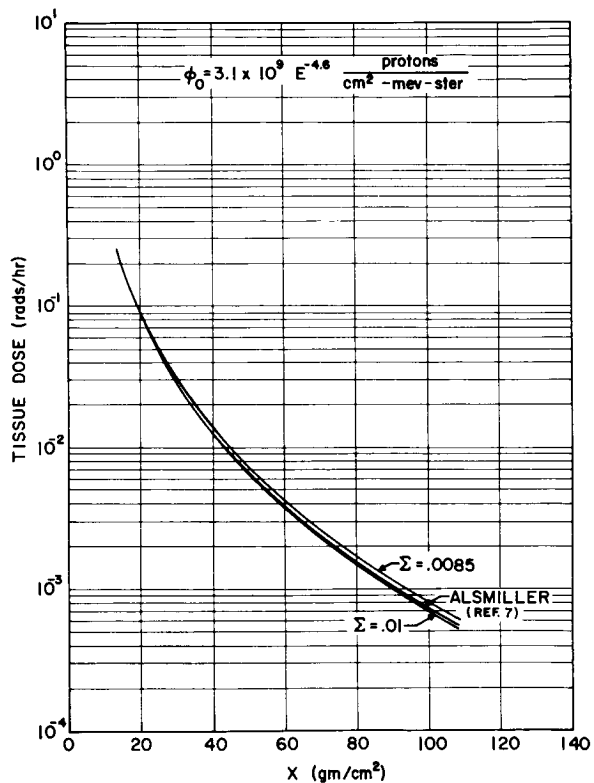


FIGURE 14.—Comparison of analytical calculation of dose to numerical methods.

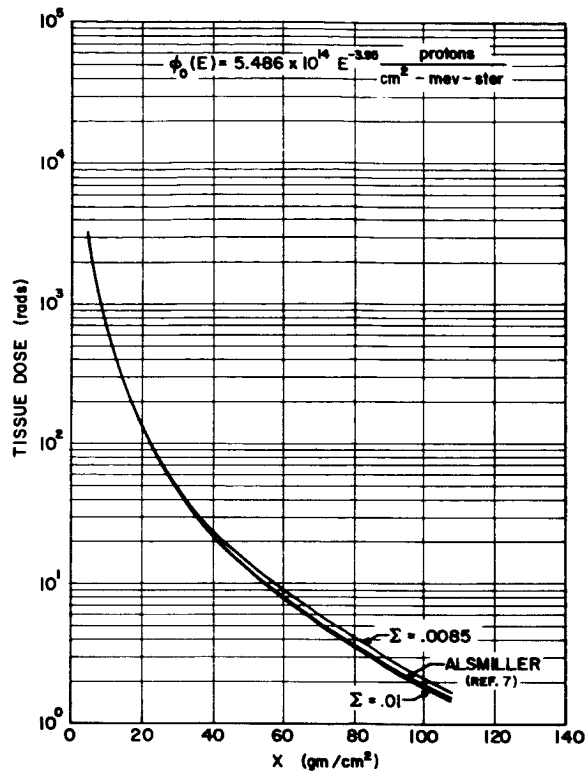


FIGURE 15.—Comparison of analytical calculation of dose to numerical methods.

REFERENCES

1. WILSON, R. R.: Phys. Rev., vol. 71, 385L, chap. 22, sec. 3, 1947.
2. STERNHEIMER, R. M.: Range-Energy Relations for Protons in Be, C, Al, Cu, Pb, and Au. Phys. Rev., vol. 115, 1959, p. 137.
3. HILL, C. W. ET AL.: Computer Programs for Shielding Problems in Manned Space Vehicles. ER-6643, Lockheed-Georgia Co., Jan. 1964.
4. EVANS, ROBLEY D.: The Atomic Nucleus, McGraw-Hill Co., 1955.
5. TROUBETZKOY, E. S.: Fast Neutron Cross Sections of Iron, Silicon, Aluminum, and Oxygen. Nuclear Development Corp. of America, NDA 2111-3, vol. C, Nov. 1959.
6. BURRELL, M. O.: The Calculation of Proton Penetration and Dose Rates. Marshall Space Flight Center, NASA TM X-53063.
7. ALSMILLER, ET AL.: Neutron Physics Div., Space Radiation Shielding Research Annual Progress Rept., Aug. 31, 1962, ORNL 62-10-29 (papers 1-10), pp. 148-155.

N65-34631

55—Local Dose From Proton and Alpha Particle Enders Behind Complex Shield Systems¹

HERMANN J. SCHAEFER

U.S. Naval School of Aviation Medicine

Flux ratios as high as 1 to 1 for protons/alpha particles in the integral rigidity spectra of some flare produced solar particle beams have been reported. Evaluation of tissue depth doses for the shield configuration of the Apollo vehicle shows that the alpha component contributes significantly to total exposure only for low shielding and only in the superficial layers of a tissue target. The fractional high LET dose due to alpha enders, however, is substantially larger than the corresponding dose from proton enders even at greater depths. Separate measurement of the high LET fraction of total dose and proper determination of RBE and QF factors, therefore, seems of even greater importance for the alpha component than for protons.

Balloon and rocket recordings of major solar flares during the maximum of the past solar cycle indicate that, for some flares, the additional particle flux contains a substantial fraction of alpha particles. The identification of alpha particles in rocket and balloon-borne counters or ionization chambers encounters some difficulties because the bulk of the alpha flux is limited to energies which correspond to rather small values of penetrating power. As a consequence, atmospheric and instrument cut-off effects severely restrict instrument response. On the other side, the low penetration of the alpha component reassures that, for a human target shielded by a space suit and wall and equipment of a vehicle, the residual radiation intensities will be substantially lower than those from protons even if the incident beam would contain equal fluxes of the two components. Nevertheless, the recordings indicate that for some large flare events the residual alpha dose rates for lower shield thicknesses are entirely comparable to proton dose rates.

¹ Research sponsored by the National Aeronautics and Space Administration under contract R-75. Opinions or conclusions contained in this report are those of the author. They are not to be construed as necessarily reflecting the view or the endorsement of the Navy Department.

Much concern has been stirred up by the communication of Freier and Webber (ref. 1) that for some flare events the flux ratio of alpha particles to protons is as high as 1 to 1 if fluxes are expressed in terms of the integral rigidity spectrum. In order to see this statement in its proper perspective for the problem of radiation hazards, one should realize that comparing a proton and alpha particle flux of the same magnetic rigidity is a rather artificial proposition. The rigidity of a charged particle is inversely proportional to the radius of curvature of its track in a magnetic field. Rigidity can also be expressed as momentum per unit charge. Rigidity and depth of penetration or range are entirely disparate magnitudes. In comparing protons and alpha particles in particular, the rigidity spectrum is in no way a measure of residual fluxes behind shields. As alpha particles have two mass units per unit charge and protons only one, equal integral fluxes of the same rigidity represent very different fluxes in terms of momentum or energy or range spectrum. The range spectrum in particular is a very useful description of particle fluxes if problems of shielding and depth doses in a human target are to be analyzed (ref. 2).

Figure 1 tries to explain the relationships involved in more detail. The upper graph shows

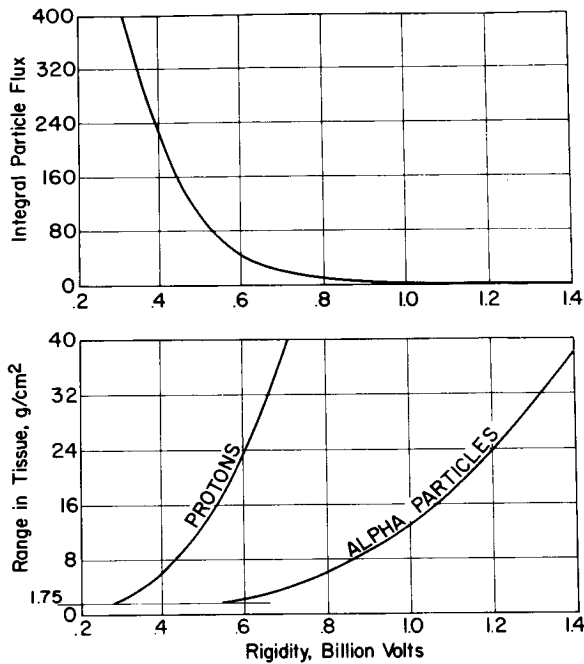


FIGURE 1.—Typical rigidity spectrum of solar particle beam and range/rigidity function of protons and alpha particles.

a typical integral rigidity spectrum of the particle flux for a large flare event. The spectrum exhibits the basic feature of all flare beams, that flux steeply drops with increasing rigidity. The lower graph of the same figure shows, over the same rigidity scale as abscissa, the ranges in tissue for protons and alpha particles. It is evident that for a given rigidity the corresponding ranges of protons and alpha particles differ greatly. For instance, for 0.6 GV rigidity, an alpha particle has a range of 2 g/cm² and a proton of almost 24 g/cm². Figure 2 shows the rigidity spectrum of the upper graph of figure 1 converted into the differential range spectrum. It is seen that the spectrum splits up into different graphs, one for protons and one for alpha particles. However, this actually simplifies the analysis because the range spectra allow direct comparisons of fluxes that would reach the same depth in tissue or shielding material. It is interesting to see that for low and very low shielding the alpha flux drops much more steeply toward greater depths than the proton flux. This indicates that possible objectionable exposures from flare

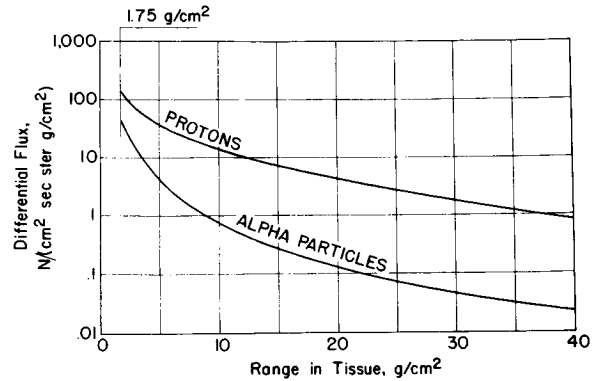


FIGURE 2.—Differential range spectra for one-to-one flux ratio of rigidity spectra.

produced alpha particles can occur only for low shielding as, for instance, for an astronaut outside the vehicle merely protected by his space suit.

It seems of special interest to carry out a detailed comparison of the depth dose distributions for the proton and alpha component of the flare spectrum of figure 2. Since the local flux in a target behind shielding contains particles of all energies from zero to very high values, the local ionization dosage is produced at LET values covering a similarly wide range from very high to low values. Therefore, a complete dosimetric evaluation would call for separate determination of the high LET fraction of the total ionization dose to which RBE factors larger than 1.0 would have to be assigned. The determination of absorbed doses for the proton and alpha component of the flare spectrum of figure 2, therefore, has been carried out separately for both the total absorbed dose and the high LET fraction of it. The results for a unidirectional beam normally incident on a semi-infinite slab of tissue are presented in figure 3. The upper graph shows total doses and the lower one fractional doses produced at LET values of 40 keV/micron_T and higher. A comparison of the total doses from protons and alpha particles shows that even at the lowest depth of 1.75 g/cm² the contribution of the alpha component is quite small and becomes altogether negligible toward greater depths. However, in extrapolating the graphs toward the left to shield thicknesses below 1.75 g/cm² one suspects that for low and very low

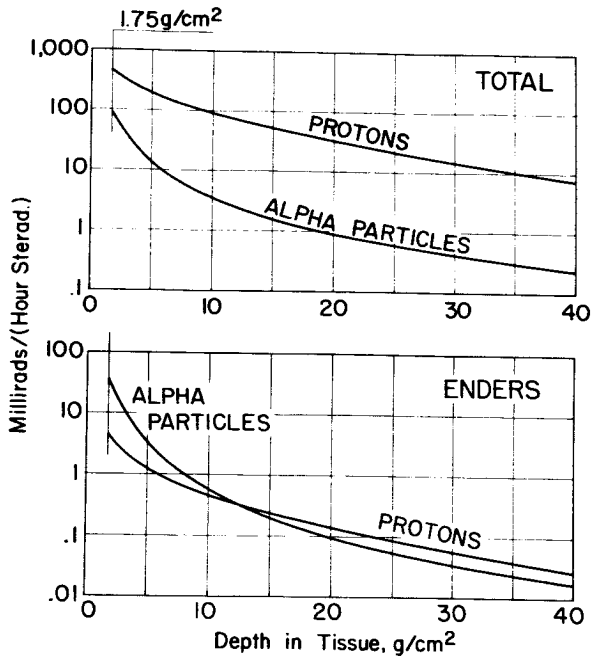


FIGURE 3.—Total and enders dose rate in tissue for unidirectional beam of flare particles.

shielding the situation becomes quite different with the alpha dose approaching and possibly surpassing the proton dose. Actual computation of doses below 1.75 g/cm² has not been carried out because the spectral section of the incident beam which would produce the absorbed dose in the superficial layers of the tissue slab is experimentally not well defined.

Radiobiologically very significant is the fact that the fractional high LET dose of the alpha component is substantially larger than the fractional proton dose down to tissue depths in excess of 10 g/cm². Furthermore, the ratio of fractional high LET to total dose for the alpha component is always substantially larger than for the proton component. For the system described in figure 3, the ratio for the alpha component starts, at 1.75 g/cm², with a value of 35 percent as compared to a value of 1 percent for the proton component at the same depth. This shows that, radiobiologically, the proton and alpha components represent two basically different quantities. For the former, the fractional high LET dose is so small that it would have to be considered only in assessments

of the long-term exposure status from repeated and extended exposures, but could be safely disregarded in measurements of acute exposures. For the latter, however, the fractional high LET dose is always a substantial part of the total dose, and the selection of proper QF or RBE factors greatly influences the assessment of acute one-time as well as of long-term exposures.

The complex problem of QF and RBE factors will not be discussed here in all its aspects. Only the obvious fact might be briefly mentioned that the larger fractional high LET dose of the alpha component can be expected to reflect in correspondingly higher mean RBE values of local exposure. Adopting the formula suggested by the RBE Committee to the ICRP (ref. 3) relating RBE to LET, one obtains, for the system of figure 3, a dependence of local RBE on depth as shown in figure 4. It is interesting to see that the RBE shows a progressively steeper slope toward smaller depths or shield thicknesses. This means that the contributions from the alpha component to the high LET dose, which at small depths are already in terms of millirad doses much larger than those from protons, become still substantially larger in terms of rem doses.

The data presented in figures 2, 3, and 4 pertain to a unidirectional beam of right angle incidence. It seems of interest to evaluate the corresponding relationships for the shielding system of an actual space vehicle. Very

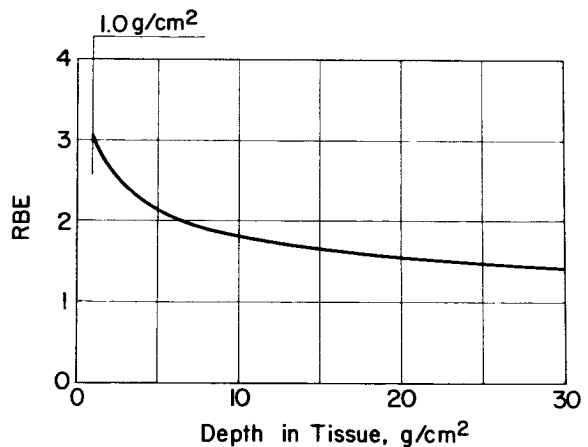


FIGURE 4.—Local RBE for Alpha component of dose for unidirectional beam of flare particles.

detailed information on the solid angle distribution of the natural shielding properties of the Apollo vehicle has been communicated by North American Aviation, Inc. (ref. 4). These data are actually more elaborate than would be needed for the purpose of a general appraisal. The minute details of the NAA system also have the disadvantage that they lead to a very complex radiation field inside the Command module with a number of structural details which are of no actual significance for assessing the radiation exposure of the astronauts. Therefore, the actual system has been simplified and rearranged for the purpose of the present investigation in such a way that an equivalent system was obtained for which the radiation field inside shows higher symmetry facilitating the analysis of the depth dose distribution in a target. The principle of rearrangement may be explained with the aid of figure 5. The left-hand sketch shows a fictitious random distribution of spherical shield sections of different thickness surrounding a spherical tissue target. It is obvious that the depth dose distribution in the target for omnidirectionally incident radiation will reflect the randomness of the shield configuration. At some point within the solid angle of minimum shield thickness, the surface dose in the target presumably will be at a maximum, although this would depend to some degree on the relative sizes and respective shield thicknesses of the adjacent solid angles. Similarly, minimum surface dose in the target

would be expected to occur within the solid angle of heaviest shielding.

The left-hand system in figure 5 is now changed into that shown in the right-hand sketch. An axis of symmetry is assumed as indicated by the vertical dash-dot line. Next, every solid angle of the actual system is changed in shape, but not in size, to a ring-shaped solid angle of constant width centered on the axis of symmetry. All angles are ordered in sequence of increasing thickness, beginning at the zenith of the equivalent system with minimum thickness and ending at the nadir with maximum thickness. It is seen by inspection that in the equivalent system, for omnidirectional irradiation, maximum surface dose in the tissue target will occur for zenith angle zero and minimum surface dose for zenith angle 180° (nadir). At the same time, these two doses are limiting cases that can never be reached at any surface point of the tissue sphere in the actual system. This follows from the fact that, for the zenith point on the target sphere, protons incident from the upper hemisphere suffer minimum attenuation since they encounter minimum thickness in the outer shield and no additional self shielding in the target, whereas for the nadir point on the target sphere, the same protons suffer maximum possible self shielding in the target. Any disarrangement in the symmetry of shield thickness distribution of the equivalent system must deteriorate the extreme condition just formulated; i.e., it will decrease the maximum dose in the zenith point of the target and increase the minimum dose in the nadir point. It is seen, then, that the depth dose distribution along the axis of symmetry through the target sphere begins, in the zenith point, with an upper limit surface dose that will never be fully reached at any target surface point in the actual system and ends, in the nadir point, with a lower limit surface dose. Furthermore, for obvious geometrical reasons, the depth dose in the center of the target sphere is the same in both systems. In other words, depth doses on the upper half of the symmetry axis represent upper limits, and on the lower half represent lower limits for the infinite variety of depth doses at corresponding radial distances in the actual system.

Table I shows the simplified equivalent system of shield distribution for the Apollo

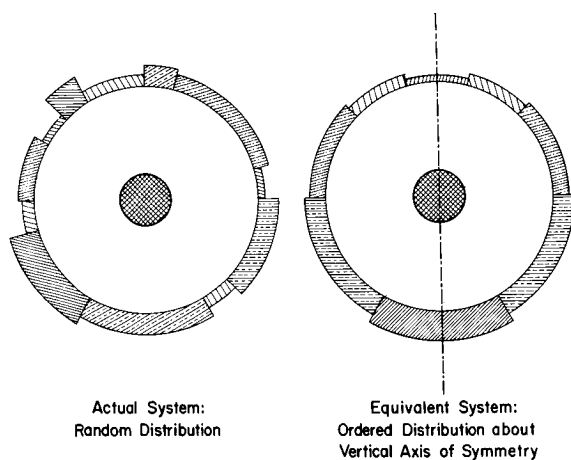


FIGURE 5.—Distribution of shield thickness about spherical target.

TABLE I

Simplified Solid Angle Breakdown of Shielding in Command Module of Apollo Vehicle

Section no.	Shield thickness, g/cm ²	Solid angle, steradians	Solid angle, % of total
C1	1.75	0.955	7.6
C2	3.5	.298	2.4
C3	5.25	.470	3.7
C4	6.5	.564	4.5
C5	7.0	1.292	10.3
C6	7.5	.571	4.5
C7	8.5	1.038	8.3
C8	8.75	.672	5.3
C9	10.75	.804	6.4
C10	11.25	.565	4.5
C11	14.25	1.109	8.8
C12	15	.949	7.6
C13	21	.799	6.4
C14	28	1.593	12.7
C15	38	.397	3.1
C16	62	.130	1.0
C17	102	.151	1.2
C18	212	.209	1.7

vehicle. It is seen that a minimum shield thickness of 1.75 g/cm² subtends a fairly large solid angle and that shield thickness varies over a very wide range. The extremely high values at the upper end correspond to solid angles of the posterior hemisphere as seen by the astronauts and are due to the large propellant tanks in the Service module. Figure 6 shows dose rates for the vertical diameter of a 30 cm tissue sphere in the center of the equivalent system as indicated in the right-hand sketch of figure 5. Four different dose rates are plotted separately, the total absorbed dose for the proton and alpha component and the number of enders per unit volume for the same two components. As pointed out before, the shaded areas indicate the width of variation that the exposure values exhibit in each case at a given radial distance from the center for different directions. It is evident that the basic characteristic of the alpha component, namely, the precipitous drop of dose rate and enders count in the initial layers of the target, which was already found for a unidirectional beam, holds also for the

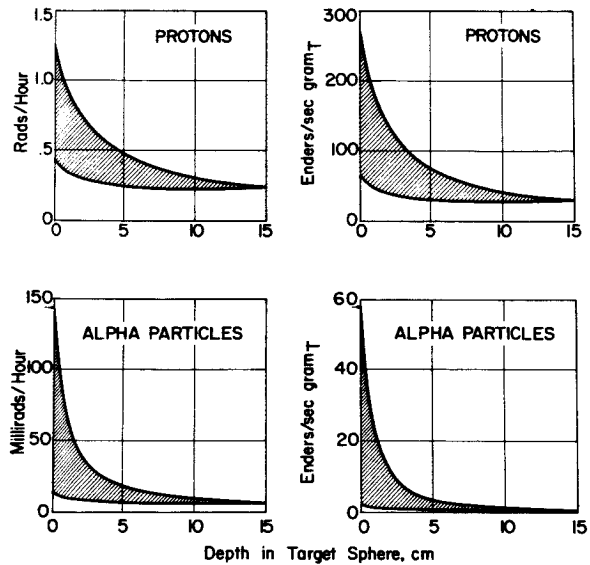


FIGURE 6.—Width of variation of radiation exposure in tissue sphere in center of Command Module for Bailey's flare spectrum.

spherical system. The graphs in figure 6 demonstrate well that this drop is substantially steeper for the alpha component as compared to protons. For the shielding system under investigation, the dose from the alpha component remains on a moderate level, constituting only 11 percent of the proton dose for the surface of the target, and drops steeply to much smaller percentages with increasing depth in the target. In comparing the enders count of alpha particles and protons, caution should be exercised because one alpha particle coming to rest deposits a substantially higher total ionization than one proton. An LET of 40 keV/micron_T as threshold for determination of the high LET fraction of the total dose corresponds to a kinetic energy of 15.5 MeV for alpha particles and of 0.6 MeV for protons. That means that an alpha ender produces a 26-times larger ionization than a proton ender. Selecting a critical LET of 25 keV/micron_T, the corresponding energies are 28 MeV for alpha particles and 1.15 MeV for protons, yielding a factor of 24 for the corresponding ionization dosages.

As indicated before and as well demonstrated by the depth dose distributions shown in

figure 6, the alpha component is a substantial contributor to exposure, mainly for shield thicknesses below the minimum value of 1.75 g/cm² for the Apollo vehicle. This does not mean that such lower shield thicknesses would not have practical importance in other circumstances. For instance, the total shielding equivalent of a space suit is about 0.3 g/cm². This value represents the combined shielding equivalent of pressure suit and heat protection suit. Still substantially smaller values are being quoted for the LEM (Lunar Excursion Module).

Estimates of alpha doses under these conditions would require the evaluation presented in this report to be extended down to lower shield thicknesses. This task encounters the basic difficulty that reliable data on the configuration of the rigidity or energy spectra in the critical region are not available. Freier and Webber expressly state in the reference quoted before (ref. 1) that "the experimental relationships of the absorber above the detector allow the rocket measurements to cover the range 30 to 120 MeV/nucleon." This corresponds to a minimum energy of 120 MeV for an alpha particle since it consists of 4 nucleons. This energy, in turn, corresponds to a range of 1.0 g/cm². Data on particle fluxes of lower penetration than 1.0 g/cm² are mostly based on indirect methods such as observations of cosmic radio noise absorption in the ionosphere. They could not possibly claim sufficient accuracy for a determination of spectral slope below 120 MeV exact enough to allow estimates of dose rates. This lack of definition is enhanced considerably by the strong dependence

on depth which the RBE exhibits for very low shield thicknesses, as discussed before in connection with figure 4.

From a dosimetric viewpoint, the important difference between the alpha and proton component of solar particle beams rests in the extremely steep drop of the radiation level in the initial layers of the absorber and, most of all, in the similarly steep drop of the local RBE. Especially the latter characteristic distinguishes the alpha exposure basically from the proton exposure. On the other side, it should be pointed out that this drop of the depth dose, even at a shield thickness as low as 1.0 g/cm², is not steep enough to qualify the alpha component as a "Radiation of Very Low Penetrating Power" in terms of the official recommendations of the National Committee of Radiation Protection in Handbook 59 (ref. 5). The criterion set by the committee (Rule III, p. 65, l.c., 5) calls for a half-value layer of less than 1 mm of soft tissue to be determined in terms of rem doses. Conceivably, the alpha component might come close to this specification for thicknesses approaching the 0.1 g/cm² level, since both rad dose and RBE exhibit a strong increase of slope toward such very low thicknesses. However, as pointed out before, available data on the energy spectrum of the incident radiation are just not accurate enough to give a conclusive answer to this particular question. All the more are radiobiological data missing on the effects of total body exposures on man or test animals with a radiation of the peculiar depth dose distribution of flare produced alpha particles.

REFERENCES

1. FREIER, P. S.; and WEBBER, W. R.: Exponential Rigidity Spectrums for Solar Flare Cosmic Rays. *J. Geophys. Res.*, vol. 68, 1963, pp. 1605-1629.
2. SCHAEFER, H. J.: Tissue Depth Doses in the High Intensity Proton Radiation Field of the Inner Van Allen Belt. BuMed Project M R005.13-1002 Subtask 1, Rept., No. 16, U.S. Naval School of Aviation Medicine (Pensacola, Fla.), 1959.
3. Report of the RBE Committee of the ICRP and ICRU. *Health Phys.* vol. 9, 1963, pp. 357-384.
4. SCHAEFER, H. J.: Dosimetric Evaluation of Data on the Solid Angle Breakdown of Shield Thickness for the Apollo Vehicle. BuMed Project MR005.13-1002 Subtask 1, Rept. No. 29 and NASA Order No. R-75. U.S. Naval School of Aviation Medicine (Pensacola, Fla.), 1964.
5. Permissible Dose From External Sources of Ionizing Radiation. Handbook 59, Nat. Bur. Std., 1954.

N65-34632

56—RBE of Protons and Alpha Particles

J. W. HAFFNER

North American Aviation, Inc.

The RBE-LET (Relative Biological Effectiveness-Linear Energy Transfer) relationship of Rossi was used as a starting point for an analytical investigation into the RBE of protons and alpha particles. Charge acquisition was handled explicitly, nuclear interactions, implicitly, in this study, which yielded analytical expressions for the RBE of protons and alpha particles. The expressions simplify considerably above the critical energies where the RBE=1. The critical energies are 10.8 MeV for protons and 249 MeV for alpha particles. Continuous energy spectra of the $E^{-\alpha}$ type were also treated. Comparisons with experimental data are presented.

INTRODUCTION

The calculation of (proton) rad doses is fairly straightforward since the rad dose refers merely to the total energy deposited per gram of material. While taking secondaries into account is somewhat troublesome, the work of Gibson (ref. 1) and others has resulted in a flux to rad dose conversion function which is generally accepted as accurate and satisfactory (fig. 1).

depends upon many factors (part of the body, type of energy of radiation, flux rate, etc.), a reasonably satisfactory dependence of the RBE on the Linear Energy Transfer (LET), has been obtained and experimentally verified (to some extent) by Rossi (fig. 2). It is the purpose of this study to investigate analytically the RBE-LET relationship of Rossi as applied to space radiations. (See ref. 2.)

DISCUSSION

The first step was to calculate the RBE for monoenergetic protons and α -particles in tissue. For this purpose, the well known expression for the range-energy relation of charged particles in matter (ref. 3) was used:

$$R = \delta E^n \tag{1}$$

where

$$\begin{aligned} R &= \text{range, gm/cm}^2 \\ E &= \text{energy, MeV} \\ \delta &\left\{ \begin{array}{l} \text{constants} \end{array} \right. \\ n &\left\{ \end{aligned}$$

For bone and muscle, these constants are (for protons):

Bone	$n = 1.779$	$\delta = 2.30 \times 10^{-3}$
Muscle	$n = 1.786$	$\delta = 2.03 \times 10^{-3}$

Taking the human body to be 50 percent bone and 50 percent muscle (the bone is weighted

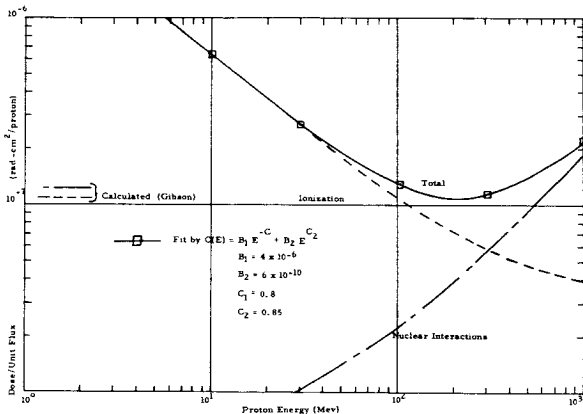


FIGURE 1.—Flux to rad dose conversion function, after Gibson.

The calculation of rem doses from rad doses is generally accomplished by use of a multiplicative correction factor called the Relative Biological Effectiveness (RBE). While this is, in principle, very complicated, since the RBE

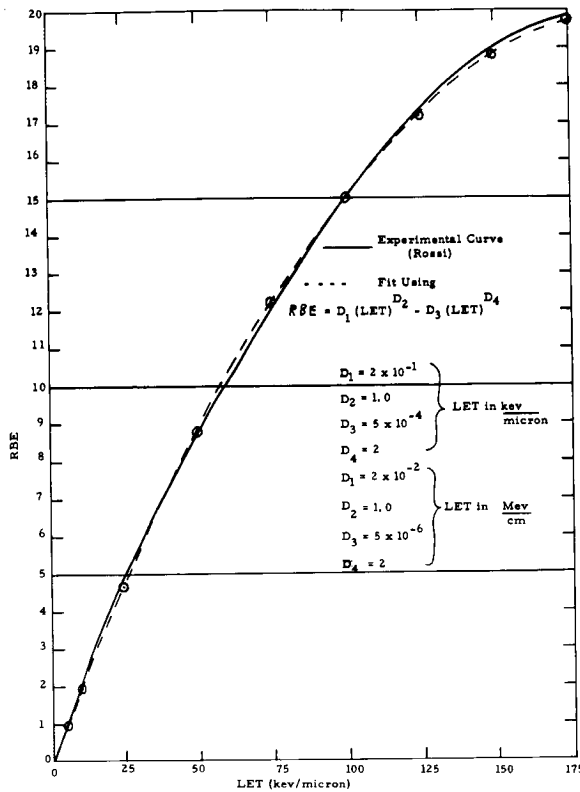


FIGURE 2.—RBE-LET relationship of Rossi.

more heavily because of the importance of the marrow), the constants for protons become

$$n = 1.7825$$

$$\delta = 2.165 \times 10^{-3}$$

For heavy charged particles, it is generally accepted (refs. 4 and 5) that

$$\frac{dE}{dx} \propto \frac{Z^2}{v^2}$$

where Z = atomic number and v = velocity of the moving heavy charged particle.

Thus, protons and alpha particles of the same Z/v will have the same $\frac{dE}{dx}$. Thus, an alpha particle will need four times the energy of a proton to have the same range as the proton. Therefore, the range-energy relation for alpha particles in tissue can be written

$$R = \delta' E^n$$

where $n = 1.7825$ (same as for protons)

$$\delta' = \frac{2.165 \times 10^{-3}}{(4)^{1.7825}} = 1.87 \times 10^{-4}$$

Range-energy relationships for protons and alpha particles in tissue and aluminum are shown in figure 3.

If a charged particle is stopped in a semi-infinite block of tissue, the total energy lost in the tissue is just the initial energy of the particle. The effective energy lost is the integral

$$\int_0^R (LET) \cdot (RBE) dx \quad (2)$$

where the integral is evaluated over the range of the particle.

The RBE as a function of LET, as shown in figure 2, can be fit over the interval

$$4 \frac{\text{keV}}{\text{micron}} \text{ to } 200 \frac{\text{keV}}{\text{micron}}$$

by a function of the form:

$$RBE = D_1 (LET) - D_2 (LET)^2 \quad (3)$$

where

$$\left. \begin{matrix} D_1 = 2 \times 10^{-2} \\ D_2 = 5 \times 10^{-6} \end{matrix} \right\} \text{LET in } \frac{\text{MeV}}{\text{cm}}$$

The RBE is unity for values of $LET \lesssim 4 \text{ keV/micron} = 40 \text{ MeV/cm}$, and the RBE may either remain constant at 20 above 200 keV/micron or decline (overkill). The effective energy lost by a particle after it has reached an RBE of 20 may be neglected in most situations.

In order to find the energies which correspond to these RBE values, the range-energy relationship is differentiated:

$$LET = \frac{dE}{dx} = \frac{1}{n\delta} \left[E_0^n - \frac{x}{\delta} \right]^{\frac{1-n}{n}} = \frac{1}{n\delta} E^{1-n} \quad (4)$$

where E_0 is the initial energy of the particle (MeV) and x is the distance (gm/cm²) traveled. Note that from this point on, it was assumed that the density of tissue was unity.

If

$$\frac{dE}{dx} = K, E_0 = (n\delta K)^{\frac{1}{1-n}} \quad (5)$$

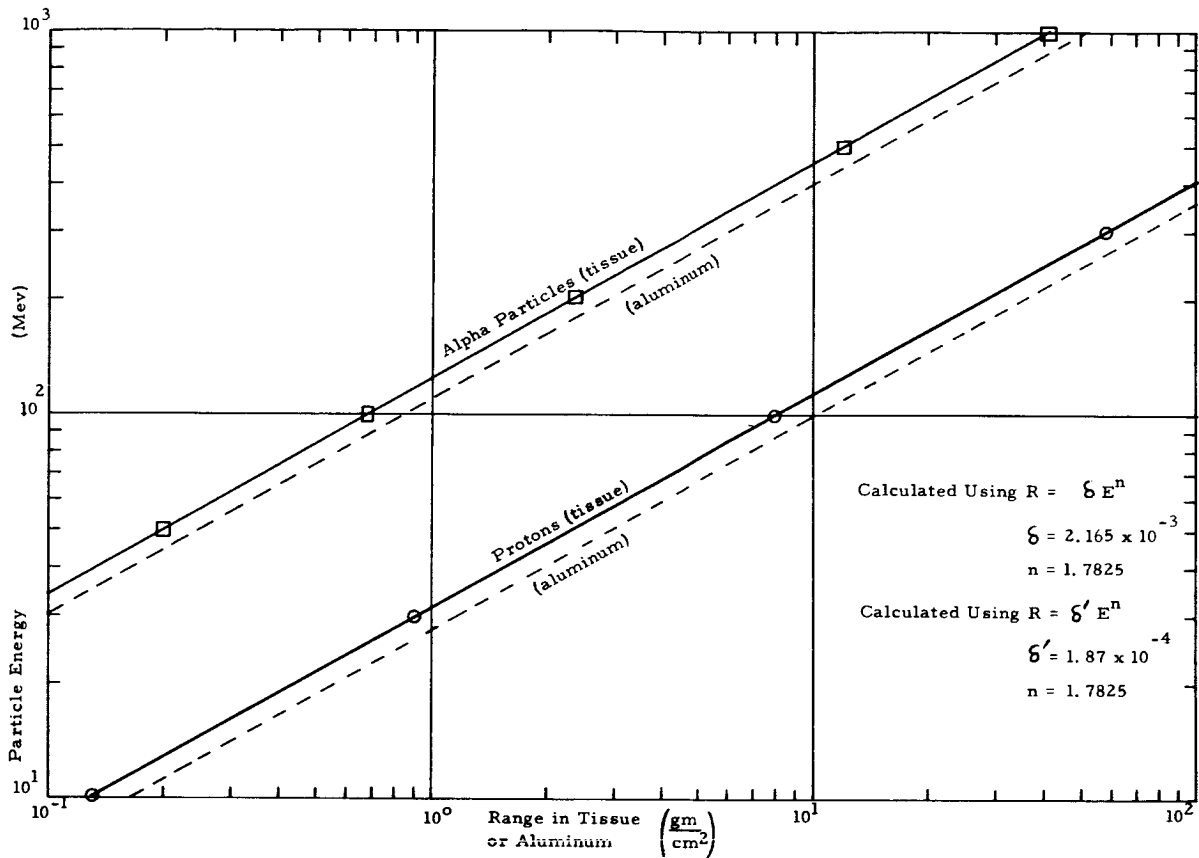


FIGURE 3.—Range-energy relationships for protons and alpha particles in tissue and aluminum.

submitting numbers yields

	For $K=40 \frac{\text{MeV}}{\text{cm}}$ (RBE=1)	For $K=2000 \frac{\text{MeV}}{\text{cm}}$ (RBE=20)
Protons.....	10.8 MeV (0.132 gm/cm ²)	0.077 MeV (1.3 × 10 ⁻³ gm/cm ²)
Alpha particles.....	249 MeV (3.52 gm/cm ²)	3.1 MeV (2 × 10 ⁻³ gm/cm ²)

The ranges (gm/cm²) of particles of these energies were obtained by using the range-energy relation of equation (1). It can be seen that the primary region of interest is between these two limits.

At this point, an analytical expression for the RBE can be obtained. It is

$$\begin{aligned}
 \text{RBE} &= \frac{\text{Effective Energy Lost}}{\text{Actual Energy Lost}} = \frac{\int (\text{LET}) \cdot (\text{RBE}) \, dx}{\int (\text{LET}) \, dx} \\
 &= \int [D_1 (\text{LET})^2 - D_2 (\text{LET})^3] dx / \int (\text{LET}) \, dx \tag{6}
 \end{aligned}$$

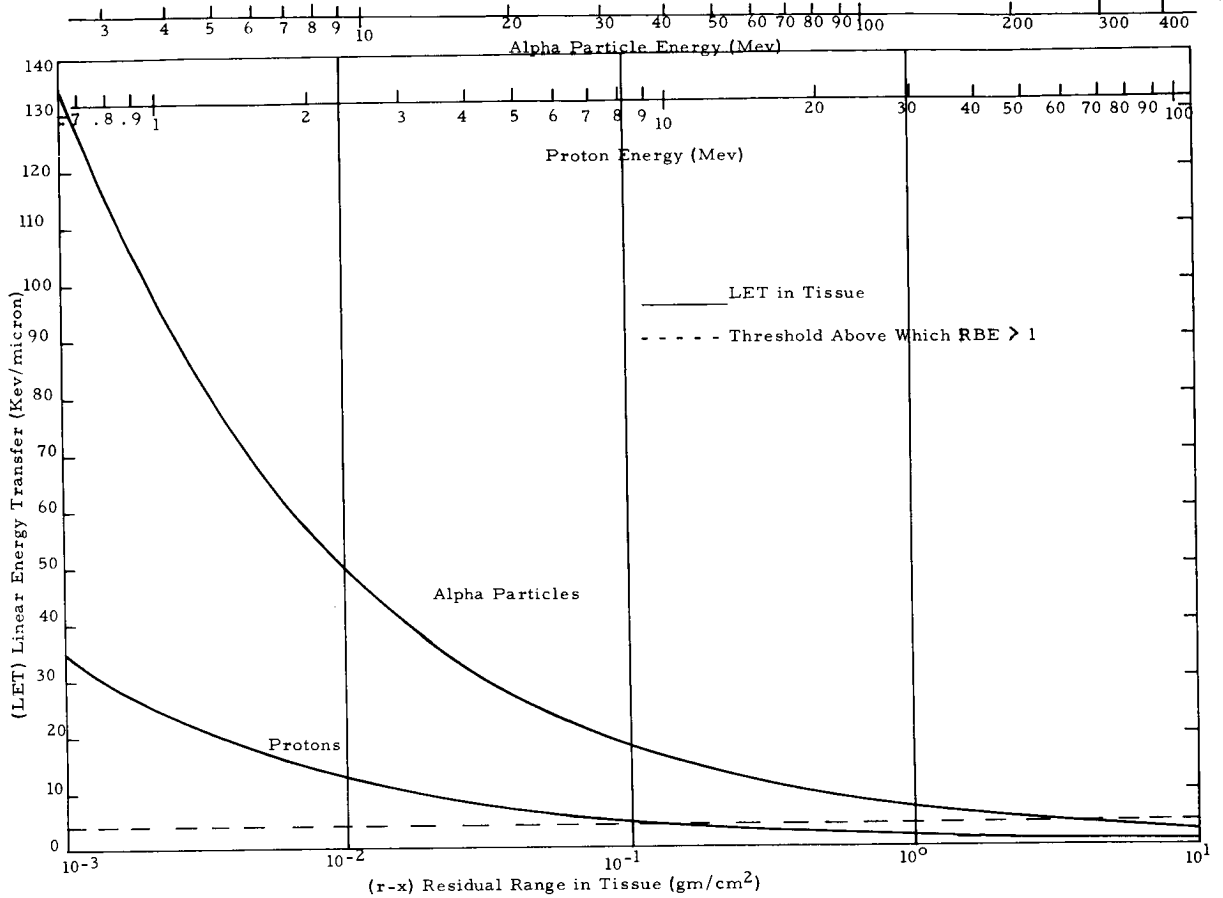


FIGURE 4.—Values of LET as functions of residual range.

Since the LET in units of x (position along the particle track) is desired, the following expression is used instead of equation (4)

$$LET = \frac{1}{n\delta} \left(\frac{R-x}{\delta} \right)^{\frac{1-n}{n}} = \frac{1}{n} \delta^{-\frac{1}{n}} (R-x)^{\frac{1-n}{n}} \quad (7)$$

Notice that this is readily obtained from equation (4) by using equation (1). Values of the LET as functions of $(R-X)$ (the residual range) are shown in figure 4. Substituting equation (7) in equation (6) yields

$$\begin{aligned} RBE &= \int_{R_1}^{R_2} \frac{1}{n} \delta^{-\frac{1}{n}} (R-x)^{\frac{1-n}{n}} dx \\ &= \int_{R_1}^{R_2} \frac{D_1}{n^2} \delta^{-\frac{2}{n}} (R-x)^{\frac{2-2n}{n}} dx \\ &\quad - \int_{R_1}^{R_2} \frac{D_2}{n^3} \delta^{-\frac{3}{n}} (R-x)^{\frac{3-3n}{n}} dx \end{aligned}$$

Integrating yields

$$RBE = \frac{\left[\frac{D_1 \delta^{-\frac{1}{n}} (R-x)^{\frac{2-n}{n}}}{n(2-n)} - \frac{D_2 \delta^{-\frac{2}{n}} (R-x)^{\frac{3-2n}{n}}}{n^2(3-2n)} \right]_{R_1}^{R_2}}{\left[(R-x)^{\frac{1}{n}} \right]_{R_1}^{R_2}}$$

Since the equations used are valid only between R_1 and R_2 , values of R greater than R_2 are not allowed. If R is less than R_1 , the LET becomes imaginary. Therefore, the RBE becomes:

$$RBE = \frac{D_1 \delta^{\frac{1}{n}} \left[1 - (R_2 - R_1)^{\frac{2-n}{n}} \right]}{n(2-n) \left[1 - (R_2 - R_1)^{\frac{1}{n}} \right]} - \frac{D_2 \delta^{-\frac{2}{n}} \left[1 - (R_2 - R_1)^{\frac{3-2n}{n}} \right]}{n^2(3-2n) \left[1 - (R_2 - R_1)^{\frac{1}{n}} \right]} \quad (8)$$

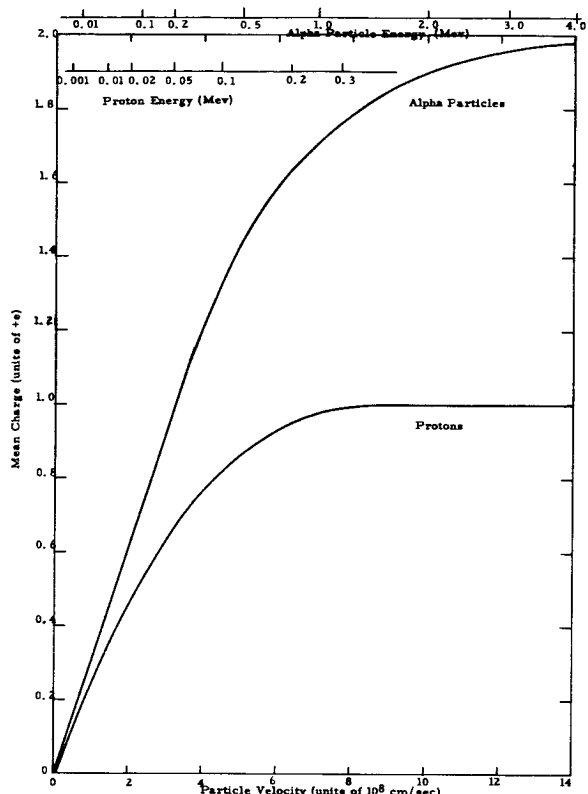


FIGURE 5.—Effective charge of protons and alpha particles near end of path.

The composite RBE obtained for the proton and alpha particles between their initial and final energies (where LET = 4 keV/micron and LET = 200 keV/micron, respectively) are:

Protons (10.8 MeV to 0.077 MeV) 2.1
Alpha particles (249 MeV to 3.1 MeV)..... 2.2

These numbers must be examined from the standpoint of effective particle charge. According to Evans (ref. 5), the alpha particle begins to lose its charge above a velocity of 1×10^9 cm/sec (2 MeV) and has lost half of its charge at $\sim 3.7 \times 10^8$ cm/sec (0.2 MeV) (fig. 5). Therefore, neglecting the alpha particle energy deposition below ~ 1 MeV is a good approximation. For protons, the corresponding velocities and energies are 6×10^8 cm/sec (0.18 MeV) and 2×10^8 cm/sec (0.02 MeV). Therefore, below ~ 0.05 MeV, the proton energy deposition can be neglected.

For proton and alpha particle energies above the upper critical energies, the RBE is taken as

one in semi-infinite tissue down to the point the particle reaches the critical energy. Therefore, the composite RBE becomes

$$\text{RBE}(E_0) = \frac{(E_0 - E_c) \cdot 1 + E_c \cdot \text{RBE}(E_c)}{E_0} \quad (9)$$

where

E_0 = particle initial energy,
MeV ($E_0 \geq E_c$)

E_c = upper critical energy (10.8 MeV for protons) (249 MeV for alpha particles)

RBE(E_c) = 2.1 for protons
= 2.2 for alpha particles

Values of the composite RBE for particle energies above E_c were calculated using the above formula.

For values of the RBE below the upper critical energies, it was easier to write the equation in terms of particle energy. Using equations (4) and (6), the formula becomes

$$\text{RBE} = \frac{\left[\frac{D_1 E^{2-n}}{n\delta(2-n)} - \frac{D_2 E^{3-2n}}{n^2\delta^2(3-2n)} \right]_{E'}}{[E]_{E'}^2} \quad (10)$$

where E_0 = initial particle energy,
MeV ($E < E_{\text{critical}}$)

E' = lower critical energy (0.077 MeV for protons) (3.1 MeV for alpha particles)

Putting in numbers yields

$$\text{RBE} = \frac{24E_0^{0.2175} + 0.59E_0^{-0.565} - 16.3}{E_0 - 0.077} \quad (\text{protons}) \quad (11)$$

$$\text{RBE} = \frac{270E_0^{0.2175} + 80E_0^{-0.565} - 396}{E_0 - 3.1} \quad (\text{alpha particles}) \quad (12)$$

The resulting RBE versus energy curves are plotted in figures 6 and 7. For monoenergetic protons, the RBE is compared with the results obtained by Schaeffer (refs. 6 and 7). Above 0.5 MeV, the present results are in good agreement with Schaeffer's. Below 0.5 MeV (~ 6 microns residual range), the present calculations predict somewhat higher RBE values. Probably saturation effects (there are only so many atoms per unit path length for the particles to

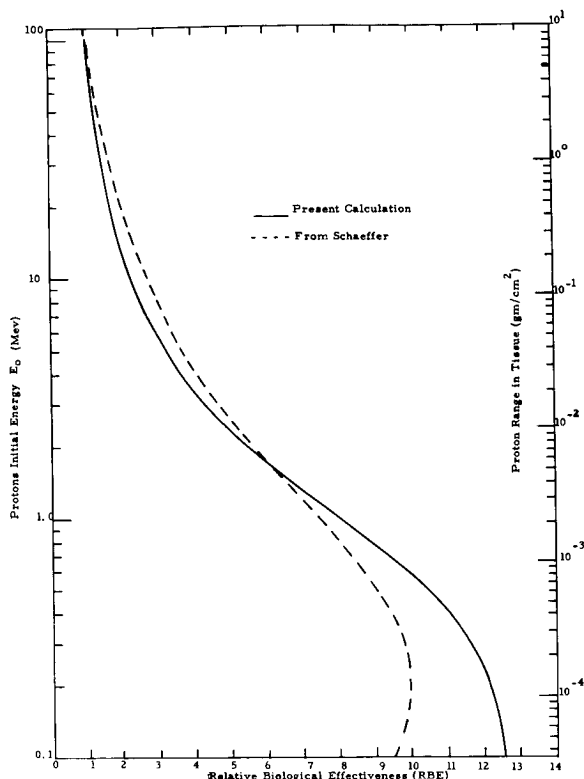


FIGURE 6.—RBE versus energy: protons in tissue.

ionize), which our present calculation did not take into account, are responsible for the differences. From the overall shielding viewpoint, the differences are unimportant.

The flux to dose conversion function for protons in a semi-infinite medium of tissue may now be obtained by multiplying equation (11) by a fit to the flux to rad dose conversion function shown in figure 1. A good fit to the graph of figure 1 is:

$$C(E) = B_1 E^{-c_1} + B_2 E^{c_2} \quad (13)$$

where $C(E)$ = flux to rad dose conversion function (rad-cm²/proton)

$$\left. \begin{aligned} B_1 &= 4 \times 10^{-6} \\ B_2 &= 6 \times 10^{-10} \\ C_1 &= 0.8 \\ C_2 &= 0.85 \end{aligned} \right\} \text{Constants}$$

The product of equations (11) and (13) is plotted in figure 8. It is seen, as expected, that low energy protons are relatively more important here than they were in figure 1.

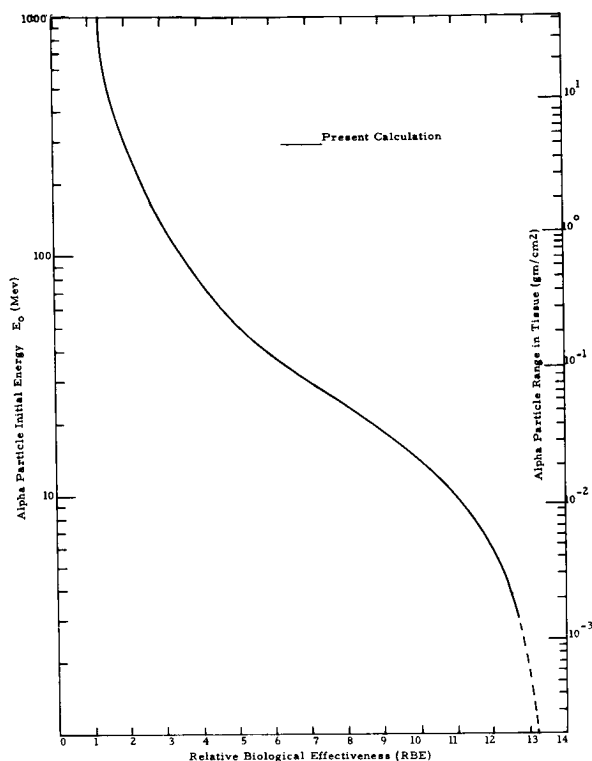


FIGURE 7.—RBE versus energy: alpha particles in tissue.

If a particle integral energy spectrum is present of the form

$$\phi(\bar{x} > E_0) = A E_0^{-\alpha} \quad (14)$$

the RBE due to particles in a given energy interval is the integral of the product of equations (10) and (14). The time integrated energy spectra of solar proton events appear to follow such a law down to ~10 MeV. Solar alpha particle spectra may follow a similar law. However, spectra behind shields will be modified thus:

$$E = [E_0^{n_s} - (E')^{n_s}]^{1/n_s} \quad (15)$$

where

- E_0 = particle energy outside shield
- E = particle energy inside shield
- E' = particle cutoff energy of shield

Relationships between incident energy E_0 , emergent energy E , and tissue thickness x for protons and alpha particles are shown in figures 9 to 12. It should be pointed out that the n_s in equation (15) is the constant for charged particles in the shield material which will generally be different from that of tissue.

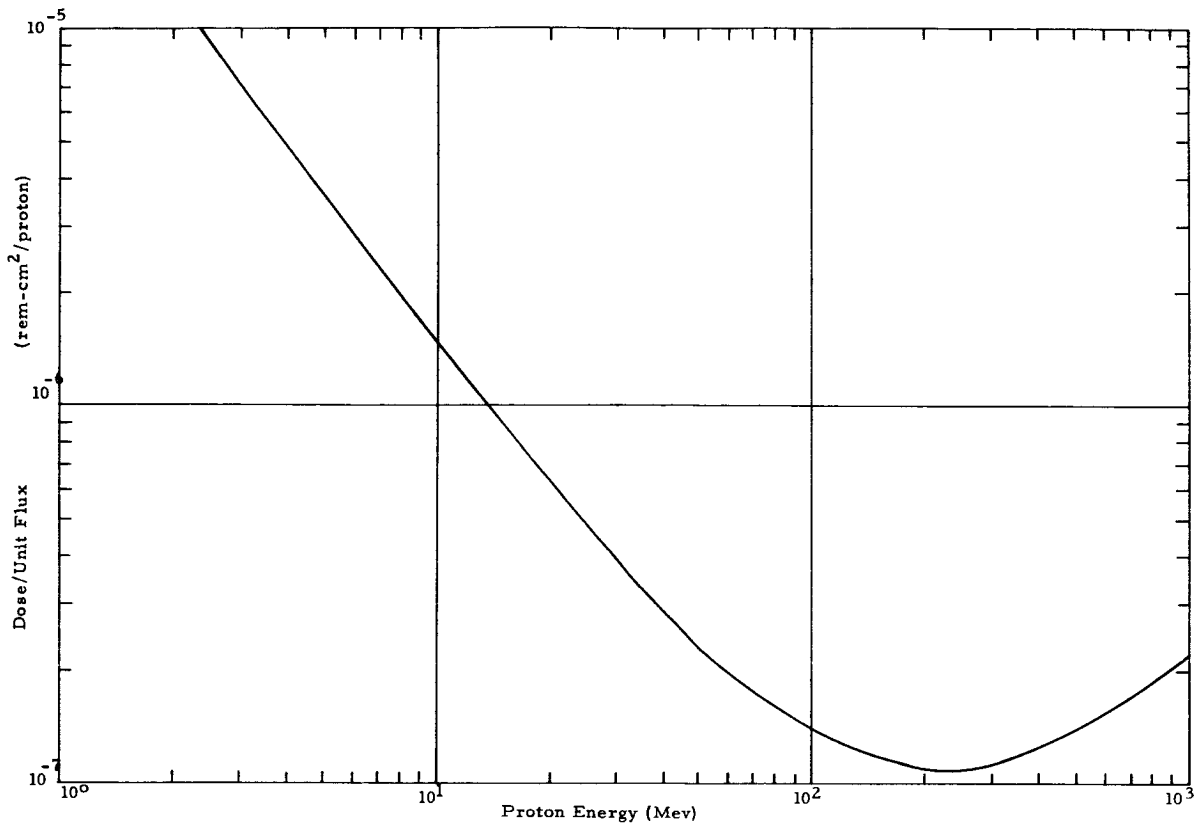


FIGURE 8.—Flux to rem dose conversion function for protons in tissue.

In table I are listed values of n and δ for various materials. In order to convert thickness (x) to the equivalent quantity in another material, the relationship is

$$X_1 = \delta_1 \left(\frac{X_2}{\delta_2} \right)^{\frac{n_1}{n_2}} \quad (16)$$

where the subscripts 1 and 2 refer to materials 1 and 2 respectively.

Substituting equation (15) into equation (14) gives as the particle energy spectrum inside the shield:

$$\begin{aligned} \phi(E > E_0) &= A[E^n + (E')^n]^{-\frac{\alpha}{n}} \\ &= AE^{-\alpha} \left[1 + \left(\frac{E'}{E} \right)^n \right]^{-\frac{\alpha}{n}} \end{aligned} \quad (17)$$

The corresponding differential energy spectrum is

$$\begin{aligned} \phi(E_0) dE &= A\alpha E_0^{-(\alpha+1)} \\ &= A\alpha E^{-(\alpha+1)} \left[1 + \left(\frac{E'}{E} \right)^n \right]^{-\frac{\alpha}{n}-1} \end{aligned} \quad (18)$$

The differential energy spectrum of particles penetrating a shield of cutoff energy E' thus peaks (inside the shield) at

$$E = E' \left(\frac{n-1}{\alpha+1} \right)^{\frac{1}{n}} \quad (19)$$

Because of the nonlinear way charged particles lose energy in matter, the effect is to "stretch" an energy interval, the stretch increasing as the cutoff energy approaches the lower limit of the interval. This results in a flattening of the spectrum at low emergent energies where the RBE is largest. Therefore, the RBE values for incident $AE^{-\alpha}$ spectra which have been attenuated through shields will be lower than might otherwise be expected, the effect being larger the steeper the incident spectrum (larger α).

The product of equations (10) and (16) cannot be integrated in closed form (which means that a closed form expression for RBE

TABLE I

Values of n and δ for Various Materials

$$\left[\text{Range} \frac{\text{gm}}{\text{cm}^2} = \delta E^n \quad (E \text{ in Mev}) \right]$$

Material	n (all heavy charged particles)	δ (protons)	δ (alpha particles)
Hydrogen.....	1.817	8.21×10^{-4}	6.61×10^{-5}
Beryllium.....	1.788	2.35×10^{-3}	1.97×10^{-4}
Carbon.....	1.787	2.22×10^{-3}	1.86×10^{-4}
Aluminum.....	1.730	3.46×10^{-3}	3.15×10^{-4}
Copper.....	1.728	4.07×10^{-3}	3.71×10^{-4}
Cadmium.....	1.708	4.97×10^{-3}	4.70×10^{-4}
Lead.....	1.680	7.18×10^{-3}	7.00×10^{-4}
Air.....	1.777	2.39×10^{-3}	2.03×10^{-4}
Water.....	1.793	1.95×10^{-3}	1.63×10^{-4}
Tissue.....	1.783	2.17×10^{-3}	1.87×10^{-4}

due to an $AE^{-\alpha}$ spectrum of particles penetrating a shield cannot be obtained). Therefore, a reasonable approximation is to assume the spectral shape is unchanged and to integrate over the energy spectrum from the energy corresponding to the differential peak inside the shield to any desired upper limit (e.g., ∞). For most shields, this energy will be above the energy where the RBE begins exceeding unity (eq. (5) *ff*). The limits are thus

$$E = E' \left(\frac{n-1}{\alpha+1} \right)^{\frac{1}{n}} \text{ to } E = \infty \quad (20)$$

Integrating the product of equations (9) and (18) over energy between the limits given by equation (20) yields:

$$\text{RBE} = 1 + \frac{\alpha}{\alpha+1} \left(\frac{\alpha+1}{n-1} \right)^{\frac{1}{n}} \frac{\Delta}{E'} \quad (21)$$

where

$\Delta = 12$ MeV for protons

$\Delta = 300$ MeV for alpha particles

Values of the RBE as a function of α for various values of $\frac{\Delta}{E'}$ are plotted in figure 13 where $n_s = 1.73$ (e.g., an aluminum shield). The same calculations are shown in figure 14, cross-plotted

to show RBE as a function of $\frac{\Delta}{E'}$ for various values of α . It is seen that, as expected, the thinner the shield and the steeper the energy spectrum (i.e., the larger the value of α) the larger the value of RBE. The reason for the shield thickness effect is that the thicker the shield the higher the energy inside the shield at which the differential energy spectrum peaks (eq. (19)) and hence the lower the RBE (figs. 6 and 7).

Thus, by obtaining an α for the desired spectrum, an E' for the shield, and a value of n_s corresponding to the shield material, the RBE for either protons or alpha particles may be calculated (so long as the shield is at least ~ 0.2 gm/cm² for protons or ~ 3.5 gm/cm² for alpha particles). While this is no real limitation for protons, for alpha particles, shields < 3.5 cm/cm² may be encountered. For this situation, graphical solutions are recommended unless a computer is used.

If finite tissue thicknesses rather than infinite tissue are considered, the way the RBE is computed enters. If the RBE is

$$\text{RBE} = \frac{\int (\text{RBE}) (\text{LET}) dx}{\int (\text{LET}) dx} \quad (22)$$

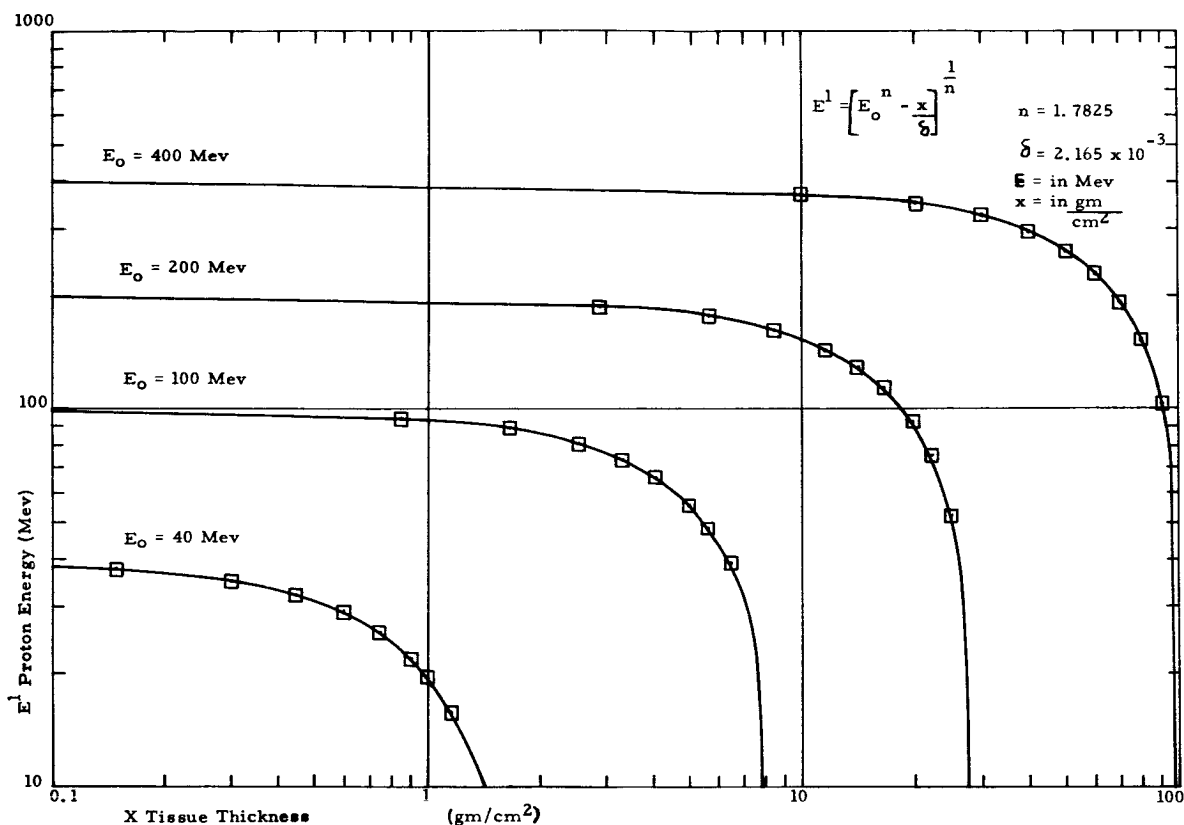


FIGURE 9.—Protons in tissue.

Then values of RBE will always be ≥ 1 . But if the RBE is taken as

$$RBE = \frac{\int (RBE)(LET)dx}{E} \quad (23)$$

then the RBE values may approach zero for thin tissue thickness. The first concept (eq. (22)) is recommended, but under certain conditions, the second concept may be far more useful. In the first case, the RBE for finite tissue sections is obtained from those for thick tissue by using the formula

$$RBE(E_0, t) = \frac{E_0 \cdot RBE(E_0) - E' \cdot RBE(E')}{E_0 - E'} \quad (24)$$

where

E_0 = particle energy as it enters tissue (MeV)

E' = particle energy as it leaves tissue (MeV)

$RBE(E)$ = RBE of particle at energy E

t = tissue thickness ($\frac{gm_2}{cm}$)

If the second concept is employed, the corresponding formula is:

$$RBE(E_0, t) = \frac{E_0 \cdot RBE(E_0) - E' \cdot RBE(E')}{E_0} \quad (25)$$

By using figures 6, 9, and 10 for protons (or figs. 7, 11, and 12 for alpha particles), it is

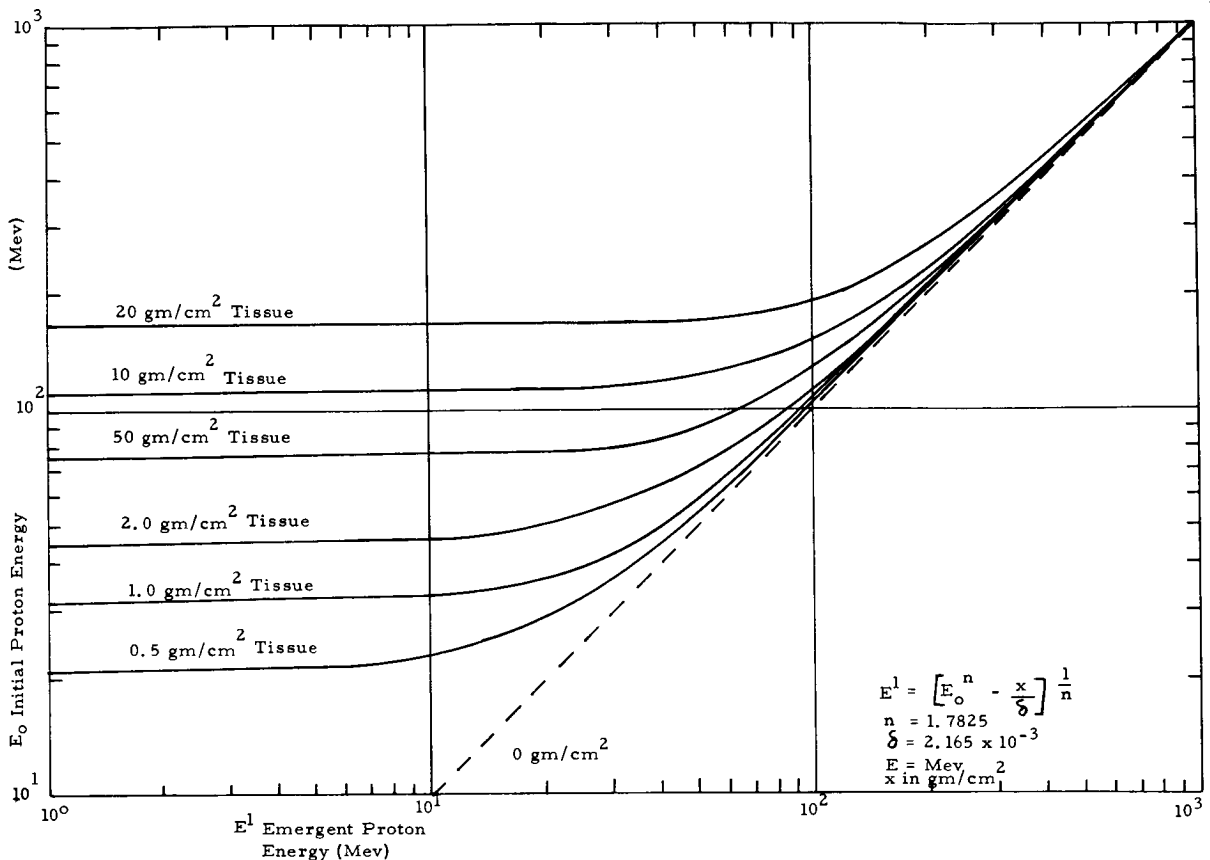


FIGURE 10.—Protons in tissue.

possible to obtain RBE values for monoenergetic protons and alpha particles in finite thicknesses of tissue.

There are relatively few experimental data to compare with the RBE values calculated herein. In table II, the data the author was able to obtain are listed (refs. 8, 9, and 10). The values <1 obviously refer to the second RBE concept for finite tissue. A detailed analysis of the data is very difficult, but it may be seen that at proton energies ≥ 100 MeV, RBE values close to one are obtained as calculated. No data for alpha particle irradiation was found, although some most certainly exist.

CONCLUDING REMARKS

RBE values have been calculated for protons and alpha particles in tissue based upon the RBE-LET relationship of Rossi. Monoener-

getic and $E^{-\alpha}$ polyenergetic spectra were considered for both infinite and finite tissue thicknesses.

The results yield RBE values varying from unity at high particle energies increasing to ~ 12 at low energies where electron acquisition becomes important. The upper critical energies (at which the LET=4 keV/micron and therefore the RBE=1) are 10.8 MeV for protons and 249 MeV for alpha particles. The composite RBE values in infinite tissue (50 percent bone and 50 percent muscle) for protons and alpha particles between their initial and final energies are 2.1 and 2.2, respectively.

Tables and graphs to facilitate the calculation of RBE values under many conditions are presented. Comparison with experiment is difficult, but the available data appear to be in agreement with the calculations.

TABLE II
Comparison of RBE Data

Group	P Energy	Effect used	Doses	Animal	RBE
LRL, UCRL-1104 Ashikawa et al. 9-13-63	730 MeV	LD ₅₀ at 6 and 30 days	600, 700 and 800 rad	Mouse	0.8 for LD ₅₀ /30, 1.3 LD ₅₀ /30 (gut vs marrow effects)
French-IAEA Sm-44/48 P. Bonet-Maury 8-7-63	157 MeV	LD ₅₀ at 8 days	790 rad	Mouse	0.77 for LD ₅₀ /8
		LD ₅₀ /30	580 rad		0.98 for LD ₅₀ /30
	592 MeV	LD ₅₀ /10	595 rad		1.06 for LD ₅₀ /10
BNL BNL-7359 Lippincott et al.	10 MeV	Progressive Epithelial Dysplasia in mouse skin	1200 rad 2000 rad	Mouse	
LRL UCRL-11015 Sondhaus et al.	150 MeV	LET Calculations		30-cm tissue sphere	1.12
BNL BNL-7343 Jesseph et al.	2 BeV	LD ₅₀ at 30 days	1.2×10^{10} to 9.7×10^{11} protons	Mouse	
USSR Saksonov et al. Sept. 1963	120 MeV	LD ₅₀		Mouse Rat	0.7
USSR Saksonov et al. Sept. 1963	660 MeV	LD ₅₀		Mouse	0.7
USSR Lebedinsky et al. USSR Acad. Sci. 1962	510 MeV	LD ₅₀		Rats	0.8
USSR Lebedinsky et al. USSR Acad. Sci. 1962	510 MeV	LD ₅₀		Dogs	1.2
USA Zeller and Allen Aerospace Med. 1962	730 MeV	Organ injury		Monkey	2.0

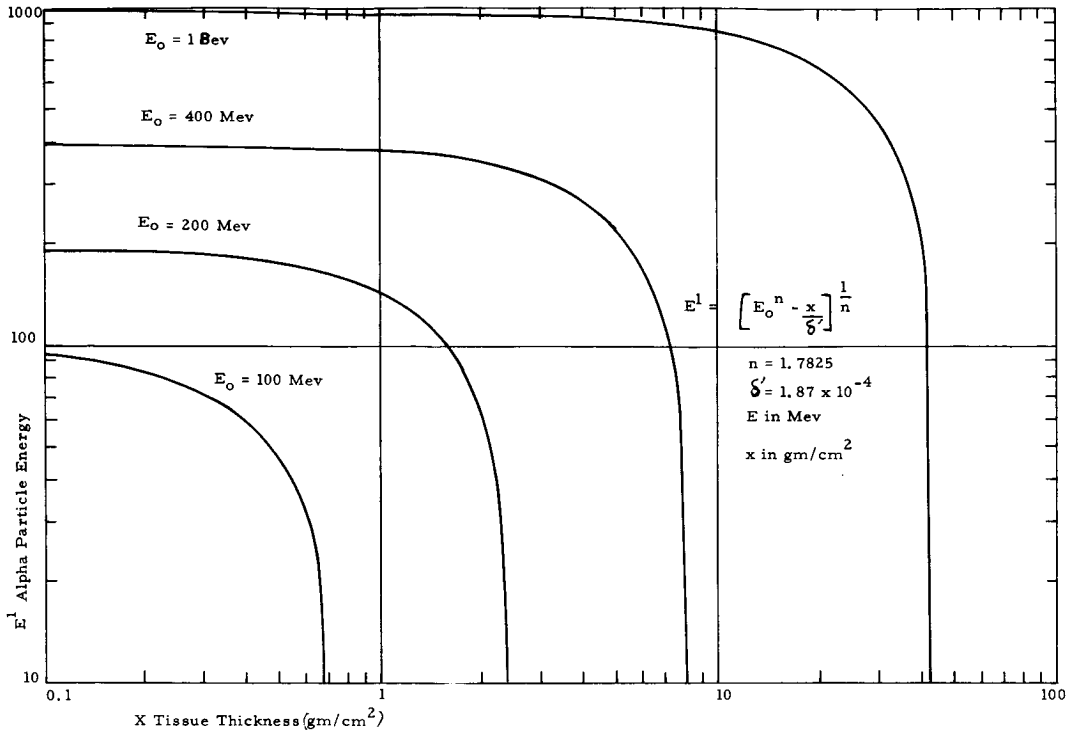


FIGURE 11.—Alpha particles in tissue.

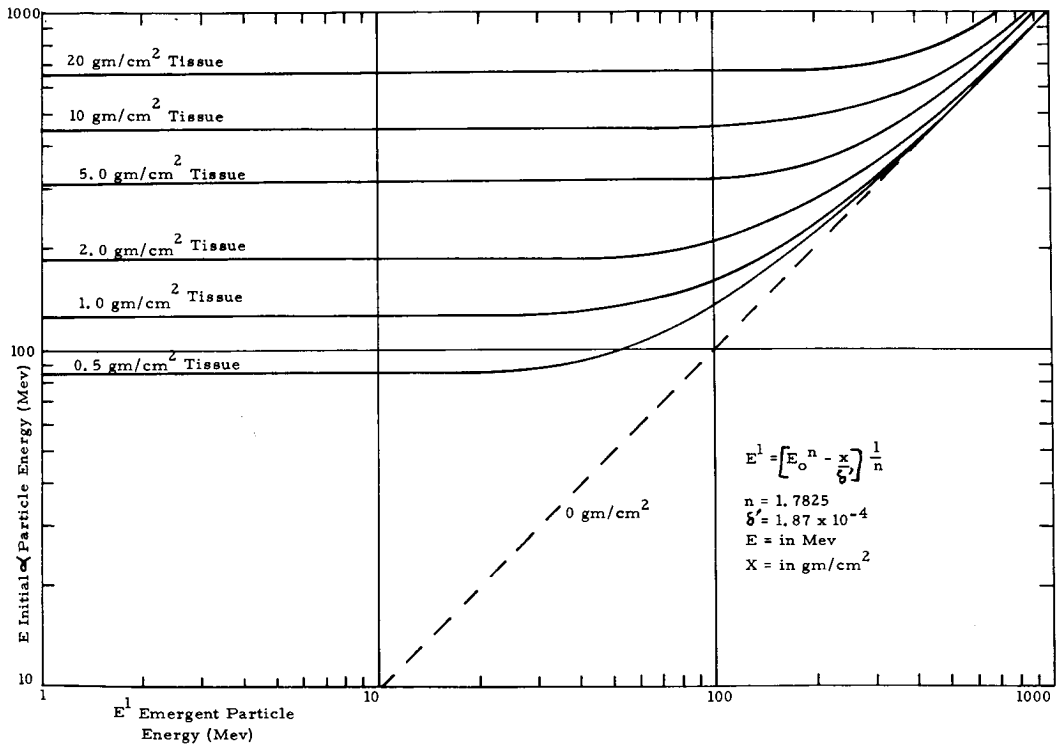


FIGURE 12.—Alpha particles in tissue.

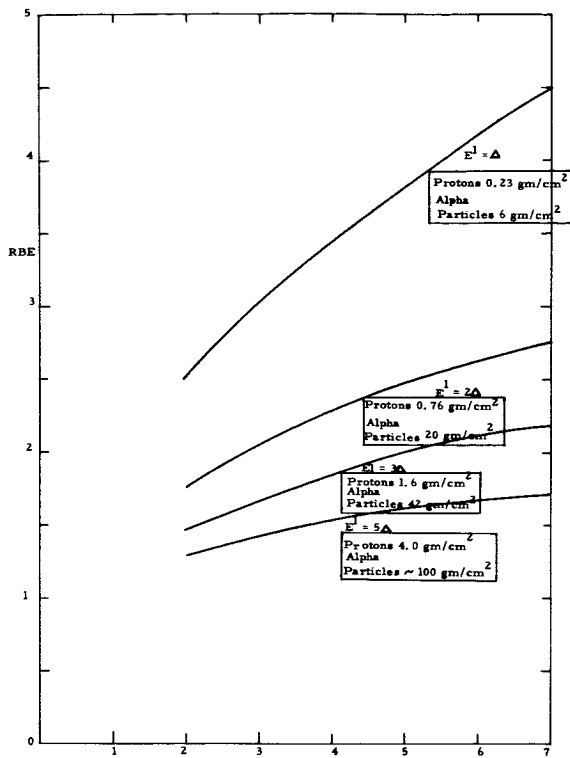


FIGURE 13.—RBE as a function of exponent α for particles attenuated by aluminum ($n_p \pm 1.73$) shields. Numbers in boxes correspond to thicknesses of aluminum shielding for each cut-off energy (E^1).

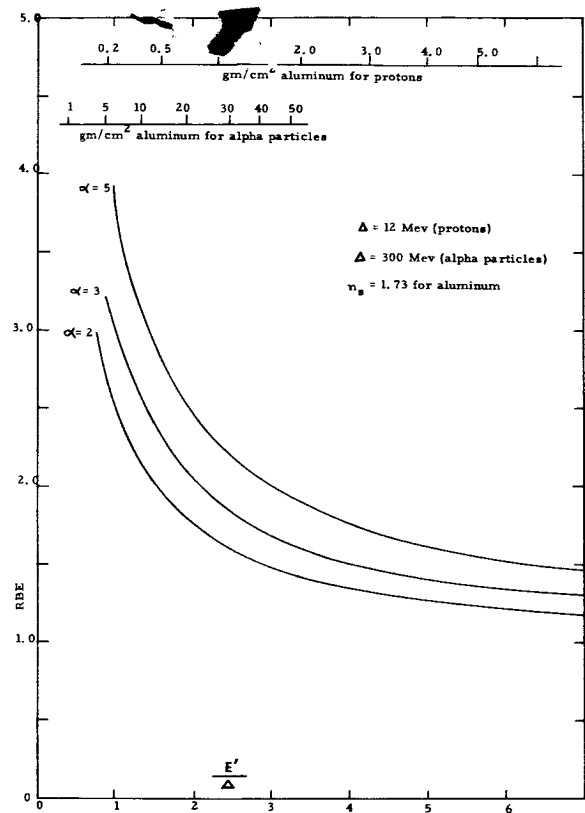


FIGURE 14.—RBE as a function of $\frac{E^1}{\Delta}$ for various values of α (E^1 =shield cut-off energy).

REFERENCES

- GIBSON, W. A.: Energy Removed From Primary Proton and Neutron Beams by Tissue. ORNL-3260, UC-34, June 1962.
- LINDENBAUM, S. J., ED.: Shielding of High Energy Accelerators. Annual Rev. Nucl. Sci., 11, 1961, p. 213.
- WEAGANT, R. A.: Proton Shielding Slide Rule. S & ID Division of North American Aviation (12-63).
- FANO, U.: Penetration of Protons, Alpha Particles, and Mesons. Annual Rev., Nucl. Sci., vol. 13, p. 1, 1963.
- EVANS, R. D.: The Atomic Nucleus, McGraw-Hill, 1955.
- SCHAEFFER, H. J.: A Note on the RBE of Proton Radiation in Space. U.S. Naval Aviation Medical Center, Jan. 1961.
- SCHAEFFER, H. J.: Local LET Spectra in Tissue for Solar Flare Protons and for Neutron-Produced Period Protons. Paper SM-44/30, Proc. IAEA Symp. on Radiological Effects of Neutron Irradiations (Brookhaven), Aug. 1963.
- SAKSONOV, P. P., ET AL.: On the Biological Effect of High Energy Protons. Proc. of 14th Intern. Astron. Congr. (Paris), 1963.
- VOLYNKIN, Y. M., ET AL.: Problems of Radiation Safety of Space Flights. Proc. of 14th Intern. Astron. Congr. (Paris), 1963.
- SONDHAUS, C. A.: Response of Mammalian Systems to Non-Uniform Space Radiation Dose. Lectures in Aerospace Medicine (Brooks AFB), 1962.

N65-34633

57—An Examination of the Relative Merits of Stochastic and Nonstatistical Methods of Computing Primary Ionization Doses

B. LILEY and G. C. SCHAEDEL

North American Aviation, Inc.

This paper will discuss several questions concerning computation of primary ionization doses for solar flare proton rigidity spectra with stochastic and nonstatistical methods. The following topics will be considered:

1. Geometrical representations for dose computations.
2. The effect of spacecraft area density distribution function parameters on the degree of geometrical detail or precision which is desirable for dose computations with nonstatistical methods. Illustration of the effect of geometry detail on dose computed for an actual spacecraft.
3. Convergence properties for the Monte Carlo method of dose computation as a function of rigidity and the geometry distribution parameters.

The necessity of accounting for nuclear collisions when computing primary ionization doses.

The effect of nuclear collisions on the convergence of the primary ionization dose.

4. Dose computational accuracy of the statistical primary ionization dose.
5. Relative merits of nonstatistical and statistical methods of dose computation (trade-offs between dose computational accuracy and cost).

SPACECRAFT GEOMETRY REPRESENTATIONS FOR DOSE COMPUTATIONS

Solid-Angle Homogenized Geometry

This geometry is generated by homogenizing the geometry in each selected solid angle and using an equivalent aluminum area density.

Elemental Solid Geometry

Another method is to represent the spacecraft geometry with a combination of spheres, cones, and other solids. This geometry can be systematically tracked to determine its equivalent area density distribution. This method will use the center point of solid angles as an average of the area density for the solid angle. This will be equivalent to homogenization to a lesser degree than the aforementioned solid-angle homogenized geometry. It should be noted that it will not be economically feasible to represent the exact vehicle without using some homogenization in equipment bays and other portions of the vehicle which contain large numbers of small components. Another tracking technique is to randomly sample the geometry, in order to avoid possible effects of homogenization.

Model Geometry

A geometry model is necessary to evaluate the statistical and nonstatistical methods of dose computation for various spacecraft area density distributions.

The inherent shielding during space missions varies considerably with the habitat of the astronaut. For example, some spacecraft have fairly good shielding effectiveness (translunar vehicles). However, the shielding of the manned lunar landing spacecraft or secondary vehicle will be somewhat less effective. When the astronaut leaves the secondary spacecraft, his shielding will be restricted to his space suit, which is even less effective.

The spacecraft interior is normally compactly fitted with equipment bays to house life support

systems, communication equipment, guidance and navigation equipment, etc. In present manned spacecraft, a region of the cabin interior is usually left unobstructed to allow for visual observation windows.

The shielding provided in the direction of the observation windows is generally only that of the vehicle skin structure or the glass of the window. In most other directions, shielding is provided by both the skin structure and the equipment bays, and by miscellaneous components, such as crew couches, etc. Except for the window region, the geometry will be rather inhomogeneous.

The analytical representation of these shields will now be defined by a simple generalized geometry model. The shielding will be defined by its solid-angle distribution as a function of area density. The distribution functions will have two basic characteristics (fig. 1): (1) a radiation window (assumed to have constant area density), which encompasses one-tenth to one-half of the unit sphere; and (2) the remainder of the unit sphere (4π steradians) which will comprise randomly selected geometry from a prescribed distribution function. The unit sphere has been divided into 4050 equal solid angles; each solid angle has a uniform area density. The distribution function for the elemental solid angles is defined by the equation in figure 2, where

X = area density (grams/cm²) of elemental solid angle

$N(X)$ = fraction of unit sphere having elemental area densities less than X

P_o = radiation window fraction of the unit sphere

X_{MIN} = radiation window area density X_o

X_{MAX} = maximum shield area density

τ = area density distribution shape parameter

The geometry distribution is generated by replacing $N(X)$ by a random number (normalized to 1.0) and computing the corresponding X .

Figure 2 also shows a sample portion of the inhomogeneous part of the unit sphere. The model geometry is defined by the standard grid. A sample grid for homogenized geometry

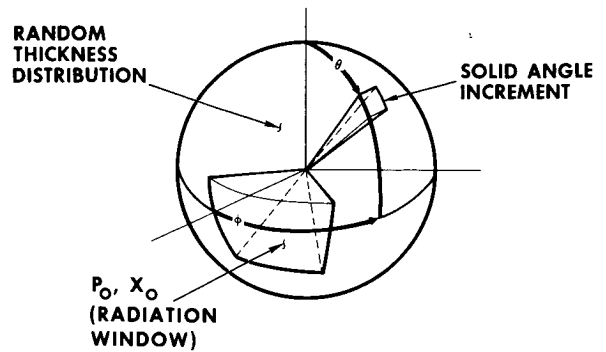


FIGURE 1.—Geometry configuration.

$$N(x) = P_o + \frac{(1-P_o)}{2} \left\{ 1 - \cos \pi \left(\frac{X - X_{MIN}}{X_{MAX} - X_{MIN}} \right) \right\}^{\frac{1}{\tau}}$$

$X_{MIN} \leq X \leq X_{MAX}$

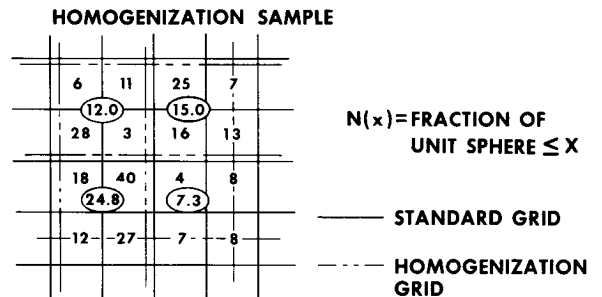


FIGURE 2.—Geometry distribution function: sample portion of inhomogeneous part of unit sphere. Model geometry is defined by the standard grid. A sample grid for homogenized geometry shows the effect of homogenization on the area density.

is indicated to show the effect of homogenization on the area density. This will be discussed in detail in another section.

Several area density distributions are shown in figure 3 as a function of τ (shape factor) for $X_o = 2$ gram/cm² and $P_o = 1/10$. Representative values of the shield parameters are as follows:

	Lunar Spacecraft	Space Suit (Includes Astronaut)
X_o -----	2.0	0.5
P_o -----	0.1	0.5
τ -----	2.0	10.0

The distribution function is not illustrated beyond 50 gm/cm² because the dose contribution for area density greater than 40 gm/cm² is negligible. For proton spectral rigidities

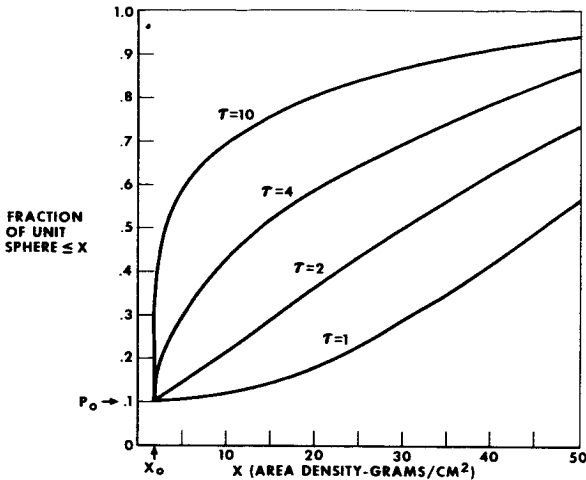


FIGURE 3.—Area density distribution as a function of τ (shape factor) for $X_o=2$ gm/cm² and $P_o=1/10$.

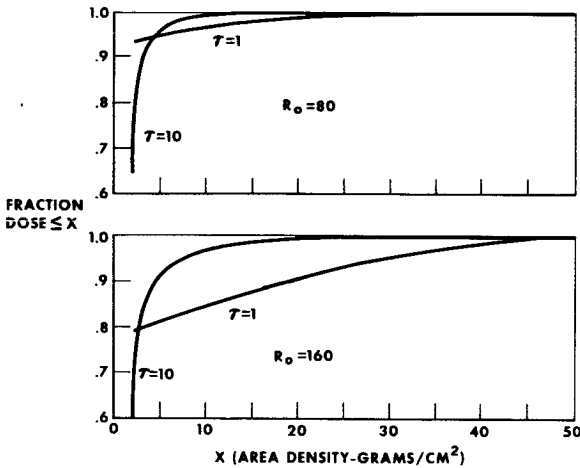


FIGURE 4.—Geometry distribution function: area density for dosages of 80 MV and 160 MV.

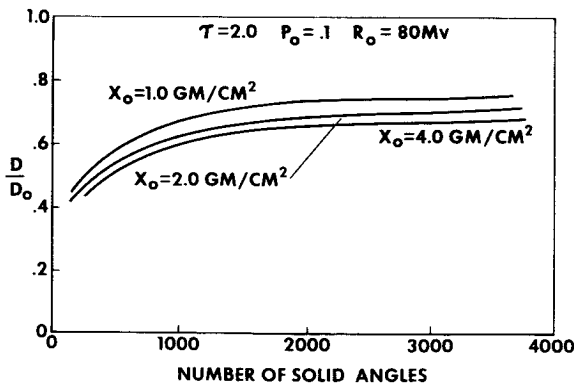


FIGURE 5.—Effect of X_o (radiation window area density) on dose computation accuracy.

of 80 MV or less, the dose contribution for area densities greater than 10 gm/cm² is relatively insignificant (fig. 4). For higher rigidities (160 MV), however, area densities to 40 gm/cm² must be considered.

EFFECT OF SOLID-ANGLE DISTRIBUTION PARAMETERS ON NONSTATISTICAL DOSE COMPUTATIONS

The model geometry, with 4,050 equal solid angles, will be defined as the reference vehicle. Doses will now be presented for various degrees of homogenization of the reference geometry and various distribution parameters. These doses will be used to discuss the importance of geometrical detail, in terms of dose, and the error tolerance of the resultant dose.

Consider the effect of X_o (radiation window area density). Figure 5 shows that the dose computation accuracy for the nonstatistical method is relatively insensitive to X_o ($\tau=2.0$ and $P_o=0.1$ at a rigidity of 80 MV). Therefore, the maximum dose accuracy and increase in accuracy as a function of increasing geometrical precision is approximately independent of X_o .

Figures 6 and 7 with $P_o=0.1$ indicate that homogenization is relatively important and that an increase in geometry detail will tend to provide an increasingly more accurate dose (up to some maximum accuracy). More detailed geometry could increase the accuracy of the dose by about 25 percent. Furthermore, even for a reasonably detailed geometry representation (minute homogenization), it is apparent that doses will only be computed to within 10 to 30 percent tolerance as a function of τ (shape factor).

Figures 6 and 7 clearly indicate that dose accuracy is practically invariant with increasing τ for $P_o>0.3$. Moreover, it is apparent that an increase in geometry detail (beyond about 500 solid angles) would result in only a small change in dose (3 to 5 percent). The maximum dose computation accuracy would be within a tolerance of 10 to 15 percent as a function of P_o . Therefore, the amount of geometry detail should be selected as a function of τ and P_o to avoid possible excessive effort

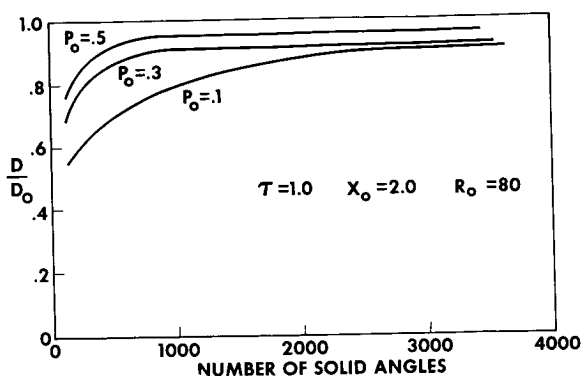


FIGURE 6.—Effect of homogenization and τ (shape factor) on dose computation accuracy.

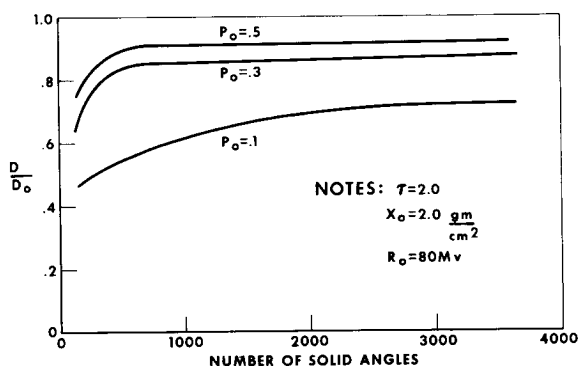


FIGURE 7.—Effect of homogenization and τ (shape factor) on dose computation accuracy.

in representation of geometrical detail without a corresponding increase in dose accuracy. In addition, the techniques which have been presented in this section can be used to estimate the dose error for moderately detailed representations.

Geometry distributions and doses for a typical spacecraft which goes from the earth to the moon are shown in figure 8. These doses were computed with both the statistical and nonstatistical methods. The geometry for the statistical dose, Master Shielding Computer Program (MSCP), is an elemental solids type of geometry. The solids are spheres, cylinders, and annular sectors from horizontal slices of a vertical cone. About 300 homogenized elemental solids were used for this particular spacecraft. The solid-angle representation used about 150 homogenized solid angles for the same spacecraft.

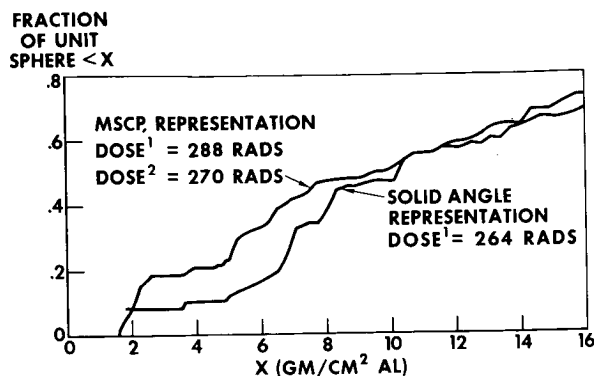


FIGURE 8.—Lunar Spacecraft thickness distribution (center point) 1. $R_0 = 80 N > 30 = 5.0 \times 10^9 P + / CM^2$; no nuclear collisions. 2. With nuclear collisions.

Figure 8 shows a relatively small decrease in dose for the solid-angle representation dose for geometry which is homogenized relative to the MSCP representation geometry. This is consistent with the conclusion of the previous section which indicated a 10 to 30 percent reduction in dose accuracy for a $P_0 = 0.1$ and a X_0 of 2.0 gm/cm^2 . The MSCP radiation window is typical of an actual vehicle. However, the relatively homogenized solid-angle geometry appears to have essentially the same geometrical distribution, except for the window. The radiation window for the solid-angle representation is an effective average of the MSCP radiation window.

CONVERGENCE PROPERTIES OF THE MONTE CARLO METHOD OF DOSE COMPUTATIONS

A modified version of the MSCP statistical dose computation program was used to obtain doses for the reference model geometry. Figure 9 shows the equivalent representation of an integral spectrum for statistical dose computation. The spectrum has been divided into ten integral spectra, which form a segmented straight-line logarithmic fit to the original spectrum. Ten random numbers are used to compute ten proton energies for one direction. The doses are completed in series for the energy interval and terminated on the tenth energy, or when a particular energy does not penetrate the shield. The direction is determined from three randomly selected direction cosines. The ten random energies and three random direction

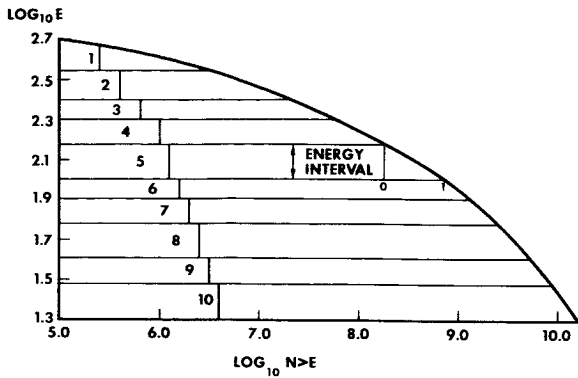


FIGURE 9.—Random energy selection: representation of an integral spectrum for statistical dose computation.

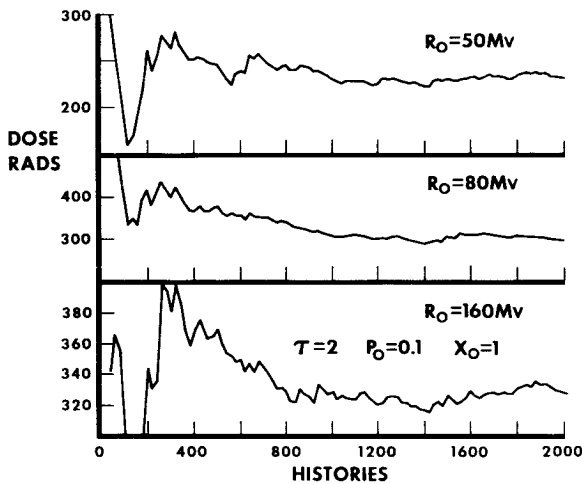


FIGURE 10.—Dose convergence as a function of X_0 (radiation window area density)=1, and rigidity, for $\tau=2.0$ and $P_0=0.1$

cosines constitute one history. Doses computed for the ten energies are weighted according to the fraction of total integral spectrum flux in the respective energy intervals. These doses are accumulated and multiplied by the total integral spectrum flux and divided by the number of histories. The remainder of this section will discuss the effect of rigidity, nuclear collisions, and geometrical parameters on dose convergence for the aforementioned statistical program.

Figures 10 and 11 illustrate dose convergence as a function of X_0 (radiation window area density) and rigidity for $\tau=2.0$ and $P_0=0.1$.

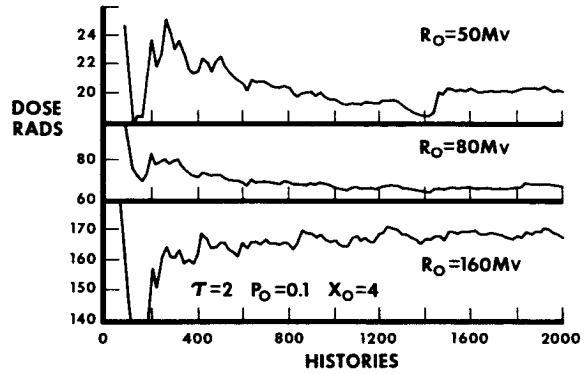


FIGURE 11.—Dose convergence as a function of $X_0=4$, and rigidity, for $\tau=2.0$ and $P_0=0.1$.

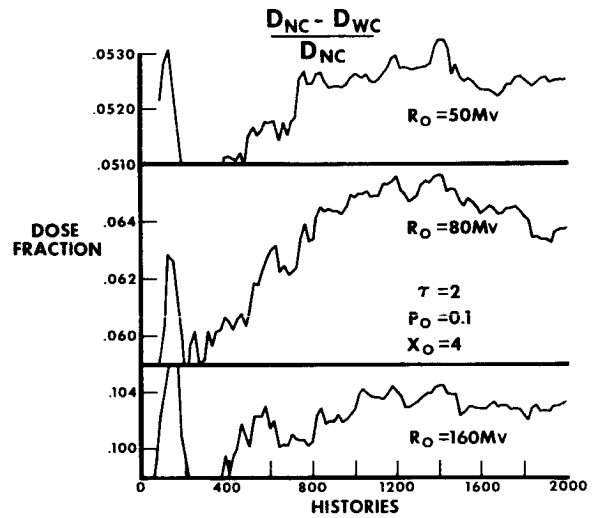


FIGURE 12.—Effect of nuclear collisions on relatively thick spacecraft ($X_0=4 \text{ gm/cm}^2$). D_{WC} and D_{NC} are the doses, with and without non-elastic nuclear collisions.

The doses (fig. 10), which converge to within 5 percent of the final dose at about 1000 histories for all rigidities when $X_0=1.0$, indicate no convergence dependence on rigidity. In figure 11, the dose converges to within 5 percent at 1450, 360, and 375 histories, respectively, for rigidities of 50, 80, and 160. At 3 percent, the respective rigidities converge at 1450, 430, and 600 histories. This indicates faster convergence for larger rigidities.

Figure 12 considers the importance of nuclear collisions for relatively thick spacecraft ($X_0=4 \text{ gm/cm}^2$). D_{WC} and D_{NC} are the doses, with and without nonelastic nuclear collisions. The

dose reduction, considering nuclear collisions, is 0.053, 0.064, and 0.103 for rigidities of 50, 80, and 160 MV, respectively. This dose reduction is sufficiently large to necessitate accounting for nuclear collision for thick vehicles ($X_0=4$). The dose reduction due to nuclear collisions converges to within 1.0 percent at 1450, 1950, and 1450 for rigidities of 50, 80, and 160, respectively. The corresponding doses converge at 1950, 1450, and 1800, for the respective rigidities. The nuclear collision dose reduction, therefore, tends to converge at about the same rate or faster than the dose without nuclear collisions for $X_0=4.0$. Nuclear collisions should also be included for this case.

Figures 13 and 14 show convergence trends as a function of τ . The dose of figure 13 converges at about 400 and 1100 histories, respectively, for 5 percent and 3 percent when the shape factor τ is 2.0. However, for a shape factor of 4.0, dose convergence occurs respectively at 1000 and 1300 histories (fig. 14). The dose, therefore, tends to converge faster for smaller values of the geometry distribution shape factor. For shape factors of 2 (fig. 15), 4 (fig. 16), and an X_0 of 2 gm/cm², the dose fraction converges to within 3 percent at about 350 histories. This indicates that the dose reduction converges much faster than the uncollided dose for $P_0=0.1$, $X_0=2.0$, and $\tau=2.0$ and 4.0. Figures 15 and 16 also indicate dose fraction ranges of (0.029 to 0.031) and (0.051 to 0.071) for rigidities of 50 and 160 MV, respectively. It is not necessary to include nuclear collisions for small rigidities. Inclusion is necessary for intermediate and large rigidities as a function of τ .

COMPUTATIONAL ACCURACY FOR STATISTICAL PRIMARY IONIZATION DOSE

In order to determine the degree of accuracy obtainable with the statistical method, the dose history distribution in figure 17 has been normalized to the dose for a 4050 solid-angle model ($\tau=2$, $P_0=0.1$, $X_0=2$, $R_0=80$). The reference grid dose was computed with the program used for the previously mentioned homogenized and standard grid doses. Neither the statistical or nonstatistical doses include

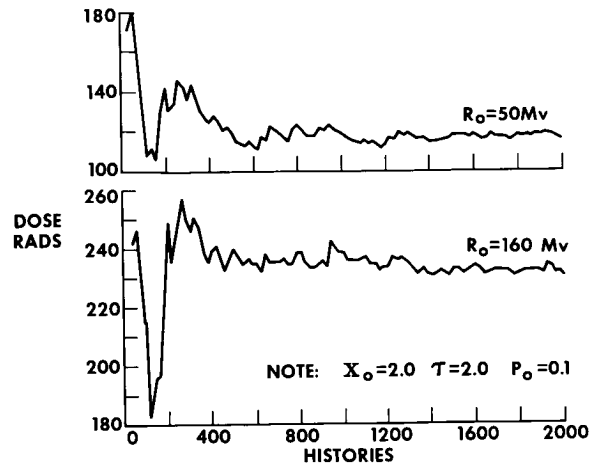


FIGURE 13.—Dose convergence—no nuclear collisions; shape factor $\tau=2.0$.

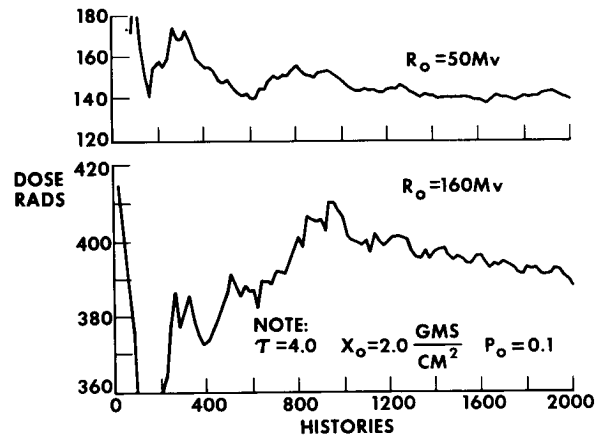


FIGURE 14.—Dose convergence—no nuclear collisions; shape factor $\tau=4.0$.

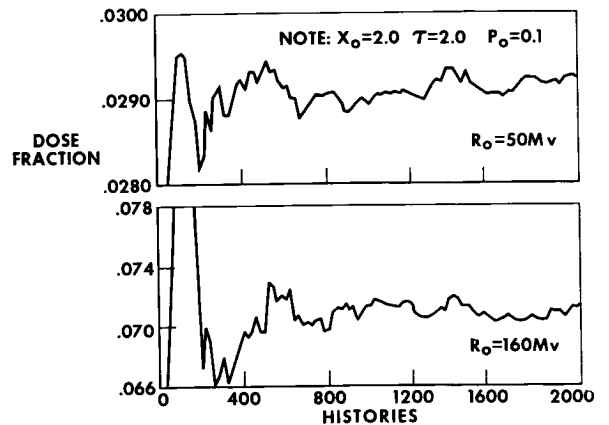


FIGURE 15.—Dose convergence $\frac{D_{NC} - D_{WC}}{D_{NC}}$; shape factor $T=2.0$.

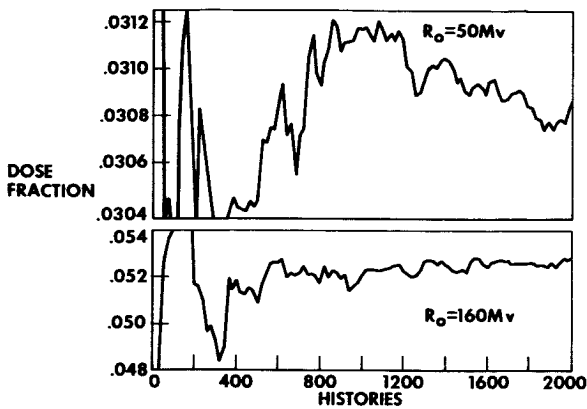


FIGURE 16.—Dose convergence— $\frac{D_{NC}-D_{WC}}{D_{NC}}$; shape factor $T=4.0$.

the dose reduction due to nuclear collisions. In figure 17, the dose converges to within 3 percent of the exact dose at about 1000 histories. At 2000 histories, the dose has converged to within 1 percent. This convergence demonstrates the potential of the Monte Carlo method of primary dose computation for rather inhomogeneous geometry.

RELATIVE MERITS OF NONSTATISTICAL AND STATISTICAL METHODS OF DOSE COMPUTATION

1. The type of analysis outlined in this paper should be used with a preliminary spacecraft distribution to determine the desirable extent of geometry detail and potential associated dose error. This will eliminate excessive effort in generating geometry representations which will yield only negligible improvement in dose computation accuracy.

2. Statistical and nonstatistical doses require about 60 seconds and 3 seconds of computer time, respectively, per computed dose. How-

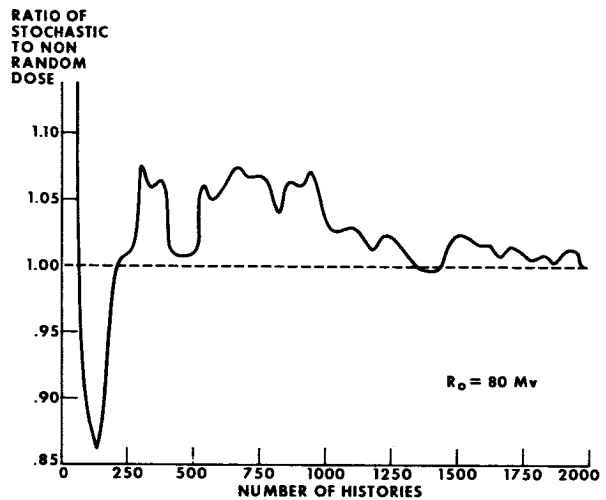


FIGURE 17.—Relative dose computational accuracy for stochastic dose program. Dose history distribution normalized to dose for a 4050 solid-angle model ($\tau=2, P_o=0.1, X_o=2, R_o=80$).

ever, the time required for geometry tracking will be large compared to both dose computation times. For example, the geometry tracking will be in the order of several minutes.

3. The necessity of accounting for dose reduction due to nuclear collisions is directly related to the shield area density distribution function and the rigidity of the proton spectrum. The inclusion of nuclear collisions in a stochastic dose calculation has a negligible effect on convergence.

4. The Monte Carlo technique should be used when extremely minute geometry is desirable because this method does not homogenize the geometry and can approach the actual dose. The nonstatistical method will necessarily result in some degree of homogenization. Homogenization will cause a smaller dose than the actual dose.

58—A Space Radiation Shielding Code For Realistic Vehicle Geometries¹

K. M. SIMPSON, C. W. HILL, and C. C. DOUGLASS

Lockheed—Georgia Company

This paper describes a computer code system which estimates primary proton and associated secondary dose at points within complex geometric configurations. Three computer programs constitute the system. The geometry program (GEOM) manipulates geometric data and computes penetration thicknesses. The geometry test program (GTEST) scans the input geometric data for character and format errors, checks for logical inconsistencies, and plots, off line, selected cross sections of the geometric representation in order that a visual inspection of the geometric configuration may be made. The dose program (DOSE) combines radiation source data and geometric data and computes the dose at specified detector points.

The purpose of the geometry program is to discover the shielding afforded a detector by a configuration of materials. To realize this purpose, a set of volume elements, representing the configuration, is constructed and a set of vectors associated with each detector is generated. The volume elements are constructed and the vectors are generated automatically by the geometry program from input data. Each volume element is defined by its material composition, density, and bounding surfaces. Four types of volume element boundaries may be used:

- Planar surfaces
- Ellipsoidal surfaces
- Elliptic cylindrical surfaces
- Elliptic conical surfaces

The coefficients for the algebraic representation of the planar and quadric surfaces are calculated by the geometry program. Data preparation for these surfaces is easy and straight-forward. These data consist of a few points, lengths, and ratios that may be obtained from engineering drawings. A planar surface is determined by the coordinates of three non-collinear points; each of the quadric surfaces is determined by three points and at most three parameters. The geometry program derives the quadric surface coefficients in a coordinate system in which the algebraic expression for the surface has a canonical form. The program then obtains the transformation necessary to compute the surface coefficients in the coordinate system common to the entire configuration. A maximum of 50 surfaces, each with unrestricted orientation, may be used to bound a volume element. Each volume element requires, in addition to the bounding surface data, the number of planar surfaces, the number of quadric surfaces, a material number, the density, and the coordinates of an internal point.

In order to reduce the amount of data required to specify a set of volume elements, a feature called "embedding" is employed. Embedding permits volume elements to be located partially, or completely, within other volume elements. Figure 1 illustrates a hollow box being specified by two volume elements—each with six bounding surfaces. Without embedding, the same hollow box would require six volume elements—each with six bounding surfaces. If two or more volume elements compete for a common region of space, dominance is assigned by the order of data input. The number of volume elements which may com-

¹ Research sponsored by George C. Marshall Space Flight Center, NASA, under contract NAS 8-11164.

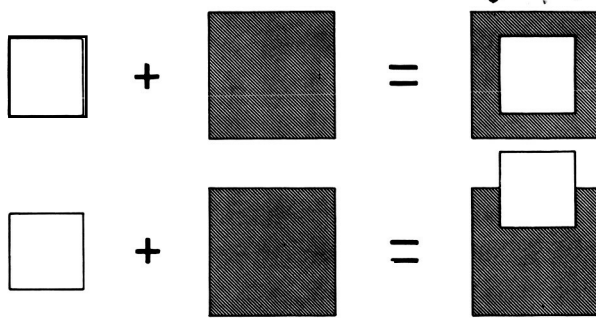


FIGURE 1.—Volume element embedding.

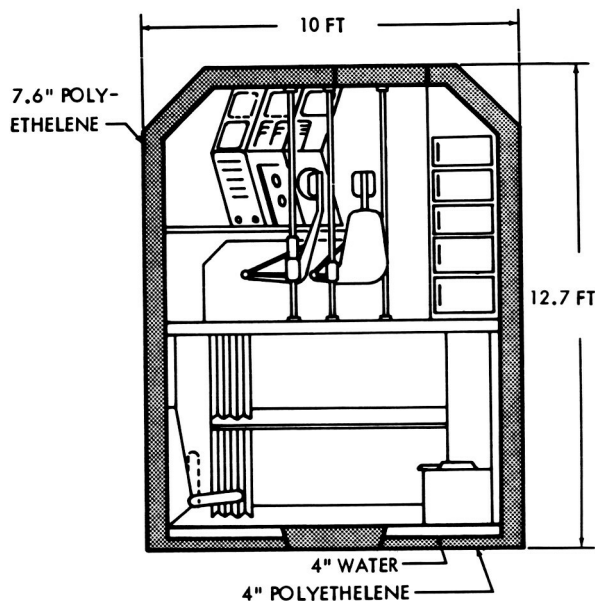


FIGURE 2.—Eight-man module.

pete for a common region of space is presently restricted to 25.

Embedding reduces considerably the number of volume elements and bounding surfaces that must be specified to represent a geometric configuration. Figure 2 illustrates a conceptual design of an interplanetary vehicle. The outer shield is simulated by two volume elements—each consisting of two planes, a cone and a cylinder. The first volume element specifies a void or an atmosphere (depending on the value assigned the density of this volume element) possessing the inner dimensions of the shield; the second volume element specifies a solid figure of polyethylene possessing the outer dimensions of the shield. The instrument console is defined in a similar manner by four

volume elements. Without embedding, 15 volume elements would be required for the instrument console. Should additional detail be desired, other volume elements may be added without changing the present data. Thus the embedding feature offers a compact way of treating complex configurations and of modifying these configurations.

In order to reduce the time spent in data generation, an option is available whereby volume elements may be rotated and translated to any desired orientation and location. An example of an application of this feature is illustrated by the following. A man model, in a sitting attitude, is constructed in a convenient coordinate system. The volume elements defining the man model are then moved into the central control position by the appropriate transformation. Two identical man model data sets are loaded with other transformations to position two other crew members at the instrument console. The same technique is used to place four prone man models in the lower half of the vehicle and one in the hatchway between stations. After a sitting man model and a prone man model have been constructed, eight simulated crew members may be positioned in the vehicle with less than an hour's work.

The geometric configuration is scanned by the geometry program in the following way. An axially symmetric figure is generated by rotating line segments about the z-axis. A rotated line segment generates a truncated conical or cylindrical shell. Each shell is approximated by six equal planar facets. Each facet is subdivided into regions until the solid angle subtended by each region at a detector is less than the input solid angle criterion for that facet. This feature permits critical shield areas to be examined more closely than others.

A vector array associated with each detector is then generated. Each vector joins the detector to the centroid of a region. Those segments of each vector which lie within volume elements are found and arranged in order from detector outward. The penetration lengths, material numbers, solid angle, and vector direction cosines are put on tape for use by the dose program.

The geometry test program is an essential adjunct to the geometry program in that it

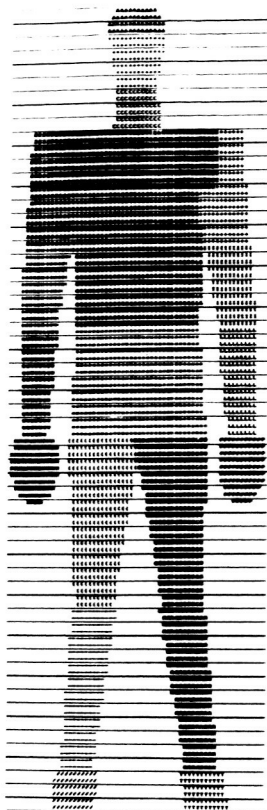


FIGURE 3.—Man model.

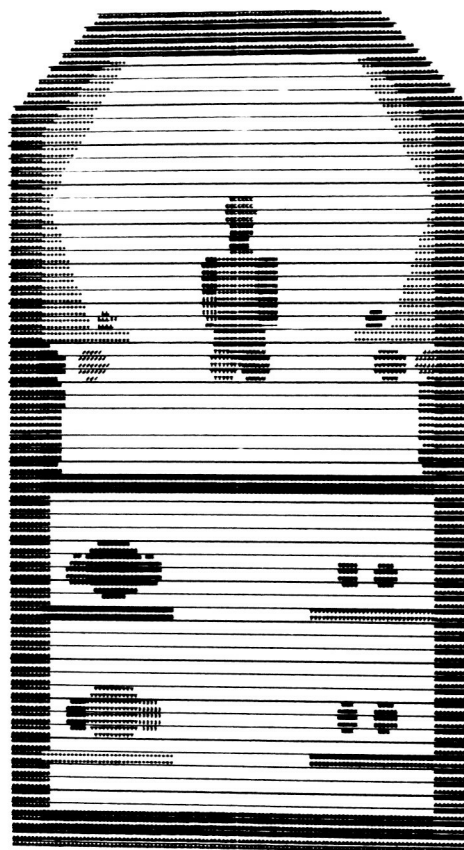


FIGURE 4.—Eight-man module vertical section.

provides computer assistance in checking geometric input data. This program first scans the input data for incorrect formats and characters. Card images containing errors are printed off-line. The program also checks for certain logical errors which would lead to ambiguity in the definition of volume elements. Erroneous volume elements are identified and printed off-line. Finally, it plots cross sections of the configuration as specified by the user. The cross sections are unrestricted in orientation. The grid size of the printer plots is variable to a maximum of 130 by 500. An alpha-numeric character is assigned each volume element appearing on the plot, and a table follows each plot indicating volume element number, density, and material number associated with each character assignment. Exhaustion of the character list, which contains 43 characters, causes a new plot to be started. This geometry test program has proved to be invaluable for verifying and correcting complex geometric data. Sample plots of the prone-man

model and the eight-man module are shown in figures 3 to 5.

The task of the dose program is to compute primary proton and related secondary dose at detector points associated with the geometric configuration. The location of the detectors with respect to the configuration and its component volume elements is in no manner restricted.

The dose program approximates the appropriate proton spectrum, differential in energy, with from one to 100 power law representations over the energy range of interest. The source and geometric data are applied to an attenuation method suggested in a preceding paper by M. O. Burrell.

The validity of the dose calculation has been tested by comparing the results to those of the Lockheed Proton Penetration Code in spherical shell shield geometry for isotropic flux. Several spectra, materials, and material combinations

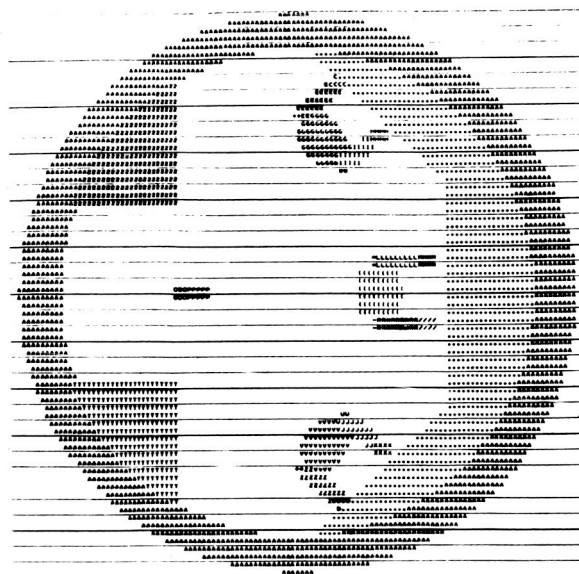


FIGURE 5.—Eight-man module horizontal section.

have been examined. Comparisons for aluminum, iron, and water are shown in figures 6-8.

For various combinations of aluminum, polyethylene, iron, and tissue, the dose program differed from LPPC by only 2 percent at most. The method appears to be satisfactory for shields less than 100 grams per square centimeter thick; investigations of thicker shields have not been conducted.

Table I displays the estimated dose values at ten detector locations in the eight-man interplanetary module shown in figure 2. Table I also indicates the effects of inboard equipment and body self-shielding on the dose values for

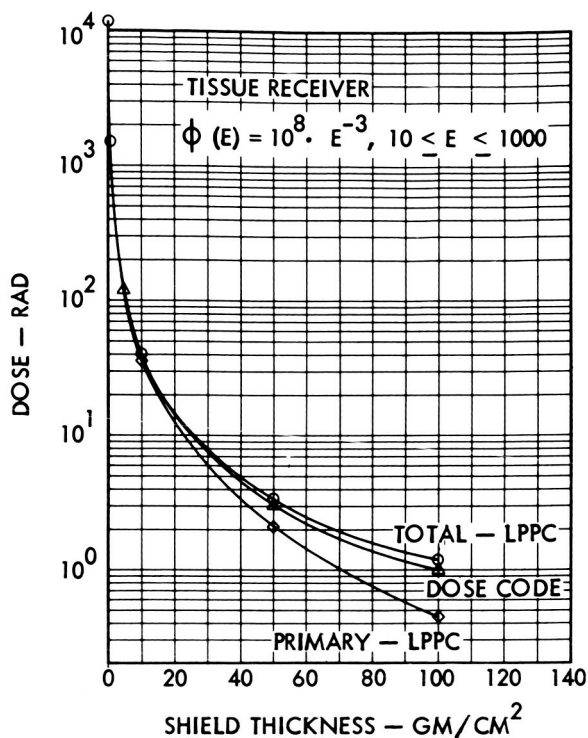


FIGURE 6.—Spherical shield aluminum.

7.6 and 1.0 inches of polyethylene shield. The crew arrangement for this configuration is: three man models are seated at the instrument console, four supine man models on the bunks, and one standing man model in the hatchway between stations. In this calculation, the average solid angle associated with each vector is 0.13 steradians, that is, an average of 97 vectors per detector.

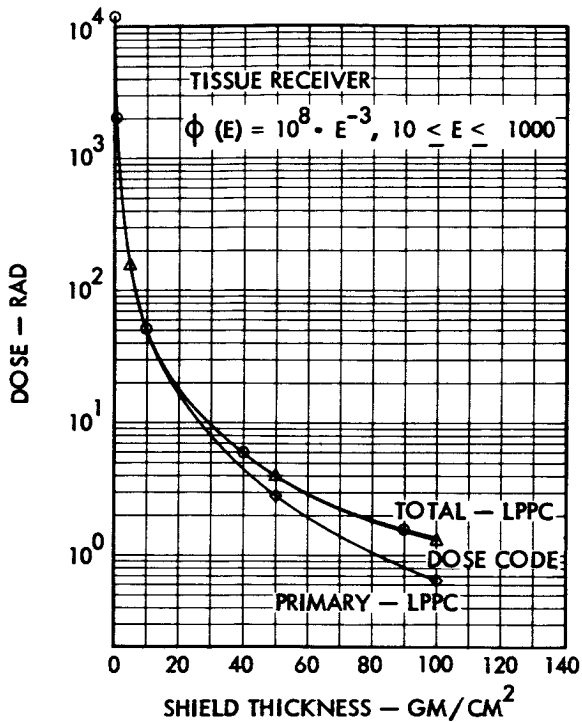


FIGURE 7.—Spherical shield iron.

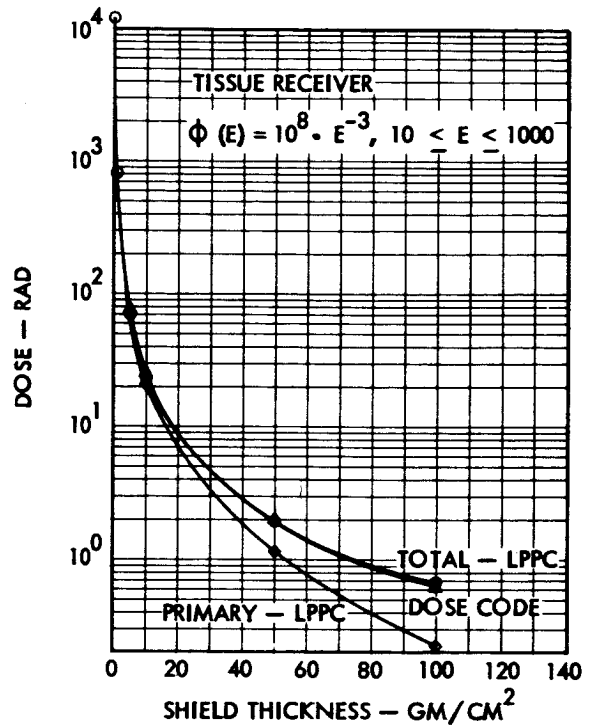


FIGURE 8.—Spherical shield water.

TABLE I
Solar Flare Dose (Rad)—Eight-Man Module

$$\left[\frac{d\phi}{dp} = 5.675 \times 10^8 \exp(-p/80), \frac{\text{protons}}{\text{cm}^2 \text{ MV}} \right]$$

Detectors	1E	1A	2E	2A	3E	3A	4E	5E	5A	6E
<i>7.6-inch Polyethylene</i>										
Shield only.....	2.87	2.87	1.49	2.07	3.00	2.51	2.36	1.59	2.08	1.62
Shield + equipment.....	1.82	1.92	1.36	1.80	2.18	2.10	1.66	1.43	1.80	1.44
Shield + crew + equipment..	1.17	0.29	0.78	0.20	1.24	0.30	1.28	0.82	0.20	0.84
<i>1.0-inch Polyethylene</i>										
Shield only.....	203.	194.	98.0	122.	198.	165.	176.	107.	124.	105.
Shield + equipment.....	83.5	95.5	91.6	96.5	116.	115.	88.6	98.1	97.4	89.5
Shield + crew + equipment..	30.4	1.87	47.6	1.16	42.1	2.12	54.4	48.9	1.23	49.7

E=Detector in eye.

A=Detector in abdomen.

1=Middle crew member at console.

2=Crew member in top bunk, head under console.

3=Crew member in hatchway.

4=Right crew member at console.

5=Crew member in top bunk, feet under console.

6=Crew member in bottom bunk, head under console.

SYMPOSIUM SUMMARY

59—Summary of the Second Symposium on Protection Against Radiations in Space

J. WARREN KELLER

NASA Headquarters

The purpose of this "Second Symposium on Protection Against Radiations in Space" was to bring the group working in the area together again to review the present status of space shielding work, and to look at the advancements that have taken place since the last symposium 2 years ago. The program was arranged so that the first three sessions were not primarily directed at the question of shielding, per se, but were concerned with the areas that actually define the shielding problem for us—the radiation environment in space, the biological effects of the radiation, and its effects on materials and components. I'd like to make a few comments regarding these first three sessions before going on.

From the session on the environment, it was apparent that data obtained during the past 2 years have not significantly altered the space radiation problem. It has been impossible to obtain much additional data on solar flares since we have been in a time of solar minimum. The problem of the artificial radiation belt had just become apparent at the time of the last meeting, and has received the principal attention since that time. This session brought out the fact that there has been a large amount of delving in detail into the existing data so as to better understand the perturbations that one has to deal with in considering the environment. Many of the questions that were with us at the time of the last meeting 2 years ago, such as which particles were trapped from the high altitude nuclear blast, have been somewhat answered in the intervening time. Of particular interest in the environment session was the work described by Dr. Vette of Aerospace

Corporation. This effort in compiling up-to-date maps of the trapped radiation represents a significant step forward in that it has the prospects of resulting in both of the principal segments of the Government concerned with space missions using the same environmental data for this component of the radiation. Hopefully, these data will be updated on a timely basis, resulting in everyone working with much more up-to-date data in the future than has been the case in the past. On the other hand, it appears that data on the detailed spectra of the low energy particles for all components of the radiation environment are insufficient. The space scientists are just as anxious for these data as are the people concerned with radiation effects and shielding, but the data are difficult to obtain. I am sure that we will see progress in this area in the future.

It was evident from the session on biological effects that large strides have been taken in that area. Two years ago, data for charged particles were very sparse, and it was necessary to rely almost entirely on neutron and gamma data. Although additional experiments have now been run using protons, most of the conclusions based on neutrons and gammas have stood up fairly well so that there has been a situation of confirming earlier thoughts on this subject. I think we must all sympathize with the people doing biological work. In the shielding or radiation effects area, we can take a piece of material, irradiate it, and see what happens. The biologist, on the other hand, has to use something other than the target that he is primarily concerned with, since he can't, for the most part, afford to experiment on

humans. He has a difficult problem of extrapolation. There were several points made in the biological effects session that stand out. One was the need for the study of combined stresses. This need was brought out by most of the speakers. Another point was the danger of indiscriminate use of recovery rates in considering the biological effects of space radiations. At least one paper pointed out the possible potential seriousness of the primary cosmic rays.

From the session dealing with radiation effects on materials and components, it was evident that, with the exception of the effects on a few particular types of materials, very long exposure times in the space environment are required to produce significant damage. It is principally with respect to the radiation effects problem for sensitive materials and components that the low energy spectral data referred to earlier are needed.

The radiation problems for three particular types of "missions" were discussed in invited papers in the meeting. These missions, which were Apollo, a Manned Orbiting Laboratory, and the Supersonic Transport, point out very dramatically the scope of the problems with respect to radiation in space. The problem for Apollo is primarily that of solar flares. For a Manned Orbiting Laboratory, it is the trapped radiation. The primary problem for the Supersonic Transport may be that imposed by the heavy nucleic component of galactic cosmic radiation. Here, we have the three primary components of the space radiation, with each represented by a mission in which that component is the controlling one. It is clear that each of these missions could potentially incur difficulties if the radiation problem were not given consideration. Consequently, each of the missions has some constraint imposed by the radiation considerations. In the case of the Supersonic Transport, the altitude at which it can operate at high latitudes is constrained by the radiation problem since one is dependent upon the earth's atmosphere for shielding. There are restrictions as to where a Manned Orbiting Laboratory can operate. An altitude must be picked which is low enough to be sufficiently free of radiation so that dose tolerances

are not exceeded. In the Apollo case, the constraint is somewhat different in that a warning system is needed to signal the occurrence of solar flares.

With regard to Apollo, a few additional comments to those that have already been made might be in order. Mr. Robbins, in his talk on the "Shielding Analysis" for Apollo, gave the following numbers for the integrated solar proton fluxes >30 MeV which would be necessary to reach the emergency dose limits for the skin and for the blood forming organs (B.F.O.) in either the LEM or the Command Module:

<i>Command Module</i>	<i>LEM</i>
2×10^{10} protons/cm ² ----(Skin)----	1.2×10^9 protons/cm ²
4.8×10^{10} protons/cm ² ----(B.F.O.)----	7×10^{10} protons/cm ²

By comparison, the best estimate of the integrated flux of solar protons >30 MeV for the largest known single group of events—that of July 1959—is 3.2×10^9 protons/cm². It is noted that this flux, for which the chance of encounter would be extremely remote, is well under that needed to produce the emergency dose limits for either the skin or the blood forming organs in the Command Module. It is also noted that in the LEM this value is below that required for the blood forming organs but does, indeed, exceed that for the skin. It should be pointed out, however, that the value given for the July 1959 series of events is integrated over the entire series. On the other hand, the mission in the LEM is constrained for other reasons to a much shorter time than is covered by this integration and, consequently, the dose limits would not be exceeded in this case either. Still another condition must be considered—that for the astronaut on the lunar surface outside the LEM. It has been determined that, with adequate warning of an event, this case can be handled in a satisfactory manner by modifying the mission so as to utilize the protection afforded by the LEM and Command Module. This case, along with the relatively high dose which could be sustained in the LEM, points out the need for the Solar Proton Alert Network which was discussed in the meeting.

Moving on to the rest of the meeting, there was a considerable amount of data presented on the interactions of radiations with matter and

the transport of radiation through matter. Consideration of secondary radiations produced by the interactions of protons with matter brings up the question as to whether or not a need exists for such data in view of the fact that it has been shown that quite thick shields must be employed before the secondaries produced in the shield become important.

Two things may be pointed out in this regard. First, there is a potential problem of secondaries produced in the body which is itself a thick shield. Secondly, in the early vehicles, such as Apollo, we are speaking of solar flares in an emergency sense. The probability of incurring a large solar flare during the Apollo mission, for instance, is very very small. If we change our sights and look at long-term missions that might be a year, two years, or three years in duration, these events can no longer be considered emergencies. We know that we will encounter solar flares. Consequently, the shielding thicknesses for such cases will increase. The need for proton secondary data then depends very much on the type of mission as well as on the nominal allowable doses which are arrived at for future missions. Also, if one is not willing to rule out the high energy proton portion of the Van Allen belt for manned orbital operations, he will encounter the need, there, for thick shields.

Two years ago most of the data presented on the interactions in, and transport through, matter were the results of theory, with very little experimental data presented. From the papers presented at this meeting, it is obvious that quite a bit of experimental data exist today for both protons and electrons, with more being generated daily. These papers, in general, pointed out the quite good agreement between theory and experiment for both protons and electrons. It should be noted that a large part of the experimental work which was reported was initiated to check out the theory and not for the generation of a large amount of parametric data.

Comparison with the last meeting indicates that the picture on shielding calculation techniques has not changed significantly. There have been refinements but, in general, the same types of calculations are being made. The

principal refinements have been in the area of provision for better defining of complicated vehicle geometry. The need for this was discussed at the last meeting. Dr. Alsmiller's paper was very interesting concerning the effectiveness of the straightahead method in handling the secondaries from protons. If the simple straightahead technique continues to prove to be adequate, consideration of secondary production may not require major changes in the codes now used for calculating doses.

A striking difference between this meeting and the last was the large amount of electron data presented at this meeting. The motivation, of course, was the existence of the artificial electron belt. Similarly, alpha particles may come in for more attention in future meetings of this type because of the large number of such particles which have been observed in solar proton events.

Besides the more conventional passive shielding, several papers dealt with magnetic or active shields. The purely magnetic shield is seen to look most attractive for vehicles needing large shielded volumes and high cutoff energies. It would seem that these types of systems must become very attractive weightwise before they would be used because of their questionable reliability compared to that of conventional bulk shielding. In any case, the application of this type of shield must be considered to be quite a number of years off. Their development presents a difficult problem requiring several significant advances in the present state-of-the-art.

There was one new shielding technique which was advanced in this meeting—that of the "plasma shield"—which has an advantage over the purely magnetic shield in that much weaker magnetic fields are required. However, the "plasma shield" concept, introduced by Dr. Levy, has many technical problems at this time. This concept, which employs electrostatic shielding for protons while using a magnetic field to control electrons, is very interesting in that it is the first really new shielding concept that has evolved in quite some time.

In conclusion, it is apparent from this meeting that the people working in the space shielding field are becoming a community—working together. This was obvious from the discussion and technical exchange during the

meeting. It appears that a large percentage of the attendees were quite well aware of most of the things going on in the field. This speaks well for the communication that has developed in this field during the past 2 years.

APPENDIX

LIST OF PARTICIPANTS

ADAMS, DUANE A.
Air Force Weapons Laboratory

ALSMILLER, FRANCES S.
Oak Ridge National Laboratory

ALSMILLER, R. G., JR.
Oak Ridge National Laboratory

ANDERS, WILLIAM A.
Manned Spacecraft Center, NASA

ANDREWS, GOULD A.
Oak Ridge Institutes of Nuclear Studies

ARNOLD, WILLIAM
Oak Ridge National Laboratory

ASHLEY, JAMES C.
Marshall Space Flight Center, NASA

AVERELL, JOHN P.
Avco-Wilmington

BAIETTI, ALBERT L.
Tracer Laboratory

BAILEY, D. K.
CRPL, National Bureau of Standards

BAILY, NORMAN A.
Hughes Research Laboratories

BARR, N. F.
U.S. Atomic Energy Commission

BARRETT, MATTHEW J.
Nuclear Utility Services, Inc.

BENJAMIN, FRED B.
NASA Headquarters

BERGER, PAUL S.
Air Force Weapons Laboratory

BERNERT, R. E.
Avco-Everett Research Laboratory

BERTINI, H.
Oak Ridge National Laboratory

BETTENHAUSEN, LEE H.
Battelle Memorial Institute

BILLINGHAM, JOHN
Manned Spacecraft Center, NASA

BINDER, DANIEL
Hughes Aircraft Company

BORELLA, HENRY M.
Edgerton, Germeshausen & Grier, Inc.

BOUQUET, FRANK L., JR.
Lockheed-California Company

BOURNE, HARRY K.
United Kingdom Scientific Mission
British Embassy

BRANDON, GEORGE W.
Manned Spacecraft Center, NASA

BRESTICKER, SAM
Grumman Aircraft Engr. Corporation

BRINOCHE, PAUL
Grumman Aircraft Engr. Corporation

BULL, HOWARD I., JR.
Westinghouse, Aerospace Division

BURKE, JOHN R.
HQ U.S. Air Force

BURRELL, MARTIN O.
Marshall Space Flight Center, NASA

BURRUS, W. R.
Oak Ridge National Laboratory

CARROLL, W. F.
Jet Propulsion Laboratory

CELNIK, JACOB
United Nuclear Corporation

CHAPMAN, G. T.
Oak Ridge National Laboratory

CHERUBINI, J. H.
High Voltage Engr. Corporation

CLARK, ROBERT S.
Air Force Weapons Laboratory

CLARK, T. G.
Oak Ridge National Laboratory

CLELAND, JOHN W.
Oak Ridge National Laboratory

CLOUTIER, R. J.
Oak Ridge Institute of Nuclear Studies

COFFEY, D. L.
Oak Ridge National Laboratory

CONDON, WILLIAM
U.S. Atomic Energy Commission

CONNOLLY, FRANCIS J.
Air Force Weapons Laboratory

CONNOR, G. B.
U.S. Atomic Energy Commission

COVEYOU, R. R.
Oak Ridge National Laboratory

COX, W. C.
Oak Ridge National Laboratory

CRAWFORD, JAMES H., JR.
Oak Ridge National Laboratory

CUPKA, A. G., JR.
Air Force Weapons Laboratory

CURTIS, STANLEY B.
The Boeing Company

DANCE, W. E.
LTV Research Center

DAVIS, HAROLD L.
Bellcomm, Inc.

DAVIS, HENRY M.
Air Force Weapons Laboratory

- DELONG, CHESTER W.
Consultant
- DEVRIES, LEONARD
Scott Air Force Base
- DUBERG, JOHN E.
Langley Research Center, NASA
- DUCKWORTH, G.
Northrop Space Laboratory
- DUGAS, DORIS J.
The Rand Corporation
- EDMONSON, N., JR.
Marshall Space Flight Center, NASA
- EKBERG, DONALD R.
General Electric Company
- ENGLER, ERICH E.
Marshall Space Flight Center, NASA
- ENZ, RICHARD W.
Air Force Weapons Laboratory
- EVANS, ROBLEY D.
Massachusetts Institute of Technology
- EWING, DEAN E.
Air Force Weapons Laboratory
- FAN, H. Y.
Purdue University
- FARRAR, R. M.
Lockheed-Georgia Company
- FERGUSON, DAVID N.
Langley Research Center, NASA
- FERGUSON, JAMES M.
U.S. Naval Rad. Defense Laboratory
- FILZ, ROBERT
Air Force Cambridge Research Laboratories
- FISH, BIRNEY R.
Oak Ridge National Laboratory
- FOELSCH, TRUTZ
Langley Research Center, NASA
- FORTNEY, R. E.
Northrop Space Laboratory
- FOX, LEO
NASA Headquarters
- FRANCIS, HEMMA E.
Union Carbide Corporation
- FREEMAN, J. W., JR.
Rice University
- FRENCH, FRANCIS W.
Mitre Corporation
- GALBRAITH, T. L.
General Electric Company
- GIBSON, W. A.
Oak Ridge National Laboratory
- GILBERT, M. B.
Air Force Cambridge Research Laboratories
- GILFILLAN, DONALD R.
ARO, Inc.
- GONSHERY, MARVIN E.
Frankford Arsenal
- GOOD, ROBERT C., JR.
General Electric Company
- GRAHN, DOUGLAS
Argonne National Laboratory
- GRAVES, GLEN A.
Los Alamos Scientific Laboratory
- GREEN, DON J.
Manned Spacecraft Center, NASA
- GUTHRIE, MIRIAM P.
Oak Ridge National Laboratory
- HAFFNER, JAMES W.
North American Aviation Company
- HAMMAN, DONALD J.
Battelle Memorial Institute
- HANSEN, KENT F.
Massachusetts Institute of Technology
- HANSEN, R. M.
Langley Research Center, NASA
- HARRIS, MILFORD D., JR.
Brooks Air Force Base
- HARNEY, E. D.
U.S. Air Force Space Systems Division
- HARRISON, ROBERT E.
Aerospace Corporation
- HARRISON, S. E.
Martin Company
- HENDRICKSON, HENRIETTA R.
Oak Ridge National Laboratory
- HENDRICKSON, JOHN R., SR.
Radio Corporation of America
- HEWITT, JOHN E.
Ames Research Center, NASA
- HIGGINS, PETER W.
Manned Spacecraft Center, NASA
- HILDERBRAND, ROBERT I.
Lewis Research Center, NASA
- HILL, CHARLES W.
Lockheed-Georgia Company
- HILL, N. W.
Oak Ridge National Laboratory
- HOENIG, W. B., JR.
Wright-Patterson Air Force Base
- HOMSEY, ROBERT J.
General Electric Company
- IRVING, DAVE C.
Oak Ridge National Laboratory
- JANDA, ROBERT J.
Goddard Space Flight Center, NASA
- JANES, G. SARGENT
Avco-Everett Research Laboratory
- JONES, ROBERT K.
Lovelace Foundation
- JORDAN, THOMAS M.
Douglas Aircraft Company
- JORDAN, W. H.
Oak Ridge National Laboratory
- JORDAN, WILLIS Y., JR.
Marshall Space Flight Center, NASA
- JUPITER, CLYDE P.
General Atomic
- KAM, FRANCIS B. K.
Oak Ridge National Laboratory
- KAPLAN, BERNARD
Air Force Institute of Technology

- KARP, IRVING M.
Lewis Research Center, NASA
- KASE, P. G.
The Martin Company
- KELLER, J. WARREN
NASA Headquarters
- KIDD, EDWIN CARSON
General Dynamics/Fort Worth
- KINNEY, W. E.
Oak Ridge National Laboratory
- KIRKBRIDE, JOHN
Edgerton, Germeshausen & Grier, Inc.
- KISTLER, VON EUGENE
Atomics International
- KLOPP, DAVID A.
IIT Research Institute
- KLOSTER, R. L.
McDonnell Aircraft Corporation
- KUHN, EDWARD
Republic Aviation Corporation
- KURITZKY, CLARENCE S.
Armed Forces Radiobiology Research Institute
- LANGLEY, ROBERT W.
Douglas Aircraft Company
- LEIMDORFER, MARTIN
Research Institute of National Defense (Sweden)
- LEVY, RICHARD H.
Avco-Everett Research Laboratory
- LILEY, BOBBY
North American Aviation Company
- LINDSAY, IAN R.
Royal Canadian Air Force
- LOVE, T. A.
Oak Ridge National Laboratory
- LUCHTER, STEPHEN
Aerojet-General Nucleonics
- LUSHBAUGH, C. C.
Oak Ridge Institute of Nuclear Studies
- MACFARLANE, GEORGE
Royal Canadian Air Force
- MAIENSCHIN, F. C.
Oak Ridge National Laboratory
- MALICH, C. W.
Ames Research Center, NASA
- MALIN, LEON
United Nuclear Corporation
- MALITSON, IRVING H.
National Bureau of Standards
- MALONE, C. FORREST
Manned Spacecraft Center, NASA
- MAR, BRIAN
The Boeing Company
- MARTIN, SHELL E.
Manned Spacecraft Center, NASA
- MASKEWITZ, BETTY F.
Oak Ridge National Laboratory
- McDERMED, ORVIS L.
General Dynamics/Astronautics
- MCDONALD, F. B.
Goddard Space Flight Center, NASA
- McGILL, BETTY L.
Oak Ridge National Laboratory
- McGUIRE, THOMAS J.
Wright-Patterson Air Force Base
- McREYNOLDS, A. W.
General Dynamics/Astronautics
- MEEKS, E. J.
U.S. Air Force
- MEREDITH, O. M.
Lockheed Missile and Space Company
- MILLER, RICHARD A.
General Dynamics/Fort Worth
- MILLER, WILLIAM E.
Langley Research Center, NASA
- MITCHELL, JOHN C.
Ling-Temco-Vought, Inc.
- MITCHELL, R. F.
Andrews Air Force Base
- MITTELMAN, P. S.
United Nuclear Corporation
- MODISETTE, J. L.
Manned Spacecraft Center, NASA
- MORE, KEITH A.
Bendix Systems Division
- MORRIS, ROBERT D.
Ames Research Center, NASA
- MOSHAFSKY, RAYMOND P.
The Boeing Company
- MUCKENTHALER, F. J.
Oak Ridge National Laboratory
- MUNSON, JOHN D.
U.S. Air Force Space Systems Division
- NEILER, J. H.
ORTEC
- NESS, NORMAN F.
Goddard Space Flight Center, NASA
- NEWSOM, BERNARD D.
General Dynamics/Astronautics
- NOLD, MAX M.
Air Force Weapons Laboratory
- O'FOGHLUDHA, FEARGHUS T.
Medical College of Virginia
- OPP, ALBERT G.
NASA Headquarters
- ORRICK, G. TIMOTHY
Bellcomm, Inc.
- PARKER, FRED
General Electric Company
- PARKER, VINCENT E.
Oak Ridge Institute of Nuclear Studies
- PEACKOCK, CHARLES L., JR.
Marshall Space Flight Center, NASA
- PEARSON, E. O.
NASA Headquarters
- PEARSON, MAYNARD D.
The Boeing Company
- PEELLE, R. W.
Oak Ridge National Laboratory
- PENNY, S. K.
Oak Ridge National Laboratory

- PEZDIRTZ, GEORGE F.
Langley Research Center, NASA
- PICCOT, ARTHUR R.
Atomics International
- PIEPER, ARTHUR G.
Naval Research Laboratory
- PIEPER, G. F.
Goddard Space Flight Center, NASA
- PORTER, FRANK
Fairport Institute, Inc.
- PRESCOTT, ARTHUR D.
Marshall Space Flight Center, NASA
- PRITCHARD, W. MAURICE
Old Dominion College
- PRUETT, ROBERT G.
Aerospace Corporation
- RAYMES, FREDERICK
North American Aviation Company
- RAZDOW, ADOLPH
Razdow Laboratories
- REETZ, ARTHUR, JR.
NASA Headquarters
- REID, NEAL E.
Goddard Space Flight Center, NASA
- RIDOLPHI, FRANK
Atomics International
- ROBBINS, DONALD E.
Manned Spacecraft Center, NASA
- ROBERTS, WILLIAM T.
Marshall Space Flight Center, NASA
- ROSEN, J. S.
General Electric Company
- ROSS, RICHARD C.
United Nuclear Corporation
- ROTH, RAYMOND E.
Oak Ridge Institute of Nuclear Studies
- RUSSAK, SIDNEY L.
Martin Company
- RUSSEL, IRVING J.
Air Force Weapons Laboratory
- SAEPOFF, G. M.
Dynasil Corporation of America
- SANTINA, R. E.
Douglas Aircraft Company
- SANTORO, R. T.
Oak Ridge National Laboratory
- SCHAEFER, HERMANN J.
Naval School of Aviation Medicine
- SCHAEFFER, N. M.
Radiation Research Associates, Inc.
- SCHNEIDER, MARION F.
Kirtland Air Force Base
- SCHULMAN, MURRAY
U.S. Atomic Energy Commission
- SCHWARZ, F. R.
Morrisville, Pennsylvania
- SCHWARZKOPF, ANSELMA
U.S. Department of Defense
- SCOTT, WALTER G., JR.
Air Force Weapons Laboratory
- SCOTT, W. WAYNE
Langley Research Center, NASA
- SELPH, WADE E.
Ling-Temco-Vought, Inc.
- SELTZER, STEPHEN M.
National Bureau of Standards
- SHAPIRO, CHARLES S.
IBM Space Guidance Center
- SHELDON, W. R.
The Boeing Company
- SHELTON, RUSSELL D.
Marshall Space Flight Center, NASA
- SHEN, S. P.
New York University
- SIMPSON, KENNETH M., JR.
Lockheed-Georgia Company
- SLATTERY, B. J., JR.
Marshall Space Flight Center, NASA
- SMITH, E. C.
Hughes Aircraft Company
- SMITH, HENRY J.
NASA Headquarters
- SONDHAUS, CHARLES
Lawrence Radiation Laboratory
- SOWLE, DAVID H.
General Dynamics/Astronautics
- SPEAKMAN, JERRY D.
Wright-Patterson Air Force Base
- SPENCER, D. F.
Jet Propulsion Laboratory
- SPICER, WILLIAM E.
Stanford Electronics Laboratories
- SPRITZER, ALBERT A.
Westinghouse Electric Company
- STAPLETON, GEORGE E.
Oak Ridge National Laboratory
- STEIN, JOSEPH A.
NASA Headquarters
- STEINER, HAROLD A.
Andrews Air Force Base
- STERN, HENRY E.
Marshall Space Flight Center, NASA
- STORTI, GEORGE M.
Langley Research Center, NASA
- STOVALL, ROBERT L.
Air Force Weapons Laboratory
- STRAYHORN, THOMAS R.
General Dynamics/Fort Worth
- SUMMERMAYS, R. M.
Ling-Temco-Vought, Inc.
- SWAN, A. G.
Brooks Air Force Base
- SWETNICK, MARTIN
NASA Headquarters
- TAKETA, S. TOM
Ames Research Center, NASA
- TOBIAS, CORNELIUS A.
University of California
- TODD, PAUL
Donner Laboratory

TROUT, OTTO F.
Langley Research Center, NASA

TRUBEY, DAVID K.
Oak Ridge National Laboratory

URBAN, EUGENE W.
Marshall Space Flight Center, NASA

VETTE, JAMES
Aerospace Corporation

VON BRAUN, WERNHER
Marshall Space Flight Center, NASA

WACHTER, JOHN W.
Oak Ridge National Laboratory

WAGNER, E. B.
Oak Ridge National Laboratory

WALKER, WILLIAM J., JR.
Air Force Weapons Laboratory

WALLACE, ROGER
Lawrence Radiation Laboratory

WARMAN, E. A.
Aerojet General Corporation

WARNEKE, CHARLES H.
McDonnell Aircraft Corporation

WATTERS, ROBERT L.
Atomics International

WEBSTER, JOHN B.
Armed Forces Radiobiology Research Institute

WEINER, HOWARD
Republic Aviation Corporation

WEISS, W. L.
ORTEC

WELLS, M. B.
Radiation Research Associates, Inc.

WHITON, JUSTIN C.
Marshall Space Flight Center, NASA

WILKIE, W. H.
Oak Ridge National Laboratory

WILLIAMSON, T. G.
University of Virginia

WILLIS, CHARLES A.
Atomic International

WITTRY, EDMUND R.
Manned Spacecraft Center, NASA

WOODSUM, H. C.
Westinghouse Astronuclear Laboratory

WRIGHT, H.
Oak Ridge National Laboratory

WRIGHT, JERRY J.
Marshall Space Flight Center, NASA

WYCKOFF, ROBERT C.
Jet Propulsion Laboratory

YOUNG, DURWARD D., JR.
Air Force Weapons Laboratory

YOUNG, GALE
Oak Ridge National Laboratory

YUSKEN, JOHN W.
Ames Research Center, NASA

ZERBY, C. D.
Union Carbide Research Institute

ZETTERBAUM, JULIUS M.
Rocketdyne

ZOBEL, WALTER
Oak Ridge National Laboratory